WOODHEAD PUBLISHING SERIES IN ELECTRONIC AND OPTICAL MATERIALS

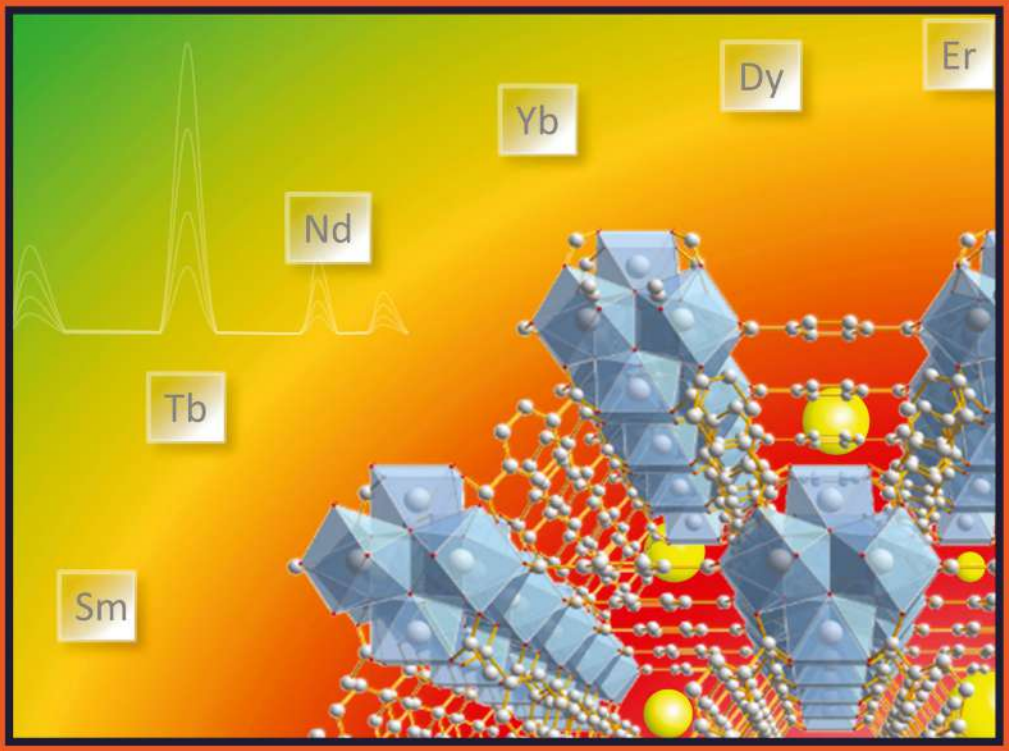

RARE EARTH METAL-ORGANIC FRAMEWORK HYBRID MATERIALS FOR LUMINESCENCE RESPONSIVE CHEMICAL SENSORS

ELSEVIER

BING YAN

Rare Earth Metal-Organic Framework Hybrid Materials for Luminescence Responsive Chemical Sensors

Woodhead Publishing Series in Electronic and Optical Materials

Rare Earth Metal-Organic Framework Hybrid Materials for Luminescence Responsive Chemical Sensors

Bing Yan
School of Chemical Science and Engineering, Tongji University, Shanghai, People's Republic of China

WP
WOODHEAD PUBLISHING
An imprint of Elsevier

Woodhead Publishing is an imprint of Elsevier
50 Hampshire Street, 5th Floor, Cambridge, MA 02139, United States
The Boulevard, Langford Lane, Kidlington, OX5 1GB, United Kingdom

Notices
Knowledge and best practice in this field are constantly changing. As new research and experience broaden our understanding, changes in research methods, professional practices, or medical treatment may become necessary.

Practitioners and researchers must always rely on their own experience and knowledge in evaluating and using any information, methods, compounds, or experiments described herein. In using such information or methods they should be mindful of their own safety and the safety of others, including parties for whom they have a professional responsibility.

To the fullest extent of the law, neither the Publisher nor the authors, contributors, or editors, assume any liability for any injury and/or damage to persons or property as a matter of products liability, negligence or otherwise, or from any use or operation of any methods, products, instructions, or ideas contained in the material herein.

ISBN: 978-0-323-91236-5 (print)
ISBN: 978-0-323-91430-7 (online)

Publisher: Matthew Deans
Acquisitions Editor: Kayla Dos Santos
Editorial Project Manager: Isabella C. Silva
Production Project Manager: Prasanna Kalyanaraman
Cover Designer: Greg Harris

Typeset by STRAIVE, India

Contents

Part III

Rare earth metal-organic frameworks hybrid materials as luminescence response chemical sensors for typical ionic analytes

Preface

Rare earths (REs), as strategic resources of the 21st century, have played a great role in both industry and the economy. Due to the unique electronic structure and physiochemical properties of rare earth ions, their compounds are important active candidates in functional materials. In particular, rare earth ions display excellent optical behaviors, such as sharp emission spectra for high color purity, broad emission bands covering the ultraviolet (UV)-visible-near-infrared (NIR) region, a wide range of lifetimes from microseconds to the second level, high luminescence quantum efficiencies, and so forth, which makes them a huge treasury of luminescent materials. In recent years, REs have attracted much attention for their wide variety of applications in the fields of lighting devices (television and computer displays, optical fibers, optical amplifiers, and lasers) and biomedical analysis (medical diagnosis and cell imaging).

Metal-organic frameworks (MOFs, also known as porous coordination polymers, or PCPs) are an emerging class of porous molecular materials constructed from metal-containing nodes (also known as secondary building units (SBUs)) and organic linkers (bridging ligands). Due to their structural and functional tunability, the area of MOFs has become one of the fastest growing fields in chemistry. MOFs embody versatile functional applications in gas storage, purification, or separation; heterogeneous catalysis or photocatalysis; optic, electronic, or magnetic materials or devices; as well as biomedicines or bioimages. Certainly, MOFs are employed as a platform for luminescent materials based on their intrinsic optical and photonic properties of metal ions and organic ligands, or guest species collaboratively assembled and/or encapsulated into their frameworks. The abundant luminescent responsive performance of MOFs provides their great potential in chemical sensing.

Rare earth metal-organic framework hybrid materials combine the virtues of both MOF materials and rare earth ions, which can create novel properties as well as functional and photofunctional applications. In particular, with rare earth ion functionalized MOF hybrid materials, luminescent RE^{3+} ions are incorporated into MOF hosts with little content, and the characteristic emission of RE^{3+} is obtained. This is identical to the traditional rare earth ion doped phosphors. Just like pure luminescent rare earth MOF materials, RE^{3+} can produce an "antenna effect" and cause a pronounced increase in the luminescence intensity through the intramolecular energy transfer process from linkers to RE^{3+}. In addition, the relatively limited content of hybrid materials often allows the

existence of luminescence of original linkers or MOFs themselves if the functionalized amount of RE^{3+} is controlled appropriately. This make it possible to exhibit multiple center luminescence for the same hybrid system and even realize luminescence color tuning or white luminescence integration. With regard to integrity, the pure rare earth MOF materials are considered in this book. Thus rare earth MOF hybrid materials encompass two main aspects: one is the pure rare earth MOFs, and the other is rare earth functionalized MOF hybrid materials.

This book consists of 6 parts, covered in 15 chapters. The first part (Chapters 1 and 2) is a general introduction to MOFs, rare earth MOFs, and rare earth functionalized MOF hybrid materials (Chapter 1); and rare earth luminescence, MOF luminescence, rare earth MOF luminescence, as well as luminescence response and chemical sensing (Chapter 2). The second part (Chapters 3, 4, and 5) gives an overview of the luminescent response mode and sensing mechanisms in rare earth metal-organic framework hybrid materials: single luminescent mode sensing (1D) (Chapter 3), dual luminescent mode (2D) for ratiometric sensing (Chapter 4), and luminescent responsive sensing mechanisms (Chapter 5). The third part (Chapters 6, 7, and 8) sheds light on rare earth metal-organic framework hybrid materials as luminescence response chemical sensors for typical ionic analytes, metal cations (I) (Chapter 6), (II) (Chapter 7), and anions (Chapter 8). The fourth part (Chapters 9, 10, and 11) focuses on rare earth metal-organic framework hybrid materials as luminescence response chemical sensors for molecules: general molecular chemicals (Chapter 9), special organic molecules (Chapter 10), and biomarkers (Chapter 11). The fifth part (Chapters 12, 13, and 14) involves rare earth metal-organic framework hybrid materials as luminescence response chemical sensors for other applications: including temperature and pH value (Chapter 12), logic gate operations (Chapter 13), and imaging applications (Chapter 14). The sixth part (Chapter 15) gives a summary and prospect for rare earth MOF hybrid materials as luminescence response chemical sensors.

Finally, I want to express my sincere gratitude to my PhD and master's students, whose research work makes up the main content of this book. I also wish to show my appreciation to my colleagues, especially to the scholars in the research fields of rare earth metal-organic frameworks, which is an important component of this book. Many colleague scholars have provided valuable reviews of the relevant topics for the instruction and outline of this book. I hope that this book will provide readers with insights into the recent developments of rare earth metal-organic framework hybrid materials for luminescent responsive chemical sensing.

Bing Yan

Part I

Introduction for rare earth metal-organic frameworks hybrid materials

Chapter 1

Metal-organic frameworks (MOFs), rare earth MOFs, and rare earth functionalized MOF hybrid materials

1.1 Metal-organic frameworks (MOFs)

Metal-organic frameworks (abbreviated as MOFs and also known as porous coordination polymers (PCPs)) are a class of porous polymeric molecular materials, consisting of metal ion nodes connected together by organic bridging ligands (linkers) (Scheme in Fig. 1.1), which are a new development in the interdisciplinary field of coordination chemistry and functional materials [1–3]. Due to their structural and functional tunability, MOFs have become one of the fastest growing research fields in inorganic chemistry. The essence of MOFs chemistry is that the frameworks are assembled by linking molecular units of well-defined shapes by chemical bonds into periodic frameworks. An important component of reticular chemistry is the deconstruction of such structures into their underlying nets to facilitate designed synthesis of materials with targeted porosity, pore size, and functionality. The organic ligands of MOFs give them flexibility and diversity in their chemical structures and functions. The synthesis of MOFs has attracted extensive attention due to the possibility of obtaining a large variety of interesting structures for a range of applications related to porous materials [4–8]. The exploration of MOFs mainly involves four categories: (1) synthesis of metal-containing nodes or coordination bonds and linker design for MOFs; (2) postsynthetic modification (PSM) of MOFs; (3) MOF hybrids or composites; and (4) potential applications of MOFs.

1.1.1 Synthesis of metal-containing nodes or coordination bonds and linker design for MOFs

In MOFs structures, a node represents a particular environment (tetrahedra, octahedra, etc.) connected to a fixed number of related points, which depends on the geometry (tetrahedral = 4, octahedral = 6, cubic = 8). Their structures can then be represented mathematically as either a discrete (zero-dimensional—0D)

Rare Earth Metal-Organic Framework Hybrid Materials for Luminescence Responsive Chemical Sensors
https://doi.org/10.1016/B978-0-323-91236-5.00003-7

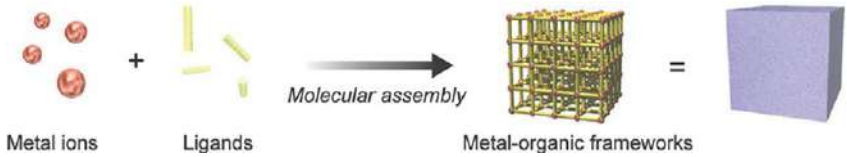

FIG. 1.1 Conceptual illustration of structuring of MOFs at microscopic/mesoscopic scales. The assembly of metal ions with organic ligands constructs molecular framework structures. *(Reproduced with permission from S. Furukawa, J. Reboul, S. Diring, K. Sumida, S. Kitagawa, Structuring of metal-organic frameworks at the mesoscopic/macroscopic scale. Chem. Soc. Rev. 43 (2014) 5700–5734. Copyright 2014 Royal Society of Chemistry.)*

or an infinite (one-dimensional—1D), two-dimensional—2D), and three-dimensional—3D)) periodic arrangement as an extended representation of the nodes. Thus the topology of a net depends on the number of nodes in a particular structure. A simplified description of MOFs structure will be considered as a metal center or metal cluster of ions connected by an organic linker. To derive the vertex symbol and the correct topology for such structures, it is important to identify the nodes according to coordination chemistry principles [9].

To understand MOFs structures, the node and the net concept are used to describe the vertex symbols in some 2D and 3D systems. **(1) 3D structures**. **(a) Uninodal structures** are based on only one type of node, which have 3 (trigonal), 4 (square planar, tetrahedral), 5 (trigonal bipyramidal), 6 (octahedral), 8 (cubic), and other higher (10 or 12) connected nodes. **(b) Binodal structures** have two geometrically different nodes in a MOFs constitutes, formed using trigonal-tetrahedral; tetrahedral-square planar; tetrahedral-octahedral and tetrahedral-cubic nodes. **(2) 2D structures**. MOFs with 2D layer structures can be described using nodal connectivity. **(a) Uninodal structures** contain 3 connected nodes, 4 connected nodes, 5 connected nodes, and 6 connected nodes, respectively. **(b) Binodal structures** in the context of the topology of MOFs based on common geometrical nodes are rare, although some topologies can be obtained based on trigonal-octahedral nodes. **(3) 3D MOFs based on 2D layers**. The 3D MOFs with 2D network topologies are pillared by rigid linkers, which can have either a simple uninodal structure or a binodal structure within the layers using the organic ligands as the linker. Either the same ligand or a completely different organic linker can be used to arrive at the 3D structure. **(4) Zeolitic imidazolate frameworks (ZIFs)**. Imidazole as the simple molecule has an ideal position between the nitrogen atoms in the structures, and behaves as a linker between the metal centers, addressing the concerns of charge neutrality. The most important topology based on the tetrahedral node is the diamond topology. These ZIF compounds have been extensively prepared for mimicking zeolite topologies [9–16].

On the other hand, the term MOFs originated from its secondary building units (SBUs) as clusters built entirely with covalent bonds [17–22].

The synthesis of SBUs can be used to direct the assembly of ordered frameworks with rigid organic linkers, which makes it highly possible to predict the chemistry of the yielded crystalline materials [17–30]. The orientation of organic linkers will result in the assembly of MOFs with predetermined structural topologies [23–30]. Generally, both SBUs (as connectors) and organic ligands (as linkers) combine to determine the final framework topology. **(1) Ditopic carboxylate linkers**. These linkers possess both ready accessibility and easily perceivable structures in combination with different SBUs: 4-connected paddlewheel clusters, 6-connected octahedral clusters, 6-connected trigonal-prismatic clusters, 12-connected clusters, and infinite chain clusters, respectively. **(2) Tritopic carboxylate linkers**. These linkers are related to different clusters: 4-connected paddlewheel clusters, 6-connected octahedral clusters, 6-connected trigonal-prismatic clusters, and multiple SBUs. **(3) Tetratopic carboxylate linkers**. These linkers appear to be very intriguing building units in MOFs constructions, especially those with tetrahedral geometry. Tetrahedral carboxylate linkers are related to different clusters: 8-connected cubical clusters, 4-connected square planar clusters, 8-connected hexagonal bipyramidal clusters, and nonregular tetrahedral carboxylate linkers. **(4) Hexatopic carboxylate linkers**. These linkers are related to 1,3-atedbenzenedicarboxylate units, 4,4′-azanediyldibenzoate units and 1,1′:3′,1″-terphenyl-4,4″-dicarboxylate units. **(5) Octatopic carboxylate linkers**. MOFs with these linkers are still rare, possibly due to the synthetic challenges in the linkers themselves, whose frameworks are based on linkers with long arms that tend to form interpenetrated structures. **(6) Mixed linkers**. They contain four types: ditopic-ditopic linear linkers, tritopic carboxylate-ditopic carboxylate linkers, carboxylate-pyridine linkers, and linkers coordinatively identical but with distinct shapes. **(7) Desymmetrized linkers**. **(8) Metallo-linkers**. These mainly involve four types with different donors: O and S donors, N and P donors, C donors, and mixed donor groups. **(9) N-heterocyclic linkers**. Organic linkers containing N donors, such as pyridine and azole derivatives, have achieved stable MOFs via N-metal coordination, including ditopic N-heterocyclic linkers and polytopic N-heterocyclic linkers [23].

1.1.2 Postsynthetic modification (PSM) of MOFs

Postsynthetic modifications (PSMs) are particularly attractive for use with MOFs materials for a variety of reasons. **(I)** The solvothermal reaction conditions to prepare most MOFs greatly limit the types of functional groups that can be functionalized by PSM. **(II)** The organic ligands in MOFs open the possibility of employing a wide range of organic transformations. **(III)** MOFs' porous structures allow reagents to access the interior of the solids for their functionalization [31–44]. Thus various functions can be imparted to MOFs by incorporating different parts of the MOF structure, including metal ions/clusters, organic linkers, and empty spaces inside the cavities (Fig. 1.2, left). A variety

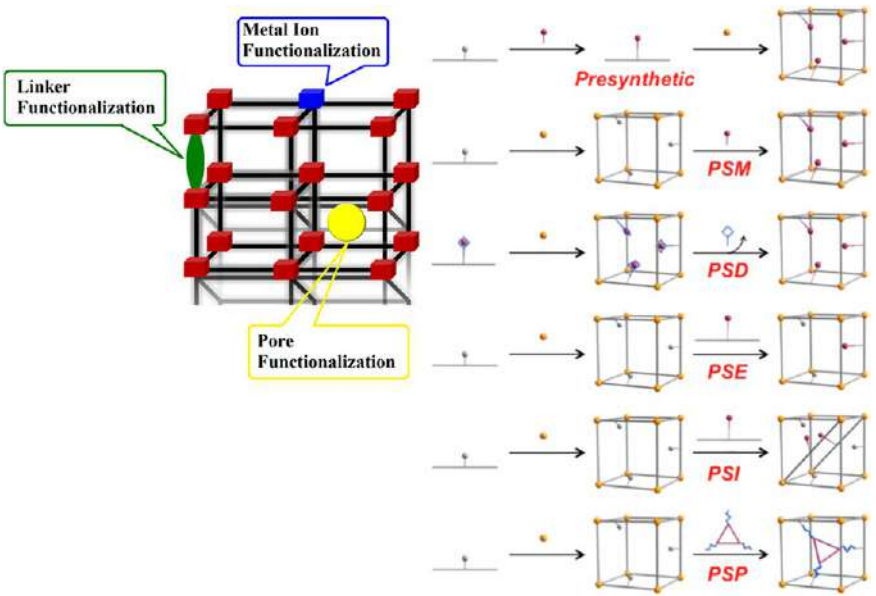

FIG. 1.2 Schematic depiction of functionalization *(left)* and PSM strategies *(right)* of MOFs: postsynthetic modification (PSM), postsynthetic deprotection (PSD), postsynthetic exchange (PSE), postsynthetic insertion (PSI), and postsynthetic polymerization (PSP). SBUs are represented as gold spheres, and ligand struts are represented by *gray* rods. *(Reproduced with permission from S. A. A. Razavi, A. Morsali, Linker functionalized metal-organic frameworks. Coord. Chem. Rev. 399 (2019) 213023 and S. M. Cohen, The postsynthetic renaissance in porous solids. J. Am. Chem. Soc. 139 (2017) 2855−2863. Copyright 2019 Elsevier and 2014 American Chemical Society.)*

of organic functional groups are functionalized to tune and optimize the host-guest chemistry of MOFs, which is a practical and rational strategy to improve MOF efficiency in different applications. Moreover, functionalization also has crucial influences on the structural properties of MOFs, such as crystallinity, porosity, flexibility, stability, and topology through induced structural changes and different types of secondary interactions. Subsequently, it is possible to synthesize functional MOFs and their hybrid materials using PSM [42].

(1) **Requirements for PSM**. MOFs require the following parameters: **(a)** Being sufficiently porous to allow access of all required reagents to the interior of the lattice. **(b)** Possessing an available functional group to undergo a chemical transformation. **(c)** Being stable to the reaction conditions. **(d)** Being stable to any byproducts produced by the reaction conditions. To date, the choices of both MOFs and reaction govern the scope of transformations that can be realized by PSM.

(2) **Types of PSM**. Broadly speaking, any change of the composition or structure of MOFs may be considered a form of PSM, such as the desolvation or activation of MOFs, the exchange of guest species from MOFs, the inclusion or encapsulation phenomena of being performed in a PSM manner, etc. In a narrow sense, however, it is important to define the different types of PSM to distinguish these chemical reactions from the previously mentioned routine handling and guest inclusion phenomena of MOFs. PSM of MOFs can be divided into three areas: (a) covalent PSM, (b) dative PSM (coordinate covalent PSM), and (c) postsynthetic deprotection (PSD) (Fig. 1.2, right). The type of chemical bond that is formed or broken during the PSM approach distinguishes each of these methods. It is important to note that these different PSM methods are not mutually exclusive, and perhaps utilize a combination of strategies to obtain materials of high complexity and functionality. In addition to achieving the desired chemical transformation, it is important that the MOFs cannot be destroyed under the reaction conditions. Indeed, PSM methods are intended to produce novel hybrid materials that retain the characteristic features of MOFs [36].

(1) Covalent PSM. This is defined as the use of a reagent to modify a component of the MOFs in a heterogeneous, postsynthetic manner to form a new covalent bond, whose target is generally the organic linker of the MOFs. Currently, covalent PSM is the most extensively investigated of the different PSM methods, and is proven to be a powerful and versatile method for introducing a broad range of chemical groups into MOFs. **(2) Dative PSM**. This type is defined as the use of a reagent that forms a dative bond with a component of the MOFs in a heterogeneous, postsynthetic manner. Not only can a ligand be added to the framework to coordinate to the SBU of the MOFs, but also a metal source can be added to the MOFs to bind to the organic linker of the MOFs, occurring through the formation of dative bonds. **(3) PSD**. This reaction is performed on the MOFs in a postsynthetic manner resulting in the cleavage of a chemical bond within an intact

framework. In principle, any kind of chemical bond can be broken during a PSD reaction to reveal a chemical functionality and produce materials with different properties. Within some highly stable MOFs, both the elimination and addition of multitopic linkers or metal ions are possible without destruction of the framework. **(4) Postsynthetic metal exchange (PSME)**. Cation doping is also widely employed in nanocrystals to tune their properties. **(5) Postsynthetic ligand exchange (PSLE)**. This represents the exchange of the key extending ligand of a framework by another similar ligand of different length or functional group, with the retention of the MOFs topology. **(6) Postsynthetic elimination and installation (PSE&I)**. Some linkers constituting the framework can be eliminated with coordination changes in the metal cluster but preservation of the infinite framework connection. If the coordination site of the adjacent metal cluster matches well with an additional linker, PSI may succeed in creating a new MOFs with higher connection numbers. **(7) Tandem PSM**. This type is used in producing MOFs with multiple functionalities otherwise difficult or infeasible to acquire by direct synthetic methods. **(i) Engineering porosity and pores by tandem PSM**. Both increased and decreased porosity can be obtained depending on the size and spatial configuration of the modified groups, whose change in porosity is moderate and limited by the constant topology of the framework. **(ii) Improving structural stability by tandem PSM**. The direct introduction of target metal ions may be subjected to low exchange rate, uncompleted conversion, decomposition of the MOFs, and others. Based on the exchanging mechanism of different metal ions, tandem PSME is useful for improving structural stability. **(iii) Modifying surface and interior by tandem PSM**. Based on the reactivity and spatial effect within the confined channels, the traditional design of the reaction pathways provides a chance to engineer either the surface or the interior of MOFs (Fig. 1.2, right) [31–44].

1.1.3 MOFs hybrids or composites

In order to satisfy the practical applications of MOFs, it is desirable to further enhance their properties and create new functionalities. MOFs composites/hybrids are materials composed of one MOFs and one or more distinct constituent materials, including other MOFs, with properties noticeably different from those of the individual components. In composite or hybrid materials, the advantages of both MOFs (structural adaptivity and flexibility, high porosity with ordered crystalline pores) and various kinds of functions (optical, electrical, magnetic, and catalytic properties) can be combined effectively, accessing new physical and chemical properties along with enhanced performance that is not attainable with the individual components. Consequently, the remarkable features of composites or hybrids resulting from the synergistic combination of both MOFs and other active components make them suitable for a wide range of applications. To date, MOFs hybrids/composites have been made with versatile active species, including metal nanoparticles/nanorods (NPs/NRs), oxides, quantum dots (QDs), polyoxometalates (POMs), polymers, graphene,

FIG. 1.3 The scheme for the composites of MOFs and functional materials. *(Reproduced with permission from Q. Zhu, Q. Xu, Metal-organic framework composites. Chem. Soc. Rev. 44 (2014) 5468–5512. Copyright 2014 Royal Society of Chemistry.)*

carbon nanotubes (CNTs), dyes, biomolecules, and so on, resulting in performance unattainable by the individual constituents (Fig. 1.3). Moreover, these hybrids or composites offer the great advantage of flexible and optimum design, which is desirable to harness the useful properties through the incorporation of various kinds of functional materials into MOFs [45–65].

(1) **MOFs-metal or metal oxide NP composites**. Porous MOFs are thermally robust and have permanent nanoscale cavities or open channels that provide powerful confinement effects, which can be utilized as supports for metal NPs with controlled sizes inside the pores, thereby circumventing the common issue of NP aggregation and benefiting their utilization in applications. In addition, some attempts have been undertaken to integrate metal oxides (especially those with magnetic or semiconducting properties) and MOFs into core-shell nanostructures [45–53].

(2) **MOFs-silica composites**. There are currently two main types of MOFs-silica composites: **(a)** incorporating dispersed silica NPs within the pores/channels of MOFs or growth of a MOFs shell on a preformed silica sphere in MOFs precursor solutions (SiO_2@MOFs); **(b)** using a silica shell as a surface coating or the mesoporous properties and processability of silica supports to promote the growth of microporous MOFs particles throughout the porous silica supports (MOFs@SiO_2) [45,54].

(3) **MOFs-organic polymer composites**. Confined polymers at nanometer scales exhibit fascinating and unexpected properties different from those in the bulk state. MOFs-organic polymer composites formed from various combinations of MOFs and organic polymers can constitute a class of composite materials with combined properties [45,55].

(4) **MOFs-QDs composites**. The versatility of functional MOFs can be extended by introducing highly luminescent semiconductor QDs within the frameworks of MOFs. In QD@MOFs composites, QDs can be stabilized against photochemical degradation through the deposition of a nanometer MOFs shell, while retaining their valuable optical properties [45].

(5) **MOFs-POM composites**. The dispersion of POMs within MOFs prevents the POMs from conglomerating and deactivating. In such POM-based MOFs, the organic ligands substitute for the oxo groups of POMs to covalently link the metallic centers. What's more, POMs can be encapsulated in the pores of MOFs through host-guest interactions to form POM@MOFs composites [45].

(6) **MOFs-carbon composites**. The exceptionally mechanical, electrical, and thermal properties of carbon materials (graphene and CNTs) commend them as valuable nanostructured fillers in MOF composites. Numerous MOFs-nanocarbon composites have been made with activated carbons, carbon monoliths, graphene oxide (GO), and CNTs, and have been intensively explored for diverse applications [45].

(7) **MOFs thin films on substrates**. The deposition of patterned thin films of MOFs on a substrate has paved the way for the nanotechnological applications of MOFs-based devices. Generally, two fabrication methods have been distinguished for the direct growth/deposition of MOFs thin films: **(a)** The substrate is added to a MOFs synthesis solution under ambient or solvothermal conditions, growing on the surface of the substrate and sometimes in solution at the same time. This growth leads to the formation of polycrystalline films where crystals are attached to the substrate surface in an intergrown and continuous fashion. **(b)** The layer-by-layer (LBL) method was developed for the facile preparation of MOFs thin films on the substrates and referred to as liquid phase epitaxy. This technique relies on the sequential deposition of monolayers of metal salts and organic linkers on a functionalized substrate. The LBL method permits the growth of smooth and homogeneous MOFs ultrathin films with diameters in the nanometer range, which achieve good control over the thickness, crystallographic orientation, and interpenetration of the MOFs multilayers [45,56–59].

(8) **MOFs@MOFs core-shell heterostructures**. The construction of multifunctional core-shell heterostructures involves two strategies. **(a)** Heteroepitaxial growth of a shell MOFs crystal on the external surface of another seed MOFs crystal could generate a composite crystal, in which the two coordination components are segregated into different regions of the crystal. This approach is based on a close crystal lattice match between the underlying MOFs substrate and the deposited MOFs. **(b)** PSM strategies include the selective reaction of the reactive residue of an organic linker and the controlled replacement of the framework metal ions or ligands, whose modification is selectively constrained to either the external surface or the internal core of the MOFs crystals [45].

(9) **MOFs-enzyme composites**. The tunable but uniform pore sizes and functionalizable pore walls of porous MOFs may make them appealing to accommodate enzymes for catalytic applications. Nevertheless, the micropore size of most MOFs precludes the entry of large-sized enzymes

and can result in only external surface attachment with low enzyme loading via adsorption and/or covalent bonding reaction [60–65].

(10) **MOFs-other molecular species composites**. Molecular materials such as organic dyes, organometallic compounds, metalloporphyrins, biomolecules, and other functional molecules can also be composed with MOFs for various applications. The use of MOFs as molecular encapsulators takes advantage of their powerful confinement effect to protect molecules from aggregation, heterogeneous distribution, and leaching. Impregnation procedures are mostly used to encapsulate these molecular materials. In addition, the self-assembly of MOFs in the presence of molecular moieties in the MOFs precursor solutions can lead to irreversible in-situ encapsulation [45].

1.1.4 Potential applications of MOFs

MOFs have unique properties as well as an extraordinary degree of variability for both the organic (ligands) and inorganic (metal ions or clusters) components of their structures, making them of interest for potential applications in practical fields (Fig. 1.4). With the input of industrial partners, some of these promising MOFs for important applications will soon be implemented in our daily lives [66–71].

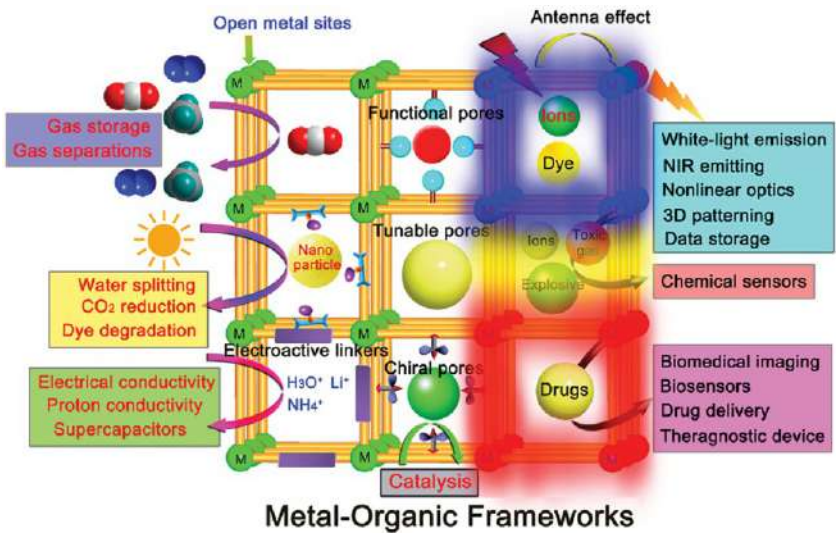

FIG. 1.4 Graphic illustration of pore and function engineering to develop multifunctional MOF materials. *(Reproduced with permission from B. Li, H. Wen, Y. Cui, W. Zhou, G. Qian, B. Chen, Emerging multifunctional metal-organic framework materials. Adv. Mater. 28 (2016) 8819–8860. Copyright 2016 Wiley.)*

1.1.4.1 MOFs for applications in adsorption, storage, and separation

First, in clean energy, MOFs are most significantly used as storage media for gases such as hydrogen and methane, and as high-capacity adsorbents to meet various separation needs [72–76]. MOFs have shown great application potential in various separations due to their tailored structures and functionalized pore surfaces, from CO_2 capture to natural gas purification, from air separation to harmful gas removal, from desulfurization to large-molecule inclusion, and from structural isomer separation to enantio-separations, in both gas-phase and liquid-phase systems. The precise tuning of MOFs material characteristics is expected to produce considerable improvements in sorbent performance, leading to reduced energy requirements for the capture process compared with current technologies. Meanwhile, the PSM availability of in-pore and outer-surface of MOFs is attractive for diverse analytical chemistry applications. MOFs have been either directly used or engineered to show excellent potential for use in air purification of toxic gases. Recently, MOFs have represented a new foreground for capturing various types of hazardous metal ion pollutants, including toxic and nuclear waste-related metal ions, which have harmful effects on human health and the environment [77–84].

MOFs are geometrically and crystallographically well-defined framework structures for the strength of coordination bonds, which are robust enough to allow the removal of the included guest species, resulting in permanent porosity. MOFs are ideal adsorbents for gas storage and separation due to their large surface areas, adjustable pore sizes, and controllable surface properties (Fig. 1.5). Currently, most of the research is focused on selective gas adsorption studies based on adsorption/desorption isotherm measurements of single gas components, which provide the predominant information for adsorbent screening. Practically, an adsorption-based process can afford molecular separation via diverse microscopic mechanisms: **(i)** thermodynamics (enthalpic)-driven, where the MOFs adsorbent expresses a relatively high affinity for a given molecule as a result of enhanced adsorbate/MOFs interactions, **(ii)** kinetics-driven, where the MOFs pore opening and its circumference constituents inflict a significant difference in the diffusivity of the adsorbate molecules, **(iii)** the combination thereof, **(iv)** conformational (entropic)-driven, where the MOFs pore size/shape permits a more efficient packing of the given molecule in a confined pore system, and **(v)** molecular sieving, where the MOFs pore aperture size/shape allows a full-size exclusion of a selected molecule. The key parameter in developing an efficient MOFs separation agent is the strong interplay between the size/shape of the targeted molecules and the structural features of the adsorbent. It needs to be pointed out that the **(i)** separation might require a dual effect conferred by a high degree of pore confinement and the presence of specific adsorption sites. Furtherly, it is more practical to consider a porous material displaying only one type of pore aperture to separate a specific molecule [76–85].

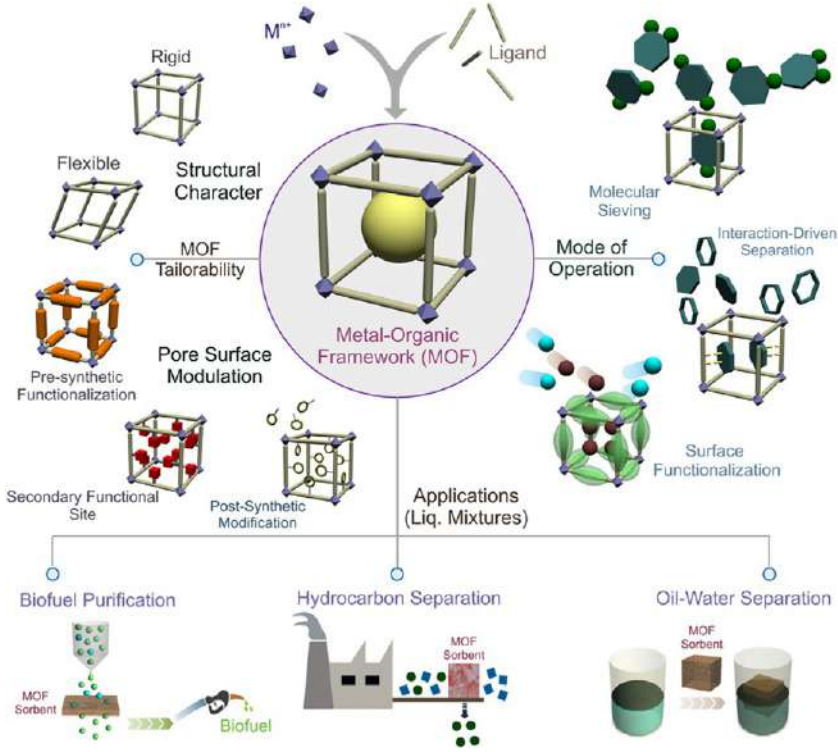

FIG. 1.5 Schematic illustration of the various possibilities of tuning the characteristics of MOFs, their modes of operation for separation, and representative applications where these compounds can be potentially applied. *(Reproduced with permission from S. Mukherjee, A. V. Desai, S. K. Ghosh, Potential of metal-organic frameworks for adsorptive separation of industrially and environmentally relevant liquid mixtures. Coord. Chem. Rev. 367 (2018) 82–126. Copyright 2018 Elsevier.)*

For selective adsorption and separation in MOFs, even membrane separation, the selection of supporting materials is the key. The large variety of MOFs available is expected to be capable of increasing selectivity, improving energy efficiency, and reducing the costs of separation processes. In addition, the ability to rationally fine-tune the structures and pore properties of MOFs at the molecular level may create unique interactions with guest molecules and thus achieve unusual functional properties for adsorptions, thereby leading to solutions of some specific scientific and engineering challenges in separations. For instance, enantio-separation can potentially be achieved by homochiral MOFs adsorbents and membranes. Homochiral MOFs not only can be easily synthesized from predesigned homochiral ligands or framework constructions, but also several PSMs of existing structures can induce framework chirality over a broad range. For adsorptive separations, most are focused on selective adsorptions, but the practical separations of a mixture involve more variables than evaluations from single-component measurements [85–89].

1.1.4.2 MOFs for applications in catalysis

The application of MOFs materials in catalysis is another hot topic [90–111]. MOFs-based catalysis involves opportunistic catalysis with metal nodes, designed catalysis with framework nodes, catalysis by homogeneous catalysts incorporated as framework struts, catalysis by MOFs-encapsulated molecular species, catalysis by metal-free organic struts or cavity modifiers, and catalysis by MOFs-encapsulated clusters. Several features make MOFs excellent candidates as heterogeneous catalysts: **(i)** an unprecedented structural diversity, **(ii)** the intrinsic hybrid organic-inorganic nature, **(iii)** the presence of uncoordinated metal sites and readily accessible organic struts, **(iv)** the potential for rational design, and **(v)** a well-defined porosity. Several structural features of MOFs can be harvested for catalytic applications: **(a)** using the metal nodes of the material when coordination vacancies are available; **(b)** using the linker as an organocatalytic site; **(c)** using the optoelectronic properties of the hybrids and ligand to metal charge transfer to trigger photocatalytic processes; **(d)** as hosts to encapsulate additional catalytic sites such as NPs, enzymes, or other moieties; **(e)** via PSM of the MOFs scaffold; **(f)** as precursors to form NPs or single site catalysts via controlled decomposition; and **(g)** combining several of the preceding features (Fig. 1.6) [101].

(1) **MOFs with intrinsic catalytic activity**. MOFs have been regarded as ideal platforms for the heterogenization of homogeneous catalysts, which can be understood as molecules arranged in a crystalline lattice and can be extended through such a crystalline lattice by crystal engineering to produce solids with intrinsic catalytic activity. Three different approaches are proposed to achieve intrinsic catalytic activity: **(i)** through the introduction of open metal sites (coordinatively unsaturated sites); **(ii)** through the creation of defects, and **(iii)** using the organic linker as a catalyst, through PSM incorporation of such sites [90–100].

(2) **MOFs as supports for metal nanoparticle (MNPs)**. MNPs are among the most important catalytic sites, whose catalytic performance in terms of activity is highly related to their size (the so-called structure sensitive reactions) for the application of MOFs. MOFs' catalytic centers are either metal ions such as Lewis acids and/or organic linkers, both of which can be tuned or modified. For example, it is relatively feasible to realize different dangling functional groups on the linkers that should improve metal-support interactions and call for the use of MOFs as supports for MNPs, which have undoubtedly proven their importance in enhancing catalytic processes. MOFs play different roles in these composites: **(a)** stabilizing MNPs within pores and controlling the uniform small particle size and distribution; **(b)** assisting in the selectivity of the reaction by sieving small substrate molecules and/or blocking oversized molecules from catalytic interactions; **(c)** altering the electronic properties of MNPs by controlling their electronic density and the electron charge transfer between the MOFs and an

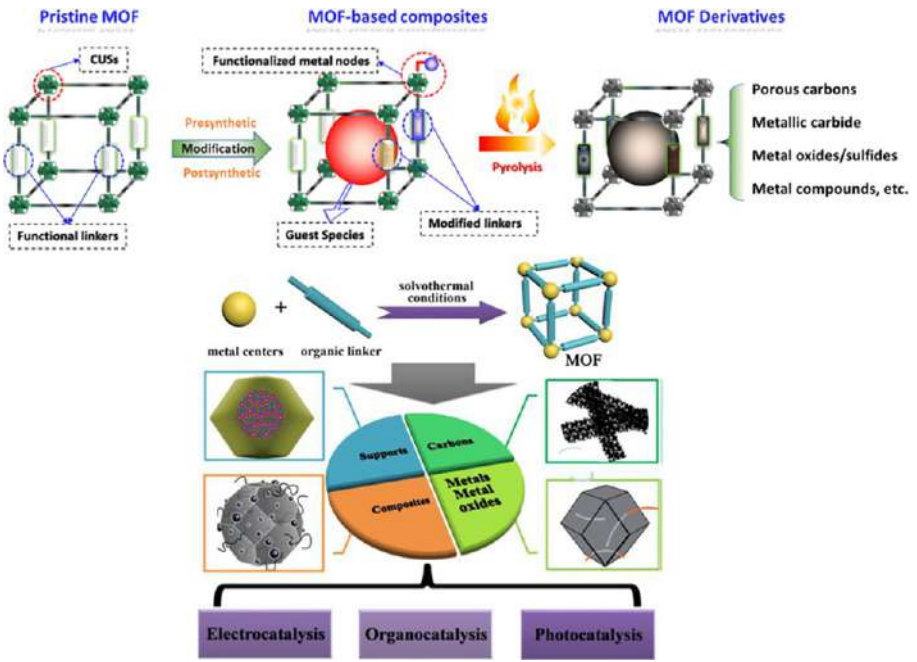

FIG. 1.6 Schematic representation of the catalytic site locations on/in different types of MOF-based catalysts *(top)*; and MOFs as supports or their derived materials for heterogeneous catalysis *(bottom)*. *(Reproduced with permission from W. Cui, G. Zhang, T. Hu, X. Bu, Metal-organic framework-based heterogeneous catalysts for the conversion of C1 chemistry: CO, CO2 and CH4. Coord. Chem. Rev. 387 (2019) 79–120 and S. Zhao, X. Song, S. Song, H. Zhang, Highly efficient heterogeneous catalytic materials derived from metalorganic framework supports/precursors. Coord. Chem. Rev. 337 (2017) 80–96. Copyright 2017 and 2019 Elsevier.)*

MNP; and **(d)** catalyzing one-pot tandem reactions in which both the MOFs and MNPs act as separate active sites in their respective reactions [90–100].

(3) **MOFs-mediated materials in heterogeneous catalyst**. MOFs can be converted to considerably more stable materials by simple posttreatments commonly involving pyrolysis. These MOFs-mediated structures retain most of the unique properties of the parent MOFs, such as the high porosity, tunable composition, and high metal loading, which is beneficial for heterogeneous catalytic applications, and they frequently outperform their conventional catalyst counterparts [90–100].

(4) **MOFs in photocatalysis**. MOFs emerge as a new type of prospective photocatalytic material, whose modular structure enables them to be facilely immobilized with photoactive sites for photocatalysis. Their metal nodes can be regarded as isolated semiconductor QDs, which can be excited directly upon light irradiation or activated by the organic linkers acting as a light absorption antenna. The availability of a large diversity of organic linkers and the rich coordination chemistry of metal cations enables the light absorption properties of the MOFs to be adjusted for efficient utilization of solar light via a judicious selection of these building units. In addition, photoactive ligands or dyes can be used directly as building blocks to fabricate the MOFs materials or these chromophores can be grafted on the organic ligands as a photoactive part via a PSM method. With all these advantages, MOFs have been applied in photocatalytic hydrogen evolution, CO_2 reduction, and pollutant degradation, as well as promotion of photocatalytic organic transformations [101–105].

(5) **Electrocatalysis on MOFs**. The potential use of MOFs as electrocatalysts is receiving increasing attention as these materials circumvent the limitations of homogeneous catalysts. Immobilizing catalysts in the solid state with various metal nodes can impact the electrochemical driving force necessary for electron transfer between the electrode and the catalyst, as well as improve the lifetime of the catalytic site and its selectivity. Using MOFs as an electrocatalyst will require an active surface area, a known propagation of charge, an optimized pore size distribution and good crystallinity. Three main electrocatalytic conversion processes are involved, which are CO_2 reduction, the hydrogen evolution reaction (HER), and the oxygen evolution reaction (OER), as well as a selection of other relevant catalytic processes [106–109].

(6) **Biomimetic catalysis**. Immobilization of biomimetic molecular catalysts in MOFs has generated many unique and highly active biomimetic MOFs hybrid catalysts, which exhibit high efficiency, selectivity, and sustainability. Biomimetic MOFs present several advantages: **(a)** uniform dispersion of active sites; **(b)** tunable hydrophobic and hydrophilic pore nature; **(c)** collaborative microenvironment; and **(d)** confined catalytic reaction pockets and transmission channels [112,113].

1.1.4.3 .MOFs for applications in magnetic and nonlinear optical (NLO) materials

The special electric, optic, and magnetic properties of MOFs provide their great potential for use in functional devices [112–122]. The diversity of magnetic exchange interactions among MOFs ranges from dimers to oligomers and their applications in infinite chains, layers, and networks, having a variety of topologies. The different forms of short-range magnetic ordering cause not only single-molecule magnets (SMMs) and single-chain magnets (SCMs), but also the long-range ordering of 2D and 3D networks is based on their ion-conducting behavior [112,113,116–119]. On the other hand, major attention is paid to the frequency doubling (second-harmonic generation, SHG) and tripling (third-harmonic generation, THG) effect for nonlinear optical (NLO) materials. Future efforts should be devoted to their potential technological applications in electrooptic devices [120–122].

MOFs based on magnetic frameworks

Depending on the origin of the magnetic phenomena, four types of MOFs can be differentiated: **(a)** magnetic MOFs with magnetic cooperativity resulting from magnetic exchange via the ligands; **(b)** spin-crossover MOFs with nodes of suitable coordination environments for this phenomenon to exist; **(c)** MOFs with magnetic relaxation with the nodes of clusters possessing an anisotropic spin ground state and showing single molecule magnet behavior; and **(d)** MOFs with a magnetocaloric effect with nodes of clusters possessing an isotropic spin ground state. **(i) Magnetic MOFs**. Magnetic exchange interactions require short distances between the metal centers, which are most commonly the spin carriers. The porosity is typically favored with the use of long linkers, which are often too long for magnetic ordering to exist at temperatures much above absolute zero. **(a) Use of short linkers**. Among the denser structures with shorter linkers, long-range magnetic order can emerge, although sorption of gases in this situation is rather atypical. **(b) Metallo-ligand approach**. A metal complex with vacant additional coordination sites is first prepared and isolated, being used in a second step as a building block towards additional metal ions. Through a suitable choice of the metallo-ligand, magnetic communication between the metal nodes can be achieved. **(c) Radical-as-ligand approach**. An alternative methodology for facilitating exchange coupling between metal centers of MOFs is the incorporation of additional spin carriers into the organic linkers such as radical ligands [112,113,116,117]. **(ii) Spin-crossover MOFs**. Cooperative effects are still necessary to make this phenomenon useful in order to have an abrupt crossover, which arises from the elastic forces present in the solid. In these systems, such a cooperativity is favored by the polymeric nature of the framework, keeping the spin-crossover centers connected even if they are not very close. The cooperativity enables this type of MOFs to show high sensitivity to the subtle structural changes occurring in metal coordination

environments upon inclusion of guest species within the porous framework. Consequently, the spin-crossover properties are tuned via PSMs of MOFs. **(a) Physisorption of gases**. **(b) Chemisorption/PSM**. **(c) MOFs with SMMs at the inorganic nodes**. SMMs are usually formed by polynuclear magnetic clusters with a large spin value and high magnetic anisotropy. One important requirement for maximizing the quantum coherence is to minimize the magnetic dipolar interactions between qubits, which can be achieved by separating these magnetic units in space. MOFs can be ideal platforms to reach this goal since they provide spatial separation at will. **(d) MOFs for magnetic refrigeration**. A magnetocaloric effect (MCE) of high interest for cooling applications is that of magnetic refrigeration. The use of magnetic MOFs for magnetic refrigerators is very appealing since they can be designed to consist of isolated paramagnetic centers that favor a large MCE, combined with higher thermal and solvent stabilities than their discrete molecular cluster analogs [112,113,118,119]. **(iii) Hybrid MOFs incorporating functional molecules in the channels**. Using this hybrid approach, two-network solids can be prepared through the self-assembly of different molecular fragments used as starting building blocks, or using a PSM method in which a molecular guest is inserted into a preformed extended network as the host lattice. **(a) SCO@MOFs**. **(b) SMM@MOFs**. **(c) Electroactive molecules@MOFs**. POMs form a class of molecular anions that have been incorporated into MOFs, which are robust species with unique electronic properties due to their ability to act as electron reservoirs or to accommodate magnetic centers [112].

MOFs for NLO

(i) Producing MOFs for NLO. Noncentrosymmetric organization is a prerequisite for the generation of NLO properties of bulk materials. In conventional methods of producing MOFs, the creation of such noncentrosymmetric structures is challenging. Not only can the coordination of the organic ligand to a metal ion yield an increase in charge transfer transitions, but it also allows organic chromophores to assemble in highly ordered geometries like octahedra and tetrahedra. This interaction produces charge transfer in several directions. In addition, this is a type of structure that is relatively easy to obtain by selecting the right combination of metal ions and organic ligands. **(ii) Ligands**. **(a) Multifunctional ligands**. One of the most successful methods for solving the problem of obtaining a noncentrosymmetric MOFs structure is using a compound as a ligand that is capable of chelating a metal ion with several functional groups in different positions. This in turn leads to different degrees of ligand deprotonation, ultimately resulting in different coordination modes upon interaction with two different metal ions. **(b) Chiral ligands**. All chiral MOFs are active for SHG, and there are some basic synthetic approaches to produce a chiral MOFs. But the presence of a chiral structure does not necessarily guarantee a high response of SHG. **(iii) Diamondoid structures**. The most likely candidates for producing crystals with NLO properties are metal ions, which have a

coordination number of 4 or 8 and are connected via a bifunctional ligand. Such components tend to form the so-called diamond structure, whose crystals inherently crystallize in a centrosymmetric space group so that the inversion center is in the middle of the C—C bond between two adjacent nodes. **(iv) New applications of MOFs in NLO**. **(a) Third-order NLO**. Third-order NLOs for MOFs have promise for use in all-optical switching in waveguides. **(b) Control of excitons**. The crystalline and organic nature of MOFs allows the existence of Coulomb-bound electron-hole pairs (excitons). The potential offered by manipulating excitons when exposed to light and electric field is the basis for modern exciton transistors and polarization lasers [120–122].

1.1.4.4 MOFs for applications in electrochemistry

MOFs and their composites show great potential in the electrochemical field for their unique properties. Creating an effective method for the large-scale production of MOFs and MOFs composites with small size and high conductivity will facilitate their rapid development in practical electrochemical applications. Electrochemistry applications are wide ranging, including electrode materials and batteries, electrocatalysis, electroanalysis, electrochemical sensing, and even the entire energy and fuel categories (Fig. 1.7) [123–137].

(I) **MOFs for batteries**. Due to their structural flexibility, low cost, and redox activity, MOFs are good candidates for electrode materials. However, the practical application of many MOFs is hampered by their poor conductivity resulting in poor cycle performance of the battery. **(i) MOFs for Li-ion batteries (LIBs)**. MOFs can be favorable to interfacial charge transport of the Li^+ insertion/extraction strain due to their high surface area and porosity. MOFs behave as positive, negative, and electrolyte materials for LIBs. **(a) Pure MOFs**. **(b) MOF composites**. The conductivity of pure MOFs materials is not good. Thus it is necessary to seek to alter the electrochemical performance by combining MOFs with other conductive materials (metal oxides, conductive polymers, single metal, and carbon materials). **(ii) MOFs for Li-S batteries**. MOFs have unparalleled synthetic flexibility and adjustable pore size, and can be used to capture and immobilize sulfur by weak host-guest interactions. **(a) Pure MOFs**. The pore structure and performance of MOFs make them promising cathode materials for Li-S battery systems. **(b) MOFs composites**. To improve the capacity and cycle stability, the composites behave as a substrate for sulfur fixation in Li-S batteries. **(c) Others**. MOFs are also more widely used in other batteries, such as Li-O_2 batteries, SIBs, and so on [125–130].

(II) **MOFs for supercapacitors (SCs)**. The direct application of MOFs as SC electrode materials is mainly faced with poor conductivity and poor mechanical/chemical stability. In order to improve the conductivity of MOFs, conjugated guest molecules with redox activity to permeate into MOFs are used and the permeable MOFs lead to an apparent increase in

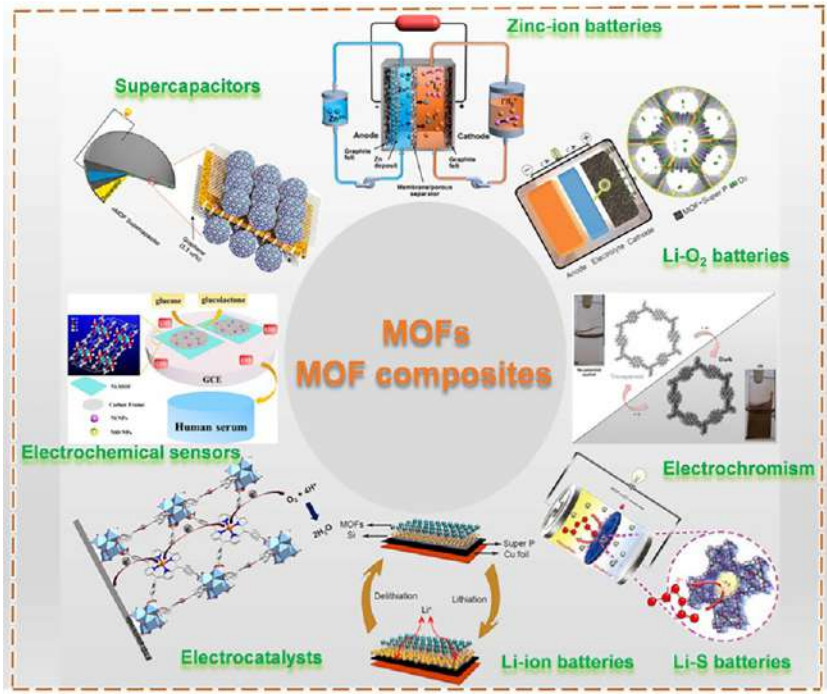

FIG. 1.7 Diagram showing MOFs and MOF composites for electrochemical applications. *(Reproduced with permission from Y. Xu, Q. Li, H. Xue, H. Pang, Metal-organic frameworks for direct electrochemical applications. Coord. Chem. Rev. 376 (2018) 292–318. Copyright 2018 Elsevier.)*

electrical conductivity. **(a) Pure MOFs**. MOFs can be directly used as novel electrode materials due to their distinct structure combined with their pseudocapacitive redox centers. **(b) MOFs composites**. Both electrical conductivity and chemical stability can be improved by combining MOFs with carbon materials, conductive polymers, etc. [130–133]

(III) **MOFs for electrocatalysts**. MOFs have potential applications in electrocatalysis as an important class of catalysts for electrochemical energy conversion reactions. This also meets the urgent need for clean and sustainable energy storage and conversion technologies, providing abundant metal active sites for electrocatalytic reactions, excellent electron transfer, and rapid mass transfer. However, the poor conductivity of MOFs requires further improvement. **(a) Pure MOFs**. **(b) MOFs composites**.

(IV) **MOFs for electrochemical sensors**. Nanostructured MOFs have important applications in electrochemical sensors, whose redox and catalytically active sites introduced through using active metal ions and/or ligands endow them with electrochemical sensing capabilities. **(a) Pure MOFs**. The application of MOFs in nonenzymatic electrochemical sensors is concerned with porphyrin MOFs constructed by porphyrin or metalloporphyrin linkers. **(b) MOFs composites**.

1.1.4.5 MOFs for applications in biomedicine

In addition, nanoscale MOFs (NMOFs) have emerged as a promising platform to develop novel nanomedicines, whose synthetic tunability can be further leveraged to fine-tune their properties for biomedical applications as well as to combine multiple therapeutic/imaging modalities into one platform to synergistically enhance therapeutic efficacy or to obtain theranostic nanomaterials. MOFs have so far shown the highest loading capacities of therapeutic molecules (drugs, cosmetics, or biological gases) associated, in most cases, with the possibility of controlling the release of their cargo. Their biodegradable character can also be modified through an adequate choice of the metal, linker, and structure (Fig. 1.8). Optimized NMOFs should have a bright future in biomedical imaging and drug delivery [138–148].

(I) **MOFs as delivery agents**. **(a) Active pharmaceutical ingredients (APIs)**. APIs are often limited by poor solubility, unfavorable pharmacokinetics, or slow biodistribution for a low drug-to-carrier molar ratio, which requires higher dosages or more potent alternative drugs to deliver therapeutically relevant concentrations. MOFs behave as promising candidates to design more efficient API vehicles due to their high pore volume and surface area, associated with a narrow pore size distribution. **(b) Antitumorals**. The usage of MOFs as drug delivery agents mostly focuses on the amount of drug loaded and the efficacy of its release. Their effect as drug carriers in cancer or tumor treatment needs attention. **(c) Pulmonary and ocular delivery**. The usage of MOFs as drug delivery agents is mostly restricted to the intravenous route. Drug delivery MOFs have been tested through pulmonary inhalation.

(II) **MOFs as protective coatings**. **(a) Enzymes**. MOFs possess pores large enough to enclose and immobilize proteins, thus enhancing their stability while facilitating their separation and recovery for future analysis. Enzyme encapsulation in MOFs still is limited by their pore size and

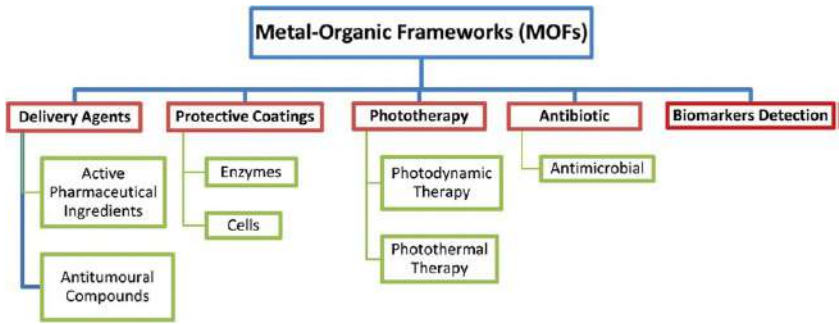

FIG. 1.8 A schematic description of the topics related to MOF applications in biomedicine. *(Reproduced with permission from R. F. Mendes, F. Figueira, J. P. Leite, L. Gales, F. A. Almeida Paz, Metal-organic frameworks: a future toolbox for biomedicine? Chem. Soc. Rev. 49 (2020) 9121—9153. Copyright 2020 Royal Chemical Society.)*

the incorporation step. Suitable linkers are required to adjust the pore size to match the enzyme configuration and polarity of the MOFs pores. **(b) Cells**. In situ MOFs synthesis can also be applied for the encapsulation of bigger bioentities, such as viruses and cells.

(III) **Phototherapy using MOFs**. Phototherapy involves the exposure of tissues to specific wavelengths of light, being in the form of photodynamic (PDT) or photothermal (PTT) therapies, whose efficiency and selectivity can be greatly improved by choosing an optimal photosensitizer (PS). MOFs are very promising candidates for a combination of PDT and PTT for their organic linker capable of creating superoxide anions, and the metal center.

(IV) **Detecting biomarkers with MOFs**. If a porous MOFs labeled with a biorecognition receptor involved in a highly specific interaction, such as antigen-antibody (immunosensing), protein-ligand, or nucleic acid base pair complementary, is combined with an efficient detecting technique, it is possible to design ultrasensitive and tunable methods for biomarker detection.

(V) **Antimicrobial activity**. MOFs can incorporate antibacterial species in their pores or even be effective themselves in killing different types of bacteria.

(VI) **Synergistic nanotherapeutics**. MOFs show great potential in biomedicine, especially in terms of cancer treatments, and NMOFs provide many opportunities for biological and medical applications. Loading of macromolecules such as proteins within NMOFs is also possible for other interesting applications such as nanovaccines. Many organic ligands within NMOFs may provide therapeutic functions by themselves, such as acting as chemotherapeutic prodrugs, photosensitizers, and fluorescent dyes. In addition, certain types of metal ions as the coordination centers may offer imaging contrast. Importantly, NMOFs in general are biodegradable by being gradually decomposed into small metal ions and organic molecules with rapid excretion and little long-term body retention, making them promising for safe in-vivo applications. In general, NMOF-based nanomedicine systems exhibit the combined benefits of both organic drug delivery systems and inorganic theranostic nanoplatforms [143–148].

1.2 Rare earth metal-organic frameworks (REMOFs)

Rare earth MOFs (REMOFs here means rare earth ions behaving as the unique framework metal centers) have garnered much interest due to a wide array of features from the marriage of rare earth ions (RE^{3+}) with MOFs. MOFs synthesized with rare earth (RE) elements (including scandium (Sc), yttrium (Y) and the series of 15 lanthanides (Ln)) are an intriguing family of MOFs from the standpoint of both structure and function. REMOFs not only can possess many of the same properties common to all MOFs families (i.e., permanent porosity,

tunable pore size/shape, accessible Lewis acidic sites), but also can display unique structures and properties owing to the high coordination numbers and distinct optical properties of RE elements. The coordination chemistry of RE ions is very diverse, with only small energetic differences between different coordination numbers and geometries, and where geometry is dictated primarily by ligand steric effects. This can make MOFs structure prediction more complicated, which also opens the door for the discovery of several new structures, composed of diverse metal nodes, and in some cases giving rise to highly connected nets, and the unique ability to merge multiple net structures using only one metal ion. Different from the transition metal ions, RE ions have unique electronic properties dictated by their 4f electron configurations. Given that the 4f orbitals are shielded from their external environment by 5s and 5p orbitals, RE ions have distinct electronic and magnetic properties that are not significantly altered by coordinating ligands. The electrons in the f block of RE^{3+} make them capable of having a larger coordination sphere. Based on the hard-soft acid-base consideration, RE^{3+} ions have affinity in relatively hard oxygen-containing linkers over other functional groups. RE^{3+} can display high coordination number and connectivity, diverse and coordination modes, which therefore exhibit great potential in constructing wide variety of MOFs. By carefully tuning the RE^{3+} node and organic linker components, REMOFs can be assembled into fascinating structures with diverse and complex topologies. The highly connective rare earth ions usually lead to the formation of condensed frameworks in the microporous range. Certainly, just as with other MOFs systems, REMOFs also have practical application value in the fields of separation, catalysis, and especially as a very promising class of materials for addressing the challenges in engineering of luminescent centers. RE^{3+} ion-bearing phosphors find numerous applications in lighting, display (light emitting diode, LED), optical communications, photonics, and biomedical devices. In addition, it should be stressed that the abundant luminescence response of REMOFs embody their versatile probe in chemical sensing [149–153].

1.2.1 REMOF structures

MOFs that are constructed using RE ions have been shown to form intricate topologies and diverse network structures. Generally, REMOF structures are classified by the identity of the metal node, being metal ions, chains, or clusters.

(1) **Metal ion nodes**. Unlike *s*-, *p*-, and *d*-block metal ions, *f*-block metal ions possess high coordination numbers as well as numerous coordination modes, unlocking a variety of structures that are not accessible through use of the former. RE^{3+} ions, especially Ln^{3+}, have a higher coordination number (in the range of 6–13) and connectivity than transition-metal ions, which are favorable for stabilizing the frameworks if all these coordination sites are utilized and bridged by organic linkers. The stable REMOFs not

only exhibit high thermal stability but also high water and chemical stability in acidic/basic solutions. Variable coordination numbers of RE^{3+} ions also make it possible to control structures and modify the pore sizes/sharps and framework interpenetration of REMOFs.

(2) **Metal chain nodes**. Rare earth oxo/hydroxo chain nodes, also called rods, are found for several REMOFs comprising carboxylic acid linkers. The formation of polymeric RE oxo/hydroxo chains tends to be favored in the presence of bridging carboxylic acid ligands. Many of the underlying design rules to construct REMOFs with RE^{3+}-chain nodes and open, porous structures have also been applied to MOFs.

(3) **Metal cluster nodes**. Controlled hydrolysis of the rare earth precursor is required to ensure the synthesis of clusters as opposed to RE chains, oxides, and hydroxides, which can be achieved using ligands as both structure-directing agents (or modulators) and capping groups to stabilize the cluster. These same clusters can be generated and stabilized during the synthesis of REMOFs, functioning as SBUs for a wide range of structures. **(a) Dinuclear clusters**. These that are 6-connected have since been found for MOFs comprising ditopic, tritopic, and mixed linkers. In addition, it should be noted that there are examples of MOFs comprising dinuclear RE cluster nodes that are 4-connected, 8-connected, and 12-connected. **(b) Trinuclear clusters**. They are common for MOFs comprising *d*-block metals, but are less commonly observed with RE metals. **(c) Tetranuclear clusters**. They focus primarily on examples with cubane-like, square planar, and rectangular tetranuclear RE clusters. **(d) Hexanuclear clusters. (e) Heptanuclear metal clusters. (f) Nonanuclear metal clusters** [149–153].

1.2.2 Some applications of REMOFs

(1) **Biological applications**. MOFs have emerged as promising candidates for drug delivery and bioimaging, while MOFs comprising RE ions may possess interesting magnetic and optical properties that can be exploited for these applications. **(a) Bioimaging**. REMOFs have also been studied for their potential in optical imaging owing, in part, to the NIR emission signatures of several of the RE^{3+} ions. In comparison to visible light, NIR light is advantageous for biological imaging since **(i)** it interacts less with biological materials, causing less potential damage to the region; **(ii)** tissue autofluorescence is low in the NIR region; and **(iii)** it scatters less, giving rise to better signals. **(b) Drug delivery**. The encapsulation of drug molecules into REMOFs-based nanocarriers has been successfully employed to increase the permeability of biofilms, change the distribution in vivo, regulate the rate of drug release, and improve stability/bioavailability. REMOFs have some of the following unique advantages as pharmaceutical carriers: **(I)** They can be simulated and designed according to the drug

characteristics, whose compositions and architecture geometries can be varied. **(II)** REMOFs have an affinity to effectively capture drug molecules with high loading doses due to their large pore volume-to-surface area ratios. **(III)** Imaging-mediated drug quantification, targeted cell delivery, and cancer treatments can be achieved by exploiting the unique optical and magnetic features. **(IV)** REMOFs can be rationally functionalized with upconversion luminescence (UCL) to serve as dual-mode drug carriers and contrast imaging agents with improved accuracy for disease diagnosis and treatment [149–153].

(2) **Catalysis**. REMOFs represent one of the emerging areas in MOFs chemistry and show excellent features for catalysis. **(I) Heterogeneous catalysis**. The metal SBUs of REMOFs are appropriate for the kinds of reactions that require strongly acidic catalytic sites. In addition, REMOFs can act as platforms to provide excellent host-guest interactions in the framework through PSM, which can be used as synergistic materials for photocatalytic purposes. However, REMOFs as heterogeneous catalysts suffer from significant underlying limitations that restrict their use for organic transformation: **(a)** Low thermal and chemical stability; **(b)** Sensitivity to oxygen and moisture, but this issue can be circumvented by introducing hydrophobic functionalities into the organic linkers, making REMOFs structures more water-resistant; **(c)** Deactivation by the coordination of basic reactants, products, or coordinating solvents at their free acidic metal sites, but this can be diminished by minimizing the defects in REMOFs structures; **(d)** the lack of a fundamental understanding of the reaction kinetics of REMOFs; and **(e)** difficulties in the large-scale synthesis of targeted REMOFs. **(II) Photocatalysts**. Designing linkers with high conjugation capable of light absorption over a wide range of wavelengths in combination with theoretical studies may shed some light on the electron transfer mechanism in REMOFs. Furthermore, the separation of photoexcited electrons and holes, facilitated by such highly conjugated linkers, combined with the LMCT process, will take full advantage of unfilled 4f orbitals of RE ions in photocatalytic transformations [149–153].

(3) **Adsorption and separations**. The inherent porosity of REMOFs has been harnessed for gas adsorption, separation, and purification processes. **(I) Adsorption**. In addition to N_2 or CO_2 gas adsorption, REMOFs have also been studied for the adsorption of liquid phase MeOH and water vapor. Such tunable pore sizes/sharps can induce highly selective gas storage and separation via a molecular sieving effect. Furthermore, the open rare earth sites and other functional sites can be easily incorporated into REMOFs and widely utilized to enhance the gas storage capacities and gas separation selectivity. Until now, REMOFs have been developed and explored for wide applications in H_2 storage, selective CO_2 capture and separation, and H_2 and CH_4 purification. Establishment of permanent porosity within REMOFs is more difficult and challenging compared with

transition metal MOFs, which is mainly due to the fact that higher coordination number and the more flexible coordination environment of RE^{3+} ions allow more small solvent molecules such as DMF and H_2O to easily occupy the coordination sites of RE^{3+} within REMOFs. **(II) Separation**. The chemical functionality, size, and shape of the pores in REMOFs can be tuned to aid in separating compounds based on size or chemical properties. A lot of REMOFs have been explored and demonstrated to have permanent porosities, making them useful for gas storage and separation. Some strategies such as the open rare earth sites, surface-functionalization, tunable pore size/sharp, interpenetration, and flexible structures within REMOFs have been simultaneously explored and widely utilized as a means to enhance the ability of selective gas storage and separation. Given the fact that some small solvent molecules can easily coordinate onto the RE^{3+}, if the coordinated solvent molecules are carefully removed, available open RE^{3+} sites should be obtained except for being occupied by the donor atoms from the neighboring organic linkers. The open RE^{3+} site formation within the pore surfaces of REMOFs is also considered to be beneficial for gas adsorption and separation [149–153].

1.3 Rare earth functionalized metal-organic framework hybrid materials (REFMOFHs)

Rare earth functionalized MOFs hybrid materials (REFMOFHs) mean that some special photoactive RE^{3+} ions (such as visible emissive Eu^{3+}, Tb^{3+}, Sm^{3+}, or Dy^{3+} and near infrared (NIR) emissive Nd^{3+}, Yb^{3+}, or Er^{3+}) are introduced into the MOF host to realize the functionalization of MOFs units and formation of the hybrid material systems. Currently, the main approach to assemble REFMOFH materials is PSM of MOFs. There are a variety of different ways to modify a MOFs in a postsynthetic manner, and each of these modification forms has the capacity to alter the physical and chemical properties of the frameworks. For REFMOFHs materials, the effective PSM strategies can be divided into six major areas (as shown in Fig. 1.9): coordinate PSM, covalent PSM, covalent and coordinate PSM, ion exchange PSM, ion doping (postsynthetic metalation or metal ion substitution) PSM, and encapsulation composition PSM. These postsynthetic methods provide the high complexity and functionality for **rare earth functionalized MOFs** hybrid materials and the desired chemical transformation should not destroy the MOFs under the reaction conditions used. Subsequently, some new hybrid materials based on RE^{3+} and MOFs can be obtained by PSM methods, which still retain the characteristic features of MOFs such as high crystallinity, high surface areas, and a structure comprising highly regular coordination bonding. It is worth pointing out that the content of the functionalized RE^{3+} in MOFs hosts is limited and small, but it still displays the effective physical property and functional performance of RE^{3+} for practical applications [154–172].

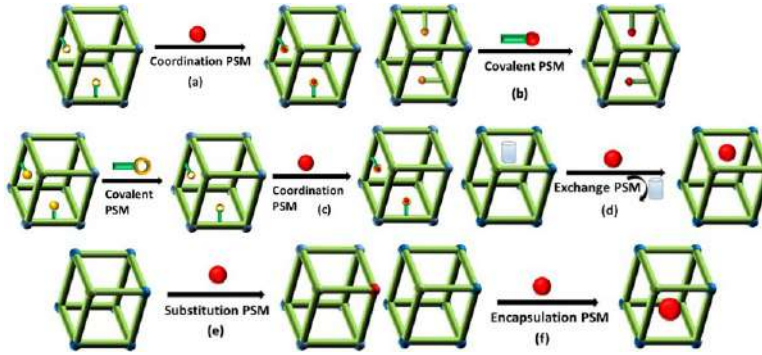

FIG. 1.9 Schematic description of postsynthetic modification (PSM) of MOFs by rare earth (RE^{3+}) ions for the corresponding hybrid materials (REFMOFHs); *red* sphere represents the rare earth species used for functionalized MOFs. *(Reproduced with permission from B. Yan, Luminescence response mode and chemical sensing mechanism for lanthanide functionalized metal-organic frameworks hybrids. Inorg. Chem. Front. 8 (2021) 201–233. Copyright 2021 Royal Chemical Society.)*

(1) **Coordinate PSM**. Coordinate PSM has the first effective approach for introducing RE^{3+} ions to achieve the final hybrid materials, using RE^{3+} species to coordinate to the free active group in MOFs (Fig. 1.9A) [155–157]. Fig. 1.10 shows an example of coordination PSM of Ga-MOF ((Ga(OH)(btec)·0.5H_2O, H_4btec = pyromellitic acid)) by double cations of both near infrared-emitting rare earth cations due to its rigid and porous structure and the presence of noncoordinating carboxylate groups. This allows the introduction of metal ions into Ga-MOF by PSM. Ag^+ can enhance visible emitting of Ln^{3+} in Ln^{3+}@Ga-MOF distinctly. Ln^{3+} (Yb^{3+}, Nd^{3+}, Er^{3+}) and Ag^+ are incorporated into the pores of Ga-MOF and used to analyze the luminescence properties of the resulting host-guest material [156].

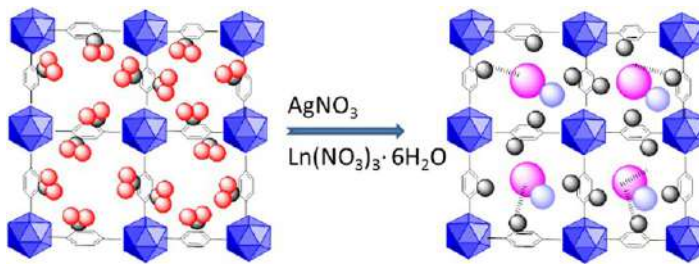

FIG. 1.10 Schematic illustration of RE^{3+} and Ag^+ incorporation into Ga-MOF. The RE, Ag, Ga, C, and O atoms are represented by *pansy*, *pink purple*, *cobalt blue*, *black*, and *red*, respectively. Hydrogen atoms and uncoordinated water molecules are excluded for clarity. *(Reproduced with permission from N. Sun, B. Yan, Near-infrared emission sensitization of lanthanide cation based on Ag + functionalized metal-organic frameworks. J. Alloys Compd. 765 (2018) 63–68. Copyright 2018 Elsevier.)*

(2) **Covalent PSM**. Covalent PSM uses a reagent to modify a component of the MOFs in a heterogeneous, postsynthetic manner to form a new covalent bond, providing a powerful and versatile method to introduce a broad range of chemical groups into MOFs (Fig. 1.9B) [158,159]. For rare earth functionalized MOF hybrid materials, covalent PSM is not a single functionalization mode, but combines with other modification paths in the hybrid materials.

(3) **Covalent and coordinate PSM**. For rare earth functionalized MOFs hybrid materials, considering that RE^{3+} should be introduced through coordinate PSM, generally covalent PSM is the prepared procedure to produce the coordinated group for further RE^{3+} coordinate PSM (Fig. 1.9C). It should be noted that the RE^{3+} ion's coordination often destroys the covalent PSM-derived MOFs, whose stability must be considered very important [158,159]. Fig. 1.11 shows the scheme for the composition of the preparation process and reaction principle of the hybrids. SBA-15 can be easily modified by the crosslinking reagent IPTES to form Si-SBA-15 through the cohydrolysis and copolycondensation process between the alkoxyl groups of IPTES and the hydroxyl groups of SBA-15. On the other hand, IRMOF-3 is synthesized in situ and then is covalently grafted to Si-SBA-15 through the addition reaction between its amino group and inner ester group of Si-SBA-15 [159].

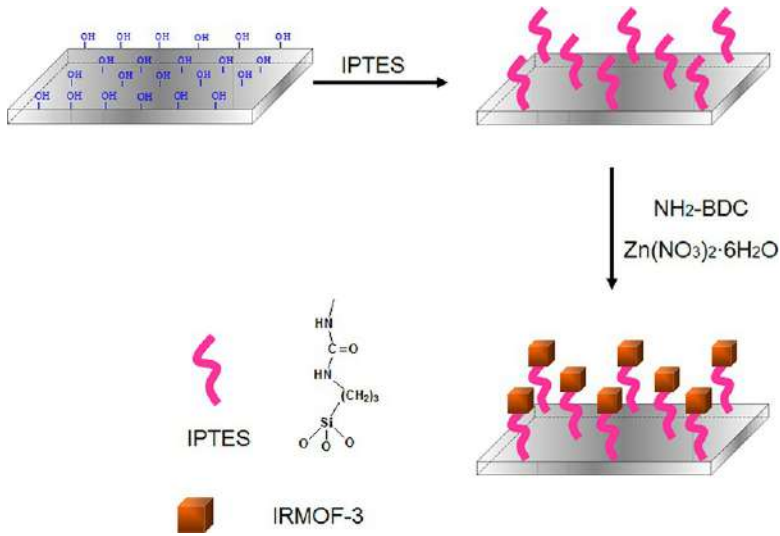

FIG. 1.11 The selected scheme for the composition of hybrid materials RE-SBA-15-Si-IRMOF-3 (RE = Eu, Tb, Nd, Yb). *(Reproduced with permission from X. Lian, B. Yan, Multi-component luminescent lanthanide hybrids of both functionalized IR-MOF-3 and SBA-15. New J. Chem. 39 (2015) 5898–5901. Copyright 2015 Royal Chemical Society.)*

(4) **Ion exchange PSM**. Ion exchange PSM is most appropriate for many anionic MOFs systems with dimethylammonium (DMA) cations in their porous structure, and so RE^{3+} cations can be introduced into the MOF via ionic exchange with DMA (Fig. 1.9D) [160–164]. For example, Fig. 1.12 shows that pillared layered hybrid materials $RE(PDA)_3^{3-}$-LDH can be prepared through ion exchange assembly of luminescent lanthanide coordination polymers $[H_2NMe_2]_3[RE(DPA)_3]$ (RE = Eu, Tb, Sm, Dy, Nd; $[H_2NMe_2]^+$=dimethyl amino cation; H_2DPA = 2,6-dipicolinic acid) and pillared layered double hydroxide (Mg-Al LDH, $Mg_6Al_2(OH)_{16}CO_3{\cdot}4H_2O$). With Mg-Al LDH interacts with $[H_2NMe_2]_3[RE(DPA)_3]$ through anion exchange ($[RE(PDA)_3]^{3-}$) and electrostatic effect to form $[RE(PDA)_3]^{3-}$-LDH [159].

(5) **Ion doping (postsynthetic metalation (or metal ion substitution) PSM)**. Ion doping PSM is easily realized for REMOFs due to the similar ion radius of lanthanide contraction. In fact, RE^{3+} ionic doping also can be extended to other trivalent metal ion MOFs such as Al, Ga, and In ions for the same valence substitution (Fig. 1.9E). A series of hybrids based on RE^{3+} ions (Eu^{3+}, Tb^{3+}, Sm^{3+}, Dy^{3+}) activated yttrium metallic organic framework of 1,3,5-benzenetricarboxylate (MOF-76(Y)) are synthesized by ion substitution under solvothermal conditions, which shows isostructure with parent MOF-76(Y) [164].

(6) **Encapsulation composition PSM**. In addition, encapsulation composition PSM permits all kinds of rare earth compounds (salts, complexes, or oxides, etc.) as small guest molecules or nanoparticles (NPs) to be introduced in MOFs hosts, providing physical composition to keep the whole

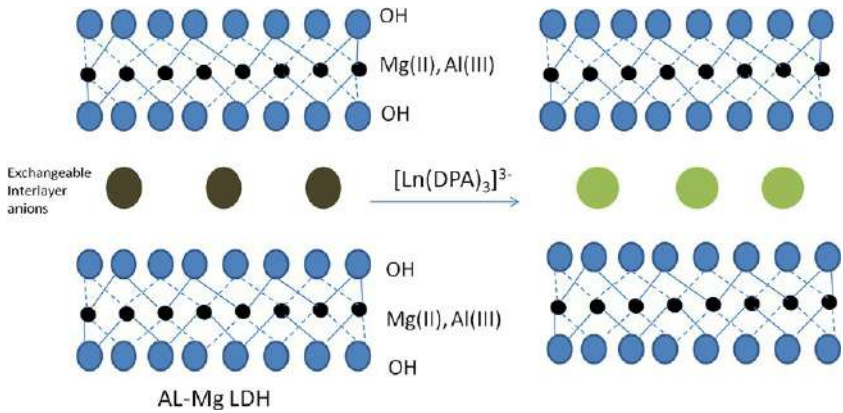

FIG. 1.12 Scheme showing synthesis procedure and predicted structure of the hybrid materials of $[RE(DPA)_3]^{3-}$-LDH, CO_3^{2-} (*gray*), $[RE(PDA)_3]^{3-}$ (*green*), OH (*blue*), Mg and Al (*black*). *(Reproduced with permission from J. Ma, B. Yan, Novel hybrid materials of lanthanide coordination polymers ion exchanged Mg-Al layered double hydroxide: multi-color photoluminescence and white color thin film. Dyes Pigments 153 (2018) 266–274. Copyright 2018 Elsevier.)*

luminescent hybrid system stable (Fig. 1.9F) [165–172]. For example, a novel strategy is demonstrated to construct photofunctional nanocomposites by composing surfactant-capped nanophosphors (upconversion luminescent $NaYF_4$:Yb^{3+}, Er^{3+}/Tm^{3+} and downconversion emissive $LaPO_4$:Ln^{3+} (Ln = Ce, Eu, Tb) NPs) and a zeolitic imidazolate framework (ZIF-8) unit. Fig. 1.13 shows the scheme for the preparation process of the nanocomposites. The PVP-NPs@ZIF-8 is synthesized through a PVP-protected process (PVP = polyvinyl pyrrolidone). This strategy involves two steps: the first step is the functionalization of nanoparticle surfaces with PVP and the second step is the crystallization of ZIF-8 [165].

Fig. 1.14 shows the scheme of a series of transparent MOFs thin films designed and prepared by assembling the lanthanide functionalized UiO-67 (Ln(TTA/TAA)@UMOF, RE = Eu, Tb, Er, Nd, TTA = 2-thenoyltrifluoroacetone, TAA = 1,1,1-trifluoropentane-2,4-dione) on the organosilane linker (L) modified Al_2O_3 (A) using RE^{3+} ions as the bridge. L is first constructed and then used to modify the surface of Al_2O_3, to obtain linker-Al_2O_3 (LA). After that, the open Lewis base site of the pyridine ring on the LA surface is coordinated with the RE^{3+} ions. Meanwhile, UMOFs are synthesized and functionalized with RE^{3+} ions (RE = Eu, Tb, Er, Nd) and β-diketone, such as TTA/TAA, by PSM. Finally, the coordination of unsaturated Eu^{3+} ions on LA is used to assemble UMOF, RE@UMOF, and RE(TTA/TAA)@UMOF, which serve as the top building blocks of the films [172].

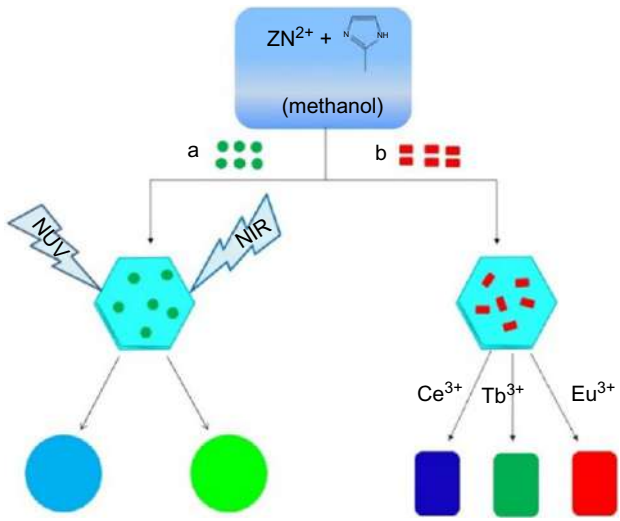

FIG. 1.13 Scheme for the preparation of nanocomposites of luminescent nanoparticles and ZIF-8 crystals, (A) upconversion nanoparticles, (B) $LaPO_4$:Ln^{3+} nanoparticles. *(Reproduced with permission from C. Liu, B. Yan, Photofunctional nanocomposites based on the functionalization of metal-organic framework by up/downconverion luminescent nanophosphors. New J. Chem. 39 (2015) 1125–1131. Copyright 2015 Royal Chemical Society.)*

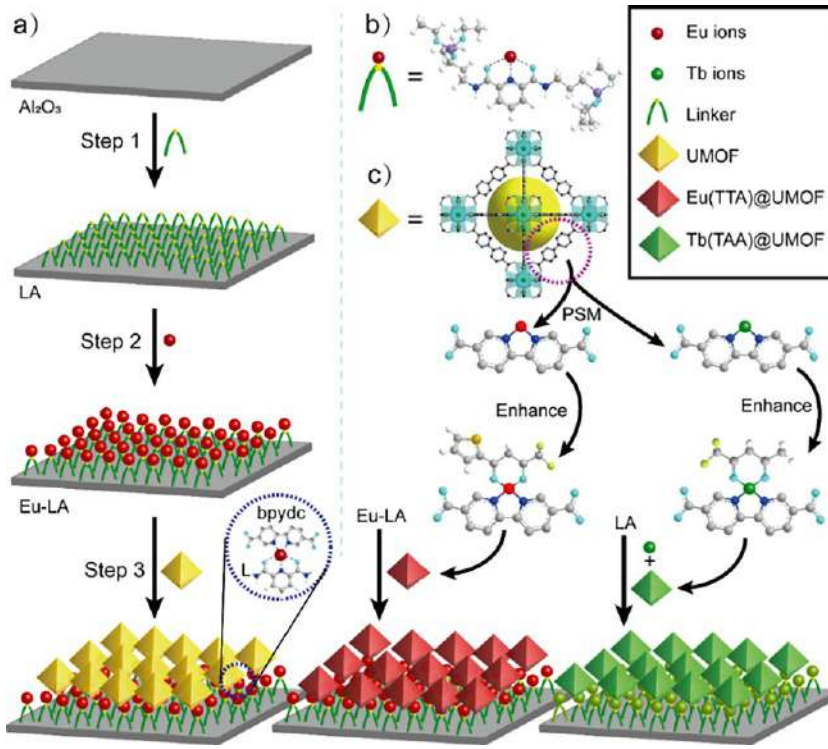

FIG. 1.14 The scheme of (A) the fabricating process of RE(TTA/TAA)@UMOF-RE-LA (RE = Eu, Tb) films; (B) the schematic diagram of Eu-L; (C) the twice PSM process of UMOF. *(Reproduced with permission from W. Ma, B. Yan, Lanthanide functionalized MOFs thin films as effective luminescent materials and chemical sensor for ammonia. Dalton Trans. 49 (2020) 15663–15671. Copyright 2020 Royal Chemical Society.)*

References

[1] N. Stock, S. Biswas, Synthesis of metal-organic frameworks (MOFs): routes to various MOF topologies, morphologies, and composites, Chem. Rev. 112 (2012) 933–969.

[2] S. Furukawa, J. Reboul, S. Diring, K. Sumida, S. Kitagawa, Structuring of metal-organic frameworks at the mesoscopic/macroscopic scale, Chem. Soc. Rev. 43 (2014) 5700–5734.

[3] R.F. Mendes, F.A. Almeida Paz, Transforming metal-organic frameworks into functional materials, Inorg. Chem. Front. 2 (2015) 495–509.

[4] G. Maurin, C. Serre, A. Cooperc, G. Ferey, The new age of MOFs and of their porous-related solids, Chem. Soc. Rev. 46 (2017) 3104–3107.

[5] C. Wang, D. Liu, W. Lin, Metal-organic frameworks as a tunable platform for designing functional molecular materials, J. Am. Chem. Soc. 135 (2013) 13222–13234.

[6] R. Lin, S. Xiang, B. Li, Y. Cui, G. Qian, W. Zhou, B. Chen, Our journey of developing multifunctional metal-organic frameworks, Coord. Chem. Rev. 384 (2019) 21–36.

[7] A. Terzopoulou, J.D. Nicholas, X. Chen, B.J. Nelson, S. Pane, J. Puigmartí-Luis, Metal-organic frameworks in motion, Chem. Rev. 120 (2020) 11175–11193.

[8] X. Zhang, B. Wang, A. Alsalme, S. Xiang, Z. Zhang, B. Chen, Design and applications of water-stable metal-organic frameworks: status and challenges, Coord. Chem. Rev. 423 (2020), 213507.
[9] S. Natarajan, P. Mahata, Metal-organic framework structures—how closely are they related to classical inorganic structures? Chem. Soc. Rev. 38 (2009) 2304–2318.
[10] A. Karmakar, A.V. Desai, S.K. Ghosh, Ionic metal-organic frameworks (iMOFs): design principles and applications, Coord. Chem. Rev. 307 (2016) 313–341.
[11] H. He, L. Hashemi, M. Hu, A. Morsali, The role of the counter-ion in metal-organic frameworks' chemistry and applications, Coord. Chem. Rev. 376 (2018) 319–347.
[12] S. Zhao, Y. Zhang, S. Song, H. Zhang, Design strategies and applications of charged metal organic frameworks, Coord. Chem. Rev. 398 (2019), 113007.
[13] S.L. Griffin, N.R. Champness, A periodic table of metal-organic frameworks, Coord. Chem. Rev. 414 (2020), 213295.
[14] S. Abednatanzi, P.G. Derakhshandeh, H. Depauw, F. Coudert, H. Vrielinck, P. Van Der Voort, K. Leus, Mixed-metal metal-organic frameworks, Chem. Soc. Rev. 48 (2019) 2535–2565.
[15] R.E. Morris, L. Brammer, Coordination change, lability and hemilability in metal-organic frameworks, Chem. Soc. Rev. 46 (2017) 5444–5462.
[16] U. Kokçam-Demir, A. Goldman, L. Esrafili, M. Gharib, A. Morsali, O. Weingart, C. Janiak, Coordinatively unsaturated metal sites (open metal sites) in metal-organic frameworks: design and applications, Chem. Soc. Rev. 49 (2020) 2751–2798.
[17] D.J. Tranchemontagne, J.L. Mendoza-Cortes, M. O'Keeffe, O.M. Yaghi, Secondary building units, nets and bonding in the chemistry of metal-organic frameworks, Chem. Soc. Rev. 38 (2009) 1257–1283.
[18] J.J. Perry IV, J.A. Perman, M.J. Zaworotko, Design and synthesis of metal-organic frameworks using metal-organic polyhedra as supermolecular building blocks, Chem. Soc. Rev. 38 (2009) 1400–1417.
[19] G. Yang, L. Hou, X. Luan, B. Wu, Y. Wang, Molecular braids in metal-organic frameworks, Chem. Soc. Rev. 41 (2012) 6992–7000.
[20] A. Schoedel, M. Li, D. Li, M. O'Keeffe, O.M. Yaghi, Structures of metal-organic frameworks with rod secondary building units, Chem. Rev. 116 (2016) 12466–12535.
[21] Z. Chen, H. Jiang, M. Li, M. O'Keeffe, M. Eddaoudi, Reticular chemistry 3.2: typical minimal edge-transitive derived and related nets for the design and synthesis of metal-organic frameworks, Chem. Rev. 120 (2020) 8039–8065.
[22] M. Li, D. Li, M. O'Keeffe, O.M. Yaghi, Topological analysis of metal-organic frameworks with polytopic linkers and/or multiple building units and the minimal transitivity principle, Chem. Rev. 114 (2014) 1343–1370.
[23] W. Lu, Z. Wei, Z. Gu, T. Liu, J. Park, J. Park, J. Tian, M. Zhang, Q. Zhang, T. Gentle III, M. Boscha, H. Zhou, Tuning the structure and function of metal-organic frameworks via linker design, Chem. Soc. Rev. 43 (2014) 5561–5593.
[24] D. Zhao, D.J. Timmons, D. Yuan, H. Zhou, Tuning the topology and functionality of metal-organic frameworks by ligand design, Acc. Chem. Res. 44 (2011) 123–133.
[25] F.A. Almeida Paz, J. Klinowski, S.M.F. Vilela, J.P.C. Tome, J.A.S. Cavaleiroc, J. Rocha, Ligand design for functional metal-organic frameworks, Chem. Soc. Rev. 41 (2012) 1088–1110.
[26] Z. Lin, J. Lu, M. Hong, R. Cao, Metal-organic frameworks based on flexible ligands (FL-MOFs): structures and applications, Chem. Soc. Rev. 43 (2014) 5867–5895.

[27] M. Eddaoudi, D.F. Sava, J.F. Eubank, K. Adila, V. Guillerm, Zeolite-like metal-organic frameworks (ZMOFs): design, synthesis, and properties, Chem. Soc. Rev. 44 (2015) 228–249.
[28] A.V. Desai, S. Sharma, S. Let, S.K. Ghosh, N-donor linker based metal-organic frameworks (MOFs): advancement and prospects as functional materials, Coord. Chem. Rev. 395 (2019) 146–192.
[29] Y. He, Y. Tan, J. Zhang, Functional metal-organic frameworks constructed from triphenylamine-based polycarboxylate ligands, Coord. Chem. Rev. 420 (2020), 213354.
[30] H. Ghasempour, K. Wang, J.A. Powell, F. ZareKarizi, X. Lv, A. Morsali, H. Zhou, Metal-organic frameworks based on multicarboxylate linkers, Coord. Chem. Rev. 426 (2021), 213542.
[31] K.K. Tanabe, S.M. Cohen, Postsynthetic modification of metal-organic frameworks—a progress report, Chem. Soc. Rev. 40 (2011) 498–519.
[32] S.M. Cohen, Postsynthetic methods for the functionalization of metal-organic frameworks, Chem. Rev. 112 (2012) 970–1000.
[33] V. Valtchev, G. Majano, S. Mintova, J. Perez-Ramırez, Tailored crystalline microporous materials by post-synthesis modification, Chem. Soc. Rev. 42 (2013) 263–290.
[34] J.D. Evans, C.J. Sumby, C.J. Doonan, Post-synthetic metalation of metal-organic frameworks, Chem. Soc. Rev. 43 (2014) 5933–5951.
[35] P. Deria, J.E. Mondloch, O. Karagiaridi, W. Bury, J.T. Hupp, O.K. Farha, Beyond post-synthesis modification: evolution of metal-organic frameworks via building block replacement, Chem. Soc. Rev. 43 (2014) 5896–5912.
[36] S.M. Cohen, The postsynthetic renaissance in porous solids, J. Am. Chem. Soc. 139 (2017) 2855–2863.
[37] T. Islamoglu, S. Goswami, Z. Li, A.J. Howarth, O.K. Farha, J.T. Hupp, Postsynthetic tuning of metal-organic frameworks for targeted applications, Acc. Chem. Res. 50 (2017) 805–813.
[38] Z. Yin, S. Wan, J. Yang, M. Kurmoo, M. Zeng, Recent advances in post-synthetic modification of metal-organic frameworks: new types and tandem reactions, Coord. Chem. Rev. 378 (2019) 500–512.
[39] Q. Yu, Z. Li, Q. Cao, S. Qu, Q. Jia, Advances in luminescent metal-organic framework sensors based on post-synthetic modification, Trends Anal. Chem. 129 (2020), 115939.
[40] C.K. Brozek, M. Dinca, Cation exchange at the secondary building units of metal-organic frameworks, Chem. Soc. Rev. 43 (2014) 5456–5467.
[41] Y. Han, J. Li, Y. Xie, G. Guo, Substitution reactions in metal-organic frameworks and metal-organic polyhedral, Chem. Soc. Rev. 43 (2014) 5952–5981.
[42] S.A.A. Razavi, A. Morsali, Linker functionalized metal-organic frameworks, Coord. Chem. Rev. 399 (2019), 213023.
[43] P. Li, X. Wang, Y. Zhao, Click chemistry as a versatile reaction for construction and modification of metal-organic frameworks, Coord. Chem. Rev. 380 (2019) 484–518.
[44] M. Xu, Q. Chen, L. Xie, J. Li, Exchange reactions in metal-organic frameworks: new advances, Coord. Chem. Rev. 421 (2020), 213421.
[45] Q. Zhu, Q. Xu, Metal-organic framework composites, Chem. Soc. Rev. 44 (2014) 5468–5512.
[46] M.L. Foo, R. Matsuda, S. Kitagawa, Functional hybrid porous coordination polymers, Chem. Mater. 26 (2014) 310–322.
[47] C. Doherty, D. Buso, A.J. Hill, S. Furukawa, S. Kitagawa, P. Falcaro, Using functional nano- and microparticles for the preparation of metal-organic framework composites with novel properties, Acc. Chem. Res. (2014) 396–405.

[48] K. Otsubo, T. Haraguchi, H. Kitagawa, Nanoscale crystalline architectures of Hofmann-type metal-organic frameworks, Coord. Chem. Rev. 346 (2017) 123–138.
[49] J.D. Sosa, T.F. Bennett, K.J. Nelms, B.M. Liu, R.C. Tovar, Y. Liu, Metal-organic framework hybrid materials and their applications, Crystals 8 (2018) 325.
[50] J. Yu, C. Mu, B. Yan, X. Qin, C. Shen, H. Xue, Huan Pang, Nanoparticle/MOF composites: preparations and applications, Mater. Horiz. 4 (2017) 557–569.
[51] Y.V. Kaneti, J. Tang, R.R. Salunkhe, X. Jiang, A. Yu, K.C. Wu, Y. Yamauchi, Nanoarchitectured design of porous materials and nanocomposites from metal-organic frameworks, Adv. Mater. 29 (2017) 1604898.
[52] H.R. Moon, D. Lim, M.P. Suh, Fabrication of metal nanoparticles in metal-organic frameworks, Chem. Soc. Rev. 42 (2013) 1807–1824.
[53] C.R. Kim, T. Uemura, S. Kitagawa, Inorganic nanoparticles in porous coordination polymers, Chem. Soc. Rev. 45 (2016) 3828–3845.
[54] N. Yuan, X. Zhang, L. Wang, The marriage of metal-organic frameworks and silica materials for advanced applications, Coord. Chem. Rev. 421 (2020), 213442.
[55] T. Kitao, Y. Zhang, S. Kitagawa, B. Wang, T. Uemura, Hybridization of MOFs and polymers, Chem. Soc. Rev. 46 (2017) 3108–3133.
[56] O. Shekhah, J. Liu, R.A. Fischer, C. Woll, MOF thin films: existing and future applications, Chem. Soc. Rev. 40 (2011) 1081–1106.
[57] A. Betard, R. A., Fischer metal-organic framework thin films: from fundamentals to applications, Chem. Rev. 112 (2012) 1055–1083.
[58] Z. Gu, J. Zhang, Epitaxial growth and applications of oriented metal-organic framework thin films, Coord. Chem. Rev. 378 (2019) 513–532.
[59] D. Bradshaw, A. Garai, J. Huo, Metal-organic framework growth at functional interfaces: thin films and composites for diverse applications, Chem. Soc. Rev. 41 (2012) 2344–2381.
[60] J. Mehta, N. Bhardwaj, S.K. Bhardwaj, K. Kim, A. Deep, Recent advances in enzyme immobilization techniques: metal-organic frameworks as novel substrates, Coord. Chem. Rev. 322 (2016) 30–40.
[61] S. Liang, X. Wu, J. Xiong, M. Zong, W. Lou, Metal-organic frameworks as novel matrices for efficient enzyme immobilization: an update review, Coord. Chem. Rev. 406 (2020), 213149.
[62] X. Lian, Y. Fang, E. Joseph, Q. Wang, J. Li, S. Banerjee, C. Lollar, X. Wang, H. Zhou, Enzyme-MOF (metal-organic framework) composites, Chem. Soc. Rev. 46 (2017) 3386–3401.
[63] R.J. Drout, L. Robison, O.K. Farh, Catalytic applications of enzymes encapsulated in metal-organic frameworks, Coord. Chem. Rev. 381 (2019) 151–160.
[64] H. Cai, Y. Huang, D. Li, Biological metal-organic frameworks: structures, host-guest chemistry and bio-applications, Coord. Chem. Rev. 378 (2019) 207–221.
[65] Q. Qiu, H. Chen, Y. Wang, Y. Ying, Recent advances in the rational synthesis and sensing applications of metal-organic framework biocomposites, Coord. Chem. Rev. 387 (2019) 60–78.
[66] R.J. Kuppler, D.J. Timmons, Q. Fang, J. Li, T.A. Makal, M.D. Young, D. Yuan, D. Zhao, W. Zhuang, H. Zhou, Potential applications of metal-organic frameworks, Coord. Chem. Rev. 253 (2009) 3042–3066.
[67] B. Li, H. Wen, Y. Cui, W. Zhou, G. Qian, B. Chen, Emerging multifunctional metal-organic framework materials, Adv. Mater. 28 (2016) 8819–8860.
[68] P. Silva, S.M.F. Vilela, J.P.C. Tome, F.A. Almeida Paz, Multifunctional metal-organic frameworks: from academia to industrial applications, Chem. Soc. Rev. 44 (2015) 6774–6803.

[69] Y. Cui, B. Li, H. He, W. Zhou, B. Chen, G. Qian, Metal-organic frameworks as platforms for functional materials, Acc. Chem. Res. 49 (2016) 483–493.
[70] X. Cai, Z. Xie, D. Li, M. Kassymova, S. Zang, H. Jiang, Nano-sized metal-organic frameworks: synthesis and applications, Coord. Chem. Rev. 417 (2020), 213366.
[71] J. Li, R.J. Kuppler, H. Zhou, Selective gas adsorption and separation in metal-organic frameworks, Chem. Soc. Rev. 38 (2009) 1477–1504.
[72] L.J. Murray, M. Dinca, J.R. Long, Hydrogen storage in metal-organic frameworks, Chem. Soc. Rev. 38 (2009) 1294–1314.
[73] M.P. Suh, H.J. Park, T.K. Prasad, D. Lim, Hydrogen Storage in metal-organic frameworks, Chem. Rev. 112 (2012) 782–835.
[74] Y. He, F. Chen, B. Li, G. Qian, W. Zhou, B. Chen, Porous metal-organic frameworks for fuel storage, Coord. Chem. Rev. 373 (2018) 167–198.
[75] H. Wang, J. Li, Microporous metal-organic frameworks for adsorptive separation of C_5-C_6 alkane isomers, Acc. Chem. Res. 52 (2019) 1968–1978.
[76] K. Sumida, D.L. Rogow, J.A. Mason, T.M. McDonald, E.D. Bloch, Z.R. Herm, T. Bae, J.R. Long, Carbon dioxide capture in metal-organic frameworks, Chem. Rev. 112 (2012) 724–781.
[77] B. Seoane, J. Coronas, I. Gascon, M.E. Benavides, O. Karvan, J. Caro, F. Kapteijna, J. Gascon, Metal-organic framework based mixed matrix membranes: a solution for highly efficient CO_2 capture? Chem. Soc. Rev. 44 (2015) 2421–2454.
[78] X. Ma, Y. Chai, P. Li, B. Wang, Metal-organic framework films and their potential applications in environmental pollution control, Acc. Chem. Res. 52 (2019) 1461–1470.
[79] T. Islamoglu, Z. Chen, M.C. Wasson, C.T. Buru, K.O. Kirlikovali, U. Afrin, M.R. Mian, O. K. Farha, Metal-organic frameworks against toxic chemicals, Chem. Rev. 120 (2020) 8130–8160.
[80] P.A. Kobielska, A.J. Howarth, O.K. Farha, S. Nayak, Metal-organic frameworks for heavy metal removal from water, Coord. Chem. Rev. 358 (2018) 92–107.
[81] G. Xu, Z. An, K. Xu, Q. Liu, R. Das, H. Zhao, Metal organic framework (MOF)-based micro/nanoscaled materials for heavy metal ions removal: the cutting-edge study on designs, synthesis, and applications, Coord. Chem. Rev. 427 (2021), 213554.
[82] J. Li, X. Wang, G. Zhao, C. Chen, Z. Chai, A. Alsaedi, T. Hayatf, X. Wang, Metal-organic framework-based materials: superior adsorbents for the capture of toxic and radioactive metal ions, Chem. Soc. Rev. 47 (2018) 2322–2356.
[83] S. Rojas, P. Horcajada, Metal-organic frameworks for the removal of emerging organic contaminants in water, Chem. Rev. 120 (2020) 8378–8415.
[84] J. Li, J. Sculley, H. Zhou, Metal-organic frameworks for separations, Chem. Rev. 112 (2012) 869–932.
[85] R. Lin, S. Xiang, H. Xing, W. Zhou, B. Chen, Exploration of porous metal-organic frameworks for gas separation and purification, Coord. Chem. Rev. 378 (2019) 87–103.
[86] T. Wang, E. Lin, Y. Peng, Y. Chen, P. Cheng, Z. Zhang, Rational design and synthesis of ultramicroporous metal-organic frameworks for gas separation, Coord. Chem. Rev. 423 (2020), 213485.
[87] X. Li, Y. Liu, J. Wang, J. Gascon, J. Li, B. Van der Bruggen, Metal-organic frameworks based membranes for liquid separation, Chem. Soc. Rev. 46 (2017) 7124–7144.
[88] S. Mukherjee, A.V. Desai, S.K. Ghosh, Potential of metal-organic frameworks for adsorptive separation of industrially and environmentally relevant liquid mixtures, Coord. Chem. Rev. 367 (2018) 82–126.
[89] J. Lee, O.K. Farha, J. Roberts, K.A. Scheidt, S.T. Nguyen, J.T. Hupp, Metal-organic framework materials as catalysts, Chem. Soc. Rev. 38 (2009) 1450–1459.

[90] Y. Huang, J. Liang, X. Wang, R. Cao, Multifunctional metal-organic framework catalysts: synergistic catalysis and tandem reactions, Chem. Soc. Rev. 46 (2017) 126–157.
[91] Y. Kang, Y. Lu, K. Chen, Y. Zhao, P. Wang, W. Sun, Metal-organic frameworks with catalytic centers: from synthesis to catalytic application, Coord. Chem. Rev. 378 (2019) 262–280.
[92] H. Konnerth, B.M. Matsagar, S.S. Chen, M.H.G. Prechtl, F. Shieh, K.C.W. Wu, Metal-organic framework (MOF)-derived catalysts for fine chemical production, Coord. Chem. Rev. 416 (2020), 213319.
[93] Q. Yang, Q. Xu, H. Jiang, Metal-organic frameworks meet metal nanoparticles: synergistic effect for enhanced catalysis, Chem. Soc. Rev. 46 (2017) 4774–4808.
[94] A. Dhakshinamoorthy, Z. Li, H. Garcia, Catalysis and photocatalysis by metal organic frameworks, Chem. Soc. Rev. 47 (2018) 8134–8172.
[95] Q. Wang, D. Astruc, State of the art and prospects in metal-organic framework (MOF)-based and MOF-derived nanocatalysis, Chem. Rev. 120 (2020) 1438–1511.
[96] Y. Wei, M. Zhang, R. Zou, Q. Xu, Metal-organic framework-based catalysts with single metal sites, Chem. Rev. 120 (2020) 12089–12174.
[97] M. Viciano-Chumillas, M. Mon, J. Ferrando-Soria, A. Corma, A. Leyva-Perez, D. Armentano, E. Pardo, Metal-organic frameworks as chemical nanoreactors: synthesis and stabilization of catalytically active metal species in confined spaces, Acc. Chem. Res. 53 (2020) 520–531.
[98] A. Bavykina, N. Kolobov, I. Son Khan, J.A. Bau, A. Ramirez, J. Gascon, Metal-organic Frameworks in heterogeneous catalysis: recent progress, new trends, and future perspectives, Chem. Rev. 120 (2020) 8468–8535.
[99] W. Cui, G. Zhang, T. Hu, X. Bu, Metal-organic framework-based heterogeneous catalysts for the conversion of C_1 chemistry: CO, CO_2 and CH_4, Coord. Chem. Rev. 387 (2019) 79–120.
[100] S. Zhao, X. Song, S. Song, H. Zhang, Highly efficient heterogeneous catalytic materials derived from metalorganic framework supports/precursors, Coord. Chem. Rev. 337 (2017) 80–96.
[101] T. Zhang, Y. Jin, Y. Shi, M. Li, J. Li, C. Duan, Modulating photoelectronic performance of metal-organic frameworks for premium photocatalysis, Coord. Chem. Rev. 380 (2019) 201–229.
[102] D. Li, M. Kassymova, X. Cai, S. Zang, H. Jiang, Photocatalytic CO_2 reduction over metal-organic framework-based materials, Coord. Chem. Rev. 412 (2020), 213262.
[103] S. Liu, C. Zhang, Y. Sun, Q. Chen, L. He, K. Zhang, J. Zhang, B. Liu, L. Chen, Design of metal-organic framework-based photocatalysts for hydrogen generation Coord, Chem. Rev. 413 (2020), 213266.
[104] D. Jiang, P. Xu, H. Wang, G. Zeng, D. Huang, M. Chen, C. Lai, C. Zhang, J. Wan, W. Xue, Strategies to improve metal organic frameworks photocatalyst's performance for degradation of organic pollutants, Coord. Chem. Rev. 376 (2018) 449–466.
[105] P. Liao, J. Shen, J. Zhang, Metal-organic frameworks for electrocatalysis, Coord. Chem. Rev. 373 (2018) 22–48.
[106] M.B. Solomon, T.L. Church, D.M. D'Alessandro, Metal-organic frameworks and their derivatives as bifunctional electrocatalysts, CrystEngComm 19 (2017) 4049–4065.
[107] J. Du, F. Li, L. Sun, Metal-organic frameworks and their derivatives as electrocatalysts for the oxygen evolution reaction, Chem. Soc. Rev. (2021), https://doi.org/10.1039/D0CS01191F.
[108] B.D. McCarthy, A.M. Beiler, B.A. Johnson, T. Liseev, A.T. Castner, S. Ott, Analysis of electrocatalytic metal-organic frameworks, Coord. Chem. Rev. 406 (2020), 213137.
[109] M. Zhao, S. Ou, C. Wu, Porous metal-organic frameworks for heterogeneous biomimetic catalysis, Acc. Chem. Res. 47 (2014) 1199–1207.

[110] K. Chen, C. Wu, Designed fabrication of biomimetic metal-organic frameworks for catalytic applications, Coord. Chem. Rev. 378 (2019) 445–465.
[111] W. Zhang, R. Xiong, Ferroelectric metal-organic frameworks, Chem. Rev. 112 (2012) 1163–1195.
[112] A.E. Thorarinsdottir, T.D. Harris, Metal-organic framework magnets, Chem. Rev. 120 (2020) 8716–8789.
[113] V. Rubio-Gimenez, S. Tatay, C. Martı-Gastaldo, Electrical conductivity and magnetic bistability in metal-organic frameworks and coordination polymers: charge transport and spin crossover at the nanoscale, Chem. Soc. Rev. 49 (2020) 5601–5638.
[114] S. Mendiratta, M. Usman, K. Lu, Expanding the dimensions of metal-organic framework research towards dielectrics, Coord. Chem. Rev. 360 (2018) 77–91.
[115] M. Kurmoo, Magnetic metal-organic frameworks, Chem. Soc. Rev. 38 (2009) 1353–1379.
[116] E. Coronado, G.M. Espallargas, Dynamic magnetic MOFs, Chem. Soc. Rev. 42 (2013) 1525–1539.
[117] G.M. Espallargas, E. Coronado, Magnetic functionalities in MOFs: from the framework to the pore, Chem. Soc. Rev. 47 (2018) 533–557.
[118] Z. Ni, J. Liu, M.N. Hoque, W. Liu, J. Li, Y. Chen, M. Tong, Recent advances in guest effects on spin-crossover behavior in Hofmann-type metal-organic frameworks, Coord. Chem. Rev. 335 (2017) 28–43.
[119] C. Wang, T. Zhang, W. Lin, Rational synthesis of noncentrosymmetric metal-organic frameworks for second-order nonlinear optics, Chem. Rev. 112 (2012) 1084–1104.
[120] V.V. Vinogradov, V.A. Milichko, E. Hey-Hawkins, A.V. Vinogradov, Metal-organic frameworks as competitive materials for non-linear optics, Chem. Soc. Rev. 45 (2016) 5408–5431.
[121] L.R. Mingabudinova, R. Medishetty, J.K. Zare, D. Mayer, M. Samoc, R.A. Fischer, Nonlinear optical properties, upconversion and lasing in metal-organic frameworks, Chem. Soc. Rev. 46 (2017) 4976–5004.
[122] Y. Xu, Q. Li, H. Xue, H. Pang, Metal-organic frameworks for direct electrochemical applications, Coord. Chem. Rev. 376 (2018) 292–318.
[123] X. Xiao, L. Zou, H. Pang, Q. Xu, Synthesis of micro/nanoscaled metal-organic frameworks and their direct electrochemical applications, Chem. Soc. Rev. 49 (2020) 301–331.
[124] L. Zhang, H. Liu, W. Shi, P. Cheng, Synthesis strategies and potential applications of metal-organic frameworks for electrode materials for rechargeable lithium ion batteries, Coord. Chem. Rev. 388 (2019) 293–309.
[125] X. Wen, Q. Zhang, J. Guan, Applications of metal-organic framework-derived materials in fuel cells and metal-air batteries, Coord. Chem. Rev. 409 (2020), 213214.
[126] R.C. Krishna Reddy, J. Lin, Y. Chen, C. Zeng, X. Lin, Y. Cai, C. Su, Progress of nanostructured metal oxides derived from metal-organic frameworks as anode materials for lithium-ion batteries, Coord. Chem. Rev. 420 (2020), 213434.
[127] M. Du, Q. Li, Y. Zhao, C. Liu, H. Pang, A review of electrochemical energy storage behaviors based on pristine metal-organic frameworks and their composites, Coord. Chem. Rev. 416 (2020), 213341.
[128] J.A. Cruz-Navarro, F. Hernandez-Garcia, G.A.A. Romero, Novel applications of metal-organic frameworks (MOFs) as redox-active materials for elaboration of carbon-based electrodes with electroanalytical uses, Coord. Chem. Rev. 412 (2020), 213263.
[129] X. Cao, C. Tan, M. Sindorob, H. Zhang, Hybrid micro-/nano-structures derived from metal-organic frameworks: preparation and applications in energy storage and conversion, Chem. Soc. Rev. 46 (2017) 2660–2677.

[130] L. Wang, Y. Han, X. Feng, J. Zhou, P. Qi, B. Wang, Metal-organic frameworks for energy storage: batteries and supercapacitors, Coord. Chem. Rev. 307 (2016) 361–381.
[131] B. Xu, H. Zhang, H. Mei, D. Sun, Recent progress in metal-organic framework-based supercapacitor electrode materials, Coord. Chem. Rev. 420 (2020), 213438.
[132] R.R. Salunkhe, Y.V. Kaneti, J. Kim, J.H. Kim, Y. Yamauchi, Nanoarchitectures for metal-organic framework-derived nanoporous carbons toward supercapacitor applications, Acc. Chem. Res. 49 (2016) 2796–2806.
[133] D. Wang, Z. Liang, S. Gao, C. Qu, R. Zou, Metal-organic framework-based materials for hybrid supercapacitor application, Coord. Chem. Rev. 404 (2020), 213093.
[134] S. Kempahanumakkagari, K. Vellingiri, A. Deep, E.E. Kwon, N. Bolan, K. Kim, Metal-organic framework composites as electrocatalysts for electrochemical sensing applications, Coord. Chem. Rev. 357 (2018) 105–129.
[135] C. Liu, J. Li, H. Pang, Metal-organic framework-based materials as an emerging platform for advanced electrochemical sensing, Coord. Chem. Rev. 410 (2020), 213222.
[136] S. Liu, C. Lai, X. Liu, B. Li, C. Zhang, L. Qin, D. Huang, H. Yi, M. Zhang, L. Li, W. Wang, X. Zhou, L. Chen, Metal-organic frameworks and their derivatives as signal amplification elements for electrochemical sensing, Coord. Chem. Rev. 424 (2020), 213520.
[137] R. Kaur, K. Kim, A.K. Paula, A. Deep, Recent advances in the photovoltaic applications of coordination polymers and metal organic frameworks, J. Mater. Chem. A 4 (2016) 3991–4002.
[138] J.D. Rocca, D. Liu, W. Lin, Nanoscale metal-organic frameworks for biomedical imaging and drug delivery, Acc. Chem. Res. 44 (2011) 957–968.
[139] C. He, D. Liu, W. Lin, Nanomedicine applications of hybrid nanomaterials built from metal-ligand coordination bonds: nanoscale metal-organic frameworks and nanoscale coordination polymers, Chem. Rev. 115 (2015) 11079–11108.
[140] M. Giménez-Marqués, T. Hidalgo, C. Serre, P. Horcajada, Nanostructured metal-organic frameworks and their bio-related applications, Coord. Chem. Rev. 307 (2016) 342–360.
[141] R.F. Mendes, F. Figueira, J.P. Leite, L. Gales, F.A.A. Paz, Metal-organic frameworks: a future toolbox for biomedicine? Chem. Soc. Rev. 49 (2020) 9121–9153.
[142] D. Wang, D. Jana, Y. Zhao, Metal-organic framework derived nanozymes in biomedicine, Acc. Chem. Res. 53 (2020) 1389–1400.
[143] S. Rojas, A. Arenas-Vivo, P. Horcajada, Metal-organic frameworks: a novel platform for combined advanced therapies, Coord. Chem. Rev. 388 (2019) 202–226.
[144] W. Zhu, J. Zhao, Q. Chen, Z. Liu, Nanoscale metal-organic frameworks and coordination polymers as theranostic platforms for cancer treatment, Coord. Chem. Rev. 398 (2019), 113009.
[145] G. Lan, K. Ni, W. Lin, Nanoscale metal-organic frameworks for phototherapy of cancer, Coord. Chem. Rev. 379 (2019) 65–81.
[146] K. Ni, T. Luo, G.T. Nash, W. Lin, Nanoscale metal-organic frameworks for cancer immunotherapy published as part of the accounts of chemical research special issue “chemistry in cancer immunotheranostics”, Acc. Chem. Res. 53 (2020) 1739–1748.
[147] J. Liu, J. Huang, L. Zhang, J. Lei, Multifunctional metal-organic framework heterostructures for enhanced cancer therapy, Chem. Soc. Rev. (2021), https://doi.org/10.1039/d0cs00178c.
[148] A. Pandey, N. Dhas, P. Deshmukh, C. Caro, P. Patil, M.L. García-Martín, B., organic frameworks for cancer therapy, imaging, and biosensing: a state-of-the-art review, Coord. Chem. Rev. 409 (2020), 213212.
[149] P. Cheng, Lanthanide metal-organic frameworks. Structure and Bonding 163 D.M.P. Mingos.

[150] B. Li, H. Wen, Y. Cui, G. Qian, B. Chen, Multifunctional lanthanide coordination polymers, Prog. Polym. Sci. 48 (2015) 40–84.
[151] F. Saraci, V. Quezada-Novoa, P.R. Donnarumm, A.J. Howarth, Rare-earth metal-organic frameworks: from structure to applications, Chem. Soc. Rev. 49 (2020) 7949–7977.
[152] A. Alzamly, M. Bakiro, S.H. Ahmed, M.A.A.R. Eaqbi, H.L. Nguyen, Rare-earth metal-organic frameworks as advanced catalytic platforms for organic synthesis, Coord. Chem. Rev. 425 (2020), 213543.
[153] S.A. Younis, N. Bhardwaj, S.K. Bhardwaj, K. Kim, A. Deep, Rare earth metal-organic frameworks (RE-MOFs): synthesis, properties, and biomedical applications, Coord. Chem. Rev. 429 (2021), 213620.
[154] B. Yan, Luminescence response mode and chemical sensing mechanism for lanthanide functionalized metal-organic frameworks hybrids, Inorg. Chem. Front. 8 (2021) 201–233.
[155] Y. Zhou, B. Yan, Imparting tunable and white-light luminescence to a nanosized metal-organic framework by controlled encapsulation of lanthanide cations, Inorg. Chem. 53 (2014) 3456–3463.
[156] N. Sun, B. Yan, Near-infrared emission sensitization of lanthanide cation based on Ag^{+} functionalized metal-organic frameworks, J. Alloys Compd. 765 (2018) 63–68.
[157] X. Xu, B. Yan, Intercalation of lanthanide cations to a layer-like metal-organic framework for color tunable and white light emission, Dalton Trans. 44 (2015) 1178–1185.
[158] X. Xu, B. Yan, Novel photofunctional hybrid materials (alumina and titania) functionalized with both MOF and lanthanide complexes through coordination bonds, RSC Adv. 4 (2014) 38761–38768.
[159] X. Lian, B. Yan, Multi-component luminescent lanthanide hybrids of both functionalized IR-MOF-3 and SBA-15, New J. Chem. 39 (2015) 5898–5901.
[160] H. Weng, B. Yan, Cadmium metal-organic frameworks: RE^{3+} ions functionalized assembly, fluorescence tuning and polymer film preparation, New J. Chem. 40 (2016) 3732–3737.
[161] G. Jia, B. Yan, Lanthanide functionalized hybrid materials of polyoxometallate based on metal-organic frameworks for multi-color luminescence, New J. Chem. 41 (2017) 12795–12800.
[162] B. Wang, B. Yan, Polyoxometalate-based metal-organic frameworks NENU-5 hybrid materials for photoluminescence tuning by introducing lanthanide ions and their functionalized soft ionogels/thin film, CrystEngComm 21 (2019) 1186–1192.
[163] B. Wang, B. Yan, Tunable multi-color luminescence and white emission in lanthanide ion functionalizedpolyoxometalate-based metal-organic frameworks hybrids and fabricated thin films, J. Alloys Compd. 777 (2019) 415–442.
[164] J. Ma, B. Yan, Novel hybrid materials of lanthanide coordination polymers ion exchanged Mg-Al layered double hydroxide: multi-color photoluminescence and white color thin film, Dyes Pigments 153 (2018) 266–274.
[165] C. Liu, B. Yan, Photofunctional nanocomposites based on the functionalization of metal-organic framework by up/downconverion luminescent nanophosphors, New J. Chem. 39 (2015) 1125–1131.
[166] T. Duan, B. Yan, Hybrids based on lanthanide ions activated yttrium metal organic frameworks: functional assembly, polymer film preparation and luminescence tuning, J. Mater. Chem. C 2 (2014) 5098–5104.
[167] C. Liu, B. Yan, Photoactive hybrid polymer films incorporated with both lanthanide complex and ZIF–8 for selectively excited multi-color luminescence, Eur. J. Inorg. Chem. (2015) 279–287.

[168] D. Mo, Z. Wang, K. Sun, X. Xie, J. Zhang, K. Cai, Core-shell metal-organic frameworks and hierarchical host–guest structures toward water-stable luminescence of lanthanide complexes in encoding beads, J. Mater. Chem. C 8 (2020) 11110–11118.
[169] J. Ma, L. Zhao, C. Jin, B. Yan, Luminescence responsive composites of rare earth metal-organic frameworks covalently linking microsphere resin, Dyes Pigments 173 (2020), 107883.
[170] J. Ma, B. Yan, Multi-component hybrid soft ionogels for photoluminescence tuning and sensing organic solvent vapors, J. Colloid Interface Sci. 513 (2018) 133–140.
[171] J. Ma, B. Yan, Multi-component luminescence responsive Eu^{3+}/Tb^{3+} hybrids based with metal-organic frameworks and zeolites A, Spectrochim. Acta A 7 (2019) 5652–5657.
[172] W. Ma, B. Yan, Lanthanide functionalized MOFs thin films as effective luminescent materials and chemical sensor for ammonia, Dalton Trans. 49 (2020) 15663–15671.

Chapter 2

Rare earth luminescence, MOFs luminescence, rare earth MOFs hybrid materials luminescence, luminescence response, and chemical sensing

2.1 Rare earth ion luminescence

Rare earth (RE) ions and their compounds are a huge treasure of luminescent materials, which can behave as both luminescent center and host. Almost all kinds of RE ions can be utilized in phosphors, and they have become the most useful species for commercial applications due to their typical luminescence processes and mechanisms. Trivalent rare earth ions (RE^{3+}) have excellent photophysical properties such as sharp emission spectra for high color purity, broad emission bands covering the ultraviolet (UV)-visible-near-infrared (NIR) region, a wide range of lifetimes from the microsecond to the second level, and high luminescence quantum efficiencies, etc. These properties of rare earth compounds have attracted much attention for a wide variety of applications in the fields of lighting devices (television and computer displays, optical fibers, optical amplifiers, lasers) and biomedical analysis (medical diagnosis and cell imaging). However, it is difficult for RE ions to directly behave as luminescent materials because of their poor light absorption abilities. As is known, the f-f transitions of RE ions are spin forbidden, so it is hard to generate efficient emission by their direct excitation. The doping of RE ions into special matrices such as metallic oxides and oxysalts is a traditionally efficient method to obtain excellent phosphors, in which the host absorption is the main energy origin for the energy transfer and sensitization of the luminescence of active RE ions. In addition, the charge transfer state (CTS) between some RE ions and their coordinated oxygen atoms also appear in some special phosphor systems. These two main wide energy absorptions can be further excited to activate RE ions, resulting in their effective luminescence. In addition, the f-f transition absorption of RE ions themselves may also be observed [1–4].

Rare Earth Metal-Organic Framework Hybrid Materials for Luminescence Responsive Chemical Sensors
https://doi.org/10.1016/B978-0-323-91236-5.00011-6

2.1.1 Atomic spectral term ($^{2S+1}L_J$) and energy level transition of trivalent rare earth (RE^{3+}) ions

The incompletely filled 4f shell of RE ions possesses single electrons and produces the nonzero spin quantum number (S). So, the spin angular momentum of RE ions splits and disturbs their orbital angular momentum (L) in the same space region, resulting in the fine splitting of orbital energy levels, the so-called spin-orbit coupling (SOC) effect. RE ions possess many single electrons and have large quantum numbers (L and S), whose SOC effect is very strong. Therefore, the common spectral term ^{2S+1}L based S and L ($2S+1$ here means the spin multiplicity) cannot show the fine energy levels of RE ions, and so it is necessary to consider the strong SOC effect and introduce the angular quantum number (J) combined with L and S. Subsequently, the electron configurations and energy levels of RE ions are presented as a spectral subterm $^{2S+1}L_J$ [4]. Therefore, for RE^{3+} ions generally, the atomic spectral term is directly represented as the atomic spectral subterm.

For all the RE ions, the number of single electrons in their 4f orbital shows a symmetrical distribution centered with the Gd^{3+} ion, so there is a common rule for their quantum number (L and S). For L and J, a so-called "gadolinium breaking effect" shows two different formulas: in front of Gd^{3+}, $J=L-S$, $L=-1/2(n(n-7))$ and behind Gd^{3+}, $J=L+S$, $L=-1/2((n-7)(n-14))$, where L can be represented as S, P, D, F, G, H, and I (using spectral symbols), respectively. So being centered on Gd^{3+}, the light RE ion (in front of Gd^{3+}) and the heavy one (behind Gd^{3+}) show the same value of L and S symmetrically except for the different J value. Fig. 2.1 presents a substantial part of the energy levels originating from the $4f^n$ configuration as a function of n for the RE^{3+} ions (the width of the bars in the figure gives the order of magnitude of the crystal field splitting). It shows the great number of possible energy level transitions for these RE^{3+} ions, revealing the great potential of RE^{3+} ions and their compounds as luminescent materials [4,5].

2.1.2 Luminescence and spectroscopy of trivalent rare earth (RE^{3+}) ions

RE^{3+} ions such as Sc^{3+}, Y^{3+}, La^{3+}, and Lu^{3+} possess a stable, empty, or filled state, so they are optically inert ions and cannot exhibit photophysical behavior. Gd^{3+} has a half-empty 4f shell and produces a very stable $^8S_{7/2}$ ground state with excitation energy higher than 32,000 cm^{-1}, whose emission is situated in the ultraviolet region (<318 nm). The $^8S_{7/2}$ level belongs to a nondegenerate orbital and cannot be split by the crystal field, so its low-temperature emission spectrum only shows a line peak originated from the transition ($^6P_{7/2} \rightarrow {}^8S_{7/2}$). Despite having the same electron configuration as Eu^{2+}, the $4f^65d$ state of Gd^{3+} is situated at a relatively high energy state, and it is impossible to observe the band emission from the $4f^65d \rightarrow 4f^7$ transition. The luminescence of Gd^{3+}

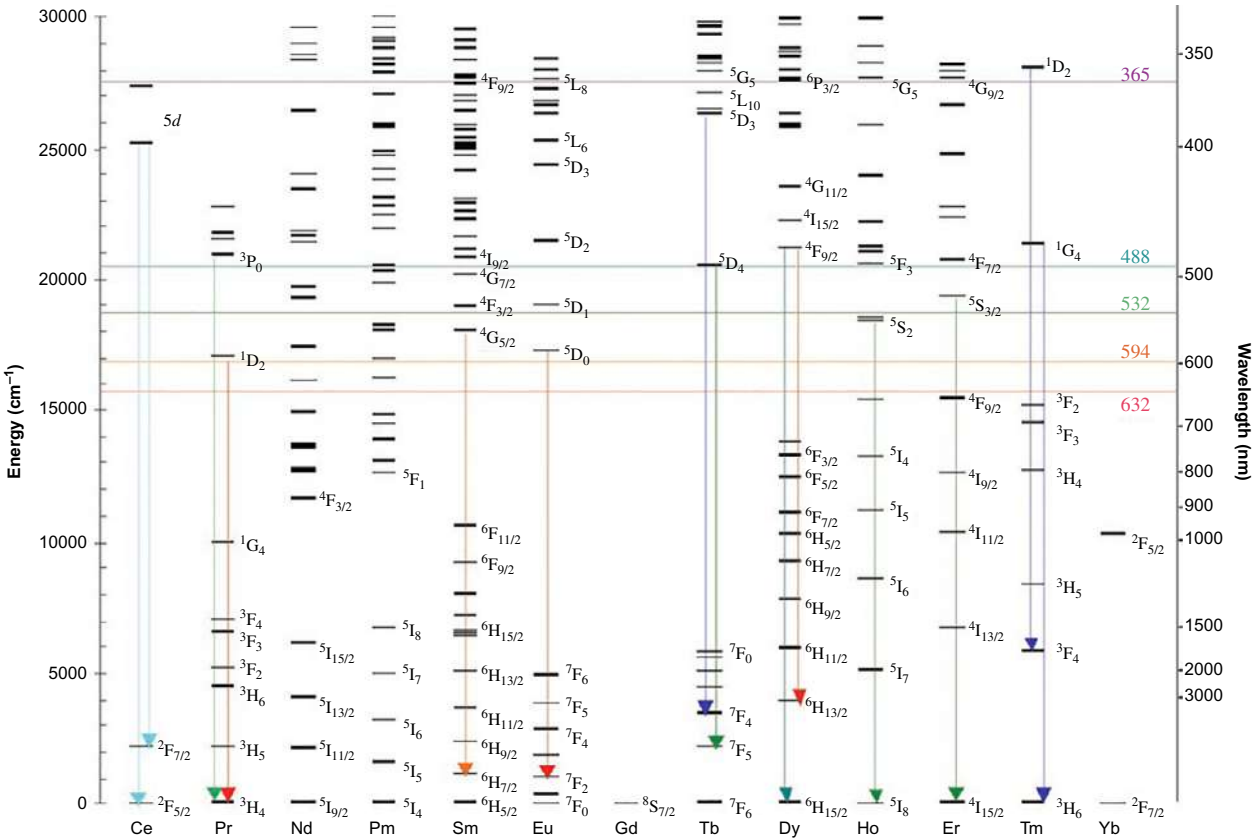

FIG. 2.1 Energy level diagram of RE^{3+} ions with dominant visible emission transitions observed in silicate glasses designated by arrows representing the approximate color of the fluorescence. Horizontal lines extending across the diagram designate the location of common organic label excitation sources labeled by wavelength in nanometers. The 365-nm line was used to excite the RE^{3+} ions. *(Reproduced with permission from M. J. Dejneka, A. Streltsov, S. Pal, A. G. Frutos, C. L. Powell, K. Yost, P. K.Yuen, U. Muller, J. Lahiri, Rare earth-doped glass microbarcodes. PNAS 100 (2003) 389–393. Copyright 2003 National Academy of Sciences of the United State of America.)*

mainly comes from the 6P → 8S transition, a line emission at 313 nm. At its high energy position, the transition emission can be observed in the host lattice with high energy optical absorption. In addition, the energy transfer is easy from the 6*P* energy level of Gd^{3+} to other RE^{3+} ions or host lattice groups. Therefore Gd^{3+} generally is considered as an inert ion just like Sc^{3+}, Y^{3+}, La^{3+}, and Lu^{3+} [6–10].

The emission spectral lines of Eu^{3+} are situated in a red color region, which corresponds to its transitions ($4f^6$) from the excited state $^5D_0$ to ^7F_J ($J = 0, 1, 2, 3, 4, 5, 6$). Because the $^5D_0$ level Eu^{3+} cannot be split by the crystal field ($J = 0$), the crystal field splitting of its ^7F_J levels is produced by the splitting of the emission transitions. The emission from its higher ^5D energy level ($^5D_1$, $^5D_2$, $^5D_3$) can also be observed. $^5D_0 \rightarrow {}^7F_J$ emission is suitable to determine the spectral features of Eu^{3+}. If Eu^{3+} is located in the lattice with inversion symmetry, the electric dipole transitions between levels of its $4f^n$ configuration are strictly forbidden by the parity selection rule, and only its weak magnetic dipole transitions or vibronic electric dipole transitions occur. If Eu^{3+} is situated in the lattice without inversion symmetry, its electric dipole transition is not strictly forbidden and shows weak spectral lines, the so-called forced electric dipole transition. These transition emissions need two conditions: (i) the crystallographic lattice of Eu^{3+} does not have an inversion symmetry center; (ii) the charge transition state is situated at the low energy level [6–10]. According to the split number of ^7F_J energy level and the transition number of the $^5D_0 \rightarrow {}^7F_J$ transition of Eu^{3+}, it is easy to predict the point group symmetry of the environment where Eu^{3+} is situated: (a) When Eu^{3+} is situated in the lattice with a strict inversion symmetry center, its allowed magnetic-dipole transition $^5D_0 \rightarrow {}^7F_1$ with orange light (about 590 nm) is dominant. (b) When Eu^{3+} is situated in the point group symmetry C_i, C_{2h} and D_{2h}, its $^5D_0 \rightarrow {}^7F_1$ transition shows three spectral lines for the splitting of three states from the completely removed degeneration of the $^7F_1$ level in the symmetric crystal field. (c) When Eu^{3+} is situated in the point group symmetry C_{4h}, D_{4h}, D_{3d}, S_6, C_{6h}, and D_{6h}, its $^7F_1$ level splits into two states to show two $^5D_0 \rightarrow {}^7F_1$ transition spectral lines. (d) When Eu^{3+} is situated in the point group symmetry Th and O_h with a high cubic symmetry, its $^7F_1$ level only has one split and shows one $^5D_0 \rightarrow {}^7F_1$ transition spectral line. On the other hand, when Eu^{3+} is situated in the lattice with a deviated inversion symmetry center, its forbidden electric dipole transition $^5D_0 \rightarrow {}^7F_0$ with red light (about 615 nm) is dominant: (i) when Eu^{3+} is situated in the point group symmetry C_s, C_n, and C_{nv}, its $^5D_0 \rightarrow {}^7F_0$ transition emission appears at 580 nm because the expanding crystal field potential energy surface transition needs to involve an odd-order crystal field term. (ii) The $^5D_0 \rightarrow {}^7F_0$ transition of Eu^{3+} cannot be split by the crystal field and shows only one emission peak, and then each peak corresponds to one crystal lattice. Therefore the number of its $^5D_0 \rightarrow {}^7F_1$ emission peaks can be utilized to predict the lattice number of point group symmetry where Eu^{3+} is located (C_s, C_n, and C_{nv}). (iii) When Eu^{3+} is situated in point groups with

low symmetry, such as triclinic crystal system C_1 and monoclinic crystal system C_s, C_2, $^7F_1$, and $^7F_2$ levels completely remove the degeneration state and are split into three and five sublevels, respectively. Subsequently, there are one $^5D_0 \rightarrow {}^7F_0$ peak, three $^5D_0 \rightarrow {}^7F_1$ peaks, and five $^5D_0 \rightarrow {}^7F_2$ peaks, respectively, where the $^5D_0 \rightarrow {}^7F_2$ transition shows the dominant red emission [1,6].

The Tb^{3+}' emission is originated from its $^5D_4 \rightarrow {}^7F_J$ transition, mainly in the green color region. In addition, the $^5D_3 \rightarrow {}^7F_J$ transition from the high energy level shows an emission mainly in the blue region, which is easily quenched by the crossing relaxation energy transfer process $Tb(^5D_3)+Tb(^7F_6) \rightarrow Tb(^5D_4)+Tb(^7F_6)$. The Sm^{3+} emission is situated in the orange-red color region, corresponding to $^4G_{5/2} \rightarrow {}^6H_J$ ($J = 5/2, 7/2, 9/2, 11/2, 13/2$) [7]. Dy^{3+} shows two main emissions in the visible light region, corresponding to $^4F_{9/2} \rightarrow {}^6H_{15/2}$ (470–500 nm, blue region) and $^4F_{9/2} \rightarrow {}^6H_{13/2}$ (570–600 nm, yellow region) [8]. Among them, the yellow emission $^4F_{9/2} \rightarrow {}^6H_{13/2}$ (570–600 nm) belongs to a hypersensitive transition. The luminescence color of Dy^{3+} often is close to white. When the hypersensitive transition of the host lattice is dominant, it shows a yellow color emission. The yellow/blue (Y/B) ratio is the important luminescence parameter. The Pr^{3+} emission color strongly depends on the host lattice of doped Pr^{3+}. The red emission derives from its $^1D_2$ level, and the green color emission comes from its $^3P_0$ level. In addition, it can show a blue emission from the $^1S_0$ level and a visible emission from the $^4f^5d$ state [8]. Nd^{3+} ($4f^3$), Er^{3+} ($4f^{11}$), and Yb^{3+} ($4f^{13}$) often show the emission in the near infrared (NIR) region. For Nd^{3+}, its emission is ascribed to three transitions of $^4F_{3/2} \rightarrow {}^4I_J$ ($J = 9/2$, 11/2, and 13/2) [11]. For Yb^{3+}, it shows a typical emission coming from its $^2F_{5/2} \rightarrow {}^2F_{7/2}$ transition. Er^{3+} exhibits emission in both NIR regions ($^4I_{13/2} \rightarrow {}^4I_{15/2}$) and the visible region ($^2H_{11/2} \rightarrow {}^4I_{15/2}$ and $^4S_{3/2} \rightarrow {}^4I_{15/2}$ transition) [8]. Tm^{3+} shows a weak blue emission originating from the $^1G_4 \rightarrow {}^3H_6$ transition [8]. Besides the line emission, some RE^{3+} ions also show a wideband emission, such as trivalent ions (Ce^{3+}, Pr^{3+}, and Nd^{3+}) and divalent ions (Eu^{2+}, Sm^{2+}, and Yb^{2+}). Ce^{3+} has only one 4f electron with excited state electron configuration $5d^1$, whose ground state $4f^1$ contains two energy levels ($^2F_{5/2}$ and $^2F_{7/2}$). So Ce^{3+} exhibits two $5d \rightarrow 4f$ transition emissions. The Ce^{3+} emission generally is situated at the ultraviolet or blue region. In a few systems, the long wavelength emission in the green or red region also can be found, in which the $5d^1$ energy level is relatively low and the crystal field strength is high [9]. The most popular divalent ion is Eu^{2+} ($4f^7$), whose $5d \rightarrow 4f$ emission changes in the range from long wavelength ultraviolet to yellow regions. Eu^{2+} mainly shows a wide band emission due to the $4f^65d \rightarrow 4f^7$ transition, which also shows line emissions under low-temperature conditions [10].

2.2 Rare earth complex molecule luminescence

Rare earth coordination compounds or complexes possess high coordination numbers and a multidimensional structure due to RE ions' large ion radius; most

of them use oxygen as the coordinated atom involving ligands of carboxylic acids, β-diketones, macrocyclic compounds, etc. RE ions only possess weak light absorption because the molar absorption coefficients of most transitions in the absorption spectra of RE^{3+} are smaller than 10 L mol^{-1} cm^{-1}; only a very limited amount of radiation is absorbed by direct excitation in the 4f levels to obtain weak luminescence. To overcome this disadvantage, Weissman has discovered an "antenna effect" within the RE complexes of organic ligands, which is based on excitation in an absorption band of the organic ligand and the subsequent intramolecular energy transfer between the organic ligands and RE ions (as shown in Fig. 2.2) [11–13]. Upon irradiation with ultraviolet radiation, organic molecules are excited to a vibrational level of the excited singlet state (S_i) and then may undergo a fast internal conversion process (IC) to relax to the lowest vibrational level of the S_1 state, which is a very quick process and easily occurs in solution due to the interaction with solvent molecules. Commonly, the excited singlet state of the organic molecule can be deactivated radiatively to the ground state, resulting in molecular fluorescence with the spin, which allows transition between two electronic states with the same spin multiplicity from S_1 to S_0. On the other hand, the excited singlet state may occur as conversion with different spin multiplicity from the singlet S_i to triplet T_i by microscopic quantum mechanics perturbation, called intersystem crossing (ISC). The excited triplet state of the organic molecule can be deactivated radiatively to the singlet ground state, resulting in molecular phosphorescence with the spin-forbidden transition from T_1 to S_0.

When an organic molecule behaves like a ligand in rare earth complexes through coordination interaction, the complex may undergo a nonradiative transition from the triplet state to an excited state of the RE ion through a so-called intramolecular energy transfer process. (The detailed scheme is provided in Fig. 2.3 to discuss the luminescence of rare earth MOF hybrid materials.) The sensitized RE^{3+} ion may undergo a radiative transition to a lower 4f state by characteristic line-like photoluminescence or may be deactivated by nonradiative processes to produce heat. From the emission transition position of

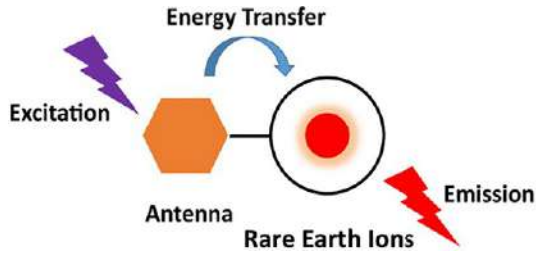

FIG. 2.2 Scheme for luminescence mechanism of rare earth complex molecules. *(Reproduced with permission from T. N. Nguyen, F. M. Ebrahim, K. C. Stylianou, Photoluminescent, upconversion luminescent and nonlinear optical metal-organic frameworks: from fundamental photophysics to potential applications. Coord. Chem. Rev. 377 (2018) 259–306. Copyright 2018 Elsevier.)*

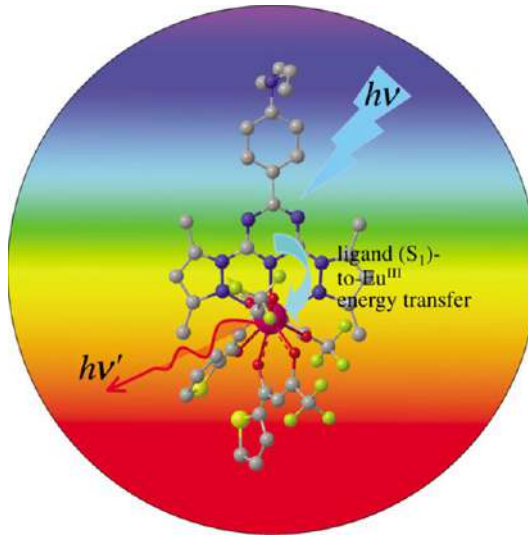

FIG. 2.3 The scheme for the singlet direct energy transfer pathway diagram *(bottom)* in complex $Eu(TTA)_3L$ (L = *N*,*N*-dialkyl aniline moiety-modified dipyrazolyltriazine derivative). *(Reprinted with permission from C. Yang, L. Fu, Y. Wang, J. Zhang, W. Wong, X. Ai, Y. Qiao, B. Zou, L. Gui, A highly luminescent europium complex showing visible-light-sensitized red emission: direct observation of the singlet pathway. Angew. Chem. Int. Ed. 43 (2004) 5010–5013. Copyright 2004 John Wiley & Sons Ltd.)*

common RE^{3+} ions, certain resonance emission levels can be determined: $^4G_{5/2}$ for Sm^{3+} (17,800 cm^{-1}), $^5D_0$ for Eu^{3+} (17,250 cm^{-1}), $^5D_4$ for Tb^{3+} (20,500 cm^{-1}), and $^4F_{9/2}$ for Dy^{3+} (20,960 cm^{-1}), respectively. If the RE^{3+} is excited to a nonemitting level, the excitation energy is dissipated via nonradiative processes until a resonance level is reached either directly by excitation in the 4f levels or indirectly by energy transfer. In this case, radiative transitions will compete with the nonradiative processes to display RE^{3+}-centered emission. So the final line emission of the RE^{3+} ion depends on the minimization of nonradiative deactivation or other emissions of molecular fluorescence and phosphorescence. To populate a resonance level of an RE^{3+} ion, the prerequisite is the lowest triplet state (Tr) of the ligand, or the complex is higher than the resonant energy level of the RE^{3+} ion. Thus the intramolecular energy transfer within the RE complexes may depend on the match between the energy of the lowest triplet level of the ligands or complexes and the resonance level of RE^{3+}. Because the position of the triplet level depends on the type of ligand, it is therefore possible to control the luminescence intensity observed for a given RE^{3+} ion by variation of the ligand [14]. The SOC interaction endows the triplet state with a partially singlet character to relax the spectral selection rules. The efficiency of the energy transfer is proportional to the overlap between the phosphorescence spectrum of the ligand and the absorption spectrum of the

RE^{3+} ion. The overlap decreases as the triplet state energy increases. Therefore the intramolecular energy migration efficiency from the organic ligands to the central RE^{3+} is the most important factor influencing the luminescence properties of RE complexes, and it depends mainly on the two energy transfer processes. One is from the lowest triplet state energy of the organic ligand to the resonant energy level from Dexter's resonant exchange interaction theory (Eq. 2.1) [15]:

$$k_{ET} = P_{da}\exp(-2R_{da}/L) = 2\pi Z^2 \int F_d(E)E_a(E)\mathrm{dE}\exp(-2R_{da}/L) \qquad (2.1)$$

where k_{ET} is the rate constant of the intermolecular energy transfer and Pda is the transition probability of the resonant exchange interaction. $2\pi Z^2/R$ is the constant relating to the specific mutual distance between the central RE^{3+} ion and its coordinated atoms. $F_d(E)$ and $E_a(E)$ are the experimental luminescent spectrum of the energy donor (ligands) and the experimental absorption spectrum of the energy acceptor (RE^{3+}), respectively; R_{da} is the intermolecular distance between donor atoms and acceptor atoms, and L is the van der Waals radius. Both R_{da} and L may be constant in intramolecular transfer processes, so k_{ET} is proportional to the overlap of $F_d(E)$ and $E_a(E)$. The other is the inverse energy transition of the thermal deactivation mechanism, shown as follows (Eq. 2.2) [16,17]:

$$k(T) = A\exp(-\Delta E/RT) \qquad (2.2)$$

Both of the two processes represent the overlap spectrum of RE^{3+}. With the decrease in the energy difference between the triplet state energy of ligands and RE^{3+}, the overlap of $F_d(E)$ and $E_a(E)$ is increased. So, it can be concluded that the larger the overlap between the luminescent spectrum of organic ligands and the emissive energy of RE^{3+}, the larger the intramolecular energy rate constant k_{ET}. In addition, the activation energy ΔE in Eq. (2.2) is equal to the energy difference ΔE(Tr-RE^{3+}), while from the formula, the inverse energy transfer rate constant $k(T)$ increased with decreasing ΔE(Tr-RE^{3+}) [18–21]. Therefore there should exist an optimal energy difference between the triplet position of organic ligands and the emissive energy level RE^{3+}; a larger or a smaller ΔE(Tr-RE^{3+}) will decrease the luminescence of RE complexes. Another possibility for sensitizing RE^{3+} luminescence is via *charge transfer states* [22–24]. This is especially the case for RE^{3+} ions that can easily be reduced to the divalent state (redox-sensitive rare earth ions), like Sm^{3+}, Eu^{3+}, and Yb^{3+}, where light can be absorbed by an intense ligand-to-metal charge transfer state (LMCT state) from which the excitation energy can be transferred to the 4f levels of the RE^{3+} ion. This process only works well if the LMCT state lies at high-enough energy. Low-lying LMCT states will partially or totally quench the luminescence. In the case of Eu^{3+}, metal-centered luminescence is totally quenched if the LMCT energy is less than 25,000 cm^{-1} [25]. Also, strongly absorbing chromophores containing d-block metals can be used for sensitizing rare earth luminescence [26]. Because these chromophores absorb in general at longer

wavelengths than the more-often used organic chromophores (typically in the visible spectral region), *d-block chromophores* are especially useful for sensitizing the near-infrared luminescence of RE^{3+} ions like Nd^{3+}, Er^{3+}, and Yb^{3+}.

In addition, Kleinerman proposes a mechanism of direct transfer of energy from the excited singlet state S_1 to the energy levels of the RE^{3+} ion [27], which is now not considered to be of great importance because it is often not efficient, due to the short lifetime of the excited singlet state. In this way, the energetic constraints from the T_1 state of the ligand can be avoided. However, owing to the lack of information regarding the emission from the excited states of the coordinated ligand and the difficulties in the determination of the ligand-localized triplet-triplet absorption spectra for rare earth chelates, it has been very difficult to prove for certain which state is responsible for the energy transfer process [28]. All the experimental work conducted on the sensitization of RE chelate luminescence seems to support the triplet pathway, whereas the singlet pathway for the sensitization of the Eu complex has not been observed experimentally [29]. Yang et al. report the successful extension of the excitation window to the visible region (460 nm) for an Eu complex, which subsequently exhibits highly efficient Eu^{3+}-centered luminescence. The sensitization mechanism is shown to take place through the singlet pathway by means of time-resolved luminescence spectroscopy, which is the first observable case of excitation energy transfer from the ligand to the luminescent states of the Eu^{3+} ion through the singlet pathway in a visible light-sensitized Eu^{3+} complex (Fig. 2.3).

2.3 MOFs luminescence

A series of novel MOFs materials have been achieved as platforms for luminescent materials for their intrinsic optical and photonic properties of metal ions and organic ligands, guest species collaboratively assembled and/or encapsulated into their frameworks. A scheme of luminescence possibilities in porous MOFs materials is shown in Fig. 2.4. MOFs materials with well-defined spatial arrangements of lumophores can give rise to several interesting luminescence activities, mainly involving metal-centered luminescence (MC), ligand-centered luminescence (LC), metal-to-ligand charger transfer (MLCT), ligand-to-metal charge transfer (LMCT), ligand-ligand charge transfer (LLCT), and metal-to-metal charge transfer (MMCT). In addition, the guest encapsulated may produce a guest-induced emission and the functionalization of MOFs may lead to a change in the MOFs' luminescence. The resulting emission features depend on the nature of MOFs structure, such as the spacing and orientation between linkers, the HOMO-LUMO gap of the linkers versus the accessible states of the metal units, the electronic configuration of the metal ions, and the bonding geometry [30]. Luminescence from MOFs containing transition metal ions in the frameworks is typically centered on the linker, but can also involve the disturbance of metal ions on linkers or even form all kinds of charge

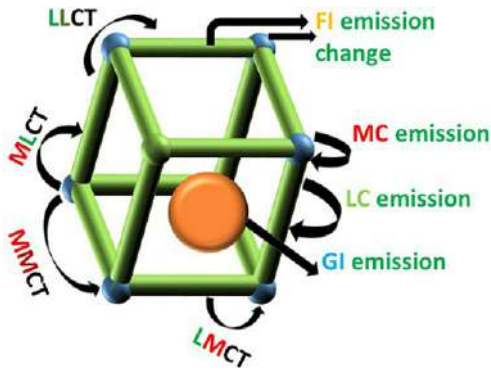

FIG. 2.4 Representation of emission possibilities in a porous MOFs: MC (metal-centered luminescence); LC (ligand-centered luminescence); MLCT (metal-to-ligand charger transfer); LMCT (ligand-to-metal charge transfer); LLCT (ligand-ligand charge transfer); MMCT (metal-to-metal charge transfer); GI (guest-induced) emission; and FI (functionalization-induced) emission change. Wherein metal centers (*blue* octahedra) are linked by organic ligands (*orange* rectangles) with an incorporated guest (*red* circle). *(Reproduced with permission from B. Yan, Luminescence response mode and chemical sensing mechanism for lanthanide functionalized metal-organic frameworks hybrids. Inorg. Chem. Front. 8 (2021) 201–233. Copyright 2021 Royal Society of Chemistry.)*

transfers between the metal ions and linker to/from each other. Paramagnetic transition metal MOFs usually show a weak emission, whose partially filled d-orbitals producing d-d ligand-field transitions may give rise to strong reabsorption and/or quenching of organic molecules' fluorescence via electron or energy transfer. MOFs of ds partition metal ions without unpaired electrons can exhibit LC luminescence [31–45].

The most common and important is LC luminescence for ligands' luminescent groups belonging to typically conjugated organic compounds to absorb in the UV and visible region, whose extended conjugation can often bring ligand HOMO/LUMO (highest occupied molecular orbital/lowest unoccupied molecular orbital) energy gaps, potentially resulting in emission energies into the visible range. For this purely LC emission, there is neither orbital mixing between ligand molecules and the metal ions coordinated nor energy transfer processes between ligand molecules. These frameworks can be considered to be arrays of single luminescence centers, whose luminescence different from the bulk ligand is primarily related to the immobilization of the ligand molecules, as upon incorporation into a framework. Certain molecular motions pertinent to the free ligand are prevented or otherwise limited, which in turn can lead to an increased quantum yield, as fewer nonradiative excitation decay pathways are available, as well as broadened emission peaks [31,33,37–42].

Additionally, the interaction between different units in MOFs may produce abundant CT luminescence. (1) LLCT emission covers luminescence from orbitals with contributions from multiple ligand molecules, or luminescence based on energy transfer from an absorber ligand to an emitter one. Typically,

aromatic MOFs ligands make their frameworks, resulting in ligand stacking, which displays the orbital mixing between ligand molecules for their π-π interactions. If multiple ligands with different oxidation/reduction potentials participate in stacking, this can also lead to charge transfer emission processes. For ligand molecules with greater separation, Förster resonance energy transfer mechanisms can move excitation from one ligand to another. However, this would depend on overlap between the emission and absorbance spectra of the two ligands, and the fact that the ligands are oriented appropriately for dipole-dipole coupling. LMCT emission can either result from orbital mixing between metal ions and ligand molecules or from absorbance on ligands followed by energy transfer onto the metal ion, where emission occurs. (2) In LMCT luminescence through orbital mixing, the LUMO is primarily based on orbitals from the metal ion, with the HOMO primarily composed of ligand orbitals. Transitions between mixed metal/ligand orbitals are responsible for luminescence, with the majority of the HOMO being contributed by metal orbitals, and the majority of the LUMO being contributed by ligand orbitals. Transition metal ions with closed d subshells (i.e., d^0 and d^{10} metals) are known to participate in LMCT luminescence, as the large gap between their HOMO and LUMO that comes from having a closed d subshell effectively prevents metal-centered emission processes. However, as metal ions with closed d subshells have high-lying LUMO energy levels; ligand molecules with similarly high-lying HOMO energy levels are generally required for LMCT in the visible range. As a result, a combination of closed subshell metals that can be partially reduced, such as the d^{10} metals Zn(II) or Cd(II) used in combination with ligand molecules that can be easily/partially oxidized and have high-lying HOMO energy levels, can often lead to LMCT luminescence. (3) In metal to ligand CT (MLCT), transitions between mixed metal/ligand orbitals are responsible for luminescence, with the majority of the HOMO being contributed by metal orbitals, and the majority of the LUMO being contributed by ligand orbitals. Like LMCT, d^{10} metals can participate in MLCT, as their large HOMO/LUMO gap prevents metal-centered luminescence in the visible range. However, as the metal and ligand contributions to the framework HOMO/LUMO are inverted relative to LMCT, so too are the oxidation/reduction requirements. Metals that can be partially oxidized, such as Cu(I) and Ag(I), can participate in MLCT luminescence with ligands that have low-lying LUMO and can be partially reduced [31,33,37–42].

MC luminescence is most often seen for MOFs materials of framework metal or doping f partition (actinide and especially lanthanide) ions. RE^{3+} ion luminescence can produce emissions covering the spectrum from UV to NIR emissions—in the case of most trivalent lanthanide ions, this emission comes from an f-f electronic transition. Because only f orbitals participate in the transition, and because these orbitals are shielded by the closed 5s and 5p orbitals, these transitions are insulated from environmental and ligand effects; luminescence resulting from these transitions is therefore extremely

sharp and characteristic for each lanthanide. However, as f-f transitions are parity-forbidden, most RE^{3+} ions have extremely poor absorption, resulting in weak emission under direct excitation. This will be discussed in more detail later [31,33,37–42].

Other guest species introduced into MOFs host produce luminescence (so-called GI (guest-induced) emission). The identity of this guest species can vary widely, from molecular organic phosphors, to fluorescent metal complexes, to metal ions or nanoparticles. These guests can either provide the entirety of an MOFs' or PCPs' or emission, or the guest's emission energy can be chosen to complement the emission from the framework, resulting in broad spectrum emission from the material. This involves three aspects: (1) "Adsorbed lumophores" through entrapping luminescent molecules or NPs in another nonemissive MOFs; (2) "Exciplex formation" through π-π interactions between adjacent conjugated linkers or between a linker and a guest molecule to produce an excited complex with typically exhibits broad, featureless luminescence; and (3) "lumophores bound to the MOFs surface" to create multifunctional MOFs. Host-guest CT depends primarily on the nature of the guest species. Dyes with conjugated or aromatic moieties can interact with the aromatic ligands of the framework through π-π interactions, resulting in Dexter electronic exchange (DEE) energy transfer mechanisms that can transfer excitation energy between the host framework and guest species. Dyes with conjugated or aromatic moieties can interact with the aromatic ligands of the framework through π-π interactions, resulting in Dexter energy transfer mechanisms that can transfer excitation energy between the host framework and guest species. Through careful selection of guest and ligand molecules with appropriate reduction/oxidation potentials, redox-mediated charge transfer can also play an important role in charge transfer, as can Förster resonance energy transfer over longer distances. When the guest species is a metal ion, often a rare earth ion, it can be chelated by free oxygen- or nitrogen-containing moieties in the ligand, or it can be located more generally in the pore. As with the previously described sensitized LMCT luminescence, chelated RE^{3+} participates in luminescence through a Dexter energy transfer process, while free RE^{3+} participates in luminescence through Förster resonance energy transfer [31,33,37–42].

Moreover, it is worth pointing out that the functionalization of MOFs through versatile PSM methods may have an influence on the luminescence of the MOFs systems, the so-called FI (functionalization-induced) emission change, which needs to be emphasized. Except for the previously mentioned guests encapsulation method for MOFs frameworks to produce GI emission, the other PSM methods to functionalize MOFs may give rise to some interaction with MOFs themselves: (1) Covalent PSM of MOFs may change the composition and structure of the linker, further changing the LC or CT luminescence. (2) Coordination PSM of MOFs may form a coordination interaction between metal ions or complexes and linkers of MOFs, affecting the LC or CT

luminescence or even producing a new MC emission for rare earth species; (3) Ionic exchange PSM of MOFs also influences the MOFs luminescence through ionic interaction, even producing the MC emission for rare earth species. This will be shown in the following discussion on luminescent rare earth functionalized MOFs hybrid materials [31,33,37–42].

2.4 Rare earth MOFs hybrid materials luminescence

For rare earth MOF hybrid materials (containing both rare earth MOFs (REMOFs) and rare earth functionalized MOFs hybrid materials (REFMOFHs)), the whole nature belongs to rare earth complexes and obeys the same intramolecular energy transfer mechanism discussed earlier. Molecular photoluminescence can be broadly characterized as fluorescence or phosphorescence. In fluorescence, an electron is excited into some singlet excited state (S_n) and quickly relaxes into the lowest singlet excited singlet state (S_1), called internal conversion (IC). Emission then occurs when the electron makes the spin-allowed transition from S_1 to the ground state (S_0). In phosphorescence, an electron is again excited into some singlet state (S_n) and relaxes into the lowest excited singlet state S_1; however, it then undergoes intersystem crossing (ISC) into the triplet excited state (T_1). Emission is associated with the spin-forbidden transition from T_1 to the ground state (S_0). For REMOFs, molecules behave as ligands or linkers to be coordinated to RE^{3+} (Fig. 2.5;

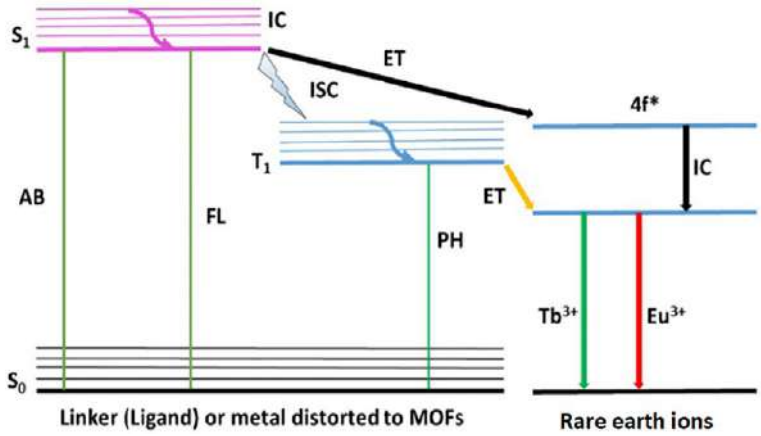

FIG. 2.5 Schematic representation of energy absorption, migration, emission, and processes in REMOFs and rare earth functionalized MOFs hybrids (REFMOFHs). A = absorption; FL = fluorescence; PH = phosphorescence; IC = internal conversion; ISC = intersystem crossing; ET = energy transfer; IC = internal conversion; S = singlet; T = triplet. Plain arrows indicate radiative transitions; curved arrows indicate nonradiative transitions. *(Reproduced with permission from B. Yan, Luminescence response mode and chemical sensing mechanism for lanthanide functionalized metal-organic frameworks hybrids. Inorg. Chem. Front. 8 (2021) 201–233. Copyright 2021 Royal Society of Chemistry.)*

right side). Consequently, by coordinating these RE^{3+} cations with conjugated organic ligands capable of transferring energy to RE^{3+} through the "antenna effect" after absorbing light energy from the environment, RE^{3+} ions can be sensitized and in turn exhibit intense luminescence. On the basis of the previously mentioned points, it can be inferred that by selecting appropriate RE^{3+} as well as suitable organic ligand/linker desired MOFs that can show excellent luminescent properties can be constructed. Here RE^{3+} serve as the central framework metal ions, and the luminescence performance depends on the type of RE^{3+} ions. For inert RE^{3+} ions such as La^{3+}, Gd^{3+}, Lu^{3+}, and Y^{3+}, their close shell electronic configurations make their MOFs materials display the luminescence of ligands or linkers. While for other RE^{3+} ions except for above mentioned, "antenna effect" appears between the T_1 of ligands or linkers to the resonant emissive energy levels of photoactive RE^{3+} ions (especially Eu^{3+} and Tb^{3+}). The effective intramolecular energy transfer process within the REMOFs may achieve the strong emission of RE^{3+}, whose efficiency is generally discussed by DEE process. This involves quenching of the donor's fluorescence by transmission of an excited electron of the donor molecule to the acceptor molecule via a nonradiative pathway applicable for short-range interactions operating between donor and acceptor (typically within 10 Å) by their orbital overlap. Although the luminescence of REMOFs depends on the energy match between ligands and RE^{3+}, when the energy match is suitable for sensitization of RE^{3+}, generally the REMOFs will mainly exhibit the luminescence of Ln^{3+} for it is the framework ion with relatively high content. On the contrary, for the situation of not having an energy match between them, the linker's luminescence displays instead of the RE^{3+} luminescence. Indeed, the high content of photoactive RE^{3+} in REMOFs limits the practical applications due to its high cost [46–52].

2.5 Luminescence for rare earth functionalized MOFs hybrid materials

For rare earth functionalized MOFs hybrid materials, luminescent RE^{3+} ions are incorporated into MOF hosts at little content and the characteristic emission of RE^{3+} is obtained. This is identical to the traditional rare earth ion doped phosphors. Just like pure luminescent REMOFs, RE^{3+} can produce an "antenna effect" and a pronounced increase in the luminescence intensity is produced through the intramolecular energy transfer process from linkers to RE^{3+}. RE^{3+} ions show weak absorbance and low quantum yields for their forbidden electronic transitions and so a strongly photo-absorbing linker is introduced to circumvent this problem. In the majority, the important energy transfer occurs from the linker T_1 to the RE^{3+} resonant emissive state. So it is significant to choose a linker for efficient intersystem crossing within the linker. The energy gap between the linker triplet state and the emitting RE excited state plays an important role in the transfer of energy from the antenna. In addition,

it needs to be stated that the relatively limited content of REFMOFHs materials often allows the existence of luminescence of the original linkers or MOFs themselves if the functionalized amount of RE^{3+} is controlled appropriately. This makes it possible to show multiple center luminescence for the same hybrid system and even to realize luminescence color tuning or white luminescence integration [53–63]. The interest in the multicolor-emitting materials, especially white light-emitting materials, stems from their wide applications in panel displays, room lighting, and other optical devices. The collaborative properties of the multiple luminescent centers in MOFs are particularly useful to develop multicolor and white-light-emitting materials. Common approaches to realize white light integration in MOFs include: (a) monochromatic emitters covering the entire visible spectrum, (b) dichromatic emitters blending blue and yellow or orange light, and (c) trichromatic emitters combining three primary colored (red, green, and blue) components. In addition, the regulation and integration of emission colors of the luminescent MOFs can also be readily implemented by modulating both chemical factors (such as RE^{3+} types and concentration) and physical parameters, like excitation wavelength. So far, tremendous efforts have been made toward the synthesis of MOFs with tunable luminescence or white light. According to the luminescent character of the main three aspects mentioned previously, these luminescent species show different spectral bands in the visible bands. For example, linker-based MOFs luminescence often is situated at the short visible region covering visible to blue to green, and even covering the wide bands of yellow color. The most commonly used RE^{3+} system is Eu^{3+}-based MOFs, whose luminescence is mainly in the red region of long wavelength, so it can be expected to realize luminescent tuning and even white luminescence integration by adjusting the luminescence center in the MOFs-based hybrid material systems, which is very useful for display and lighting devices or barcoding. Although luminescent MOFs-based OLED devices have not yet been realized, it is theoretically feasible to incorporate nanoscale electroluminescent MOFs between two conductors for such useful electronic devices. Nanoscale luminescent REFMOFHs materials are expected to be fabricated into thin films for straightforward and instant sensing devices in the future [53–63].

Duan et al. prepared a Y-MOF (MOF-76(Y), $Y(1,3,5\text{-}BTC)_n \cdot H_2O$, H_3BTC = benzene tricarboxylic acid) and then used RE^{3+} ions (Eu^{3+}, Tb^{3+}, Sm^{3+}, Dy^{3+}) as activators to obtain a series of luminescent REMOF hybrids. The color-tunable luminescence of these hybrid MOF systems is realized by adjusting the doping concentration ratio of RE^{3+} or varying the excitation wavelength (Fig. 2.6; top, left). Polymer films based on them are also prepared for the purpose of extending the application fields. Interestingly, the photoluminescent color of MOF-76(Y):10 mol% Eu/10 mol%Tb can be tuned from yellow, yellow-green, warm white to orange by changing the excitation wavelength from 300 to 380 nm. Fig. 2.6 (top, right) shows the corresponding CIE chromaticity diagram of MOF-76(Y):10 mol% Eu/10 mol%Tb under different

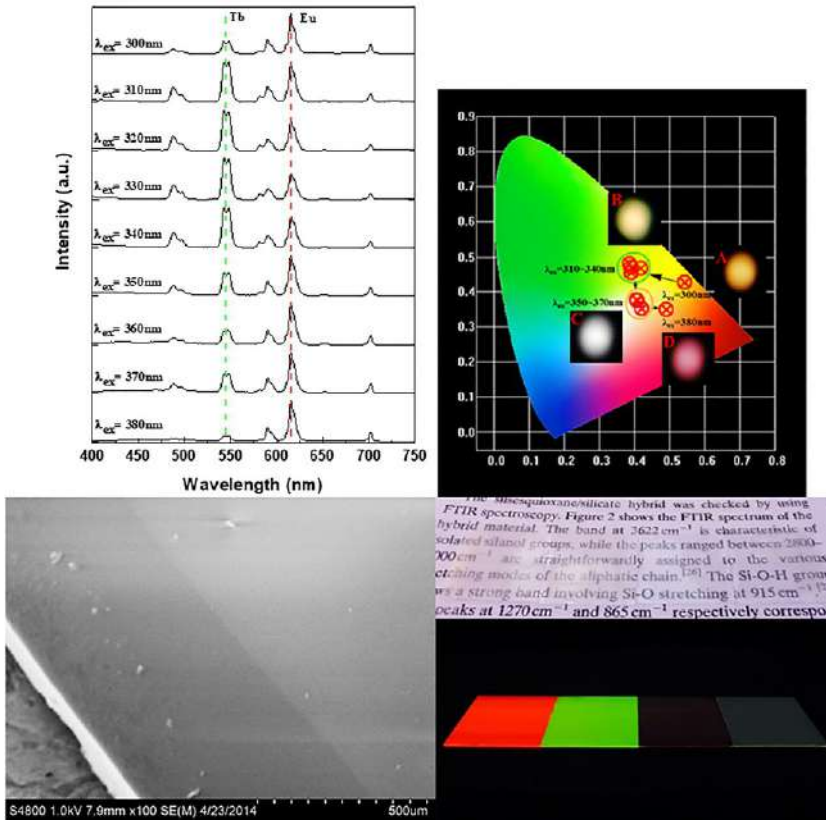

FIG. 2.6 *(Top, left)* Emission spectra of MOF-76(Y):10 mol% Eu/10 mol% Tb under excitation ranging from 300–380 nm and CIE *x-y* chromaticity diagram of MOF-76(Y):10 mol% Eu/10 mol% Tb under different excitation wavelength. *(Top, right)* The luminescence of 10 mol% Eu/10 mol% Tb under the excitation of (A) 300 nm, (B) 330 nm, (C) 360 nm, and (D) 380 nm. *(Bottom, left)* SEM image of NMOF-76:Eu polymer film. *(Bottom, right)* Images of the NMOF-76:RE^{3+} (RE = Eu, Tb, Sm, Dy) polymer film under sunlight and in the ultraviolet box (under 254 nm excitation). *(Reproduced with permission from T. Duan, B. Yan, Lanthanide ions (Eu3+, Tb3+, Sm3+, Dy3+) activated ZnO embedded zinc 2,5-pridinedicarboxylic metal organic frameworks for luminescent application. J. Mater. Chem. C 3 (2015) 2823–2830. Copyright 2014 Royal Society of Chemistry.)*

excitation wavelengths (300–380 nm). There is a little difference between the excitation spectra monitored by 616 nm (Eu^{3+}: $^5D_0 \rightarrow {}^7F_2$) and 548 nm ($Tb^{3+}$: $^5D_4 \rightarrow {}^7F_5$). The excitation band of Tb^{3+} ranging from 250-350 nm is much broader than Eu^{3+} from 250 to 310 nm; in the meantime, there is an excitation line centered at 392 nm in the excitation monitored by 616 nm (Eu^{3+}: $^5D_0 \rightarrow {}^7F_2$). Therefore when the wavelength changes from 300 nm to 380 nm, the different energy-absorbing trends of Eu^{3+} and Tb^{3+} yield various photoluminescence colors. The SEM image of NMOF-76: Eu fabricated polymer film

is shown in Fig. 2.6 (bottom, left). Both NMOF-76(Y): Eu and NMOF-76(Y): Tb fabricated polymer films show their characteristic transition emission (red and green color) under 295 nm excitation. While NMOF-76(Y): Sm and NMOF-76(Y):Dy fabricated polymer films present relatively weak luminescence, it can be observed that, besides the characteristic emission lines of Sm^{3+} and Dy^{3+}, there is a broad band located in 400–500 nm that can be attributed to the luminescence of the polymer matrix. NMOF-76(Y): Ln polymer films are transparent under sunlight, while showing emission of red, green, pink, and cold white in the ultraviolet box (254 nm excitation) (Fig. 2.6; bottom, right) [54].

Lu et al. prepared a MOF-based monolayer luminescent thin film (Fig. 2.7). A rare earth complex (Eu^{3+}, Tb^{3+} and Yb^{3+}) was introduced to the Al-MOF (MOF-253) by PSM first, and then the MOFs modified by PSM could be assembled on quartz through functional linkers with the ability to coordinate and sensitize rare earth ions (Eu^{3+}, Tb^{3+}, and Yb^{3+}), as the prepared MOF thin film is a dense and transparent monolayer with a high degree of coverage. Under the different excitation wavelengths, the thin film can emit white, red, and green light and NIR luminescence. In the structure of MOF-253, one-dimensional (1D) infinite chains of AlO_6 corner-sharing octahedral are built by connecting bpydc (bpydc = 2,2′-bipyridine-5,5′-dicarboxylic) linkers to construct rhombic-shaped pores. The functionalized plates, (Eu^{3+})-quartz, could be further immersed in a suspension of MOF-253 in toluene to realize step 3, the formation of Al-MOF(Eu^{3+})-quartz (Fig. 2.7). The Eu^{3+} ion is used as a linker to connect the MOF-253 and the functionalized plates. The transparent Eu-HBA-functionalized quartz plates (Al-MOF(Eu^{3+})-quartz) turn opaque upon contact with the suspension of MOF-253 in dry toluene under vigorous sonication. The SEM images of the modified quartz plates (Al-MOF(Eu^{3+})-quartz) reveal that the coverage degree and packing degree are both highly satisfactory, although some spots with less surface coverage can be observed in Fig. 2.7A and B (bottom). Then, the thin film is transparent in the photograph (Fig. 2.7C; bottom). The thickness of the thin film should be less than 100 nm [56].

Lu et al. further fabricated a near-UV white LED based on RE^{3+} functionalized MOF hybrids (Fig. 2.8). Lanthanide complexes are first encapsulated in MOFs (MOF-253) by the postsynthetic method (PSM), and then the modified MOF-253 is introduced into organic polymer by suitable monomer functionalization to achieve polymer hybrid materials based on MOFs. The MOF-based polymer is assembled on a near-UV GaN chip to realize a near-UV white LED (Fig. 2.8; top). Functionalization of MOF-253-Eu1-TTA with ethyl methacrylate (EMA) leads to MOF-253-Eu1-TTA-EMA (MOF-EMA). The transparent hybrid materials (MOF-PEMA) are finally prepared from the radical polymerization of the monomer EMA and MOF-EMA. The amount of EMA is kept the same and additional MOF-EMA amounts equivalent to 3.5% and 10% (weight ratio) are denoted as MOF-PEMA-3.5 and MOF-PEMA-10. Under excitation at 395 nm, the emission spectra of MOF-PEMA-3.5 and MOF-PEMA-10 are

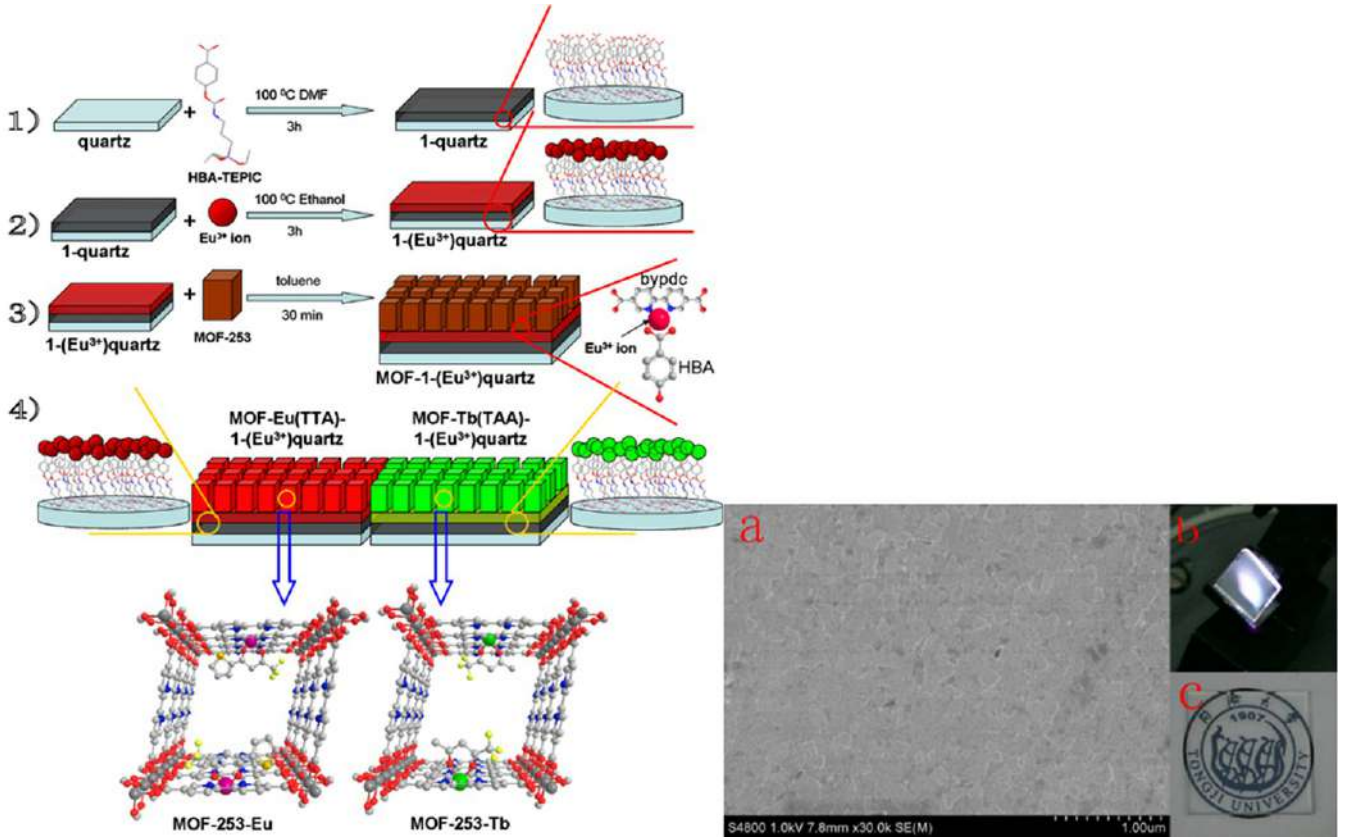

FIG. 2.7 *(Left)* The procedure to prepare the thin film materials based on PSM and functional linker: (1) A1-MOF-quartz, (2) A1-MOF-(Eu^{3+})quartz, (3) A1-MOF(Eu^{3+}) quartz and (4) A1-MOF-Eu(TTA)-1(Eu^{3+})quartz and A1-MOF-Tb(TAA)(Tb^{3+})quartz. *(Right)* SEM images of A1-MOF(Eu^{3+})quartz thin film (A) viewed from surface, the white light from A1-MOF(Eu^{3+})quartz under the light of 390 nm (B) and the photograph of A1-MOF(Eu^{3+})quartz thin film (C). *(Reproduced with permission from Y. Lu, B. Yan, A novel luminescent monolayer thin film based on postsynthetic method and functional linker. J. Mater. Chem. C 2 (2014) 5526–5532. Copyright 2014 Royal Society of Chemistry.)*

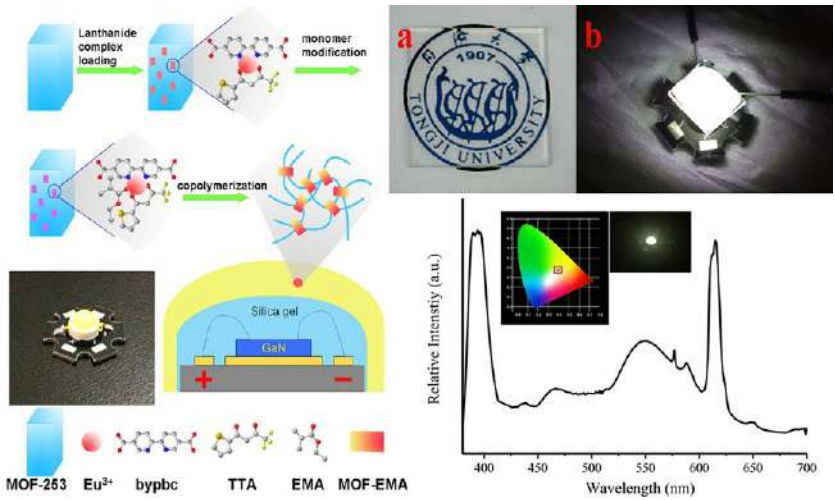

FIG. 2.8 *(Left)* Procedure for obtaining MOF-PEMA LED; the inset is the LED based on MOF-PEMA. *(Middle)* (A) The photograph of MOF-PEMA-3.5 hybrid materials and (B) the bright white light from MOF-PEMA-3.5 hybrid materials under excitation by 395 nm GaN chip. *(Right)* Electroluminescent spectrum of MOF-PEMA-10 LED; the inset is the CIE plot, and the photograph is the warm white light from the MOF-PEMA-10 LED under 350 mA. *(Reproduced with permission from Y. Lu, B. Yan, Lanthanide organic-inorganic hybrids based on functionalized metal-organic frameworks (MOFs) for near-UV white LED. Chem. Commun. 50 (2014) 15443–15446. Copyright 2014 Royal Society of Chemistry.)*

similar to MOF-253-Eu1-TTA, which is constructed by a broad band from MOF-253 (550 nm) and a narrow band from the Eu^{3+} ion (614 nm). Moreover, the luminescent intensity of MOF-PEMA-10 is obviously stronger than that of MOF-PEMA-3.5 in THF solution with the same concentration, proving the integrity of the framework during polymerization. MOF-PEMA-3.5 hybrid material has high transparency and could emit bright white light under excitation by a 395-nm GaN chip (Fig. 2.8; middle). MOF-PEMA can be further assembled on a near-UV GaN chip to realize a near-UV white LED. The electroluminescent spectrum of a MOF-PEMA-10 LED is shown in Fig. 2.8 (bottom). The MOF-PEMA-10 white LED operated at 350 mA shows warm white light with CCT of 3742 K ($X=0.39$, $Y=0.38$) and a promising CRI (R_a) of 87.34. The general CRI is designated by the symbol R_a, which is the average value of R_1 to R_8. MOF-PEMA-10 LEDs have higher R values than the commercial YAG: Ce^{3+} white LED (whose R_a is 78). The white light from the MOF-PEMA LED can be adjusted by altering the content of MOF-EMA in the polymer. The LED assembled from MOF-PEMA-3.5 shows natural white light, the color coordinates being $X=0.33$, $Y=0.34$, with a CCT of 5603 K. The white light operated by the MOF-PEMA LED can be changed from cold white to warm white [58].

Lu et al. also used a similar MOF (MOF-253) for luminescent barcoding, in which the barcoding is realized by PSM to introduce RE^{3+} (Eu^{3+}, Tb^{3+}, and Sm^{3+}). The emission intensity of each RE^{3+} is proportional to its amount in the MOF, resulting in unique luminescent barcodes that depend on the RE^{3+} ratios and compositions. Luminescence studies demonstrated that the different RE^{3+} compositions could result in unique and discernible barcoded signals. The emission of MOF-253-Tb_xEu_{1-x} displays the characteristic transition of the Eu^{3+} ion and Tb^{3+} ion with excitation at 330 nm (Fig. 2.9A; top). With an increase in the amount of Eu^{3+} ion and a decrease in the amount of Tb^{3+} ion, their characteristic emission intensities increase and decrease accordingly. That means we can quantitatively control the luminescent intensities of the two emitting RE^{3+} by controlling the RE^{3+} composition. Their relative intensities can be reflected as unique and visible color, which corresponds with three distinct barcodes. The points of emission of

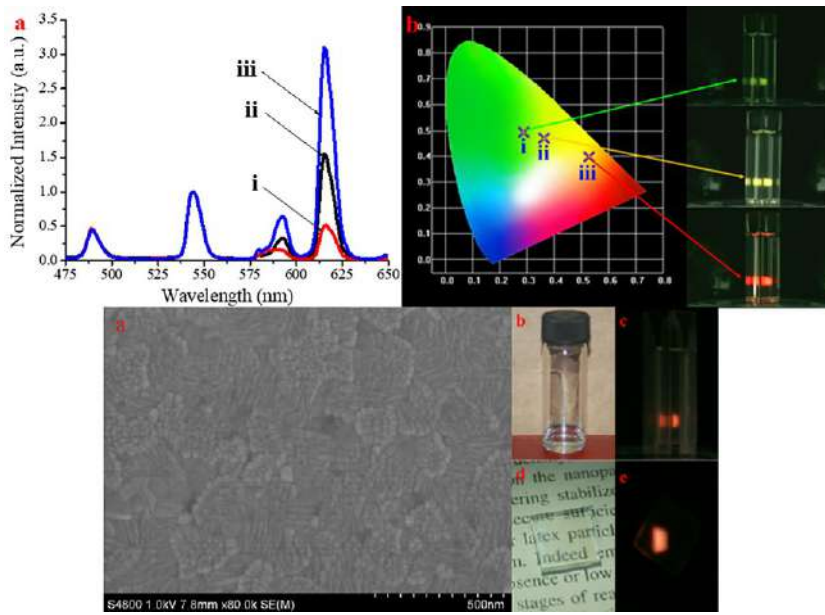

FIG. 2.9 *(Top)* (A) Eu^{3+} and Tb^{3+} emission spectra recorded under excitation at 330 nm, normalized to the Tb^{3+} signal, (B) Color-code of the barcode readout in the CIE chromaticity diagram and the photograph of the MOF-253-based barcoded material (dispersed in ethanol) under excitation at 330 nm; i, ii, and iii are MOF-253-$Tb_{0.999}Eu_{0.001}$, MOF-253-$Tb_{0.995}Eu_{0.005}$, and MOF-253-$Tb_{0.99}Eu_{0.01}$, respectively. *(Bottom)* (A) SEM of ITO glass-supported luminescent thin films of MOF-253-RE-1, the photograph of IL-MOF-RE (B) and under excitation at 330 nm (C), the photograph of thin film constructed by MOF-253-RE-1 (D) and the red light from the thin film under excitation at 330 nm (E). *(Reproduced with permission from Y. Lu, B. Yan, Luminescent lanthanide barcodes based on postsynthetic modified nanoscale metal-organic frameworks. J. Mater. Chem. C 2 (2014) 7411–7416. Copyright 2014 Royal Society of Chemistry.)*

MOF-253-$Tb_{0.95}Eu_{0.05}$, MOF-253-$Tb_{0.99}Eu_{0.01}$, and MOF-253-$Tb_{0.995}Eu_{0.005}$ in the CIE chromaticity diagram are green ($X=0.2876$, $Y=0.4915$), yellow ($X=0.3630$, $Y=0.4698$), and red ($X=0.5276$, $Y=0.3980$), respectively (Fig. 2.9B; top). An ionic liquid, 1-(2-hydroxyethyl)-3-methyl imidazolium bromide (IL), was chosen as the matrix to disperse MOF-253-RE-1, recorded as IL-MOF-RE, which is clear (about 70°C) and can emit the luminescent barcoded signal under 330 nm (Fig. 2.9B and C; bottom). ITO glass-supported luminescent thin films of MOF-253-RE-1 are prepared by direct spin-coating, like the thin films constructed by nanoscale MOF-76. In the photograph, the thin film is transparent (Fig. 2.9D; bottom) and emits the luminescent barcoded signal under 330 nm (Fig. 2.9E; bottom). From SEM images (Fig; 2.9A; bottom), the surface of the thin film is continuous and defect-free over a large area [61].

Zhou et al. developed a barcoded system based on RE^{3+} functionalized MOF films that contained multiple emission bands, which relied on tuning the emission intensities of RE^{3+} in multiple bands. Varying the filtered dye loading generated distinct ratiometric optical signatures or codes. To achieve the conceptual barcoding function of RE^{3+}@MIL-100 (In) films, they designed an encoding strategy based on tuning their emission intensities in multiple bands through a luminescence reabsorbed process. As shown in Fig. 2.10 (top), two of the emission bands of RE^{3+}@MIL-100 (In) films (488 and 544 nm emissions for Tb^{3+}@MIL-100 (In), and 616 nm and 701 nm for Eu^{3+}@MIL-100 (In) are employed for the demonstration. For the filtered dyes, fluorescein isothiocyanate (FL) and methylene blue (MB) are selected for respective Tb^{3+}@MIL-100 (In) and Eu^{3+}@MIL-100 (In) films for the reasons of high extinction coefficients and overlapping absorption spectra with only one of the two emission bands of RE^{3+}@MIL-100 (In) films. The concentrations of the dyes are adjusted in four levels. With an increase in the amount of filtered dyes, the filtered emissions intensities (I_{code}) fall accordingly, due to the reabsorbed light processes (Fig. 2.10A (bottom, left) and B (top)). At high dye concentration, the intensity of I_{code} is reduced up to 15% for Tb^{3+}@MIL-100 (In) and 33% for Eu^{3+}@MIL-100 (In) film compared the isolated RE^{3+}@MIL-100 (In) films. In contrast, the intensities of unfiltered emissions (I_{ref}) barely changed. Consequently, four ratiometric intensity ratios were generated for both Tb^{3+}@MIL-100 (In) and Eu^{3+}@MIL-100 (In) films, which gave rise to four optical codes, respectively. To facilitate the interpretation and human qualification, ratiometric optical signals are transferred to color-related codes (Fig. 2.10C and D; bottom, left). The emission bands (I_{code}/I_{ref}) are represented by distinctive colors, and their intensities are reflected in the display. As expected, it exhibits dual emissions of Eu^{3+} and Tb^{3+} upon excitation at the same wavelength. Three emission bands (488, 544, and 615 nm) of Eu^{3+}/Tb^{3+}@MIL-100 (In) film were chosen as the spectral signals for realizing the barcoding function (Fig. 2.10A; bottom, right). Of them, 488 (I_{code1}) and 615 nm (I_{code2}) emissions were filtered by FL and MB dyes, respectively. On the contrary, 615 nm emission was unfiltered and served as reference (I_{ref}) for the

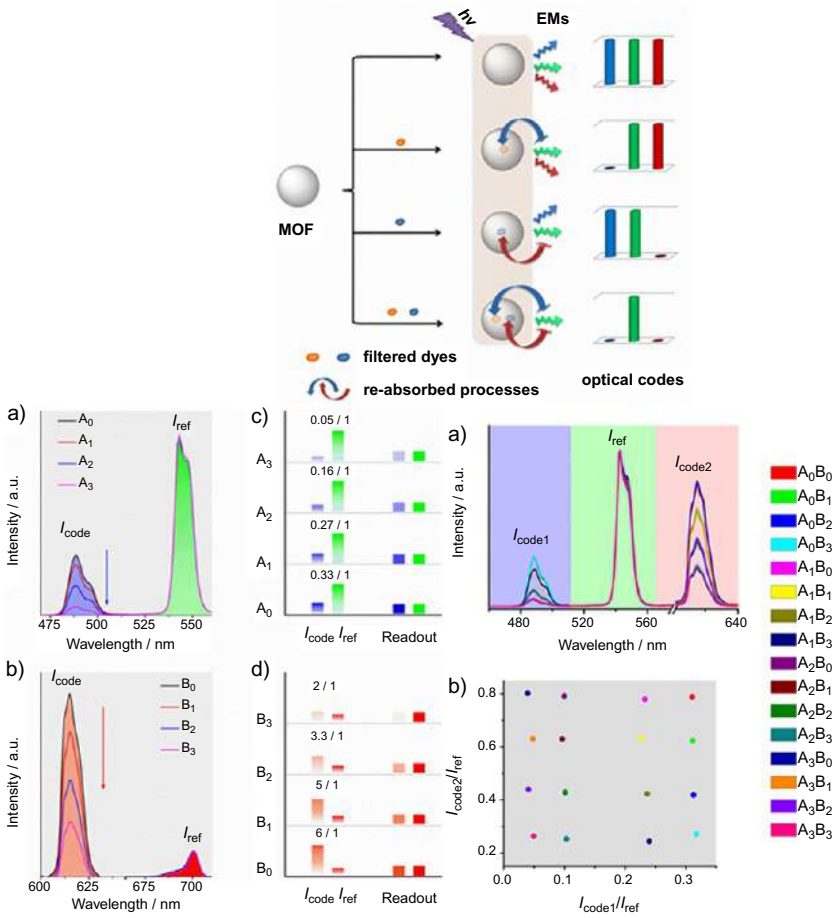

FIG. 2.10 *(Top)* Schematic illustration of the encoding strategy based on tuning the multiple emission bands of lanthanide luminescent MOFs. Blue and red emissions can be tuned by controlling filtered dye loading, while the green emission is not adsorbed and serves as an internal reference to generate ratiometric optical codes. *(Middle)* Emission spectra of encoding (A) Tb^{3+}@MIL-100 (In) and (B) Eu^{3+}@MIL-100 (In) films. Both 488 and 615 nm emissions (I_{code}) are tuned in four increments by varying the loading concentration of fluorescein isothiocyanate or methylene blue, respectively. In contrast, 544 and 701 nm emissions ($I_{ref.}$) remain constant. Here, the encoding Tb^{3+}@MIL-100 (In) and Eu^{3+}@MIL-100 (In) films are defined as A and B, while their subscripts in A and B are used to differentiate the films with different dye loaded amounts. For instance, A0 and B3 mean Tb^{3+}@MIL-100 (In) film with free fluorescein isothiocyanate loading and Eu^{3+}@MIL-100 (In) film with maximum methylene blue loading, respectively, while (C) and (D) are the color-coded schematic of the barcoded readout, which are derived from (A) and (B), respectively. *(Bottom)* (A) Emission spectra of Eu^{3+}/Tb^{3+}@MIL-100 (In) films with various dye (FL and MB) loading combinations. The loading concentration of both FL and MB are set at four levels, leading to 4^2 ratiometric codes. (B) Two-dimensional (2D) matrix of the ratiometric codes derived from (A), revealing that the ratiometric codes can be well separated and identified. *(Reproduced with permission from Y. Zhou, B. Yan, Ratiometric multiplexed barcodes based on luminescent metal organic framework films. J. Mater. Chem. C 3 (2015) 8413–8418. Copyright 2014 Royal Society of Chemistry.)*

filtered emissions. Similarly, the concentration of FL and MB dyes were both set at four levels, leading to 16 combinations in total. Since the information of the combinations can be carried by their emission intensities in multiple bands, each of the combinations correlates to one 2D ratiometric code (I_{code1}/I_{ref}, I_{code2}/I_{ref}), which is calculated by the ratios of two filtered intensities (I_{code1} and I_{code2}) to one reference intensity (I_{ref}). The 2D ratiometric codes are arranged in a matrix (Fig. 2.10B; bottom, right), demonstrating that the optical codes can be well separated and identified [62].

2.6 Luminescence response for chemical sensing of rare earth MOFs hybrid materials

The luminescent sensors utilize UV light to produce the glow of the analyte in the visible region of the spectrum. This excited light produces a signal visible to the naked eye. On the other hand, the chemodosimeter offers an irreversible recognition of an analyte, providing high selectivity in terms of analytes. This recognition process is less affected by the external factors. Both MOFs themselves and their rare earth hybrid materials are potential candidates for luminescent sensing of all kinds of analytes [37,64–84].

2.6.1 Luminescence response and chemical sensing in MOFs-based material

For MOFs as luminescence-based chemosensors, several pathways have been examined to elucidate the interaction with foreign species, but luminescence continues to be the most preferred and relatively easiest mechanism to interpret. Fig. 2.11 shows a descriptive scheme of the different approaches to construct MOFs-based luminescence sensors. Actually, the assignment of a particular effect can be ascribed qualitatively but the concurrent presence of multiple processes has been commonly observed in MOFs, whose exact contributions of all effects involved in the emission process are not trivial. The key parameters to develop any chemical sensor include sensitivity, selectivity, response time, stability of the material, and reusability of the probe. Detectability makes luminescence more attractive than light absorption since it is more sensitive and even small numbers of photons can be detected using photon-counting techniques, even in the absence of a large background signal. Several potential transduction mechanisms are possible in luminescent MOFs: **(a) solvochromatic shifts; (b) alteration of the electronic structure via changes in the coordination sphere; (c) fluorescence quenching by adsorbed species; and (d) exciplex formation**. MOFs with broadly varied fluorometric sensing properties have been developed by the design strategies of crystal engineering, structure-property correlations, and functionalization, resulting in large and extensive interests. The sensing research domains contain a number of crucial sensing

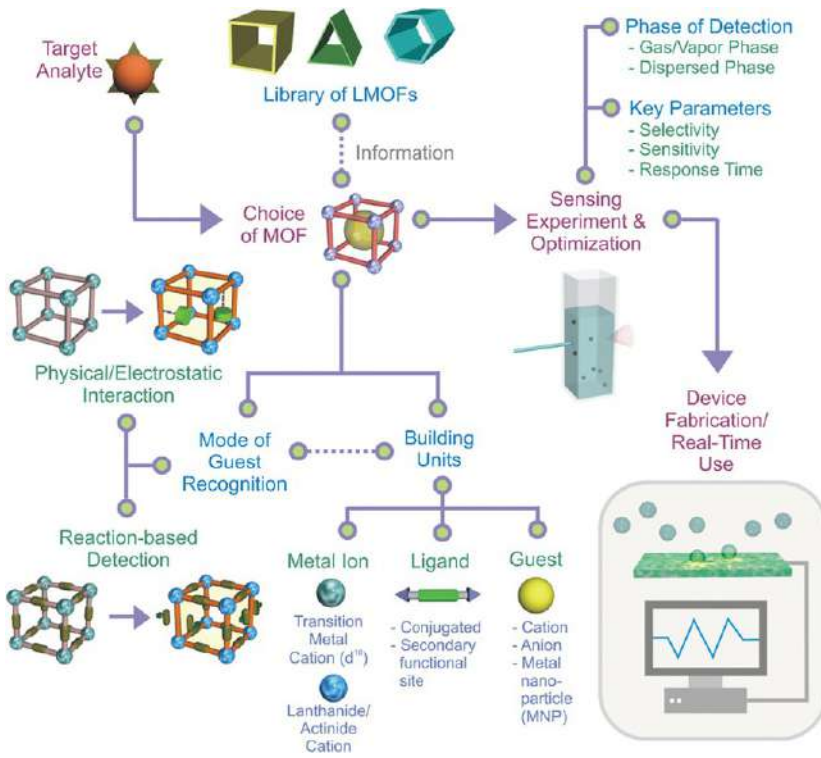

FIG. 2.11 Schematic outline of the various steps involved in development of luminescent MOFs (LMOFs) for sensing applications, along with the considerations at every step. *(Reproduced with permission from W. P. Lustig, S. Mukherjee, N. D. Rudd, A. V. Desai, J. Li, S. K. Ghosh, Metal-organic frameworks: functional luminescent and photonic materials for sensing applications. Chem. Soc. Rev. 46 (2017) 3242–3285. Copyright 2017 Royal Chemical Society.)*

species. What's more, new classes of MOFs sensory materials utilizing advanced signal transduction by devices based on MOFs photonic crystals and thin films are being developed. **(1) It must exhibit luminescence response (intensity or wavelength) to an interaction with an analyte ("Turn−On" for enhancement or "Turn−Off" for quenching)**. Generally, a change in the luminescence intensity or profile pattern of the MOFs materials can be utilized as a probe to recognize the presence of interacting species. Typically, intensity change is the usual mode of detection in the case of MOFs, with enhancement or quenching being a by-product of the nature of interaction or electronic characteristics of the guest involved. Depending on the extent and the character of interaction, either or both electron and energy transfer mechanisms are found to have a role in directing the change of luminescence intensity or peak shifts. Changes in intensity can also appear when a sensitizer is directly involved in the

interaction process with the guest. This observation is commonly noticed for rare earth MOFs hybrid materials, wherein the organic ligands transfer energy to the HOMO of the RE^{3+} cations. Once the organic ligands interact with any incoming guest molecule, the nature of the interaction is directly reflected in the emission intensities of the RE^{3+}, either as an enhanced signal or depletion of the emission intensity. Unfortunately, the intensity change may not always be the precise mode of recognition, which sometimes involves a false response or an erroneous observation triggered by changes in the local environment of the species. The more reliable and efficient pathway would be the appearance of a new peak or the disappearance of a peak accompanied by a new emission peak. This "Turn−On" response usually signifies selective binding to the luminescent group, which is a sensitive method to detect. Another approach to obtain "Turn−On" signals is by modulation of the appended secondary functional sites in a ligand system having an original dark or weakly emitted signal. Such an approach, commonly referred to as a chemodosimeter, is a much more reliable pathway for both selective and sensitive response. **(2) The response must have some analyte specificity (selectivity for sensing), which is optimally reversible**. Selectivity is probably the basic premise for development of any sensor. While the molecular sieving effect has been the most reliable approach to attain selectivity in MOFs, efforts are ongoing to tune the pore surface character to segregate competing analytes based on affinity to the framework. **(3) The response must be detectable (acceptable limit of detection (LOD))**. MOFs, by virtue of their porous character, are inherently sensitive receptors owing to the preconcentration effect; the feature of permanent porosity enables them to be suitable host matrices at the molecular level. The size, shape, and nature of the porous channels in MOFs are directly related to adsorption kinetics and strongly influence the rate at which the signal is generated and conveyed. In the majority of the cases, the guest species are physisorbed in the MOFs pores and hence can be desorbed with antagonistic stimuli with relatively lesser energy demand. **(4) Stability of the material, especially chemical inertness and hydrolytic stability, continues to inhibit the promotion to the level of practical implementation**. In addition to stability, another pertinent challenge for MOFs in seeking real-time applicability as gas/vapor sensors is the ability of the majority of MOFs to adsorb water, whose presence can substantially hinder the sensitivity and response time, and in some cases compromise the energy effectiveness of the detection system on account of stronger binding. The key to MOFs as sensory materials lies in the features bestowed on them by the building units and their subsequent assembly, as the ability to tap structure-property correlation to fabricate target-specific systems is a distinct advantage over its congeners. It is feasible that MOFs can incorporate and tune signal transduction centers in the system, which equips them to function as communication devices in addition to the primary role of being host matrices for a range of analytes. **(5) Other considerations such as ionic character, acidity/basicity, hydrophobicity, polarizability, pore apertures, etc**. These

properties of MOFs are largely affected by the choice of the ligand, metal, or guest. **(i) Ligands**. The ligand in MOFs is π-conjugated organic molecules, which shorten the HOMO-LUMO gap and promote radiative decay. The preferred emission in the visible region of MOFs requires that organic ligands with green or red emissions be selected for sensing due to their greater suitability. **(ii) Pore surface modulation**. It becomes an attractive mode of design strategy to discriminate between competing guest molecules by preferred binding tendencies. The presence of Lewis acidic/basic sites or π-electron rich/poor surfaces renders the desired attributes for screening target species. **(iii) Metal ions**. Paramagnetic transition metals are known to be strong quenchers of luminescence to promote nonradiative emission by inducing electron or energy transfer from the excited organic ligand. Metal ions with larger coordination spheres, higher coordination numbers, or flexible coordination modes can be chosen for modifying the luminescence. (iv) **Secondary building units (SBUs)**. The size of the SBUs can alter the bandgaps of the MOFs, which is of considerable significance as a majority of the reported stable MOFs compounds are built around rigid SBUs. (v) **Guest molecules in MOFs**. These species are not coordinated directly to the MOFs and have a role in dictating their emission feature; their nature, size, and interaction strength determine the extent of their role in regulating the MOF properties. **(6) Key parameters for seeking real-time applicability**. Among the considerations for a sensor material to seek potential real-time application, stability to air/moisture and in certain cases to varying chemical environments is a primary factor and a core issue, along with selectivity and sensitivity under operating conditions. In addition to hydrolytic stability, functional MOFs with resistance to degradation over a wide pH range or in biological fluids are the current target of research in this regard [37,40,60–84].

2.6.2 MOFs-based materials primarily display special advantages for chemical sensing

(1) Sensitivity and selectivity. The high surface area and structural tenability of MOFs can provide them abundant interaction with guest species, which gives them the high sensitivity crucial for developing efficient sensors. The versatile pore or channel structure and functional position of MOFs provide them with high selectivity. Therefore various analytes can be selectively recognized through size exclusion of the porosity of MOFs, where the orifices of the MOFs assist as a sieve to permit the specific moiety to enter the cavity present inside MOFs. The entering moiety can develop a coordination with the active sites (acceptor) in the MOFs structure, readily changing their electronic structure and the corresponding photophysical performance. Various functionalities can serve as binding sites for MOFs for targeting the specific analytes, which is expected to construct MOFs with multifunctional sites to collaboratively induce their preferential and highly sensitive and selective binding with different species. The microporous structure can act as a molecular sieve by blocking

oversized molecules and hence increasing the sensitivity and selectivity of the detection system. **(2) Sensing mechanism**. The crystalline framework structure and energy transfer process of MOFs materials are beneficial for understanding the sensing mechanism. The distinct crystalline assemblies of MOF-assisted detectors permit the exploration of the detecting principle of the frameworks based on MOFs at the molecular level, whose exceedingly tunable structure nature assures the optimization and specific design of sensors. **(4) Multiple luminescence response**. The multiple luminescent centers (especially for REFMOFHs materials) easily lend themselves to potential applications for ratiometric or even intelligent sensing for complicated systems. The different metal ions or mixed ligands or guests, having diverse luminescent properties, can be hosted into a MOF structure with the aim of divulging self-calibration in the detecting systems. On the basis of sensing materials, MOFs can be applied to develop the engineering of the next generation MOF-based sensing devices, which rely on the combination of MOFs light-harvesting ability, understanding energy transfer processes within a framework, and application of MOF-based functions to sensing enhancement. **(5) PSM chemistry**. Linkers with carefully designed functionalities can be used as supports for MOFs, posing molecular specificity to host-guest interactions. On the other hand, the detection ability of MOF-based sensors can also be increased by PSM.

References

[1] G. Blasse, B.C. Grabmaier, Luminescent Materials, Springer, Berlin, 1994.

[2] G. Blasse, Vibronic transitions in rare earth spectroscopy, Int. Rev. Phys. Chem. 11 (1992) 71–100.

[3] E.G. Moore, A.P.S. Samuel, K.N. Raymond, From antenna to assay: lessons learned in lanthanide luminescence, Acc. Chem. Res. 42 (2009) 542–552.

[4] M.J. Dejneka, A. Streltsov, S. Pal, A.G. Frutos, C.L. Powell, K. Yost, P.K. Yuen, U. Muller, J. Lahiri, Rare earth-doped glass microbarcodes, PNAS 100 (2003) 389–393.

[5] T.N. Nguyen, F.M. Ebrahim, K.C. Stylianou, Photoluminescent, upconversion luminescent and nonlinear optical metal-organic frameworks: from fundamental photophysics to potential applications, Coord. Chem. Rev. 377 (2018) 259–306.

[6] W.T. Carnall, P.R. Fields, K. Rajnak, Electronic energy levels of the trivalent lanthanide aquo ions. IV. Eu^{3+}, J. Chem. Phys. 49 (1968) 4450–4455.

[7] W.T. Carnall, P.R. Fields, K. Rajnak, Electronic energy levels of the trivalent lanthanide aquo ions. III. Tb^{3+}, J. Chem. Phys. 49 (1968) 4447–4449.

[8] W.T. Carnall, P.R. Fields, K. Rajnak, Electronic energy levels in the trivalent lanthanide aquo ions. I. Pr^{3+}, Nd^{3+}, Pm^{3+}, Sm^{3+}, Dy_{3+}, Ho^{3+}, Er^{3+}, and Tm^{3+}, J. Chem. Phys. 49 (1968) 4424–4442.

[9] B. Di Bartolo, Optical Interaction in Solids, Wiley, New York, 1968.

[10] G. Blasse, G.J. Dirksen, A. Meijerink, The luminescence of ytterbium(II) in strontium tetraborate, Chem. Phys. Lett. 167 (1990) 41–44.

[11] G.A. Crosby, R.E. Whan, R.M. Alire, Intramolecular energy transfer in rare earth chelates—role of the triplet state, J. Chem. Phys. 34 (1961) 743–748.

[12] S.I. Weissman, Intramolecular energy transfer: the fluorescence of complexes of europium, J. Chem. Phys. 10 (1942) 214–217.

[13] G.A. Crosby, R.E. Whan, J. Freeman, Spectroscopic studies of rare earth chelates, J. Phys. Chem. 66 (1962) 2493–2499.
[14] S. Sato, M. Wada, Relations between intramolecular energy transfer efficiencies and triplet state energies in rare earth β-diketone chelates, Bull. Chem. Soc. Jpn. 43 (1970) 1955–1962.
[15] D.L. Dexter, A theory of sensitized luminescence in solids, J. Chem. Phys. 21 (1944) 836–850.
[16] T.D. Brown, T.M. Shepherd, Factors affecting the quantum efficiencies of fluorescent terbium(III) chelates in the solid state, J. Chem. Soc. Dalton Trans. (1973) 336–341.
[17] V. Balzani, L. Moggi, M.F. Manfrin, F. Bolletta, Quenching and sensitization process of coordination compounds, Coord. Chem. Rev. 15 (1975) 321–433.
[18] S. Wu, Y. Wu, Y. Yang, Rare earth(iii) complexes with indole-derived acetylacetones II. Luminescent intensity for europium(iii) and terbium(iii) complexes, J. Alloys Compd. 180 (1992) 399–402.
[19] Y.S. Song, B. Yan, Z.X. Chen, Different crystal structure and photophysical properties of rare earth complexes with 5-bromonicotinic acid, J. Solid State Chem. 177 (2004) 3805–3814.
[20] B. Yan, B. Zhou, Photophysical properties of dysprosium complexes with aromatic carboxylic acids by molecular spectroscopy, J. Photochem. Photobiol. A Chem. 171 (2005) 181–186.
[21] Q. Wang, B. Yan, X. Zhang, Photophysical properties of novel rare earth complexes with long chain mono-eicosyl cis-butene dicarboxylate, J. Photochem. Photobiol. A Chem. 174 (2005) 119–124.
[22] S. Petoud, J.C.G. Bunzli, T. Glanzman, C. Piguet, Q. Xiang, R.P. Thummel, Influence of charge-transfer states on the Eu(III) luminescence in mononuclear triple helical complexes with tridentate aromatic ligands, J. Lumin. 82 (1999) 69–79.
[23] W.M. Faustino, O.L. Malta, G.F. de Sa, Intramolecular energy transfer through charge transfer state in lanthanide compounds: a theoretical approach, J. Chem. Phys. 122 (2005) 317–325.
[24] A. Daleo, A. Picot, A. Beeby, J.A.G. Williams, B. Le Guennic, C. Andraud, O. Maury, Efficient sensitization of europium, ytterbium, and neodymium functionalized tris-dipicolinate lanthanide complexes through tunable charge-transfer excited states, Inorg. Chem. 47 (2008) 10258–10268.
[25] W.H. Fonger, C.W. Struck, Eu^{3+} ^5D resonance quenching to the charge-transfer states in Y_2O_2S, La_2O_2S, and LaOCl, J. Chem. Phys. 52 (1970) 6364–6371.
[26] M.D. Ward, Transition-metal sensitized near-infrared luminescence from lanthanides in d-f heteronuclear arrays, Coord. Chem. Rev. 251 (2007) 1663–1677.
[27] M. Kleinerman, Energy migration in lanthanide chelates, Bull. Am. Phys. Soc. 9 (1964) 265–269.
[28] C. Yang, L. Fu, Y. Wang, J. Zhang, W. Wong, X. Ai, Y. Qiao, B. Zou, L. Gui, A highly luminescent europium complex showing visible-light-sensitized red emission: direct observation of the singlet pathway, Angew. Chem. Int. Ed. 43 (2004) 5010–5013.
[29] J. Yang, G. Zhu, H. Wang, Application of the co-luminescence effect of rare earths: simultaneous determination of trace amounts of samarium and europium in solution, Analyst 114 (1989) 1417–1419.
[30] J. Hao, X. Xu, H. Fei, L. Li, B. Yan, Functionalization of metal-organic frameworks for photoactive materials, Adv. Mater. 30 (2018) 1705634.
[31] M.D. Allendorf, C.A. Bauer, R.K. Bhaktaa, R.J.T. Houka, Luminescent metal-organic frameworks, Chem. Soc. Rev. 38 (2009) 1330–1352.
[32] Y. Cui, Y. Yue, G. Qian, B. Chen, Luminescent functional metal-organic frameworks, Chem. Rev. 112 (2012) 1126–1162.
[33] J. Heine, K. Muller-Buschbaum, Engineering metal-based luminescence in coordination polymers and metal-organic frameworks, Chem. Soc. Rev. 42 (2013) 9232–9242.

[34] M.L.P. Reddy, S. Sivakumar, Lanthanide benzoates: a versatile building block for the construction of efficient light emitting materials, Dalton Trans. 42 (2013) 2663–2678.
[35] V. Stavila, A.A. Talin, M.D. Allendorf, MOF-based electronic and optoelectronic devices, Chem. Soc. Rev. 43 (2014) 5994–6010.
[36] Y. Cui, J. Zhang, H. He, G. Qian, Photonic functional metal-organic frameworks, Chem. Soc. Rev. 47 (2018) 5740–5785.
[37] Y. Zhang, S. Yuan, G. Day, X. Wang, X. Yang, H. Zhou, Luminescent sensors based on metal-organic frameworks, Coord. Chem. Rev. 354 (2018) 28–45.
[38] B. Yan, Photofunctional Rare Earth Hybrid Materials, Springer Publishers, 2017.
[39] W.P. Lustig, J. Li, Luminescent metal-organic frameworks and coordination polymers as alternative phosphors for energy efficient lighting devices, Coord. Chem. Rev. 373 (2018) 116–147.
[40] T. Rasheed, F. Nabeel, Luminescent metal-organic frameworks as potential sensory materials for various environmental toxic agents, Coord. Chem. Rev. 401 (2019), 213065.
[41] H. Kaur, S. Sundriyal, V. Pachauri, S. Ingebrandt, K. Kim, A.L. Sharma, A. Deep, Luminescent metal-organic frameworks and their composites: potential future materials for organic light emitting displays, Coord. Chem. Rev. 401 (2019), 213077.
[42] J. Liu, Z. Luo, Y. Pan, A.K. Singh, M. Trivedi, A. Kumar, Recent developments in luminescent coordination polymers: designing strategies, sensing application and theoretical evidences, Coord. Chem. Rev. 406 (2020), 213145.
[43] H. Yin, X. Yin, Metal – organic frameworks with multiple luminescence emissions: designs and applications, Acc. Chem. Res. 53 (2020) 485–495.
[44] A.M. Rice, C.R. Martin, V.A. Galitskiy, A.A. Berseneva, G.A. Leith, N.B. Shustova, Photophysics modulation in photoswitchable metal – organic frameworks, Chem. Rev. 120 (2020) 8790–8813.
[45] T. Gorai, W. Schmitt, T. Gunnlaugsson, Highlights of the development and application of luminescent lanthanide based coordination polymers, MOFs and functional nanomaterials, Dalton Trans. 50 (2021) 770–784.
[46] B. Yan, Luminescence response mode and chemical sensing mechanism for lanthanide functionalized metal-organic frameworks hybrids, Inorg. Chem. Front. 8 (2021) 201–233.
[47] C. Wei, L. Ma, H. Wei, Z. Liu, Z. Bian, C. Huang, Advances in luminescent lanthanide complexes and applications, Sci. China Technol. Sci. 61 (2018) 1265–1285.
[48] C.M.G. dos Santos, A.J. Harte, S.J. Quinn, T. Gunnlaugsson, Recent developments in the field of supramolecular lanthanide luminescent sensors and self-assemblies, Coord. Chem. Rev. 252 (2008) 2512–2527.
[49] J. Rocha, L.D. Carlos, F.A. Almeida Paza, D. Ananiasa, Luminescent multifunctional lanthanides-based metal-organic frameworks, Chem. Soc. Rev. 40 (2011) 926–944.
[50] Y. Cui, B. Chen, G. Qian, Lanthanide metal-organic frameworks for luminescent sensing and light-emitting applications, Coord. Chem. Rev. 273–274 (2014) 76–86.
[51] T. Gorai, W. Schmitt, T. Gunnlaugsson, Highlights of the development and application of luminescent lanthanide based coordination polymers, MOFs Funct. Nanomater. (2021), https://doi.org/10.1039/d0dt03684f.
[52] D. Hu, Y. Song, L. Wang, Nanoscale luminescent lanthanide-based metal-organic frameworks: properties, synthesis, and applications, J. Nanopart. Res. 17 (2015) 310.
[53] Y. Zhou, B. Yan, Imparting tunable and white-light luminescence to a nanosized metal-organic framework by controlled encapsulation of lanthanide cations, Inorg. Chem. 53 (2014) 3456–3463.

[54] T. Duan, B. Yan, Lanthanide ions (Eu^{3+}, Tb^{3+}, Sm^{3+}, Dy^{3+}) activated ZnO embedded zinc 2,5-pridinedicarboxylic metal organic frameworks for luminescent application, J. Mater. Chem. C 3 (2015) 2823–2830.
[55] T. Duan, B. Yan, Hybrids based on lanthanide ions activated yttrium metal organic frameworks: functional assembly, polymer film preparation and luminescence tuning, J. Mater. Chem. C 2 (2014) 5098–5104.
[56] Y. Lu, B. Yan, A novel luminescent monolayer thin film based on postsynthetic method and functional linker, J. Mater. Chem. C 2 (2014) 5526–5532.
[57] X. Xu, B. Yan, Intercalation of lanthanide cations to a layer-like metal-organic framework for color tunable and white light emission, Dalton Trans. 44 (2015) 1178–1185.
[58] Y. Lu, B. Yan, Lanthanide organic-inorganic hybrids based on functionalized metal-organic frameworks (MOFs) for near-UV white LED, Chem. Commun. 50 (2014) 15443–15446.
[59] Y. Zhou, B. Yan, Lanthanides post-functionalized nanocrystalline metal-organic frameworks for tunable white-light emission and orthogonal multi-readout thermometry, Nanoscale 7 (2015) 4063–4069.
[60] J. Wu, B. Yan, Lanthanides post-functionalized Indium metal-organic frameworks (MOFs) for luminescence tuning, polymer film preparation and near-UV white LED assembly, Dalton Trans. 45 (2016) 18585–18590.
[61] Y. Lu, B. Yan, Luminescent lanthanide barcodes based on postsynthetic modified nanoscale metal-organic frameworks, J. Mater. Chem. C 2 (2014) 7411–7416.
[62] Y. Zhou, B. Yan, Ratiometric multiplexed barcodes based on luminescent metal organic framework films, J. Mater. Chem. C 3 (2015) 8413–8418.
[63] X. Shen, B. Yan, Barcoded materials based on photoluminescent hybrid system of lanthanide ions-doped metal organic framework and silica via ion exchange, J. Colloid Interface Sci. 468 (2016) 220–226.
[64] L.E. Kreno, K. Leong, O.K. Farha, M. Allendorf, R.P. Van Duyne, J.T. Hupp, Metal-organic framework materials as chemical sensors, Chem. Rev. 112 (2012) 1105–1125.
[65] F. Yi, D. Chen, M. Wu, L. Han, H. Jiang, Chemical sensors based on metal-organic frameworks, ChemPlusChem 81 (2016) 67–690.
[66] I. Stassen, N. Burtch, A. Talin, P. Falcaro, D.M. Allendorfc, R. Ameloot, An updated roadmap for the integration of metal-organic frameworks with electronic devices and chemical sensors, Chem. Soc. Rev. 46 (2017) 3185–3241.
[67] W.P. Lustig, S. Mukherjee, N.D. Rudd, A.V. Desai, J. Li, S.K. Ghosh, Metal-organic frameworks: functional luminescent and photonic materials for sensing applications, Chem. Soc. Rev. 46 (2017) 3242–3285.
[68] E.A. Dolgopolova, A.M. Rice, C.R. Martin, N.B. Shustova, Photochemistry and photophysics of MOFs: steps towards MOF-based sensing enhancements, Chem. Soc. Rev. 47 (2018) 4710–4728.
[69] S.A. Diamantis, A. Margariti, A.D. Pournara, G.S. Papaefstathiou, M.J. Manos, T. Lazarides, Luminescent metal-organic frameworks as chemical sensors: common pitfalls and proposed best practices, Inorg. Chem. Front. 5 (2018) 1493–1511.
[70] R. Lin, S. Liu, J. Ye, X. Li, J. Zhang, Photoluminescent metal-organic frameworks for gas sensing, Adv. Sci. 3 (2016) 1500434.
[71] Y. Li, A. Xiao, B. Zou, H. Zhang, K. Yan, Y. Lin, Advances of metal-organic frameworks for gas sensing, Polyhedron 154 (2018) 83–97.
[72] H. Li, S. Zhao, S. Zang, J. Li, Functional metal-organic frameworks as effective sensors of gases and volatile compounds, Chem. Soc. Rev. 49 (2020) 6364–6401.

[73] K. Müller-Buschbaum, F. Beuerle, C. Feldmann, MOF based luminescence tuning and chemical/physical sensing, Microporous Mesoporous Mater. 216 (2015) 171–199.
[74] Q. Yu, Z. Li, Q. Cao, S. Qu, Q. Jia, Advances in luminescent metal-organic framework sensors based on post-synthetic modification, Trends Anal. Chem. 129 (2020), 115939.
[75] B. Chen, S. Xiang, G. Qian, Metal-organic frameworks with functional pores for recognition of small molecules, Acc. Chem. Res. 43 (2010) 1115–1124.
[76] Y. Li, Temperature and humidity sensors based on luminescent metal-organic frameworks, Polyhedron 179 (2020), 114413.
[77] Z. Liao, J. Zhang, E. Yu, Y. Cui, Recent progress in metal-organic frameworks for precaution and diagnosis of Alzheimer's disease, Polyhedron 151 (2018) 554–567.
[78] Y. Hao, S. Chen, Y. Zhou, Y. Zhang, M. Xu, Recent progress in metal-organic framework (MOF) based luminescent chemodosimeters, Nanomaterials 9 (2019) 974.
[79] J.H. Jung, J.H. Lee, J.R. Silverman, G. John, Coordination polymer gels with important environmental and biological applications, Chem. Soc. Rev. 42 (2013) 924–936.
[80] Z. Hu, B.J. Deibert, J. Li, Luminescent metal-organic frameworks for chemical sensing and explosive detection, Chem. Soc. Rev. 43 (2014) 5815–5840.
[81] X. Fang, B. Zong, S. Mao, Metal-organic framework-based sensors for environmental contaminant sensing, Nano-Micro Lett. 10 (2018) 64.
[82] H. Wang, W.P. Lustig, J. Li, Sensing and capture of toxic and hazardous gases and vapors by metal-organic frameworks, Chem. Soc. Rev. 47 (2018) 4729–4756.
[83] J. Tang, X. Ma, J. Yang, D. Feng, X. Wang, Recent advances in metal-organic frameworks for pesticide detection and adsorption, Dalton Trans. 49 (2020) 14361–14372.
[84] L. Chen, D. Liu, J. Peng, Q. Du, H. He, Ratiometric fluorescence sensing of metal-organic frameworks: tactics and perspectives, Coord. Chem. Rev. 404 (2020), 213113.

Part II

Luminescent response mode and sensing mechanisms in rare earth metal-organic frameworks hybrid materials

Chapter 3

Single mode for luminescence responsive chemical sensing in rare earth metal-organic framework hybrid materials

3.1 Introduction for luminescence response of metal-organic frameworks

The permanent porosity of MOFs can be perturbed and further induced by an encapsulated or interacting guest species, which can alter multiple aspects of the photophysical properties (light absorption and emission) of the MOF host. Color change that is visible to the naked eye becomes the most preferred signal for sensing, and provides a simple and convenient method of detection since it does not require instrumentation. For example, an exchange of solvent guest molecules in a crystal lattice of MOFs will shift their emission spectrum to tune the corresponding color, which is utilized to identify a guest molecule through a guest-dependent color change. In addition, some ionic species also have a similar colorimetric effect, whose spectroscopic change can potentially be used as a sensing signal. Depending on the electronic nature of the analytes, either quenching or enhancing the luminescence of MOFs materials can occur, which can be attributed to either (both) electron transfer or (and) energy transfer between the analytes and the MOFs. For luminescence quenching, nitroaromatics are known as strong quenchers due to their high electron affinity, and paramagnetic metal ions (Mn^{2+}, Co^{2+}, Ni^{2+}, and Cu^{2+}) are capable of quenching fluorescence due to their inducing of ligand-metal charger transfer (LMCT) to relax the excitation energy through a nonradiative pathway. On the other hand, electron-rich species such as benzene derivatives with electron-donating substituents can enhance MOFs' luminescence due to their ability to donate an electron from an excited state to the lowest unoccupied molecular orbit (LUMO) or conduction band (CB) of the MOFs. In addition, the capture of an analyte results in the shift of an emission peak or a new emission peak in the visible range different from a dark background, which is called guest-induced emission. This has two main advantages: (i) monitoring the evolution

Rare Earth Metal-Organic Framework Hybrid Materials for Luminescence Responsive Chemical Sensors
https://doi.org/10.1016/B978-0-323-91236-5.00001-3

of a new emission peak is more sensitive than comparing the changes in emission intensity of the same peak for higher detection limits; (ii) the intensity change of an emission is not always specific and molecules of similar electronic properties for similar intensity response can affect the selectivity. Currently, the most widely observed sensing mechanism for analyte detection is electron transfer through host-guest interactions of the analyte, whose LUMOs being at lower energy level than the MOFs makes the electron transfer possible from MOFs to guest analytes. Another important factor affecting the sensing behavior is the energy transfer between analyte and MOFs, which greatly depends on the overlapping region between the absorbance of analyte and emission of the MOFs. They both can give nonemissive or weakly emissive MOFs owing to the nonradiative relaxation. The shifting in wavelength can be activated by interaction of the MOFs host and special analytes [1–4].

Certainly, external stimuli can also shift the emission maximum [1–29]. Fig. 3.1 shows a schematic description of relevant luminescence processes to tune MOFs luminescence and related sensing options for analytes [1]. For rare

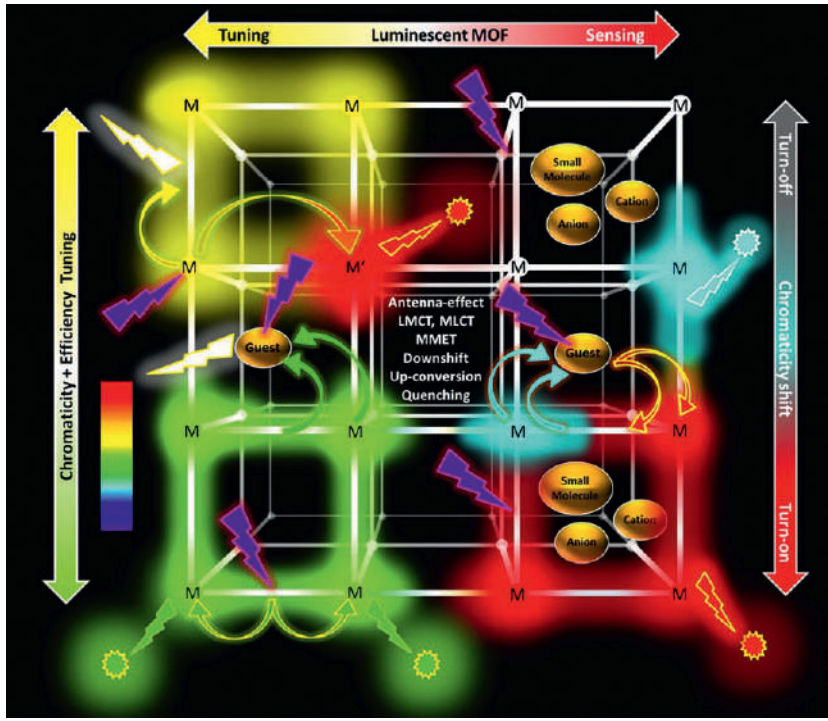

FIG. 3.1 Schematic depiction of relevant luminescence processes for the tuning of MOF luminescence and related sensing options for molecules and ions. *(Reproduced with permission from reference K. Müller-Buschbaum, F. Beuerle, C. Feldmann, MOF based luminescence tuning and chemical/physical sensing, Microp. Mesop. Mater. 216 (2015) 171–199. Copyright 2015 Elsevier.)*

earth MOF hybrid materials (REMOFHs), especially for rare earth functionalized MOF hybrid materials (REFMOFHs), energy transfer between MOFs or their linkers and rare earth (RE^{3+}) ions is common for luminescence responsive sensing of analytes. To date, there are four main luminescence response modes: luminescence quenching ("Turn-Off"), luminescence enhancement ("Turn-On"), luminescence enhancement-quenching-enhancement ("Turn-On-Off-On") and ratiometric luminescence (RL) detection. Among these, "Turn-Off" is most extensive; it is based on luminescence quenching resulting from the interaction between the analyte and the fluorophore, leading to an energy transfer from the fluorophore to the analyte or even a collapse of the frameworks. On the other hand, the luminescent sensing of "Turn-On" detection is based on a new emission peak evolving from a dark background or the luminescence intensity increasing to show the apparent color change. The "Turn-On-Off-On" mode mainly involves some transitional metal ions, Cu^{2+}, Ag^{+} or Fe^{3+}, whose cointroduction in REMOF hybrid materials sometimes results in the composed effect. Multicenter photo responses (especially dual emission) have great application potential in ratiometric or self-calibrating sensing [7].

Signal and response are two important concepts that should clearly be discriminated from each other in sensing fields. Signal is the emission spectrum generated by luminescent MOFs upon light irradiation without any analyte in the solution, which greatly depends on the structural features of luminescent MOFs and existing close relationship with the structure (called the signal-structure approach). Response is defined as the change in luminescent signal of the MOFs in the presence of an analyte, involving both intensity and wavelength of the luminescent spectrum of the host MOFs. The one-dimensional (1D) produced response means that the host MOFs change with just intensity or only wavelength in the presence of analytes, which can be observed when the generated signal by a luminescent MOFs is only singularly emissive, based on just ligand or metal-based emissions, or dual emissive based on the same ligand. In some cases, the 1D responses can be combined with a two-dimensional (2D) response. A 1D response is observed for the changes in emission intensity of MOFs materials in the presence of an analyte and can be classified as enhancement (Turn-On) or quenching (Turn-Off). Generally, 1D response-based "Turn-On" behavior is more suitable than "Turn-Off" because of increased environmental interference effects in the dark background and reduction in accuracy and precision of the signal-to-noise ratio. It should be stated that, for evaluation of 1D ("Turn-On" or "Turn-Off") behaviors, all sensing parameters (response, selectivity, sensitivity, time, and detection limit) must be considered and compared comprehensively.

In fact, each single luminescence process can be influenced by chemical and (or) physical parameters, resulting in an emission intensity change or an emission wavelength shift. Fig. 3.2 gives a typical example: the reduction of the luminescence intensity by quenching leading to a "Turn-Off" effect of the emission quenching of the lanthanide (Ln^{3+}) ion containing MOFs lattices in the

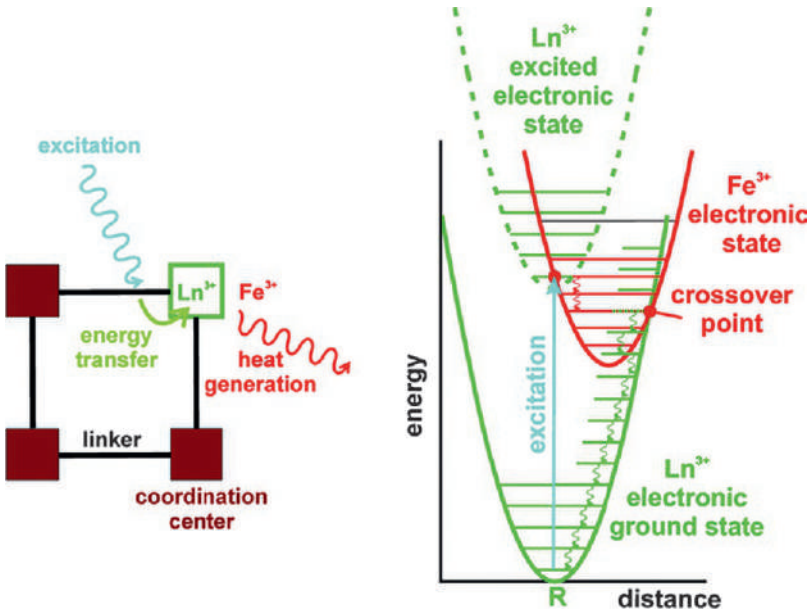

FIG. 3.2 Scheme illustrating quenching and "Turn-Off" of the emission of lanthanide ion (Ln^{3+}) containing MOF lattices in the presence of open-shell transition metal ions such as Fe^{3+} due to vibronic relaxation from the Ln^{3+} excited electronic state to the Ln^{3+} ground state via an electronic state on Fe^{3+}. *(Reproduced with permission from reference K. Müller-Buschbaum, F. Beuerle, C. Feldmann, MOF based luminescence tuning and chemical/physical sensing, Microp. Mesop. Mater. 216 (2015) 171–199. Copyright 2015 Elsevier.)*

presence of open-shell d-metal ions such as Fe^{3+}, whose underlying quenching mechanism can be illustrated based on the simple harmonic oscillator model. After excitation of the Ln^{3+} via its 4f states, electronic states of the open-shell Fe^{3+} can allow a relaxation via vibronic states only into the electronic ground state of the Ln^{3+} ion. Subsequently, no emission of light but only heat generation is observed. Such effects are widely used for sensing and selective differentiation of open shell d-metal ions (e.g., Fe^{3+}) and closed shell ds-metal ions (e.g., Zn^{2+}). A very similar quenching effect is also observed if molecules with high-energy vibronic states (—OH, —CN, $—NO_2$ functionalities) are coordinated to the coordination center of the MOFs lattice, whose coordination is also therefore widely used for MOFs-based sensing. Certainly, such transition metal ions as Fe^{3+} can affect the excitation state of MOFs linkers to further affect the subsequent energy transfer to Ln^{3+} ions [1].

3.2 "Turn-off" luminescence response chemical sensing for rare earth metal-organic framework hybrid materials

The principle of using MOFs-based materials as luminescent probes depends on the variation in luminescence intensity before and after their interaction with analytes. However, luminescence quenching is the most typical phenomenon and may be caused by several factors, such as photoinduced electron transfer (PET), fluorescence (Förster) resonance energy transfer (FRET), intermolecular charge transfer, excited-state intermolecular proton transfer, and excimer/exciplex. PET can be explained by predicting electron distribution and energy of the LUMO and the highest occupied molecular orbit (HOMO). As far as we know, two typical quenching phenomena appear: (i) dynamic quenching, occurring from the collision between the excited-stated fluorophore and the quencher; (ii) static quenching, occurring because of the formation of nonemissive intermediates [4,30–32]. For both REMOFs and REFMOFHs, the luminescence quenching of the "Turn-Off" effect mainly derives from the interaction between analytes and RE^{3+} ions or linkers in the MOFs or their hybrid materials, which influences the energy transfer from linkers to RE^{3+} within the MOFs hybrids. Here some examples are given.

Sun et al. chose 5-((2′-cyano-[1,1′-biphenyl]-4-yl)-methoxy) isophthalic acid (H_2L) as a linking ligand to construct 2D layer structural RE-MOFs, $[RE(L)(HCOO)(H_2O)]_n$ (RE = Eu, Gd, Ho, and Tb), whose free N atoms can interact with some transition metal ions and play a key role in the sensing process through their luminescence intensity changes. Both Eu-MOF and Tb-MOF exhibit excellent recyclable, selective, and sensitive detection of Cr(III) and Cr(VI) ions and can be used to detect them. As shown in Fig. 3.3 (left), only the Cr^{3+} ion has a significant emission-quenching effect on luminescence of the two MOFs, implying they both can be regarded as hopeful candidates for selective recognizing of the Cr^{3+} ion. Furthermore, the Stern-Volmer (SV) quenching curve for the Cr^{3+} ion is nearly linear at low concentrations, which deviates from the linear correlation with the increase of concentration illustrates the existence of both static and dynamic quenching processes. The calculated detection limits (LOD) of the Cr^{3+} ion are 1.5 and 1.9 μmol L^{-1} for Eu-MOF and Tb-MOF, respectively. The partial overlap between the Cr^{3+} absorption and the excitation bands of the two MOFs may cause Cr^{3+} ions to absorb the energy of the excitation, resulting in their luminescence quenching. In addition, the —CN group of L^{2-} ligands remains uncoordinated for the weak coordination interaction with Cr^{3+}, leading to energy migration and luminescence quenching. Thus the energy absorption and weak coordination interaction may have a synergistic effect on the quenching of fluorescence intensity. They also found Cr(VI) (CrO_4^{2-} and $Cr_2O_7^{2-}$) anions have a striking quenching effect

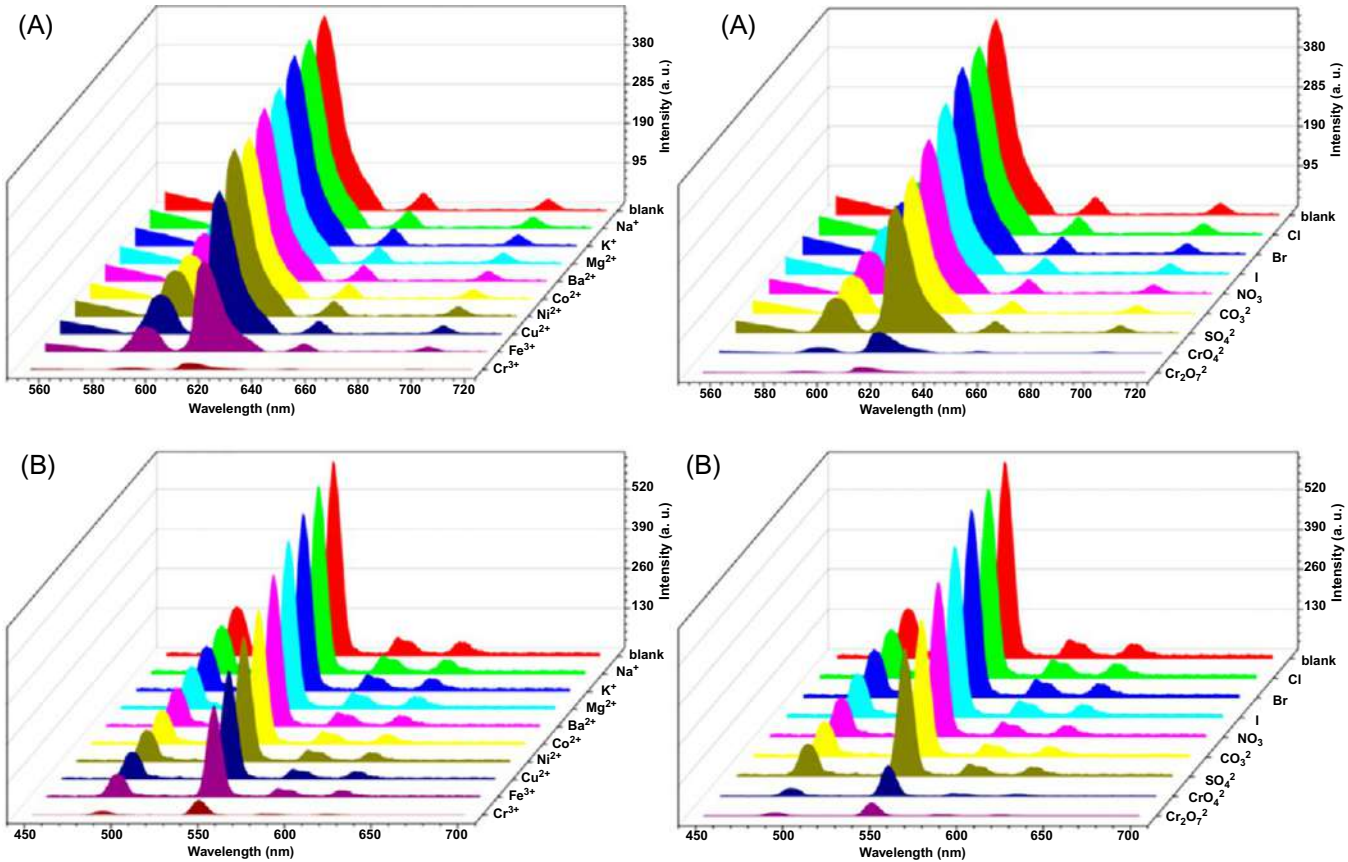

FIG. 3.3 Emission spectra of Eu-MOF (A) and Tb-MOF (B) dispersed in various cations *(left)* and anions *(right)*. *(Reproduced with permission from reference Z. Sun, M. Yang, Y. Ma, L. Li, Multi-responsive luminescent sensors based on two-dimensional lanthanide-metal organic frameworks for highly selective and sensitive detection of Cr(III) and Cr(VI) ions and benzaldehyde, Cryst. Growth Des. 17 (2017) 4326–4335. Copyright 2017 American Chemical Society.)*

on the fluorescence of two RE-MOFs, whereas other anions have no or only minor effects on the fluorescence intensity (Fig. 3.3 (right)). The plots of all titration experiments deviate from linearity with the concentration increasing, demonstrating that both static and dynamic quenching happened simultaneously. The LOD are calculated as low as 1.2 (CrO_4^{2-}), 1.0 ($Cr_2O_7^{2-}$) for Eu-MOF, and 1.8 (CrO_4^{2-}), and 2.1 ($Cr_2O_7^{2-}$) μmol L^{-1} for Tb-MOF. The extensive overlap of the absorption bands of anions with the excitation bands of the two MOFs cause the energy of the excitation light to be strongly absorbed by Cr(VI) anions, reducing the efficiency of the energy transfer from the ligand to the RE^{3+} due to luminescence quenching [33].

Liu et al. reported a luminescent Eu-MOF, $[Eu_2(MTBC)(OH)_2(DMF)_3(H_2O)_4]\cdot 2DMF\cdot 7H_2O$ for detecting both Cu^{2+} and UO_2^{2+} with high sensitivity, among other selected monovalent, divalent, trivalent metal cations based on a "Turn-Off" mechanism with LOD to Cu^{2+} ion of 17.2 μg/L and to UO_2^{2+} ions of 309.2 μg/L. As shown in Fig. 3.4A (left), this phenomenon occurs only in the presence of Cu^{2+} and UO_2^{2+}, and the influence from other metal cations on the luminescence of Eu-MOF is negligible. The ability to perceive this interaction with the naked eye under 365 nm light, as shown in Fig. 2.4B (left), reveals potential for the use of Eu-MOF as a luminescent probe for Cu^{2+} and UO_2^{2+} through exploitation of this cogent phenomenon. K_{SV} of Eu-MOF treated with various metal cation solutions is determined as 2251.4 and 3631.5 M^{-1}, respectively, indicating a selective quenching capacity for these cations. The most logical mechanism is an energy transfer process that occurs from the interaction of Cu^{2+} and UO_2^{2+} with Eu-MOF. As shown in the inset of Fig. 3.4A (right), the excitation of Eu-MOF at 345 nm can be strongly absorbed by UO_2^{2+}, creating competition between them for optical excitation. The mantle area between the UV-vis spectrum of the Cu^{2+}-loaded sample and the emission spectrum of Eu-MOF clearly demonstrates the reabsorption of the emitted light from Eu-MOF, which may also contribute to the luminescence quenching phenomenon observed. Moreover, from Fig. 3.4B (right), the $^5D_0$ lifetimes of the Cu^{2+}- or UO_2^{2+}-loaded hybrids significantly decrease compared to the pure Eu-MOF, which establishes that energy transfer occurs throughout the adsorption process. The energy transfer efficiencies between Eu-MOF and Cu^{2+} and UO_2^{2+} are 57% and 16%, respectively, verifying the fact that the LOD toward Cu^{2+} is much lower than UO_2^{2+} [34].

Li et al. synthesized a white-light-emitting material through three isomorphic 1D chain-like REMOFs based on L-*O*,*O*′-dibenzoyl tartaric acid (L-DBTA), whose luminescent sensing of metal cations was carried out, exhibiting good responses for both Mn^{2+} and Ag^+ ions via luminescence color change (LCC). Fig. 3.5A and B shows that the emission intensity of $\{Et_3NH[(Sm_{0.2}Eu_{0.2}Tb_{0.6})(L\text{-}DBTA)_2(CH_3OH)_2(H_2O)_2]\cdot 2H_2O\}_n$ (SmEuTb-MOF) decreases drastically with increasing Ag^+ and Mn^{2+} concentration. The intensity of the blue component (400–550 nm) of SmEuTb-MOF is almost entirely quenched as the concentration of Ag^+ increases to 5×10^{-7} M, which contributes to the LCC from white to red. For the sensing sensitivity of SmEuTb-MOF to Mn^{2+} ions, the luminescent

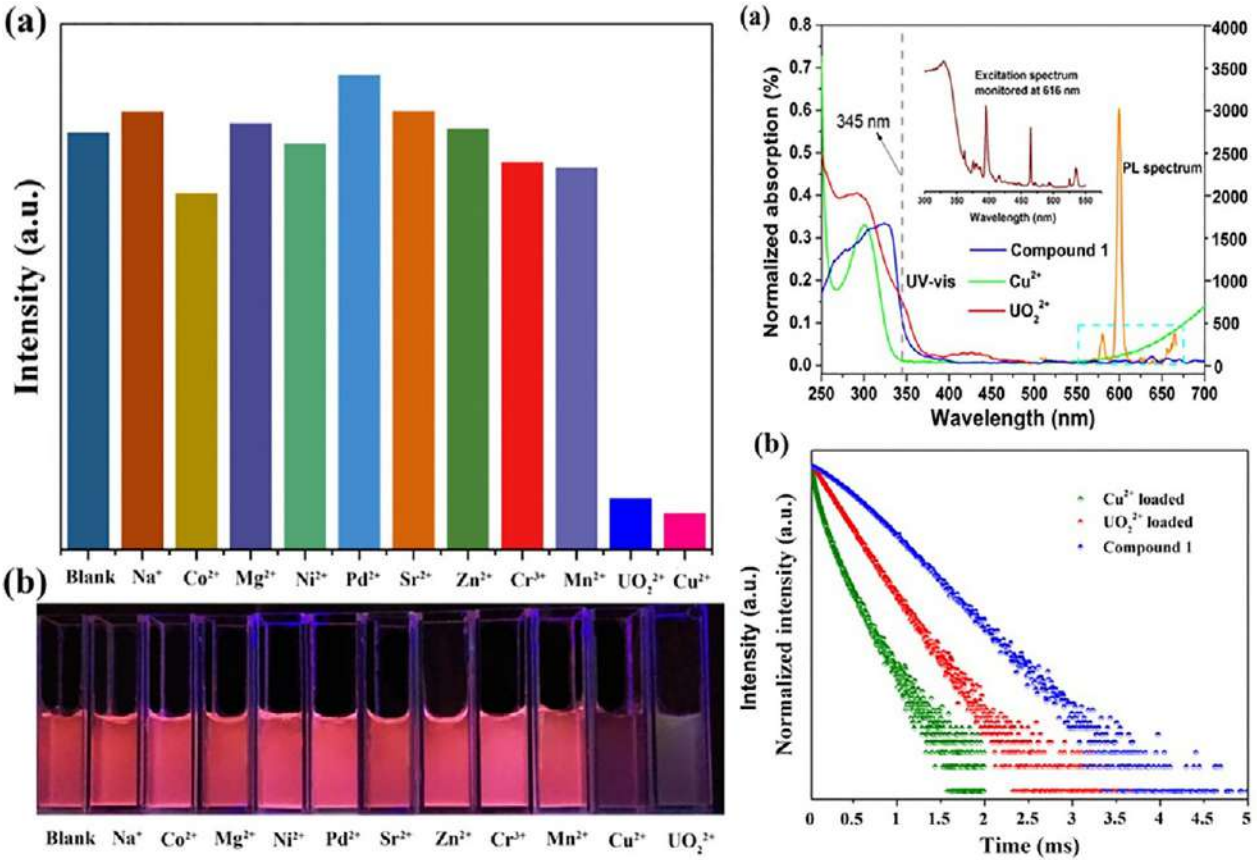

FIG. 3.4 *(Left)* (A) Luminescence intensity ($\lambda_{Em} = 616$ nm, $\lambda_{Ex} = 345$ nm) of Eu-MOF immersed in 300 mg/L M^{n+} solutions ($M^{n+} = Na^+$, Co^{2+}, Mg^{2+}, Ni^{2+}, Pd^{2+}, Sr^{2+}, Zn^{2+}, Cr^{3+}, Mn^{2+}, UO_2^{2+}, and Cu^{2+}). (B) Corresponding photograph of the luminescence of Eu-MOF immersed in various metal cation solutions. *(Right)* (A) Combined UV-vis absorption spectra of Eu-MOF, and Cu^{2+}- and UO_2^{2+}-loaded species, as well as the photoluminescence spectrum of Eu-MOF. Inset: excitation spectrum of compound 1 monitored at 616 nm. (B) The photoluminescence decay time of Eu^{3+} centers in free, Cu^{2+}- and UO_2^{2+}-loaded Eu-MOF monitored at 616 nm. *(Reproduced with permission from reference W. Liu, Y. Wang, L.Song, M. A. Silver, J. Xie, L. Zhang, L. Chen, J. Diwu, Z. Chai, S. Wang, Efficient and selective sensing of Cu^{2+} and UO_2^{2+} by a europium metal-organic framework, Talanta 196 (2019) 515–522. Copyright 2019 Elsevier.)*

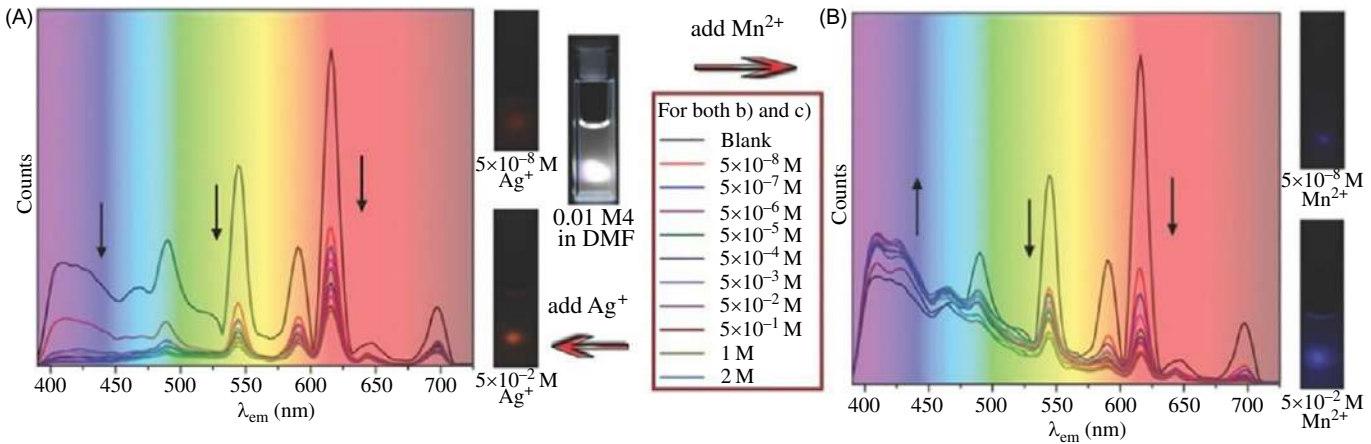

FIG. 3.5 (A) Luminescence spectra of the sensor with distinct concentrations of Ag^+ ions, and photographs of Ag^+@REMOF with Ag^+ ion concentrations of 5×10^{-8} M and 5×10^{-2} M. (B) Luminescence spectra of the sensor with distinct concentrations of Mn^{2+} ions, and photographs of Mn^{2+}@REMOF with Mn^{2+} ion concentrations of 5×10^{-8} M and 5×10^{-2} M. *(Reproduced with permission from reference Y. Li, S. Li, P. Yan, X. Wang, X. Yao, G. An, G. Li, Luminescence-colour-changing sensing of Mn^{2+} and Ag^+ ions based on a white-light-emitting lanthanide coordination polymer, Chem. Commun. 53 (2017) 5067–5070. Copyright 2017 Royal Chemical Society.)*

intensities of the green component (544 nm) and the red component (614 nm) evidently decrease with increasing Mn^{2+} ion concentration. Interestingly, the fluorescent intensity of the blue component (400–550 nm) increases. Therefore the blue-light emission dominates the emission with continuous addition of Mn^{2+} ions, which results in an LCC from white to blue. The luminescence lifetime of Ag^{+}@SmEuTb-MOF in DMF/water solution dramatically decreases, indicating the existence of interactions between analytes and sensor. Upon introduction of Ag^{+} ions, the ligand emission reveals a hypsochromic shift, illustrating an increase in the energy level of the π^* orbits of the ligand, resulting in an increment in the energy gap between the π^* level of the ligand and the resonance energy level of the RE^{3+} ions, which facilitates ligand-to-RE^{3+} ion energy transfer. As a result, the ligand emission (blue color) is quenched and so the RE^{3+} ion emission (red and green color) dominates. In contrast, introduced Mn^{2+} ions induce a bathochromic shift in the ligand emission, indicating a decrease in its π^* energy level, which blocks the energy transfer pathway from the π^* to the RE^{3+} ions. Therefore the ligand emission (blue color) increases and the RE^{3+} luminescence (red and green color) decreases substantially [35].

Yan's group has done extensive work on "Turn-Off" sensing based on luminescence quenching [36–39]. Qu et al. applied a straightforward PSM path to fabricate a hybrid material Tb^{3+}@MOF-SO_3^- as a luminescence sensor to biomarker *trans, trans*-muconic acid (*t*-MA) of benzene based on luminescence quenching. The luminescence of Tb^{3+}@MOF-SO_3^- suspension is totally quenched only by *tt*-MA (Fig. 3.6A; left). Notably, as shown in Fig. 3.6B (left), the emission intensity of Tb^{3+} ions at 544 nm in aqueous suspension of Tb^{3+}@MOF-SO_3^-/*tt*-MA contrasts sharply with that in aqueous suspension of Tb^{3+}@MOF-SO_3^-/other urine chemicals. Fig. 3.6A (right) shows gradual decreases of ligands-based emission and typical Tb^{3+} ions appearance as the *tt*-MA concentration increases from 0 to 200 $\mu g \cdot mL^{-1}$. When the concentration of *tt*-MA is 5 $\mu g\ mL^{-1}$, nearly half the intensity of the typical Tb^{3+} emission at 544 nm is quenched. When the *tt*-MA concentration is 100 $\mu g\ mL^{-1}$, the QE value of the typical Tb^{3+} emission is up to 92%, though the blue emission band of ligands can still be observed. Interestingly, under irradiation with a UV lamp, Tb^{3+}@MOF-SO_3^- test papers show visible luminous variation from light green to natty blue after soaking in various concentrations of *tt*-MA aqueous solutions (from 0 to 100 $\mu g\ mL^{-1}$) (Fig. 3.6B; right), demonstrating the good response sensitivity of Tb^{3+} ions to *tt*-MA. In the range of low concentrations of *tt*-MA from 0 to 20 $\mu g\ mL^{-1}$, a certain linear relationship ($R^2 = 0.97$) yields a linear curve, with K_{SV} to be calculated as 0.27932 mL μg^{-1} (Fig. 3.6C; right). The LOD is estimated to be 0.1 $\mu g\ mL^{-1}$ (ppm). The strong absorption from 230 to 285 nm is largely overlapped by the absorption band of MOF-SO_3^- and Tb^{3+}@MOF-SO_3^-, whose competitive absorption and the inefficient ligand-metal energy transfer can quench the emission of both ligand and Tb^{3+} ions. Moreover, the mechanism of dynamic quenching between the excited-stated Tb^{3+}@MOF-SO_3^- and *tt*-MA can be mainly responsible for the quenching effect of *tt*-MA on the luminescence of Tb^{3+} ions [36].

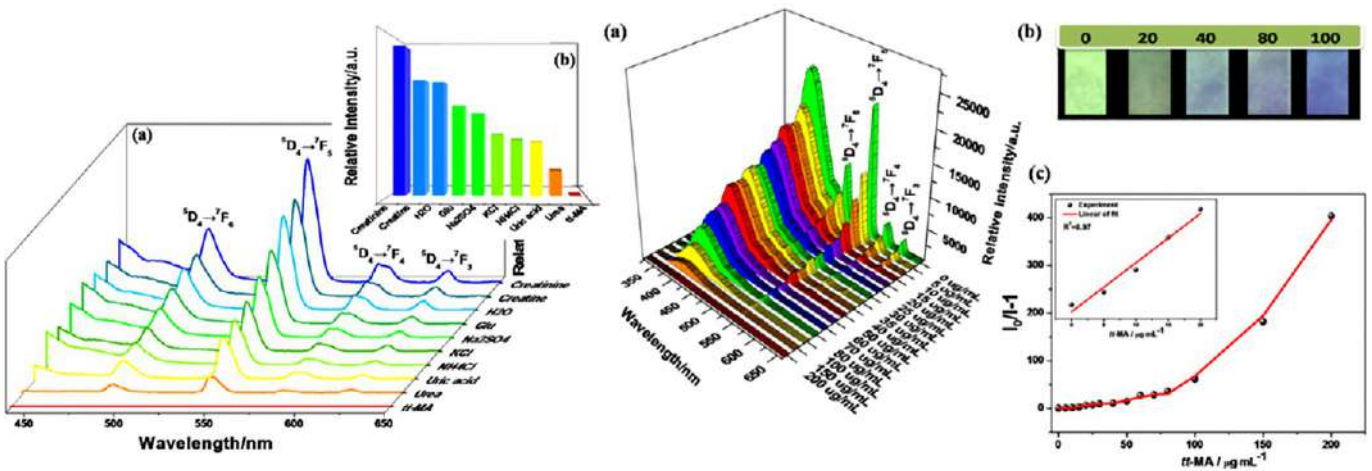

FIG. 3.6 *(Left)* Emission spectra of Tb^{3+}@MOF-SO_3^- in different aqueous solutions of common ingredients in urine, (A) and the emission intensities (B) of the main peak at 544 nm assigned to the $^5D_4 \rightarrow {}^7F_5$ transition of Tb^{3+} ($\lambda_{ex} = 291$ nm). *(Right)* (A) Emission spectra of Tb^{3+}@MOF-SO_3^- dispersed in aqueous solutions with different concentrations of *tt*-MA ($\lambda_{ex} = 291$ nm); (B) optical images of test paper under 254 nm UV light irradiation after immersing into aqueous solutions with different concentrations of *tt*-MA; (C) the *S-V* curve of I_0/I^{-1} versus concentration of *tt*-MA. *(Reproduced with permission from reference X. Qu, B. Yan, Ln(III)-functionalized metal-organic frameworks hybrid systems: luminescence properties and sensor for trans, trans-muconic acid as a biomarker of benzene, Inorg. Chem. 57 (2018) 7815–7824. Copyright 2018 American Chemical Society.)*

Qu et al. synthesized $\{[NH_2(CH_3)_2]_4{\cdot}[Cd_6(pdda)_4(HTz)_{1.5}(H_2O)_6]{\cdot}0.75DMF{\cdot}3.5H_2O\}_n$ and fabricated its hybrid Tb^{3+}@Cd-MOF (H_2pdda = 3, 5-di(2, 4-dicarboxylphenyl)pyridine, HTz = 1H-tetrazole) by cation exchange, which is proven for the practical luminescent detection of biomarker dichloroanilines (3, 4(5)-DCA) (Fig. 3.7; top) [37]. Under UV lamp irradiation, 3, 4(5)-DCA can

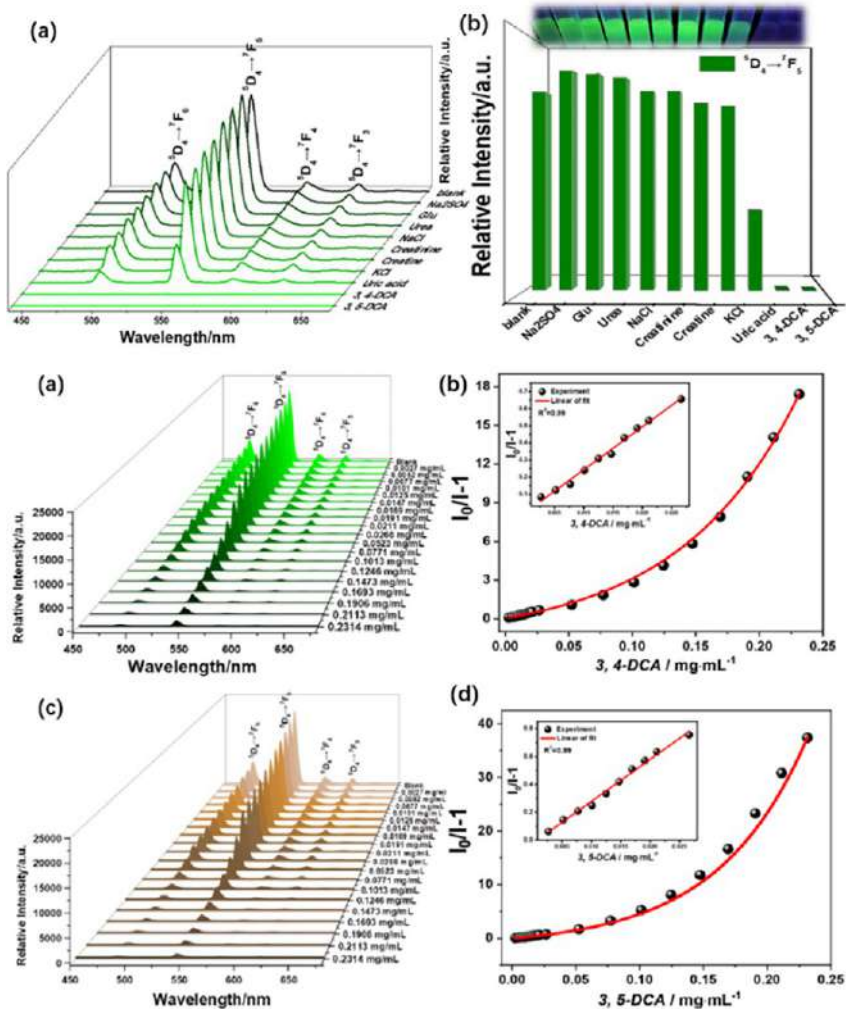

FIG. 3.7 *(Top)* The emission spectra (A) and intensities (B) at 545 nm of Tb^{3+}@Cd-MOF suspensions containing various urine chemicals. Inset for photographs under a 365-nm UV light. *(Bottom)* The emission spectra *S-V* curve of I_0/I^{-1} versus concentration of Tb^{3+}@Cd-MOF dispersed in DMF with different concentrations of 3, 4-DCA (A,B) and 3, 5-DCA (C,D). *(Reproduced with permission from reference X. Qu, B. Yan, Zn(II)/Cd(II)-based metal-organic frameworks: crystal structures, ln (III)-functionalized luminescence and chemical sensing of dichloroaniline as pesticide biomarker, J. Mater. Chem. C 8 (2020) 9427–9439. Copyright 2020 Royal Society of Chemistry.)*

induce a visible color change from green to colorless and differences in the effect of different urine chemicals on the Tb^{3+}@Cd-MOF emission (Fig. 3.7; top, inset). As shown in Fig. 3.7A and C (bottom), a gradual decrease in the emission of Tb^{3+}@Cd-MOF is observed upon the increasing concentrations of 3, 4(5)-DCA from 0 to 0.2314 mg mL^{-1}, both of which are nonlinear and match with the first-order exponential equation for the diffusion-controlled quenching processes. In the range of low content from 0 to 0.0266 mg mL^{-1}, it exhibits a good linear correlation ($R^2 = 0.99$) as the concentration of 3, 4(5)-DCA increases (Fig. 3.7B and D; bottom). The LODs are calculated to be 3.3 and 2.6 ppm, respectively. In addition, the quenching sensitivity of 3, 5-DCA to hybrids is better than that of 3, 4-DCA, which may originate from different host-guest effects. The specific interactions between dichloroaniline and the Tb^{3+} ion are attributed to the quenching induced by the interfilter effect (IFE). As the concentrations are above 0.0523 mg mL^{-1}, the decreases in lifetime values just confirm the existence of dynamic quenching for the probe toward 3, 4(5)-DCA. The excitation spectra of Tb^{3+}@Cd-MOF show significant blue shifts with the appearances of new peaks at about 285 nm and the diminishing of the original emission peaks at 300 nm, which gives direct proof for the existence of strong static quenching. These results suggest that more than one quenching mechanism exists in the sensing process: IFE at low concentrations and dynamic as well as static quenching at high concentrations of 3, 4(5)-DCA [37].

Lian et al. prepared a hybrid Eu^{3+}@Hf-MOF by coordinate postsynthetic modification (PSM), displaying an MPA (methyl phosphoric acid)-induced luminescence quenching, which is due to the metal-ligand charge tranfer (MLCT) from MPA to Hf^{6+} and generation of exciplex. It can be applied in wastewater detection, and with finer selectivity, high sensitivity (LOD = 0.4 ppm), and large linear range (10^{-7}–10^{-3} M) [38]. Fig. 3.8A (left) for the excitation spectrum shows a blue shift contrast with Hf-MOF for the energy transfer from the ligand to the Eu^{3+} ions. The approach for sensing of organic phosphoric chemical warfare agents (OPCWAs) is further supported by using luminescence measurement (Fig. 3.8B; left), and there is no obvious change in the luminescence intensity except MPA. The emission of Eu^{3+} to MPA has dropped markedly and quickly; the difference of $^5D_0 \rightarrow {}^7F_2$ emission between blank and testing samples is several times that of others (Fig. 3.8C; left). In consideration of the strong Brönsted acidity of Hf-MOF and deprotonation of phosphoric acid, the strong electron donor oxygen radical anion (R—O^-) is generated via the deprotonation of MPA, and CT occurs from donor to the excited-state Hf_{12} cluster as an electron acceptor, subsequently forming exciplex. Finally, the energy transfer from HfMOF to Eu^{3+} is forbidden and can result in luminescence quenching (Fig. 3.8; right) [38].

Qu et al. synthesized an anionic Cd-MOF, $\{[NH_2(CH_3)_2]_2 \cdot [Cd_{3.5}(bdba)(Hbdba)(H_2O)_{1.5}]\}_n$ (H_5bdba = 2, 5-bis(3′,5′-dicarboxylphenyl)-benzoic acid), further functionalized to a Tb^{3+}@Cd-MOF hybrid for sensing the biomarker diphenyl phosphate (DPP) [39]. The emission spectra and intensities in

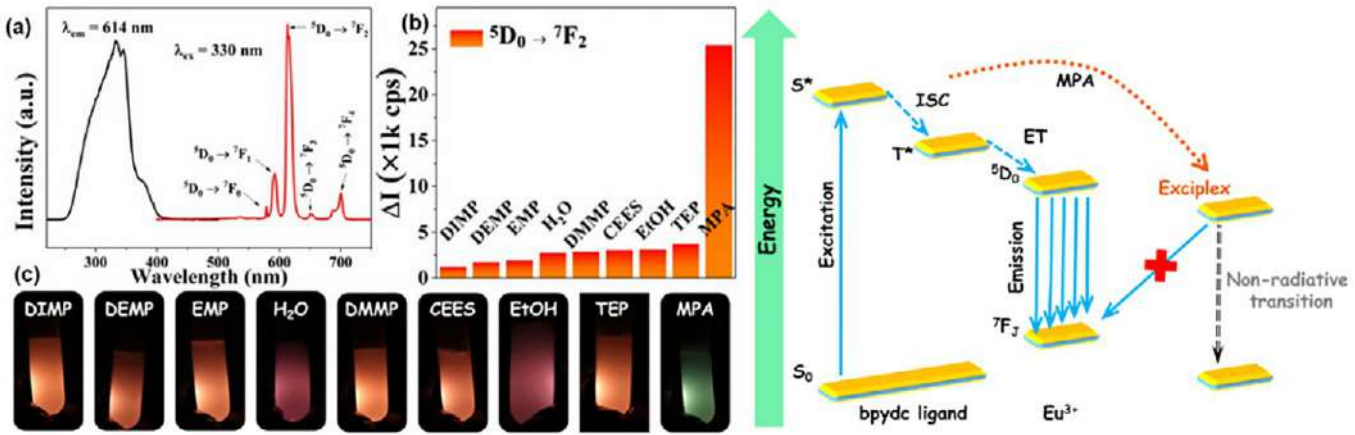

FIG. 3.8 *(Left)* (A) Luminescent spectra of Eu^{3+}@Hf-MOF in solid state; (B) the histogram of $^5D_0 \rightarrow {}^7F_2$ emission of Eu@1 in various solutions of OPCWAs; (C) photographs of Eu^{3+}@Hf-MOF in suspensions with various OPCWAs. *(Right)* Mechanism of the MPA-induced quenching. *(Reproduced with permission from reference X. Lian, B. Yan, Trace detection of organophosphorus chemical warfare agents in wastewater and plants by luminescent UiO-67(hf) and evaluating the bioaccumulation of organophosphorus chemical warfare agents, ACS Appl. Mater. Interf. 10 (2018) 14869–14876. Copyright 2018 American Chemical Society.)*

Tb^{3+}@Cd-MOF suspensions containing DPP contrast sharply with other urine chemicals (Fig. 3.9; top). Under the irradiation of a UV device, DPP can exclusively induce a visible color change from bright-green to colorless (Fig. 3.9; top, inset). As shown in Fig. 3.9A (bottom), a gradual decrease in the luminescence of Tb^{3+}@Cd-MOF suspensions is observed with the increasing concentrations of DPP from 0 to 0.5226 mg mL^{-1}. Within the full range of concentrations, the corresponding relationship curve exhibits a good linear correlation ($R^2 = 0.98$) (Fig. 3.9B; bottom). The absorption bands of DPP, H_5bdba ligand, Cd-MOF, and the hybrid show competitive absorption between DPP and the Tb^{3+}@Cd-MOF. The concentration-dependent lifetime measurement for Tb^{3+}@Cd-MOF to DPP validates the existence of the dynamic quenching mechanisms. In addition, the excitation spectra peak of Tb^{3+}@Cd-MOF displays gradual red shifts of 6 nm with relative high concentration of DPP (0.5226 mg mL^{-1}), proving the existence of static quenching.

3.3 "Turn-On" luminescence response chemical sensing for rare earth metal-organic framework hybrid materials

For "Turn-On" luminescence response sensing in rare earth MOFs hybrid materials, the reported example is relatively much less than those of the "Turn-Off" mode. Some "Turn-On" mode sensors are based on the introduction of a quenching transducer and then realization of the luminescence enhancement. Herein, such works will be ascribed to the "Turn-On-Off-On" mode and will be separately discussed in the next section. Sun et al. prepared a RE^{3+} PSM Ga-MOF hybrid (RE = Eu, Tb, Sm, Dy). Upon 314-nm excitation, Eu-Ga-MOF, Tb-Ga-MOF, and Eu/Tb-Ga-MOF all exhibited their respective strong sharp emission bands. However, Sm-Ga-MOF and Dy-Ga-MOF showed very similar emission to MIL-61 and almost no luminescence of Sm^{3+} and Dy^{3+}, which can be effectively sensitized by co-PSM Ag^+. In addition, single-phase white-light emitters based on the resulting 4d-4f heterometallic co-PSM MOFs hybrid could be realized. Furthermore, Sm-Ga-MOF showed more highly sensitive and selective sensing toward Ag^+ [40]. Gamonal et al. used two isostructural Ln-MOFs, including an amino group as the sensitive recognition center for NO_2 molecules. A gas-sensing mechanism exploiting RE^{3+} luminescence modulation upon NO_2 adsorption was demonstrated. The transfer of energy from the ligands to Ln^{3+} was strongly dependent on the presence of NO_2, resulting in an unprecedented photoluminescent sensing scheme. Thereby, NO_2 exposition triggered either a reversible enhancement or a decrease in the luminescence intensity to the LRE^{3+} ion [41].

Zhou et al. demonstrated a water sensor based on a dual-emitting Eu-MOF from a 2-aminoterephthalic acid (atpt) ligand with responsive fluorescence inherent in its intramolecular charge transfer (ICT) process [42]. This ICT process can be rapidly Turn-On in the presence of water, owing to its ability to

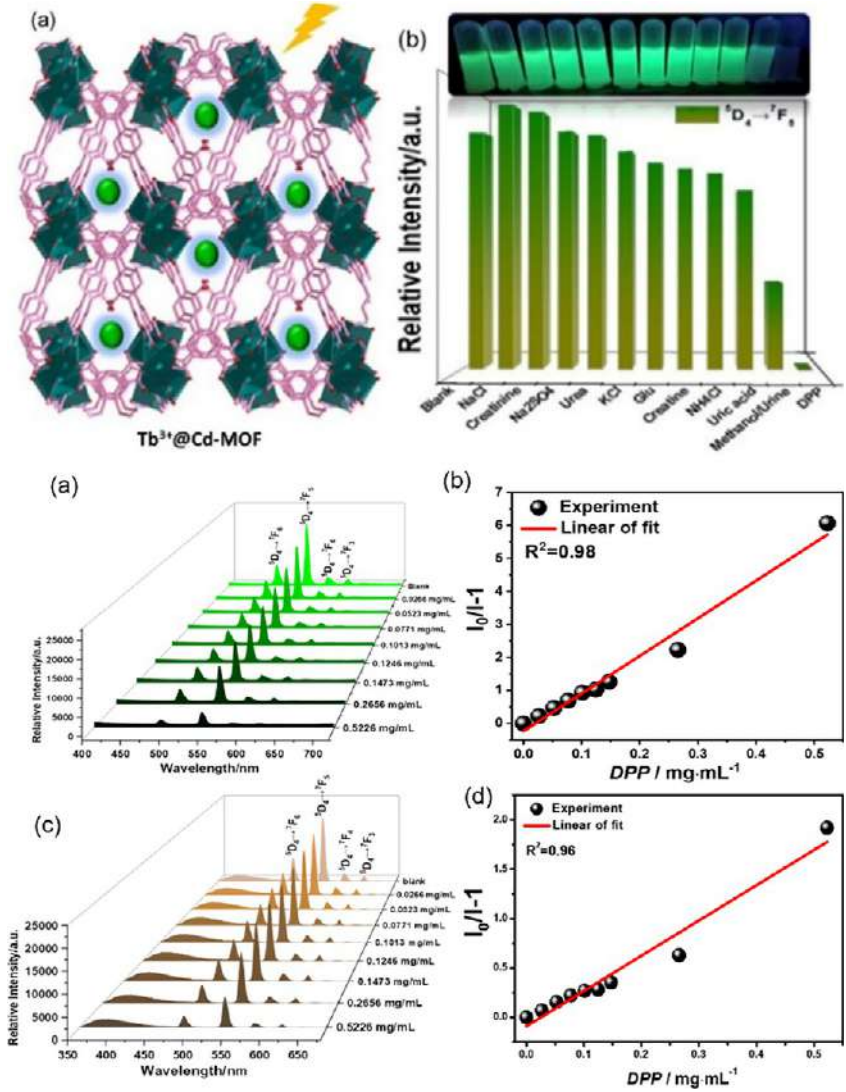

FIG. 3.9 *(Top)* (A) Scheme for Cd-MOF containing uncoordinated carbonyl groups pointing to the pores acting as PSM site for Tb^{3+} functionalization; (B) Intensities at 544 nm of Tb^{3+}@Cd-MOF suspensions containing various urine chemicals. Inset, the corresponding photographs of different suspensions under a 365-nm UV light. *(Bottom)* (A) The emission spectra of Tb^{3+}@Cd-MOF dispersed in methanol with different concentrations of DPP, and (B) *S-V* curve of I_0/I^{-1} versus concentration of DPP. (C) Emission spectra of Tb^{3+}@Cd-MOF dispersed in reconstituted urine samples with different concentrations of DPP, and (D) *S-V* curve of I_0/I^{-1} versus concentration of DPP. *(Reproduced with permission from reference X. Qu, B. Yan, A Cd-based MOF containing uncoordinated carbonyl groups as lanthanide post-synthetic modification sites and chemical sensing of diphenyl phosphate as fame retardant biomarker, Inorg. Chem. 59 (2020) 15088–15100. Copyright 2020 American Chemical Society.)*

boost and stabilize the ICT state. The significant ratiometric luminescence response induced by water makes Eu-MOF undergo a distinct change of emitting color from red to blue, which is favorable for visual analysis with the naked eye. The emission color change of Eu-MOF is very sensitive, which is observable by the naked eye from red to magenta in the presence of a low water content of 1% (v/v) (Fig. 3.10A; left). From the CIE coordinates in Fig. 3.10B (left), the calculated chromaticity progressively moves from red to blue, and a linear relationship between the CIE coordinate and water content can be established, suggesting the feasibility of quantitative water sensing by monitoring the luminescence color by the naked eye or with a CCD camera. The emission spectra of atpt in various solvents (acetone, DMF, ethanol, water) are recorded (Fig. 3.10A; right). With the increase of solvent polarity from cyclohexane to water, the emission of atpt undergoes a distinct red shift, which supports

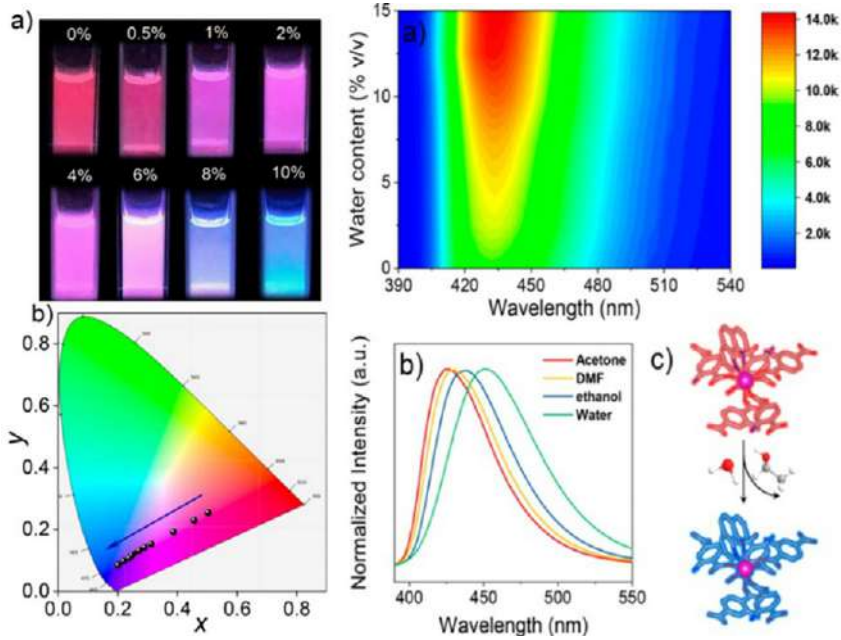

FIG. 3.10 *(Left)* (A) Photographs of Eu-MOF in DMF containing different water contents (0.05%–10%, v/v) under 365-nm irradiation by a UV lamp. (B) The CIE chromaticity coordinates calculated from the emission spectra presented in (A, *left*) showing the linear shift from *red* to *blue* region with increasing water content from 0% to 10% (v/v). *(Right)* (A) color-coded contour map showing emission spectra of atpt ligand in DMF with various water contents (0%–15%, v/v). (B) Emission spectra of atpt (1×10^{-7} M) in water and different organic solvents (acetone, DMF, ethanol). The emission spectra are normalized to the same intensity. (C) Schematic illustration of luminescent-sensing mechanism of Eu-MOF toward water. *(Reproduced with permission from reference Y. Zhou, D. Zhang, W. Xing, J. Cuan, Y. Hu, Y. Cao, N. Gan, Ratiometric and turn-on luminescence detection of water in organic solvents using a responsive europium-organic framework, Anal. Chem. 91 (2019) 4845–4851. Copyright 2019 American Chemical Society.)*

the charge transfer nature of the emissive state. The ICT state can be further stabilized by efficient hydrogen bonding with water, owing to its smaller size and low steric hindrance. The effective stabilization of the ICT state is reflected by the maximum emission wavelength that occurs in water (Fig. 3.10B; right). In addition to the stabilization, the hydrogen bonding of water with carboxylic oxygen increases the electron affinity of the electron acceptor (carboxyl group), promoting the charge flow from the donor to the acceptor (amino group) and favoring the ICT process. The ICT emission is subsequently switched on for water's boosting formation and effective stabilization (Fig. 3.10C; right) [42].

Wang et al. developed a dual-signal probe based on a boric acid (BA)-functionalized REMOF (BA-Eu-MOF) with 5-boronobezene-1, 3-dicarboxylic acid (5-bop) ligand for the detection of Hg^{2+} and CH_3Hg^+ [43], as 5-bop provides reaction sites for Hg^{2+} and CH_3Hg^+. Owing to the electron-withdrawing effect of the BA group, the "antenna" effect of the ligand was passivating and BA-Eu-MOF showed weak red emission in water. Upon addition of Hg^{2+} or CH_3Hg^+ into the system, a transmetalation reaction takes place, i.e., BA groups are replaced by Hg^{2+} or CH_3Hg^+; therefore the "antenna" effect of the ligand is triggered, leading to the enhancement of red emission. As Hg^{2+} or CH_3Hg^+ concentration increases, the red emission is gradually enhanced, and the color change is also observed with the naked eye under 365-nm ultraviolet light. To verify the specific recognition of BA-Eu-MOF toward Hg^{2+} or CH_3Hg^+ ions, a series of fluorescence tests in the presence of various metal ions were performed, and the results are shown in Fig. 3.11. The results showed that, under the same conditions, only Hg^{2+} or CH_3Hg^+ lead to remarkable fluorescence enhancement [43].

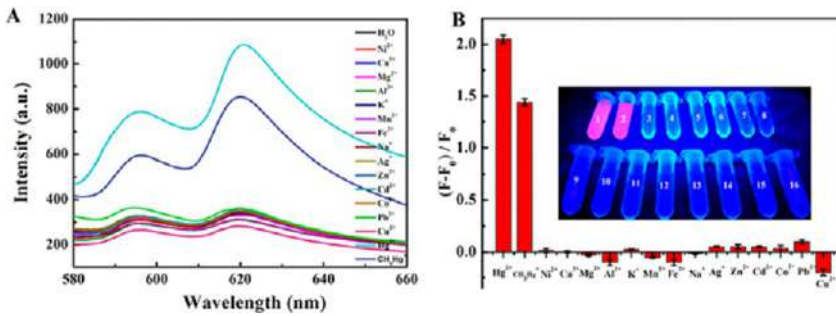

FIG. 3.11 (A) Fluorescence spectra of BA-Eu-MOF toward various metal ions at the same concentrations (120 μM). (B) $(F - F_0)/F_0$ of different metal ions; the inset shows the detection system of BA-Eu-MOF (0.3 mg mL^{-1}) in response to 120 μM concentrations of different metal ions under UV light at 365 nm (the *white* numbers correspond to the ions below from left to right). *(Reproduced with permission from reference H. Wang, X. Wang, M. Liang, G. Chen, R. Kong, L. Xia, F. Qu, A boric acid-functionalized lanthanide metal-organic framework as a fluorescence "turn-on" probe for selective monitoring of Hg^{2+} and CH_3Hg^+, Anal. Chem. 92 (2020) 3366–3372. Copyright 2020 American Chemical Society.)*

Luo et al. reported on luminescence "Turn-On" sensors for Gsp (gossypol, a natural toxin concentrated in cottonseeds that poses great risks with consumption of cottonseed products and is used extensively throughout the food industry) using near-infrared (NIR) emitting RE-MOFs [44], which is further identified as a "Turn-On" of Yb-NH_2-TPDC photoluminescence due to the "antenna effect" of Gsp. In the absence of Gsp, a solid Yb-NH_2-TPDC sample under acetone, when excited between 300 and 475 nm, exhibits the characteristic Yb^{3+} NIR emission band at 940–1060 nm corresponding to the $^2F_{5/2} \rightarrow {}^2F_{7/2}$ transition of Yb^{3+} (Fig. 3.12A; top). Intriguingly, incubating Yb-NH_2-TPDC with Gsp led to a red-shift of the long wavelength edge of the excitation band of Yb^{3+} from 475 nm as observed in the blank sample to 550 nm (Fig. 3.12B; top). Compared to the blank sample, a decrease in Yb^{3+} intensity in the presence of Gsp is also noted when Yb-NH_2-TPDC is excited between 340 and 400 nm. The observed extension of the excitation range of Yb^{3+} to longer wavelengths in the presence of Gsp is consistent with the fact

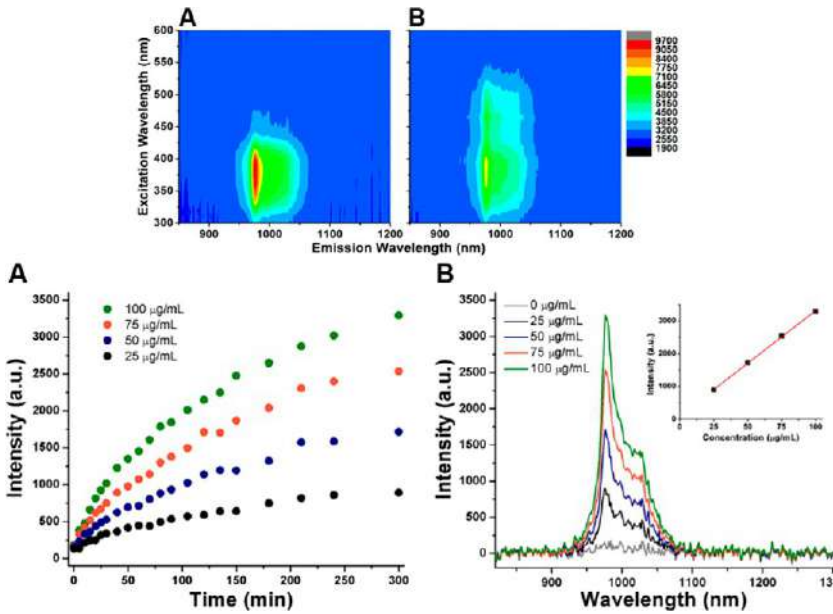

FIG. 3.12 *(Top)* Excitation-emission maps of Yb-NH_2-TPDC (A) in the absence of Gsp and (B) in the presence of Gsp. *(Bottom)* Gsp-sensing experiments using Yb-NH_2-TPDC. (A) Kinetics of Yb^{3+} luminescence of Yb-NH_2-TPDC emission at 976 nm in response to Gsp solutions of different concentrations (100 μg/mL, *green*; 75 μg/mL, *orange*; 50 μg/mL, *blue*; 25 μg/mL, *black*). (B) Emission spectra of Yb-NH_2-TPDC samples in response to different Gsp concentrations at 300 min (100 μg/mL, *green*; 75 μg/mL, *orange*; 50 μg/mL, *blue*; 25 μg/mL, *black*; *blank*, *gray*; calibration curve, inset). *(Reproduced with permission from reference T. Luo, P. Das, D. L. White, C. Liu, A. Star, N. L. Rosi, Luminescence "turn-on" detection of gossypol using Ln^{3+}-based metal-organic frameworks and Ln^{3+} salts, J. Am. Chem. Soc. 142 (2020) 2897–2904. Copyright 2020 American Chemical Society.)*

that it can either directly act as a sensitizer for the Yb^{3+} ions or modify the sensitization wavelength of the NH_2-TPDC linker via formation of Schiff base product. Fig. 3.12A (bottom) shows the evolution of Yb^{3+} intensity at 976 nm as a function of time, where data points at 0 min represent intensity measured immediately after the addition of Gsp solutions. Upon addition of Gsp, Yb^{3+} emission gradually increases over 300 min. With an equal amount of incubation time, stronger Yb^{3+} intensity correlates with higher Gsp concentration in the 25–100 μg/mL range (Fig. 3.12B; bottom). At 300 min, Yb^{3+} intensity follows a linear dependence with Gsp concentration between 25 μg/mL and 100 μg/mL (Fig. 3.12B; bottom, inset), and therefore is suitable for quantification of Gsp in this concentration range. Interference from background molecules present in realistic samples, such as cottonseed oil and cottonmeals, does not induce Yb^{3+} PL (white bars in Fig. 3.12C; bottom). To assess the Gsp detection performance of Yb-NH_2-TPDC in the presence of background substances, Yb^{3+} intensity at 976 nm in response to Gsp (100 μg/mL) without interference is compared to intensity in the presence of interference (shaded bars in Fig. 3.12C; bottom).

Xu et al. assembled a multicomponent hybrid material via the integration of Eu-MOFs and organic dyes (methylred, MR). The carboxylic acid group of MR offers the possibility of covalent linking to the amino group-rich Eu-MOFs to yield MR@Eu-MOFs, which contain two emission centers, MR and Eu^{3+}. Both of the emission centers show pH-induced intensity changes, which can be constructed for monitoring BAs, the indicators of food spoilage and alkaline matter [45]. As shown in Fig. 3.13 (left), the luminescence intensity of Eu^{3+} decreases at 613 nm (F_{Eu}: threefold) and the maximum emission wavelength of MR increases (F_{MR}: 44-fold), leading to the emission color of the MR@Eu-MOFs changing from red to blue under a UV lamp. The MR@Eu-MOFs (40 mg) are solidified into a CMC-Na hydrogel to easily prepare a portable sensor. When the hydrogels are exposed to the HI vapor, the pH will increase due to the basicity of HI. Fig. 3.13A and B (right) shows that the luminescence intensities of F_{Eu} and F_{MR} change with the HI aqueous solution concentration and the exposure time. Saturation is reached after 25 min for all concentrations; the luminescence spectra are given in Fig. 3.13C (right). The emission intensity of Eu^{3+} decreases, while the MR-based emission increases as the HI concentration increases, and the hydrogel color gradually changes from red to blue-violet, to blue (Fig. 3.13D; right). The HI concentration is quantitatively analyzed using the response signals, being defined as the ratio of F_{MR} to F_{Eu} (Fig. 3.13E; right). It shows a good linear relationship ($R^2 = 0.9903$) between the response signals and the HI vapor concentration ranged in 0–250 μM, and a LOD of 0.1 μM [45].

Liu et al. used a PSM cation exhange method to prepare a Eu^{3+} functionalized PbMOF hybrids (Eu^{3+}@Pb-MOF) [46], which can be designed to be a "Turn-On" probe of fleroxacin. With the addition of fleroxacin into the solution, the intensity of $^5D_0 \rightarrow {}^7F_J$ ($J = 0$–4) transitions of Eu^{3+} ions are extremely enhanced. As depicted in Fig. 3.14A and B, Eu^{3+}@Pb-MOF has different

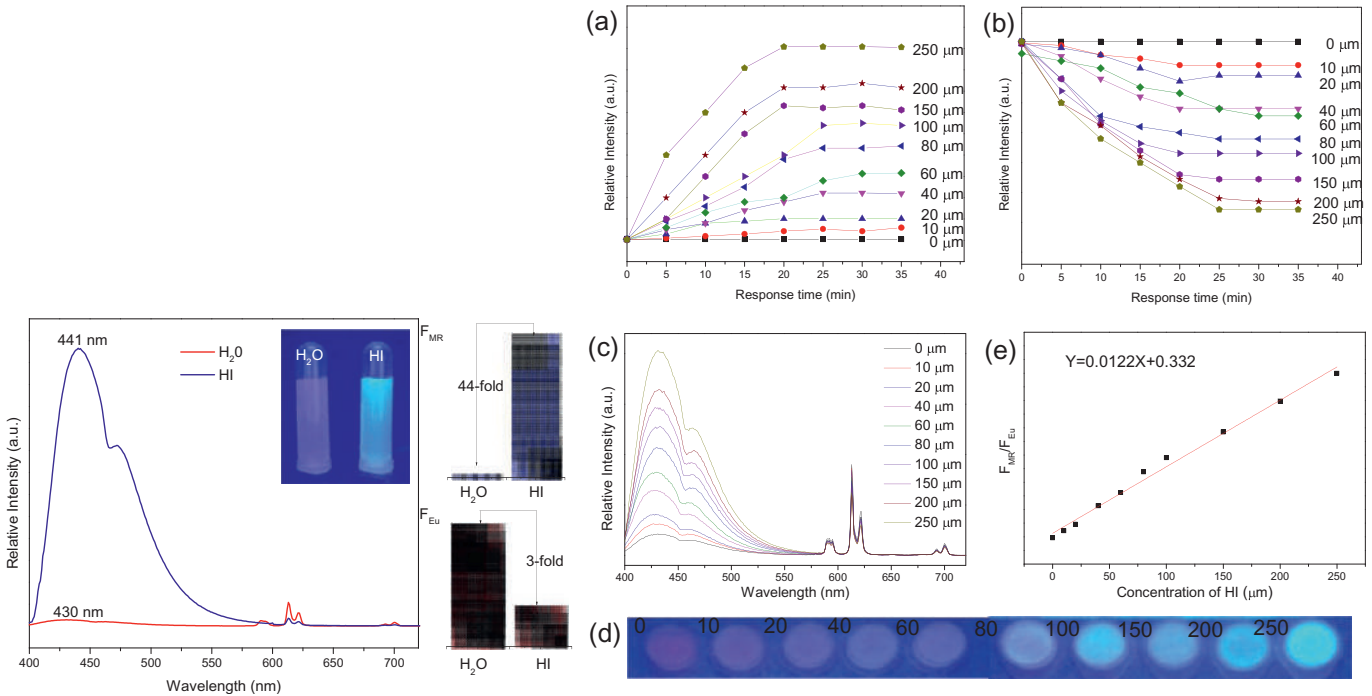

FIG. 3.13 *(Left)* The emission spectra of MR@Eu-MOFs and comparison of F_{MR} and F_{Eu} before and after being treated by HI at an excitation wavelength of 370 nm. Inset for the optical photograph under 365-nm UV-light irradiation. *(Right)* Emission intensity of F_{MR} (A) and F_{Eu} (B) in different times (0–35 min) upon exposure to HI at concentrations from 0 to 250 μM ($\lambda_{ex} = 370$ nm); concentration-dependent emission spectra (C) and corresponding optical photograph under 365-nm UV-light irradiation (D) of MR@Eu-MOFs sensory hydrogel with different concentrations of HI from 0 to 250 μm; (E) the linear fitted curve showing F_{MR}/F_{Eu} vs. HI concentration, $\lambda_{ex} = 370$ nm. *(Reproduced with permission from reference X. Xu, X. Lian, J. Hao, C. Zhang, B. Yan, Double stimuli-responsive fluorescent center for food spoilage monitoring based on dye covalent modified EuMOFs: from sensory hydrogel to logic device, Adv. Mater. 29 (2017) 1702298. Copyright 2017 WILEY-VCH.)*

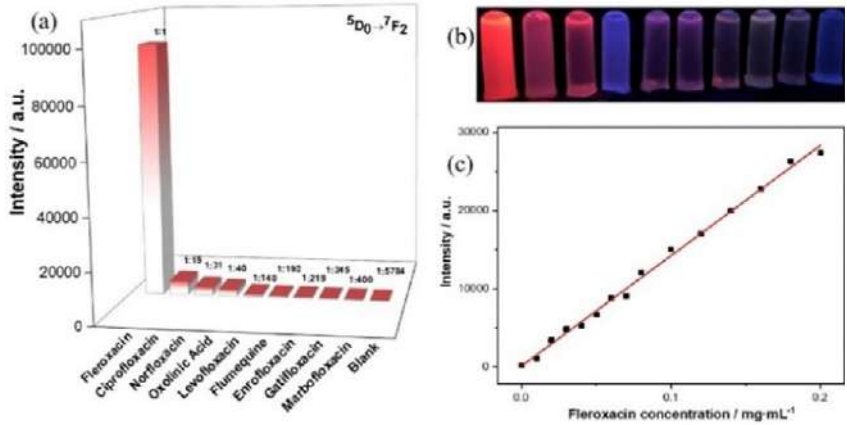

FIG. 3.14 (A) Emission intensities of the main peak at 612 nm assigned to $^5D_0 \rightarrow {}^7F_2$ transition of Eu^{3+} ($\lambda_{ex} = 377$ nm); (B) the inset shows the photograph of the Eu^{3+}@Pb-MOF aqueous suspensions containing different quinolone drugs under 365-nm UV light; the order is the same as that in (A); and (C) The fitting curve of the emission intensity (613 nm) of Eu^{3+}@Pb-MOF vs. fleroxacin concentration. *(Reproduced with permission from reference T. Liu, X. Qu, B. Yan, A highly sensitive and selective "turn-on" fluorescent probe of fleroxacin in human serum and urine based on Eu^{3+} functionalized metal-organic framework, Dalton Trans. 48 (2019) 17945–17952. Copyright 2019 Royal Society of Chemistry.)*

degrees of luminescence response to the quinolone drugs, and the ratios between the intensity of fleroxacin and that of others at 612 nm are marked in the figure. The luminescence titration experiment reveals an obvious linear relationship ($R^2 = 0.9954$) between the emission intensity of solutions at 613 nm and the concentrations of fleroxacin in the experimental range with LOD of 43.91 ng/m (Fig. 3.14C). The mechanism of luminescence enhancement can be easily attributed to the self-assembly of Eu^{3+} ions with β-diketonate. The structure of fleroxacin contains a β-diketone moiety and produces the effective coordination interaction and "antenna effect" on Eu^{3+} [47].

Sun et al. used a feasible method for *N*-methylformamide (NMF) detection with a hybrid (Eu^{3+}@Ga-MOF) [48]. As shown in Fig. 3.15A (left), upon addition of NMF to the suspensions of Eu^{3+}@Ga-MOF, the luminescence intensity of Eu^{3+} at 613 nm is enhanced significantly, while the ligand emission is suppressed. A bright red color can be observed with the naked eye under a UV lamp. The intensity of the $^5D_0 \rightarrow {}^7F_2$ transition increased by five times in the presence of NMF from the Fig. 3.15B (left). Only NMF induced a distinct color change of Eu^{3+}@Ga-MOF from dark to bright red under a UV lamp, which can act as a sign indicating the emergence of DMF in individual performance (inset of Fig. 3.15B; left). The recycling performance of Eu^{3+}@Ga-MOF as a urinary NMF sensor is shown in Fig. 3.15A (right). After four cycles, every circle expresses corresponding enhancement and recovery of the luminescence intensity. As shown in Fig. 3.15B (right), under UV irradiation, the luminescent

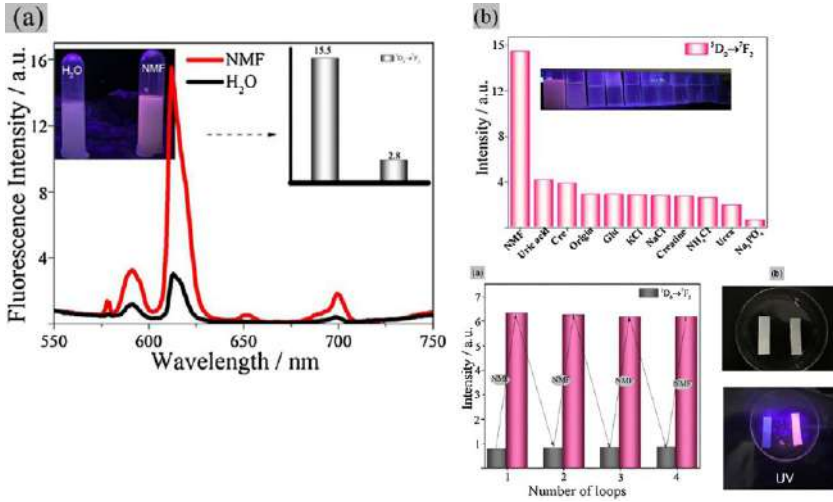

FIG. 3.15 *(Left)* (A) The luminescence spectra of Eu^{3+}@Ga-MOF in the absence and presence of NMF, respectively. Inset: the changes of luminescence intensity (613 nm) and luminescence color (under UV-light irradiation of 256 nm) induced by addition of NMF; (B) the corresponding luminescence intensity ($^5D_0 \rightarrow {}^7F_2$ transition) of Eu^{3+}@Ga-MOF with various urine components. Inset in (B): the corresponding photograph under irradiation of UV light (254 nm). *(Right)* (A) Luminescence intensities of Eu^{3+}@Ga-MOF at 613 nm during three consecutive enhancement and recovering cycles. (B) The prepared test paper in the absence and in the presence of NMF with the irradiation of UV lamp. *(Reproduced with permission from reference N. Sun, B Yan, Fluorescence detection of urinary N-methylformamide for biomonitoring of human occupational exposure to N,N-dimethylformamide by Eu(III) functionalized MOFs, Sens. Actuators B Chem. 261 (2018) 153–160. Copyright 2018 Elsevier.)*

color of the test card smeared with the suspension of NMF-Eu^{3+}@Ga-MOF (NMF: 0.01 M) is bright red by the naked eye, which can be used to judge the degree of DMF intoxication in an individual through the color change.

3.4 "Turn-on-off-on" luminescence response chemical sensing for rare earth metal-organic framework hybrid materials

In nature, the "Turn-On-Off-On" luminescent response belongs to a kind of "Turn-On" mode if we consider the final response to a special analyte. Generally, here "Turn-On-Off" is the strategy or path to realize the final "Turn-On" effect. In order to distinguish it from the direct "Turn-On" mode, it will be strengthened separately. Zeng et al. synthesized a dual-emission multivariate Eu^{3+}@Al-MOF by sequential mixed-ligand self-assembly and a PSM method. The hybrid possessed two emission bands: the strong blue emission from ligands sensitive to hypochlorite and the red emission from Eu^{3+} almost invariable. Thus it can realize the ratiometric luminescence "On-Off" sensing of HCl with LOD of

0.094 μM. In addition, the suppressed blue emission is recovered after the addition of ascorbic acid (AA) that consumes ClO^- via the redox reaction. Therefore it can be further employed for the RL "On-Off-On" sensing of AA [49].

More research projects are using co-PSM metal ions to quench the luminescence of RE^{3+} functionalized MOF hybrids, realizing the "Turn-On-Off" effect, and then responding to the analyte to result in the subsequent "Turn-On" response. The most commonly used co-PSM metal ion is currently Cu^{2+} [49–56]. Using Tb^{3+} and 1,3,5-benzenetricarboxylate (BTC), and Cu^{2+} as the signal modulator as well as a recognition unit, Liu et al. proposed a novel and effective rare earth functionalized MOF fluorescent sensor (Cu-BTC/Tb) for amyloid β-peptide (Aβ) monomer, a biomarker for Alzheimer's disease (AD) [50]. Specifically, Cu-BTC/Tb, created by a PSM strategy, is almost nonemissive due to the quenching effect of Cu^{2+} in the MOCP; exhilaratingly, the presence of Aβ1–40 triggered a significant emission enhancement of Cu-BTC/Tb assay due to the high binding affinity of Aβ1–40 for Cu^{2+} and the subsequent suppression of the quenching effect. The Tb-MOF alone emits strong time-resolve luminescence; however, when Tb^{3+} is introduced into Cu-BTC by the PSM method, the formed Cu-BTC/Tb is very weakly emissive due to the quenching effect of Cu^{2+} to Tb^{3+}. Interestingly, the subsequent addition of Aβ1–40 induces a strong emission to an originally nonemitting Cu-BTC/Tb owing to the specific interaction between Cu^{2+} and Aβ1–40 (Fig. 3.16; left). To evaluate the sensing performance of the as-synthesized Cu-BTC/Tb toward Aβ1–40, the emission variations at 545 nm corresponding to the Tb^{3+} $^5D_4 \rightarrow {}^7F_5$ transition were checked with different concentrations of Aβ1–40 (Fig. 3.16; right). The luminescence intensities of Cu-BTC/Tb suspensions (mole ratio, Cu:Tb = 1:5) increased gradually upon incremental concentrations of Aβ1–40 Fin, and an eight times fluorescence enhancement vs. the initial emission intensity was observed. The intensity at 545 nm correlates well with the concentration of Aβ1–40 in the range of 1–550 nM with a detection limit of 0.3 nM. They checked the influence of Aβ1–40 on the fluorescence intensity of Tb-BTC/Tb^{3+}, with no obvious fluorescence sensitization of Tb-BTC/Tb^{3+} by Aβ1–40 observed. The increasing luminescence lifetime proved the increase of signal intensity of Cu-BTC/Tb from the strong interaction between Cu^{2+} and the residues H6, H13, H14, and the N-terminus in Aβ1–40 [50].

Lian et al. synthesized a phosphonate MOF and its Eu^{3+} hybrid Eu^{3+}/Cu^{2+}@Al-MOF, whose Eu^{3+} luminescence rebounds in the presence of uric acid. This "On-Off-On" pattern is utilized for detecting uric acid, which is the final metabolite of purine (Fig. 3.17; top, left) [51]. As shown in Fig. 3.17 (top, right), only uric acid induces a remarkable rebound in the luminescence intensity of Eu^{3+} at 612 nm. Uric acid can't influence the luminescence of Eu^{3+}@Al-MOF, but a Eu^{3+}/Cu^{2+}@Al-MOF hybrid shows almost no luminescence emission; the quench effect of Cu^{2+} for 4f-4f emission of Eu^{3+} is obvious. However, with the addition of uric acid into Eu^{3+}/Cu^{2+}@Al-MOF suspensions, the luminescent intensity is

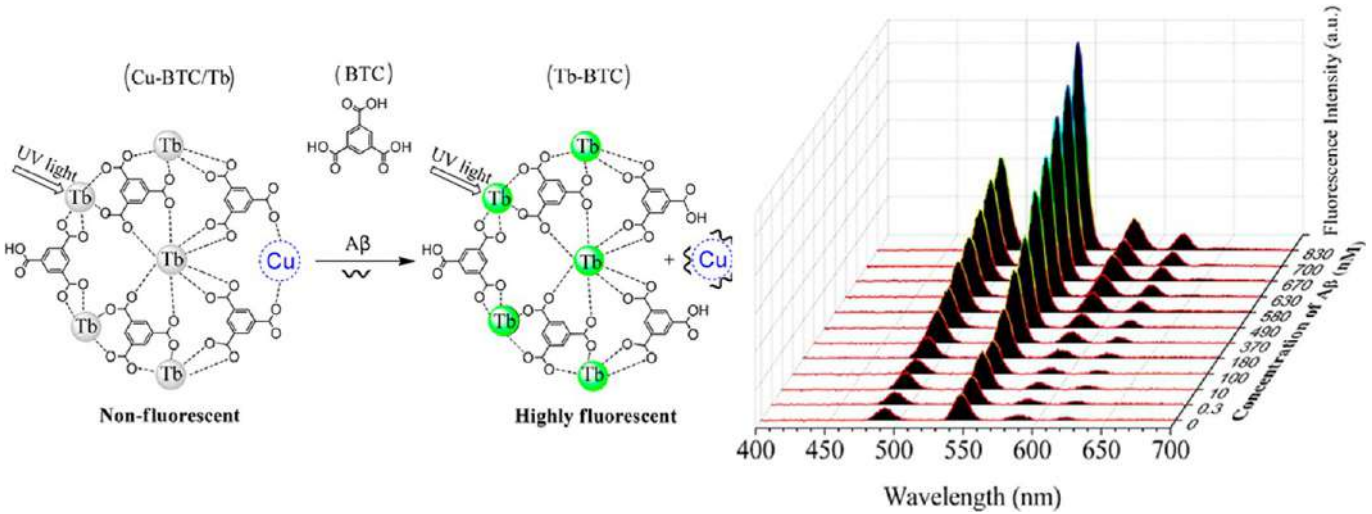

FIG. 3.16 *(Left)* Schematic diagram of LMOCP (Cu-BTC/Tb) assay for Aβ1–40. *(Right)* Fluorescence variation of Cu-BTC/Tb upon the addition of Aβ1–40 with different concentrations 0, 0.3, 10, 100, 180, 370, 490, 580, 630, 670, 700, and 830 nM. The detection was conducted in a mixed solution of DMSO and HEPES buffer (10 mM, pH 7.4) (volume ratio = 2:1). *(Reproduced with permission from reference B. Liu, H. Shen, Y. Hao, X. Zhu, S. Li, Y. Huang, P. Qu, M. Xu Lanthanide functionalized metal-organic coordination polymer: toward novel turn-on fluorescent sensing of amyloid β-peptide, Anal. Chem. 90 (2018) 12449–12455. Copyright 2018 American Chemical Society.)*

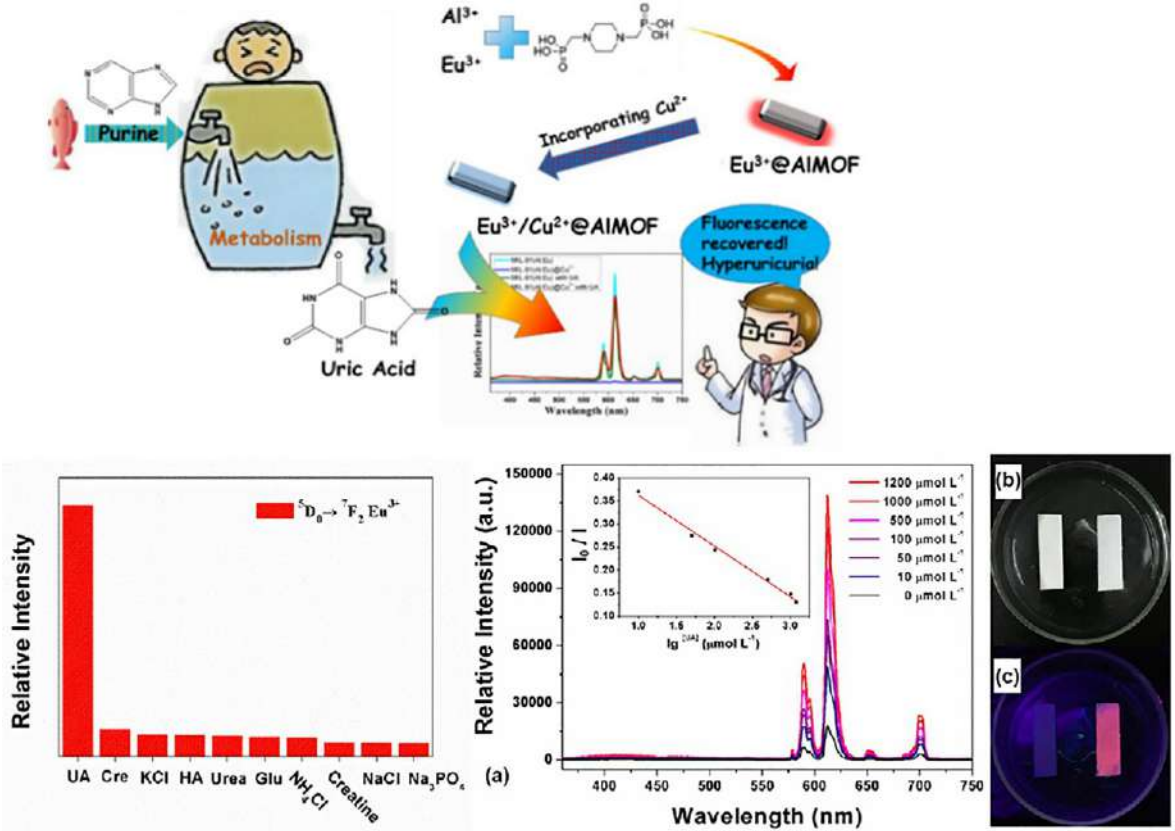

FIG. 3.17 *(Top, left)* The diagrammatic drawing of the whole sensing mechanism and process. *(Top, right)* The histogram based on the intensity of the $^5D_0 \rightarrow {}^7F_2$ transition of Eu^{3+} in Eu^{3+}/Cu^{2+}@Al-MOF toward various urine chemicals. *(Bottom)* (A) The luminescence spectra of Cu^{2+}@Al-MOF in the presence of different concentrations of uric acid aqueous solution, and the plot of I_0/I versus the logarithm of the concentration of uric acid; (D) and (C) are the test papers under light and UV irradiation. *(Reproduced with permission from reference X. Lian, B. Yan, Phosphonate MOFs composite as off-on fluorescent sensor for detecting purine metabolite uric acid and diagnose hyperuricuria, Inorg. Chem. 56 (2017) 6802–6808. Copyright 2017 American Chemical Society.)*

recovered. They found a good linear relationship ($R = 0.991$) between the intensity ratios of $^5D_0 \rightarrow {}^7F_J$ transition (I_0/I) and the logarithm of uric acid concentration with LOD of 1.6 μmol L^{-1}. The test paper is shown in Fig. 3.17B and C (bottom); under UV irradiation, the luminescent color of the test paper that was immersed in the urine containing 1000 μmol L^{-1} uric acid is relucent red, and the other test paper treated with low-concentration uric acid shows almost no luminescence [51].

Hao et al. designed a luminescent nanoprobe based on a Eu^{3+}/Cu^{2+}@Zr-MOF hybrid. The implantation of Cu^{2+} not only can tune the luminescence of Eu^{3+} via an energy transfer process but also can serve as reactive sites for urinary thiodiglycolic acid (TDGA) as a biomarker for carcinogenic vinyl chloride monomer (VCM) [52]. In contrast to TDGA, the addition of these components only causes negligible changes in the luminescence spectra intensities (Fig. 3.18A). Under a UV lamp irradiation, only TDGA induces a visible color change from colorless to red, which can be easily distinguished by the naked eye. As shown in Fig. 3.18B, the emission signals of Eu^{3+} in the hybrid are found to gradually increase with the increasing additional amount of TDGA

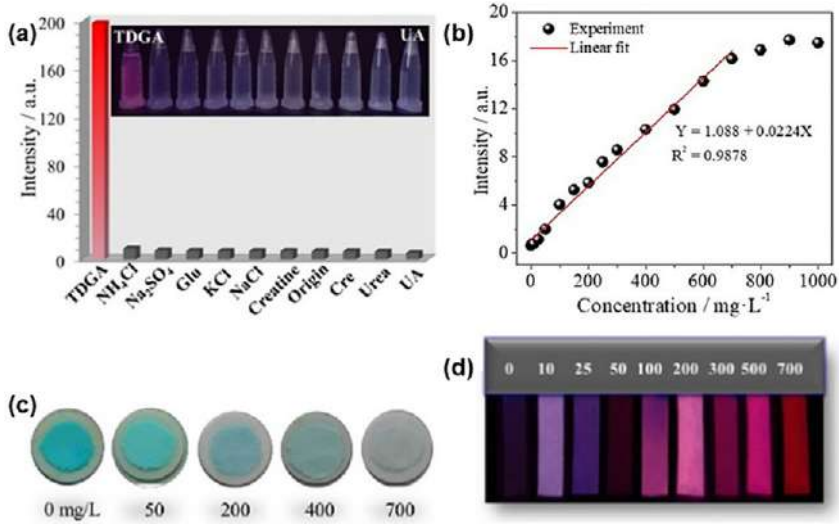

FIG. 3.18 (A) Luminescence intensities (the $^5D_0 \rightarrow {}^7F_2$ transition, 614 nm) of Eu^{3+}/Cu^{2+}@Zr-MOF toward various urine components ($\lambda_{ex} = 310$ nm). Inset in (B): the corresponding photographs under a UV lamp (254 nm). (B) Plot of intensity of Eu^{3+}/Cu^{2+}@Zr-MOF at 614 nm vs. TDGA concentration over the linear range 0–700 mg L^{-1}. (C) Photographs showing the color changes of the Eu^{3+}/Cu^{2+}@Zr-MOF sample treated by different concentrations of TDGA. (D) Optical images of test paper under 254 nm UV light after immersing into urine spiked with different concentrations of TDGA. *(Reproduced with permission from reference J. Hao, X. Xu, X. Lian, C. Zhang, B. Yan, A luminescent 3d-4f-4d MOF nanoprobe as a diagnosis platform for human occupational exposure to vinyl chloride carcinogen, Inorg. Chem. 56 (2017) 11176–11183. Copyright 2018 American Chemical Society.)*

and tend to saturate when exceeding 700 mg/L. This linear relationship can be fitted with an R^2 of 0.9878 with LOD of 89 ng mL^{-1} for TDGA. As shown in Fig. 3.18C, the colors of the Eu^{3+}/Cu^{2+}@Zr-MOF change from brilliant blue to light blue, and finally are almost colorless with the increasing concentration of TDGA (0–700 mg/L). The strong complexation ability of TDGA for Cu^{2+} causes the leakage of Cu^{2+} from Eu^{3+}@Zr-MOF hybrids and weakens its quenching effect on Eu^{3+}'s emission, thus leading to luminescence enhancement with the faded sample color. Moreover, the luminescent colors of the prepared test stripe change from dark to dark red, faint red, purplish red, and finally bright red with increasing TDGA content (Fig. 3.18D) [52].

Ji et al. designed a strategy for the detection of aspartic acid (Asp) based on a PSM MOF Cu^{2+}/Tb^{3+}@Zn-MOF. Subsequently, the luminescence-quenched hybrid was developed as a luminescence "Turn-On" probe for Asp with LOD of 0.54 ppm. In addition, this "On-Off-On" pattern was further used to construct an advanced analytical model based on an IMPLICATION-type logic gate [53]. Zhang et al. utilized PSM Eu^{3+}/Cu^{2+}@In-MOF luminescent hybrid film, realizing luminescence "Turn-On-Off-On" sensing of gaseous H_2S at room temperature with an LOD of 0.535 ppm. The sensor was designed based on the strong affinity of H_2S with Cu^{2+}. Forming CuS, the "antenna effect" between the ligand and Eu^{3+} is recovered, resulting in the "Turn-On" emission of Eu^{3+} [54]. Besides Cu^{2+}-Eu^{3+} co-PSM MOF hybrid systems, a similar sensing mode can also be adopted for Cu^{2+}-Tb^{3+} PSM MOF hybrids [55]. Zheng et al. also tried the "Turn-On-Off-On" responsive sensing research based on Tb^{3+} PSM Cu-MOFs hybrids [54,55]. They first synthesized a Cu-MOF and its hybrid Tb^{3+}@Cu-MOF via PSM for sensing H_2S. The obtained hybrid emitted a weak typical Tb^{3+} ion emission and strong LC emission. Interestingly, H_2S, as a strong electron donor, can strongly enhance the luminescence of Tb^{3+} through its superior affinity for Cu^{2+} ions. So, the hybrid belongs to a "Turn-On-Off-On" ratiometric luminescent probe for H_2S detection with LOD 1.20 μM [56]. Then they designed and developed two novel hybrids based on a Tb^{3+}/Yb^{3+}-cofunctionalized Cu-MOF that display broad ligand-centered emission and weak typical Tb^{3+} ion emission. Similarly, it is used as a ratiometric luminescent sensor ("Turn-On-Off-On" response for Tb^{3+} luminescence) for the metabolic product NMF of DMF in the human body (LOD = 0.02 mμM). Sun et al. designed a luminescent probe based on Tb^{3+}/Cu^{2+} MOFs for beamed monitoring of urinary sarcosine, a differential metabolite indicating the progression of prostate cancer (PCa). The incorporation of Cu^{2+} not only tunes the luminescence of Tb^{3+} via the LMET process but it also provides available sites for sarcosine. Cu^{2+}/Tb^{3+}@Ga-MOFs present significantly enhanced luminescence ("Turn-On-Off-On") toward sarcosine [57].

Lian et al. provide a composite hydrogel Fe^{3+}/Eu^{3+}-MOF@SA for the diagnosis of penicillin anaphylaxis. Penicillamine is the metabolite of penicillin and can be detected by Fe^{3+}/Eu^{3+}-MOF@SA both in aqueous solution or serum. More significantly, the determination of β-lactamase by Fe^{3+}/Eu^{3+}-MOF@SA

is achieved through a "Turn-On-Off-On" luminescence trigger pattern [58]. Fe^{3+} has been found to be able to quench the Fe^{3+}/Eu^{3+}-MOF's emission, and penicillamine has a strong affinity for Fe^{3+} and quenches on the luminescence of Fe^{3+}/Eu^{3+}-MOF. Thereby, luminescence enhancement of Fe^{3+}/Eu^{3+}-MOF@SA in the presence of penicillamine is demonstrated in Fig. 3.19A (top), showing an expeditious response to penicillamine of about a 32-fold increase. The luminescence data are accounted for and compared in Fig. 3.19B (top), and only penicillamine can induce this remarkable rebound in the luminescence of Eu^{3+}. The luminescence color of Fe^{3+}/Eu^{3+}-MOF@SA changed from colorless to red, after the addition of penicillamine (Fig. 3.19C; top). As shown in Fig. 3.19A (middle), the luminescence signal of Fe^{3+}/Eu^{3+}-MOF@SA is found to gradually increase with the concentration of β-lactamase. The fitting curve of β-lactamase concentration vs. luminescent intensity (I_3) is plotted in Fig. 3.19B (middle), with LOD of 1.25 U mL^{-1}. As shown in Fig. 3.19C (middle), the luminescent colors of the cordiform hydrogels changed from dark to bright red with rise of the concentration of β-lactamase. Therefore, a MOFs-based composite hydrogel Fe^{3+}/Eu^{3+}-MOF@SA is provided for the diagnosis of penicillin anaphylaxis, which reflects the enzymatic hydrolysis profiles of penicillin via β-lactamase through an "On-Off-Off-On" fluorescence trigger pattern [58].

3.5 Both "Turn-On" and "Turn-Off" luminescence response chemical sensing on different analytes for rare earth MOF hybrid materials

In fact, in the view of different analytes, the rare earth MOFs hybrid material as a probe often shows different luminescence responses, even contrary to each other. They may correspond to different responsive mechanisms and they respond to different effects in spite of a similar mechanism. Therefore rare earth MOF hybrid materials can be developed as an extensive and universal probe for luminescence response chemical sensing. Here we give some examples to show this point.

Wang et al. prepared a Gd^{3+} MOF with 5,5′-(anthracene-9,10-diyl)diisophthalic acid (H_4adip), $[Gd_2(adip)(H_2adip)(NMP)_2]\cdot DMF\cdot 3H_2O$ (Gd-MOF, NMP = *N*-methylpyrrolidone; DMF = *N*,*N*-dimethylformamide) with a 3-D framework and a strong ligand-based blue emission [59]. It can be applied as a multifunctional chemical sensor for UO_2^{2+}, PO_4^{3-} with excellent selectivity, sensitivity, and antiinterference. The fluorescence titration experiment showed that the emission intensity of a Gd-MOF-H_2O suspension progressively decreases by increasing the UO_2^{2+} ion concentration from 0 to 1000 μM (Fig. 3.20A; left). In the 0–20 μM concentration range of UO_2^{2+}, the K_{SV} is 4.05×10^4 M^{-1} with an LOD of 1.42 μM. In aqueous solution, the emission spectrum of the Gd-MOF overlaps the UO_2^{2+} adsorption spectrum significantly. Therefore the important reason for fluorescence quenching may be the FRET mechanism. In addition, the fluorescence quenching response is also affected

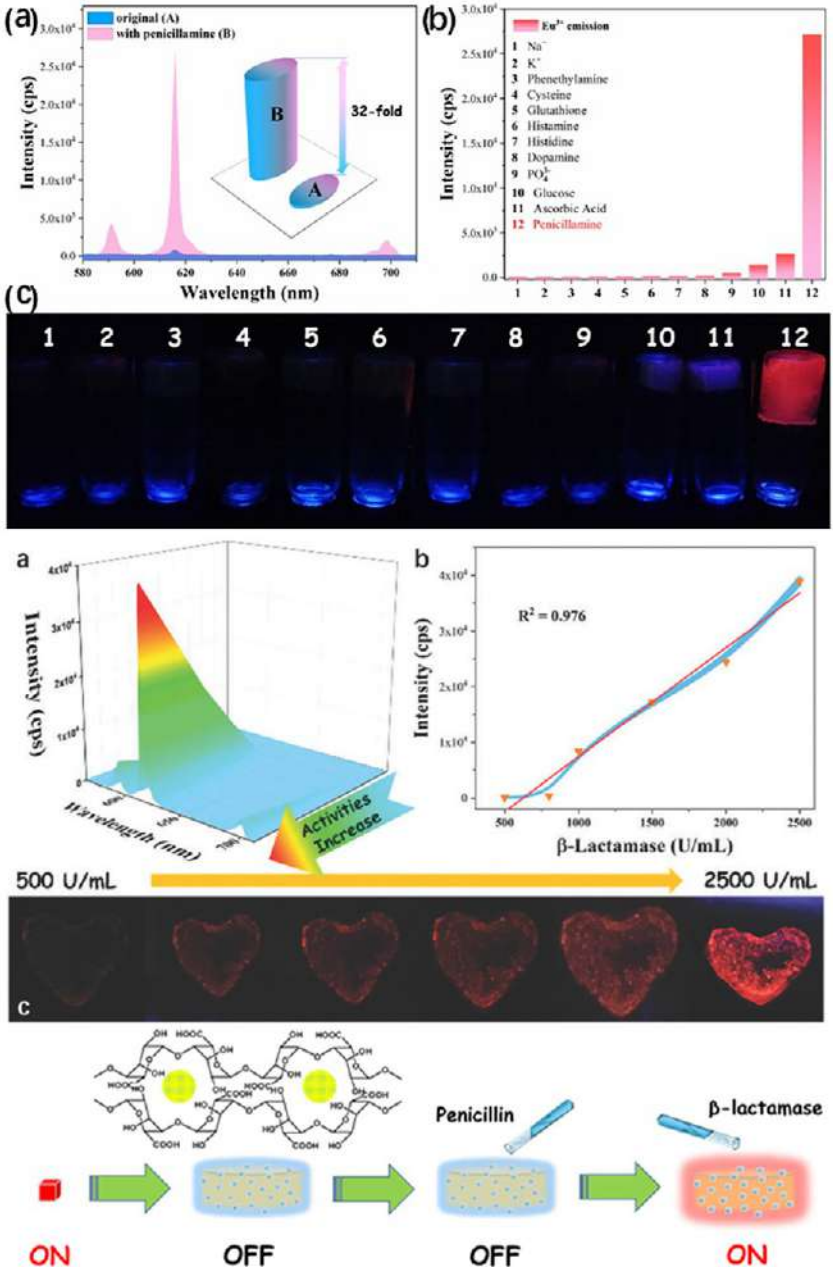

FIG. 3.19 *(Top)* (A) The emission enhancement effect of penicillamine on Fe^{3+}/Eu^{3+}-MOF@SA hydrogel; the inset is the comparison of the intensities; (B) emission intensities of Fe^{3+}/Eu^{3+}-MOF@SA to various chemicals under excitation at 325 nm; (C) the corresponding photographs of (B) under UV radiation. *(Middle)* (A) Luminescence responses of Fe^{3+}/Eu^{3+}-MOF@SA hydrogels for the β-lactamase concentration changes; (B) linear curve between intensities of Fe^{3+}/Eu^{3+}-MOF@SA and the β-lactamase concentrations with error bars; (C) corresponding photographs of the Fe^{3+}/Eu^{3+}-MOF@SA hydrogels to the various β-lactamase serum solution. *(Bottom)* The scheme for a MOFs-based hybrid hydrogel Fe^{3+}/Eu^{3+}-MOF@SA and the determination of β-lactamase by this hydrogel through a "Turn-On-Off-On" luminescence trigger pattern. *(Reproduced with permission from reference X. Lian, B. Yan, Diagnosis of penicillin allergy: a MOFs-based composite hydrogel for detecting β-lactamase in serum, Chem. Commun. 55 (2019) 241–244. Copyright 2019 Royal Society of Chemistry.)*

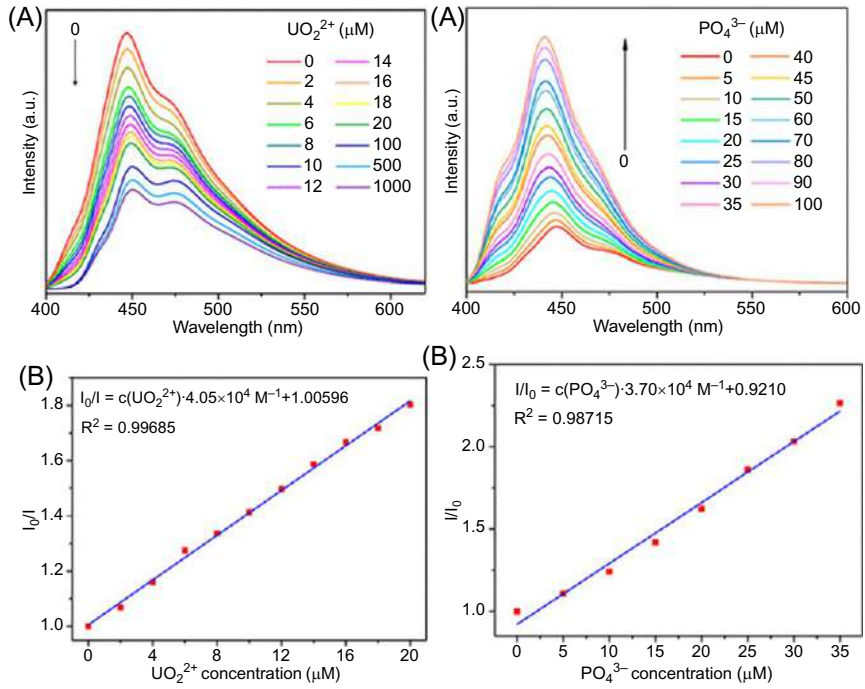

FIG. 3.20 (A) Emission spectra of a GdMOF-H_2O suspension after the addition of different concentrations of UO_2^{2+} *(left)* and PO_4^{3-} *(right)* under excitation at 372 nm. (B) SV curve for UO_2^{2+} *(left)* and PO_4^{3-} *(right)* in the concentration range of 0–20 μM. *(Reproduced with permission from reference M. Wang, Z. Liu, X. Zhou, H. Xiao, Y. You, W. Huang, Anthracene-based lanthanide coordination polymer: structure, luminescence, and detections of UO_2^{2+}, PO_4^{3-}, and 2-thiazolidinethione-4-carboxylic acid in water, Inorg. Chem. 59 (2020) 18027–18034. Copyright 2020 American Chemical Society.)*

by competitive absorption. From the fluorescence titration spectra, on the gradual addition of a very low concentration of the PO_4^{3-} solution to a Gd-MOF-H_2O suspension (Fig. 3.20A; right), fluorescence enhancement is observed when PO_4^{3-} is added to the Gd-MOF-H_2O suspension. The slope of the linear relationship between the PO_4^{3-} concentration in the 0–35 μM concentration range and I/I_0 is $3.70 \times 10^4\ M^{-1}$ with a detection limit of 1.55 μM. The protons in the H_2adip^{2-} ligand may react with OH^- ions under a certain alkalinity, destroying the conjugate system and electron transfer, thereby affecting the luminescence of the Gd-MOF-H_2O suspension. The carboxylic acid groups react with OH^- ions to form deprotonated carboxylates, leading to fluorescence "Turn-On" in the 9.4–11.50 pH range [59].

Chen et al. assembled a luminescent Eu-MOF with tubular channels based on 5,5′-methylenebis-(2,4,6-trimethyl)isophthalic acid ($H_4BTMIPA$) with $[H_2N(CH_3)_2]^+$ ions as counter ions located in the channels, whose cation exchange between $[H_2N(CH_3)_2]^+$ and metal ions can selectively sense Fe^{3+} and Al^{3+} ions through fluorescence quenching and enhancement [60].

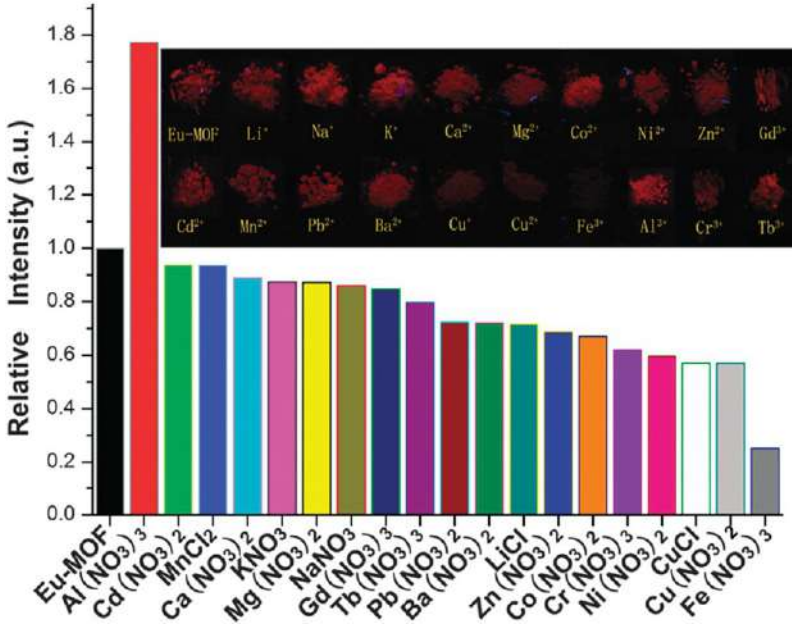

FIG. 3.21 Photoluminescence intensity of the $^5D_0 \rightarrow {}^7F_2$ transition (617 nm) of 1 treated with different metal ions (10^{-3} M) in DMF solution for 72 h. Inset: the colors of the treated samples with different metal ions under the irradiation of UV light of 365 nm. *(Reproduced with permission from reference Z. Chen, Y. Sun, L. Zhang, D. Sun, F. Liu, Q. Meng, R. Wang, D. Sun, A tubular europium–organic framework exhibiting selective sensing of Fe^{3+} and Al^{3+} over mixed metal ions, Chem. Commun. 49 (2013) 11557–11559. Copyright 2013 Royal Chemical Society.)*

The luminescent properties are recorded and shown in Fig. 3.21. Interestingly, most metal ions have varying degrees of quenching effects on the luminescence intensity. When Al^{3+} ions are present, the luminescence intensity is enhanced compared to the original one. Under the irradiation of UV light of 365 nm, the samples after being immersed in DMF solutions containing different metal ions showed red color, except for Fe^{3+} ions that showed dark color. These results indicate that complex Eu-MOFs can selectively sense Fe^{3+} ions through fluorescence quenching and Al^{3+} ions through fluorescence enhancement. To further prove that the fluorescence quenching and enhancement are caused by a cation exchange process, a sensing mechanism was further proposed: Fe^{3+} and Al^{3+} were exchanged with the $[H_2N(CH_3)_2]^+$ cations in the channels at the low concentration, leading to partial fluorescence quenching and enhancement gradually [60].

Kukka et al. investigated the optimal conditions for solvothermal-assisted synthesis of Eu-BDC-NH_2 MOF to improve their sensing capacity toward some selected target metal species [61]. The sensing potential of luminescent MOFs was explored for detection of toxic metal ions through two approaches, i.e., a direct chemosensing and an indirect biomolecule-mediated sensing approach.

In the former, Eu-MOF exhibited noticeable turn-off fluorescence behavior, especially with Hg^{2+} ions (i.e., a high Stern∼Volmer quenching constant (K_{SV}) of $6.42 \times 10^5\ M^{-1}$ and LOD of 0.007 M). In the latter, a nanocomposite of MOF-cyanocobalamin is characterized by a highly selective "Turn-On" luminescence response toward Co^{2+} ions ($K_{SV} = -6.25 \times 10^3\ M^{-1}$; LOD = 0.7 M).

References

[1] K. Müller-Buschbaum, F. Beuerle, C. Feldmann, MOF based luminescence tuning and chemical/physical sensing, Microp. Mesop. Mater. 216 (2015) 171–199.

[2] Y. Zhang, S. Yuan, G. Day, X. Wang, X. Yang, H. Zhou, Luminescent sensors based on metal–organic frameworks, Coord. Chem. Rev. 354 (2018) 28–45.

[3] T. Rasheed, F. Nabeel, Luminescent metal–organic frameworks as potential sensory materials for various environmental toxic agents, Coord. Chem. Rev. 401 (2019), 213065.

[4] J. Liu, Z. Luo, Y. Pan, A.K. Singh, M. Trivedi, A. Kumar, Recent developments in luminescent coordination polymers: designing strategies, sensing application and theoretical evidences, Coord. Chem. Rev. 406 (2020), 213145.

[5] H. Yin, X. Yin, Metal–organic frameworks with multiple luminescence emissions: designs and applications, Acc. Chem. Res. 53 (2020) 485–495.

[6] T. Gorai, W. Schmitt, T. Gunnlaugsson, Highlights of the development and application of luminescent lanthanide based coordination polymers, MOFs and functional nanomaterials, Dalton Trans. 50 (2021) 770–784.

[7] B. Yan, Luminescence response mode and chemical sensing mechanism for lanthanide functionalized metal-organic frameworks hybrids, Inorg. Chem. Front. 8 (2021) 201–233.

[8] C.M.G. dos Santos, A.J. Harte, S.J. Quinn, T. Gunnlaugsson, Recent developments in the field of supramolecular lanthanide luminescent sensors and self-assemblies, Coord. Chem. Rev. 252 (2008) 2512–2527.

[9] J. Rocha, L.D. Carlos, F.A. Almeida Paza, D. Ananiasa, Luminescent multifunctional lanthanides-based metal–organic frameworks, Chem. Soc. Rev. 40 (2011) 926–940.

[10] J. Hao, X. Xu, H. Fei, L. Li, B. Yan, Functionalization of metal-organic frameworks for photoactive materials, Adv. Mater. 30 (2018) 1705634.

[11] L.E. Kreno, K. Leong, O.K. Farha, M. Allendorf, R.P. Van Duyne, J.T. Hupp, Metal–organic framework materials as chemical sensors, Chem. Rev. 112 (2012) 1105–1125.

[12] F. Yi, D. Chen, M. Wu, L. Han, H. Jiang, Chemical sensors based on metal–organic frameworks, ChemPlusChem 81 (2016) 675–690.

[13] I. Stassen, N. Burtch, A. Talin, P. Falcaro, D.M. Allendorfc, R. Ameloot, An updated roadmap for the integration of metal–organic frameworks with electronic devices and chemical sensors, Chem. Soc. Rev. 46 (2017) 3185–3241.

[14] W.P. Lustig, S. Mukherjee, N.D. Rudd, A.V. Desai, J. Li, S.K. Ghosh, Metal–organic frameworks: functional luminescent and photonic materials for sensing applications, Chem. Soc. Rev. 46 (2017) 3242–3285.

[15] E.A. Dolgopolova, A.M. Rice, C.R. Martin, N.B. Shustova, Photochemistry and photophysics of MOFs: steps towards MOF-based sensing enhancements, Chem. Soc. Rev. 47 (2018) 4710–4728.

[16] S.A. Diamantis, A. Margariti, A.D. Pournara, G.S. Papaefstathiou, M.J. Manos, T. Lazarides, Luminescent metal–organic frameworks as chemical sensors: common pitfalls and proposed best practices, Inorg. Chem. Front. 5 (2018) 1493–1511.

[17] R. Lin, S. Liu, J. Ye, X. Li, J. Zhang, Photoluminescent metal–organic frameworks for gas sensing, Adv. Sci. 3 (2016) 1500434.
[18] Y. Li, A. Xiao, B. Zou, H. Zhang, K. Yan, Y. Lin, Advances of metal–organic frameworks for gas sensing, Polyhedron 154 (2018) 83–97.
[19] H. Li, S. Zhao, S. Zang, J. Li, Functional metal–organic frameworks as effective sensors of gases and volatile compounds, Chem. Soc. Rev. 49 (2020) 6364–6401.
[20] Q. Yu, Z. Li, Q. Cao, S. Qu, Q. Jia, Advances in luminescent metal-organic framework sensors based on post-synthetic modification, Trends Anal. Chem. 129 (2020), 115939.
[21] B. Chen, S. Xiang, G. Qian, Metal–organic frameworks with functional pores for recognition of small molecules, Acc. Chem. Res. 43 (2010) 1115–1124.
[22] Y. Li, Temperature and humidity sensors based on luminescent metal-organic frameworks, Polyhedron 179 (2020), 114413.
[23] Z. Liao, J. Zhang, E. Yu, Y. Cui, Recent progress in metal–organic frameworks for precaution and diagnosis of Alzheimer's disease, Polyhedron 151 (2018) 554–567.
[24] Y. Hao, S. Chen, Y. Zhou, Y. Zhang, M. Xu, Recent progress in metal–organic framework (MOF) based luminescent chemodosimeters, Nanomaterials 9 (2019) 974.
[25] Z. Hu, B.J. Deibert, J. Li, Luminescent metal–organic frameworks for chemical sensing and explosive detection, Chem. Soc. Rev. 43 (2014) 5815–5840.
[26] X. Fang, B. Zong, S. Mao, Metal–organic framework-based sensors for environmental contaminant sensing, Nano-Micro Lett. 10 (2018) 64.
[27] H. Wang, W.P. Lustig, J. Li, Sensing and capture of toxic and hazardous gases and vapors by metal–organic frameworks, Chem. Soc. Rev. 47 (2018) 4729–4756.
[28] J. Tang, X. Ma, J. Yang, D. Feng, X. Wang, Recent advances in metal–organic frameworks for pesticide detection and adsorption, Dalton Trans. 49 (2020) 14361–14372.
[29] L. Chen, D. Liu, J. Peng, Q. Du, H. He, Ratiometric fluorescence sensing of metal-organic frameworks: tactics and perspectives, Coord. Chem. Rev. 404 (2020), 213113.
[30] T.F.S. Mahapatra, A. Dey, H. Singh, S.S. Hossain, A.K. Mandal, A. Das, Two-dimensional lanthanide coordination polymer nanosheets for detection of FOX-7, Chem. Sci. 11 (2020) 1032–1042.
[31] Y. Liu, Y. Lu, B. Zhang, L. Hou, Y. Wang, Post-synthetic functionalization of Ni-MOF by Eu^{3+} ions: luminescent probe for aspartic acid and magnetic property, Inorg. Chem. 59 (2020) 7531–7538.
[32] C. Fan, X. Lv, M. Tian, Q. Yu, Y. Mao, W. Qiu, H. Wan, G. Liu, A terbium(III)-functionalized zinc(II)-organic framework for fluorometric determination of phosphate, Microchim. Acta 187 (2020) 84.
[33] Z. Sun, M. Yang, Y. Ma, L. Li, Multi-responsive luminescent sensors based on two-dimensional lanthanide – metal organic frameworks for highly selective and sensitive detection of Cr(III) and Cr(VI) ions and benzaldehyde, Cryst. Growth Des. 17 (2017) 4326–4335.
[34] W. Liu, Y. Wang, L. Song, M.A. Silver, J. Xie, L. Zhang, L. Chen, J. Diwu, Z. Chai, S. Wang, Efficient and selective sensing of Cu^{2+} and UO_2^{2+} by a europium metal-organic framework, Talanta 196 (2019) 515–522.
[35] Y. Li, S. Li, P. Yan, X. Wang, X. Yao, G. An, G. Li, Luminescence-colour-changing sensing of Mn^{2+} and Ag^{+} ions based on a white-light-emitting lanthanide coordination polymer, Chem. Commun. 53 (2017) 5067–5070.
[36] X. Qu, B. Yan, Ln(III)-functionalized metal-organic frameworks hybrid systems: luminescence properties and sensor for *trans, trans*-muconic acid as a biomarker of benzene, Inorg. Chem. 57 (2018) 7815–7824.

[37] X. Qu, B. Yan, Zn(II)/Cd(II)-based metal-organic frameworks: crystal structures, Ln(III)-functionalized luminescence and chemical sensing of dichloroaniline as pesticide biomarker, J. Mater. Chem. C 8 (2020) 9427–9439.

[38] X. Lian, B. Yan, Trace detection of organophosphorus chemical warfare agents in wastewater and plants by luminescent UiO-67(Hf) and evaluating the bioaccumulation of organophosphorus chemical warfare agents, ACS Appl. Mater. Interf. 10 (2018) 14869–14876.

[39] X. Qu, B. Yan, A Cd-based MOF containing uncoordinated carbonyl groups as lanthanide post-synthetic modification sites and chemical sensing of diphenyl phosphate as fame retardant biomarker, Inorg. Chem. 59 (2020) 15088–15100.

[40] N. Sun, B. Yan, Ag^{+}-induced photoluminescence enhancement in lanthanide post-functionalized MOFs and Ag^{+} sensing, Phys. Chem. Chem. Phys. 19 (2017) 9174–9180.

[41] A. Gamonal, C. Sun, A.L. Mariano, E. Fernandez-Bartolome, E. Guerrero-SanVicente, B. Vlaisavljevich, J. Castells-Gil, C. Marti-Gastaldo, R. Poloni, R. Wannemacher, J. -Cabanillas-Gonzalez, J. Sanchez Costa, Divergent adsorption-dependent luminescence of amino-functionalized lanthanide metal–organic frameworks for highly sensitive NO_2 sensors, J. Phys. Chem. Lett. 11 (2020) 3362–3368.

[42] Y. Zhou, D. Zhang, W. Xing, J. Cuan, Y. Hu, Y. Cao, N. Gan, Ratiometric and turn-on luminescence detection of water in organic solvents using a responsive europium-organic framework, Anal. Chem. 91 (2019) 4845–4851.

[43] H. Wang, X. Wang, M. Liang, G. Chen, R. Kong, L. Xia, F. Qu, A boric acid-functionalized lanthanide metal–organic framework as a fluorescence "turn-on" probe for selective monitoring of Hg^{2+} and CH_3Hg^{+}, Anal. Chem. 92 (2020) 3366–3372.

[44] T. Luo, P. Das, D.L. White, C. Liu, A. Star, N.L. Rosi, Luminescence "turn-on" detection of gossypol using Ln^{3+}-based metal–organic frameworks and Ln^{3+} salts, J. Am. Chem. Soc. 142 (2020) 2897–2904.

[45] X. Xu, X. Lian, J. Hao, C. Zhang, B. Yan, Double stimuli-responsive fluorescent center for food spoilage monitoring based on dye covalent modified EuMOFs: from sensory hydrogel to logic device, Adv. Mater. 29 (2017) 1702298.

[46] B. Wang, B. Yan, A turn-on fluorescent probe Eu^{3+} functionalized Ga-MOF integrated with logic gate operation for detecting ppm-level ciprofloxacin (CIP) in urine, Talanta 208 (2020), 120438.

[47] T. Liu, X. Qu, B. Yan, A highly sensitive and selective "turn-on" fluorescent probe of fleroxacin in human serum and urine based on Eu^{3+} functionalized metal-organic framework, Dalton Trans. 48 (2019) 17945–17952.

[48] N. Sun, B. Yan, Fluorescence detection of urinary N-methylformamide for biomonitoring of human occupational exposure to N,N-dimethylformamide by Eu(III) functionalized MOFs, Sens. Actuators B Chem. 261 (2018) 153–160.

[49] Y. Zeng, H. Zheng, J. Gu, G. Cao, W. Zhuang, J. Lin, R. Cao, Z. Lin, Dual-emissive metal–-organic framework as a fluorescent "switch" for ratiometric sensing of hypochlorite and ascorbic acid, Inorg. Chem. 58 (2019) 13360–13369.

[50] B. Liu, H. Shen, Y. Hao, X. Zhu, S. Li, Y. Huang, P. Qu, M. Xu, Lanthanide functionalized metal–organic coordination polymer: toward novel turn-on fluorescent sensing of amyloid β-peptide, Anal. Chem. 90 (2018) 12449–12455.

[51] X. Lian, B. Yan, Phosphonate MOFs composite as off-on fluorescent sensor for detecting purine metabolite uric acid and diagnose hyperuricuria, Inorg. Chem. 56 (2017) 6802–6808.

[52] J. Hao, X. Xu, X. Lian, C. Zhang, B. Yan, A luminescent 3d-4f-4d MOF nanoprobe as a diagnosis platform for human occupational exposure to vinyl chloride carcinogen, Inorg. Chem. 56 (2017) 11176–11183.

[53] G. Ji, T. Zheng, X. Gao, Z. Liu, A highly selective turn-on luminescent logic gates probe based on postsynthetic MOF for aspartic acid detection, Sens. Actuators B. Chem. 284 (2019) 91–95.
[54] J. Zhang, F. Liu, J. Gan, Y. Cui, B. Li, Y. Yang, G. Qian, Metal-organic framework film for fluorescence turn-on H_2S gas sensing and anti-counterfeiting patterns, Sci. China-Mater. 62 (2019) 1445–1453.
[55] X. Zheng, R. Fan, Y. Song, A. Wang, K. Xing, X. Du, P. Wang, Y. Yang, A highly sensitive turn-on ratiometric luminescent probe based on postsynthetic modification of Tb^{3+}@Cu-MOF for H_2S detection, J. Mater. Chem. C 5 (2017) 9943–9951.
[56] X. Zheng, R. Fan, H. Lu, B. Wang, J. Wu, P. Wang, Y. Yang, A dual-emitting Tb(iii)&Yb(iii)-functionalized coordination polymer: a "turn-on" sensor for N-methylformamide in urine and a "turn-off" sensor for methylglyoxal in serum, Dalton Trans. 48 (2019) 14408–14417.
[57] N. Sun, B. Yan, A fluorescence probe based on Tb^{3+}/Cu^{2+} co-functionalized MOFs to urinary sarcosine detection, Analyst 143 (2018) 2349–2355.
[58] X. Lian, B. Yan, Diagnosis of penicillin allergy: a MOFs-based composite hydrogel for detecting β-lactamase in serum, Chem. Commun. 55 (2019) 241–244.
[59] M. Wang, Z. Liu, X. Zhou, H. Xiao, Y. You, W. Huang, Anthracene-based lanthanide coordination polymer: structure, luminescence, and detections of UO_2^{2+}, PO_4^{3-}, and 2-thiazolidinethione-4-carboxylic acid in water, Inorg. Chem. 59 (2020) 18027–18034.
[60] Z. Chen, Y. Sun, L. Zhang, D. Sun, F. Liu, Q. Meng, R. Wang, D. Sun, A tubular europium–organic framework exhibiting selective sensing of Fe^{3+} and Al^{3+} over mixed metal ions, Chem. Commun. 49 (2013) 11557–11559.
[61] P. Kukkar, D. Kukkar, H. Sammi, K. Singh, M. Rawat, P. Singh, S. Basud, K. Kim, A facile means for the improvement of sensing properties of metal-organic frameworks through control on the key synthesis variables, Sens. Actuators: B. Chem. 271 (2018) 157–163.

Chapter 4

Dual mode for ratiometric luminescence responsive chemical sensing for rare earth metal-organic framework hybrid materials

4.1 Dual mode for ratiometric luminescence (RL) responsive chemical sensing of MOFs materials

MOFs possess an important advantage over other candidate classes for chemosensory materials because of their exceptional structural tunability and properties. Luminescent sensing using MOFs is a simple, intuitive, and convenient method to recognize species, but the method has limitations, such as insufficient chemical selectivity and signal loss. MOFs contain versatile building blocks (linkers or ligands) with special chemical reactivity, and postsynthetic modification (PSM) provides an opportunity to exploit and expand their unique properties. The linkers in most MOFs contain aromatic subunits that can readily display luminescence after ultraviolet or visible (typically blue) excitation, and this is the main luminescent nature of most MOFs, including forming versatile charge transfer between metal ions and ligand linkers. MOFs' luminescence from metal nodes, ligands, and encapsulated guests or PSM functionalization offers an excellent luminescence response in analysis and detection. However, MOFs-based monochromatic fluorescence probes are limited by concentration and the effects of ambient and excitation light intensity, resulting in low detection accuracy. To overcome this defect, MOFs-based RL sensors have been proposed and rapidly developed. Sometimes the emission peak of host luminescent MOFs is based on two different maximum peaks, called dual emissive MOFs, which originate from different sources and have different efficacy in the presence of analytes. As a result, they can be applied as ratiometric sensors. Although singular emissive MOFs with one type of emission center can generate a 1D response and is good enough for quantitative analysis of an analyte, some sensing parameters like selectivity, sensitivity, detection limit, and linearity range are poor in combination with instrumental methods. Dual emissive

Rare Earth Metal-Organic Framework Hybrid Materials for Luminescence Responsive Chemical Sensors
https://doi.org/10.1016/B978-0-323-91236-5.00002-5

MOFs with two different emission centers and 2D ratiometric response are excellent candidates for improving the sensing parameters of luminescent MOFs, especially sensitivity and selectivity, whose improvement can be concluded because of a self-calibrating or self-referencing mechanism from different but correlated emission centers, which results in minimization of the external influence and interfering effects. Considering the luminescence nature within MOFs building units and relevant guests, rare earth MOFs hybrid materials belong to ideal systems to realize dual emission and RL sensing. Herein, the dual emission and RL sensing in MOF materials, rare earth MOFs, and rare earth functionalized MOFs hybrid materials are outlined. Dual luminescent centers are created with different luminescent bands in the visible region [1–4].

For luminescence intensity measurement and luminescence response ("Turn-On" and "Turn-Off") detection, the effects of concentration, environment, and excitation light intensity result in low accuracy of detection for MOFs-based monochromatic fluorescence sensors. To ameliorate this drawback, another luminescence signal is introduced to construct a MOF-based RL sensor. The emission intensities at two wavelengths is independent of the preceding interfering factors, so the RL sensors can eliminate these shortcomings of single luminescence sensing by self-calibration of dual emission and achieve accurate detection. By contrast, RL sensors can avoid the preceding limitations and provide accurate detection through self-calibration with two emissive bands. From the representation of present experimental results, the RL detection mechanism can be summarized as follows: (1) for two emissions with "Turn-On" and "Turn-Off," one emission increases while another decreases; (2) for two emissions with "Turn-On" or "Turn-Off," one emission changes (increased or decreased) while another keeps the same intensity; (3) for the same change of the two emissions, both increase or decrease in varying degrees. With these diverse combinations of luminescence intensity change, many RL sensors are developed for all kinds of applications. According to previous work, the tactics of ratio sensing based on dual-emission MOFs could be summarized in the following parts: (i) Synthesis of self-illuminating MOFs based on MC and LC or introducing a specific target to bridge the two emissions; (ii) Combining single-emissive MOFs with a guest chromophore such as QDs, dyes, and NPs. (iii) Encapsulating two guest chromophores into the frameworks of nonemissive MOFs (Fig. 4.1) [1].

4.1.1 MOFs′ intrinsic dual emission

MOFs with intrinsic dual emission are mainly constructed using three paths: (a) mixed RE^{3+} ions to form double emitters, i.e., the bimetallic mixed rare earth MOFs; (b) combining two luminescent ligands to emit dual luminescence, as a bridge to cause the energy transfer between the metal center and ligands; (c) composing a single RE^{3+} ion and luminescent ligand [1–23]. **(I) Bimetallic-based MOFs**. Bimetallic MOFs are typically based on RE^{3+} ions such as

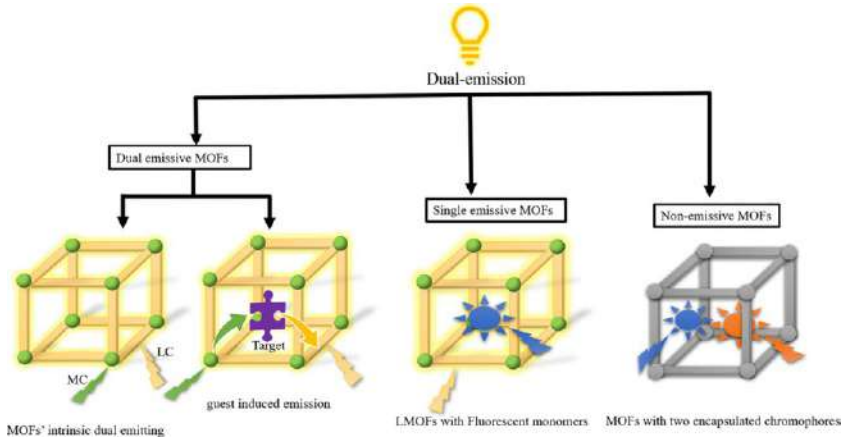

FIG. 4.1 MOFs-based ratiometric fluorescence probes synthesized by different design schemes. MC: metal-center emission, LC: ligand-centered emission. *(Reproduced with permission from L. Chen, D. Liu, J. Peng, Q. Du, H. He, Ratiometric fluorescence sensing of metal-organic frameworks: tactics and perspectives. Coord. Chem. Rev. 404 (2020) 213113. Copyright 2020 Elsevier.)*

RE-MOFs or mixed RE^{3+}-metal REM-MOFs, which can generate strong emissions arising from f-f or f-d energy transfer when exposed to UV light and can be adjusted by appropriate adjacent chromophores. Eu^{3+} and Tb^{3+} are widely applied among various RE^{3+} ions because of the large Stokes shift and relatively long lifetimes. The emission wavelengths of the mixed RE-MOFs can be tuned by adjusting the Eu^{3+}/Tb^{3+} ratios. In addition, the emission of Eu^{3+} in mixed RE-MOFs can be sensitized by Tb^{3+}. Thus bimetallic RE-MOFs with dual emission upon one excitation can allow construction of an RL sensor with cheap and easy-to-use materials. REM-MOFs contain mixed metal ions that can link with each other through the organic ligand, and intervention on one of the metal ions (transition metal ions) could impact another metal ion (RE^{3+}), so as to adjust their properties. Unfortunately, different chemical and physical characteristics of d and f electrons make it harder to synthesize REM-MOFs than homometallic MOFs. Therefore RE-MOFs are more popular than REM-MOFs in the field of MOF-based RL detection. RE^{3+} ions are often used as the center node in both RE-MOFs and REM-MOFs. In addition, RE^{3+} ions can also be used for modifying and mixing with other non-RE-MOFs. However, the intrinsic dual-emissive MOFs with mixed or functionalized RE^{3+} ions are rarer than MOFs that simultaneously incorporate different ligands for Kasha's rule to allow only the lowest excited state to emit [1–14]. **(II) Ligand-based MOFs**. Organic ligands in MOFs are often used to link metal ions or metal clusters to form stable and porous frameworks, whose functionalization precisely embodies the designability and tunability and easily regulates the luminescence of MOFs. Common modifications of nonfluorescent ligands to produce fluorescence are hydroxylation, carboxylation, and amination. Generally, in MOFs constructed

with only one kind of ligand, it is hard to simultaneously excite two emissions with the antenna effect, except for such single ligands as 2,5-dihydroxyterephthalic acid (H_2DHT), whose excited-state intramolecular proton-transfer (ESIPT) chromophore in protic solvent often shows dual emission from both the initial excited form (a keto or enol) and the proton-transferred tautomer. This feature is also preserved in the MOFs and is the simplest way to construct a MOF-based RL sensor. However, the introduction of mixed ligands in MOFs provides more possibilities, and the sensor is more designable, having achieved a new level of rational design and construction, including the synergetic coordination of different ligands with metal ions. The two ligands in MOFs should have structural similarities (the geometry, functional side groups, acid strength, and rigidity of the linkers) and often produce close emissions, which makes it very difficult to demand a special design to achieve ratio detection, so that the mixed-ligand MOFs sound reasonable, but are not common. Hence, more ingenious methods for achieving RL sensing by guest-induced fluorescence have been developed, which retain better selectivity while being easier to implement [1–4,15–21]. **(III) Target analyst-induced ratio luminescence**. The selective binding of analytes can activate an intense emission of the originally low-emitting or nonemitting MOFs, namely guest-induced emissions. To further improve selectivity, an analyte-dependent RL sensing method is developed in which the analyte can be a switch that turns on dual emission [1–4,22,23].

4.1.2 Single-emissive MOFs with fluorescent guests

As a class of porous materials, MOFs provide a special platform to stabilize functional species, causing the specific behavior within the defined pores. Actually, through the leading of quantities of fluorophores (e.g., QDs and fluorescent dyes) into their pores, various sorts of MOF-based composites have been produced as novel functional materials for optical devices [1,24–39]. **(I) Dyes@MOFs**. Dyes are diffusely applied as colorants, photographic sensitizers, markers, and fluorescent sensors, but dyes face the problem of aggregation-caused quenching (ACQ) [1,24,25]. **(II) NPs@MOFs** Nanomaterial fluorescent sensors, especially those based on MOFs, are attracting special attention owing to their strong encapsulation capabilities, adjustable pore sizes, and large specific surface area. Correspondingly, MOFs can be expanded by encapsulating nanoparticles (NPs) such as noble metal NPs and QDs within them, forming NPs@MOFs nanocomposites. The NPs@MOFs can also work as RL probes; sensors of multicolor luminescent species functionalized NPs, such as the noble metal NPs, QDS, and carbon dots (CDs), have received considerable attention due to their elevated photostability, good water dispersibility, and enriched separation capacity toward analytes. **(i) Noble metal NPs@MOFs**. The most commonly adopted nanomaterials in MOFs are the noble metal NPs, including gold NPs (AuNPs) and silver NPs (AgNCs). In general, the combination of the noble metal NPs and MOFs is a mutually beneficial method and, apart from this, QDs with highly fluorescent performance are other

kinds of nanomaterials that are usually combined with MOFs. The most common QDs in MOFs are metal semiconductor QDs and carbon QDs. **(ii) QDs@MOFs**. QDs have their own clear merits of broad absorption spectra, high fluorescent quantum yields, good photostability, and long fluorescence lifetime, and they have gradually taken the place of the ordinary fluorophores, with broad applications in microarrays, fluorescence imaging, and immunoassays. MOFs can be a good shell for their porosity and stable framework. Methods for preparing QDs@MOFs composites include: (a) fixing functional or nanoscale objects in MOFs, known as "ships in ships" and "bottles around ships" methods. (b) photochemical deposition of semiconductor NPs onto the surface of the skeleton. The core-shell composite is constructed of MOFs with QDs, showing an enhancement of light harvesting via energy transfer from the QDs to the MOFs. It is this energy transfer that increased MOF-based fluorescence and decreased QD-based fluorescence, forming a ratio fluorescence RL probe. (c) CDs@MOFs. Comparatively, low toxic carbon quantum dots are developed and used in combination with MOFs for the development of an RL sensor. They are generally spherical and are classified into amorphous and crystalline forms, wherein the crystalline form less than 10 nm in size is carbon quantum dots (CQDs) and the single layer of graphite structure is the graphene quantum dots (GQDs). As promising emerging fluorescent labels, these carbon NPs have wide application in cellular imaging, bioimaging, and sensing. The composite CQDs@MOF are utilized for the construction of an RL sensor to selectively accumulate target analytes and increase the sensitivity of the measurement [1,27–34].

4.1.3 Nonemissive MOFs with encapsulated chromophores

Apart from the MOFs-based luminescence, there are reports of luminescence from fluorophores introduced into the nonemissive MOFs or bound to the surface through PSM [1,35,39]. For rare earth MOF hybrid materials, RE^{3+} ions have one emissive center, and can compose the other emissive center from other rare earth ions or linkers, or other guests. Based on the origin of the luminescence, there are three classes of dual-emission RE-contained MOFs: (1) emission from RE^{3+} and other materials; (2) emission from the Eu/Tb ion and the ligand; (3) emission from mixed-RE ions. Due to the different nature of illuminant centers, the RE-functionalized MOFs can detect species as the self-calibration probes through the different variation trends of signals. Three strategies to obtain dual-emission materials are summarized, including embedding additional luminescence species, modulating the "antenna effect," and mixed-RE-based MOFs (Fig. 4.2). The introduction of photoactive RE^{3+} to the MOF hosts may produce new luminescent signals at different positions from that of the MOFs linker, but this depends on the intramolecular energy transfer (antenna effect) from the MOFs (linkers) to the RE^{3+} ion. Controlling the RE^{3+} content in MOFs hybrids may create multiple luminescent centers. The nature of the unique luminescent centers may cause different responses

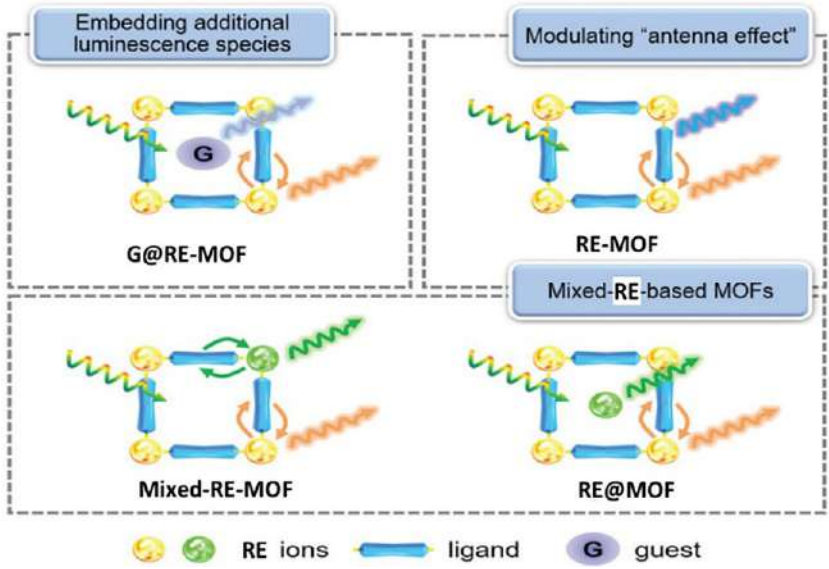

FIG. 4.2 Schematic representation of the three strategies to build dual-center emission RE-MOFs reported so far. *(Reproduced with permission from Y. Zhao, D. Li, Lanthanide-functionalized metal-organic frameworks as ratiometric luminescent sensors. J. Mater. Chem. C 8 (2020) 12739–12754. Copyright 2020 Royal Chemical Society.)*

(ratiometric sensing) to sensing species, which may provide a new opportunity for luminescence research with applications to chemical sensing.

4.2 Dual rare earth ion luminescence for ratiometric luminescence sensing in rare earth metal-organic framework hybrid materials

The dual RE^{3+} ion luminescence for RL sensing mainly focuses on the mixed rare earth MOFs materials, which contains two photoactive RE^{3+} centers through the ion substitution of one RE^{3+} using another RE^{3+} [10,40–56]. Due to the similar coordination characteristics and ionic radii, mixed-RE^{3+} MOFs, including the EuCe-MOF [40], the EuGd-MOF [41], the EuDy-MOF [42], and especially major EuTb-MOF [10,43–51,53–56], can be easily prepared by one-pot synthesis or ion exchange or coordinative PSM functionalization. By doping two or more RE^{3+} ions at the same crystallographically equivalent positions, the MOFs are endowed with two emission sources from RE^{3+} ions. Among them, EuTb-MOF or EuTb-functionalized MOFs have been studied extensively in the detection of temperature [10,43–51].

Li et al. reported a sensor $Tb_{97.11}Eu_{2.89}$-L_1 (H_6L_1 = hexakis-(4-carboxylatophenoxy)cyclotriph-osphazene) for ratiometric detection of trace water in

CH_3CN [54], which displays variable colors at different water content levels in CH_3CN detected with the naked eye from optical photos taken under ultraviolet light (254 nm) illumination. As the water content increases from 0% to 17.6%, the color of $Tb_{97.11}Eu_{2.89}$-L_1 changes from red-orange, yellow, to green (Fig. 4.3A; top). Upon excitation at 280 nm, the emission intensity of

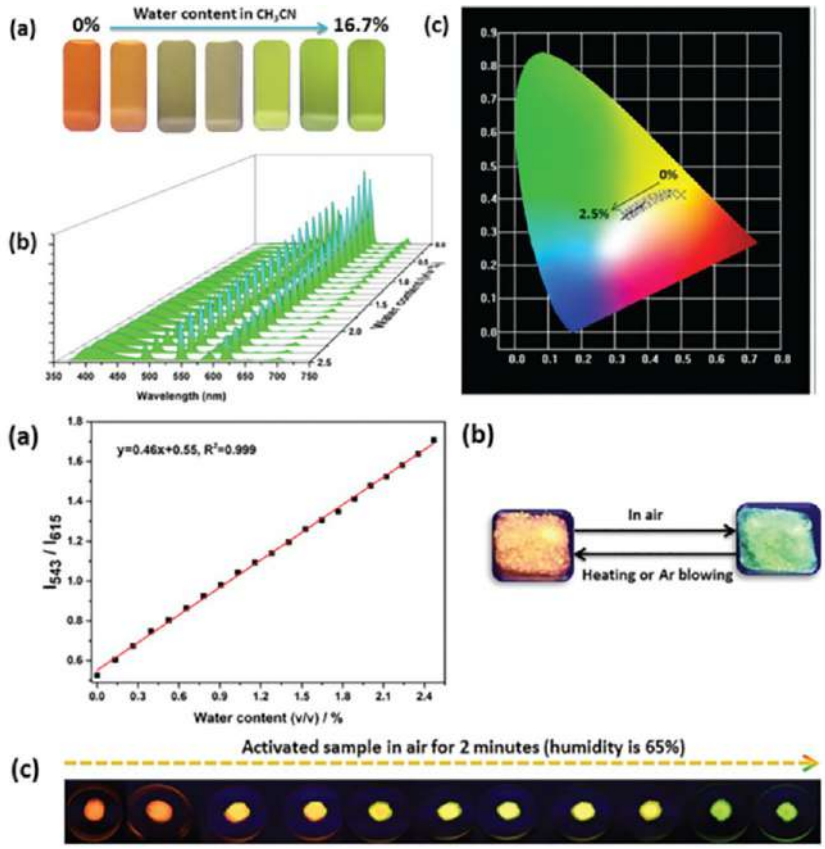

FIG. 4.3 *(Top)* (A) Optical images of $Tb_{97.11}Eu_{2.89}$-L1 under a 254-nm UV lamp after treatment with various amounts of water in CH_3CN. (B) The fluorescence spectra of $Tb_{97.11}Eu_{2.89}$-L1 at different amounts of water. (C) CIE chromaticity coordinates of $Tb_{97.11}Eu_{2.89}$-L1 after treatment with various amounts of water at an excitation wavelength of 280 nm. *(Bottom)* (A) The linear relationship between the fluorescence intensity I_{543}/I_{615} and the water content. (B) Optical images showing fluorescence switch of the as-synthesized sensor $Tb_{97.11}Eu_{2.89}$-L1 upon heating or Ar blowing and then cooling in air. (C) Optical images showing the fluorescence changes of the CH_3CN-exchanged $Tb_{97.11}Eu_{2.89}$-L1 sensor in air. All the solids are dispersed on the glass slides upon 254-nm UV lamp irradiation. *(Reproduced with permission from B. Li, W. Wang, Z. Hong, E. M. El-Sayed, D. Yuan, Ratiometric fluorescence detection of trace water in an organic solvent based on bimetallic lanthanide metal-organic frameworks. Chem. Commun. 55 (2019) 6926–6929. Copyright 2019 Royal Society of Chemistry.)*

$Tb_{97.11}Eu_{2.89}$-L_1 enhanced upon contacting water in CH_3CN, and a further increase in the water content in CH_3CN leads to a decrease in the emission intensities of Tb^{3+} and Eu^{3+} and an increase in that of the ligand. As the water content increases from 0% to 2.5% (*v*/v%), the characteristic luminescence shows an intensity reduction of 75% for the $^5D_0 \rightarrow {}^7F_2$ transition of Eu^{3+}, 18% for the $^5D_4 \rightarrow {}^7F_5$ transition of Tb^{3+}, and an increase of 345% for the ligand (Fig. 4.3B; top). The emission spectra of $Tb_{97.11}Eu_{2.89}$-L_1 at different water contents (0%–2.5%) in CH_3CN exhibit a chromaticity shift from orange, yellow, to white according to the change in the intensity ratio between the ligand, Tb^{3+}, and Eu^{3+} peaks. In addition, the corresponding chromaticity coordinate changes from (0.500, 0.413) to (0.330, 0.348) (Fig. 4.3C; top). As the water content increases, the fluorescence intensity of Eu^{3+} quenches more significantly than that of Tb^{3+}, which eventually leads to an increase in I_{543}/I_{615}. The linear regression equation of ratiometric fluorescence and water content change from 0% to 2.5% can be written with the correlation coefficients R^2 reaching up to 0.999 (Fig. 4.3A; bottom). To visually demonstrate the color change of $Tb_{97.11}Eu_{2.89}$-L_1 accompanying water absorption/release processes, the investigators simply deposited small amounts of the as-synthesized compound $Tb_{97.11}Eu_{2.89}$-L_1 onto glass slides (Fig. 4.3B; bottom). The solid crystals $Tb_{97.11}Eu_{2.89}$-L_1 containing DMA solvent molecules in pores changed the color slowly from red-orange to green in air upon irradiation under a 254-nm UV lamp (Fig. 4.3C; bottom) [10].

Zhao et al. designed and applied a 2′-fluoro-[1,1′:4′,1″-terphenyl]-3,3″,5,5″-tetracarboxylic acid (H_4FTPTC) with suitable triplet energy excited state to construct a luminescent RE-MOF for cryogenic temperature sensing [51]. They developed a new Tb^{3+}/Eu^{3+} mixed RE-MOF system $Tb_{1-x}Eu_x$FTPTC ($x = 0.05, 0.1, 0.2$), which featured excellent linear responses to temperature with high relative sensitivity in the cryogenic range of 25–125 K. The mixed $Tb_{0.95}Eu_{0.05}$FTPTC has a significantly different temperature dependence of luminescent behavior (Fig. 4.4A and B). Apparently, the luminescence behavior of the Tb^{3+} and Eu^{3+} ions within $Tb0._{95}Eu_{0.05}$FTPTC is typical of the Tb^{3+} -to-Eu^{3+} energy transfer process, which can be enhanced via a thermally driven phonon-assisted energy transfer mechanism. The intensity ration of Tb^{3+} at 543 nm and Eu^{3+} at 613 nm can serve as a ratiometric parameter for self-calibrating temperature measurement. As depicted in Fig. 4.4C, the intensity ratio Δ ($=I_{Tb}/I_{Eu}$) of the $Tb_{0.95}Eu_{0.05}$FTPTC as a function of temperature (T) exhibits an excellent linear relationship in the cryogenic regime from 25 to 125 K with the correlation coefficient of $R^2 = 0.97$ [51].

Lian et al. realized a near-infrared pumped luminescent MOF thermometer $Nd_{0.577}Yb_{0.423}$BDC-F_4, with near-infrared fluorescence and excellent sensitivity in the physiological temperature range (293–313 K), which may be potentially applied for biomedical systems [52]. Fig. 4.5 (left) shows the schematic representation of the energy transfer processes in our RE-MOF. As illustrated in Fig. 4.5A (right), the intensity of the $^2F_{5/2} \rightarrow {}^2F_{7/2}$ (Yb^{3+}, 980 nm) transition

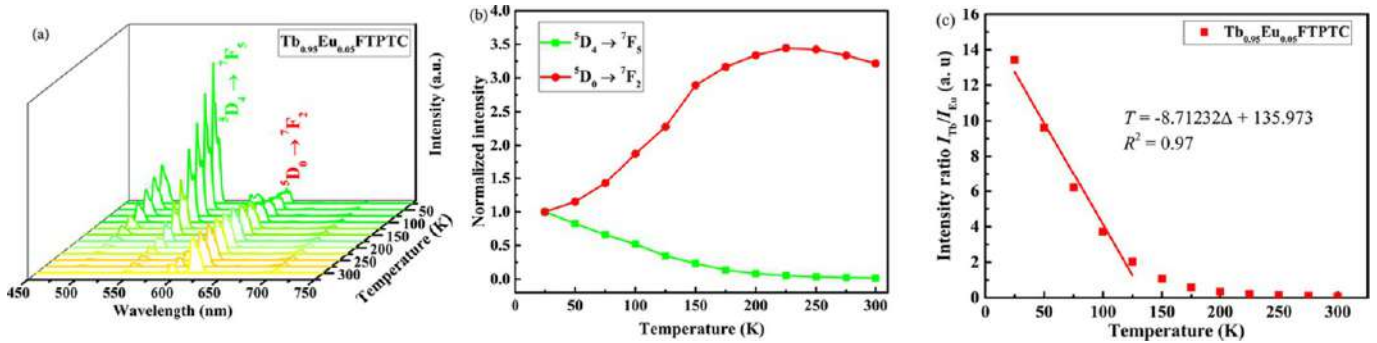

FIG. 4.4 (A) Emission spectrum of $Tb_{0.95}Eu_{0.05}$FTPTC from 25 to 300 K. (B) Temperature-dependent normalized luminescence intensity of Tb^{3+} ($^5D_4 \rightarrow {}^7F_5$, 544 nm) and Eu^{3+} ($^5D_0 \rightarrow {}^7F_2$, 614 nm) for $Tb_{0.95}Eu_{0.05}$FTPTC. (C) Intensity ratio I_{Tb}/I_{Eu} and the fitted curve for $Tb_{0.95}Eu_{0.05}$FTPTC from 25 to 300 K. *(Reproduced with permission from D. Zhao, D. Yue, L. Zhang, K. Jiang, G. Qian, Cryogenic luminescent Tb/Eu-MOF thermometer based on a fluorine-modified tetracarboxylate ligand. Inorg. Chem. 57 (2018) 12596–12602. Copyright 2018 American Chemical Society.)*

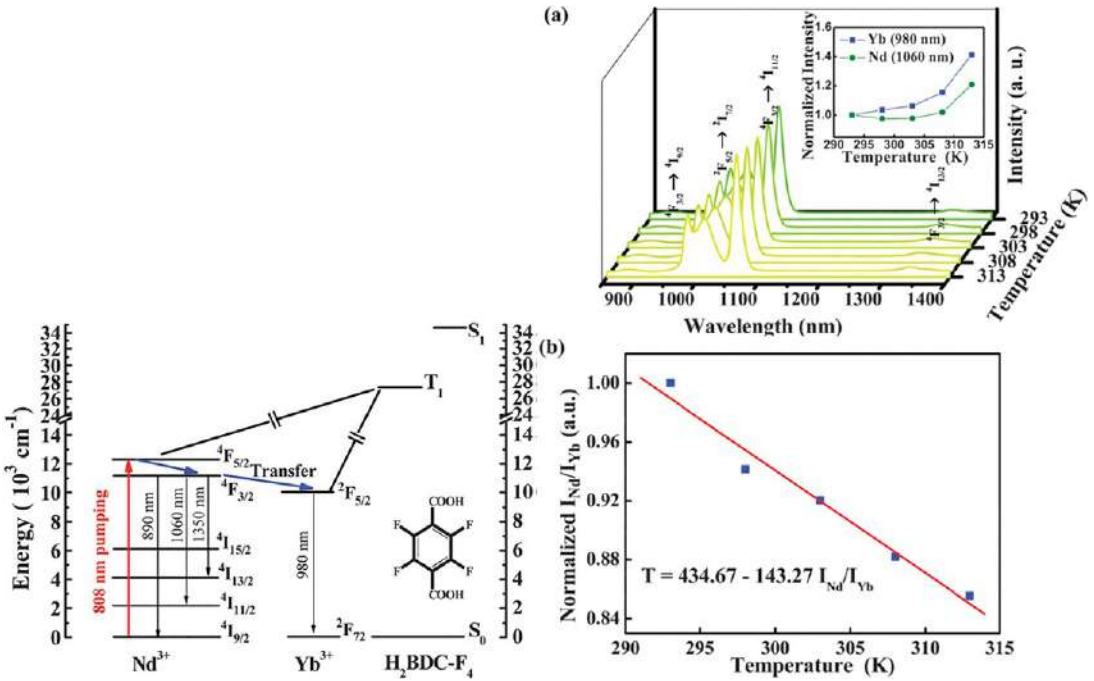

FIG. 4.5 *(Left)* Schematic representation of energy processes in RE-MOFs. *(Right)* (A) Emission spectra of $Nd_{0.577}Yb_{0.423}BDC\text{-}F_4$ in the range of 293–313 K excited at 808 nm; inset: temperature dependence of the normalized intensity of the corresponding transitions. (B) Temperature-dependent intensity ratio of Nd^{3+} (1060 nm) to Yb^{3+} (980 nm) and the fitted curve for $Nd_{0.577}Yb_{0.423}BDC\text{-}F_4$. *(Reproduced with permission from X. Lian, D. Zhao, Y. Cui, Y. Yang, G. Qian, A near infrared luminescent metal-organic framework for temperature sensing in the physiological range. Chem. Commun. 51 (2015) 17676–17679. Copyright 2015 Royal Society of Chemistry.)*

strongly increases as the temperature increases, while the intensity of the $^4F_{3/2} \rightarrow {}^4I_{11/2}$ (Nd^{3+}, 1060 nm) transition starts to increase until the temperature rises to 308 K. The inset of Fig. 4.5A (right) clearly shows the temperature dependence for the normalized intensity of the corresponding emissions. Furthermore, the increase of the Yb^{3+} emission is significantly different from YbBDC-F_4, with no emission band excited at 808 nm. This phenomenon is a typical energy transfer process, which can be attributed to efficient energy transfer from the Nd^{3+} to Yb^{3+} ions and enhances with the increase in temperature based on a thermally driven phonon-assisted transfer mechanism. For $Nd_{0.577}Yb_{0.423}$BDC-F_4, the intensity ratio of two emissions, the $^4F_{3/2} \rightarrow {}^4I_{11/2}$ (Nd^{3+}, 1060 nm) and $^2F_{5/2} \rightarrow {}^2F_{7/2}$ (Yb^{3+}, 980 nm), can be applied as the thermometric parameter in ratiometric luminescent thermometers, allowing self-calibrating measurement of the temperature based on the emission spectra. As shown in Fig. 4.5B (right), the calibration curve approximately follows a linear relationship between the I_{Nd}/I_{Yb} ratio and the temperature with a correlation coefficient $R^2 = 0.966$, which demonstrates that $Nd_{0.577}Yb_{0.423}$ BDC-F_4 is an excellent luminescent thermometer within the temperature range from 293 to 313 K [52].

Zhou et al. report an orthogonal multireadout nanothermometer in relation to the emission intensity ratio as well as the decay time and luminescence color of Eu^{3+}/Tb^{3+}@Zr-MOF nanocrystals, which are prepared via PSM functionalization with RE^{3+} cations of a robust UiO type Zr-MOF bearing the 2,2′-bipyridyl moiety [53]. As shown in Fig. 4.6A (left), Eu^{3+}/Tb^{3+}@Zr-MOF displays an exactly contrary thermal dependence with respect to the emissions of Tb^{3+} and Eu^{3+}. As the temperature rises, the Tb^{3+} emission intensity decreases sharply, while the Eu^{3+} emission significantly increases. The decay time of $^5D_4$ declines dramatically with temperature rising from 100 to 300 K, while the lifetime of $^5D_0$ increases from 0.666 ms at 100 K to 0.701 ms at 200 K (Fig. 4.6B; left). These phenomena indicate the occurrence of the Tb^{3+} to Eu^{3+} energy transfer in Eu^{3+}/Tb^{3+}@Zr-MOF. As shown in Fig. 4.6C (left), the values of η_{ET} are essentially unchanged in the low temperature range of 100–175 K, above which a rapid increase of η_{ET} is observed. It suggests that the Tb^{3+} to Eu^{3+} energy transfer process can be rationalized by the thermally driven phonon-assisted Förster transfer mechanism. The thermal sensitive luminescence properties enable Eu^{3+}/Tb^{3+}@Zr-MOF to serve as a nanoplatform for temperature sensing (Fig. 4.6D; right). For the intensity ratio-based temperature readout, the ratiometric parameter is defined as the ratio of the intensities of $^5D_4 \rightarrow {}^7F_5$ of Tb^{3+} (544 nm) and $^5D_0 \rightarrow {}^7F_2$ of Eu^{3+} (616 nm). Fig. 4.6A (right) illustrates the thermometric response curve measured for Eu^{3+}/Tb^{3+}@Zr-MOF nanocrystals, plotting the emission intensity ratio as a function of temperature. These data show the best thermometric sensitivity of 47.98% K^{-1} at 140 K (Fig. 4.6B; right), which is the largest one measured so far for the thermometers using the same intensity ratio technique. When setting a minimum sensitivity value of 2.5% K^{-1} as the quality limit, an optimal operation range of

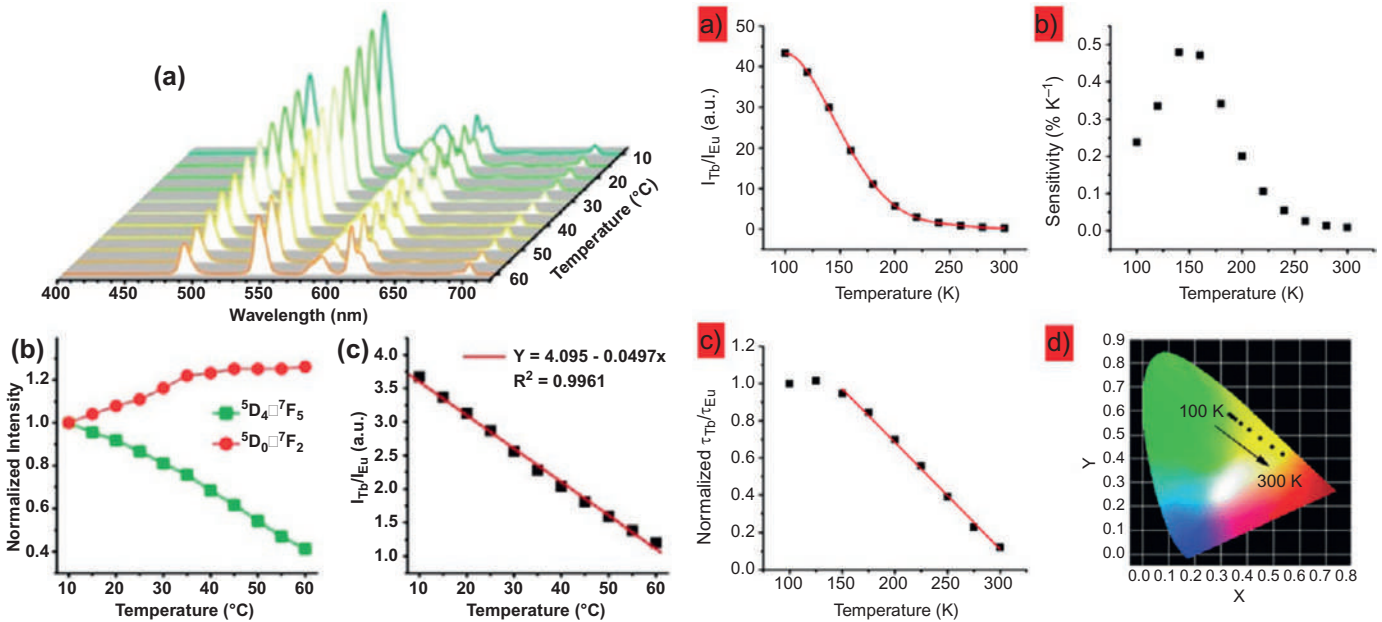

FIG. 4.6 *(Left)* (A) Temperature-dependent emission spectra ($\lambda_{ex} = 340$ nm) of Eu^{3+}/Tb^{3+}@Zr-MOF nanocrystals. Spectra were normalized to the total integrated intensity. (B) The $^5D_4$ and $^5D_0$ lifetimes of Eu^{3+}/Tb^{3+}@Zr-MOF as a function of temperature. (C) Temperature dependence of the Tb^{3+} to Eu^{3+} energy transfer efficiency (η_{ET}) in Eu^{3+}/Tb^{3+}@Zr-MOF. *(Right)* Eu^{3+}/Tb^{3+}@Zr-MOF nanocrystals show multireadout orthogonal detection of temperature. (A) Thermometric response curve plotting $I_{Tb}(^5D_4 \rightarrow {}^7F_5)/I_{Eu}(^5D_0 \rightarrow {}^7F_2)$ vs. temperature. (B) The relative thermometric sensitivity determined from (A). (C) $\tau_{Tb}(^5D_4 \rightarrow {}^7F_5)/\tau_{Eu}(^5D_0 \rightarrow {}^7F_2)$ as a function of temperature. (D) Thermal dependence of the luminescence color. *(Reproduced with permission from Y. Zhou, B. Yan, Lanthanides post-functionalized nanocrystalline metal-organic frameworks for tunable white-light emission and orthogonal multi-readout thermometry. Nanoscale 7 (2015) 4063–4069. Copyright 2015 Royal Chemical Society.)*

100–260 K can be achieved. For the readout based on decay times, similarly, the normalized luminescence lifetime ratio of $^5D_4$ and $^5D_0$ (τ_{Tb}/τ_{Eu}) of Eu^{3+}/Tb^{3+}@Zr-MOF is defined as a thermometric parameter. Fig. 4.6C (right) plots the dependence of I_{Tb}/I_{Eu} on temperature, which reveals a good linear relationship between normalized τ_{Tb}/τ_{Eu} and temperature within the range of 150–300 K with a slope of 0.57% K^{-1}. In addition, Eu^{3+}/Tb^{3+}@Zr-MOF nanocrystals can be developed as a colorimetric thermometer. As depicted in Fig. 4.6D (right), the chromaticity diagram coordinates transformed from the temperature-dependent emission spectra shift from green to orange (Fig. 4.6A; left). This indicates that the variation of ambient temperature can be estimated by observing the luminescence color of Eu^{3+}/Tb^{3+}@Zr-MOF using the naked eye or a CCD camera [53].

Qin et al. developed luminescent, bimetallic MOFs as luminescent sensors for NMF with a focus on Eu^{3+} and Tb^{3+} MOFs as visible emitters with red and green emission [53]. The concentration dependence of the emission spectra (0–1) of the mixed MOFs [$Eu_xTb_{1-x}(FDA)_3$] ($x = 0.01, 0.02, 0.2, 0, 2$, respectively; H_2FDA = 2,5-furandicarboxylic acid) are illustrated in Fig. 4.7A.

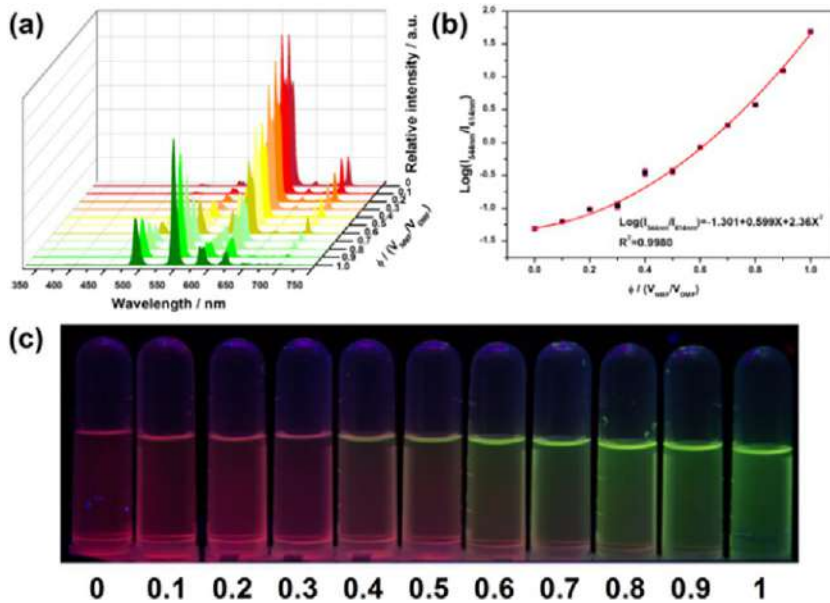

FIG. 4.7 (A) Suspension-state luminescent spectra of $[Eu_{0.1}Tb_{1.9}(FDA)_3(DMF)_2]\cdot 2DMF$ in volume ratio (ϕ) of NMF/DMF from 0 to 1 excited at 300 nm; (B) the correlation curve for the response of the sensor toward the NMF in the volume ratio from 0 to 1; and (C) the corresponding luminescence images of $[Eu_{0.1}Tb_{1.9}(FDA)_3(DMF)_2]\cdot 2DMF$ under UV light. *(Reproduced with permission from S. Qin, X. Qu, B. Yan, A self-calibrating bimetallic lanthanide metal-organic luminescent sensor integrated with logic gate operation for detecting N-methylformamide. Inorg. Chem. Front. 5 (2018) 2971–2977. Copyright 2018 Royal Society of Chemistry.)*

Notably, with the increasing concentration of NMF, the intensity of the Tb^{3+} luminescence in hybrid substantially increases, while contrary to the Eu^{3+} emission. A concentration-dependent curve shows a good linear relationship, which is represented as the concentration versus intensity ratio ($^5D_0 \rightarrow {}^7F_2/{}^5D_4 \rightarrow {}^7F_5$ defined the ratiometric parameter I_{544nm}/I_{614nm}) and further confirms that the hybrid is a self-calibrating luminescent sensor (Fig. 4.7B). As illustrated in Fig. 4.7C, the concentration-dependent luminescence emission of the hybrid is systematically tuned from red to green at different concentrations of NMF. Furthermore, the luminescence color changes make it particularly easy to use a sensitive luminescent colorimetric ratiometric for visualizing the NMF concentration over a wide range [54].

4.3 Ligand (linker) and RE^{3+} ions through energy transfer "antenna effect" for ratiometric luminescence sensing in rare earth metal-organic framework hybrid materials

Most of the reported RE-MOFs are monochromatic and exhibit an emission from an RE^{3+} ion or an organic ligand. As the "antenna effect" is very sensitive to the coordination environment, the incomplete energy transfer by modulating the "antenna effect" through rational ligand design or regulating the external conditions will lead to dual-emitting materials with emissions from both RE^{3+} and the ligand [57–72].

Zhou et al. described a new strategy for the generation of ratiometric MOF thermometers, illustrated by imparting an additional Eu^{3+} luminescence to a robust MOF with intrinsic ligand-based emission to form a dual-emissive hybrid for highly sensitive temperature sensing over the physiologic temperature range [57]. The dual emissions of the hybrid have different thermal dependencies, thus enabling their intensity ratio to be highly sensitive to the temperature. To examine the feasibility of the Eu^{3+}@Zr-MOF for ratiometric thermometry, the temperature-dependent photoluminescence properties were studied (Fig. 4.8; left). Eu^{3+}@Zr-MOF exhibits an exactly contrary thermal dependence with respect to the emissions of linkers and Eu^{3+}. With the temperature increases, the Eu^{3+} emission intensity declines, while the ligand emission significantly increases. The significant luminescence enhancement of the linker as well as the decrease in Eu^{3+} emission in the Eu^{3+}@Zr-MOF hybrid may be attributed to the back energy transfer (BEnT) from Eu^{3+} cations to linker. Temperature-dependent emission lifetimes (Eu^{3+}) of the MOF hybrid are recorded for the determination of K_b and E_a (Fig. 4.8A; right). The decay time of Eu^{3+} reduced with the increase of temperature, while the decay time of the ligand emission slightly increased as the temperature elevated. This phenomenon further verifies the BEnT from Eu^{3+} to MOF. These results indicate the occurrence of the back energy transfer from Eu^{3+} to the bpydc linkers embedded in the framework. The calculated K_{BEnT} enhances with the increase of temperature (Fig. 4.8B; right). The slope of the Arrhenius plots for K_{BEnT} is 1.98,

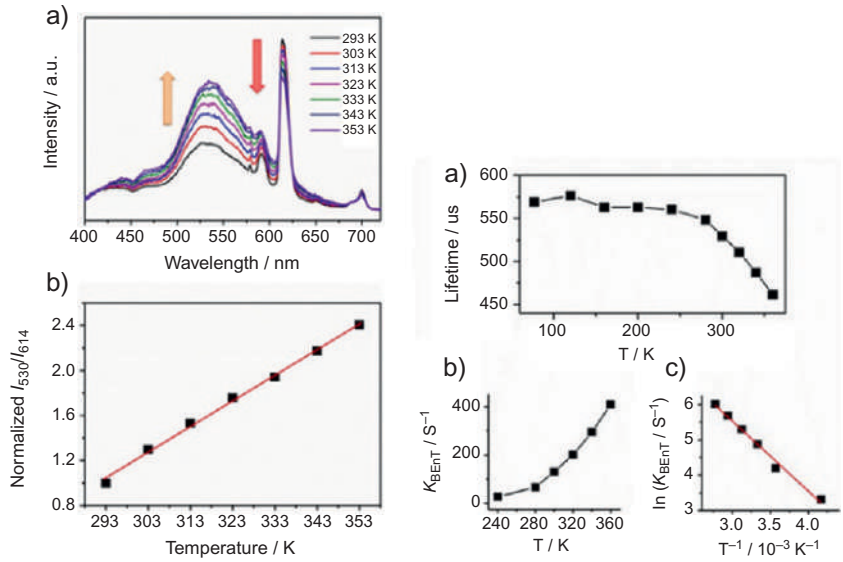

FIG. 4.8 *(Left)* (A) Temperature-dependent emission spectra of Eu^{3+}@Zr-MOF; and (B) the intensity ratio of ligand (530 nm) to Eu^{3+} (614 nm) as a function of temperature. Ratios are normalized to the value at 293 K. *(Right)* (A) Temperature-dependence of luminescence lifetime of Eu^{3+} in Eu^{3+}@Zr-MOF; (B) Thermometric response curve plotting back energy transfer rate (K_{BEnT}) vs. temperature; and (C) Arrhenius plots for back K_{BEnT} constants of Eu^{3+}@Zr-MOF. *(Reproduced with permission from Y. Zhou, B. Yan, Ratiometric detection of temperature using responsive dual-emissive MOF hybrids. J. Mater. Chem. C 3 (2015) 9353–9358. Copyright 2015 Royal Society of Chemistry.)*

resulting in a value of 44 kJ mol^{-1} for activation energy E_a (Fig. 4.8C; right). It is interesting, for such an LMET process to take place from Eu^{3+} to ligand is not common [57].

Xu et al. encapsulated Eu^{3+} cations into MIL-124 ($Ga_2(OH)_4(C_9O_6H_4)$) and used it to detect Fe^{3+}/Fe^{2+} ions via fluorescence quenching of the dual-emission centers (Eu^{3+} and MOF) [58]. Although both Fe^{2+} and Fe^{3+} ions significantly quenched the Eu^{3+} emission, the emission colors of the two ions were different and easily distinguished under UV light. Therefore, Eu^{3+}@MIL-124 can selectively sense Fe^{2+} and Fe^{2+} ions via the different quenching effects on Eu^{3+} and the MOF. To detect Fe^{2+} and Fe^{3+} in water, a test paper was immersed in aqueous solutions of the metal ions, and the fluorescent colors changed from red to dark red, faint dark red, and black with an increase in Fe^{3+} (Fig. 4.9A). When the test paper was immersed in aqueous solutions with various concentrations of Fe^{2+}, the color changed from red to blue, as shown in Fig. 4.9B. The quenching effect of Fe^{3+} on Eu^{3+}@MIL-124 is ascribed to the partial replacement of Ga^{3+} by Eu^{3+}, and its substitution is the main reason for the fluorescence quenching due to Fe^{2+} [58]. Sun et al. presented a facile, rapid, and selective strategy for

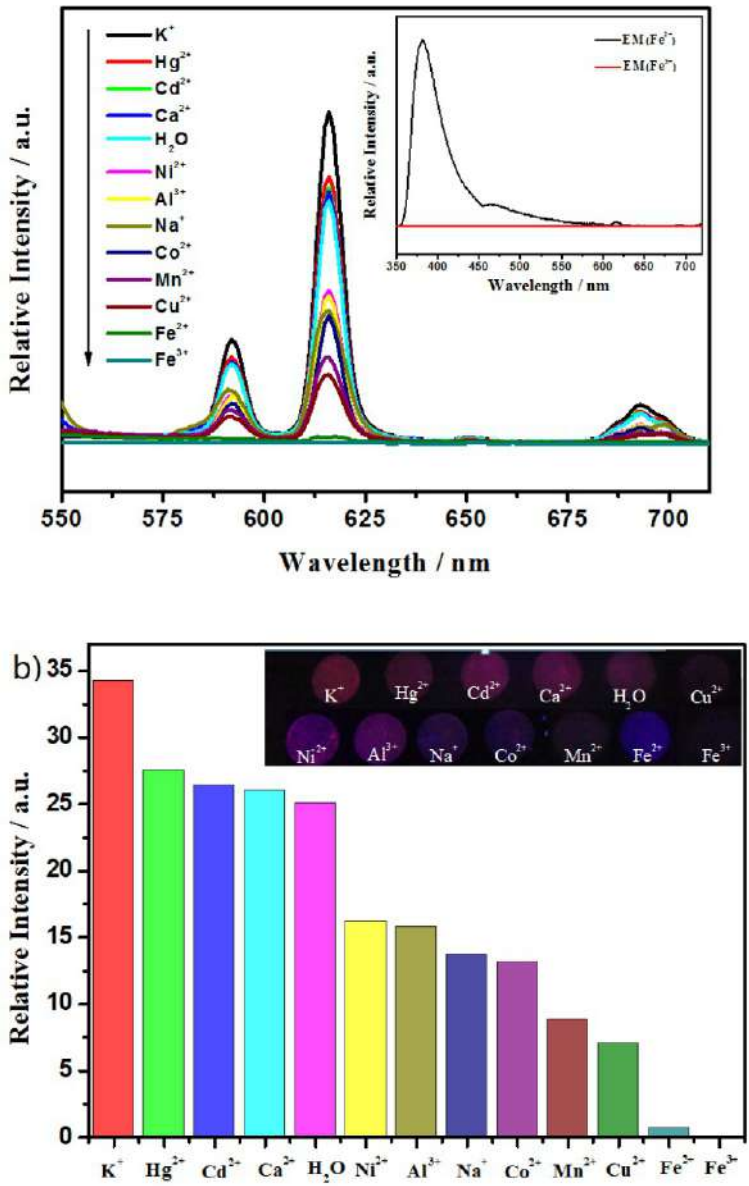

FIG. 4.9 (A) PL spectra of Eu^{3+}@MIL-124 dispersed into different aqueous solution of various metal ions (10^{-2} mol L^{-1}) and the inset is Fe^{2+} (*blank line*) and Fe^{3+} (*red line*). (B) The luminescence intensity of the $^4D_0$-$^7F_2$ of Eu^{3+}@MIL-124 interacting with different metal ions in 10^{-2} mol L^{-1} aqueous solution of MCl_n ($\lambda_{ex} = 298$ nm), and inset is the corresponding photographs under UV-light irradiation at 254 nm. *(Reproduced with permission from X. Xu, B. Yan, Eu(III)-functionalized MIL-124 as fluorescent probe for highly selectively sensing ions and organic small molecules especially for Fe(III) and Fe(II). ACS Appl. Mater. Interfaces 7 (2015) 721–729. Copyright 2015 American Chemical Society.)*

ratiometric sensing of carbonate ions based on heterobimetallic Eu/Pt-MOFs with bpydc as linker, which has dual emissions from the ligand and Eu^{3+}. The interaction with CO_3^{2-} drastically enhances the luminescence intensity of Eu^{3+}, and the maximum ratio of the two intensities ($I_{Eu(614)}/I_{Ligand}$) increases upon the addition of carbonate ions. This may be an efficient tool for analytical monitoring of trace CO_3^{2-} in real samples because of the high orientation selectivity for CO_3^{2-} [59].

Zhou et al. examined the capability of Eu^{3+}@bpy-UiO nanohybrids for volatile organic compound (VOC) sensing [60]. Fig. 4.10A shows the emission spectra of Eu^{3+}@bpy-UiO after exposure to different VOCs, and the intensity ratio of the ligand-based emission to the Eu^{3+} emission (I_L/I_{Eu}) significantly depended on the VOCs. Moreover, the ratiometric luminescence of Eu^{3+}@bpy-UiO was highly responsive to different concentrations of VOCs and mixed VOCs. Fig. 4.10B shows the one-to-one correlation between the resulting I_L/I_{Eu} and the encapsulated VOCs. The ratiometric emission intensity and luminescence quantum yield (Φ) of the VOC-included Eu^{3+}@bpy-UiO are related to a unique, 2D readout (I_L/I_{Eu}, Φ) arranged in a decoded map (Fig. 4.10C). These readouts show that one can precisely differentiate the VOCs using this dual-readout process [60].

Xu et al. prepared a portable luminescent RE-MOF film by in-situ growing of nanoscale SUMOF-6-Eu on an oxidation-treated nonwoven polypropylene surface (NMOFs@O-PP) (Fig. 4.11; left), which was then conducted to determine the luminescence response to O_2. Upon excitation at 395 nm, emission intensities at 557 nm and 614 nm were measured after exposure to each P_{O2}. As shown in Fig. 4.11A (left), the Eu^{3+} luminescence intensities at 614 nm decreased gradually with the increase of P_{O2}. However, the ligand-based emission intensities centered at 557 nm have been shown to be invariant under different P_{O2} values simultaneously, meaning that the emission can potentially provide a reference signal that allows for the quantification of O_2 by the sensor. The chromaticity coordinates calculated from the emission spectra (Fig. 4.11A; left) shift from the orange region to the green region. Furthermore, the luminescence decay time ($^5D_0 \rightarrow {}^7F_2$) of NMOFs@O-PP substantially changed upon exposure to O_2 at different P_{O2} values, which supports the fact that ratiometric luminescence responses toward O_2 can be rationalized by the guest-dependent energy transfer from H_2bpydc ligands to Eu^{3+} cations. Good linearity ($R^2 = 0.99765$) can be seen from the Stern-Volmer plots of coated NMOFs@O-PP, as shown in Fig. 4.11B (left). The K_{SV} and the R_0/R ($P_{O2} = 1$) are estimated to be 6.73 and 7.66, respectively. The LOD is estimated to be 0.45%, which is obtained from the emission intensities of the sensor under 100% N_2 for 20 times. The luminescence intensities of coated NMOFs@O-PP films were continuously recorded by alternating the atmosphere between 1 atm of O_2 and 1 atm of N_2 for 7 cycles. As demonstrated in Fig. 4.11 (right, top), at room temperature, the sensor worked successfully as a ratiometric luminescent O_2 probe with I_{Eu}/I_L values between 5.91 for

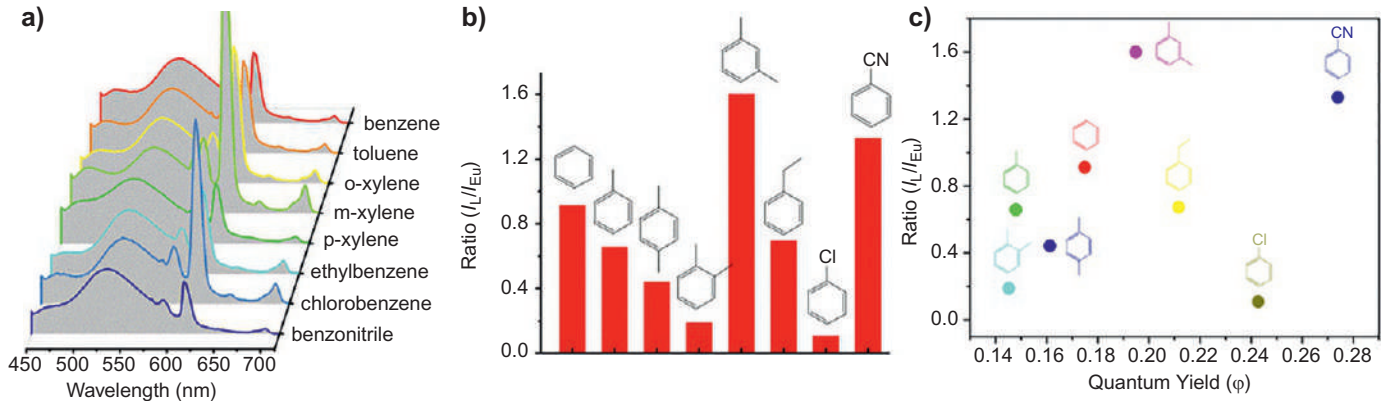

FIG. 4.10 The emission spectra (A) and I_L/I_{Eu} intensity ratios (B) of Eu^{3+}@UiO-bpy after the encapsulation of VOCs and (C) A 2D decoded map of the aromatic VOCs based on the emission intensity ratio (I_L/I_{Eu}) and quantum yield (Φ) responses of the Eu^{3+}@bpy-UiO nanocomposite. *(Reproduced with permission from Y. Zhou, B. Yan, A responsive MOF nanocomposite for decoding volatile organic compounds. Chem. Commun. 52 (2016) 2265–2268. Copyright 2016 Royal Society of Chemistry.)*

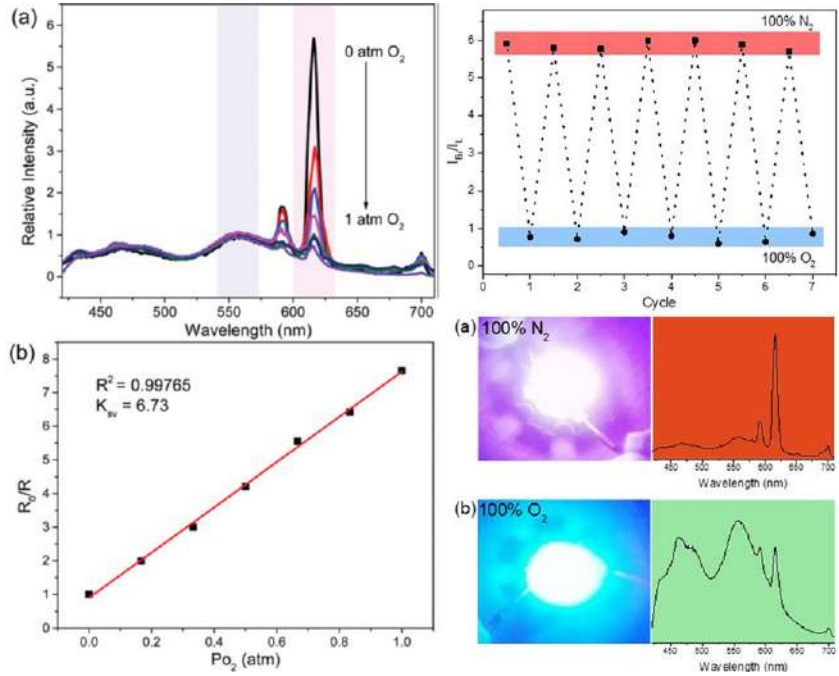

FIG. 4.11 *(Left)* (A) Emission spectra of coated NMOFs@O-PP film at different oxygen partial pressures P_{O2} and (B) Stern-Volmer plots showing R_0/R vs. O_2 partial pressure P_{O2} for the coated NMOFs@O-PP film, $\lambda_{ex} = 395$ nm. *(Right) (Top)* Luminescence intensity ratio (I_{Eu}/I_L) values of coated NMOFs@O-PP films under repeated cycles of 1 atm O_2 and 1 atm N_2 conditions, $\lambda_{ex} = 395$ nm. *(Bottom)* Photographs of 395-nm LED modified by coated NMOFs@O-PP and emission spectra of coated NMOFs@O-PP under 100% N_2 (A) and 100% O_2 (B). *(Reproduced with permission from X. Xu, B. Yan, Nanoscale LnMOF-functionalized nonwoven fibers protected by a polydimethylsiloxane coating layer as a highly sensitive ratiometric oxygen sensor. J. Mater. Chem. C 4 (2016) 8514–8521. Copyright 2016 Royal Society of Chemistry.)*

1 atm N_2 and 0.77 for 1 atm O_2, with reversible O_2 quenching and good N_2 recovering properties. The coated NMOF-PP film was also fabricated on the outer surface of a commercial 395-nm blue-light light-emitting diode (LED) to construct a simple color-changing ratiometric O_2 sensor, which enables easy identification of O_2 concentration by the change in the light color. As seen in Fig. 4.11A (right, bottom), a bright red emission can be observed by the naked eye when a modified LED is exposed to 100% N_2; under 100% O_2, the obvious red emission of the modified LED turns to green light mainly originating from the emission of the ligand due to a sharp decrease in the Eu^{3+}-based emission (Fig. 4.11B; right, bottom) [61].

More recently, Xu et al. fabricated ZnO-doped UiO-MOF heterostructures (ZnO@UiO-MOFs) and tuned them into a dual-emitting material (I_{614} and I_{470}) by introducing Eu^{3+} by coordinated PSM to UiO-MOFs and controlling the

excitation wavelength [62]. Reduced aldehyde molecules could build a bridge via the charge transfer from ZnO to Eu^{3+} to increase the intensity of I_{614} and realize selective sensing. The open connected channels and high surface area of UiO-MOFs could facilitate the effective adsorption of aldehydes, leading to a low detection limit (42 ppb for FA, 58 ppb for AA, and 66 ppb for ACA). The efficient charge transfer from the MOFs to ZnO can lead to reusable detectors for aldehyde gases. In addition, the MOFs show stable and reliable fluorescent responses for aldehydes at different temperatures (25–65°C), which makes them suitable for practical applications, e.g., vehicle detection. After exposure to the main volatile gases (10 ppm) at 25°C for 30 min, the photoluminescence responses were recorded and are compared in Fig. 4.12A (left). The results revealed that various volatile gases displayed markedly different effects on the PL of Eu^{3+}@ZUM (Fig. 4.12B; left). Most of the volatile gases do not cause any significant change in the intensity of the sensor ($I_{614}/I_{470} = 2.3 \pm 0.1$), which gives a faint blue-white light (inset of Fig. 4.12B; left). In contrast, the composite shows a significant increased effect of Eu^{3+}-based PL emission after exposure to FA. The relative ratio (I_{614}/

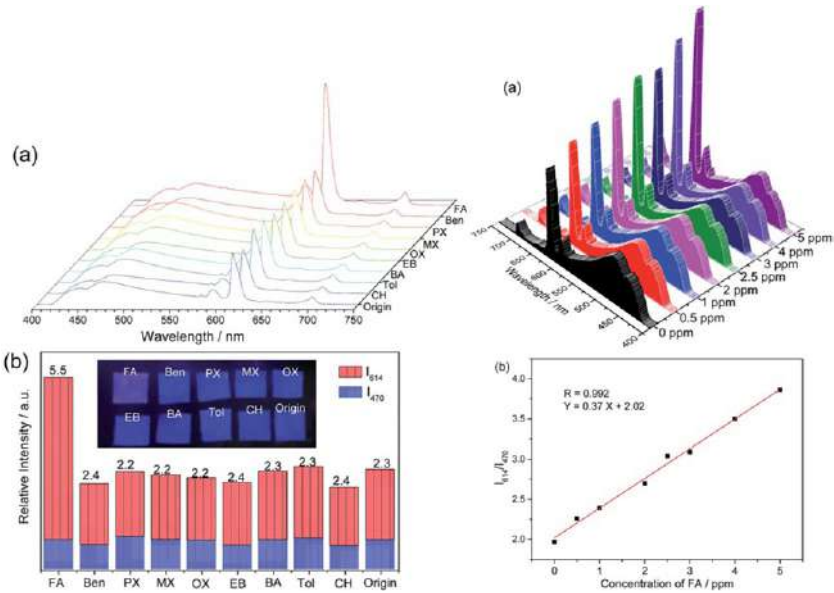

FIG. 4.12 *(Top)* The PL intensities (I_{614} and I_{470}) of Eu^{3+}@ZUM test paper after exposure to various polluting gases in vehicles ($\lambda_{ex} = 365$ nm). *(Bottom)* (A) PL emission spectra of Eu^{3+}@ZUM test paper at different concentrations of FA ranging from 0 to 5 ppm and (B) the linear fitted curve showing I_{614}/I_{470} vs. FA concentration for the Eu^{3+}@ZUM test paper, $\lambda_{ex} = 365$ nm. *(Reproduced with permission from X. Xu, B. Yan, Eu(III)-functionalized ZnO@MOFs heterostructures: integration of pre-concentration and efficient charge transfer as ppb-level sensing platform for volatile aldehyde gases in vehicles. J. Mater. Chem. A 5 (2017) 2215–2223. Copyright 2017 Royal Society of Chemistry.)*

$I_{470} = 5.5$) exhibits a 2.4-fold increase compared to that before exposure to FA, leading to the color of the test paper changing from blue to red that can be observed with the naked eye under UV light (inset of Fig. 4.12B; left). To further prove the fluorescence response of Eu^{3+}@ZUM to aldehyde species, concentration-dependent studies on the PL properties were carried out. Fig. 4.12 (right) presents the changes in PL intensity of the Eu^{3+}@ZUM test paper after exposure to various concentrations (0–5 ppm) of FA gas at 25°C for 30 min. The results revealed that the emission intensity of Eu^{3+} regularly increases with the successive increase of FA in the range of 0–5 ppm (Fig. 4.12A; right). The plot of relative intensities (I_{614}/I_{470}) versus the concentration of FA gas in Fig. 4.12B (right) reveals a good linear relationship between them. In addition, the high sensitivity of Eu^{3+}@ZUM toward all the target aldehydes can be attributed to two factors. One is the open connected channels and high surface area of MOFs that can facilitate the effective adsorption of aldehydes. The other is the increased surface electrons of ZnO, which can easily capture oxygen molecules for the reaction to occur [62].

Zhang et al. constructed a luminescent Ln^{3+} exchange PSM MOF hybrid (Eu^{3+}@Zn-MOF) to detect formaldehyde (FA) in water and food. The two luminescent centers of Eu^{3+}@Zn-MOF had completely different responses to FA, which could offer a reference for each other, so a precise self-calibrating luminescent detector for FA could be designed. Based on this, a portable self-calibrating luminescent logic detector capable of gradient detection of FA was designed [63]. As shown in Fig. 4.13A, the luminescence of Eu^{3+} (λ_{614nm}) is quenched completely after immersion in FA, while the luminescence of Zn-MOF (λ_{405nm}) has a remarkable enhancement compared with other

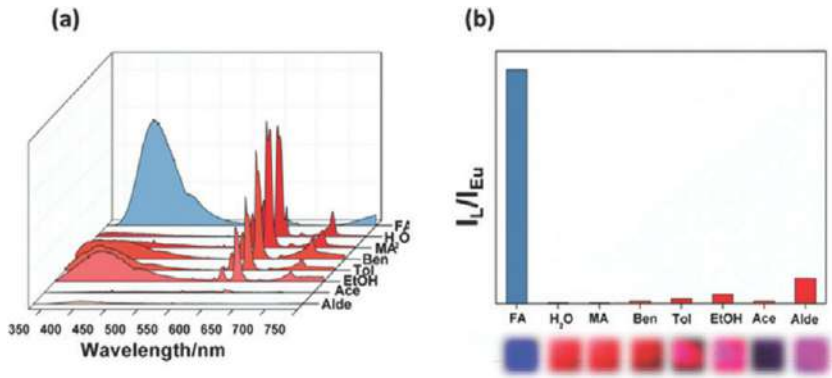

FIG. 4.13 (A) Luminescent spectra of Eu^{3+}@Zn-MOF dispersed in different solutions when excited at 313 nm; (B) histogram for I_L/I_{Eu} of Eu^{3+}@Zn-MOF undergoes various solutions (the inset is the photo of different solutions under UV lights). *(Reproduced with permission from Y. Zhang, B. Yan, A portable self-calibrating logic detector for gradient detection of formaldehyde based on luminescent metal organic frameworks. J. Mater. Chem. C 7 (2019) 5652–5657. Copyright 2020 Royal Society of Chemistry.)*

solvents. The remarkable change can also be clearly distinguished by the naked eye under UV light irradiation, as shown in the inset of Fig. 4.13B [63].

Gao et al. reported a series of water-stable MOFs with three emitting centers for tunable emissions $[RE(TCPB)(DMF)_3]_n$ (RE = Eu, Tb, and Gd, H_3TCPB = 1,3,5-tris(1-(2-carboxyphenyl)-1H-pyrazol-3-yl)benzene, DMF = *N*,*N*′-dimethylformamide), which are easily synthesized by simultaneously doping red-emitting Eu^{3+} and green-emitting Tb^{3+} into the same framework. The versatile $Eu_{0.67}Tb_{0.33}$-TCPB is applied to conveniently distinguish different nitroaromatic pollutants and multidimensional ratiometric sensing $CrO_4^{2-}/Cr_2O_7^{2-}$ [72]. As shown in Fig. 4.14A–C, $CrO_4^{2-}/Cr_2O_7^{2-}$ exhibit significant quenching effects on all the ligand-Eu^{3+}-Tb^{3+} emissions and the corresponding quenching efficiencies upon addition of $CrO_4^{2-}/Cr_2O_7^{2-}$ are calculated to be 91.7%, 73.9%, and 76.0% for CrO_4^{2-}, and 95.3%, 79.8%, and 81.8% for/$Cr_2O_7^{2-}$. These results clearly indicate that toxic $CrO_4^{2-}/Cr_2O_7^{2-}$ could be effectively detected by $Eu_{0.67}Tb_{0.33}$-TCPB. The linear correlation between $\log(I_{386}/I_{545})/\log(I_{386}/I_{616})$ and concentration (C) of $CrO_4^{2-}/Cr_2O_7^{2-}$ can be linearly fitted (Fig. 4.14D and E). The low LOD rank $Eu_{0.67}Tb_{0.33}$-TCPB sensors are almost the most sensitive CP-based luminescent sensors reported for detecting $CrO_4^{2-}/Cr_2O_7^{2-}$ in water. Sensing of $CrO_4^{2-}/Cr_2O_7^{2-}$ can be improved by recording the concentration-dependent evolution of $\log(I_{386}/I_{545})$ and $\log(I_{386}/I_{616})$, and a novel 3D code recognition can be mapped out for further 3D ratiometric sensing (Fig. 4.14F). When concentration is added as the third dimension, the 3D code recognition can further distinguish $CrO_4^{2-}/Cr_2O_7^{2-}$. This provides a new perspective for luminescent sensing compared with sensors based on single or dual emissions [72].

4.4 Embedding additional luminescent species for ratiometric luminescence sensing in rare earth metal-organic framework hybrid materials

Due to the high surface area, regular channels, and abundant interaction sites, MOFs are potential platforms to encapsulate the luminescent species in their channels or on their surface to build dual-emitting materials. By one-pot synthesis or PSM, the illuminant guests are highly dispersed in the rigid skeleton of MOFs and their emission is stronger than the isolated one [73–75].

Cui et al. incorporated an organic dye perylene into a porous Eu-MOF, ZJU-88 ($[Eu_2(QPTCA)(NO_3)_2(DMF)_4]\cdot(CH_3CH_2OH)_3$) to form a ZJU-88 ⊃ perylene composite, and made use of the dual emission from organic dyes and Eu^{3+} ions to realize ratiometric temperature sensing in a physiological temperature range (Fig. 4.15; left). As expected, the ZJU-88 ⊃ perylene composite features a red emitting of Eu^{3+} at 615 nm and an appended blue emitting around 473 nm of perylene dyes, whose luminescent intensity ratios correlate linearly very well to temperatures in the range of 20°C to 80°C. To assess the potential of ZJU-88 ⊃ perylene as a ratiometric thermometer, the temperature-dependent photoluminescent properties were investigated (Fig. 4.15A; right). With the

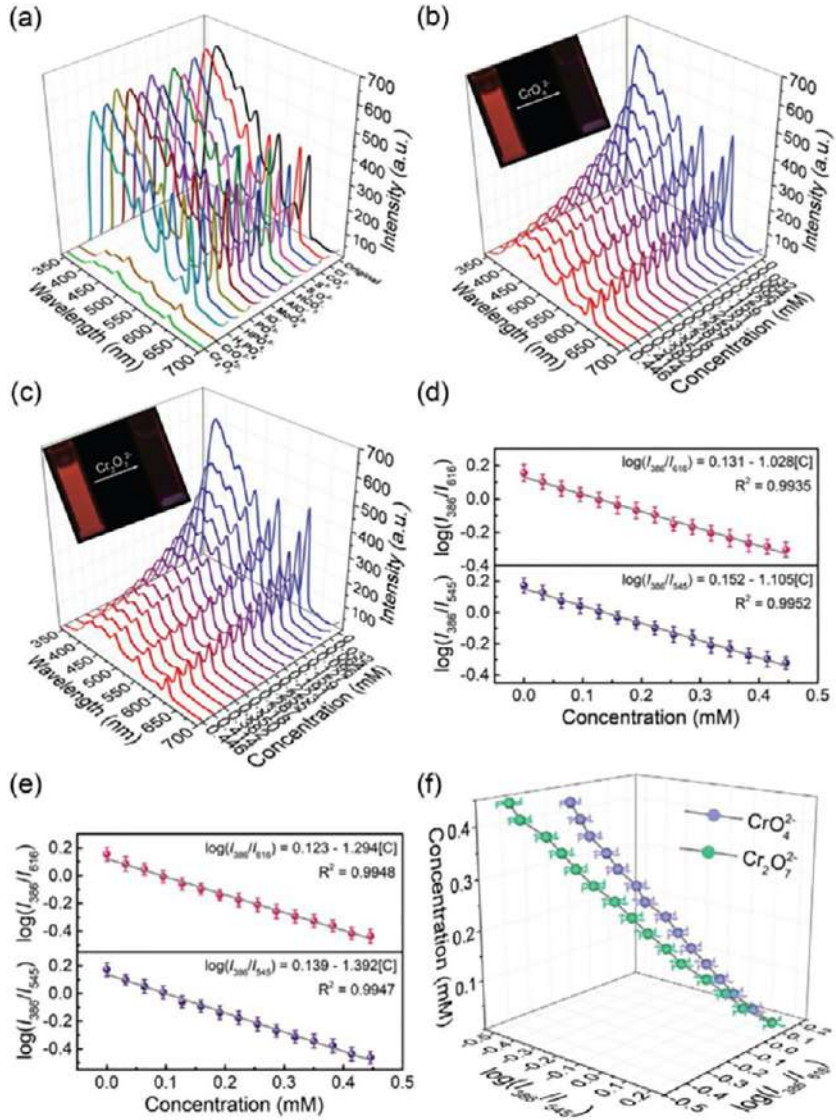

FIG. 4.14 (A) Emission spectra of $Eu_{0.67}Tb_{0.33}$-TCPB toward different anions in aqueous solution with concentration of 1×10^{-6} m under excitation at 325 nm. (B) Emission spectra of $Eu_{0.67}Tb_{0.33}$-TCPB dispersed in water upon incremental addition of CrO_4^{2-}. (C) Emission spectra of $Eu_{0.67}Tb_{0.33}$-TCPB upon incremental addition of $Cr_2O_7^{2}$. (D) Fitting curve of $Eu_{0.67}Tb_{0.33}$-TCPB quenched by CrO_4^{2-}. (E) Fitting curve of $Eu_{0.67}Tb_{0.33}$-TCPB quenched by $Cr_2O_7^{2}$. (F) The derived 3D ratiometric sensing of $CrO_4^{2-}/Cr_2O_7^{2-}$ when concentration is added as the third dimension. The inset shows the luminescence color change after adding $CrO_4^{2-}/Cr_2O_7^{2-}$ under UV light. *(Reproduced with permission from E. J. Gao, S. Y. Wu, J. Wang, M. C. Zhu, Y. Zhang and V. P. Fedin, Water-stable lanthanide coordination polymers with triple luminescent centers for tunable emission and efficient self-calibration sensing wastewater pollutants. Adv. Opt. Mater. 8 (2020) 1901659. Copyright 2020 Wiley.)*

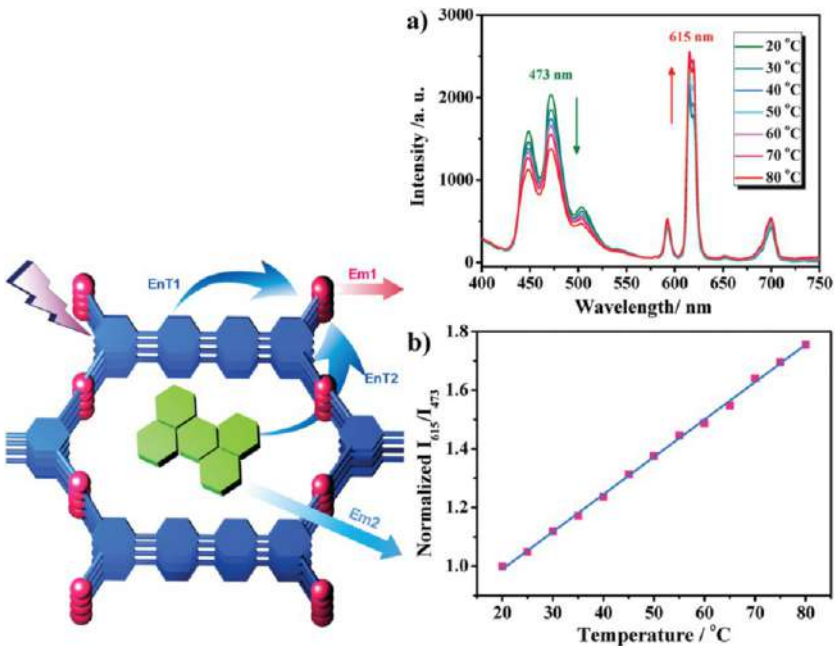

FIG. 4.15 *(Left)* Scheme for the design of dual-emitting ZJU-88 ⊃ perylene composite (EnT: energy transfer, Em: emission). *(Right)* (A) Emission spectra of ZJU-88 ⊃ perylene recorded from 20°C to 80°C, excited at 388 nm. (B) Temperature-dependent intensity ratio of Eu^{3+} (615 nm) to perylene (473 nm) and the fitted curve for ZJU-88 ⊃ perylene. *(Reproduced with permission from Y. Cui, R. Song, J. Yu, M. Liu, Z. Wang, C. Wu, Y. Yang, Z. Wang, B. Chen, G. Qian, Dual-emitting MOF⊃dye composite for ratiometric temperature sensing. Adv. Mater. 27 (2015) 1420–1425. Copyright 2015 Wiley.)*

increase of temperature from 20°C to 80°C, the luminescence intensity at 473 nm of perylene dye in ZJU-88 ⊃ perylene substantially decreased due to the thermal activation of nonradiative-decay pathways, while the intensity of the $^5D_0 \rightarrow {}^7F_2$ transition of Eu^{3+} at 615 nm increased. The significant luminescence decreases of perylene as well as the enhancement in emission of Eu^{3+} in ZJU-88 ⊃ perylene may be attributed to the energy transfer from perylene molecules to Eu^{3+} ions. Fig. 4.15B (right) plots the ratio of the two luminescence intensities at 615 nm (Eu^{3+}) and 473 nm (perylene) versus temperature, normalized to this intensity ratio at 20°C. There is a very good linear relationship between the intensity ratio and temperature with correlation coefficient 0.998, where I_{615} and I_{473} are the luminescence intensity of Eu^{3+} and perylene dye, respectively.

Dong et al. encapsulated strongly blue light-emitting nitrogen and sulfur-codoped CDs (N,S-CDs) in the frameworks of a Eu-MOF, whose dual-emission nanohybrid (Eu-MOFs/N,S-CDs) was developed as a sensitive and visual colorimetric sensor for water contents in organic solvents (Fig. 4.16; top). Because

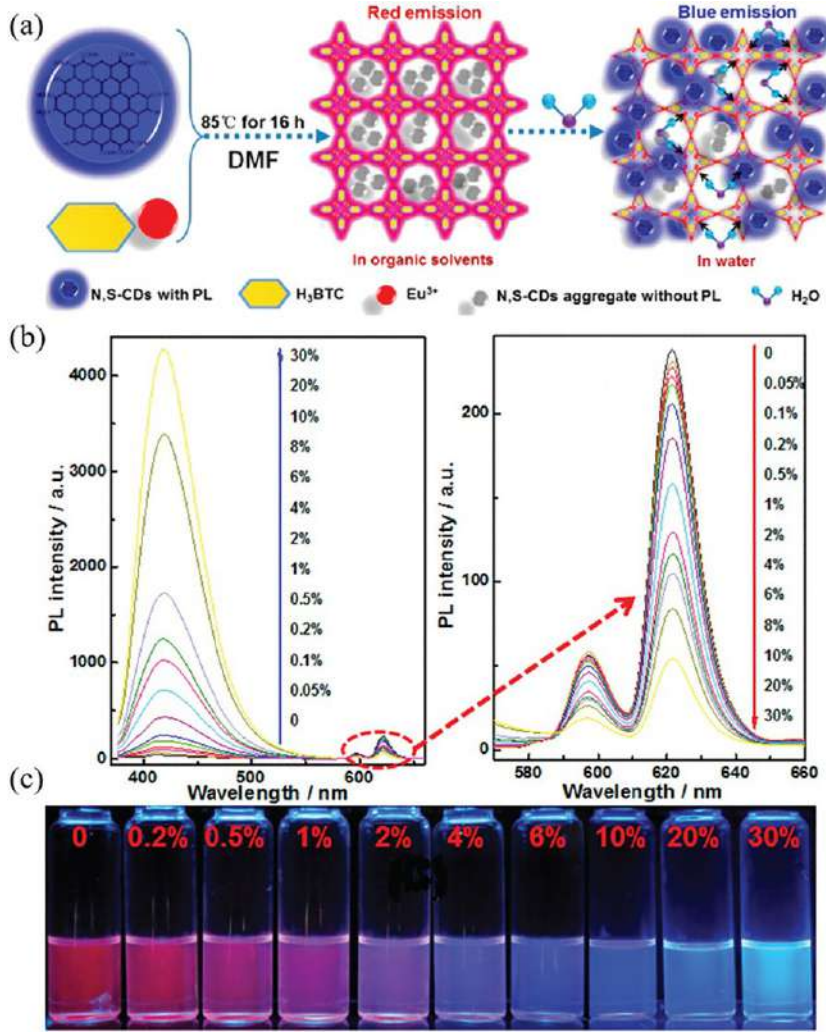

FIG. 4.16 (A) Scheme of synthesis and detection of water in the CDs@Eu-MOF. (B) PL spectra and (C) the related photos of the CDs@Eu-MOF in ethanol upon adding different contents of water under 365-nm excited light. *(Reproduced with permission from Y. Dong, J. Cai, Q. Fang, X. You, Y. Chi, Dual-emission of lanthanide metal-organic frameworks encapsulating carbon-based dots for ratiometric detection of water in organic solvents. Anal. Chem. 88 (2016) 1748–1752. Copyright 2016 American Chemistry Society.)*

the Eu-MOF/N,S-CD composites emit red light in organic solvents and blue light in water, a colorimetric sensor may be established based on the luminescent properties of the Eu-MOF/N,S-CD composites. As shown in Fig. 4.16A (bottom), upon gradually increasing the water content in ethanol, the intensity of the blue emission peak shows continuous enhancement. The luminescent

intensity of the blue emission increases linearly with the water content in the range of 0%–10% (*v*/v). Conversely, the red emission peaks decrease contrarily as the water content is increased (Fig. 4.16B; bottom). It can be seen that the luminescent intensity of the red emission is quite sensitive to the water content in the range of 0%–10% (the luminescent intensity is directly proportional to the water content in the range 0%–4%). As shown in Fig. 4.16C (bottom), the changes in luminescent intensities of the emission peaks result in continuous PL color changes from red to blue. The color change is quite sensitive when the water content is lower than 10%. Even a slight increase of the water content in ethanol can cause an obvious color change [74].

Xu et al. encapsulated CDs with a strong fluorescence activity into MOF-253, and the emissions of both the CDs and Eu^{3+} formed the dual-emissive Eu^{3+}/CDs@MOF-253. In a solution in the absence of Hg^{2+}, it exhibited both characteristic emissions of the CDs and Eu^{3+} ($I_{Eu}/I_{CD} = 1.5$) with a faint blue light (Fig. 4.17A). In contrast, in the presence of Hg^{2+}, the emission changed from blue to red under UV light, corresponding to quenching of the CD emission. Hg^{2+} has less of an influence on the emission of Eu^{3+} in Eu^{3+}/CDs@MOF-253, which led to a colorimetric and ratiometric fluorescence Hg^{2+} sensor. The quenching effect of Hg^{2+} on the CDs in Eu^{3+}/CDs@MOF-253 is attributed to the coordination between Hg^{2+} and functional groups in the CDs. Fig. 4.17B shows the relative photoluminescence (PL) intensities (I_{Eu}/I_{CD}) versus the concentration of Hg^{2+}. The LOD is estimated to be 13 nM [75].

4.5 Single rare earth functionalized metal-organic framework hybrid materials for ratiometric luminescence sensing

Harbuzaru et al. reported the synthesis, structure, and sensing properties of an Eu-MOF, ITQMOF-3-Eu of 1,10-phenanthroline-2,9-dicarboxylic acid, which combines an optical fiber to show a linear photoluminescence response and achieve the self-calibration of the emitting signal within this pH range. The excitation spectra of ITQMOF-3-Eu recorded at both room temperature and 12 K (Fig. 4.18A; left) display a series of sharp lines assigned to the $^7F_0 \rightarrow {}^5D_{2-0}$ and $^5L_6$ Eu^{3+} intra-$4f^6$ transitions and several intense and broad bands in the UV region with a maximum at around 350 nm, attributed to ligand excited states. The sharp lines in the emission spectra (Fig. 4.18B; left) are assigned to transitions between the first excited nondegenerate $^5D_0$ state and the $^7F_{0-4}$ levels of the fundamental Eu^{3+} septet. There are two different Eu^{3+} environments, which is indicated by two lines at approximately 579.0 nm (17,272 cm^{-1}) and 580.7 nm (17, 221 cm^{-1}) in the 300 K spectrum (ascribed to Eu_2 and Eu_1 sites) for the nondegenerate $^5D_0 \rightarrow {}^7F_0$ transition (inset in Fig. 4.18; left), and the local-field splitting of the $^7F_1$ level into six Stark components (Fig. 4.18B; left). Surprisingly, in contrast with the behavior of site Eu_1, the $^5D_0 \rightarrow {}^7F_0$ transition intensity of site Eu_2 increases with temperature (Fig. 4.17B; left, inset). The increase of the $^5D_0 \rightarrow {}^7F_0$ transition intensity of

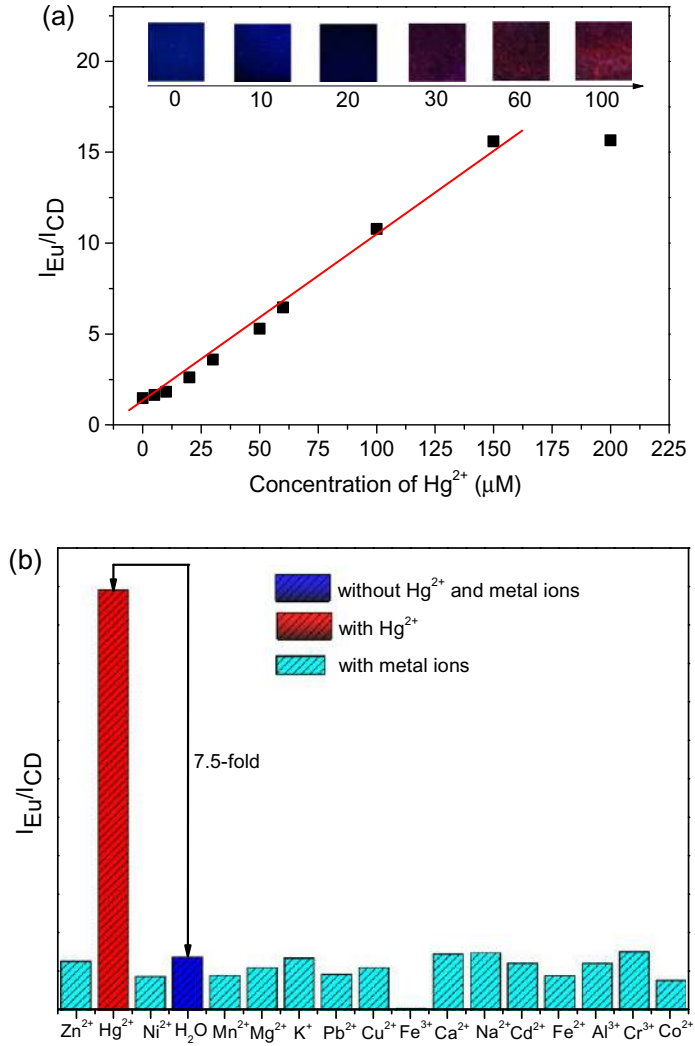

FIG. 4.17 (A) Line relationship between I_{Eu}/I_{CD} and $C_{Hg}{}^{2+}$ ($\lambda_{ex} = 360$ nm). Inset shows photographs of the test plates treated by different concentrations of Hg^{2+}; (B) Comparison of the PL intensity of I_{Eu}/I_{CD} for Eu^{3+}/CDs@MOF-253 dispersed in aqueous solutions of metal ions. *(Reproduced with permission from X. Xu, B. Yan, Fabrication and application of ratiometric and colorimetric fluorescent probe for Hg2 + based on dual-emissive metal-organic framework hybrids with carbon dots and Eu3 +. J. Mater. Chem. C 4 (2016) 1543–1549. Copyright 2016 Royal Society of Chemistry.)*

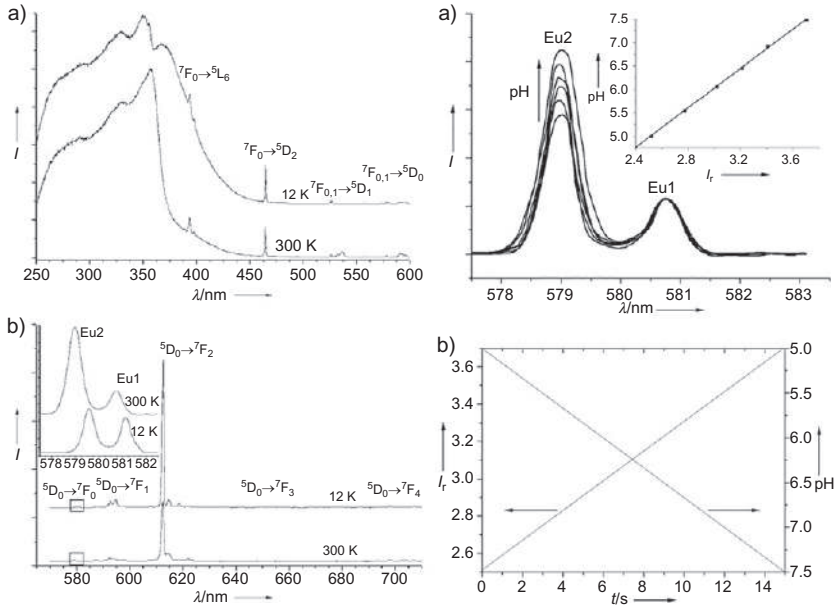

FIG. 4.18 *(Left)* (A) Excitation spectra of ITQMOF-3-Eu crystals recorded at 300 K and 12 K with the emission monitored at 612.3 nm. (B) Emission spectra of ITQMOF-3-Eu recorded at 300 K and 12 K under 350-nm excitation. The inset shows an expansion of the Eu^{3+} $^5D_0 \rightarrow {}^7F_0$ emission region. *(Right)* (A) Intensity variation of the Eu_2 $^5D_0 \rightarrow {}^7F_0$ transition from high (pH 7.5) to low (pH 5) pH values; the inset shows the linear variation of I_r with the pH value. (B) Time variation of I_r with the pH change from 5 to 7.5 in ramping mode (measured with a glass electrode). *(Reproduced with permission from B. V. Harbuzaru, A. Corma, F. Rey, J. L. Jorda, D. Ananias, L. D. Carlos, J. Rocha, A miniaturized linear pH sensor based on a highly photoluminescent self-assembled europium(III) metal-organic framework. Angew. Chem. Int. Edi. 48 (2009) 6476–6479. Copyright 2009 Wiley.)*

Eu_2 with temperature is likely to arise from changes induced in the local site geometry of the dimers, which is clearly evidenced by the blue shift of the $^5D_0 \rightarrow {}^7F_0$ energy with temperature in the range 12–300 K (Fig. 4.18B; left, inset). Most interestingly, this sensor requires no calibration because only one of the two Eu^{3+} emitting sites is affected by the pH variation in the range 5 to 7.5. By following the intensity ratio (Ir) of the $^5D_0 \rightarrow {}^7F_0$ emissions of the two Eu^{3+} types (Fig. 4.18A; right), it is possible to determine the pH of the solution to be analyzed. In this pH range, the relation between the Eu_2/Eu_1 (579.0 nm/580.5 nm) peak intensities I_r and the pH value present a good linearity ($R = 0.9997$) (Fig. 4.18B; right).

Eu^{3+} can be controlled to produce a dual-emission center. Although the emission position is the same for Eu^{3+}, its luminescent performance changes as the surrounding conditions change. Lu et al. reported a ratiometric pH sensor based on nanoscale PSM MOF-253. Two types of Eu^{3+} with different excitation wavelengths are simultaneously present in MOF-253 (Fig. 4.19; top). One of the

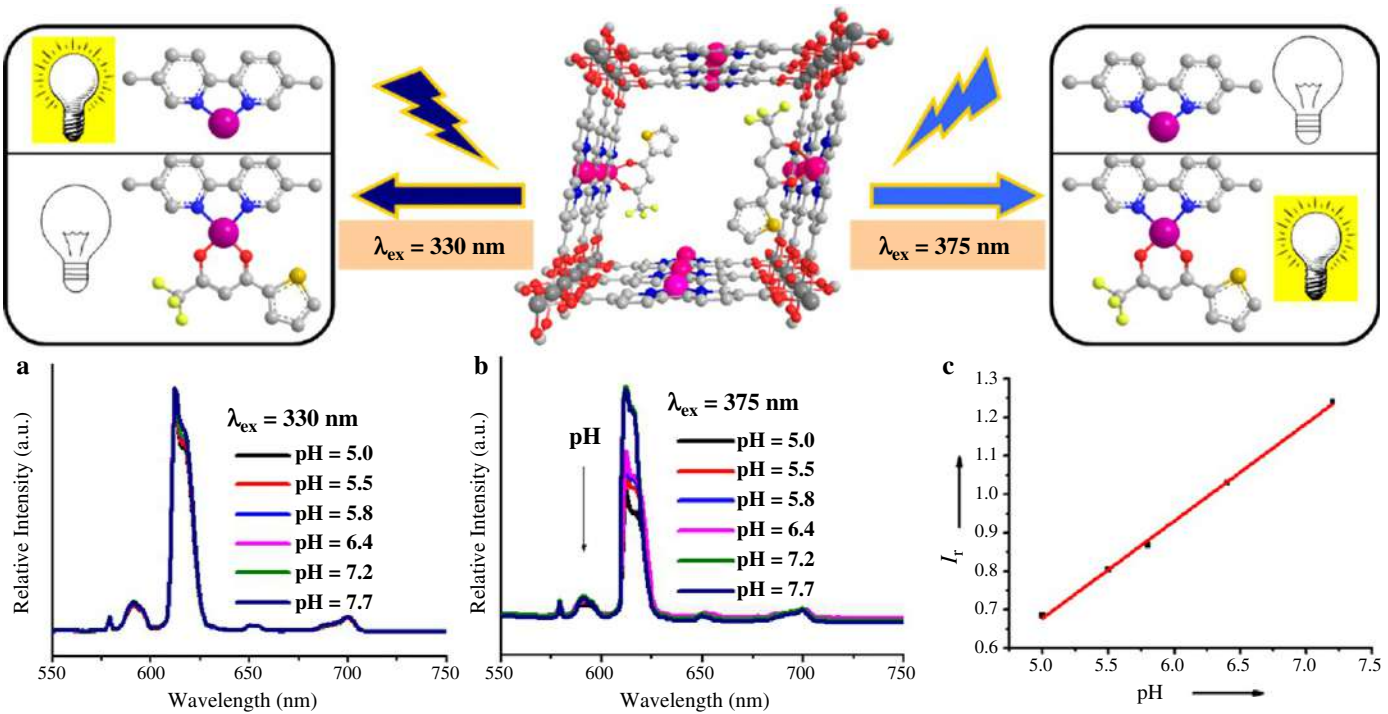

FIG. 4.19 *(Top)* Scheme of MOF-253 modified by Eu^{3+} complex with TTA with two types of Eu^{3+} (Eu_1 and Eu_2). *(Bottom)* The emission spectra of MOF-253-Eu-TTA in different pH aqueous solution, $\lambda_{ex} = 330$ nm (A), 375 nm (B); (C) the linear variation of the $^5D_0 \rightarrow {}^7F_2$ emission intensity ratio (I_r) of the two types of Eu^{3+}. *(Reproduced with permission from Y. Lu, B. Yan, A ratiometric fluorescent pH sensor based on nanoscale metalorganic frameworks (MOFs) modified by europium(III) complexes. Chem. Commun. 50 (2014) 13323–13326. Copyright 2015 Royal Society of Chemistry.)*

ions is insensitive to the pH, and the other one is sensitive to the pH value. In PSM, the Eu^{3+} ions have two different coordination environments; Eu_1 is only linked to the bipyridine, and Eu_2 is linked to both bipyridine and TTA. The broad band at 330 nm is assigned to the excitation of Eu_1, and the broad band at 375 nm is mostly from the excitation of Eu_2 due to the energy absorption via TTA. The weakened sensitization causes the excitation wavelength of Eu_2 to be at 375 nm and not 330 nm (Fig. 4.19; bottom). The sensor has a linear response in the pH range from 5.0 to 7.2, which is required for work with biological fluids, such as blood and culture cell media [76].

References

[1] L. Chen, D. Liu, J. Peng, Q. Du, H. He, Ratiometric fluorescence sensing of metal-organic frameworks: tactics and perspectives, Coord. Chem. Rev. 404 (2020), 213113.
[2] B. Yan, Lanthanide functionalized metal-organic frameworks hybrid systems to create multiple luminescent centers for chemical sensing, Acc. Chem. Res. 50 (2017) 2789–2798.
[3] Y. Zhao, D. Li, Lanthanide-functionalized metal-organic frameworks as ratiometric luminescent sensors, J. Mater. Chem. C 8 (2020) 12739–12754.
[4] S.Y. Wu, H. Min, W. Shi, P. Cheng, Multicenter metal-organic framework-based ratiometric fluorescent sensors, Adv. Mater. 32 (2020) 1805871.
[5] Y. Cue, F. Chen, X. Yin, A ratiometric fluorescence platform based on boric acid-functional Eu-MOF for sensitive detection of H_2O_2 and glucose, Biosens. Bioelectron. 135 (2019) 208–215.
[6] L. Li, J. Cheng, Z. Liu, L. Song, Y. You, X. Zhou, W. Huang, Ratiometric luminescent sensor of picric acid based on the dual-emission mixed lanthanide coordination polymer, ACS Appl. Mater. Interfaces 10 (2018) 44109–44115.
[7] W. Liu, X. Dai, Y. Wang, L. Song, L. Zhang, D. Zhang, J. Xie, L. Chen, D. Juan, J. Wang, Z. Chai, S. Wang, Ratiometric monitoring of thorium contamination in natural water using a dual-emission luminescent europium organic framework, Environ. Sci. Technol. 53 (2019) 332–341.
[8] J. Zhou, H. Li, H. Zhang, H. Li, W. Shi, P. Cheng, A bimetallic lanthanide metalorganic material as a self-calibrating color-gradient luminescent sensor, Adv. Mater. 27 (2015) 7072–7077.
[9] K. Miyata, Y. Konno, T. Nakanishi, A. Kobayashi, M. Kato, K. Fushimi, Y. Hasegawa, Chameleon luminophore for sensing temperatures: control of metal-to-metal and energy back transfer in lanthanide coordination polymers, Angew. Chem. Int. Ed. 52 (2013) 6413–6416.
[10] B. Li, W. Wang, Z. Hong, E.M. El-Sayed, D. Yuan, Ratiometric fluorescence detection of trace water in an organic solvent based on bimetallic lanthanide metal-organic frameworks, Chem. Commun. 55 (2019) 6926–6929.
[11] A. Cadiau, C.D.S. Brites, P.M.F.J. Costa, R.A.S. Ferreira, J. Rocha, L.D. Carlos, Ratiometric nanothermometer based on an emissive Ln^{3+}-organic framework, ACS Nano 7 (2013) 7213–7218.
[12] D. Dang, B. An, Y. Bai, G. Zheng, J. Niu, Three-dimensional homochiral manganese-lanthanide frameworks based on chiral camphorates with multicoordination modes, Chem. Commun. 49 (2013) 2243–2245.
[13] S. Zhan, M. Li, X. Zhou, J. Wang, J. Yang, D. Li, When Cu_4I_4 cubane meets Cu3(pyrazolate)3 triangle: dynamic interplay between two classical luminophores functioning in a reversibly thermochromic coordination polymer, Chem. Commun. 47 (2011) 12441–12443.

[14] S. Liao, W. Gu, L. Yang, T. Li, J. Tian, L. Wang, M. Zhang, X. Liu, Series of novel 3D heterometallic frameworks based on the co(II) coordination chains and ln(III) coordination layers, Cryst. Growth Des. 12 (2012) 3927–3936.
[15] E.A. Dolgopolova, A.M. Rice, C.R. Martin, N.B. Shustova, Photochemistry and photophysics of MOFs: steps towards MOF-based sensing enhancements, Chem. Soc. Rev. 47 (2018) 4710–4728.
[16] Q. Du, P. Wu, P. Dramou, R. Chen, H. He, One-step fabrication of a boric acid functionalized lanthanide metal-organic framework as a ratiometric fluorescence sensor for the selective recognition of dopamine, New J. Chem. 43 (2019) 1291–1298.
[17] J.E. Kwon, S.Y. Park, Advanced organic optoelectronic materials: harnessing excited-state intramolecular proton transfer (ESIPT) process, Adv. Mater. 23 (2011) 3615–3642.
[18] B. Bhattacharya, A. Halder, L. Paul, S. Chakrabarti, D. Ghoshal, Eye-catching dual-fluorescent dynamic metal-organic framework senses traces of water: experimental findings and theoretical correlation, Chem. Eur. J. 22 (2016) 14998–15005.
[19] W. Zhang, Q. Li, J. Cheng, K. Cheng, X. Yang, Y. Li, X. Zhao, X. Wang, Ratiometric luminescent detection of organic amines due to the induced lactam-lactim tautomerization of organic linker in a metal-organic framework, ACS Appl. Mater. Interfaces 9 (2017) 31352–31356.
[20] D. Wang, Z. Hu, S. Xu, D. Li, Q. Zhang, W. Ma, H. Zhou, J. Wu, Y. Tian, Fluorescent metal-organic frameworks based on mixed organic ligands: new candidates for highly sensitive detection of TNP, Dalton Trans. 48 (2019) 1900–1905.
[21] J. Bitzer, W. Kleist, Synthetic strategies and structural arrangements of isoreticular mixed-component metal-organic frameworks, Chem. Eur. J. 25 (2019) 1866–1882.
[22] X. Lin, G. Gao, L. Zheng, Y. Chi, G. Chen, Encapsulation of strongly fluorescent carbon quantum dots in metal- organic frameworks for enhancing chemical sensing, Anal. Chem. 86 (2014) 1223–1228.
[23] Z. Dou, J. Yu, Y. Cui, Y. Yang, Z. Wang, D. Yang, G. Qian, Luminescent metal-organic framework films as highly sensitive and fast-response oxygen sensors, J. Am. Chem. Soc. 136 (2014) 5527–5530.
[24] H. Fu, X. Wu, L. Ma, F. Wang, J. Zhang, Dual-emission SG_7@MOF sensor via SC-SC transformation: enhancing the formation of excimer emission and the range and sensitivity of detection, ACS Appl. Mater. Interfaces 10 (2018) 18012–18020.
[25] D. Yan, Y. Tang, H. Lin, D. Wang, Tunable two-color luminescence and host-guest energy transfer of fluorescent chromophores encapsulated in metal-organic frameworks, Sci. Rep. 4 (2014) 4337.
[26] K. Wang, N. Li, J. Zhang, Z. Zhang, F. Dang, Size-selective QD@MOF core-shell nanocomposites for the highly sensitive monitoring of oxidase activities, Biosens. Bioelectron. 87 (2017) 339–344.
[27] K. Cai, M. Zeng, F. Liu, N. Liu, Z. Huang, Y. Song, L. Wang, BSA-AuNPs@Tb-AMP metal-organic frameworks for ratiometric fluorescence detection of DPA and Hg^{2+}, Luminescence 32 (2017) 1277–1282.
[28] C. Dai, C. Yang, X. Yan, Ratiometric fluorescent detection of phosphate in aqueous solution based on near infrared fluorescent silver nanoclusters/metal-organic shell composite, Anal. Chem. 87 (2015) 11455–11459.
[29] C. Fan, X. Lv, F. Liu, L. Feng, M. Liu, Y. Cai, H. Liu, J. Wang, Y. Yang, H. Wang, Silver nanoclusters encapsulated into metal-organic frameworks with enhanced fluorescence and specific ion accumulation toward the microdot array-based fluorimetric analysis of copper in blood, ACS Sens. 3 (2018) 441–450.

[30] J. Aguilera-Sigalat, D. Bradshaw, Synthesis and applications of metal-organic framework-quantum dot (QD@MOF) composites, Coord. Chem. Rev. 307 (2016) 267–291.
[31] Z. Long, J. Jia, S. Wang, L. Kou, X. Hou, M.J. Sepaniak, Visual enantioselective probe based on metal organic framework incorporating quantum dots, Microchem. J. 110 (2013) 764–769.
[32] M.L. Desai, S. Jha, H. Basu, R.K. Singhal, P.K. Sharma, S.K. Kailasa, Microwave-assisted synthesis of water-soluble Eu^{3+} hybrid carbon dots with enhanced fluorescence for the sensing of Hg^{2+} ions and imaging of fungal cells, New J. Chem. 42 (2018) 6125–6133.
[33] J. Hao, F. Liu, N. Liu, M. Zeng, Y. Song, L. Wang, Ratiometric fluorescent detection of Cu^{2+} with carbon dots chelated Eu-based metal-organic frameworks, Sens. Actuators B Chem. 245 (2017) 641–647.
[34] Y. Dong, J. Cai, Q. Fang, X. You, Y. Chi, Dual-emission of lanthanide metalorganic frameworks encapsulating carbon-based dots for ratiometric detection of water in organic solvents, Anal. Chem. 88 (2016) 1748–1752.
[35] R. Jalili, A. Khataee, M.R. Rashidi, R. Luque, Dual-colored carbon dot encapsulated metal-organic framework for ratiometric detection of glutathione, Sens. Actuators B Chem. 297 (2019) 8.
[36] Y. Ma, G. Xu, F. Wei, Y. Cen, Y. Ma, Y. Song, X. Xu, M. Shi, S. Muhammad, Q. Hu, A dual-emissive fluorescent sensor fabricated by encapsulating quantum dots and carbon dots into metal-organic frameworks for the ratiometric detection of Cu^{2+} in tap water, J. Mater. Chem. C 5 (2017) 8566–8571.
[37] Y. Ma, G. Xu, F. Wei, Y. Cen, X. Xu, M. Shi, X. Cheng, Y. Chai, M. Sohail, Q. Hu, One-pot synthesis of a magnetic, ratiometric fluorescent nanoprobe by encapsulating Fe_3O_4 magnetic nanoparticles and dual-emissive rhodamine B modified carbon dots in metal-organic framework for enhanced HClO sensing, ACS Appl. Mater. Interfaces 10 (2018) 20801–20805.
[38] K. Wang, H. Ren, N. Li, X. Tan, F. Dang, Ratiometric fluorescence sensor based on cholesterol oxidase-functionalized mesoporous silica nanoparticle@ZIF-8 core-shell nanocomposites for detection of cholesterol, Talanta 188 (2018) 708–713.
[39] L. Xu, G. Fang, J. Liu, M. Pan, R. Wang, S. Wang, One-pot synthesis of nanoscale carbon dots-embedded metal-organic frameworks at room temperature for enhanced chemical sensing, J. Mater. Chem. A 4 (2016) 15880–15887.
[40] D. Yue, Y. Huang, L. Zhang, K. Jiang, X. Zhang, Y. Cui, Y. Yu, G. Qian, Ratiometric luminescence sensing based on a mixed Ce/Eu metal-organic framework, J. Mater. Chem. C 6 (2018) 2054–2059.
[41] T. Xia, J. Wang, K. Jiang, Y. Cui, Y. Yang, G. Qian, A Eu/Gd-mixed metal-organic framework for ultrasensitive physiological temperature sensing, Chin. Chem. Lett. 29 (2018) 861–864.
[42] H. Li, W. Han, R. Lv, A. Zhai, X. Li, W. Gu, X. Liu, Dual-function mixed-lanthanide metal – organic framework for ratiometric water detection in bioethanol and temperature sensing, Anal. Chem. 91 (2019) 2148–2154.
[43] Y. Cui, F. Zhu, B. Chen, G. Qian, Metal-organic frameworks for luminescence thermometry, Chem. Commun. 51 (2015) 7420–7431.
[44] Y. Cui, W. Zou, R. Song, J. Yu, W. Zhang, Y. Yang, G. Qian, A ratiometric and colorimetric luminescent thermometer over a wide temperature range based on a lanthanide coordination polymer, Chem. Commun. 50 (2014) 719–721.
[45] D. Zhao, X. Rao, J. Yu, Y. Cui, Y. Yang, G. Qian, Design and synthesis of an MOF thermometer with high sensitivity in the physiological temperature range, Inorg. Chem. 54 (2015) 11193–11199.
[46] Y. Cui, H. Xu, Y. Yue, Z. Guo, J. Yu, Z. Chen, J. Gao, Y. Yang, G. Qian, B. Chen, A luminescent mixed-lanthanide metal-organic framework thermometer, J. Am. Chem. Soc. 134 (2012) 3979–3982.

[47] X. Rao, T. Song, J. Gao, Y. Cui, Y. Yang, C. Wu, B. Chen, G. Qian, A highly sensitive mixed lanthanide metal – organic framework self-calibrated luminescent thermometer, J. Am. Chem. Soc. 135 (2013) 15559–15564.
[48] D. Zhao, D. Yue, K. Jiang, L. Zhang, C. Li, G. Qian, Isostructural Tb^{3+}/Eu^{3+} codoped metal organic framework based on pyridine-containing dicarboxylate ligands for ratiometric luminescence temperature sensing, Inorg. Chem. 58 (2019) 2637–2644.
[49] Y. Wei, R. Sa, Q. Li, K. Wu, Highly stable and sensitive LnMOF ratiometric thermometers constructed with mixed ligands, Dalton Trans. 44 (2015) 3067–3074.
[50] Y. Zhou, B. Yan, F. Lei, Postsynthetic lanthanides functionalization of nanosized metal-organic frameworks for highly sensitive ratiometric luminescent nanothermometers, Chem. Commun. 50 (2014) 15235–15238.
[51] D. Zhao, D. Yue, L. Zhang, K. Jiang, G. Qian, Cryogenic luminescent Tb/Eu-MOF thermometer based on a fluorine-modified tetracarboxylate ligand, Inorg. Chem. 57 (2018) 12596–12602.
[52] X. Lian, D. Zhao, Y. Cui, Y. Yang, G. Qian, A near infrared luminescent metal-organic framework for temperature sensing in the physiological range, Chem. Commun. 51 (2015) 17676–17679.
[53] Y. Zhou, B. Yan, Lanthanides post-functionalized nanocrystalline metal-organic frameworks for tunable white-light emission and orthogonal multi-readout thermometry, Nanoscale 7 (2015) 4063–4069.
[54] S. Qin, X. Qu, B. Yan, A self-calibrating bimetallic lanthanide metal-organic luminescent sensor integrated with logic gate operation for detecting N-methylformamide, Inorg. Chem. Front. 5 (2018) 2971–2977.
[55] J. Ye, J. Lin, Z. Mo, C. He, H. Zhou, J. Zhang, X. Chen, Mixed-lanthanide porous coordination polymers showing range tunable ratiometric luminescence for O_2 sensing, Inorg. Chem. 56 (2017) 4238–4243.
[56] D. Chen, C. Sun, Y. Peng, N. Zhang, H. Si, C. Liu, M. Du, Ratiometric fluorescence sensing and colorimetric decoding methanol by a bimetallic lanthanide-organic framework, Sens. Actuators B-Chem. 265 (2018) 104–109.
[57] Y. Zhou, B. Yan, Ratiometric detection of temperature using responsive dual-emissive MOF hybrids, J. Mater. Chem. C 3 (2015) 9353–9358.
[58] X. Xu, B. Yan, Eu(III)-functionalized MIL-124 as fluorescent probe for highly selectively sensing ions and organic small molecules especially for Fe(III) and Fe(II), ACS Appl. Mater. Interfaces 7 (2015) 721–729.
[59] N. Sun, B. Yan, Rapid and facile ratiometric detection of CO_3^{2-} based on heterobimetallic metal-organic frameworks (Eu/Pt-MOFs), Dyes Pigments 142 (2017) 1–7.
[60] Y. Zhou, B. Yan, A responsive MOF nanocomposite for decoding volatile organic compounds, Chem. Commun. 52 (2016) 2265–2268.
[61] X. Xu, B. Yan, Nanoscale LnMOF-functionalized nonwoven fibers protected by a polydimethylsiloxane coating layer as a highly sensitive ratiometric oxygen sensor, J. Mater. Chem. C 4 (2016) 8514–8521.
[62] X. Xu, B. Yan, Eu(III)-functionalized ZnO@MOFs heterostructures: integration of preconcentration and efficient charge transfer as ppb-level sensing platform for volatile aldehyde gases in vehicles, J. Mater. Chem. A 5 (2017) 2215–2223.
[63] Y. Zhang, B. Yan, A portable self-calibrating logic detector for gradient detection of formaldehyde based on luminescent metal organic frameworks, J. Mater. Chem. C 7 (2019) 5652–5657.
[64] C. Li, J. Huang, H. Zhu, L. Liu, Y. Feng, G. Hu, X. Yu, Dual-emitting fluorescence of Eu/Zr-MOF for ratiometric sensing formaldehyde, Sens. Actuator B-Chem. 253 (2017) 275–282.

[65] R. He, Y. Wang, H. Ma, H. Yin, Q. Liu, Eu^{3+}-functionalized metal-organic framework composite as ratiometric fluorescent sensor for highly selective detecting urinary 1-hydroxypyrene, Dyes Pigments 151 (2018) 342–347.

[66] X. Du, R. Fan, L. Qiang, P. Wang, Y. Song, K. Xing, X. Zheng, Y. Yang, Encapsulation and sensitization of Ln^{3+} within indium metal-organic frameworks for ratiometric Eu^{3+} sensing and linear dependence of white-light emission, Cryst. Growth Des. 17 (2017) 2746–2756.

[67] K. Luan, R. Meng, C. Shan, J. Cao, J. Jia, W. Liu, Y. Tang, Terbium functionalized micelle nanoprobe for ratiometric fluorescence detection of anthrax spore biomarker, Anal. Chem. 90 (2018) 3600–3607.

[68] Y. Zhang, B. Yan, A ratiometric fluorescent sensor with dual response of Fe^{3+}/Cu^{2+} based on europium post-modified sulfone-metal-organic frameworks and its logical application, Talanta 197 (2019) 291–298.

[69] Y. Cheng, H. Zhang, B. Yang, J. Wu, Y. Wang, B. Ding, J. Huo, Y. Li, Highly efficient fluorescence sensing of phosphate by dual-emissive lanthanide MOFs, Dalton Trans. 47 (2018) 12273–12283.

[70] S. Wu, M. Zhu, Y. Zhang, M. Kosinova, V.P. Fedin, E. Gao, A water-stable lanthanide coordination polymer as multicenter platform for ratiometric luminescent sensing antibiotics, Chem. Eur. J. 26 (2020) 3137–3144.

[71] L. Yu, Q. Zheng, H. Wang, C. Liu, X. Huang, Y. Xiao, Double-color lanthanide metal-organic framework based logic device and visual ratiometric fluorescence water microsensor for solid pharmaceuticals, Anal. Chem. 92 (2020) 1402–1408.

[72] E.J. Gao, S.Y. Wu, J. Wang, M.C. Zhu, Y. Zhang, V.P. Fedin, Water-stable lanthanide coordination polymers with triple luminescent centers for tunable emission and efficient self-calibration sensing wastewater pollutants, Adv. Opt. Mater. 8 (2020) 1901659.

[73] Y. Cui, R. Song, J. Yu, M. Liu, Z. Wang, C. Wu, Y. Yang, Z. Wang, B. Chen, G. Qian, Dual-emitting MOF⊃dye composite for ratiometric temperature sensing, Adv. Mater. 27 (2015) 1420–1425.

[74] Y. Dong, J. Cai, Q. Fang, X. You, Y. Chi, Dual-emission of lanthanide metal-organic frameworks encapsulating carbon-based dots for ratiometric detection of water in organic solvents, Anal. Chem. 88 (2016) 1748–1752.

[75] X. Xu, B. Yan, Fabrication and application of ratiometric and colorimetric fluorescent probe for Hg^{2+} based on dual-emissive metal-organic framework hybrids with carbon dots and Eu^{3+}, J. Mater. Chem. C 4 (2016) 1543–1549.

[76] Y. Lu, B. Yan, A ratiometric fluorescent pH sensor based on nanoscale metalorganic frameworks (MOFs) modified by europium(III) complexes, Chem. Commun. 50 (2014) 13323–13326.

Chapter 5

Luminescence responsive sensing mechanism in rare earth metal-organic framework hybrid materials

5.1 The luminescence responsive sensing mechanism for metal-organic framework-based materials

Razavi et al. have tried to communicate between structural features, signal generation, detection mechanism, and response production in luminescent MOFs to gain more insight into their design and application as sensors [1]. They have gathered and classified their findings based on "structure-signal" and "mechanism-response" approaches, which include (i) chemical nature of organic and inorganic building blocks or structural features of MOFs, (ii) luminescent signal of host MOFs, (iii) sensing mechanism of analyte detection, and (iv) specific response (signal change in MOFs in presence of analytes) of MOFs toward analytes, respectively [1]. Luminescent MOFs with special building blocks, including organic ligand and metal ion/clusters, can create a specific photoluminescent signal. In addition, unique types of responses can be observed due to the particular mechanism to detect the analytes using luminescent MOFs materials, whose main close relationships can be further discussed (Fig. 5.1). The typical sensing mechanisms in luminescent MOFs are introduced in the following sections (Fig. 5.2).

5.1.1 Overlap mechanism

When the absorption band of the nonemissive analyte has an effective overlap with the emission band of the fluorophore or donor in MOFs, the resonance energy transfer (RET) process can occur from the fluorophore in MOFs to the analyte when they are coupled by a dipole-dipole interaction [1,2]. Here, this mechanism is effective in signal transduction. Moreover, the extent of the RET process depends on the distance between the fluorophore of MOFs and analyte. RET can dramatically enhance fluorescence-quenching efficiency to improve sensitivity. In addition, the overlapping of the excitation band of the

Rare Earth Metal-Organic Framework Hybrid Materials for Luminescence Responsive Chemical Sensors
https://doi.org/10.1016/B978-0-323-91236-5.00006-2

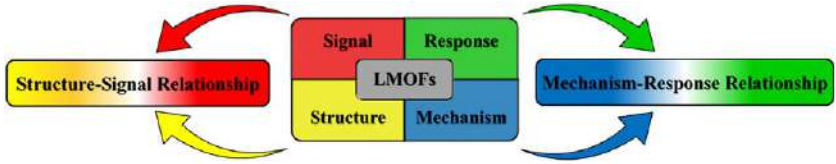

FIG. 5.1 Schematic description for the points in development of luminescent MOFs. *(Reproduced with permission from S. A. A. Razavi, A. Morsali, Metal ion detection using luminescent-MOFs: principles, strategies and roadmap. Coord. Chem. Rev. 415 (2020) 213299. Copyright 2020 Elsevier.)*

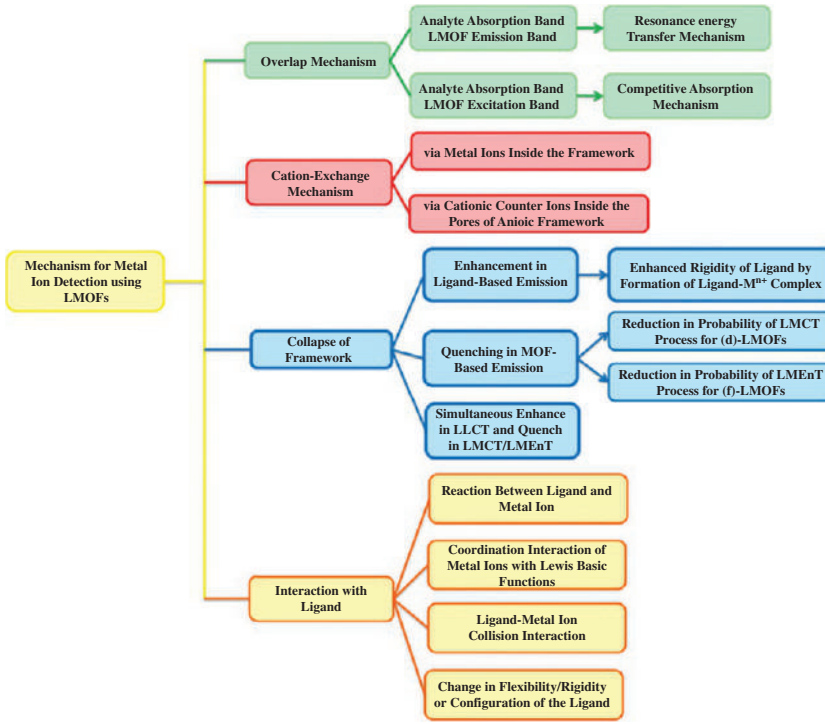

FIG. 5.2 Schematic description for possible mechanisms for analyte detection using luminescent MOFs (LMOFs). *(Reproduced with permission from S. A. A. Razavi, A. Morsali, Metal ion detection using luminescent-MOFs: principles, strategies and roadmap. Coord. Chem. Rev. 415 (2020) 213299. Copyright 2020 Elsevier.)*

fluorophore of MOFs with the absorption band of the analyte can also lead to competitive adsorption of light by fluorophore and analyte [3], in which analytes can adsorb energy of excitation light as well as the fluorophore and ultimately this competition for light adsorption leads to fluorescent quenching in MOFs emissions. Considering the different nature of absorption and excitation

bands (absorption band refers to all absorbed photon energies to excite electrons from the S_0 ground state to any excited state, like S_n ($n > 0$), while excitation band refers to specific absorbed photon energies to excite electrons from the S_0 ground state to only the S_1 excited state) [4], it is recognizable that the fluorophore excitation band-analyte absorption band overlap is confident to discuss about possible mechanisms in fluorescence quenching of MOFs. The overlap mechanism shows a more specific response than other mechanisms, such as structural collapse or interaction with functional ligands.

5.1.2 Structural collapse mechanism

Another possible mechanism in analyte detection by luminescent MOFs is collapse of the structure (or structural change), which can be easily distinguished using PXRD and ICP analyses. This mechanism will result in reduction in probability of the ligand-metal charger transfer (LMCT) process in (*d*)-MOFs and ligand-metal resonant energy transfer (LMRET) process in (*f*)-MOFs, whose proper response is one-dimensional (1D) quenching in the luminescent MOFs-based emission peak [5–8]. Sometimes ligand-based emission can be observed due to ligand-metal ion coordination after luminescent MOF structure destruction [9–11]. The major problem is that sensors developed based on this mechanism are not stable, and great challenges in stability and recyclability still exist [1].

5.1.3 Ion exchange mechanism

Ion exchange is another possible mechanism, mainly for both cation and anion detection using luminescent MOFs, in which cation exchange is very extensive and common. For a luminescent neutral MOFs, it is based on exchanging the analyte cation and cation (metal ion) inside the framework (also called ion substitution). For a luminescent anionic MOFs, analyte cations can be exchanged with both cationic counter ions inside the pores for framework neutralization (usually $NH_2Me_2^+$ or NH_4^+) and cations (metal ions) as inorganic building blocks inside the framework. Generally, the exchange between cations inside the pores of luminescent anionic MOFs should perform faster than that inside the framework, because the latter exchange needs a stronger driving force than the former for metal-carboxylate bond cleavage, except for diffusion. If the RE^{3+} ions are engaged in the exchange mechanism, it can predict what kind of signal transduction and response can take place to observe RE^{3+} sensitization efficiently. If the analyte cation is exchanging with RE^{3+} ions, the intensity of characteristic peaks of (*f*)-MOFs will decrease with the 1D quenching response (RE^{3+} ions can be encapsulated in the pores, anchored to the ligand, or applied as inorganic building blocks in luminescent MOFs structure) [1].

5.1.4 Linker-analytes interaction mechanism

The most practical mechanism for detection of analytes using (*d*)-MOFs or (*f*)-MOFs is based on interaction between the organic linker and analytes, to influence their energy transfer or charge transfer. Although the organic linker being functional or nonfunctional has critical effects on the detection mechanism, both "Turn-On" and "Turn-Off" responses can be generated through linker-analytes interaction. In the case of functional ligands with Lewis basic guest-interactive sites, coordination interaction between the functional ligand and some analytes can change the electron density, rigidity, or conformation of the ligand. Depending on the nature of the changes in the structure of the organic linker or framework, luminescence enhancement and quenching are observed. Sometimes interaction between linker and analytes may introduce some changes in structural features of the ligand (without structural collapse or framework destruction), such as a change in conformation, flexibility, or rigidity of ligands. In this condition, such structural changes lead to specific kinds of responses toward specific analytes. Functional ligands are mostly applied as guest interactive sites to detect and interact with analytes, especially metal ions; they can interact with metal ions through different methods like electrostatic interactions and coordination interactions. If such interactions lead to photoinduced electron transfer (PET) or fluorescent resonance energy transfer (FRET) from luminescent MOFs to analytes, the produced response is based on quenching in emission of the host MOFs. On the contrary, if such interactions lead to higher efficiency in radiative relaxation, the produced response is based on enhancement in emission spectra of the luminescent MOFs. In the case of luminescent MOFs with nonfunctional ligands containing an aromatic or aliphatic skeleton, it seems that identification of the detection mechanism is somewhat harder, because there are no predesigned guest interactive sites within the framework. But in these cases, some of the analyses such as using the Stern-Volmer (SV) equation, calculation of fluorescence lifetime decay, investigation of overlap mechanism, and collapse of the framework are beneficial for more details about factors involved in signal transduction.

5.1.5 Common mechanistic pathways involved in luminescence sensing

Fig. 5.3 presents the syntheses of luminescent MOFs (LCPs), their application in luminescence sensing, and common mechanistic pathways involved in luminescence sensing. **(1) Förster resonance energy transfer (FRET).** This is the nonradiative transfer of energy from a donor (MOFs linker) to an acceptor (analyte) molecule, which leads to both decline in luminescence intensity as well as excited state lifetime of the donor and it enhances the excited state lifetime as well as emission intensity of the acceptor. This process is also distance dependent and hence can be used to investigate Coulombic interaction between

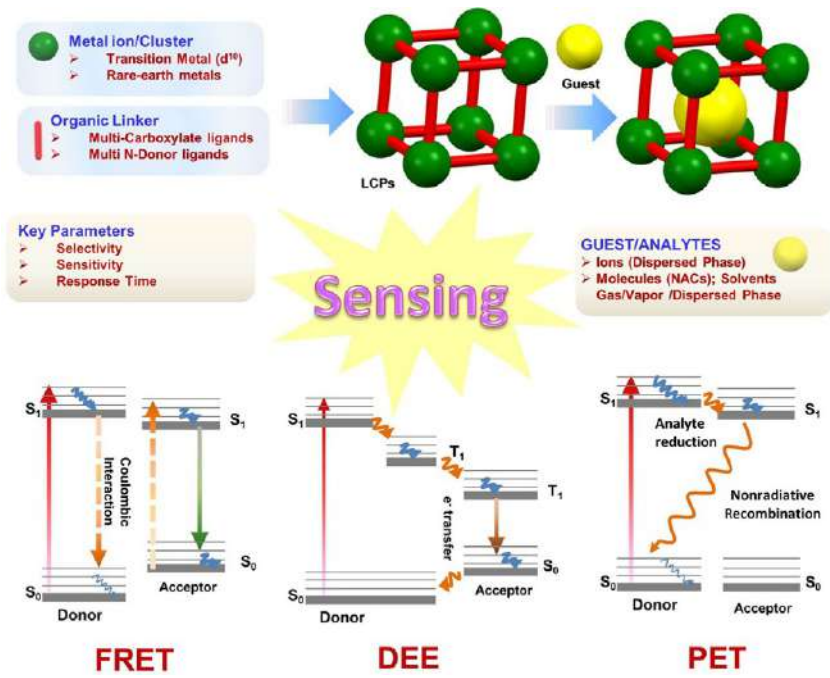

FIG. 5.3 Schematic presentation for synthesis of LCPs and general mechanisms of sensing by luminescent MOFs (LCPs). *(Reproduced with permission from J. Liu, Z. Luo, Y. Pan, A. K. Singh, M. Trivedi, A. Kumar, Recent developments in luminescent coordination polymers: designing strategies, sensing application and theoretical evidences. Coord. Chem. Rev. 406 (2020) 213145. Copyright 2020 Elsevier.)*

molecules. **(2) Dexter electron exchange (DEE).** This process involves quenching of the donor's fluorescence by transmission of an excited electron of the donor molecule to the acceptor molecule via a nonradiative pathway by orbital overlap between the donor and acceptor, which is applicable in the case of short-range interactions operating between donor and acceptor (typically within 10 Å). Electron transfer can also be possible by concerted or two-step processes. **(3) Photo-induced electron transfer (PET).** This is similar to DEE, involving transmission of the excited electron from donor to acceptor via a nonradiative pathway, while it is a redox process and results in the quenching of luminescence. This phenomenon proceeds through charge recombination followed by regeneration of the ground state donor/acceptor species, with concomitant release of excess energy in the form of heat. **(4) A diverse set of sensing mechanisms are possible based on complexation between donor-acceptor (sensing probe-analyte) species.** Tuning of HOMO and LUMO energy levels by complexation of analyte with probe may be reflected in the luminescence energy as well as intensity of the probe. Sensitization or the antenna effect is a process whereby the analyte acts as a strong photon absorber,

and then transfers the absorbed excitation energy to the luminescent probe, thereby resulting in enhancement in the emission intensity. This is especially relevant to metal center-based luminescence, especially for rare earth-based sensors having spin-forbidden f-f transitions and hence are difficult to excite directly.

5.2 The LMET for luminescence response on chemical sensing in rare earth metal-organic framework hybrid materials

Combinations of different functional or nonfunctional organic ligands with different inorganic moieties can result in versatile types of luminescent signals when using MOFs as probes for analyte detection. As we known, for MOFs hosts themselves, all kinds of interaction between metal ions and ligands are possibly involved, which determine the final photophysical properties of the whole hybrid [12–19]. Therefore, for rare earth MOFs hybrid materials, they mainly perform the influence on these interactions [12,20,21]. Therefore, when RE^{3+} ions behave as the central metal ions for rare earth MOFs materials or the photoactive ions for rare earth functionalized MOFs hybrid materials, these hybrids may respond to analytes. The most common interaction occurs between analytes and metal ion or linkage, or both of them, in MOFs. Subsequently, analytes may change the interaction and energy transfer from ligand to RE^{3+} (LMET). In a broad sense, almost all the luminescence responses of rare earth MOFs hybrid materials for sensing analytes are ascribed as the influences on the LMET process in the hybrid system in the final analysis [13,16,17,22–30]. Therefore LMET is too extensive and common to be excessively emphasized. Herein some recent examples are given on this point [31].

MOFs allow for sensible choices of metal ions and suitable ligands of various functionalities. It is easy to introduce fluorescent functions through metal ions, ligands, guest molecules or postsynthetic modification (PSM) functionalization due to the bonding interactions between ligands and metal ions. Simultaneously, ligand-metal charge transfer increases the fluorescence function. Fig. 5.4 shows the diverse emitting mechanisms for tunable luminescent MOFs to affect the LMET processes, including metal-centered (MC) emission (e.g., ligand-to-metal charge transfer (LMCT)), ligand-centered (LC) emission (e.g., metal-to-ligand charge transfer (MLCT)), guest-introduced emission, and so on [1–5,12–19,22–30]. LMCT and MLCT are mainly associated with relative height of the lowest excited state energy levels in MOFs. If the energy of the lowest excited state level of the organic ligand is lower than that of the metal ions, then the charge will transfer from the metal ions to the organic ligands to emit light, i.e., the process of LMCT. Conversely, the charge will transfer from the ligands to the metal ions, i.e., the process of MLCT (Fig. 5.4; top). MC is often found in rare earth MOFs (RE-MOFs) or RE functionalized MOFs hybrids, whose RE^{3+} ions' luminescence needs to be

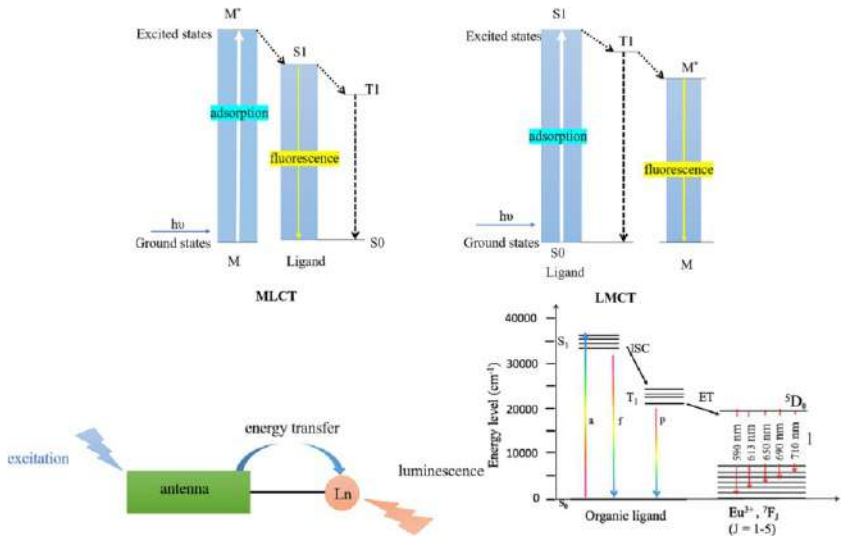

FIG. 5.4 *(Top)* Mechanism of MLCT and LMCT. *(Bottom, Left)* Antenna effect for lanthanide luminescence. *(Bottom, Right)* Schematic diagram of Eu-MOF with the antenna effect. ["a": absorption; "f": fluorescence; "p": phosphorescence; "l": luminescence. ISC: intersystem crossing; ET: energy transfer; S: singlet; and T: triplet.] *(Reproduced with permission from S. A. A. Razavi, A. Morsali, Metal ion detection using luminescent-MOFs: principles, strategies and roadmap. Coord. Chem. Rev. 415 (2020) 213299, J. Heine, K. Mueller-Buschbaum, Engineering metal-based luminescence in coordination polymers and metal-organic frameworks. Chem. Soc. Rev. 42 (2013) 9232–9242, Z. Yang, M. Wang, X. Wang, X. Yin, Boric-acid-functional lanthanide metal organic frameworks for selective ratiometric fluorescence detection of fluoride ions. Anal. Chem. 89 (2017) 1930–1936. Copyright 2020 Elsevier, 2013 Royal Chemical Society, and 2017 American Chemical Society.)*

sensitized by the organic ligands due to the Laporte forbidden f-f transitions. Ligands or linkers can coordinate with rare earth (mainly lanthanide (Ln)) ions, resulting in energy transfer from the ligand to the RE^{3+} ions, vividly referred to as the "antenna effect" (Fig. 5.4; bottom, left). In fact, the essence of this "antenna effect" is the LMCT, e.g., in an Eu-MOF composed of Eu^{3+} and ligand, the emission of Eu^{3+} is sensitized by the ligand through the LMCT, also called the "antenna effect" (Fig. 5.4; bottom, right). LC emission is based on the emission of the ligands used in the assembly of MOFs, mostly relying on the charge transfer, i.e., MLCT, LLCT, and the intraligand charge transfer (ILCT). The MLCT luminescence of MOFs is the process of energy transfer from metal ions to ligands after the metal ions are illuminated by light, resulting in the metal excited states changing into the ligand excited states, and then returning to S_0 to emit fluorescence. The stronger the reducibility of metal ions, the stronger the oxidizability of the ligands, and the more likely MLCT occurs. The π-electrons in an organic ligand with an aromatic moiety or an extended p-system have significant contributions to luminescence, which can be classified as LLCT

and LC or ILCT. Actually, the luminescent properties of MOFs are not only controlled by the metal clusters or ligands; they can also be adjusted by the interactions among them.

Zhang et al. chose a MOFs-based hybrid as the signal transducer to construct a dual-functional intelligent logic detector, which could visually and simultaneously two-dimensionally (2D) monitor pyrethroid (PYRs) exposure time and exposure extent [32]. 3-Phenoxybenzoic acid (3-PBA) and 3-phenoxybenzaldehyde (3-PBD) have a different quenching effect toward Eu^{3+} emission under different excitations of 313 nm and 322 nm. As shown in Fig. 5.5A (left), the Eu^{3+}@Hf-MOF treated by 3-PBA (3-PBD) has the same PXRD pattern as the pristine one, indicating that the quenching effect can't be ascribed to the framework collapse of Eu^{3+}@Hf-MOF. From Fig. 5.5B (left), the unchanged lifetimes of Eu^{3+} in 3-PBA/3-PBD are strong evidence to prove the absence of interaction between them. Fig. 5.5C (left) shows the UV-vis spectra of 3-PBA and 3-PBD; the absorption of 3-PBD has completely overlapped the excitation of 313 nm and 322 nm, while the absorption of 3-PBA can only overlap the excitation of 313 nm. Hence, the excitation light absorbed by the ligand has been reduced, which further decreases the antenna effect between the ligand and Eu^{3+}. From Fig. 5.5D (left), with the addition of 3-PBA, the red shift of the excitation band can be clearly observed, so it can be inferred that there is an exciplex formed by the framework of Eu^{3+}@Hf-MOF and 3-PBA, which causes the obvious red shift of the maximum excitation. As shown in Fig. 5.5A (right), if the concentration is higher, the extent of exposure is more severe. A light red light can be seen and "W (weak)" is shown by the logic detector, indicating that the exposure extent is weak (Fig. 5.5B; right). For better application of the intelligent logic detectors, Eu^{3+}@Hf-MOF is solidified into a hydrogel of CMC-Na to prepare a portable sensor. By putting the prepared hydrogel into simulated urine of the three different concentrations of 3-PBA, the gels exhibited clearly visible luminescence color transitions from light red to colorless under the UV lamp (Fig. 5.5C; right). The developed hydrogel enables Eu^{3+}@Hf-MOF to be an intelligent and portable tool for the construction of dual-functional logic detectors to monitor pyrethroid exposure two-dimensionally [32].

Hao et al. generated a series of RE-based MOFs (RE = Sm, Dy, Nd, Yb, Er) by encapsulating the RE^{3+} cations into MIL-121 (Al-MOF) crystals (aluminum pyromellitate or $Al(OH)(H_2btec)\cdot H_2O$, H_4btec = pyromellitic acid) for its non-coordinating carboxylate groups, which are amenable to PSM by a coordination reaction with RE^{3+} cations [33]. However, the luminescence of RE^{3+}@Al-MOF is very weak, since the ligand H_4btec cannot effectively sensitize the luminescence of RE^{3+} (Fig. 5.6; right, top). Ag^+ is used to enhance the fluorescence of RE^{3+}@Al-MOF so as to obtain a strong emission. Furthermore, as a sensing probe for Ag^+, Sm^{3+}@Al-MOF shows a higher selectivity and sensitivity for Ag^+ in aqueous solution. The luminescence measurements (Fig. 5.6; left) illustrate that only Ag^+ can induce a significant luminescence enhancement of Sm^{3+}

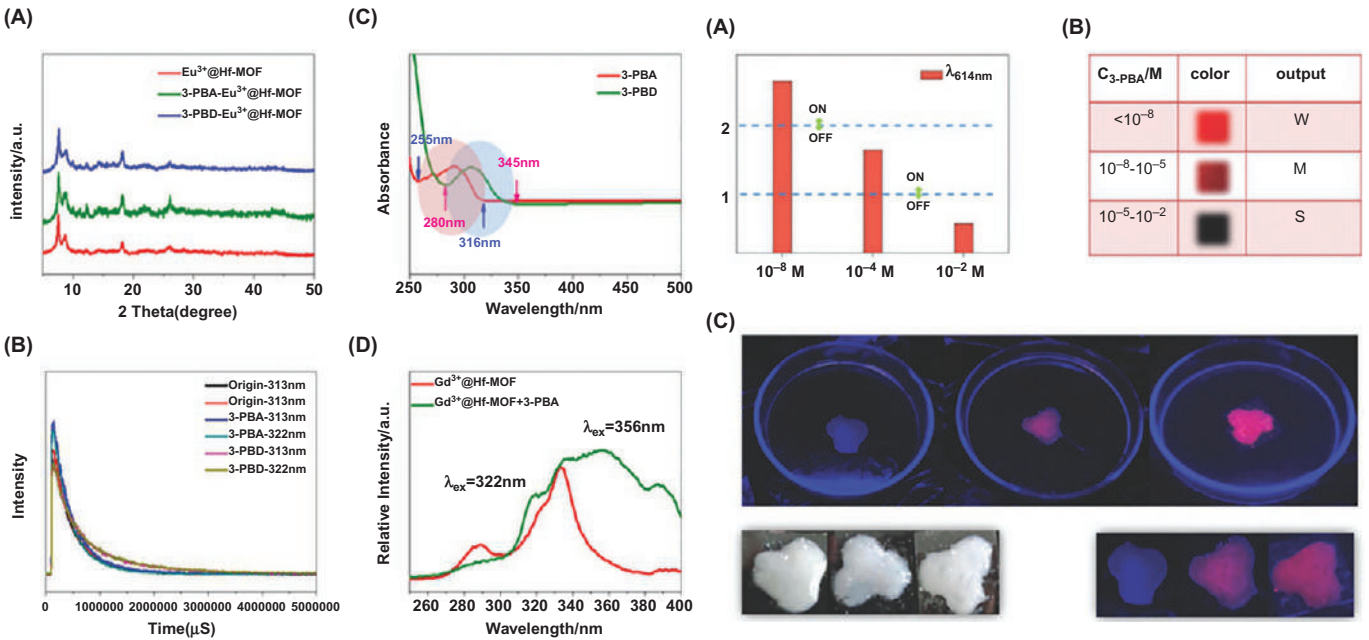

FIG. 5.5 *(Left)* (A) The PXRD patterns of Eu^{3+}@Hf-MOF and Eu^{3+}@Hf-MOF after treated with 3-PBA and 3-PBD; (B) Luminescence decay curves of Eu^{3+}@Hf-MOF and Eu^{3+}@Hf-MOF immersed in 3-PBA and 3-PBD under the excitation of 313 nm and 322 nm, respectively; (C) The UV-vis spectrum of Eu^{3+}@Hf-MOF immersed in 3-PBA (*red* line) and 3-PBD (*green* line); (D) Excitation spectra of Gd^{3+}@Hf-MOF (*red* line) and Gd^{3+}@Hf-MOF in 3-PBA (*green* one). *(Right)* (A) Column diagram of the fluorescence intensity: the dashed line shows the threshold; (B) corresponding color, outputs, and different concentrations of 3-PBA of the logic detector; (C) photographs of the composite Eu^{3+}@Hf-MOF hydrogels and hydrogels in different concentrations of 3-PBA (from left to right: 10^{-2} M, 10^{-5} M, 10^{-8} M). *(Reproduced with permission from Y. Zhang, X. Lian, B. Yan, A point-of-care diagnostics logic detector based on glucose oxidase immobilized lanthanide functionalized metal-organic frameworks. J. Mater. Chem. C 8 (2020) 3023–3028. Copyright 2020 Royal Society of Chemistry.)*

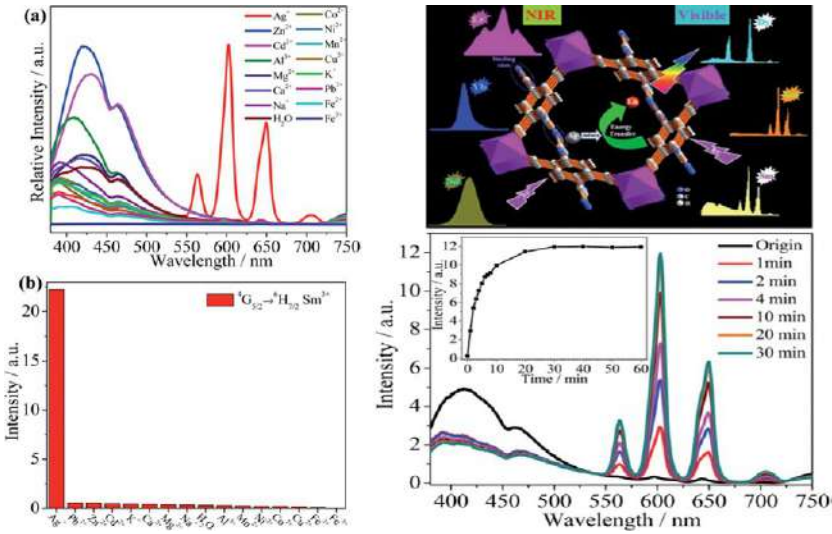

FIG. 5.6 *(Left)* (A) Suspension-state PL spectra and (B) the relative intensities of $^5G_{5/2} \rightarrow {}^6H_{7/2}$ at 603 nm for Sm^{3+}@Al-MOF dispersed in aqueous solutions containing different metal ions (10 mM) when excited at 320 nm. *(Right, Top)* The schematic description for the luminescence enhancement of RE^{3+}-doped (RE = Sm, Dy, Nd, Yb, Er) MOFs by Ag^+. *(Right, Bottom)* Variation of fluorescence intensity of Sm^{3+}@MIL-121 at 603 nm with immersion time in Ag^+ solution (10 mM), $\lambda_{ex} = 320$ nm; inset: a fluorescence intensity plot depending on the immersion time. *(Reproduced with permission from J. Hau, B. Yan, Ag+-sensitized lanthanide luminescence in Ln3+ post-functionalized metal-organic frameworks and Ag+ sensing. J. Mater. Chem. C 3 (2015) 4788–4792. Copyright 2015 Royal Society of Chemistry.)*

and no remarkable luminescence responses are observed upon the addition of other metal ions. As demonstrated in Fig. 5.6 (right, bottom), the Ag^+-induced luminescence enhancement reaction is very fast. The intensity of the highest peak at 603 nm increased more than 7.0 times in 1 min and to a constant value in 30 min. The luminescence intensity of Sm^{3+}@Al-MOF is proportional to Ag^+ concentrations in the range of 0–500 mM and the detection limit (LOD) of Sm^{3+}@MIL is estimated to be 0.09 mM [33].

Peng et al. constructed a luminescent sensor based on a Tb^{3+}-functionalized Zr-MOF (Tb^{3+}@UiO-66-$(COOH)_2$, Tb^{3+}@Zr-MOF), which exhibits many attractive sensing properties toward thiabendazole (TBZ). Moreover, the probe was employed to determine TBZ in real orange samples, in which good recoveries from 98.41% to 104.48% were obtained. It only took 35 min for the whole process of detection of TBZ in real orange samples, providing a reliable and rapid method for monitoring the TBZ in real orange samples (Fig. 5.7; top). The luminescent properties are given in Fig. 5.7A (bottom); among all the tested chemicals, only TBZ caused a distinct quenching effect on the fluorescent intensity, while Vitamin C and citric acid showed a slight decrease, and the other 14 chemicals showed no obvious changes in luminescence intensity.

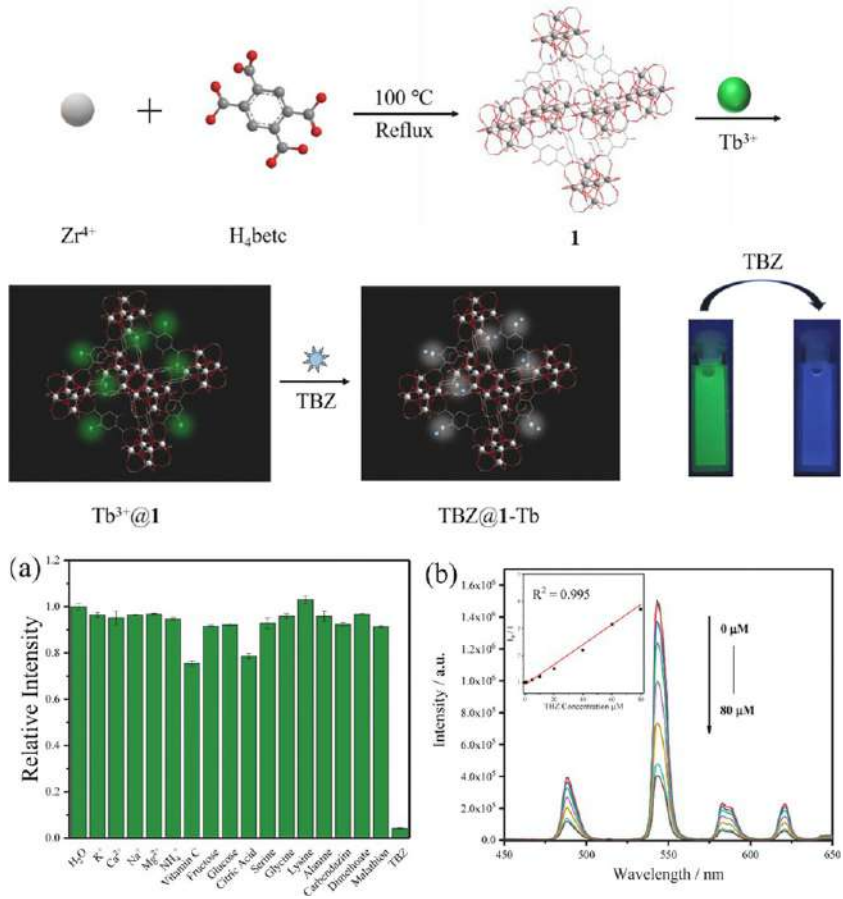

FIG. 5.7 *(Top)* Schematic diagram for the synthesis of Tb^{3+}@Zr-MOF (Zr-MOF = 1) and selective sensing for TBZ. *(Bottom)* The fluorescence intensity of the 544 nm of Tb^{3+}@Zr-MOF (A) treated with various constituents in oranges; (B) the emission spectra of Tb^{3+}@Zr-MOF with different concentrations of TBZ (0–80 μM). The inset is the relationship between the concentration of TBZ and I_0/I. *(Reproduced with permission from X. Peng, G. Bao, Y. Zhong, L. Zhang, K. Zeng, J. He, W. Xiao, Y. Xia, Q. Fan, H. Yuan, Highly sensitive and rapid detection of thiabendazole residues in oranges based on a luminescent Tb3+-functionalized MOF. Food Chem. 343 (2021) 128504. Copyright 2021 Elsevier.)*

As illustrated in Fig. 5.7B (bottom), the emission intensity of the probe at 544 nm decreased obviously with the increase of the concentration of TBZ, and showed good linearity in the range of 0 to 80 μM. The sensitivity and LOD were derived quantitatively with a value of K_{sv} of 3.5×10^4 M^{-1} and a linear correlation coefficient (R^2) of 0.995 (inset of Fig. 5.7B; bottom), indicating the Tb^{3+}@Zr-MOF) can monitor TBZ with good quantitative analysis.

The LOD was calculated to be 0.271 μM. These results indicate that the Tb^{3+}@Zr-MOF) can quantitatively detect TBZ in oranges. The possible mechanism is that, based on the coordination interactions of the Tb^{3+} ion with Zr-MOF and TBZ, energy transfers from Zr-MOF to the TBZ molecule, which reduces the LMET from the linker of Zr-MOF to the Tb^{3+} ion and further leads to the quenching effect [34].

5.3 The photo-induced energy transfer (PET) and fluorescence (Förster) resonance energy transfer (FRET) for luminescence response for chemical sensing in rare earth metal-organic framework hybrid materials

There are two common mechanistic pathways for MOFs materials in luminescence sensing: photo-induced electron transfer (PET) and fluorescent (Förster) resonance energy transfer (FRET), especially for the majority of MOFs with LC luminescence or all types of CT ones. The energy transfer process mainly focuses on the probe (often molecule system, linkers of MOFs) and the analytes (especially molecular species). In this regard, the character of MOFs sensing is identical to a small molecule system. FRET is the nonradiative transfer of energy from a donor to an acceptor molecule, which is also distance dependent and hence can be used to investigate Coulombic interaction between molecules. On the other hand, PET is similar to DEE, which involves transmission of excited electrons from donor to acceptor via a nonradiative pathway; however, this is a redox process and results in the quenching of luminescence. Tuning of HOMO and LUMO energy levels by complexation of the analyte with a probe may be reflected in the luminescence energy as well as the intensity of the probe. This is especially relevant to MC luminescence, especially for lanthanide-based sensors having spin-forbidden f-f transitions that are hence difficult to excite directly [35]. But in fact, neither PET nor FRET are common in MOFs materials and are even rarer in rare earth MOF hybrid materials.

5.3.1 PET for luminescence response in chemical sensing

Herein, several recent works on PET for MOFs-based materials are introduced. Wang et al. designed and synthesized two Zr-MOFs, which showed intense luminescence in water and could be solely quenched by trace amounts of Fe^{3+} ions with LOD toward Fe^{3+} ions of 212 and 16 ppb, respectively. The efficient luminescent quenching effect is attributed to the PET between Fe^{3+} ions and the ligands in these MOFs [36]. Bej et al. synthesized Cd^{2+}- and Zn^{2+}-based MOFs for the selective identification of m-xylene in a pool of other isomers by fluorometric methods. Inhibition of the PET process is the prime reason for luminescence enhancement, owing to the comparable molecular orbital energies for m-xylene in comparison with *o*- and *p*-xylene [37]. Fan et al. designed an unprecedented self-penetrated Zn-MOF as a multiresponse chemosensor in

detecting dichloronitroaniline pesticide and nitrofuran antibiotics in water with an LOD (116 ppb) for DCN pesticide, 16 ppb for NFT antibiotic, and 12 ppb for NTZ antibiotic, respectively. In addition, the mechanisms of luminescence quenching were revealed from the viewpoint of IFE and PET [38]. Tang et al. developed a hybrid via PSM of a Zr-MOF through an efficient click reaction with 1-ethynylpyrene for 2,4,6-trinitrophenol (PA) detection. The hybrid showed an 85% luminescence quenching efficiency with 0.203 mMPA and an LOD of 4.5×10^{-7} M. The hydrogen bond interaction promotes PET between the MOFs-based hybrid and PA, leading to better selectivity for PA detection over TNT [39].

Yang et al. synthesized two La-MOFs ($\{[La_4(Cmdcp)_6(H_2O)_9]\}_n$ (La-MOF1, 3D) and $\{[La_2(Cbdcp)_3(H_2O)_{10}]\}_n$ (La-MOF2, 2D), H_3CmdcpBr (H_3CbdcpBr) =*N*-carboxymethyl ((4-carboxybenzyl))-3,5-dicarboxylpyridinium bromide), which could absorb the carboxyfluorescein (FAM)-tagged probe DNA (P-DNA) and quench the luminescence of FAM via a PET process. The nonemissive P-DNA@La-MOF hybrids thus formed in turn functioned as sensing platforms to distinguish conservative linear, single-stranded RNA sequences of Sudan virus [40]. In addition, increasing the concentration of target SUDV RNA sequences led to a gradual increase in the fluorescence intensity until saturation was observed at a concentration of 50 nM for both P-DNA@La-MOF1 and P-DNA@La-MOF2 (Fig. 5.8; top), whose fluorescence intensities showed the anticipated linear relationships with the concentration of the target RNA sequences (inset of Fig. 5.8; top), giving an LOD of 112 pM with an RSD of 1.2% and 67 pM with an RSD of 1.1%, respectively. The introduction of completely complementary target Sudan virus RNA T_{20} resulted in marginal fluorescence enhancement, with the recovery efficiency (RE) approaching 0.62 ± 0.03 for P-DNA@La-MOF1 and 0.78 ± 0.02 for P-DNA@La-MOF2 (Fig. 5.8; bottom). In addition, the fluorescence recovery induced by T_{20} showed much higher concentration dependence in comparison to that by T_1 and T_2 (Fig. 5.8; bottom). They extended the length of target SUDV RNA sequences from 20 (T_{20}) to 30 (T_{30}) and 40 (T_{40}) nucleobases. As shown in Fig. 5.8 (bottom), introducing T_{30} and T_{40} to both systems also resulted in decent fluorescence enhancement, with RE values being 0.49 and 0.37 for P-DNA@La-MOF1 and 0.63 and 0.50 for P-DNA@La-MOF2. Under these conditions, the LODs were 806 pM for T_{30} and 1016 pM for T_{40} of the P-DNA@La-MOF1 system and 83 pM for T_{30} and 92 pM for T_{40} of the P-DNA@La-MOF2 system. Such results may be rationalized from the structural traits of MOFs. With the conjugated π-electron system in MOFs and aromatic nucleotide bases in the probe DNA, the two La-MOFs absorb P-DNA through electrostatic and π-stacking interactions to form hybrids and quench the fluorescence of the FAM via a PET process [40].

Lian et al. used a hetero bimetallic-organic framework (Ag^+/Tb^{3+}@MOFs) and mercaptan linker to build a versatile platform for sensing and decontaminate CS lachrymator [41]. MOFs-SH is used as the detector for CS based upon the thiolene reaction. The photos of these suspensions under UV light also display obvious

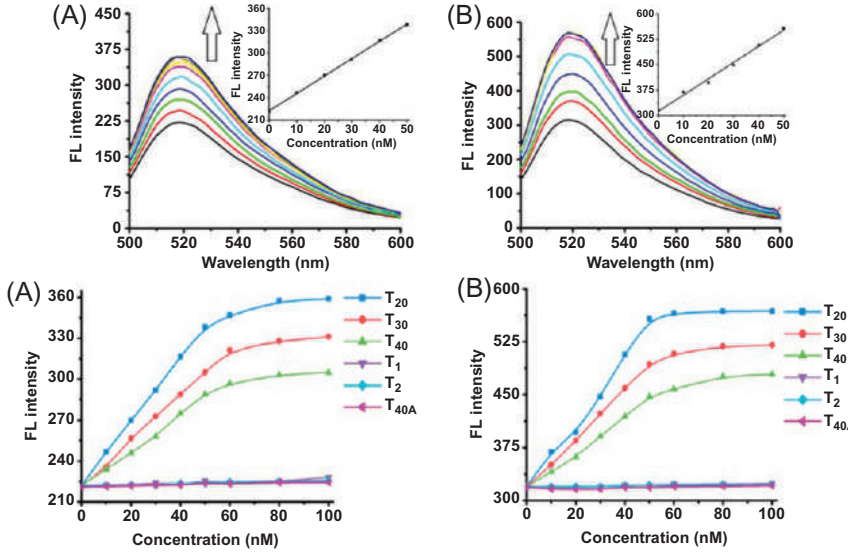

FIG. 5.8 *(Top)* Fluorescence spectra of the P-DNA@La-MOF system (50 nM/45 μM for P-DNA@La-MOF1 (A), 50 nM/40 μM for P-DNA@La-MOF2 (B)) incubated with T_{20} at varying concentrations. Inset: plot of the fluorescence intensity at 518 nm versus the concentration of T_{20}. *(Bottom)* Fluorescence recovery of P-DNA@La-MOF1 (A, 50 nM/45 μM) and P-DNA@La-MOF2 (B, 50 nM/40 μM) systems by target T_{20}, T_{30}, T_{40}, T_1, T_2, and T_{40A}. A at varying concentrations. *(Reproduced with permission from S. Yang, W. Zhao, P. Hu, K. Wu, Z. Jiang, L. Bai, M. Li, J. Chen, Lanthanum-based metal-organic frameworks for specific detection of Sudan virus RNA conservative sequences down to single-base mismatch. Inorg. Chem. 56 (2017) 14880–14887. Copyright 2017 American Chemical Society.)*

luminescence extinction from bright green to dark (Fig. 5.9; top, left), which exhibits conspicuous significant luminescence quenching effects. However, the luminescence of Ag^+/Tb^{3+}@MOFs has maintained even if it encounters a CS molecule. Concentration-dependent studies on the photoluminescence were carried out, revealing a good linear relationship ($R^2 = 0.9987$) between the logarithm of intensities ratios and the molar concentration of CS in aqueous solutions (Fig. 5.9; top, right) over the range 1.0×10^{-7}–5.0×10^{-5} mol L^{-1} with LOD as 32.1 ppb. This may be the chemical bond between the CS molecule and MOFs-SH framework. For Ag^+/Tb^{3+}@MOFs and MOFs-SH (Fig. 5.9A; bottom), such aspects can play an important role, where the organic ligand bpydc has excited states in a region relevant for an LMET to Tb^{3+}. Hence, the interdiction of emission is confirmed and a PET pathway is proposed in the following (Fig. 5.9B and C; bottom). When structures with high HOMO levels appear around Ag^+/Tb^{3+}@MOFs, such as CS-SH, the electrons in the HOMO of CS-SH will be transferred to the empty HOMO of Ag^+/Tb^{3+}@MOF, resulting

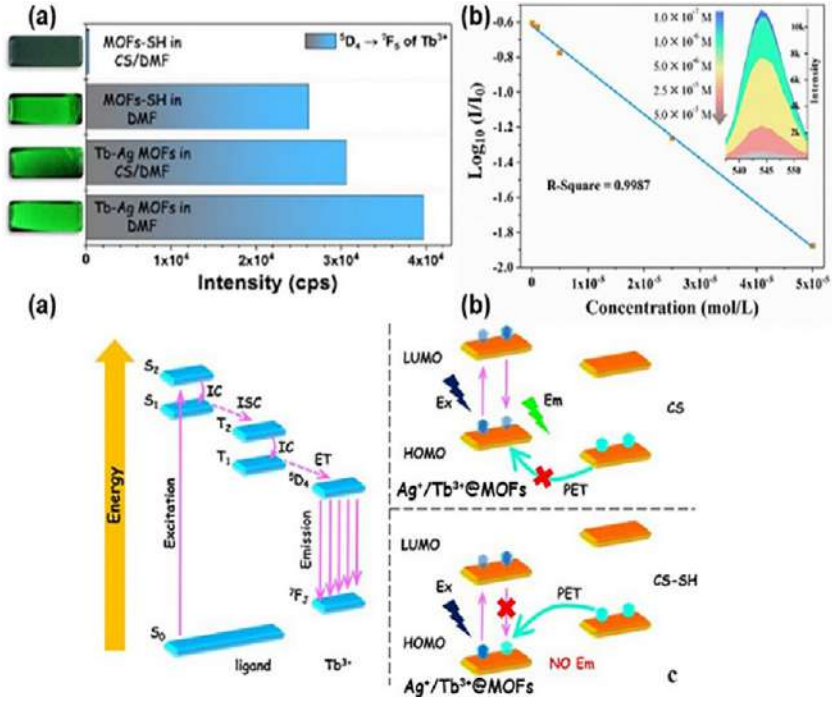

FIG. 5.9 *(Top)* (A) The histogram for the emission of $^5D_4 \rightarrow {}^7F_5$ transition of Ag^+/Tb^{3+}@MOFs or MOFs-SH toward pure DMF or CS/DMF solution; (B) Linear relationship curve between $\log_{10}(I_i/I_0)$ with concentration of CS in water and the partial spectra between 535 and 555 nm (insert). *(Bottom)* (A) Jablonski diagram for ligand and Tb^{3+}; (B, C) schematic diagram of HOMO and LUMO of different materials or structures, and scheme of PET pathway, Ex = excitation, Em = emission. *(Reproduced with permission from X. Lian, B. Yan, Antineoplasticmitoxantrone monitor: a sandwimixed matrix membrane (MMMs) based on luminescent MOFs-hydrogel hybrid. Sens. Actuators B Chem. 281 (2019) 168–174. Copyright 2019 Elsevier.)*

in forbidden electronic transitions and no luminescence can be observed. The PET process will happen in the resulting structure of MOFs-SH with CS [41].

5.3.2 FRET for luminescence response in chemical sensing

For the FRET mode of sensing, there are some reports on MOF probes. Here we only give some comments on the typical research over the past several years [42–49]. Ding et al. prepared two kinds of luminescent Zr-MOFs as the energy donor and stimuli-responsive polymers conjugated to fluorophores as energy acceptors, forming a FRET nanosystem. Ratiometric sensing of pH (3.0 and 8.0 under 420-nm excitation and by ratioing the emission peaks at 645 and 530 nm) and temperature (25°C to 50°C under 550-nm excitation and by ratioing the emission peaks at 810 and 695 nm) was accomplished by monitoring

luminescence [42]. Afzalinia et al. presented a luminescent biosensor based on "sandwich-type" hybridization of oligonucleotides and the FRET strategy to determine the MicroRNA-155 (miRNA-155) expression levels as a cancer biomarker. A modified La-MOF and Ag NPs were used as the energy donor-acceptor pairs in luminescence quenching through the FRET process, and the surface of both was conjugated with different 5′-amino-labeled ssDNA strands (aptamers) [43]. Qu et al. designed a luminescence sensor platform by the interaction of aggregation/dispersion AuNPs with Tb-MOFs. AuNPs can effectively quench the luminescence of Tb-MOFs, involving FRET as well as IFE and dynamic quenching effect (DQE). The linear range of PSA is achieved from 1 to 100 ng/mL with a detection limit of 0.36 ng/mL [44]. Sun et al. reported a thiol-labeled adenosine triphosphate (ATP) binding aptamer covalently linked on the surface of AuNPs. The dispersed AuNPs can quench the luminescence of the Tb-MOFs at 547 nm with an excitation wavelength of 290 nm, which is similarly ascribed to the combined action of FRET and IFE [45]. Cao et al. reported the FRET properties of a 2D Cd-MOF, which was encapsulated with two guest dyes, acridine orange (AO) and rhodamine B (RhB), in its honeycomb-type nanochannel. Cd-MOF serves as an energy funnel that harvests high energy excitation and channels it onto AO and then onto RhB [46]. Khatun et al. constructed a luminescent pillared paddle-wheel Zn-MOF, whose highly ordered arrangement and good overlap between the emission and absorption spectra of these two complementary energy donor and acceptor units enabled ligand-to-ligand FRET, allowing the MOF to display exclusively DPTTZ-centric blue emission (410 nm) regardless of the excitation of either chromophore at different wavelengths. Zn-MOF displayed an Hg^{2+} -specific luminescence signal, demonstrating its selective detection of Hg^{2+} [47]. Cai et al. studied a series of dye@Zn-MOF, featuring a unique mechanism of tandem FRET among the MOF host and the multiple dye guests [48]. Xiao et al. synthesized a Cd-MOF and fabricated it into an unparalleled luminescence-silent system CrO_4^{2-}@Cd-MOFs by PSM. First, this probe displayed quenching of luminescence intensity for CrO_4^{2-} ions originating from the FRET mechanism. Further, the fluorescent intensity of the CrO_4^{2-}@Cd-MOFs system could be recovered for sensing ascorbic acid for the elimination of the FRET process [49].

Xia et al. utilized an Eu(III) postfunctionalized Zr(IV)-based MOF (UiO-66 $(COOH)_2$, Eu^{3+}@Zr-MOF) as an independently luminescent probe for sensing bilirubin (BR) in human serum, a biomarker of jaundice in hepatitis. From Fig. 5.10A (top), it can be clearly seen that there is a large spectral overlap from 380 to 510 nm between the ligand-based emission of compound Eu^{3+}@Zr-MOF and absorption of BR, which can lead to an effective FRET process and hinder the ligand-to-Eu energy transfer to reduce the emission intensity of Eu^{3+} in Zr-MOF. As shown in Fig. 5.10B (top), the red emission at 614 nm of Eu^{3+} in Eu^{3+}@Zr-MOF is markedly suppressed after introducing BR, and its intensity continuously declines with increasing the BR content. At the same time, a discernible quenched phenomenon can be observed for the blue ligand-centered

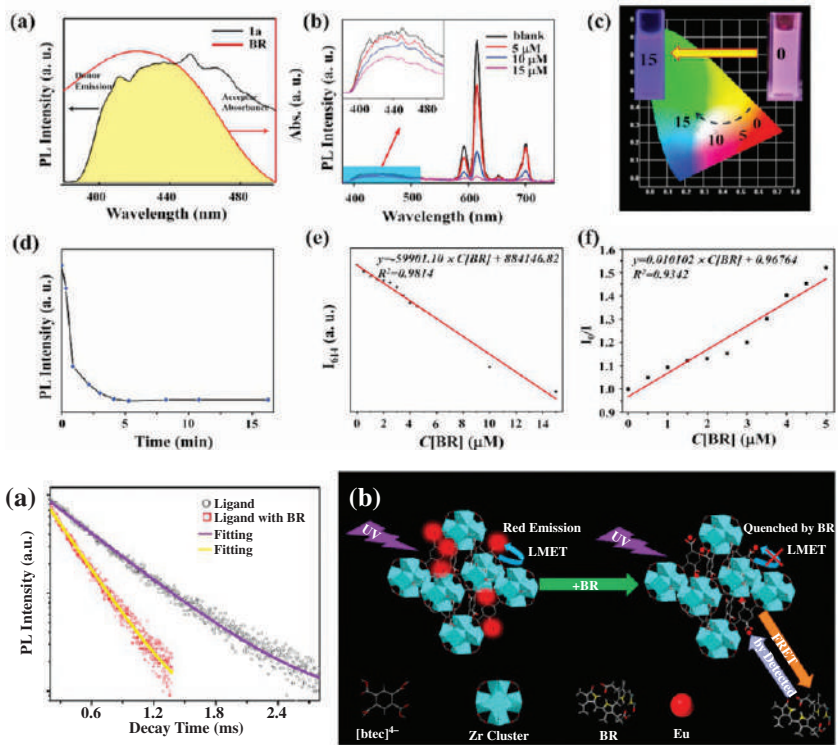

FIG. 5.10 *(Top)* The absorption spectrum of BR and emission spectrum of sample Eu^{3+}@Zr-MOF (A). The emission spectra of Eu^{3+}@Zr-MOF suspensions containing different concentrations of BR in PBS; inset shows partial enlargement of the *blue* ligand-centered emission bands (B). The evolution of CIE chromaticity coordinates and luminescent colors (inset) caused by different concentrations of BR (C). The time-dependent luminescent intensity curve of Eu^{3+}@Zr-MOF suspension monitored at 614 nm with a BR concentration of 15 μM (D, $\lambda_{ex} = 320$ nm). Luminescent intensity of Eu^{3+}@Zr-MOF at 614 nm versus BR concentration plot (E), as well as the linear relationship between I_0/I and BR concentration from 0 to 5 μM (F). *(Bottom)* The decay curves of ligand-based emissions with and without 15 μM BR (A), and the schematic diagram of the sensing mechanism of BR by Eu^{3+}@Zr-MOF (B). *(Reproduced with permission from C. Xia, Y. Xu, M. Cao, Y. Liu, J. Xia, D. Jiang, G. Zhou, R. Xie, D. Zhang, H. Li, A selective and sensitive fluorescent probe for bilirubin in human serum based on europium(III) post-functionalized Zr(IV)-based MOFs. Talanta 212 (2020) 120795. Copyright 2020 Elsevier.)*

emission when BR is present (inset in Fig. 5.10B; top). The direct visual result caused by luminescence variation after introducing BR is that the emission color of Eu^{3+}@Zr-MOF systematically varies from red to pale cyanine under UV excitation (insert in Fig. 5.10C; top), whose chromaticity coordinates calculated from the emission spectra shift from (0.52, 0.31) to (0.28, 0.27) as the BR concentration increases from 0 to 15 μM. Additionally, from the time-dependent emission intensity curve of the 614-nm emission peak in

Fig. 5.10D (top), the fluorescent response rate of Eu^{3+}@Zr-MOF to BR is very fast. Extending the contact time to 5 min, the luminescence barely decreases further and remains unchanged. The dependence of intensity for Eu^{3+}@Zr-MOF at 614 nm on the BR concentration is plotted in Fig. 5.10E (top). A linear correlation can be fitted in the low concentration from 0 to 5 μM with K_{SV} of $1.01 \times 10^5\ mol^{-1}$ (Fig. 5.10F; top), whose LOD and limit of quantification (LOQ) to BR are estimated to be 0.45 μM and 1.5 μM. The luminescent quenching of the Eu^{3+}@Zr-MOF caused by the addition of BR being attributed to the FRET process can be further verified by the large spectral overlap between the ligand-based emission of Eu^{3+}@Zr-MOF and absorption of BR seen in Fig. 5.10A (top). In addition, the occurrence of the FRET process between the BR and ligands can also be proven by the variation of the fluorescence lifetime of the ligand-based emission with or without BR (Fig. 5.10A; bottom); the corresponding high FRET efficiency is calculated as 55.92% between the probe Zr-MOF and BR. The inherent natures of the molecular structure of BR and Zr-MOF allow for several interactions between them, such as interaction between the free –COOH of BR and the unsaturated Zr (IV) sites, the possible hydrogen bonding between the hydroxyl groups of Eu^{3+}@Zr-MOF and free –COOH of BR, and the π-π interaction between Eu^{3+}@Zr-MOF and the aromatic rings of BR. These preceding intermolecular forces will cause Eu^{3+}@Zr-MOF to be close to BR as much as possible, to finally effectively promote the FRET process. As shown in Fig. 5.10B (bottom), a strong red emission originates from the LMET process: the FRET process between the ligands and BR occurs and begins to compete with the LMET process between the ligands and Eu^{3+}. The energy absorbed by the ligand is no longer transmitted to Eu^{3+}, then quenching the bright red emission from Eu^{3+} in Zr-MOF [50].

Hao et al. first reported a designed luminescent Eu^{3+}@Ga-MOF sensor, whose luminescence can be effectively quenched by 1-hydroxypyrene (1-HP) via a FRET process, thus achieving recognition of 1-HP [51]. As shown in Fig. 5.11A (top), upon the addition of 1-HP (1 mg/mL) to the suspension of, a significant decrease (77%) in the luminescence intensity of Eu^{3+} at 614 nm can be observed, leading to the emission color of the hybrid changing from red to colorless. Of particular note is that the fluorescent response rate of the hybrid probe toward 1-HP is very fast, as illustrated by the time-dependent emission spectra and intensity curve (Fig. 5.11B; top). The interaction between 1-HP and the MOF linker causes the luminescence quenching. The LUMOs energy level of the ligands (donor) is obviously lower than that of the 1-HP (acceptor), indicating the absence of the PET process in the luminescence quenching by 1-HP. The efficiency of the FRET depends on the extent of spectral overlap between the donor's emission spectrum and the acceptor's absorption spectrum. The donor-acceptor (ligand-1-HP) distance (r) and Förster distance (R_0) in this study were also calculated. This also facilitated the occurrence of the FRET process between the Ga-MOF ligands and 1-HP. The bright red emissions of Eu^{3+}@Ga-MOF are based on the LMET process: the ligands

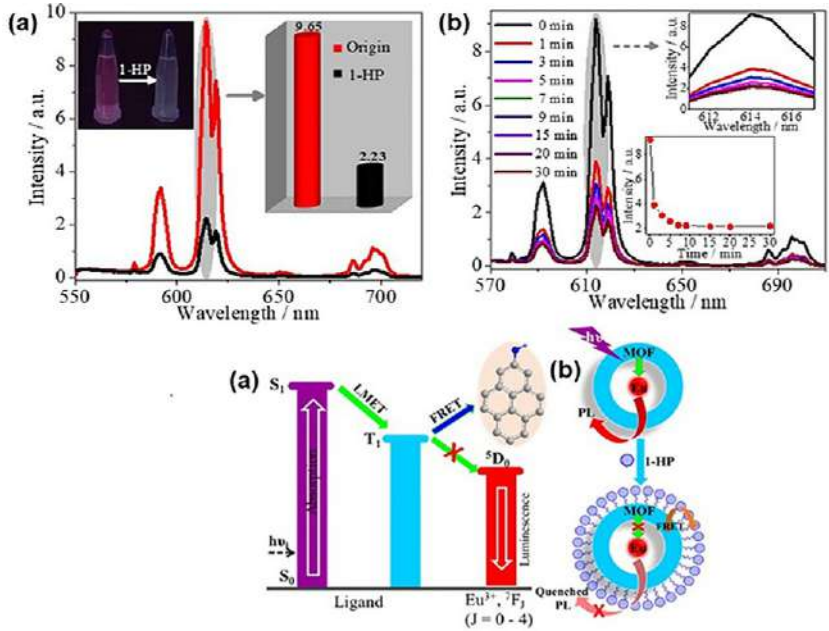

FIG. 5.11 *(Top)* (A) Suspension-state luminescence spectra of Eu^{3+}@Ga-MOF before and after being treated by 1-HP (1 mg/mL). Inset: The changes in the emission intensity (614 nm) and luminescence colors of Eu^{3+}@Ga-MOF induced by the addition of 1-HP; (B) Emission spectra of Eu^{3+}@Ga-MOF suspensions upon exposure to 1-HP at various time intervals ($\lambda_{ex} = 302$ nm) and the emission intensity at 614 nm as a function of exposure time in the inset. *(Bottom)* (A) Simplified scheme of the LMET and FRET process in Eu^{3+}@Ga-MOF with 1-HP; (B) Scheme of the mechanism of 1-HP sensing by Eu^{3+}@Ga-MOF. *(Reproduced with permission from J. Hao, B. Yan, Determination of urinary 1-hydroxypyrene for biomonitoring of human exposure to polycyclic aromatic hydrocarbons carcinogens by a lanthanide-functionalized metal-organic framework sensor. Adv. Funct. Mater. 27 (2017) 1603856. Copyright 2017 Wiley-VCH.)*

strongly absorb UV light and transfer the absorbed energy to Eu^{3+}, thus facilitating the luminescence of Eu^{3+} and endowing Eu^{3+}@Ga-MOF with the Eu^{3+}'s characteristic emission (Fig. 5.11; bottom). However, in the presence of 1-HP, the FRET process between the ligands and 1-HP competes with the LMET process through suppressing or blocking the energy transfer from the ligands to Eu^{3+}. As a result, the emission of Eu^{3+}@Ga-MOF is restricted or quenched, and thus 1-HP is detected (Fig. 5.11; bottom) [51].

Lian et al. fabricated a sandwiched mixed matrix membrane (MMM) based on a MOF-hydrogel hybrid and achieved ppb-level sensitivity and good selectivity for detecting mitoxantrone in serum among other analogous antineoplastics [52]. MMM in mitoxantrone solution had a much more enervated emission than the original MMM to realize its detection (Fig. 5.12A; top). As shown in Fig. 5.12B (top), various analytes induced different effects on the luminescence of the suspension; however, mitoxantrone exhibited the most remarkable

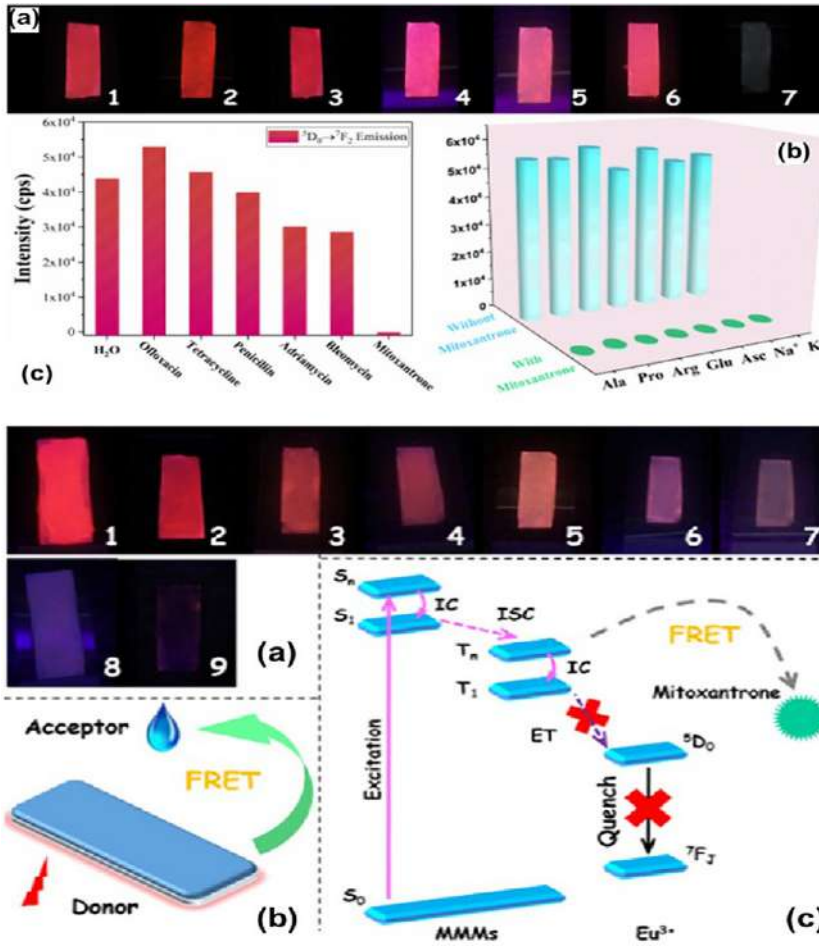

FIG. 5.12 *(Top)* (A) The photographs of MMM hydrogels under UV irradiation after addition for H_2O (1), ofloxacin (2), tetracycline (3), penicillin (4), adriamycin (5), bleomycin (6), and mitoxantrone (7); (B) luminescence intensity of MMMs at 614 nm toward various drugs; (C) luminescence responses of MMMs toward mitoxantrone in the presence of background of other various serum components. *(Bottom)* (A) Photographs of MMMs after addition of serum with different concentrations of mitoxantrone (1–9: 10^{-3}–100 μM); (B) and (C) FRET process between MMMs and mitoxantrone. *(Reproduced with permission from X. Lian, Y. Zhang, J. Wang, B. Yan, Antineoplastic mitoxantrone monitor: a sandwich mixed matrix membrane (MMMs) based on luminescent MOFs-hydrogel hybrid. Inorg. Chem. 59 (2020) 10304–10310. Copyright 2020 American Chemical Society.)*

quenching effect. There is no evidence that the interfering substances can affect the selectivity of the detection platform (Fig. 5.12C; top). The ribbon hydrogel MMM also exhibited a distinct luminescence under UV radiation, which could be observed by the naked eye (Fig. 5.12A; bottom). Overall, the presence of the FRET process between MMM and mitoxantrone was ratified (Fig. 5.12B;

bottom). In this process, the donor is the luminescence center Eu^{3+} and the acceptor is the quencher mitoxantrone. The MMMs strongly absorb photons and the energy is transferred to Eu^{3+}, thus endowing MMMs to display the Eu^{3+}'s characteristic emission. However, in the presence of mitoxantrone, the FRET process restrains the energy transfer from MMMs to Eu^{3+} (Fig. 5.12C; bottom).

5.4 Special interactions for luminescence response on chemical sensing in rare earth metal-organic framework hybrid materials

Besides the general metal ions and linkers or ligands within MOF materials, some special interactions still exist that affect the luminescence response to be applied in sensing. They include hydrogen bonding or $\pi \rightarrow \pi$ interactions in MOFs hosts; some reactions (coordination, redox, and precipitation, etc.) even occur between building blocks of MOFs and analytes [52–62]. Although these interactions do not seem to be very common, they still have useful and attractive significance for this field.

5.4.1 Hydrogen bonding for luminescence response on chemical sensing

Comparatively, some research studies have reported on hydrogen bonding for luminescent responsive sensing. This section offers comments on some works involving MOFs materials [52–58]. Kahn et al. synthesized a Zn-MOF, whose luminescence and electron-rich nature allow it to be utilized for selective sensing of Fe^{3+} and 2,4,6-trinitrophenol (TNP) in water, with LOD of 3.7 and 1.8 ppm, respectively. This mechanistic evidence revealed that a combination of strong hydrogen bonding with FRET and PET processes was synchronously responsible for the quenching of the luminescence intensity of Zn-MOF [52]. Zhu et al. used an amino-group functionalized MOF NH_2-UiO-66 to obtain a drastic luminescence enhancement at 455 nm induced by F^- ions with LOD of 0.229 mg L^{-1}, whose luminescent sensing mechanism can be ascribed to the formation of hydrogen bonds between the guest F^- anions and the free amino groups in NH_2-UiO-66 to result in incremental electron transfer from ligands to Zr-oxo clusters [53]. Sharma et al. reported on the synthesis of a hydroxyl-functionalized MOF for rapid and efficient sensing of NACs and examined in detail its luminescence-quenching mechanisms. In chloroform, quenching takes place primarily by exciton migration to the ground-state complex formed between the MOF and the analytes. A combination of hydrogen-bonding interactions and π-π stacking interactions are responsible for luminescence quenching, and this observation is supported by single-crystal structures [54]. Liu et al. revealed the underlying principles for the sensing mechanism by comprehensively studying the analyte-sensor interactions. They discovered that the hydrogen bond

showed multifunctions during the detecting processes that, on the one hand, served as the electron transfer bridge and, on the other hand, reinforced the π-π stacking [55]. Tehrani et al. synthesized two urea-containing MOFs (namely TMU-35 and TMU-36), whose urea functional group can interact favorably through hydrogen bonding with carbonyl compounds and thus they are potential candidates for carbonyl compound sensing. When the pillaring linker containing a benzene core (TMU-35) is replaced by the pillaring linker containing a naphthalene core (TMU-36), luminescence-sensing ability toward carbonyl compounds is dramatically quenched [56]. Pentyala et al. synthesized a Zn-MOF with specific binding sites for guest molecules, whose sensing interaction with alcohol gas was studied. It was argued that the sensing mechanism was based on the exchange of Zn-coordinated water against alcohol molecules. The unfavorable loss of hydrogen bonds when replacing water against alcohol in the structure could be partially balanced by van der Waals interactions between alcohol alkyl chains and the aromatic rings of the linker molecules [57]. Mallick et al. reported a luminescent Zr-based MOFs, which exhibited an unprecedentedly low LOD of 66 nM for amines in aqueous solution. Markedly, this ultralow detection was driven by hydrogen bonding interactions between the linker and the hosted amines [58].

For rare earth functionalized MOFs hybrid materials sensing via hydrogen bonding interaction, Hao et al. designed an Eu^{3+} PSM Ga-MOF hybrid (Eu^{3+}@Ga-MOF) to detect ammonia gas and its biological metabolite of ammonia in the human body (urinary urea), which represents a rare example of a reported luminescent sensor that can realize both pollutant environmental monitoring and biological indicator detection (scheme in Fig. 5.13; left) [59]. The solid-state luminescent measurements are recorded and compared in Fig. 5.13 (right, top). Interestingly, most organic vapors have a negligible effect on the luminescence of hybrid film, except in the case of NH_3, which induces a remarkable reduction (76%) of luminescence intensity of Eu^{3+} at 614 nm. In accordance with the change in luminescence spectra, under the irradiation of a UV lamp, only the hybrid film absorbed NH_3 shows a significantly darker luminescence than that from the original one (inset of Fig. 5.13B; right, top). More importantly, the hybrid also realizes the determination of the biological metabolite (urinary urea) of inhaled ammonia gas in the human body. For the suspension-state fluorescent in Fig. 5.13A (right, bottom), notably only urea induced a twofold enhancement in the emission intensity at 614 nm. The hydrogen bonds between ammonia or urea and ligands affect the energy transfer efficiency from ligand to Eu^{3+} ions since the luminescence intensity of RE^{3+} crucially depends on the efficiency of the ligand to Eu^{3+} energy transfer. With the presence of ammonia, the ligands' emission has a bathochromic shift of 24 nm, indicating a decrease of the π^* energy level of the ligands by the hydrogen bonds. On the contrary, urea induces a hypochromatic shift (27 nm) in the emission of the ligands, demonstrating an increased energy level of the π^* orbits of the ligands by the hydrogen bonds. So, the sensing mechanism for ammonia

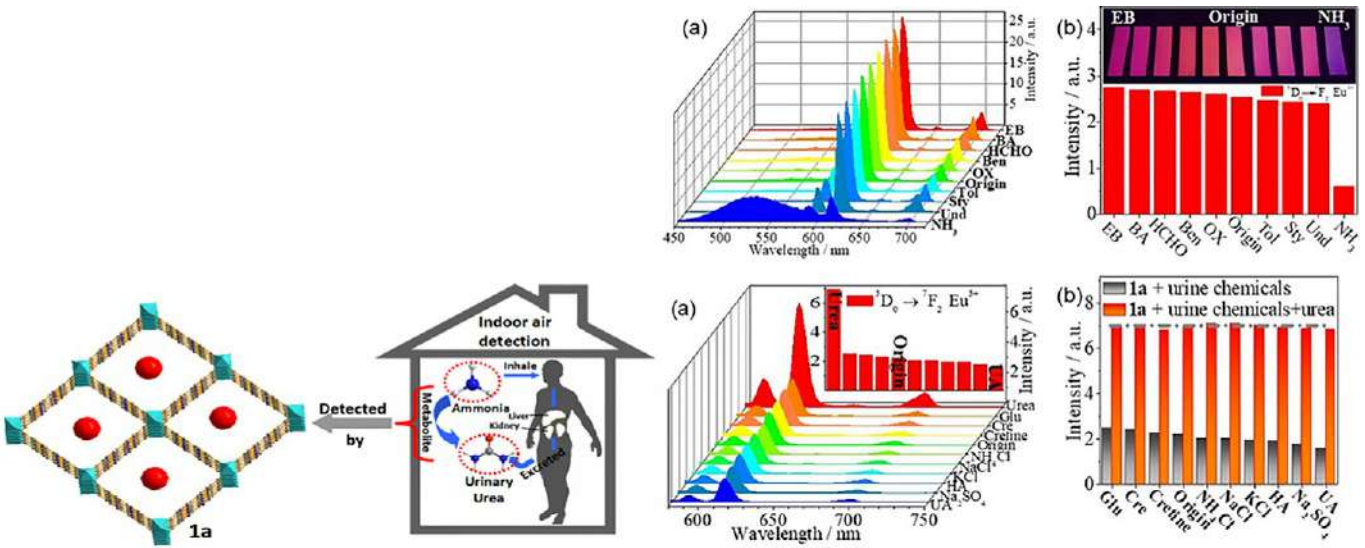

FIG. 5.13 *(Left)* Schematic of the synthesis of nanocrystal Eu^{3+}@Ga-MOF as a luminescent sensor for indoor ammonia and its biological metabolite (urinary urea) in the human body. *(Right, Top)* (A) PL spectra of Eu^{3+}@Ga-MOF film after exposure to various indoor gas pollutants for 1 h; (B) the relative emission intensities at 614 nm ($\lambda_{ex} = 338$ nm); the inset shows the corresponding photographs under 365 nm UV-light irradiation. *(Right, Bottom)* (A) Suspension-state PL spectra and the relative intensities of $^5D_0 \rightarrow {}^7F_2$ at 614 nm (inset of a) for Eu^{3+}@Ga-MOF dispersed in various urine chemicals (10^{-2} M, $\lambda_{ex} = 338$ nm); (B) Luminescence responses of Eu^{3+}@Ga-MOF (1 mg/mL) upon the addition of urea (0.01 M) in the presence of a background of various urine chemicals (0.02 M) in aqueous solution ($\lambda_{ex} = 338$ nm). *(Reproduced with permission from J. Hao, B. Yan, Simultaneous determination of indoor ammonia pollution and its biological metabolite in human body by use of a recyclable nanocrystalline lanthanide functionalized MOF. Nanoscale 8 (2016) 2881–2886. Copyright 2016 RSC Society of Chemistry.)*

or urea is based on their hydrogen bond interaction with Eu^{3+}@Ga-MOF ligands, which changes the excited-state energy level of ligands, thus affecting the ligand-to-Eu^{3+} energy transfer efficiency, consequently leading to different luminescent emissions.

5.4.2 Coordination interaction for luminescence response on chemical sensing

Lian et al. prepared an Eu^{3+} functionalized Sc-MOF as a "Turn-On" fluorescent switch for phenylglyoxylic acid (PGA) for a coordination interaction between Eu^{3+} and PGA [60]. The Eu^{3+}-functionalized Sc-MOF with carboxyl-rich synthesized by a mixed-ligand strategy can effectively sensitize the luminescence of Eu^{3+} through the LMCT process, and the PGA surrounding can enhance the emission of Eu^{3+} -functionalized MOFs (Eu^{3+}@Sc-MOF). Moreover, the on-site monitoring of PGA in urine by a paper-based fluorescent probe integrated with a smartphone was also proposed (Fig. 5.14; top). Compared with the excitation spectrum of original Eu^{3+}@Sc-MOF (Fig. 5.14A; bottom), the maximum excitation peak of the spectrum of Eu^{3+}@Sc-MOF with PGA shifted to 322 nm, and the intensity of the maximum excitation peak was much stronger than the original spectrum in the same experimental conditions. As shown in Fig. 5.14B (bottom), only PGA can induce a significant luminescence enhancement of Eu^{3+}, indicating that Eu^{3+}@Sc-MOF could be a potential sensor with excellent selectivity for PGA in an aqueous environment. The pictures of the luminescence changes of Eu^{3+}@Sc-MOF suspensions over time are recorded by successive photographs (Fig. 5.14C; bottom). The luminescence enhancement is reproduced in Fig. 5.14A (bottom), and the calculated LOD value is 4.16 ppb. The lifetime of Eu^{3+}@Sc-MOF suspension with additional PGA is much larger than others; there is an interaction between Eu^{3+} and PGA molecules and there is a new complex structure in the Eu^{3+}@Sc-MOF with the PGA suspension. The diketone group in the PGA molecule is a familiar excellent structure for Eu^{3+} sensitization. The appropriate interatomic distance is also favorable for this speculation. The calculated results based on the DFT revealed the possible complex structure is stable in the suspension system.

5.4.3 Reduction reaction for luminescence response for chemical sensing

Hao et al. fabricated an Eu^{3+}/Ag^{+} functionalized MOFs hybrid (Eu^{3+}/Ag^{+}@Zr-MOF) as a luminescent sensor for indoor formaldehyde (FA). The implantation of Ag^{+} ions could produce the simultaneous luminescence of both Eu^{3+} and the organic ligands in the MOF to form a dual-emitting hybrid [61] as shown in Fig. 5.15 (top). The FA sensing by the Ag^{+}/Eu^{3+} codoped MOFs was achieved by its induced emission change. The pure Eu^{3+}@Zr-MOF only gives the characteristic emission of Eu^{3+}. With the presence of Ag^{+}, the Ag^{+}/Eu^{3+} codoped

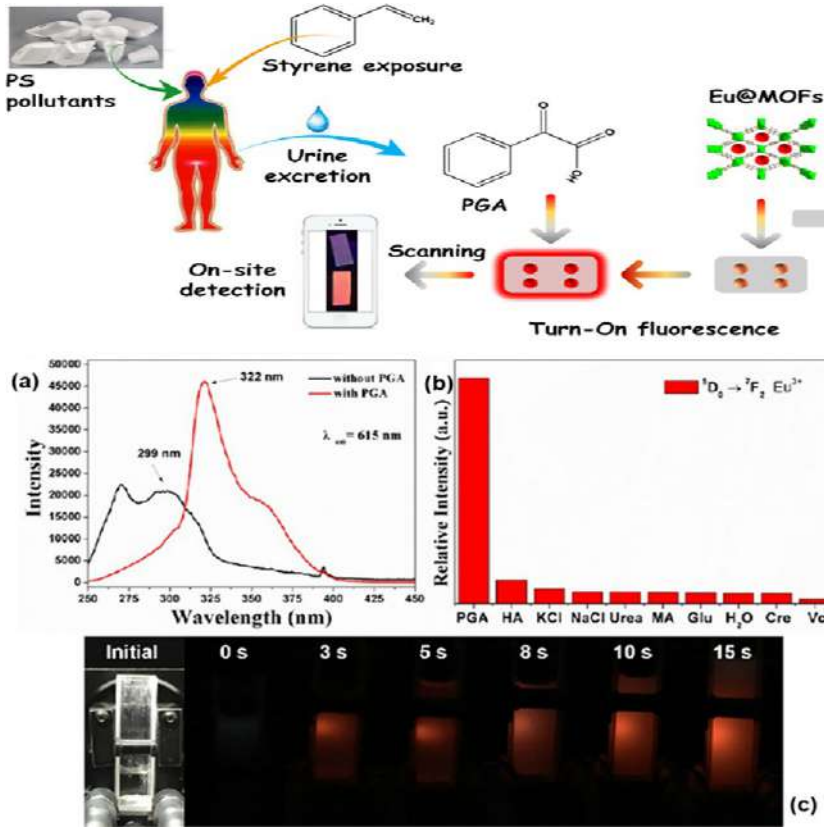

FIG. 5.14 *(Top)* The schematic diagram of the "Turn-On" luminescence switch for on-site detecting of urinary PGA. *(Bottom)* (A) The excitation spectra of Eu^{3+}@Sc-MOF with or without PGA; (B) the histogram for the luminescence of Eu^{3+}@Sc-MOF ($^5D_0 \rightarrow {}^7F_2$ transition of Eu^{3+}) toward different urine chemicals under excitement at 322 nm; (C) successive photographs of the Eu^{3+}@Sc-MOF with addition of PGA solution for different times (0–15 s). *(Reproduced with permission from X. Lian, T. Miao, X. Xu, C. Zhang, B. Yan, Eu3 + functionalized Sc-MOFs: turn-on fluorescent switch for ppb-level biomarker of plastic pollutant polystyrene. Biosens. Bioelectron. 97 (2017) 299–304. Copyright 2017 Elsevier.)*

MOF also has the emission of the organic ligands accompanied by the decrease of the Eu^{3+} emission, since Ag^+ changes the organic ligands' electronic structure and affects the ligand-to-Eu^{3+} energy transfer process. The energy gap between S_1 and T_1 of the organic ligands is calculated to be 12,300 cm^{-1}. Such a high energy gap (>5000 cm^{-1}) is favorable for the intersystem crossing process (Fig. 5.15A; bottom) and gives the emission of organic ligands. Contrarily, the energy gap between the T_1 (21,598) and $^5D_0$ level of Eu^{3+} (17,500 cm^{-1}) exceeds the optimal $\triangle E$ (~2500 cm^{-1}) due to the presence of Ag^+, weakening the ligand-to-Eu^{3+} energy transfer efficiency and decreasing the Eu^{3+}'s

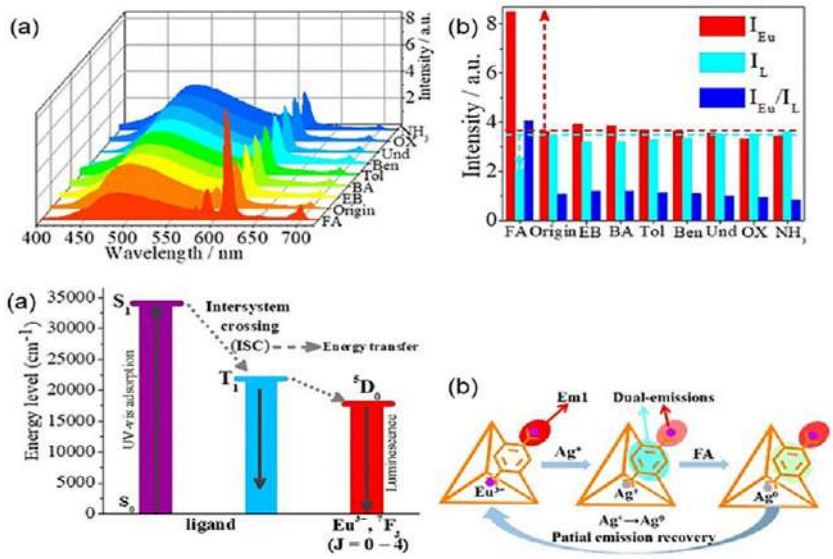

FIG. 5.15 *(Top)* The luminescence spectra (A) and the intensities (I_{Eu}, I_L, and I_{Eu}/I_L) (B) of Eu^{3+}/Ag^{+}@Zr-MOF films after being treated with various indoor polluted gases. *(Bottom)* (A) Simplified schematic diagram of the LMET process in Eu^{3+}/Ag^{+}@Zr-MOF; (B) Schematic illustration of the mechanism of FA sensing by Eu^{3+}/Ag^{+}@Zr-MOF. *(Reproduced with permission from J. Hao, B. Yan, A dual-emitting 4d-4f metal-organic framework as a self-calibrating luminescent sensor for indoor formaldehyde pollution. Nanoscale 8 (2016) 12047–12053. Copyright 2016 RSC Society of Chemistry.)*

emission. FA has the tendency to interact with the Ag^{+} in hybrids and thus to affect the hybrid's electronic structure and energy transfer process. In this way, the FA sensing is achieved by its redox reaction with Ag^{+} and the induced luminescence change of the hybrid (Fig. 5.15B; bottom).

5.4.4 Precipitation reaction for luminescence response in chemical sensing

Xu et al. selected two Ln-MOFs to provide high color purity and accurate measurements, and Ag^{+}/Eu^{3+}@UiO-67 was the working luminescence center and Tb-MOF was the reference luminescence center [62]. The coordinated Ag^{+} reduced the efficiency of the energy transfer from UiO-67 to Eu^{3+}, which can be proven by quantum yields (4%) and luminescence lifetime study (undetectable) (Fig. 5.16; top). The reduced lifetime indicates a dynamic quenching mechanism and that the quenching is due to the interaction of Ag^{+} and the excited ligand molecule. Considering the strong affinity between Ag^{+} and Cl^{-} to bring about a precipitation reaction, they examined the potential of Ag^{+}/Eu^{3+}@UiO-67 for Cl^{-} detection. As shown in Fig. 5.16A–C (bottom),

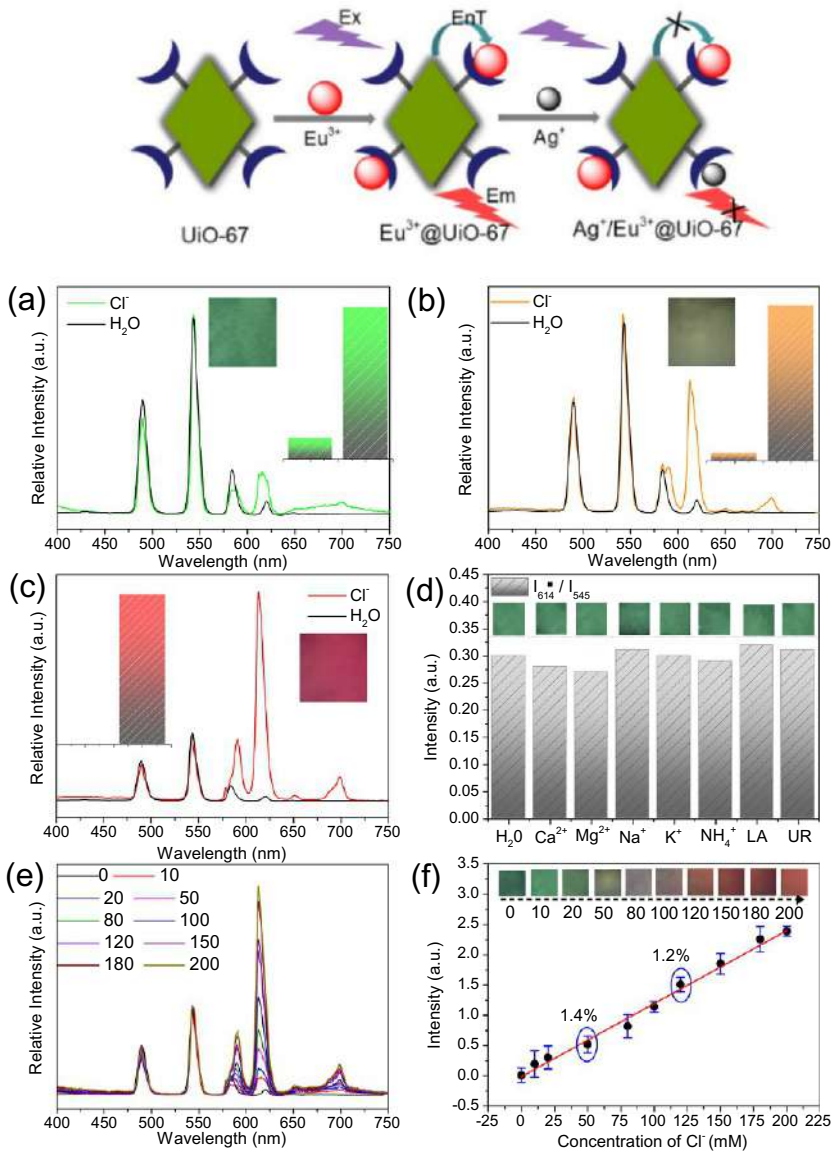

FIG. 5.16 *(Top)* Simplified illustration showing the Ag^+ induced luminescence quenching of Eu^{3+} in Ag^+/Eu^{3+}@UiO-67. *(Bottom)* Luminescence response of MCP-1 (A), MCP-2 (B), and MCP-3 (C) toward Cl^- (1 mL, 100 mM); the insets show the corresponding luminescence photographs and luminescence intensity of I_{614}/I_{545}; (D) luminescence response of MCP-2 toward various sweat components in their physiological level; the insets give the corresponding photographs; (E) concentration-dependent emission spectra of MCP-2 upon adding Cl^- (0–200 mM); (F) the linear fitted curve showing the luminescence intensity of I_{614}/I_{545} vs. Cl^- concentration for MCP-2; the insets show every concentration photograph; $\lambda_{ex} = 365$ nm and UV-light irradiation is 365 nm. *(Reproduced with permission from X. Xu, B. Yan, Fluorescent wearable platform for sweat Cl− analysis and logic smart-device fabrication based on color adjustable lanthanide MOFs. J. Mater. Chem. C 7 (2018) 1863–1869. Copyright 2017 RSC Society of Chemistry.)*

the presence of Cl^- triggers an apparent enhancement in the Eu^{3+} -based emission (24.6-fold for 614 nm). Under a UV lamp, a bright red color can be observed. By integrating DUT-101 with Ag^+/Eu^{3+}@UiO-67, a luminescence sensor to monitor Cl^- can be developed using Ag^+/Eu^{3+}@UiO-67 for the signal processing and DUT-101 for the signal calibration. In contrast to Cl^-, a color conversion cannot be observed for any of the added components under a 365-nm UV lamp (inset of Fig. 5.16D; bottom). The emission spectra are shown in Fig. 5.16E (bottom) and reflect the Cl^- sensor response to artificial sweat. Upon a gradual increase in the concentration of Cl^-, the Eu^{3+} emission intensity progressively increases, and the Tb^{3+}-based emission intensity is invariant. The luminescent colors of the sensing cotton piece change from green to yellow, and then orange and red as the Cl^- concentrations increase, under 365-nm UV light irradiation. As shown in Fig. 5.16F (bottom), a good linear correlation is observed over the concentration range, and the relationship can be fitted with a correlation coefficient (R^2) of 0.99752 with an LOD of 0.1 mM.

References

[1] S.A.A. Razavi, A. Morsali, Metal ion detection using luminescent-MOFs: principles, strategies and roadmap, Coord. Chem. Rev. 415 (2020) 213299.

[2] F.S. Wouters, Förster resonance energy transfer and fluorescence lifetime imaging, in: U. Kubitscheck (Ed.), Fluorescence Microscopy, 2017, https://doi.org/10.1002/9783527687732.ch13.

[3] S.Y. Wu, H. Min, W. Shi, P. Cheng, Multicenter metal-organic framework-based ratiometric fluorescent sensors, Adv. Mater. 32 (2020) 1805871.

[4] Y. Cui, Y. Yue, G. Qian, B. Chen, Luminescent functional metal-organic frameworks, Chem. Rev. 112 (2012) 1126–1162.

[5] J. Hao, B. Yan, Amino-decorated lanthanide (III)-organic extended frameworks for multicolor luminescence and fluorescence sensing, J. Mater. Chem. C 2 (2014) 6758–6764.

[6] Z. Zhou, Y. Han, X. Xing, S. Du, Microporous lanthanide metal-organic frameworks with multiple 1D channels: tunable colors, white-light emission, and luminescent sensing for iron(II) and iron(III), ChemPlusChem 81 (2016) 798–803.

[7] S. Dang, T. Wang, F. Yi, Q. Liu, W. Yang, Z. Sun, A nanoscale multiresponsive luminescent sensor based on a terbium(III) metal-organic framework, Chem. Eur. J. 10 (2015) 1703–1709.

[8] W. Liu, X. Huang, C. Xu, C. Chen, L. Yang, W. Dou, W. Chen, H. Yang, W. Liu, A multi-responsive regenerable europium-organic framework luminescent sensor for Fe^{3+}, CrVI anions, and picric acid, Chem. Eur. J. 22 (2016) 18769–18776.

[9] L. Cao, F. Shi, W. Zhang, S. Zang, T. Mak, Selective sensing of Fe^{3+} and Al^{3+} ions and detection of 2,4,6-trinitrophenol by a water-stable terbium-based metal-organic framework, Chem. Eur. J. 21 (2015) 15705–15712.

[10] B. Liu, C. Sun, Y. Chen, Nucleotide/Tb^{3+} coordination polymer as a luminescent nanosensor: synthesis and sensing of iron(II) in human serum, J. Mater. Chem. B 2 (2014) 1661–1666.

[11] Y. Kang, X. Zheng, L. Jin, A microscale multi-functional metal-organic framework as a fluorescence chemosensor for Fe(III), Al(III) and 2-hydroxy-1-naphthaldehyde, J. Colloid Interface Sci. 471 (2016) 1–6.

[12] K. Müller-Buschbaum, F. Beuerle, C. Feldmann, MOF based luminescence tuning and chemical/physical sensing, Microporous Mesoporous Mater. 216 (2015) 171–199.

[13] Y. Zhang, S. Yuan, G. Day, X. Wang, X. Yang, H. Zhou, Luminescent sensors based on metal-organic frameworks, Coord. Chem. Rev. 354 (2018) 28–45.
[14] T. Rasheed, F. Nabeel, Luminescent metal-organic frameworks as potential sensory materials for various environmental toxic agents, Coord. Chem. Rev. 401 (2019) 213065.
[15] H. Yin, X. Yin, Metal – organic frameworks with multiple luminescence emissions: designs and applications, Acc. Chem. Res. 53 (2020) 485–495.
[16] T. Gorai, W. Schmitt, T. Gunnlaugsson, Highlights of the development and application of luminescent lanthanide based coordination polymers, MOFs and functional nanomaterials, Dalton Trans. 50 (2021) 770–784.
[17] B. Yan, Luminescence response mode and chemical sensing mechanism for lanthanide functionalized metal-organic frameworks hybrids, Inorg. Chem. Front. 8 (2021) 201–233.
[18] J. Rocha, L.D. Carlos, F.A. Almeida Paza, D. Ananiasa, Luminescent multifunctional lanthanides-based metal-organic frameworks, Chem. Soc. Rev. 40 (2011) 926–940.
[19] J. Hao, X. Xu, H. Fei, L. Li, B. Yan, Functionalization of metal-organic frameworks for photoactive materials, Adv. Mater. 30 (2018) 1705634.
[20] X. Song, S. Song, H. Zhang, in: P. Cheng (Ed.), Lanthanide Metal–Organic Frameworks, Springer Publishers, 2015, pp. 109–144.
[21] J. Xiao, L. Song, M. Liu, X. Wang, Z. Liu, Intriguing pH-modulated luminescence chameleon system based on postsynthetic modified dual-emitting Eu^{3+}@Mn-MOF and its application for histidine chemosensor, Inorg. Chem. 59 (2020) 6390–6397.
[22] L.E. Kreno, K. Leong, O.K. Farha, M. Allendorf, R.P. Van Duyne, J.T. Hupp, Metal-organic framework materials as chemical sensors, Chem. Rev. 112 (2012) 1105–1125.
[23] F. Yi, D. Chen, M. Wu, L. Han, H. Jiang, Chemical sensors based on metal-organic frameworks, ChemPlusChem 81 (2016) 67–690.
[24] I. Stassen, N. Burtch, A. Talin, P. Falcaro, D.M. Allendorfc, R. Ameloot, An updated roadmap for the integration of metal-organic frameworks with electronic devices and chemical sensors, Chem. Soc. Rev. 46 (2017) 3185–3241.
[25] W.P. Lustig, S. Mukherjee, N.D. Rudd, A.V. Desai, J. Li, S.K. Ghosh, Metal-organic frameworks: functional luminescent and photonic materials for sensing applications, Chem. Soc. Rev. 46 (2017) 3242–3285.
[26] E.A. Dolgopolova, A.M. Rice, C.R. Martin, N.B. Shustova, Photochemistry and photophysics of MOFs: steps towards MOF-based sensing enhancements, Chem. Soc. Rev. 47 (2018) 4710–4728.
[27] S.A. Diamantis, A. Margariti, A.D. Pournara, G.S. Papaefstathiou, M.J. Manos, T. Lazarides, Luminescent metal-organic frameworks as chemical sensors: common pitfalls and proposed best practices, Inorg. Chem. Front. 5 (2018) 1493–1511.
[28] Q. Yu, Z. Li, Q. Cao, S. Qu, Q. Jia, Advances in luminescent metal-organic framework sensors based on post-synthetic modification, Trends Anal. Chem. 129 (2020) 115939.
[29] Y. Hao, S. Chen, Y. Zhou, Y. Zhang, M. Xu, Recent progress in metal-organic framework (MOF) based luminescent chemodosimeters, Nanomaterials 9 (2019) 974.
[30] L. Chen, D. Liu, J. Peng, Q. Du, H. He, Ratiometric fluorescence sensing of metal-organic frameworks: tactics and perspectives, Coord. Chem. Rev. 404 (2020) 213113.
[31] J. Heine, K. Mueller-Buschbaum, Engineering metal-based luminescence in coordination polymers and metal-organic frameworks, Chem. Soc. Rev. 42 (2013) 9232–9242.
[32] Y. Zhang, X. Lian, B. Yan, A point-of-care diagnostics logic detector based on glucose oxidase immobilized lanthanide functionalized metal-organic frameworks, J. Mater. Chem. C 8 (2020) 3023–3028.
[33] J. Hau, B. Yan, Ag^{+}-sensitized lanthanide luminescence in Ln^{3+} post-functionalized metal-organic frameworks and Ag^{+} sensing, J. Mater. Chem. C 3 (2015) 4788–4792.

[34] X. Peng, G. Bao, Y. Zhong, L. Zhang, K. Zeng, J. He, W. Xiao, Y. Xia, Q. Fan, H. Yuan, Highly sensitive and rapid detection of thiabendazole residues in oranges based on a luminescent Tb^{3+}-functionalized MOF, Food Chem. 343 (2021) 128504.

[35] J. Liu, Z. Luo, Y. Pan, A.K. Singh, M. Trivedi, A. Kumar, Recent developments in luminescent coordination polymers: designing strategies, sensing application and theoretical evidences, Coord. Chem. Rev. 406 (2020) 213145.

[36] B. Wang, Q. Yang, C. Guo, Y. Sun, L.H. Xie, J.R. Li, Stable Zr(IV)-based metal-organic frameworks with predesigned functionalized ligands for highly selective detection of Fe(III) ions in water, ACS Appl. Mater. Interfaces 9 (2017) 10286–10295.

[37] S. Bej, R. Das, N. Murmu, P. Banerjee, Selective identification and encapsulation of biohazardous m-xylene among a pool of its other constitutional C_8 alkyl isomers by luminescent d^{10} MOFs: a combined theoretical and experimental study, Inorg. Chem. 59 (2020) 4366–4376.

[38] L. Fan, F. Wang, D. Zhao, Y. Peng, Y. Deng, Y. Luo, X. Zhang, A self-penetrating and chemically stable zinc (II)-organic framework as multi-responsive chemo-sensor to detect pesticide and antibiotics in water, Appl. Organomet. Chem. (2020) e5960.

[39] Y. Tang, H. Wu, J. Chen, J. Jia, J. Yu, W. Xu, Y. Fu, Q. He, H. Cao, J. Cheng, A highly fluorescent metal organic framework probe for 2,4,6-trinitrophenol detection via post-synthetic modification of UiO-66-NH_2, Dyes Pigments 167 (2019) 10–15.

[40] S. Yang, W. Zhao, P. Hu, K. Wu, Z. Jiang, L. Bai, M. Li, J. Chen, Lanthanum-based metal-organic frameworks for specific detection of Sudan virus RNA conservative sequences down to single-base mismatch, Inorg. Chem. 56 (2017) 14880–14887.

[41] X. Lian, B. Yan, Antineoplasticmitoxantrone monitor: a sandwimixed matrix membrane (MMMs) based on luminescent MOFs-hydrogel hybrid, Sens. Actuators B Chem. 281 (2019) 168–174.

[42] Z. Ding, C. Wang, S. Wang, L. Wu, X. Zhang, Light-harvesting metal-organic framework nanoprobes for ratiometric fluorescence energy transfer-based determination of pH values and temperature, Microchim. Acta 186 (2019) 476.

[43] A. Afzalinia, M. Mirzaee, Ultrasensitive fluorescent miRNA biosensor based on a "sandwich" oligonucleotide hybridization and fluorescence resonance energy transfer process using an Ln (III)-MOF and Ag nanoparticles for early cancer diagnosis: application of central composite design, ACS Appl. Mater. Interfaces 12 (2020) 16076–16087.

[44] F. Qu, Y. Ding, X. Lv, L. Xia, J. You, W. Han, Emissions of terbium metal-organic frameworks modulated by dispersive/agglomerated gold nanoparticles for the construction of prostate-specific antigen biosensor, Anal. Bioanal. Chem. 411 (2019) 3979–3988.

[45] C. Sun, S. Zhao, F. Qu, W. Han, J. You, Determination of adenosine triphosphate based on the use of fluorescent terbium(III) organic frameworks and aptamer modified gold nanoparticles, Microchim. Acta 187 (2020) 34.

[46] L. Cao, H. Li, H. Xu, Y. Wei, S. Zang, Diverse dissolution-recrystallization structural transformations and sequential Förster resonance energy transfer behavior of a luminescent porous Cd-MOF, Dalton Trans. 46 (2017) 11656–11663.

[47] A. Khatun, D.K. Panda, N. Sayresmith, M.G. Walter, S. Saha, Thiazolothiazole-based luminescent metal-organic frameworks with ligand-to-ligand energy transfer and Hg^{2+}-sensing capabilities, Inorg. Chem. 58 (2019) 12707–12715.

[48] H. Cai, W. Lu, C. Yang, M. Zhang, M. Li, C. Che, D. Li, Tandem Föster resonance energy transfer induced luminescent ratiometric thermometry in dye-encapsulated biological metal-organic frameworks, Adv. Opt. Mater. 7 (2019) 1801149.

[49] J. Xiao, J. Liu, M. Liu, G. Ji, Z. Liu, Fabrication of a luminescence-silent system based on a post-synthetic modification Cd-MOFs: a highly selective and sensitive turn-on luminescent probe for ascorbic acid detection, Inorg. Chem. 58 (2019) 6167–6174.
[50] C. Xia, Y. Xu, M. Cao, Y. Liu, J. Xia, D. Jiang, G. Zhou, R. Xie, D. Zhang, H. Li, A selective and sensitive fluorescent probe for bilirubin in human serum based on europium(III) post-functionalized Zr(IV)-based MOFs, Talanta 212 (2020) 120795.
[51] J. Hao, B. Yan, Determination of urinary 1-hydroxypyrene for biomonitoring of human exposure to polycyclic aromatic hydrocarbons carcinogens by a lanthanide-functionalized metal-organic framework sensor, Adv. Funct. Mater. 27 (2017) 1603856.
[52] X. Lian, Y. Zhang, J. Wang, B. Yan, Antineoplastic mitoxantrone monitor: a sandwich mixed matrix membrane (MMMs) based on luminescent MOFs-hydrogel hybrid, Inorg. Chem. 59 (2020) 10304–10310.
[53] S. Khan, P. Das, S.K. Mandal, Design and construction of a luminescent and highly stable 3D metal-organic framework with a $[Zn_4(\mu_3\text{-}OH)_2]^{6+}$ core, Inorg. Chem. 59 (2020) 4588–4600.
[54] H. Zhu, J. Huang, Q. Zhou, Z. Lv, C. Li, G. Hu, Enhanced luminescence of NH_2-UiO-66 for selectively sensing fluoride anion in water medium, J. Lumin. 208 (2019) 67–74.
[55] A. Sharma, D.W. Kim, J.H. Park, S. Rakshit, J. Seong, G.H. Jeong, O.H. Kwon, M.S. Lah, Mechanistic insight into the sensing of nitroaromatic compounds by metal-organic frameworks, Commun. Chem. 2 (2019) 39.
[56] L. Liu, X. Chen, J. Qiu, C. Hao, New insights into the nitroaromatics detection mechanism of the luminescent metal-organic framework sensor, Dalton Trans. 44 (2015) 2897–2906.
[57] A.A. Tehrani, H. Abbasi, L. Esrafili, A. Morsali, Urea-containing metal-organic frameworks for carbonyl compounds sensing, Sensors Actuators B Chem. 256 (2018) 706–710.
[58] V. Pentyala, P. Davydovskaya, M. Ade, R. Pohle, G. Urban, Metal-organic frameworks for alcohol gas sensor, Sensors Actuators B Chem. 222 (2016) 904–909.
[59] A. Mallick, A.M. El-Zohry, O. Shekhah, J. Yin, J.T. Jia, H. Aggarwal, A.H. Emwas, O.F. Mohammed, M. Eddaoudi, Unprecedented ultralow detection limit of amines using a thiadiazole-functionalized Zr(IV)-based metal-organic framework, J. Am. Chem. Soc. 141 (2019) 7245–7249.
[60] J. Hao, B. Yan, Simultaneous determination of indoor ammonia pollution and its biological metabolite in human body by use of a recyclable nanocrystalline lanthanide functionalized MOF, Nanoscale 8 (2016) 2881–2886.
[61] X. Lian, T. Miao, X. Xu, C. Zhang, B. Yan, Eu^{3+} functionalized Sc-MOFs: turn-on fluorescent switch for ppb-level biomarker of plastic pollutant polystyrene, Biosens. Bioelectron. 97 (2017) 299–304.
[62] J. Hao, B. Yan, A dual-emitting 4d-4f metal-organic framework as a self-calibrating luminescent sensor for indoor formaldehyde pollution, Nanoscale 8 (2016) 12047–12053.

Part III

Rare earth metal-organic frameworks hybrid materials as luminescence response chemical sensors for typical ionic analytes

Chapter 6

Rare earth metal-organic framework hybrid materials for luminescence responsive chemical sensing of metal ions (I)

6.1 Luminescence responsive sensing of Fe^{3+} using rare earth metal-organic framework hybrid materials

Iron species are essential for virtually all organisms due to their functions as a cofactor in central cellular processes such as respiration, DNA synthesis and repair, ribosome biogenesis, and metabolism, among others. In this regard, how to effectively probe the iron ion becomes a challenging issue, particularly with the emergence of fluorescent imaging technology. Biological iron species are commonly found in the +2 (ferrous) and +3 (ferric) oxidation states. Designing a sensor with specificity for ferrous over ferric is difficult, due to iron's propensity for oxidation within aqueous and aerobic conditions. A luminescent probe to detect Fe^{3+} in environmental and biological systems mainly depends on the quenching effect on luminescence of MOFs by metal cations, which originates from three approaches: the interaction between metal cations and organic ligands, the collapse of the crystal structure by metal cations, and the cation exchange of central cations in a framework with targeted cations. The sensing of Fe^{2+} and even both Fe^{2+} and Fe^{3+} or Fe^{2+} against Fe^{3+} is expected to be studied deeply. The sensing of Fe^{3+} is universal and there are many probes based on rare earth MOF hybrid material systems [1–58].

Zhou et al. demonstrated a strategy to fabricate a luminescent rare earth functionalized MOF by encapsulating Eu^{3+} cations in the pores of MIL-53-COOH (Al) nanocrystals (Al-MOF) [2], which was developed as a highly selective and sensitive probe for detection of Fe^{3+} in aqueous solutions. In addition, the possible sensing mechanism is based on cation exchange between Fe^{3+} and the framework Al^{3+} in Al-MOF. Luminescent responses of Eu^{3+}@Al-MOF toward aqueous solutions of various metal cations can be seen in Al-MOF. Only Fe^{3+} shows a significant quenching effect on the luminescence. The remarkable quenching effect can be further confirmed by the photograph of the Eu^{3+}@Al-MOF suspension under UV-light irradiation (Fig. 6.1A; top). The emitted

Rare Earth Metal-Organic Framework Hybrid Materials for Luminescence Responsive Chemical Sensors
https://doi.org/10.1016/B978-0-323-91236-5.00016-5

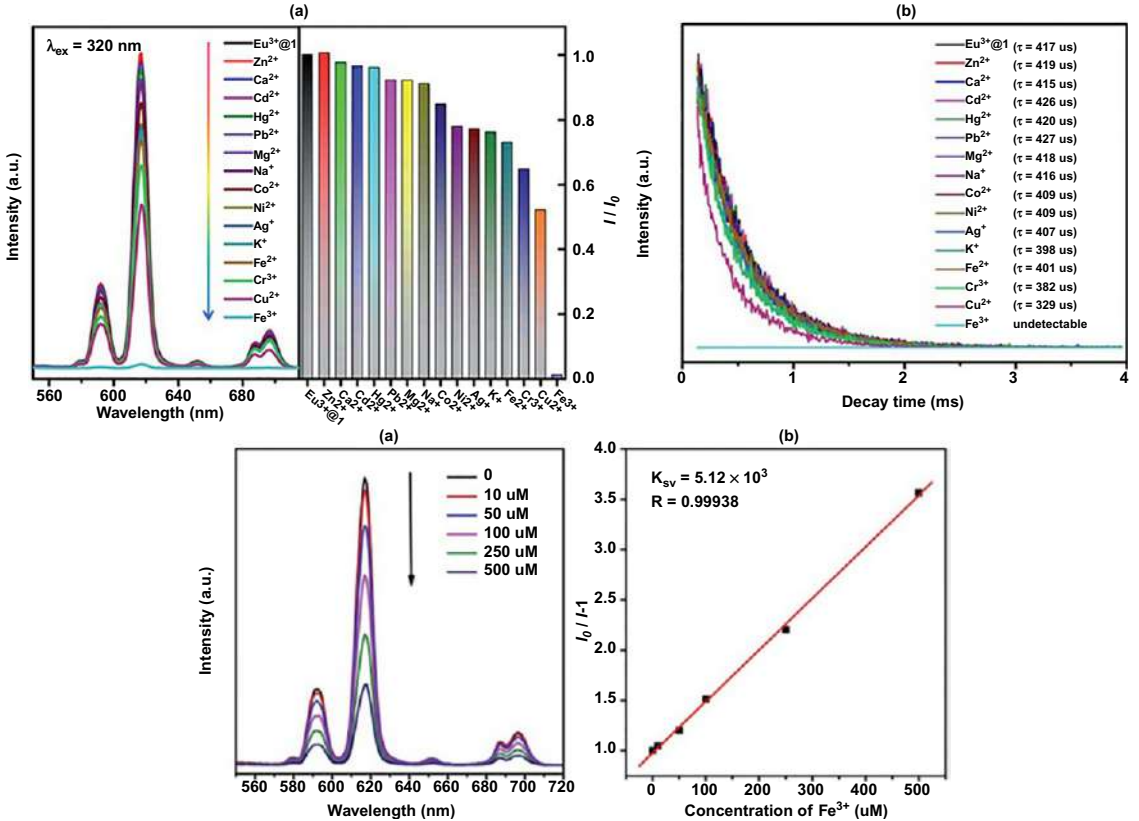

FIG. 6.1 *(Top)* Responses of the fluorescence (A) and lifetime (B) of Eu^{3+}@Al-MOF (0.4 mg L^{-1}) toward aqueous solution of various metal cations (5 mM). Both the emission spectra and lifetimes were collected at the excitation wavelength of 320 nm. I and I_0 denote the fluorescence intensity of Eu^{3+}@Al-MOF with and without metal ions of interest, respectively. *(Bottom)* Emission spectra (A) and K_{sv} curve (B) of Eu^{3+}@Al-MOF (0.4 g L^{-1}) nanocrystals in aqueous solutions in the presence of various concentrations of Fe^{3+} under excitation at 320 nm (Al-MOF = MIL-53-COOH). *(Reproduced with permission from Y. Zhou, H. Chen, B. Yan, An Eu3+ post-functionalized nanosized metal-organic framework for cation exchange-based Fe3+-sensing in an aqueous environment. J. Mater. Chem. A 2 (2014) 13691–13697. Copyright 2015 Royal Chemical Society.)*

visible red light of the Eu^{3+}@Al-MOF suspension is essentially completely quenched when in contact with the aqueous solution of Fe^{3+}. These results indicate the high selectivity of Eu^{3+}@Al-MOF for the sensing and specific recognition of Fe^{3+} in an aqueous environment. In addition, the quenching effect of Fe^{3+} on the luminescence of Eu^{3+}@Al-MOF is evaluated by the fluorescence decay time of Eu^{3+} (Fig. 6.1B; top). Cu^{2+} and Fe^{3+} exhibit varying degrees of decline in the fluorescence lifetime. A luminescence titration upon the addition of $Fe(NO_3)_3$ to Eu^{3+}@Al-MOF was further conducted (Fig. 6.1A; bottom), and the emission intensity of the Eu^{3+}@Al-MOF suspension declined sharply with the increase of Fe^{3+} concentration from 0 to 0.5 mM. Fig. 6.1B (bottom) shows the K_{sv} curve of Eu^{3+}@Al-MOF nanocrystals with Fe^{3+}. The linear correlation coefficient (R) is 0.99938. The K_{sv} value is calculated as 5.12×10^3, which reveals a strong quenching effect on the Eu^{3+}@Al-MOF luminescence. It is speculated that a static quenching process is dominant because the absorption spectrum of Eu^{3+}@Al-MOF shows an obvious difference after contact with Fe^{3+}. The limit of detection (LOD) for Fe^{3+} was determined as 0.5 mM, whose low value meets the requirements for intracellular sensing and imaging of Fe^{3+} [2].

.

Shen et al. prepared the Eu^{3+} ion modified bio-MOF-1 by ionic exchange and further introduced some ligands (TTA) by gas diffusion ("ship-in-bottle") to improve the luminescence first (Fig. 6.2; top, left), after which they studied its application in the sensing of metal ions [4]. The relative intensities of $^5D_0 \rightarrow {}^7F_2$ at 616 nm from their suspension-state photoluminescent spectra are shown in Fig. 6.2 (top, right). Both Cr^{3+} and Cu^{2+} produced the marked quenching of the luminescent intensity of Eu^{3+}@ bio-MOF-1 hybrids. In particular, the introduction of Fe^{3+} almost quenches the luminescence of Eu^{3+}@ bio-MOF-1 hybrids. These results may be related to the interaction between different metal ions and bio-MOF-1 and the exchange of Eu^{3+}. On checking the Eu^{3+} content of Eu^{3+}@bio-MOF-1 after sensing of Fe^{3+}, it decreased from 1.52% to 1.29%, suggesting the exchange reaction between Eu^{3+} and Fe^{3+}. In Fig. 6.2A (bottom), the luminescence intensity of Eu^{3+} decreases gradually while the concentration of Fe^{3+} is increasing. When the concentration reaches 1 mmol L^{-1}, the emission intensity of Eu^{3+} is sharply weakened. Fig. 6.2B (bottom) shows the K_{sv} curve of Eu^{3+}@ bio-MOF-1 with Fe^{3+}. The linear correlation coefficient (R) is 0.994 with the linear range from 0 to 500 μmol/L. The K_{sv} value is calculated as 3.38×10^3, which reveals a strong quenching effect on the Eu^{3+}@ bio-MOF-1 luminescence.

Xing et al. used an Eu-MOF, $[H_2N(Me)_2][Eu_3(OH)(bpt)_3(H_2O)_3](DMF)_2{\cdot}(H_2O)_4$ with a one-dimensional (1D) channel from the rare trinuclear $[Eu_3(OH)(COO)_9]$ clusters and biphenyl-3,4,5-tricarboxylic acid (H_3bpt), which is a promising luminescent probe for sensing Fe^{3+} in aqueous solution [15]. The resulting suspensions were analyzed by using a luminescence spectrophotometer, and the highest intensities at 612 nm are presented in Fig. 6.3A. A considerable quenching effect for Fe^{3+} was observed, the other

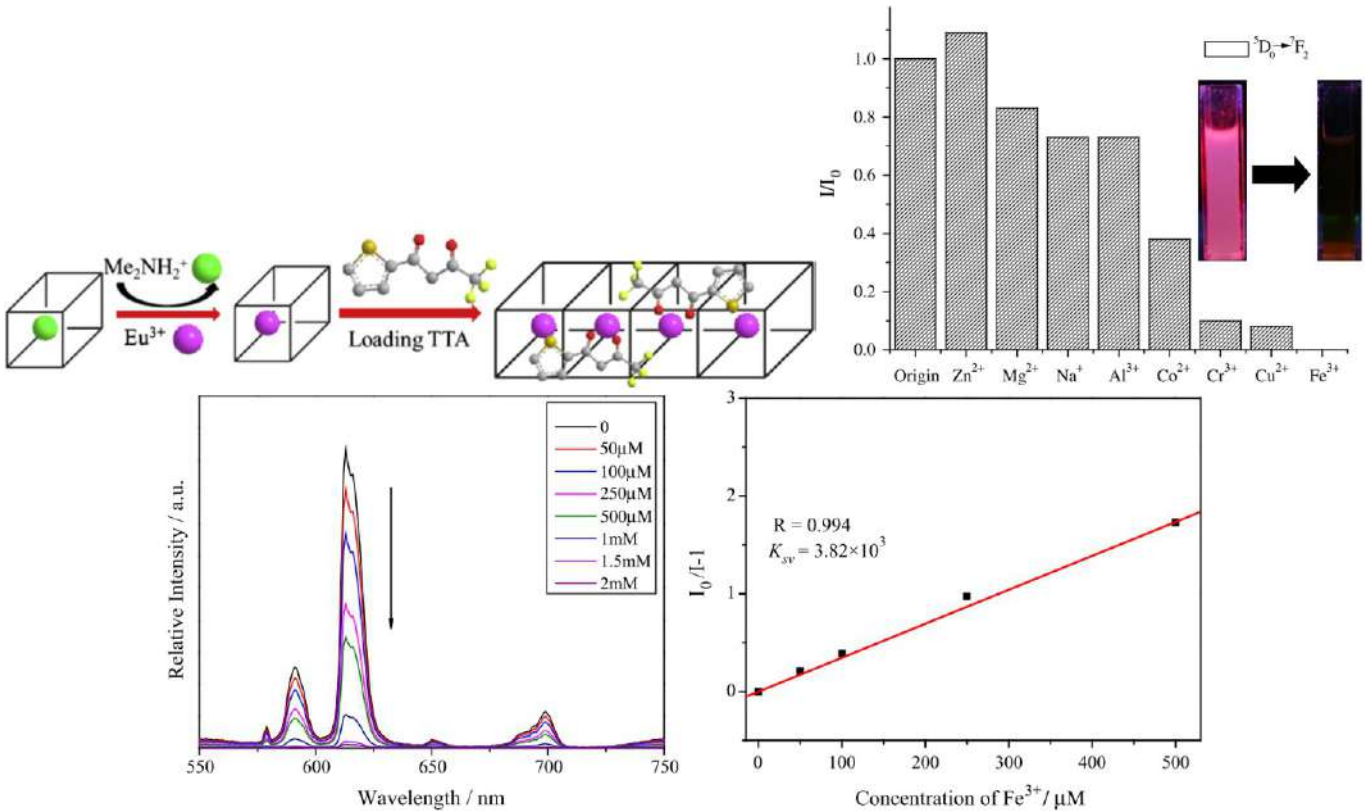

FIG. 6.2 *(Top) (Left)* The selected scheme for the synthesis procedures of Eu^{3+} functionalized bio-MOF-1 (Eu^{3+}@bio-MOF-1) via cation exchange and the encapsulation of TTA with the "ship-in-bottle" method; *(Right)* The relative intensities of $^5D_0 \rightarrow {}^7F_2$ at 616 nm for Eu^{3+}@bio-MOF-1 in different metal ion DMF solutions when excited at 332 nm. *(Bottom)* Emission spectra (A) and K_{sv} curve (B) of Eu^{3+}@ bio-MOF-1 in various concentrations of Fe^{3+} aqueous solutions under excitation at 317 nm. *(Reproduced with permission from X. Shen, B. Yan, Photofunctional hybrids of lanthanide functionalized bio-MOF-1 for fluorescence tuning and sensing. J. Colloid Interface Sci. 451 (2015) 63–68. Copyright 2015 Elsevier.)*

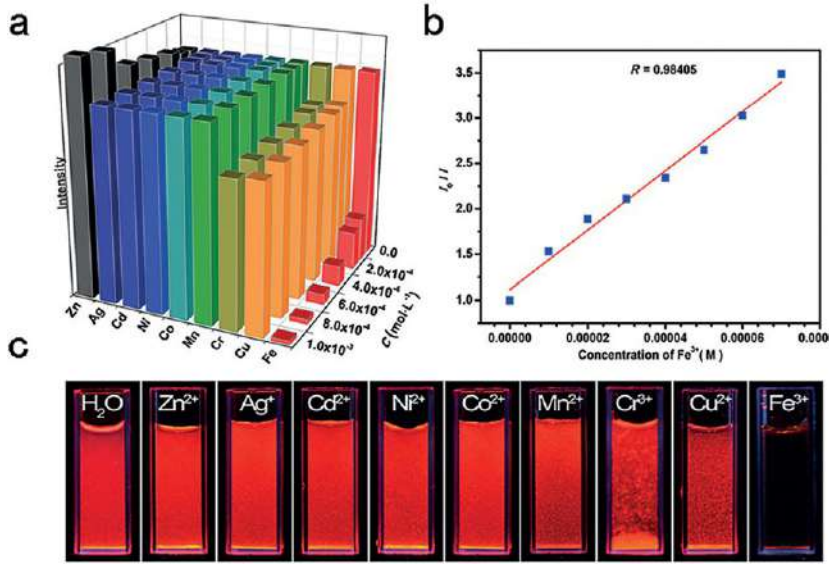

FIG. 6.3 (A) Luminescence intensities of Eu-MOF dispersed in aqueous solutions containing different metal ions at different concentrations. (B) Stern-Volmer (SV) plot for Fe^{3+}. (C) Digital photographs of solutions of Eu-MOF in the presence of different metal ions under a portable UV light. *(Reproduced with permission from S. Xing, Q. Bing, L. Song, G. Li, J. Liu, Z. Shi, S. Feng, R. Xu, The uncommon channel-based Ln-MOFs for highly selective Fe3 + detection and superior rhodamine B adsorption. Chem. A Eur. J. 2016, 22 (201) 16230–16235. Copyright 2016 Wiley.)*

metal ions having no significant effect on the luminescence intensity of Eu-MOF. The luminescence intensity of Eu-MOF was reduced by 98.5% at a concentration of 0.01 M of Fe^{3+} compared with that in its absence, indicating that this can be considered as a highly selective sensor for Fe^{3+} ions. The selectivity for Fe^{3+} was confirmed by photographs showing the response of Eu-MOF to different metal ions (Fig. 6.3C). The quenching efficiency can be quantitatively estimated by K_{sv}, with the value of K_{sv} for Fe^{3+} being 32,666 M^{-1} (Fig. 6.3B). The emission quenching results demonstrate that the pathway from the ligand to the emissive center is blocked upon the addition of Fe^{3+}.

Li et al. prepared Eu^{3+} postfunctionalized UiO-66-type MOF through a facile hydrothermal approach and developed it as a highly selective luminescent sensor for probing Fe^{3+} in aqueous solution (Fig. 6.4 (top, left)). The free carboxylic acids can be readily modulated by tunable defects in assembling a UiO-66 framework and treated as the PSM sites. In order to identify the potential of Eu^{3+}@UiO-66(20) toward sensing of metal ions, the luminescence spectra of the MOF suspension were recorded upon addition of different metal ions. As shown in Fig. 6.4 (top, right), among the tested cations, only the Fe^{3+} ion induced a distinct quenching effect on the fluorescence of Eu^{3+}@UiO-66 (20). A concentration-dependent fluorescence titration experiment was carried

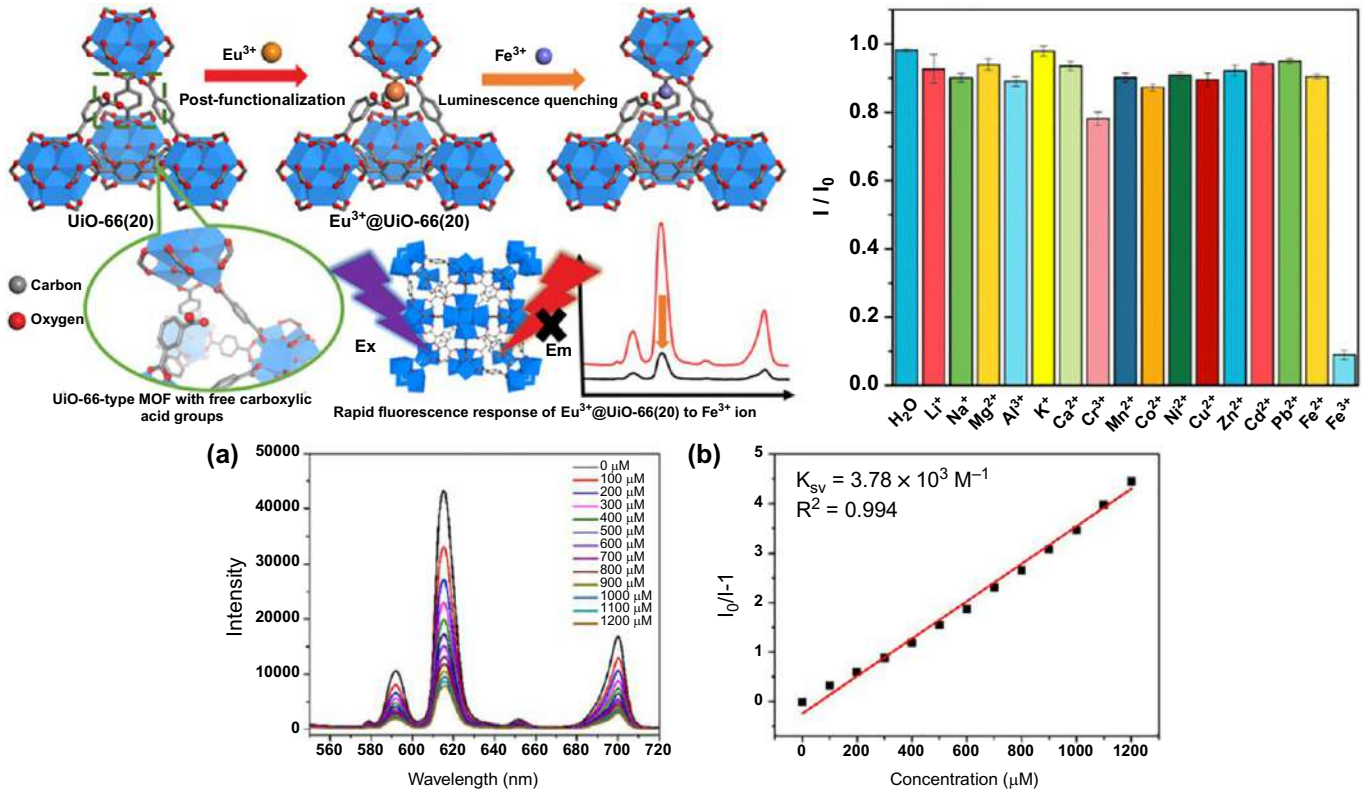

FIG. 6.4 *(Top, Left)* Schematic description of the process for sensing Fe^{3+} based on the luminescence. *(Top, Right)* Photoluminescence intensity of the $^5D_0 \rightarrow {}^7F_2$ transition ($\lambda_{em} = 615$ nm) of Eu^{3+}@UiO-66(20) treated with different metal ions (1 mM) in aqueous solution. *(Bottom)* (A) The fluorescent emission spectra of Eu^{3+}@UiO-66(20) in the presence of different concentrations of Fe^{3+} ion from 0 to 1200 μM; (B) Linear relationship of a fluorescence intensity at 615 nm as a function of Fe^{3+} ion concentration. *(Reproduced with permission from L. Li, S. Shen, W. Ai, S. Song, Y. Bai, H. Liu, Facilely synthesized Eu3+ post-functionalized UiO-66-type metal-organic framework for rapid and highly selective detection of Fe3+ in aqueous solution. Sens. Actuators B 267 (2018) 542–548. Copyright 2018 Elsevier.)*

out. As demonstrated in Fig. 6.4A (bottom), the luminescence intensity of the $^5D_0 \rightarrow {}^7F_2$ transition at 615 nm gradually quenched upon the addition of different concentrations of Fe^{3+} from 0 to 1200 μM. Fig. 6.4B (bottom) shows the K_{sv} curve of Eu^{3+}@UiO-66(20) with the Fe^{3+} ion. The linear correlation coefficient (R^2) is 0.994 and the quenching coefficient K_{sv} value is calculated as $3.78 \times 10^3\ M^{-1}$, which reveals a strong quenching effect on the MOF. The LOD for Fe^{3+} is determined as 12.8 μM. The quenching process follows a static mechanism rather than a dynamic mechanism. It may be a competition of absorption of the light source energy and the electronic interaction between the Fe^{3+} and benzene dicarboxylate moieties. The adsorbed Fe^{3+} ions on MOF effectively filter the light, also decreasing the probability of energy transfer from organic ligands to Eu^{3+} and subsequently quenching the luminescence of the Eu^{3+} ion.

Sheta et al. reported a La-MOF $[La(AIP)(Phen)(H_2O)_2(DMF)_2(Cl)_2]_n$ constructed from the reaction of π-electron-rich rigid ligand 5-amino-isophthalic acid (AIP) and 1,2-phenylenediamine (Phen), whose strong emission was efficiently quenched by addition of Fe^{3+} traces, even in the presence of other metal ions. Moreover, this study was extended to detect Fe^{3+} in both pure water and wastewater [38]. As shown in Fig. 6.5A, the La-MOFs show a red-shifted emission, whose luminescent behavior can be attributed to π-π* and π-n molecular orbital transitions within the aromatic rings of the carboxylate and diamine ligands. As shown in Fig. 6.5B, only Fe^{3+} induces a strong level of quenching for the luminescent intensity of La-MOF-M1, whereas the others have a slightly decreased or increased effect or a negligible effect on the emission intensities. Meanwhile, Fig. 6.5B shows a quenching and efficiency enhancing diagram, which indicates a highly selective sensing of Fe^{3+} by La-MOF through the quenching effect. As shown in Fig. 6.5C, the emission intensity of La-MOF is significantly quenched as the Fe^{3+} concentration increases. The linear correlation between PL intensity of La-MOF at $\lambda_{em} = 558$ nm and concentration of the Fe^{3+} in the given range from 1.0 μM to 500 μM is represented in (Fig. 6.5D) and the inset shows the luminescence quenching histogram of La-MOF upon the Fe^{3+} concentration increasing. The LOD is found to be 1.35 μM, and the LOQ equal to 4.08 μM, whereas the dynamic linear range is 18–450 μM. The luminescent spectra of La-MOF upon progressive addition of Fe^{3+} are recorded as shown in (Fig. 6.5C). In this system, La-MOF acts as a donor and Fe^{3+} acts as an acceptor. Hence, the change in PL intensity of La-MOF upon addition of Fe^{3+} is due to an interaction between La-MOF and Fe^{3+} (quenching phenomena). By applying the Stern-Völmer equation in the obtained data and from the linear calibration curve (Fig. 6.5D), it is calculated that the critical transfer distance is 1.49 Å. The quenching mechanism is an efficient energy transfer between the donor and acceptor that may take place, which is in good agreement with the mechanism of FRET occurring during the donor-acceptor interaction. The slopes of the La-MOF plots being directly proportional to the temperature indicates a dynamic type quenching mechanism between La-MOF and Fe^{3+}.

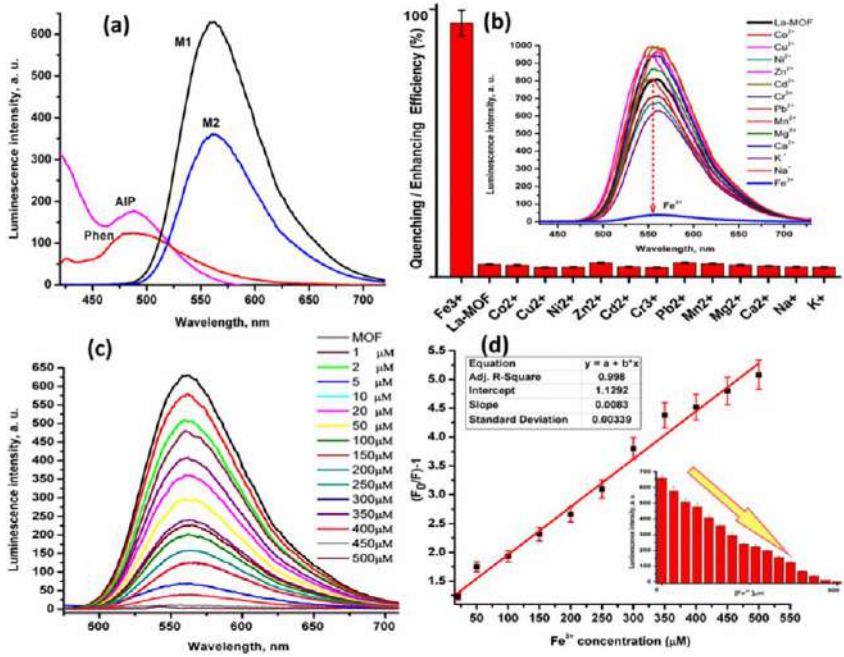

FIG. 6.5 (A) The luminescent spectra of La-MOFs (M1 & M2), AIP, and Phen; (B) The luminescent quenching efficiency histogram of La-MOF (inset is the luminescent spectra of La-MOF upon exposure to 0.4 mM concentration of different metal ions); (C) The PL spectra of La-MOF titration upon incremental addition of different concentrations of Fe^{3+}; (D) The linear relationship between emission intensity of La-MOF and different concentrations of Fe^{3+} (inset is the luminescent quenching histogram of La-MOF). *(Reproduced with permission from S. M. Sheta, S. M. El-Sheikh, M. M. Abd-Elzaher, A. R. Wassel, A novel nano-size lanthanum metal-organic framework based on 5-amino-isophthalic acid and phenylenediamine: photoluminescence study and sensing applications. Appl. Organomet. Chem. 33 (2019) e4777. Copyright 2019 Wiley.)*

6.2 Luminescence responsive sensing of Fe^{2+} or Fe^{3+}/Fe^{2+} using rare earth metal-organic framework hybrid materials

The sensing of Fe^{2+} and even both Fe^{2+} and Fe^{3+} or Fe^{2+} against Fe^{3+} are expected to be studied deeply [58–62]. Liu et al. constructed a luminescent nucleotide/Tb^{3+} MOF with a recognition function for Fe^{2+} ions by means of the component flexibility of MOFs (as shown in Fig. 6.6; top, left). The fluorescent response of Tb-ADP-Phen to Fe^{2+} in aqueous solution is shown. In the presence of Fe^{2+}, the fluorescence of Tb-ADP-Phen is strongly quenched. Approximately 30 nM Fe^{2+} can produce an obvious reduction of fluorescence (signal/noise ratio > 3: 1) (Fig. 6.7; top, right). The fluorescence intensity of Tb-ADP-Phen gradually decreases with an increase in Fe^{2+} concentration, and there is a good linear correlation in the concentration range of 30 nM^{-3} mM Fe^{2+} (inset of Fig. 6.6; top, right). The LOD is approximately

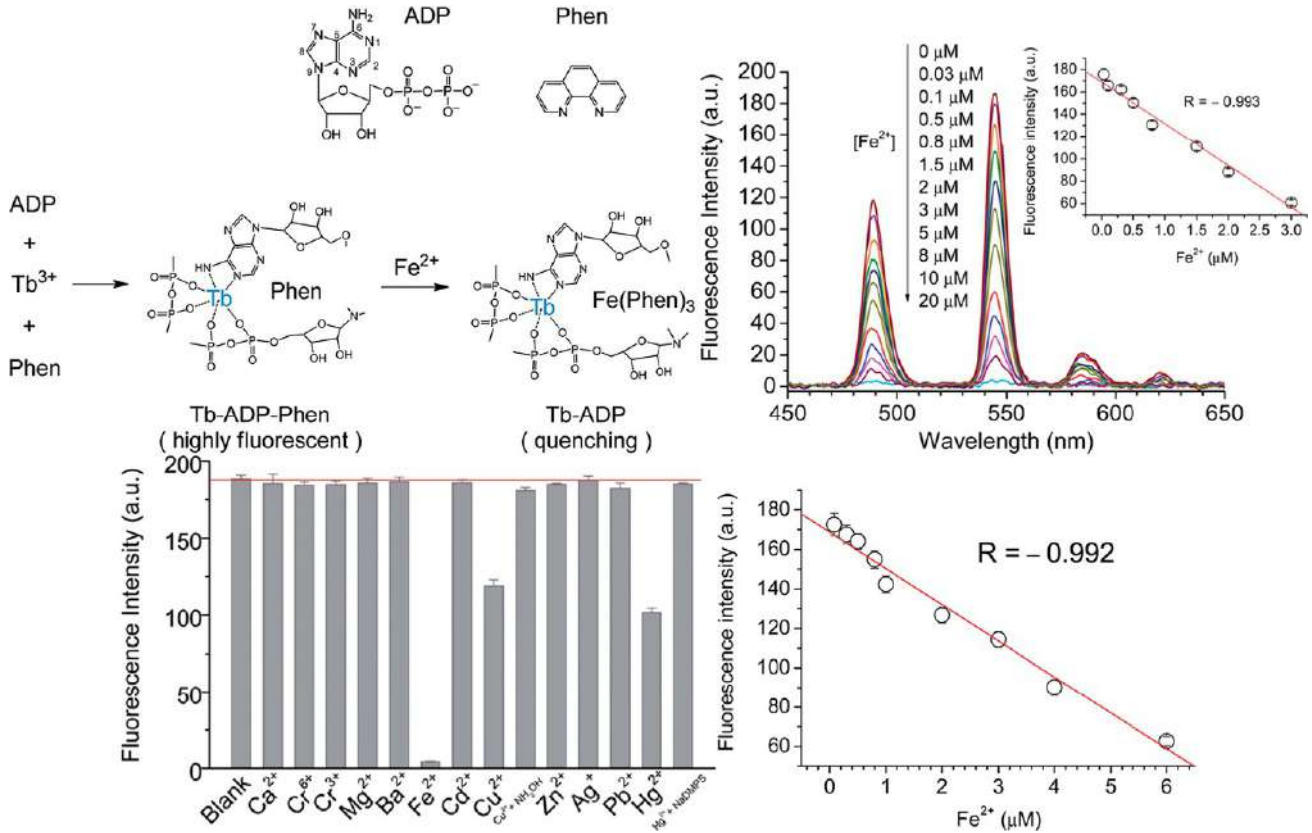

FIG. 6.6 *(Top, Left)* Schematic diagram of the Tb-ADP-Phen coordination polymer for sensing Fe^{2+}. *(Top, Right)* Fluorescence quenching of the Tb-ADP-Phen CP in the presence of Fe^{2+} in HEPES buffer (100 mM, pH 7.4). The inset shows the linear relationship between the fluorescence intensity of the Tb-ADP-Phen CP and the concentration of Fe^{2+}. *(Bottom, Left)* Selectivity of the determination of Fe^{2+} by the Tb-ADP-Phen-based method. The concentrations of the interfering metal ions are 20 mM. *(Bottom, Right)* Determination of Fe^{2+} in human serum by the Tb-ADP-Phen-based method. *(Reproduced with permission from B. Liu, C. Sun, Y. Chen, Nucleotide/Tb3 + coordination polymer as a luminescent nanosensor: synthesis and sensing of iron(II) in human serum. J. Mater. Chem. B 2 (2014) 1661–1666. Copyright 2014 Royal Chemical Society.)*

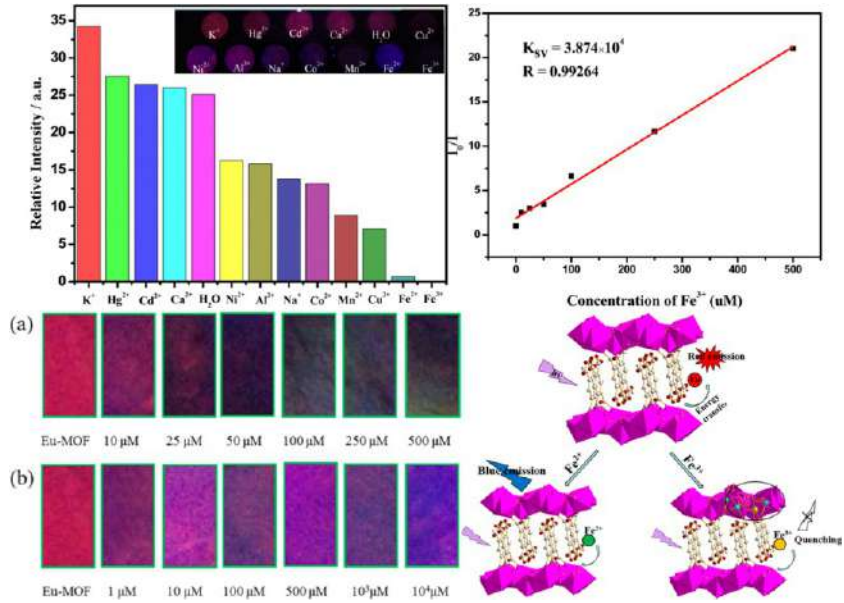

FIG. 6.7 *(Top, Left)* Luminescence intensity of the $^5D_0 \rightarrow {}^7F_2$ of Eu^{3+}@MIL-124 interacting with different metal ions in 1×10^{-2} mol/L aqueous solution of MCl_n (excitation monitored at 298 nm). The inset is the corresponding photographs under UV-light irradiation at 254 nm. *(Top, Right)* K_{sv} curve of Eu^{3+}@MIL-124 in aqueous solutions in the presence of various concentrations of Fe^{3+} under excitation at 298 nm. *(Bottom, Left)* Optical images of the Eu^{3+}@MIL-124 test paper after immersion into solution with different concentrations of (A) Fe^{3+} and (B) Fe^{2+} for 1 min. *(Bottom, Right)* Simplified schematic illustration of the luminescence quenching mechanism of Eu^{3+}@MIL-124 by Fe^{3+} and Fe^{2+} ions. *(Reproduced with permission from X. Xu, B. Yan, Eu(III)-functionalized MIL-124 as fluorescent probe for highly selectively sensing ions and organic small molecules especially for Fe(III) and Fe(II). ACS Appl. Mater. Interfaces 7 (2015) 721–729. Copyright 2015 American Chemical Society.)*

30 nM based on a signal-to-noise ratio of 3:1. They attribute the fluorescence quenching of Tb-ADP-Phen by Fe^{2+} to the formation of a $Fe(Phen)_3$ complex due to the higher stability of $Fe(Phen)_3$ compared to $Tb(Phen)_3$. Selectivity of the fluorescence response of Tb-ADP-Phen to Fe^{2+} is shown. They tested the fluorescence quenching of the Tb-ADP-Phen MOFs in the presence of common metal ions as interferents. As shown in Fig. 6.6 (top, right), under identical conditions, only the addition of Fe^{2+} produced strong fluorescence quenching. The selective fluorescence quenching of Tb-ADP-Phen by Fe^{2+} can be attributed to two factors: (1) an exclusive chromogenic agent for Fe^{2+} and a specific binding ability to Fe^{2+}; (2) only the produced $Fe(Phen)_3$ can significantly quench the fluorescence of Tb-ADP-Phen due to the overlap of the UV-vis absorption of $Fe(Phen)_3$ with the maximum emission of Tb-ADP-Phen. They further applied this material to detect Fe^{2+} ions in human serum by time-resolved fluorimetry. The fluorescence intensity of

Tb-ADP-Phen at 545 nm against the concentration of Fe^{2+} produced a linear correlation in the range of 80 nM–6 μM ($R^2 = 0.992$) (Fig. 6.6; bottom, right). The lowest detectable concentration of Fe^{2+} in serum was approximately 80 nM. Therefore, the current method can satisfy not only the determination of Fe^{2+} but can also effectively eliminate the interference of nonspecific autofluorescence [58].

Xu et al. prepared a layerlike structure, MIL-124 ($Ga_2(OH)_4(C_9O_6H_4)$), and chose for it a parent framework for RE^{3+}-doped luminescent MOFs through encapsulating Eu^{3+} cations in MIL-124, which was developed as a highly selective and sensitive fluorescence probe targeting Fe^{3+} and Fe^{2+} ions in aqueous solutions. The different quenching effects lead to changes of emitting color under UV-light irradiation and the luminescence color changes are completely consistent with the variation tendency of the emission spectra in the inset of Fig. 6.7 (top, left). For the Fe^{2+} and Fe^{3+} ions, although they both seriously quench the emission of Eu^{3+}, their emission colors are different and easy to distinguish under UV light (inset of Fig. 6.7; top, left). Fe^{2+} can completely quench the emission of Eu^{3+} but retain the emission of MOF, causing the blue light. However, Fe^{3+} ions not only can quench the emission of Eu^{3+} but also can have a quenching effect on the emission of MOF, which leads to the dark under UV light. And upon the introduction of Fe^{3+} to the mixture of Eu^{3+}@MIL-124 and other metal cations, the fluorescence is significantly quenched. Fe^{3+} totally quenches the emission of pure MOF while Fe^{2+} ions have no significant quenching effect. The emission intensity of the Eu^{3+}@MIL-124 suspension declines sharply with the increase of Fe^{3+} concentration from 0 to 500 μM. As shown in Fig. 6.7 (top, right), the linear correlation coefficient (R) in the K_{sv} curve of Eu^{3+}@MIL-124 with Fe^{3+} is 0.99264 and the K_{sv} value is calculated as 3.874×10^4, which reveals a strong quenching effect on the Eu^{3+}@MIL-124 luminescence. They developed a fluorescence test paper for rapid detection of metal ions. As shown in Fig. 6.7A (bottom, left), under the irradiation of UV light of 254 nm, the colors changed from red to dark red, faint dark red, and finally black with the increase of Fe^{3+}. The least concentration of detection of Fe^{3+} by the fluorescence test paper was 50 μM. At the same time, when immersing the test paper in various concentrations of Fe^{2+} aqueous solution, the color changed from red to blue as shown in Fig. 6.7B (bottom, left), indicating obvious differences with Fe^{3+}. Considering these results, it can distinguish the colors of different intensities by the naked eye. They speculate that the remarkable quenching effect of Eu^{3+}@MIL-124 by Fe^{3+} and Fe^{2+} results from the transformation of the patented framework MIL-124 (Ga) to MIL-124 (Fe) via the cation exchange. Therefore the quenching effect on Eu^{3+} should be attributed to the interaction between metal ions and organic ligands. The quenching effect on Eu^{3+}@MIL-124 by Fe^{3+} can be attributed to the partial replacement of Ga^{3+} and the substitution of Eu^{3+}, whereas substitution of Eu^{3+} is the main reason for the fluorescence quenching by Fe^{2+} (Fig. 6.7; bottom, right).

Maity et al. designed and developed an La-based blue light-emitting fluorescent MOF (La-MOF) and have utilized it to detect Fe^{3+} and Fe^{2+} from aqueous solutions in a very selective and time-effective fashion. No appreciable fluorescence quenching happens in the case of Fe^{2+}, whereas Fe^{3+} completely quenches the fluorescence in less than 1 min (Fig. 6.8A; top). H_2O_2 can oxidize Fe^{2+} to Fe^{3+} in situ in the detection system, which leads to a gradual decrease in fluorescence with increasing Fe^{3+} concentration (Fig. 6.8B and C; top). However, no such changes occur in the absence of peroxide, whose optimum peroxide concentration required for the complete oxidation of the Fe^{2+} (0.5 mM) is found to be 1.5 mM (Fig. 6.8B; top). There is no significant quenching of the MOF fluorescence in neat peroxide solutions (Fig. 6.8C; top). It is observed that among all the employed metal ions, only Fe^{3+} can significantly quench the fluorescence (Fig. 6.8D; top). The K_{sv} value is calculated to be 1.52×10^4 L mol^{-1} at the low concentration region of 0–55 μL with almost 90% quenching efficiency using a 340 μM Fe^{3+} solution (Fig. 6.8E and F; top), suggesting a strong interaction between host and Fe^{3+} cation. The LOD for Fe^{3+} is calculated to be 3.6 ppm. The ascorbic acid reduces the trapped Fe^{3+} to Fe^{2+} within the pores, and the latter due to its poor affinity to the MOF pores leaches out upon a gentle sonication within 5 min (Fig. 6.8; bottom). This is visible from no color change in the sample (remains brown; see inset photographs of Fig. 6.8; bottom). In principle, such an exchange of La^{3+} by Fe^{3+} in the framework can also give rise to fluorescence quenching. So, strong Fe^{3+}(guest)-La-MOF(host) interactions within the pore might be the actual reason for the fluorescence quenching, and this may form a nonfluorescent ground state complex (Fig. 6.8; bottom).

6.3 Luminescence responsive sensing of Cu^{2+} using rare earth metal-organic framework hybrid materials

The detection of Cu^{2+} in the human body is an essential issue in medicine, because Cu^{2+} plays considerable roles in living organisms, particularly in the brain. The sensing of Cu^{2+} in the environment and biological systems is extremely important. For example, Alzheimer's disease and Wilson's disease are related to the homeostasis of Cu^{2+}. There are extensive reports of Cu^{2+} sensing by rare earth MOF hybrid material probes [63–84].

Liu et al. used H_4L to construct four isostructural RE-MOFs, $[H_2N(Me)_2][Ln_3(L)_2(HCOO)_2(DMF)_2(H_2O)]$ (RE = Eu, Tb, Gd and Dy), showing unusual nanocage-based 3D frameworks with trinuclear RE^3 clusters. Eu-MOF reveals excellent luminescent sensing for Cu^{2+} ions [65]. The luminescence spectra of Eu-MOF dispersed in DMF solution containing the same concentrations of metal nitrates were studied (Fig. 6.9A). Interestingly, the Cu^{2+} ion showed a significant quenching effect on the luminescence intensity of Eu-MOF; in contrast, other metal ions enhanced luminescence intensity to a degree, indicating highly selective sensing of Eu-MOF for Cu^{2+} ions. This unique quenching effect in Eu-MOF possibly results from the stronger affinity of pyridine N atoms in

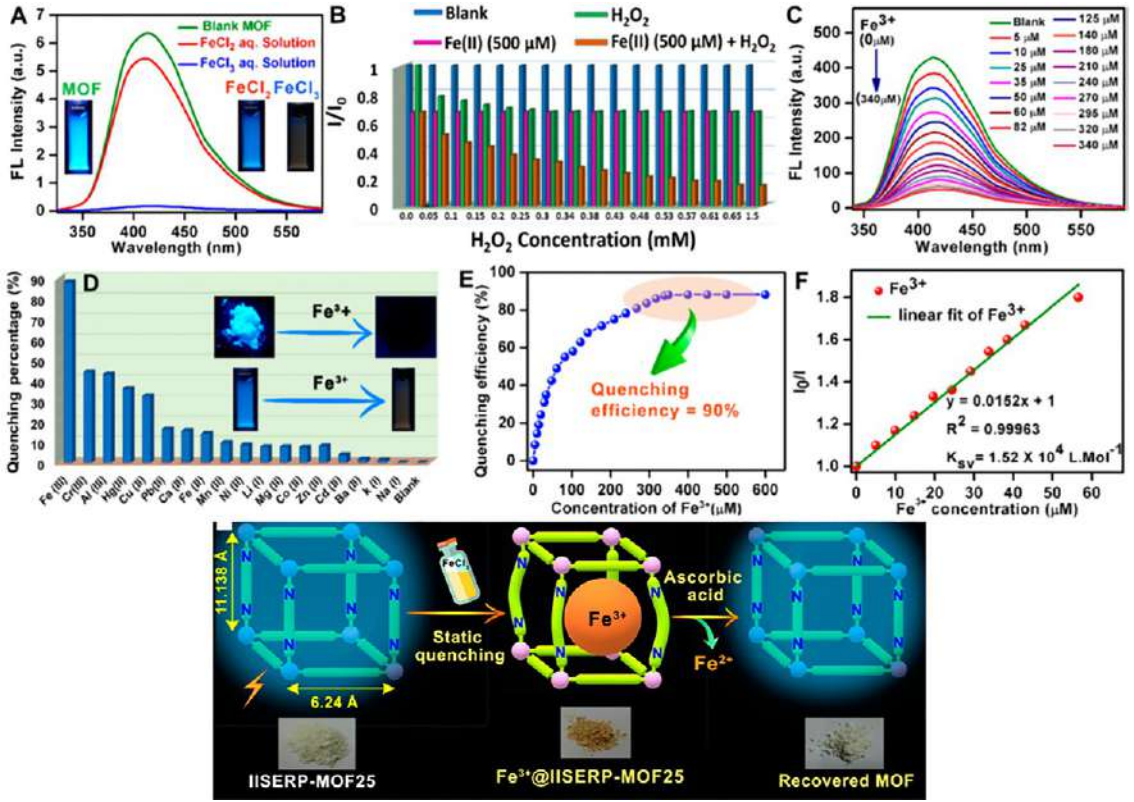

FIG. 6.8 *(Top)* (A) Solution-state fluorescence spectra of La-MOF and in the presence of Fe^{2+} or Fe^{3+}. (B) Relative fluorescence intensity of MOF (*blue* columns) after addition of different amounts of peroxide (*green* columns) to the neat MOF solution, in the presence of only Fe^{2+} (*pink* columns) and in the presence of both Fe^{2+} (500 μM) and peroxide (*brown* columns). This generates Fe^{3+} in situ. (C) Fluorescence quenching efficiency of $FeCl_3$ solution of varying concentrations. (D) Solid state and liquid state fluorescence quenching of La-MOF by Fe^{3+} ions in the presence of different metal ions, including Fe^{2+}. Excitation was at 300 nm, and emission was obtained at 413 nm. (E) The quenching efficiency of Fe^{3+} ions. (F) Activated La-MOF changes color from colorless to *brown* upon soaking in 0.33 mM $FeCl_3$ solution: a Stern-Volmer plot of the dilute concentrations of Fe^{3+} (aq) showing linearity. *(Bottom)* Mechanism of static fluorescence quenching phenomenon of IISERP-MOF25 via ground-state nonfluorescent complex formation with Lewis acidic Fe^{3+} ions. MOF has a pore window of dimensions 11.138 × 6.24 Å, able to accommodate Fe^{3+}, while it interacts weakly with Fe^{2+} because of its larger size, which facilitates its leaching. *(Reproduced with permission from R. Maity, D. Chakraborty, S. Nandi, A. K. Yadav, D. Mullangi, C. P. Vinod, R. Vaidhyanathan, Aqueous-phase differentiation and speciation of Fe3 + and Fe2 + using water-stable photoluminescent lanthanide-based metal-organic framework. ACS Appl. Nano Mater. 2019, 2, 5169–5178. Copyright 2019 American Chemical Society.)*

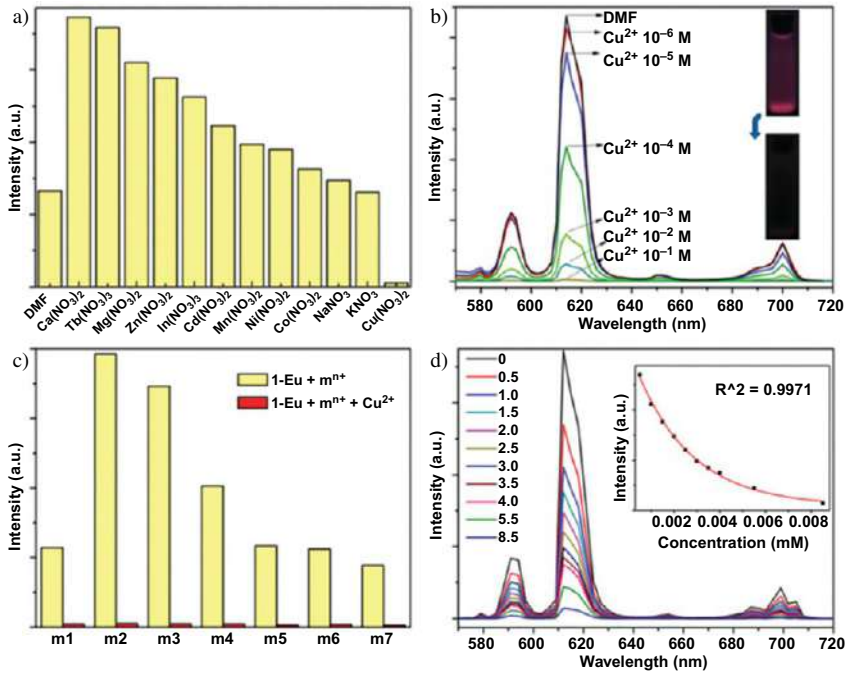

FIG. 6.9 (A) Luminescence intensity at 615 nm of Eu-MOF treated with different metal ions (10^{-2} M) in DMF solutions. (B) Luminescence spectra of Eu-MOF in DMF solutions with $Cu(NO_3)_2$ at different concentrations, and color changes of Eu-MOF in DMF after adding Cu^{2+} (10^{-2} M) under UV light. (C) Luminescence intensity at 615 nm of Eu-MOF dispersed in DMF with addition of different mixed ions (10^{-1} M) (m1: blank; m2: $Na^{+}/Mg^{2+}/Ca^{2+}$; m3: Mg^{2+}/Ca^{2+}; m4: Zn^{2+}/Cd^{2+}; m5: Co^{2+}/Ni^{2+}; m6: $Zn^{2+}/Cd^{2+}/Ni^{2+}$; m7: $Zn^{2+}/Cd^{2+}/Co^{2+}$) and Cu^{2+}-incorporated systems (10^{-2} M). (D) Luminescence spectra of Eu-MOF in DMF in the presence of different amounts of Cu^{2+} (inset: the plot of intensity versus Cu^{2+} concentration). *(Reproduced with permission from B. Liu, W. Wu, L. Hou, Y. Wang, Four uncommon nanocage-based Ln-MOFs: highly selective luminescent sensing for Cu2 + ions and selective CO2 capture. Chem. Commun. 50 (2014) 8731—8734. Copyright 2014 Royal Chemical Society.)*

L^{4-} toward Cu^{2+}, as well as from the smaller ionic radius of Cu^{2+}, which renders Cu^{2+} ions more readily able to contact with the pyridine N atom than other metal ions and, as a result, decreases the efficiency of energy transfer from L^{4-} linkers to f-f transitions of Eu^{3+} centers. As illustrated in Fig. 6.9B, the luminescence intensity of Eu-MOF is almost completely quenched at a $Cu(NO_3)_2$ concentration of 10^{-2} M. The quenching coefficient K_{sv} of $2350 \pm 40\ M^{-1}$ is obtained from the luminescent data. It is very striking that the luminescence intensity of Eu-MOF shows no significant change after adding the different mixed metal ions (Fig. 6.9C), while the luminescence intensity is close to complete quenching once the Cu^{2+} ion (10^{-2} M) is incorporated. Furthermore, the titration experiments of Cu^{2+} ions in Eu-MOF and mixed ion systems were also studied (Fig. 6.9D). The luminescence intensity at

615 nm versus the volume ratio of Cu^{2+} ions can be well fitted by a single exponential function, establishing a diffusion-controlled process for the Cu^{2+} ion luminescent quenching behavior [65].

Lian et al. reported a facile route for the synthesis of core-shell structure microspheres based on silica and $[H_2NMe_2]_3[RE(dpa)_3]$ (RE = Eu, Tb, Sm, Dy, Nd, and Yb; $[H_2NMe_2]^+$ = dimethylamino cation; dpa = 2-dipicolinate) [68]. The core-shell structure materials SiO_2@RE-dpa displayed excellent optical properties for applications in the development of white-light devices or sensors for small organic molecules or Cu^{2+}. The luminescence spectra and histogram are shown in Fig. 6.10 (top), and only Cu^{2+} reveals a conspicuous quenching effect on the luminescence originated from the f-f transition of Eu^{3+}. Well-dispersed suspensions in DMF of the core-shell microspheres at various concentrations of Cu^{2+} produced a decrease in the luminescence intensity of SiO_2@Eu-dpa microspheres with an increase in the content of Cu^{2+} from 0 to 500 μM (Fig. 6.10A; bottom). The luminescence Turn-Off effect of Cu^{2+} on SiO_2@Eu-dpa is also easily observed by the naked eye. In addition, they also compared the sensitivity of different sensing materials with silica cores or without cores for the detection of Cu^{2+}. As demonstrated in Fig. 6.10B (bottom), the value of the quenching effect coefficient K_{sv} ($2.93 \times 10^4\ M^{-1}$) of core-shell materials exhibits an increase of more than 20% over that of the pure Eu-dpa complex ($2.29 \times 10^4\ M^{-1}$). The core-shell structure materials enhanced the selectivity and showed higher sensitivity than a pure MOF system. This selective sensing of Cu^{2+} is achieved due to the complete destruction of the original crystal framework, leading to the luminescence of Eu^{3+} disappearing [68].

Zhao et al. assembled a luminescent terbium MOF with fascinating pyridyl nitrogen atoms, $[Tb_3(L)_2(HCOO)(H_2O)_5]\cdot DMF\cdot 4H_2O$ (Tb-MOF, H_4L = 4,4′-(pyridine-3,5-diyl)diisophthalic acid) [69], which can detect Cu^{2+} ions with high selectivity and sensitivity due to its luminescence being nearly entirely quenched in *N*,*N*-dimethylformamide (DMF) solution and a biological system. Cu^{2+} exhibits a drastic quenching effect on the luminescence of Tb-MOF, while other metal ions have no significant effect on the emission except for Cu^{2+} (Fig. 6.11A; left). The luminescence intensity of the Cu^{2+} incorporated Tb-MOF is more than 21 times weaker than that of Tb-MOF with no metal ion incorporated (Fig. 6.11B; left). As shown in Fig. 6.11 (right), the luminescence intensity of Tb-MOF gradually decreases with increasing concentration of Cu^{2+} such that the probe can reach 10^{-6} mol/L. The weak bonding between Cu^{2+} and the N atom site of the organic ligand might partly quench the singlet and triplet excited states of the ligand-to-Tb^{3+} optically active core, which may also increase the interaction between the pyridyl Lewis basic sites and Cu^{2+} cations. Such interactions can decrease the ligands' antenna efficiency and further magnify the f-f transitions of Tb^{3+} cations, resulting in the quenching.

Du et al. reported an Eu-MOF $\{[Eu_2(abtc)_{1.5}(H_2O)_3(DMA)]\cdot H_2O\cdot DMA\}_n$ (DMA = *N*,*N*-dimethylacetamide, H_4abtc), which is a rare example of a highly selective and sensitive luminescence probe for benzaldehyde and Cu^{2+}. As

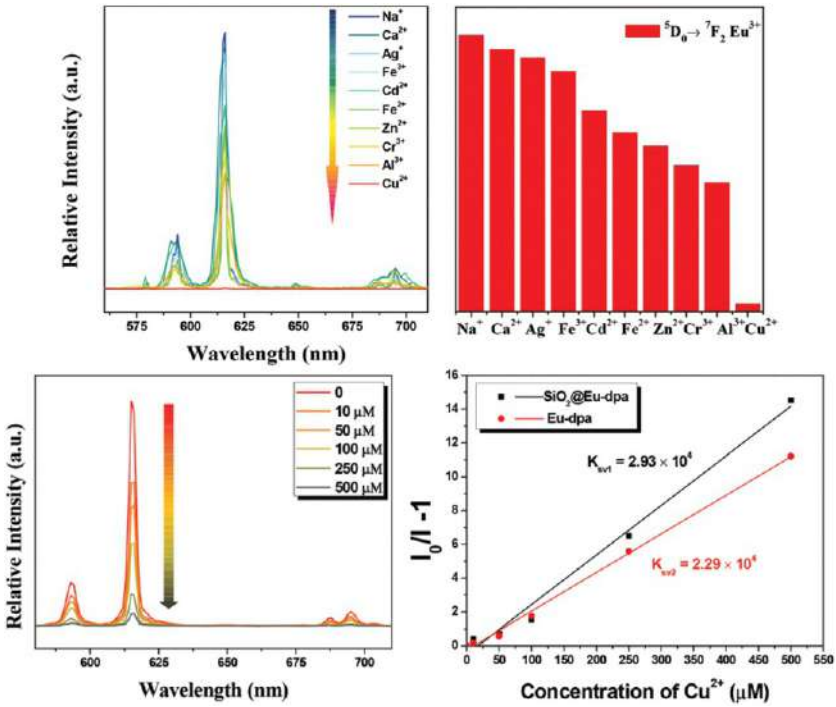

FIG. 6.10 *(Top)* Responses of the fluorescence of SiO_2@Eu-dpa to DMF solutions of various metal cations (5 mM). All the emission spectra are recorded at an excitation wavelength of 300 nm. *(Bottom)* Emission spectra of SiO_2@Eu-dpa (A) and linear fitting curve of the luminescence intensity of SiO_2@Eu-dpa (*black*) and pure Eu-dpa complex (*red*) (B) in DMF suspensions in the presence of various concentrations of Cu^{2+} under excitation at 285 nm. *(Reproduced with permission from X. Lian, B. Yan, Novel core-shell structure microspheres based on lanthanide complexes for white-light emission and fluorescence sensing. Dalton Trans. 45 (2016) 2666–2673. Copyright 2016 Royal Chemical Society.)*

shown in Fig. 6.12A, the luminescence intensities of M-incorporated Eu-MOF suspensions are heavily dependent on the species of metal ions. In particular, the luminescence intensity of Cu^{2+}-incorporated Eu-MOF is dramatically quenched compared with that of the initial Eu-MOF in water, which can be further confirmed by a photograph of the Eu-MOF suspension under UV light (as shown in the inset of Fig. 6.12B). As can be seen from Fig. 6.12C, the interference from conventional metal cations can be neglected, further convincing proof of the high selectivity of Eu-MOF for Cu^{2+} detection for practical use. The addition of Eu-MOF to the solutions of metal ions results in a visible color change of the solution for Cu^{2+}, while no such visible color change is observed upon the addition of Eu-MOF to other metal-ion solutions (Fig. 6.12D). In addition, the pictures of Cu^{2+}@Eu-MOF show a color change of Eu-MOF from orange to green, indicating that Eu-MOF displays unique colors upon

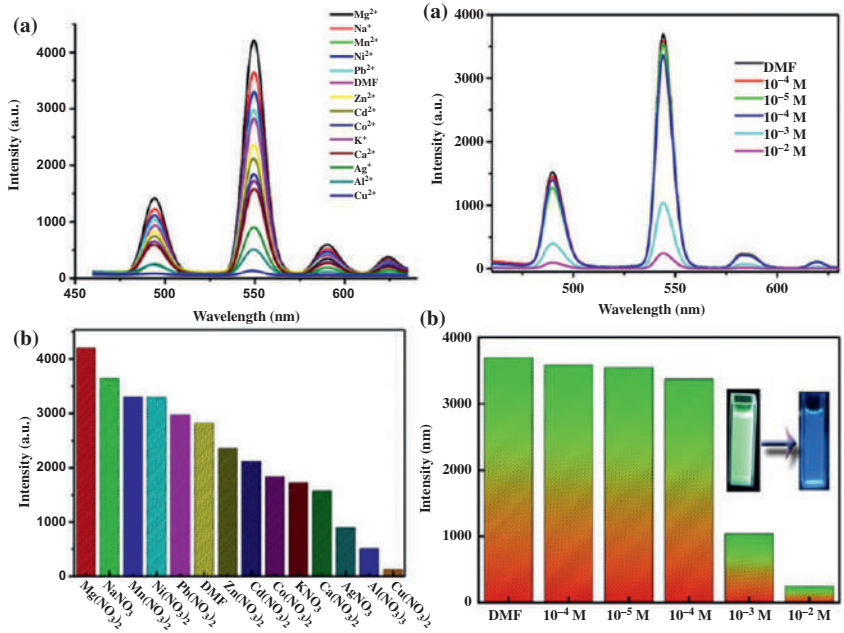

FIG. 6.11 *(Left)* (A) Luminescence spectra of Tb-MOF and (B) the comparison of the luminescence intensity of Tb-MOF with different metal ions (10^{-2} M) in DMF solutions. *(Right)* (A) Luminescence spectra of compound Tb-MOF in DMF solutions with $Cu(NO_3)_2$ at different concentrations, and (B) the comparison of the luminescence intensity of compound Tb-MOF with different concentrations and color changes of Tb-MOF in DMF after adding Cu^{2+}. *(Reproduced with permission from J. Zhao, Y. Wang, W. Dong, Y. Wu, D. Li, Q. Zhang, A robust luminescent Tb(III)-MOF with Lewis basic pyridyl sites for the highly sensitive detection of metal ions and small molecules. Inorg. Chem. 55 (2016) 3265–3271. Copyright 2016 American Chemical Society.)*

metal-ion encapsulation and can be considered as a universal naked-eye detector for Cu^{2+}. Cu^{2+} can rapidly diffuse into the adaptable channels or interlayer of Eu-MOF and be recognized by the terminal Lewis basic sites and/or the carboxylate group, whose interactions between Cu^{2+} ions and ligands minimize the energy transfer efficiency, thus decreasing the luminescent intensity.

6.4 Luminescence responsive sensing of Zn^{2+} using rare earth metal-organic framework hybrid materials

Zn^{2+} plays key roles in mammals, such as in (a) the reversible hydration rate of CO_2 in carbonic anhydrase, (b) the hydrolysis of C-terminal amino acids in the peptide chains of carboxypeptidase and N-terminal amino acids in the peptide chains of aminopeptidase, and (c) the hydrolysis of phosphate monoester in alkaline phosphatase of colibacillus. In addition, the Zn^{2+} ion participates in

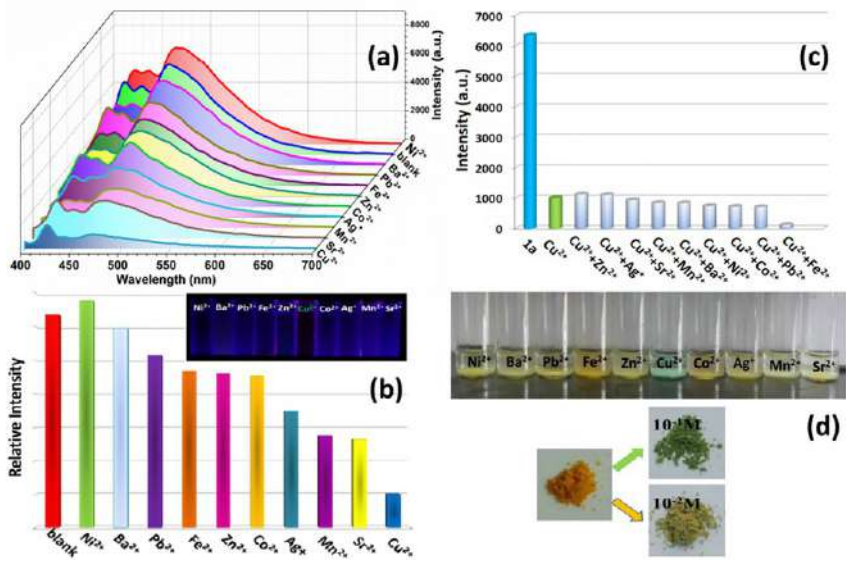

FIG. 6.12 (A) Emission spectra of 1a in diverse metal-ion aqueous solutions. (B) Comparisons of the luminescence intensity of Mn^{+}@Eu-MOF. Inset: Photograph of M^{n+}@Eu-MOF under UV-light irradiation at 365 nm. (C) Luminescence intensity of Eu-MOF upon the addition of Cu^{2+} in the presence of a background of metal ions. (D) Color changes in the aqueous suspension of Eu-MOF with different metal ions and Eu-MOF soaked in aqueous solutions containing $Cu(NO_3)_2$ with 10^{-1} and 10^{-2} M, respectively. *(Reproduced with permission from P. Du, W. Gu, X. Liu, Multifunctional three-dimensional europium metal – organic framework for luminescence sensing of benzaldehyde and Cu2 + and selective capture of dye molecules. Inorg. Chem. 55 (2016) 7826–7828. Copyright 2016 American Chemical Society.)*

various biological activities, including insulin secretion, neural-signal transmission, and metalloenzyme regulation, as well as those that occur in the course of certain diseases, such as Alzheimer's disease, infantile diarrhea, and diabetes. Therefore the detection of Zn^{2+} in body fluids is of extreme importance for human health, especially for growth and intelligent development, due to the serious impact on our body induced by either an excess or a deficiency. However, probes based on RE^{3+} luminescence have not made great progress, and there are even fewer Zn^{2+} sensors that can be used for in-site detection, due to their poor water stability [85,86].

Song et al. prepared three MOF $[REL(NO_3)_3]_n{\cdot}2C_4H_8O_2$ (RE-MOF, RE = Nd, Eu, Tb) based on an asymmetric ligand L (2,2′-((2-(pyridin-4-yl)-2-((2-(((thiophen-2-ylmethyl)carbamoyl)phenoxy) methyl) propane-1.3-diyl) bis(oxy))bis(*N*-(thiophen-2-ylmethyl)benzamid). All the emission spectra of the treated films were obtained at the maximum excitation wavelength at 309 nm (Fig. 6.13; top). For Eu-MOF@PMMA, Zn^{2+} exerts a quenching effect on Eu^{3+} emission and an enhancing one on the emission characteristic of $\pi^* \rightarrow \pi$. As for Tb-MOF@PMMA, the emission originated from the $f \rightarrow f$

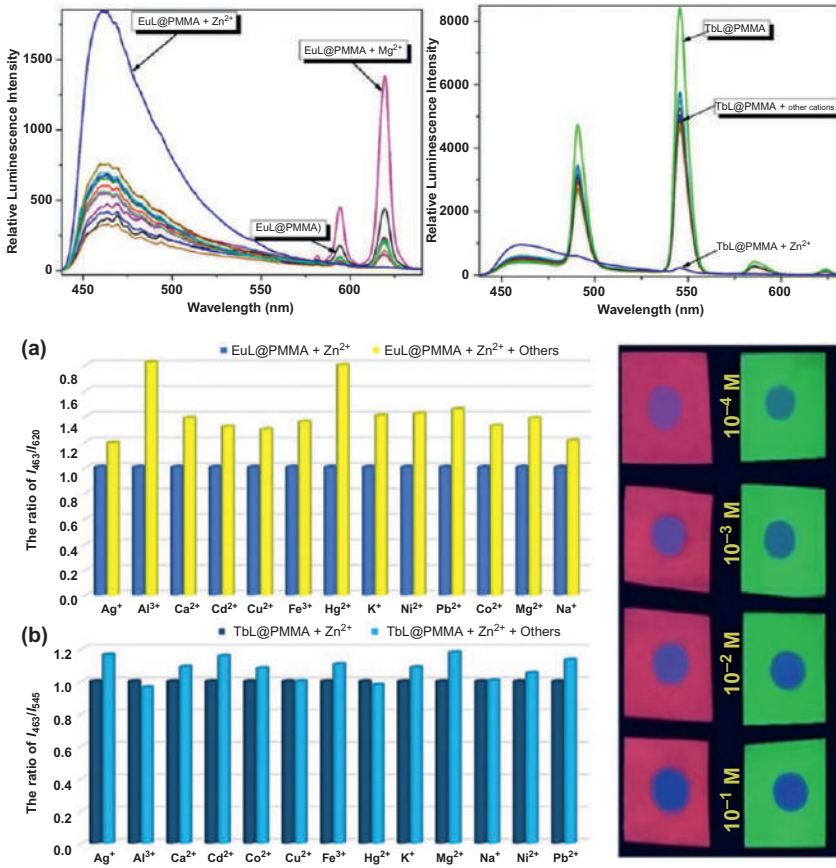

FIG. 6.13 *(Top)* Emission spectra of Eu-MOF@PMMA *(left)* and Tb-MOF@PMMA *(right)* excited at 309 nm upon immersion in metal cations (0.1 M). *(Bottom, Left)* (A) Ratio of I_{463}/I_{620} of Eu-MOF@PMMA in the presence of various cations and Zn^{2+} combinations (10^{-1} M) solution. (B) Ratio of I_{463}/I_{545} of Tb-MOF@PMMA in the presence of various cations and Zn^{2+} combinations (10^{-1} M) solution. *(Bottom, Right)* Photograph of Eu-MOF@PMMA *(top)* and Tb-MOF@PMMA *(bottom)* excited at 254 nm under a handheld UV lamp upon addition of one drop of Zn^{2+} (10^{-1}, 10^{-2}, 10^{-3}, and 10^{-4} M). *(Reproduced with permission from X. Song, H. Meng, Z. Lin, L. Wang, 2D lanthanide coordination polymers: synthesis, structure, luminescent properties, and ratiometric sensing application in the hydrostable PMMA-doped hybrid films. ACS Appl. Polym. Mater. 2 (2020) 1644–1655. Copyright 2020 American Chemical Society.)*

transition of Tb^{3+} is almost quenched completely by Zn^{2+} selectively. Therefore effective luminescent detection can be achieved in a self-calibrating way by comparing the relative luminescence intensities from different emitting centers (I_{463}/I_{545} or I_{463}/I_{620}). The cation-exchange mechanism may work upon immersing Eu-MOF@PMMA and Tb-MOF@PMMA in a Zn^{2+} solution, in which a stronger coordination interaction exists between L and Zn^{2+} than L and Eu^{3+}/Tb^{3+} due to the right Lewis acidity and ion size of Zn^{2+} with the

aid of a hydrophobic PMMA matrix. Upon immersing Eu-MOF@PMMA and Tb-MOF@PMMA into a mixture of Zn^{2+} and other cations, respectively, their emission spectra show negligible changes with the ratio of I_{463}/I_{620} for Eu-MOF@PMMA and I_{463}/I_{546} for Tb-MOF@PMMA, as shown in Fig. 6.13 (bottom, left). The preparation process of the as-prepared hybrid films acting as ratiometric luminescence sensors for Zn^{2+} is simple and has a high yield. For practical application, they performed real-time monitoring of Zn^{2+} by doping the detection solution on the hybrid films (Fig. 6.13; bottom, right), both of which displayed a quick luminescence response by the appearance of bright blue fluorescence under a UV lamp, and the observed minimum LOD can be 10^{-4} M [86].

6.5 Luminescence responsive sensing of multimetal cations using rare earth metal-organic framework hybrid materials

Zhang et al. constructed five novel three-dimensional (3D) RE-MOFs by 4-(3′,5′-dicarboxylphenoxy) phthalic acid (H_4dcppa), and used $\{[Eu_2K_2(dcppa)_2(H_2O)_6]\cdot mH_2O_n$ (Eu-MOF) and binding of metal ions through Lewis base interactions for Fe^{3+} and Cu^{2+} ions with luminescent quenching. The highest emission peak at 614 nm of Eu^{3+} was monitored under the perturbation of various cations, as depicted in Fig. 6.14 (top. left). Most interestingly, the luminescence intensities of the M^{n+}-Eu-MOF heavily relied on the identity of metal ions. The significant luminescent quenching effect of Fe^{3+} and Cu^{2+} ions was very clearly observed. Moreover, the pictures of M^{n+}-Eu-MOF at room temperature show the incorporation of Fe^{3+} or Cu^{2+} and rendered Eu-MOF from bright to brown or blue, which can be obviously observed with the unaided eye. The luminescence intensity of Eu-MOF gradually decreases with increasing concentration of Fe^{3+} and Cu^{2+} (Fig. 6.14; bottom). The decrease of the luminescence intensity is still clearly observed when Eu-MOF is immersed in 5×10^{-6} Fe^{3+} solution (10^{-6} mol/L Cu^{2+} solution), indicating that its LOD as a luminescent probe can reach 10^{-6} mol/L. As shown in the inset of Fig. 6.14 (bottom), the values of K_{sv} are 4.3×10^4 L/mol for Fe^{3+} and 5.2×10^4 L/mol for Cu^{2+}. The possible luminescence quenching mechanism of Eu-MOF by Fe^{3+} and Cu^{2+} is shown in Fig. 6.14 (top, right), which may follow two processes: one is that the paramagnetic effect of encapsulated Fe^{3+} and Cu^{2+} ions is responsible for the quenching of the luminescence over a short period. The other is the interaction between Fe^{3+} or Cu^{2+} and oxygen atoms (through Lewis basic sites that the pores bond with), resulting in inefficient energy transfer between ligand and Eu^{3+}, leading to immediate photoluminescence quenching [87].

Du et al. synthesized a series of RE-MOFs with mixed ligands, namely $\{[RE(dpc)(H_2O)_2]\cdot(Hbibp)_{0.5}\}_n$. Particularly, Eu-MOF acts as a multiresponsive luminescent sensor toward Fe^{3+} and Cu^{2+} with high sensitivity, selectivity, and stability [88]. As shown in Fig. 6.15 (top), the introduction of Fe^{3+} or

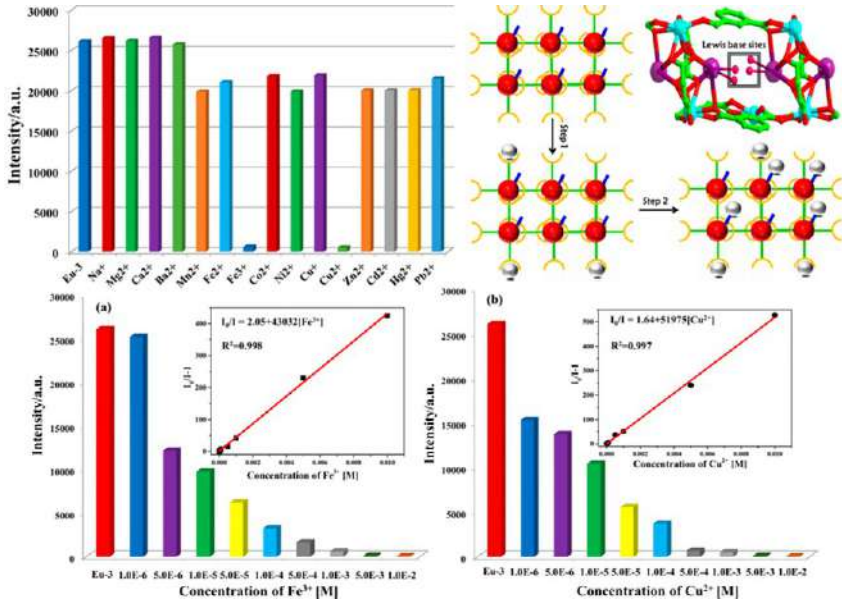

FIG. 6.14 *(Top, Left)* Photoluminescence intensity of Eu-MOF ($^5D_0 \rightarrow {}^7F_2$ transition) treated with 10^{-3} M MCl_x for 2 h, excited at 315 nm. *(Top, Right)* Scheme for possible luminescence quenching mechanism of Eu-MOF by Fe^{3+} and Cu^{2+} ions. *(Bottom)* Comparison of the luminescence intensity of Eu-MOF immersed in different concentrations of Fe^{3+} (A) and Cu^{2+} (B) in ethanol solutions. Inset: Stern-Volmer plot of Eu-MOF quenched by Fe^{3+} and Cu^{2+}. *(Reproduced with permission from H. Zhang, R. Fan, W. Chen, J. Fan, Y. Dong, Y. Song, X. Du, P. Wang, Y. Yang, 3D Lanthanide metal – oganic frameworks based on mono-, tri-, and heterometallic tetranuclear clusters as highly selective and sensitive luminescent sensor for Fe3+ and Cu2+ ions. Cryst. Growth Des. 16 (2016) 5429–5440. Copyright 2016 American Chemical Society.)*

Cu^{2+} cations produces a striking quenching effect of intensities, demonstrating that the Eu-MOF exerts a selective luminescence response toward Fe^{3+} and Cu^{2+}. When the concentration of Fe^{3+} or Cu^{2+} is raised to 360 μL, the luminescence intensity decreases to 94.66% or 91.11%, respectively (see Fig. 6.15A; bottom). Quantitatively, the luminescence intensity versus [Fe^{3+}] and [Cu^{2+}] plots shows good linear correlation at low concentrations ($R^2 = 0.9885$ for Fe^{3+} and 0.9863 for Cu^{2+}) (Fig. 6.15B and C; bottom). The K_{sv} value of the Eu-MOF for the Fe^{3+} and Cu^{2+} cations is calculated to be $4.84 \times 10^3\ M^{-1}$ and $4.62 \times 10^3\ M^{-1}$, respectively. The LOD values are obtained as follows: 1.32×10^{-5} M for Fe^{3+} and 2.53×10^{-5} M for Cu^{2+}, respectively. However, accompanied by the increase of concentration, the plots of I_0/I versus concentration of cations deviate from the linear correlation, indicating that the process of luminescence quenching is involved in the coexistence of static and dynamic mechanisms. Studies reveal that the UV-vis absorption spectrum of the Fe^{3+} ion is located in the range of 270 to 350 nm, which is a wide range overlapped with the excitation wavelength of the Eu-MOF (296 nm); on the contrary, the

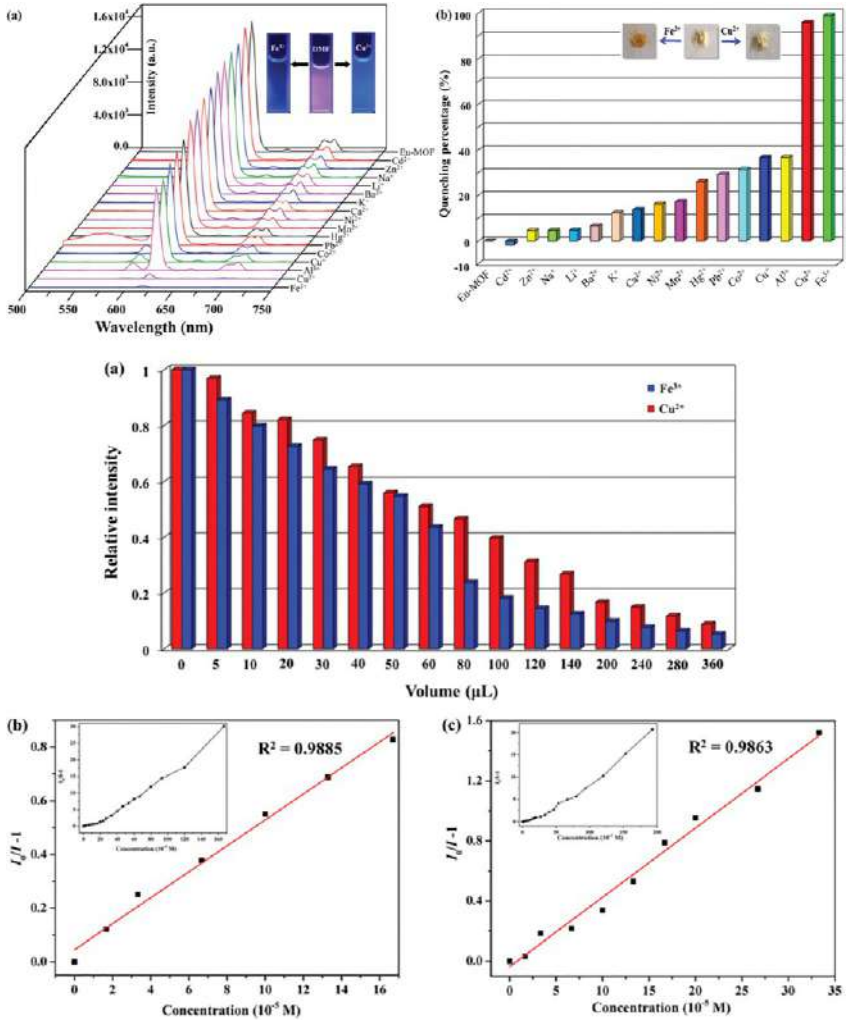

FIG. 6.15 *(Top)* (A) Luminescence spectra of the Eu-MOF dispersed in different metal cations in DMF solutions (inset: the color changes after adding Fe^{3+}/Cu^{2+} ions under 365 nm ultraviolet light). (B) Luminescence quenching percentage of the Eu-MOF ($^5D_0 \rightarrow {}^7F_2$) dispersed into different DMF solutions of various cations. *(Bottom)* (A) Concentration-dependent luminescence intensities of the Eu-MOF by addition of different volumes of Fe^{3+} and Cu^{2+} (1×10^{-2} M). Linear SV curves for the Eu-MOF by gradual addition of Fe^{3+} ions (B) and Cu^{2+} ions (C) in DMF solution (inset: nonlinear SV plot of ions). *(Reproduced with permission from Y. Du, H. Yang, R. Liu, C. Shao, L. Yang, A multi-responsive chemosensor for highly sensitive and selective detection of Fe3+, Cu2+, Cr2O72− and nitrobenzene based on a luminescent lanthanide metal-organic framework. Dalton Trans. 49 (2020) 13003–13016. Copyright 2020 Royal Chemical Society.)*

absorption spectrum of the Cu^{2+} ion shows no significant overlap with the excitation spectrum of the Eu-MOF. In the 3D framework of Eu-MOF, the uncoordinated carboxyl O or imidazolyl N atoms from dpc^{4-} or bibp ligands may act as Lewis basic sites to be incorporated into Fe^{3+} or Cu^{2+} ions. Meanwhile, the weak interactions between Fe^{3+} or Cu^{2+} and O or N atoms may disturb the singlet and triplet excited states of ligands and reduce the energy transfer efficiency from the ligands to the Eu^{3+} centers, thus leading to the luminescence quenching of the Eu-MOF [88]. This versatile probe for both Fe^{3+} and Cu^{2+} is found only rarely.

Wang et al. reported two 3D neutral MOFs, $\{[Eu(BIPA\text{-}TC)_{0.5}(DMA)_2(NO_3)]\cdot DMA\cdot H_2O\}_n$ (Eu1-MOF) and $\{[Eu_2(BIPA\text{-}TC)_{1.5}(DMA)_3(H_2O)_2]\cdot 2DMA\cdot 2H_2O_n$ (Eu2-MOF), via a solvent regulation strategy [89]. As is shown in Fig. 6.16A, all metal cations exhibited quenching effects for Eu1-MOF, but no selectivity was exhibited. The quenching efficiency of Fe^{3+} was 93.1%. Quantitatively, the

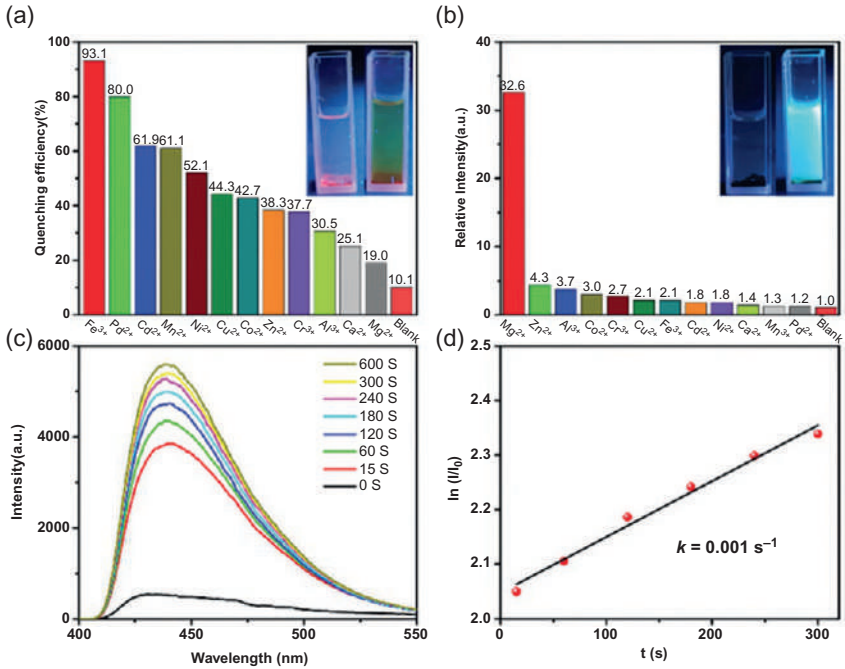

FIG. 6.16 (A) Quenching efficiency of Eu1-MOF containing metal ions at 0.25 mmol/L (inset, images before and after addition of Fe^{3+}); (B) fluorescence enhancement ratio of 2-Eu containing metal ions at 0.25 mmol/L (inset, images before and after addition of Mg^{2+}); (C) time-dependent fluorescence intensity of the suspension after adding 200 μL Mg^{2+} solution; and (D) the fitting of its first-order reaction kinetic equation. *(Reproduced with permission from X. Wang, Y. Wang, X. Wang, K. Lu, W. Jiang, P. Cui, H. Hao, F. Dai, Two series of ln-MOFs by solvent induced self-assembly demonstrating the rapid selective sensing of Mg2 + and Fe3 + cations. Dalton Trans. 49 (2020) 15473–15480. Copyright 2020 Royal Chemical Society.)*

quenching efficiency was analyzed using the Stern-Volmer equation, whose K_{sv} of Eu1-MOF was calculated to be 3.89×10^3 and 3.19×10^3 M^{-1} for Fe^{3+}. However, for Eu2-MOF, Mg^{2+} had the most obvious effect by fluorescence enhancement and other metal cations had ignorable influence, revealing that it has the best sensitivity toward Mg^{2+} (Fig. 6.16B). The emission intensity correspondingly enhances with the increase in the Mg^{2+} concentration, which reveals the Turn-On fluorescence sensing of Eu2-MOF. In addition, the detection limit calculated is about 1.53×10^{-10} mol/L. The time-reliant fluorescence response was also investigated and, as displayed in Fig. 6.16C, the fluorescence intensity displayed a clear enhancement after 15 s, and at 600 s, the fluorescence intensity increased by 10.4 times compared to the blank. Most overlaps between the absorption spectra of the Fe^{3+} solution and the excitation spectrum of Eu1-MOF were observed, suggesting the competitive absorption mechanism may be responsible for the quenching effect. As for Eu2-MOF, because Mg^{2+} ions have a high charge-to-size ratio, and conjugated organic ligands with rich π electrons can act as an electron donor. It is likely that strong electrostatic interactions exist between ligands and Mg^{2+} ions. The fluorescence enhancement can be largely enucleated by the donor-acceptor electron-transfer mechanism [89].

References

[1] S. Cai, S. Zheng, J. Fan, T. Xiao, J. Tan, W. Zhang, A new sensor based on luminescent terbium-organic framework for detection of Fe^{3+} in water, Inorg. Chem. Commun. 14 (2011) 937–939.

[2] Y. Zhou, H. Chen, B. Yan, An Eu^{3+} post-functionalized nanosized metal–organic framework for cation exchange-based Fe^{3+}-sensing in an aqueous environment, J. Mater. Chem. A 2 (2014) 13691–13697.

[3] W. Sun, J. Wang, G. Zhang, Z. Liu, A luminescent terbium MOF containing uncoordinated carboxyl groups exhibits highly selective sensing for Fe^{3+} ions, RSC Adv. 4 (2014) 55252–55255.

[4] X. Shen, B. Yan, Photofunctional hybrids of lanthanide functionalized bio-MOF-1 for fluorescence tuning and sensing, J. Colloid Interface Sci. 451 (2015) 63–68.

[5] X. Shen, B. Yan, Photoactive rare earth complexes for fluorescence tuning and sensing cations (Fe^{3+}) and anions ($Cr_2O_7^{2-}$), RSC Adv. 5 (2015) 6752–6757.

[6] S. Dang, T. Wang, F. Yi, Q. Liu, W. Yang, Z. Sun, A nanoscale multiresponsive luminescent sensor based on a terbium(III) metal–organic framework, Chem. Asian J. 10 (2015) 1703–1709.

[7] X. Dong, R. Wang, J. Wang, S. Zang, T.C.W. Mak, Highly selective Fe^{3+} sensing and proton conduction in a water-stable sulfonate–carboxylate Tb–organic-framework, J. Mater. Chem. A 3 (2015) 641–647.

[8] S. Zhang, J. Yang, H. Wu, Y. Liu, J. Ma, Systematic investigation of high-sensitivity luminescent sensing for polyoxometalates and iron(III) by MOFs assembled with a new resorcin[4]arene-functionalized tetracarboxylate, Chem. A Eur. J. 21 (2015) 15806–15819.

[9] K. Zheng, K. Lou, C. Zeng, S. Li, Z. Nie, S. Zhong, Hybrid membrane of agarose and lanthanide coordination polymer: a selective and sensitive Fe^{3+} sensor, Photochem. Photobiol. 91 (2015) 814–818.

[10] H. Weng, B. Yan, A flexible Tb(III) functionalized cadmium metal organic framework as fluorescent probe for highly selectively sensing ions and organic small molecules, Sens. Actuators B 228 (2016) 702–708.
[11] S. Pal, P.K. Bharadwaj, A luminescent terbium MOF containing hydroxyl groups exhibits selective sensing of nitroaromatic compounds and Fe(III) ions, Cryst. Growth Des. 16 (2016) 5852–5858.
[12] L. Zhou, W. Deng, Y. Wang, G. Xu, S. Yin, Q. Liu, Lanthanide-potassium biphenyl-3,3′-disulfonyl-4,4′-dicarboxylate frameworks: gas sorption, proton conductivity, and luminescent sensing of metal ions, Inorg. Chem. 55 (2016) 6271–6277.
[13] J. Wang, M. Jiang, L. Yan, R. Peng, M. Huangfu, X. Guo, Y. Li, P. Wu, Multifunctional luminescent Eu(III)-based metal-organic framework for sensing methanol and detection and adsorption of Fe(III) ions in aqueous solution, Inorg. Chem. 55 (2016) 12660–12668.
[14] Y. Li, D. Wang, Z. Liao, Y. Kang, W. Ding, X. Zheng, L. Jin, Luminescence tuning of the Dy–Zn metal–organic framework and its application in the detection of Fe(III) ions, J. Mater. Chem. C 4 (2016) 4211–4217.
[15] S. Xing, Q. Bing, L. Song, G. Li, J. Liu, Z. Shi, S. Feng, R. Xu, The uncommon channel-based Ln-MOFs for highly selective Fe^{3+} detection and superior rhodamine B adsorption, Chem. A Eur. J. 22 (201) (2016) 16230–16235.
[16] R. Li, X. Qu, Y. Zhang, H. Han, X. Li, Lanthanide–organic frameworks constructed from naphthalenedisulfonates: structure, luminescence and luminescence sensing properties, CrstEngComm 18 (2016) 5890–5900.
[17] D. Wang, L. Sun, C. Hao, Y. Yan, Z. Liang, Lanthanide metal–organic frameworks based on a 1,2,3-triazole-containing tricarboxylic acid ligand for luminescence sensing of metal ions and nitroaromatic compounds, RSC Adv. 6 (2016) 57828–57834.
[18] K. Xu, F. Wang, S. Huang, Z. Yu, J. Zhang, J. Yu, H. Gao, Y. Fu, X. Li, Y. Zhao, Selective fluorescence detection of anilines and Fe^{3+} ions by two lanthanide metal–organic frameworks, RSC Adv. 6 (2016) 91741–91747.
[19] Y. Wu, G. Xu, W. Dong, J. Zhao, D. Li, J. Zhang, X. Bu, Anionic lanthanide MOFs as a platform for iron-selective sensing, systematic color tuning, and efficient nanoparticle catalysis, Inorg. Chem. 56 (2017) 1402–1411.
[20] R.F. Bogale, Y. Chen, J. Ye, Y. Yang, A. Rauf, L. Duan, P. Tian, G. Ning, Highly selective and sensitive detection of 4-nitrophenol and Fe^{3+} ion based on a luminescent layered terbium (III) coordination polymer, Sens. Actuators B 245 (2017) 171–178.
[21] W. Yan, C. Zhang, S. Chen, L. Han, H. Zheng, Two lanthanide metal-organic frameworks as remarkably selective and sensitive bifunctional luminescence sensor for metal ions and small organic molecules, ACS Appl. Mater. Interfaces 9 (2017) 1629–1634.
[22] H.N. Abdelhamid, A. Bermejo-Gómez, B. Martín-Matute, X. Zou, A water-stable lanthanide metal-organic framework for fluorimetric detection of ferric ions and tryptophan, Microchim. Acta 184 (2017) 3363–3371.
[23] R.F. Bogale, Y. Chen, J. Ye, S. Zhang, Y. Li, X. Liu, T. Zheng, A. Raufa, G. Ning, A terbium (III)-based coordination polymer for selective and sensitive sensing of nitroaromatics and ferric ion: synthesis, crystal structure and photoluminescence properties, New J. Chem. 41 (2017) 12713–12720.
[24] Z. Sun, Y. Li, Y. Ma, L. Li, Dual-functional recyclable luminescent sensors based on 2D lanthanide-based metal-organic frameworks for highly sensitive detection of Fe^{3+} and 2,4-dinitrophenol, Dyes Pigm. 146 (2017) 263–271.
[25] Y. Tang, C. Wang, S. Chen, H. Dai, A terbium(III) organic framework as a fluorescent probe for selectively sensing of organic small molecules and metal ions especially nitrobenzene and Fe^{3+}, J. Coord. Chem. 70 (2017) 3996–4007.

[26] F. Zhao, X. Guo, Z. Dong, Z. Liu, Y. Wang, 3D LnIII-MOFs: slow magnetic relaxation and highly sensitive luminescence detection of Fe^{3+} and ketones, Dalton Trans. 47 (2018) 8972–8982.

[27] L. Liu, Y. Wang, R. Lin, Z. Yao, Q. Lin, L. Wang, Z. Zhang, S. Xiang, Two water-stable lanthanide metal–organic frameworks with oxygen-rich channels for fluorescence sensing of Fe(III) ions in aqueous solution, Dalton Trans. 47 (2018) 16190–16196.

[28] L. Xua, Y. Xu, X. Li, Z. Wang, T. Sun, X. Zhang, Eu^{3+}/Tb^{3+} functionalized Bi-based metal–organic frameworks toward tunable white-light emission and fluorescence sensing applications, Dalton Trans. 47 (2018) 16696–16703.

[29] L. Li, S. Shen, W. Ai, S. Song, Y. Bai, H. Liu, Facilely synthesized Eu^{3+} post-functionalized UiO-66-type metal-organic framework for rapid and highly selective detection of Fe^{3+} in aqueous solution, Sens. Actuators B 267 (2018) 542–548.

[30] K. Shang, J. Sun, D. Hu, X. Yao, L. Zhi, C. Si, J. Liu, Six Ln (III) coordination polymers with a semirigid tetracarboxylic acid ligand: bifunctional luminescence sensing, NIR-luminescent emission, and magnetic properties, Cryst. Growth Des. 18 (2018) 2112–2120.

[31] Y. Huang, H. Chen, Y. Wang, Y. Ren, Z. Li, L. Li, Y. Wang, A channel-structured Eu-based metal–organic framework with a zwitterionic ligand for selectively sensing Fe^{3+} ions, RSC Adv. 8 (2018) 21444–21450.

[32] J. Gu, Y. Cai, Y. Liu, X. Liang, A.M. Kirillov, New lanthanide 2D coordination polymers constructed from a flexible ether-bridged tricarboxylate block: synthesis, structures and luminescence sensing, Inorg. Chim. Acta 469 (2018) 98–104.

[33] F. Yang, G. Yang, Y. Wu, Y. Yan, J. Liu, R. Gao, W. Zhang, Y. Wang, Ln(III)-MOFs (Ln = Tb, Eu, Dy, and Sm) based on triazole carboxylic ligand with carboxylate and nitrogen donors with applications as chemical sensors and magnetic materials, J. Coord. Chem. 71 (2018) 2702–2713.

[34] H. Xu, Y. Dong, Y. Wu, W. Ren, T. Zhao, S. Wang, J. Gao, An -OH group functionalized MOF for ratiometric Fe^{3+} sensing, J. Solid State Chem. 258 (2018) 441–446.

[35] Y. Wang, R. Huang, J. Zhang, G. Cheng, H. Yang, Lanthanide (Tb^{3+}, Eu^{3+})-functionalized a new one dimensional Zn-MOF composite as luminescent probe for highly selectively sensing Fe^{3+}, Polyhedron 148 (2018) 178–183.

[36] X. Song, Y. Wang, J. Yan, X. Chen, Y. Meng, Z. Tan, Enhancing the Fe^{3+} sensing sensitivity by energy transfer and phase transformation in a bimetallic lanthanide metal-organic framework, ChemistrySelect 3 (2018) 9564–9570.

[37] Y. Su, J. Yu, Y. Li, S.F.Z. Phua, G. Liu, W. Lim, X. Yang, R. Ganguly, C. Dang, C. Yang, Y. Zhao, Versatile bimetallic lanthanide metal-organic frameworks for tunable emission and efficient fluorescence sensing, Commun. Chem. 1 (2018) 12.

[38] S.M. Sheta, S.M. El-Sheikh, M.M. Abd-Elzaher, A.R. Wassel, A novel nano-size lanthanum metal–organic framework based on 5-amino-isophthalic acid and phenylenediamine: photoluminescence study and sensing applications, Appl. Organomet. Chem. 33 (2019), e4777.

[39] S. Hussain, X. Chen, W.T.A. Harrison, M.R.J. Elsegood, S. Ahmad, S. Li, S. Muhammad, D. Awoyelu, Synthesis, crystal structures and photoluminescent properties of one-dimensional europium(III)- and terbium(III)-glutarate coordination polymers, and their applications for the sensing of Fe^{3+} and nitroaromatics, Front. Chem. 7 (2019) 728.

[40] W. Chen, L. Li, X. Li, L. Lin, G. Wang, Z. Zhang, L. Li, Y. Yu, Layered rare earth-organic framework as highly efficient luminescent matrix: the crystal structure, optical spectroscopy, electronic transition, and luminescent sensing properties, Cryst. Growth Des. 19 (2019) 4754–4764.

[41] J. Zhang, S.B. Peh, J. Wang, Y. Du, S. Xi, J. Dong, A. Karmakar, Y. Ying, Y. Wang, D. Zhao, Hybrid MOF-808-Tb nanospheres for highly sensitive and selective detection of acetone vapor and Fe^{3+} in aqueous solution, Chem. Commun. 55 (2019) 4727–4730.

[42] W. Yang, J. Li, Z. Xu, J. Yang, Y. Liu, L. Li, A Eu-MOF/EDTA-NiAl-CLDH fluorescent micromotor for sensing and removal of Fe^{3+} from water, J. Mater. Chem. C 7 (2019) 10297–10308.

[43] Y. Wu, M. Lin, D. Liu, M. Liu, J. Qian, Two-dimensional Cd(II) coordination polymer encapsulated by Tb^{3+} as a reversible luminescent probe for Fe^{3+}, RSC Adv. 9 (2019) 34949–34957.

[44] W. Wang, Q. Gao, X. Li, J. Wang, C. Wang, Y. Zhang, X. Bu, A water-stable lanthanide-coordination polymer with free Lewis site for fluorescent sensing of Fe^{3+}, Chin. Chem. Lett. 30 (2019) 75–78.

[45] X. Zhang, J. Hua, J. Li, T. Liu, J. Wang, X. Ma, A bifunctional luminescent coordination polymer as recyclable sensor for detecting TNP and Fe^{3+} with high selectivity and sensitivity, Inorg. Chim. Acta 486 (2019) 556–561.

[46] Y. Qin, J. Feng, S. Yu, J. Zhang, Z. Li, G. Li, Identification performance of two luminescent lanthanide–organic frameworks, Polyhedron 161 (2019) 40–46.

[47] G.E. Gomez, M. dos Santos Afonso, H.A. Baldoni, F. Roncaroli, G.J.A.A. Soler-Illia, Luminescent lanthanide metal organic frameworks as chemosensing platforms towards agrochemicals and cations, Sensors 19 (2019) 1260.

[48] P. Wu, L. Xia, M. Huangfu, F. Fu, M. Wang, B. Wen, Z. Yang, J. Wang, Lanthanide-based metal-organic frameworks containing "V-shaped" tetracarboxylate ligands: synthesis, crystal structures, "naked-eye" luminescent detection, and catalytic properties, Inorg. Chem. 59 (2020) 264–273.

[49] Z. Li, X. Zhu, E. Gao, S. Wu, Y. Zhang, M. Zhu, Bifunctional luminescent Eu metal–organic framework for sensing nitroaromatic pollutants and Fe^{3+} ion with high sensitivity and selectivity, Appl. Organomet. Chem. 35 (2020), e6136.

[50] Q. Xu, G. Dong, R. Cui, X. Li, 3D lanthanide-coordination frameworks constructed by a ternary mixed-ligand: crystal structure, luminescence and luminescence sensing, CrstEngComm 22 (2020) 740–750.

[51] X. Liu, L. Du, R. Li, N. Ma, M. You, X. Feng, Different effects in the selective detection of aniline and Fe^{3+} by lanthanide-based coordination polymers containing multiple reactive sites, CrstEngComm 22 (2020) 2837–2844.

[52] G. Liang, S. Wang, M. Xu, H. Chen, G. Liang, L. Gui, X. Wang, 2D lanthanide coordination polymers constructed from a semi-rigid tricarboxylic acid ligand: crystal structure, luminescence sensing and color tuning, CrstEngComm 22 (2020) 6161–6169.

[53] X. Yin, S. Li, B. Liao, Water-stable ln-exclusive metal-organic framework for highly selective sensing of Fe^{3+} ions, Dyes Pigm. 174 (2020), 108035.

[54] X. Cheng, J. Hu, J. Li, M. Zhang, Tunable emission and selective luminescence sensing for nitro- pollutants and metal ions based on bifunctional lanthanide metal-organic frameworks, JOL 221 (2020), 117100.

[55] L. Hou, Y. Song, F. Lang, Z. Wang, L. Wang, Fluorometric determination of Fe^{3+} and polychlorinated benzenes based on Tb^{3+}-pyromellitic acid coordination polymer, J. Ind. Eng. Chem. 90 (2020) 145–151.

[56] C. Yang, C. Jiang, M. Zhang, X. Chen, P. Zou, R. Yang, H. Rao, G. Wang, A multifunctional Eu-based coordination polymer luminescent sensor for highly sensitive and selective detection of Fe^{3+} and acetone, Polyhedron 175 (2020), 114216.

[57] P. Jia, Z. Wang, Y. Zhang, D. Zhang, W. Gao, Y. Su, Y. Li, C. Yang, Selective sensing of Fe^{3+} ions in aqueous solution by a biodegradable platform based lanthanide metal organic framework, Spectrochim. Acta A Mol. Biomol. Spectrosc. 230 (2020), 118084.

[58] B. Liu, C. Sun, Y. Chen, Nucleotide/Tb^{3+} coordination polymer as a luminescent nanosensor: synthesis and sensing of iron(II) in human serum, J. Mater. Chem. B 2 (2014) 1661–1666.

[59] X. Xu, B. Yan, Eu(III)-functionalized MIL-124 as fluorescent probe for highly selectively sensing ions and organic small molecules especially for Fe(III) and Fe(II), ACS Appl. Mater. Interfaces 7 (2015) 721–729.

[60] Z. Zhou, Y. Han, X. Xing, S. Du, Microporous lanthanide metal–organic frameworks with multiple 1D channels: tunable colors, white-light emission, and luminescent sensing for iron(II) and iron(III), ChemPlusChem 81 (2016) 798–803.

[61] R. Maity, D. Chakraborty, S. Nandi, A.K. Yadav, D. Mullangi, C.P. Vinod, R. Vaidhyanathan, Aqueous-phase differentiation and speciation of Fe^{3+} and Fe^{2+} using water-stable photoluminescent lanthanide-based metal-organic framework, ACS Appl. Nano Mater. 2 (2019) 5169–5178.

[62] E. Gao, M. Zhu, Y. Zhang, M. Kosinova, V.P. Fedin, S. Wu, Logic operation for differentiation and speciation of Fe^{3+} and Fe^{2+} based on two-dimensional metal–organic frameworks with tunable emissions, Appl. Organomet. Chem. (2020), e6129.

[63] Z. Hao, X. Song, M. Zhu, X. Meng, S. Zhao, S. Su, W. Yang, S. Song, H. Zhang, One-dimensional channel-structured Eu-MOF for sensing small organic molecules and Cu^{2+} ion, J. Mater. Chem. A 1 (2013) 11043–11050.

[64] Z. Hao, G. Yang, X. Song, M. Zhu, X. Meng, S. Zhao, S. Song, H. Zhang, A europium(III) based metal–organic framework: bifunctional properties related to sensing and electronic conductivity, J. Mater. Chem. A 2 (2014) 237–244.

[65] B. Liu, W. Wu, L. Hou, Y. Wang, Four uncommon nanocage-based Ln-MOFs: highly selective luminescent sensing for Cu^{2+} ions and selective CO_2 capture, Chem. Commun. 50 (2014) 8731–8734.

[66] C. Liu, B. Yan, Highly effective chemosensor of a luminescent silica@lanthanide complex-@MOF heterostructured composite for metal ion sensing, RSC Adv. 5 (2015) 101982–101988.

[67] L. Zhang, A. Liu, Y. Liu, J. Shen, C. Du, H. Hou, A luminescent europium metal–organic framework with free phenanthroline sites for highly selective and sensitive sensing of Cu^{2+} in aqueous solution, Inorg. Chem. Commun. 56 (2015) 137–141.

[68] X. Lian, B. Yan, Novel core–shell structure microspheres based on lanthanide complexes for white-light emission and fluorescence sensing, Dalton Trans. 45 (2016) 2666–2673.

[69] J. Zhao, Y. Wang, W. Dong, Y. Wu, D. Li, Q. Zhang, A robust luminescent Tb(III)-MOF with Lewis basic pyridyl sites for the highly sensitive detection of metal ions and small molecules, Inorg. Chem. 55 (2016) 3265–3271.

[70] Q. Liu, J. Yang, F. Guo, L. Jin, W. Sun, Facile fabrication of MIL-103(Eu) porous coordination polymer nanostructures and their sorption and sensing properties, Dalton Trans. 45 (2016) 5841–5847.

[71] S. Wang, T. Cao, H. Yan, Y. Li, J. Lu, R. Ma, D. Li, J. Dou, J. Bai, Functionalization of microporous lanthanide-based metal-organic frameworks by dicarboxylate ligands with methyl-substituted thieno[2,3-b]thiophene groups: sensing activities and magnetic properties, Inorg. Chem. 55 (2016) 5139–5151.

[72] P. Du, W. Gu, X. Liu, Multifunctional three-dimensional europium metal-organic framework for luminescence sensing of benzaldehyde and Cu^{2+} and selective capture of dye molecules, Inorg. Chem. 55 (2016) 7826–7828.

[73] S. Wang, R. Ma, Z. Chen, Y. Li, T. Cao, C. Zhou, J. Bai, Solvent- and metal-directed lanthanide-organic frameworks based on pamoic acid: observation of slow magnetization relaxation, magnetocaloric effect and luminescent sensing, Sci. China: Chem. 59 (2016) 948–958.

[74] H. Weng, B. Yan, A Eu(III) doped metal-organic framework conjugated with fluorescein-labeled single-stranded DNA for detection of Cu(II) and sulfide, Anal. Chim. Acta 988 (2017) 89–95.

[75] R. Ma, Z. Chen, S. Wang, Q. Yao, Y. Li, J. Lu, D. Li, J. Dou, Solvent-induced assembly of two helical Eu(III) metal-organic frameworks and fluorescence sensing activities towards nitrobenzene and Cu^{2+} ions, J. Solid State Chem. 252 (2017) 142–151.

[76] E. Zhou, C. Qin, D. Tian, X. Wang, B. Yang, L. Huang, K. Shao, Z. Su, A difunctional metal–organic framework with Lewis basic sites demonstrating turn-off sensing of Cu^{2+} and sensitization of Ln^{3+}, J. Mater. Chem. C 6 (2018) 7874–7879.

[77] Z. Sun, H. Li, G. Sun, J. Guo, Y. Ma, L. Li, Design and construction of lanthanide metal-organic frameworks through mixed-ligand strategy: sensing property of acetone and Cu^{2+}, Inorg. Chim. Acta 469 (2018) 51–56.

[78] N. Liu, H. Liu, J. Lu, Z. He, Z. Wang, S. Wang, Y. Li, Y. Huang, Syntheses, structures, fluorescence sensing and magnetic properties of two coordination polymers based on 5-(benzimidazol-2-yl) isophthalic acid ligand, Inorg. Chim. Acta 469 (2018) 515–522.

[79] Y. Liang, L. Luo, Y. Li, B. Ling, B. Chen, X. Wang, T. Luan, A luminescent probe for highly selective Cu^{2+} sensing using a lanthanide-doped metal organic framework with large pores, Eur. J. Inorg. Chem. 2019 (2019) 206–211.

[80] J. Luo, B. Liu, X. Zhang, R. Liu, A Eu^{3+} post-functionalized metal-organic framework as fluorescent probe for highly selective sensing of Cu^{2+} in aqueous media, J. Mol. Struct. 1177 (2019) 444–448.

[81] Z. Sun, J. Sun, L. Xi, J. Xie, X. Wang, Y. Ma, L. Li, Two novel lanthanide metal-organic frameworks: selective luminescent sensing for nitrobenzene, Cu^{2+}, and MnO_4^-, Cryst. Growth Des. 20 (2020) 5225–5234.

[82] X. Peng, G. Bao, Y. Zhong, J. He, L. Zeng, H. Yuan, Highly selective detection of Cu^{2+} in aqueous media based on Tb^{3+}-functionalized metal-organic framework, Spectrochim. Acta A Mol. Biomol. Spectrosc. 240 (2020), 118621.

[83] Z. Ma, J. Shi, M. Wang, L. Tian, Lanthanide-organic complex with uncoordinated Lewis basic triazolyl sites as multi-responsive sensor for nitrobenzene, Cu^{2+} and MnO_4^-, Dyes Pigm. 185 (2021) 10893.

[84] X. Zhou, J. Peng, C. Wen, Z. Liu, X. Wang, J. Wu, Y. Ou, Tuning the structure and Zn(II) sensing of lanthanide complexes with two phenylimidazophenanthrolines by acetonitrile hydrolysis, CrstEngComm 19 (2017) 6533–6539.

[85] X. Song, H. Meng, Z. Lin, L. Wang, 2D lanthanide coordination polymers: synthesis, structure, luminescent properties, and ratiometric sensing application in the hydrostable PMMA-doped hybrid films, ACS Appl. Polym. Mater. 2 (2020) 1644–1655.

[86] R. Wang, X. Dong, H. Xu, R. Pei, M. Ma, S. Zang, H. Hou, T.C.W. Mak, A super water-stable europium–organic framework: guests inducing low-humidity proton conduction and sensing of metal ions, Chem. Commun. 50 (2014) 9153–9156.

[87] H. Zhang, R. Fan, W. Chen, J. Fan, Y. Dong, Y. Song, X. Du, P. Wang, Y. Yang, 3D Lanthanide metal-organic frameworks based on mono-, tri-, and heterometallic tetranuclear clusters as highly selective and sensitive luminescent sensor for Fe^{3+} and Cu^{2+} ions, Cryst. Growth Des. 16 (2016) 5429–5440.

[88] Y. Du, H. Yang, R. Liu, C. Shao, L. Yang, A multi-responsive chemosensor for highly sensitive and selective detection of Fe^{3+}, Cu^{2+}, $Cr_2O_7^{2-}$ and nitrobenzene based on a luminescent lanthanide metal-organic framework, Dalton Trans. 49 (2020) 13003–13016.

[89] X. Wang, Y. Wang, X. Wang, K. Lu, W. Jiang, P. Cui, H. Hao, F. Dai, Two series of ln-MOFs by solvent induced self-assembly demonstrating the rapid selective sensing of Mg^{2+} and Fe^{3+} cations, Dalton Trans. 49 (2020) 15473–15480.

Chapter 7

Rare earth metal-organic framework hybrid materials for luminescence responsive sensing of metal ions (II)

7.1 Luminescence responsive sensing of Hg^{2+} using rare earth metal-organic framework hybrid materials

Mercury, an extremely toxic heavy metal and a dangerous contaminant, is widely used in thermometers, barometers, manometers, float valves, and other devices. Ionic mercury is easily converted into neurotoxic methylmercury by bacteria when it enters the environment. Bioaccumulated mercury in the food chain may enter the human body and can cause a variety of diseases. Mercury(II) ion is one of the most toxic pollutants, and is widely distributed in the air, water, and soil through natural and human activities. Mercury(II) can accumulate in the human body, leading to brain damage and other chronic diseases. Mercury pollutants have become a serious and urgent global problem due to their potential to do great harm to the environment and to human health. The water-soluble mercuric ion (Hg^{2+}) is one of the most stable inorganic forms of mercury, and is nonbiodegradable and bioaccumulable through the food chain. Even at very low concentrations, it can damage brain, kidneys, and nervous system [1–6]. Therefore the development of highly selective functional materials to detect and simultaneously remove Hg^{2+} is urgently needed for environmental protection, as well as to ensure human health [4–12].

Tan et al. attempted to design and prepare rare earth coordination polymer nanoparticles (CPNPs) with a photoinduced electronic transfer (PET) fluorescence sensing function and to use this nanosensor to detect Hg^{2+} in aqueous solution. The nanoparticles were composed of adenine (Ad), Tb^{3+}, and dipicolinic acid (DPA), denoted as Ad/Tb/DPA CPNPs [7]. Under light excitation, the nitrogen atom of adenine may transfer its electron to DPA and prevent the intramolecular energy transfer from DPA to Tb^{3+}, leading to fluorescence quenching by the Ad/Tb/DPA CPNPs. Hg^{2+} ions have a high affinity to N atoms and can be used to disrupt the PET process. So, the presence of Hg^{2+} may enhance the fluorescence of Ad/Tb/DPA CPNPs by the coordination of Hg^{2+} with adenine

Rare Earth Metal-Organic Framework Hybrid Materials for Luminescence Responsive Chemical Sensors
https://doi.org/10.1016/B978-0-323-91236-5.00007-4

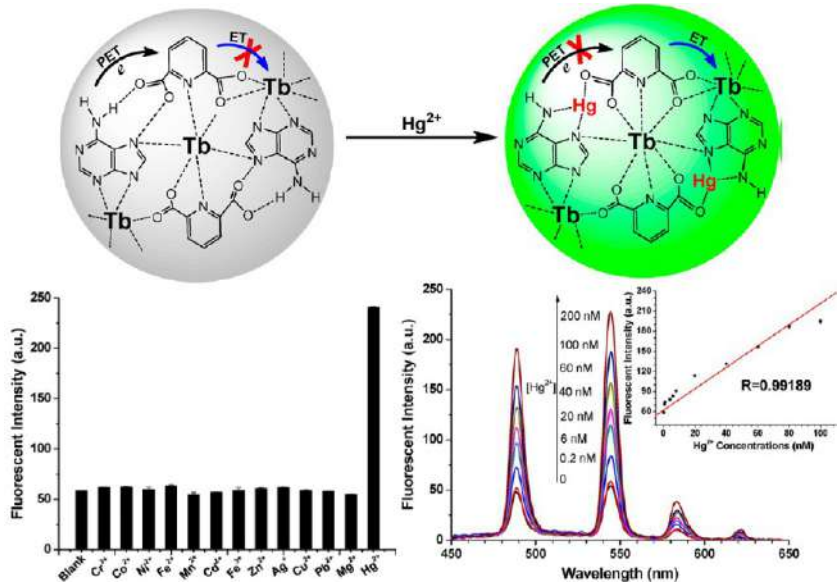

FIG. 7.1 *(Top)* Scheme for coordination polymer nanoparticle (CPNP)Ad/Tb/DPA for sensing of Hg^{2+} by photoinduced electron transfer (PET). *(Bottom, left)* Effect of various metal ions (1 μM) on the fluorescence intensity of Ad/Tb/DPA CPNPs at 545 nm. *(Bottom, right)* Fluorescence emission spectra of Ad/Tb/DPA CPNPs in the presence of different concentrations of Hg^{2+} solution (0, 0.2, 6, 20, 40, 60, 100, 200 nM). Inset: Linear relationship between the fluorescence intensity of Ad/Tb/DPA CPNPs at 545 nm and Hg^{2+} concentration. *(Reproduced with permission from H. Tan, B. Liu, Y. Chen, Lanthanide coordination polymer nanoparticles for sensing of mercury(II) by photoinduced electron transfer, ACS Nano 6 (2012) 10505–10511. Copyright 2012 American Chemical Society.)*

(Fig. 7.1; top). As shown in Fig. 7.1 (bottom, left), only the addition of Hg^{2+} results in a significant fluorescence enhancement. The high selectivity of Ad/Tb/DPA CPNPs to Hg^{2+} is ascribed to the fact that Hg^{2+} possesses a much higher binding ability to the N atoms of adenine and the carboxylic acid group of DPA than other metal ions, and to the higher stability constant of the Hg^{2+} ion with DPA than that of other ions. The unusual selectivity of Ad/Tb/DPA CPNPs to Hg^{2+} is appropriate for application to the detection of trace Hg^{2+} in environmental water samples. The fluorescence response of Ad/Tb/DPA CPNPs to Hg^{2+} with different concentrations is shown in Fig. 7.1 (bottom, right). The fluorescence of Ad/Tb/DPA CPNPs is enhanced gradually with the increase of Hg^{2+} concentrations from 0 to 200 nM. There is a linear fluorescence response to Hg^{2+} in the concentration range of 0.2–100 nM. The detection limit (LOD) is 0.2 nM on the basis of a signal-to-noise ratio of 3:1 [7].

Li et al. constructed an inner filter effect (IFE)-based Turn-On sensor through selecting Eu^{3+}-based coordination polymer nanoparticles (CPNPs) as the

fluorophore and imidazole-4,5-dicarboxylic acid (Im) as the absorber [10]. The Eu/IPA CPNPs are built from the self-assembly of Eu^{3+} and isophthalic acid (IPA), which can emit strong red fluorescence. Upon the addition of Im, a significant decrease in the fluorescence of Eu/IPA CPNPs was observed, due to Im having a strong absorption band that greatly overlaps with the excitation spectrum of Eu/IPA CPNPs to filter out the excitation energy of Eu/IPA CPNPs through the internal filter effect (IFE). Im can react with Hg^{2+} to form a stable Hg/Im complex due to its high affinity to Hg^{2+}. The introduction of Hg^{2+} causes Im to be released from the surface of Eu/IPA CPNPs to form a Hg/Im complex, leading to the suppression of the IFE of Im. In the presence of Hg^{2+}, therefore, a recovered fluorescence of Eu/IPA CPNPs through the formation of a Hg/Im complex would be observed (Fig. 7.2; top). As shown in Fig. 7.2A (middle), only the addition of Hg^{2+} results in a significant enhancement in the fluorescence of the Eu/IPA-Im complex, indicating that its highly specific fluorescence response to Hg^{2+} can be attributed to the higher affinity of Im to Hg^{2+} than other metal ions. Upon the addition of Im, an obvious decrease in the fluorescence of Eu/IPA CPNPs is observed. Such quenching behavior can even be observed by the naked eye under a common UV lamp (Fig. 7.2B; middle). Under optimized conditions, the fluorescence changes of the Eu/IPA-Im complex in the presence of Hg^{2+} with different concentrations were then investigated. As shown in Fig. 7.2 (bottom), the fluorescence of the Eu/IPA-Im complex is enhanced with gradually increasing Hg^{2+} concentration. The fluorescence intensity of the Eu/IPA-Im complex at 615 nm displays a linear correlation to the Hg^{2+} concentration from 2 nM to 2 mM. The LOD for Hg^{2+} is estimated to be about 2 nM. Moreover, the proposed Eu/IPA CPNP-based fluorescent sensor has the advantages of a Turn-On work mode with high sensitivity and selectivity and a fast response to determine the levels of Hg^{2+} in urine samples for practical application [10].

Xia et al. chose 4,4′,4″-*s*-triazine-1,3,5-triyltri-*p*-aminobenzoic acid (H_3TATAB) to construct a terbium MOF, Tb(TATAB)·$(DMF)_4(H_2O)(MeOH)_{0.5}$ (Tb-MOF) for Hg^{2+} sensing. The Tb-MOF exhibited good water stability and could exclusively probe Hg^{2+} even in the presence of other interferential metal ions [11]. The emission intensity of Tb-MOF is gradually quenched with a Hg^{2+} concentration increasing from 0 to 1×10^{-2} M (Fig. 7.3A; left). The luminescent response to Hg^{2+} ions is immediate and reaches a plateau after only 1 min. Quantitatively, the quenching effect can be analyzed with a K_{sv} (Stern-Volmer quenching constant) value of 4851 M^{-1}. There is a good linear relationship between I_0/I and [Hg^{2+}] over a wide concentration range (Fig. 7.3B; left), indicating that either dynamic or static quenching is taking place. The one-dimensional (1D) pore channel system may be beneficial for the diffusion and accumulation of Hg^{2+} in the framework, which leads to a low LOD, estimated to be 4.4 nM based on a signal-to-noise ratio of 3:1, which is even lower than the maximum permitted level of Hg^{2+} in drinking water (2 ppb, 10 nm). As shown in Fig. 7.3A (bottom), the addition of Hg^{2+} causes a significant luminescence

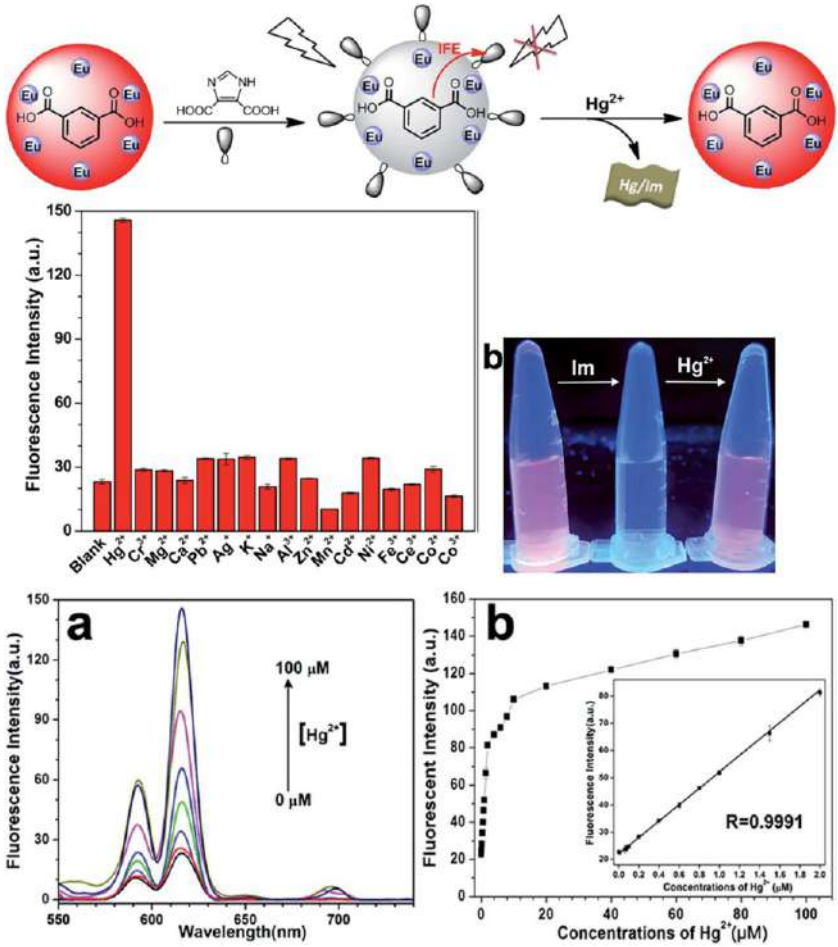

FIG. 7.2 *(Top)* Schematic illustration of the changes in the fluorescence of Eu/IPA CPNPs induced by imidazole-4,5-dicarboxylic acid (Im) and Hg^{2+}. *(Middle)* (A) Fluorescence responses of the Eu/IPA-Im complex to different metal ions (each 100 mM). The reactions were performed in Tris-HCl buffer (25 mM, pH 7.0) with 26.5 mg mL^{-1} of the Eu/IPA CPNPs, 320 mM of Im and 100 mM of Hg^{2+} or other metal ions at room temperature; the total volume was 100 mL. The excitation wavelength is 250 nm. (B) Photograph of 26.5 mg mL^{-1} of Eu/IPA CPNPs in the absence and presence of 320 mM of Im with and without 100 mM Hg^{2+} under a 365-nm UV lamp. *(Bottom)* (A) Excitation spectrum of 26.5 mg mL^{-1} of Eu/IPA CPNPs *(black line)* and the absorption spectrum of 320 mM of pure Im *(red line)*. The emission wavelength was fixed at 615 nm to record the excitation spectrum of Eu/IPA CPNPs. (B) Absorption spectra of the Eu/IPA-Im complex in the presence of Hg^{2+} with different concentrations (0, 0.5, 5, 10, 30, 50, and 100 mM). *(Reproduced with permission from Q. Li, C. Wang, H. Tan, G. Tang, J. Gao, C. Chen, A turn on fluorescent sensor based on lanthanide coordination polymer nanoparticles for the detection of mercury(II) in biological fluids, RSC Adv. 6 (2016) 17811–17817. Copyright 2016 Royal Chemical Society.)*

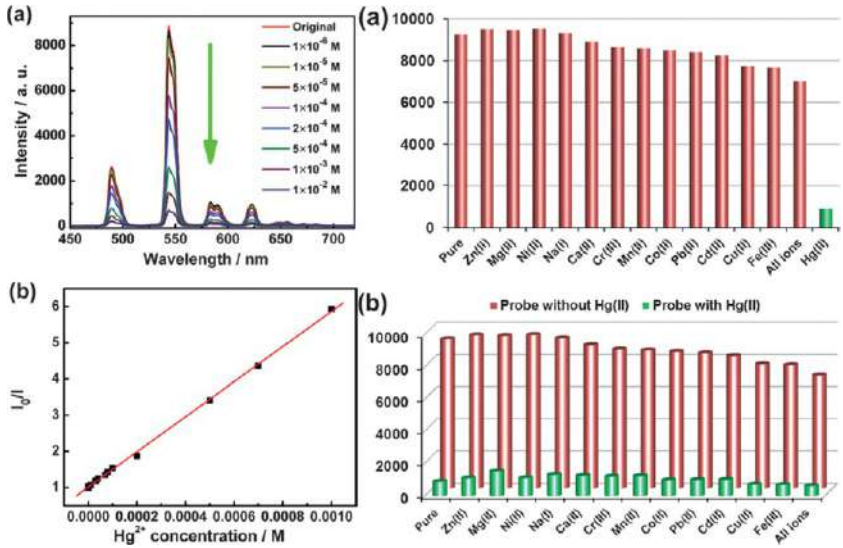

FIG. 7.3 *(Left)* (A) Luminescent emission spectra (excited at 350 nm) of Tb-MOF in Hg^{2+} solutions with different concentrations. (B) Stern-Volmer plots of I_0/I versus Hg^{2+} concentration and the fitting line in water ($R^2 = 0.999$, $K_{sv} = 4851\ M^{-1}$). *(Right)* Luminescence intensity histograms of Tb-MOF dispersed in water with the addition of different metal ions (A) and subsequent addition of Hg^{2+} ion (B). The concentrations of interferential metal ions and Hg^{2+} ion both are 1 mm. Emission intensities at the $^5D_4 \rightarrow {}^7F_5$ transition ae selected. *(Reproduced with permission from T. Xia, T. Song, G. Zhang, Y. Cui, Y. Yang, Z. Wang, G. Qian, A terbium metal–organic framework for highly selective and sensitive luminescence sensing of Hg^{2+} ions in aqueous solution, Chem. A Eur. J. 22 (2016) 18429–18434. Copyright 2016 Wiley.)*

quenching, while no remarkable luminescence changes are observed when other ions are involved. Fig. 7.3B (bottom) demonstrates that there is little change in quenching efficiency with the coexistence of other metal ions as compared to that in the presence of only Hg^{2+}. Hg^{2+} possesses a much higher binding ability with the N atoms, and the interaction between N atoms and Hg^{2+} disturbs the energy transfer from H_3TATAB to Tb^{3+} ions. What is more, the space between nitrogen atoms in triazine and imino groups is more suitable to interact with the larger ionic radius of Hg^{2+} than with other metal ions. The group further detected the concentration of Hg^{2+} in different natural water sources (river water, drinking water, and tap water) by the standard addition method, whose results indicate that the probe has good precision and satisfactory reproducibility, and might be practically used to detect Hg^{2+} in environmental samples [11].

7.2 Luminescence responsive sensing of Cd^{2+} using rare earth metal-organic framework hybrid materials

Among various heavy metal ions, Cd^{2+} is one of the most dangerous ions due to its high toxicity and carcinogenicity. It is widely used in many fields, including industry, agriculture, and military affairs. These sources lead to a high level of cadmium exposure and contamination. Furthermore, toxic Cd^{2+} can be easily absorbed and accumulated in plants and other organisms. This may result in serious diseases and even certain forms of cancer. Bearing in mind the elevated risks related to human health, qualitative and quantitative detection of cadmium can be considered a goal of primary importance. Cd^{2+}, with its high toxicity and carcinogenicity to humans and the environment, has attracted considerable attention [13–18]. Thus it is significant to sense Cd^{2+} in the water for environmental protection. For Cd^{2+}, many kinds of rare earth MOF hybrid materials show the Turn-On luminescence response and Cd^{2+} behaves as a heavy metal ion to enhance the linker's absorption to transfer effective energy to Ln^{3+} [19–24].

Hao et al. utilized the facile yet versatile postsynthetic approach to fabricate a highly efficient luminescent hybrid by encapsulating Eu^{3+} cations into the pores of UiO-66(Zr)-$(COOH)_2$ (Zr-MOF), developed as a fluorescent probe for Cd^{2+} and a sensor [19]. As shown in Fig. 7.4 (left), with Cr^{3+}, Fe^{2+}, and Cu^{2+}, the luminescence of Eu^{3+} is almost quenched. By contrast, the interaction with Cd^{2+} drastically enhances the luminescence intensity, with a maximum of more than 8.0 times as much as that of the original. As a result, when irradiated under UV light, only Cd^{2+} can induce a red-colored luminescence, which can be

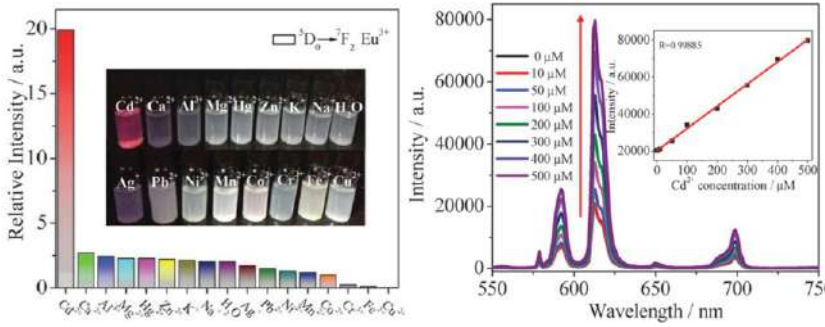

FIG. 7.4 *(Left)* Suspension-state luminescent spectra relative intensities of $^5D_0 \rightarrow {}^7F_2$ at 614 nm for Eu^{3+}@Zr-MOF dispersed in various metal ion aqueous solutions (10 mM) when excited at 322 nm. Inset: the corresponding photographs under UV-light irradiation. *(Right)* Fluorescence intensity of Eu^{3+}@Zr-MOF at 614 nm as a function of Cd^{2+} concentration in aqueous solution ($\lambda_{ex} = 322$ nm). Inset: linear relationship of the emission intensity of Eu^{3+}@Zr-MOF enhanced by Cd^{2+} ions. *(Reproduced with permission from J. Hao, B. Yan, A water-stable lanthanide-functionalized MOF as a highly selective and sensitive fluorescent probe for Cd^{2+}, Chem. Commun. 51 (2015) 7737–7740. Copyright 2015 Royal Chemical Society.)*

clearly seen by the naked eye, while no visible change can be observed upon the addition of other metal ions (inset of Fig. 7.4). The group measured the fluorescence responses of Eu^{3+}@Zr-MOF in the presence of different concentrations of Cd^{2+}. As demonstrated in Fig. 7.4 (right), when the Cd^{2+} concentration increased from 0 to 500 mM, the emission intensity of Eu^{3+}@Zr-MOF was gradually enhanced and showed a good linear relationship ($R^2 = 0.99885$) between the emission intensity of Eu^{3+} at 614 nm and the concentration of Cd^{2+}. The LOD of Eu^{3+}@Zr-MOF toward Cd^{2+} was calculated to be 0.06 mM. The Cd^{2+}-induced fluorescence enhancement reaction is very fast. The emission intensity of Eu^{3+} ions at 614 nm has been increased to more than 7.0 times in 1 min and to a constant value in 8 min. The real samples, containing different concentrations of Cd^{2+} in tap water and lake water, were regularly analyzed by Eu^{3+}@Zr-MOF, indicating that this probe can be practically used to quantitatively detect Cd^{2+} in water samples. A proposed mechanism of luminescence enhancement induced by Cd^{2+} ions is that Cd^{2+} ions interact with the Lewis basic carboxylic oxygen sites within Eu^{3+}@Zr-MOF and facilitate the efficiency of energy transformation from ligands to Eu^{3+} ions, which results in a more efficient energy transition from ligands to Eu^{3+} for the following reasons: the coordination of Cd^{2+} to reduce various nonradiative deactivations and decrease energy loss; Cd^{2+} ions' heavy atom effect to promote intersystem crossing energy transfer (S_1–T_1); the Cd^{2+}' d^{10} closed shell electronic configuration and its ligand-to-metal (Cd^{2+}) charge transfer (LMCT) to change the energy level of the excited state of the ligands, to make the energy-matching between the ligands and Eu^{3+} more suitable [19].

Liu et al. prepared a Eu^{3+} functionalized MOF CPM-17-Zn-Eu with appropriate synthesis conditions (Fig. 7.5; top), which possesses the similar zeolite-type topologies structures but different properties with as-synthesized CPM-17-Zn [20]. This highly efficient luminescent RE-MOF is fabricated by encapsulating Eu^{3+} cations into the channels of CPM-17-Zn, resulting in a highly selective, strongly sensitive, and rapidly detective fluorescent probe. CPM-17-Zn-Eu was selected to recognize Cd^{2+} ions in aqueous solutions with a Turn-On Eu^{3+} characteristic luminescence. As shown in Fig. 7.5 (bottom, left), the photoluminescence intensity of CPM-17-Zn-Eu is largely dependent on the metal ion-water solutions, whose intensity is enhanced by about 4.0 times with the addition of Cd^{2+} compared with that of the aqueous solutions. Only Cd^{2+} could induce a red-colored luminescence that can be clearly seen under UV light irradiation, and the addition of other metal ions could not induce visible change. In Fig. 7.5 (bottom, right), the luminescence intensity of CPM-17-Zn-Eu incorporated with Cd^{2+} shows a strong dependence on the concentration of the metal ion, whose luminescence intensity is enhanced proportionally to the concentration of Cd^{2+}. Quantitatively, this enhancing effect can be rationalized with the linear correlation coefficient (R) of 0.99883 and K_{sv} value of $4.95 \times 10^3\ M^{-1}$. The enhancing effect on luminescence of CPM-17-Zn-Eu by Cd^{2+} ions can be ascribed to the fact that

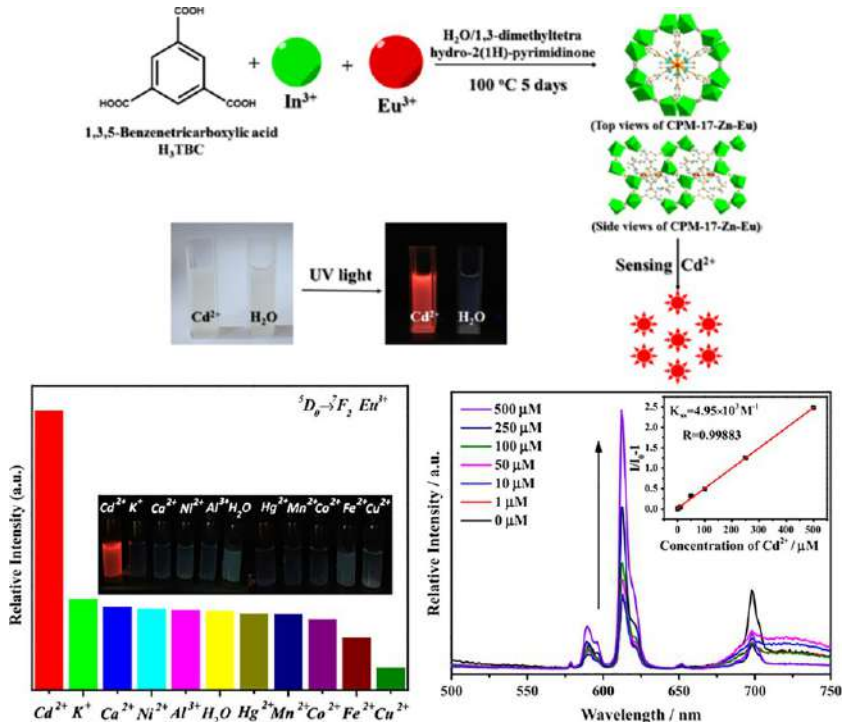

FIG. 7.5 *(Top)* Schematic description for the synthetic procedure of CPM-17-Zn-Eu and the fluorescent enhancement of CPM-17-Zn-Eu by Cd^{2+}. *(Bottom, left)* (A) Suspension-state photoluminescent spectra and (B) the relative intensities of $^5D_0 \rightarrow {}^7F_2$ at 613 nm for CPM-17-Zn-Eu dispersed in various metal ion aqueous solutions upon excitation at 294 nm. The inset: the corresponding photographs under UV-light irradiation. *(Bottom, right)* Emission spectra of CPM-17-Zn-Eu in aqueous solutions in the presence of various concentrations of Cd^{2+} under excitation at 294 nm and the inset is the K_{sv} curve (linear relationship of the emission intensity) of CPM-17-Zn-Eu enhanced by Cd^{2+} ions. *(Reproduced with permission from C. Liu, B. Yan, Zeolite-type metal organic frameworks immobilized Eu^{3+} for cation sensing in aqueous environment, J. Colloid Interface Sci. 459 (2015) 206–211. Copyright 2015 Elsevier.)*

Cd^{2+} ions interact with the third COO^- group of H_3BTC ligand within CPM-17-Zn-Eu and facilitate the efficiency of energy transformation from ligands to Eu^{3+} ions. This is because it can induce more efficient intermolecular energy transfer from ligand to lanthanide ions, when they are added into some MOFs [20].

Xu et al. assembled an Eu-based MOF (UiO-66-NH_2-Eu) [21], whose amino group, an electron-donating group in UiO-66-NH_2-Eu, can be used as a binding site to bind with metal ions. It behaves as a highly selective and sensitive fluorescence probe targeting Cd^{2+} ions in aqueous solutions through an impressive enhancing phenomenon of the typical Eu^{3+} luminescence (Fig. 7.6; top, left). In particular, this approach has been successfully applied to determine the

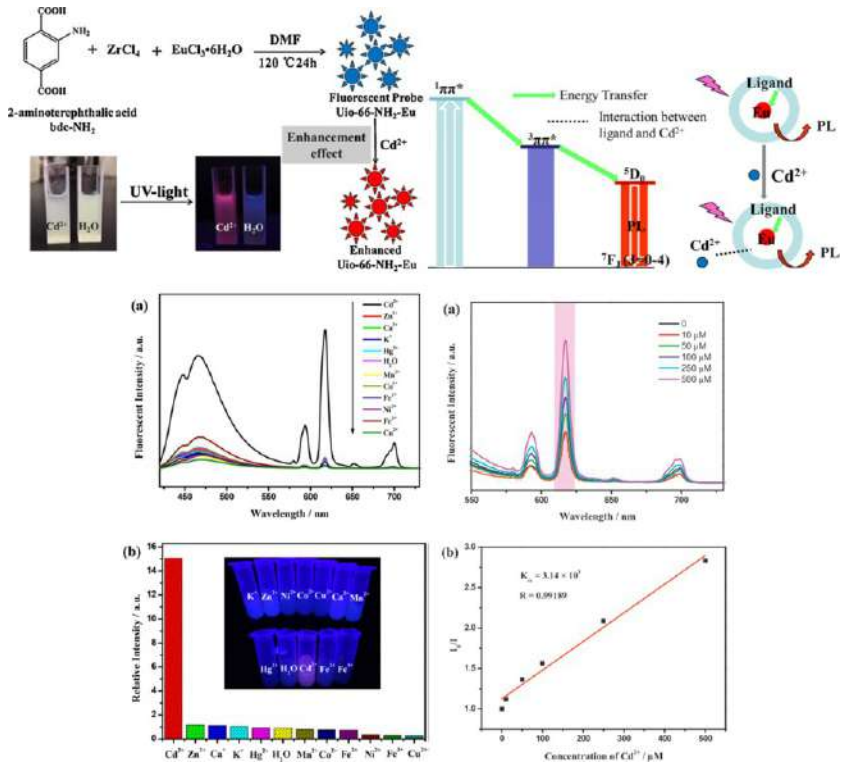

FIG. 7.6 *(Top, left)* Schematic representation for and fluorescent enhancement chemosensor of Cd^{2+} by UiO-66-NH_2-Eu. The inset is a clear photograph under UV-light irradiation at 365 nm of the sensing effect. *(Top, right)* Simplified schematic diagrams showing ligand-metal energy transformation (LMET) for luminescence emission ($^1\pi\pi^*$ and $^3\pi\pi^*$ are the singlet state and triplet state of ligands) and the influence of Cd^{2+} on LMET. *(Bottom, left)* PL spectra of UiO-66-NH_2-Eu (3 mg) (A) and the luminescence intensity of the $^5D_0 \rightarrow {}^7F_2$ of UiO-66-NH_2-Eu (B) dispersed into different aqueous solutions of various metal ions (10^{-2} M) (excitation monitored at 395 nm). The inset is the corresponding photographs under UV-light irradiation at 365 nm. *(Bottom, right)* Emission spectra (A) and K_{sv} curve (B) of UiO-66-NH_2-Eu in aqueous solutions in the presence of various concentrations of Cd^{2+} under excitation at 395 nm. *(Reproduced with permission from X. Xu, B. Yan, Eu(III) functionalized Zr-based metal-organic framework as excellent fluorescent probe for Cd^{2+} detection in aqueous environment, Sens. Actuators B 222 (2016) 347–353. Copyright 2016 Elsevier.)*

concentration of Cd^{2+} in environmental samples. A simplified ligand ($^1\pi\pi^*$) → ligand ($^3\pi\pi^*$) → Eu^{3+*} energy transformation is shown in Fig. 7.6 (top, right). Therefore, they attribute the enhancement of luminescent intensity of UiO-66-NH_2-Eu to the fact that Cd^{2+} leads a more efficient energy transfer from ligands to Eu^{3+}. The photoluminescence properties of M^{n+}@UiO-66-NH_2-Eu are recorded and compared in Fig. 7.6A (bottom, left). The histogram shows about 13 times as much as that of the original one after

immersing into a 0.01 mol L^{-1} Cd^{2+} aqueous solution for a few minutes (Fig. 7.6B; bottom, left). The remarkable enhancement effect by Cd^{2+} can be further confirmed by the photograph of the UiO-66-NH_2-Eu suspension under UV-light irradiation (the inset of Fig. 7.6B; bottom, left). The emitted visible red light of the UiO-66-NH_2-Eu suspension is completely enhanced when in contact with the aqueous solution of Cd^{2+}. It is obvious that the luminescence intensity at 617 nm of Eu^{3+} is gradually enhanced as the concentration of the metal cations increases (Fig. 7.6A; bottom, right). Based on the experimental data in Fig. 7.6B (bottom, right), the linear correlation coefficient (R) in the K_{sv} curve of UiO-66-NH_2-Eu with Cd^{2+} is 0.99189. The high sensitivity allows the existence of a small amount of Cd^{2+} ions to be easily identified [21].

7.3 Luminescence responsive sensing of Pb^{2+} using rare earth metal-organic framework hybrid materials

As is commonly known, Pb^{2+} ions are one of the most toxic heavy metal ions, and are widely used in our daily life and usually contained in batteries, gasoline, and pigments. After entering the human body, this ion will damage the functions of the kidneys, reproductive system, nervous system, and brain cells. As a common pollutant, Pb^{2+} ions have extensively been a concern and the Environmental Protection Agency (EPA) recommends that it should not exceed 0.015 ppm in drinking water. Among the heavy metals, Pb^{2+} is often encountered in the environment and continues to be one of the most hazardous. A wide variety of diseases including digestive, reproductive, neurological, and developmental disorders have been attributed to excessive Pb^{2+} concentration in the body. Hence, selective sensing of Pb^{2+} seems to be very important [25–27]. There are few examples of luminescence sensing of Pb^{2+} using MOF-based probes [28–32].

Zeng et al. developed a colorimetric sensing method for Pb^{2+} based on bimetallic RE-MOFs, $Tb_{1.7}Eu_{0.3}(BDC)_3{\cdot}(H_2O)_4$ (TbEu-MOF) [30]. As shown in Fig. 7.7A (top), the emission color of the TbEu-MOF changes from red-orange to green with a concentration of Pb^{2+} ranging from 0.25 to 10 mM, and the luminescence intensity of TbEu-MOF decreases with the increased concentration of Pb^{2+}. They studied the response of TbEu-MOF for 10 mM of Pb^{2+} after the MOFs-ion interaction for different periods of time (Fig. 7.7B; top). The color of the TbEu-MOF changes from red-orange to green as the reaction time increases. The luminescence color reached steady state after 18 min, which indicates that the binding of Pb^{2+} to TbEu-MOF is fast and the method is applicable for rapid detection of Pb^{2+}. In order to evaluate the sensing performance of TbEu-MOF probes for real analysis, they applied it in the colorimetric sensing of Pb^{2+} contained in three Pb^{2+}-polluted environmental water samples. As shown in Fig. 7.7C (top), TbEu-MOF can be employed as a promising colorimetric sensing probe for Pb^{2+} monitoring in real time for field screen analysis.

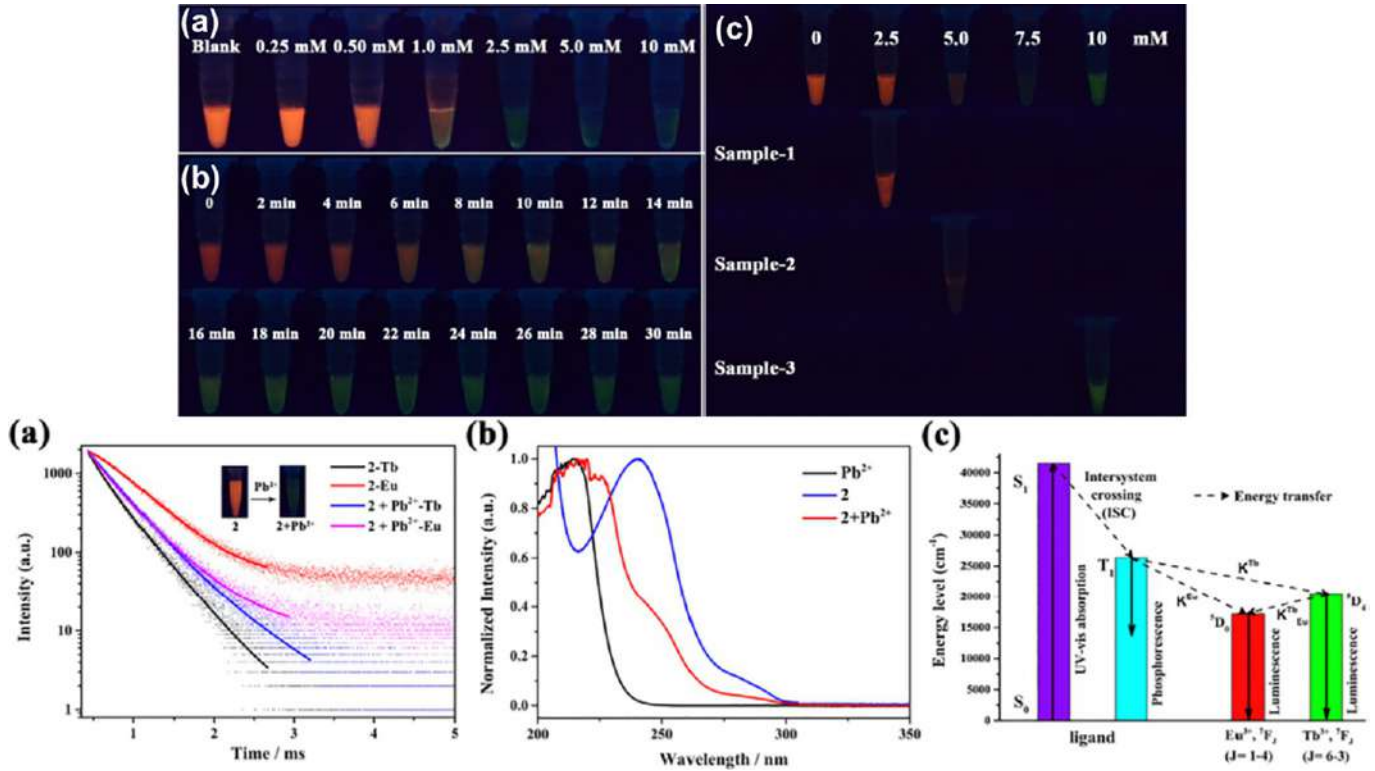

FIG. 7.7 *(Top)* (A) A photograph of the solutions containing the mixture of $Tb_{1.7}Eu_{0.3}(BDC)_3{\cdot}(H_2O)_4$ (0.125 mg mL^{-1}) with Pb^{2+} at different concentrations taken 6 h after the mixing. (B) The color changed after different periods of time upon the mixing of $Tb_{1.7}Eu_{0.3}(BDC)_3{\cdot}(H_2O)_4$ (0.125 mg mL^{-1}) and Pb^{2+} (10 mM). (C) A photograph taken 30 min after the mixing of $Tb_{1.7}Eu_{0.3}(BDC)_3{\cdot}(H_2O)_4$ particles (0.125 mg mL^{-1}) with three lead-polluted water samples. (Total volume is 100 μL). *(Bottom)* (A) Fluorescence decay curves of $Tb_{1.7}Eu_{0.3}(BDC)_3{\cdot}(H_2O)_4$ (marked as 2) in the absence and presence of Pb^{2+}, monitored at 546 nm (Tb^{3+}) and 616 nm (Eu^{3+}), respectively. The system is excited at 280 nm; (B) the UV-vis absorption spectra of Pb^{2+}, $Tb_{1.7}Eu_{0.3}(BDC)_3{\cdot}(H_2O)_4$, and the mixture of $Tb_{1.7}Eu_{0.3}(BDC)_3{\cdot}(H_2O)_4$ and Pb^{2+}; and (C) simplified schematic diagram of the ligand-metal energy transfer for the emission (S_0 is the ground state of the ligand; S_1 and T_1 are the singlet state and triplet state of the ligand, respectively) and the energy transfer between the lowest excited states $^5D_0$ and $^5D_4$ of the Eu^{3+} and Tb^{3+} as metallic centers. *(Reproduced with permission from X. Zeng, Y. Zhang, J. Zhang, H. Hu, X. Wu, Z. Long, X. Hou, Facile colorimetric sensing of Pb^{2+} using bimetallic lanthanide metal-organic frameworks as luminescent probe for field screen analysis of lead-polluted environmental water, Microchem. J. 134 (2017) 140–145. Copyright 2017 Elsevier.)*

To calibrate the fluorescence decay curves in Fig. 7.7A (bottom), the average lifetime of Tb^{3+} (monitored at 546 nm) increases in the presence of Pb^{2+}, while the average lifetime of Eu^{3+} decreases. This result is consistent with the emission color change of TbEu-MOF. In addition, the UV-vis spectra suggest almost no absorption at 312 nm, as shown in Fig. 7.7B (bottom), which excludes the absorption effect of Pb^{2+}. Therefore the sensing mechanism of this colorimetric method can be explained by the modulation of the energy transfer processes in TbEu-MOF, as depicted in Fig. 7.7C (bottom), which decreases the intensity of the $^5D_0 \rightarrow {}^7F_2$ transition of Eu^{3+} at 616 nm and increases that of the $^5D_4 \rightarrow {}^7F_5$ transition of Tb^{3+} at 546 nm [30].

Li et al. selected mixed 4-(pyridin-3-yloxy)-phthalic acid (H_2ppda) and 1,4-naphthalenedicarboxylic acid (H_2nbdc) to synthesize a Tb-MOF $[Tb(ppda)(npdc)_{0.5}(H_2O)_2]_n$, whose free oxygen atoms of the ether bond can serve as the functional sites to tune their purposeful properties [31]. It acts as an effective luminescent sensor for Pb^{2+} ions, with a low LOD. As shown in Fig. 7.8A (top), the photoluminescence spectra of the samples dispersed in different metal cations displayed four typical transitions of Tb^{3+} ions. It should be noted that a strong enhancement effect on the luminescence intensity of Tb-MOF is induced by the Pb^{2+} ions. As shown in Fig. 7.8B (top), the fluorescence enhancement efficiency of Pb^{2+} ions at a concentration of 1.0×10^{-3} M for the $^5D_4 \rightarrow {}^7F_5$ emission peak of Tb-MOF is 89.9%, implying a promising sensing ability for Pb^{2+} ions. The luminescence titration experiments in Fig. 7.8A (bottom) showed that the fluorescence intensity of TbMOF gradually increases with the increasing concentration of Pb^{2+} ions. As depicted in Fig. 7.8B (bottom), a good linear relationship at low concentrations is obtained and the K_{sv} value is $1.05 \times 10^5\ M^{-1}$. Furthermore, the LOD of the Pb^{2+} ion is calculated to be 9.44×10^{-5} M. This enhancement mechanism should be based on a dynamic mechanism. A bonding interaction between the Lewis basic site of the oxygen atom of the ether bond in Tb-MOF and Pb^{2+} ions may affect the ligand-metal charge transfer and make the energy transfer process more efficient, to enhance the luminescence of Tb^{3+} [31].

7.4 Luminescence responsive sensing of Cr^{3+} using rare earth metal-organic framework hybrid materials

Chromium is an important element and exists in the two common oxidation states of Cr(III) and Cr(VI) ions. The toxicity of chromium in different valences is quite different. The Cr(III) ion is an important biological trace element and is widely used in industrial production, whereas excessive Cr(III) ions in the body can combine with DNA, leading to mutations or malignant cells. In addition, Cr(VI) species are poisonous pollutants in ecological, environmental, and biological systems, due to their broad utilization in modern industry and agriculture, and they have been classified as a serious pollutant by the U.S. Environmental Protection Agency. Additionally,

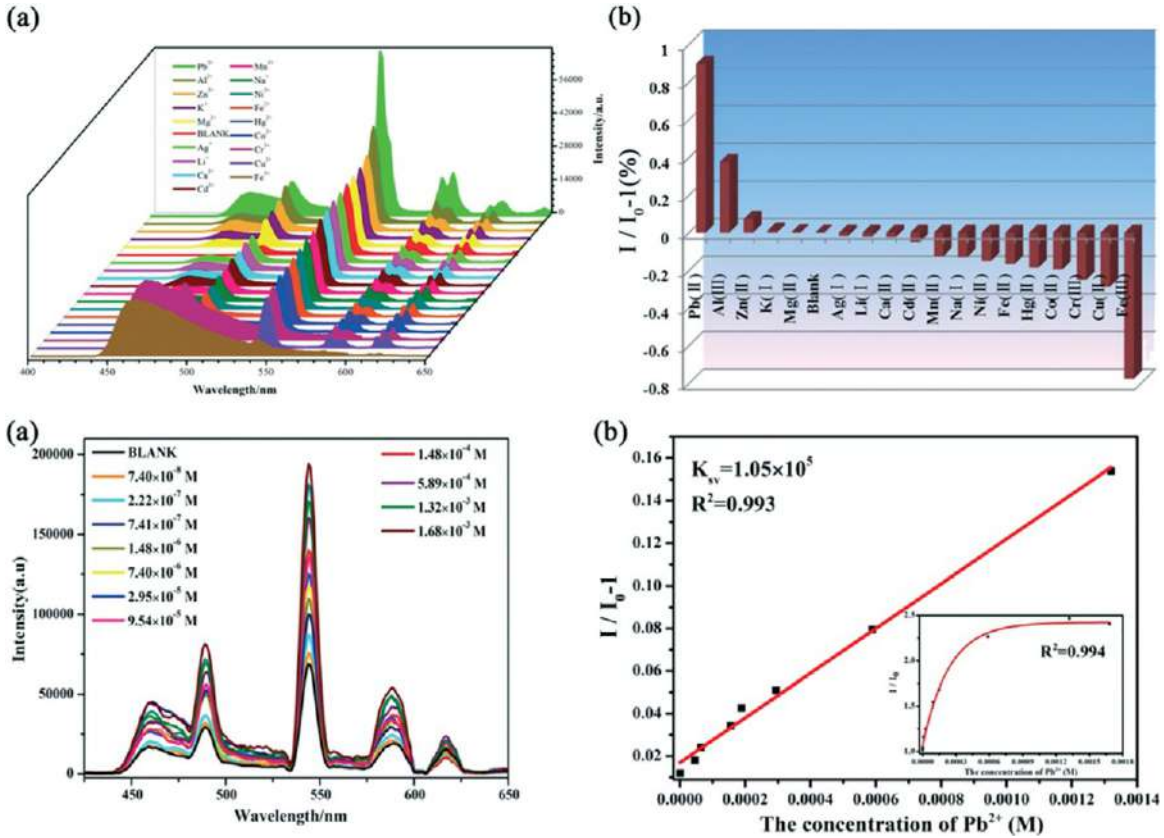

FIG. 7.8 *(Top)* (A) Luminescent spectra of Tb-MOF dispersed in aqueous solutions with various cations. (B) Enhancing efficiency of Tb-MOF dispersed in various cations. *(Bottom)* (A) Fluorescence spectra of Tb-MOF after addition of different concentrations of Pb^{2+}. (B) The linear Stern-Volmer plot of Tb-MOF detecting Pb^{2+} (inset: the nonlinear Stern-Volmer plot of Tb-MOF). *(Reproduced with permission from Z. Li, Z. Zhan, M. Hu, A luminescent terbium coordination polymer as a multifunctional water-stable sensor for detection of Pb^{2+} ions, PO_4^{3-} ions, $Cr_2O_7^{2-}$ ions, and some amino acids, CrystEngComm 22 (2020) 6727–6737. Copyright 2020 Royal Chemical Society.)*

long-term exposure to Cr(VI) ions, even at low concentrations, can cause several adverse health effects such as allergic reactions, hereditary genetic defects, and even lung cancers. Excessive hexavalent chromium (more than 10 ppm) has a lethal effect on aquatic organisms, and the content of Cr(VI) ions in the body must be less than 3 ppm. Therefore it is a significant issue to detect chromium ions sensitively and rapidly in water or edible resources, which is meaningful in environmental protection and food security [33–37]. Cr(VI) ions exist in the environment as anions ($Cr_2O_7^{2-}$ and CrO_4^{2-}), which will be touched on in the following chapter. Here some examples are given of the rare earth MOF hybrid materials for luminescent responsive sensing of Cr(III) (Cr^{3+}) [38–44].

Liu et al. chose an unexplored ligand 4′-[4,2′;6′,4″]-terpyridin-4′-yl-biphenyl-4-carboxylic acid (H_4tpbpc) to synthesize an Eu-MOF ($[Eu_2(tpbpc)_4 \cdot CO_3 \cdot 4H_2O] \cdot DMF \cdot$solvent), which behaves as a sensor for detecting Cr^{3+} ions in aqueous solutions simultaneously [42]. As shown in Fig. 7.9, the bright red fluorescence is

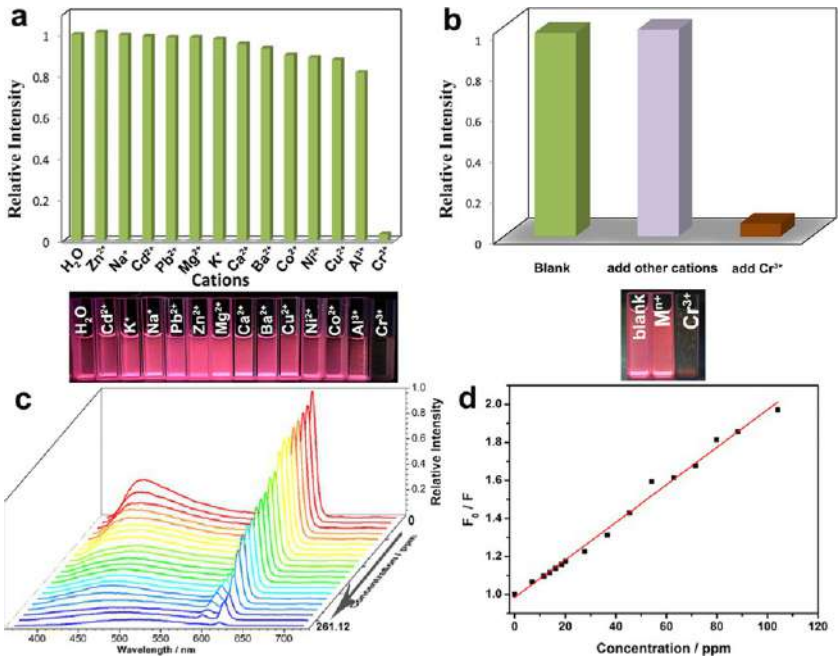

FIG. 7.9 (A) *(Top)* Relative intensities at 618 nm ($^5D_0 \rightarrow {}^7F_2$) for Eu complex dispersed in different metal ion aqueous solutions upon excitation at 343 nm. *(Bottom)* Corresponding photographs under irradiation of 365-nm UV light. (B) *(Top)* Relative intensities at 618 nm for Eu complex, blank *(green)*, addition of other mixed cations *(purple)*, and addition of Cr^{3+} metal ions *(brown)*. *(Bottom)* Corresponding photographs under irradiation of 365-nm UV light. (C and D) Emission spectra of Eu complex in water solution (excited at 343 nm) at different concentrations and a Stern-Volmer plot of Cr^{3+} ion. *(Reproduced with permission from J. Liu, G. Ji, J. Xiao, Z. Liu, Ultrastable 1D europium complex for simultaneous and quantitative sensing of Cr(III) and Cr(VI) ions in aqueous solution with high selectivity and sensitivity, Inorg. Chem. 56 (2017) 4197–4205. Copyright 2017 American Chemical Society.)*

completely quenched when a certain number of Cr^{3+} ions are added into the system. The inset of Fig. 7.9A shows the strong red emission of the suspension and addition of other M^{n+}, which can be easily captured by the naked eye under a 365-nm UV lamp, and its brightness disappears with higher concentrations of Cr^{3+} addition. With increasing concentration of Cr^{3+} ions, the luminescence intensities gradually decrease and the emission peak has an obvious red shift. The calculated LOD of the Cr^{3+} ion is 3.64 ppm. As shown in Fig. 7.9D, the Stern-Volmer quenching curve for the Cr^{3+} ion is nearly linear at low concentrations with a linear fit correlation coefficient of 0.992 and a K_{sv} value of $5.14 \times 10^2\ M^{-1}$. The quenching mechanism of the Eu complex in the presence of Cr^{3+} can be assigned to two primary factors. The overlap between the emission spectra of the Eu complex and the UV-vis absorption spectra of the Cr^{3+} ion solution makes it possible for the Cr^{3+} ion to adsorb the emission light of the Eu complex to decrease the luminescence intensities. Additionally, three N atoms from three pyridyl rings of each $tpbpc^-$ ligand are free and provide open Lewis base sites for additional metal ions, whose further interaction between them causes the $\pi \rightarrow \pi^*$ transition absorption band to move to a longer wavelength, hence minimizing the energy transfer from the $tpbpc^-$ ligands to the Eu(III) ions and attenuating the fluorescence intensity [42].

7.5 Luminescence responsive sensing of Al^{3+} using rare earth metal-organic framework hybrid materials

Aluminum is used extensively in our daily lives and is also an important metal element applied in industrial production. Moreover, on the one hand, with the massive use of aluminum products, more and more Al^{3+} ions are exposed to the air and enter the human body through food and drinking water. Its maximum intake is estimated to be 7 mg kg^{-1} body weight per week. However, Al^{3+} is toxic and environmentally harmful. Due to the frequent use of aluminum vessels and foil, the risk of Al^{3+} ion absorption by the human body is increasing. Al^{3+} has been implicated as a fatal factor in Alzheimer's disease, and it also prevents plant growth on acid grounds. Further study has confirmed that high aluminum content in food will cause early aging, and also can further cause brain nerve degeneration, memory loss, intelligence, and even senile dementia. When the amount of aluminum accumulation in the body exceeds 5–16 times the normal level, it can inhibit the absorption of phosphorus in the intestine and interfere with the normal calcium and phosphorus metabolism in the body. Long-term exposure to a high concentration of Al^{3+} pollution in the living environment may cause internal environmental changes and result in metabolic dysfunction. Al^{3+} also affects blood glucose levels in the body. Thus the development of selective and sensitive Al^{3+} chemsensors is an urgent need [45–50]. There are some reports on luminescence sensing of Al^{3+} using MOF-based hybrid probes [51–61].

Hao et al. prepared a series of rare earth (RE = Eu, Tb, Sm, and Dy) MOFs (MOF-LIC-1) with 2-aminoterephthalic acid and selected Eu-MOF as a

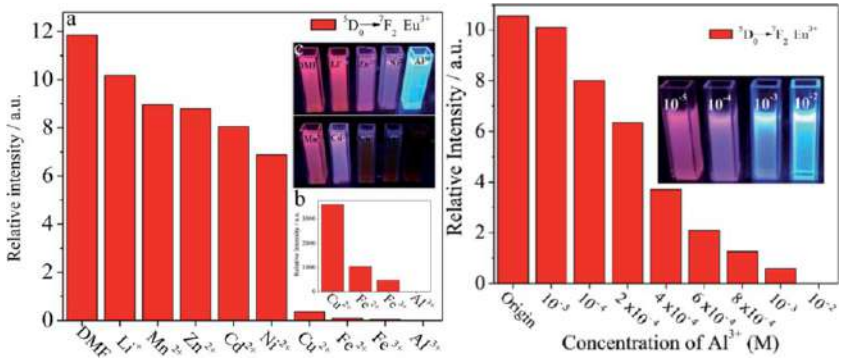

FIG. 7.10 *(Left)* (A) The luminescence intensity of the $^5D_0 \rightarrow {}^7F_2$ transition of Eu-MOF interacting with different metal ions in 10^{-2} mol L^{-1} DMF solution of MCl_z (excited and monitored at 365 nm). The insets show the relative intensity of Eu-MOF with respect to Cu^{2+}, Fe^{2+}, Fe^{3+}, and Al^{3+} (B) and the images of M^{z+}-Eu-MOF under UV-light irradiation at 365 nm (C), respectively. *(Right)* Comparison of the luminescence intensity of Eu-MOF in DMF solutions in the presence of various concentrations of Al^{3+} under excitation at 365 nm. *(Reproduced with permission from J. Hao, B. Yan, Amino-decorated lanthanide(III) organic extended frameworks for multi-color luminescence and fluorescence sensing, J. Mater. Chem. C 2 (2014) 6758–6764. Copyright 2014 Royal Chemical Society.)*

representative sample to examine the potential of the material for the sensing of metal ions, which shows highly selective and sensitive luminescence sensing for Al^{3+} ions [51]. In addition, the luminescence color change can be easily distinguished with the naked eye under UV-light irradiation. The luminescent properties are recorded and are compared in Fig. 7.10 (left); the quenching effects of Cu^{2+}, Fe^{2+}, Fe^{3+}, and Al^{3+} are highly pronounced, particularly for Al^{3+} ions. Different quenching effects lead to the changes of emitting color under UV-light irradiation. For the Li^+, Mn^{2+}, Zn^{2+}, Cd^{2+}, and Ni^{2+} ions, along with an increasing quenching effect, the emission intensity at 614 nm gradually decreases, whereas the ligand-centered emission in the range of 450–550 nm appears, leading to the emission color changes from red to pink. For the Cu^{2+}, Fe^{2+}, Fe^{3+}, and Al^{3+} ions, although they all seriously quench the emission of Eu^{3+}, their emission colors are different and are easy to distinguish under UV light. This is because Al^{3+} completely quenches the emission of only Eu^{3+}, whereas the emission of the ligand still exists, causing the bright blue light, as shown in Fig. 7.10C (left). Cu^{2+}, Fe^{2+}, and Fe^{3+} ions not only can quench the emission of Eu^{3+} but can also have quenching effects on the emission of the ligand, whose emission colors under UV light are dark. As shown in Fig. 7.10 (right) for the Al^{3+}-loaded sample, the luminescence intensity of Eu^{3+} decreases gradually with an increase in the concentration of Al^{3+}. As a result, under UV-light irradiation of 365 nm with an increase in Al^{3+}, the colors of the Al^{3+}-loaded samples changed from red to blue. They further speculated on a possible sensing mechanism. Al^{3+}-loaded Eu-MOF changes and collapses the crystal structure [51].

Ding et al. employed a rigid asymmetrical tricarboxylate ligand p-terphenyl-3,4″,5-tricarboxylic acid (H_3L) and isolated a unique heterometallic BaLa-MOF, $\{[Ba_3La_{0.5}(\mu_3\text{-}L)_{2.5}(H_2O)_3(DMF)]\cdot(3DMF)\}_n$, which exhibits highly selective and sensitive sensing of Al^{3+} over other cations [53]. The BaLa-MOF sample was employed as a luminescent probe and was investigated for the sensing of diverse metal ions, for it can exhibit strong visible blue light when excited by ultraviolet light. As shown in Fig. 7.11A, only Al^{3+} ions have a significant fluorescence-quenching effect, while other metal ions only have a slight effect on the fluorescent intensity. As shown in Fig. 7.11, when Al^{3+} concentrations gradually increase, the fluorescent intensity of BaLa-MOF gradually decreases. As shown in Fig. 7.11C and D, the fluorescent intensity linearly decreases with Al^{3+} concentration varying from 5 to 60 μM. To further investigate the correlation between quenching result and Al^{3+} concentration, a

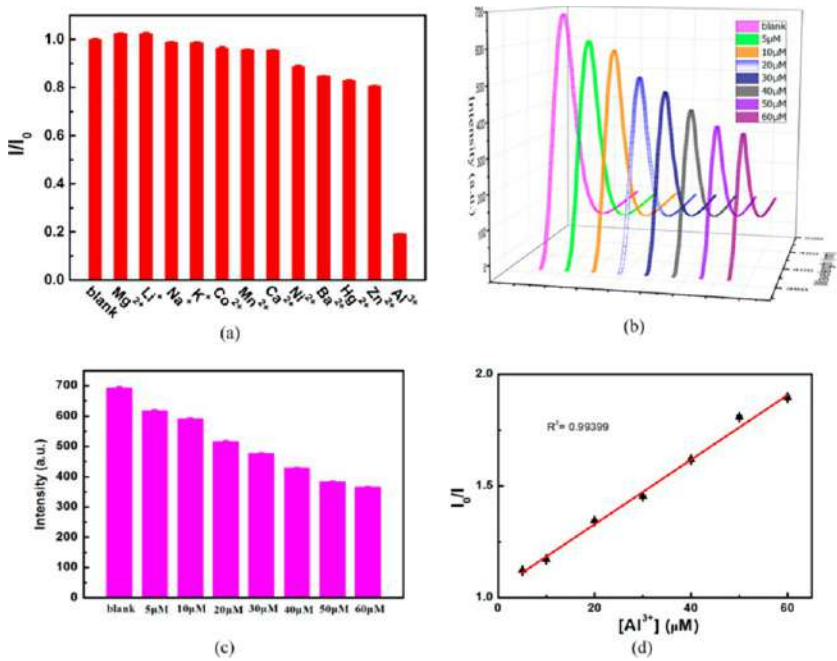

FIG. 7.11 (A) Comparison of the luminescence intensity of BaLa-MOF at 374 nm incorporating aqua solutions (10^{-4} M) upon the addition of various different cations. (B) Liquid luminescence spectra of 1 under different concentrations of Al^{3+} aqueous solution. (C) Comparison of the luminescence intensity of BaLa-MOF under different concentrations of Al^{3+} aqueous solution. (D) Linear luminescence intensity vs. Al^{3+} concentration plot. *(Reproduced with permission from B. Ding, S. Liu, Y. Cheng, C. Guo, X. Wu, J. Guo, Y. Liu, Y. Li, Heterometallic alkaline earth–lanthanide BaII–LaIII microporous metal–organic framework as bifunctional luminescent probes of Al^{3+} and MnO_4^-, Inorg. Chem. 55 (2016) 4391–4402. Copyright 2016 American Chemical Society.)*

linear fluorescent intensity vs. Al^{3+} concentration plot was made (Fig. 7.11D), to which a K_{sv} value calculated to be 1.445×10^4 L·mol^{-1} can be fitted and a low LOD (0.19 μM) is found, for a high quenching efficiency. They speculated that Al^{3+} may be diffused into the channels of BaLa-MOF or attached to its surface rapidly, and the encapsulated Al^{3+} ions are responsible for the quenching of the luminescence [53].

7.6 Luminescence responsive sensing of Ag^+ using rare earth metal-organic framework hybrid materials

Because of human activities, the Ag^+ content in the vicinities of sewage outfalls, electroplating plants, mine waste sites, and silver-iodide seeded areas has increased. Ag^+ can accumulate in the human body through the food chain and drinking water. In addition, Ag^+ ions are known to bind with various metabolites, including amine, imidazole, and carboxyl groups, and inactivate sulfhydryl enzymes. Therefore the presence of Ag^+ will result in several pathological disorders, such as cell toxicity and organ failure. Ag^+ ions can accumulate in an organism through the biological chain and water circulation system, causing silver ion poisoning, leading to cell damage and organ failure. Thus it is of considerable importance for the environment and human health to establish an Ag^+ detection method with high sensitivity and high selectivity [62–73].

Hao et al. chose MIL-121 ($Al(OH)(H_2btec)\cdot H_2O$) ($H_4btec$ = pyromellitic acid), which contains two extra free carboxylic acid functions per ligand with interesting porosity for a parent framework, as a good candidate to bind with RE^{3+} cations, whose hybrids (Eu^{3+}@MIL-121) have been developed as highly selective and sensitive fluorescence probes targeting Ag^+ ions in aqueous solutions [67]. As shown in Fig. 7.12 (top, left), various metal ions show markedly different effects on the luminescence of Eu^{3+} ions. The interaction with Ag^+ drastically enhanced the luminescence intensity, with a maximum of over 5.0 times that of the original. As a result, only the sample immersed in aqueous solution containing Ag^+ provided direct information (red luminescent color) visible to the naked eye when irradiated under UV light at 254 nm, as shown in the inset of Fig. 7.12 (top, left). In addition, the enhancement effect of Ag^+ on the luminescence of Eu^{3+}@MIL-121 was evaluated by the fluorescence decay time of Eu^{3+}. Fig. 7.12 (top, right) shows that the emission lifetimes of Eu^{3+}@MIL-121 significantly increase from 0.21 to 0.98 ms in the presence of Ag^+. This observation is in good agreement with the results of PL spectra. Fig. 7.12 (bottom, left) shows the time-response PL spectra (A) and curves (B) within 4 h, respectively. With increasing interaction time between Ag^+ and Eu^{3+}@MIL-121, the emission intensity of the sample is continuously enhanced. From the inset of Fig. 7.12A (bottom, left), it can be seen that when the Eu^{3+}@MIL-121 was treated with an Ag^+ solution for 5 min, the highest peak at 614 nm increased to an intensity of over 2.0 times that of the original peak. This indicates that the Ag^+-induced fluorescence enhancement reaction is fast. As demonstrated in Fig. 7.13A (bottom, right), the emission intensity of

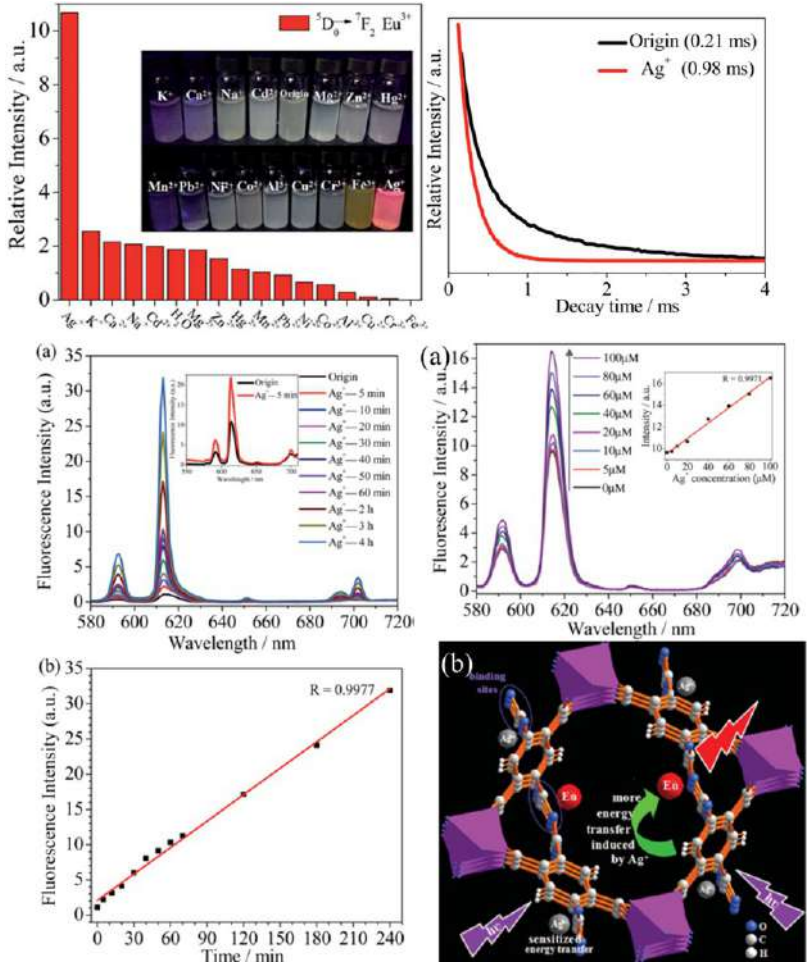

FIG. 7.12 *(Top, left)* Suspension-state PL spectra relative intensities of $^5D_0 \rightarrow {}^7F_2$ at 614 nm for Eu^{3+}@MIL-121 dispersed in aqueous solutions containing different metal ions (10 mM) when excited at 315 nm. The inset in (B) are the corresponding images under UV-light irradiation at 254 nm. *(Top, right)* Fluorescence lifetime of Eu^{3+}@MIL-121 in the absence *(black)* and presence *(red)* of Ag^+ in aqueous solution. *(Bottom, Left)* (A) Variation of fluorescence intensity of Eu^{3+}@MIL-121 at 614 nm with immersion time in Ag^+ solution, $\lambda_{ex} = 315$ nm; the inset is the corresponding change in emission intensity when treated with Ag^+ for 5 min. (B) Linear relationship of the fluorescence intensity at 614 nm as a function of interaction time. *(Bottom, right)* (A) Fluorescence intensity of Eu^{3+}@MIL-121 at 612 nm as a function of Ag^+ concentration in aqueous solution ($\lambda_{ex} = 315$ nm). Inset: linear relationship of Eu^{3+}@MIL-121 enhanced by Ag^+ aqueous solution. (B) Illustration of the fluorescence enhancement of Eu^{3+}@MIL-121 by Ag^+. *(Reproduced with permission from J. Hao, B. Yan, Highly sensitive and selective fluorescent probe for Ag^+ based on a Eu^{3+} post-functionalized metal–organic framework in aqueous media, J. Mater. Chem. A 2 (2014) 18018–18025. Copyright 2014 Royal Chemical Society.)*

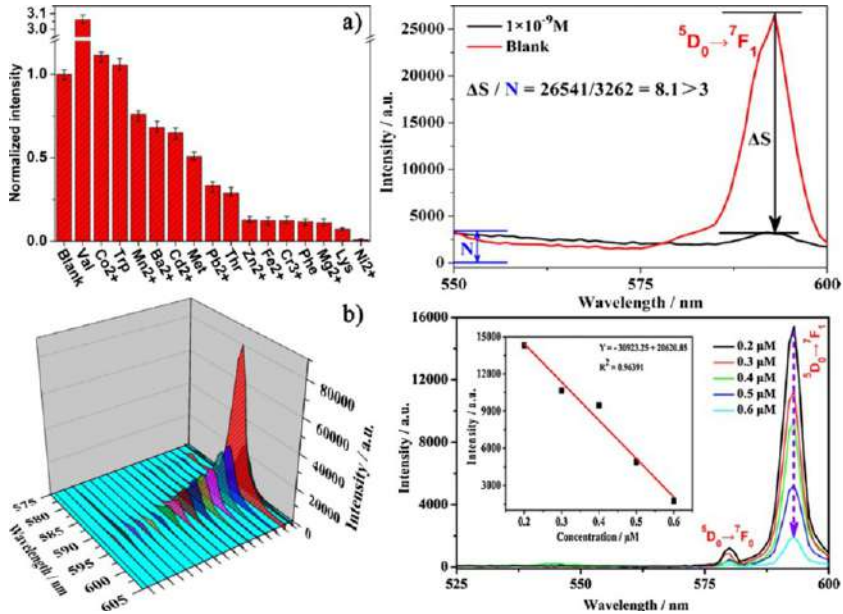

FIG. 7.13 *(Left)* (A) The histogram shows that Val increases Eu-MOF centered luminescence by three times and Ni^{2+} quenched the Eu-MOF centered luminescence absolutely; (B) 3D luminescence spectra of Eu-MOF reacts with 16 species of Val, Co^{2+}, Trp, Mn^{2+}, Ba^{2+}, Cd^{2+}, Met, Pb^{2+}, Thr, Zn^{2+}, Fe^{2+}, Cr^{3+}, Phe, Mg^{2+}, Lys and Ni^{2+}. *(Right, top)* The LOD for sensing Ni^{2+} is an ultrasensitive value of 1.0×10^{-9} M. *(Right, bottom)* Luminescence intensity decreases as the concentration of Ni^{2+} increases. Inset: the linearity of luminescence intensity versus the concentration of Ni^{2+} at 592 nm. *(Reproduced with permission from K. Zheng, Z. Liu, Y. Huang, F. Chen, C. Zeng, S. Zhong, S. W. Ng, Highly luminescent Ln-MOFs based on 1,3-adamantanediacetic acid as bifunctional sensor, Sens. Actuators B 257 (2018) 705–713. Copyright 2018 Elsevier.)*

the Eu^{3+}@MIL-121 suspension increased in accordance with the increase of Ag^{+} concentration from 0 to 100 mM. In other words, the fluorescence response of Eu^{3+}@MIL-121 toward Ag^{+} is linear when measured in the range 0–100 mM of Ag^{+} (inset of Fig. 7.12A; bottom, right). From these data, they estimated the LOD of Eu^{3+}@MIL121 to be 0.1 mM. The enhancement of luminescent intensity of Eu^{3+}@MIL-121 to Ag^{+} can be attributed to causing more efficient energy transfer from ligands to Eu^{3+} ions, as depicted in Fig. 7.12B (bottom, right) [67].

7.7 Luminescence responsive sensing of Co^{2+}/Ni^{2+} using rare earth metal-organic framework hybrid materials

Cobalt, as an essential trace element in the human body, plays a crucial role in the synthesis of vitamin B_{12} and hemoglobin. Because cobalt deficiency and excessive intake will seriously affect human health, the detection of cobalt is very important. As we all know, many nickel compounds dissolve easily in

water. Nickel is found in all soil and is emitted from volcanoes, and it is also found in meteorites and on the ocean floor. Unfortunately, nickel and its compounds have no characteristic odor or taste. Increased exposure to Ni^{2+} can cause several diseases such as dermatitis, pneumonitis, asthma, several problems of the central nervous system, and even cancer of the lungs and nasal cavity. Thus the detection of Ni^{2+} is of utmost importance in biological, industrial, and comestible samples [74]. There are a few works on the luminescence sensing of Co^{2+}/Ni^{2+} using MOF-based probes [75–78].

Zheng et al. adopted 1,3-adamantanediacetic acid (H_2ADA) to construct a series of RE-MOFs with the formula of $[RE(ADA)_{1.5}(phen)]_n$ (RE-MOF, $RE^{3+} = Eu^{3+}$, Gd^{3+}, Tb^{3+}, La^{3+}, Ce^{3+}, Pr^{3+}, Nd^{3+}, Y^{3+}). It is very interesting to find that the Eu-MOF (1a) can sense Ni^{+} [77]. The histogram (Fig. 7.13A; left) which was monitored at 592 nm ($^5D_0 \rightarrow {}^7F_1$ transition) shows more obviously about the luminescence change of 1a after reacting with different species, indicating Eu-MOF is a highly selective sensor. Then, the mixed solutions are placed at the room temperature to react for 24 h. 3D luminescence spectra (inset of Fig. 7.13B; left) of these solutions displays that only Ni^{2+} quenched the Eu^{3+}-centered luminescence absolutely (Fig. 7.13A; right). The LOD for sensing Ni^{2+} is an ultrasensitive value of 1.0×10^{-9} M. The result reveals that 1a is a highly sensitive Ni^{2+} sensor, and it is the most sensitive chemosensor for sensing Ni^{2+}. Further investigation reveals there is a good linear relationship between luminescence intensity (monitored at 592 nm) and the Ni^{2+} concentration (0.2–0.6 μM), it fits a linear equation of $R^2 = 0.964$ (Fig. 7.13B; right). The quenching mechanism caused by the addition of Ni^{2+} might be explained by a ligand-to-metal charge transfer (LMCT) mechanism [77].

Xie et al. prepared $Sc_2(NH_2\text{-}BDC)_3$ (Sc-MOF) crystals with relatively uniform morphology and size as a probe for Co^{2+} and Ni^{2+} ion detection through the fluorescence quenching effect [78]. As shown in Fig. 7.14A and B (left), the addition of metal ions and anionic solutions barely gave rise to a slight change in fluorescence intensity, except it exhibited an obvious quenching effect once Ni^{2+} and Co^{2+} ions were added to the suspension. At the same time, as can be observed intuitively from the inset in Fig. 7.14A (right), once Ni^{2+} and Co^{2+} are added, the corresponding fluorescence intensity immediately dramatically decreases compared with the pristine material under the ultraviolet lamp with an excitation wavelength of 365 nm. In addition, the distinct quenching effect can be certified directly through a naked eye comparison of the pristine suspension and the suspension containing Co^{2+} ions under the ultraviolet lamp (the inset in Fig. 7.14A; right), in which the bright blue fluorescence of Sc-MOF can be obviously weakened as soon as Co^{2+} ions are added into the suspension. Furthermore, there is a better linear correlation ($R^2 = 0.98$) between the fluorescence intensity and the concentration of Co^{2+} ions in the range from 0.1 to 7 μM (Fig. 7.14B; right). Moreover, the corresponding LOD of Co^{2+} ions is determined to be 22.44 nM (approximately 1.3 ppb). Some defects exist with the formation of Sc hydroxyls in the as-prepared Sc-MOF crystal, which is inclined to interact with the entered Co^{2+}/Ni^{2+} ions into the framework of

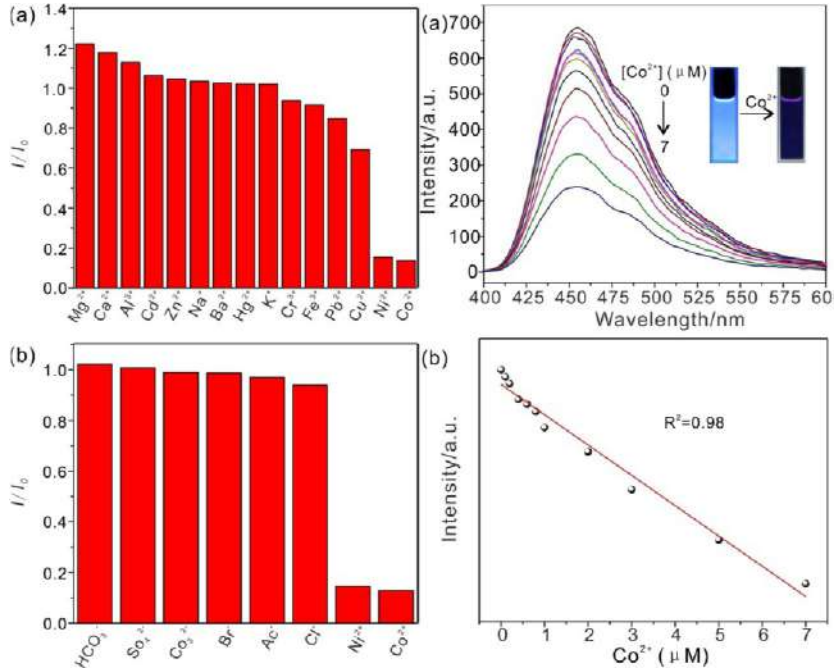

FIG. 7.14 *(Left)* Selectivity of the Sc-MOF toward Ni^{2+} and Co^{2+} detection: fluorescence response of Sc-MOF in the presence of 2 μM various (A) cations and (B) anions in ethanol solution ($\lambda_{ex} = 335$ nm). *(Right)* (A) Fluorescence spectra of the Sc-MOF suspension upon the addition of various concentrations of Co^{2+} under excitation at 335 nm (Inset: Photographs of fluorescence emission change under a ultraviolet lamp with $\lambda_{ex} = 365$ nm of Sc-MOF in ethanol upon the addition of Co^{2+}); (B) linear fitting plot between the fluorescence intensity of Sc-MOF and the concentration of Co^{2+}. *(Reproduced with permission from C. Xie, Z. Yu, W. Tong, K. Shehzad, W. Xu, J. Wang, J. Liu, Insights into the fluorescence sensing mechanism of scandium-based metal-organic frameworks by solid-state NMR spectroscopy. ChemistrySelect 4 (2019) 5291–5299. Copyright 2019 Wiley.)*

Sc-MOF. The electrons are transferred from the framework to the unoccupied orbitals of Co^{2+}/Ni^{2+}, leading to fluorescent quenching [78].

7.8 Luminescence responsive sensing of f-block metal ions using rare earth metal-organic framework hybrid materials

On the other hand, Ce^{3+} species are poisonous pollutants to eco- and biosystems [79]. Contamination from uranium sources has become a global concern due to the rapid expansion of nuclear science and technology during the last century. This element could be readily found in various public accessible industries, such as uranium mining and processing, glass manufacturing, and nuclear power stations, which all share a significant hazard to human health. Radiotoxicity accompanied by chemotoxicity is what makes the ingestion or inhalation of uranium a

problem that could lead to serious kidney damage, disruption of bioactive molecules (enzymes), as well as a series of other violent health problems [80–83].

Zhang et al. used H_3L (2-(6-carboxypyridin-3-yl)terephthalic acid) to prepare new RE-MOFs with the formula $[RE_4(\mu 6\text{-}L)_2(\mu\text{-}HCOO)(\mu_3\text{-}OH)_3(\mu_3\text{-}O)(DMF)_2(H_2O)_4]_n$ (RE = Tb, Eu, Gd, Dy, and Er), among which Tb-MOF disclosed a high detection ability to sense Ce^{3+} cations through the quenching of luminescence [84]. The luminescent behavior of the obtained dispersions was investigated (Fig. 7.15; top), revealing a remarkable effect of Ce^{3+} on quenching the luminescence of Tb-MOF. In contrast, other RE^{3+} ions showed almost no influence on luminescence intensity of DMF dispersion of Tb-MOF. These data suggest that Tb-MOF acts as a remarkable luminescent probe to detect Ce^{3+} cations. Fig. 7.15 (bottom) shows the influence of Ce^{3+} concentration on the emission quenching of Tb-MOF, exhibiting a linear dependence between the Ce^{3+} concentration and quenching efficiency (Fig. 7.15B; bottom). This quenching behavior can be rationalized with a K_{sv} value of 279.4 M^{-1} for Ce^{3+} ions. A possible mechanism is suggested on the basis of the suppression of LRET (luminescence resonance energy transfer) and the enhancement of intermolecular electron transfer [84].

Liu et al. presented an investigation of a luminescent Eu-MOF, for multifunctional applications as a luminescent sensor of UO_2^{2+} cations, which directly affects the luminescence signal with a rapid response. As shown in Fig. 7.16A, with the increase of the UO_2^{2+} concentration, the luminescence intensity of Eu-MOF attenuated sharply as well. The quenching process could also be more quantitatively described by plotting the quenching ratio (denoted as $(I_0 - I)/I_0\%$) against uranium concentration, as exhibited in Fig. 7.16B. Additionally, the quenching process could be well fitted with $R^2 = 0.95$. The UO_2^{2+} adsorption kinetics and isotherms were also investigated to confirm the correlation between the luminescence evolution and uranium adsorption process. As shown in Fig. 7.16C, with a contact time increase, the adsorption of uranium increased as well, taking only about 60 min to reach equilibrium. As for the sorption isotherm demonstrated in Fig. 7.16D, it is obvious that a similar evolution process is observed for both the concentration-dependent luminescence evolution and the adsorption isotherm, which is direct evidence for the inherent correlation between these two processes. The LOD is toward UO_2^{2+} ion is determined as c. 309.2 μg L^{-1}, which is a relative high value and may be induced by the inefficient energy transfer from the ligand to the guest UO_2^{2+} ions. Nevertheless, the sensor is still promising for application in high-level contaminated areas. On the other hand, the method proposed in this contribution could be directly used for probing UO_2^{2+} contamination over a wide concentration range (309.2 μg L^{-1} to 800 mg L^{-1}) in order to confirm the performance of the material in a real environmental sample for the determination of UO_2^{2+} contamination. The most logical mechanism to be construed from the aforementioned data is an energy transfer process that occurs from the interaction of UO_2^{2+} with the framework [85]. Gomez et al. also reported on luminescent Tb-MOFs evaluated and employed as chemical sensors for agrochemical and cationic species, with LOD of 2.9 ppm for $[UO_2^{2+}]$ [86].

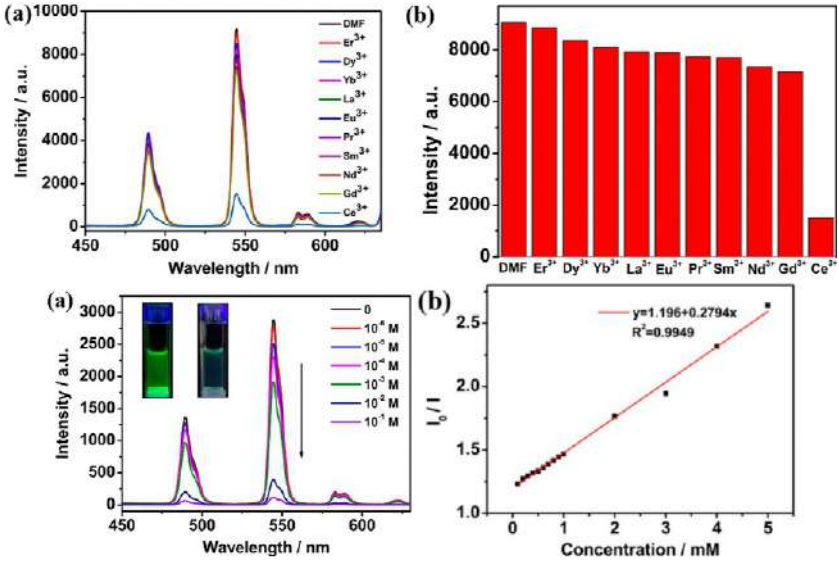

FIG. 7.15 *(Top)* Luminescence spectra (A) and intensities of the $^5D_4 \rightarrow {}^7F_5$ transition (B) of Tb-MOF dispersed in DMF solutions of different RE^{3+} ions (10^{-2} M lanthanide nitrate, 2 mL DMF, 2 mg TbMOF). *(Bottom)* (A) Luminescence spectra of Tb-MOF dispersed in DMF solutions of $Ce(NO_3)_3$ (10^{-1}–10^{-6} M, 2 mL DMF, 2 mg TbMOF); inset shows the color of solutions under UV light before *(left)* and after *(right)* addition of Ce^{3+} (10^{-2} M). (B) Linear dependence between the quenching efficiency and the concentration of Ce^{3+} in the range of 0.1–5 mM. *(Reproduced with permission from Q. Zhang, J. Wang, A. M. Kirillov, W. Dou, C. Xu, C. Xu, L. Yang, R. Fang, W. Liu, Multifunctional Ln−MOF luminescent probe for efficient sensing of Fe^{3+}, Ce^{3+}, and acetone, ACS Appl. Mater. Interfaces 10 (2018) 23976–23986. Copyright 2018 American Chemical Society.)*

Song et al. presented a luminescent Eu-MOF, $[Eu_2(FDC)_3(DMA)_2]\cdot 4H_2O$ (H_2FDC = 2,5-furandicarboxylic acid, DMA = *N*,*N*-dimethylacetamide), which showed high hydrolytic stability over a wide range of pH values (from 2 to 12) [87]. As depicted in Fig. 7.17A (left), the luminescence intensity decreased as the Th^{4+} concentration increased. Specifically, the intensity decreased to about 30.94% of the initial value at the Th^{4+} concentration of 1.08×10^{-4} mol L^{-1} by monitoring the luminescence intensity at 616 nm and was almost completely quenched when the concentration reached 6.47×10^{-4} mol L^{-1}. Such a distinct quenching characteristic is suitable for the quantitative determination of Th^{4+} contamination in aqueous solution. As shown in Fig. 7.17B (left), the linear correlation in the concentration range of 0–6.47×10^{-4} mol L^{-1} with $R^2 = 0.939$ clearly demonstrates its potential as a Th^{4+} probe. In order to investigate the detection capacity of the compound Eu-MOF, the LOD was determined to be 3.49×10^{-5} mol L^{-1}, which is close to the WHO standard of 1.06×10^{-6} mol L^{-1}. As shown in Fig. 7.17 (right, top), in the distinct and intriguing phenomenon of the luminescence intensity, a decrease of Eu-MOF occurs when treated with Th^{4+} solutions while negligible luminescence intensity change occurs for other metal ion solutions and anions.

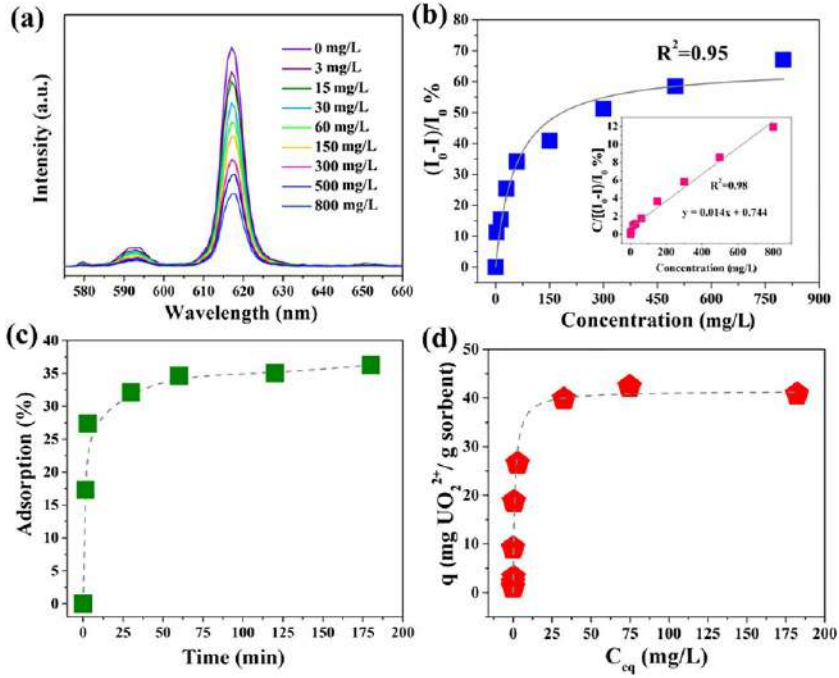

FIG. 7.16 (A) Luminescence spectra of compound 1 in varied concentrations of *v*. (B) The correlation between the quenching ratio versus concentration simulated by a Langmuir model. The inset is the correlation between $C/[(I_0 - I)/I_0]\%$ versus UO_2^{2+} concentration. (C) The *v* adsorption kinetics curve ($C_0 = 10$ mg L^{-1}). (D) Adsorption isotherm curve of v simulated by a Langmuir model. *(Reproduced with permission from W. Liu, Y. Wang, L. Song, M.A. Silver, J. Xie, L. Zhang, L. Chen, J. Diwu, Z. Chai, S. Wang, Efficient and selective sensing of Cu^{2+} and UO_2^{2+} by a europium metal-organic framework, Talanta 196 (2019) 515–522. Copyright 2019 Elsevier.)*

The quenching constant K_{sv} was determined as 6.68×10^4 toward Th^{4+}, suggesting that Eu-MOF exhibits a predominant selectivity toward Th^{4+} ions, suitable for serving as Th^{4+} sensors being applied in environmentally relevant systems. As displayed in Fig. 7.17 (right, bottom), elemental mapping measurements confirmed that the successfully adsorbed Th^{4+} ions were uniformly distributed on the surface of the crystal following the distribution of Eu (Fig. 7.17D; right, bottom) and O (Fig. 7.17E; right, bottom) atoms which are in situ incorporated into the framework. The quenching of the luminescence was induced by the direct interaction between the emission center and the guest Th^{4+} ions, which led to efficient energy transfer responsible for the luminescence quenching observed after Th^{4+} loading. The competitive sorption of the excitation light should be another reason for the decrease of the luminescence intensity, for the absorption peak of Eu-MOF is partially overlapped by the absorption of Th^{4+} at 290 nm [87].

In fact, some rare earth MOF hybrid materials often display an extensive probe for luminescence response to multimetal ions [88–91]. Ding et al.

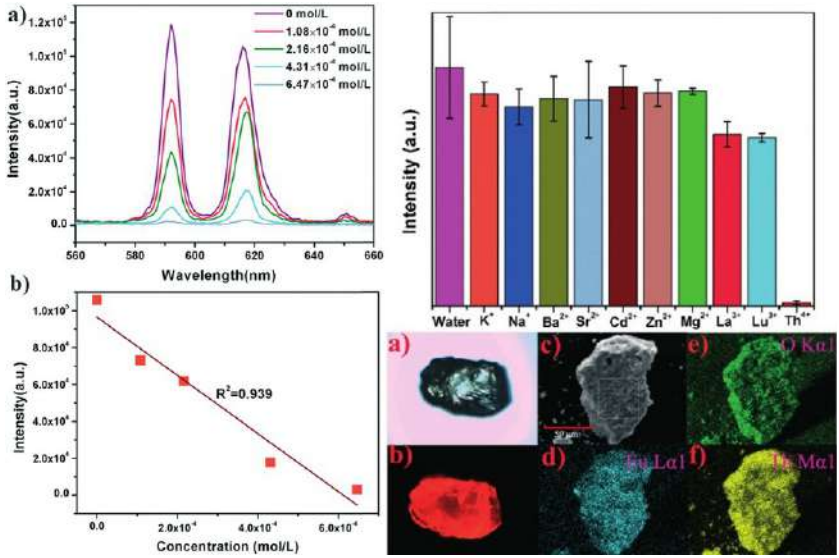

FIG. 7.17 *(Left)* (A) Luminescence spectra of Eu-MOF in Th^{4+} solutions with various concentrations at pH = 3. (B) The simulated correlation between luminescence intensity and Th^{4+} concentration in 616 nm wavelength. *(Right, top)* Luminescence intensity of Eu-MOF immersed in 1×10^{-3} mol L^{-1} various metal cation solutions (monitored at 616 nm and excited at 290 nm). *(Right, bottom)* (A) The initial crystal morphology of Eu-MOF 1 under daylight. (B) The luminescence photos of Eu-MOF excited by 365 nm UV light. (C) Microphotograph of Th^{4+}-loaded Eu-MOF. (D–F) Eu, O and Th elemental mapping of Th^{4+}-loaded Eu-MOF. *(Reproduced with permission from L. Song, W. Liu, Y. Wang, L. Chen, X. Wang, S. Wang, A hydrolytically stable europium–organic framework for the selective detection of radioactive Th^{4+} in aqueous solution, CrystEngComm 21 (2019) 3471–3477. Copyright 2019 Royal Chemical Society.)*

prepared four 4d-4f hetero-MOFs: $[RECd_2(Pbc)_4(Meimdc)\ (H_2O)]\cdot 3H_2O$ (RECd-MOF, RE = Eu, Tb, Sm, Dy) (HPbc = 4-(4-pyridinyl)benzoic acid; H_3Meimdc = 2-methyl-1*H*-4,5-imidazole-dicarboxylic acid) [91]. EuCd-MOF can capture Ag^+, Cu^{2+}, Zn^+, Co^{2+}, and Ni^{2+} cations and shows a cation-dependent colorimetric response, which indicates the potential for naked sensing. The powder sample of EuCd-MOF is immersed in an aqueous solution containing different 0.1 M $M(NO_3)_x$ and the emission spectra of Eu^{3+} ions are measured (Fig. 7.18; top). In stark contrast, most metal cations exhibit an enhancement effect for the luminescent intensities. In particular, the interaction with Mg^{2+} drastically enhanced the luminescent intensity, with a maximum of more than 3.9 times as much as that of the parent MOF. However, the Ag^+, Cu^{2+}, Zn^+, Co^{2+}, and Ni^{2+} cations exhibited a complete quenching effect on the luminescence of EuCd-MOF. Furthermore, the reduction of luminescence intensity is still clearly observed when compound EuCd-MOF is soaked in a 1×10^{-5} mol L^{-1} Cu^{2+} solution, suggesting that the detection limit of compound EuCd-MOF as a Cu^{2+} probe is much lower, with the sensitivity $Cu^{2+} > Ag^+ \approx Co^{2+} \approx Ni^{2+} \approx Zn^{2+}$. Interestingly, the process of soaking is

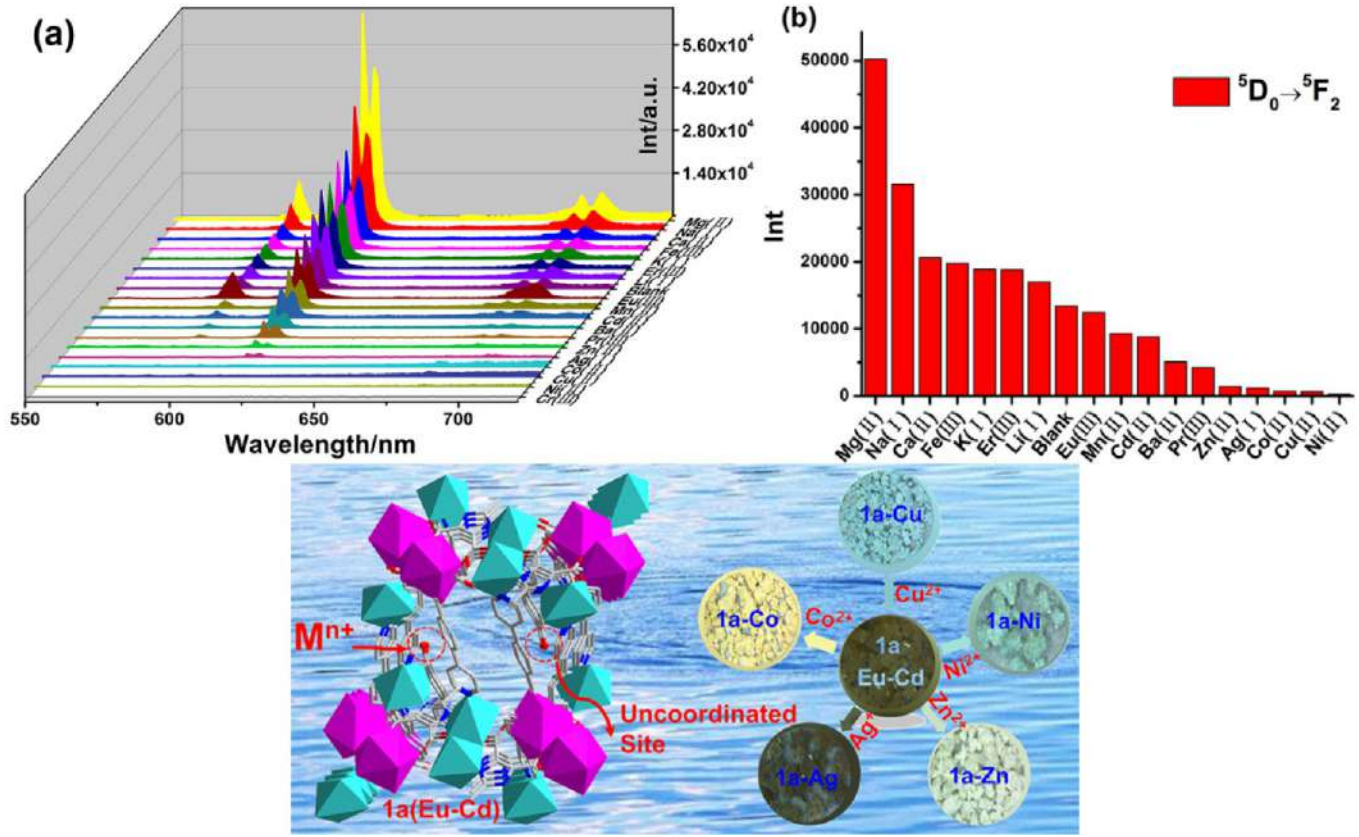

FIG. 7.18 *(Top)* (A) Emission spectra of 1a introduced into various 0.1 M aqueous cations solution. (B) Luminescent intensities at 616 nm of 1a treated with various 0.1 M aqueous cation solutions. *(Bottom)* Crystal photographs of compound 1a dispersed into various 0.1 M aqueous $M(NO_3)_x$ solutions. *(Reproduced with permission from L. Ding, L. Liu, Q. Shi, Y. Sun, Y. Wang, Y. Chen, Luminescent 3D lanthanide–cadmium heterometal–organic frameworks with chemical stability and selective luminescent sensing, Inorg. Chem. 56 (2017) 14850–14858. Copyright 2017 American Chemical Society.)*

accompanied by visible changes in color. After being immersed in these aqueous solutions of 0.1 mol L^{-1} ($M(NO_3)_x$) (M = Ag^+, Cu^{2+}, Zn^+, Co^{2+}, and Ni^{2+}) for 3 days, respectively, the surfaces of the crystals of EuCd-MOF are covered with the powder of metal cations and the crystals turn blue in $Cu(NO_3)_2$ solution, green in $Ni(NO_3)_2$ solution, light yellow in $Zn(NO_3)_2$ solution, dark brown in $AgNO_3$ solution, and yellow in $Co(NO_3)_2$ solution, respectively, which makes it easy to distinguish by the naked eye (Fig. 7.18; bottom). The uncoordinated $OCOO^-$ ion of Pbc^- ligands points to the channels and provides binding sites for metal ions. The distance between the uncoordinated $OCOO^-$ atoms is 4.2622 Å, so appropriate ionic radii of metal cations, such as Ag^+, Cu^{2+}, Zn^+, Co^{2+}, and Ni^{2+}, lead to the easy combination of metal cations and the uncoordinated $OCOO^-$ ion. The interaction between uncoordinated $OCOO^-$ ions and metal cations is expected to perturb the singlet and triplet excited states of ligands, which will affect antenna efficiency and further decrease the energy transitions from ligands to Eu^{3+} ions to lead to the luminescence quenching [91].

References

[1] M.A. Verity, W.J. Brown, Hg^{2+} induced kidney necrosis. Subcellular localization and structure-linked lysosomal enzyme changes, Am. J. Pathol. 61 (1970) 57–74.

[2] R.K. Zalups, Molecular interactions with mercury in the kidney, Pharmacol. Rev. 52 (2000) 113–143.

[3] J. Randerson, Even 'safe' mercury levels harm brain, New Sci. 178 (2003) 7.

[4] X. Cui, L. Zhu, J. Wu, Y. Hou, P. Wang, Z. Wang, M. Yang, A fluorescent biosensor based on carbon dots-labeled oligodeoxyribonucleotide and graphene oxide for mercury (II) detection, Biosens. Bioelectron. 63 (2015) 506–512.

[5] S. Wang, B. Lin, L. Chen, N. Li, J. Xu, J. Wang, Y. Yang, Y. Qi, Y. She, X. Shen, X. Xiao, Branch-migration based fluorescent probe for highly sensitive detection of mercury, Anal. Chem. 90 (2018) 11764–11769.

[6] N. Chen, Y. Zhang, H. Liu, X. Wu, A. Wu, High-performance colorimetric detection of Hg^{2+} based on triangular silver nanoprisms, ACS Sens. 1 (2016) 521–527.

[7] H. Tan, B. Liu, Y. Chen, Lanthanide coordination polymer nanoparticles for sensing of mercury(II) by photoinduced electron transfer, ACS Nano 6 (2012) 10505–10511.

[8] B. Liu, Y. Huang, X. Zhu, Y. Hao, Y. Ding, W. Wei, Q. Wang, P. Qu, M. Xu, Smart lanthanide coordination polymer fluorescence probe for mercury(II) determination, Anal. Chim. Acta 912 (2016) 139–145.

[9] S. Zhao, L. Wu, J. Feng, S. Song, H. Zhang, An ideal detector composed of a 3D Gd-based coordination polymer for DNA and Hg^{2+} ion, Inorg. Chem. Front. 3 (2016) 376–380.

[10] Q. Li, C. Wang, H. Tan, G. Tang, J. Gao, C. Chen, A turn on fluorescent sensor based on lanthanide coordination polymer nanoparticles for the detection of mercury(II) in biological fluids, RSC Adv. 6 (2016) 17811–17817.

[11] T. Xia, T. Song, G. Zhang, Y. Cui, Y. Yang, Z. Wang, G. Qian, A terbium metal–organic framework for highly selective and sensitive luminescence sensing of Hg^{2+} ions in aqueous solution, Chem. A Eur. J. 22 (2016) 18429–18434.

[12] X. Xu, B. Yan, Fabrication and application of a ratiometric and colorimetric fluorescent probe for Hg^{2+} based on dual-emissive metal–organic framework hybrids with carbon dots and Eu^{3+}, J. Mater. Chem. C 4 (2016) 1543–1549.

[13] R.R. Lauwerys, A.M. Bernard, H.A. Reels, Cadimium markers as predictors of nephrotoxic effects, Clin. Chem. 40 (1994) 1391–1394.
[14] L. Xue, C. Liu, H. Jiang, Highly sensitive and selective fluorescent sensor for distinguishing cadmium from zinc ions in aqueous media, Org. Lett. 11 (2009) 1655–1658.
[15] L. Pari, P. Murugavel, S.L. Sitasawad, K.S. Kumar, Cytoprotective and antioxidant role of diallyl tetrasulfide on cadmium induced renal injury: an in vivo and in vitro study, Life Sci. 80 (2007) 650–658.
[16] G.F. Nordberg, R.F.M. Herber, L. Alessio (Eds.), Cadmium in the Human Environment: Toxicity and Carcinogenicity, Oxford University Press, Oxford, 1992.
[17] C.C. Bridges, R.K. Zalups, Molecular and ionic mimicry and the transport of toxic metals, Toxicol. Appl. Pharmacol. 204 (2005) 274–308.
[18] H.N. Kim, W.X. Ren, J.S. Kim, J. Yoon, Fluorescent and colorimetric sensors for detection of lead, cadmium, and mercury ions, Chem. Soc. Rev. 41 (2012) 3210–3244.
[19] J. Hao, B. Yan, A water-stable lanthanide-functionalized MOF as a highly selective and sensitive fluorescent probe for Cd^{2+}, Chem. Commun. 51 (2015) 7737–7740.
[20] C. Liu, B. Yan, Zeolite-type metal organic frameworks immobilized Eu^{3+} for cation sensing in aqueous environment, J. Colloid Interface Sci. 459 (2015) 206–211.
[21] X. Xu, B. Yan, Eu(III) functionalized Zr-based metal-organic framework as excellent fluorescent probe for Cd^{2+} detection in aqueous environment, Sens. Actuators B 222 (2016) 347–353.
[22] D. Wang, J. Liu, Z. Liu, A chemically stable europium metal-organic framework for bifunctional chemical sensor and recyclable on–off–on vapor response, J. Solid State Chem. 251 (2017) 243–247.
[23] N. Liu, H. Liu, J. Lu, Z. He, Z. Wang, S. Wang, Y. Li, Y. Huang, Syntheses, structures, fluorescence sensing and magnetic properties of two coordination polymers based on 5-(benzimidazol-2-yl) isophthalic acid ligand, Inorg. Chim. Acta 469 (2018) 515–522.
[24] W. Liao, M. Wei, J. Mo, P. Fu, Y. Fan, M. Pan, C. Su, Acidity and Cd^{2+} fluorescent sensing and selective CO_2 adsorption by a water-stable Eu-MOF, Dalton Trans. 48 (2019) 4489–4494.
[25] S. Lv, J. Liu, C. Li, N. Zhao, Z. Wang, S. Wang, A novel and universal metal-organic frameworks sensing platform for selective detection and efficient removal of heavy metal ions, Chem. Eng. J. 375 (2019) 122111.
[26] J. Liu, J. Hou, J. Liu, X. Jing, L. Li, J. Du, Pyrazinyl-functionalized Zr(iv)-MOF for ultrasensitive detection of tyrosine/TNP and efficient CO_2/N_2 separation, J. Mater. Chem. C 7 (2019) 11851–11857.
[27] H.N. Rubin, M.M. Reynolds, Amino-incorporated tricarboxylate metal-organic framework for the sensitive fluorescence detection of heavy metal ions with insights into the origin of photoluminescence response, Inorg. Chem. 58 (2019) 10671–10679.
[28] L. Li, Q. Chen, Z. Niu, X. Zhou, T. Yang, W. Huang, Lanthanide metal–organic frameworks assembled from a fluorene-based ligand: selective sensing of Pb^{2+} and Fe^{3+} ions, J. Mater. Chem. C 4 (2016) 1900–1905.
[29] X. Zhang, P. Li, W. Gao, F. Liu, J. Liu, Construction of three lanthanide metal-organic frameworks: synthesis, structure, magnetic properties and highly selective sensing of metal ions, J. Solid State Chem. 244 (2016) 6–11.
[30] X. Zeng, Y. Zhang, J. Zhang, H. Hu, X. Wu, Z. Long, X. Hou, Facile colorimetric sensing of Pb^{2+} using bimetallic lanthanide metal-organic frameworks as luminescent probe for field screen analysis of lead-polluted environmental water, Microchem. J. 134 (2017) 140–145.
[31] Z. Li, Z. Zhan, M. Hu, A luminescent terbium coordination polymer as a multifunctional water-stable sensor for detection of Pb^{2+} ions, PO_4^{3-} ions, $Cr_2O_7^{2-}$ ions, and some amino acids, CrystEngComm 22 (2020) 6727–6737.

[32] J. Lin, Q. Cheng, J. Zhou, X. Lin, R.C.K. Reddy, T. Yang, G. Zhang, Five 3D lanthanide-based coordination polymers with 3,3,6T13 topology: structures and luminescent sensor for Hg^{2+} and Pb^{2+} ions, J. Solid State Chem. 270 (2019) 339–345.
[33] A.D. Dayan, A.J. Paine, Mechanisms of chromium toxicity, carcinogenicity and allergenicity: review of the literature from 1985 to 2000, Hum. Exp. Toxicol. 20 (2001) 439–451.
[34] R. Lv, J. Wang, Y. Zhang, H. Li, L. Yang, S. Liao, W. Gu, X. Liu, An amino-decorated dual-functional metal – organic framework for highly selective sensing of Cr(iii) and Cr(vi) ions and detection of nitroaromatic explosives, J. Mater. Chem. A 4 (2016) 15494–15500.
[35] A. Levina, P.A. Lay, Mechanistic studies of relevance to the biological activities of chromium, Coord. Chem. Rev. 249 (2005) 281–298.
[36] U.S. Department of Health and Human Services, Toxicological Profile for Chromium, Public Health Service Agency for Toxic Substances and Diseases Registry, Washington, DC, 1991.
[37] K.L. Witt, M.D. Stout, R.A. Herbert, G.S. Travlos, G.E. Kissling, B.J. Collins, M.J. Hooth, Mechanistic insights from the NTP studies of chromium, Toxicol. Pathol. 41 (2013) 326–342.
[38] D. Cai, H. Guo, L. Wen, C. Liu, Fabrication of hierarchical architectures of Tb-MOF by a "green coordination modulation method" for the sensing of heavy metal ions, CrystEngComm 15 (2013) 6702–6708.
[39] H. Wang, L. Zhou, Y. Wang, Q. Liu, Terbium-biphenyl-3,3′-disulfonyl-4,4′-dicarboxylate framework with sulfonate sites for luminescent sensing of Cr^{3+} ion, Inorg. Chem. Commun. 73 (2016) 94–97.
[40] H. Weng, B. Yan, Multi-color luminescence and sensing of rare earth hybrids by ionic exchange modification, J. Fluoresc. 26 (2016) 1497–1504.
[41] Y. Wang, H. Yang, G. Cheng, Y. Wu, S. Lin, A new Tb(III)-functionalized layer-like Cd MOF as luminescent probe for high-selectively sensing of Cr^{3+}, CrystEngComm 19 (2017) 7270–7276.
[42] J. Liu, G. Ji, J. Xiao, Z. Liu, Ultrastable 1D europium complex for simultaneous and quantitative sensing of Cr(III) and Cr(VI) ions in aqueous solution with high selectivity and sensitivity, Inorg. Chem. 56 (2017) 4197–4205.
[43] H. Ma, L. Wang, J. Chen, X. Zhang, L. Wang, N. Xu, G. Yang, P. Cheng, A multi-responsive luminescent sensor for organic small-molecule pollutants and metal ions based on a 4d–4f metal–organic framework, Dalton Trans. 46 (2017) 3526–3534.
[44] K. Zheng, Z. Liu, Y. Jiang, P. Guo, H. Li, C. Zeng, S.W. Ng, S. Zhong, Ultrahigh luminescence quantum yield lanthanide coordination polymer as a multifunctional sensor, Dalton Trans. 47 (2018) 17432–17440.
[45] C.J. Gibbs, Intraneuronal aluminum accumulation in amyotrophic lateral sclerosis and Parkinsonism-dementia of Guam, Science 217 (1982) 1053–1055.
[46] D.P. Perl, A.R. Brody, Alzheimer's disease: X-ray spectrometric evidence of aluminum accumulation in neurofibrillary tangle-bearing neurons, Science 208 (1980) 297–299.
[47] G.D. Fasman, Aluminum and Alzheimer's disease: model studies, Coord. Chem. Rev. 149 (1996) 125–165.
[48] M. Shyamal, P.M. Mazumdar, S. Maity, G.P. Sahoo, G. Salgado-Moran, A. Misra, Pyrene scaffold as real-time fluorescent turn-on chemosensor for selective detection of trace-level Al(III) and its aggregation-induced emission enhancement, J. Phys. Chem. A 120 (2016) 210–220.
[49] V.K. Gupta, A.K. Jain, G. Maheshwari, Aluminum(III) selective potentiometric sensor based on morin in poly(vinyl chloride) matrix, Talanta 72 (2007) 1469–1473.
[50] T.P. Flaten, Aluminium as a risk factor in Alzheimer's disease, with emphasis on drinking water, Brain Res. Bull. 55 (2001) 187–196.

[51] J. Hao, B. Yan, Amino-decorated lanthanide(III) organic extended frameworks for multi-color luminescence and fluorescence sensing, J. Mater. Chem. C 2 (2014) 6758–6764.
[52] L. Cao, F. Shi, W. Zhang, S. Zang, T.C.W. Mak, Selective sensing of Fe^{3+} and Al^{3+} ions and detection of 2,4,6-trinitrophenol by a water-stable terbium-based metal–organic framework, Chem. Eur. J. 21 (2015) 15705–15712.
[53] B. Ding, S. Liu, Y. Cheng, C. Guo, X. Wu, J. Guo, Y. Liu, Y. Li, Heterometallic alkaline earth–lanthanide BaII–LaIII microporous metal–organic framework as bifunctional luminescent probes of Al^{3+} and MnO_4^-, Inorg. Chem. 55 (2016) 4391–4402.
[54] X. Liu, H. Lin, Z. Xiao, W. Fan, A. Huang, R. Wang, L. Zhang, D. Sun, Multifunctional lanthanide–organic frameworks for fluorescent sensing, gas separation and catalysis, Dalton Trans. 45 (2016) 3743–3749.
[55] Y. Kang, X. Zheng, L. Jin, A microscale multi-functional metal-organic framework as a fluorescence chemosensor for Fe(III), Al(III) and 2-hydroxy-1-naphthaldehyde, J. Colloid Interface Sci. 471 (2016) 1–6.
[56] X. Zhou, J. Cheng, L. Li, Q. Chen, Y. You, H. Xiao, W. Huang, A europium(III) metal-organic framework as ratiometric turn-on luminescent sensor for Al^{3+} ions, Sci. China Mater. 61 (2018) 752–757.
[57] X. Wang, Z. Huang, J. Du, X. Wang, N. Gu, X. Tian, Y. Li, Y. Liu, J. Huo, B. Ding, Hydrothermal preparation of five rare-earth (Re = Dy, Gd, Ho, Pr, and Sm) luminescent cluster-based coordination materials: the first MOFs-based ratiometric fluorescent sensor for lysine and bifunctional sensing platform for insulin and Al^{3+}, Inorg. Chem. 57 (2018) 12885–12899.
[58] Z. Zhan, Y. Jia, D. Li, X. Zhang, M. Hu, A water-stable terbium-MOF sensor for the selective, sensitive, and recyclable detection of Al^{3+} and CO_3^{2-} ions, Dalton Trans. 48 (2019) 15255–15262.
[59] D. Chen, Y. Zheng, S. Fang, A polyhedron-based porous Tb(III)–organic framework with dual emissions for highly selective detection of Al^{3+} ion, Inorg. Chem. Commun. 117 (2020) 107967.
[60] H. Guo, N. Wu, R. Xue, H. Liu, L. Li, M. Wang, W. Yao, Q. Li, W. Yang, Multifunctional Ln-MOF luminescent probe displaying superior capabilities for highly selective sensing of Fe^{3+} and Al^{3+} ions and nitrotoluene, Colloids Surf. A 585 (2020) 124094.
[61] M. Chen, K. Wu, W. Pan, N. Huang, R. Li, J. Chen, Selective and recyclable tandem sensing of PO_4^{3-} and Al^{3+} by a water-stable terbium-based metal–organic framework, Spectrochim. Acta A Mol. Biomol. Spectrosc. 247 (2021) 119084.
[62] G. Aragay, J. Pons, A. Merkoci, Recent trends in macro-, micro-, and nanomaterial-based tools and strategies for heavy-metal detection, Chem. Rev. 111 (2011) 3433–3458.
[63] T.Q. Duong, J.S. Kim, Fluoro- and chromogenic chemodosimeters for heavy metal ion detection in solution and biospecimens, Chem. Rev. 110 (2010) 6280–6301.
[64] C. Hao, L. Xua, C. Xing, H. Kuang, L. Wang, C. Xu, Oligonucleotide-based fluorogenic sensor for simultaneous detection of heavy metal ions, Biosens. Bioelectron. 36 (2012) 174–178.
[65] Q. Feng, J. Wu, G. Chen, F. Cui, T. Kim, J. Kim, A mechanistic study of the antibacterial effect of silver ions on *Escherichia coli* and *Staphylococcus aureus*, J. Biomed. Mater. Res. 52 (2000) 662–668.
[66] M. Yamanaka, K. Hara, J. Kudo, Bactericidal actions of a silver ion solution on *Escherichia coli*, studied by energy-filtering transmission electron microscopy and proteomic analysis, Appl. Environ. Microbiol. 71 (2005) 7589–7593.
[67] J. Hao, B. Yan, Highly sensitive and selective fluorescent probe for Ag^+ based on a Eu^{3+} post-functionalized metal–organic framework in aqueous media, J. Mater. Chem. A 2 (2014) 18018–18025.
[68] J. Hao, B. Yan, Ag^+-sensitized lanthanide luminescence in Ln^{3+} post-functionalized metal–organic frameworks and Ag^+ sensing, J. Mater. Chem. A 3 (2015) 4788–4792.

[69] N. Sun, B. Yan, Ag^+-induced photoluminescence enhancement in lanthanide post-functionalized MOFs and Ag^+ sensing, Phys. Chem. Chem. Phys. 19 (2017) 9174–9180.
[70] N. Sun, B. Yan, A reliable amplified fluorescence-enhanced chemosensor (Eu-MIL-61) for the directional detection of Ag^+ in an aqueous solution, Dalton Trans. 46 (2017) 875–881.
[71] J. Liu, L. Yu, F. Han, F. Chen, F. Cheng, A thioether-containing luminescent metal-organic framework for highly selective and sensitive detection of Ag(I) ion, J. Solid State Chem. 270 (2019) 45–50.
[72] D. Liu, G. Dong, X. Wang, F. Nie, X. Li, A luminescent Eu coordination polymer with near-visible excitation for sensing and its homologues constructed from 1,4-benzenedicarboxylate and 1H-imidazo[4,5-f][1,10]-phenanthroline, CrystEngComm 22 (2020) 7877–7887.
[73] K. Ge, D. Wang, Z. Xu, R. Chu, A luminescent Eu(III)-MOF for selective sensing of Ag^+ in aqueous solution, J. Mol. Struct. 1208 (2020) 127862.
[74] S. Biswas, S. Acharyya, D. Sarkar, S. Gharami, T.K. Mondal, Novel pyridyl based azo-derivative for the selective and colorimetric detection of nickel(II), Spectrochim. Acta A 159 (2016) 157–162.
[75] H. Yang, F. Wang, Y. Tan, Y. Kang, T. Li, J. Zhang, Charge matching on designing neutral cadmium–lanthanide–organic open frameworks for luminescence sensing, Chem. Asian J. 7 (2012) 1069–1073.
[76] Z. Cui, Zhang, S. Liu, L. Zhou, W. Li, J. Zhang, Anionic lanthanide metal–organic frameworks: selective separation of cationic dyes, solvatochromic behavior, and luminescent sensing of Co(II) ion, Inorg. Chem. 57 (2018) 11463–11473.
[77] K. Zheng, Z. Liu, Y. Huang, F. Chen, C. Zeng, S. Zhong, S.W. Ng, Highly luminescent Ln-MOFs based on 1,3-adamantanediacetic acid as bifunctional sensor, Sens. Actuators B 257 (2018) 705–713.
[78] C. Xie, Z. Yu, W. Tong, K. Shehzad, W. Xu, J. Wang, J. Liu, Insights into the fluorescence sensing mechanism of scandium-based metal-organic frameworks by solid-state NMR spectroscopy, ChemistrySelect 4 (2019) 5291–5299.
[79] L. Wang, J. He, Q. Yang, X. Lv, J. Li, D. Chen, X. Ding, X. Huang, Q. Zhou, Abnormal pinocytosis and valence-variable behaviors of cerium suggested a cellular mechanism for plant yield reduction induced by environmental cerium, Environ. Pollut. 230 (2017) 902–910.
[80] G. Mathews, N. Nagaiah, M.B. Karthik Kumar, M.R. Ambika, Radiological and chemical toxicity due to ingestion of uranium through drinking water in the environment of Bangalore, India, J. Radiol. Prot. 35 (2015) 447–455.
[81] P.A. Bryant, Chemical toxicity and radiological health detriment associated with the inhalation of various enrichments of uranium, J. Radiol. Prot. 34 (2014) N_1–N_6.
[82] M. Yazzie, S.L. Gamble, E.R. Civitello, D.M. Stearns, Uranyl acetate causes DNA single strand breaks in vitro in the presence of ascorbate (vitamin C), Chem. Res. Toxicol. 16 (2003) 524–530.
[83] K.L. Cooper, E.J. Dashner, R. Tsosie, Y.M. Cho, J. Lewis, L.G. Hudson, Inhibition of poly(ADP-ribose)polymerase-1 and DNA repair by uranium, Toxicol. Appl. Pharmacol. 291 (2016) 13–20.
[84] Q. Zhang, J. Wang, A.M. Kirillov, W. Dou, C. Xu, C. Xu, L. Yang, R. Fang, W. Liu, Multifunctional Ln – MOF luminescent probe for efficient sensing of Fe^{3+}, Ce^{3+}, and acetone, ACS Appl. Mater. Interfaces 10 (2018) 23976–23986.
[85] W. Liu, Y. Wang, L. Song, M.A. Silver, J. Xie, L. Zhang, L. Chen, J. Diwu, Z. Chai, S. Wang, Efficient and selective sensing of Cu^{2+} and UO_2^{2+} by a europium metal-organic framework, Talanta 196 (2019) 515–522.

[86] G.E. Gomez, M. dos Santos Afonso, H.A. Baldoni, F. Roncaroli, G.J.A.A. Soler-Illia, Luminescent lanthanide metal organic frameworks as chemosensing platforms towards agrochemicals and cations, Sensors 19 (2019) 1260.

[87] L. Song, W. Liu, Y. Wang, L. Chen, X. Wang, S. Wang, A hydrolytically stable europium–organic framework for the selective detection of radioactive Th^{4+} in aqueous solution, CrystEngComm 21 (2019) 3471–3477.

[88] H. Wu, H. Chen, M. Fu, R. Li, P. Ma, J. Wang, J. Niu, A PHBA-functionalized organic-inorganic hybrid polyoxometalate as a luminescent probe for selectively sensing chromium and calcium in aqueous solution, Dyes Pigments 171 (2019) 107696.

[89] Z. Zhan, X. Liang, X. Zhang, Y. Jia, M. Hu, A water-stable europium-MOF as a multifunctional luminescent sensor for some trivalent metal ions (Fe^{3+}, Cr^{3+}, Al^{3+}), PO_4^{3-} ions, and nitroaromatic explosives, Dalton Trans. 48 (2019) 1786–1794.

[90] Y. Wu, D. Liu, M. Lin, J. Qian, Zinc(II)-based coordination polymer encapsulated Tb^{3+} as a multi-responsive luminescent sensor for Ru^{3+}, Fe^{3+}, CrO_4^{2-}, $Cr_2O_7^{2-}$ and MnO_4^-, RSC Adv. 10 (2020) 6022–6029.

[91] L. Ding, L. Liu, Q. Shi, Y. Sun, Y. Wang, Y. Chen, Luminescent 3D lanthanide–cadmium heterometal–organic frameworks with chemical stability and selective luminescent sensing, Inorg. Chem. 56 (2017) 14850–14858.

Chapter 8

Rare earth metal-organic framework hybrid material for luminescence responsive chemical sensing of anions

8.1 Rare earth metal-organic framework hybrid materials for luminescence responsive chemical sensing of fluoride (F^-) ions

Fluoride is an essential trace element in the human body; however, intake of excessive fluoride can cause serious health problems, including dental and skeletal fluorosis. The fluoride ion (F^-) is considered one of the most serious pollutants in water because of its high toxicity. The World Health Organization (WHO) has set a maximum limit of F^- ions in drinking water of 1.5 ppm because of the critical threat to human health [1–5]. As a result, it is vital to monitor the concentrations of F^- ions in aqueous solution with high selectivity and sensitivity. There are some reports on luminescent chemical sensing of F^- using rare earth MOF hybrid materials [6–12].

Wan et al. used boric acid to tune the optical properties of Eu^{3+} MOFs (Eu-MOF) with 5-boronoisophthalic acid (5-bop) for dual luminescence and to improve their selectivity for the determination of F^- ions. The ratiometric luminescent detection of F^- ions was validated with the dual emission at single excitation [9]. They revealed that the rational selection of functional ligands can improve the sensing efficiency through tuning their optical properties and enhancing the selectivity toward targets (Fig. 8.1; top). The dual emission of Eu-MOF was recorded with the F^- concentration ranging from 0 to 500 μM (Fig. 8.1A and B; bottom). The intensity ratio at 625 and 366 nm decreased to 0.26 from the original value of 0.93 when 100 μM F^- was tested. An excellent linear relationship was observed between the intensity ratio and F^- concentration ranged between 4 and 80 μM. Thus Eu-MOF has interesting prospects for the quantitative detection of F^- ions with the detection limits (LOD) of 2 μM or 0.034 mg L^{-1} (Fig. 8.1C; bottom). When F^- was added into the Eu-MOF solution gradually, the bright red luminescence faded away with decreasing intensity, while the color also changed from red to blue (inset of Fig. 8.1A;

Rare Earth Metal-Organic Framework Hybrid Materials for Luminescence Responsive Chemical Sensors
https://doi.org/10.1016/B978-0-323-91236-5.00008-6

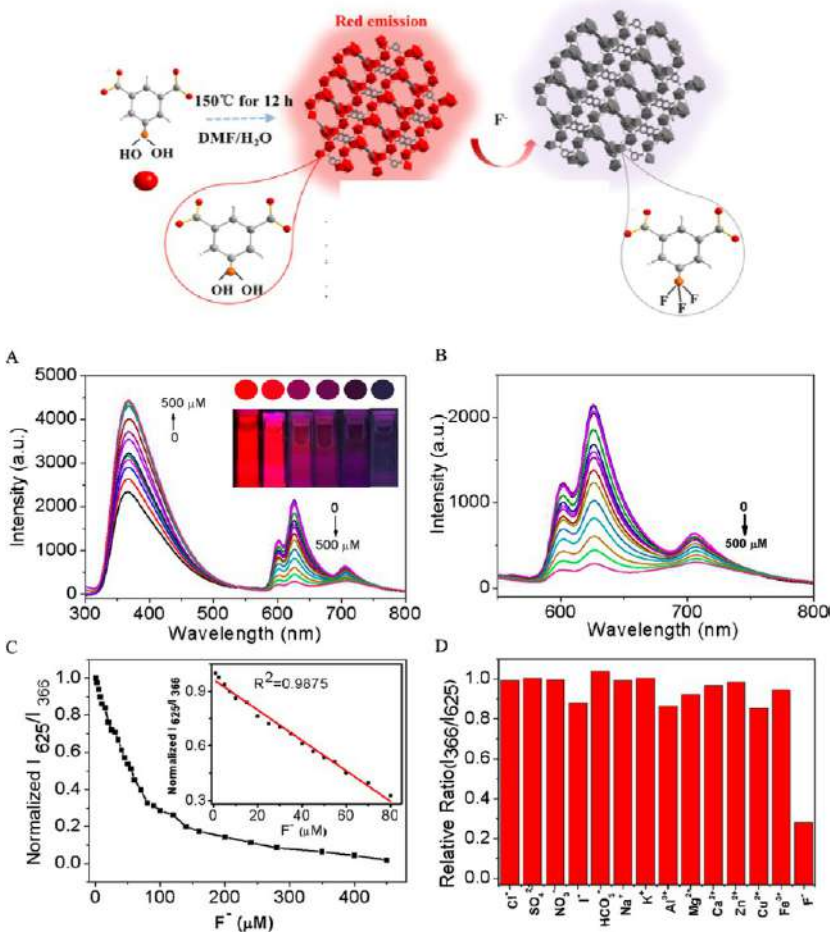

FIG. 8.1 *(Top)* Schematic description of Eu-MOF fluorescent sensing of fluoride ions. *(Bottom)* (A) Fluorescence spectra ($\lambda_{ex} = 275$ nm) of 0.2 mg mL^{-1} Eu-MOF upon the addition of fluoride at different concentrations. Inset shows photographs of the mixture solution to illustrate the color and intensity change at different concentrations of fluoride. (B) The part amplification of the emission profile in panel (A). (C) Plot of the intensity ratio of I_{625}/I_{366} vs. fluoride concentration. (D) Luminescence ratio of I_{625}/I_{366} from the responses of Eu-MOF in the presence of 100 μM fluoride and 500 μM interference ions. *(Reproduced with permission from Z. Yang, M. Wang, X. Wang, X. Yin, Boric-acid-functional lanthanide metal–organic frameworks for selective ratiometric fluorescence detection of fluoride ions, Anal. Chem. 89 (2017) 1930–1936. Copyright 2017 American Chemical Society.)*

bottom). The change in color and intensity can be easily distinguished by the naked eye, compared with the single intensity change from the emission of Eu^{3+} ions. Under identical conditions, only F^- shows the remarkable luminescence change, while only a negligible change is observed from the other ions (Fig. 8.1D; bottom). Eu-MOF's high selectivity to F^- ions is due to its high

affinity between boric acid and F^-, which is generally considered to be a strong covalent interaction between boron and F^- and the change from sp^2 trigonal boron $-B(OH)_2$ to sp^3 hybridized $-BF_3$. The disrupted π-π conjugation of 5-bop decreases the intersystem crossing efficiency with the addition of F^-, leading to the increasing emission of 5-bop and the decreasing intensity from Eu^{3+} ions for the strong electron-withdrawing property of F^- [9].

Zheng et al. reported a "Turn-On" fluorescent probe for sensing F^- ions based on Tb^{3+}-functionalized Zr-MOFs with mixed ligands. Postcoordinated encapsulation generated the Tb^{3+}-loaded luminescent Tb^{3+}@Zr-MOF, which was then applied in sensing anions in an aqueous solution [10]. As shown in Fig. 8.2 (top), F^- can extremely enhance the emission of Tb^{3+}. The dark colors of suspensions serve as foils to that of F^-, which displays a bright green color (inset of Fig. 8.2; top). As can be seen in Fig. 8.2 (bottom, left), when F^- is added to the other anion solution, the luminescence intensity of Tb^{3+} is apparently increased compared to that in the absence of F^-. This indicates that sensing of F^- ions by the Tb^{3+}@Zr-MOF has good antiinterference, vital for fluorescent probes. A concentration-dependent luminescence analysis of Tb^{3+}@Zr-MOF was performed and is shown in Fig. 8.2 (bottom, right); the emission intensity obviously is enhanced with the increasing content of F^-. The curve of emission intensity of Tb^{3+}@Zr-MOF versus the concentration of F^- is plotted in the inset of Fig. 8.2 (bottom, right), and it can be rationalized by the linear fit. This linear correlation can be fitted as a function of the equation with a correlation coefficient of 0.9884 and LOD of 0.35 ppm.

Wang et al. designed and prepared Y-MOF nanoplates of TCCP as the porphyrin-based planar ligand. Customarily, TCCP (4,4,4,4-(porphine-5,10,15,20-tetrayl) tetrakis (benzoic acid)) exhibits a bright red fluorescence at 645 nm. After the formation of Y-MOF nanoplates (YTMNs), the fluorescence was quenched via the photoinduced electron transfer (PET) effect [12]. Apart from those used for coordination with ligands, the redundant open metal sites provide the binding or adsorption positions and high probability of replacement toward F^-. Meanwhile, F^- has the smallest radius in all kinds of anions, which causes F^- to exhibit the facile replacement of solvent H_2O in the YTMNs unit cell. A strong Lewis acid-base interaction occurs between YTMNs and F^-. The strong electronegativity of F^- sufficiently changes the original pathway of PET from TCCP to Y^{3+} and then recovers the fluorescence of TCCP. In view of these distinctive host-guest responses, F^- induced a rapid fluorescence recovery of YTMNs with high sensitivity and selectivity. As shown in Fig. 8.3A, the fluorescence intensity of the YTNMs nanoprobe increases with the growing additions of F^-, leading to a linear response in ΔF to F^- (Fig. 8.3B). The calibration equation is described, with a linear range from 0.05 to 8 ppm and with R^2 of 0.992. The LOD of the proposed method for F^- detection is calculated to be 8.5 ppb. As can be seen from Fig. 8.3C and D, only F^- ions induce a sufficient fluorescence response, while a negligible response is observed from other interferents.

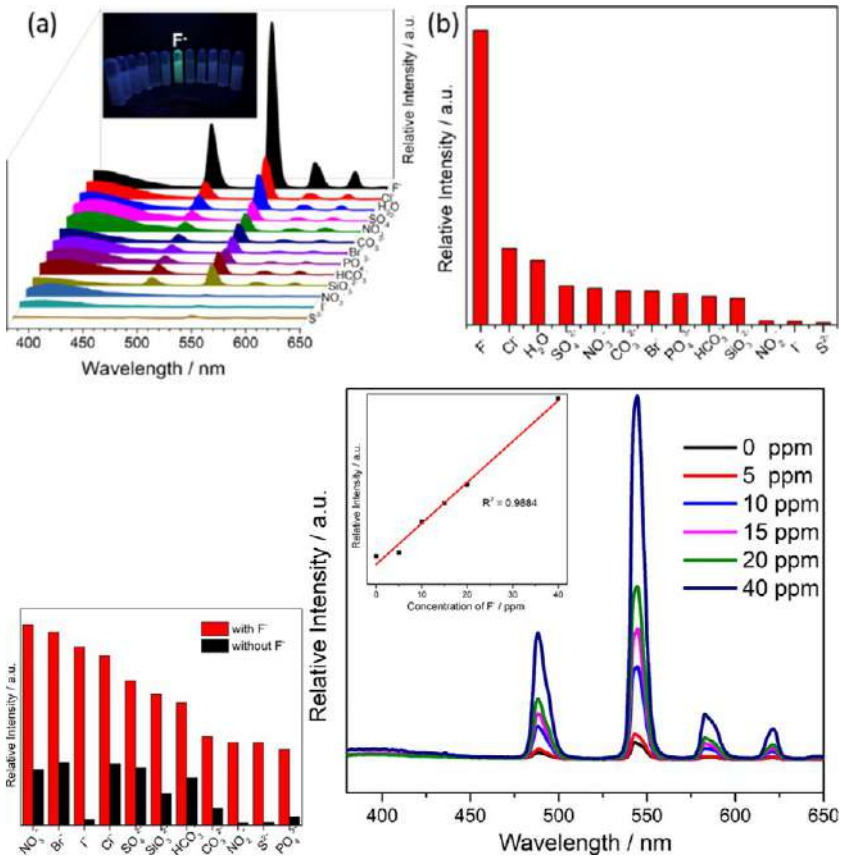

FIG. 8.2 *(Top)* (A) Emission spectra of Tb^{3+}@Zr-MOF dispersed in different anion solutions (excited at 302 nm). The inset is the corresponding photographs under UV-light irradiation. *(Bottom, left)* Luminescence intensity (545 nm) of Tb^{3+}@Zr-MOF with or without F^- in the presence of the background of the other anions in aqueous solution. *(Bottom, right)* Emission spectra of Tb^{3+}@Zr-MOF excited at 302 nm under different F^- concentrations. The inset is the linear relationship between F^- concentration and luminescence intensity of Tb^{3+}. *(Reproduced with permission from H. Zheng, X. Lian, S. Qin, B. Yan, Novel "turn-on" fluorescent probe for highly selectively sensing fluoride in aqueous solution based on Tb^{3+}-functionalized metal–organic frameworks, ACS Omega 3 (2018) 12513–12519. Copyright 2018 American Chemical Society.)*

8.2 Rare earth metal-organic framework hybrid materials for luminescence responsive chemical sensing of other simple anions (S^{2-}, HS^-, and SCN^-)

Sulfide is widely produced in the production process of sulfuric acid, dyes, and cosmetics. Sulfide ion (S^{2-}) can combine with H^+ in acidic solution, generating more toxic H_2S or HS^-. H_2S can participate in the process of cardiovascular diastolic as antioxidant. In addition, it is related to high blood pressure,

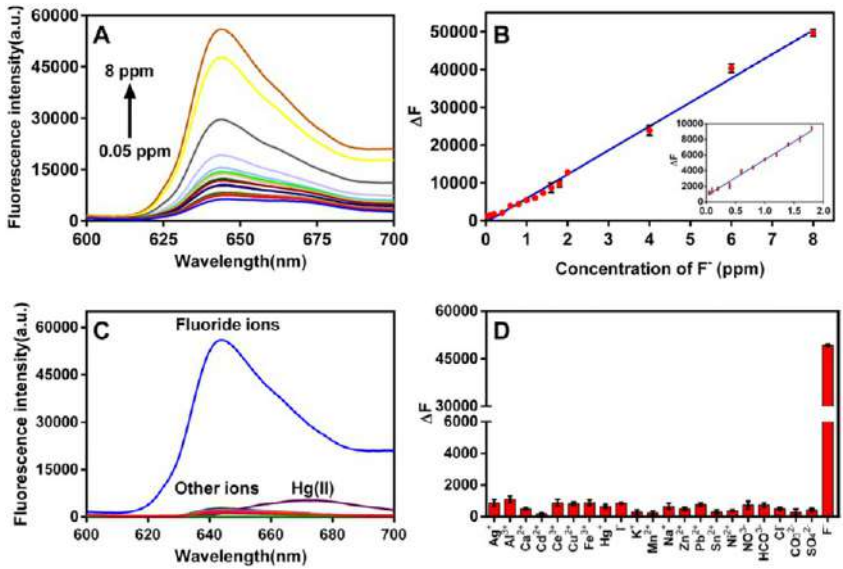

FIG. 8.3 The fluorescence spectrum (A) of YTMNs nanoprobe and corresponding calibration curve (B) with the growing concentrations of F^- (0.05, 0.1, 0.2, 0.4, 0.6, 0.8, 1, 1.2, 1.4, 1.6, 1.8, 2, 4, 6, 8 ppm). The final fluorescence spectrum (C) and corresponding net fluorescence (D) of the YTMNs nanoprobe after reaction with fluoride ions (8 ppm) and various interfering ions (40 ppm). *(Reproduced with permission from X. Wang, C. Chu, Y. Wu, Y. Deng, J. Zhou, M. Yang, S. Zhang, D. Huo, C. Hou, Synthesis of yttrium(III)-based rare-earth metal-organic framework nanoplates and its applications for sensing of fluoride ions and pH. Sens. Actuators B Chem. 321 (2020) 128455. Copyright 2020 Elsevier.)*

cirrhosis, and Down's syndrome. Hydrogen sulfide is a colorless, corrosive, and exceedingly poisonous gas, which can be directly absorbed by the human lungs, giving rise to diseases in the respiratory and nervous systems, and can even cause death [13–15]. Rare earth MOF hybrid materials have been applied for the sensing of these anions [16–18].

Weng et al. assembled a luminescent hybrid material by adjusting the ratio of FAM-ssDNA (carboxyfluorescein-labeled single strand DNA) and Eu^{3+} @Bio-MOF-1, which can emit the characteristic fluorescence of both FAM and Eu^{3+} [16]. The luminescent intensities of FAM at 520 nm and Eu^{3+} at 614 nm are comparable. The introduction of Cu^{2+} can quench the luminescence of FAM while the luminescence of Eu^{3+} is enhanced. The Cu^{2+}@MOFs hybrid can then be further used for the detection of anions; in low concentrations of S^{2-}, the luminescence of Eu^{3+} can decrease with an increase of S^{2-}. Fig. 8.4 (left) shows that at a concentration of 10^{-5} mol L^{-1}, S^{2-} shows a greatly decreased emission at 614 nm, which is significantly different than other anions. To further explore this fluorescence quenching of S^{2-}, concentration-dependent experiments were carried out. As is shown in Fig. 8.4 (right, top), the emission intensity of Cu^{2+}@MOFs hybrid suspension declines with the

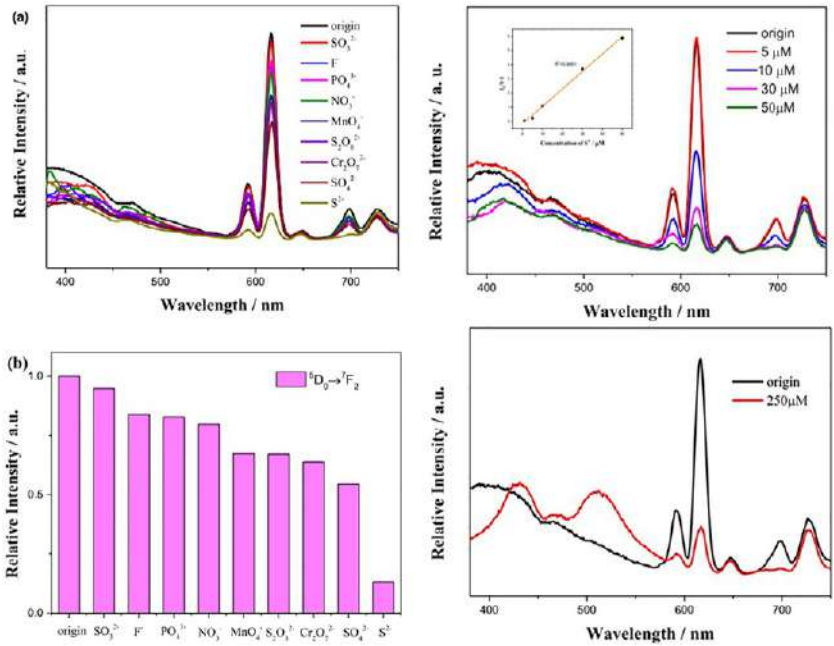

FIG. 8.4 *(Left)* (A) Luminescent spectra of Cu^{2+}@Bio-MOF-1 dispersed into aqueous solutions of various anions with the concentration of 10^{-5} mol L^{-1} when excited at 323 nm; (B) Emission intensity of the $^5D_0 \rightarrow {}^7F_2$ of Cu^{2+}@Bio-MOF-1 with different anions. *(Right, top)* Emission spectra of Cu^{2+}@ Bio-MOF-1 in different concentrations of S^{2-}; inset is the plot of $(I/I_0)^{-1}$ versus the logarithm of the concentration of S^{2-}. *(Right, bottom)* Emission spectra of Cu^{2+}@ Bio-MOF-1 in S^{2-} at a concentration of 250 mM. *(Reproduced with permission from H. Weng, B. Yan, A Eu(III) doped metal-organic framework conjugated with fluorescein-labeled single-stranded DNA for detection of Cu(II) and sulfide, Anal. Chim. Acta 988 (2017) 89–95. Copyright 2017 Elsevier.)*

increase of S^{2-} concentration from 0 to 50 mM. As is shown in the inset of Fig. 8.4 (right, top), there is a good linear relationship ($R^2 = 0.9951$) between the concentration of S^{2-} and the luminescent intensity at 614 nm, with a K_{sv} value of 1.2306×10^5 and LOD of 1.3 mM. However, as the concentration of S^{2-} rises to 250 mM, there is an interesting phenomenon: an emission located at about 520 nm occurs, as is shown in Fig. 8.4 (right, bottom). The emission spectra are similar to Cu^{2+}@MOFs hybrid, in which Cu^{2+} is not involved. That means the existence of S^{2-} can eliminate the influence of Cu^{2+} toward the Cu^{2+} @MOFs hybrid step by step.

Wang et al. designed a triple-wavelength-region sensing procedure and utilized it as a trifunctional luminescent color change (LCC) path for the detection of anions, cations, and organic small molecules. In this system, La^{3+}, Eu^{3+}, and Tb^{3+} ions were three independent luminescence centers, which led to a synergism effect on the final luminescence color [17]. As shown in Fig. 8.5 (top), the luminescence spectra of the blank sample and the majority of anion ions@La/Eu/Tb-dcbba remain almost the same in terms of the ratios of I_{544}/I_{616} being

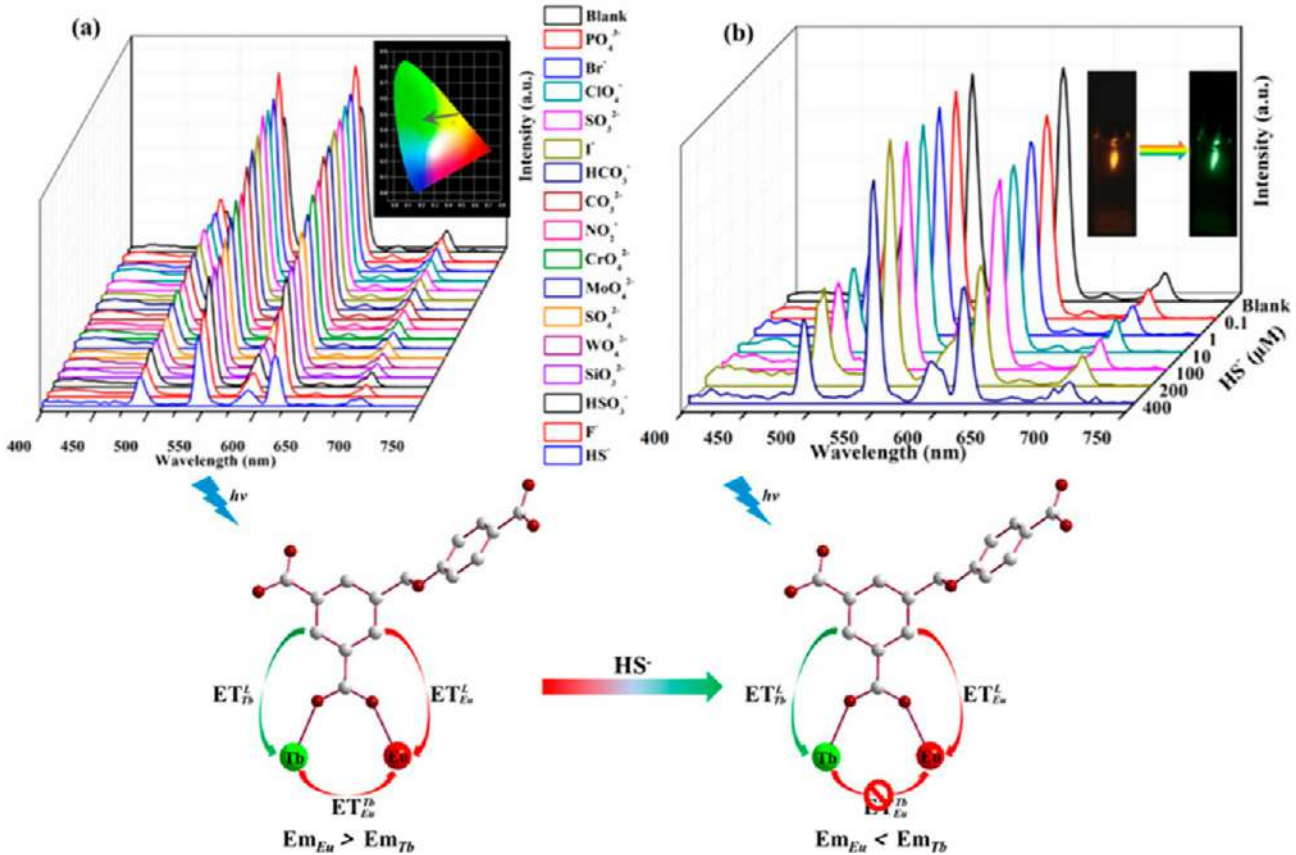

FIG. 8.5 (A) Emission spectra of X^{x-}@La/Eu/Tb-dcbba excited at 300 nm (inset: the corresponding CIE coordinates change of HS^-@ La/Eu/Tb-dcbba 4). (B) Emission spectra of La/Eu/Tb-dcbba toward different concentrations of HS^- ions (inset: the corresponding luminescence photograph with HS^- ion concentration from 0 to 400 μM). *(Bottom)* Schematic illustrations of the mechanism of La/Eu/Tb-dcbba detecting HS^- ions. *(Reproduced with permission from X. Wang, X. Yao, Q. Huang, Y. Li, G. An, G. Li, Triple-wavelength-region luminescence sensing based on a color tunable emitting lanthanide metal organic framework, Anal. Chem. 90 (2018) 6675–6682. Copyright 2018 American Chemical Society.)*

about 1. However, the luminescence spectra of HS^-@La/Eu/Tb-dcbba show obvious LCC phenomena compared to other X^{n-}@La/Eu/Tb-dcbba systems, with the ratios of I_{544}/I_{616} closing to 1.4, exhibiting an obvious LCC from orange to green. According to Fig. 8.5B (top), the intensity of I_{544} shows negligible change when the content of HS^- ions is increased gradually. However, the intensity of I_{616} shown evidently decreases, exhibiting an obvious LCC phenomenon from orange to blue. The excellent selectivity and visible LCC phenomena boost the potential for applications for detection of HS^- ions via the LCC process. La/Eu/Tb-dcbba is conducted by the in situ doping of La^{3+}, Eu^{3+}, and Tb^{3+} ions with a molar ratio of $La_{0.88}/Eu_{0.02}/Tb_{0.10}$. Although the content of the Tb^{3+} ions is almost five times that of the Eu^{3+} ions, the characteristic peaks of Eu^{3+} ions at 616 nm are stronger than those of Tb^{3+} ions at 544 nm when La/Eu/Tb-dcbba is excited at 300 nm, which can be attributed to an energy transfer from the Tb^{3+} to Eu^{3+} ions. Weak interactions (such as hydrogen bonds) may exist between the HS^- ions and the other sections of the frameworks. This may further break the energy transfer from Tb^{3+} to Eu^{3+} ions, which results in the decreasing emission of Eu^{3+} ions (Fig. 8.5; bottom) [17].

As one of the important inorganic anions, thiocyanate (SCN^-) acts as an antimicrobial agent, widely used in fabric dyeing, photographing, electroplating baths, and so on. However, high concentrations of SCN^- in living cells may lead to protein dialysis [19,20]. A few works have reported on the luminescence sensing of SCN^- via rare earth MOF hybrid probes [21,22].

Li et al. designed a nanoprobe based on luminous Eu(III) complex-functionalized Fe_3O_4 nanoparticles encapsulated into zeolitic imidazolate framework materials (nano-ZIF-8, Fig. 8.6; top), whose core-shell-like nano-ZIF-8 can simultaneously detect ClO^- and SCN^- in ultrapure water. Fig. 8.6A (middle) shows the emission change of nano-ZIF-8 upon incremental addition of ClO^- in ultrapure water. The introduction of ClO^- from 0 to 100 μM results in a gradual decrease in these two emission peaks, accompanied by an obvious fluorescent color change from red to colorless under a UV lamp (inset of Fig. 8.6A; middle), which is due to the stronger binding ability of ClO^- and Eu^{3+}, releasing the free nonfluorescent PDA. Moreover, the emission intensity at 613 nm displays a good linear relationship with ClO^- concentration in the range of 0–0.50 μM ($R^2 = 0.9938$) (Fig. 8.6B; middle). As illustrated in Fig. 8.6C (middle), only ClO^- induces significant fluorescence quenching at 590 nm and 613 nm, and no or negligible changes in emission intensity at 613 nm (F_{613} nm) are observed in the presence of even excessive amounts (5 equiv.) of the other various anions investigated (Fig. 8.6C; middle, black bar), proving the high selectivity of nano-ZIF-8 toward ClO^-. The results shown in Fig. 8.6C (middle) (red bar) indicate that the values of F_{613} nm are almost identical to those of nano-ZIF-8-ClO^- alone, and the specificity of nano-ZIF-8 is good enough to detect ClO^- in the presence of other anions in water. In addition, the obtained quenching fluorescence system nano-ZIF-8-ClO^- is utilized to detect SCN^- in ultrapure water. As depicted in Fig. 8.6A

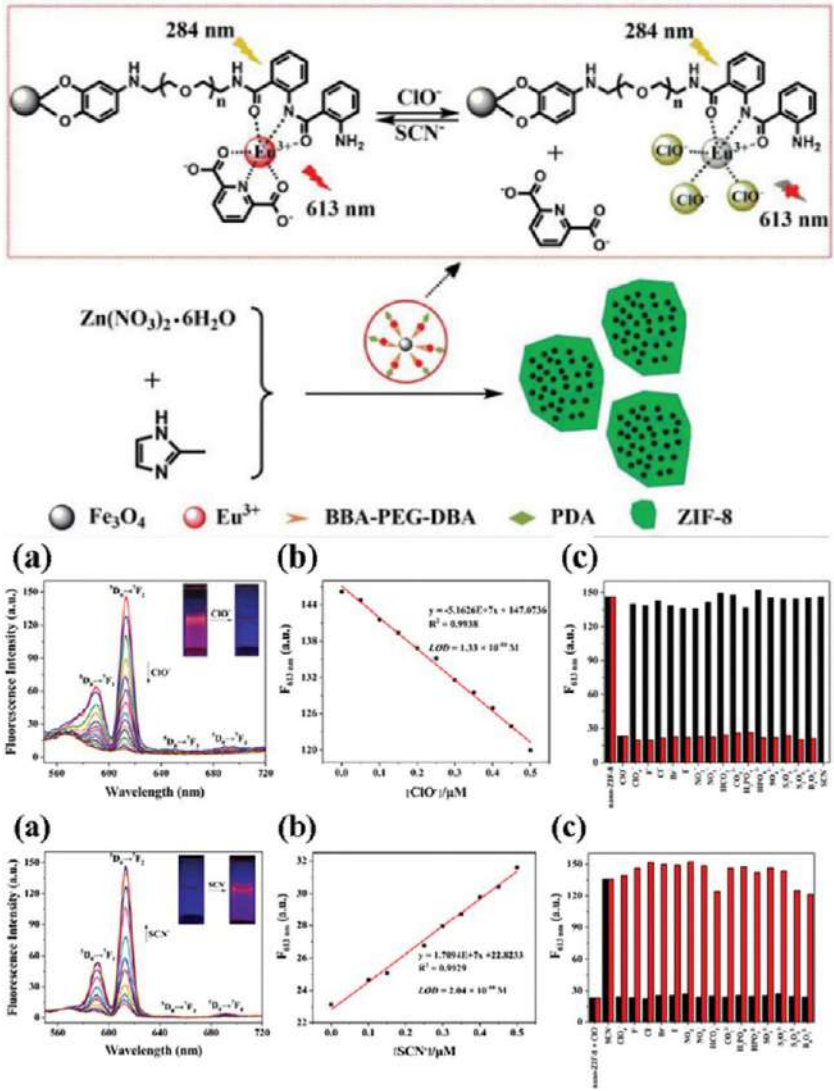

FIG. 8.6 *(Top)* Schematization for the encapsulation of Eu(III) complex-functionalized Fe_3O_4 into ZIF-8 for detecting ClO^- and SCN^-. *(Middle)* (A) Change in emission spectra of the nano-ZIF-8-ClO^- system with the incremental addition of SCN^- (5, 10, 15, 20, 25, 30, 35, 40, 45, 50, 60, 70, 80, 90, 100 μM) in ultrapure water. Inset: Fluorescent images of the nano-ZIF-8-ClO^- system solution before *(left)* and after *(right)* addition of SCN^- under a 284-nm UV lamp. (B) Determination of the LOD of the nano-ZIF-8-ClO^- system for sensing SCN^- in ultrapure water. (C) Fluorescence responses at 613 nm of the nano-ZIF-8-ClO^- system to SCN^- (1 equiv.) and other various interference anions (5 equiv.) under identical conditions. *Black bar*: Nano-ZIF-8-ClO^- + anions (250 μM), *red bar*: nano-ZIF-8-ClO^- + anions (250 μM) + SCN^- (50 μM). ($\lambda_{ex} = 284$ nm). *(Bottom)* (A) Change in emission spectra of nanocomposite nano-ZIF-8 with the incremental addition of ClO^- (5, 10, 15, 20, 25, 30, 35, 40, 45, 50, 60, 70, 80, 90, 100 μM) in ultrapure water. Inset: Fluorescent images of nano-ZIF-8 solution before *(left)* and after *(right)* addition of ClO^- under a 284-nm UV lamp. (B) Determination of the LOD of nano-ZIF-8 for sensing ClO^- in ultrapure water. (C) Fluorescence responses at 613 nm of nano-ZIF-8 to ClO^- (1 equiv.) and other various interference anions (5 equiv.) under identical conditions. *Black bar*: Nano-ZIF-8 + anions (250 μM), *red bar*: nano-ZIF-8 + anions (250 μM) + ClO^- (50 μM). ($\lambda_{ex} = 284$ nm). *(Reproduced with permission from C. Li, J. Hai, S. Li, B. Wang, Z. Yang, Luminescent magnetic nanoparticles encapsulated in MOFs for highly selective and sensitive detection of ClO^-/SCN^- and anti-counterfeiting, Nanoscale 10 (2018) 8667–8676. Copyright 2018 Royal Chemical Society.)*

(bottom), with excitation at 284 nm, the quenched fluorescence emission by ClO^- is gradually enhanced with incremental addition of SCN^-, and the value of F_{613} nm increases approximately 11.06-fold with the addition of 2.0 equiv. of SCN^-. Simultaneously, the fluorescent color of the solution changed from colorless to red under a UV lamp (inset of Fig. 8.6A; bottom). The reason for the fluorescence enhancement by SCN^- is the oxidation-reduction reaction between ClO^- and SCN^- causing the coordination of Eu^{3+} with PDA. Furthermore, the fluorescence intensity at 613 nm also shows a good linear relationship with SCN^- concentration in the range of 0–0.50 μM ($R^2 = 0.9929$) (Fig. 8.6B; bottom). The LOD of the nano-ZIF-8-ClO^- system for sensing SCN^- is calculated as 0.204 nM. Fig. 8.6C (bottom) (black bar) shows that only SCN^- results in remarkable fluorescence enhancement at 590 nm and 613 nm, indicating high selectivity of the fluorescence quenched system, nano-ZIF-8-ClO^-, toward SCN^-. As shown in the red bar of Fig. 8.6C (bottom), the values of F_{613} nm are nearly identical to those of nano-ZIF-8-ClO^--SCN^-, suggesting that other various interfering anions have negligible effects on the fluorescence response of the nano-ZIF-8-ClO^- system to SCN^-.

There is application potential for nano-ZIF-8 as a solid-state nanoprobe for sensing ClO^- and SCN^- visually. Encouraged by the aforementioned discoveries, the group further tested the usefulness of the nanocomposite, nano-ZIF-8, as a solid-state nanoprobe for sensing ClO^- and SCN^- in coated filter papers. As can be seen from Fig. 8.7, after dipping increasing amounts of ClO^-, the red fluorescence gradually diminished without interference of the background fluorescence under a 284-nm UV light (Fig. 8.7A). Additionally, with further treatment of increasing amounts of SCN^- by the same method, the nonfluorescent filter paper changed to red again with more and more obvious fluorescence, which can be easily detected by the naked eye (Fig. 8.7B). The sensing of ClO^- and SCN^- by nano-ZIF-8 is hardly affected by the presence of other anions, as their presence exhibits only negligible changes in the fluorescence of nano-ZIF-8 and nano-ZIF-8-ClO^- under a 284-nm UV light (Fig. 8.7C and D), confirming that our nanocomposite, nano-ZIF-8, can be utilized as a solid-state nanoprobe for sensing ClO^- and SCN^-.

8.3 Rare earth metal-organic framework hybrid materials for luminescence responsive chemical sensing of main group element oxysalt anions

The superoxide anion ($O_2{\cdot}^-$) is very important in medical and biological research due to its being a critical intermediate in many physiological and toxicological mechanisms of pathogens, responsible for cell signals and some diseases, including cancer, diabetes and neurodegenerative diseases. $O_2{\cdot}^-$ should be kept constant under normal conditions as it will lead to the peroxidation of body lipids and can induce cancer, progressive neurodegenerative diseases,

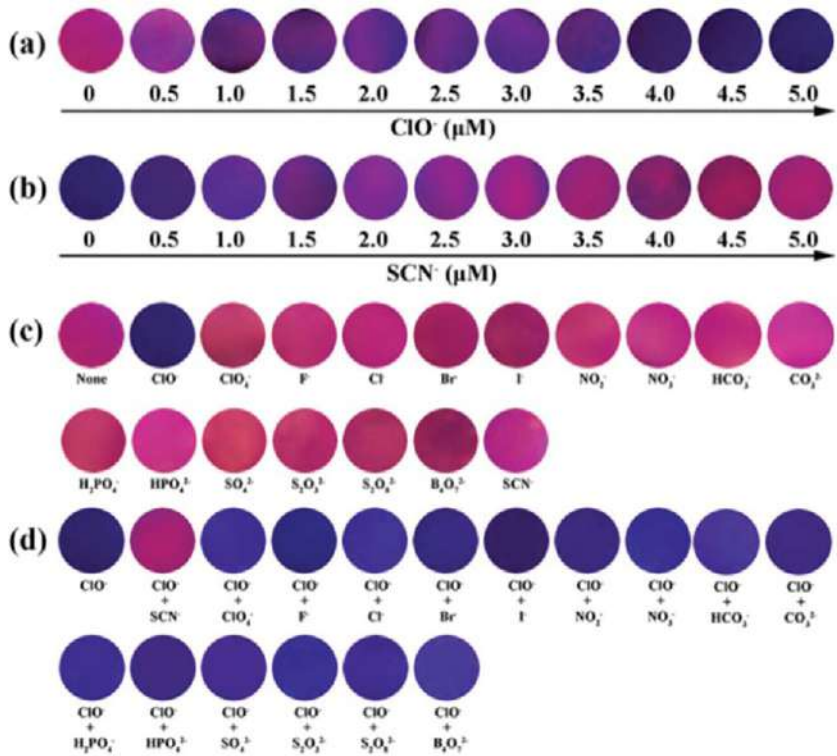

FIG. 8.7 *(Top)* (A) Photographs of filter papers containing nano-ZIF-8 in the presence of increasing amounts of ClO^- in ultrapure water under a 284-nm UV light. (B) Photographs of filter papers containing nano-ZIF-8 in the presence of increasing amounts of SCN^- in ultrapure water under a 284-nm UV light. (C) Photographs of filter papers containing nano-ZIF-8 in the presence of various anions in ultrapure water under a 284-nm UV light. (D) Photographs of filter papers containing nano-ZIF-8 and ClO^- in the presence of various anions in ultrapure water under a 284-nm UV light. *(Reproduced with permission from C. Li, J. Hai, S. Li, B. Wang, Z. Yang, Luminescent magnetic nanoparticles encapsulated in MOFs for highly selective and sensitive detection of ClO^-/SCN^- and anti-counterfeiting, Nanoscale 10 (2018) 8667–8676. Copyright 2018 Royal Chemical Society.)*

cardiovascular disease, and hepatitis as the body releases excessive $O_2\cdot^-$ [23–26]. Thus it is very important to obtain real-time analysis and detection of $O_2\cdot^-$.

Liu et al. designed a ratiometric fluorescent nanosensor for $O_2\cdot^-$ detection with gold nanoparticles (AuNPs)-bovine serum albumin (AuNPs-BSA)@terbium/guanosine monophosphate disodium (Tb/GMP) nanoscale coordination polymers (NCPs) (AuNPs-BSA@Tb/GMP NCPs). The abundant hydroxyl and amino groups of AuNPs-BSA act as binding points for the self-assembly of Tb^{3+} and GMP to form core-shell AuNPs-BSA@Tb/GMP NCP nanosensors. The obtained probe exhibited the characteristic luminescence of both AuNPs-BSA and Tb/GMP NCPs. The AuNPs-BSA not only acts as a template to

accelerate the growth of Tb/GMP NCPs, but also can be used as the reference luminescence for the detection of $O_2{\cdot}^-$. The resulting AuNPs-BSA@Tb/GMP NCP ratiometric luminescence nanosensor for the detection of $O_2{\cdot}^-$ demonstrated high sensitivity and selectivity with a wide linear response range (14 nM–10 μM) and a low LOD (4.7 nM) [27].

The hypochlorite anion (ClO^-), which is regarded as one of the most biologically significant reactive oxygen species (ROSs), originates from the peroxidation process of hydrogen peroxide (H_2O_2) and the Cl^- ion, catalyzed by the heme-containing enzyme myeloperoxidase (MPO) in activated neutrophils to defend against pathogen invasion, playing a vital role in the immune system against inflammation and microorganisms in the human body, Proper levels of ClO^- in biological systems are beneficial to humans, but ClO^- overproduction can cause damage and is associated with various health problems. Furthermore, ClO^- is extensively utilized as a household bleaching agent and tap water disinfectant; however, an excessive amount of ClO^- in tap water can also cause harm to humans [28–31]. Some research has been carried out on rare earth MOF hybrid materials for sensing ClO^- [22,32,33].

Zeng et al. adopted multivariate MOFs to introduce a second strong fluorescent center into the MOF-253 framework, where various amounts of $H_2N\text{-}BPDC^{2-}$ and $BPyDC^{2-}$ ligands are facilely integrated into multivariate MOF-253 (denoted as BPyDC@MOF-253-NH_2). The Eu^{3+} encapsulated multivariate Eu/BPyDC@MOF-253-NH_2 (Fig. 8.8; left, top) display both the high blue emission of $H_2N\text{-}BPDC^{2-}$ ligands and the red emission of Eu^{3+} cations. With the ClO^- content increasing, the blue emission of Eu/BPyDC@MOF-253-NH_2 is gradually quenched, while the red emission remains almost stable. Subsequently, a dual-emissive 5-5-Eu/BPyDC@MOF-253-NH_2 was employed as a ratiometric nanosensor for the "On-Off" sensing of ClO^-, where the blue emission acts as a detection signal and the red emission serves as a reference signal. In order to quantitatively determine hypochlorite concentration by the proposed "On-Off" sensing system, the dose-dependent fluorescence was carried out under optimal sensing conditions (Fig. 8.8; right). With an increase in hypochlorite concentration from 0.1 to 30 μM, the fluorescent intensities of the blue emission centered at 471 nm gradually decreased, while those of the red emission at 614 nm were almost unchanged (Fig. 8.8A; right). So, the blue emission at 471 nm was employed as a detection signal while the red emission at 614 nm was used as reference signal. The calibration curve based on the ratio of fluorescent intensities between the blue and red emissions (I_{471}/I_{614}) versus hypochlorite concentration was established with a correlation coefficient (R^2) of 0.9930 (Fig. 8.8B; right). The LOD for ClO^- is 0.094 μM. In that fluorescent "Turn-Off" sensing system, the energy transfer from MIL-53(Al)-NH_2 to ClO^- is realized by hydrogen bonding between amino groups and ClO^- (N—H···OCl^-) that shortens their distance and thus act as a bridge for the energy transfer. Based on this discussion, a possible quenching mechanism is proposed (Fig. 8.8; left, top). First, ClO^- is swiftly adsorbed into

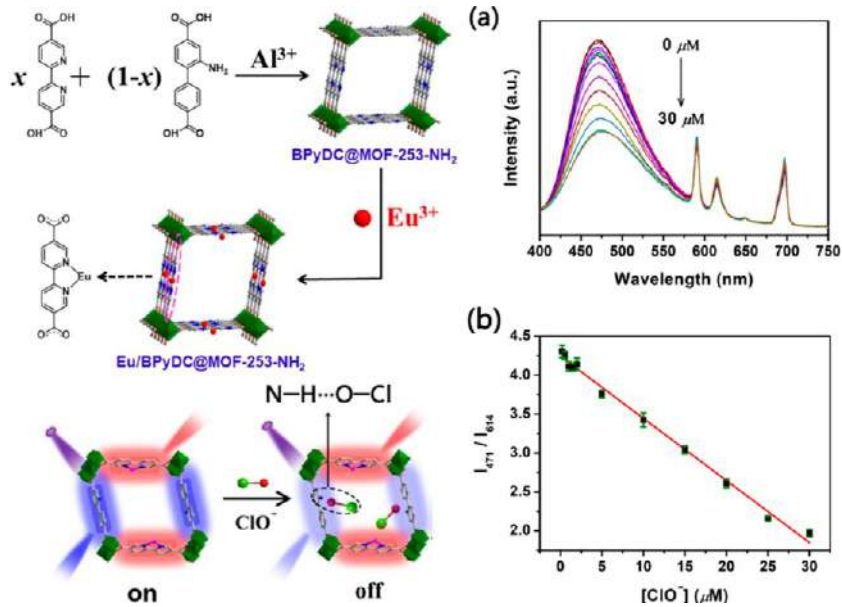

FIG. 8.8 *(Left, top)* Syntheses and structures of multivariate Eu/BPyDC@MOF-253-NH_2. *(Left, bottom)* Proposed mechanism of the fluorescent "switch." *(Right)* (A) ClO^- dose-dependent fluorescent spectra of 5-5-Eu/BPyDC@MOF-253-NH_2 suspensions under the optimal sensing conditions and (B) the calibration curve for the detection of ClO^-. *(Reproduced with permission from Y. Zeng, H. Zheng, J. Gu, G. Cao, W. Zhuang, J. Lin, R. Cao, Z. Lin, Dual-emissive metal–organic framework as a fluorescent "switch" for ratiometric sensing of hypochlorite and ascorbic acid, Inorg. Chem. 58 (2019) 13360–13369. Copyright 2019 American Chemical Society.)*

5-5-Eu/BPyDC@MOF-253-NH_2 through the large channels of the framework, and then the distance between amino groups in the H_2N-$BPDC^{2-}$ ligands and ClO^- is shortened by hydrogen bonding interactions (N—H···OCl^-). This may serve as a bridge for charge transfer between H_2N-$BPDC^{2-}$ ligands in hybrid and ClO^-, leading to the fluorescence quenching.

Since nitrite can prevent the production of *Clostridium botulinum*, a toxic microorganism, it improves the safety of meat products. In addition, nitrite combined with myoglobin can be more stable, so it is often used to improve the appearance and freshness of meat. However, some unscrupulous merchants will use high nitrite content in order to seek higher profits, which can easily lead to toxicity and cause intestinal cancer or gastric carcinoma. Thus it is of great practical significance to measure the existing content of NO_2^- in drinking water or foods [34–37]. Some research work has been reported on rare earth functionalized MOF hybrid materials for luminescent sensing of NO_2^- [38,39].

Wu et al. employed a typical In-MOF (In(OH)bpydc, H_2bpydc = biphenyl-5,5′-dicarboxylic acid) to perform as a carrier and "antenna" to encapsulate Tb^{3+}, which has proven to be suitable for the detection of NO_2^- in aqueous solution. In addition, a fast and effective sensing plate was designed to detect NO_2^-.

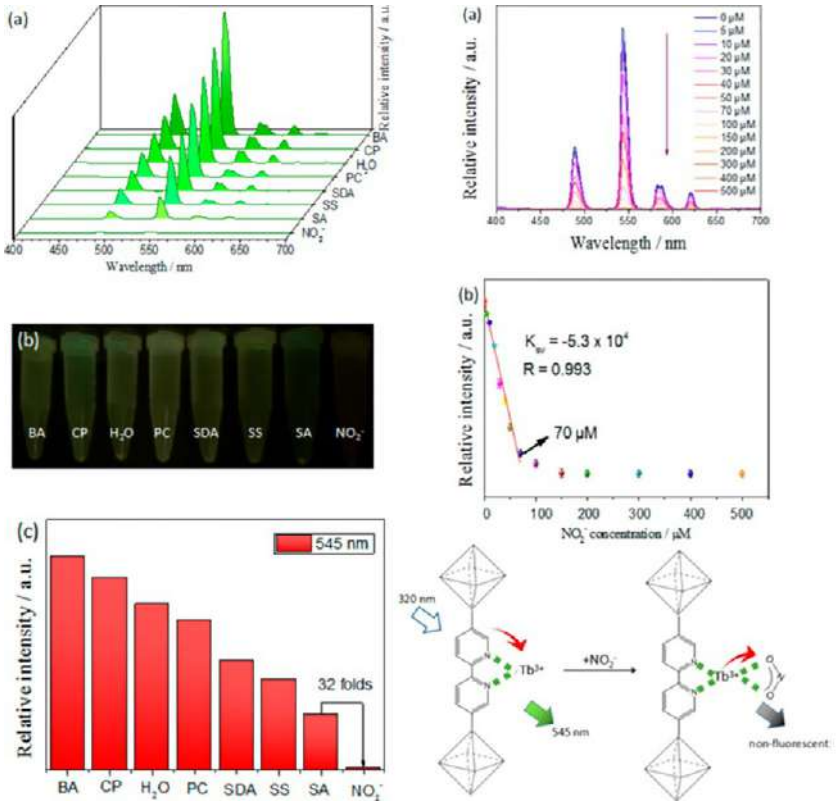

FIG. 8.9 *(Left)* (A) The luminescence intensity of the Tb^{3+}@In-MOF dispersed into different food preservative aqueous solutions (excitement monitored at 320 nm). (B) Corresponding photographs under UV-light irradiation at 320 nm. (C) Luminescence intensity at 545 nm of Tb^{3+}@In-MOF dispersed into different food preservative aqueous solutions. *(Right, top)* (A) Emission spectra and (B) K_{sv} curve of Tb^{3+}@In-MOF in aqueous solutions in the presence of various concentrations of NO_2^- under excitation at 320 nm. *(Right, bottom)* Scheme of Tb^{3+}@In-MOF coordinates with NO_2^-, leading to energy transfer and fluorescent quenching. *(Reproduced with permission from J. Wu, B. Yan, Luminescent hybrid Tb^{3+} functionalized metal–organic frameworks act as food preservative sensor and water scavenger for NO_2^-, Ind. Eng. Chem. Res. 57 (2018) 7105–7111. Copyright 2018 American Chemical Society.)*

The luminescent properties recorded and compared in Fig. 8.9A (left) indicate that only NO_2^- has the distinct quenching effect on the fluorescence and leads to a dark emission, while the luminescent emissions of others can be observed clearly. Considering Fig. 8.9B (left), the photograph suggests that only NO_2^- causes this quenching effect and leads to the dark luminescence. For clear observation and comparison, we can compare the Tb^{3+} characteristic transitions at 545 nm with each other, as shown in Fig. 8.9C (left). The relative luminescent intensity of the probe in NO_2^- aqueous solution can be virtually ignored, whereas the fluorescent intensity of the larger one (SA) is about 32 times greater than that

of NO_2^-. To better understand the luminescence quenching that is caused by NO_2^-, concentration-dependent research experiments on the luminescence properties of Tb^{3+}@In-MOF in NO_2^- solutions were carried out, as described in Fig. 8.9A (right, top). With the existence of NO_2^- ions, the intensity of Tb^{3+}@In-MOF decreases gradually with the increase of NO_2^- content from 0 to 500 μM. The peak intensity at 545 nm declines swiftly and linearly from 0 to 70 μM, followed by a gradual decrease to 150 μM; it tends to be stable eventually. This quenching effect can be rationalized quantitatively within the range of NO_2^- concentration from 0 to 70 μM and a fitting linear equation with a slope $K_{sv} = -5.3 \times 10^4$ and a linear correlation coefficient $R = 0.993$. The Tb^{3+}@In-MOF does not collapse and the structure is not damaged by NO_2^-, so the luminescent quenching effect by NO_2^- is due to the interaction of Tb^{3+} with NO_2^- to lead to energy transfer. The NO_2^- ion is an electron-rich system with electron-donating ability (a nucleophile), while the Tb^{3+} has an empty orbit. Both of them form a coordination bond easily, as shown in Fig. 8.9 (right, bottom). The existence of the Dexter energy transfer (DEE) between Tb^{3+} and NO_2^- causes NO_2^- to often serve as a luminescent quencher for Tb^{3+}.

Phosphate ions play a critical role in transduction, energy storage, and gene construction in biological systems, and are usually used as fertilizers for food production. Along with the large quantities used in modern agriculture and industry, phosphate is inevitably released into the aqueous environment. Excessive phosphate in water can cause severe environmental pollution, such as eutrophication, and can cause aquatic plants to bloom, which can deplete the dissolved oxygen level, release algal toxins into the water environment, and lead to the decay and death of vegetation and aquatic life. Thus many countries and organizations have established regulations for the use of phosphate as a convenient indicator or tracer of organic pollution in water bodies. The detection requirement of PO_4^{3-} discharge criteria in a water environment is reported to be around 0.2–10 mg P L^{-1} (6.4×10^{-6} to 3.2×10^{-4} mol L^{-1}) [40–44]. Rare earth MOF hybrid materials have been reported for luminescent sensing of phosphate-based ions [11,45–52].

Zhang et al. developed a luminescent hybrid sensor Eu@BUC-14 ([(4-Hap)$_4$(Mo_8O_{26})], 4-ap = 4-aminopyridine) for detecting PO_4^{3-} in aqueous environments [48]. The design rationale and sensing process are illustrated in Fig. 8.10 (top). After the addition of PO_4^{3-} anions, the energy transfer process from ligand to Eu^{3+} cations can be partially interrupted by the strong interaction between PO_4^{3-} anions and Eu^{3+} cations, resulting in the luminescence of Eu@BUC-14 being quickly quenched, and eventually realizing the detection process. Obvious fluorescence change is visible to the naked eye in the detection process under a UV lamp, making it more practical. Moreover, Eu@BUC-14 exhibits a positive adsorption capacity of 57.9 mg P g^{-1} toward PO_4^{3-} at room temperature. The adsorption process can lead to a quick fluorescent response in the detection process by preconcentrating PO_4^{3-}. As shown in Fig. 8.10A (bottom, left), the emission intensity at 617 nm gradually decreases

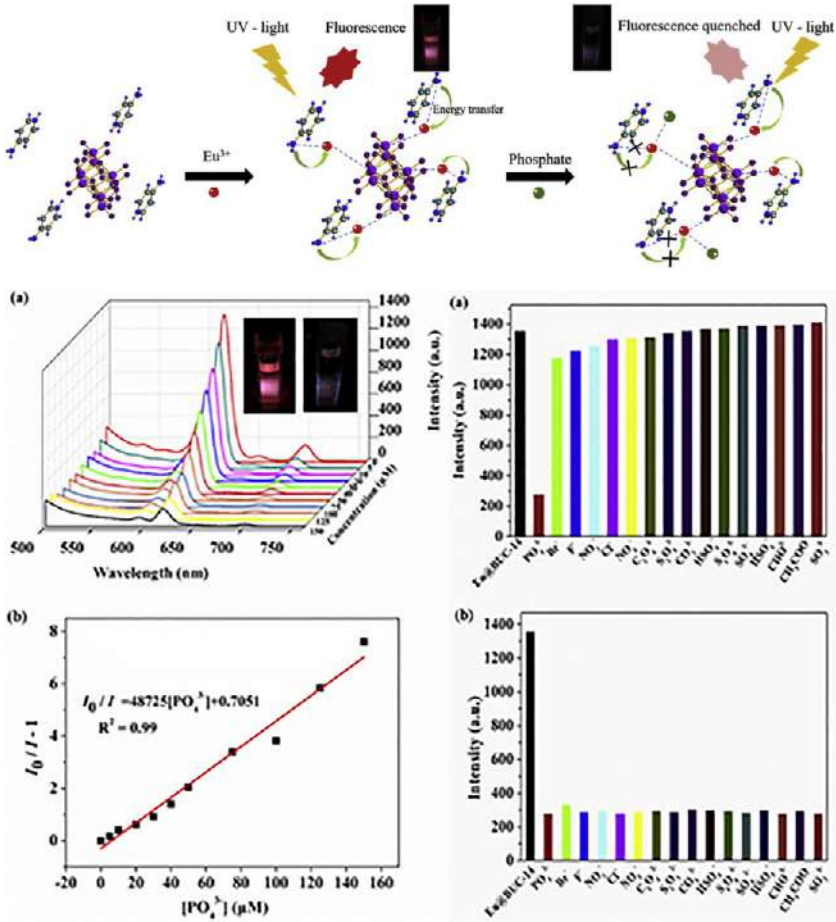

FIG. 8.10 *(Top)* A schematic illustration of synthesis of Eu@BUC-14 and the recognition process of PO_4^{3-}. *(Bottom, left)* (A) Fluorescent spectra of Eu@BUC-14 in aqueous solutions with different concentration of PO_4^{3-} under $\lambda_{ex} = 312$ nm at room temperature. The inset pictures show the color of aqueous solutions with Eu@BUC-14 under UV illumination at 312 nm without *(left)* and with PO_4^{3-} *(right)* addition, respectively; (B) the Stern-Volmer plot of Eu@BUC-14 is quenched by a PO_4^{3-} aqueous solution. *(Bottom, right)* (A) Comparison of the luminescence intensity at 617 nm of Eu@BUC-14 toward different anions (100 mM); (B) the effects of different coexistent anions (100 mM) on the luminescence intensity at 617 nm of Eu@BUC-14 after 100 mM PO_4^{3-} solution was added ($\lambda_{ex} = 312$ nm). *(Reproduced with permission from Y. Zhang, S. Sheng, S. Mao, X. Wu, Z. Li, W. Tao, I.R. Jenkinson, Highly sensitive and selective fluorescent detection of phosphate in water environment by a functionalized coordination polymer, Water Res. 163 (2019) 114883. Copyright 2019 Elsevier.)*

with the concentration of PO_4^{3-} rising from 5 to 150 mM, and the fluorescence quenching reaches nearly 90% of the PO_4^{3-} concentration of 150 mM, which can be visually represented as in Fig. 8.10A (bottom, left) (inset). Fig. 8.10B (bottom, left) shows that the quenching effect can be rationalized by S-V with a good linear correlation of the concentration in the range of 5–150 mM.

The K_{sv} value of Eu@BUC-14 for PO_4^{3-} is calculated as $4.87 \times 10^4\ M^{-1}$, demonstrating the high quenching efficiency of PO_4^{3-} on the emission of the probe and the LOD (0.88 mM) is far below the detection requirement. In Fig. 8.10A (bottom, right), PO_4^{3-} exhibits a drastic quenching effect on the luminescence emission, which demonstrates the high selectivity of Eu@BUC-14 toward PO_4^{3-}. The selectivity results demonstrate that the luminescent intensity Eu@BUC-14 in the solution with mixed anions changes very slightly compared to the solution with only PO_4^{3-} as seen in Fig. 8.10B (bottom, right) [48].

Chen et al. synthesized luminescent water-stable $\{[Tb(Cmdcp)(H_2O)_3]_2(NO_3)_2{\cdot}5H_2O\}_n$ (Tb-MOF, $H_3CmdcpBr$ = *N*-carboxymethyl-(3,5-dicarboxyl)pyridinium bromide) and used it for the recyclable sensing of PO_4^{3-} in tandem [51]. Tb-MOF acts as a fluorescent sensor for PO_4^{3-} by the luminescence "Turn-Off" mechanism, with high selectivity over other anions. Halogen ions and oxygen-containing anions show different levels of quenching effects, with PO_4^{3-} exhibiting the most significant quenching toward the luminescence intensity of Tb-MOF (Fig. 8.11A; top), whose

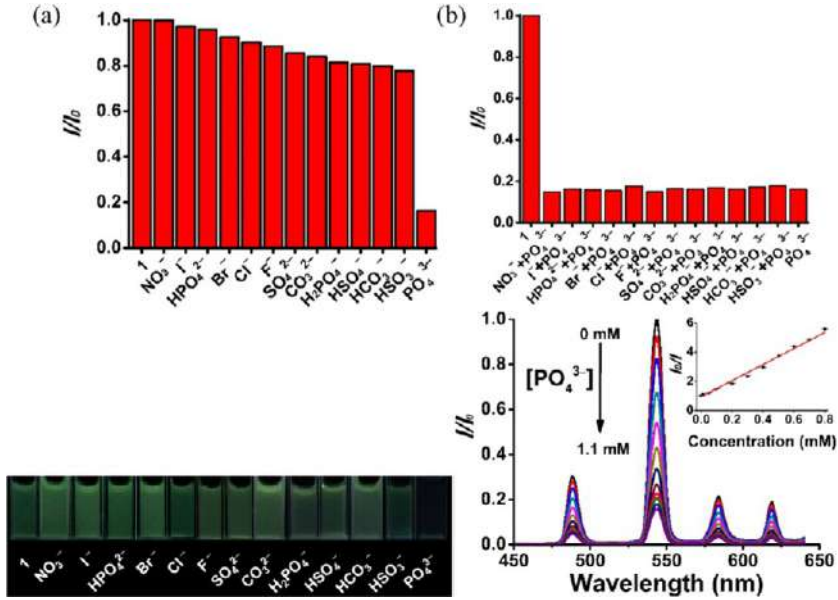

FIG. 8.11 *(Top).* (A) The luminescence intensity at 545 nm of Tb-MOF treated with 1 M different anions and 10 mM PO_4^{3-} upon excitation at 380 nm in DMF/H_2O (v:v = 1:1). (B) The luminescence intensity at 545 nm of PO_4^{3-}@Tb-MOF upon the addition of 100 times the concentration of other anions under excitation at 380 nm. *(Bottom, left)* The emission of Tb-MOF seen by the naked eye under the existence of different anions when irradiated under UV light (365 nm). *(Bottom, right)* The emission intensity changes upon increasing the PO_4^{3-} loading. Inset: Stern-Volmer plot of Tb-MOF treated with incremental PO_4^{3-} concentration (λ_{ex} = 380 nm). *(Reproduced with permission from M. Chen, K. Wu, W. Pan, N. Huang, R. Li, J. Chen, Selective and recyclable tandem sensing of PO_4^{3-} and Al^{3+} by a water-stable terbium-based metal–organic framework, Spectrochim. Acta A Mol. Biomol. Spectrosc. 247 (2021) 119084. Copyright 2021 Elsevier.)*

luminescence quenching is not interfered with by other anions (100 equiv.) (Fig. 8.11B; top). Notably, the quenching of the green emission of Tb-MOF by PO_4^{3-} can be clearly identified by the naked eye under UV light (365 nm) (Fig. 8.11; bottom, left). With the increased concentration of PO_4^{3-} from 0 to 1.1 mM, the fluorescence intensity of Tb-MOF also decreases sharply (Fig. 8.11; bottom, right). The quenching effect can be calculated quantitatively by the S-V equation and the quenching constant K_{sv} of Tb-MOF to PO_4^{3-} is 5491 M^{-1}. The LOD of 1.1 μM is inferred by the linear relationship ranging from 0 to 0.8 mM. Meanwhile, a weak coordination effect exists between PO_4^{3-} and Tb^{3+} in the structure of Tb-MOF [51].

As a polyatomic anion, carbonate salts are extensively used in the manufacture of glass, rayon, rubber, plastic, paper, printing ink, cosmetics, toothpaste, and food. Furthermore, carbonate salts have vital roles in agricultural planting, soil science, hydrology, and geology. In spite of these wide applications in various processes, the carbonate ion is toxic in large doses and has a strong caustic effect on the gastrointestinal tract, causing severe abdominal pain, vomiting, diarrhea, and even death. Therefore there is an urgent demand to develop a simple, fast, responsive chemosensor for identification of carbonate ions without interference from endogenous substrates [52–54]. Some works have been reported on rare earth MOF hybrid materials for luminescent sensing of CO_3^{2-} [55,56].

Zhan et al. utilized 4-(pyridin-3-yloxy)-phthalic acid (H_2ppda) and oxalic acid (H_2ox) as organic linkers with the Tb^{3+} ion to synthesize a luminescent MOF, namely $[Tb(ppda)(ox)_{0.5}(H_2O)_2]_n$ (Tb-MOF), which proved to be an excellent selective and sensitive fluorescent probe for sensing CO_3^{2-} ions [56]. As shown in Fig. 8.12 (top), the fluorescence intensities of the different suspension solutions of Tb-MOF were reduced to varying degrees. Uniquely, the CO_3^{2-} ion had the highest quenching influence on the intensity of Tb-MOF, implying the great potential of Tb-MOF as a probe for the CO_3^{2-} ion. The LOD is 3.76×10^{-7} M (0.38 μM) (Fig. 8.12A; bottom). In addition, the luminescence intensity obeys the equation with the K_{sv} value of 1.78×10^3 M^{-1} (as shown in Fig. 8.12B; bottom), revealing that the CO_3^{2-} ion displays a high quenching efficiency on the emission of compound Tb-MOF. The introduction of the CO_3^{2-} ion may cause energy dissipation through the collision interaction and further decrease the energy transfer from the $ppda^{2-}$ ligands to the Tb^{3+} centers, resulting in the luminescence quenching of Tb-MOF [56].

Lian et al. synthesized a rare earth functionalized hybrid material MIL-125 (Ti)-AM-Eu based on the ligand 2-aminoterephthalic acid (NH_2-H_2BDC) and $Ti(OiPr)_4$. After covalent PSM and Eu^{3+} functionalization, which displays excellent photoluminescence features and luminescence sensing properties for PO_4^{3-} and $C_2O_4^{2-}$ anions. As shown in Fig. 8.13A (top), the intensity ratio of the ligand emission to Eu^{3+} emission (I_L/I_{Eu}) is significantly influenced by anions. Compared with the primitive emission spectra of MIL-125(Ti)-AM-Eu,

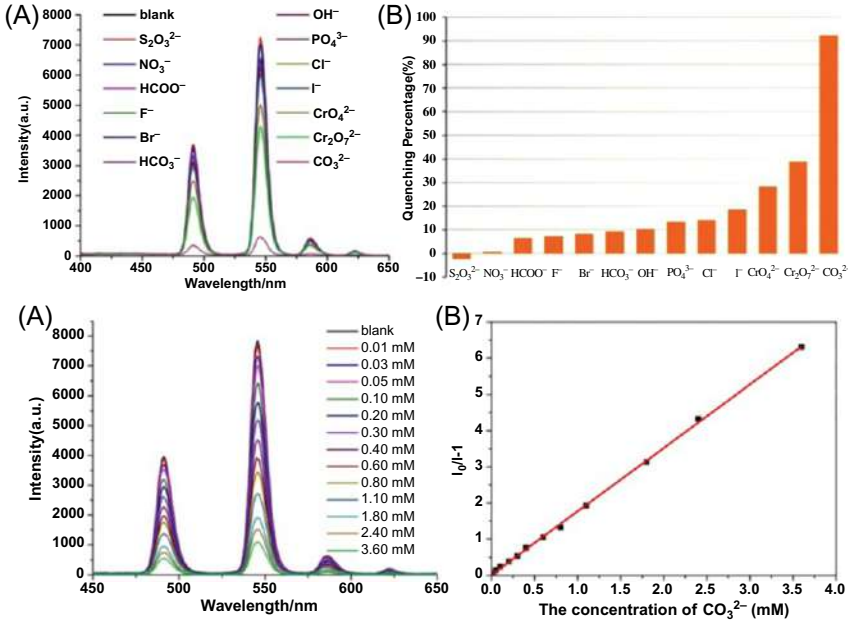

FIG. 8.12 *(Top)* (A) Luminescent spectra in the presence of different anions dispersed in aqueous solution; (B) the quenching efficiency of Tb-MOF in the presence of different anions dispersed in aqueous solution. *(Bottom)* (A) Luminescent spectra of Tb-MOF dispersed in aqueous solutions in the presence of various concentrations of CO_3^{2-} ions; (B) the linear Stern-Volmer curve in a low concentration range of CO_3^{2-} ions. *(Reproduced with permission from Z. Zhan, Y. Jia, D. Li, X. Zhang, M. Hu, A water-stable terbium-MOF sensor for the selective, sensitive, and recyclable detection of Al^{3+} and CO_3^{2-} ions, Dalton Trans. 48 (2019) 15255–15262. Copyright 2019 Royal Chemical Society.)*

the spectra of anion incorporated MIL-125(Ti)-AM-Eu exhibit different degrees of variation in the intensity ratio. The values of the intensity ratio (I_L/I_{Eu}) of different spectra are also displayed in Fig. 8.13B (top), among which the phosphate and oxalate incorporated MIL-125(Ti)-AM-Eu has the largest I_L/I_{Eu}. The interaction like the coordinate bond between the anions and Eu^{3+} affects even the blocking of the energy transfer between the MIL-125(Ti)-AM moiety and Eu^{3+} during excitation. In the primitive MIL-125(Ti)-AM-Eu, the MIL-125(Ti)-AM moiety absorbs and transfers energy to Eu^{3+} under excitation. However, the effect of the MIL-125(Ti)-AM moiety and Eu^{3+} is weakened by the addition of anions. The ratiometric luminescence responses of the MIL-125(Ti)-AM-Eu hybrid toward different anions can be exploited to differentiate these anions. As shown in Fig. 8.13B (top), there is a one-to-one correspondence between the resulting I_L/I_{Eu} and the encapsulated anions. A dual-readout orthogonal identification pattern is demonstrated in connection to both the emission intensity ratio (I_L/I_{Eu}) and the quantum yield of MIL-125 (Ti)-AM-Eu. As shown in Fig. 8.13 (bottom, left), most of these coordinates are

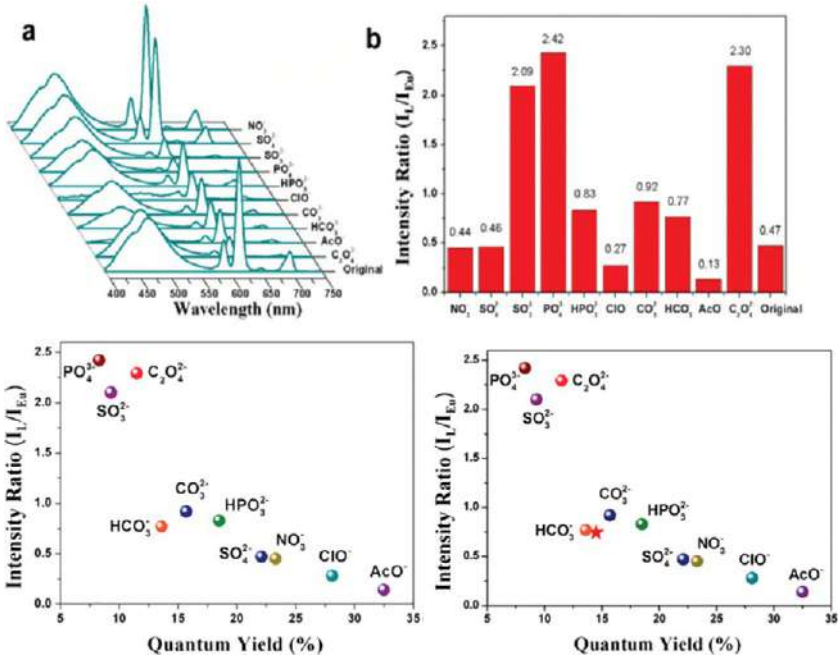

FIG. 8.13 *(Top)* The emission spectra (A) and luminescence intensity ratios (I_L/I_{Eu}) (B) of IL-125 (Ti)-AM-Euu after the encapsulation of different anions. *(Bottom, left)* The two-dimensional plan of the anions based on the emission intensity ratio (I_L/I_{Eu}) and quantum yield of MIL-125(Ti)-AM-Eu toward various anion accommodation. *(Bottom, right)* The coordinate *(red star)* of an unknown anion is close to that of the bicarbonate ion in the two-dimensional plane, suggesting that the unknown anion could be recognized as bicarbonate. *(Reproduced with permission from X. Lian, B. Yan, A postsynthetically modified MOF hybrid as a ratiometric fluorescent sensor for anion recognition and detection, Dalton Trans. 45 (2016) 18668–18675. Copyright 2016 Royal Chemical Society.)*

separated and identified in the 2D plane, suggesting that one can accurately differentiate these anions through our method. In Fig. 8.13 (bottom, right), the emission intensity ratio and quantum yield of nitrate-MIL-125(Ti)-AM-Eu and sulfate-MIL-125(Ti)-AM-Eu are close to that of the primordial one. Due to the stable structure and saturated coordination numbers, almost no interaction exists between these two kinds of anions and MIL-125(Ti)-AM-Eu [57].

8.4 Rare earth metal-organic framework hybrid materials for luminescence responsive chemical sensing of transition metal oxysalts anions

The Cr(VI) ion is an internationally recognized ingestion poison and inhalation extreme poison, and often exists in the waste of metal processing, electroplating, and the leather industry. It can invade the human body through digestion,

respiratory tract, skin, and mucous membranes. Contact of Cr(VI) ions with skin may cause a skin allergy. Inhalation may cause cancer and genetic defects [58–60]. Compared with other anions, the reports on Cr(VI) ion sensing by rare earth MOF hybrid materials are extensive [61–91].

CrO_4^{2-} is the most important form of the Cr(VI) ion and its sensing is very important in water or other recyclable resources for environmental protection and ecological security [92]. It is worth noting that rare earth MOF hybrid materials-based luminescence sensors used to detect CrO_4^{2-} have hitherto been relatively scarce [61–63]. Liu et al. presented a highly stable luminescent cationic MOF, $[Eu_7(mtb)_5(H_2O)_{16}]\cdot NO_3\cdot 8DMA\cdot 18H_2O$ (denoted as Eu-MOF, H_4mtb = 4-[tris(4-carboxyphenyl)methyl]benzoic acid), which can be used for quantitative and instant detection of CrO_4^{2-} anions over a wide concentration range (1 ppb to 300 ppm). The detection capability is highly sensitive and selective, leading to chromate sensing capability in real environmentally relevant systems with a high ionic strength, such as seawater and natural lake water. On the basis of this speculation, the solid/liquid ratio is reduced from 1.5 to 0.5 mg mL^{-1} to investigate the luminescence behavior at a relatively low concentration (less than 10 ppm) in detail, to determine the LOD (Fig. 8.14; top). The deionized water system detection was selected first with an LOD to be as low as 0.56 ppb (Fig. 8.14A; top), whose slope is obtained from the linear fit of the CrO_4^{2-} concentration-dependent luminescence intensity (monitored at 616 nm) curve in the low concentration region (Fig. 8.14B; top). As shown in Fig. 8.14A (bottom), the spectra of samples in the presence of all other anions exhibit almost identical features, whereas only the emission spectrum of the chromate ion-soaked sample exhibits a striking quenching effect on the emission intensity of Eu-MOF. These results indicate the superior selective luminescence quenching property of Eu-MOF toward CrO_4^{2-} ions over that of other anionic species. Besides these anions, the environmentally abundant cations are selected to investigate their influence on the luminescence spectra of Eu-MOF and a negligible luminescence intensity reduction was seen after the addition of these cations (Fig. 8.14B and D; bottom). The quenching constants (K_{sv}) are quantified to be as large as 3.3×10^4. The group further investigated the performance of Eu-MOF in natural water, fresh lake water, which again confirmed the real application of Eu-MOF as a sensitive and quantitative chromate sensor in natural water systems [61].

Liu et al. chose a rigid polycarboxylic acid 3,3′,5,5′-azoxybenzenetetracarboxylic acid (H_4L) as the ligand and Eu(III) to design a luminescent sensor, $\{[Eu_2(HL)_2(H_2O)_4]\cdot 3H_2O\}_n$ (Eu-MOF), for rapidly sensing CrO_4^{2-} ions from mixed anions [63]. Furthermore, the repeatability tests indicated Eu-MOF has good photostability and can be reused in the preceding two detection systems. As displayed in Fig. 8.15 (top), the luminescence is significantly quenched, when CrO_4^{2-} is introduced into the suspension of Eu-MOF-H_2O containing other anions. As shown in Fig. 8.15A (bottom) for titration experiments, upon increasing the concentration of CrO_4^{2-}, the

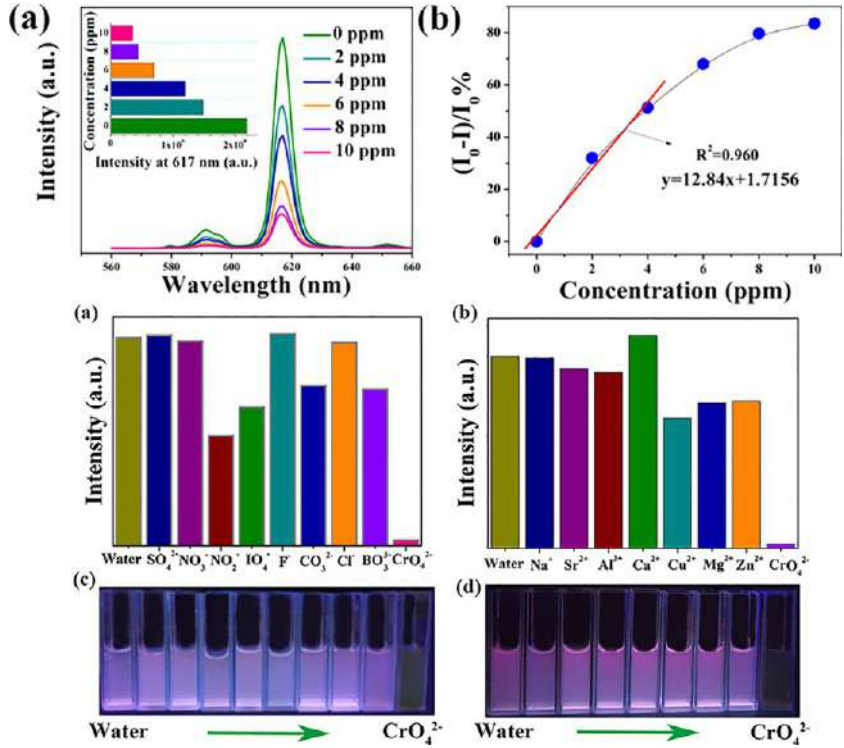

FIG. 8.14 *(Top)* (A) Luminescence spectra of Eu-MOF in chromate deionized water solution with a concentration from 0 to 10 ppm. The inset shows the emission intensity evolution of Eu-MOF at different concentrations, monitored at 616 nm. (B) Plot showing the quenching ratio of emission intensity (measured at 616 nm) of Eu-MOF as a function of the chromate concentration; the data points in the low-concentration range from 0 to 4 ppm are fitted in a linear relationship to obtain the slope. *(Bottom)* (A, B) Luminescence intensity of $^5D_0 \rightarrow {}^7F_2$ of Eu^{3+} at 616 nm of Eu-MOF dispersed in different aqueous solutions of various anions and cations. (C) Corresponding luminescence photograph of Eu-MOF immersed in different anion solutions (excited at 365 nm). (D) Corresponding luminescence photograph of Eu-MOF immersed in different cation solutions (excited at 365 nm). *(Reproduced with permission from W. Liu, Y. Wang, Z. Bai, Y. Li, Y. Wang, L. Chen, L. Xu, J. Diwu, Z. Chai, S. Wang, Hydrolytically stable luminescent cationic metal organic framework for highly sensitive and selective sensing of chromate anions in natural water systems, ACS Appl. Mater. Interfaces 9 (2017) 16448–16457. Copyright 2017 American Chemical Society.)*

luminescence of Eu-MOF is gradually quenched. In the meantime, a significant red shift (18 nm) is observed with the increase of CrO_4^{2-} concentration, which may be caused by the solvatochromism effect. The luminescence quenching efficiency can also be quantitatively illustrated with the plot showing CrO_4^{2-} ions, which is linear at low concentration (Fig. 8.15B; bottom),

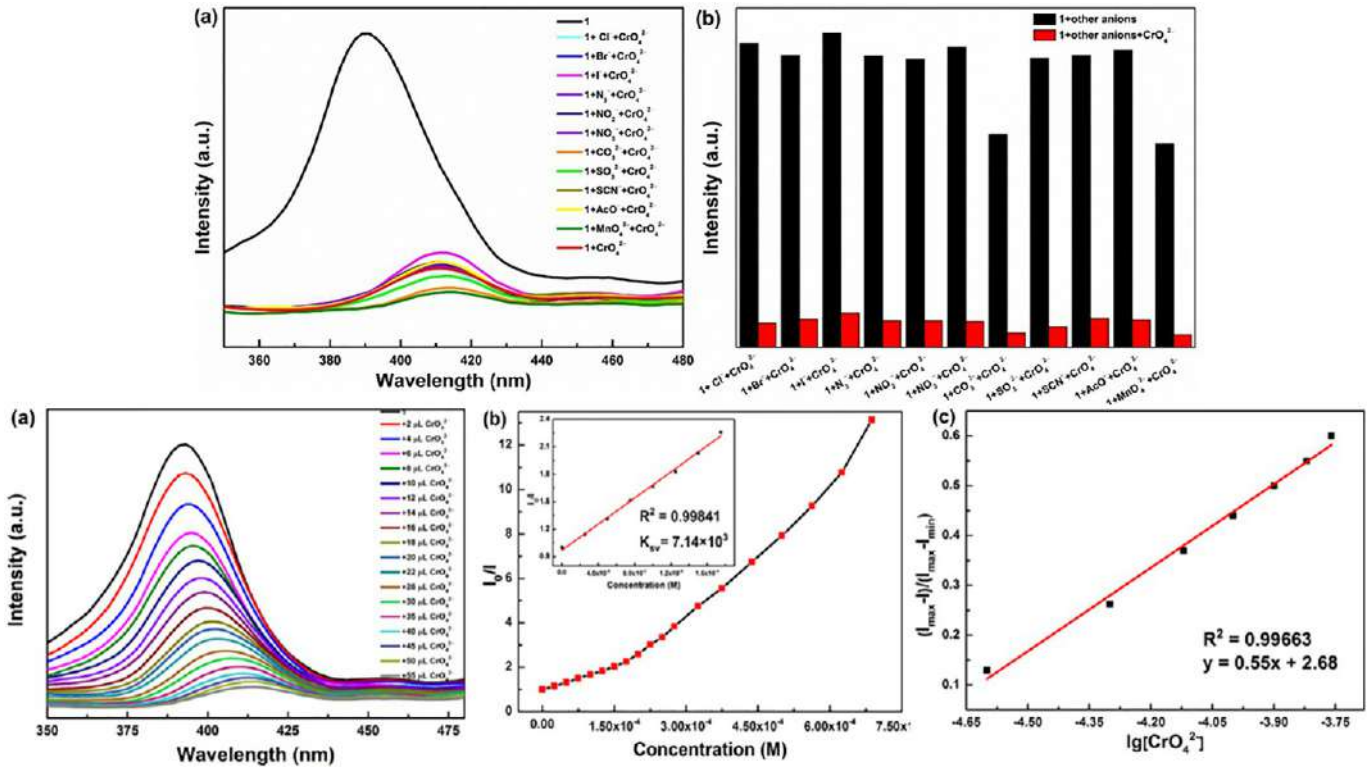

FIG. 8.15 *(Top)* (A) The luminescence intensities of Eu-MOF interacting with different anions in aqueous solution with and without CrO_4^{2-} ions. (B) The luminescence intensities of Eu-MOF upon the addition of different anions before and after CrO_4^{2-} addition. *(Bottom)* (A) The luminescence change of Eu-MOF upon incremental addition of CrO_4^{2-} ions. (B) Stern-Volmer plot for the titration experiments. (C) $(I_{max} - I)/(I_{max} - I_{min})$ vs. lg $[CrO_4^{2-}]$ plot for the titration experiments. *(Reproduced with permission from Y. Liu, X. Lv, X. Zhang, L. Liu, J. Xie, Z. Che, Eu(III)-organic complex as recyclable dual-functional luminescent sensor for simultaneous and quantitative sensing of 2,4,6-trinitrophenol and CrO_4^{2-} in aqueous solution, Spectrochim. Acta A Mol. Biomol. Spectrosc. 239 (2020) 118497. Copyright 2020 Elsevier.)*

with a K_{sv} value of $7.14 \times 10^3\ M^{-1}$. From the luminescence titration plot of $(I_{max} - I)/(I_{max} - I_{min})$ vs. $\lg[CrO_4^{2-}]$, the LOD for CrO_4^{2-} can be calculated as 1.60×10^{-5} M (Fig. 8.15C; bottom). A fluorescent resonant energy transfer (FRET) mechanism exists in the quenching process of CrO_4^{2-} to Eu-MOF. In addition, the O atoms from CrO_4^{2-} ions may interact with −OH groups from terminal water molecules in Eu-MOF through hydrogen bonding interactions in aqueous solution, resulting in an energy transfer from Eu-MOF to CrO_4^{2-} [63].

Gao et al. chose biphenyl-3′-nitro-3,4′,5-tricarboxylic acid (H_3L) as an organic linker with the Eu(III) to construct $[EuL(H_2O)_3]\cdot 3H_2O\cdot 0.75DMF$ (Eu-MOF), which displays a quenching effect on $Cr_2O_7^{2-}$ [65]. As demonstrated in Fig. 8.16 (top), only the $Cr_2O_7^{2-}$ anion gave a significant fluorescence quenching effect. As shown in Fig. 8.16 (bottom), a series of titration experiments was performed. The luminescence intensities decreased as the concentration of $Cr_2O_7^{2-}$ increased, and those of Eu-MOF were almost completely

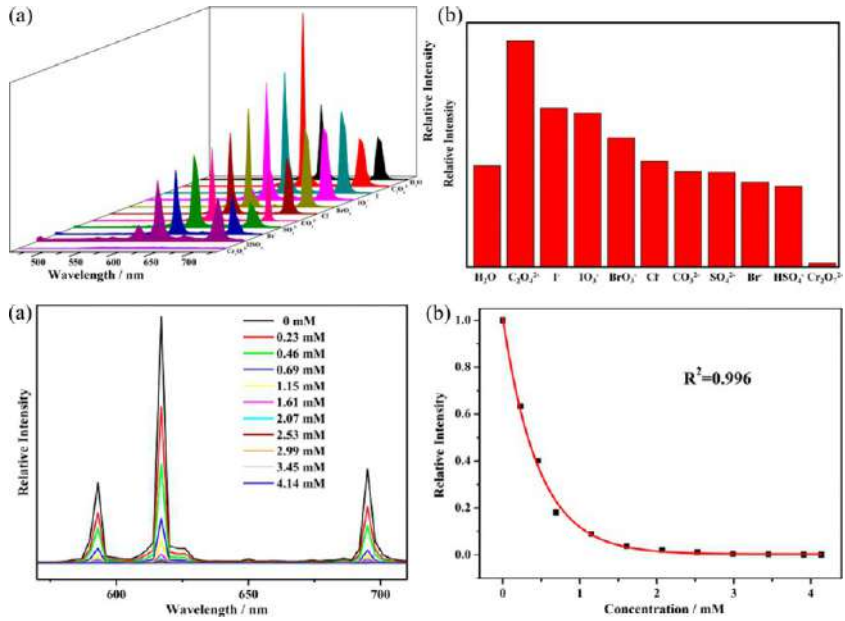

FIG. 8.16 *(Top)* (A) Luminescence spectra and (B) luminescence intensity at 614-nm intensities of Eu-MOF in various anions or pure solvents when excited at 395 nm. *(Bottom)* (A) Luminescence spectra of Eu-MOF@ $Cr_2O_7^{2-}$@H_2O suspensions with $Cr_2O_7^{2-}$ concentration varying from 0 to 4.14 mM (excited at 395 nm). (B) The plot of relative intensity vs. $Cr_2O_7^{2-}$ concentration. *(Reproduced with permission from R. Gao, F. Guo, N. Bai, Y. Wu, F. Yang, J. Liang, Z. Li, Y. Wang, Two 3D isostructural Ln(III)-MOFs: displaying the slow magnetic relaxation and luminescence properties in detection of nitrobenzene and $Cr_2O_7^{2-}$, Inorg. Chem. 55 (2016) 11323–11330. Copyright 2016 American Chemical Society.)*

quenched at a concentration of 4.14 mM. The relationship between the relative luminescence intensity and the concentration of $Cr_2O_7^{2-}$ also can be fitted as given in the following formula, with $R^2 = 0.996$. The mechanism of luminescence quenching is attributed to two aspects: one is the $Cr_2O_7^{2-}$ anions absorbed on the surface of the target complexes, and the other is the competition for the excitation energy between the $Cr_2O_7^{2-}$ anions themselves and the Eu-MOF framework due to their weak interactions [65].

Duan et al. developed a hybrid material, Y(BTC)(DMF):0.1Eu (Eu1-MOF, H_3BTC = 1,3,5-benzenetricarboxylic acid, whose immersion in aqueous solution causes its coordination with six water molecules to form a new structure ([Y(BTC)$(H_2O)_6]_2$:0.1Eu, Eu2-MOF). In an aqueous environment, Eu1-MOF acts as a luminescent probe of Cr(VI) anion species, which shows a relatively low and broad linear range. As shown in Fig. 8.17 (top), under the high anion concentration sensing procedure, the Cr(VI) anion species shows a remarkable quenching effect on europium emission. The luminescence quenching caused by $Cr_2O_7^{2-}$ along with CrO_4^{2-} is understandable due to a hydrolysis process,

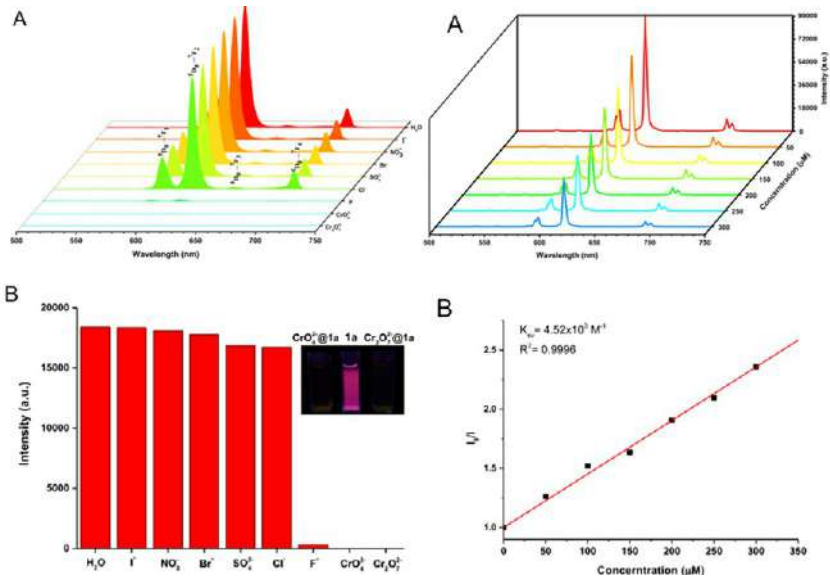

FIG. 8.17 *(Left)* (A) Suspension-state luminescent spectra and (B) intensities of $^5D_0 \rightarrow {}^7F_2$ at 616 nm for Eu1-MOF dispersed in different anions in aqueous solution when excited at 295 nm. *(Right)* (A) Emission spectra of Eu1-MOF in aqueous solutions in the presence of various concentrations of $Cr_2O_7^{2-}$ under excitation of 300 nm; (B) K_{sv} curve of Eu1-MOF in aqueous solutions in the presence of various concentrations of $Cr_2O_7^{2-}$ under excitation of 300 nm. *(Reproduced with permission from T. Duan, B. Yan, H. Weng, Europium activated yttrium hybrid microporous system for luminescent sensing toxic anion of Cr(VI) species, Microporous Mesoporous Mater. 217 (2015) 196–202. Copyright 2015 Elsevier.)*

resulting in transformation between $Cr_2O_7^{2-}$ and CrO_4^{2-}, as shown in the following: $Cr_2O_7^{2-} + H_2O = 2HCrO_4^- = 2H^+ + 2CrO_4^{2-}$. As depicted in Fig. 8.17 (right), the structure of Eu2-MOF is retained in the anions' aqueous solution except for the F^- aqueous solution. The linear correlation coefficients of $Cr_2O_7^{2-}$ and CrO_4^{2-} are 0.9996 and 0.9999, respectively, indicating that the quenching effect of Cr(VI) species on 1a fits the S-V mode well. The K_{sv} is calculated as $4.52 \times 10^3\ M^{-1}$ and $1.18 \times 10^3\ M^{-1}$, for $Cr_2O_7^{2-}$ and CrO_4^{2-}, respectively. This reveals that $Cr_2O_7^{2-}$ has a stronger quenching effect on Eu1-MOF luminescence than CrO_4^{2-}. The LODs for $Cr_2O_7^{2-}$ and CrO_4^{2-} are determined to be 0.04 mM and 0.03 mM, respectively. Eu^{3+} sites in Eu2-MOF are in interaction with the $Cr_2O_7^{2-}$ (or CrO_4^{2-}) anion, at the same time resulting in a requirement for higher energy than before, to generate a charge transfer from O to Cr(VI), whose remarkable quenching effect results from interaction of $Cr_2O_7^{2-}/CrO_4^{2-}$ with Eu^{3+} ions, which influence the efficiency of the antenna effect and lead to a decrease of luminescence signals [77].

Yu et al. constructed two RE-MOFs (Eu-MOF and Tb-MOF), $[Eu_2(HICA)(BTEC)(H_2O)_2]_n$ and $\{[Tb_2(HICA)\text{-}(BTEC)(H_2O)_2]\cdot 2.5H_2O\}_n$ (H_3ICA = 4,5-imidazoledicarboxylic acid, H_4BTEC = 1,2,4,5-benzenetetracarboxylic acid). Furthermore, the Eu-MOF and Tb-MOF can be used as excellent luminescent sensors of $CrO_4^{2-}/Cr_2O_7^{2-}$ ions in water. All the anion analytes show different degrees of the fluorescence quenching effect for Eu-MOF and Tb-MOF in water, while the CrO_4^{2-} and $Cr_2O_7^{2-}$ ions show obvious luminescence quenching effects (Fig. 8.18; top). Moreover, the high antiinterference ability toward $CrO_4^{2-}/Cr_2O_7^{2-}$ anions was preceded by competition experiments. To better understand the sensitivity of Eu-MOF and Tb-MOF toward $CrO_4^{2-}/Cr_2O_7^{2-}$ ions, the group performed quantitative luminescent titration experiments by adding different concentrations from 10 to 1000 μM of $CrO_4^{2-}/Cr_2O_7^{2-}$ ions into water. Fig. 8.18 clearly shows that the luminescent intensities of Eu-MOF and Tb-MOF decrease with the increase of $CrO_4^{2-}/Cr_2O_7^{2-}$ content. The K_{sv} for $CrO_4^{2-}/Cr_2O_7^{2-}$ ions were calculated to be about $1.915 \times 10^4\ M^{-1}$ and $1.141 \times 10^4\ M^{-1}$ for Eu-MOF and $1.14 \times 10^4\ M^{-1}$ and $8.23 \times 10^3\ M^{-1}$ for Tb-MOF. A competition exists between CrO_4^{2-} and $Cr_2O_7^{2-}$ ions and ligands of RE-MOFs for the absorption of light source energy. The analytes can effectively reduce the energy transfer from ligands to metal sites, thus inhibiting the luminescence of RE^{3+} [88].

The permanganate ion (MnO_4^-), a strong oxidizing agent, is utilized for a variety of purposes in analytical chemistry, agriculture, municipal water treatment, human health and safety, medicine, groundwater remediation, and aquaculture. Potassium permanganate is used in the fish production stage of pond aquaculture to treat a variety of fish diseases; however, potassium permanganate aqueous solution has not been authoritatively recognized as a desired aquaculture therapeutant, because it has side effects when the concentration is too high that can give rise to aquatic ecological risks; only potassium permanganate solution with low concentration has positive applications for disinfecting

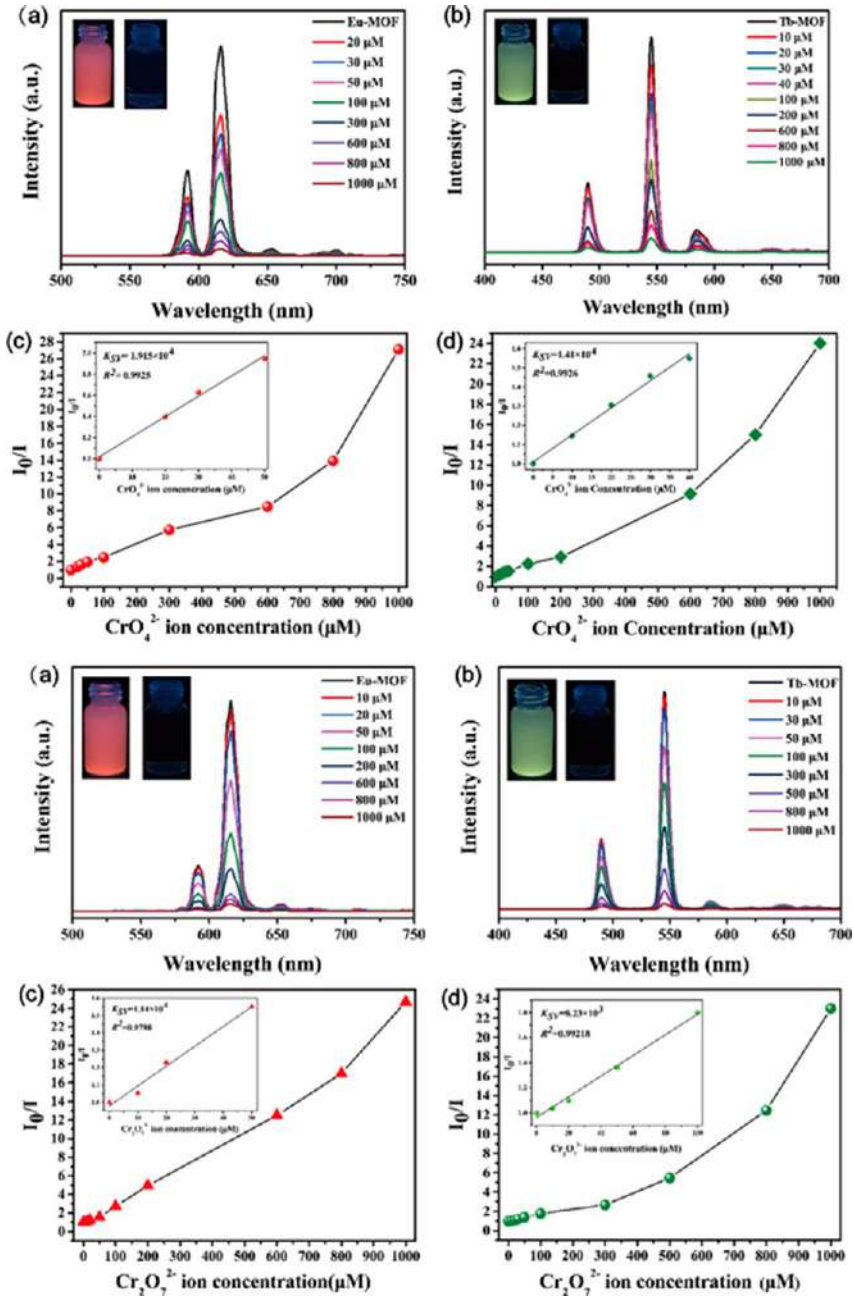

FIG. 8.18 *(Top)* Luminescent titration of Eu-MOF (A) and Tb-MOF (B) upon incremental addition of CrO_4^{2-}. S-V plots of Eu-MOF (C) and Tb-MOF (D) upon different concentrations of CrO_4^{2-} ions (inset: the linearity relationship of luminescent quenching at low concentrations). *(Bottom).* Luminescent spectra of Eu-MOF (A) and Tb-MOF (B) upon incremental addition of $Cr_2O_7^{2-}$ ions. S-V plot of Eu-MOF (C) and Tb-MOF (D) upon different concentrations of $Cr_2O_7^{2-}$ ions (inset: the linearity relationship of luminescent quenching at low concentration). *(Reproduced with permission from H. Yu, M. Fan, Q. Liu, Z. Su, X. Li, Q. Pan, X. Hu, Two highly water-stable imidazole-based Ln-MOFs for sensing Fe^{3+}, $Cr_2O_7^{2-}$/CrO_4^{2-} in a water environment, Inorg. Chem. 59 (2020) 2005–2010. Copyright 2020 American Chemical Society.)*

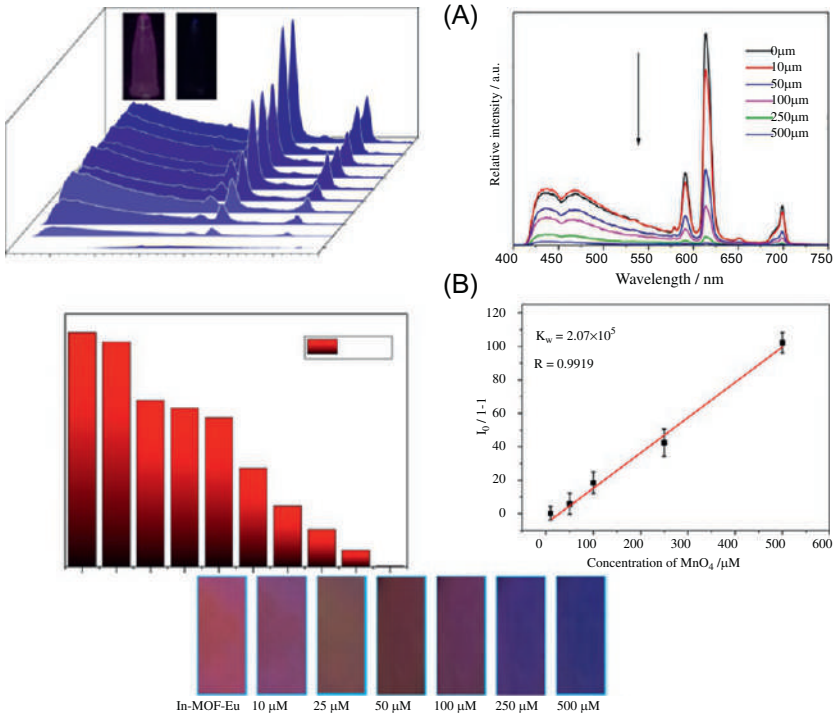

FIG. 8.19 *(Top, left)* (A) Luminescence intensity of the In-MOF-Eu dispersed into different aqueous solutions of various anions (0.5 mM) (3 mg/3 mL) (excitation monitored at 360 nm). The inset is the corresponding photographs under UV-light irradiation at 365 nm. (B) Luminescence intensity of the $^5D_0 \rightarrow {}^7F_2$ of In-MOF-Eu dispersed into different aqueous solutions of various anions (0.5 mM). *(Top, right)* (A) Emission spectra and (B) K_{sv} curve of In-MOF-Eu in aqueous solutions in the presence of various concentrations of MnO_4^- under excitation at 360 nm. *(Bottom)* Optical images of the In-MOF-Eu test paper after immersion into solution with different concentrations of MnO_4^- for 1 min. *(Reproduced with permission from J. Wu, B. Yan, Eu(III)-functionalized In-MOF (In(OH) bpydc) as fluorescent probe for highly selectively sensing organic small molecules and anions especially for $CHCl_3$ and MnO_4^-, J. Colloid Interface Sci. 504 (2017) 197–205. Copyright 2017 Elsevier.)*

[93,94]. There are some reports on rare earth MOF hybrids for sensing of MnO_4^- or both MnO_4^- and Cr(VI) oxysalts [95–106].

Wu et al. synthesized a hybrid of In-MOF, In(OH)bpydc (bpydc = biphenyl-5,5′-dicarboxylate) imparting additional luminescent Eu^{3+} ions for sensing anions, especially MnO_4^- [96]. The luminescence intensity of In-MOF-Eu dispersed into different aqueous solutions of various anions (10^{-2} M) (3 mg/3 mL) (excitement monitored at 360 nm) is presented in Fig. 8.19 (top, left); a striking phenomenon can be noted, which is that MnO_4^- has a distinct quenching effect on the luminescent emission and leads to a dark emission, but the luminescent emissions of the rest can be observed easily. It should be noted that, based on the concentration of these anions, the luminescence intensity of the In-MOF-Eu in

$Cr_2O_7^{2-}$ has decreased, but there is a clear discrimination with MnO_4^-. Also, the naked eye can distinguish their dark solutions from the bright red one of NO_3^- according to the inset of Fig. 8.19A (top, left). A histogram of Fig. 8.19B (top, left) manifests that the luminescence intensity of the $^5D_0 \rightarrow {}^7F_2$ of In-MOF-Eu dispersed into different aqueous solutions of MnO_4^- can be virtually ignored. For better understanding, fluorescence quenching concentration-dependent studies of the luminescence properties of In-MOF-Eu when MnO_4^- was present were carried out. As demonstrated in Fig. 8.19A (top, right), the emission intensity of the In-MOF-Eu suspension declined sharply with the increase of MnO_4^- concentration from 0 to 500 μM. Quantitatively, this quenching effect can be rationalized (Fig. 8.19B; top, right) with the linear correlation coefficient (R) of In-MOF-Eu with MnO_4^- of 0.9919. The K_{sv} value is 2.07×10^5 and the LOD is 1.47×10^{-4} μM. This result argues that the quenching effect is caused by the competition of MnO_4^- with the organic ligand for absorption of light energy, finally reducing the efficiency of energy transfer from the ligand to the Eu^{3+}. Optical images of Fig. 8.19 (bottom) describe that, under the irradiation of UV light of 254 nm, the fluorescent colors of the test paper change from bright red to dark red, faint red, and finally black with increase of MnO_4^-. The naked eye can distinguish the colors of the different intensities, thus making the detection simple and portable [96].

Xu et al. prepared a fluorescent heterometallic layered framework, $\{[Eu_2Na(Hpddb)(pddb)_2\ (CH_3COO)_2]\cdot 2.5(DMA)\}_n$ (Eu-MOF, 4,4′-(pyridine-2,6-diyl) dibenzoic acid = H_2pddb), whose sensing property of $Cr_2O_7^{2-}$ and MnO_4^- was also investigated [104]. As illustrated in Fig. 8.20A, typical halide anions and inorganic acid radicals only negligibly weaken the emission intensity of Eu-MOF, with the quenching efficiency varying between 0.12% and 11.37% (Fig. 8.20B). Instead, the intensity for the $^5D_0 \rightarrow {}^7D_2$ transition of Eu-MOF was severely decreased in the presence of trace contents of $Cr_2O_7^{2-}$ and MnO_4^- anions, with a quenching efficiency up to 91.2% and 70.8% (Fig. 8.20B). Fluorescence titration experiments of Eu-MOF were further undertaken by the gradual addition of concentrated $Cr_2O_7^{2-}$ and MnO_4^- solutions (1.0×10^{-2} M) into the dispersion of Eu-MOF in DMF (0.1 mg mL^{-1}). As shown in Fig. 8.20C, the emission intensity of Eu-MOF at 615 nm obviously decreased with the increase in $Cr_2O_7^{2-}$ and MnO_4^-. When the concentration of $Cr_2O_7^{2-}$ was 800 μM, the emission of Eu-MOF F was completely quenched. Good linear correlations were observed for the plots of I_0/I vs. $[Cr_2O_7^{2-}]/[MnO_4^-]$ over the concentration range from 0 to 500/800 μM (Fig. 8.20D). The linear variation in the low concentration region is mainly due to static quenching, whereas the steep curve at high concentrations is presumably due to dynamic quenching. A linear treatment of the plot affords $K_{sv} = 6.45 \times 10^3$ L mol^{-1}, $R^2 = 0.9913$ for $Cr_2O_7^{2-}$ and $K_{sv} = 2.84 \times 10^3$ L mol^{-1}, $R^2 = 0.9956$ for MnO_4^-. Additionally, the LODs of Eu-MOF for $Cr_2O_7^{2-}$ and MnO_4^- are calculated to be 5.35 μM and 5.99 μM [104].

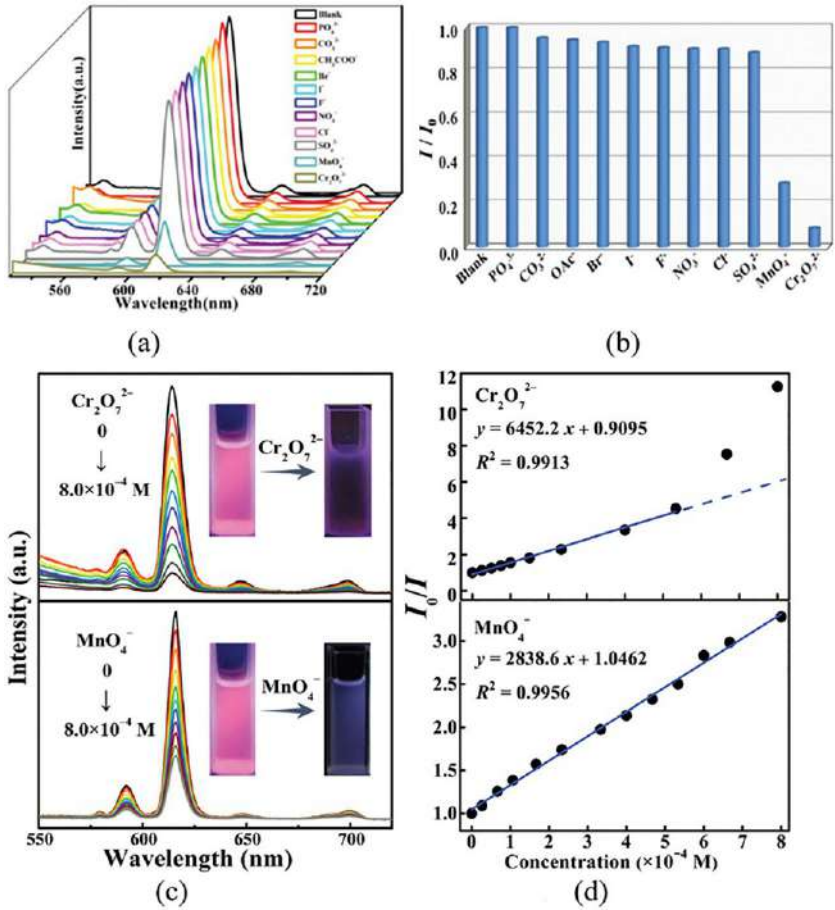

FIG. 8.20 (A) Emission spectra of Eu-MOF dispersed in DMF in the absence and presence of selected inorganic anions upon excitation at 394 nm. (B) Quenching efficiency of Eu-MOF by different inorganic anions. (C) Fluorescence titration of Eu-MOF upon incremental addition of concentrated $Cr_2O_7^{2-}$ and MnO_4^- anions (inset: optical images of Eu-MOF in the presence of $Cr_2O_7^{2-}$ and MnO_4^- anions under irradiation of 365 nm UV light). (D) Plot of I_0/I vs. $[Cr_2O_7^{2-}]/[MnO_4^-]$ (the *blue solid lines* represent the linear fit to the Stern-Volmer equation). *(Reproduced with permission from S. Xu, J. Shi, B. Ding, Z. Liu, X. Wang, X. Zhao, E. Yang, A heterometallic sodium(I)–europium(III)-organic layer exhibiting dual-responsive luminescent sensing for nitrofuran antibiotics, $Cr_2O_7^{2-}$ and MnO_4^- anions, Dalton Trans. 48 (2019) 1823–1834. Copyright 2019 Royal Chemical Society.)*

References

[1] J.J. Clarkson, J. McLoughlin, Role of fluoride in oral health promotion, Int. Dent. J. 50 (2000) 119–128.

[2] A.A. Mohammadi, M. Yousefi, M. Yaseri, M. Jalilzadeh, A.H. Mahvi, Skeletal fluorosis in relation to drinking water in rural areas of West Azerbaijan, Iran, Sci. Rep. 7 (2017) 17300.

[3] A. Rashid, D. Guan, A. Farooqi, S. Khan, S. Zahir, S. Jehan, S.A. Khattak, M.S. Khan, R. Khan, Fluoride prevalence in groundwater around a fluorite mining area in the flood plain of the River Swat, Pakistan, Sci. Total Environ. 635 (2018) 203–215.

[4] A. Rasool, A. Farooqi, T. Xiao, W. Ali, S. Noor, O. Abiola, S. Ali, W. Nasim, A review of global outlook on fluoride contamination in groundwater with prominence on the Pakistan current situation, Environ. Geochem. Health 40 (2018) 1265–1281.

[5] Q. Zhao, C. Zhang, S. Liu, Y. Liu, K.Y. Zhang, X. Zhou, J. Jiang, W. Xu, T. Yang, W. Huang, Dual-emissive polymer dots for rapid detection of fluoride in pure water and biological systems with improved reliability and accuracy, Sci. Rep. 5 (2015) 16420.

[6] J. Zhou, W. Shi, N. Xu, P. Cheng, Highly selective luminescent sensing of fluoride and organic small molecule pollutants based on novel lanthanide metal–organic frameworks, Inorg. Chem. 52 (2013) 8082–8090.

[7] Y. Wan, W. Sun, J. Liu, Z. Liu, A 3D porous luminescent terbium metal-organic framework for selective sensing of F^- in aqueous solution, Inorg. Chem. Commun. 80 (2017) 53–57.

[8] D. Wang, J. Liu, Z. Liu, A chemically stable europium metal-organic framework for bifunctional chemical sensor and recyclable on–off–on vapor response, J. Solid State Chem. 251 (2017) 243–247.

[9] Z. Yang, M. Wang, X. Wang, X. Yin, Boric-acid-functional lanthanide metal–organic frameworks for selective ratiometric fluorescence detection of fluoride ions, Anal. Chem. 89 (2017) 1930–1936.

[10] H. Zheng, X. Lian, S. Qin, B. Yan, Novel "turn-on" fluorescent probe for highly selectively sensing fluoride in aqueous solution based on Tb^{3+}-functionalized metal–organic frameworks, ACS Omega 3 (2018) 12513–12519.

[11] Q. Wang, J. Li, M. Zhang, X. Li, A luminescent Eu(III)-based metal-organic framework as a highly effective sensor for cation and anion detections, Sens. Actuators B Chem. 258 (2018) 358–364.

[12] X. Wang, C. Chu, Y. Wu, Y. Deng, J. Zhou, M. Yang, S. Zhang, D. Huo, C. Hou, Synthesis of yttrium(III)-based rare-earth metal-organic framework nanoplates and its applications for sensing of fluoride ions and pH, Sens. Actuators B Chem. 321 (2020) 128455.

[13] C.A. Wagner, Hydrogen sulfide: a new gaseous signal molecule and blood pressure regulator, J. Nephrol. 22 (2009) 173–176.

[14] J.W. Calvert, S. Jha, S. Gundewar, J.W. Elrod, A. Ramachandran, C.B. Pattillo, C.G. Kevil, D.J. Lefer, Hydrogen sulfide mediates cardioprotection through Nrf_2 signaling, Circ. Res. 105 (2009) 365–374.

[15] A. Kumar, S. Samanta, A. Singh, M. Roy, S. Singh, S. Basu, M.M. Chehimi, K. Roy, N. Ramgir, M. Navaneethan, Y. Hayakawa, A.K. Debnath, D.K. Aswal, S.K. Gupta, Fast response and high sensitivity of ZnO nanowires-cobalt phthalocyanine heterojunction based H_2S sensor, ACS Appl. Mater. Interfaces 7 (2015) 17713–17724.

[16] H. Weng, B. Yan, A Eu(III) doped metal-organic framework conjugated with fluorescein-labeled single-stranded DNA for detection of Cu(II) and sulfide, Anal. Chim. Acta 988 (2017) 89–95.

[17] X. Wang, X. Yao, Q. Huang, Y. Li, G. An, G. Li, Triple-wavelength-region luminescence sensing based on a color tunable emitting lanthanide metal organic framework, Anal. Chem. 90 (2018) 6675–6682.

[18] Y. Xu, P. Chen, T. Gao, H. Li, P. Yan, Improved luminescence properties by the self-assembly of lanthanide compounds with a 1-D chain structure for the sensing of CH_3COOH and toxic HS^- anions, CrystEngComm 21 (2019) 5965–5972.

[19] R. Ihalin, V. Loimaranta, J. Tenovuo, Origin, structure, and biological activities of peroxidases in human saliva, Arch. Biochem. Biophys. 445 (2006) 261–268.
[20] A.K. Chandra, Goitrogen in food: cyanogenic and flavonoids containing plant foods in the development of goiter, Bioact. Foods Promot. Health (2010) 691–716.
[21] Y. Zhang, P. Zhang, H. Yin, J. Cheng, Y. Kang, A EuIII-MOF with bis(2-carboxyethyl) isocyanurate for luminescence sensing of Fe^{3+} and SCN^- ions, Z. Anorg. Allg. Chem. 643 (2017) 1126–1130.
[22] C. Li, J. Hai, S. Li, B. Wang, Z. Yang, Luminescent magnetic nanoparticles encapsulated in MOFs for highly selective and sensitive detection of ClO^-/SCN^- and anti-counterfeiting, Nanoscale 10 (2018) 8667–8676.
[23] Z. Li, T. Liang, S. Lv, Q. Zhuang, Z. Liu, A rationally designed upconversion nanoprobe for in vivo detection of hydroxyl radical, J. Am. Chem. Soc. 137 (2015) 11179–11185.
[24] P. Li, W. Zhang, K. Li, X. Liu, H. Xiao, W. Zhang, B. Tang, Mitochondria-targeted reaction-based two-photon fluorescent probe for imaging of superoxide anion in live cells and in vivo, Anal. Chem. 85 (2013) 9877–9881.
[25] X. Shen, Q. Wang, Y. Liu, W. Xue, L. Ma, S. Feng, M. Wan, F. Wang, C. Mao, Manganese phosphate self-assembled nanoparticle surface and its application for superoxide anion detection, Sci. Rep. 6 (2016) 28989.
[26] Y. Dong, J. Cai, Q. Fang, X. You, Y. Chi, Dual-emission of lanthanide metal-organic frameworks encapsulating carbon-based dots for ratiometric detection of water in organic solvents, Anal. Chem. 88 (2016) 1748–1752.
[27] N. Liu, J. Hao, K. Cai, M. Zeng, Z. Huang, L. Chen, B. Peng, P. Li, L. Wang, Y. Song, Ratiometric fluorescence detection of superoxide anion based on AuNPs-BSA@Tb/GMP nanoscale coordination polymers, Luminescence 33 (2018) 119–124.
[28] N.M. Domigan, T.S. Charlton, M.W. Duncan, C.C. Winterbourn, A.J. Kettle, Chlorination of tyrosyl residues in peptides by myeloperoxidase and human neutrophils, J. Biol. Chem. 270 (1995) 16542–16548.
[29] X. Han, Z. Wang, M. Chen, X. Zhang, C. Tang, Z. Wu, Acute responses of microorganisms from membrane bioreactors in the presence of NaOCl: protective mechanisms of extracellular polymeric substances, Environ. Sci. Technol. 51 (2017) 3233–3241.
[30] M.D. Rees, C.L. Hawkins, M.J. Davies, Hypochlorite-mediated fragmentation of hyaluronan, chondroitin sulfates, and related N-acetyl glycosamines: evidence for chloramide intermediates, free radical transfer reactions, and site-specific fragmentation, J. Am. Chem. Soc. 125 (2003) 13719–13733.
[31] L.A. Ramos, K.R. Prieto, E.T.G. Cavalheiro, C.C.S. Cavalheiro, Determination of hypochlorite in bleaching products with flower extracts to demonstrate the principles of flow injection analysis, J. Chem. Educ. 82 (2005) 1815–1817.
[32] Y. Zeng, H. Zheng, J. Gu, G. Cao, W. Zhuang, J. Lin, R. Cao, Z. Lin, Dual-emissive metal–organic framework as a fluorescent "switch" for ratiometric sensing of hypochlorite and ascorbic acid, Inorg. Chem. 58 (2019) 13360–13369.
[33] Y. Zeng, H. Zheng, X. He, G. Cao, B. Wang, K. Wu, Z. Lin, Dual-emissive metal–organic framework: a novel turn-on and ratiometric fluorescent sensor for highly efficient and specific detection of hypochlorite, Dalton Trans. 49 (2020) 9680–9687.
[34] C.G. Kevil, D.J. Lefer, Review focus on inorganic nitrite and nitrate in cardiovascular health and disease, Cardiovasc. Res. 89 (2011) 489–491.
[35] Y.M. Ko, J.H. Park, K.S. Yoon, Nitrite formation from vegetable sources and its use as a preservative in cooked sausage, J. Sci. Food Agric. 97 (2017) 1774–1783.

[36] Y. Sun, A. Li, X. Zhang, F. Ma, Regulation of dissolved oxygen from accumulated nitrite during the heterotrophic nitrification and aerobic denitrification of *Pseudomonas stutzeri* T_{13}, Appl. Microbiol. Biotechnol. 99 (2015) 3243–3248.

[37] Q. Liu, X. Yan, J. Guo, D. Wang, L. Li, F. Yan, L. Chen, Spectrofluorimetric determination of trace nitrite with a novel fluorescent probe, Spectrochim. Acta A Mol. Biomol. Spectrosc. 73 (2009) 789–793.

[38] J. Wu, B. Yan, Luminescent hybrid Tb^{3+} functionalized metal–organic frameworks act as food preservative sensor and water scavenger for NO_2^-, Ind. Eng. Chem. Res. 57 (2018) 7105–7111.

[39] S. Zhu, L. Zhao, B. Yan, A novel spectroscopic probe for detecting food preservative NO_2^-: citric acid functionalized metal-organic framework and luminescence sensing, Microchem. J. 155 (2020) 104768.

[40] D.F. Caffrey, T. Gunnlaugsson, Displacement assay detection by a dimeric lanthanide luminescent ternary Tb(III)ecyclen complex: high selectivity for phosphate and nitrate anions, Dalton Trans. 43 (2014) 17964–17970.

[41] S. Banerjee, M. Bhuyan, B. Konig, Tb(III) functionalized vesicles for phosphate sensing: membrane fluidity controls the sensitivity, Chem. Commun. 49 (2013) 5681–5683.

[42] B. Lin, J. Xu, K. Lin, M. Li, M. Lu, Low-cost automatic sensor for in situ colorimetric detection of phosphate and nitrite in agricultural water, ACS Sens. 3 (2018) 2541–2549.

[43] W. Cheng, J. Sue, W. Chen, J. Chang, J. Zen, Activated nickel platform for electrochemical sensing of phosphate, Anal. Chem. 82 (2010) 1157–1161.

[44] J. Yang, Y. Dai, X. Zhu, Z. Wang, Y. Li, Q. Zhuang, J. Shi, J. Gu, Metal–organic frameworks with inherent recognition sites for selective phosphate sensing through their coordination-induced fluorescence enhancement effect, J. Mater. Chem. 3 (2015) 7445–7452.

[45] H. Xu, Y. Xiao, X. Rao, Z. Dou, W. Li, Y. Cui, Z. Wang, G. Qian, A metal–organic framework for selectively sensing of PO_4^{3-} anion in aqueous solution, J. Alloys Compd. 509 (2011) 2552–2554.

[46] Y. Cheng, H. Zhang, B. Yang, J. Wu, Y. Wang, B. Ding, J. Huo, Y. Li, Highly efficient fluorescence sensing of phosphate by dual-emissive lanthanide MOFs, Dalton Trans. 47 (2018) 12273–12283.

[47] Z. Zhan, X. Liang, X. Zhang, Y. Jia, M. Hu, A water-stable europium-MOF as a multifunctional luminescent sensor for some trivalent metal ions (Fe^{3+}, Cr^{3+}, Al^{3+}), PO_4^{3-} ions, and nitroaromatic explosives, Dalton Trans. 48 (2019) 1786–1794.

[48] Y. Zhang, S. Sheng, S. Mao, X. Wu, Z. Li, W. Tao, I.R. Jenkinson, Highly sensitive and selective fluorescent detection of phosphate in water environment by a functionalized coordination polymer, Water Res. 163 (2019) 114883.

[49] Z. Li, Z. Zhan, M. Hu, A luminescent terbium coordination polymer as a multifunctional water-stable sensor for detection of Pb^{2+} ions, PO_4^{3-} ions, $Cr_2O_7^{2-}$ ions, and some amino acids, CrystEngComm 22 (2020) 6727–6737.

[50] D. Shi, X. Yang, Y. Ma, M. Niu, R.A. Jones, Construction of 14-metal lanthanide nanorings with NIR luminescence response to ions, Chem. Commun. 56 (2020) 8651–8654.

[51] M. Chen, K. Wu, W. Pan, N. Huang, R. Li, J. Chen, Selective and recyclable tandem sensing of PO_4^{3-} and Al^{3+} by a water-stable terbium-based metal–organic framework, Spectrochim. Acta A Mol. Biomol. Spectrosc. 247 (2021) 119084.

[52] N. Abramova, S. Levichev, A. Bratov, The influence of CO_2 on ISFETs with polymer membranes and characterization of a carbonate ion sensor, Talanta 81 (2010) 1750–1754.

[53] S. Tavakoli-Kivi, R.T. Bailey, T.K. Gates, A salinity reactive transport and equilibrium chemistry model for regional-scale agricultural groundwater systems, J. Hydrol. 572 (2019) 274–293.
[54] C.M. Phillips-Lander, S.R. Parnell, L.E. McGraw, M.E.E. Madden, Carbonate dissolution rates in high salinity brines: implications for post-Noachian chemical weathering on mars, Icarus 307 (2018) 281–293.
[55] N. Sun, B. Yan, Rapid and facile ratiometric detection of CO_3^{2-} based on heterobimetallic metal-organic frameworks (Eu/Pt-MOFs), Dyes Pigm. 142 (2017) 1–7.
[56] Z. Zhan, Y. Jia, D. Li, X. Zhang, M. Hu, A water-stable terbium-MOF sensor for the selective, sensitive, and recyclable detection of Al^{3+} and CO_3^{2-} ions, Dalton Trans. 48 (2019) 15255–15262.
[57] X. Lian, B. Yan, A postsynthetically modified MOF hybrid as a ratiometric fluorescent sensor for anion recognition and detection, Dalton Trans. 45 (2016) 18668–18675.
[58] C.M. Thompson, C.R. Kirman, D.M. Proctor, L.C. Haws, M. Suh, S.M. Hays, J.G. Hixon, M. A. Harris, A chronic oral reference dose for hexavalent chromium-induced intestinal cancer, J. Appl. Toxicol. 34 (2014) 525–536.
[59] E.A. Katayev, Y.A. Ustynyuk, J.L. Sessler, Receptors for tetrahedral oxyanions, Coord. Chem. Rev. 250 (2006) 3004–3037.
[60] A. Zhitkovich, Importance of chromium–DNA adducts in mutagenicity and toxicity of chromium(VI), Chem. Res. Toxicol. 18 (2005) 3–11.
[61] W. Liu, Y. Wang, Z. Bai, Y. Li, Y. Wang, L. Chen, L. Xu, J. Diwu, Z. Chai, S. Wang, Hydrolytically stable luminescent cationic metal organic framework for highly sensitive and selective sensing of chromate anions in natural water systems, ACS Appl. Mater. Interfaces 9 (2017) 16448–16457.
[62] L. Gao, J. Zhang, L. Zhai, X. Wang, L. Fan, T. Hu, Gas adsorption and fluorescent sensing properties of two porous lanthanide metal–organic frameworks based on 3,5-bis(2-carboxyphenoxy)-benzoic acid, Polyhedron 165 (2019) 171–176.
[63] Y. Liu, X. Lv, X. Zhang, L. Liu, J. Xie, Z. Che, Eu(III)-organic complex as recyclable dual-functional luminescent sensor for simultaneous and quantitative sensing of 2,4,6-trinitrophenol and CrO_4^{2-} in aqueous solution, Spectrochim. Acta A Mol. Biomol. Spectrosc. 239 (2020) 118497.
[64] X. Shen, B. Yan, Photoactive rare earth complexes for fluorescence tuning and sensing cations (Fe^{3+}) and anions ($Cr_2O_7^{2-}$), RSC Adv. 5 (2015) 6752–6757.
[65] R. Gao, F. Guo, N. Bai, Y. Wu, F. Yang, J. Liang, Z. Li, Y. Wang, Two 3D isostructural Ln (III)-MOFs: displaying the slow magnetic relaxation and luminescence properties in detection of nitrobenzene and $Cr_2O_7^{2-}$, Inorg. Chem. 55 (2016) 11323–11330.
[66] H. Weng, B. Yan, A flexible Tb(III) functionalized cadmium metal organic framework as fluorescent probe for highly selectively sensing ions and organic small molecules, Sens. Actuators B 228 (2016) 702–708.
[67] J. Liu, G. Li, W. Liu, Q. Li, B. Li, R.W. Gable, L. Hou, S.R. Batten, Two unusual nanocage-based Ln-MOFs with triazole sites: highly fluorescent sensing for Fe^{3+} and $Cr_2O_7^{2-}$, and selective CO_2 capture, ChemPlusChem 81 (2016) 1299–1304.
[68] L. Liu, X. Qiu, Y. Wang, Q. Shi, Y. Sun, Y. Chen, NIR emission and luminescent sensing of a lanthanide–organic framework with Lewis basic imidazole and pyridyl sites, Dalton Trans. 46 (2017) 12106–12113.
[69] H. He, S. Chen, D. Zhang, R. Hao, C. Zhang, E. Yang, X. Zhao, A micrometer-sized europium(III)–organic framework for selective sensing of the $Cr_2O_7^{2-}$ anion and picric acid in water systems, Dalton Trans. 46 (2017) 13502–13509.

[70] C. Yang, J. Zheng, W. Cai, F. Guo, Y. Wang, Two isostructural Ln-MOFs showing luminescent sensing (Eu) and slow magnetic relaxation (Dy) properties, Dalton Trans. 47 (2018) 15656–15660.

[71] Y. Tao, P. Zhang, J. Liu, X. Chen, X. Guo, H. Jin, J. Chai, L. Wang, Y. Fan, Multi-responsive luminescent sensor based on three-dimensional lanthanide metal–organic framework, New J. Chem. 42 (2018) 19485–19493.

[72] X. Guo, P. Wang, J. Xu, L. Shen, Y.T. Sun, X. Chen, S. Jing, L. Wang, Y. Fan, A 2D zinc coordination polymer constructed from long and flexible N-containing tricarboxylate ligand for encapsulating Ln^{3+} ions and luminescent sensing, Inorg. Chim. Acta 479 (2018) 213–220.

[73] X. Shi, X. Qu, J. Chai, C. Tong, Y. Fan, L. Wang, Stable coordination polymers with linear dependence color tuning and luminescent properties for detection of metal ions and explosives, Dyes Pigm. 170 (2019) 107583.

[74] X. Hou, C. Yan, X. Xu, A. Liang, Z. Song, S. Tang, Two-dimensional layered lanthanide diphosphonates: synthesis, structures and sensing properties toward Fe^{3+} and $Cr_2O_7^{2-}$, Dalton Trans. 49 (2020) 3809–3815.

[75] L. Duan, C. Zhang, P. Cen, X. Jin, C. Liang, J. Yang, X. Liu, Stable Ln-MOFs as multi-responsive photoluminescence sensors for the sensitive sensing of Fe^{3+}, $Cr_2O_7^{2-}$, and nitrofuran, CrystEngComm 22 (2020) 1695–1704.

[76] Y. Wang, Y. Yu, J. Lu, Y. Li, S. Wang, D. Li, J. Dou, A 2D lanthanum coordination polymer as a multiresponsive luminescent chemosensor with fast response and high sensitivity, J. Solid State Chem. 283 (2020) 121173.

[77] T. Duan, B. Yan, H. Weng, Europium activated yttrium hybrid microporous system for luminescent sensing toxic anion of Cr(VI) species, Microporous Mesoporous Mater. 217 (2015) 196–202.

[78] X. Zhang, Z. Zhan, X. Liang, C. Chen, X. Liu, Y. Jia, M. Hu, Lanthanide-MOFs constructed from mixed dicarboxylate ligands as selective multi-responsive luminescent sensors, Dalton Trans. 47 (2018) 3272–3282.

[79] Y. Liu, J. Ma, C. Xu, Y. Yang, M. Xia, H. Jiang, W. Liu, A water-stable lanthanide coordination polymer as a multiresponsive luminescent sensor for Fe^{3+}, Cr(VI) and 4-nitrophenol, Dalton Trans. 47 (2018) 13543–13549.

[80] X. Wang, J. Li, C. Jiang, P. Hu, B. Li, T. Zhang, H. Zhou, An efficient strategy for improving the luminescent sensing performance of a terbium(III) metal–organic framework towards multiple substances, Chem. Commun. 54 (2018) 13271–13274.

[81] J. Zou, L. Li, S. You, Y. Liu, H. Cui, J. Cui, S. Zhang, Two luminescent lanthanide(III) metal–organic frameworks as chemosensors for high-efficiency recognition of Cr(VI) anions in aqueous solution, Dalton Trans. 47 (2018) 15694–15702.

[82] J. Li, R. Lia, X. Li, Construction of metal–organic frameworks (MOFs) and highly luminescent Eu(III)-MOF for the detection of inorganic ions and antibiotics in aqueous medium, CrystEngComm 20 (2018) 4962–4972.

[83] C. Chen, X. Zhang, P. Gao, M. Hu, A water stable europium coordination polymer as fluorescent sensor for detecting Fe^{3+}, CrO_4^{2-}, and $Cr_2O_7^{2-}$ ions, J. Solid State Chem. 258 (2018) 86–92.

[84] X. Li, J. Tang, H. Liu, K. Gao, X. Meng, J. Wu, H. Hou, A highly sensitive and recyclable Ln-MOF luminescent sensor for the efficient detection of Fe^{3+} and CrVI anion, Chem. Asian J. 14 (2019) 3721–3727.

[85] Q. Liu, S. Zhang, J. Yang, K. Yue, A water-stable La-MOF with high fluorescence sensing and supercapacitive performances, Analyst 144 (2019) 4534–4544.

[86] D. Sheng, F. Sun, Y. Yu, Y. Wang, J. Lu, Y. Li, S. Wang, J. Dou, D. Li, 1-D multifunctional Ln-CPs: luminescence probes for Fe^{3+} and Cr(VI) and uncommon discriminative detection between $Cr_2O_7^{2-}$ and CrO_4^{2-} of Tb-CP in various media, JOL 213 (2019) 140–150.

[87] Z. Li, W. Cai, X. Yang, A. Zhou, Y. Zhu, H. Wang, X. Zhou, K. Xiong, Q. Zhang, Y. Gai, Cationic metal–organic frameworks based on linear zwitterionic ligands for $Cr_2O_7^{2-}$ and ammonia sensing, Cryst. Growth Des. 20 (2020) 3466–3473.

[88] H. Yu, M. Fan, Q. Liu, Z. Su, X. Li, Q. Pan, X. Hu, Two highly water-stable imidazole-based Ln-MOFs for sensing Fe^{3+}, $Cr_2O_7^{2-}$/CrO_4^{2-} in a water environment, Inorg. Chem. 59 (2020) 2005–2010.

[89] W. Gao, A. Zhou, H. Wei, C. Wang, J. Liu, X. Zhang, Water-stable LnIII-based coordination polymers displaying slow magnetic relaxation and luminescence sensing properties, New J. Chem. 44 (2020) 6747–6759.

[90] D. Liu, G. Dong, X. Wang, F. Nie, X. Li, A luminescent Eu coordination polymer with near visible excitation for sensing and its homologues constructed from 1,4-benzenedicarboxylate and 1H-imidazo[4,5-f][1,10]-phenanthroline, CrystEngComm 22 (2020) 7877–7887.

[91] H. Guo, N. Wu, R. Xue, H. Liu, M. Wang, W. Yao, X. Wang, W. Yang, An Eu(III)-functionalized Sr-based metal-organic framework for fluorometric determination of Cr(III) and Cr(VI) ions, Microchim. Acta 187 (2020) 374.

[92] L. Wen, X. Zheng, K. Lv, C. Wang, X. Xu, Two amino-decorated metal-organic frameworks for highly selective and quantitatively sensing of Hg-II and Cr-VI in aqueous solution, Inorg. Chem. 54 (2015) 7133–7135.

[93] C.C. Willhite, V.S. Bhat, G.L. Ball, C.J. McLellan, Emergency do not consume/do not use concentrations for potassium permanganate in drinking water, Hum. Exp. Toxicol. 32 (2013) 275–298.

[94] A.V. Desai, B. Manna, A. Karmakar, A. Sahu, K.A. Ghosh, A water-stable cationic metal-organic framework as a dual adsorbent of oxoanion pollutants, Angew. Chem. Int. Ed. 55 (2016) 7811–7815.

[95] B. Ding, S. Liu, Y. Cheng, C. Guo, X. Wu, J. Guo, Y. Liu, Y. Li, Heterometallic alkaline earth–lanthanide baII–LaIII microporous metal–organic framework as bifunctional luminescent probes of Al^{3+} and MnO_4^-, Inorg. Chem. 55 (2016) 4391–4402.

[96] J. Wu, B. Yan, Eu(III)-functionalized In-MOF (In(OH)bpydc) as fluorescent probe for highly selectively sensing organic small molecules and anions especially for $CHCl_3$ and MnO_4^-, J. Colloid Interface Sci. 504 (2017) 197–205.

[97] J. Shi, P. Xu, X. Wang, B. Ding, X. Zhao, E. Yang, A dual-responsive luminescent terbium(III) chain for selective sensing of Fe^{3+} and MnO_4^- ions, Z. Anorg. Allg. Chem. 644 (2018) 1598–1606.

[98] J. Wei, J. Yi, M. Han, B. Li, S. Liu, Y. Wu, L. Ma, D. Li, A water-stable terbium(III)–organic framework as a chemosensor for inorganic ions, nitro-containing compounds and antibiotics in aqueous solutions, Chem. Asian J. 14 (2019) 3694–3701.

[99] Z. Dong, F. Zhao, L. Zhang, Z. Liu, Y. Wang, Two novel lanthanide metal–organic frameworks: selective luminescent sensing for nitrobenzene, Cu^{2+}, and MnO_4^-, Cryst. Growth Des. 20 (2020) 5225–5234.

[100] Z. Sun, J. Sun, L. Xi, J. Xie, X. Wang, Y. Ma, L. Li, A white-light-emitting lanthanide metal–organic framework for luminescence turn-off sensing of MnO_4^- and turn-on sensing of folic acid and construction of a "turn-on plus" system, New J. Chem. 44 (2020) 10239–10249.

[101] J. Zhao, P. Liu, Z. Dong, Z. Liu, Y. Wang, Eu(III)-organic framework as a multi-photoluminescence sensor for efficient detection of 1-naphthol, Fe^{3+} and MnO_4^- in water, Inorg. Chim. Acta 511 (2020) 119843.

[102] X. Shia, Y. Fan, J. Xu, H. Qi, J. Chai, J. Sun, H. Jin, X. Chen, P. Zhang, L. Wang, Layer-structured lanthanide coordination polymers constructed from 3,5-bis (3,5-dicarboxylphenyl)-pyridine ligand as fluorescent probe for nitroaromatics and metal ions, Inorg. Chim. Acta 483 (2018) 473–479.

[103] J. Jin, G. Yang, Y. Liu, S. Cheng, J. Liu, D. Wu, Y. Wang, Two series of microporous lanthanide–organic frameworks with different secondary building units and exposed Lewis base active sites: sensing, dye adsorption, and magnetic properties, Inorg. Chem. 58 (2019) 339–348.

[104] S. Xu, J. Shi, B. Ding, Z. Liu, X. Wang, X. Zhao, E. Yang, A heterometallic sodium(I)–europium(III)-organic layer exhibiting dual-responsive luminescent sensing for nitrofuran antibiotics, $Cr_2O_7^{2-}$ and MnO_4^- anions, Dalton Trans. 48 (2019) 1823–1834.

[105] J. Ma, W. Liu, Effective luminescence sensing of Fe^{3+}, $Cr_2O_7^{2-}$, MnO_4^- and 4-nitrophenol by lanthanide metal–organic frameworks with a new topology type, Dalton Trans. 48 (2019) 12287–12295.

[106] T. Sun, P. Wang, R. Fan, W. Chen, S. Hao, Y. Yang, Functional microscale single phase white emission lanthanide MOF for tunable fluorescent sensing and water quality monitoring, J. Mater. Chem. C 7 (2019) 3598–3606.

Part IV

Rare earth metal-organic frameworks hybrid materials as luminescence response chemical sensors for typical molecular analytes

Chapter 9

Rare earth metal-organic framework hybrid materials for luminescence responsive chemical sensing of general molecules

Compared to the ion analytes, molecule species are very abundant and complicated, involving both inorganic and organic molecules. The most common molecules are the organic chemicals and pollutants, which are of increasing concern due to environmental biological hazards. Many of the organic chemicals are volatile organic solvents (especially organic amines and benzenes). They are utilized in practical laboratories for both scientific research and industrial production. However, precise sensing of these molecules based on a luminescence response is very difficult. Nowadays the research mainly focuses on some limited organic solvent molecules, such as acetone, pyridine, tetrahydrofuran, trichloromethane, organic amine, and organic aromatics. Both volatile organic solvents and their vapors can be detected in solution and the gas state. Among these, atmospheric benzene homologues (BTEX) are noted for their extensive use. For volatile organic compounds (VOCs) with similar composition and structure or properties, a dual-readout identification scheme can be established. The inorganic and organic pollutants have been studied extensively for their importance in environmental fields. Among these, the inorganic pollutants such as amine gas and organic pollutants like formaldehyde are commonly studied due to their representation in public or confined spaces. In addition, some important organic molecules, including biomolecules, antibiotics/drugs, and nitroaromatics explosives are discussed separately in Chapter 10. The special organic and polymeric chemicals used in industrial applications are also worth noting, as they are important for the health of workers. However, the direct detection of these chemical products cannot reflect their actual harmfulness exactly, and so the trend is to detect their metabolites. This will be discussed in Chapter 11, which covers biomarkers.

Rare Earth Metal-Organic Framework Hybrid Materials for Luminescence Responsive Chemical Sensors
https://doi.org/10.1016/B978-0-323-91236-5.00013-X

9.1 Rare earth metal-organic framework hybrid materials for luminescence responsive chemical sensing of inorganic molecules

The sensing of molecular oxygen (O_2) is of great practical significance in many fields, including metallurgy, the chemical industry, environmental monitoring, and life sciences. Optical techniques have become more and more attractive due to their features of noninvasive operation, rapid response, full reversibility, extremely low detection limits, inertness to strong electric or magnetic fields, and ability to enable remote and microarea oxygen monitoring in special situations [1–4]. In fact, nowadays, nearly half of the electrochemical O_2 probe market has been superseded by optical sensors. O_2 has been known as a strong dynamic quencher of luminescence and O_2 molecular quenching of RE-MOFs supposedly results from the deactivation of triplet state organic ligands by the triplet state of O_2 ($^3O_2$), which then disrupts the antenna effect. But this process has little interaction with the singlet state of organic ligands, whose emission can be retained. Therefore the luminescent response process can be easily realized through rare earth MOF hybrid systems. To date, some reports have concentrated on rare earth MOF hybrid material probes for luminescence responsive chemical sensing of molecular O_2 [5–10].

Weng et al. chose Bio-MOF-1 as a host material to prepare its Tb^{3+} hybrid material via a cation exchange method and then investigated the optical properties of Tb^{3+}@Bio-MOF-1 towards O_2. Sm^{3+}@TiO_2 was assembled with Tb^{3+}@Bio-MOF-1 and subsequently the oxygen-sensing properties of the hybrid were explored after spreading the complex on ethanol. This showed that the luminescent intensity of Tb^{3+} decreased with increasing O_2 content while the luminescent intensity of Sm^{3+} was enhanced, suggesting that this method can be used as a promising ratio-dependent O_2 sensing material. As is shown in Fig. 9.1 (left, top), the emission spectra of Tb^{3+}@Bio-MOF-1 with varying concentration of O_2 (0%, 10%, 21%, 40%, 100%) were recorded ranging from 360 to 700 nm when excited at 327 nm. The emission of Tb^{3+}@Bio-MOF-1 with its maximum at 545 nm was easily quenched by O_2. The LOD of the obtained materials was estimated at 0.49%. The mechanism of luminescent quenching due to Tb^{3+} ions towards O_2 has been shown in Fig. 9.1 (left, bottom): due to the energy transfer (EnT) between ligand and RE^{3+} ions, which is also known as the antenna effect, the characteristic luminescence of RE^{3+} ions can be obtained. However, O_2 contact with these MOFs can cause the deactivation of triplet state organic ligands and further affect the ligand-to-metal energy transfer (LMET). Meanwhile, an appropriate thermally activated energy back transfer (BEnT) also exists, to prolong the triplet-state lifetime of ligands, resulting in a decrease in RE^{3+} ion emissions. Fig. 9.1 (right, top) shows that the luminescent intensity of Sm^{3+}@TiO_2 increases with varying concentration of O_2 (0%, 21%, 40%, 60%, 80%, 100%) ranging from 395 to 750 nm when excited at 359 nm; the emission at 613 nm is enhanced by O_2. The LOD is calculated as 1.78%. The mechanism is further represented in Fig. 9.1 (right,

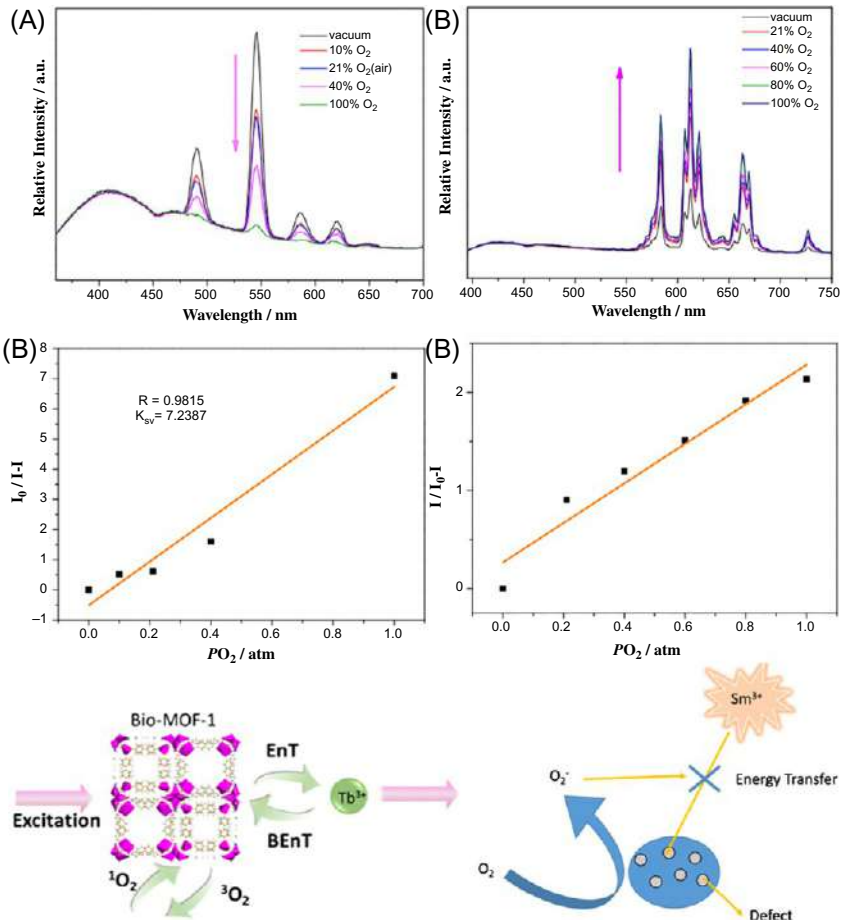

FIG. 9.1 *(Left, Top)* (A) Emission spectra and (B) K_{sv} curve of Tb^{3+}@Bio-MOF-1 with varying concentration of O_2 under the excitation of 327 nm. The luminescent intensity in a pure N_2 environment is denoted as I_0 while the luminescent intensity in different concentrations of O_2 is denoted as I. *(Left, Bottom)* Schematic representation of the energy transfer processes and O_2 quenching processes in Tb^{3+}@Bio-MOF-1. EnT: energy transfer from the ligand to the metal ion; BEnT: energy back transfer. *(Right, Top)* (A) Emission spectra and (B) luminescent intensity curve of Sm^{3+}@TiO_2 in varying concentrations of O_2 under the excitation of 359 nm. Examining the intensity data at 613 nm, the luminescent intensity in a pure nitrogen environment is denoted as I_0 while the luminescent intensity in different concentration of O_2 is denoted as I. *(Right, Bottom)* Schematic representation of mechanism for the luminescent enhancement of Sm^{3+}@TiO_2 towards O_2. *(Reproduced with permission from H. Weng, X. Xu, B. Yan, Novel multicomponent photofunctional nanohybrids for ratio-dependent oxygen sensing. J. Colloid Interface Sci. 502 (2017) 8–15. Copyright 2017 Elsevier.)*

bottom). There are defects in the TiO_2 samples that can act as energy acceptors for Sm^{3+}. When O_2 is present, they are adsorbed on the surface of TiO_2 and electrons are withdrawn from the inner region of TiO_2, especially the defects forming the energy acceptor. As a result, the energy transfer is hindered. On

the contrary, when O_2 is desorbed from the surface, the electrons released by surface O_2 are captured by the inner defects of TiO_2, which can serve as the energy acceptors for Sm^{3+} once again. That means the energy transfer between acceptor defects and Sm^{3+} is influenced by O_2 [8].

Xia et al. chose 1,4-naphthalenedicarboxylic acid (1,4-H_2NDC) with a suitable high triplet level to construct a Eu-MOF for the O_2 sensors. Then, they fabricated the MOF-integrated optical fiber sensing device by immobilizing Eu-MOF and silica fiber into PDMS film for portable, on-site, and real-time O_2 detection [10]. As shown in Fig. 9.2A (top), the obtained PDMS film⊃Eu-MOF is mechanically robust, flexible, and resilient to mechanical stress and can be easily handled. After the deaeration, the free-standing film was highly transparent with a BET surface area of 6.05 m^2g^{-1} (Fig. 9.2B; top), indicating that it was free of cracks and macroscopic defects, which is important for the transmission of fluorescent signals in O_2 sensing. When exposed to a portable ultraviolet lamp, the PDMS film⊃EuNDC emitted the

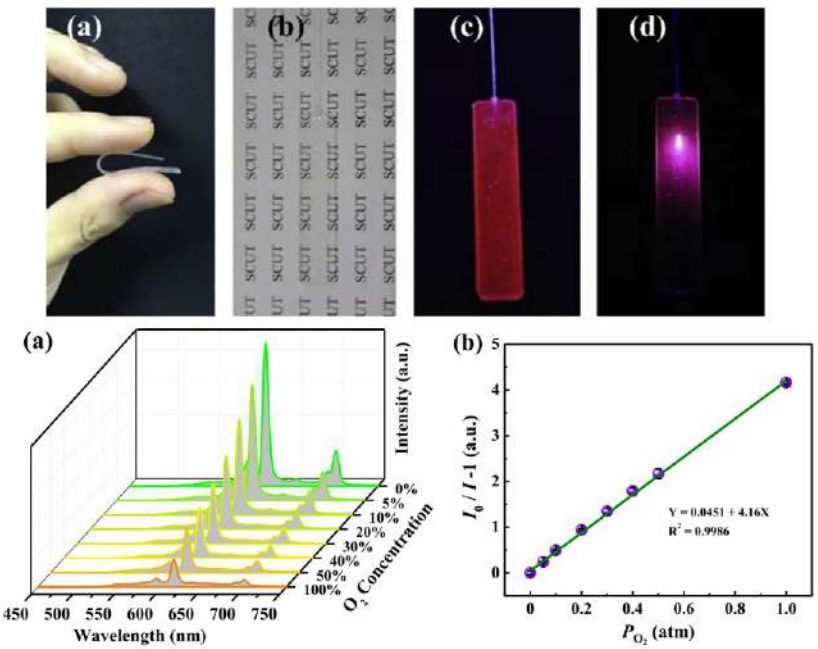

FIG. 9.2 *(Top)* (A, B) Photographs demonstrating the good elasticity and transparency of PDMS film⊃Eu-MOF. (C, D) Fluorescent images of PDMS film⊃Eu-MOF lluminated with portable ultraviolet lamp and 365 nm fiber-coupled LED light source, respectively. *(Bottom)* (A) The PL emission spectra of Eu-MOF integrated optical fiber sensor at various concentrations of O_2 in N_2 and (B) the corresponding linear regression fitting results of the Stern-Volmer plots. *(Reproduced with permission from T. Xia, L. Jiang, J. Zhang, Y. Wan, Y. Yang, J. Gan, Y. Cui, Z. Yang, G. Qian, A fluorometric metal-organic framework oxygen sensor: from sensitive powder to portable optical fiber device. Microporous Mesoporous Mater. 305 (2020) 110396. Copyright 2020 Elsevier.)*

bright and homogeneous characteristic red light of Eu^{3+} ions (Fig. 9.1C; top). When a 365-nm LED light source was introduced into the PDMS film⊃EuNDC through integrated silica fiber, cone-shaped visible photoluminescence could be found at the edge of the fiber end (Fig. 9.2D; top). They further combined it with an LED light source, filters, and luminescent spectrometer into a detection device, and used it for remote O_2 detection. As shown in Fig. 9.2A (bottom), the optical fiber sensor maintains the characteristic emissions of Eu^{3+} ions. The luminescence emission intensity gradually decreases with the increase of oxygen partial pressure. The characteristic emission intensities of $^5D_0 \rightarrow {}^7F_2$ transition are extracted out separately and plotted in Fig. 9.2B (bottom), which quenches up to 80.6% at pure O_2. There is a good linear relationship of I_0/I vs. P_{O2} with $K_{sv} = 4.16$ and $I_0/I_{100} = 5.17$, revealing an outstanding O_2 sensory device, with the theoretical O_2 sensing resolution of optical fiber sensor could be better than 50 ppm [10].

Many organic reactions need to occur under anhydrous conditions, and even trace amounts of water greatly impede the yield and impose restrictions on the reaction rate, and can even be dangerous. Similarly, the detection of water vapor or relative humidity in the environment is also very important for the storage of grain and wood products, preservation of chemical agents, and moisture-proofing of fireworks [11–13]. There are some reports on rare earth MOF hybrid materials for luminescence sensing of trace water [14–25].

Wu et al. established a colorimetric sensor based on a Tb^{3+}-functionalized In-MOF of 2,2′-bipyridine-5,5-dicarboxylic acid and *p*-CDs (carbon dots), *p*-CDs/In-MOF and Tb^{3+}@*p*-CDs/In-MOF. As shown in Fig. 9.3 (left), as the water content in ethanol increased gradually, the red emission peak of *p*-CDs decreased significantly. Simultaneously, the characteristic emission peak of the green Tb^{3+} decreased gradually. A very distinct color gradient can be observed with an increase in water content in ethanol (Fig. 9.3B; left). Further study of the optical spectra was performed under excitation of 360-nm UV light; Fig. 9.3 (left) demonstrates the intensity ratio of the two emission wavelengths (I_{545}/I_{605}) against water content with a good linear correlation ($R^2 = 0.96$). The LOD is estimated to be 0.28% from the linear relationship in Fig. 9.3C (left). The mechanism of the luminescence response of Tb^{3+} @*p*-CDs/In-MOF towards water in organic solvents is illustrated in Fig. 9.3 (right, top). When *p*-CDs is stronger than that of Tb^{3+} and eventually shows a red luminescent color for Tb^{3+}@*p*-CDs/In-MOF dispersed in aqueous solution, due to the agglomeration effect, red light is quenched and only green light is shown. The decrease in the characteristic emission intensity of Tb^{3+} is because of the O-H oscillations in water molecules towards the luminescence of Tb^{3+}. Furthermore, to examine the humidity-sensing properties of Tb^{3+} @*p*-CDs/In-MOF, test plates were first prepared, whose luminescence intensity of 605 nm gradually decreased as the RH increased from 33.0% to 85.1% (Fig. 9.3A; right, bottom). These ratios of I_{545}/I_{605} were 0.65, 0.71, 0.76, and 0.84, respectively, showing a good linear relationship of I_{545}/I_{605} vs. RH in

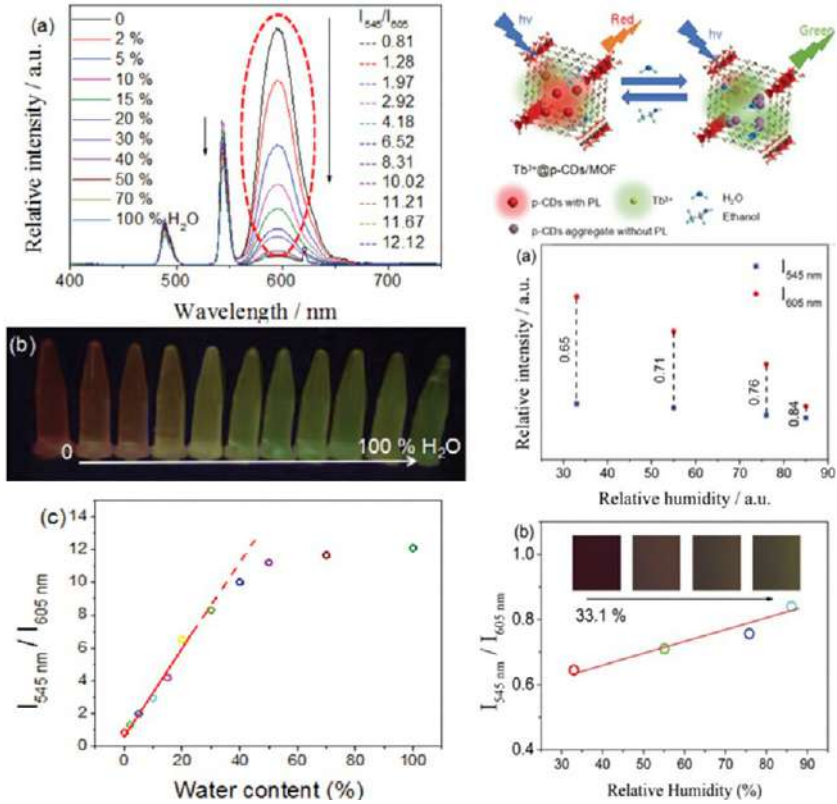

FIG. 9.3 *(Left)* (A) Luminescent spectra ($\lambda_{ex} = 360$ nm) of Tb^{3+}@*p*-CDs/MOF in ethanol upon addition of different amounts of water and ratios of I_{545}/I_{605}. (B) Visual PL photographs of Tb^{3+}@*p*-CDs/MOF dispersed in ethanol with various water content under UV light at 365 nm. (C) Linear relationship of I_{545}/I_{605} vs. water content in ethanol. *(Right, Top)* Mechanism of the PL response of Tb^{3+}@*p*-CDs/MOF towards water in organic solvents. *(Right, Bottom)* (A) Changes in the corresponding values of I_{545} and I_{605} and ratio of I_{545}/I_{605}. (B) Linear relationship of I_{545}/I_{605} vs. RH. Insets are RH photographs. *(Reproduced with permission from J. Wu, Bing Yan, A dual-emission probe to detect moisture and water in organic solvents based on green-Tb3+ post-coordinated metal-organic frameworks with red carbon dots. Dalton Trans. 46 (2017) 7098–7105. Copyright 2017 Royal Chemical Society.)*

ethanol ($R^2 = 0.91$) (Fig. 9.3B; right, bottom). The inset of Fig. 9.3B (right, bottom) shows the test plates under irradiation by UV visible light at 365 nm, resulting in different colors of light that can be identified and distinguished by the naked eye [18].

Wehner et al. reported on a yellow-emitting composite material as a ratiometric water detector by utilization of two luminescent MOFs as the shell, combined with Fe_3O_4/SiO_2 microparticles as the core, which added

superparamagnetism to the hybrid material's ratiometric sensing, combined with signal augmentation upon magnetic harvesting. Both luminescence centers, Tb^{3+} and Eu^{3+}, showed a rather similar course in luminescence decay. This resulted in a blue shift of the resulting chromaticity for higher H_2O concentrations (Fig. 9.4; top). Fig. 9.4B (top) compares the luminescence decreases for the $^5D_4 \rightarrow {}^7F_5$ transition of Tb^{3+} and for the $^5D_0 \rightarrow {}^7F_4$ transition of Eu^{3+} and illustrates a similar decrease rate for both RE^{3+} with increasing H_2O content. A low LOD can be calculated with 0.03% (20 mg) water content. For ratiometric sensing applications, the hybrids Eu-BDC, Tb-bipy@Fe_3O_4/SiO_2 were constructed. Both luminescence bands of Eu^{3+} and Tb^{3+} showed a decreasing intensity with increasing water content. The increase of water concentration showed the same trend, e.g., 3% H_2O resulted in a luminescence decrease of the $^5D_4 \rightarrow {}^7F_5$ transition of Tb^{3+} to 1.8% of its original intensity, while the $^5D_0 \rightarrow {}^7F_4$ intensity of Eu^{3+} was reduced to 11.1% of the original intensity (Fig. 9.4B; middle). Thus, the ratio of the intensity of the Eu^{3+} and the Tb^{3+} transitions differed, thereby indicating different and increasing water content. This results in a red shift of the chromaticity that is also visible with the naked eye (Fig. 9.4; top and bottom). Both detector systems are also applicable to an "on-the-fly" analysis outside a laboratory, as they are visible to the naked eye. Additional advantages are obtained by the magnetic separation possibilities [23].

Hydrogen peroxide (H_2O_2) is one of the reactive oxygen species (ROS) and an essential participant in food, enzyme catalysis, and environmental detection. Moreover, H_2O_2 is an effective biomarker of several cellular processes, including protein folding, growth, signaling, differentiation, and migration in the cells. Aberrant accumulation of H_2O_2 results in oxidative stress and the level of H_2O_2 is also connected to aging and some serious diseases. Therefore H_2O_2 plays an important role as a signaling molecule in monitoring human health and life, and it is urgent and necessary to develop a rapid, sensitive H_2O_2 detection strategy for earlier diagnosis and treatment. H_2O_2 is a bridge in the assays of many enzymes and their products; their assays can be achieved by the assay of H_2O_2. Therefore, whether from the elucidation of its biological role as a messenger molecule in living bodies or an important analyte in enzyme-based assays, the detection of H_2O_2 is of great significance [26–30]. Some works have been reported on the luminescence sensing of H_2O_2 using rare earth MOF hybrid probes [31–34].

Qi et al. designed and synthesized a type of luminescence-indicating PA-Tb-Cu-MOF nanoznzyme for the catalytic reaction of H_2O_2, whose fluorescence intensity directly indicated the concentration of H_2O_2. This MOF nanoenzyme consisted of the luminescent Tb^{3+} ion, catalytic Cu^{2+}, and *m*-phthalic acid (PA) as a bridging ligand. The catalytic reaction of H_2O_2 can occur as in Fig. 9.5 (left, top): the reaction extent (concentration) of H_2O_2 is luminescently monitored in real time during catalysis. The catalytic activity of PA-Tb-Cu-MOF for the reaction of ascorbic acid (AA) and H_2O_2 is evaluated by means of the

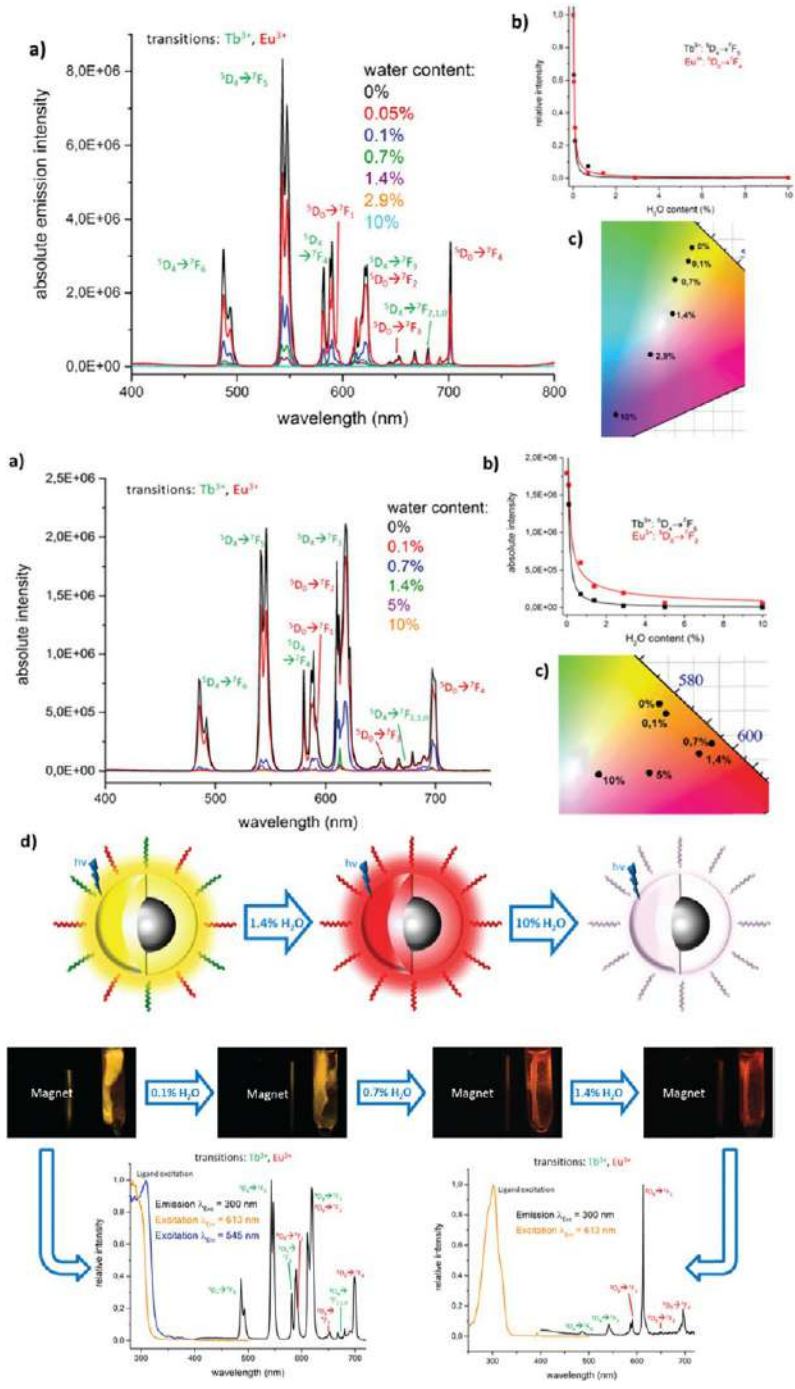

FIG. 9.4 See figure legend on opposite page

fluorescence of the complex of Tb^{3+} and oxidized AA. As shown in Fig. 9.5 (left, bottom), very weak fluorescence can be observed from the solution containing H_2O_2, AA, and Tb^{3+}(curve a), suggesting that there is a very small amount of oxidized AA, i.e., the reaction of H_2O_2 and AA can hardly happen in the absence of a catalyst. After the addition of Cu^{2+}, the solution becomes weakly fluorescent (Fig. 9.5; left, bottom, curve B), showing that the Cu^{2+} ion has a certain catalytic activity for the reaction of AA and H_2O_2. In the presence of PA-Tb-Cu-MOF containing an equal molar quantity of Cu^{2+} in the solution, however, the fluorescence intensity of the solution of AA and H_2O_2 is immediately enhanced up to 80-fold (Fig. 9.5; left, bottom, curve C and curve A). Luminescent catalytic determination of H_2O_2 by the PA-Tb-Cu-MOF nanoenzyme was assessed. As shown in Fig. 9.5A (right), the fluorescence intensity of PA-Tb-Cu-MOF increased steadily with the concentration of H_2O_2. There was an excellent linear correlation between the fluorescence intensity of PA-Tb-Cu-MOF and the concentration of H_2O_2 in the range of 0–500 μM and the LOD was 0.2 μM. As shown in Fig. 9.5B (left, bottom), only H_2O_2 could cause a strong fluorescence enhancement. The excellent selectivity is a result of the special catalysis of PA-Tb-Cu MOF to the H_2O_2 oxidation reaction [32].

Recent biological studies have indicated that hydrogen sulfide (H_2S) is associated with various physiological and pathological processes; for example, H_2S can be produced in the lung and airway tissues via the actions of two H_2S-generating enzymes, cystathionine β-synthase (CBS) and/or cystathionine γ-lyase (CSE). And serum H_2S levels are significantly reduced in asthma patients, considered as an early-detection biomarker for asthma. The fluorescence-based detecting methods are preferred due to their high sensitivity, simplicity, short response time, noninvasive nature, and real-time monitoring ability [35–38].

FIG. 9.4, CONT'D *(Top)* Detection of different concentrations of water with the composite material Eu-BDC, Tb-bipy@Fe_3O_4/SiO_2: emission and excitation spectra of the composite after contact with, the solvent hexane containing defined amounts of H_2O (A) relative course of intensity of the dominant Eu^{3+} and Tb^{3+} transitions for increasing water content fitted with an exponential function (B), and the resulting chromaticity shift for different water content shown in a CIE color diagram (C). *(Middle)* Detection of different concentrations of water with the composite material Eu-BDC, Tb-bipy@Fe_3O_4/SiO_2: emission and excitation spectra of the composite after contact with the solvent hexane containing defined amounts of H_2O (A), relative course of the intensity of the dominant Eu^{3+} and Tb^{3+} transitions for increasing water content fitted with an exponential function (B), resulting chromaticity shift for different water content shown in a CIE color diagram (C) and schematic depiction of the luminescent core/shell system, indicating a chromaticity change for different water content (D). *(Bottom)* Ratiometric and colorimetric "on-the-fly" detection of water with the composite Eu-BDC,Tb-bipy@Fe_3O_4/SiO_2: depiction of the color shift of the composite for different water concentrations *(top)* and corresponding emission and excitation spectra for a water concentration of 0% *(bottom left)* and 1.4% *(bottom right). (Reproduced with permission from T. Wehner, M. T. Seuffert, J. R. Sorg, M. Schneider, K. Mandel, G. Sextl, K. Muller-Buschbaum, Composite materials combining multiple luminescent MOFs and superparamagnetic microparticles for ratiometric water detection. J. Mater. Chem. C 5 (2017) 10133–10142. Copyright 2017 Royal Chemical Society.)*

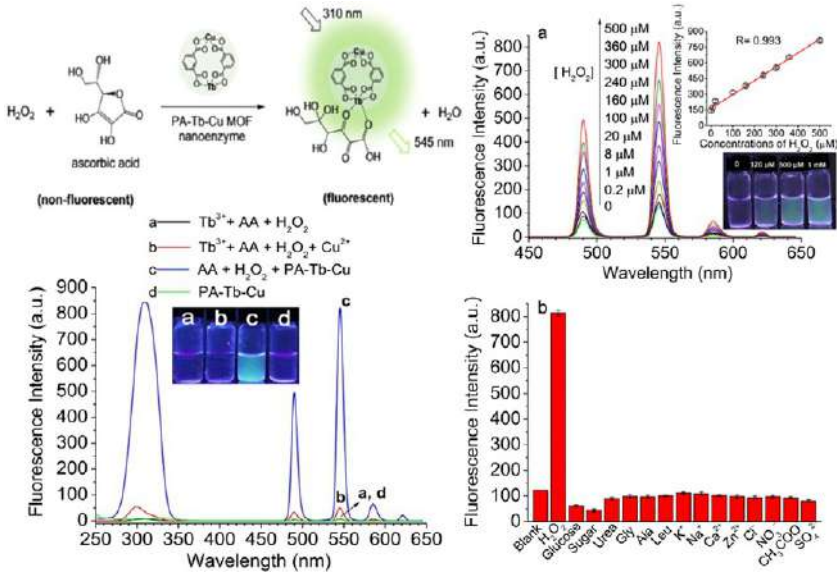

FIG. 9.5 *(Left, Top)* Scheme for luminescent catalytic assay of H_2O_2 using PA-Tb-Cu-MOF nanoznzyme and ascorbic acid. *(Left, Bottom)* Excitation and emission spectra of Tb^{3+}+AA +H_2O_2 (A), Tb^{3+}+AA+H_2O_2 + Cu^{2+} (B), PA-Tb-Cu MOF + AA+H_2O_2 (C) and PA-Tb-Cu-MOF (D). The concentrations of AA, H_2O_2, Cu^{2+}, Tb^{3+}, and PA-Tb-Cu-MOF are 2 mM, 500 μM, 0.267 mM, 0.267 mM and 0.235 mg mL^{-1}, respectively. Inset is the corresponding color photograph under a common 300-nm UV lamp. *(Right)* (A) Luminescent catalytic determination of H_2O_2 in the presence of PA-Tb-Cu-MOF and 2 mM AA in HAc-NaAc buffer (10 mM, pH 5.05). Inset: the linear relationship between the concentration of H_2O_2 and the fluorescence of PA-Tb-Cu-MOF; Color photograph of different concentrations of H_2O_2 under a common 300-nm UV lamp. (B) Effect of interfering substances (500 μM) on the catalytic determination of H_2O_2. *(Reproduced with permission from Z. Qi, L. Wang, Q. You, Y. Chen, PA-Tb-Cu MOF as luminescent nanoenzyme for catalytic assay of hydrogen peroxide. Biosens. Bioelectron. 96 (2017) 227–232. Copyright 2017 Elsevier.)*

Some works have been published on rare earth MOF hybrid materials for luminescence sensing of H_2S [39–46].

Gao et al. presented a ratiometric sensor CDs@ZIF-8@GMP/Tb for H_2S based on Cu^{2+}-mediated fluorescence of Tb-MOFs doped with CDs, which was fabricated by the self-assembly of Tb^{3+} and guanosine monophosphate (GMP) on the surface of ZIF-8 loaded with CDs (CDs@ZIF-8) [42]. GMP/Tb moiety was employed as a response signal due to the On-Off-On behaviors of Tb^{3+} fluorescence upon the sequential addition of Cu^{2+} and H_2S, while CDs@ZIF-8 served as a reference signal because of the good stability of CDs fluorescence in the presence of Cu^{2+} and/or H_2S. As shown in Fig. 9.6A (top), with the increase of H_2S concentration, the Tb^{3+} fluorescence was enhanced gradually, whereas the CDs fluorescence showed negligible changes. Fig. 9.6B (top) showed the intensity ratio of the emission of Tb^{3+}

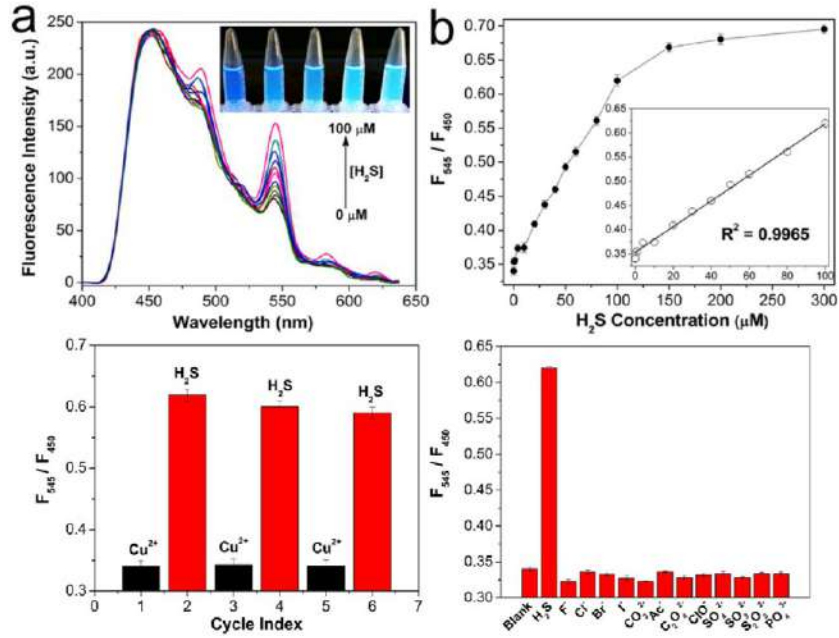

FIG. 9.6 *(Top)* Emission spectra (A) and F_{545}/F_{450} changes (B) of CDs@ZIF-8@GMP/Tb-Cu^{2+} complex in the presence of H_2S with different concentrations. Inset (A) is fluorescent images of CDs@ZIF-8@GMP/Tb-Cu^{2+} complex in the presence of H_2S under UV lamp. The concentrations of H_2S from left to right are 0, 3, 10, 50, 100 μM. Inset (B) is the linear calibration plots of F_{545}/F_{450} against H_2S concentrations. *(Bottom, Left)* Reversible F_{545}/F_{450} changes of CDs@ZIF-8@GMP/Tb upon cyclic treatment with Cu^{2+} and H_2S. *(Bottom, Right)* The detection selectivity of CDs@ZIF-8@GMP/Tb as a ratiometric sensor in the presence of 100 μM various anions. *(Reproduced with permission from J. Gao, Q. Li, C. Wang, H. Tan, Copper (II)-mediated fluorescence of lanthanide coordination polymers doped with carbon dots for ratiometric detection of hydrogen sulfide. Sens. Actuators B 253 (2017) 27–33. Copyright 2017 Elsevier.)*

and CDs, F_{545}/F_{450}, increased from 0.34 to 0.69 upon the increase of H_2S concentration from 0 to 300 μM with a good linear relationship ($R^2 = 0.9964$); the LOD was calculated as 150 nM. Moreover, the H_2S sensing and the concomitant fluorescent changes were clearly visible under a UV lamp, where the blue fluorescence of the sensor suspension turned cyan upon the addition of H_2S (inset of Fig. 9.6A; top). In this case, a color change can be identified by the unaided eye, even at an H_2S concentration as low as 3 μM. Fig. 9.6 (bottom, left) shows that the changes of F_{545}/F_{450} are reversible and repeatable upon the alternate addition of Cu^{2+} and H_2S. Even after three repeated cycles, the F_{545}/F_{450} still remains more than 90% of the original value. As can be seen from Fig. 9.6 (bottom, right), upon adding H_2S to the analysis system, F_{545}/F_{450} is significantly increased. The presence of these anions is not able to switch on the fluorescence of Tb^{3+} quenched by Cu^{2+}, which is attributed to the stronger

binding ability of H_2S to Cu^{2+} than to other anions. The level of H_2S in serum samples was determined with the sensor to test its practicality, and the test showed that the recoveries of H_2S in serum samples were more than 96% and the relative standard deviations were less than 1.58% [42].

Zhang et al. developed a luminescent MOF film through postfunctionalization of MIL-100(In) with linker 1,3,5-benzenetricarboxylic acid (H_3BTC). As shown in Fig. 9.7A and B (top, left), Eu^{3+} and Cu^{2+} ions can be simultaneously postfunctionalized on the extra carboxylate acid of MIL-100(In) film. Cu^{2+} ions have been found to be able to quench the emission of Eu^{3+} ions. As a result, the emission of Eu^{3+} ions in this film is at the off state. However, Cu^{2+} ions may drop from the coordination site with the presence of S^{2-} because of the strong affinity between them, resulting in the fluorescence "Turn-On" of Eu^{3+} ions (Fig. 9.7B; top, left). They found that the reaction of Cu^{2+} and H_2S could also take place in the absence of water and, therefore, with the presence of gaseous H_2S, the characteristic emission of Eu^{3+} ions in MIL-100(In)@Eu^{3+}/Cu^{2+} would be enhanced with the recovery of the antenna effect (Fig. 9.7C; top, left). As shown in Fig. 9.7 (top, right), H_2S gas induces a large increase in the fluorescence intensity of Eu^{3+} emission, which effectively differentiates H_2S from other gases. As shown in Fig. 9.7A (bottom), when the concentration of H_2S increased from 3 to 115 ppm, the fluorescence intensity of MIL-100(In)@Eu^{3+}/Cu^{2+} film was gradually enhanced. In Fig. 9.7B (bottom), the enhancing curve at lower H_2S concentrations displays a good linear relationship with $R^2 = 0.99945$, suggesting that H_2S can be detected quantitatively using this film. The LOD of MIL-100(In)@Eu^{3+}/Cu^{2+} film to H_2S is calculated to be 0.535 ppm [45].

Ammonia (NH_3) is an important and extensively used industrial material, but it is also an extremely toxic chemical even at low concentrations. Ammonia has a higher over-standard rate and is the most significant indoor air pollutant. It is a colorless, volatile and corrosive gas with a pungent odor and is harmful to human health. It irritates the eyes, nose, throat, respiratory tract and skin, which can lead to vomiting, headaches, pneumonedema, respiratory disease, permanent blindness, and even death [47–50]. Some research has been reported on the luminescence sensing of NH_3 using rare earth MOF hybrid material as probes [51–54].

Wang et al. selected $(\{[Eu_2(L)_3\cdot(H_2O)_2\cdot(DMF)_2]\cdot 16H_2O\}_n$ (Eu-MOF, H_2L = 1,4-bis (5-carboxy-1H- benzimidazole-2-yl) benzene)) to further explore the function derived from the chemical analyte as a recyclable "On-Off-On" vapo-luminescent sensor for HCl and NH_3. As shown in Fig. 9.8 (left, top), under irradiation of 365-nm UV light, the red luminescence of Eu-MOF visually disappears when exposed to HCl vapors, and eventually turns to blue luminescence after 5 min; the HCl-treated sample can also be drifted back to red luminescence after 2 min with exposure to NH_3 vapors. In consideration of reversibility, the spectral changes at 618 nm were monitored upon alternating exposure to HCl and NH_3 vapors over several HCl-NH_3 cycles (Fig. 9.8; right).

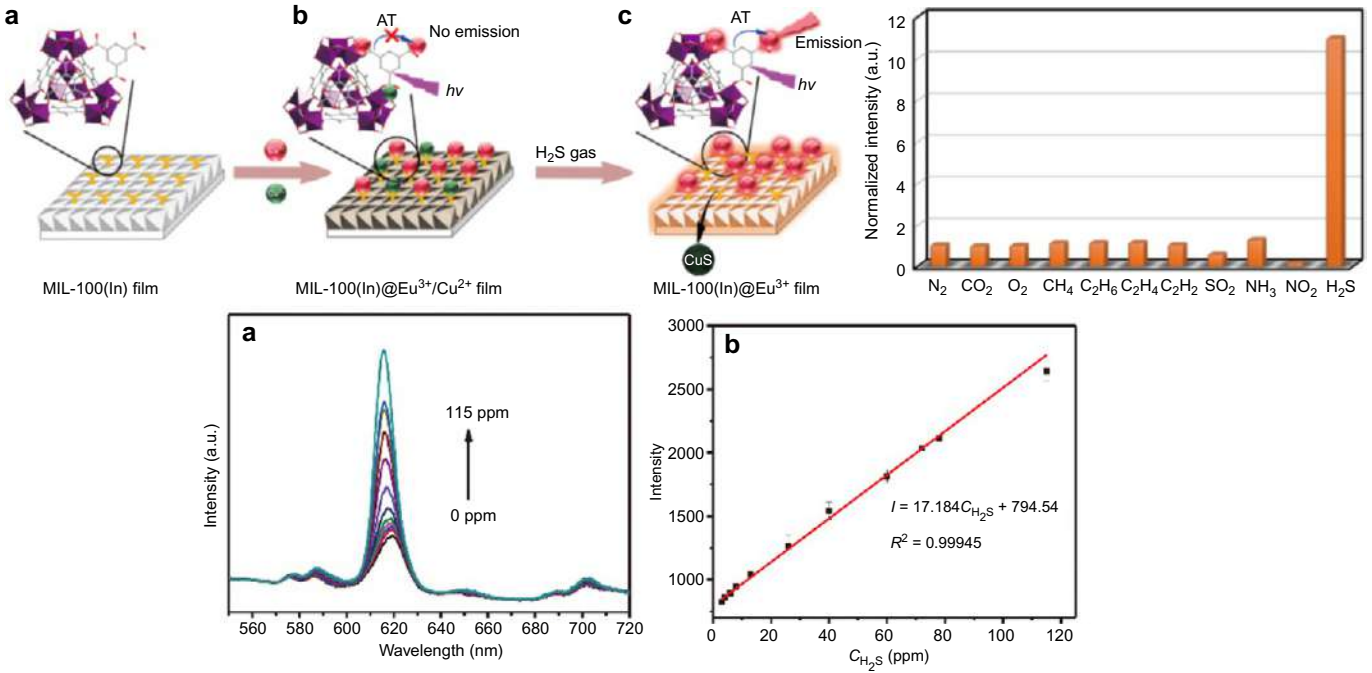

FIG. 9.7 *(Top, Left)* Schematic diagram of the fluorescence Turn-On sensor for H_2S gas of MIL-100(In)@Eu^{3+}/Cu^{2+} film. (A) The supertetrahedra of MIL-100(In) film and the coordinated BTC ligands; fluorescence state of MIL-100(In)@ Eu^{3+}/Cu^{2+} film in (B) absence and (C) presence of H_2S. *(Top, Right)* The enhancement fold of the emission intensity of $^5D_0 \rightarrow {}^7F_2$ transition of Eu^{3+} of MIL-100(In)@E Eu^{3+}/Cu^{2+} film towards various gases (1% *v*/v diluted with N_2) at 40°C. *(Bottom)* Emission spectra (A) and K_{sv} curve (B) of MIL-100(In)@ Eu^{3+}/Cu^{2+} film in the presence of different concentrations of H_2S at 40°C. *(Reproduced with permission from J. Zhang, F. Liu, J. Gan, Y. Cui, B. Li, Y. Yang, G. Qian, Metal-organic framework film for fluorescence turn-on H2S gas sensing and anti-counterfeiting patterns. Sci. China Mater. 62 (2019) 1445–1453. Copyright 2019 Springer.)*

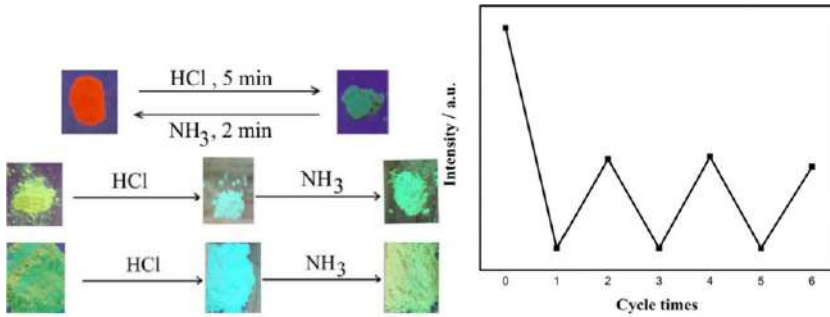

FIG. 9.8 *(Left, Top)* Luminescence pictures of UV-light irradiation of 365 nm for a recyclable On-Off-On luminescent response. *(Left, Middle)* Control experiment of powder sample of free ligand. *(Left, Bottom)* Control experiment of mixture sample of the ligand and $Eu(NO_3)_3$. *(Right)* Cycle tests for recyclable On-Off-On luminescent response. *(Reproduced with permission from D. Wang, J. Liu, Z. Liu, A chemically stable europium metal-organic framework for bifunctional chemical sensor and recyclable on-off-on vapor response. J. Solid State Chem. 251 (2017) 243–247. Copyright 2017 Elsevier.)*

The luminescent colors of the sample changed from chartreuse to blue after exposure to HCl vapors and further became bright green after exposure to NH_3 vapors (Fig. 9.8; left, middle). Then, the ligand and $Eu(NO_3)_3$ were mechanically mixed and ground evenly; after that the obtained sample was selected for vapo-luminescent sensing experiments using the same procedure (Fig. 9.8; left, bottom) The results showed that the luminescent color of the sample changed from chartreuse to blue after exposure to HCl vapors and further became chartreuse after exposure to NH_3 vapors. Eu^{3+} dissociates from Eu-MOF in the acid conditions caused by HCl, while the coordination of Eu^{3+} with carboxyl is re-formed to its basic condition caused by NH_3 [53].

Currently, removal of NO_x in industrial settings is handled through an energy-intensive, catalyst-driven process. Among the most common pollutants, nitrogen dioxide (NO_2) is a toxic gas that is generated by combustion processes at high temperatures and can cause inflammation of the airways and even death at high concentrations. It also plays a pivotal role in the formation of smog and acid rain and is central to the formation of ground level ozone, all being associated with adverse health effects. The standard way to measure NO_2 in almost all air quality studies has been to use surface-conversion techniques to convert NO_2 to NO and to subsequently detect the NO by chemiluminescence. Nevertheless, for low-concentration measurements, this methodology is still affected by interference and is costly or difficult to implement in the field [55–58]. A few works have been reported on rare earth MOF hybrid materials as probes for sensing NO_x [59–61].

Gamonal et al. demonstrated a gas-sensing mechanism exploiting RE^{3+} luminescence modulation upon NO_2 adsorption [60]. The transfer of energy from the organic ligands to RE^{3+} is strongly dependent on the presence of

NO_2, resulting in an unprecedented photoluminescent sensing scheme. Thereby, NO_2 exposition triggers either a reversible enhancement or a decrease in the luminescence intensity, depending on the RE^{3+} (Eu or Tb). The results for both RE-MOFs of 2-amino-1,4-benzene dicarboxylic acid (H_2N-BDC) are plotted in panels a and b of Fig. 9.9. The exposure of Tb-MOF to 5 ppm of NO_2 results in a decrease in the luminescent intensity of ~20% monitored at

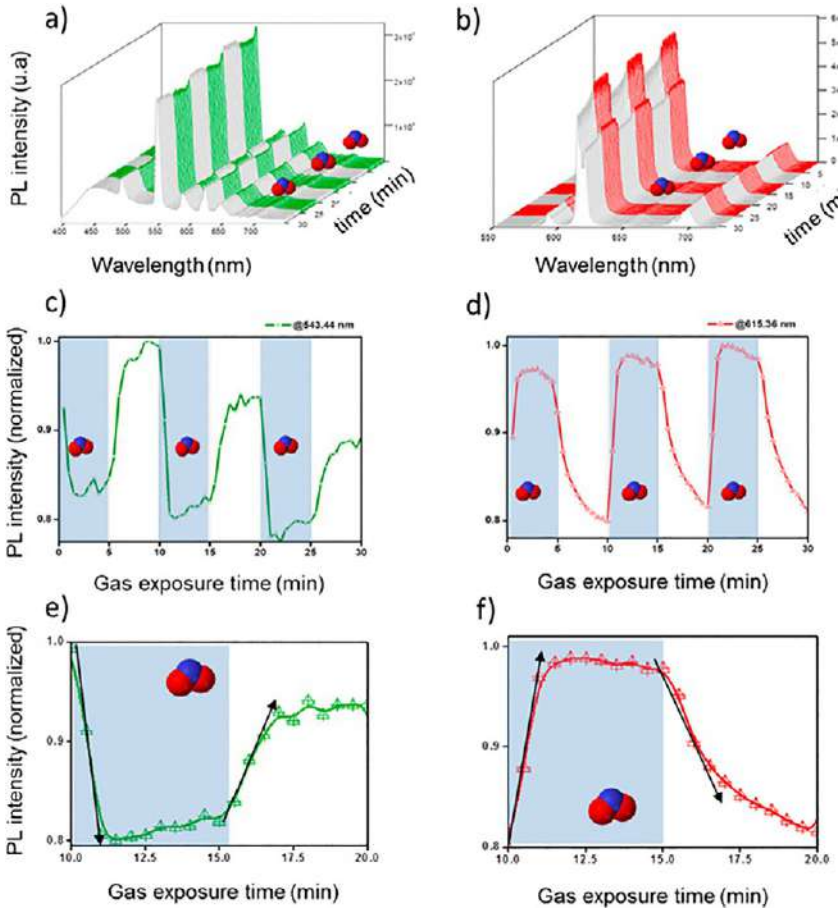

FIG. 9.9 Evolution of PL spectra in (A) Tb-MOF and (B) Eu-MOF during three NO_2/PSA cycles. Luminescent intensity (C) at 543 nm for Tb-MOF and (D) at 615 nm for Eu-MOF as a function of time (the NO_2 exposition is denoted by the shaded areas). Single-cycle sensing evolution illustrating the divergent behavior of (E) Tb-MOF and (F) Eu-MOF. *(Reproduced with permission from A. Gamonal, C. Sun, A. L. Mariano, E. Fernandez-Bartolome, E. Guerrero-SanVicente, B. Vlaisavljevich, J.R Castells-Gil, C. Marti-Gastaldo, R. Poloni, R. Wannemacher, J. Cabanillas-Gonzalez, J. S. Costa, Divergent adsorption-dependent luminescence of amino-functionalized lanthanide metal–organic frameworks for highly sensitive NO2 sensors. J. Phys. Chem. Lett. 11 (2020) 3362–3368. Copyright 2020 American Chemical Society.)*

the emission peak (543 nm) and reaching a plateau after 2 min. Subsequent exposure of Tb-MOF to PSA leads to recovery of the emission intensity within a similar time frame. Contrary to the behavior of Tb-MOF, exposure of Eu-MOF to 5 ppm of NO_2 leads to an increase in luminescence of ~20% during 90 s until it reaches a plateau. Replacement of the NO_2 flux by PSA leads to a return of the emission intensity to the original level. The lowest sensed NO_2 concentrations with this set-up are 0.5 ppm for Tb-MOF (LOD of 1.8 ppm) and 1 ppm for Eu-MOF (LOD of 2.2 ppm). The reversible change in the luminescence intensity of Tb-MOF and Eu-MOF must be associated with the interaction of NO_2 with the RE-MOF. Panels A and B of Fig. 9.9 show no noticeable spectral shifts or changes in the crystal field splitting in the emission lines upon gas absorption. There are also no changes in the relative intensity between the specific transitions upon NO_2 uptake [60].

Sulfur dioxide (SO_2) is an air pollutant and has been studied extensively in toxicology; it is mainly generated from volcanic eruptions and the combustion of fossil fuels and is a noticeable component of the atmosphere. Excessive inhalation of SO_2 can cause respiratory and allergic reactions. In the human body, SO_2 has been found to be able to dilate blood vessels and lower blood pressure, so it is increasingly considered as a gasotransmitter. The benefits of SO_2 gas in the atmosphere may influence the habitat suitability for plant communities and animal life. Excessive intake of SO_2 for human beings can cause acute symptoms and severe adverse effects, such as lung cancer, respiratory diseases, neurological disorders, and cardiovascular disease [62–64]. There are few reports of rare earth MOF hybrid materials for luminescent sensing on SO_2 [64–66].

Wang et al. reported a specially designed bimetallic lanthanide MOF material as a luminescent sensor of sulfite and sulfur dioxide, composed of reactive Ce^{4+} ion, fluorescent Tb^{3+} ion, and *m*-phthalic acid (*m*-PA) as a bridging ligand and also an antenna molecule for the luminescence of the Tb^{3+} ion. The use of the Ce^{4+} ion was inspired by the Ce^{4+}-based chemiluminescence system in flow injection analysis (FIA), in which the chemiluminescence reaction sensitizes the emission of some added fluorescent reagents. This led to the idea of using the reaction of Ce^{4+} to sensitize Tb^{3+} to emit light by assembling Ce^{4+} and Tb^{3+} together to form an ingenious integrated lanthanide sensor [64].

Zhang et al. fabricated an Eu(III)-MOF film on common glass for fluorescence sensing of gaseous SO_2, whose strong characteristic Eu^{3+} emissions can be fast and remarkably quenched by SO_2 gas [66]. As shown in Fig. 9.10 (top, left), most gases show limited quenching effect on the fluorescence intensity of the film. In contrast, SO_2 gas induced a large and instant decrease of the fluorescence intensity of Eu^{3+} emissions (quenching 98.33%). The fluorescence responses of Eu-MOF film were further investigated in different concentrations of SO_2 three times. As shown in Fig. 9.9 (top, right), a good relationship ($R^2 = 0.998$) of the fluorescent intensity with the concentration of SO_2 can be established in the range of 0–200 ppm. Additionally, in the range of 0–25 ppm, the plots of fluorescence intensity versus the concentration of

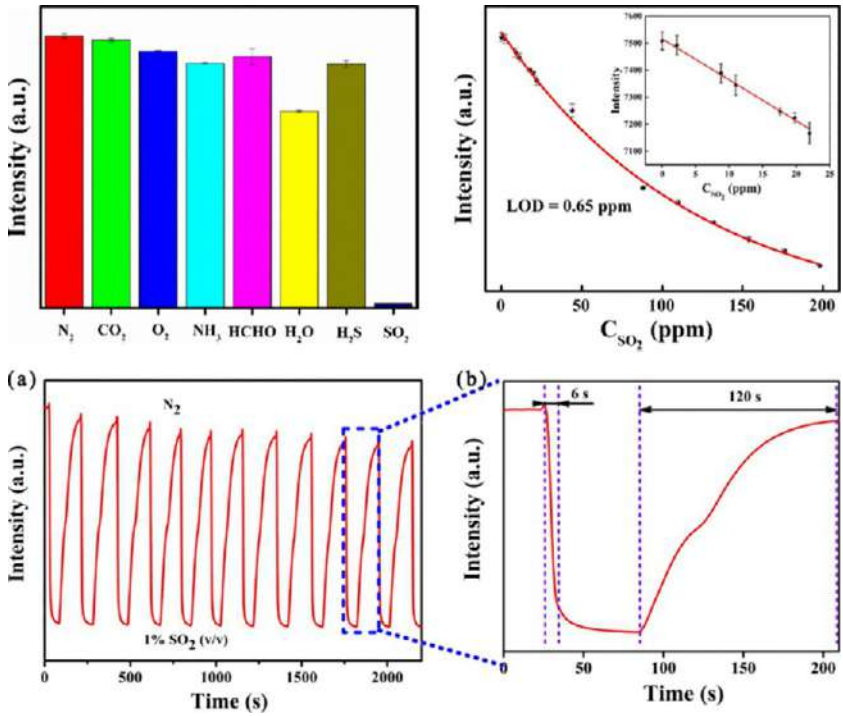

FIG. 9.10 *(Top, Left)* The intensity of the $^5D_0 \rightarrow {}^7F_2$ transition of Eu^{3+} of the Eu-MOF film towards various gases (1% *v*/v diluted with N_2) after 5 min of gas calibration. *(Top, Right)* Concentration dependence of the fluorescence intensity. The inset is the fluorescence intensity in the concentration of 0–25 ppm. *(Bottom)* (A) Reversible luminescence quenching of the Eu-MOF film upon alternating exposure to 1% SO_2 and N_2; (B) The response and recovery time of the Eu-MOF film. *(Reproduced with permission from J. Zhang, T. Xia, D. Zhao, Y. Cui, Y. Yang, G. Qian, In situ secondary growth of Eu(III)-organic framework film for fluorescence sensing of sulfur dioxide. Sens. Actuators B 260 (2018) 63–69. Copyright 2018 Elsevier.)*

SO_2 can follow an excellent linear relationship ($R^2 = 0.994$) and the LOD is estimated as 0.65 ppm. Fig. 9.10A (bottom) exhibits the recyclability of the Eu-MOF film, whose luminescence intensity exhibits an excellent quenching effect to 1% (*v*/v) SO_2 and a recovery ability in N_2 in at least 10 cycles. The fluorescence intensity of the Eu-MOF film can recover to 88.2% of the initial intensity in N_2 after 10 cycles. It is worth noting that the response time of this film to 1% SO_2 is as short as 6 s (Fig. 9.10B; bottom). The significant aspect of the charge transfer process is that the presence of the electron withdrawing molecules causes the charge transfer from the ligand to these molecules and thus dissipates the energy. As a result, the absorbed energy of the ligand will be dissipated by SO_2 instead of sensitizing the Eu^{3+} ion, leading to the quenching of the luminescence [66].

9.2 Rare earth metal-organic framework for luminescence responsive chemical sensing of general organic molecules

As the main sources of atmospheric pollution, general organic molecules, or known volatile organic compounds (VOCs), have posed various threats to homeland security as well as human health risks. They are present in indoor/outdoor air, as a consequence of the release from chemical industries, cosmetics, building blocks, and other sources. Therefore effective detection of VOCs is of great importance for both environmental and health issues. Although a number of luminescent MOFs show great promise in sensing VOCs in solution, fluorescence sensing of trace solvent vapors is still challenging due to their low vapor pressures at room temperature. Thus the luminescence detection in the vapor phase is much more difficult than in the liquid form [67–69]. Acetone is a highly volative and flammable VOC, which is easy for humans to absorb, such as through breath and skin exposure. Absorbed acetone can be distributed over the body, which can lead to metabolism disorders, diabetes, and other serious health effects. Several methods have been proposed to detect acetone [70,71]. For rare earth MOF hybrid materials, the reports on luminescence sensing of acetone are the most extensive [72–88].

Wang et al. prepared a hybrid luminescent coating of Tb^{3+}@MOF-5/ZnO and developed it as a highly selective luminescent probe targeting acetone. The luminescence response of the Tb^{3+}@MOF-5/ZnO to the various organic molecules is displayed in Fig. 9.11 (top, left), and it was found that the luminescence intensity of $^5D_4 \rightarrow {}^7F_5$ transition of Tb^{3+} was largely dependent on organic molecules. The luminescence intensity of the Tb^{3+}@MOF-5/ZnO significantly quenches only in acetone. It was found that the luminescence intensity gradually decreased as the concentration of acetone increased, as shown in Fig. 9.11 (top, right) and (bottom, left). The luminescence intensity was almost undetectable when the acetone content reached 6 vol%. As shown in Fig. 9.11 (top, right) at low concentrations of acetone (up to 0.14 M, 1 vol%), a linear increase in (I_0/I) was observed ($K_{sv} = 6.7\ M^{-1}$). With increasing concentration of acetone, the S-V plots diverge from linearity and begin to bend upwards in acetone (Fig. 9.11; top, right and bottom, left). The LOD is about 0.08 M. The titration experiments indicate high sensitivity of the Tb^{3+}@MOF-5/ZnO towards acetone, making it an excellent candidate for the detection of acetone. Tb^{3+}@MOF-5/ZnO was immersed in the solution containing acetone and a series of other analytes. As shown in Fig. 9.11 (bottom, right), when Tb^{3+}@MOF-5/ZnO is immersed in the mixed analytes (6 vol% other analyte +6 vol% acetone), the measurement of the luminescence intensity shows that the luminescence is quenched completely, indicating that the selectivity for acetone is not interfered with by the existence of other analytes. Acetone absorbs most of the energy and only a small fraction of energy is transferred through the ligand to the Tb^{3+} ions, which illustrates the decreased or fully quenched luminescence intensity of Tb^{3+}@MOF-5/ZnO upon addition of acetone [77].

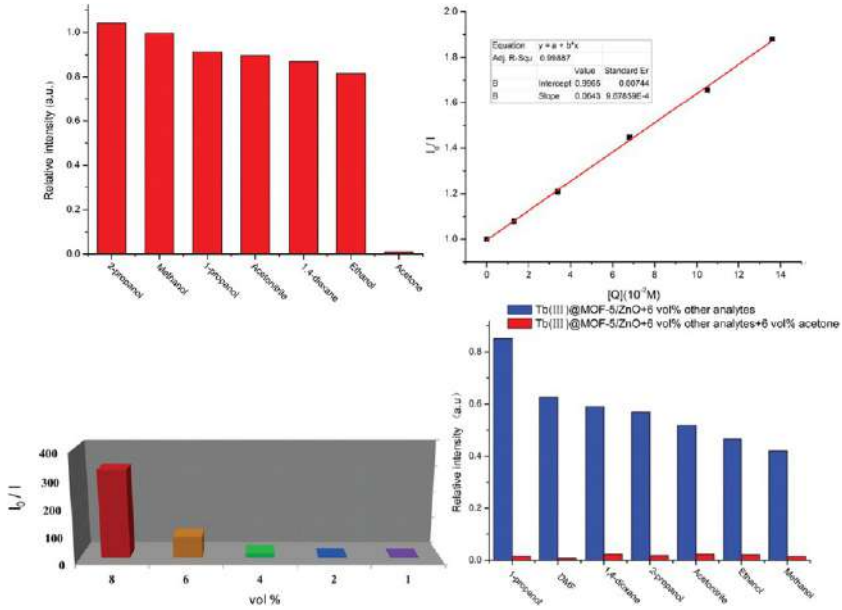

FIG. 9.11 *(Top, Left)* Diagrams of the $^5D_4 \rightarrow {}^7F_5$ transition intensities of the Tb^{3+}@MOF-5/ZnO at 546 nm in various small organic molecules ($\lambda_{ex} = 299$ nm). *(Top Right)* Plot of I_0/I of the Tb^{3+}@MOF-5/ZnO (at 546 nm) vs. concentration of acetone in lower concentration ranges (0–1 vol%) of acetone (up to 0.14 M, 1 vol%). *(Bottom, Left)* Plot of I_0/I of the Tb^{3+}@MOF-5/ZnO (at 546 nm) vs. concentration of acetone in higher concentration ranges of acetone (1–8 vol%). *(Bottom, Right)* The $^5D_4 \rightarrow {}^7F_5$ transition intensities of the Tb^{3+}@MOF-5/ZnO upon the addition of different analytes (*blue*) and subsequent addition of acetone (*red*) ($\lambda_{ex} = 299$ nm). *(Reproduced with permission from Y. Wang, F. Zhang, Z. Fang, M. Yu, Y. Yang, K Wong, Tb(III) postsynthetic functional coordination polymer coatings on ZnO micronanoarrays and their application in small molecule sensing. J. Mater. Chem. C 4 (2016) 8466–8472. Copyright 2016 Royal Chemical Society.)*

Zhang et al. obtained five RE-MOFs formulated as $[RE_4(\mu_6\text{-}L)_2(\mu\text{-}HCOO)(\mu_3\text{-}OH)_3(\mu_3-O)(DMF)_2(H_2O)_4]_n$ {RE = Tb, Eu, Gd, Dy, and Er} with 2-(6-carboxypyridin-3-yl)terephthalic acid (H_3L) ligand, which revealed a unique capability of Tb-MOF for sensing acetone with high efficiency and selectivity. The emission spectra of Tb-MOF (after being dispersed in organic solvents) showed typical bands for Tb^{3+} ions (Fig. 9.12A; left). However, the intensity of the main transition ($^5D_4 \rightarrow {}^7F_5$) was significantly affected by solvent, especially for acetone, which provoked a strong luminescence quenching. Furthermore, the effect of the acetone amount on the luminescence quenching of Tb-MOF was investigated in DMF-acetone suspensions (Fig. 9.12; right). The emitted visible green light of the suspension of Tb-MOF in DMF faded upon an addition of acetone, followed by a gradual decrease of the $^5D_4 \rightarrow {}^7F_5$ transition intensity. Analysis of the emission and absorption spectra suggests that there is an energy transfer between L^{3-} and acetone, indicating a

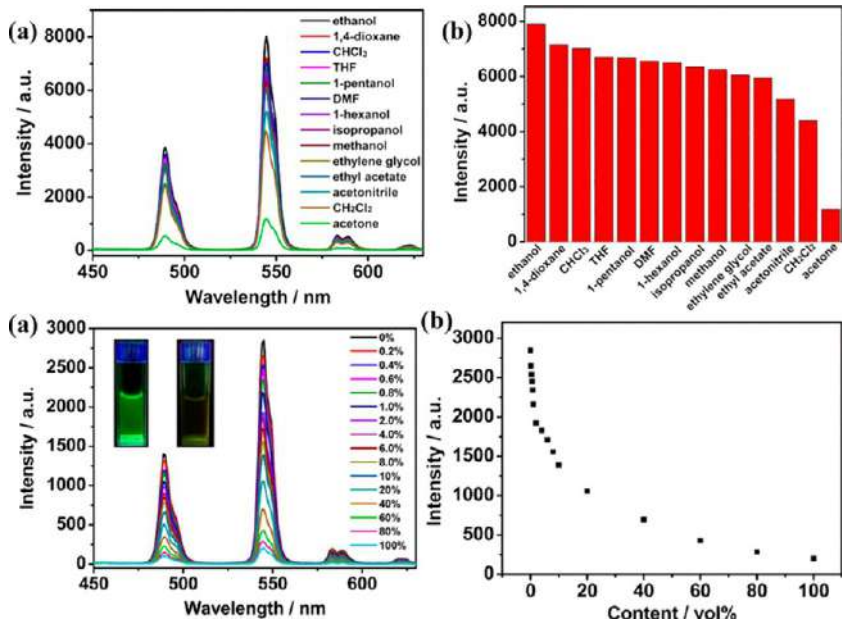

FIG. 9.12 *(Top)* Luminescence spectra (A) and intensities of the $^5D_4 \rightarrow {}^7F_5$ transition (B) for Tb-MOF dispersed in various organic solvents (2 mL, 2 mg Tb-MOF). *(Bottom)* (A) Luminescence spectra of Tb-MOF dispersed in DMF-acetone solution (2 mL total volume; 2 mg Tb-MOF) with different volume content of acetone; inset shows color of DMF *(left)* and acetone *(right)* solutions under UV light. (B) Luminescence intensities of the $^5D_4 \rightarrow {}^7F_5$ transition (544 nm) of Tb-MOF with an increasing volume content of acetone in DMF-acetone solution. *(Reproduced with permission from Q. Zhang, J. Wang, A. M. Kirillov, W. Dou, C. Xu, C. Xu, L. Yang, R. Fang, W. Liu, Multifunctional Ln−MOF luminescent probe for efficient sensing of Fe3+, Ce3+, and acetone. ACS Appl. Mater. Interfaces 10 (2018) 23976–23986. Copyright 2018 American Chemical Society.)*

sort of competitiveness between the compound excitation and the acetone absorption [81].

Hao et al. prepared Eu-based MOF (MIL-121, $Al(OH)(H_4btec)\cdot H_2O$, H_4btec = pyromellitic acid) crystals (Eu^{3+}@MIL-121) and utilized them as a fluorescence probe for organic small molecule pollutants. Fig. 9.13 (left) shows the emission spectra of Eu^{3+}@MIL-121 treated by different solvents, including chloroform and acetone, which exhibited the most noticeable enhancing and quenching effects, respectively. It is noticeable that the luminescent intensity of the suspension of Eu^{3+}@MIL-121 increased with the addition of chloroform, as shown in Fig. 9.13A (right), and the enhancement was nearly proportional to the content of chloroform (inset of Fig. 9.13A; right). Conversely, addition of acetone into the standard suspension of Eu^{3+}@MIL-121 led to a significant decrease of the fluorescence intensity, which almost disappeared at an acetone content of 8 vol% (Fig. 9.13B; right). This decreasing trend of the largest luminescent intensities of Eu^{3+} at 615 nm versus the volume ratio of acetone can be

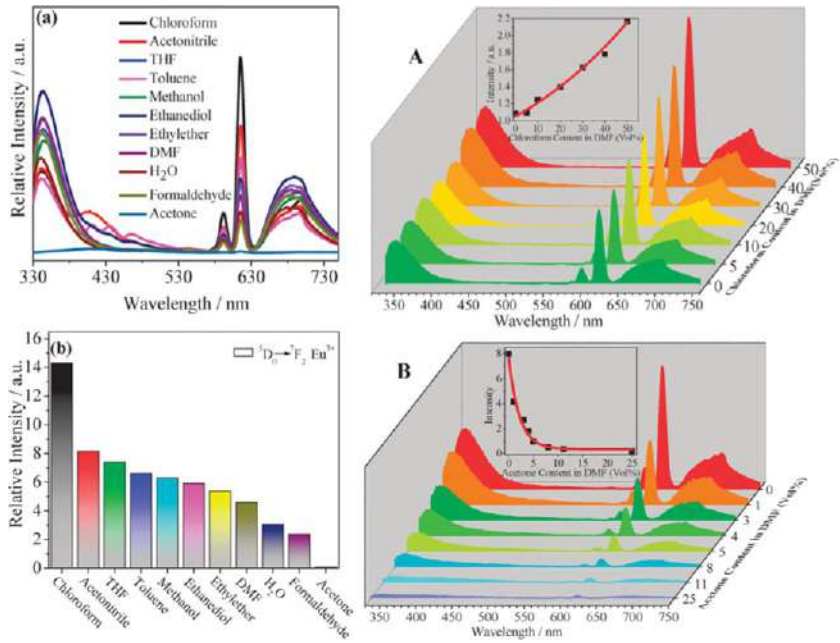

FIG. 9.13 *(Left)* (A) Luminescent spectra and (B) the $^5D_0 \rightarrow {}^7F_2$ transition intensities of Eu^{3+}@MIL-121 dispersed into various pure solvents when excited at 315 nm. *(Right)* The emission spectra of Eu^{3+}@MIL-121 DMF suspension in the presence of various content of (A) chloroform and (B) acetone solvent, respectively (excited at 315 nm). The insets in (A) and (B) show the $^5D_0 \rightarrow {}^7F_2$ transition intensity of Eu^{3+} for DMF suspension of Eu^{3+}@MIL-121 as a function of chloroform and acetone content, respectively. *(Reproduced with permission from J. Hao, B. Yan, Ln3 + post-functionalized metal–organic frameworks for color tunable emission and highly sensitive sensing of toxic anions and small molecules. New J. Chem. 40 (2016) 4654–4661. Copyright 2016 Royal Chemical Society.)*

well fitted with a first-order exponential decay (inset of Fig. 9.13B; right), implying that luminescence quenching of Eu^{3+}@MIL-121 by acetone is diffusion controlled. The absorption band of H_4btec within the hybrid partially overlaps with the absorption band of acetone, whose competitive absorption between acetone and H_4btec in the range of 250 to 350 nm affects the absorption of H_4btec, reducing the efficiency of LMET to cause the energy transfer between ligands and acetone. The influence of chloroform on LMET is important, as energy absorbed by chloroform is transferred to ligands to increase the efficiency of LMET and enhance the luminescence of Eu^{3+}@MIL-121 [89].

Wang et al. assembled a Eu-MOF with 2,2′,3,3′-oxidiphthalic acids (H_4ODA) as efficient sensitizing units, which showed a unique luminescent response to methanol, in contrast to *n*-propanol and ethanol. The luminescent spectra of Eu-MOF were largely changed when subjected to the different solvent molecules, particularly for methanol and acetone, for which the most

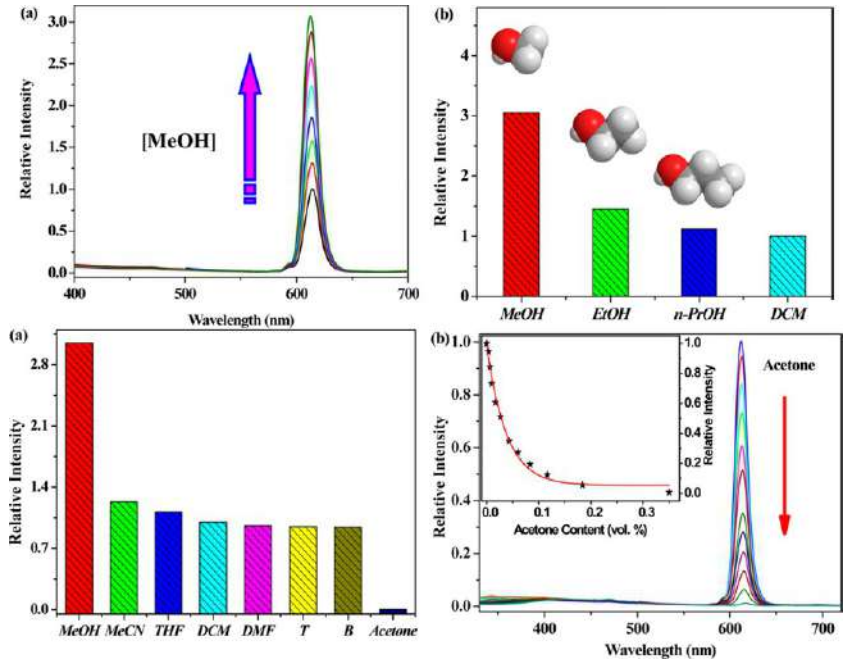

FIG. 9.14 *(Top)* (A) Fluorescence spectra of Eu-MOF (60 μM) dichloromethane emulsion as a function of the methanol concentration (from bottom: 0.0, 0.06, 0.23, 0.46, 0.83, 1.31, 1.96, and 2.60 vol%). (B) Fluorescence responses of Eu-MOF at 614 nm to the addition of alcohols (2.60 vol%) when excited at 305 nm. *(Bottom)* (A) The $^5D_0 \rightarrow {}^7F_2$ transition intensities of Eu-MOF when immersed into various pure solvents with excitation at 305 nm. (B) Family of luminescence spectra of Eu-MOF (60 μM) upon adding acetone. The inset picture exhibits the PL intensity of the Eu-MOF emulsion with the change of acetone content. *(Reproduced with permission from J. Wang, M. Jiang, L. Yan, R. Peng, M. Huangfu, X. Guo, Y. Li, P. Wu, Multifunctional luminescent Eu(III)-based metal-organic framework for sensing methanol and detection and adsorption of Fe(III) ions in aqueous solution. Inorg. Chem. 55 (2016) 12660–12668. Copyright 2016 American Chemical Society.)*

remarkable enhancement and quenching effects were found, respectively (Fig. 9.14A; bottom). As shown in Fig. 9.14A (top), the addition of methanol led to a gradual increase of the luminescence intensity of Eu-MOF at 614 nm up to 3.1 times the enhanced efficiency. Such Turn-On luminescence switching initiated by methanol molecules is probably due to hydrogen-bonding interactions with the terminal water molecules in the framework, alleviating the O-H high energy vibrations to lead to an increase in emission intensities. The presence of *n*-propanol leaves the fluorescence intensity almost unchanged under the same experimental conditions (Fig. 9.14B; top). Considering that the pore size (4.1 Å) of Eu-MOF is bigger than that of methanol (kinetic diameter 3.8 nm) but smaller than that of ethanol and *n*-propanol, the remarkable size selectivity for the sensing of alcohols mainly depends on the size constraint effect of the host pore and the guest analytes. In addition, the fluorescence intensities of the Eu-MOF/dichloromethane standard emulsion are gradually reduced

by the gradual increase of the acetone content and almost disappear when the acetone content is up to 0.35 vol% (Fig. 9.14B; bottom). Acetone shows a wide absorption overlaying the absorbing band of H_4ODA, whose competitive adsorption weakens the energy transfer from the $HODA^{3-}$ sensitizer to Eu^{3+} to bring about a reduction of the luminescence intensity.

Zheng et al. prepared a series of Eu^{3+}-functionalized MOF materials (Eu-MOF) based on the PSM of the parent MOF (UMCM-NH_2) (ligands of 2-amino-1,4-benzenedicarboxylate (NH_2-BDC) and 4,4′,4″-benzene-1,3,5-triyl-tribenzoic acid (H_3BTB) and 2,3-pyrazinedicarboxylic anhydride for covalent PSM), which showed an extremely selective and rapid response to THF compared to the other sensing organic molecules and could be easily distinguished by the naked eye under UV-light irradiation [90]. As shown in Fig. 9.15 (top),

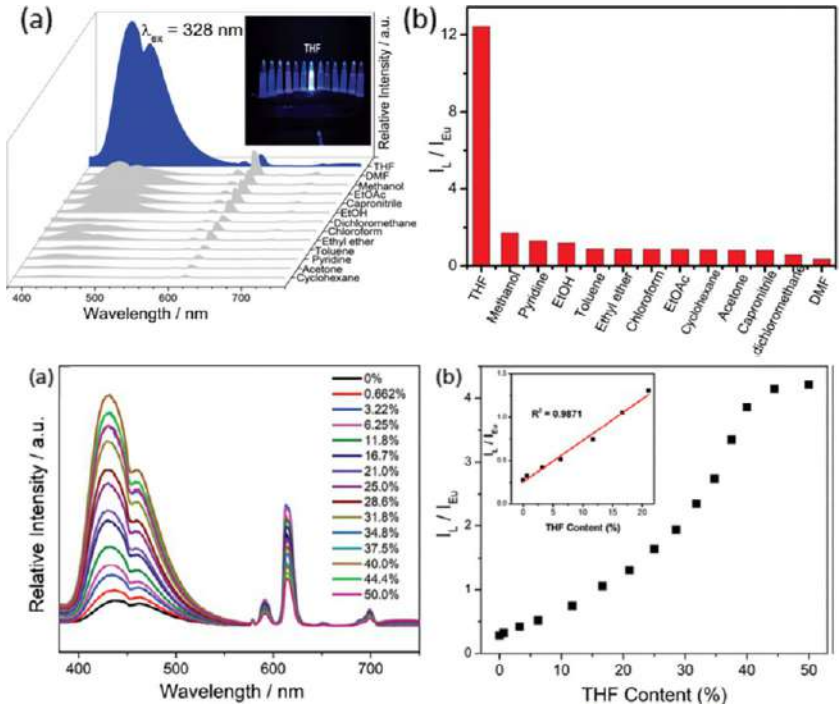

FIG. 9.15 *(Top)* (A) Emission spectra of Eu-MOF dispersed in different organic molecules (2.5 mg/3 mL) (excited at 328 nm). The inset is the corresponding photographs under UV-light irradiation at 365 nm. (B) The luminescence intensity ratio (I_L/I_{Eu}) of Eu-MOF with the different organic molecules. *(Bottom)* (A) The luminescence spectra of Eu-MOF dispersed in DMF with increasing THF content; (B) the changes of I_L/I_{Eu} with increasing THF content. The insets show the linearity between I_L/I_{Eu} and the THF content (0%–21%). *(Reproduced with permission from H. Zheng, X. Lian, S. Qin, B. Yan, Lanthanide hybrids of covalently-coordination cooperative post-functionalized metal–organic frameworks for luminescence tuning and highly selectively sensing of tetrahydrofuran. Dalton Trans. 47 (2018) 6210–6217. Copyright 2018 Royal Chemical Society.)*

the luminescence intensities of Eu^{3+} ($^5D_0 \rightarrow {}^7F_2$) of Eu-MOF immersed in various solvents are almost quenched to a different extent compared to the solid state. On the other hand, it is worth mentioning that the emission bands of the linkers within the Eu-MOF are extremely enhanced when THF is added. The luminescence intensity ratio (I_L/I_{Eu}) of THF-induced emission is calculated as 12.44, which is much higher than the other organic molecule-induced luminescence intensity ratios. As shown in the inset of Fig. 9.15A (top), these dark colors of the solvents serve as foils to that of THF, which displays a bright cyan-blue color under UV-light irradiation. As shown in Fig. 9.15A (bottom), the emission spectra of the system changed very obviously with the increment of THF content. As expected, the intensity ratio of ligands and Eu^{3+} (I_L/I_{Eu}) increased with the proportion of THF added, and when the volume fraction of THF increased to 50%, the values of I_L/I_{Eu} were almost constant (Fig. 9.15B; bottom). The linearity can be fitted with the correlation coefficient (R^2) calculated as 0.9871 and the LOD for THF is calculated as 0.76% from the slope of the linear relationship in the inset of Fig. 9.15B (bottom). This result is due to the existence of the lone pair of electrons in the O that belongs to the furan ring and unmodified free NH_2, which can form a hydrogen bond and cause the enhancement effects [90].

Wu et al. synthesized highly fluorescent In-MOF (In(*OH*)bpydc, H_2bpydc = biphenyl-5,5′-dicarboxylic acid)) imparting additional luminescent Eu^{3+} ions for sensing organic molecules, especially chloroform with a significant spectral response. The dual-emitting MOF hybrid exhibited a distinctly different response to $CHCl_3$, one of which was almost unchanged, while the other intrinsic broad emission had a remarkable enhancement, leading to an obvious change in color. The luminescent responses of In-MOF-Eu towards small molecules of various organics are recorded in Fig. 9.16 (left) at $\lambda_{ex} = 360$ nm. The change of emission of In-MOF-Eu can be divided into two main parts: characteristic emission of Eu^{3+} and ligand central emission. As shown in the inset of Fig. 9.16 (left), these dark colors of organics serve as foils to that of chloroform, leading to the notable distinction by the naked eye. As depicted in the time-response emission spectra and curves within 35 min of Fig. 9.16 (right), just for 5 min, the luminescence intensity at 490 nm of In-MOF-Eu reached a constant value and after that, the height was raised just a little. As time passed, the luminescence intensity at 490 nm of In-MOF-Eu rose sharply in 5 min, before a slow increase for the remaining 30 min (as shown in the inset of Fig. 9.16B; right). Only the ligand-central emission became stronger, indicating that $CHCl_3$ has the only effect on the ligand. The effects of luminescent enhancement of In-MOF-Eu are caused by hydrogen-bonding interaction, whose N atom as a hydrogen-bonding donor can decrease the electron deficiency by bonding to hydrogen bonding-accepting analytes.

Lian et al. synthesized a rare earth functionalized material based on MIL-125(Ti)-NH_2 (ligands of 2-amino-1,4-benzenedicarboxylate (NH_2-BDC) and 2,3-pyrazinedicarboxylic anhydride for covalent PSM) by the covalent

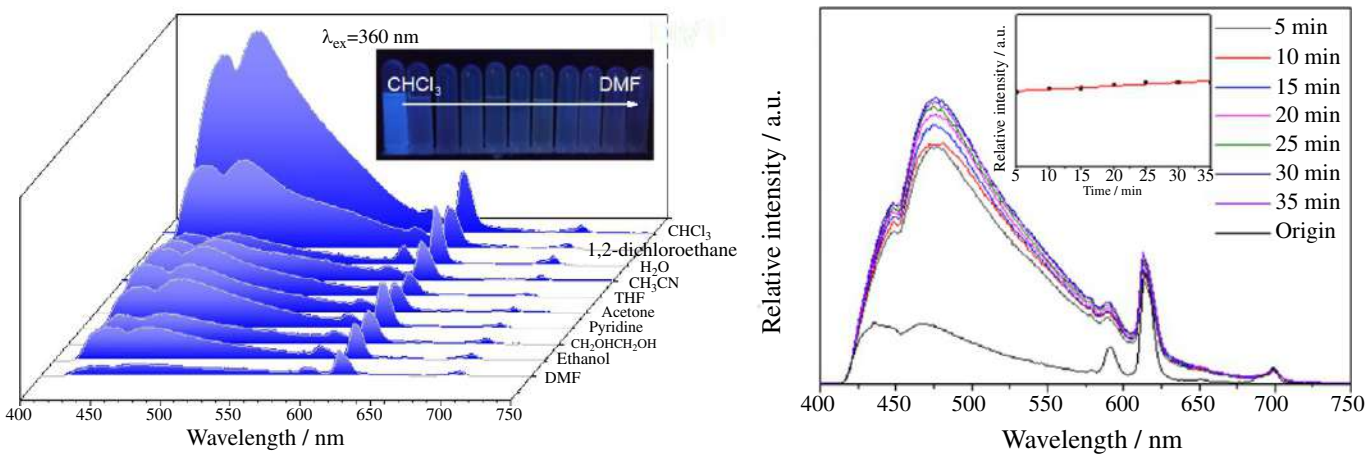

FIG. 9.16 *(Left)* Luminescence intensity of the In-MOF-Eu dispersed into different organic molecule solvents (3 mg/3 mL) (excitation monitored at 360 nm). The inset is the corresponding photographs under UV-light irradiation at 365 nm. *(Right)* Variation of fluorescence intensity of In-MOF-Eu with different immersion time in $CHCl_3$ ($\lambda_{ex} = 360$ nm). *(Reproduced with permission from J. Wu, B. Yan, Eu(III)-functionalized in-MOF (In(OH)bpydc) as fluorescent probe for highly selectively sensing organic small molecules and anions especially for CHCl3 and MnO4 −. J. Colloid Interface Sci. 504 (2017) 197–205. Copyright 2017 Elsevier.)*

postsynthetic modification and it showed photocatalytic oxidation properties of α-phenethyl alcohol. The luminescence of MIL-125(Ti)-AM-Eu becomes weak and even is quenched in the presence of acetophenone and this process can be used as a new fluorescence sensor for detecting α-phenethyl based on photocatalytic oxidation. Towards expanding the application of MIL-125(Ti)-AM-Eu in the detection of organic small molecules, the group proposed to design a Turn-On/Turn-Off luminescent sensor for α-phenethyl alcohol combined with the catalytic performance and fluorescence spectrum of MIL125(Ti)-AM-Eu (Fig. 9.17; left). Fig. 9.17 (right) shows the fluorescence response of MIL-125(Ti)-AM-Eu immersed in α-phenethyl alcohol for different times, and the reaction system is exposed to UV irradiation. The fluorescence signal gradually becomes weaker with time. This phenomenon is similar to the fluorescence quenching, and as shown in the inset of Fig. 9.17 (right), it can be easily distinguished by the naked eye. When α-phenethyl alcohol is adsorbed inside the channels of MIL-125(Ti)-AM-Eu, a fast photocatalytic effect occurs upon UV irradiation. The hydroxyl groups will be oxidized with the photocatalytic effect impelled by MIL-125(Ti)-AM-Eu, yielding the photooxidation products of alcohols [91].

Chen et al. presented a Tb-MOF material of linker 4,4′-oxybis(benzoic acid) (H_2oba) with 3-amino1,2,4-triazole (Hatz) as the directing reagent, which could realize fast recognition of *p*-xylene (PX) vapor and nitrobenzene (NB) vapor. A homemade setup was fabricated by placing a MOF-coated thin paper into the cuvette, followed by adding one drop of organic compound into the cuvette (Fig. 9.18A). As shown in Fig. 9.18B, the time-dependent emission spectrum

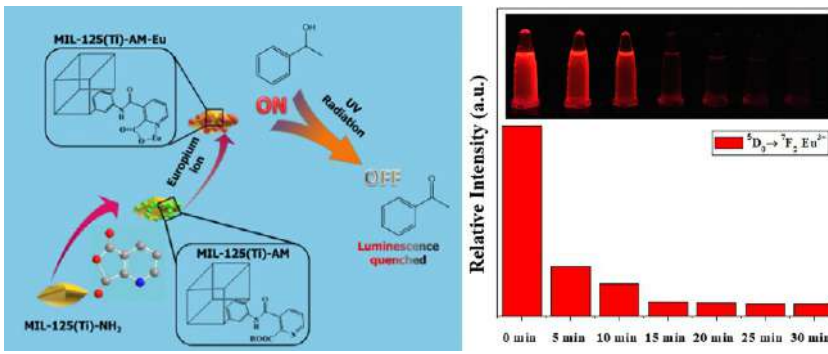

FIG. 9.17 *(Left)* Schematic of synthesis of MIL-125(Ti)-AM-Eu as a Turn-On/Off fluorescent sensor for α-phenethyl alcohol. The solvent molecules (including DMF and H_2O) and counterions that could coordinate with Eu^{3+} are omitted for simplicity. *(Right)* The $^5D_0 \rightarrow {}^7F_2$ transition intensity ratios from the emission spectra of MIL-125(Ti)-AM-Eu introduced into α-phenethyl alcohol after UV radiation for different times. *(Reproduced with permission from X. Lian, B. Yan, A post-synthetic modified MOF hybrid as heterogeneous photocatalyst for α-phenethyl alcohol and reusable fluorescence sensor. Inorg. Chem. 55 (2016) 11831–11838. Copyright 2016 American Chemical Society.)*

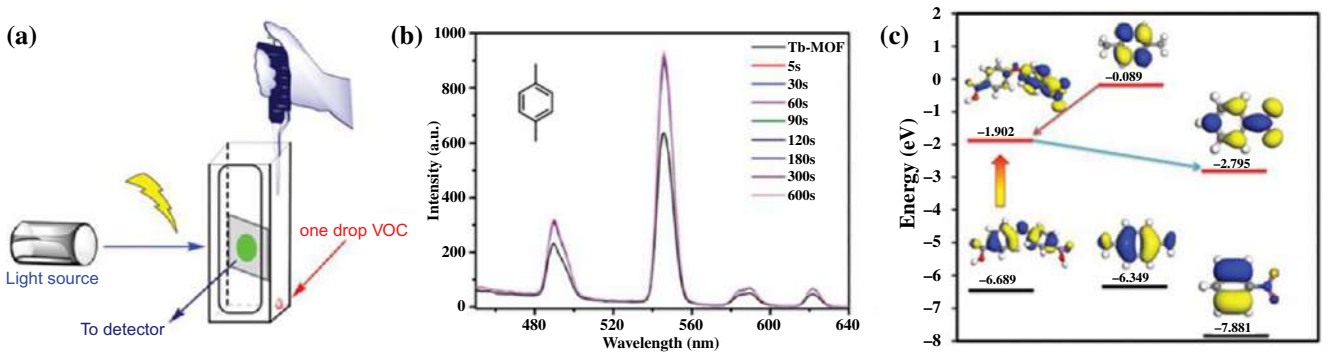

FIG. 9.18 (A) The homemade device for VOC vapor detection. (B) Time-dependent emission spectrum for the Tb-MOF in the PX atmosphere. (C) The calculated energy levels for the H_2oba ligand and the analyte molecules. *(Reproduced with permission from D. Chen, N. Zhang, C. Liu, M. Du, Template-directed synthesis of a luminescent Tb-MOF material for highly selective Fe3 + and Al3 + ion detection and VOC vapor sensing. J. Mater. Chem. C 5 (2017) 2311–2317. Copyright 2017 Royal Chemical Society.)*

showed that the response rate of the Tb-MOF for PX vapor was 5 s with a 40% fluorescence enhancement, and the increased fluorescence intensity was stable within 5 min without an obvious change. This may be attributed to the photo-induced donor-acceptor electron transfer between the antenna ligand and analyte molecules adsorbed on the surface of the MOF particles. The energy levels of the antenna ligand H_2oba were calculated using the DFT theory, and the results are shown in Fig. 9.18D, which indicates that PX has a higher LUMO energy level than that of the H_2oba ligand. PX has a high-lying π^*-type LUMO orbital that is above the singlet state energy of the ligand, so the excited electrons of PX are easily transferred to the LUMO of the ligand, resulting in fluorescence enhancement [92].

Wu et al. investigated a Eu^{3+}-functionalized In-MOF (In(*OH*)bpydc, H_2bpydc = 2,2′-bipyridine-5,5′- dicarboxylic acid) hybrid system (In-MOF-Eu) with dual emission for fluorescence sensing of benzene homologues (BTEX) in both vapor and liquid phases. A fluorescence test paper and a 2D-decoded map were designed to provide the potential for the convenient distinction of BTEX. The images in Fig. 9.19B (left) show the different luminescence colors produced. The luminescence color of most BTEX compounds is either blue or green. However, one of them is quite unique: Br-benzene shows dark red light. The CIE chromaticity diagram and related values are obtained when the compounds are excited at 360 nm (as shown in Fig. 9.19C and D; left), and various BTEX compounds locate in two main color regions of green and blue. Only the emission of the Br-benzene is near the white-yellow area, with the colors being the same as those in the images (Fig. 9.19B; left). Images of filter text paper shown in Fig. 9.19 (right, top) indicate that under the irradiation of UV light of 365 nm, the fluorescence of the test paper of alkyl benzene changes from dark blue to bright green, whereas the fluorescence of the test paper of halogenated benzenes changes from dark blue to red. The potential application of In-MOF-Eu for detecting BTEX volatiles has been investigated. All samples were placed under a vapor atmosphere of BTEX for around 1 h, and the final results are shown in Fig. 9.19 (right, bottom) [93].

Zhao et al. assembled a luminescent Tb-MOF ($[Tb_3(L)_2(HCOO)(H_2O)_5]\cdot DMF\cdot 4H_2O$ (H_4L = 4,4′-(pyridine-3,5-diyl)diisophthalic acid), whose luminescence was nearly entirely quenched in a *N*,*N*-dimethylformamide (DMF) solution and biological system. In addition, Tb-MOF still had high detection for the trace content of nitromethane with 70 ppm. As shown in Fig. 9.20 (left), the intensities of the emission peaks largely depend on the solvent molecules, especially nitromethane, which shows a significant quenching effect. A batch of emulsions of Tb-MOF in DMF with gradually increasing nitromethane concentrations were prepared to monitor emissive responses. It was found that the luminescent intensity of the suspension of T-MOF decreased with the addition of nitromethane, which almost disappeared at the content of 70 ppm (Fig. 9.20A and B; right). The fluorescence decrease was nearly proportional to the nitromethane concentration. The effect of guest organic small molecules on LMET plays a key role for its emission efficiency determines the luminescent intensity [94].

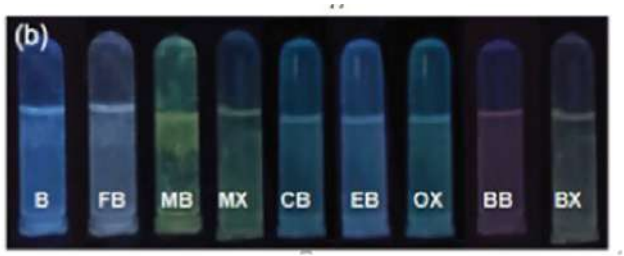

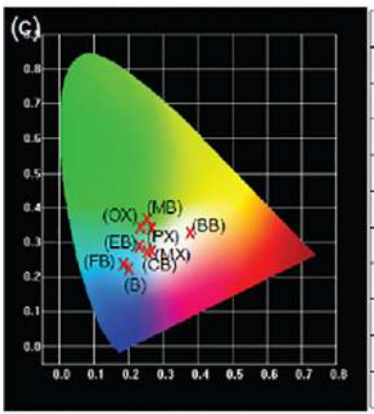

(d) CIE chromaticity diagram

Abbreviation	Compounds	CIE
B	Benzene	(0.18, 0.23)
FB	F-Benzene	(0.18, 0.20)
MB	Methylbenzene	(0.25, 0.36)
MX	m-Xylene	(0.23, 0.28)
CB	Cl-Benzene	(0.25, 0.26)
EB	Ethylbenzene	(0.23, 0.29)
OX	o-Xylene	(0.25, 0.34)
BB	Br-Benzene	(0.38, 0.31)
PX	p-Xylene	(0.23, 0.34)

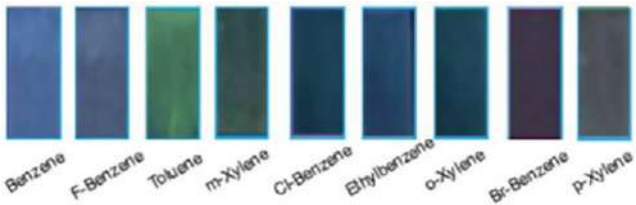

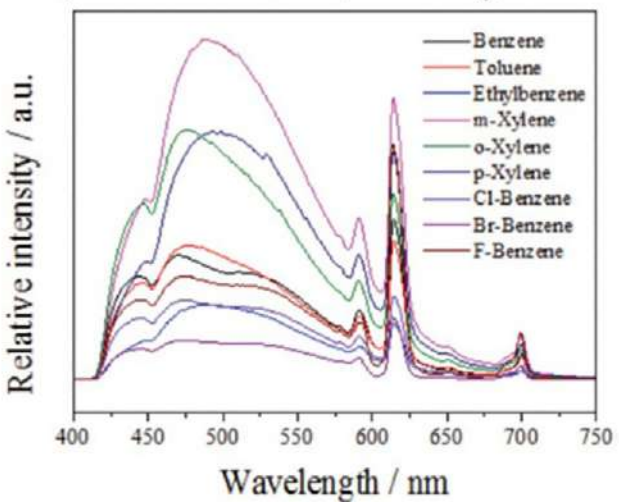

FIG. 9.19 *(Left)* (A) Corresponding images obtained under UV-light irradiation at 365 nm for In-MOF-Eu dispersed in various alkyl-benzene solvents (3 mg/3 mL). (B) CIE chromaticity diagram obtained under excitation at 360 nm. (C) Related values of the CIE chromaticity diagram. *(Right, Top)* Optical images of the In-MOF-Eu test paper obtained after immersion into solution with different types of BTEX. *(Right, Bottom)* Luminescence intensities of the In-MOF-Eu sample exposed to the vapor atmosphere of different BTEX compounds (excited at $\lambda_{ex} = 360$ nm). *(Reproduced with permission from J. Wu, B. Yan, A europium ion post-functionalized indium metal–organic framework hybrid system for fluorescence detection of aromatics. Analyst 142 (2017) 4633–4637. Copyright 2017 Royal Chemical Society.)*

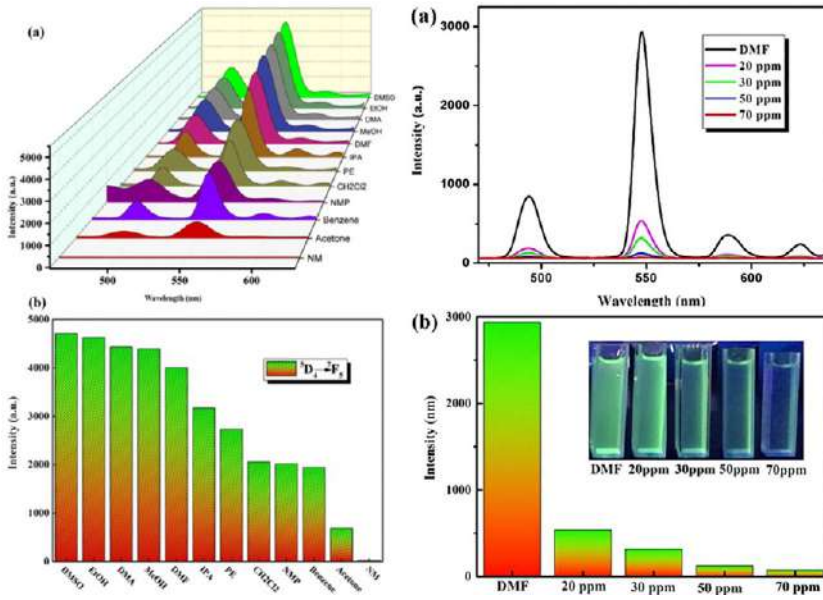

FIG. 9.20 *(Left)* (A) Luminescence spectra and (B) the $^5D_4 \rightarrow {}^7F_5$ transition intensities of Tb-MOF in various organic pure solvents when excited at 327 nm. *(Right)* (A) Luminescence spectra of Tb-MOF at different nitromethane concentrations in DMF (excited at 327 nm). (B) Corresponding emission intensities of the $^5D_4 \rightarrow {}^7F_5$ transition with color change. *(Reproduced with permission from J. Zhao, Y. Wang, W. Dong, Y. Wu, D. Li, Q. Zhang, A robust luminescent Tb (III)-MOF with Lewis basic pyridyl sites for the highly sensitive detection of metal ions and small molecules. Inorg. Chem. 55 (2016) 3265–3271. Copyright 2016 American Chemical Society.)*

9.3 Rare earth metal-organic framework hybrid materials for luminescence responsive chemical sensing of general organic pollutant molecules

Besides the general organic solvents or vapor molecules, with industrial development and population increases, the discharge of organic effluents and other chemical wastes has increased tremendously, becoming one of the greatest concerns for environmental protection and health hazard issues. Many gas phase hazardous chemicals still exist, such as the aldehydes or amines, among others, which are widely present both in outdoor and indoor air and are considered to be an important group of air pollutants due to its short- or long-term adverse health effects on human beings. Considering this, determining the level of pollutant gases in vehicles under exposure conditions is crucial for public health [95–99]. There are extensive reports on the luminescence responsive sensing of these pollutants using rare earth MOF hybrid materials as probes [100–128]. Here only a few examples are described.

Min et al. selected a La-centered MOF ($\{[La(hisp)(Hhisp)(H_2O)_2]\cdot 2H_2O\}_n$, La-MOF, H_2hisp = 5-hydroxyisophthalic acid) as the matrix for functionalization by PSM to construct a hybrid Tb@La-MOF for small organic molecule sensing. It displays particularly high selectivity and sensitivity for acetaldehyde. Fixing the excitation wavelength at 333 nm, the related emission spectra of Tb@La-MOF in diverse solvents were collected in Fig. 9.21A (top). Fig. 9.21B (top) was obtained by picking out the emission peak intensity stemming from the representative $^5D_4 \rightarrow {}^7F_5$ transition of Tb^{3+}. In Fig. 9.21 (top), it's very easy to distinguish the "wall" and "bar" of acetaldehyde from other molecules. Simply by using a UV lamp, the inset of Fig. 9.21B (top) clearly shows that acetaldehyde can be sorted out from some small organic molecules by the naked eye. As shown in Fig. 9.21 (right), the emission of Tb@La-MOF in ethanol with acetaldehyde differs a bit from the situation in the acetaldehyde

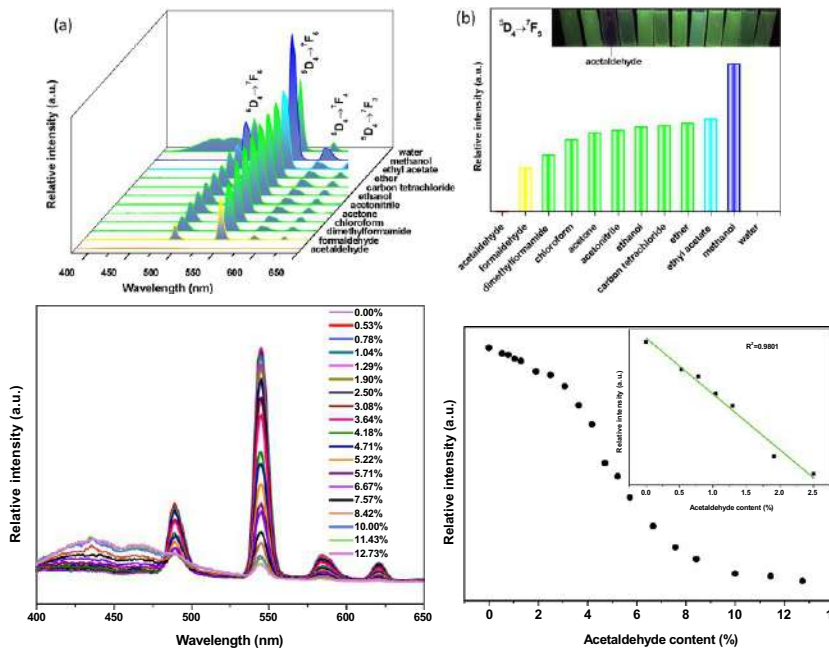

FIG. 9.21 *(Top)* (A) Emission spectra of Tb@La-MOF (3 mg) suspended in different solvents (3 mL) at an excitation wavelength of 333 nm; (B) Corresponding emission intensity histogram selected from the peak arising from $^5D_4 \rightarrow {}^7F_5$ transition of Tb^{3+}. (Inset) The photograph of Tb@La-MOF in a series of different small molecular solvents under 310 nm UV light. *(Bottom)* (A) Emission spectra of Tb@La-MOF dispersed in ethanol with different volume fractions of acetaldehyde (λ_{ex} = 334 nm); (B) Variation of the luminescence intensity of Tb@La-MOF with acetaldehyde content at 545 nm; the inset shows the corresponding linear relationship in the low concentration range (0%–2.70%). *(Reproduced with permission from J. Min, X. Qu, B. Yan, Tb post-functionalized La (III) metal organic framework hybrid probe for simple and highly sensitive detection of acetaldehyde. Sens. Actuators B 300 (2019) 126985. Copyright 2019 Elsevier.)*

aqueous solution. The linear relation expression between the content of acetaldehyde and the luminescence of Tb@La-MOF can be fitted by the equation, with R^2 of 0.9801 and the LOD of the acetaldehyde in ethanol calculated as 0.66% (volume fraction). The energy absorbed by the ligand is reduced, thereby further weakening the antenna effect, resulting in a reduction in the amount of energy transfer from the ligand to Tb^{3+}. In addition, hydrogen bonding interaction between free hydroxyl groups in Tb@La-MOF and the aldehyde group in acetaldehyde is another major factor, which might lead to the decreasing efficiency of ligand-to-metal energy transfer to a weakening of fluorescence intensity [102].

Li et al. synthesized a dual-emitting hetero-MOF and its incorporation of Eu^{3+} (Eu/Zr-MOF with linker of 2-aminoterephthalic acid). Under excitation of 365 nm, the fluorescence images and CIE chromaticity coordinate values for Eu/Zr-MOF in organic small molecule solvents are shown in Fig. 9.22 (top). Formaldehyde exhibits a prominent enhancing effect on 465-nm emission of Eu/Zr-MOF, leading to a conspicuous alteration of fluorescent color upon other small molecules. As shown in Fig. 9.22 (bottom), for two concentration series of formaldehyde (0–10 and 0–160 ppm), the ratio of fluorescent intensity at 465 and 615 nm is nearly linearly proportional to the amount of formaldehyde. This is because with formaldehyde added, the emission intensity of the

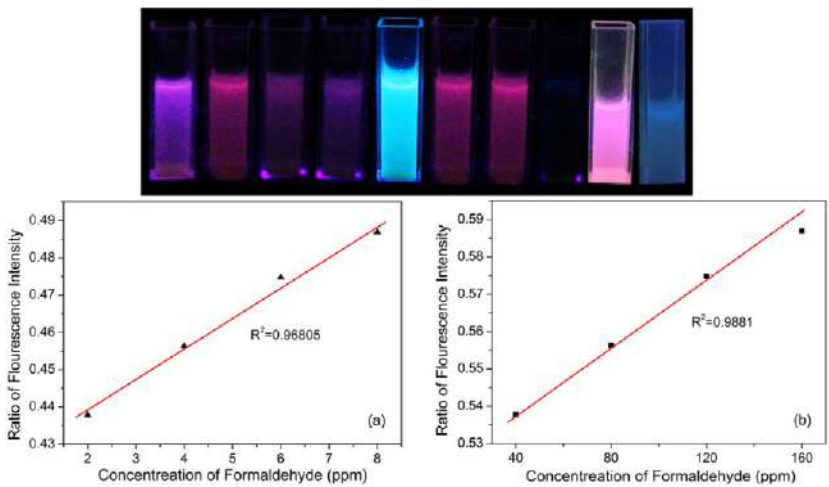

FIG. 9.22 *(Top)* Fluorescence image of Eu/Zr-MOF in organic small molecule solvent (from left: benzene, acetone, dichloromethane, cyclohexane, formaldehyde, acetonitrile, ethyl acetate, 4-butylbenzaldehyde tert-butylbenzaldehyde, DMF and deionized water, respectively). *(Bottom)* The intensity ratio of two emitting bands for Eu/Zr-MOF dependent on formaldehyde concentration. *(Reproduced with permission from C. Li, J. Huang, H. Zhu, L. Liu, Y. Feng, G. Hu, X. Yu, Dual-emitting fluorescence of Eu/Zr-MOF for ratiometric sensing formaldehyde. Sens. Actuators B 253 (2017) 275–282. Copyright 2017 Elsevier.)*

ligand-centered charger transfer band is drastically enhanced, while the trend of characteristic $^5D_0 \rightarrow {}^7F_2$ emission of Eu^{3+} at 615 nm increases slowly. The LOD of formaldehyde is 0.2 ppm. Formaldehyde is absorbed into the micropores of Eu/Zr-MOF, and part of them are involved in the reaction with amino groups in the structure of Eu/Zr-MOF. Under the photoexcitation, an adding electron transfer from the amino group containing lone pair electrons in 2-aminoterephthalate to the positively charged formaldehyde may lead to the fluorescence enhancement at 465 nm [104].

Shi et al. reported two unique 3D isostructural luminescent MOFs, $[RE(H_2DMPhIDC)_3\ (H_3DMPhIDC)]_n$ (RE = Eu, Tb; $H_3DMPhIDC$ = 2-(3,4-dimethylphenyl)-1H-imidazole-4,5-dicarboxylic acid), which show high sensitivity and quick response towards the presence of trace amounts of benzaldehyde. As shown in Fig. 9.23 (top, left), the luminescent intensity of the $^5D_0 \rightarrow {}^7F_2$ transition for the Eu^{3+} ion or of the $^5D_4 \rightarrow {}^7F_5$ transition for the Tb^{3+} ion in the suspensions heavily depends on the type of solvent: there is almost no characteristic emission of Eu^{3+} ion for benzaldehyde. As shown in Fig. 9.23 (top, right), it can be clearly seen that the fluorescence intensity gradually decreases with increasing benzaldehyde content, which indicates that both Eu-MOF and Tb-MOF are promising fluorescent probe for detecting benzaldehyde. In addition, they investigated the fluorescent quenching properties of other aromatic aldehydes. The emission spectra (Fig. 9.23; bottom, left) showed that the three aromatic aldehydes can also efficiently quench the fluorescence. Upon the addition of benzaldehyde, close contact may occur between Eu-MOF and benzaldehyde. It is most likely that the antenna effect in Eu-MOF is weakened by benzaldehyde through O—H⋯O hydrogen bonds between the imidazole dicarboxylate ligands and benzaldehyde molecules, leading to the energy transformation to reduce the LMET efficiency, leading to the quenching effect on the luminescent intensity (Fig. 9.23; bottom, right) [106].

Ma et al. synthesized RE-MOFs, $\{[RE_2(L)_2(H_2O)_2]\cdot 5H_2O\cdot 6DMAC\}_n$, [RE = Eu, Tb; H_3L = 4,4′-(((5-carboxy-1,3-phenylene)bis(azanediyl))bis(carbonyl))dibenzoic acid, DMAC = *N*,*N*′-dimethylacetamide], both of which exhibited a luminescence sensing response to 4-nitrophenol (4-NP). Taking the effect of nitro aromatic compounds on Eu-MOF as an example, it is found that 4-NP can significantly quench Eu-MOF. As the 4-NP (0.1–10.0 mM) content gradually increases, the luminescence intensity of Eu-MOF at 619 nm gradually decreases, which shows a good linear correlation between the amount of 4-NP and the relative fluorescence intensity in a low linear range of 0–1.0 mM ($R^2 = 0.9819$) with an LOD of 7.6×10^{-5} M and K_{sv} of 5352 M^{-1} (Fig. 9.24). By comparing the UV-visible absorption spectra of 4-NP with the excitation spectra of Eu-MOF and Tb-MOF, it is found that there is a significant overlap between the absorption peaks and the excitation peaks, whose quenching effect on the two MOFs may be attributed to their energy competitive absorption [123].

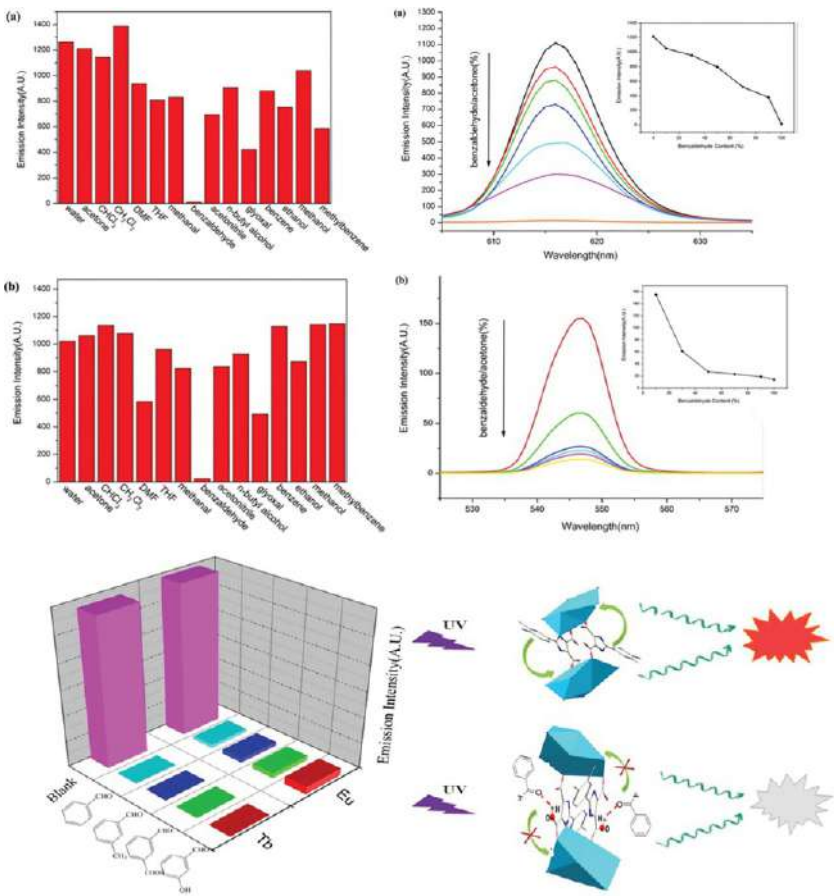

FIG. 9.23 *(Top, Left)* (A) Photoluminescence intensity of the $^5D_0 \rightarrow {}^7F_2$ transition of Eu-MOF dispersed in different solvents, excited at 345 nm. (B) The $^5D_4 \rightarrow {}^7F_5$ transition intensity of Tb-MOF dispersed in different solvents, excited at 332 nm. *(Top, Right)* (A) Emissive response spectra of Eu-MOF for benzaldehyde in acetone solution with different benzaldehyde volume concentrations (inset is a graph of the fluorescence intensity of Eu-MOF, acetone as a function of benzaldehyde content). (B) Emissive response spectra of Tb-MOF for benzaldehyde in acetone solution with different benzaldehyde volume concentrations (inset is a graph of the fluorescence intensity of Tb-MOF, acetone as a function of benzaldehyde content). *(Bottom, Left)* View of the fluorescence intensity of Eu-MOF and Tb-MOF with four different aromatic analytes. *(Bottom, Right)* Luminescence quenching effect of Eu-MOF induced by benzaldehyde through a reduction of the antenna efficiency inside Eu-MOF, which may be due to the H-bond interactions between benzaldehyde and the organic ligands. *(Reproduced with permission from B. Shi, Y. Zhong, L. Guo, G. Li, Two dimethylphenyl imidazole dicarboxylate-based lanthanide metal-organic frameworks for luminescence sensing of benzaldehyde. Dalton Trans. 44 (2015) 4362–4369. Copyright 2015 Royal Chemical Society.)*

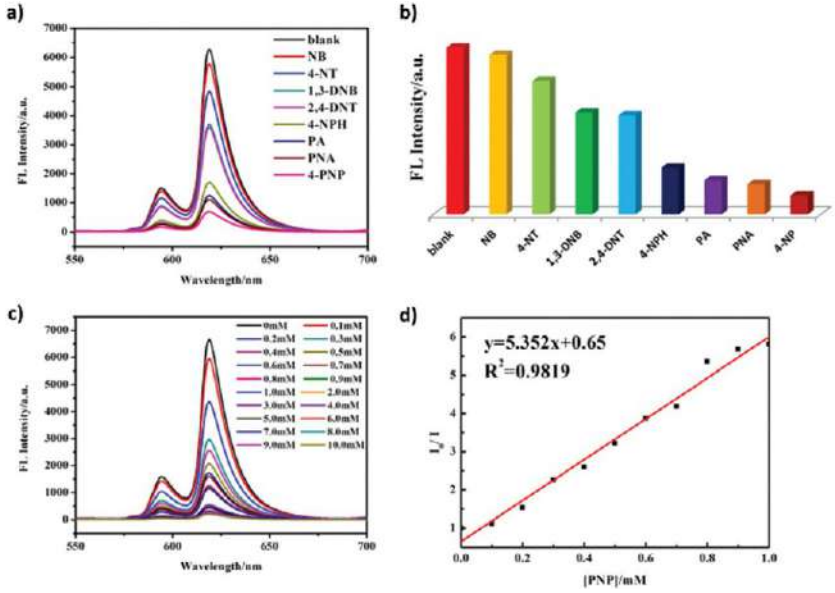

FIG. 9.24 (A) Luminescence intensity at 619 nm of Eu-MOF dispersed in aqueous solutions of different nitro aromatic compounds, when excited at 394 nm. (B) Nitro aromatic compound selectivity of Eu-MOF (I_0/I) in H_2O. (C) Luminescence responses of Eu-MOF towards different concentrations of 4-NP (0–1.0 mM) in H_2O ($\lambda_{ex} = 394$ nm). (D) Stern-Volmer plot of I_0/I versus increasing concentrations of 4-NP. *(Reproduced with permission from J. Ma, W. Liu, Effective luminescence sensing of Fe3 +, Cr2O72 −, MnO4 − and 4-nitrophenol by lanthanide metal–organic frameworks with a new topology type. Dalton Trans. 48 (2019) 12287–12295. Copyright 2019 Royal Chemical Society.)*

References

[1] X. Wang, O.S. Wolfbeis, Optical methods for sensing and imaging oxygen: materials, spectroscopies and applications, Chem. Soc. Rev. 43 (2014) 3666–3761.

[2] Z. Dou, J. Yu, Y. Cui, Y. Yang, Z. Wang, D. Yang, G. Qian, Luminescent metal-organic framework films as highly sensitive and fast-response oxygen sensors, J. Am. Chem. Soc. 136 (2014) 5527–5530.

[3] R. Lin, S. Liu, J. Ye, X. Li, J. Zhang, Optical methods for sensing and imaging oxygen: materials, spectroscopies and applications, Adv. Sci. 3 (2016) 1500434.

[4] Y. Xu, S. Liu, J. Liu, L. Zhang, D. Chen, J. Chen, Y. Ma, J. Zhang, Z. Dai, X. Zou, In situ enzyme immobilization with oxygen-sensitive luminescent metal-organic frameworks to realize "all-in-one" multifunctions, Chem. A Eur. J. 25 (2019) 5463–5471.

[5] J. Demel, P. Kubat, F. Millange, J. Marrot, I. Císarova, K. Lang, Lanthanide-porphyrin hybrids: from layered structures to metal – organic frameworks with photophysical properties, Inorg. Chem. 52 (2013) 2779–2786.

[6] X. Xu, B. Yan, Nanoscale LnMOF-functionalized nonwoven fiber protected by polydimethysiloxane coating layer as highly sensitive ratiometric oxygen sensor, J. Mater. Chem. C 4 (2016) 8514–8521.

[7] J. Ye, J. Lin, Z. Mo, C. He, H. Zhou, J. Zhang, X. Chen, Mixed-lanthanide porous coordination polymers showing range tunable ratiometric luminescence for O_2 sensing, Inorg. Chem. 56 (2017) 4238–4243.
[8] H. Weng, X. Xu, B. Yan, Novel multicomponent photofunctional nanohybrids for ratio-dependent oxygen sensing, J. Colloid Interface Sci. 502 (2017) 8–15.
[9] X. Qiao, Z. Ma, L. Si, W. Ding, G. Xu, Doping metal-organic framework with a series of europium-antenna cations: obviously improved spectral response for O_2 gas via long-range energy rollback procedure, Sens. Actuators B Chem. 299 (2019), 126978.
[10] T. Xia, L. Jiang, J. Zhang, Y. Wan, Y. Yang, J. Gan, Y. Cui, Z. Yang, G. Qian, A fluorometric metal-organic framework oxygen sensor: from sensitive powder to portable optical fiber device, Microporous Mesoporous Mater. 305 (2020), 110396.
[11] G.A. Meshram, V.D. Patil, Chemoselective synthesis of 1,1-diacetates from aldehydes using anhydrous Cobalt(II) bromide under solvent-free conditions, Synth. Commun. 40 (2010) 442–449.
[12] S. Okur, M. Kus, F. Ozel, V. Aybek, M. Yilmaz, Humidity adsorption kinetics of calix[4]arene derivatives measured using QCM technique, Talanta 81 (2010) 248–251.
[13] A. Pinkert, K.N. Marsh, S. Pang, Reflections on the solubility of cellulose, Ind. Eng. Chem. Res. 49 (2010) 11121–11130.
[14] L.V. Meyer, F. Schönfeld, A. Zurawski, M. Mai, C. Feldmann, K. Müller-Buschbaum, A blue luminescent MOF as a rapid turn-off/turn-on detector for H_2O, O_2 and CH_2Cl_2, MeCN: $3\,\infty[Ce(Im)_3ImH]\cdot ImH$, Dalton Trans. 44 (2015) 4070–4079.
[15] Y. Yu, J. Ma, Y. Dong, Luminescent humidity sensors based on porous Ln^{3+}-MOFs, CrstEngComm 14 (2012) 7157–7160.
[16] S. Mohapatra, B. Rajeswaran, A. Chakraborty, A. Sundaresan, T.K. Maji, Bimodal magneto-luminescent dysprosium (DyIII)-potassium (KI)-oxalate framework: magnetic switchability with high anisotropic barrier and solvent sensing, Chem. Mater. 25 (2013) 1673–1679.
[17] U. Huizi-Rayo, A. Zabala-Lekuona, A. Terenzi, C.M. Cruz, J.M. Cuerv, A. Rodrıguz-Dieguez, J. Angel Garcıa, J.M. Seco, E.S. Sebastian, J. Ceped, Influence of thermally induced structural transformations on the magnetic and luminescence properties of tartrate-based chiral lanthanide organic-frameworks, J. Mater. Chem. C 8 (2020) 8243–8256.
[18] J. Wu, B. Yan, A dual-emission probe to detect moisture and water in organic solvents based on green-Tb^{3+} post-coordinated metal-organic frameworks with red carbon dots, Dalton Trans. 46 (2017) 7098–7105.
[19] J.M. Stangl, D. Dietrich, A.E. Sedykh, C. Janiak, K. Muller-Buschbaum, Luminescent MOF polymer mixed matrix membranes for humidity sensing in real status analysis, J. Mater. Chem. C 6 (2018) 9248–9257.
[20] H. Li, W. Han, R. Lv, A. Zhai, X. Li, W. Gu, X. Liu, Dual-function mixed-lanthanide metal – organic framework for ratiometric water detection in bioethanol and temperature Sensing, Anal. Chem. 91 (2019) 2148–2154.
[21] Y. Gao, M. Hilbers, H. Zhang, S. Tanase, Designed synthesis of multiluminescent materials using lanthanide metal-organic frameworks and carbon dots as building-blocks, Eur. J. Inorg. Chem. (2019) 3925–3932.
[22] Z. Wei, L. Ren, X. Xiao, Q. Zhang, J. Huang, R. Liu, S. Zhao, W. Xu, Biomimetic mineralization of nanoscale lanthanide metal-organic frameworks with thermo-sensitive polymer as organic ligands for solvent recognition and water detection, J. Solid State Chem. 277 (2019) 594–601.
[23] T. Wehner, M.T. Seuffert, J.R. Sorg, M. Schneider, K. Mandel, G. Sextl, K. Muller-Buschbaum, Composite materials combining multiple luminescent MOFs and superparamagnetic microparticles for ratiometric water detection, J. Mater. Chem. C 5 (2017) 10133–10142.

[24] J. Zhao, X. Qu, B. Yan, Lanthanide coordination polymers of viologen carboxylic acid: crystal structures and luminescence response tuning, J. Photochem. Photobiol. A Chem. 390 (2020), 112296.
[25] P. Majee, P. Daga, D.K. Singha, D. Saha, P. Mahata, S.K. Mondal, A lanthanide doped metal-organic framework demonstrated as naked eye detector of a trace of water in organic solvents including alcohols by monitoring the turn-on of luminescence, J. Photochem. Photobiol. A Chem. 402 (2020), 112830.
[26] M. Zhang, D. Wang, Z. Geng, P. Li, Z. Sun, W. Xu, Effect of heat shock protein 90 against ROS-induced phospholipid oxidation, Food Chem. 240 (2018) 642–647.
[27] K. Chang, Z. Liu, X. Fang, H. Chen, X. Men, Y. Yuan, K. Sun, X. Zhang, Z. Yuan, C. Wu, Enhanced phototherapy by nanoparticle-enzyme via generation and photolysis of hydrogen peroxide, Nano Lett. 17 (2017) 4323–4329.
[28] P. Jia, Y. Zhou, X. Zhang, Y. Zhang, H. Dai, Cyanobacterium removal and control of algal organic matter (AOM) release by UV/H_2O_2 pre-oxidation enhanced Fe(II) coagulation, Water Res. 131 (2018) 122–130.
[29] C.E. Paulsen, K.S. Carroll, Cysteine-mediated redox signaling: chemistry, biology, and tools for discovery, Chem. Rev. 113 (2013) 4633–4679.
[30] Y. Nosaka, A.Y. Nosaka, Generation and detection of reactive oxygen species in photocatalysis, Chem. Rev. 117 (2017) 11302–11336.
[31] H. Tan, C. Ma, Q. Li, L. Wang, F. Xu, S. Chen, Y. Song, Functionalized lanthanide coordination polymer nanoparticles for selective sensing of hydrogen peroxide in biological fluids, Analyst 139 (2014) 5516–5522.
[32] Z. Qi, L. Wang, Q. You, Y. Chen, PA-Tb-Cu MOF as luminescent nanoenzyme for catalytic assay of hydrogen peroxide, Biosens. Bioelectron. 96 (2017) 227–232.
[33] X. Zheng, R. Fan, K. Xing, A. Wang, X. Du, P. Wang, Y. Yang, Dual-emissive nanocomposites based on Eu(III) functionalized Cu(I)-coordination polymer for ratiometric fluorescent sensing and integrating Boolean logic operations, J. Mater. Chem. C 6 (2018) 6229–6239.
[34] Y. Cui, F. Chen, X. Yin, A ratiometric fluorescence platform based on boric-acid-functional Eu-MOF for sensitive detection of H_2O_2 and glucose, Biosens. Bioelectron. 135 (2019) 208–215.
[35] H. Kimura, Hydrogen sulfide: its production and functions, Exp. Physiol. 96 (2011) 833–835.
[36] Y. Wen, H. Wang, S. Kho, S. Rinkiko, X. Sheng, H. Shen, Y. Zhu, Hydrogen sulfide protects HUVECs against hydrogen peroxide induced mitochondrial dysfunction and oxidative stress, PLoS One 8 (2013), e53147.
[37] P. Wang, G. Zhang, T. Wondimu, B. Ross, R. Wang, Hydrogen sulfide and asthma, Exp. Physiol. 96 (2011) 847–852.
[38] Y. Chen, C. Zhu, Z. Yang, J. Chen, Y. He, Y. Jiao, W. He, L. Qiu, J. Cen, Z. Guo, A ratiometric fluorescent probe for rapid detection of hydrogen sulfide in mitochondria, Angew. Chem. Int. Ed. 52 (2013) 1688–1691.
[39] X. Zhang, Q. Hu, T. Xia, J. Zhang, Y. Yang, Y. Cui, B. Chen, G. Qian, Turn-on and ratiometric luminescent sensing of hydrogen sulfide based on metal – organic frameworks, ACS Appl. Mater. Interfaces 8 (2016) 32259–32265.
[40] A. Buragohain, S. Biswas, Cerium-based azide- and nitro-functionalized UiO-66 frameworks as turn-on fluorescent probes for the sensing of hydrogen sulphide, CrstEngComm 18 (2016) 4374–4381.
[41] X. Zheng, R. Fan, Y. Song, A. Wang, K. Xing, X. Du, P. Wang, Y. Yang, A highly sensitive turn-on ratiometric luminescent probe based on postsynthetic modification of Tb^{3+}@Cu-MOF for H_2S detection, J. Mater. Chem. C 5 (2017) 9943–9951.

[42] J. Gao, Q. Li, C. Wang, H. Tan, Copper (II)-mediated fluorescence of lanthanide coordination polymers doped with carbon dots for ratiometric detection of hydrogen sulfide, Sens. Actuators B 253 (2017) 27–33.
[43] L. Chen, H. Tan, F. Xu, L. Wang, Terbium (III) coordination polymer-copper (II) compound as fluorescent probe for time-resolved fluorescence 'turn-on' detection of hydrogen sulfide, Luminescence 33 (2018) 161–167.
[44] X. Zhang, L. Fang, K. Jiang, H. He, Y. Yang, Y. Cui, B. Li, G. Qian, Nanoscale fluorescent metal-organic framework composites as a logic platform for potential diagnosis of asthma, Biosens. Bioelectron. 130 (2019) 65–72.
[45] J. Zhang, F. Liu, J. Gan, Y. Cui, B. Li, Y. Yang, G. Qian, Metal-organic framework film for fluorescence turn-on H_2S gas sensing and anti-counterfeiting patterns, Sci. China Mater. 62 (2019) 1445–1453.
[46] Z. Wang, X. Wang, J. Li, W. Li, G. Li, Eu^{3+}/TFA functionalized MOF as luminescent enhancement platform: a ratiometric luminescent sensor for hydrogen sulfide in aqueous solution, J. Inorg. Organomet. Polym. Mater. 29 (2019) 2124–2132.
[47] Y. Wang, Q. Mu, G. Wang, Z. Zhou, Sens. Actuators B Chem. 145 (2010) 847–853.
[48] X. Liu, N. Chen, B. Han, X. Xiao, G. Chen, I. Djerdj, Y. Wang, Nanoscale 7 (2015) 14872–14880.
[49] J. Wang, P. Yang, X. Wei, ACS Appl. Mater. Interfaces 7 (2015) 3816–3824.
[50] C. Chen, L. Cai, B. Tan, Y. Zhang, X. Yang, J. Zhang, Ammonia detection by using flexible Lewis acidic sites in luminescent porous frameworks constructed from a bipyridinium derivative, Chem. Commun. 51 (2015) 8189–8192.
[51] I.A. Ibarra, T.W. Hesterberg, J. Chang, J.W. Yoon, B.J. Holliday, S.M. Humphrey, Molecular sensing and discrimination by a luminescent terbium-phosphine oxide coordination material, Chem. Commun. 49 (2013) 7156–7158.
[52] J. Hao, B. Yan, Simultaneous determination of indoor ammonia pollution and its biological metabolite in human body by use of a recyclable nanocrystalline lanthanide functionalized MOF, Nanoscale 8 (2016) 2881–2886.
[53] D. Wang, J. Liu, Z. Liu, A chemically stable europium metal-organic framework for bifunctional chemical sensor and recyclable on-off-on vapor response, J. Solid State Chem. 251 (2017) 243–247.
[54] Z. Li, W. Cai, X. Yang, A. Zhou, Y. Zhu, H. Wang, X. Zhou, K. Xiong, Q. Zhang, Y. Gai, Cationic metal – organic frameworks based on linear zwitterionic ligands for $Cr_2O_7^{2-}$ and ammonia sensing, Cryst. Growth Des. 20 (2020) 3466–3473.
[55] M.E. Jenkin, S.R. Utembe, R.G. Derwent, Modelling the impact of elevated primary NO_2 and HONO emissions on regional scale oxidant formation in the UK, Atmos. Environ. 42 (2008) 323–336.
[56] T.C. Brueggemann, M.D. Przybylski, S.P. Balaji, F.J. Keil, Theoretical investigation of the mechanism of the selective catalytic reduction of nitrogen dioxide with ammonia on H-form zeolites and the role of nitric and nitrous acids as intermediates, J. Phys. Chem. C 114 (2010) 6567–6587.
[57] G.W. Peterson, J.J. Mahle, J.B. DeCoste, W.O. Gordon, J.A. Rossin, Extraordinary NO_2 removal by the metal-organic framework Uio-66-NH_2, Angew. Chem. Int. Ed. 55 (2016) 6235–6238.
[58] S. Bhattacharyya, R. Han, J.N. Joshi, G. Zhu, R.P. Lively, K.S. Walton, D.S. Sholl, S. Nair, Stability of zeolitic imidazolate frameworks in NO_2, J. Phys. Chem. C 123 (2019) 2336–2346.
[59] D.F. Sava Gallis, D.J. Vogel, G.A. Vincent, J.M. Rimsza, T.M. Nenof, NO_x adsorption and optical detection in rare earth metal – organic frameworks, ACS Appl. Mater. Interfaces 11 (2019) 43270–43277.

[60] A. Gamonal, C. Sun, A.L. Mariano, E. Fernandez-Bartolome, E. Guerrero-SanVicente, B. Vlaisavljevich, J.R. Castells-Gil, C. Marti-Gastaldo, R. Poloni, R. Wannemacher, J. Cabanillas-Gonzalez, J.S. Costa, Divergent adsorption-dependent luminescence of amino-functionalized lanthanide metal – organic frameworks for highly sensitive NO_2 sensors, J. Phys. Chem. Lett. 11 (2020) 3362–3368.

[61] F.G. Moscoso, J. Almeida, A. Sousaraei, T. Lopes-Costa, A.M.G. Silva, J. Cabanillas-Gonzalez, L. Cunha-Silva, J.M. Pedrosa, Luminescent MOF crystals embedded in PMMA/PDMS transparent films as effective NO_2 gas sensors, Mol. Syst. Des. Eng. 5 (2020) 1048–1056.

[62] X. Wang, H. Jin, C. Tang, J. Du, Significance of endogenous sulphur-containing gases in the cardiovascular system, Clin. Exp. Pharmacol. Physiol. 37 (2010) 745–752.

[63] X. Pan, Sulfur oxides: sources, exposures and health effects, Encycl. Environ. Health 3 (2011) 290–296.

[64] B. Yuliarto, M.F. Ramadhani, N.L.W. Nugraha, K.A. Septiani, Hamam, Enhancement of SO_2 gas sensing performance using ZnO nanorod thin films: the role of deposition time, J. Mater. Sci. 52 (2016) 4543–4554.

[65] L. Wang, Y. Chen, A reaction-triggered luminescent Ce^{4+}/Tb^{3+} MOF probe for the detection of SO_2 and its derivatives, Chem. Commun. 56 (2020) 6965–6968.

[66] J. Zhang, T. Xia, D. Zhao, Y. Cui, Y. Yang, G. Qian, In situ secondary growth of Eu(III)-organic framework film for fluorescence sensing of sulfur dioxide, Sens. Actuators B 260 (2018) 63–69.

[67] D.T. McQuade, A.E. Pullen, T.M. Swager, Conjugated polymer-based chemical sensors, Chem. Rev. 100 (2000) 2537–2574.

[68] J. Wang, M. Li, D. Li, A dynamic luminescent and entangled MOF as a qualitative sensor for volatile organic solvents and a quantitative monitor for acetonitrile vapour, Chem. Sci. 4 (2013) 1793–1801.

[69] F. Yi, Y. Wang, J. Li, D. Wu, Y. Lan, Z. Sun, An ultrastable porous metal-organic framework luminescent switch towards aromatic compounds, Mater. Horiz. 2 (2015) 245–251.

[70] Y. Li, H. Song, Q. Chen, K. Liu, F. Zhao, W. Ruan, Z. Chang, Two coordination polymers with enhanced ligand-centered luminescence and assembly imparted sensing ability for acetone, J. Mater. Chem. A 2 (2014) 9469–9473.

[71] M. Righettoni, A. Tricoli, S.E. Pratsinis, Si:WO_3 sensors for highly selective detection of acetone for easy diagnosis of diabetes by breath analysis, Anal. Chem. 82 (2010) 3581–3587.

[72] Y. Xiao, L. Wang, Y. Cui, B. Chen, F. Zapata, G. Qian, Molecular sensing with lanthanide luminescence in a 3D porous metal-organic framework, J. Alloys Compd. 484 (2009) 601–604.

[73] W. Yang, J. Feng, H. Zhang, Facile and rapid fabrication of nanostructured lanthanide coordination polymers as selective luminescent probes in aqueous solution, J. Mater. Chem. 22 (2012) 6819–6823.

[74] S. Dang, X. Min, W. Yang, F. Yi, H. You, Z. Sun, Lanthanide metal-organic frameworks showing luminescence in the visible and near-infrared regions with potential for acetone sensing, Chem. A Eur. J. 19 (2013) 17172–17179.

[75] Z. Hao, G. Yang, X. Song, M. Zhu, X. Meng, S. Zhao, S. Song, H. Zhang, A europium(III) based metal-organic framework: bifunctional properties related to sensing and electronic conductivity, J. Mater. Chem. A 2 (2014) 237–244.

[76] S. Wang, T. Cao, H. Yan, Y. Li, J. Lu, R. Ma, D. Li, J. Dou, J. Bai, Functionalization of microporous lanthanide-based metal – organic frameworks by dicarboxylate ligands with methyl-substituted thieno[2,3-b]thiophene groups: sensing activities and magnetic properties, Inorg. Chem. 55 (2016) 5139–5151.

[77] Y. Wang, F. Zhang, Z. Fang, M. Yu, Y. Yang, K. Wong, Tb(III) postsynthetic functional coordination polymer coatings on ZnO micronanoarrays and their application in small molecule sensing, J. Mater. Chem. C 4 (2016) 8466–8472.
[78] Q. Liu, J. Yang, F. Guo, L. Jin, W. Sun, Facile fabrication of MIL-103(Eu) porous coordination polymer nanostructures and their sorption and sensing properties, Dalton Trans. 45 (2016) 5841–5847.
[79] K. Wang, Y. Ma, H. Tang, Lanthanide coordination polymers as luminescent for the selective and recyclable detection of acetone, Crystals 7 (2017) 199.
[80] M. Han, S. Wang, Z. Li, Z. Zhou, D. Li, L. Ma, Y. Wang, Significant centre metallic effects on the sensing properties of two isostructural lanthanide metal-organic frameworks, Inorg. Chem. Commun. 79 (2017) 12–16.
[81] Q. Zhang, J. Wang, A.M. Kirillov, W. Dou, C. Xu, C. Xu, L. Yang, R. Fang, W. Liu, Multifunctional Ln – MOF luminescent probe for efficient sensing of Fe^{3+}, Ce^{3+}, and acetone, ACS Appl. Mater. Interfaces 10 (2018) 23976–23986.
[82] F. Zhao, X. Guo, Z. Dong, Z. Liu, Y. Wang, 3D LnIII-MOFs: slow magnetic relaxation and highly sensitive luminescence detection of Fe^{3+} and ketones, Dalton Trans. 47 (2018) 8972–8982.
[83] Z. Sun, H. Li, G. Sun, J. Guo, Y. Ma, L. Li, Design and construction of lanthanide metal-organic frameworks through mixed-ligand strategy: sensing property of acetone and Cu^{2+}, Inorg. Chim. Acta 469 (2018) 51–56.
[84] J. Zhang, S. Bo Peh, J. Wang, Y. Du, S. Xi, J. Dong, A. Karmakar, Y. Ying, Y. Wang, D. Zhao, Hybrid MOF-808-Tb nanospheres for highly sensitive and selective detection of acetone vapor and Fe^{3+} in aqueous solution, Chem. Commun. 55 (2019) 4727–4730.
[85] X. Han, J. Yang, Y. Liu, J. Ma, Nine coordination polymers assembled with a novel resorcin [4]arene tetracarboxylic acid: selective luminescent sensing of acetone and Fe^{3+} ion, Dyes Pigments 160 (2019) 492–500.
[86] C. Yang, C. Jiang, M. Zhang, X. Chen, P. Zou, R. Yang, H. Rao, G. Wang, A multifunctional Eu-based coordination polymer luminescent sensor for highly sensitive and selective detection of Fe^{3+} and acetone, Polyhedron 175 (2020), 114216.
[87] J. Huang, P. Wu, Controlled assembly of luminescent lanthanide-organic frameworks via post-treatment of 3D-printed objects, Nano-Micro Lett. 13 (2021) 15.
[88] J. Zhou, W. Shi, H. Li, H. Li, P. Cheng, Experimental studies and mechanism analysis of high-sensitivity luminescent sensing of pollutional small molecules and ions in Ln_4O_4 cluster based microporous metal – organic frameworks, J. Phys. Chem. C 118 (2014) 416–426 (Benzene acetone).
[89] J. Hao, B. Yan, Ln^{3+} post-functionalized metal-organic frameworks for color tunable emission and highly sensitive sensing of toxic anions and small molecules, New J. Chem. 40 (2016) 4654–4661.
[90] H. Zheng, X. Lian, S. Qin, B. Yan, Lanthanide hybrids of covalently-coordination cooperative post-functionalized metal-organic frameworks for luminescence tuning and highly selectively sensing of tetrahydrofuran, Dalton Trans. 47 (2018) 6210–6217.
[91] X. Lian, B. Yan, A postsynthetic modified MOF hybrid as heterogeneous photocatalyst for α-phenethyl alcohol and reusable fluorescence sensor, Inorg. Chem. 55 (2016) 11831–11838.
[92] D. Chen, N. Zhang, C. Liu, M. Du, Template-directed synthesis of a luminescent Tb-MOF material for highly selective Fe^{3+} and Al^{3+} ion detection and VOC vapor sensing, J. Mater. Chem. C 5 (2017) 2311–2317.

[93] J. Wu, B. Yan, A europium ion post-functionalized indium metal-organic framework hybrid system for fluorescence detection of aromatics, Analyst 142 (2017) 4633–4637.
[94] J. Zhao, Y. Wang, W. Dong, Y. Wu, D. Li, Q. Zhang, A robust luminescent Tb(III)-MOF with Lewis basic pyridyl sites for the highly sensitive detection of metal ions and small molecules, Inorg. Chem. 55 (2016) 3265–3271.
[95] N.A. Rakow, K.S. Suslick, A colorimetric sensor array for odour visualization, Nature 406 (2000) 710–713.
[96] M. Riediker, R. Williams, R. Devlin, T. Griggs, P. Bromberg, Exposure to particulate matter, volatile organic compounds, and other air pollutants inside patrol cars, Environ. Sci. Technol. 37 (2003) 2084–2093.
[97] M. Mandalakis, E.G. Stephanou, Y. Horii, K. Kannan, Emerging contaminants in car interiors: evaluating the impact of airborne PBDEs and PBDD/Fs, Environ. Sci. Technol. 42 (2008) 6431–6436.
[98] R. Benigni, L. Passerini, Carcinogenicity of the aromatic amines: from structure-activity relationships to mechanisms of action and risk assessment, Mutat. Res. 511 (2002) 191–206.
[99] S.A. Lawrence, Amines: Synthesis, Properties and Applications, Cambridge University Press, Cambridge, 2004.
[100] P. Wu, J. Wang, Y. Li, C. He, Z. Xie, C. Duan, Luminescent sensing and catalytic performances of a multifunctional lanthanide-organic framework comprising a triphenylamine moiety, Adv. Funct. Mater. 21 (2011) 2788–2794.
[101] X. Xu, B. Yan, Eu(III)-functionalized ZnO@MOF heterostructures: integration of preconcentration and efficient charge transfer for the fabrication of a ppb-level sensing platform for volatile aldehyde gases in vehicles, J. Mater. Chem. A 5 (2017) 2215–2223.
[102] J. Min, X. Qu, B. Yan, Tb post-functionalized La (III) metal organic framework hybrid probe for simple and highly sensitive detection of acetaldehyde, Sens. Actuators B 300 (2019), 126985.
[103] Y. Wang, G. Zhang, F. Zhang, T. Chu, Y. Yang, A novel lanthanide MOF thin film: the highly performance self-calibrating luminescent sensor for detecting formaldehyde as an illegal preservative in aquatic product, Sens. Actuators B 251 (2017) 667–673.
[104] C. Li, J. Huang, H. Zhu, L. Liu, Y. Feng, G. Hu, X. Yu, Dual-emitting fluorescence of Eu/Zr-MOF for ratiometric sensing formaldehyde, Sens. Actuators B 253 (2017) 275–282.
[105] Y. Wang, Y. Wu, C. Zhou, L. Cao, H. Yang, A new bimetallic lanthanide metal-organic framework as a self-calibrating sensor for formaldehyde, Inorg. Chem. Commun. 89 (2018) 5–9.
[106] B. Shi, Y. Zhong, L. Guo, G. Li, Two dimethylphenyl imidazole dicarboxylate-based lanthanide metal-organic frameworks for luminescence sensing of benzaldehyde, Dalton Trans. 44 (2015) 4362–4369.
[107] P. Du, W. Gu, X. Liu, Multifunctional three-dimensional europium metal – organic framework for luminescence sensing of benzaldehyde and Cu^{2+} and selective capture of dye molecules, Inorg. Chem. 55 (2016) 7826–7828.
[108] Z. Sun, M. Yang, Y. Ma, L. Li, Multi-responsive luminescent sensors based on two-dimensional lanthanide – metal organic frameworks for highly selective and sensitive detection of Cr(III) and Cr(VI) ions and benzaldehyde, Cryst. Growth Des. 17 (2017) 4326–4335.
[109] Y. Kang, X. Zhen, L. Jin, A microscale multi-functional metal-organic framework as a fluorescence chemosensor for Fe(III), Al(III) and 2-hydroxy-1-naphthaldehyde, J. Colloid Interface Sci. 471 (2016) 1–6.

[110] H. Huang, W. Gao, X. Zhang, A. Zhou, J. Liu, 3D LnIII-MOFs: displaying slow magnetic relaxation and highly sensitive luminescence sensing of alkylamines, CrstEngComm 21 (2019) 694–702.
[111] K. Xu, F. Wang, S. Huang, Z. Yu, J. Zhang, J. Yu, H. Gao, Y. Fu, X. Li, Y. Zhao, Selective fluorescence detection of anilines and Fe^{3+} ions by two lanthanide metal-organic frameworks, RSC Adv. 6 (2016) 91741–91747.
[112] G. Chakraborty, P. Das, S.K. Mandal, Strategic construction of highly stable metal-organic frameworks combining both semi-rigid tetrapodal and rigid ditopic linkers: selective and ultrafast sensing of 4-nitroaniline in water, ACS Appl. Mater. Interfaces 10 (2018) 42406–42416.
[113] Y. Shi, W. Wang, G. Tang, Y. Zhang, M. Li, Z. Wu, Robust lanthanide metal-organic frameworks with highly sensitive sensing of aniline and slow magnetization relaxation behaviors, Polyhedron 153 (2018) 122–127.
[114] Y. Pu, Z. Yu, F. Wang, Y. Fu, T. Yan, H. Cheng, Selective fluorescence sensing of p-nitroaniline and Fe^{3+} ions by luminescent Eu-based metal-organic framework, Sensor Rev. 39 (2019) 149–161.
[115] M. Shen, Z. Wei, L. Xu, B. Liu, H. Jiao, A mixed matrix Eu-4,4′-biphenyldicarboxylate coordination polymer film as a fluorescence turn-off sensor to aniline vapor, J. Solid State Chem. 269 (2019) 87–93.
[116] J. Liang, M.Y.B. Zulkifli, S. Choy, Y. Li, M. Gao, B. Kong, J. Yun, K. Liang, Metal – organic framework – plant nanobiohybrids as living sensors for on-site environmental pollutant detection, Environ. Sci. Technol. 54 (2020) 11356–11364.
[117] Y. Hidalgo-Rosa, M.A. Treto-Suárez, E. Schott, X. Zarate, D. Páez-Hernández, Sensing mechanism elucidation of a europium(III) metal-organic framework selective to aniline: a theoretical insight by means of multiconfigurational calculations, J. Comput. Chem. 41 (2020) 1956–1963.
[118] X. Zhao, Y. Shi, M. Pang, W. Zhang, Y. Li, Facile fabrication of Eu-1,4-NDC-fcu-MOF particles for sensing of benzidine, Main Group Chem. 19 (2020) 117–124.
[119] L. Cao, F. Shi, W. Zhang, S. Zang, T.C.W. Mai, Selective sensing of Fe^{3+} and Al^{3+} ions and detection of 2,4,6-trinitrophenol by a water-stable terbium-based metal-organic framework, Chem. A Eur. J. 21 (2015) 15705–15712.
[120] Y. Tao, P. Zhang, J. Liu, X. Chen, X. Guo, H. Jin, J. Chai, L. Wang, Y. Fan, Multi-responsive luminescent sensor based on three dimensional lanthanide metal-organic framework, New J. Chem. 42 (2018) 19485–19493.
[121] Y. Liu, J. Ma, C. Xu, Y. Yang, M. Xia, H. Jiang, W. Liu, A water-stable lanthanide coordination polymer as a multiresponsive luminescent sensor for Fe^{3+}, Cr(VI) and 4-nitrophenol, Dalton Trans. 47 (2018) 13543–13549.
[122] X. Xin, M. Zhang, S. Ji, H. Dong, L. Zhang, A luminescent ytterbium(III)-organic framework for highly selective sensing of 2,4,6-trinitrophenol, J. Solid State Chem. 262 (2018) 186–190.
[123] J. Ma, W. Liu, Effective luminescence sensing of Fe^{3+}, $Cr_2O_7^{2-}$, MnO_4^- and 4-nitrophenol by lanthanide metal-organic frameworks with a new topology type, Dalton Trans. 48 (2019) 12287–12295.
[124] M. Jiang, L. Yu, Y. Zhou, J. Jia, X. Si, W. Dong, Z. Tian, J. Zhao, D. Li, A novel d-f heterometallic CdII-EuIII metal-organic framework as a sensitive luminescent sensor for the dual detection of ronidazole and 4-nitrophenol, Z. Anorg. Allg. Chem. 646 (2020) 268–274.
[125] J. Zhao, P. Liu, Z. Dong, Z. Liu, Y. Wang, Eu(III)-organic framework as a multi-responsive photoluminescence sensor for efficient detection of 1-naphthol, Fe^{3+} and MnO_4^- in water, Inorg. Chim. Acta 511 (2020), 119843.

[126] S. Dang, T. Wang, F. Yi, Q. Liu, W. Yang, Z. Sun, A nanoscale multi-responsive luminescent sensor based on a terbium(III) metal-organic framework, Chem. Asian J. 10 (2015) 1703–1709.

[127] Y. Zhou, Y. Shi, B. Geng, Q. Bo, Highly water-stable novel lanthanide wheel cluster organic frameworks featuring coexistence of hydrophilic cage-like chambers and hydrophobic nano-sized channels, ACS Appl. Mater. Interfaces 9 (2017) 5337–5347.

[128] Y. Wang, Y. Yu, J. Lu, Y. Li, S. Wang, D. Li, J. Dou, A 2D lanthanum coordination polymer as a multi-responsive luminescent chemosensor with fast response and high sensitivity, J. Solid State Chem. 283 (2020), 121173.

Chapter 10

Rare earth metal-organic framework hybrid materials for luminescence responsive chemical sensing of special molecule species

10.1 Rare earth metal-organic framework hybrid materials for luminescence responsive chemical sensing of biomolecular species

Common biomolecular species include amino acids, proteins, and nucleic acids, among others. Amino acids, as essential ingredients of proteins needed by living organisms, are crucially involved in the health of the human body. Many amino acids are involved in almost all physiological activities in vivo and the proper balance of various amino acids is a precondition for human health. Lack of any amino acid will affect the immune system and other normal functions. In recent years, the content of various amino acids in serum has become an important indicator for disease screening. Sensing of certain amino acids is important in nutritional analysis and diagnosis of diseases [1,2].

Aspartic acid (Asp) is widely used in medicine, food, and chemicals. In particular, the L-Asp form becomes a part of proteins used in the human body, and is also involved in the synthesis of essential amino acids. It can be used as a carrier to deliver electrolytes to the myocardium, improving the myocardial systolic function. In clinical therapy, it can also be used for treating hypertension, heart disease, and other disorders.

Both tyrosine (Tyr) and tryptophan (Trp) are nutritional amino acids, which are closely related to metabolism, growth, and development of humans and animals. Tyr is widely used in the food, feed, medical, and chemical industries. Excessive or insufficient Tyr may cause depression, uric aciduria, albinism, Parkinson's disease, and other diseases. Trp is an important raw material to prepare the neurotransmitter serotonin.

L-Cysteine (Cys) is one of the basic amino acids in vivo with many physiological effects, such as relieving the degree of poisoning from toxic substances

Rare Earth Metal-Organic Framework Hybrid Materials for Luminescence Responsive Chemical Sensors
https://doi.org/10.1016/B978-0-323-91236-5.00014-1

or drugs, promoting hair growth, and protecting humans from radiation. Moreover, excessive Cys in vivo is often related to some diseases. Therefore the detection of Cys is important for human health.

Lysine (Lys), as a precursor of carnitine biosynthesis, has a key effect on the β-oxidation of fatty acids. Lys is also considered to be involved in decomposition and metabolism and then results in irreversible α-aminoadipate formation via a saccharopine pathway. Superfluous lysine may also lead to congenital metabolic disorders such as ascystinuria or hyperlysinemia in plasma and urine [3–10].

Thus the detection of amino acids in fields such as nutritional analysis and disease diagnosis is particularly important. Luminescent probes possess comparatively high sensitivity, good selectivity, and recyclability, making them a good choice for detecting different amino acids [11–16]. Notably, Cys is a typical amino acid with an active sulfhydryl group (–SH) that has strong affinity for some heavy metal ions. Therefore heavy metal ion-containing probes with high sensitivity and selectivity are needed for Cys sensing. Sun et al. designed and synthesized two anionic Ln-K-MOFs, namely $\{[RE_2K(bpda)_4(C_2H_5OH)]\cdot(H_3O)\cdot(H_2O)_x\}_n$ (RE = Eu, Tb; H_2bpda = 2,2′-bipyridine-6,6′-dicarboxylic acid), where K^+ was utilized to link the subunits and for further constructing of the anionic framework. Additionally, the introduction of K^+ in the structure also resulted in long RE-RE distances (8.15–13.24 Å) and limited the energy transfer between RE^{3+} ions. Fe^{3+}@Eu-K-bpda achieved sensitive detection of the emission spectra of Cys (Fig. 10.1A). The emission at 615 nm gradually recovered with the Cys concentration and reached a maximum at about 100 mM of Cys. The recovery of the red emission could also be easily observed by the naked eye (Fig. 10.1B). Luminescent intensities corresponding to a series of Cys concentrations can be fitted to a linear relationship in a wide concentration range of 0–50 mM with an R^2 of 0.9976 and an LOD of 0.149 mM. In addition, the luminescence response of Cu^{2+}@Eu-K-bpda was also investigated and the emission intensities corresponding to increased concentrations of Cys are listed in Fig. 10.1C. A well-fitted linear relationship was also obtained for quantitative Cys detection (Fig. 10.1D), which displays a slightly worse sensitivity (LOD = 0.301 mM) but over a broader concentration range (0∼100 mM) [13].

Liu et al. synthesized a Ni-MOF $\{[Ni_2(odip)(H_2O)_4(DMF)]\cdot DMF\cdot 2H_2O\}$ with a 5,5′-oxidiisophthalic acid (H_4odip) ligand, whose functionalized Eu^{3+}@Ni-MOF hybrid exhibited good fluorescence selectivity, sensitivity, and recyclability for Asp within 10 types of common amino acids (L-aspartic acid (Asp), L-leucine (Leu), L-isoleucine (Ile), L-histidine (His), L-cysteine (Cys), L-tyrosine (Tyr), L-threonine (Thr), L-valine (Val), phenylalanine (Phe), and L-proline (Pro)). Most amino acids exhibited negligible influences except for Asp (Fig. 10.2A; left), which showed a significant quenching behavior as demonstrated in Fig. 10.2B (left). The fluorescence intensity of Eu^{3+}@Ni-MOF decreased gradually as the Asp concentration increased (Fig. 10.2C; left). The plot of I_0/I vs. Asp concentration [C] (mmol/L) can be well fitted by an

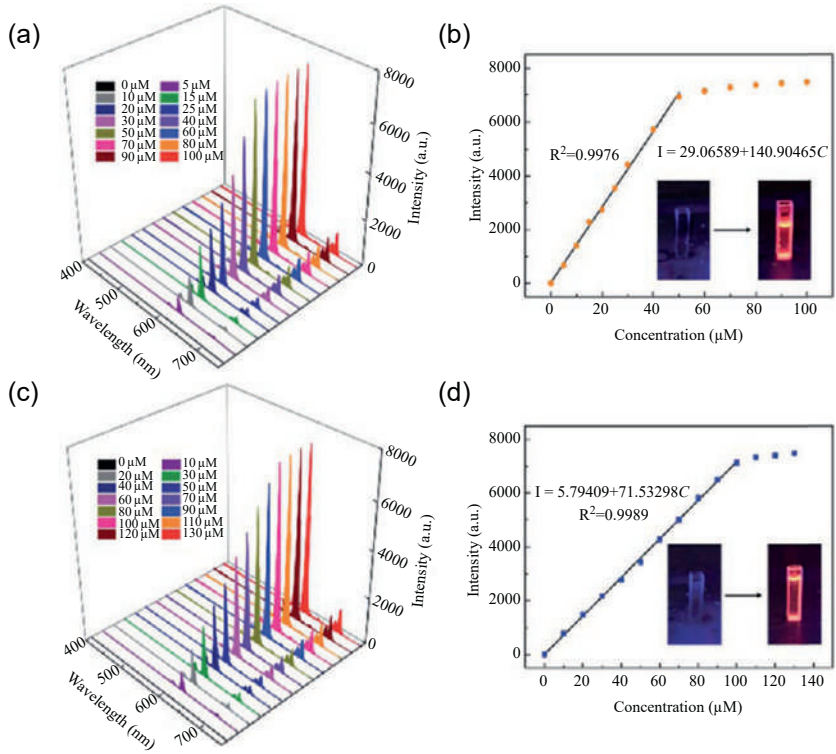

FIG. 10.1 (A) Emission spectra of probe Fe^{3+}@Eu-K-bpda with different L-cysteine (Cys) concentrations. (B) The linear relationship between I_{615} and Cys concentrations in the range of 0–50 mM; inset shows the corresponding photograph under a UV lamp. (C) Emission spectra of probe Cu^{2+}@Eu-K-bpda with different Cys concentrations. (D) The linear relationship between I_{615} and Cys concentrations in the range of 0–100 mM. *(Reproduced with permission from T. Sun, R. Fan, R. Xiao, T. Xing, M. Qin, Y.Liu, S. Hao, W. Chen, Y. Yang, Anionic Ln-MOF with tunable emission for heavy metal ion capture and L-cysteine sensing in serum. J. Mater. Chem. A 8 (2020) 5587–5594. Copyright 2020 Royal Chemical Society.)*

exponential function relationship (Fig. 10.2D; left), indicating the coincidence of dynamic and static quenching processes. At low concentrations, the quenching constant K_{sv} was calculated to be 1.565×10^3 L/mol in the range of 0–1.136 mmol/L. The detection limit (LOD) was calculated to be 2.51 mmol/L. As shown in Fig. 10.2A (right), when excited at 332 nm, there was an intense luminescent spectrum at 615 nm, but the luminescence was quenched visibly once aspartic acid (0.03 mmol) was added. Meanwhile, multiple cycles of the sensing experiment of Asp were performed (Fig. 10.2B; right). After being recycled five times, Eu^{3+}@Ni-MOF still mostly maintained its luminescent intensity after washing. The result illustrates that the luminescence of Eu^{3+}@Ni-MOF is almost totally quenched after 150 s (Figs. 10.2C and D; right).

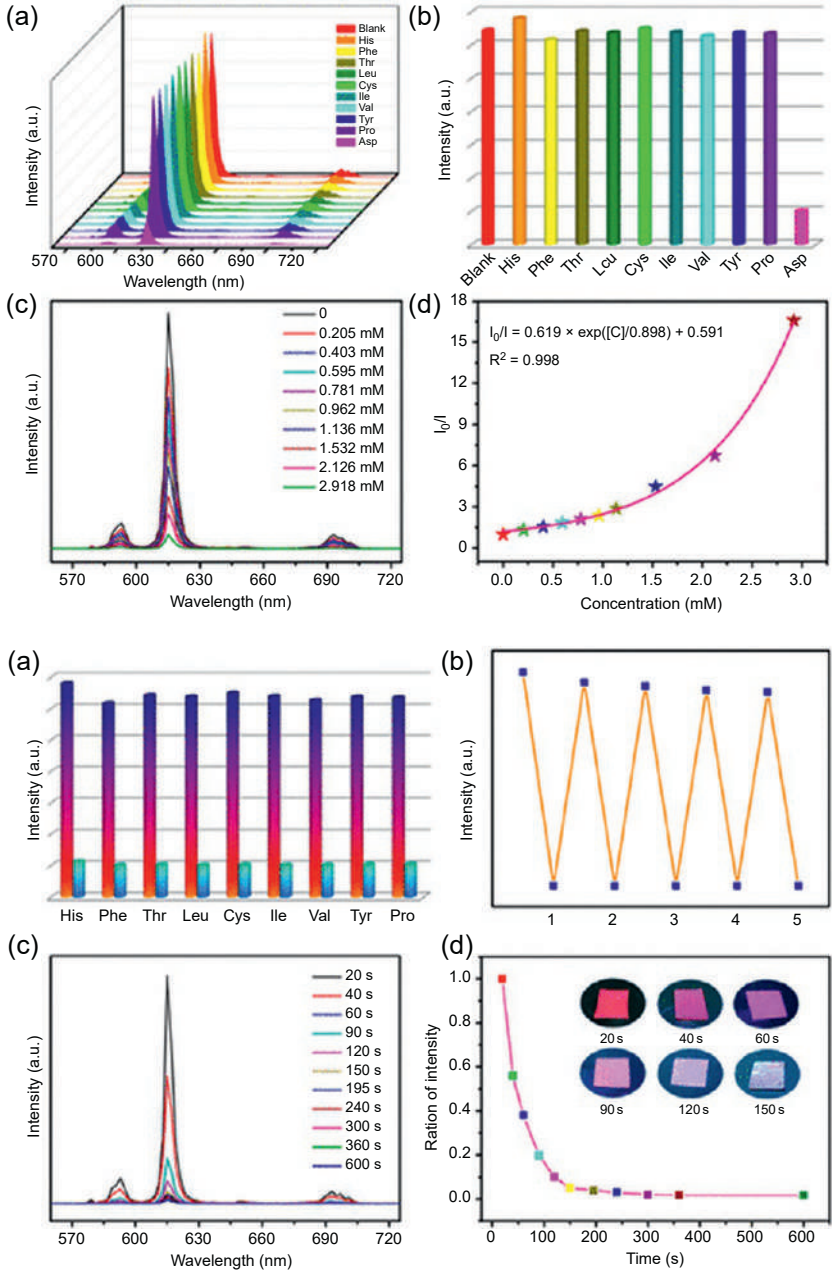

FIG. 10.2 *(Top)* (A) Luminescent spectrum of Eu^{3+}@Ni-MOF; (B) luminescent intensity at 615 nm; (C) luminescent spectra with different aspartic acid concentrations; (D) and the correlation between I_0/I vs. aspartic acid concentration. *(Bottom)* (A) Luminescent intensity (I_{615}) of Eu^{3+}@Ni-MOF vs. different amino acids (colors) and upon the addition of aspartic acid (*blue*); (B) luminescent intensity (I_{615}) after five recycles; (C) emission spectra at different times; and (D) luminescent intensity (I_{615}) at different times (inset: color changes of test papers under UV light). *(Reproduced with permission from Y. Liu, Y. Lu, B. Zhang, L. Hou, Y. Wang, Post-synthetic functionalization of Ni-MOF by Eu3 + ions: luminescent probe for aspartic acid and magnetic property. Inorg. Chem. 59 (2020) 7531–7538. Copyright 2020 American Chemical Society.)*

Under ultraviolet light irradiation of 254 nm, the red luminescence of the test papers faded gradually. The interactions between Asp and Eu^{3+}@Ni-MOF caused the energy loss resulting in luminescence quenching [14].

Li et al. synthesized a Tb-MOF based on 4-(pyridin-3-yloxy)-phthalic acid (H_2ppda) and 1,4-naphthalene -dicarboxylic acid (H_2nbdc), namely, $[Tb(ppda)(npdc)_{0.5}(H_2O)_2]_n$, which acted as a luminescent sensor for amino acids with high selectivity and sensitivity that discerned tyrosine (Tyr) and tryptophan (Trp) with the characteristic emission of Tb^{3+} ions and ligand luminescence in aqueous solution, respectively. With the same concentrations (1.0×10^{-3} M), different natural amino acids show different influences on the luminescence intensities of Tb-MOF (Fig. 10.3; top). Tyr quenched the fluorescence of Tb-MOF to a certain extent, with a quenching efficiency of 56.76%, while Trp had little variation in the emission at 545 nm caused by the $^5D_4 \rightarrow {}^7F_5$ transition ofTb^{3+}, but the emission at 465 nm induced by the ligands was significantly enhanced. As shown in Fig. 10.3A and C (bottom), the luminescence of Tb-MOF differed greatly when it was immersed in concentrations of Tyr. It was found that the emission intensity of Tb^{3+} located at 545 nm decreased regularly. And with the addition of Trp at different concentrations, the H_2npdc emission at 465 nm gradually increased with the continuous increase of Trp concentration. The relationship between the quenching effect and the Tyr or Trp concentration was further examined through the Stern-Volmer equation, linearly fitted with the values of K_{sv} and the LOD for Tyr and Trp of $4.01 \times 10^5\ M^{-1}$ and 1.43×10^{-5} M, and $2.60 \times 10^5\ M^{-1}$ and 6.99×10^{-5} M, respectively (Fig. 10.3B and D; bottom). It can be deduced that the luminescence quenching of compound Tb-MOF induced by Trp or Tyr may be attributed to the interactions of competitive absorption of energy [16].

DNA is a very important biomacromolecule, containing the biological instructions that make each species unique. So, sensitive, rapid, and cost-effective detection of specific DNA is of great importance to gene expression analysis, clinical diagnostics, environmental monitoring, and antibioterrorism [17–19]. Fortunately, MOFs have recently been demonstrated to be a sensing platform for fluorescent detection of DNA and proteins. Compared with conventional nanomaterial-based fluorescent sensing platforms, MOFs not only possess simpler preparation procedures, but also exhibit higher quenching efficiency and discriminating ability of single-base mismatch. However, the construction of DNA sensors based on luminescent rare earth MOF hybrid materials remains to be further exploited [20–22].

Tang et al. explored the application of a luminescent Eu-MOF of 1,3,5-benzenetricarboxylic acid (H_3BTC) for sensitive detection of DNA. Because of the π-rich structure of BTC for providing a conjugated π-electron system and the intrinsic fluorescence quenching ability of the metal cations of MOCPs, the Eu-MOF is reasonably able to absorb single-stranded DNA (ssDNA) and quench its labeled fluorescence of 6-carboxyfluorescein (FAM) (Fig. 10.4; right, top). Upon the introduction of complementary target DNA (tDNA), however, the FAM labeled ssDNA (FAM-DNA) will be released from the Eu-MOF

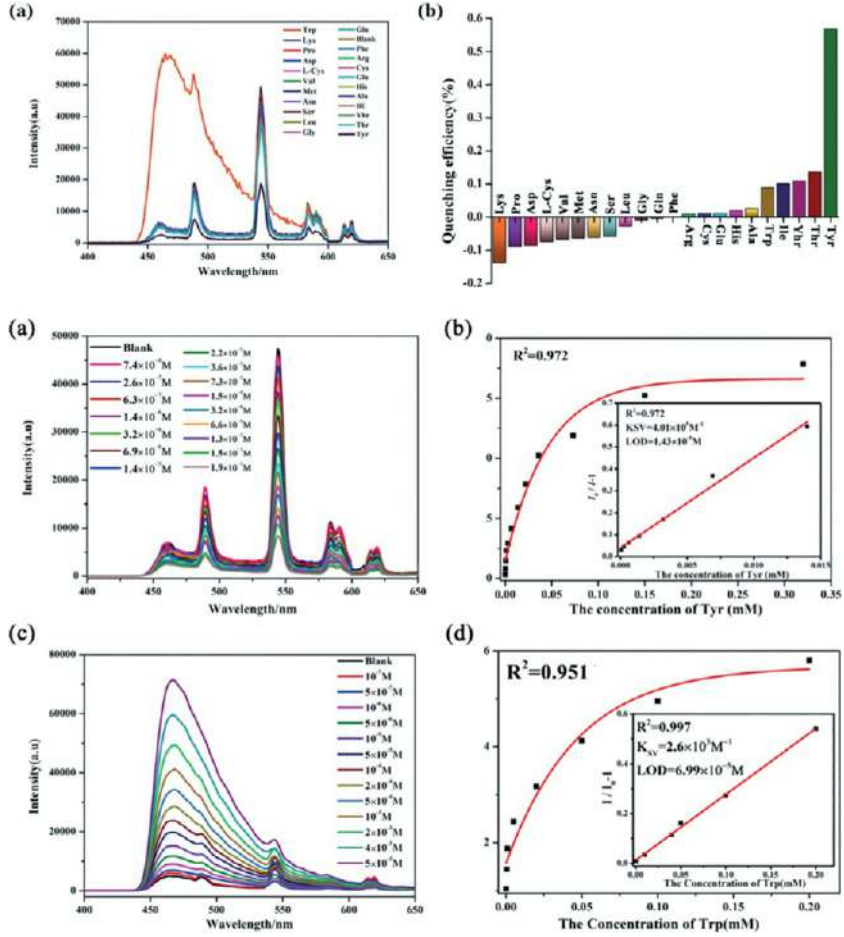

FIG. 10.3 *(Top)* (A) Fluorescence response of Tb-MOF in various amino acids and (B) quenching efficiency of Tb-MOF for detecting different amino acids. *(Bottom)* (A) Luminescent spectra of Tb-MOF dispersed in the presence of various amounts of Tyr. (B) Nonlinear Stern-Volmer plot of Tyr; inset: the linear Stern-Volmer plot of Tyr. (C) Luminescent spectra of Tb-MOF dispersed in the presence of various amounts of Trp. (D) Nonlinear Stern-Volmer plot of Trp, inset: the linear Stern-Volmer curves of Trp. *(Reproduced with permission from Z. Li, Z. Zhan, M. Hu, A luminescent terbium coordination polymer as a multifunctional water-stable sensor for detection of Pb2 + ions, PO43 − ions, Cr2O72 − ions, and some amino acids. CrstEngComm 22 (2020) 6727–6737. Copyright 2020 Royal Chemical Society.)*

surface to form a double-stranded DNA (dsDNA), leading to the recovery of the labeled FAM fluorescence. Nevertheless, the red fluorescence of Eu-MOF itself remains unchanged during the interaction process (binding and releasing) of the FAM-DNA probe with the Eu-MOF. As shown in Fig. 10.4A (left), the fluorescence of the Eu-MOF/FAM-DNA hybrid is highly sensitive to tDNA and is

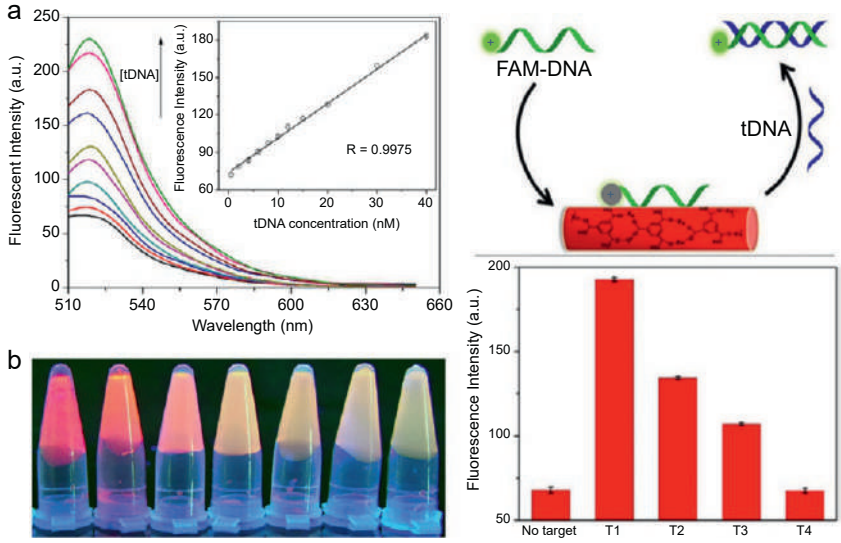

FIG. 10.4 *(Left)* (A) Emission spectra of the Eu-MOF/FAM-DNA complex in the presence of tDNA with different concentrations (from 0 to 400 nM). Inset is the plot of fluorescent intensity at 520 nm of FAM-DNA as a function of the tDNA concentration. (B) Visual fluorescence color changes of Eu-MOF/FAM-DNA complex upon the addition of different concentrations of tDNA (from left to right: 0, 10, 20, 50, 100, 200, 500 nM). *(Right, Top)* Schematic illustration of (A) fabrication process of Eu-MOF and (B) sensing principle and corresponding changes in emission spectra and color for the DNA fluorescent assay. *(Right, Bottom)* Fluorescent responses of the Eu-MOF/FAM-DNA complex to complementary target (T_1, tDNA), single-base mismatched target (T_2), two-base mismatched target (T_3), and noncomplementary target (T_4). *(Reproduced with permission from G. Tang, J. Gao, C. Wang, H. Tan, Luminescent lanthanide coordination polymer as a platform for DNA colorimetric detection. Sens. Actuators B 244 (2017) 571–576. Copyright 2017 Elsevier.)*

gradually enhanced with the increase of tDNA concentration. The gradually enhanced fluorescent intensity also suggests that the Eu-MOF/FAM-DNA hybrid is appropriate for the quantification of tDNA. The inset of Fig. 10.4A (left) outlines the relationship between the fluorescent intensity of the Eu-MOF/FAM-DNA hybrid complex at 520 nm and the concentration of tDNA. A good linear relationship is seen ($R = 0.9975$) between the fluorescent intensity at 520 nm and the concentration of tDNA in the range of $0.5 \sim 40$ nM. The LOD of the sensor is calculated to be 0.09 nM. Additionally, due to the unchanged fluorescence of Eu-MOF, the tDNA-induced fluorescence changes can be easily observed under a UV lamp. From Fig. 10.4B (left), the color of the Eu-MOF/FAM-DNA hybrid solution gradually turned from red to yellow-green upon the titration with tDNA, which enabled the tDNA to be detected by the naked eye. As shown in Fig. 10.4 (right, bottom), compared with the Eu-MOF/FAM-DNA hybrid alone, the fluorescent intensity of FAM-DNA at 520 nm performed remarkable enhancement for the complementary target T_1 (tDNA). In

addition, almost no changes in the fluorescence of the Eu-MOF/FAM-DNA hybrid were observed after the addition of a noncomplementary target T_4. These results indicate that the hybrid-based sensor has a high selectivity for targeting DNA, and even single-base mismatched nucleotides can be distinguished [21].

Thiamines are also called vitamin B_1. It is an important small biomolecule, and when an organism lacks thiamines, the following responses can appear in turn: dry beriberi, wet beriberi, Wernicke encephalopathy, Korsakoff syndrome, among others. In view of the close relationship of thiamines with human health, their effective detection is significant. Wang et al. presented the synthesis and structure of rare earth MOFs and the sensing behavior of the Tb-MOF, which exhibited highly selective and sensitive detection of thiamines at very low concentration due to the strong intermolecular force between Tb-MOF and thiamines [23]. Ascorbic acid (AA, vitamin C) also exhibits multiple functions as an antioxidant and enzyme cofactor. AA as an antioxidant is widely used in food, animal feed, beverages, and pharmaceutical formulations. However, its abnormal expression also induces several diseases [24–26]. The luminescence sensing of AA by RE-MOF hybrid materials has been lightly explored [27,28].

Zeng et al. reported a Tb-MOF, $\{[Tb(Cmdcp)(H_2O)_3]_2(NO_3)_2{\cdot}5H_2O\}_n$ by a zwitterionic carboxylate ligand *N*-carboxymethyl-(3,5-dicarboxyl)pyridinium bromide ($H_3CmdcpBr$), as a luminescent probe for sensing AA through a luminescence "Off-On" mechanism. The sensing process could be directly observed with the naked eye, and was transferable to urine and serum samples with a satisfactory near-quantitative recovery, yielding a potent sensor of Tb-MOF for AA in biological media. The Fe^{3+}@Tb-MOF sensor exhibits a fast response for AA in aqueous solution even at a lower concentration. With 0.05 mM AA, the luminescence intensity of Fe^{3+}@Tb-MOF increased to saturation in 2 min, as shown in Fig. 10.5A (top). As demonstrated in Fig. 10.5B (top), the emission intensity of Fe^{3+}@Tb-MOF increases linearly with the increase of the AA concentration in the range of 0–1.25 mM (inset of Fig. 10.5B; top), giving rise to a detection limit of 5.9 μM for AA [28].

Alkaline phosphatase (ALP) is one of the most widely distributed enzymes in the human body, and it is mainly involved in the regulation of the cell-signaling network by removing phosphate groups from biomolecules such as nucleotides and proteins. However, the abnormal expression of ALP is often associated with serious diseases including prostate cancer, bone disease, and liver diseases. In addition, ALP is crucial to adjusting the level of pyrophosphate ion (PPi) by hydrolyzing PPi to phosphate ion (Pi), which facilitates mineral precipitation and growth and prevents excess vascular calcification [29–31]. Therefore, it is highly desirable to develop a convenient and sensitive method for ALP detection in order to accurately evaluate the role of ALP in physiological and pathological processes [32,33].

Wang et al. developed red-emitting Tb-GMP-Eu nanohybrids to detect the activity of alkaline phosphatase by utilizing GMP as the bridge ligand to self-

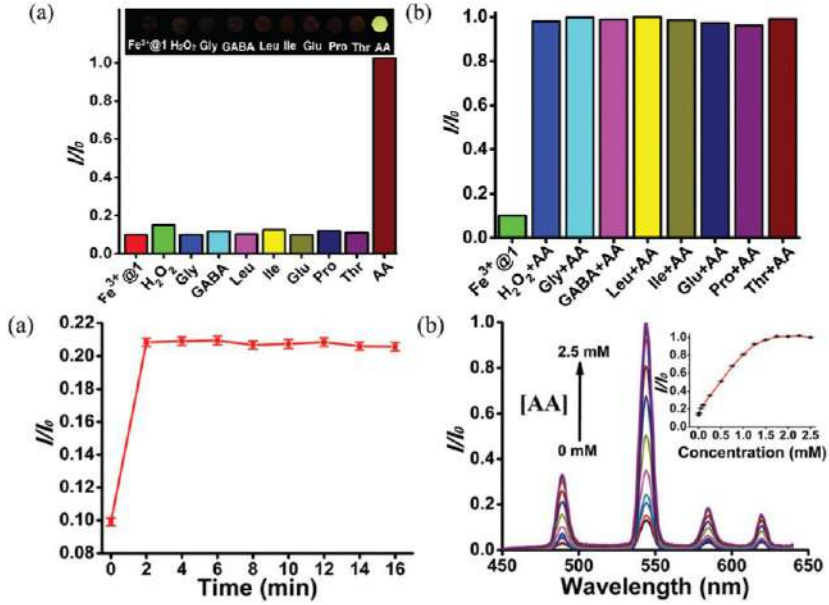

FIG. 10.5 *(Top)* (A) The luminescence intensity at 545 nm of Fe^{3+}@Tb-MOF treated with 10 mM of various interfering substances (H_2O_2, Gly, GABA, Leu, Ile, Glu, Pro, Thr, AA) upon excitation at 380 nm. Inset: The luminescence of Fe^{3+}@Tb-MOF seen with the naked eye under the existence of different substances when irradiated under UV light (365 nm). (B) The luminescence intensity at 545 nm of Fe^{3+}@Tb-MOF upon the addition of an equal concentration of other interferential substances and AA under excitation at 380 nm. *(Bottom)* (A) The emission intensity of Fe^{3+}@Tb-MOF with AA (0.05 mM) with different immersion times ($\lambda_{ex} = 380$ nm, $\lambda_{em} = 545$ nm). (B) The fluorescence spectra of Fe^{3+}@Tb-MOF treated with incremental AA concentration ($\lambda_{ex} = 380$ nm). *(Reproduced with permission from K. Wu, L. Qin, C. Fan, S. Cai, T. Zhang, W. Chen, X. Tang, J. Chen, Sequential and recyclable sensing of Fe3+ and ascorbic acid in water with a terbium (III)-based metal–organic framework. Dalton Trans. 48 (2019) 8911–8919. Copyright 2019 Royal Chemical Society.)*

assemble with Tb^{3+} and Eu^{3+} in Tris-HCl buffer solution. As shown in Fig. 10.6A (top), the fluorescence intensity of Tb-GMP-Eu gradually decreased with the increase of ALP concentration, and a good linear relationship between the fluorescence intensity and ALP concentration was obtained over the range from 0.05 to 20 U L^{-1} (inset of Fig. 10.6B; top). The fitting regression equation can be expressed with $R^2 = 0.9973$ and an LOD of 0.004 U L^{-1}. The proposed fluorescence-sensing method was also applied to evaluate the inhibitory effect of the ALP inhibitor. When the activity of ALP was inhibited by Na_3VO_4, GMP could not be dephosphorylated any longer, and the fluorescence quenching effect was hindered accordingly. As shown in Fig. 10.6B (bottom), the fluorescence quenching was limited in proportion to the amount of Na_3VO_4 added in the reaction system. The regression equation has $R^2 = 0.9982$, and an LOD of 0.027 nM for Na_3VO_4. With the addition of

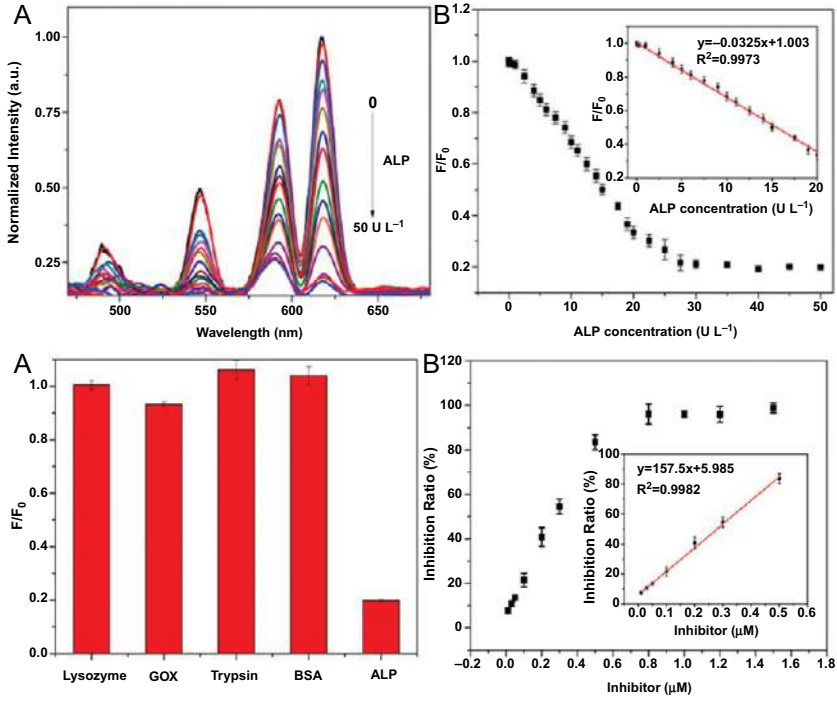

FIG. 10.6 *(Top)* (A) Fluorescence emission spectra of Tb-GMP-Eu CPNs (0.12 mg mL^{-1}) in the presence of different concentrations of ALP from 0 to 50 U L^{-1} in Tris-HCl buffer solution (10 mM, pH 7.4). (B) Plot of F/F_0 versus the concentration of ALP from 0.05 to 20 U L^{-1} (where F_0 and F refer to the fluorescence intensities of Tb-GMP-Eu CPNs before and after addition of ALP, respectively). Inset: The calibration curve with a linear relationship from 0.05 to 20 U L^{-1}. $\lambda_{ex} = 290$ nm and $\lambda_{em} = 618$ nm. *(Bottom)* (A) The fluorescence intensity ratio (F/F_0) in response to tested substances including lysozyme, glucose oxidase (GOX), trypsin, bovine serum albumin (BSA), and ALP, where F and F_0 are the fluorescence intensities at 618 nm in the presence and absence of the tested substances, respectively. The concentration was 40 U L^{-1} for ALP and 0.25 mg mL^{-1} for other targets. (B) Plot of enzyme inhibition efficiency (I%) in the presence of different concentrations of Na_3VO_4 from 0 to 1.5 mM. Inset: The linear regression curve with a linear relationship from 0 to 0.8 mM. *(Reproduced with permission from F. Wang, X. Hu, J. Hu, Q. Peng, B. Zheng, J. Du, D. Xiao, Fluorescence assay for alkaline phosphatase activity based on energy transfer from terbium to europium in lanthanide coordination polymer nanoparticles. J. Mater. Chem. B 6 (2018) 6008–6015. Copyright 2019 Royal Chemical Society.)*

ALP in the sensing system, the phosphate group in the GMP ligand is cleaved, resulting in interruption of energy transfer from Tb^{3+} to Eu^{3+}, leading to the quenching of Tb-GMP-Eu to show the characteristic red emission of Eu^{3+} [32].

Cui et al. synthesized Eu-MOF hollow spheres with Eu^{3+} as the metal node and H_2BBDC (5-boronobenzene-1,3-dicarboxylic acid) as ligand, which exhibited dual emission at 370 and 623 nm, respectively, similar to the corresponding emission from BBDC and Eu^{3+} ions. Since glucose can be catalyzed to produce

H_2O_2 by glucose oxidase (GOx), it is also an appropriate probe for glucose detection. In the presence of GOx, when glucose concentration increased, the emission at 354 nm was enhanced, while the emission at 623 nm decreased, corresponding to the emissions from BBDC and Eu^{3+}, respectively (Fig. 10.7A). A good linear correlation was obtained between the intensity ratio and glucose concentration in the range from 0.1 to 4 μM, with a coefficient of determination of $R^2 = 0.9824$ (Fig. 10.7C) and an LOD of 0.0643 μM. As illustrated in Fig. 10.7D, when the concentration of glucose increased, strong red fluorescence diminished and gradually changed to blue. The dual fluorescence probe was easily differentiated by the naked eye and showed a high tolerance of concentration interference. CIE chromaticity coordination confirmed the color changes (Fig. 10.7B). Under the identical conditions, no significant changes of the fluorescence intensity in the presence of saccharides and amino acids were found, except for glucose (Fig. 10.7E) because of the high selective catalysis of glucose with GOx. It is obvious that other materials have little interference with the reaction of Eu-MOF and glucose (Fig. 10.7F) [34].

Folic acid (FA), known as a water-soluble chemical compound in the vitamin B group, is widely distributed in fresh fruits, vegetables, meat, and other foods. FA plays an essential role in the synthesis of proteins and nucleic acids and is involved in amino acid metabolism, which is helpful to the production and maintenance of new cells for preventing cancer. FA deficiency can cause megaloblastic anemia, leucopenia, and other signs and symptoms, and it disturbs the synthesis of DNA and cell division, which affects the hematopoietic cells and neoplasms. Adequate FA in pregnant women can prevent some birth defects such as low body weight, infant cleft palate, and congenital malformation. FA detection with high sensitivity and selectivity is urgently required and significant in preventing diseases related to FA deficiency [35,36].

Dong et al. obtained a single-phase white-light-emitting mixed rare earth MOF $[Eu_{0.06}Tb_{0.04}Gd_{0.9}(HDPNC)_{1.5}\ (H_2O)(DMF)]\cdot 2H_2O$ (EuTbGd-MOF, H_3DPNC = 5-(3′,5′−dicarboxylphenyl) nicotinic acid) under 365-nm excitation by adjusting the molar ratio of RE^{3+} and different excitation wavelengths, with the CIE coordinates of (0.3328, 0.3296). The fluorescence intensity of EuTbGd-MOF was gradually enhanced with the incremental addition of FA (Fig. 10.8B). Taking the emission intensity at 462 nm as a reference, a good linear correlation ($R^2 = 0.9983$) exists between the emission intensity ratios (I/I_0) and the concentration of FA, as shown in Fig. 10.8C, which can be quantitatively explained in the range of 0–18 mM with the LOD of 0.0883 mM. It is interesting to note that the fluorescence response of EuTbGd-MOF toward FA is almost undisturbed by the addition of other interferential substances (Fig. 10.8D), indicating its high sensitivity toward FA in the aqueous system. Moreover, the recycling capability and stability of a sensor is important and meaningful for practical application in fluorescence sensing for FA (Fig. 10.8E). The well-scattered FA molecules in the aqueous solutions may be adsorbed on the surface of the MOFs, promoting possible host-guest

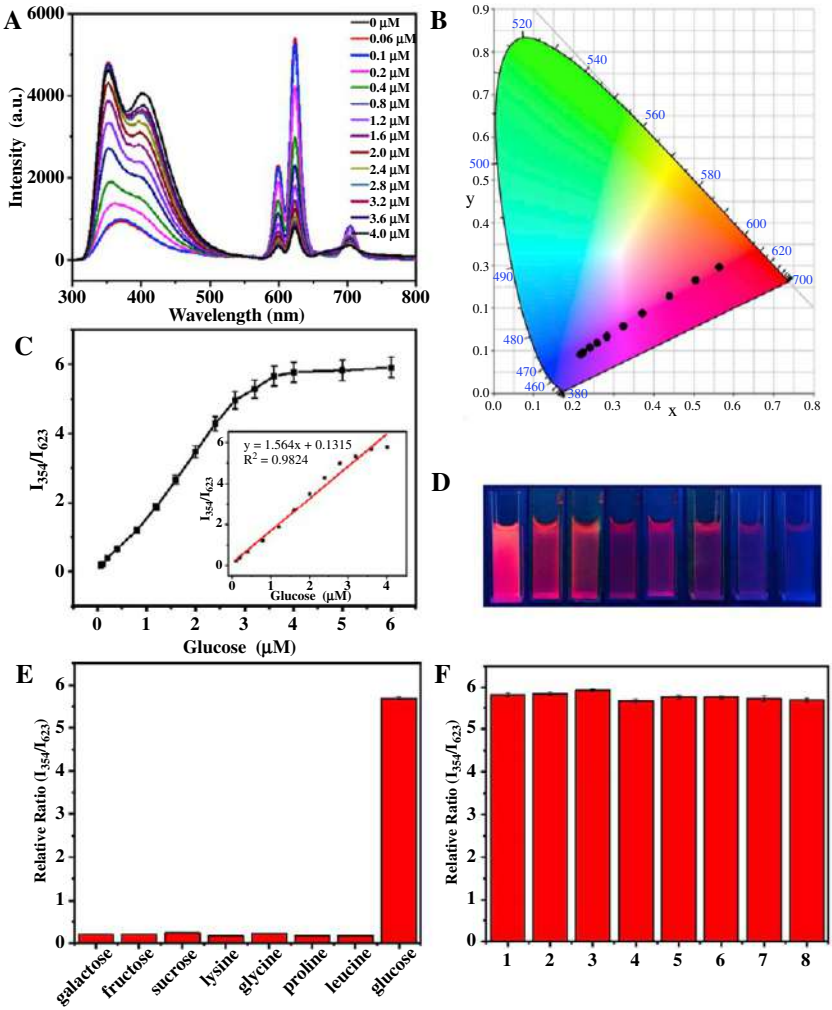

FIG. 10.7 (A) Fluorescence spectra of reaction solution with the addition of glucose at different concentrations under the excitation of 270 nm. (B) CIE chromaticity coordinates of reaction solution with the addition of glucose at different concentrations. (C) Plot of the intensity ratio of I_{354}/I_{623} vs. glucose concentration under UV irradiation. (D) Images of the mixture solution at different concentrations of glucose. (E) Comparison of fluorescence ratio of Eu-MOF in the presence of other biologically relevant species at the excitation of 270 nm. (F) Fluorescence ratio of Eu-MOF in response to 4 μM glucose and 20 μM other biologically relevant species as the interference, (1) glucose +galactose, (2) glucose+fructose, (3) glucose+sucrose, (4) glucose+lysine, (5) glucose+glysine, (6) glucose+proline, (7) glucose+leucine, (8) glucose. *(Reproduced with permission from Y. Cui, F. Chen, X. Yin, A ratiometric fluorescence platform based on boric-acid-functional Eu-MOF for sensitive detection of H_2O_2 and glucose. Biosens. Bioelectron. 135 (2019) 208–215. Copyright 2019 Elsevier.)*

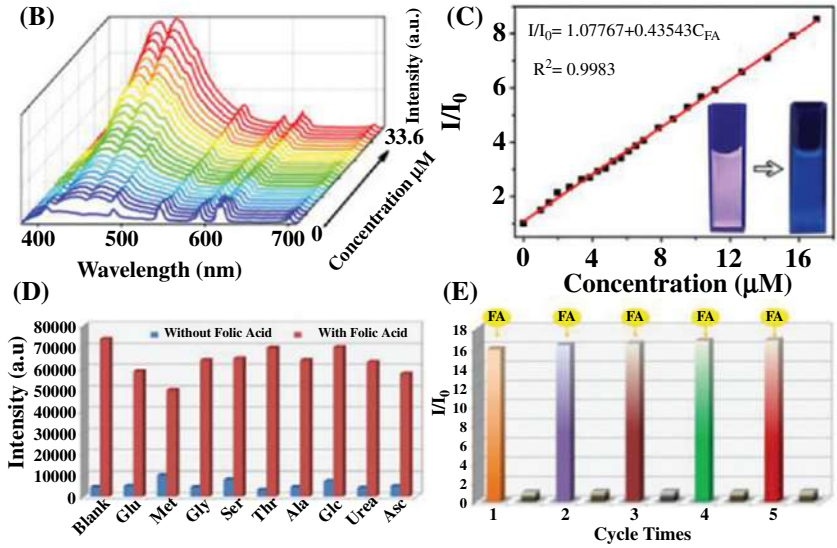

FIG. 10.8 (B) The emission spectra of $Eu_{0.06}Tb_{0.04}Gd_{0.9}$-MOF in aqueous solution ($\lambda_{ex} = 365$ nm) with an incremental addition of FA to the aqueous solution. (C) The Stern-Volmer plots of I/I_0 for FA with different concentrations; insets show the corresponding photographs under irradiation of 365-nm UV light. (D) The fluorescence intensity at 462 nm of $Eu_{0.06}Tb_{0.04}Gd_{0.9}$-MOF toward different organism-related substances in the absence and presence of FA ($\lambda_{ex} = 365$ nm). (E) The intensity of I/I_0 during five consecutive enhancement and regeneration cycles. *(Reproduced with permission from Z. Dong, F. Zhao, L. Zhang, Z. Liu, Y. Wang, A white-light-emitting lanthanide metal-organic framework for luminescence turn-off sensing of MnO4 − and turn-on sensing of folic acid and construction of a "turn-on plus" system. New J. Chem. 44 (2020) 10239–10249. Copyright 2019 Royal Chemical Society.)*

interactions. The mechanism of Turn-On fluorescence may be explained based on the donor-acceptor electron-transfer mechanism.

Liu et al. prepared a Cu-BTC/Tb MOF hybrid (BTC = 1,3,5-benzenetricarboxylate) for Turn-On fluorescence detection of Aβ1–40. When Tb^{3+} was introduced into the Cu-BTC MOF by the PSM method, the formed Cu-BTC/Tb was very weakly emissive due to the quenching effect of Cu^{2+} to Tb^{3+}. Interestingly, the subsequent addition of Aβ1–40 induced a strong emission to an originally nonemitting Cu-BTC/Tb, owing to the specific interaction between Cu^{2+} and Aβ1–40. By combining the characteristics of long-lived luminescence of Tb^{3+} ions, the quenching behavior of Cu^{2+}, and the specific binding between Cu^{2+} and Aβ1–40, a sensor platform with high sensitivity for Aβ1–40 was achieved [37]. Tian et al. established a label-free, selective, and sensitive luminescent sensing platform for tyrosinase (TYR) activity monitoring and its inhibitor screening using an AMP-Tb/Ag^{+} MOFs nanoparticle. By taking advantage of the specific binding and redox properties of Ag^{+} incorporated into the AMP-Tb network and dopamine (DA) as the product of the model substrate tyramine, the enzymatic

reaction and the signal change of the sensing platform were effectively linked. The cooperative effect of a weakened energy transfer from AMP to Tb^{3+} by altering the electronic structure of Ag^{+} and an efficient photoinduced election transfer (PET) process caused by dopaquinone facilitated the luminescence quenching of Tb^{3+}. Thus this luminescent sensing platform can be employed for quantitative evaluation of TYR activity, showing a good linear range for TYR activity from 0.08 to 0.20 U mL^{-1} with a low LOD of 0.004 U mL^{-1}. This sensing platform is very promising in clinical diagnosis and drug screening for TYR-associated diseases [38]. Wu et al. prepared a water-stable MOF of $\{[Tb(Cmdcp)(H_2O)_3]_2(NO_3)_2 \cdot 5H_2O\}_n$ ($H_3CmdcpBr$ = *N*-carboxymethyl-(3,5-dicarboxyl) pyridinium bromide), which functions as an effective fluorescent sensor for the label-free detection of dopamine (DA) with an LOD of 0.41 μM. Under the optimum condition of 80°C, pH 9 for 80 min in Tris-HCl with natural ambient oxygen, DA polymerizes to give polydopamine (pDA), which adheres to the surface of this MOF and quenches its green luminescence thoroughly. The sensing process is visible to the naked eye under 365-nm UV light irradiation due to the partial overlap of its excitation spectrum with the absorption spectrum of pDA. The sensing process is also adaptable in biological fluids of serum and urine, with satisfactory recoveries ranging from 96.14% to 104.32% [39].

10.2 Rare earth metal-organic framework hybrid materials for luminescence responsive chemical sensing of antibiotics and drugs

Antibiotics are widely applied drugs for treating human and animal diseases as well as bacterial infections in the aquaculture and agriculture fields. However, their widespread application has resulted in increased antibiotic residues appearing in grains, animals, and even in drinking water. Long-term intakes of the contaminated foods could result in severe disorders, such as immunity decline, allergic reactions, hereditary genetic defects, and various types of cancers. Overuse of antibiotics has led to serious antibiotic residues in both aquatic products and domestic water, which are having detrimental impacts on environmental safety and human health. Most antibiotics cannot easily degrade naturally, and thus they pose serious ecological and health risks. High levels of antibiotic residues resulting from abuse and mismanagement have already been monitored in the ecological water environment [40–42]. Many efforts have been made in this area to find a convenient and efficient method using rare earth MOF hybrid materials for detecting residual antibiotics [43–68].

Yu et al. designed and fabricated an excitation wavelength-independent chemosensor to detect antibiotics in water. An anionic framework of $[Me_2NH_2][Tb_3(dcpcpt)_3(HCOO)]\cdot DMF\cdot 15H_2O$ (Tb-MOF, $H_3dcpcpt$ = 3-(3,5-dicarboxylphenyl)-5-(4-carboxylphenl)-1H-1,2,4-triazole, DMF = *N*,*N*′-dimethylformamide) and a cationic dye of rhodamine B (RhB) were selected to prepare the RhB@Tb-MOF hybrid by the ion-exchange process. According to

Fig. 10.10A (top), nitrofuran antibiotics (NZF and NFT) presented obvious luminescent quenching of the sensor, while others exhibited low or even a smaller quenching effect. The alternation of excitation wavelength had little influence on the value of quenching efficiencies by monitoring the luminescent intensity at 545 nm (Fig. 10.9B; top). In order to assess the detection sensitivity of RhB@Tb-MOF toward NZF and NFT, quantitative luminescent titration experiments were carried out. As shown in Fig. 10.9C and D (top), the emission intensity of the sensor decreased dramatically when the nitrofuran concentration increased from 0 to 0.10 mM, featuring heavy dependence on the concentration of nitrofuran antibiotic. A detailed S-V analysis further revealed that near-linear correlation exists between the quenching efficiency and the amount of nitrofuran antibiotic, indicating that either a static or dynamic mechanism exists in the quenching process (Fig. 10.9C; top). By monitoring at 545 nm, the LOD toward NZF and NFT is as low as 0.502 μM (99 ppb) and 0.448 μM (106 ppb), respectively. The luminescence intensity of RhB@Tb-MOF shows slight changes in the presence of excesses of other antibiotics (Fig. 10.9E and F; top). For the detection of quinolone antibiotics, remarkably, RhB@Tb-MOF presents an obvious luminescent color-changing process from yellow to blue after adding quinolones such as CPFX and NFX, while other antibiotics exhibit yellow light emission (Fig. 10.9A; bottom); like those in detecting nitrofurans, quantitative titration experiments of RhB@Tb-MOF toward CPFX and NFX were performed. According to Fig. 10.9B–D (bottom), the luminescent color of the samples obviously turned from yellow to white, and then to blue. With the increase of CPFX and NFX concentrations, the intensities of the Tb^{3+} and RhB components decreased rapidly, but the ligand component remained the same for NFX and even increased for CPFX (Fig. 10.9B and D; bottom). Therefore, the blue light emission gradually dominated the emission with continuous addition of CPFX and NFX, resulting in a luminescent color-changing process from yellow to white to blue. According to Fig. 10.10F (bottom), the luminescent color of the samples turned to white when the CPFX or NFX concentration was 4 mM and turned to blue when the concentration was 7 mM. In addition, the plots of relative intensities (I_{441}/I_{583}) versus the concentration of quinolone antibiotics revealed a good linear relationship ($R^2 = 0.99878$ for CPFX and 0.99306 for NFX). The LODs were estimated to be 0.21 μM (69 ppb) and 0.17 μM (53 ppb) for CPFX and NFX, respectively. One possible sensing mechanism toward nitrofuran and quinolone antibiotics could be the PET from the sensor to the LUMO of the analytes. Another possible mechanism is the energy allocation and transfer inner filter effect (IFE), which decides the sensitivity of RhB@Tb-MOF to the two kinds of antibiotics [45].

Dong et al. designed and synthesized a series of $Eu_{1-x}Tb_x$-MOFs using a flexible ligand H_4L (5,5′-(propane-1,3-diylbis(oxy))di-isophthalic acid). A submicrometer bimetallic $Eu_{0.3}Tb_{0.7}$-MOF with homogeneous morphology was achieved and the group further fabricated a MOF-based membrane combined

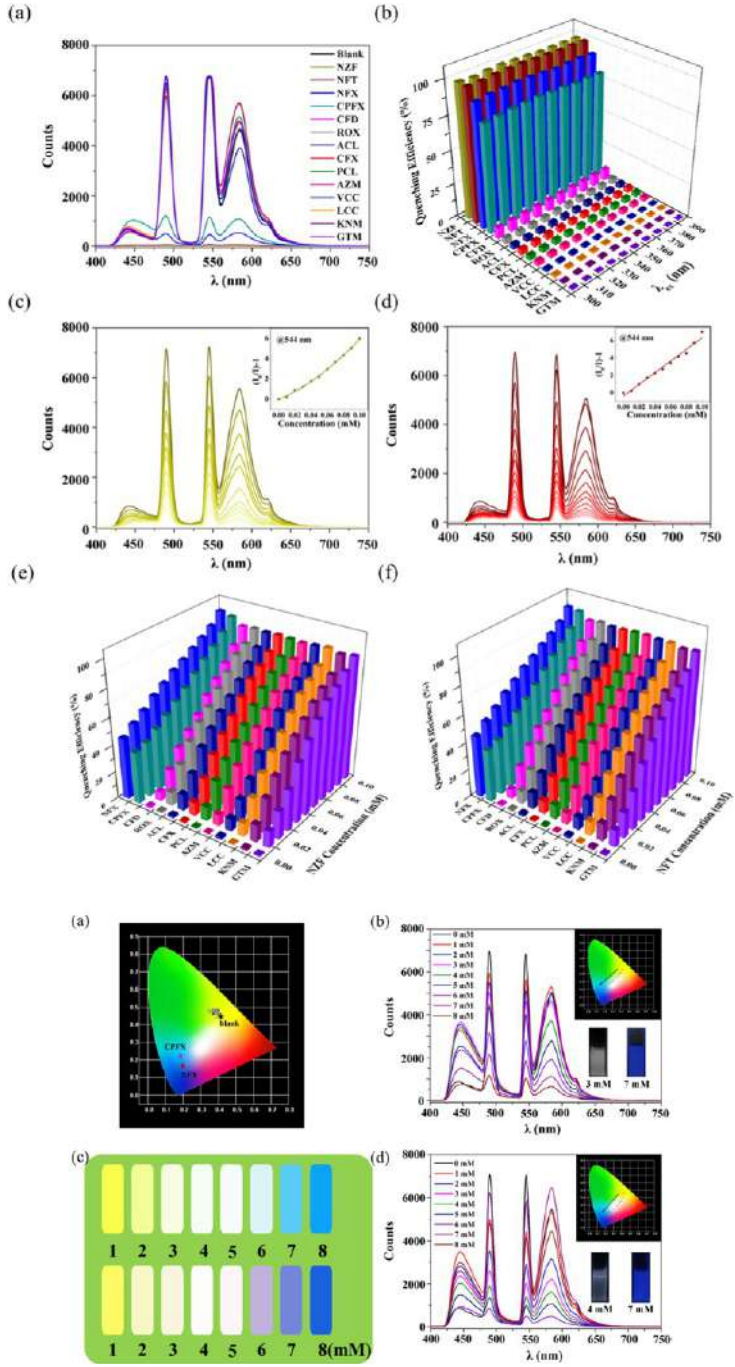

FIG. 10.9 *(Top)* (A) Effect on the emission spectra of 1 g/L RhB@Tb-MOF well dispersed in water with isovolumetric 0.01 M antibiotic aqueous solution; (B) fluorescence quenching of RhB@Tb-MOF by different antibiotics under different excitation wavelengths at room temperature;

(Continued)

with polymer materials, which can act as a self-calibrating luminescent probe for efficiently sensing different antibiotics within a certain concentration range through 2D readouts based on the emission intensity ratio. Additionally, they introduced these bimetallic $Eu_{1-x}Tb_x$-MOFs to monitor the concentration of ornidazole (ODZ) as a prototype system. The luminescent emission spectra of $Eu_{1-x}Tb_x$-MOFs ($x = 0$, 1.0, 0.35, and 0.60) in various concentrations of ODZ are shown in Fig. 10.10A–D. The luminescence intensities of Eu^{3+} and Tb^{3+} in $Eu_{1-x}Tb_x$-MOFs ($x = 0$, 1.0, 0.35, and 0.60) gradually decreased along with increasing concentration of ODZ, and the photograph of liquid samples shows that a 365-nm UV lamp displays the color change of these $Eu_{1-x}Tb_x$-MOFs before and after the reaction. The K_{sv} values for these $Eu_{1-x}Tb_x$-MOFs were calculated to be 0.06, 0.06, 0.04, and 0.03 L/mol, respectively, revealing a high quenching efficiency of ODZ in the emission of these $Eu_{1-x}Tb_x$-MOFs. Moreover, variable spectra of the $Eu_{0.3}Tb_{0.7}$-MOF membrane in different concentrations of ODZ are shown in Fig. 10.10E. The LOD of the $Eu_{0.3}Tb_{0.7}$-MOF-10 h membrane as a luminescent probe for detecting ODZ can reach 2 ppm from the fluorescence quenching curve. The emission color changed from saffron yellow to colorless with ultraviolet light at 365 nm (the inset in Fig. 10.10E). As shown in Fig. 10.10F, the results are in keeping with the original ones after the experiment was repeated six times, indicating that the $Eu_{0.3}Tb_{0.7}$-MOF membrane as an antibiotic probe can be reused effectively. The reduced luminescent intensity is caused by the adsorption of ODZ in the UV-Vis region, as well as the collision interaction between structures and free ODZ energy consumption. They applied $Eu_{0.3}Tb_{0.7}$-MOF membranes to monitor the ODZ solution using as-prepared lake water, proving the viability of this promising application in real samples.

Yang et al. employed the difunctional 2-(4-pyridyl)-terephthalic acid (H_2pta) as an organic linker with RE^{3+} ions to construct two series of RE-MOFs ([RE

FIG. 10.9, CONT'D, (C) effect on the emission spectra of 1 g/L RhB@Tb-MOF well dispersed in water with different concentrations of NZF at room temperature; and (D) effect on the emission spectra of 1 g/L RhB@Tb-MOF well dispersed in water with different concentrations of NFT at room temperature. (E) Luminescence quenching efficiency of RhB@Tb-MOF with 1 mM antibiotic aqueous solution upon adding different concentrations of NZF. (F) Luminescence quenching efficiency of RhB@Tb-MOF with 1 mM antibiotic aqueous solution upon adding different concentrations of NFT. The inset spectra are SV plots. *(Bottom)* (A) Effect on the luminescence color of 1 g/L RhB@Tb-MOF well dispersed in water with isovolumetric 0.01 M antibiotic aqueous solution; (B) effect on the emission spectra of 1 g/L RhB@Tb-MOF well dispersed in water with different concentrations of NFX; (C) the luminescence color of RhB@Tb-MOF with different concentrations of NFX and CPFX; (D) effect on the emission spectra of 1 g/L RhB@Tb-MOF well dispersed in water with different concentrations of CPFX. The inset spectra are CIE diagrams. The inset photographs are RhB@Tb-MOF under a 365-nm UV lamp after adding quinolone antibiotic at a certain concentration. *(Reproduced with permission from M. Yu, Y. Xie, X. Wang, Y. Li, G. Li, Highly water-stable dye@ln-MOFs for sensitive and selective detection toward antibiotics in water. ACS Appl. Mater. Interfaces 11 (2019) 21201–21210. Copyright 2019 American Chemical Society.)*

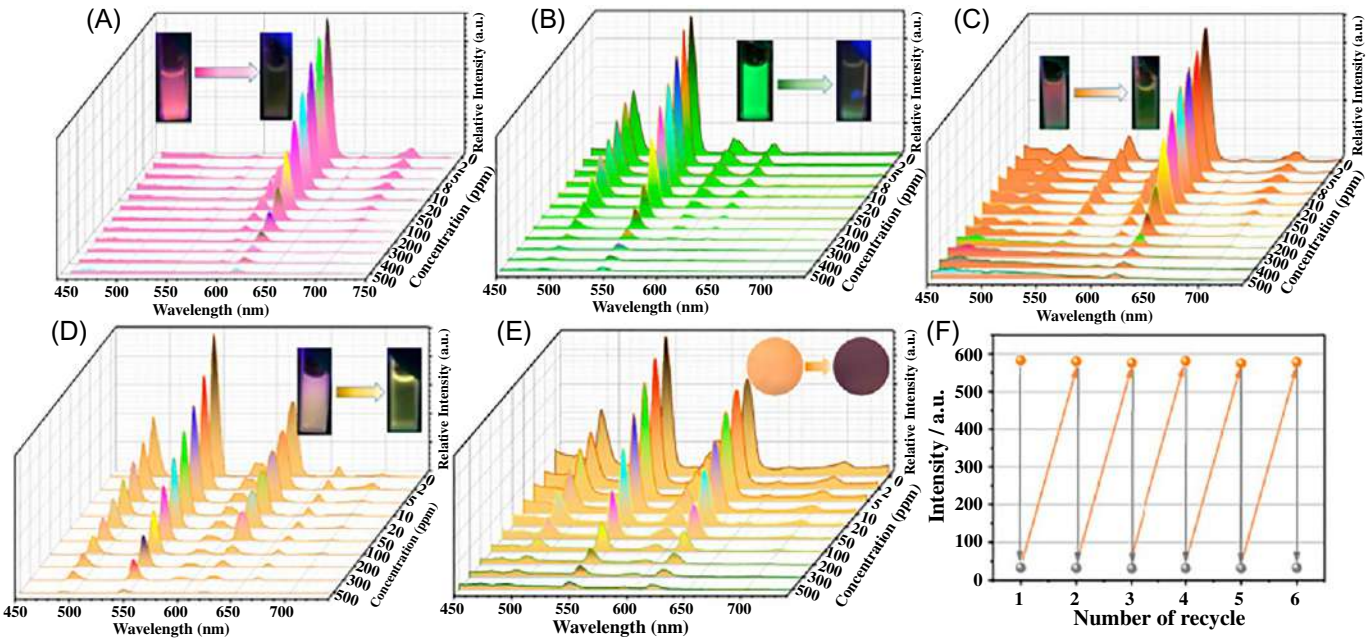

FIG. 10.10 Emission spectra of compounds $Eu_{1-x}Tb_x$-MOF ($x = 0$ (A), 1.0 (B), 0.35 (C) and 0.60 (D)) recorded in different concentrations of ODZ excited at 330 nm. Insert: Luminescent images of 1, 2, 8, and 10 before and after the luminescence reaction under 365-nm UV light. (E) Emission spectra of the bimetallic $Eu_{0.3}Tb_{0.7}$-MOF-10 h membrane recorded in different concentrations of ODZ excited at 330 nm. Insert: Luminescent images of the membrane before and after the luminescence reaction under 365-nm UV light. (F) Luminescent intensity (544 nm) of the membrane containing $Eu_{0.3}Tb_{0.7}$-MOF-10 h after being recycled five times. *(Reproduced with permission from J. Dong, S. Hou, B. Zhao, Bimetallic lanthanide-organic framework membranes as a self-calibrating luminescent sensor for rapidly detecting antibiotics in water. ACS Appl. Mater. Interfaces 12 (2020) 38124–38131. Copyright 2020 American Chemical Society.)*

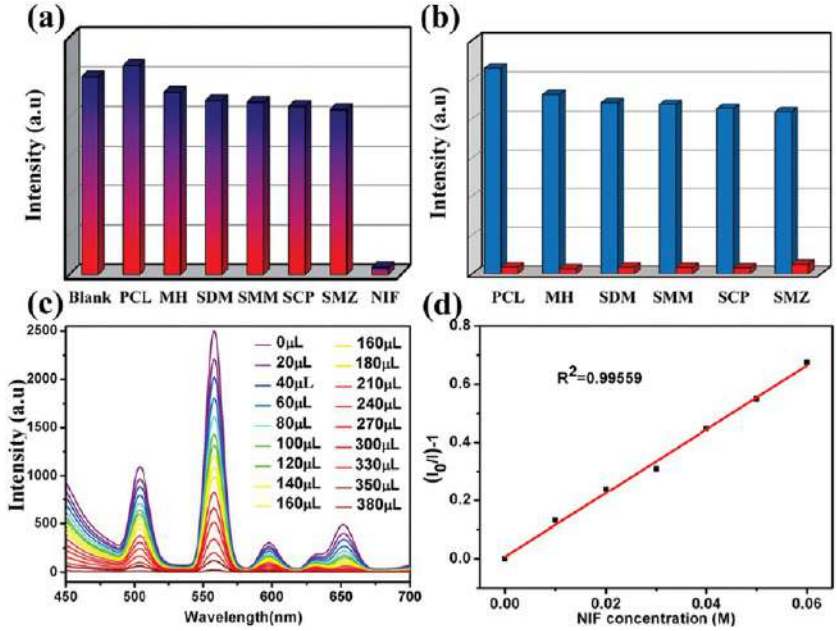

FIG. 10.11 (A) The luminescence intensity (546 nm) of Tb-MOF treated with 0.01 M concentrations of various different antibiotics in DMF; (B) the luminescence intensity (546 nm) of Tb-MOF dispersed in DMF with the addition of different antibiotics (0.01 M) (PCL, MH, SDM, SMM, SCP, SMZ) and NIF-incorporated systems (0.01 M); (C) the luminescence spectra of Tb-MOF in DMF solution with NIF at different concentrations; and (D) a plot of the relative luminescence intensity versus NIF concentration. *(Reproduced with permission from L. Duan, C. Zhang, P. Cen, X. Jin, C. Liang, J. Yang, X. Liu, Stable ln-MOFs as multi-responsive photoluminescence sensors for the sensitive sensing of Fe3+, Cr2O72−, and nitrofuran. CrstEngComm 22 (2020) 1695–1704. Copyright 2020 Royal Chemical Society.)*

$(pta)_5(Hpta)(H_2O)_4]\cdot xH_2O$ (RE = Eu, Gd) and $RE(Hpta)(C_2O_4)]\cdot 3H_2O$ (RE = Tb, Dy, Er, Ho). Furthermore, the Tb-MOF can also be used for quantitatively detecting the concentrations of nitrofuran (NIF) in DMF solution. For the Tb-MOF, most antibiotics displayed a relatively small influence on the emissions, or a gradual change in the luminescent intensity (Fig. 10.11A). NIF, however, presented a drastic quenching effect of 96% on the luminescence. Subsequently, fluorescence titration experiments were performed to check the detection sensitivity of Tb-MOF toward NIF (Fig. 10.11C). From the linear fitting of the S-V plots, the calculated K_{sv} value for NIF was $1.1 \times 10^4\ M^{-1}$ (Fig. 10.11D). The calculated LOD for NIF was 8.1×10^{-5} M. As shown in Fig. 10.11B, in the presence of other interfering antibiotics, the luminescence quenching effect of Tb-MOF caused by NIF was hardly influenced at all, illustrating that Tb-MOF can effectively detect NIF with an exceptional antiinterference ability. NIF can drastically absorb the energy of the excitation light from Tb-MOF, reducing

the efficiency of the energy transformation from the ligand to the Tb^{3+} ions, which definitely induces the luminescence quenching effect. The adsorption of NIF in the UV-Vis region, as well as the collision interaction between the structures and free NIF, consumes the energy and suppresses the intensity [56].

Tetracycline antibiotics (TCs) are a commonly used type of antibiotic for treating infections; however, the overuse of TCs has adversely affected human health and the ecosystem. Thus detection of TCs in water is important, but challenging. Li et al. developed a luminescent $[Tb(HL)L(H_2O)]_n$ (Tb-MOF, H_2L = salicylic acid) for immediate detection of oxytetracycline (OTC) and tetracycline (TC). As shown in Fig. 10.12 (top), the time-dependent emission spectra show a significant decrease in the luminescence of Tb-MOF after its reaction with OTC and TC for 1 min. The rapid sensing results imply that Tb-MOF can be used to monitor OTC and TC in real time and in situ. As shown in Fig. 10.12A (top), after the reacting of 0.2 mM^{-1} suspension with OTC and TC for 1 min, the luminescence is quenched significantly; the color changes from green to colorless under 365-nm UV light (Fig. 10.12B; top) can be distinguished by the naked eye. Further investigation found that anions (Fig. 10.12C and D; top) and cations (Fig. 10.12E and F; top) have little effect on the luminescence of Tb-MOF. Thus, among the 27 tested species of antibiotics, anions, and cations, only OTC and TC quenched the luminescence of Tb-MOF (Fig. 10.12G; top). As shown in Fig. 10.12A and C (bottom), the luminescence of Tb-MOF suspension decreased gradually with the OTC/TC concentration increasing. Meanwhile, the color of the suspension changed from green to colorless under irradiation of a UV lamp (insets of Fig. 10.12A and C). The linearity relationship between the luminescence and OTC/TC concentration is quantitatively illustrated in Fig. 10.12B and D (bottom), which shows the linear correlation coefficients (R^2) of OTC and TC are 0.991 and 0.986, respectively. The K_{sv} values are calculated as $2.18 \times 10^4\ M^{-1}$ for OTC and $1.39 \times 10^4\ M^{-1}$ for TC. Meanwhile, the LOD of Tb-MOF toward OTC and TC are estimated to be 1.95 and 2.77 nM, respectively. The UV light cannot reach the sensor and excite Tb-MOF through the antenna effect, which can be ascribed to the strong inner filter effect (IFE) [61].

Qin et al. synthesized ultrathin Cd-MOF/Tb^{3+} fluorescent nanosheets by a reaction between Cd^{2+} and 2,3-PDC (2,3-pyridinedicarboxylate) ions, whose strong fluorescence can be very sensitively quenched by Cefixime antibiotic in aqueous solution. Fig. 10.13A (top) depicts the emission spectra of the Cd-MOF/Tb^{3+} nanosheet suspension after adding various antibiotics with the same concentration. Only CFX strongly quenches the fluorescence. Fig. 10.13B (top) exhibits the histograms of the emission intensity at 546 nm after introducing various antibiotics with the concentration of 10 μM into the Cd-MOF/Tb^{3+} nanosheets suspension. Fig. 10.13C (top) investigates the fluorescence changes of the system with interfering antibiotics before and after introducing CFX antibiotic. Fig. 10.13D (top) displays the correlation between the relative fluorescence intensity of the system after adding 10 μM CFX and the duration. Within the initial 20 s, the value of I/I_0 dramatically falls; and after

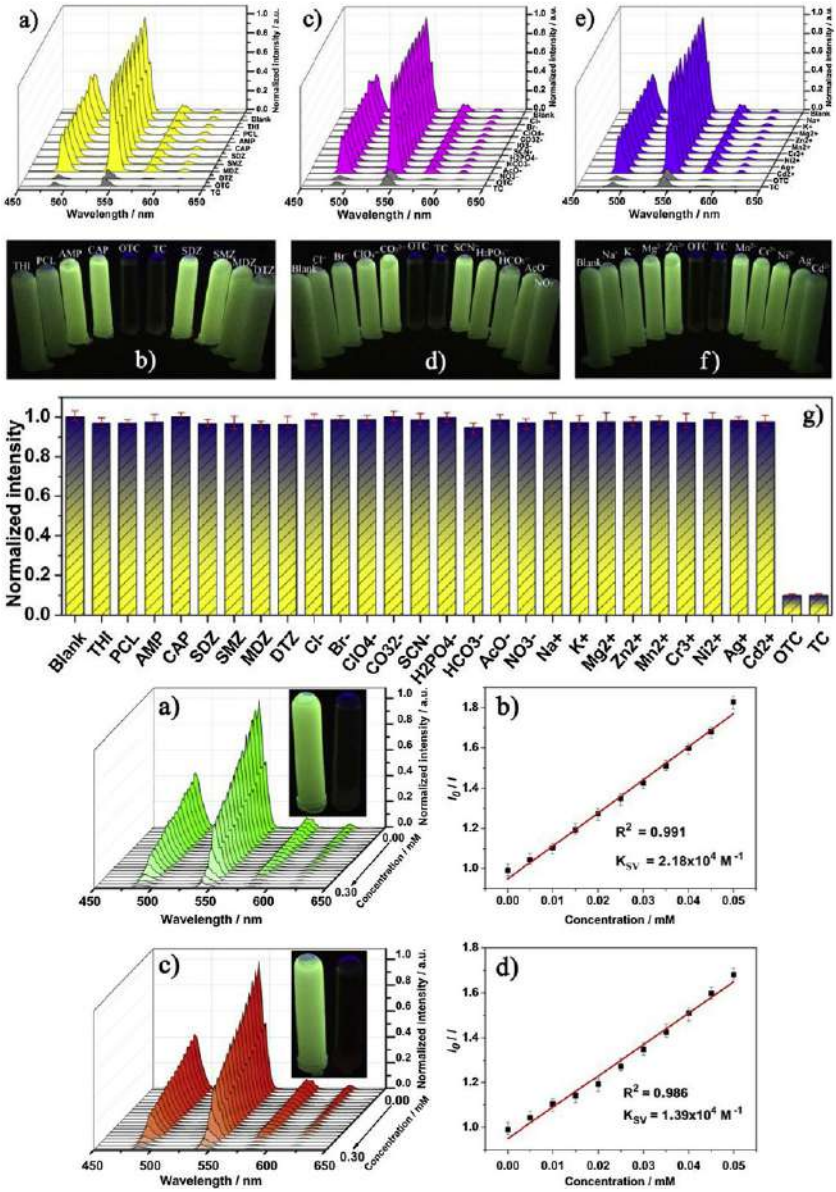

FIG. 10.12 *(Top)* 3D luminescence monitoring of 0.2 mM Tb-MOF reacting with various TCs (A), anions (C), and cations (e) for 1 min; photographs showing the solutions of Tb-MOF reacting with TCs (B), anions (D), and cations (F) under 365-nm UV light; (G) column diagram of luminescence comparison (at 542 nm) while Tb-MOF reacts with various species. *(Bottom)* The emission spectra of Tb-MOF suspension reacting with various concentrations of OTC (A) and TC (C); S-V plot for the luminescence quenching of Tb-MOF by OTC (B) and TC (D) at room temperature. Insets show changes of luminescence under UV light (365 nm) after adding OTC and TC. *(Reproduced with permission from C. Li, C. Zeng, Z. Chen, Y. Jiang, H. Yao, Y. Yang, W. Wong, Luminescent lanthanide metal-organic framework test strip for immediate detection of tetracycline antibiotics in water. J. Hazard. Mater. 384 (2020) 121498. Copyright 2020 Elsevier.)*

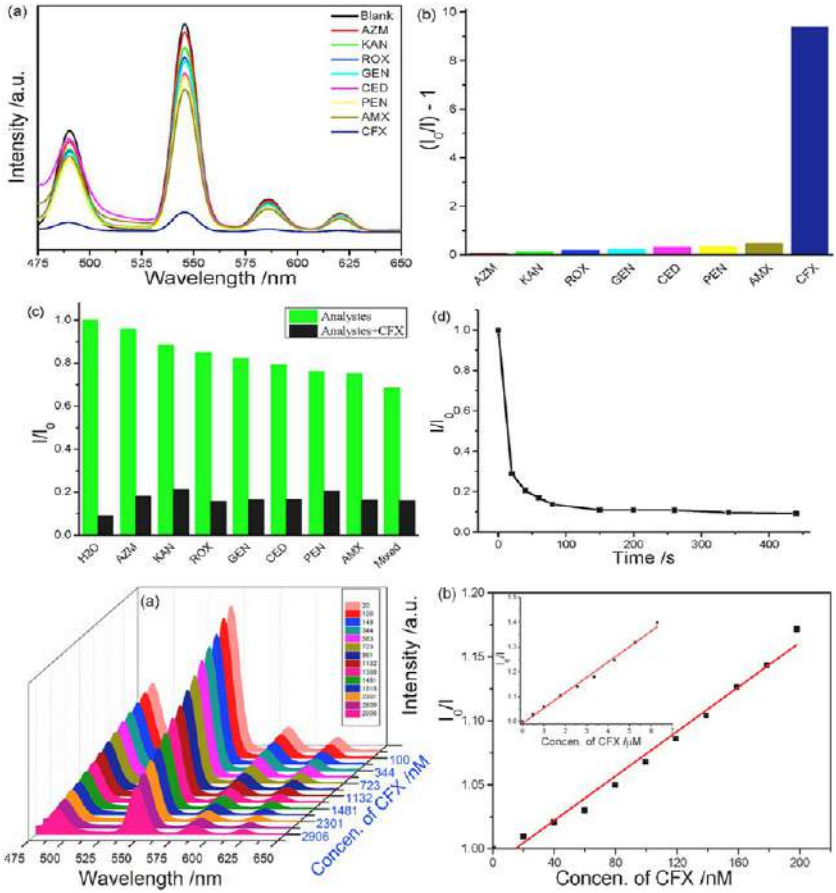

FIG. 10.13 *(Top)* (A) Effect on the emission spectra of 50 μg mL^{-1} Cd-MOF/Tb^{3+} nanosheets colloidal suspension with isovolumetric 10 μM antibiotics aqueous solution; (B) fluorescence quenching efficiency of various antibiotics for Cd-MOF/Tb^{3+} nanosheets at room temperature; (C) the interfering tests of other antibiotics to CFX; (D) the fluorescence intensity changes of the present probe with the duration after introducing 10 μM CFX. *(Bottom)* (A) The emission spectra of Cd-MOF/Tb^{3+} nanosheets suspension after adding CFX with various concentrations under UV excitation of 294 nm; (B) The linear relationships between the I_0/I value of Cd-MOF/Tb^{3+} sample before (the inset) and after exfoliation and concentrations of CFX in the low concentration range. *(Reproduced with permission from G. Qin, J. Wang, L. Li, F. Yuan, Q. Zha, W. Bai, Y. Ni, A highly water-stable cd-MOF/Tb3 + ultrathin fluorescence nanosheets for ultrasensitive and selective detection of Cefixime. Talanta 221 (2021) 121421. Copyright 2021 Elsevier.)*

450 s, the value of I/I_0 slowly declines. Fig. 10.13A (bottom) depicts the emission spectra of the Cd-MOF/Tb^{3+} nanosheets suspension after introducing CFX with various concentrations. With the concentration increase of CFX in the system, the emission intensity of the system gradually decreases. At the low concentration region, a nearly linear correlation is visible (Fig. 10.13B; bottom), from which the Cd-MOF/Tb^{3+} samples before and after exfoliation have the

highest K_{sv} value of 6.16×10^4 and 8.7×10^5 M^{-1} toward CFX, respectively. The LOD of Cd-MOF/Tb^{3+} samples before and after exfoliation toward CFX are separately calculated as 559 and 26.7 nM. The PET and the IFE effects simultaneously exist between Cd-MOF/Tb^{3+} nanosheets and CFX, leading to high sensibility and selectivity for detection of CFX [63].

Liu et al. described a sensitive luminescent probe based on a 3D chiral Cd-MOF, $[(CH_3)_2NH_2][Cd(bpdc)_{1.5}]\cdot 2DMA$ (H_2bpdc = 4,4′-biphenyldicarboxylate acid), for the enantioselective recognition and determination of quinine and quinidine. Additional chiral binding sites were introduced into the pores of the framework of Cd-MOF via exchanging dimethylamine cations with the *N*-benzylquininium cations to prepare the compound Cd-MOF-C, and Eu^{3+} ions are then introduced into the host as the luminescent center. In view of the multiple chiral centers in the channels and the excellent fluorescence properties of the hybrid Cd-MOF-C-Eu, it was designed to be a luminescent probe for the enantioselective recognition of the enantiomers quinine and quinidine. As is illustrated in Fig. 10.14, the fluorescence of suspensions is obviously quenched with the

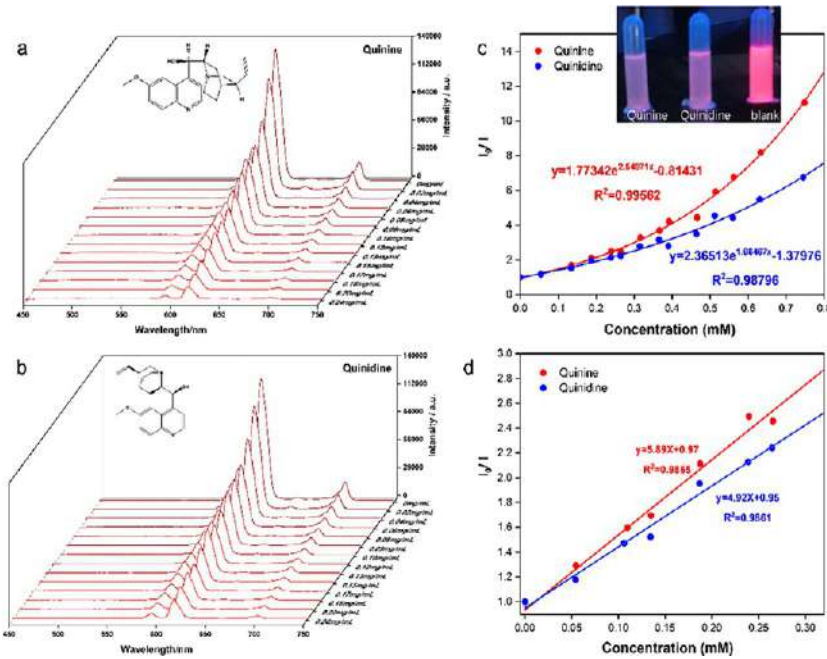

FIG. 10.14 The emission spectra of Cd-MOF-C-Eu dispersed in DMA solutions of (A) quinine and (B) quinidine at different concentrations ranging from 0 to 0.24 mg mL^{-1} (λ_{ex} = 313 nm). The fitting curve of I_0/I versus concentration of quinine and quinidine (C) at full range concentrations and (D) at lower concentrations. The insert picture is the photograph of Cd-MOF-C-Eu dispersed in blank DMA solutions, DMA solutions of quinine and quinidine (0.2 mg mL^{-1}). *(Reproduced with permission from T. Liu, X. Qu, B. Yan, A sensitive metal-organic frameworks nanosensor with cation-introduced chirality for enantioselective recognition and determination of quinine and quinidine in human urine. J. Mater. Chem. C 8 (2020) 14579–14586. Copyright 2020 Royal Chemical Society.)*

gradual addition of quinine and quinidine. In fact, with more enantiomers added, the difference between fluorescence intensities of the suspensions can even be detected by the naked eye (Fig. 10.14 inset picture). When the concentrations of the analytes ranged from 0 to 0.24 mg·mL^{-1}, the quantitative relationships between I_0/I and the concentrations of the analytes could be fitted to the equations in Fig. 10.14C, with the K_{sv} value for quinine being 4522 M^{-1} and for quinidine 3937 M^{-1}, respectively. The S-V plots of the probe obtained by the linear fitting of I_0/I and [C] are indicated in Fig. 10.14D with a good correlation ($R^2 = 0.9865$ and 0.9861, respectively). The K_{sv} values for quinine and quinidine are 5890 and 4920 M^{-1}, respectively. It is calculated that the LOD of Cd-MOF-C-Eu for quinine and quinidine are 19.12 and 23.91 μg L^{-1}, respectively. That means the sensor Cd-MOF-C-Eu can be used as an effective quantitative fluorescent probe for the determination of quinine and quinidine at low concentrations ranging from 0 to 0.086 mg mL^{-1}. Multiple quenching mechanisms are responsible for the luminescence quenching effects of Cd-MOF-C-Eu toward the analytes [65].

Sha et al. designed a fluorescence resonance energy transfer (FRET) aptasensor for quantitative detection of 17b-estradiol (E2), an important endocrine-disrupting compound [66]. Streptavidin was immobilized on the synthesized MIL-53-NH_2 by covalent bonding, and further linked with the biotin-modified E2 aptamer (apt) through specific bonding between avidin and biotin to obtain the FRET donor probe (MIL-53-apt). Meanwhile, complementary DNA (cDNA) modified $Ru(bpy)_3^{2+}$-doped silica nanoparticles ($RuSiO_2$-cDNA) were prepared through covalent bonding. They act as the FRET acceptor probe, since its absorption spectrum shows a large overlap with the emission spectrum of MIL-53-apt. In the presence of E2, aptamer-modified donor probes tend to bind with E2, owing to their higher selectivity and affinity. The hybridization of MIL-53-apt and $RuSiO_2$-cDNA is through complementary base pairing, which shortens the distance between the two probes to lead to FRET. Subsequently, when different concentrations of E2 are present in the system, the strong specific recognition between E2 aptamer and E2 destroys the energy transfer process to varying extents. This causes the recovery of the fluorescence of MIL-53-apt and the fluorescence of $RuSiO_2$-cDNA is quenched, as shown in Fig. 10.15A (top). The calibration curve with a satisfying linear correlation coefficient ($R^2 = 0.99573$) was acquired between the fluorescence intensity ratio (I_{428}/I_{608}) and concentration logarithm of E2, in the range between 0.5 and 1000 nM. Moreover, the corresponding linear regression equation of the sensor estimates the LOD to be 0.2 nM in Fig. 10.15B (top). The proposed sensing strategy based on FRET shows good sensitivity for detection of E2. Some properties of the biosensor affecting its application in real samples have been explored in Fig. 10.15 (bottom). Considering the possible interference of substances in serum, NaCl, $CaCl_2$, $MgCl_2$, L-histidine, urea, glucose, estriol, progesterone, and their mixture (all substances interfering with E2) were selected to replace the detection target E2 for fluorescence detection in Fig. 10.15A (bottom), suggesting high selectivity of the sensor for 17b-estradiol. Moreover,

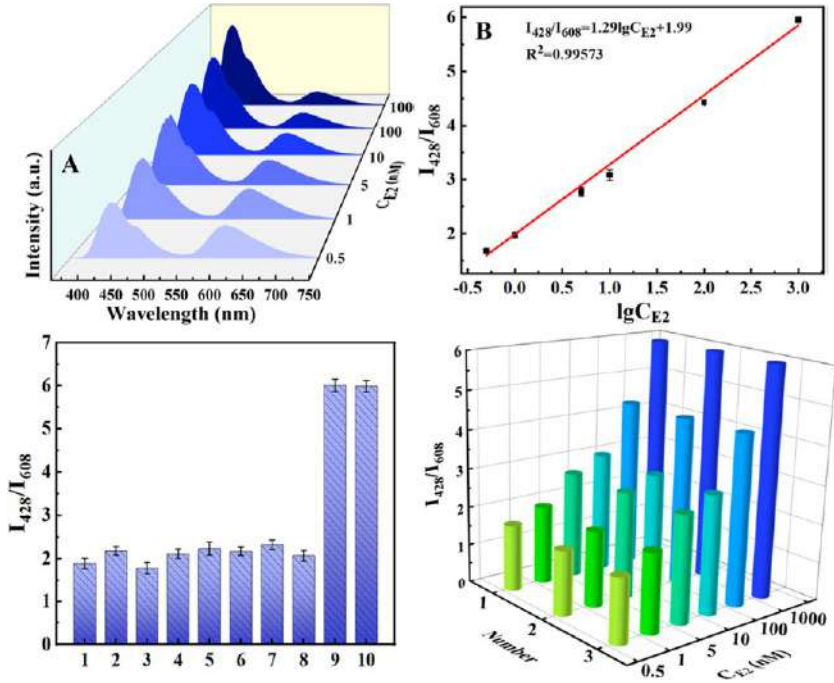

FIG. 10.15 *(Top)* (A) Fluorescence spectrum of this aptasensor with the presence of different concentrations of E2 (0.5–1000 nM) in pH = 8.0 TE buffer (λ_{ex} = 329 nm). (B) The corresponding calibration curves. Error bars were calculated based on the results of three experiments. *(Bottom)* (A) The selectivity of the constructed FRET aptasensor in the presence of different interfering substances (including: 1-NaCl, 2-$CaCl_2$, 3-$MgCl_2$, 4-L-Histidine, 5-urea, 6-glucose, 7-estriol, 8-progesterone, 9-mixture and 10-E2). Error bars were calculated based on the results of three experiments. (B) The reproducibility of three time tests for different E2 concentrations. *(Reproduced with permission from H. Sha, B. Yan, Design of a ratiometric fluorescence sensor based on metal organic frameworks and Ru(bpy)32 +-doped silica composites for 17β-Estradiol detection. https://www.ru.nl/science/analyticalchemistry/ J. Colloid Interface Sci. 583 (2021) 50–57. Copyright 2021 Elsevier.)*

three times repeated detection of different E2 concentrations, with relative standard deviation (RSD) from 1.5% to 4.1%, as shown in Fig. 10.15B (bottom), indicates that the sensor had satisfactory reproducibility for the determination of E2 [66].

Liu et al. selected an ionic MOF, $[(Me)_4N]_2[Pb_6K_6(m\text{-BDC})_9(OH)_2]\cdot H_2O$ (PbK-MOF) for further functionalization to a series of hybrids, RE^{3+}@PbK-MOF (RE = Eu, Tb, Sm and Dy) via cation exchange of RE^{3+} ion. The hybrid Eu^{3+}@PbK-MOF could be developed as a "Turn-On" fluorescent probe of fleroxacin in human serum and urine with high sensitivity and selectivity. As depicted in Fig. 10.16 (left), Eu^{3+}@PbK-MOF had different degrees of fluorescence response to the quinolone drugs, and the ratios between

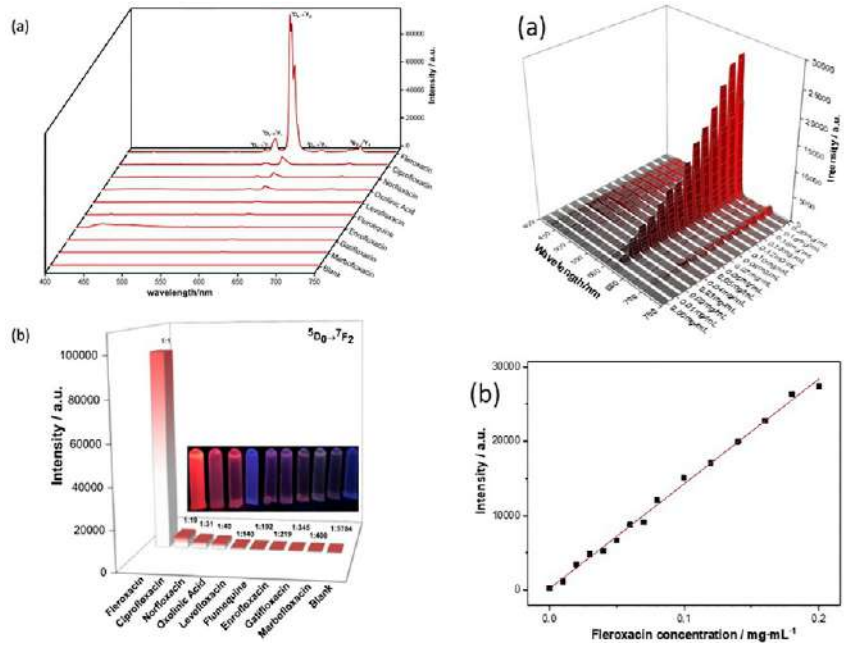

FIG. 10.16 *(Left)* (A) Emission spectra of the Eu^{3+}@PbK-MOF aqueous suspensions containing different quinolone drugs; (B) emission intensities of the main peak at 612 nm assigned to $^5D_0 \rightarrow {}^7F_2$ transition of Eu^{3+} ($\lambda_{ex} = 377$ nm). The insert shows the photograph of the Eu^{3+}@PbK-MOF aqueous suspensions containing different quinolone drugs under 365-nm UV light; the order is the same as that in (B). *(Right)* (A) Emission spectra of the Eu^{3+}@PbK-MOF dispersed in aqueous solutions with different concentrations of fleroxacin, (B) The fitting curve of the emission intensity (613 nm) of Eu^{3+}@PbK-MOF vs. fleroxacin concentration. *(Reproduced with permission from T. Liu, X. Qu, B. Yan, A highly sensitive and selective "turn-on" fluorescent probe of fleroxacin in human serum and urine based on Eu3 + functionalized metal-organic framework. Dalton Trans. 48 (2019) 17945–17952. Copyright 2019 Royal Chemical Society.)*

the fluorescence response intensity of fleroxacin and that of others at 612 nm are marked in the figure. As is observed in Fig. 10.16 (right), the intensities of the fluorescence responses increased gradually with the concentration of the fleroxacin solution. Furthermore, it is encouraging that an obvious linear relationship (correlation coefficient $R^2 = 0.99541$) is present between the emission intensity of solutions at 613 nm and the concentrations of fleroxacin in the experimental range. The LOD of Eu^{3+}@PbK-MOF toward fleroxacin is calculated to be 43.91 ng/mL. The mechanism of fluorescence enhancement can be easily attributed to the self-assembly of Eu^{3+} ions with β-diketonate. As far as the sensitivity of fleroxacin to the fluorescence of Eu^{3+}@PbK-MOF is concerned, a high concentration of fleroxacin coordinated to Eu^{3+} in the framework replaces the coordination H_2O molecules, and then enhances the characteristic emission of Eu^{3+} ions [68].

10.3 Rare earth metal-organic framework hybrid materials for luminescence sensing of nitroaromatic explosives (NAE) and other special dangerous species

Organophosphorus chemical warfare agents (OPCWAs) are organophosphorus esters or acids with high toxicity applied in warfare, terrorism, and pesticides. Due to their volatility and lack of color and odor, they can cause contamination of ground, air, surface, and water and rapid absorption and action through inhalation. OPCWAs are extremely insidious and dangerous to effectively inhibit acetylcholine esterase, shutting down pulmonary muscle control and causing death by oxygen deprivation within minutes. Therefore, detection and neutralization of OPCWAs have received anticipated attention given the recent conflict and subsequent ISIS terrorist organization. The fast, sensitive, and selective detection of OPCWAs is therefore critical to minimize exposure for both humans and the environment [69–71]. Some works have been reported on the luminesence sensing of OPCWAs using rare earth MOF hybrid probes [72–76].

Lian et al. chose dense Hf_{12} cluster MOFs as a subject to synthesize a luminescent sensor (Eu@Hf-MOF). The reactivity of the Hf_{12} cluster and the excellent luminescence of Eu^{3+} encouraged exploration of the sensing performance of Eu@Hf-MOF for OPCWAs. The methanephosphonic acid (MPA) induced a prominent fluorescence quenching effect, and an exciplex mechanism was presented after detailed confirmation. This detection method was further verified in domestic wastewater and a satisfactory outcome was obtained. As shown in Fig. 10.17B (top), in MPA-containing suspension, the emission of Eu^{3+} has dropped markedly and quickly; the difference of $^5D_0 \rightarrow {}^7F_2$ emission (ΔI) between blank and testing samples is several times that of others. This change can also be observed by the naked eye (Fig. 10.17C; top). Fig. 10.16A (bottom) shows that when Eu@Hf-MOF was added into the solution of MPA of 10^{-4}, 10^{-3}, 10^{-2} M with excesses of other chemicals, the intensity change at 614 nm displayed a similar pattern to that with MPA only. To explore the sensitivity of Eu@Hf-MOF to detect a trace quantity of MPA in wastewater, a batch of Eu@Hf-MOF suspensions in wastewater with different concentrations of MPA (10^{-7}–10^{-3} M) was prepared and their emission spectra are recorded in Fig. 10.17B (bottom). As the concentration of MPA gradually increased, the emission intensity of Eu^{3+} progressively decreased. The curve of emission intensity of Eu@Hf-MOF vs. the MPA concentration is plotted in Fig. 10.17C (bottom), and a good linear relationship between them is observed within the concentration of MPA from 10^{-7} M to 10^{-3} M. This linear correlation can be fitted with a correlation coefficient (R^2) of 0.9757 and an LOD of 0.4 ppm [73].

Xu et al. described a noninvasive approach that uses a glove sensor for rapid on-site detection of OPs by a ratiometric fluorescence method, which gives a clear color change. The new single-use wearable "lab-on-a-glove" device that

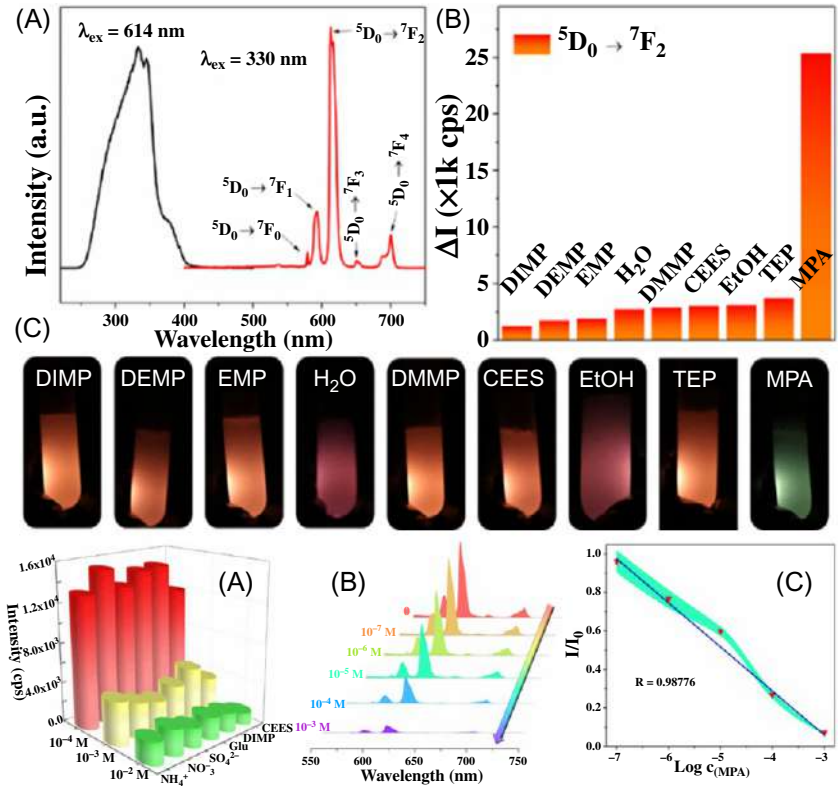

FIG. 10.17 *(Top)* (A) Photoluminescent spectra of Eu@Hf-MOF in solid state; (B) the histogram of $^5D_0 \rightarrow {}^7F_2$ emission of Eu@Hf-MOF in various solutions of OPCWAs; (C) photographs of Eu@Hf-MOF in suspensions with various OPCWAs. *(Bottom)* (A) Intensity of the luminescence of Eu@Hf-MOF in various appendices solutions (NH_4^+, NO_3^-, SO_4^{2-}, Glu, DIMP, and CEES) with different MPA concentrations (10^{-4} M, 10^{-3} M, and 10^{-2} M); (B) emission spectra of Eu@Hf-MOF suspensions in wastewater with different concentrations of MPA; (C) fitting curve of I/I_0 vs. concentration of MPA. *(Reproduced with permission from X. Lian, B. Yan, Trace detecting OPCWAs in wastewater and plant by a luminescent Uio-67(Hf) and evaluation bioaccumulation of OPCWAs. ACS Appl. Mater. Interfaces 10 (2018) 14869–14876. Copyright 2018 American Chemical Society.)*

can withstand mechanical deformations includes CMC aerogel containing two fluorescent materials (Eu-MOFs and CDs) fabricated on a stretchable and flexible nitrile glove. Eu-MOFs with bright red emission act as a working fluorescence center, and their fluorescence can be quenched by target OP (CP) due to the competitive absorption effect. Blue mission CDs that have no response to CP serve as a reference fluorescence center. The glove-based fluorescent measurements required swipe sampling (collector) and fluorescent analysis (sensor) on the same finger, as illustrated in Fig. 10.18A (right, top). Dynamic mechanical deformation and bending studies demonstrated resilience against

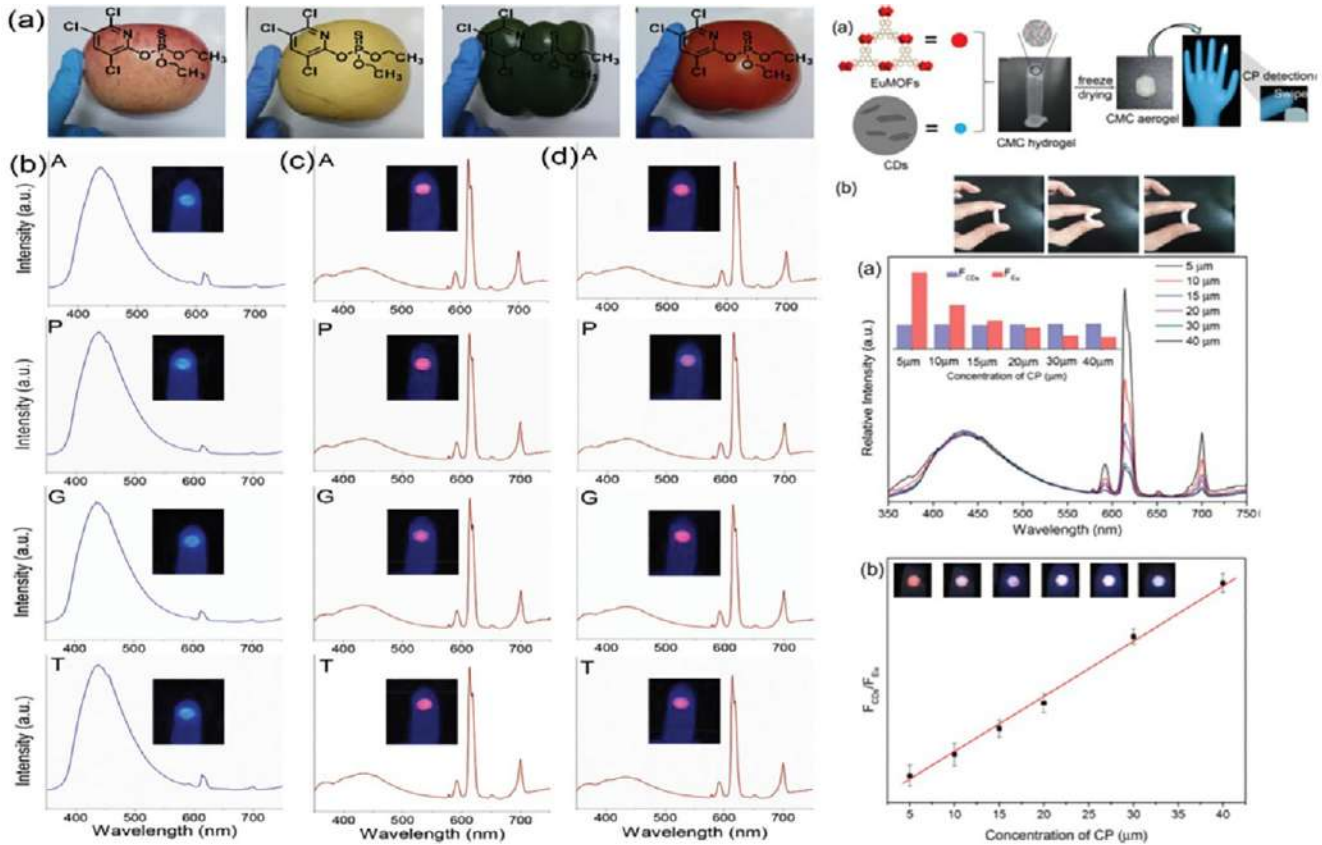

FIG. 10.18 *(Left)* Wearable glove sensor for CP detection on the surfaces of different agricultural products: apple, pear, green pepper, and tomato. (A) The swiping pictures for the glove sensor on different agricultural product surfaces for sampling; fluorescence emission spectra of the sensing glove on different agricultural product surfaces contaminated by CP (B), EtOH (C), and DM (D), $\lambda_{ex} = 365$ nm; insets of (B), (C), and (D) are the corresponding photographs under UV-light irradiation of 365 nm. *(Right, Top)* (A) Simple schematic illustration of the wearable CP monitoring device containing MOF loading, CMC hydrogel freeze-drying, and swipe process; (B) pictures of dynamic mechanical deformation of the CMC aerogel. *(Right, Bottom)* (A) Concentration-dependent emission spectra of the glove sensor upon different concentrations of CP from 5 to 40 μm; the inset is the emission intensity of CDs at 445 nm (F_{CDs}) and Eu-MOFs at 614 nm (F_{Eu}) in different concentrations of CP ($\lambda_{ex} = 365$ nm); (B) the linear fitted curve showing F_{CDs}/F_{Eu} versus CP contention ($\lambda_{ex} = 365$ nm); insets are the corresponding photographs of the glove sensor treated by different concentrations of CP under 365-nm UV-light irradiation. *(Reproduced with permission from X. Xu, B. Yan, X. Lian, Wearable glove sensor for non-invasive organophosphorus pesticide detection based on a double-signal fluorescence strategy. Nanoscale 10 (2018) 13722–13729. Copyright 2018 Royal Chemical Society.)*

mechanical deformations, as expected in real-life applications of the new chemical sensing glove (Fig. 10.18; right, top). Then, they tested the potential of the glove sensor for CP detection on different agricultural products (fruits and vegetables). Fig. 10.18A (left) shows the photographs of the glove sensor after swiping the skin surface of apple (A), pear (P), green pepper (G), and tomato (T) with 100 μM of CP. The optical images of this glove sensor for different samples under the irradiation of a UV lamp are recorded. As shown in Fig. 10.18B (left), a blue color is observed for glove-based swiping and sensing of CP on these agricultural products. In contrast, no color change occurred in the blank experiments involving the same sample surfaces but without CP (Fig. 10.18C; left). Similarly, a red color was observed in control experiments using DM (100 μM) contaminated surface (Fig. 10.18D; left). As expected, the presence of CP (100 μM) triggered an apparent quench of the Eu^{3+}-based emission of the glove sensor, as shown in Fig. 10.18B (left). The intensity ratios of F_{CDs} and F_{Eu} show 45.5-, 47.8-, 46.6- and 45.7-fold increase for apple, pear, green pepper and tomato, respectively. However, no clear intensity change in CDs or Eu^{3+}-based emission is found in the blank (Fig. 10.18C; left) and control experiments (Fig. 10.18D; left). Considering that our main goal is to obtain quantitative information for the presence of OP, concentration-dependent studies on the luminescent properties of the sensing glove were carried out. As exhibited in Fig. 10.18A (right, bottom), the emission intensity of Eu^{3+} decreases gradually as the contaminated CP concentration increases from 5 to 40 μM, whereas that of CDs is nearly constant. Meanwhile, the relative PL intensities (F_{CDs}/F_{Eu}) also increased as the CP concentration increased. Fig. 10.18B (right, bottom) presents the relative luminescent intensities (F_{CDs}/F_{Eu}) versus the concentration of CP. A good linear correlation ($R^2 = 0.99529$) is observed over the 5–40 μM concentration range, and the LOD is determined to be 89 nM. As shown in the inset of Fig. 10.18B (right, bottom), the colors of the sensor changed from brilliant orange-red to dark purple and faint blue as the concentration of CP increased from 5 to 40 μM; these observations can be clearly seen. The concentration-induced color change or double-readout assay of the glove sensor is reliable for real samples [74].

Nitroaromatic compounds (NACs) are highly volatile in nature, which makes them an important class of explosives. When a conventional explosive detonates, relatively unstable chemical bonds convert into more stable bonds, which produces kinetic energy in the form of thermal energy and blast. The transformation from less stable bonds to more stable bonds is exothermic. The NACs in the biosphere are mostly industrial chemicals such as explosives, dyes, polyurethane foams, herbicides, insecticides, and solvents. Various NAC explosives, including trinitrotoluene (TNT), tetryl, and picric acid (PA), are known. TNT is a constituent in many explosive compositions and is quite heavily used in civilian and military applications. However, the illicit use of NACs is also prevalent these days. As well as being explosive in nature, NACs are toxic and are environmental pollutants that can cause serious health

problems like skin diseases, and eye, liver, and neurological damage. The detection of explosives is immensely important due to the constant intimidation from terrorist attacks worldwide. In addition, explosives need to be handled at manufacturing sites and mining locations. NACs are electron-deficient in nature and can easily form charge-transfer complexes with electron-rich moieties. An ideal chemosensor for NACs would be an ensemble involving a π-electron-rich fluorophore [76–84]. Extensive research has been carried out on the luminescence sensing of NACs by rare earth MOF hybrid materials [48,85–130].

Zhang et al. synthesized five Cd(II)-RE(III) hetero-MOFs [CdCl(*L*)$Eu_xTb_y(H_2O)(DMA)](NO_3)\cdot 3DMA$ (IFMC-36-Eu_xTb_y, H_3L = 4,4′,4″-((2,2′,2″-(nitrilotris(methylene))tris (1H-benzo[d]-imidazole-2,1-diyl)) tris(methylene)) tribenzoic acid). The solvent-dependent luminescent behavior of IFMC-36-Eu showed a potential application in detection of the small molecule pollutant nitrobenze (NB) by significant fluorescence quenching. The luminescence spectrum of the IFMC-36-Eu sample dispersed in DMA is shown in Fig. 10.19A (left). To examine the potential of IFMC-36-Eu toward sensing of small molecules, the luminescence properties of IFMC-36-Eu in different solvent emulsions were

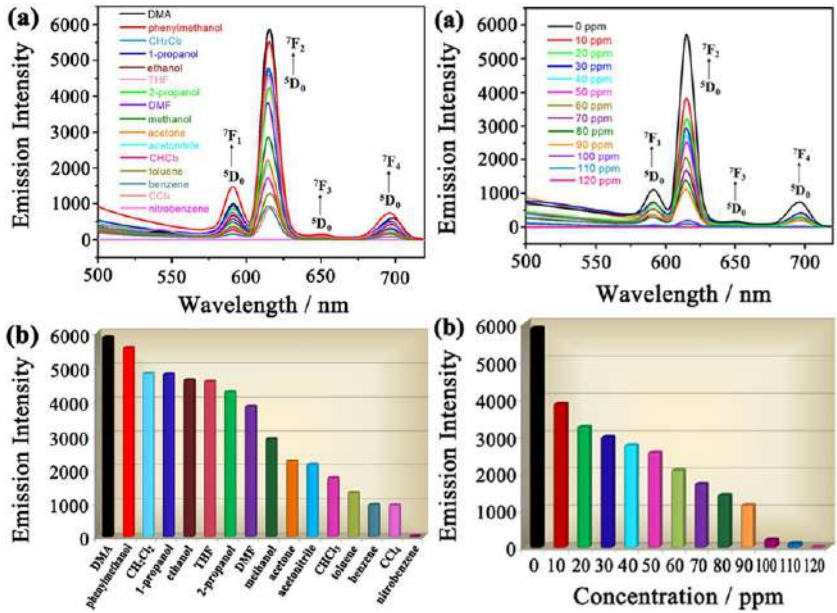

FIG. 10.19 *(Left)* (A) Emission spectra and (B) the $^5D_0 \rightarrow {}^7F_2$ transition intensities of IFMC-36-Eu introduced into various pure solvents when excited at 367 nm. *(Right)* (A) Emission spectra and (B) the $^5D_0 \rightarrow {}^7F_2$ transition intensities of IFMC-36-Eu introduced into different concentrations of nitrobenzene in DMA (excited at 367 nm). *(Reproduced with permission from S. Zhang, D. Du, J. Qin, S. Li, W. He, Y. Lan, Z. Su, 2D Cd(II)–Lanthanide(III) heterometallic – organic frameworks based on metalloligands for tunable luminescence and highly selective, sensitive, and recyclable detection of nitrobenzene. Inorg. Chem. 53 (2014) 8105–8113. Copyright 2014 American Chemical Society.)*

investigated (Fig. 10.19A; left). The most intriguing feature was that the luminescent intensity of the $^5D_0 \rightarrow {}^7F_2$ transition at 617 nm of Eu^{3+} was largely dependent on the solvent molecules (Fig. 10.19B; left), and the physical interaction between the solute and solvent played a vital role. Notably, the emission intensity exhibited significant quenching behaviors, especially in the case of NB. As shown in Fig. 10.19A (right), the luminescence intensity of the IFMC-36-Eu suspension significantly decreased into 55.7% at an NB concentration of only 50 ppm, and was almost completely quenched at 120 ppm (Fig. 10.19B; bottom). The excellent fluorescence quenching response to NB can be attributed to the PET mechanism. The finely ground powder of IFMC-36-Eu can be dispersed well in the solution, enabling NB to be closely adhered to the surface of the MOF particles and facilitate possible host-guest interactions. The electron transfer from the electron-donating framework with rich π-electrons to the highly electron-deficient NB molecule adsorbed on the surface of the MOF particles can take place upon excitation, resulting in fluorescence quenching [85].

Wang et al. selected H_4L (5,5′-(pyridine-2,5-diyl)-isophthalic acid) as the π-conjugated ligands to get a $[Eu_6(L)_3(HL)_2(H_2O)_{10}]\cdot 10H_2O \cdot x$(solvent) (Eu-MOF) that exhibits a combination of uncoordinated Lewis-base sites and terminally coordinated aqua ligands, which exhibit high sensitivity and selectivity toward *o*-, *m*-, and *p*-NP (NP = nitrophenol). As shown in Fig. 10.20 (top, left), *o*-, *m*-, and *p*-NP can almost completely quench the emission of Eu-MOF. The fluorescence intensity decreased continuously upon incremental addition of an ethanol *o*-, *m*-, and *p*-NP solution into a standard Eu-MOF emulsion in ethanol (Fig. 10.20; top, right and bottom). The fluorescence quenching by *o*-, *m*- and *p*-NP can be detected at very low concentrations (0.33, 0.67, and 0.17 mM, respectively) with extremely high sensitivity. The relative luminescent intensity (I_0/I) versus the *o*-, *m*-, and *p*-NP concentrations are shown in insets of Fig. 10.20 (top, right) and (bottom) to further quantify the quenching efficiency. Notably, the I_0/I versus the *o*-, *m*-, and *p*-NP concentration plots bend upwards rather than being the typically linear plots, which may be due to the presence of simultaneous static and dynamic quenching. There are no interactions between *o*-, *m*-, and *p*-NP and the Eu^{3+} ions and changes in emission intensity are related to the interactions between them and the ligands L^{4-}. The quenching mechanism may be attributed to the following: (i) electron transfer upon excitation from the conduction band (CB) of MOFs to the LUMOs of analytes; (ii) competitive absorption between MPFs and analytes; (iii) the electrostatic interactions between the hydroxyl groups of the analytes and the free Lewis-base sites of pyridine rings in Eu-MOF [86].

Wang et al. prepared an Eu-MOF, $[Eu_2(L)_2(DMAC)_2]\cdot nH_2O$ (H_4L = 5-(bis (4-carboxybenzyl) amino)-isophthalic acid, DMAC = *N*,*N*′-dimethylacetamide), which exhibited an excellent luminescent sensing of TNP. To obtain a stable suspension, the crystal samples of Eu-MOF were finely ground and immersed in DMAC by ultrasonication treatment for 30 min. Then the maximum luminescent intensity of Eu-MOF was reduced by 22.27%, 25.88%, 28.03%, 28.78%, and 75.08%, respectively, when the content of nitroaromatic

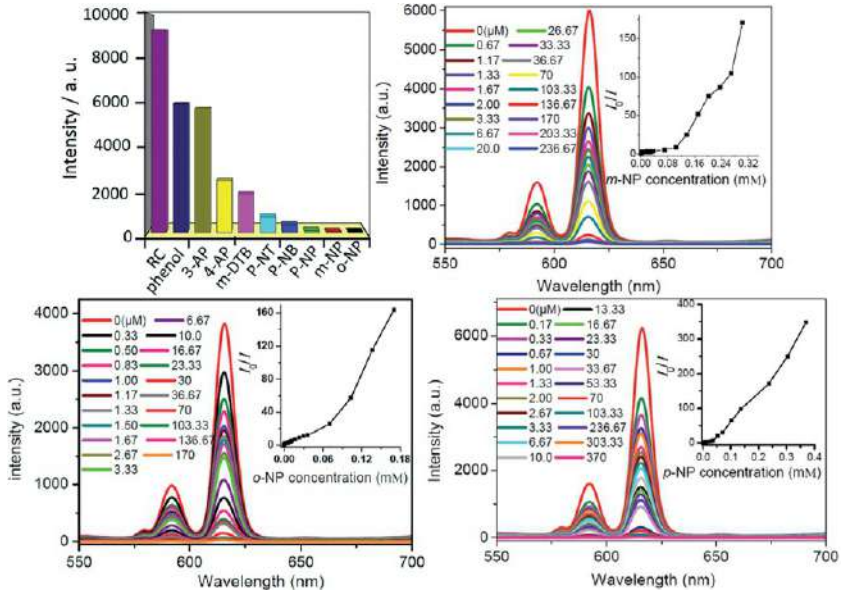

FIG. 10.20 *(Top, Left)* Luminescence intensity of 1 dispersed in ethanol on the addition of different analytes (0.1 M). RC (resorcinol), 3-AP (3-aminophenol), 4-AP (4-aminophenol), *m*-DTB (*m*-dinitrobenzene), *p*-NT (*p*-n nitrotoluene), NB (nitrobenzene), *p*-NP (*p*-nitrophenol), *m*-NP (*m*-nitrophenol), and *o*-NP (*o*-nitrophenol). Emission intensity at 616 nm was selected. Effect on the emission spectra of 1 dispersed in ethanol upon incremental addition of an NP ethanol solution ($\lambda_{ex} = 358$ nm). Inset: Stern-Volmer plot of I_0/I versus the NP concentration: *(Top, Right)* for *m*-NP and *(Bottom)* for *o*-NP and *p*-NP. *(Reproduced with permission from Y. Wang, Q. Tan, H. Liu, W. Sun, Z. Liu, A luminescent europium MOF containing Lewis basic pyridyl site for highly selective sensing of o-, m- and p-nitrophenol. RSC Adv. 5 (2015) 86614–86619. Copyright 2015 Royal Chemical Society.)*

compounds was 120 μL (10 mM, in DMAC solution) (Fig. 10.21A). This suggests that the quenching efficiencies of Eu-MOF follow the sequence of TNP > 2,6-DNT > 2,4-DNT > NB > *m*-DNB (Fig. 10.21B). The quenching efficiency can be quantitatively explained by the S-V equation with K_{sv} estimated as $1.39 \times 10^3\ M^{-1}$ for NB, $1.9 \times 10^3\ M^{-1}$ for *m*-DNB, $2.33 \times 10^3\ M^{-1}$ for 2,4-DNT, $2.4 \times 10^3\ M^{-1}$ for 2,6-DNT, and $3.58 \times 10^4\ M^{-1}$ for TNP, respectively. For Eu-MOF, TNP is the most efficient quencher with an LOD of 4.66×10^{-4} mM, suggesting its extremely high detection sensitivity toward TNP. In addition, the luminescent intensity and quenching ability of Eu-MOF exhibited negligible changes after being used for four repeated cycles (Fig. 10.21D). Generally, the CB of a MOF lies at a higher energy than the lowest LUMOs energy of nitroaromatic compounds, and leads to a luminescent quenching. It was found that the LUMOs energies are in good agreement with the maximum quenching efficiency observed for TNP. In addition, there may be another luminescent quenching mechanism in this work, such as FRET.

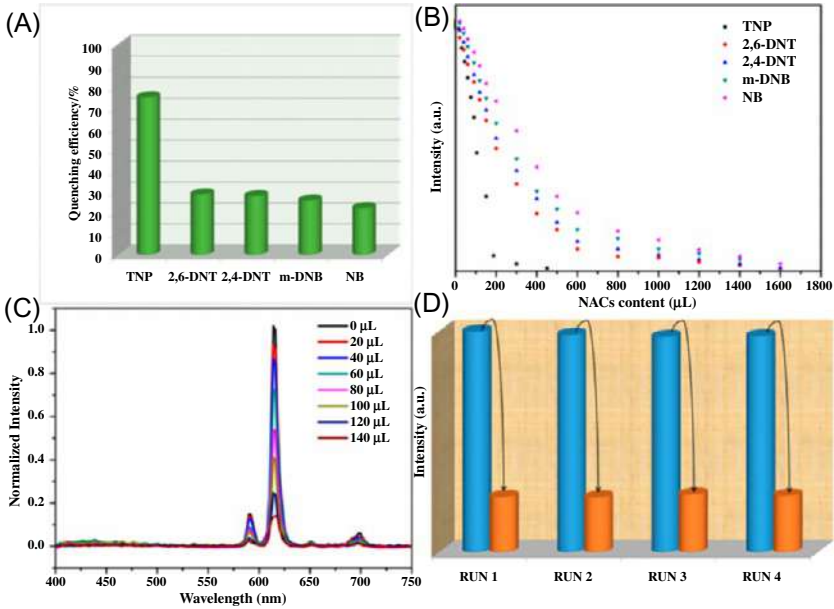

FIG. 10.21 (A) Quenching efficiency of Eu-MOF for various nitroaromatic compounds. (B) The relationships between emission intensities and nitroaromatic compounds. (C) Emission spectra of Eu-MOF dispersed in DMAC upon incremental addition of TNP solution in DMAC. (D) Reproducibility of Eu-MOF dispersed in DMAC with TNP solution of 120 μL. *(Reproduced with permission from X. Wang, P. Yan, Y. Li, G. An, X. Yao, G. Li, Highly efficient white-light emission and UV-visible/NIR luminescence sensing of lanthanide metal–organic framework. Cryst. Growth Des. 17 (2017) 2178–2185. Copyright 2017 American Chemical Society.)*

Wang et al. constructed a luminescent Tb-MOF, $[Tb_4(L)_6(H_2O)_8]$ (H_2L = 4-{bis(4-benzoic) amino}-4H-1,2,4-triazole) that exhibited multiresponsive behavior toward nitromethane, while also being able to detect trace amounts of NACs with a rapid response in both liquid and vapor phases. The sensing behavior of Tb-MOF toward other NACs such as nitrobenzene (NB), 1,4-dinitrobenzene (1,4-DNB), 2-nitrotoluene (2-NT), 2,4-dinitrotoluene (2,4-DNT), 1,3-dinitrotoluene (1,3-DNB), and 2,4,6-trinitrophenol (TNP) in aqueous solution was also investigated (Fig. 10.22A and B; top). With the addition of 70 ppm of TNP, the emission could be quenched by 98.5%, showing a high selectivity and sensitivity toward TNP in aqueous solution. The time-dependent emission spectra showed the different luminescence responses to the vaporized analytes, especially for NB and 2-NT (94% and 85%). The diffusion-controlled process was responsible for explaining the identically fast and remarkable fluorescence quenching response for NB and 2-NT (Fig. 10.22; bottom). The energy of the excited light can be strongly absorbed by TNPN either in the aqueous or vapor phase, t, which reduces the probability of energy transfer from the H_2L ligand to Tb^{3+}, and ultimately results in luminescence quenching. Once the TNP molecules are captured onto the surface of the

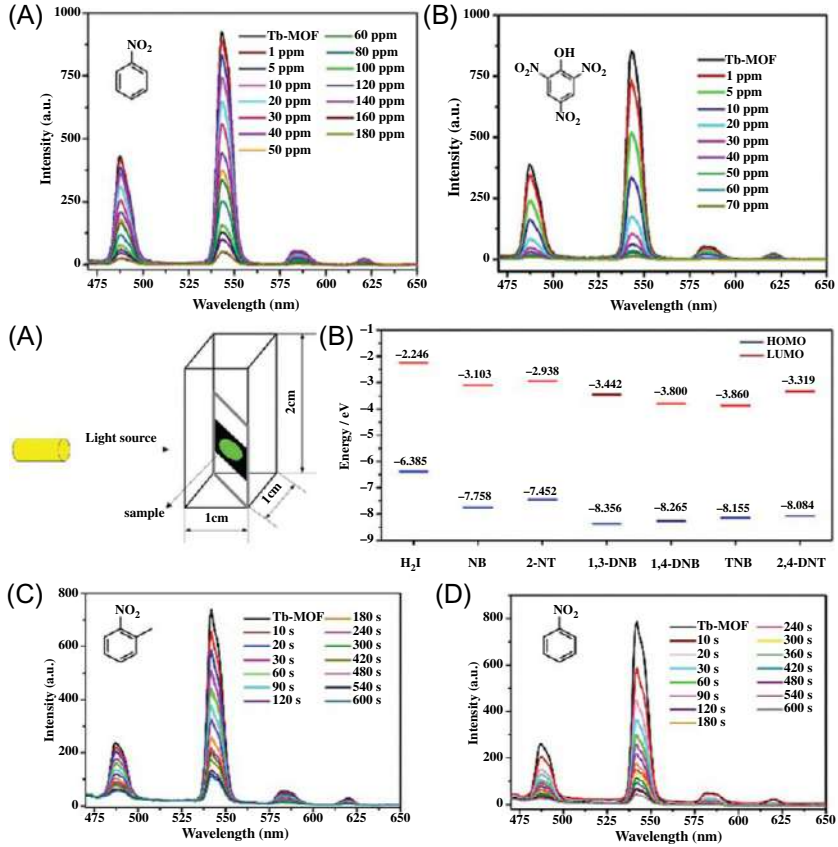

FIG. 10.22 *(Top)* Fluorescence titration of Tb-MOF dispersed in aqueous solution with the gradual addition of NB (A) and TNP (B). *(Bottom)* (A) The homemade setup for the NACs vapor detection. (B) The calculated energy levels of the H_2L ligand and the selected NACs. Time-dependent emission spectrum of Tb-MOF in NB vapor (C) and 2-NT vapor (D). *(Reproduced with permission from X. Wang, J. Li, C. Jiang, P. Hu, B. Li, T. Zhang. H. Zhou, An efficient strategy for improving the luminescent sensing performance of a terbium(III) metal-organic framework towards multiple substances. Chem. Commun. 54 (2018) 13271–13274. Copyright 2018 Royal Chemical Society.)*

Tb-MOF, the luminescence quenching can be attributed to the competition of the absorption of light source energy and PET [105].

Mukherjee et al. synthesized two RE-MOFs, $[\{Dy(2N_3\text{-}TPA)_2(H_2O)(CH_3OH)\}]_\infty$(Dy-NMOF1) and $[\{Dy_4(5N_3\text{-}IPA)_6(DMF)_3(H_2O)_4\}(DMF)(H_2O)_2]_\infty$ (Dy-NMOF2) from two carboxylate ligands (2-azidoterephthalate ($2N_3$-TPA) and 5-azidoterephthalate ($5N_3$-IPA)), with immobilized azide functionalities oriented toward the pore surfaces, which were exploited as fluorescent probes for the detection of various nitro analytes such as nitrotoluene (NT), nitrobenzene (NB), 2,6-dinitrotoluene (DNT), 4-nitrobenzoic acid (4-NBA), picric acid (PA), etc. The fluorescence titration profile of PA (Fig. 10.23; top) clearly indicates that complete attenuation of intensity

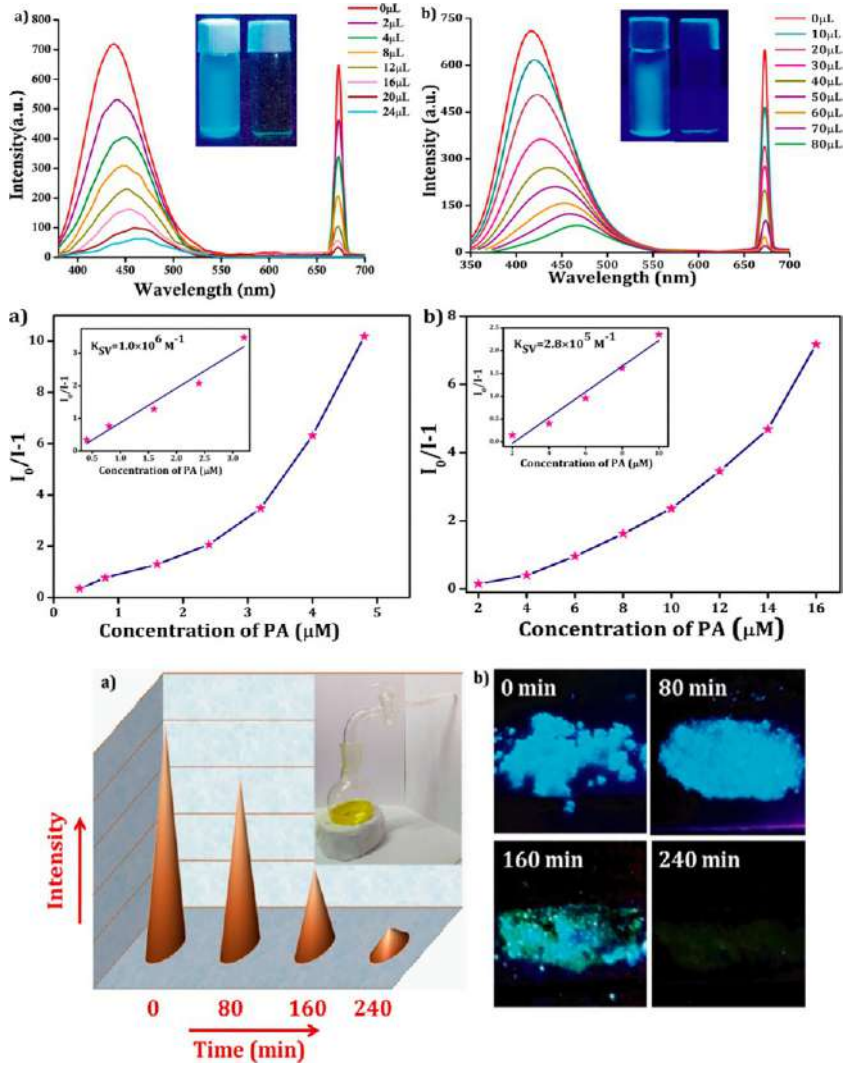

FIG. 10.23 *(Top)* Effect on the emission spectrum of aqueous suspensions of (A) Dy-NMOF1 and (B) Dy-NNMOF2 upon incremental addition of PA. The insets show visual color changes of (A) Dy-NMOF1 and (B) Dy-NNMOF2 before and after titrating with PA under UV radiation. *(Middle)* SV plot of PA in water suspensions of (A) Dy-NMOF1 and (B) Dy-NNMOF2. Insets: linear fitting within the lower concentration region with R^2 values of 0.97 for (A) and 0.98 for (B). *(Bottom)* (A) Aqueous solution of PA exposed to solid Dy-NMOF11. (B) Optical images of a solid sample under UV light at various time intervals. *(Reproduced with permission from S. Mukherjee, S. Ganguly, A. Chakraborty, A. Mandal, D. Das, Green synthesis of self assembled nanospherical dysprosium MOFs: selective and efficient detection of picric acid in aqueous and gas phase. ACS Sustain. Chem. Eng. 7 (2019) 819–830. Copyright 2018 American Chemical Society.)*

occurs upon addition of 24 and 80 μL of a 0.5 mM solution of PA in Dy-NMOF1(2). The naked eye blue emission of both NMOFs under UV radiation becomes completely dark upon addition of the requisite amount of PA in the respective NMOF suspensions. Evidently, the quenching efficiencies of the nitro analytes fall in the order PA ≫ DN > NBA > NB > NT, which agrees well with the order of their π acidity. As depicted in Fig. 10.23 (middle) (S-V plot for PA), it is quite clear that the nature of the plot remains linear in the lower concentration region, while at higher concentration it deviates from linearity considerably, presumably due to the concurrent presence of static and dynamic quenching processes, self-absorption, and/or certain kinds of FRET pathways between the PA and the NMOFs. K_{sv} values for PA detection are 1.0×10^6 and 2.8×10^5 M^{-1} using Dy-NMOF1(2). The LODs for PA sensing are 0.04 μM and 0.125 μM for Dy-NMOF1(2) for the high sensitivity. These data clearly demonstrate that a FRET process is operative between PA and NMOFs, whereas for other nitro analytes fluorescence quenching is merely due to a PET mechanism. So, due to the combined effect of two processes (PET and RRET), the high quenching constants for PA sensing are encountered. The researchers selected Dy-NMOF1 to study detection phenomena in the vapor phase; a rapid decrease in the fluorescence intensity could be observed by the naked eye within 4 h of exposure (Fig. 10.23; bottom) [112].

Wu et al. reported a Tb-MOF based on H_4MDIA (5,5′-methylenediisophthalic acid): $[Tb(HMDIA)(H_2O)_3]\cdot H_2O$, which allowed naked-eye detection of explosives in ethanol. The luminescence responses of Tb-MOF to various aromatic compounds were investigated by the addition of PA, NB, DNT, aniline (A), TNT, toluene (T), and benzene (B) at concentrations of 0.33 mM in ethanol [122]. As shown in Fig. 10.24B, the fluorescence intensity of a Tb-MOF suspension hardly changes with the addition of A, T, and B. However, a significant quenching of the emission intensity is observed in the presence of PA, TNT, DNT, and NB, with the quenching efficiency decreasing in the following order: PA > TNT > DNT > NB. In this case, the fluorescence quenching of Tb-MOF originated from PET from its excited state to the NAC. When up to 0.33 mM PA was added to an ethanol suspension of Tb-MDIA (0.33 g/L), the quenching efficiency reached >98% (Fig. 10.24A). The LOD for PA is approximately 5×10^{-7} M, indicating that Tb-MDIA has good sensitivity for PA as a Turn-Off luminescent sensory material. Fitting the data to the linear S-V equation gives a $K_{sv} = 63{,}708$ M^{-1}. The visible green light from the original Tb-MOF disappears after the addition of PA under UV radiation. The Tb-MOF framework exhibits different detection performances for PA and TNT, whose different quenching mechanisms for TNT and PA may originate from supramolecular interactions (e.g., hydrogen bonding) between the Tb-MOF framework and hydroxyl groups in the PA molecules. The quenching effect for *p*-NP is almost the same as that for PA, different from *m*-NP and *o*-NP. These results indicate that only NPs with suitable

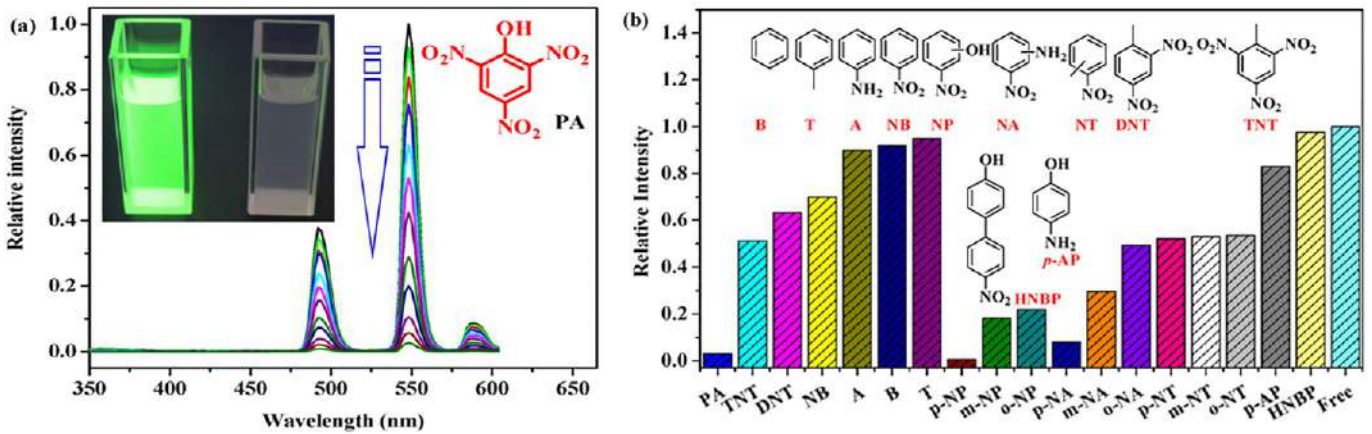

FIG. 10.24 (A) Luminescent emission spectra of Tb-MOF in ethanol (0.33 g/L) with added PA (0.33 mM). The inset shows that the visible green light emitted from the original Tb-MOF complex disappeared after PA (0.33 mM) incorporation under 365-nm UV radiation. (B) Fluorescence responses of Tb-MOF to different selected analytes (0.33 mM). The inset shows the molecular structures of the analytes. Excitation is at 305 nm. *(Reproduced with permission from P. Wu, L. Xia, M. Huangfu, F. Fu, M. Wang, B. Wen, Z. Yang, J. Wang, Lanthanide-based metal–organic frameworks containing "V-shaped" tetracarboxylate ligands: synthesis, crystal structures, "naked-eye" luminescent detection, and catalytic properties. Inorg. Chem. 59 (2020) 264–273. Copyright 2020 American Chemical Society.)*

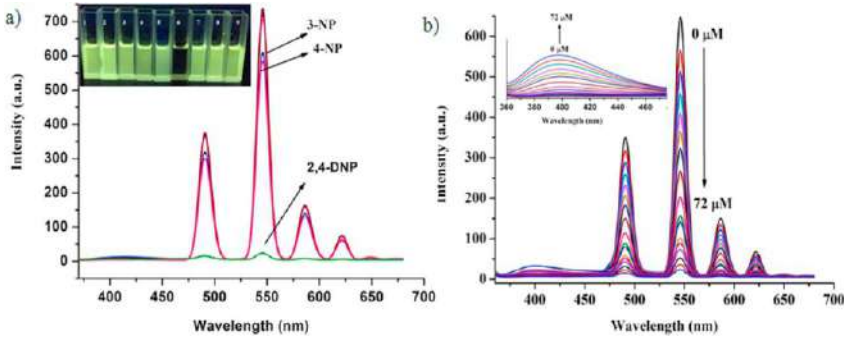

FIG. 10.25 (A) Fluorescence spectra of Tb-MOF (2 mL, 10 μM) in DMF with 1 equiv. of NACs ($\lambda_{ex} = 350$ nm, slit width: 5,5) (Inset: the photographs of fluorescence colors of Tb-MOF with nitroaromatic compounds.1: Tb-MOF, 2: MB, 3: DMB, 4: 3-NP, 5: 4-NP, 6: 2, 4-DNP, 7: 2,4-DNT, 8: 1,3-DNT, 9: NT); (B) Luminescence titration spectra of Tb-MOF (2 mL, 10 μM) with 2, 4-DNP (0–72 μM) in DMF (Inset: the luminescence emission increasing at 408 nm with the addition of 2,4-DNP). *(Reproduced with permission from Z. Xu, X. He, Y. He, X. Zhao, M. Batmunkh, H. Li, Y. Wang, J. Cao, T. Ma, A luminescent terbium coordination complex as multifunctional sensing platform. Talanta 208 (2020) 120363. Copyright 2020 Elsevier.)*

configurations facilitate the formation of hydrogen bonds between the hydroxyl groups and framework. The selective detection of PA is based on the combined effects of hydrogen-bonding interactions, electron transfer, and size matching [122].

Xu et al. designed and synthesized a Tb-MOF, $Tb(HL)(EtOH)_2(NO_3)_2$ (H_2L = 2,6-bis-(5-pyridin-4-yl-1H-[1,2,4]triazol-3-yl)-pyridine), with the ability to sense 2,4-DNP compound by "Turn-Off" fluorescence. It should be noted that the emission intensity peak of Tb-MOF was highly quenched and a weak emission centered at 408 nm was generated after addition of 2,4-DNP, as compared to the minor effect of other competing nitro compounds (Fig. 10.25A). As shown in Fig. 10.25B, after incremental addition of 2,4-DNP, the sequential fluorescence quenching can be clearly observed. The limit of detection from the linear regression curve plot of 2, 4-DNP is found to be 1.69 μM. When 2,4-DNP is added into the solution of Tb-MOF, accompanied by the quenching of the luminescence of Tb-MOF, the weak emission at 408 nm being generated means the H_2L is released, which can also confirm the decomposition of the Tb-MOF (Fig. 10.25B). The result shows that the sensing mechanism of 2, 4-DNP is the coordination of 2,4-DNP with the Tb^{3+} cation to lead to the decomposition of the Tb-MOF [127].

References

[1] P. Chandrasekhar, A. Mukhopadhyay, G. Savitha, J.N. Moorthy, Remarkably selective and enantiodifferentiating sensing of histidine by a fluorescent homochiral Zn-MOF based on pyrenetetralactic acid, Chem. Sci. 7 (2016) 3085–3091.

[2] A. Yang, S. Hou, Y. Shi, G. Yang, D. Qin, B. Zhao, Stable lanthanide-organic framework as a luminescent probe to detect both histidine and aspartic acid in water, Inorg. Chem. 58 (2019) 6356–6362.
[3] M. Rekharsky, H. Yamamura, M. Kawai, Y. Inoue, Critical difference in chiral recognition of N-Cbz-D/L-aspartic and glutamic acids by mono- and bis(trimethylammonio)-cyclodextrins, J. Am. Chem. Soc. 123 (2001) 5360–5361.
[4] J.L. Johnson, Aspartic acid as a precursor for glutamic acid and glycine, Brain Res. 67 (1974) 358–362.
[5] J. Liu, J. Hou, J. Liu, X. Jing, L. Li, J. Du, Pyrazinyl-functionalized Zr(iv)-MOF for ultrasensitive detection of tyrosine/TNP and efficient CO^2/N^2 separation, J. Mater. Chem. C 7 (2019) 11851–11857.
[6] S.A. Murfitt, P. Zaccone, X. Wang, A. Acharjee, Y. Sawyer, A. Koulman, L.D. Roberts, A. Cooke, J. Griffin, Metabolomics and lipidomics study of mouse models of type 1 diabetes highlights divergent metabolism in purine and tryptophan metabolism prior to disease onset, J. Proteome Res. 17 (2018) 946–960.
[7] M. Kishino, M. Kondoh, T. Hirasawa, Enhanced L-cysteine production by overexpressing potential L-cysteine exporter genes in an L-cysteine-producing recombinant strain of *Corynebacterium glutamicum*, Biosci. Biotechnol. Biochem. 83 (2019) 2390–2393.
[8] Y.I. Mahmoud, S.S. Sayed, Effects of L-cysteine on lead acetate induced neurotoxicity in albino mice, Biotech. Histochem. 91 (2016) 327–332.
[9] H.N. Abdelhamid, A. Bermejo-Gómez, B. Martín-Matute, X. Zou, A water-stable lanthanide metal-organic framework for fluorimetric detection of ferric ions and tryptophan, Microchim. Acta 184 (2017) 3363–3371.
[10] H. Weng, B. Yan, A sliver ion fabricated lanthanide complex as a luminescent sensor for aspartic acid, Sens. Actuators B 253 (2017) 1006–1011.
[11] X. Qian, W. Gong, F. Wang, Y. Lin, G. Ning, A pyrylium-based colorimetric and fluorimetric chemosensor for the selective detection of lysine in aqueous environment and real sample, Tetrahedron Lett. 56 (2015) 2764–2767.
[12] D. Dousa, J. Brichac, P. Gibala, P. Lehnert, Rapid hydrophilic interaction chromatography determination of lysine in pharmaceutical preparations with fluorescence detection after post-column derivatization with o-phtaldialdehyde, J. Pharm. Biomed. Anal. 54 (2011) 972–978.
[13] X. Wang, Z. Huang, J. Du, X. Wang, N. Gu, X. Tian, Y. Li, Y. Liu, J. Huo, B. Ding, Hydrothermal preparation of five rare-earth (Re = Dy, Gd, Ho, Pr, and Sm) luminescent cluster-based coordination materials: the first MOFs-based ratiometric fluorescent sensor for lysine and bifunctional sensing platform for insulin and Al^{3+}, Inorg. Chem. 57 (2018) 12885–12899.
[14] X. Wang, X. Wang, Y. Yuan Liu, J. Huo, Y. Li, Q. Wang, K. Liu, B. Ding, Ultrasonic preparation of near-infrared emission cluster-based YbIII and NdIII coordination materials: ratiometric temperature sensing, selective antibiotics detection and "turn-on" discrimination of L-arginine, Ultrason. Sonochem. 59 (2019), 104734.
[15] T. Sun, R. Fan, R. Xiao, T. Xing, M. Qin, Y. Liu, S. Hao, W. Chen, Y. Yang, Anionic Ln–MOF with tunable emission for heavy metal ion capture and L-cysteine sensing in serum, J. Mater. Chem. A 8 (2020) 5587–5594.
[16] Y. Liu, Y. Lu, B. Zhang, L. Hou, Y. Wang, Post-synthetic functionalization of Ni-MOF by Eu^{3+} ions: luminescent probe for aspartic acid and magnetic property, Inorg. Chem. 59 (2020) 7531–7538.
[17] D. Yang, L. Lu, S. Feng, M. Zhu, First ln-MOF as a trifunctional luminescent probe for the efficient sensing of aspartic acid, Fe^{3+} and DMSO, Dalton Trans. 49 (2020) 7514–7524.

[18] Z. Li, Z. Zhan, M. Hu, A luminescent terbium coordination polymer as a multifunctional water-stable sensor for detection of Pb^{2+} ions, PO_4^{3-} ions, $Cr_2O_7^{2-}$ ions, and some amino acids, CrstEngComm 22 (2020) 6727–6737.
[19] X. Zhao, R. Tapec-Dytioco, W. Tan, Ultrasensitive DNA detection using highly fluorescent bioconjugated nanoparticles, J. Am. Chem. Soc. 125 (2003) 11474–11475.
[20] H. Zhang, F. Li, B. Dever, X.-F. Li, X.C. Le, DNA-mediated homogeneous binding assays for nucleic acids and proteins, Chem. Rev. 113 (2012) 2812–2841.
[21] J. Tian, N. Cheng, W. Xing, X. Sun, Cobalt phosphide nanowires: efficient nanostructures for fluorescence sensing of biomolecules and photocatalytic evolution of dihydrogen from water under visible light, Angew. Chem. Int. Ed. 54 (2015) 5493–5497.
[22] S. Zhao, L. Wu, J. Feng, S. Song, H. Zhang, An ideal detector composed of a 3D Gd-based coordination polymer for DNA and Hg^{2+} ion, Inorg. Chem. Front. 3 (2016) 376–380.
[23] G. Tang, J. Gao, C. Wang, H. Tan, Luminescent lanthanide coordination polymer as a platform for DNA colorimetric detection, Sens. Actuators B 244 (2017) 571–576.
[24] S. Yang, W. Zhao, P. Hu, K. Wu, Z. Jiang, L. Bai, M. Li, J. Chen, Lanthanum-based metal-organic frameworks for specific detection of Sudan virus RNA conservative sequences down to single-base mismatch, Inorg. Chem. 56 (2017) 14880–14887.
[25] Y. Wang, N. Du, X. Zhang, Y. Wang, Y. Xing, F. Bai, L. Sun, Z. Shi, Functional sensing materials based on lanthanide N-heterocyclic polycarboxylate crystal frameworks for detecting thiamines, Cryst. Growth Des. 18 (2018) 2259–2269.
[26] Q. Li, Z. Zhang, W. Yao, J. Li, J. Yang, A novel ternary system for the determination of ascorbic acid concentration based on resonance Rayleigh scattering, Anal. Methods 7 (2015) 9963–9970.
[27] H. Meng, D. Yang, Y. Tu, J. Yan, Turn-on fluorescence detection of ascorbic acid with gold nanolcusters, Talanta 165 (2017) 346–350.
[28] D. Yue, D. Zhao, J. Zhang, L. Zhang, K. Jiang, X. Zhang, Y. Cui, Y. Yang, B. Chen, G. Qian, A luminescent cerium metal-organic framework for the turn-on sensing of ascorbic acid, Chem. Commun. 53 (2017) 11221–11224.
[29] Y. Zeng, H. Zheng, J. Gu, G. Cao, W. Zhuang, J. Lin, R. Cao, Z. Lin, Dual-emissive metal-organic framework as a fluorescent "switch" for ratiometric sensing of hypochlorite and ascorbic acid, Inorg. Chem. 58 (2019) 13360–13369.
[30] K. Wu, L. Qin, C. Fan, S. Cai, T. Zhang, W. Chen, X. Tang, J. Chen, Sequential and recyclable sensing of Fe^{3+} and ascorbic acid in water with a terbium(III)-based metal–organic framework, Dalton Trans. 48 (2019) 8911–8919.
[31] D. Goltzman, D. Miao, Encyclopedia of Endocrine Diseases, Elsevier, New York, 2004, pp. 164–169.
[32] Y. Liu, K.S. Schanze, Conjugated polyelectrolyte-based real-time fluorescence assay for alkaline phosphatase with pyrophosphate as substrate, Anal. Chem. 80 (2008) 8605–8612.
[33] S.G. Julien, N. Dube, S. Hardy, M.L. Tremblay, Inside the human cancer tyrosine phosphatome, Nat. Rev. Cancer 11 (2011) 35–49.
[34] C. Wang, G. Tang, H. Tan, Pyrophosphate ion-triggered competitive displacement of ssDNA from a metal–organic framework and its application in fluorescent sensing of alkaline phosphatase, J. Mater. Chem. B 6 (2018) 7614–7620.
[35] B. Liu, H. Shen, D. Liu, Y. Hao, X. Zhu, Q. Shen, P. Qu, M. Xu, Citrate/Tb lanthanide coordination polymer nanoparticles: preparation and sensing of guanosine-5-monophosphate, Sens. Actuators B 300 (2019), 126879.
[36] Y. Cui, F. Chen, X. Yin, A ratiometric fluorescence platform based on boric-acid-functional Eu-MOF for sensitive detection of H_2O_2 and glucose, Biosens. Bioelectron. 135 (2019) 208–215.

[37] D. Chavez-Garacıa, K. Juarez-Moreno, C.H. Campos, E.M. Tejeda, J.B. Alderete, G.A. Hirata, Cytotoxicity, genotoxicity and uptake detection of folic acid-functionalized green upconversion nanoparticles Y2O3/Er3+, Yb3+ as biolabels for cancer cells, J. Mater. Sci. 53 (2018) 6665–6680.

[38] Z. Dong, F. Zhao, L. Zhang, Z. Liu, Y. Wang, A white-light-emitting lanthanide metal-organic framework for luminescence turn-off sensing of MnO_4^- and turn-on sensing of folic acid and construction of a "turn-on plus" system, New J. Chem. 44 (2020) 10239–10249.

[39] B. Liu, H. Shen, Y. Hao, X. Zhu, S. Li, Y. Huang, P. Qu, M. Xu, Lanthanide functionalized metal-organic coordination polymer: toward novel turn-on fluorescent sensing of amyloid β-peptide, Anal. Chem. 90 (2018) 12449–12455.

[40] Y. Tian, Z. Zhang, N. Gao, P. Huang, F. Wu, A label-free luminescent assay for tyrosinase activity monitoring and inhibitor screening with responsive lanthanide coordination polymer nanoparticles, Spectrochim. Acta A Mol. Biomol. Spectrosc. 228 (2020), 117751.

[41] K. Wu, M. Chen, N. Huang, R. Li, W. Pan, W. Zhang, W. Chen, J. Chen, Facile and recyclable dopamine sensing by a label-free terbium(III) metal-organic framework, Talanta 221 (2021), 121399.

[42] J.L. Martinez, Environmental pollution by antibiotics and by antibiotic resistance determinants, Environ. Pollut. 157 (2009) 2893–2902.

[43] K. Kümmerer, Antibiotics in the aquatic environment—a review—part I, Chemosphere 75 (2009) 417–434.

[44] Q. Zhang, G. Ying, C. Pan, Y. Liu, J. Zhao, Comprehensive evaluation of antibiotics emission and fate in the river basins of China: source analysis, multimedia modeling, and linkage to bacterial resistance, Environ. Sci. Technol. 49 (2015) 6772–6782.

[45] J. Li, R. Li, X. Li, Construction of metal–organic frameworks (MOFs) and highly luminescent Eu(III)-MOF for the detection of inorganic ions and antibiotics in aqueous medium, CrstEngComm 20 (2018) 4962–4972.

[46] Z. Wang, L. Zhou, T. Zhao, L. Cai, X. Guo, P. Duan, Q. Sun, Hierarchical self-assembly and chiroptical studies of luminescent 4d-4f cages, Inorg. Chem. 57 (2018) 7982–7992.

[47] M. Yu, Y. Xie, X. Wang, Y. Li, G. Li, Highly water-stable dye@ln-MOFs for sensitive and selective detection toward antibiotics in water, ACS Appl. Mater. Interfaces 11 (2019) 21201–21210.

[48] J. Wei, J. Yi, M. Han, B. Li, S. Liu, Y. Wu, L. Ma, D. Li, A water-stable terbium(III)–organic framework as a chemosensor for inorganic ions, nitro-containing compounds and antibiotics in aqueous solutions, Chem. Asian J. 14 (2019) 3694–3701.

[49] S. Xu, J. Shi, B. Ding, Z. Liu, X. Wang, X. Zhao, E. Yang, A heterometallic sodium(I)-europium(III)-organic layer exhibiting dual-responsive luminescent sensing for nitrofuran antibiotics, $Cr_2O_7^{2-}$ and MnO_4^- anions, Dalton Trans. 48 (2019) 1823–1834.

[50] J. Zhang, L. Gao, Y. Wang, L. Zhai, X. Niu, T. Hu, A bifunctional 3D Tb-based metal–organic framework for sensing and removal of antibiotics in aqueous medium, CrstEngComm 21 (2019) 7286–7292.

[51] C. Li, F. Zhang, X. Li, G. Zhang, Y. Yang, A luminescent Ln-MOF thin film for highly selective detection of nitroimidazoles in aqueous solutions based on inner filter effect, JOL 205 (2019) 23–29.

[52] M. Yu, X. Yao, X. Wang, Y. Li, G. Li, White-light-emitting decoding sensing for eight frequently-used antibiotics based on a lanthanide metal-organic framework, Polymers 11 (2019) 99.

[53] L. Jia, S. Guo, J. Xu, X. Chen, T. Zhu, T. Zhao, A ratiometric fluorescent nano-probe for rapid and specific detection of tetracycline residues based on a dye-doped functionalized nanoscaled metal–organic framework, Nanomaterials 9 (2019) 976.

[54] J. Dong, S. Hou, B. Zhao, Bimetallic lanthanide-organic framework membranes as a self-calibrating luminescent sensor for rapidly detecting antibiotics in water, ACS Appl. Mater. Interfaces 12 (2020) 38124–38131.

[55] S. Wu, M. Zhu, Y. Zhang, M. Kosinova, V.P. Fedin, E. Gao, A water-stable lanthanide coordination polymer as multicenter platform for ratiometric luminescent sensing antibiotics, Chem. A Eur. J. 26 (2020) 3137–3144.

[56] B. Li, Y. Jiang, Y. Sun, Y. Wang, M. Han, Y. Wu, L. Ma, D. Li, The highly selective detecting of antibiotics and support of noble metal catalysts by a multifunctional Eu-MOF, Dalton Trans. 49 (2020) 14854–14862.

[57] X. Wang, W. Wei, K. Zhang, S. Du, A stable LnMOF as a highly efficient and selective luminescent sensor for detecting malachite green in water and real samples, RSC Adv. 10 (2020) 6129–6134.

[58] L. Duan, C. Zhang, P. Cen, X. Jin, C. Liang, J. Yang, X. Liu, Stable ln-MOFs as multi-responsive photoluminescence sensors for the sensitive sensing of Fe^{3+}, $Cr_2O_7^{2-}$, and nitrofuran, CrstEngComm 22 (2020) 1695–1704.

[59] S. Sun, X. Sun, Q. Sun, E. Gao, J. Zhang, W. Li, Europium metal-organic framework containing helical metal-carboxylate chains for fluorescence sensing of nitrobenzene and nitrofunans antibiotics, J. Solid State Chem. 292 (2020), 121701.

[60] H. Yang, P. Xu, X. Wang, X. Zhao, E. Yang, A highly stable (4, 8)-connected Tb-MOF exhibiting efficiently luminescent sensing towards nitroimidazole antibiotics, Z. Anorg. Allg. Chem. 646 (2020) 23–29.

[61] L. Yu, H. Chen, J. Yue, X. Chen, M. Sun, J. Hou, K.A. Alamry, H.M. Marwani, X. Wang, S. Wang, Europium metal-organic framework for selective and sensitive detection of doxycycline based on fluorescence enhancement, Talanta 207 (2020), 120297.

[62] Q. Xu, G. Dong, R. Cui, X. Li, 3D lanthanide-coordination frameworks constructed by a ternary mixed-ligand: crystal structure, luminescence and luminescence sensing, CrstEngComm 22 (2020) 740–750.

[63] C. Li, C. Zeng, Z. Chen, Y. Jiang, H. Yao, Y. Yang, W. Wong, Luminescent lanthanide metal-organic framework test strip for immediate detection of tetracycline antibiotics in water, J. Hazard. Mater. 384 (2020), 121498.

[64] X. Lian, Y. Zhang, J. Wang, B. Yan, Antineoplastic mitoxantrone monitor: a sandwiched mixed matrix membrane (MMMs) based on luminescent MOFs-hydrogel hybrid, Inorg. Chem. 59 (2020) 10304–10310.

[65] G. Qin, J. Wang, L. Li, F. Yuan, Q. Zha, W. Bai, Y. Ni, A highly water-stable cd-MOF/Tb^{3+} ultrathin fluorescence nanosheets for ultrasensitive and selective detection of Cefixime, Talanta 221 (2021), 121421.

[66] G.E. Gomez, M. dos Santos Afonso, H.A. Baldoni, F. Roncaroli, G.J.A.A. Soler-Illia, Luminescent lanthanide metal organic frameworks as chemosensing platforms towards agrochemicals and cations, Sensors 19 (2019) 1260.

[67] T. Liu, X. Qu, B. Yan, A sensitive metal-organic frameworks nanosensor with cation-introduced chirality for enantioselective recognition and determination of quinine and quinidine in human urine, J. Mater. Chem. C 8 (2020) 14579–14586.

[68] H. Sha, B. Yan, Design of a ratiometric fluorescence sensor based on metal organic frameworks and $Ru(bpy)_3^{2+}$-doped silica composites for 17β-Estradiol detection, J. Colloid Interface Sci. 583 (2021) 50–57. https://www.ru.nl/science/analyticalchemistry/.

[69] B. Wang, B. Yan, A turn-on fluorescent probe Eu^{3+} functionalized Ga-MOF integrated with logic gate operation for detecting ppm-level Ciprofloxacin (CIP) in urine, Talanta 208 (2020), 120438.

[70] T. Liu, X. Qu, B. Yan, A highly sensitive and selective "turn-on" fluorescent probe of fleroxacin in human serum and urine based on Eu^{3+} functionalized metal-organic framework, Dalton Trans. 48 (2019) 17945–17952.
[71] G.H. Dennison, M.R. Johnston, Mechanistic insights into the luminescent sensing of organophosphorus chemical warfare agents and simulants using trivalent lanthanide complexes, Chem. A Eur. J. 21 (2015) 6328–6338.
[72] V. Kumar, E.V. Anslyn, A selective turn-on fluorescent sensor for sulfur mustard simulants, J. Am. Chem. Soc. 135 (2013) 6338–6344.
[73] G. Yue, S. Su, N. Li, M. Shuai, X. Lai, D. Astruc, P. Zhao, Gold nanoparticles as sensors in the colorimetric and fluorescence detection of chemical warfare agents, Coord. Chem. Rev. 311 (2016) 75–84.
[74] X. Lian, B. Yan, A dual-functional bimetallic-organic framework nanosensor for detection and decontamination of lachrymator in drinking water, Sens. Actuators B 281 (2019) 168–174.
[75] X. Lian, B. Yan, Trace detecting OPCWAs in wastewater and plant by a luminescent Uio-67 (Hf) and evaluation bioaccumulation of OPCWAs, ACS Appl. Mater. Interfaces 10 (2018) 14869–14876.
[76] X. Xu, B. Yan, X. Lian, Wearable glove sensor for non-invasive organophosphorus pesticide detection based on a double-signal fluorescence strategy, Nanoscale 10 (2018) 13722–13729.
[77] B. Wang, X. Lian, B. Yan, Recyclable Eu^{3+} functionalized Hf-MOF fluorescent probe for urinary metabolites of some organophosphorus pesticides, Talanta 214 (2020), 120856.
[78] W. Wei, K. Zhang, X. Wang, S. Du, Construction of a highly stable lanthanide metal-organic framework for effective detection of aryl-organophosphorus flame retardants in simulated wastewater and fruit juices, Inorg. Chim. Acta 511 (2020), 119840.
[79] P. Kovacic, R. Somanathan, Nitroaromatic compounds: environmental toxicity, carcinogenicity, mutagenicity, therapy and mechanism, J. Appl. Toxicol. 34 (2014) 810–824.
[80] K.S. Ju, R.E. Parales, Nitroaromatic compounds, from synthesis to biodegradation, Microbiol. Mol. Biol. Rev. 74 (2010) 250–272.
[81] Y. Ma, S. Wang, L. Wang, Nanomaterials for luminescence detection of nitroaromatic explosives, Trends Anal. Chem. 65 (2015) 13–21.
[82] K.K. Kartha, A. Sandeep, V.K. Praveen, A. Ajayaghosh, Detection of nitroaromatic explosives with fluorescent molecular assemblies and pi-gels, Chem. Rec. 15 (2015) 252–265.
[83] F. Akhgari, H. Fattahi, Y.M. Oskoei, Recent advances in nanomaterial-based sensors for detection of trace nitroaromatic explosives, Sens. Actuators B 221 (2015) 867–878.
[84] S. Shanmugaraju, P.S. Mukherjee, π-Electron rich small molecule sensors for the recognition of nitroaromatics, Chem. Commun. 51 (2015) 16014–16032.
[85] M.E. Germain, M.J. Knapp, Optical explosives detection: from color changes to fluorescence turn-on, Chem. Soc. Rev. 38 (2009) 2543–2555.
[86] M. Chhatwal, R. Mittal, R.D. Gupt, S.K. Awasthi, Sensing ensembles for nitroaromatics, J. Mater. Chem. C 6 (2018) 12142–12158.
[87] S. Zhang, D. Du, J. Qin, S. Li, W. He, Y. Lan, Z. Su, 2D Cd(II)-Lanthanide(III) heterometallic-organic frameworks based on metalloligands for tunable luminescence and highly selective, sensitive, and recyclable detection of nitrobenzene, Inorg. Chem. 53 (2014) 8105–8113.
[88] Y. Wang, Q. Tan, H. Liu, W. Sun, Z. Liu, A luminescent europium MOF containing Lewis basic pyridyl site for highly selective sensing of *o*-, *m*- and *p*-nitrophenol, RSC Adv. 5 (2015) 86614–86619.
[89] D.K. Singha, P. Majee, S.K. Mondal, P. Mahata, A Eu-doped Y-based luminescent metal–organic framework as a highly efficient sensor for nitroaromatic explosives, Eur. J. Inorg. Chem. 2015 (2015) 1390–1397.

[90] X. Liu, H. Lin, Z. Xiao, W. Fan, A. Huang, R. Wang, L. Zhang, D. Sun, Multifunctional lanthanide–organic frameworks for fluorescent sensing, gas separation and catalysis, Dalton Trans. 45 (2016) 3743–3749.

[91] S. Pal, P.K. Bharadwaj, A luminescent terbium MOF containing hydroxyl groups exhibits selective sensing of nitroaromatic compounds and Fe(III) ions, Cryst. Growth Des. 16 (2016) 5852–5858.

[92] S. Wang, T. Cao, H. Yan, Y. Li, J. Lu, R. Ma, D. Li, J. Dou, J. Bai, Functionalization of microporous lanthanide-based metal-organic frameworks by dicarboxylate ligands with methyl-substituted thieno[2,3-b]thiophene groups: sensing activities and magnetic properties, Inorg. Chem. 55 (2016) 5139–5151.

[93] R. Gao, F. Guo, N. Bai, Y. Wu, F. Yang, J. Liang, Z. Li, Y. Wang, Two 3D isostructural Ln (III)-MOFs: displaying the slow magnetic relaxation and luminescence properties in detection of nitrobenzene and $Cr_2O_7^{2-}$, Inorg. Chem. 55 (2016) 11323–11330.

[94] D. Wang, L. Sun, C. Hao, Y. Yan, Z. Liang, Lanthanide metal–organic frameworks based on a 1,2,3-triazole-containing tricarboxylic acid ligand for luminescence sensing of metal ions and nitroaromatic compounds, RSC Adv. 6 (2016) 57828–57834.

[95] F. Zhang, Y. Wang, T. Chu, Z. Wang, W. Li, Y. Yang, A facile fabrication of electrodeposited luminescent MOF thin films for selective and recyclable sensing of nitroaromatic explosives, Analyst 141 (2016) 4502–4510.

[96] R.F. Bogale, Y. Chen, J. Ye, Y. Yang, A. Rauf, L. Duan, P. Tian, G. Ning, Highly selective and sensitive detection of 4-nitrophenol and Fe^{3+} ion based on a luminescent layered terbium (III) coordination polymer, Sens. Actuators B 245 (2017) 171–178.

[97] S. Srivastava, B.K. Gupta, R. Gupta, Lanthanide-based coordination polymers for the size-selective detection of nitroaromatics, Cryst. Growth Des. 17 (2017) 3907–3916.

[98] X. Wang, P. Yan, Y. Li, G. An, X. Yao, G. Li, Highly efficient white-light emission and UV-visible/NIR luminescence sensing of lanthanide metal-organic framework, Cryst. Growth Des. 17 (2017) 2178–2185.

[99] R.F. Bogale, Y. Chen, J. Ye, S. Zhang, Y. Li, X. Liu, T. Zheng, A. Raufa, G. Ning, A terbium (III)-based coordination polymer for selective and sensitive sensing of nitroaromatics and ferric ion: synthesis, crystal structure and photoluminescence properties, New J. Chem. 41 (2017) 12713–12720.

[100] H. He, S. Chen, D. Zhang, R. Hao, C. Zhang, E. Yang, X. Zhao, A micrometer-sized europium(III)-organic framework for selective sensing of the $Cr_2O_7^{2-}$ anion and picric acid in water systems, Dalton Trans. 46 (2017) 13502–13509.

[101] Z. Sun, Y. Li, Y. Ma, L. Li, Dual-functional recyclable luminescent sensors based on 2D lanthanide-based metal-organic frameworks for highly sensitive detection of Fe^{3+} and 2,4-dinitrophenol, Dyes Pigments 146 (2017) 263–271.

[102] X. Zhou, Y. Zhu, L. Li, T. Yang, J. Wang, W. Huang, Lanthanide-organic frameworks based on terphenyl-tetracarboxylate ligands: syntheses, structures, optical properties and selective sensing of nitro explosives, Sci. China Chem. 60 (2017) 1130–1135.

[103] T. Xia, F. Zhu, Y. Cui, Y. Yang, Z. Wang, G. Qian, Highly selective luminescent sensing of picric acid based on a water-stable europium metal-organic framework, J. Solid State Chem. 245 (2017) 127–131.

[104] S. Wang, L. Shan, Y. Fan, J. Jia, J. Xu, L. Wang, Fabrication of Ln-MOFs with color-tunable photoluminescence and sensing for small molecules, J. Solid State Chem. 245 (2017) 132–137.

[105] R. Ma, Z. Chen, S. Wang, Q. Yao, Y. Li, J. Lu, D. Li, J. Dou, Solvent-induced assembly of two helical Eu(III) metal-organic frameworks and fluorescence sensing activities towards nitrobenzene and Cu^{2+} ions, J. Solid State Chem. 252 (2017) 142–151.

[106] M. Han, S. Wang, Z. Li, Z. Zhou, D. Li, L. Ma, Y. Wang, Significant centre metallic effects on the sensing properties of two isostructural lanthanide metal-organic frameworks, Inorg. Chem. Commun. 79 (2017) 12–16.
[107] X. Wang, J. Li, C. Jiang, P. Hu, B. Li, T. Zhang, H. Zhou, An efficient strategy for improving the luminescent sensing performance of a terbium(III) metal–organic framework towards multiple substances, Chem. Commun. 54 (2018) 13271–13274.
[108] K. Shang, J. Sun, D. Hu, X. Yao, L. Zhi, C. Si, J. Liu, Six Ln (III) coordination polymers with a semirigid tetracarboxylic acid ligand: bifunctional luminescence sensing, NIR-luminescent emission, and magnetic properties, Cryst. Growth Des. 18 (2018) 2112–2120.
[109] S. Lu, Y. Liu, Z. Duan, Z. Wang, M. Li, X. He, Improving water-stability and porosity of lanthanide metal-organic frameworks by stepwise synthesis for sensing and removal of heavy metal ions, Cryst. Growth Des. 18 (2018) 4602–4610.
[110] Y. Gao, Y. Qi, K. Zhao, Q. Wen, J. Shen, L. Qiu, W. Mou, An optical sensing platform for the dual channel detection of picric acid: the combination of rhodamine and metal-organic frameworks, Sens. Actuators B 257 (2018) 553–560.
[111] X. Zhang, Z. Zhan, X. Liang, C. Chen, X. Liu, Y. Jia, M. Hu, Lanthanide-MOFs constructed from mixed dicarboxylate ligands as selective multi-responsive luminescent sensors, Dalton Trans. 47 (2018) 3272–3282.
[112] X. Shi, Y. Fan, J. Xu, H. Qi, J. Chai, J. Sun, H. Jin, X. Chen, P. Zhang, L. Wang, Layer-structured lanthanide coordination polymers constructed from 3,5-bis (3,5-dicarboxylphenyl)-pyridine ligand as fluorescent probe for nitroaromatics and metal ions, Inorg. Chim. Acta 483 (2018) 473–479.
[113] M. Raizada, F. Sama, M. Ashafaq, M. Shahid, M. Khalid, M. Ahmad, Z.A. Siddiqi, Synthesis, structure and magnetic studies of lanthanide metal–organic frameworks (Ln–MOFs): aqueous phase highly selective sensors for picric acid as well as the arsenic ion, Polyhedron 139 (2018) 131–141.
[114] S. Mukherjee, S. Ganguly, A. Chakraborty, A. Mandal, D. Das, Green synthesis of self assembled nanospherical dysprosium MOFs: selective and efficient detection of picric acid in aqueous and gas phase, ACS Sustain. Chem. Eng. 7 (2019) 819–830.
[115] Q. Tang, Y. Sun, H. Li, J. Wu, Y. Liang, Z. Zhang, Hexanuclear 3d-4f metal-organic cages assembled from a carboxylic acid-functionalized tris-triazamacrocycle for highly selective fluorescent sensing of picric acid, Appl. Organomet. Chem. 33 (2019), e4814.
[116] J. Cheng, Z. Liu, D. Wang, K. Chen, Y. You, X. Zhou, Fluorene-based lanthanide coordination polymer: structure, luminescence and sensing of picric acid, Appl. Organomet. Chem. 33 (2019), e5168.
[117] S. Khullar, S. Singh, P. Das, S.K. Mandal, Luminescent lanthanide-based probes for the detection of nitroaromatic compounds in water, ACS Omega 4 (2019) 5283–5292.
[118] Q. Chen, J. Cheng, J. Wang, L. Li, Z. Liu, X. Zhou, Y. You, W. Huang, A fluorescent Eu(III) MOF for highly selective and sensitive sensing of picric acid, Sci. China Chem. 62 (2019) 205–211.
[119] S. Hussain, X. Chen, W.T.A. Harrison, M.R.J. Elsegood, S. Ahmad, S. Li, S. Muhammad, D. Awoyelu, Synthesis, crystal structures and photoluminescent properties of one-dimensional europium(III)- and terbium(III)-glutarate coordination polymers, and their applications for the sensing of Fe^{3+} and nitroaromatics, Front. Chem. 7 (2019) 728.
[120] X. Shi, X. Qu, J. Chai, C. Tong, Y. Fan, L. Wang, Stable coordination polymers with linear dependence color tuning and luminescent properties for detection of metal ions and explosives, Dyes Pigments 170 (2019), 107583.

[121] L. Ren, Y. Cui, A. Cheng, E. Gao, Water-stable lanthanide-based metal-organic frameworks for rapid and sensitive detection of nitrobenzene derivatives, J. Solid State Chem. 270 (2019) 463–469.

[122] F. Zhang, S. Chen, S. Nie, J. Luo, S. Lin, Y. Wang, H. Yang, Waste PET as a reactant for lanthanide MOF synthesis and application in sensing of picric acid, Polymers 11 (2019) 2015.

[123] Z. Sun, J. Sun, L. Xi, J. Xie, X. Wang, Y. Ma, L. Li, Two novel lanthanide metal-organic frameworks: selective luminescent sensing for nitrobenzene, Cu^{2+}, and MnO_4^-, Cryst. Growth Des. 20 (2020) 5225–5234.

[124] P. Wu, L. Xia, M. Huangfu, F. Fu, M. Wang, B. Wen, Z. Yang, J. Wang, Lanthanide-based metal-organic frameworks containing "V-shaped" tetracarboxylate ligands: synthesis, crystal structures, "naked-eye" luminescent detection, and catalytic properties, Inorg. Chem. 59 (2020) 264–273.

[125] Y. Du, H. Yang, R. Liu, C. Shao, L. Yang, A multi-responsive chemosensor for highly sensitive and selective detection of Fe^{3+}, Cu^{2+}, $Cr_2O_7^{2-}$ and nitrobenzene based on a luminescent lanthanide metal-organic framework, Dalton Trans. 49 (2020) 13003–13016.

[126] Z. Li, X. Zhu, E. Gao, S. Wu, Y. Zhang, M. Zhu, Bifunctional luminescent Eu metal–organic framework for sensing nitroaromatic pollutants and Fe^{3+} ion with high sensitivity and selectivity, Appl. Organomet. Chem. 35 (2020), e6136.

[127] H. Guo, N. Wu, R. Xue, H. Liu, L. Li, M. Wang, W. Yao, Q. Li, W. Yang, Multifunctional Ln-MOF luminescent probe displaying superior capabilities for highly selective sensing of Fe^{3+} and Al^{3+} ions and nitrotoluene, Colloids Surf. A Physicochem. Eng. Asp. 585 (2020), 124094.

[128] Y. Liu, X. Lv, X. Zhang, L. Liu, J. Xie, Z. Chen, Eu(III)-organic complex as recyclable dual-functional luminescent sensor for simultaneous and quantitative sensing of 2,4,6-trinitrophenol and CrO_4^{2-} in aqueous solution, Spectrochim. Acta A Mol. Biomol. Spectrosc. 239 (2020), 118497.

[129] Z. Xu, X. He, Y. He, X. Zhao, M. Batmunkh, H. Li, Y. Wang, J. Cao, T. Ma, A luminescent terbium coordination complex as multifunctional sensing platform, Talanta 208 (2020), 120363.

[130] Z. Ma, J. Shi, M. Wang, L. Tian, Lanthanide-organic complex with uncoordinated Lewis basic triazolyl sites as multi-responsive sensor for nitrobenzene, Cu^{2+} and MnO_4^-, Dyes Pigments 185 (2021), 108930.

Chapter 11

Rare earth metal-organic framework hybrid materials for luminescence responsive chemical sensing of biomarkers

11.1 Biomarkers and their chemical sensing

Biomonitoring means monitoring the contents of chemicals and their metabolites from biomaterials (blood, urine, gases, etc.) in the human body, and the produced nonharmful biological effect level. The comparison between the determined value and the standard one is utilized to evaluate the extent of bodily exposure to a chemical substance and its potential influence on health. Therefore it provides an important value for evaluating the dangerous factors in occupational health monitoring and the effect of environmental hygiene in production. Environmental monitoring alone cannot reflect the total amount of noxious substances to which different paths (respiratory tract, digestive tract, and skin, among others) are exposed, as the level of noxious substances in the environment is not the same as that of such substances touching and being absorbed into a human body and it cannot effectively reflect the distinction of individual differences. Biological monitoring can provide the internal dosage and any harmless effects of the human body touching noxious chemical substances and can reveal the implications of contact with pollutants for bodily health. This information can be utilized to assess and determine the touching issue between the individual or crowd and the special substance in order to provide the relationship between external contact and internal dose. Subsequently, biological monitoring is an effective supplement to environmental monitoring and has practical value in risk assessment of environmental health, and may not only aid in carrying out effective health protection but also provide a method to assess the efficiency of controls and precautions. Proper selection of biomarkers that represent health and disease states is vital for disease diagnosis and treatment by detecting disease before it manifests [1–5].

Biomarkers are the indicator of biological monitoring. The National Research Council (NRC) describes a biomarker as an indicator to reflect the state of a biological system or condition, which can be considered as a tool

Rare Earth Metal-Organic Framework Hybrid Materials for Luminescence Responsive Chemical Sensors
https://doi.org/10.1016/B978-0-323-91236-5.00005-0

to investigate the relationship between the touching external chemicals and health lesion. The working group of the National Institutes of Health defines a biomarker as a characteristic that is objectively measured and evaluated as an indicator of normal biological processes, pathogenic processes, or pharmacological responses to a therapeutic intervention. The International Programme on Chemical Safety put forward the generalized definition of biomarker as a determined index to reflect the interaction between a biological system and external chemical, physical, and biological factors. As the incipient biological signals to indicate the toxicological effect of pollutants, a biomarker has been developed and applied in the research of the metabolic process and pathological mechanism. A biomarker is designated as a substance or activity that can be objectively measured and evaluated as an indicator for a normal biological process, pathogenic process, or pharmacological responses to a therapeutic intervention. In medicine, a biomarker is a metric characteristic to reflect the severity or presence of some disease state. More generally, a biomarker is anything that can be used as an indicator of a particular disease state or some other physiological state of an organism. Biomarkers include genes, proteins, genetic variations, and differences in metabolic expression from different sources such as body fluids or tissues. A biomarker can be a substance that is introduced into an organism as a means to examine organ function or other aspects of health. It can be a substance whose detection indicates a particular disease state. More specifically, a biomarker indicates a change in the expression or state of a protein that correlates with the risk for or progression of a disease or with the susceptibility of the disease to a given treatment [1–5].

Biomarkers can be classified based on different parameters, including their characteristics, such as imaging biomarkers or molecular biomarkers. Molecular biomarkers can be used to refer to nonimaging biomarkers that have biophysical properties, which allow them to be measured in biological samples and include nucleic acid-based biomarkers such as gene mutations or polymorphisms and quantitative gene expression analysis, peptides, proteins, lipids metabolites, and other small molecules. Biomarkers can also be classified based on their application, such as diagnostic biomarkers, staging of disease biomarkers, disease prognosis biomarkers (cancer biomarkers), and biomarkers for monitoring the clinical response to an intervention. Another category of biomarkers includes those used in decision making during early drug development. For instance, pharmacodynamic biomarkers are markers of a certain pharmacological response and are of special interest in dose optimization studies. **(a) Molecular biomarkers.** They can be discovered using basic and acceptable platforms such as genomics and proteomics. **(b) Metabolomics approach.** This approach is introduced to refer specifically to the analysis of metabolic responses to drugs or diseases, which becomes a major area of research as the study of complex biological systems used to identify biomarkers for various diseases. **(c) Lipidomics approach. (d) Tissue-based biomarkers.** A cancer biomarker usually refers to a substance or process that is indicative of the

presence of cancer in the body, whose biomarker may be a molecule secreted by a tumor or a specific response of the body to the presence of cancer. Ideally, such biomarkers can be assayed in noninvasively collected biofluids such as blood or serum. (**e**) **Imaging biomarkers.** These are usually noninvasive, and produce intuitive, multidimensional results. When combined with other sources of information, they can be very useful to clinicians seeking to make a diagnosis; they can also help monitor or trace substances in vivo and identify their metabolites or remains in the body as a pharmacokinetics assay [2,6].

In fact, for chemists, the special molecule species are convenient for consideration as biomarkers to realize the application for diagnosing and monitoring diseases. Currently, many types of chemical markers (proteins, metabolites, small molecules, volatile organic compounds (VOCs), pH value, etc.) in all kinds of biological fluids (blood, urine, sweat, breath, saliva, interstitial fluid, seminal fluid, nipple aspirate fluid, tears, stool, and cerebrospinal fluid) can be indicative in disease diagnosis and monitoring. Fig. 11.1 displays the main body fluids containing disease-related chemical markers. The sources of chemical markers, categorized into noninvasive and invasive groups, are presented in the following subsections [1,7–10].

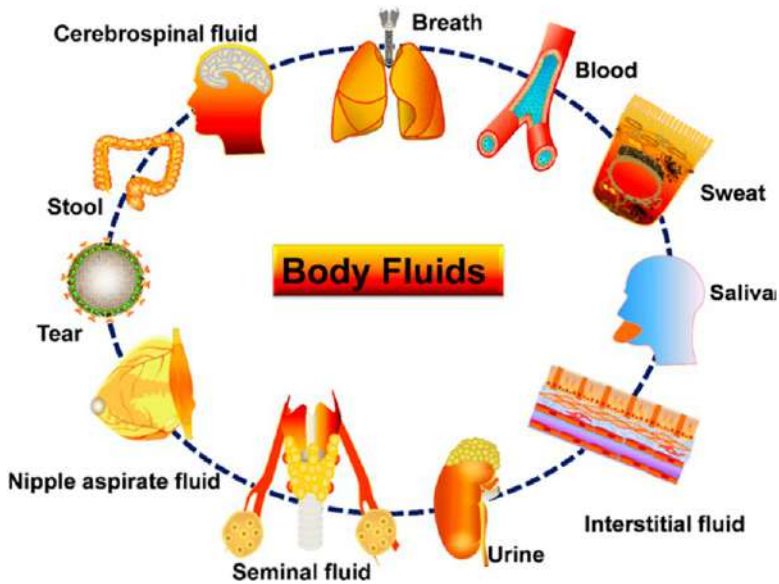

FIG. 11.1 Schematic description for main sources of disease-related chemical markers in body fluid systems. *(Reproduced with permission from Y. Y. Broza, X. Zhou, M. Yuan, D. Qu, Y. Zheng, R. Vishinkin, M. Khatib, W. Wu, H. Haick, Disease detection with molecular biomarkers: from chemistry of body fluids to nature-inspired chemical sensors. Chem. Rev. 119 (2019) 11761–11817. Copyright 2019 American Chemical Society.)*

11.2 Rare earth metal-organic framework materials for luminescence responsive chemical sensing of biomarkers

Pure MOF materials utilized for sensing of biomarkers are few and mainly employ rare earth MOF hybrid materials using photoactive Eu^{3+} or Tb^{3+} as central framework metal ions. The early works were focused on the anthrax biomarker DPA (dipicolinic acid) as a convenient biomarker for *Bacillus anthracis* [11–20]. Anthrax is one of the acute infectious diseases that infects both animals and humans. *B. anthracis* has been reported as a potential bioterrorism agent since the anthrax attack in the United States in 2001, and still attracts broad attention throughout the world. A number of attempts have been made to detect bacillus spores using bacteriology, serology/immunoassays, and polymerase chain reactions (PCR). Rapid, sensitive, and straightforward detection of bacillus spores is crucial for disease and bioterrorism prevention. Recently, optical techniques for DPA (a unique biomarker and major constituent of bacterial spores) detection have attracted wide attention due to their low cost, fast response, and easy portability [11–22]. Tan et al. employed a hydrophilic lanthanide/nucleotide coordination polymer constructed by spontaneous self-assembling of Tb^{3+} and adenosine monophosphate (AMP) as a receptor platform for direct detection of DPA in aqueous solution [11]. Due to the coordination of DPA with Tb^{3+} on the surface of the AMP/Tb, significant enhancement in the fluorescent intensity of AMP/Tb was obtained and the enhanced fluorescence intensity of AMP/Tb displayed a good linear response to DPA concentrations in the range from 20 nM to 20 μM with a detection of limit (LOD) of 10 nM. The presented receptor platform has the advantage of allowing simple, direct analysis for DPA without requiring complicated preparation processes or extra steps of surface modification. They also synthesized another Tb-based MOF, $[Tb(BTC)(H_2O)_6]$, in aqueous medium to conveniently and reliably quantify DPA. The mixing of the Tb-MOF fluorescence probe with DPA led to a fairly quick reduction in the photoluminescence signal. The PL-quenching signal maintained a highly linear relationship with increasing DPA concentrations in the range of 1 nM to 5 mM with a very low LOD (0.04 nM) [12]. Gao et al. reported a facile and novel strategy for detection of the anthrax biomarker DPA in aqueous solution using heterobinuclear (Tb^{3+} and Eu^{3+}) rare earth coordination polymer NPs with one type of nucleotide (guanosine 5′-monophosphate (GMP)) as the smart ratiometric luminescent probe [13]. This construction was based on the use of GMP as the bidendate ligand to assemble with Tb^{3+}/Eu^{3+} ions to form a GMP-Tb/Eu network, in which the N atoms in the guanosine subunit and the phosphate groups of GMP could be coordinated with Tb^{3+} and Eu^{3+}. Interestingly, GMP can effectively sensitize Tb^{3+} luminescence but can hardly switch on Eu^{3+} luminescence. Fortunately, weak luminescence from Eu^{3+} can be improved by energy transfer from Tb^{3+} to Eu^{3+}, which essentially constitutes a simple and smart dual-emission nanoprobe. Moreover, upon exposure to the anthrax biomarker DPA, Tb^{3+} luminescence is largely enhanced

while Eu^{3+} luminescence is gradually decreased, producing a sensitive ratiometric response presenting apparent visual luminescence color changes. This technique can be applied to visual real-time monitoring of the release of DPA during the germination of *B. subtilis* spores, harmless simulants of *B. anthracis*. Zhang et al. demonstrated a ratiometric luminescent sensor of DPA based on a dual-emissive MOF hybrid by encapsulation of Tb^{3+} cations into an anionic MOF through a cation exchange process. The Tb^{3+}@MOF hybrid well inherited the intrinsic ligand emission of the host framework and the Tb^{3+} emission. The Tb^{3+} emission within the MOF hybrid was significantly enhanced in the presence of DPA molecules owing to the occurrence of antenna sensitization upon the formation of the Tb-DPA complex, while the ligand emission was insensitive to DPA [14]. Chen et al. constructed a ratiometric fluorescent composite system for DPA optical sensing, denoted as RB-Eu-BTC, using a rhodamine-derived molecule as sensing probe (RB) and luminescent MOF Eu-BTC as supporting substrate, respectively. RB-Eu-BTC was supposed to depict ratiometric sensing behavior toward DPA along with good selectivity and precision. Its Eu^{3+} emission section showed an emission Turn-Off effect toward DPA, while its rhodamine emission section showed an emission Turn-On effect toward DPA. Both sensing channels showed linear response and good selectivity toward DPA [15]. Similarly, Shi et al. reported an optical sensing hybrid with two sensing channels of both colorimetric sensing and ratiometric fluorescent sensing for the detection of DPA, which was constructed using luminescent MOF as the supporting substrate and arhodamine-like dye as the sensing probe. LOD (limit of detection) value was low, at 4.5 μM, with good selectivity. Its Eu^{3+} emission component was quenchable by DPA, contrary to the rhodamine emission. The sensing mechanism was revealed as the combination of a rhodamine structural transformation initiated by DPA-released protons and an emission quenching caused by energy transfer from Eu(BTC) to DPA (pyridine ring) [16].

Zhang et al. presented a direct and rapid strategy for colorimetric detection of the *Bacillus anthracis* biomarker DPA using Tb^{3+}/Eu^{3+} codoped hybrid (Tb/Eu@bio-MOF-1). Three different Tb^{3+}/Eu^{3+} molar ratios Tb/Eu@bio-MOF-1 were prepared to study the effect of Tb^{3+} ion concentration on sensor performance, whose DPA sensing spectra are shown in Fig. 11.2. For the MOF with Tb^{3+}/Eu^{3+} molar ratio of 2.55 (Fig. 11.2A), after adding DPA, Tb^{3+} emission was gradually increased, while Eu^{3+} emission was first weakened and then enhanced at high DPA concentration. For the MOF with Tb^{3+}/Eu^{3+} molar ratio of 9.5 (Fig. 11.2B), the Tb^{3+} emission was almost unchanged; while the Eu^{3+} emission was weakened with the increase of DPA concentration. In the case of MOF with Tb^{3+}/Eu^{3+} molar ratio of 5.89 (Fig. 11.2C), with DPA addition, Tb^{3+} emission at 545 nm was gradually enhanced while the Eu^{3+} emission at 615 nm was significantly weakened. More interestingly, this Tb/Eu@bio-MOF-1 with moderate Tb/Eu ratio exhibited visual colorimetric sensing: its fluorescent color changed from orange-red to green after different

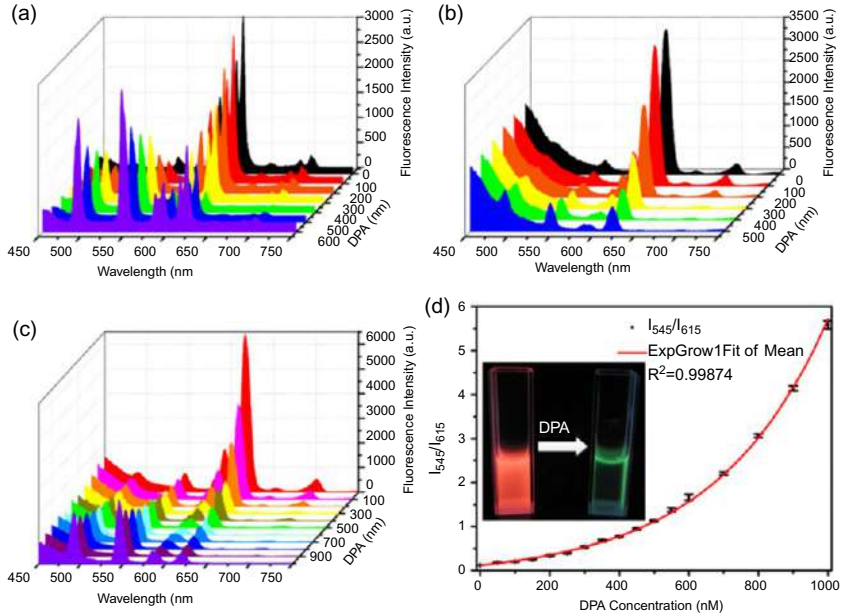

FIG. 11.2 DPA sensing spectra of the Tb/Eu@bio-MOF-1 with the final molar ratios of Tb^{3+}/Eu^{3+} as (A) 2.55, (B) 9.5, and (C) 5.89. (D) Plots of the relationship between the integrated intensity (I_{545}/I_{615}) of Tb/Eu@bio-MOF-1 ($Tb^{3+}/Eu^{3+} = 5.89$) and DPA concentrations from 50 nM to 1 μM. Inset: visible color changes of Tb/Eu@bio-MOF-1 under 254 nm UV light. *(Reproduced with permission from Y. Zhang, B. Li, H. Ma, L. Zhang, Y. Zheng, Rapid and facile ratiometric detection of an anthrax biomarker by regulating energy transfer process in bio-metal-organic framework. Biosens. Bioelectron. 85 (2016) 287–293. Copyright 2015 Elsevier.)*

concentrations of DPA were added, recognizable with the naked eye under UV light (Fig. 11.2D). When introducing different concentrations of DPA, the intensity values at 545 nm and 615 nm show opposite changes and the intensity ratio I_{545}/I_{615} increases exponentially; the intensity ratio I_{545}/I_{615} is fitted well with a single exponential and an R of 99.87%. The LOD for DPA is calculated to be 34 nM. DPA chelates with Tb^{3+} ions and forms a ligand-to-metal energy transfer (LMET). Then the reversible energy transfer tendency between Tb^{3+} and Eu^{3+} enhances their response signal [17].

Wu et al. used NH_2BTC (2-amino-1,3,5-benzenetricarboxylate) with a dual functional group to construct a rare earth-based MOF, NH_2-MOF-76(Eu) (Eu-MOF1), which is a rare nonluminescent. Interestingly, the luminescence properties of Eu-MOF1 can be selectively restored by DPA solution with $\sim 10^5$-fold "Turn-On" enhancement, even in the presence of other potentially disturbing aromatic compounds. Moreover, the interaction between DPA and Eu-MOF results in the structural transformation (single-crystal to single-crystal phase transition) from Eu-MOF1 to Eu-MOF2. As shown in Fig. 11.3A (top), the fluorescence intensity of the peak at 614 nm gradually increases in the DPA

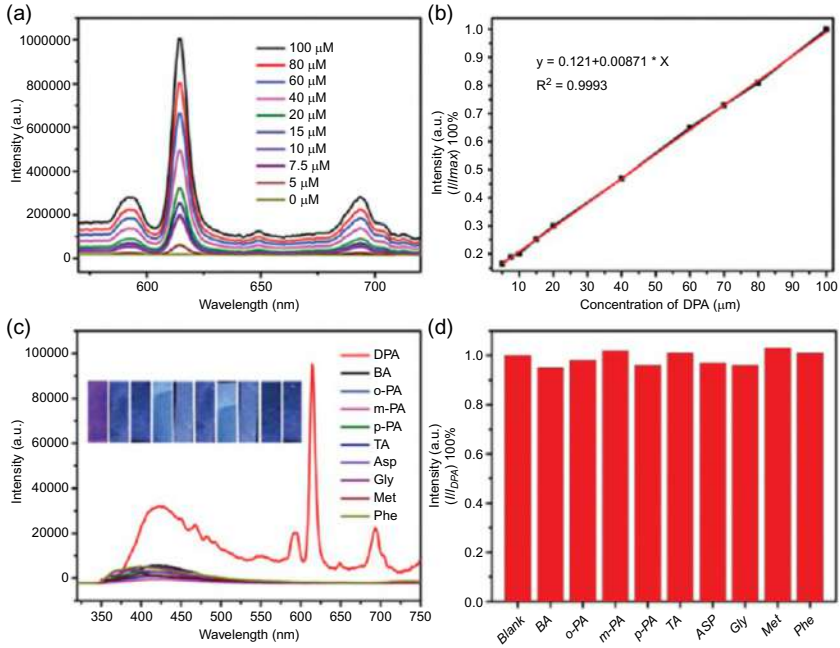

FIG. 11.3 *(Top)* (A) Variations in the luminescence spectra of Eu-MOF1 (0.1 mg mL^{-1}) as a function of DPA concentration varying from 0 to 100 mM (excited at 250 nm). (B) Linear relationships between the fluorescence intensity (I/I_{max}) and concentration of DPA. *(Bottom)* (A) Fluorescence spectra of Eu-MOF1 in EtOH solution under interferents (100 mM). Inset shows photographs of luminescence test paper toward different interferents. (B) Fluorescence intensity of Eu-MOF1 in EtOH solution under DPA (60 mM) and interferents (100 mM) existing at the same time. *(Reproduced with permission from D. Wu, Z. Zhang, X. Chen, L. Meng, C. Li, G. Li, X. Chen, Z. Shi, S. Feng, A non-luminescent Eu-MOF-based "turn-on" sensor towards an anthrax biomarker through single-crystal to single-crystal phase transition. Chem. Commun. 55 (2019) 14918–14921. Copyright 2019 Royal Chemical Society.)*

concentration range of $0 \sim 100$ mM. The linear response between the fluorescence intensity at 614 nm and the DPA concentration fits well with $R^2 = 0.9993$ (Fig. 11.3B; top). As can be seen in Fig. 11.3A (bottom), except for DPA, the fluorescence intensity of Eu-MOF1 shows a negligible luminescent response, indicating the "Turn-On" fluorescence recovery for highly selective detection of DPA. Changes in the luminescence spectra of Eu-MOF1 to DPA with and without such interfering agents are nearly indistinguishable from each other (Fig. 11.3B; bottom). Fluorescent paper based with Eu-MOF1 was prepared for real-scenario tests. The blue-emitting test strip turned red immediately toward DPA under a UV lamp at 254 nm (inset of Fig. 11.3A; bottom). The "Turn-On" luminescence recovery was ascribed to DPA, as the "antenna" molecule transferring energy to Eu^{3+} ions [18].

In addition, biomarkers for the polycyclic aromatic hydrocarbon (PAH) 1-hydroxypyrene (1-HP) detection have been reported. Sun et al. synthesized a new sulfonylcalix[4]arene-based dinuclear terbium molecular container and utilized it as a fluorescence probe for the detection of 1-HP. The sulfonylcalix[4]arene ligand can serve not only as an efficient antenna ligand to promote the LMET, but also can provide a suitable cavity to accommodate 1-HP. Promising fluorescence-quenching effects are due to the enhancement in the host-guest intermolecular charge transfer and the decrease in the LMET after the formation of the stable host-guest complex [23]. Zhou et al. demonstrated a robust microcrystalline MOF (NU-1000) of Zr(*IV*)ions and tetraethyl 4,4′,4″,4‴-(pyrene-1,3,6,8-tetrayl) tetrabenzoic acid (TBAPy) ligands with a highly fluorescent pyrene core, which exhibited sensitive luminescence detection of urinary 1-HP. The pyrene core within NU-1000 behaves as the signal converter, whose luminescence is significantly quenched by 1-HP owing to its efficient π-π charge transfer interactions with pyrene cores. The pore confinement effect of the molecular-sized channel of NU-1000 facilitates the preconcentration of 1-HP within NU-1000, which makes 1-HP contact with NU-1000 more sufficient, therefore enhancing the detection efficiency [24].

Asthma is a common chronic disorder, and decreased hydrogen sulfide (H_2S) production in the lungs has been considered as an early detection biomarker for asthma. However, the detection of H_2S in biological systems remains a challenge, because it requires the designed sensors to have the following features: nanoscale size, good biocompatibility, real-time detection, high selectivity/sensitivity, and good water stability. Zhang et al. suggested the potential of using the nanoscale fluorescent MOF hybrids Eu^{3+}/Ag^{+}@UiO-66-$(COOH)_2$ as a logic platform for tentative diagnosis of asthma by detecting the biomarker H_2S. This INHIBIT logic gate based on Eu^{3+}@UiO-66-$(COOH)_2$ can be produced by choosing Ag^{+} and H_2S as inputs and by monitoring the fluorescent signal (I_{615}) as an output. The fluorescent studies indicated that the Eu^{3+}/Ag^{+}@UiO-66-$(COOH)_2$ exhibited excellent selectivity, extreme sensitivity (LOD: 23.53 μM), and real-time in-situ detection of H_2S. Further, MTT analysis in $PC1_2$ cells showed that the EAUC possesses low cytotoxicity and favorable biocompatibility that are suitable for the detection of the biomarker H_2S in vivo, as demonstrated by the successful detection of spiked H_2S in the diluted serum samples. This work thus presents the possibility of using a MOF-based logic platform for tentative diagnosis of asthma in clinical medicine [25].

Cheng and Shi's group have carried out research using rare earth MOFs for fluorescence chemical sensing on biomarkers [26,27]. They demonstrated a judicious selection of luminescent RE^{3+} centers and ligands to form SBUs to construct a family of RE-ZMOFs with zeolitic topology and formula $[RE_{48}(NO_3)_{48}(bpdc)_{48}]\cdot G_x$ (RE = Tb, Eu; G = guest; H_2bpdc = 2,2′-bipyridine-6,6′-dicarboxylic acid) together with the mixed-crystal variants Eu_xTb_{1-x}-ZMOF [26]. One of these mixed crystals, MZMOF-3, exhibited fluorescence

detection of lysophosphatidic acid (LPA) as a biomarker for ovarian cancer and other gynecologic cancers. Linear correlation between the integrated fluorescence intensity and the concentration of LPA was observed, enabling quantitative analysis of LPA in physiologically relevant ranges (1.4–43.3 μM). Physiological concentrations of LPA in plasma typically vary from 0.1 to 6.3 μM, whereas danger levels for ovarian cancer are indicated by concentrations on the order of 43.1 μM. There was a linear relationship with a slope of 0.05010 ± 0.00179, indicating that MZMOF-3 is a self-referencing sensor and requires no additional calibration of luminescence intensity (Fig. 11.4). The increased intensity of Eu^{3+} transitions and the decreased intensity of Tb^{3+} transitions induced by energy transfer from Tb^{3+} to Eu^{3+} ions are significantly enhanced in the presence of LPA [26].

More recently, the researchers synthesized Eu-MOF with mixed ligands, $\{[Eu(TDA)(H_2BTEC)_{0.5}(H_2O)_3]\cdot H_2O\}_n$ (H_2TDA = thiazolidine 2,4-dicaboxylic acid, H_4btec = 1,2,4,5-benzenetetracarboxylic acid), applied for qualitative and quantitative recognition of serotonin (5-hydroxytryptamine, HT), a neurotransmitter, and its main metabolite 5-hydroxyindole-3-acetic acid (HIAA) as biomarkers for carcinoid tumors [27]. Highly luminescent quenching of Eu-MOF occurs upon the incremental addition of HT and HIAA. The LODs were calculated to be 0.66 and 0.54×10^{-6} m for HT and HIAA, respectively, lower than danger levels for carcinoid tumors. So Eu-MOF can quantitatively detect HT and HIAA in

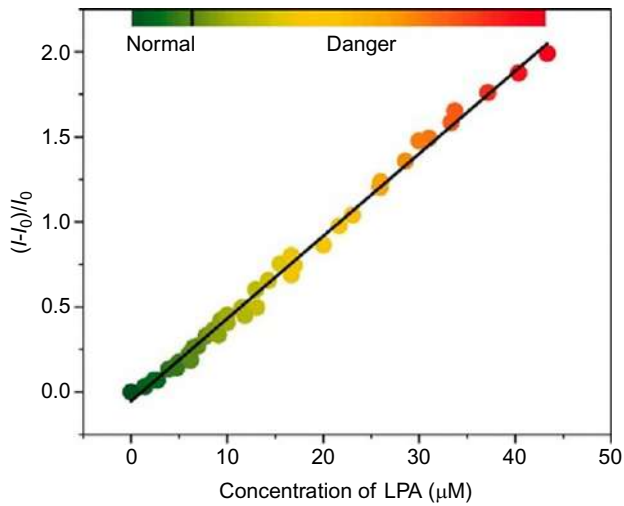

FIG. 11.4 Integrated luminescence intensity changes of MZMOF-3 suspended in MeOH toward 0.03, 0.10, and 0.13 mM LPA. *(Reproduced with permission from S. Zhang, W. Shi, P. Cheng, M. J. Zaworotko, A mixed-crystal lanthanide zeolite-like metal-organic framework as a fluorescent indicator for lysophosphatidic acid, a cancer biomarker. J. Am. Chem. Soc. 137 (2015) 12203–12206. Copyright 2015 American Chemical Society.)*

physiologically relevant ranges lower than danger levels for carcinoid patients. For HT, as shown in Fig. 11.5A and B, negligible changes of emissions were observed when the system was treated with other blood plasma components except for HT. With regard to HIAA, urine components also have no obvious influence on Eu-MOF's emission (Fig. 11.5A and B). As a result, only HT and HIAA induce a visible color change of Eu-MOF 1 from red to colorless under UV light, which can be easily distinguished with the naked eye (Fig. 11.5A and B). Fig. 11.5A and B show that the decrease in the emission intensity at 616 nm induced by HT and HIAA is not affected in the background of other blood plasma and urine ingredients, demonstrating a high antijamming capability and superior selectivity of Eu-MOF. The calculation using the DFT method shows that the LUMO's energy level of the ligands (donor) is obviously lower than that of the analytes (acceptor), indicating the absence of the photo-induced electron transfer (PET) process around the luminescent quenching of HT and HIAA by Eu-MOF [27].

Zhao et al. demonstrated that Cu-based metal-organic gel (Cu-MOG) can serve as an amplification platform for fluorescence anisotropy (FA) assay for its sensitive detection of a common cancer biomarker, prostate specific antigen (PSA) [28]. The dye-labeled probe aptamer (PA) product was adsorbed onto the benzimidazole derivative-containing Cu-MOG via electrostatic incorporation and strong π-π stacking interactions, which significantly increases the FA value due to the enlargement of the molecular volume of the PA/Cu-MOG complex. With the introduction of target PSA, the FA value was obviously decreased on account of the specific recognition between PSA and PA, which resulted in the detachment of PA from the surface of MOG. The linear range was from 0.5–8 ng mL^{-1}, with an LOD of 0.33 ng mL^{-1}. This tactic could also be extended to other tumor marker detections simply by changing the corresponding aptamer [28]. Du et al. reported the synthesis of a fluorescent material UiO-66-PSM based on the covalent attachment of MOFs (UiO-66-NH_2) and 2,3,4-trihydroxybenzaldehyde (THBA) via a postsynthetic modification (PSM) strategy. It could detect free bilirubin sensitively and selectively. The interaction between free bilirubin and UiO-66-PSM may contribute to the change of the fluorescence behaviors, resulting in an efficient fluorescence resonance energy transfer (FRET). The method was validated by the detection of free bilirubin in human serum samples, a key biomarker for jaundice [29]. Wu et al. synthesized three isostructural MOFs with different rare earth centers solvothermally, which displayed strong regulated emissions by adjustable metal-organic coordination interactions. Among them, Ho(III)-MOF could quantitatively detect phenylglyoxylic acid (PGA, a biomarker of ethylbenzene and styrene (EB/S) representing the internal dose of EB/S exposure) with the highest sensitivity in physiologically relevant ranges. The mechanism study of luminescent responses toward PGA further explained its excellent sensitivity and selectivity for sensing PGA. The facile, accurate, fast, and recyclable sensing system relying on LCP materials provides a convenient approach for developing sensing platforms with adjustable emissions for assessment of the intoxication level of EB/S [30].

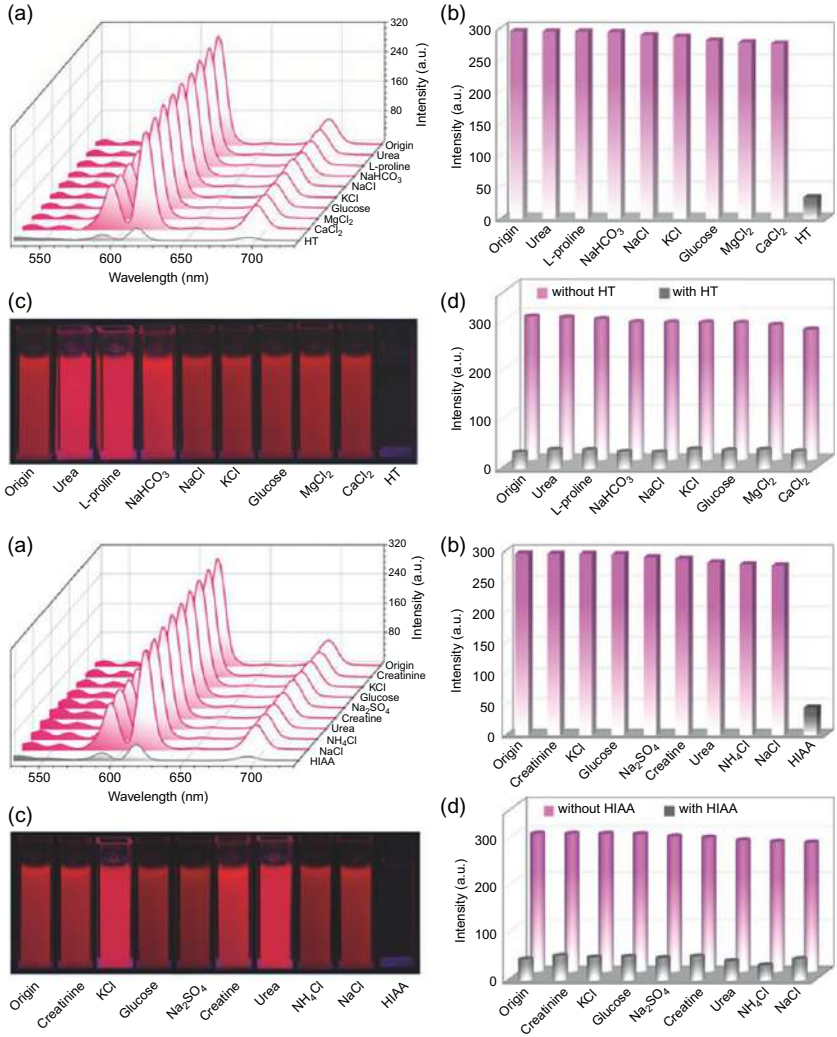

FIG. 11.5 (A) Luminescence spectra and (B) intensities of Eu-MOF suspensions with various urine components, as well as the corresponding photographs under (C) a 254-nm UV light. (D) Luminescence responses of Eu-MOF toward (*top*) HT and (*right*) HIAA in the presence of background of other various urine components. *(Reproduced with permission from S. Wu, Y. Lin, J. Liu, W. Shi, G. Yang, P. Cheng, Rapid detection of the biomarkers for carcinoid tumors by a water stable luminescent lanthanide metal–organic framework sensor. Adv. Funct. Mater. 28 (2018) 1707169. Copyright 2018 Wiley.)*

Qu et al. prepared a Tb-MOF with a three-dimensional (3D) anhydrous framework, whose asymmetric unit comprised one Tb(III) ion, one pddb (H_2pddb = 4,4′-(pyridine-2,6-diyl)dibenzoic acid), a half of ox^{2-} anions, and one phen [31]. The coordinative free double N-sites of pddb ligands directly into the rectangular pores, suggesting that there can be some interactions

between these sites and acidic analytes. The fluorescence sensing can be a convenient and effective way of detecting 2-thiazolidinethione-4-carboxylic acid (TTCA, as a biomarker of CS_2) in urine. The emission spectrum of the Tb-MOF aqueous suspension was entirely quenched only by TTCA (Fig. 11.6A). Under UV-lamp irradiation, only TTCA could induce a visible color change from light green to colorless and the differences in the effects of different urine chemicals on the Tb-MOF emission could be easily distinguished by the naked eye (Fig. 11.6A; inset). Under illumination with a UV lamp, Tb-MOF test papers showed distinct color changing from bright green to blue, which could be observed readily by the naked eye after immersion treatment of Tb-MOF test paper (Fig. 11.6B). Within the full range concentrations of TTCA from 0 to 0.6 mg mL^{-1}, the corresponding relationship curve is nonlinear, but in the range of low content of TTCA, from 0 to 0.2 mg mL^{-1}, the luminescence quenching efficiency can be quantitatively expressed by a linear S-V curve ($R^2 = 0.98$); K_{sv} is calculated as 13.57 mL mg^{-1}, with LOD of 0.001 mg mL^{-1} [31].

As an important neurotransmitter of the central nervous system, 5-hydroxy tryptamine (HT) remains constant in blood plasma of healthy human bodies. Oversecretion of HT by carcinoid cells can bring an inevitably high risk of malignant tumors, resulting simultaneously in the gathering of 5-hydroxyindole-3-acetic acid (HIAA) in the urine due to the metabolite of HT. Therefore, both HT and HIAA are regarded as the most important biomarkers of carcinoid cells in patients, and the monitoring of HT and HIAA in urine and/or blood

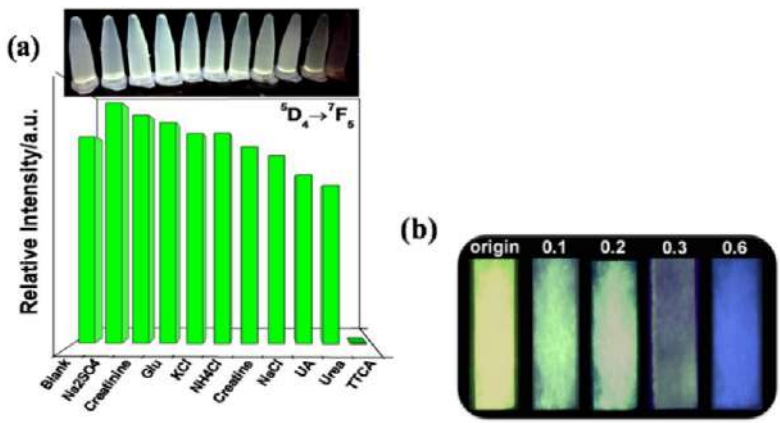

FIG. 11.6 (A) The main peak at 545 nm assigned to the $^5D_4 \rightarrow {}^7F_5$ transition of Tb(III) in Tb-MOF dispersed into aqueous solutions of common urinary chemicals. Inset, the photographs of Tb-MOF aqueous solutions containing various urine chemicals under a 365-nm UV light. (B) Optical images of test paper under UV light irradiation. *(Reproduced with permission from X. Qu, B. Yan, A highly stable Tb(III)-based metal-organic framework: structure, photoluminescence and chemical sensing of 2-thiazolidinethione-4-carboxylic acid as a biomarker of CS2. Inorg. Chem. 58 (2019) 524–534. Copyright 2019 American Chemical Society.)*

plasma is thus strongly significant for the early diagnosis and early cure of carcinoids. Yang et al. synthesized a Tb-MOF formulated as $\{[Tb(H_2O)(TPA)(ox)]\cdot 0.5H_2O\}_n$ via employing 6-(1H-1,2,4- triazol-1-yl)pyridine-2-carboxylate (TPA) and oxalate (ox) as antenna and bridging ligands. Furthermore, the Tb-MOF showed fast and effective responses toward the biomarkers of carcinoid cells with a strong S-V quenching constant (K_{SV}) and LOD of $8.95 \times 10^3\ M^{-1}$ and 0.72 μM for HT as well as $1.18 \times 10^4\ M^{-1}$ and 0.95 μM for HIAA. To quantitatively evaluate the sensing ability of neurotransmitters, luminescent titration experiments were performed by stepwise addition of HT and HIAA into the homogeneous suspension of Tb-MOF, and the emission phenomena of the hybrid were monitored. Severe luminescent quenching of Tb-MOF appeared to be caused by the introduction of HT and HIAA (Fig. 11.7A). When HT and HIAA increased up to 9×10^{-4} mol L^{-1}, the I_{542} of Tb-MOF decreased by 94.4% and 95.6%. Apart from the decreased I_{542}, both analytes could decolorize the green Tb-MOF suspension to colorless through a UV-lamp irradiation of 254 nm (inset of Fig. 11.7A), suggesting a naked eye-detectable recognition by Tb-MOF of HT or HIAA. The fluorescence quenching of Tb-MOF was closely related to the concentration of HT and HIAA, whose decay curves of I_0/I at 542 nm accord with a first-order exponential equation at low concentrations of HT and HIAA, indicating a diffusion-dominated quenching mechanism (Fig. 11.7B). Quantitative regression of the linear portions of I_0/I versus [HT] and [HIAA] affords a correlation coefficient $R^2 = 0.9982$ at a low concentration range (Fig. 11.7E), signifying intrinsically powerful discrimination of Tb- on HT or HIAA that is imperceptibly disturbed by excess interfering substances. Regeneration and recyclability of the Tb-MOF sensor were also evaluated. As shown in Fig. 11.7F, after five continuous recycles, both the I_{542} and quenching percentage of the recycled Tb-MOF changed insignificantly as compared to the initial sample. The UV-Vis absorption spectra indicate that both HT and HIAA superimpose well with the excitation data of Tb-MOF, so both Tb-CP and HIAA or HT can absorb the photoexcitation energy effectively, but competitively. The fluorescent quenching of Tb-MOF by HT or HIAA is attributed to the synergistic effect of more favorable absorption toward the excitation light energy and the sensor-analyte interaction, both of which cut off the energy transfer from TPA^- to the Tb^{3+} ion [32].

11.3 Rare earth functionalized metal-organic framework hybrid materials for luminescence responsive chemical sensing of biomarkers

Urine hippuric acid (HA) is the ultimate and major metabolite of toluene and is considered a biological indicators of toluene exposure. Approximately 80% of inhaled toluene is excreted in urine as HA, whose concentration is proportional to the level of toluene exposure. Hao et al. developed an Eu^{3+} -functionalized MOF (Eu^{3+}@Al-MOF, with linker of 1,2,4,5-benzenetetracarboxylic acid

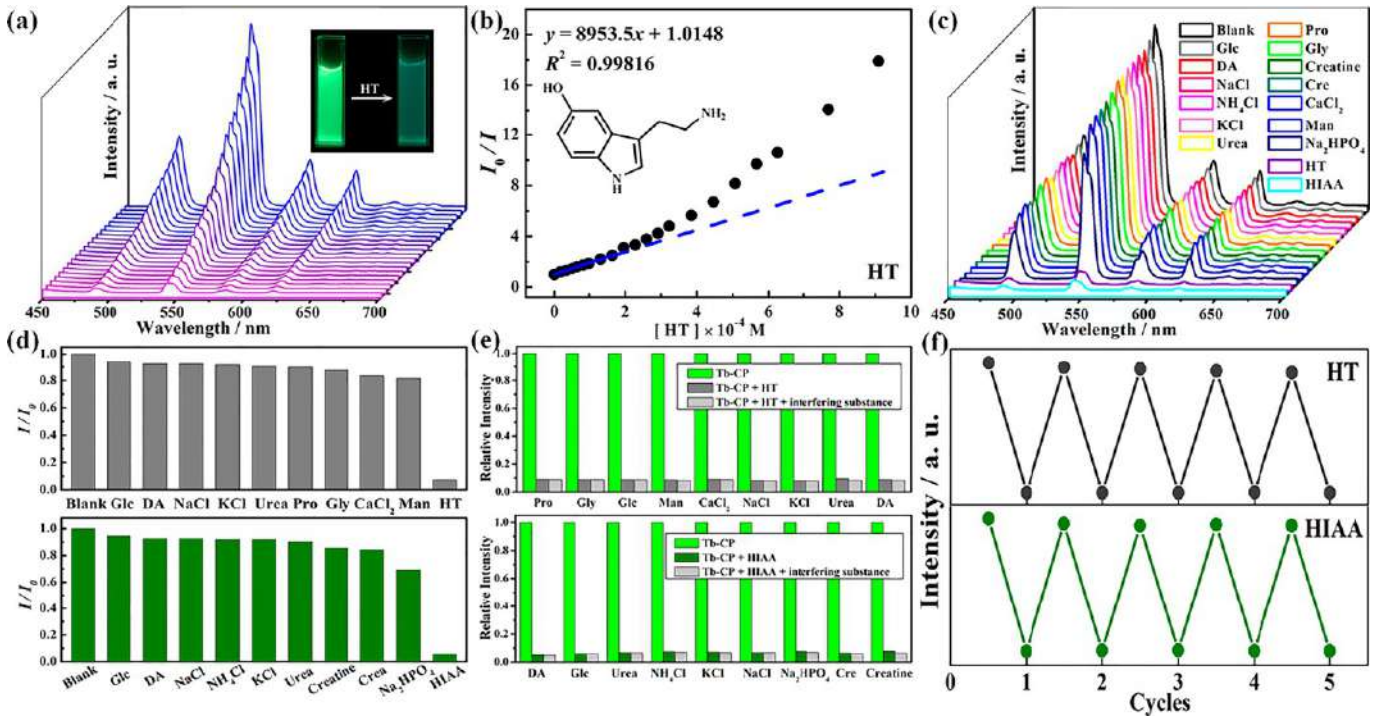

FIG. 11.7 (A) Luminescence spectra of Tb-MOF in the presence of different concentrations of HT. (B) Stern-Volmer equation of HT at room temperature (Inset: luminescence change after adding HT under UV-light irradiation of 254 nm). (C) Emission spectra of Tb-MOF dispersed in water in the absence and presence of various substances in the blood plasma and urine. (D) Emission intensity of 542 nm for Tb-MOF in the presence of various substances in the blood plasma and urine. (E) Fluorescence response of Tb-MOF toward HT and HIAA in the presence of one of the other competing substances. (F) Recyclability of Tb-MOF implemented with HT or HIAA. *(Reproduced with permission from H. Yang, P. Xu, B. Ding, X. Wang, Z. Liu, H. Zhao, X. Zhao, E. Yang, Isostructural lanthanide coordination polymers with high photoluminescent quantum yields by effective ligand combination: crystal structures, photophysical characterizations, biologically relevant molecular sensing, and anti-counterfeiting ink application. Cryst. Growth Des. 20 (2020) 7615–7625. Copyright 2020 American Chemical Society.)*

(H_4btec)) with extremely high water toleration as a fluorescent probe for HA in urine. The suspension-state luminescent measurements (Fig. 11.8A) show that only HA induces a remarkable reduction of luminescence intensity of Eu^{3+}@Al-MOF at 614 nm. In accordance with the changes in fluorescence spectra, under the irradiation of a UV lamp, only HA incorporated Eu^{3+}@Al-MOF showed a significantly darker luminescence than that from the original one, distinguished easily by the naked eye (inset of Fig. 11.8A). To evaluate the sensitivity of Eu^{3+}@ Al-MOF toward HA, fluorescence titration experiments were carried out (Fig. 11.8B). A good linear relationship ($R = 0.997$) was found between the emission intensity ratios ($I_0/I - 1$) and the logarithm of HA concentration over the range from 0.05 to 8 mg mL^{-1}. The LOD was determined as 9 μg mL^{-1}, sufficient for detection of millimolar concentrations of HA in urine. The regenerable performance for a sensor is shown in Fig. 11.8C. With five runs performed by sequential addition of HA and

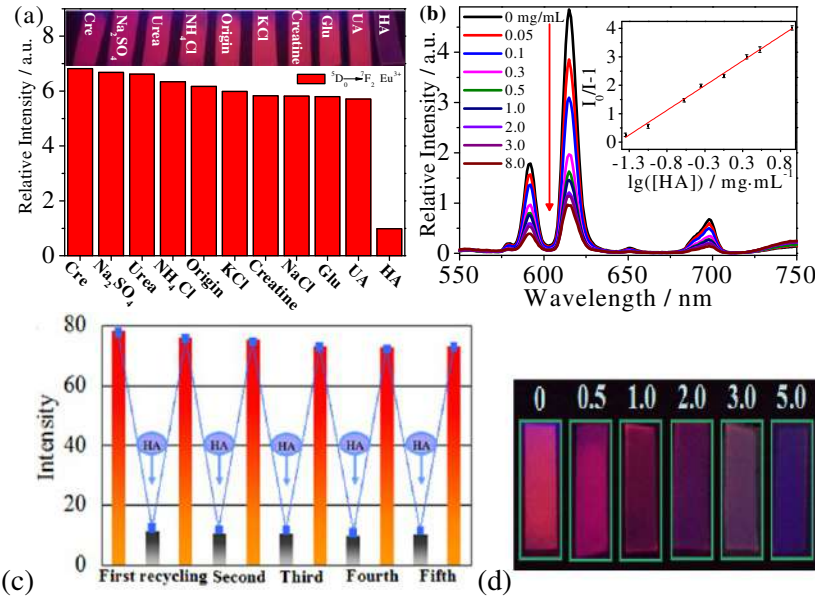

FIG. 11.8 (A) The relative intensities of $^5D_0 \rightarrow {}^7F_2$ at 614 nm for Eu^{3+}@Al-MOF dispersed in various metal ion aqueous solutions (10 mM) ($\lambda_{ex} = 315$ nm). (B) The luminescence spectra of Eu^{3+}@Al-MOF in the presence of different concentrations of HA aqueous solutions ($\lambda_{ex} = 315$ nm), and the plot of $I_0/I - 1$ versus the logarithm of the concentration of HA; Inset in (B): the corresponding photographs under 254-nm UV-light irradiation; (C) The luminescence intensity of Eu^{3+}@Al-MOF at 614 nm after five recycles. ($\lambda_{ex} = 315$ nm); and (D) Optical images under 254-nm UV-light irradiation of the test paper after immersing into urines with different concentrations (mg mL^{-1}) of spiked HA for 1 min. *(Reproduced with permission from J. Hao, B. Yan, Recyclable lanthanide-functionalized MOF hybrids to determine hippuric acid in urine as biological indices of toluene exposure. Chem. Commun. 51 (2015) 14509–14512. Copyright 2015 Royal Society of Chemistry.)*

ultrasonic washing, the luminescent intensity of the recycled Eu^{3+}@Al-MOF was well consistent with that of the original one, suggesting that Eu^{3+}@ Al-MOF can be reused to detect HA. Under the irradiation of UV light of 254 nm, the fluorescent colors of the test paper changed from bright red to dark red, faint red, and finally black when soaked in 0.5, 1.0, 2.0, 3.0, and 5.0 mg mL^{-1} of HA spiked urines (Fig. 11.8D). To the naked eye, the colors of different intensities could be distinguished, thus allowing the degree of toluene intoxication to be judged [33]. Furthermore, Qin et al. tried a more extensive sensing system with functionalized MOF ($Ga_2(OH)_4(C_9O_6H_4$, Ga-MOF, with linker 1,2,4-benzenetetracarboxylic acid (H_3btc)) hybrid Ga-MOF@Eu^{3+} by coordination postsynthetic modification Eu^{3+} cations, which exhibited the strong luminescence of the Eu^{3+} ion and could extensively sense the biological metabolites of benzene derivatives (toluene, xylene, and ethylbenzene) in urine [34].

Hao et al. fabricated an Eu^{3+} PSM-functionalized MOF hybrid Eu^{3+}@Ga-MOF with nanosize and intense luminescence [35]. It could both detect ammonia gas among various indoor air pollutants and simultaneously detect a biological metabolite of ammonia in the human body (urinary urea). The joint determination of indoor environmental ammonia and the urinary urea in the human body can comprehensively reflect real ammonia exposure and intoxication of humans. As shown in Fig. 11.9A, only urea induced a twofold enhancement in the emission intensity of Eu^{3+}@Ga-MOF at 614 nm, while nearly no fluorescence intensity change was observed in the presence of others. This indicates Eu^{3+}@Ga-MOF can selectively recognize urea in aqueous solutions. The emission intensity enhancement induced by urea was not affected by the coexisting components (Fig. 11.9B), further confirming that Eu^{3+}@Ga-MOF is a highly selective probe for urea. As illustrated in Fig. 11.9C, it was observed that the fluorescence intensity of Eu^{3+}@Ga-MOF at 614 nm increased linearly with the concentration of urea in the range of 0.6–50 mg mL^{-1}. Urea could be directly detected at concentrations as low as 0.6 mg mL^{-1}, sufficient for detection of millimolar concentrations of urea in urine. They tested the response rate and regenerated ability of the Eu^{3+}@Ga-MOF sensor for urea. After five consecutive cycles of enhancing and recovery, the luminescent intensity of Eu^{3+}@Ga-MOF in water was comparable to the initial state (Fig. 11.9D) [35].

Lian et al. synthesized a phosphonate Al-MOF (MIL-91(Al: Eu)) and modified it to a hybrid material to detect uric acid [36]. The nonblooming hybrid Cu^{2+}@Al-MOF(Al: Eu) can be used for detecting uric acid due to the rebound of luminescence in the presence of uric acid [36]. It provides a novel method for the convenient and nimble diagnosis of hyperuricuria (Fig. 11.10; left). The luminescence intensity of Cu^{2+}@Al-MOF(Al: Eu) at 612 nm gradually increased with increasing uric acid concentration. They fit a linear relationship between the fluorescence intensity (612 nm) of Cu^{2+}@Al-MOF(Al: Eu) vs. the content of uric acid, and found a good linear relationship ($R = 0.991$) between the intensity ratios of $^5D_0 \rightarrow {}^7F_J$ transition (I_0/I) and the logarithm of uric acid concentration over the range from 10 to 1200 μmolL^{-1} with LOD of 1.6

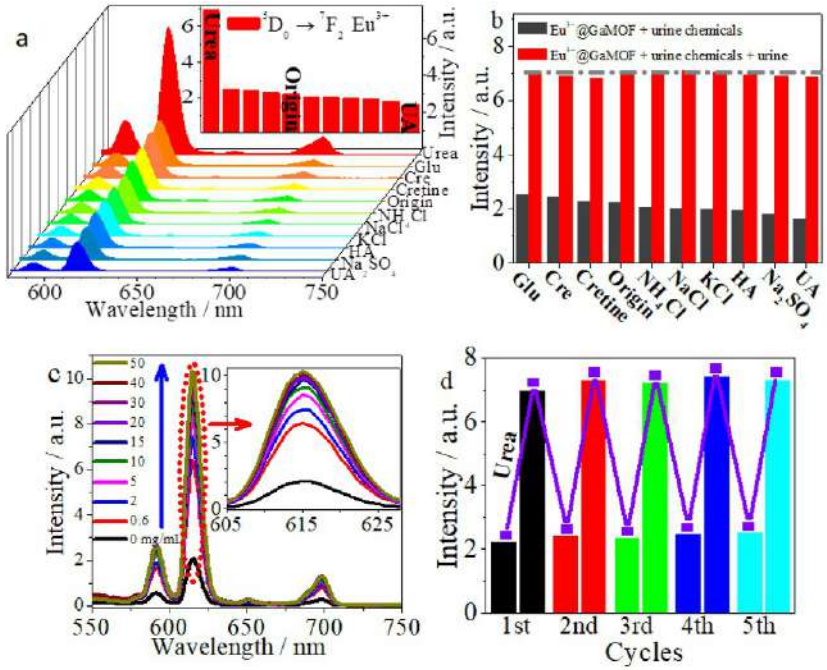

FIG. 11.9 (A) Suspension-state luminescent spectra and the relative intensities of $^5D_0 \rightarrow {}^7F_2$ at 614 nm (inset of A) for Eu^{3+}@Ga-MOF dispersed in various urine chemicals (10^{-2} M, $\lambda_{ex} = 338$ nm); (B) Luminescence responses of Eu^{3+}@Ga-MOF (1 mg mL^{-1}) upon the addition of urea (0.01 M) in the presence of a background of various urine chemicals (0.02 M) in aqueous solution ($\lambda_{ex} = 338$ nm); (C) Luminescence spectra of Eu^{3+}@Ga-MOF under different concentrations of urea aqueous solution ($\lambda_{ex} = 338$ nm); and (D) the regeneration cycles of Eu^{3+}@Ga-MOF sensor used in detecting urea. *(Reproduced with permission from J. Hao, B. Yan, Simultaneous determination of indoor ammonia pollution and its biological metabolite in human body by use of a recyclable nanocrystalline lanthanide functionalized MOF. Nanoscale 8 (2016) 2881–886. Copyright 2016 RSC Society of Chemistry.)*

μmolL^{-1} (Fig. 11.10A; right). Real urine samples from normal people were collected and about 420 μmolL^- 1of uric acid was added. The concentration of uric acid using Cu^{2+}@Al-MOF(Al: Eu) suspended solution was determined as 429 μmolL^{-1}, very close to the actual value. Moreover, the test paper was infiltrated in real urine with various concentrations of uric acid (200 and 1000 μmol L^{-1}) and then exposed to air for drying. With the naked eye, the colors of the test papers could be distinguished, thus allowing a determination as to whether or not the subject suffered from hyperuricuria (Fig. 11.10B and C; right) [36].

Hao et al. designed a luminescent Eu-MOF hybrid for qualitative and quantitative analysis of urinary 1-HP. [37] As shown in Fig. 11.11A, upon addition of 1-HP (1 mg mL^{-1}) to the suspension of Eu^{3+}@Ga-MOF (MIL-61, with linker 1,2,4,5-benzenetetracarboxylic acid (H_4btec)), a significant decrease (77%) in

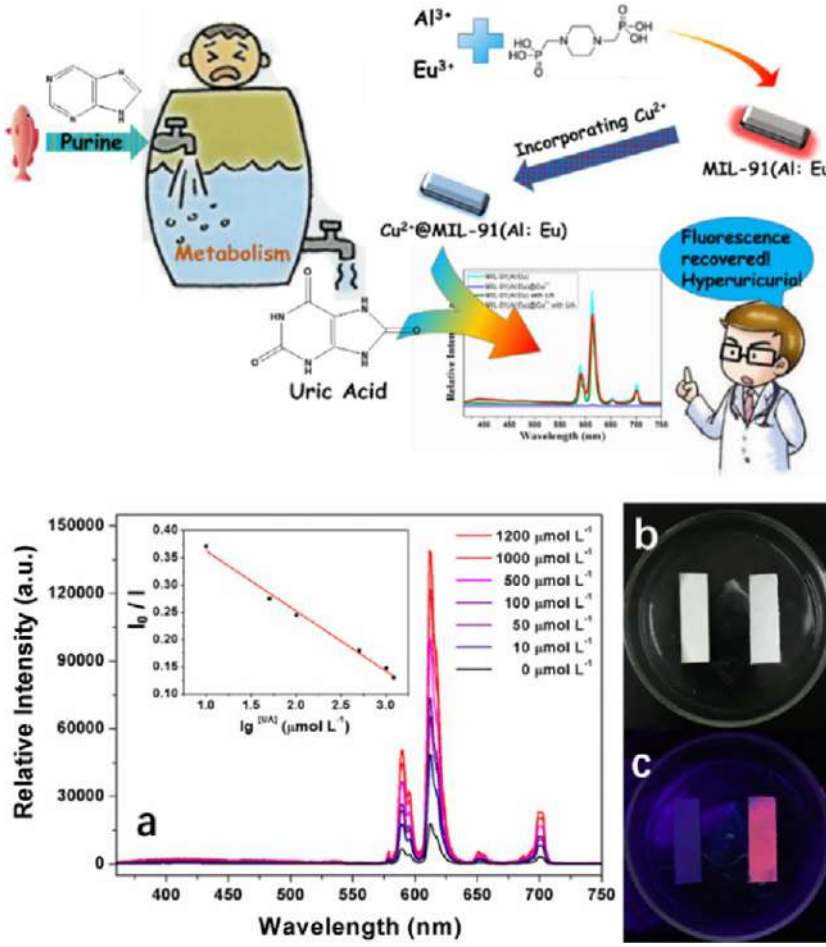

FIG. 11.10 *(Top)* Scheme for the Cu^{2+}@Al-MOF(Al: Eu) hybrid as Off-On fluorescent sensor for detecting purine metabolite uric acid and diagnose hyperuricuria; *(Bottom)* The histogram on the basis of the intensity of $^5D_0 \rightarrow {}^7F_2$ transition of Eu^{3+} in Cu^{2+}@Al-MOF(Al: Eu) toward various urine chemicals; (A) The luminescence spectra of Cu^{2+}@Al-MOF(Al: Eu) in the presence of different concentrations of uric acid aqueous solution, and the plot of I_0/I versus the logarithm of the concentration of uric acid; (B) and (C) are the test papers under light and UV irradiation. *(Reproduced with permission from X. Lian, B. Yan, Phosphonate MOFs composite as off-on fluorescent sensor for detecting purine metabolite uric acid and diagnose hyperuricuria. Inorg. Chem. 56 (2017) 6802–6808. Copyright 2017 American Chemical Society.)*

the luminescence intensity of Eu^{3+} at 614 nm could be observed, leading to its emission color changing from red to colorless as seen by the naked eye under a UV lamp (inset of Fig. 11.11B). Moreover, a 1-HP urine test paper was developed and the optical images under the irradiation of UV light of 254 nm were recorded. As shown in Fig. 11.11C, the emission colors of the test papers

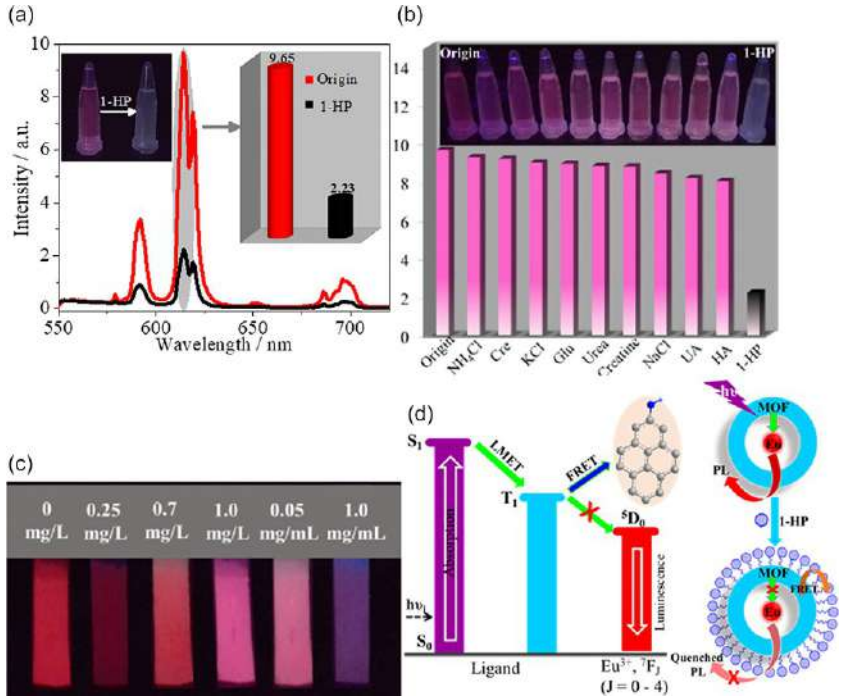

FIG. 11.11 (A) Suspension-state luminescence spectra of Eu^{3+}@Ga-MOF before and after being treated by 1-HP (1 mg mL^{-1}), Inset in (A): the changes in the emission intensity (614 nm) and luminescence colors of Eu^{3+}@Ga-MOF induced by the addition of 1-HP; (B) Intensities (the $^5D_0 \rightarrow {}^7F_2$ transition) of Eu^{3+}@Ga-MOF suspensions with various urine components. Inset in (B): the corresponding photographs under a UV lamp (254 nm); (C) Optical images of test paper under 254-nm UV light irradiation after immersing into urine spiked with different amounts of 1-HP. Simplified schematic diagram of LMET and FRET process in Eu^{3+}@Ga-MOF with 1-HP; and (D) The schematic illustration of the mechanism of 1-HP sensing by Eu^{3+}@Ga-MOF. *(Reproduced with permission from J. Hao, B. Yan, Determination of urinary 1-hydroxypyrene for biomonitoring of human exposure to polycyclic aromatic hydrocarbons carcinogens by a lanthanide-functionalized metal-organic framework sensor. Adv. Funct. Mater. 27 (2017) 1603856. Copyright 2017 Wiley.)*

changed from brilliant red to dark red, faint red, and finally colorless with increasing concentration of 1-HP from 0 to 1 mg mL^{-1}. These different colors could be easily distinguished by the naked eye allowing simple evaluation of the intoxication degree of PAHs. The luminescence quenching is typically attributed to a FRET mechanism. In the presence of 1-HP, the FRET process between the ligands and 1-HP competes with the LMET process through suppressing or blocking the energy transfer from the ligands to Eu^{3+}. So the emission of Eu^{3+}@Ga-MOF is restricted or quenched, and thus 1-HP is detected (Fig. 11.11D) [37]. In addition, He et al. chose an anionic 3D MOF of JXNU-4 as a parent

compound to host Eu^{3+} cations by uncoordinated carboxylate oxygen atoms in its pores, which was also developed as a fluorescent probe for urine 1-HP. In the presence of 1-HP, Eu^{3+}@JXNU-4 exhibited 1-HP- and Eu^{3+} -based dual emission. The intensity of the 1-HP emission increased with the concentration of 1-HP increasing, while the Eu^{3+} emission receded in the meantime. The ratio value of 1-HP emission at 502 nm (I_{502}) and Eu^{3+} emission at 616 nm (I_{616}) versus the concentration of 1-HP revealed a good linear relationship. This provides a ratiometric fluorescence sensor with high sensitivity to 1-HP in urine [38].

VCM (vinyl chloride monomer) exposure can result in angiosarcoma and hepatocellular cancer. TDGA (urinary thiodiglycolic acid), a detectable metabolite of VCM in human urine, is considered to be a sensitive biomarker of VCM and reflects the internal dose of human exposure to VCM. Hao et al. designed a hybrid material (Cu^{2+}/Eu^{3+}-Zr^{4+}-MOF, with linker H_4btec) as a luminescent sensor to detect TDGA [39]. The design principle of probing TDGA was to introduce the reactive site (Cu^{2+}) for TDGA into the framework as the TDGA-responding site. Cu^{2+} has been found to be able to quench Eu^{3+}'s luminescence. TDGA has a strong affinity for Cu^{2+} and can weaken the quenching effect of Cu^{2+} on the emission of Eu^{3+}. Thereby, in the presence of TDGA, the enhanced luminescence of Cu^{2+}/Eu^{3+}-Zr^{4+}-MOF can be observed. In contrast to TDGA, the additions of these components only cause negligible changes in the luminescence spectra (Fig. 11.12A), which induces a visible color change from colorless to red to be distinguished by the naked eye. Fig. 11.12B reveals that the TDGA-induced fluorescence enhancement response is unaffected in the background of other coexisting urine ingredients, demonstrating the good anti-interference performance and high selectivity of Cu^{2+}/Eu^{3+}-Zr^{4+}-MOF for TDGA. The LOD is 89 ng mL^{-1} for TDGA, more than 200 times lower than the threshold value of 20 mg L^{-1} for a healthy person, which fulfills the critical requirement of tracing the urinary TDGA levels for early diagnosis of VCM poisoning. The colors of the Cu^{2+}/Eu^{3+}-Zr^{4+}-MOF powders change from brilliant blue to light blue, and finally are almost colorless, with the increasing concentration of TDGA from 0 to 700 mg/L, i.e., TDGA's addition bleaches the blue color of the powders out (Fig. 11.12C), in good agreement with the actual TDGA amount. The luminescent colors of the test stripes changed from dark to dark red, faint red, purplish red, and finally bright red when soaked in urine samples with increasing TDGA content (seen from the optical images in Fig. 11.12D). To the naked eye, the colors of different intensities can be distinguished so as to easily evaluate the intoxication degree of human exposure to VCM [39].

Lian et al. provided an unreported Turn-On fluorescence switch for independent detecting of phenylglyoxylic acid (PGA) in serum and urine with high selectivity, based on the luminescent Eu@Sc-MOF hybrid with MIL-53 type configuration (linkers terephthalic acid (H_2BDC) replaced with isophthalic acid (H_2IPA)) [40]. The on-site monitoring of PGA in urine by a paper-based fluorescent probe integrated with smartphone was also proposed (Fig. 11.13A).

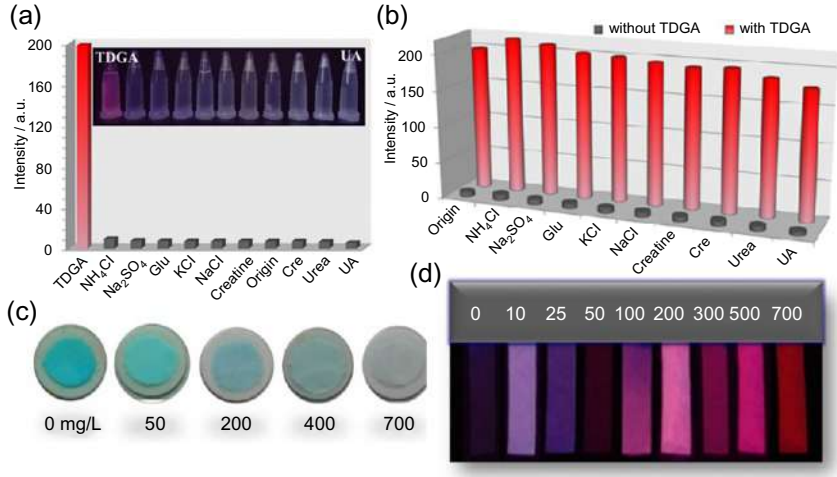

FIG. 11.12 (A) Suspension-state luminescence intensities (the $^5D_0 \rightarrow {}^7F_2$ transition, 614 nm) of Cu^{2+}/Eu^{3+}-Zr^{4+}-MOF toward various urine components ($\lambda_{ex} = 310$ nm). Inset in (B): the corresponding photographs under a UV lamp (254 nm). Luminescence responses of Cu^{2+}/Eu^{3+}-Zr^{4+}-MOF toward TDGA in the presence of background of other various urine components ($\lambda_{ex} = 310$ nm); (B) Luminescence responses of Cu^{2+}/Eu^{3+}-Zr^{4+}-MOF toward TDGA in the presence of background of other various urine components ($\lambda_{ex} = 310$ nm); (C) Photographs showing the color changes of the Cu^{2+}/Eu^{3+}-Zr^{4+}-MOF sample after treated by different concentrations of TDGA and (D) Optical images of test paper under 254-nm UV light irradiation after immersing into urine spiked with different concentrations of TDGA (mg/L). *(Reproduced with permission from J. Hao, X. Xu, X. Lian, C. Zhang, B. Yan, A luminescent 3d-4f-4d MOF nanoprobe as a diagnosis platform for human occupational exposure to vinyl chloride carcinogen", Inorg. Chem. 56 (2017) 11176–11183. Copyright 2017 American Chemical Society.)*

They further investigated the time-response characteristic of the Eu@Sc-MOF sensor toward PGA; pictures of the fluorescence changes over time were recorded by successive photographs. As demonstrated in Fig. 11.13B, the PGA-caused fluorescence enhancement phenomenon was very fast. Such a macroscopic phenomenon can be seen in 5 s, indicating that Eu@Sc-MOF can be used as a convenient and fast sensor for PGA. The calculated LOD value is 4.16 ppb. In addition, the LOD experiment in real urine with the addition of MA (0.01 M) and HA (0.01 M) was conducted again. The Eu@Sc-MOF sensor exhibited excellent potential as before (linear range: $0.02 \sim 0.4$ mg mL^{-1}, $R = 0.9925$, LOD = 10.8 ppb). The LOD is much lower than the critical value of 0.25 mg mL^{-1} of PGA, which is proposed by the American Conference of Governmental Industrial Hygienists (ACGIH). A paper-based probe for rapid and on-site detection of PGA was developed, which undergoes an obvious fluorescence color switch from navy to red under a 356-nm UV lamp, which can be readily observed (Fig. 11.13C). The LOD is approximately 0.197 mg mL^{-1}, less than the benchmark value recommended by ACGIH (0.25 mg mL^{-1}) [40].

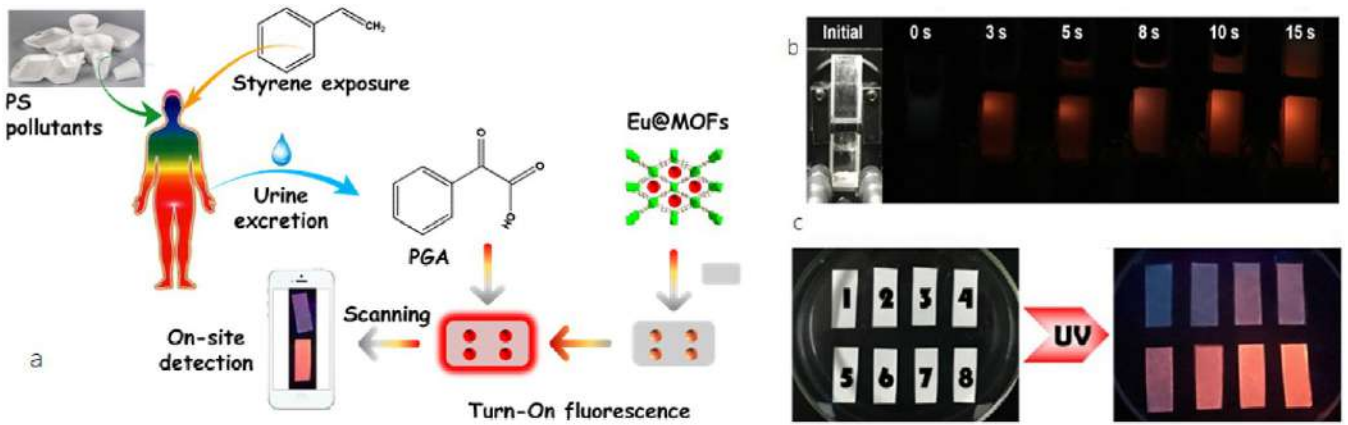

FIG. 11.13 (A) The schematic diagram of the turn-on fluorescence switch for on-site detecting of urinary PGA; (B) Successive photographs of the Eu^{3+}@Sc-MOF with addition of PGA solution for different times (0∼5 s); and (C) Optical images under 365-nm UV light irradiation of the test paper after immersing into urine spiked with different concentrations (0, 0.02, 0.05, 0.1, 0.2, 0.25, 0.4, and 0.5 mg mL^{-1}, the test paper labeled as 1–8, respectively). *(Reproduced with permission from X. Lian, T. Miao, X. Xu, C. Zhang, B. Yan, Eu3 + functionalized Sc-MOFs: turn-on fluorescent switch for ppb-level biomarker of plastic pollutant polystyrene in serum and urine and on-site detection by smartphone. Biosens. Bioelectron. 97 (2017) 299–304. Copyright 2017 Elsevier.)*

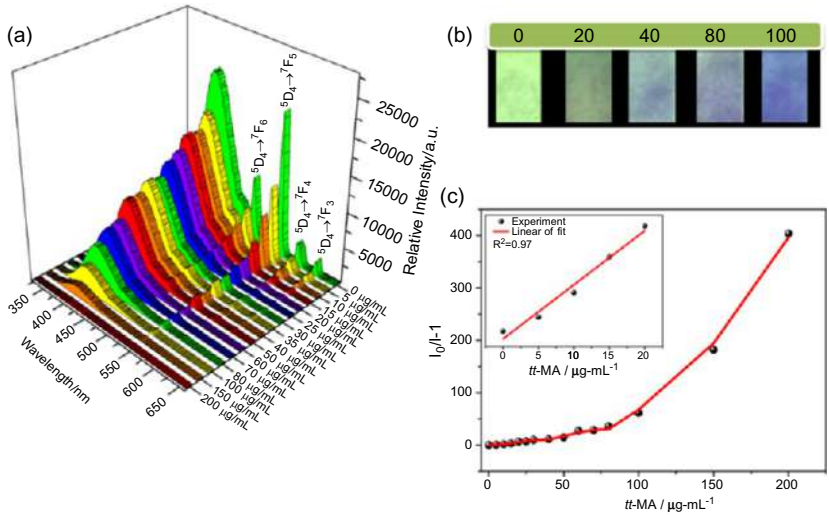

FIG. 11.14 (A) Emission spectra of Tb^{3+}@MOF-SO 3^- dispersed in aqueous solutions with different concentrations of *tt*-MA ($\lambda_{ex} = 291$ nm). (B) Optical images of test paper under 254-nm UV light irradiation after immersing into aqueous solutions with different concentrations of *tt*-MA. (C) The S-V curve of $I_0/I - 1$ versus concentration of *tt*-MA. *(Reproduced with permission from X. Qu, B. Yan, Ln(III)-functionalized metal-organic frameworks hybrid system: luminescence properties and sensor for trans, trans-muconic acid as a biomarker of benzene. Inorg. Chem. 57 (2018) 7815–7824. Copyright 2018 American Chemical Society.)*

Urinary *trans*, *trans*-muconic acid (*tt*-MA) is widely used, usually as a benzene metabolite, as a biological biomarker of environmental and occupational exposure to this xenobiotic. Qu et al. presented an alternative approach to preparing a highly luminescent hybrid Tb(III)@MOF-SO_3^- (main linker of 2-sulfonylterephthalate (2-H_2stp)) [41]. As shown in Fig. 11.14A, gradual decreases of the fluorescence emissions of ligands and typical Tb^{3+} ions were observed in Tb^{3+}@MOF-SO 3^- aqueous suspensions as the *tt*-MA concentration increased from 0 to 200 μg·mL^{-1}. When the concentration of *tt*-MA was 5 μg mL^{-1}, nearly half the intensity of the typical Tb^{3+} emission at 544 nm was quenched, with a quenching efficiency of 49%, while there were almost no conspicuous emissions of both detected when the *tt*-MA concentration was 200 μg·mL^{-1}. Under irradiation with a UV lamp, Tb^{3+}@MOF-SO 3^- test papers showed visible luminous variation from light green to nattier blue after soaking in various concentrations of *tt*-MA aqueous solutions (from 0 to 100 μg mL^{-1}) (Fig. 11.14B). However, in the range of low concentrations of *tt*-MA from 0 to 20 μg mL^{-1}, the S-V equation shows a certain linear relationship ($R^2 = 0.97$), and yield a linear curve by which K_{sv} can be calculated as 0.27932 mL·μg^{-1} (Fig. 11.14C) [41].

Carbaryl is the most frequently used carbamate pesticide in the agriculture field and is associated with a series of potentially adverse health impacts,

including neurological disorders and cancer. 1-Naphthol (1-N), a metabolite of the insecticide carbaryl, is an established human biomarker used for assessing food intake and environmental exposure. Qin et al. utilized a hybrid material Eu^{3+}@MOF-253 as a highly efficient recyclable luminescent probe for the detection of biomarker 1-N of exposure to carbaryl with excellent sensitivity and rapid response time [42]. An extensive fluorescence quenching was presented by the 1-N, and the fluorescence color turned from red to green in the fluorescence photographs and could be visualized with the naked eye. The LOD was determined to be 7 $\mu g\ mL^{-1}$, far below the maximum permissible intake standard 0.008 $mg\ kg^{-1}$ as reported by the ACGIH. Indicator boxes were made increasingly mobile to better characterize concentrations in humans through mobile monitors. The simulated diagram and photograph are presented in Fig. 11.15A and B. The sensor device consists mainly of three parts, which are the sensory unit, the colorimetric card, and the UV lamp. The sensory unit consists of a test paper and measuring jug. The main function of this unit is to react with the urinary sample. The colorimetric assays developed for fluorescence of the results can be distinguished by the naked eye.

N-methylformamide (NMF), the major metabolite of the DMF in the human body, is regarded as a biomarker of DMF intoxication and represents the internal dose of DMF exposure in the human body. Sun et al. developed a feasible method for NMF detection with a luminescent Eu^{3+}-functionalized MOF hybrid [43]. The luminescence of the hybrid material could be significantly increased only by NMF even though in the presence of other chemical components of urine. Moreover, a portable test card was also made for immediate detection. Qin et al. designed a ratiometric fluorescence hybrid probe Eu^{3+}/CDs@MIL-53 by encapsulating luminescent carbon dots (CDs) and Eu^{3+} into the MIL-53 host

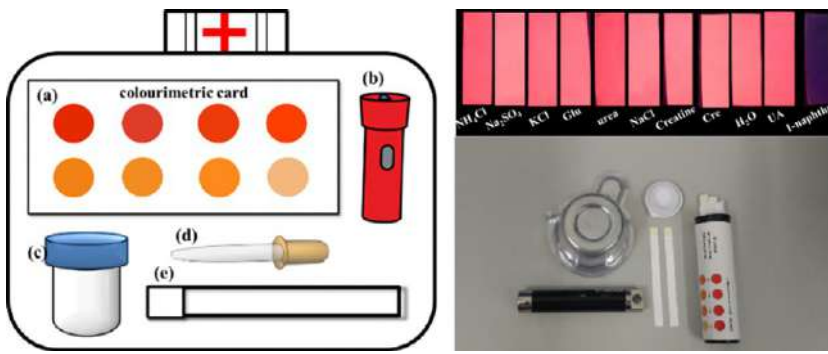

FIG. 11.15 (A) Simulated diagram of the indicator box. (a) colorimetric card; (b) ultraviolet lamp; (c) measuring jug; (d) dropper; (e) test paper. (B) Photograph of the indicator box. Inset: the photo of test paper under UV lamp. *(Reproduced with permission from S. Qin, B. Yan, A facile indicator box based on Eu3+ functionalized MOF hybrid for the determination of 1-naphthol, a biomarker for carbaryl in urine. Sens. Actuators B 259 (2018) 125–132. Copyright 2018 Elsevier.)*

to yield the dual-emitting center [44]. The prepared fluorescent probe is a promising dual-functional sensor with high selectivity and sensitivity for the detection and recognition of diaminotoluene (TDA), a metabolite of toluene diisocyanates (TDI) that has been associated with an increased risk of occupational asthma. The ratio of ($I_{C\text{-}dots}/I_{Eu}$) increases with increased TDA concentrations. Phenylamine has been recognized as one of the most important industrially relevant ingredients and a crucial intermediate in chemical products. However, its internal exposure detection in humans remains largely elusive due to the lack of a potent monitoring method. Qin et al. also achieved a probe based on Tb^{3+} functionalized hybrid Tb@MOF-253 through post-synthetically modified MOFs [45]. The synthesized Tb^{3+}@MOF-253 exhibited a strong luminescence of Tb^{3+} originated from efficient energy transfer from the ligand, which could sense the biological metabolite *p*-aminophenol (PAP) of the phenylamine in human urine. Linear correlation between the integrated fluorescence intensity and the concentration of PAP enables the quantitative analysis of PAP in physiological ranges (0.005–5 mg mL^{-1}) with low LOD (5 μg mL^{-1}). Furthermore, a simple and rapid smartphone-based medical portable test paper was developed.

Sweat components provide plentiful potential biomarkers to indicate the health state of a subject. Xu et al. demonstrated a novel, wearable device that uses fluorescence detection technology to noninvasively monitor Cl^- in sweat. The wearable Cl^- monitoring platform integrates a flexible host material (cotton piece) and two fluorescent materials (Tb-MOFs (DUT-101) and Ag^+/Eu^{3+}@UiO-67) by simple ultrasonic loading. Instead of using a large circuit board, this device is comfortable for human body contact and can be worn routinely. Here Ag^+/Eu^{3+}@UiO-67 is the working fluorescence center and DUT-101 is the reference fluorescence center. After characterizing the performance, flexibility, and stability of the sensing device, quantitative Cl^- measurements were performed with high selectivity and sensitivity [46]. Sun et al. designed a luminescent probe based on Tb^{3+}/Cu^{2+} heterometallic MOFs for beamed monitoring of urinary sarcosine, a differential metabolite that can indicate the progression of prostate cancer (PCa). The fluorescence probe presented high selectivity toward sarcosine in the urine. It also displayed good sensitivity with a comparatively low detection limit and fast response to sarcosine within 5 min [47]. Homovanillic acid (HVA) is one of the major metabolites of catecholamine in humans. An elevated level of HVA in urine and blood has been associated with many diseases, including catecholamine-secreting tumors. Consequently, detection of the biomarker HVA in urine is an effective strategy to detect cancer precursors and early stage cancers. Qin et al. fabricated a fluorescence probe by integrating RE^{3+} with MOFs, which showed a good response toward HVA and exhibited ratiometric detection of HVA, rendering it an excellent candidate for sensing devices. Thus they designed a logic gate operation integrating the probe with logical operations for the intelligent sensing of HVA [48]. Wang et al. designed a microporous luminescent probe based on a fluorescein (FS)

dianion dye functionalized zinc MOF, FS@Zn-MOF, to effectively detect trichloroacetic acid (TCA) in human urine, which is a biomarker or biometabolite of trichloroethylene (TCE). This study showed that the luminescence intensity ratio of the peaks at 518 nm and 411 nm correlated well linearly to the concentration of TCA with a rapid response time of less than 30 s while disregarding the interference of other coexisting species in urine. It also exhibited excellent sensitivity with a detection limit of 1.22 ppm/7.46 μmol L^{-1} [49]. The detection of 4-aminophenol (4-AP), which is a biomarker of aniline and represents the internal dose of aniline exposure in the human body, has attracted much attention in recent years. Jin et al. prepared a bifunctionalized luminescent MOF, Eu@MOF-253-CH, through encapsulating the methyl groups and the Eu^{3+} cations into MOF-253. This study showed that the bifunctionalized Eu@MOF-253-CH_3 could specifically recognize 4-AP upon luminescence quenching, while refraining from the interference of other coexisting species in urine. The Eu@MOF-253-CH_3 hybrid as a 4-AP sensor also displayed excellent performance, including high water tolerance, good pH-independent stability, fast response, great selectivity, and elevated sensitivity (0.5 $\mu g \cdot mL^{-1}$), attributed to the N-viologenized ligand. These results suggest that the bifunctionalized Eu@MOF-253-CH_3 can act as a promising sensor to practically monitor 4-AP concentration in the human urine system, and then to realize the screening and prediagnosis of human health [50]. By means of PSM treatment of the UiO-66 derivative with -SO_3H, Min et al. prepared a luminescent hybrid material, Tb^{3+}@UiO-66-SO_3H, which was further developed as a fluorescent probe for the sensing of trans, trans-muconic acid (*tt*-MA, a biomarker of benzene), being closely related to human health. Notably, Tb^{3+}@UiO-66-SO_3H could realize highly sensitive and selective detection of *tt*-MA (detection limit, 0.58 μM, 0.083 ppm) [51]. Yan has summarized the progress on this topic in his review [52].

Wang et al. prepared a unique Y-MOF, which can be utilized to combine FAM-labeled NH-ssDNA to construct the rarely reported but excellent hybrid FAM-labeled NH-ssDNA/Y-MOF sensing platform for CRP Ab (C-reactive protein autoantibody) in human serum solution, which provides an effective method for detecting biomarkers of ALA (amoeba liver abscess) [53]. The protein-aptamer binding strategy was used: (1) the aptamer for CRP Ab, namely, ssDNA, is a DNA sequence with specific binding with CRP Ab; (2) 5-carboxyfluorescein (FAM) was modified by aptamer, which can be investigated on a fluorescent spectrum; (3) to further improve the sensitivity of the CRP Ab detection process, the amino group was modified by 3′-ssDNA to fabricate NH-ssDNA, which easily strengthens hydrogen-bonding interactions with Y-MOF and CRP; (4) Y-MOF was utilized as a highly sensitive sensing platform, which attracts CRP, CRP Ab, and NH-ssDNA through hydrogen-bonding interactions (Fig. 11.16; top, left). Different from other proteins, only NH-ssDNA's fluorescent intensity can be influenced dramatically by CRP Ab (Fig. 11.16; top, right). Therefore Y-MOF/NH-ssDNA is a rarely reported

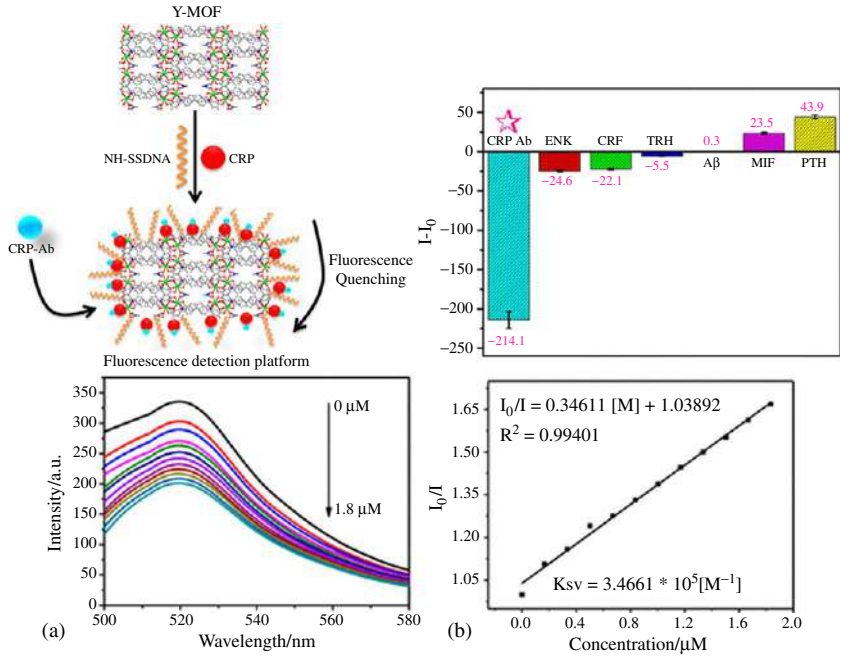

FIG. 11.16 *(Top, Left)* Schematic description for the illustration of the CRP Ab detection process by the hybrid FAM-labeled NH-ssDNA/Y-MOF sensing platform. *(Top, Right)* Fluorescent intensity variable values ($I - I_0$) when Y-MOF is added to different CRP Ab and some analogue proteins of CRP Ab (I_0 and I represent the fluorescent intensity of Y-MOF before and after adding CRP Ab and some analogue proteins of CRP Ab). *(Bottom)* (A) Fluorescent spectrum of NH-ssDNA after adding different concentrations of CRP Ab in 2.5 nM CRP; (B) fluorescent ratio of NH-ssDNA after adding different concentrations of CRP Ab in 2.5 nM CRP. *(Reproduced with permission from X. Wang, X. Mao, Z. Zhang, R. Guo, Y. Zhang, N. Zhu, K. Wang, P. Sun, J. Huo, X. Wang, B. Ding, Solvothermal and ultrasonic preparation of two unique cluster-based coordination materials: metal-organic framework-based ratiometric fluorescent biosensor for an ornidazole and ronidazole and sensing platform for a biomarker of amoeba liver abscess. Inorg. Chem. 59 (2020) 2910–2922. Copyright 2020 American Chemical Society.)*

hybrid MOF-based sensing platform that behaves with high selectivity for CRP Ab. Although FAM-labeled NH-ssDNA has an emission peak located at 525 nm, when different concentrations of CRP Ab are directly added into the solutions only containing FAM-labeled NH-ssDNA, FAM-labeled NH-ssDNA's fluorescent intensity gradually decreases. After CRP Ab is added into the mixture solution of Y-MOF and 0.5 mM CRP solution, a new excellent linear relationship between CRP Ab concentration and NH-ssDNA fluorescent ratio is obtained, with R^2 of 0.99401 and a Ksv value of 3.4661×10^5 [M^{-1}] (Fig. 11.16; bottom). Therefore the result also reveals that, through the protein-aptamer binding strategy, the Y-MOF sensing platform's sensitivity for CRP Ab was improved. The sensing performance improvement by

Y-MOF and CRP could be because CRP may have specific protein-aptamer binding with CRP Ab, which can lead to a further quenching effect through the strength of the hydrogen-bond interactions [53].

Qu et al. used 3,5-di(2,4-dicarboxylphenyl)pyridine (H_4pdda) and 1H-tetrazole (HTz) to synthesize a MOF, $\{[NH_2(CH_3)_2]_4 \cdot [Cd_6(pdda)_4(HTz)_{1.5}(H_2O)_6] \cdot 3/4DMF \cdot 7/2H_2O\}_n$ (Cd-MOF) ($[NH_2(CH_3)_2]^+$ = dimethyl ammonium cation), which showed a single-crystal to single-crystal (SC-SC) phase transition in pure water. Moreover, Tb^{3+}-functionalized Cd-MOF hybrids, Tb(III)@Cd-MOF, were fabricated by straightforward cation-exchange modification to replace $[NH_2(CH_3)_2]^+$ ions in channels of Cd-MOF with Tb^{3+} ions, which is proven as a promising sensor with the potential of practical detection of biomarker dichloroanilines (3,4-DCA and 3,5-DCA) (urinary dichloroanilines) through fluorescence spectrometry [54]. The results clearly show that the emission spectra and intensities in Tb(III)@Cd-MOF suspensions containing 3,4-DCA and 3,5-DCA contrast sharply with that in Tb(III)@Cd-MOF suspensions containing other urine compounds (Fig. 11.17; top). Under UV-lamp irradiation, 3,4-DCA and 3,5-DCA can induce a visible color change from green to colorless and the differences in the effect of different urine chemicals on Tb(III)@Cd-MOF emission can be easily distinguished with the naked eye (Fig. 11.17; top). These indicate Tb(III)@Cd-MOF can serve as a chemosensor for selective recognition of 3,4-DCA and 3,5-DCA in DMF. As shown in Fig. 11.17A and C (bottom), a gradual decrease in the fluorescence emissions of the Tb(III)@Cd-MOF sensor was observed upon the increasing concentrations of 3,4-DCA and 3,5-DCA from 0 to 0.2314 mg mL^{-1}. Within the full range of concentrations from 0 to 0.2314 mg mL^{-1}, the corresponding relationship curves of both are nonlinear and match with a first-order exponential equation, suggesting diffusion-controlled quenching processes. Nonetheless, in the range of low content, from 0 to 0.0266 mg mL^{-1}, the S-V plot of Tb(III)@Cd-MOF exhibits a good linear correlation ($R^2 = 0.99$) as the concentration of 3,4-DCA and 3,5-DCA increases (Fig. 11.17B and D). The Ksv values for Tb(III)@Cd-MOF toward 3,4-DCA and 3,5-DCA are 25.11 and 30.21 mL mg^{-1}, respectively. The LODs are calculated to be 0.0033 mg mL^{-1} (3.3 ppm) and 0.0026 mg mL^{-1} (2.6 ppm), respectively. When the concentrations of 3,4-DCA and 3,5-DCA are in the low range, the fluorescence quenching mechanism is mainly based on the internal filter effect (IFE). But when the concentrations continue to increase, the quenching mechanisms are transformed into dynamic and static quenching [54].

Qu et al. selected an appropriate semirigid polycarboxylate, 2,5-bis(3′,5′-dicarboxylphenyl)benzoic acid (H_5bdba) to synthesize an anionic framework, $\{[NH_2(CH_3)_2]_2 \cdot [Cd_{3.5}(bdba)(Hbdba)(H_2O)_{1.5}]\}_n$ (Cd-MOF) with accessible uncoordinated −COOH groups on Hbdba pointing toward the rhombus channels. In addition, Tb(III)-functionalized hybrids Tb(III)@Cd-MOF were initially prepared by coordinated PSM to incorporate luminescent Tb(III) ions into the structure and this was further developed as a highly sensitive and selective luminescent probe for detection of the biomarker diphenyl phosphate (DPP) based on multiquenching effects [55]. The results exhibited that the

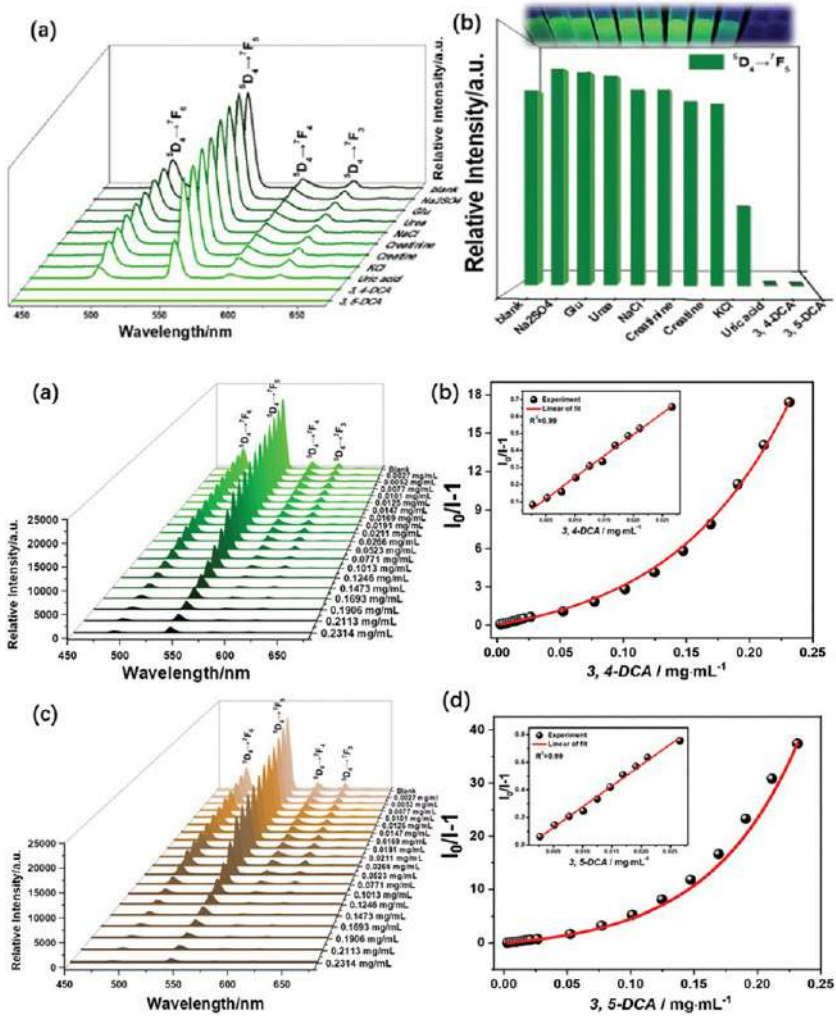

FIG. 11.17 *(Top)* The (A) emission spectra and (B) emission intensities at 545 nm of Tb(III)@Cd-MOF suspensions containing various urine chemicals: Inset, the photographs of Tb(III)@Cd-MOF suspensions under a 365-nm UV light. *(Bottom)* The emission spectra of Tb(III)@Cd-MOF dispersed in DMF with different concentrations of 3,4-DCA (A) and 3,5-DCA (C). S-V curve of $I_0/I-1$ versus concentration of 3,4-DCA (B) and 3,5-DCA (D). *(Reproduced with permission from X. Qu, B. Yan, Zn(II)/Cd(II)-based metal-organic frameworks: crystal structures, Ln(III)-functionalized luminescence and chemical sensing of dichloroaniline as pesticide biomarker. J. Mater. Chem. C 8 (2020) 9427–9439. Copyright 2020 Royal Chemical Society.)*

emission spectra and intensities related to Tb^{3+}@Cd-MOF/methanol suspensions in the presence of DPP contrasted sharply with those of other urine chemicals (Fig. 11.18; top). Under irradiation of a UV device, DPP can exclusively lead to an obvious color difference from bright-green to colorless, which can be readily caught by the naked eye (Fig. 11.18; top, inset). To examine the capacity

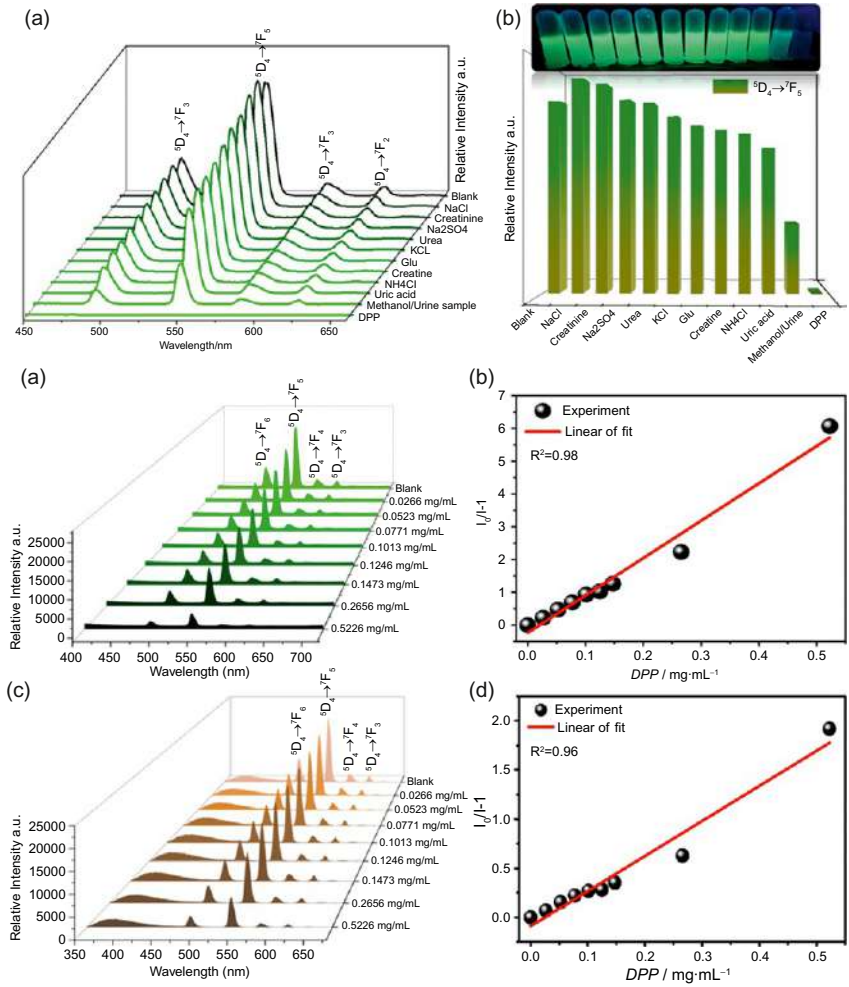

FIG. 11.18 *(Top)* (A) Emission spectra and (B) emission intensities related to the $^5D_4 \rightarrow {}^7F_5$ transition of Tb^{3+}@Cd-MOF/methanol suspensions treated by different urine chemicals. Inset: Corresponding photographs of different suspensions under 365-nm UV light. *(Bottom)* (A) Emission spectra of Tb^{3+}@Cd-MOF/methanol suspensions with different concentrations of DPP and (B) S-V curve of $I_0/I - 1$ versus content of DPP. (C) Emission spectra of Tb(III)@Cd-MOF scattered in methanol-reconstituted urine samples with different concentrations of DPP and (D) S-V curve of $I_0/I - 1$ versus content of DPP. *(Reproduced with permission from X. Qu, B. Yan, A cd-based MOF containing uncoordinated carbonyl groups as lanthanide post-synthetic modification sites and chemical sensing of diphenyl phosphate as flame retardant biomarker. Inorg. Chem. 59 (2020) 15088–15100. Copyright 2020 American Chemical Society.)*

of Tb^{3+}@Cd-MOF to detect trace amounts of DPP, luminescence titration experiments were implemented through the drop-by-drop addition of DPP to the Tb^{3+}@Cd-MOF/methanol suspension. As shown in Fig. 11.18A (bottom), a gradual depression in the characteristic emissions of Tb^{3+}@Cd-MOF/

methanol suspensions was observed as the concentrations of DPP increased from 0 to 0.5226 mg mL^{-1}. Within the whole range of concentrations, the corresponding curve fit exhibited a good linear correlation ($R^2 = 0.98$) when the content of DPP increased gradually (Fig. 11.18B; bottom). The Ksv values for Tb^{3+}@Cd-MOF toward DPP and the LOD can be calculated as 11.61 mL mg^{-1} and 0.022 mg mL^{-1} according to the equation 3Sb/k, 86, which shows that Tb^{3+}@Cd-MOF has good sensitivity to DPP molecules in methanol for the realization of quantifiable sensing. In addition, dynamic quenching occurs based on the collision effect between the excited-stated host and the guest quencher, while static quenching arises upon generation of nonemissive intermediates. In addition, the static quenching effect usually originates from the strong interaction between the luminophor and quenching analyte, which is responsible for the direct change of the excitation energy. These demonstrate that more than one quenching mechanism is at work in the DPP sensing process [55].

References

[1] Y.Y. Broza, X. Zhou, M. Yuan, D. Qu, Y. Zheng, R. Vishinkin, M. Khatib, W. Wu, H. Haick, Disease detection with molecular biomarkers: from chemistry of body fluids to nature-inspired chemical sensors, Chem. Rev. 119 (2019) 11761–11817.

[2] R. Huss, Chapter 19—Biomarkers, in: Translational Regenerative Medicine, 2015, pp. 235–241.

[3] K. Strimbu, J.A. Tavel, What are biomarkers? Curr. Opin. HIV AIDS 5 (2010) 463–466.

[4] A. Mishra, M. Verma, Cancer biomarkers: are we ready for the prime time? Cancer 2 (2010) 190–208.

[5] J. Rhea, R.J. Molinaro, Cancer biomarkers: surviving the journey from bench to bedside, Med. Lab. Obs. 43 (2011) 10–12.

[6] K. W., Biomarkers—predictive, surrogate parameters—a concept definition, in: G. Schmitz, S. Endres, D. Götte (Eds.), Biomarker, Schattauer, Germany, 2008.

[7] M. Swierczewska, G. Liu, S. Lee, X. Chen, High-sensitivity nanosensors for biomarker detection, Chem. Soc. Rev. 41 (2012) 2641–2655.

[8] L. Wu, X. Qu, Cancer biomarker detection: recent achievements and challenges, Chem. Soc. Rev. 44 (2015) 2963–2997.

[9] X. He, X. Hu, T.D. James, J. Yoon, H. Tian, Multiplexed photoluminescent sensors: towards improved disease diagnostics, Chem. Soc. Rev. 46 (2017) 6687–6696.

[10] R. Gui, H. Jin, X. Bu, Y. Fu, Z. Wang, Q. Liu, Recent advances in dual-emission ratiometric fluorescence probes for chemo/biosensing and bioimaging of biomarkers, Coord. Chem. Rev. 383 (2019) 82–103.

[11] H. Tan, C. Ma, L. Chen, F. Xu, S. Chen, L. Wang, Nanoscaled lanthanide/nucleotide coordination polymer for detection of an anthrax biomarker, Sens. Actuators B 190 (2014) 621–626.

[12] N. Bhardwaj, S. Bhardwaj, J. Mehta, K. Kim, A. Deep, Highly sensitive detection of dipicolinic acid with a water-dispersible terbium-metal organic framework, Biosens. Bioelectron. 86 (2016) 799–804.

[13] N. Gao, Y. Zhang, P. Huang, Z. Xiang, F. Wu, L. Mao, Perturbing tandem energy transfer in luminescent heterobinuclear lanthanide coordination polymer nanoparticles enables real-time

monitoring of release of the anthrax biomarker from bacterial spores, Anal. Chem. 90 (2018) 7004–7011.
[14] D. Zhang, Y. Zhou, J. Cuan, N. Gan, A lanthanide functionalized MOF hybrid for ratiometric luminescence detection of an anthrax biomarker, CrstEngComm 20 (2018) 1264–1270.
[15] L. Chen, Z. Fang, Modifying luminescent metal-organic frameworks with rhodamine dye: aiming at the optical sensing of anthrax biomarker dipicolinic acid, Inorg. Chim. Acta 477 (2018) 51–58.
[16] K. Shi, Z. Yang, L. Dong, B. Yu, Dual channel detection for anthrax biomarker dipicolinic acid: the combination of an emission turn on probe and luminescent metal-organic frameworks, Sens. Actuators B 266 (2018) 263–269.
[17] Y. Zhang, B. Li, H. Ma, L. Zhang, Y. Zheng, Rapid and facile ratiometric detection of an anthrax biomarker by regulating energy transfer process in bio-metal-organic framework, Biosens. Bioelectron. 85 (2016) 287–293.
[18] D. Wu, Z. Zhang, X. Chen, L. Meng, C. Li, G. Li, X. Chen, Z. Shi, S. Feng, A non-luminescent Eu-MOF-based "turn-on" sensor towards an anthrax biomarker through single-crystal to single-crystal phase transition, Chem. Commun. 55 (2019) 14918–14921.
[19] K. Cai, M. Zeng, F. Liu, N. Liu, Z. Huang, Y. Song, L. Wang, BSA-AuNPs@Tb-AMP metal-organic frameworks for ratiometric fluorescence detection of DPA and Hg^{2+}, Luminescence 32 (2017) 1277–1282.
[20] J. Li, Y. Wu, C. Yang, R. Zhu, K. Zhao, For the optical detection of anthrax biomarker using a luminescent rare earth-organic framework modified by rhodamine molecules: synthesis, characterization and two sensing channels, Spectrochim. Acta A Mol. Biomol. Spectrosc. 203 (2018) 397–403.
[21] K. Xing, R. Fan, S. Gai, X. Zheng, P. Wang, Y. Yang, Europium-functionalized flexible luminescent zeolite-like supramolecular assembly for ratiometric anthrax biomarker determination, ACS Appl. Mater. Interfaces 11 (2019) 36081–36089.
[22] K. Yi, X. Zhang, L. Zhang, Eu^{3+}@metal-organic frameworks encapsulating carbon dots as ratiometric fluorescent probes for rapid recognition of anthrax spore biomarker, Sci. Total Environ. 743 (2020), 140692.
[23] C. Sun, L. Zhang, J. Wang, Z. Chen, F. Dai, Sensitive and selective urinary 1-hydroxypyrene detection by dinuclear terbium-sulfonylcalixarene complex, Dalton Trans. 47 (2018) 8301–8306.
[24] Y. Zhou, Q. Yang, J. Cuan, Y. Wang, N. Gan, Y. Cao, T. Li, A pyrene-involved luminescent MOF for monitoring 1-hydroxypyrene, a biomarker for human intoxication of PAH carcinogens, Analyst 143 (2018) 3628–3634.
[25] X. Zhang, L. Fang, K. Jiang, H. He, Y. Yang, Y. Cui, B. Li, G. Qian, Nanoscale fluorescent metal-organic framework composites as a logic platform for potential diagnosis of asthma, Biosens. Bioelectron. 130 (2019) 65–72.
[26] S. Zhang, W. Shi, P. Cheng, M.J. Zaworotko, A mixed-crystal lanthanide zeolite-like metal-organic framework as a fluorescent indicator for lysophosphatidic acid, a cancer biomarker, J. Am. Chem. Soc. 137 (2015) 12203–12206.
[27] S. Wu, Y. Lin, J. Liu, W. Shi, G. Yang, P. Cheng, Rapid detection of the biomarkers for carcinoid tumors by a water stable luminescent lanthanide metal-organic framework sensor, Adv. Funct. Mater. 28 (2018) 1707169.
[28] T. Zhao, Z. Peng, D. Yuan, S. Zhen, C. Huang, Y. Li, Metal-organic gel enhanced fluorescence anisotropy for sensitive detection of prostate specific antigen, Spectrochim. Acta A 192 (2018) 328–332.

[29] Y. Du, X. Li, X. Lv, Q. Jia, Highly sensitive and selective sensing of free bilirubin using metal-organic frameworks-based energy transfer process, ACS Appl. Mater. Interfaces 9 (2017) 30925–30932.
[30] S. Wu, M. Zhu, Y. Zhang, M. Kosinova, V.P. Fedin, E. Gao, Luminescent sensors based on coordination polymers with adjustable emissions for detecting biomarker of pollutant ethylbenzene and styrene, Appl. Organomet. Chem. 35 (2021), e6058.
[31] X. Qu, B. Yan, A highly stable Tb(III)-based metal-organic framework: structure, photoluminescence and chemical sensing of 2-thiazolidinethione-4-carboxylic acid as a biomarker of CS_2, Inorg. Chem. 58 (2019) 524–534.
[32] H. Yang, P. Xu, B. Ding, X. Wang, Z. Liu, H. Zhao, X. Zhao, E. Yang, Isostructural lanthanide coordination polymers with high photoluminescent quantum yields by effective ligand combination: crystal structures, photophysical characterizations, biologically relevant molecular sensing, and anti-counterfeiting ink application, Cryst. Growth Des. 20 (2020) 7615–7625.
[33] J. Hao, B. Yan, Recyclable lanthanide-functionalized MOF hybrids to determine hippuric acid in urine as biological indices of toluene exposure, Chem. Commun. 51 (2015) 14509–14512.
[34] S. Qin, J. Hao, X. Xu, X. Lian, B. Yan, Highly sensing probe for biological metabolite of benzene series pollutants based on recyclable Eu^{3+} functionalized metal-organic frameworks hybrids, Sens. Actuators B 253 (2017) 852–859.
[35] J. Hao, B. Yan, Simultaneous determination of indoor ammonia pollution and its biological metabolite in human body by use of a recyclable nanocrystalline lanthanide functionalized MOF, Nanoscale 8 (2016) 2881–2886.
[36] X. Lian, B. Yan, Phosphonate MOFs composite as off-on fluorescent sensor for detecting purine metabolite uric acid and diagnose hyperuricuria, Inorg. Chem. 56 (2017) 6802–6808.
[37] J. Hao, B. Yan, Determination of urinary 1-hydroxypyrene for biomonitoring of human exposure to polycyclic aromatic hydrocarbons carcinogens by a lanthanide-functionalized metal-organic framework sensor, Adv. Funct. Mater. 27 (2017) 1603856.
[38] R. He, Y. Wang, H. Ma, S. Yin, Q. Liu, Eu^{3+}-functionalized metal-organic framework composite as ratiometric fluorescent sensor for highly selective detecting urinary 1-hydroxypyrene, Dyes Pigm. 151 (2018) 342–347.
[39] J. Hao, X. Xu, X. Lian, C. Zhang, B. Yan, A luminescent 3d-4f-4d MOF nanoprobe as a diagnosis platform for human occupational exposure to vinyl chloride carcinogen, Inorg. Chem. 56 (2017) 11176–11183.
[40] X. Lian, T. Miao, X. Xu, C. Zhang, B. Yan, Eu^{3+} functionalized Sc-MOFs: turn-on fluorescent switch for ppb-level biomarker of plastic pollutant polystyrene in serum and urine and on-site detection by smartphone, Biosens. Bioelectron. 97 (2017) 299–304.
[41] X. Qu, B. Yan, Ln(III)-functionalized metal-organic frameworks hybrid system: luminescence properties and sensor for trans, trans-muconic acid as a biomarker of benzene, Inorg. Chem. 57 (2018) 7815–7824.
[42] S. Qin, B. Yan, A facile indicator box based on Eu^{3+} functionalized MOF hybrid for the determination of 1-naphthol, a biomarker for carbaryl in urine, Sens. Actuators B 259 (2018) 125–132.
[43] N. Sun, B. Yan, Fuorescence detection of urinary N-methylformamide for biomonitoring of human occupational exposure to N,N-dimethylformamide by Eu(III) functionalized MOFs, Sens. Actuators B 261 (2018) 153–160.
[44] S. Qin, B. Yan, The point-of-care colorimetric detection of the biomarker of phenylamine in the human urine with smartphone based on Tb^{3+} functionalized metal-organic framework, Anal. Chim. Acta 1012 (2018) 82–89.

[45] S. Qin, B. Yan, Dual-emissive ratiometric fluorescent probe based on Eu^{3+}/C-dots@MOF hybrids for the biomarker diaminotoluene sensing, Sens. Actuators B 272 (2018) 510–517.
[46] X. Xu, B. Yan, Fluorescent wearable platform for sweat cl^{-} analysis and logic smart-device fabrication based on color adjustable lanthanide MOFs, J. Mater. Chem. C 6 (2018) 1863–1869.
[47] N. Sun, B. Yan, A fluorescence probe based on Tb^{3+}/Cu^{2+} co-functionalized MOFs to urinary sarcosine detection, Analyst 143 (2018) 2349–2355.
[48] S. Qin, B. Yan, An AND logic gate-based fluorescence probe for the detection of homovanillic acid, an indicator of the tumor, JOL 211 (2019) 431–436.
[49] B. Wang, B. Yan, A dual-emitting dye@MOF crystalline probe serving as a platform for ratiometric sensing the biomarker of trichloroethylene (TCE) carcinogen in the human urine, CrstEngComm 21 (2019) 4637–4643.
[50] Y. Jin, B. Yan, A bi-functionalized metal-organic framework based on N-methylation and Eu^{3+} post-synthetic modification for highly sensitive detection of 4-aminophenol (4-AP), a biomarker for aniline in urine, Talanta 227 (2021), 122209.
[51] J. Min, X. Qu, B. Yan, Covalent-coordination tandem functionalization of metal-organic framework (UiO-66) as a hybrid probe for luminescence detection of trans, trans-muconic acid as a biomarker of benzene and Fe^{3+}, Analyst 146 (2021) 3052–3061.
[52] B. Yan, Photofunctional MOFs based hybrid materials for chemical sensing application on biomarkers, J. Mater. Chem. 7 (2019) 8155–8175.
[53] X. Wang, X. Mao, Z. Zhang, R. Guo, Y. Zhang, N. Zhu, K. Wang, P. Sun, J. Huo, X. Wang, B. Ding, Solvothermal and ultrasonic preparation of two unique cluster-based coordination materials: metal – organic framework-based ratiometric fluorescent biosensor for an ornidazole and ronidazole and sensing platform for a biomarker of amoeba liver abscess, Inorg. Chem. 59 (2020) 2910–2922.
[54] X. Qu, B. Yan, Zn(II)/Cd(II)-based metal-organic frameworks: crystal structures, Ln(III)-functionalized luminescence and chemical sensing of dichloroaniline as pesticide biomarker, J. Mater. Chem. C 8 (2020) 9427–9439.
[55] X. Qu, B. Yan, A cd-based MOF containing uncoordinated carbonyl groups as lanthanide post-synthetic modification sites and chemical sensing of diphenyl phosphate as flame retardant biomarker, Inorg. Chem. 59 (2020) 15088–15100.

Part V

Rare earth metal-organic frameworks hybrid materials as luminescence response chemical sensors for others and applications

Chapter 12

Rare earth metal-organic framework hybrid materials for luminescence responsive chemical sensing of temperature and pH value

12.1 Rare earth metal-organic framework hybrid materials for luminescence sensing of temperature

Temperature is a fundamental physical parameter whose measurement is crucial in both scientific investigations and technological developments [1]. The luminescence thermometry method exploits the relationship between temperature and luminescence behaviors to realize temperature sensing and mapping from the spectral and spatial analysis of the luminescence generated from the object [2]. Temperature-dependent luminescent behaviors include the variation of spectral positions and shape, the changes in luminescence intensity or decay lifetime, and the changes in anisotropy. Based on these variable parameters, luminescence thermometry is commonly classified into intensity-based, lifetime-based, wavelength-based, and ratiometric methods [1,3]. **(1) Intensity-based luminescence thermometry.** Temperature sensing is achieved through the analysis of luminescence intensity. Temperature-induced changes in the luminescence intensity are generally caused by the thermal activation of nonradiative deactivation pathways [3–6]. Changes in luminescence intensity caused by temperature are easy to detect, but the process is often susceptible to errors due to changes in probe concentration, excitation power, or detection efficiency. Indeed, even if all the experimental conditions, such as concentration of luminescence centers, excitation wavelength, and light source power, are kept constant during the measurements, the absorption and scatter cross-section may vary from sample to sample. These drawbacks reduce the accuracy and thus make this method inappropriate for precise temperature sensing. **(2) Lifetime-based luminescence thermometry.** This method is based on the temperature dependence of the lifetime [3,4,7]. Unlike the luminescence intensity, the lifetime value is independent of the concentration, size, or

Rare Earth Metal-Organic Framework Hybrid Materials for Luminescence Responsive Chemical Sensors
https://doi.org/10.1016/B978-0-323-91236-5.00010-4

geometry of probes. Additionally, it is not affected by light scattering, reflection, or the intensity fluctuation of the excitation source. However, lifetime determination requires a more sophisticated read-out and a time-consuming computational treatment. Moreover, this method is less available for large-area gradient temperature sensing and cannot be used to realize dynamic measurements in which temperature variations occur at time intervals shorter than or equal to the lifetime of the luminescence. **(3) Wavelength-based luminescence thermometry.** The wavelength or frequency shift of luminescence spectra can be correlated with the temperature values [3,4]. Although this method may be sufficiently sensitive for practical temperature detection, its broad emission band introduces some difficulties in accurately identifying the maximum luminescence wavelength. **(4) Ratiometric luminescence thermometry.** This method exploits the intensity ratio of two independent transitions from the same materials whose luminescence spectra consist of several bands to detect temperature [1,3–6]. In ratiometric thermometry, the temperature sensing is independent of the concentration and inhomogeneity of luminescent centers as well as the optoelectronic drifts of excitation source and detectors, and thus overcomes the main drawbacks of intensity-based measurements of only one transition [8]. This self-referenced thermometry method can guarantee a precise and absolute temperature measurement without the need for calibration. Therefore ratiometric luminescence thermometry is a preferred method for temperature sensing.

Thermographic phosphor thermometry is a noninvasive spectroscopic technique for temperature measurement based on phosphor emission temperature dependence. In the last decade, many RE^{3+} -based thermometers have been reported, covering a wide temperature range, from cryogenic ($T < 100$ K) to physiological (298–323 K) values. Among MOF-based materials and their multifunctional heater-thermometer nanoplatforms are employed. The mixed rare earth (RE, RE′) approach is generally based on the dual-emission of Tb^{3+} and Eu^{3+} within MOFs to construct ratiometric thermometers. Such materials involve three energy transfer processes: Tb^{3+} -to-Eu^{3+}, ligand-to-Eu^{3+}, and ligand-to-Tb^{3+}, and display the characteristic transition emission of Eu^{3+} and Tb^{3+} ions. Although most research on this MOF-based hybrid thermometry is based on the Tb^{3+}/Eu^{3+} emission ratio, a few papers explore the emission of an organic chromophore (usually involving an excited triplet state) and RE^{3+}. The implementation of these rare-earth MOF hybrid materials as ratiometric thermometers in diverse applications has been extensively revised in the past decade [9–38].

Cui et al. realized a luminescent mixed rare earth MOF approach to explore luminescent thermometers, whose targeted self-referencing luminescent thermometer $Eu_{0.0069}Tb_{0.9931}$-DMBDC (DMBDC = 2,5-dimethoxy-1,4-benzenedicarboxylate) based on two emissions of Tb^{3+} at 545 nm and Eu^{3+} at 613 nm with high sensitivity at a wide range from 10 to 300 K. The temperature dependence of the emission spectra of Tb-DMBDC, Eu-DMBDC, and $Eu_{0.0069}Tb_{0.9931}$-DMBDC from 10 to 300 K is illustrated in Fig. 12.1A–C

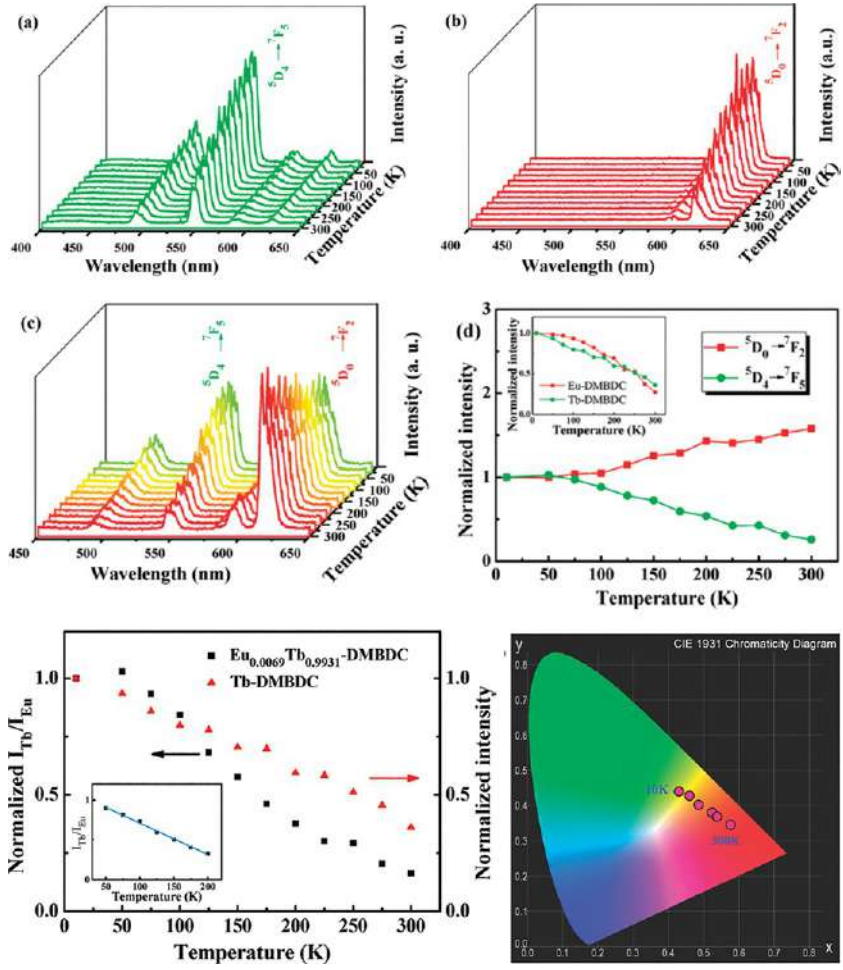

FIG. 12.1 *(Top)* Emission spectra of (A) Tb-DMBDC, (B) Eu-DMBDC, (C) $Eu_{0.0069}Tb_{0.9931}$-DMBDC recorded between 10 and 300 K (excited at 355 nm from the third harmonic of a Nd: YAG laser), and (D) temperature dependence of integrated intensities of the $^5D_4 \rightarrow {}^7F_5$ (534–562 nm) and $^5D_0 \rightarrow {}^7F_2$ (605–633 nm) transitions for $Eu_{0.0069}Tb_{0.9931}$-DMBDC. (Inset) Temperature-dependent integrated intensity of the $^5D_4 \rightarrow {}^7F_5$ transition of Tb-DMBDC and $^5D_0 \rightarrow {}^7F_2$ transition of Eu-DMBDCF. *(Bottom, Left)* Temperature dependence of the integrated intensity ratio of Tb^{3+} (545 nm) to Eu^{3+} (613 nm) for $Eu_{0.0069}Tb_{0.9931}$-DMBDC (*black squares*), and temperature dependence of integrated intensity of Tb^{3+} (545 nm) for Tb-DMBDC (*red triangles*). (Inset) Fitted curves of the integrated intensity ratio for $Eu_{0.0069}Tb_{0.9931}$-DMBDC from 50 to 200 K. *(Bottom, Right)* CIE chromaticity diagram showing the luminescence color of $Eu_{0.0069}Tb_{0.9931}$-DMBDC at different temperatures. *(Reproduced with permission from Y. Cui, H. Xu, Y. Yue, Z. Guo, J. Yu, Z. Chen, J. Gao, Y. Yang, G. Qian, B. Chen, A luminescent mixed-lanthanide metal-organic framework thermometer. J. Am. Chem. Soc. 134 (2012) 3979–3982. Copyright 2012 American Chemical Society.)*

(top), and the integrated intensities of the $^5D_4 \rightarrow {}^7F_5$ (Tb^{3+}, 545 nm) and $^5D_0 \rightarrow {}^7F_2$ (Eu^{3+}, 613 nm) transitions are shown in Fig. 12.1D (top). The luminescent intensity of both Tb^{3+} and Eu^{3+} in Tb-DMBDC and Eu-DMBDC decreased gradually as the temperature increased, which is normal due to the thermal activation of nonradiative-decay pathways. The emission intensity of the Tb^{3+} ions in $Eu_{0.0069}Tb_{0.9931}$-DMBDC decreased, while that of the Eu^{3+} increased with the temperature. Such temperature-dependent emission spectra are repeatable and reversible. As shown in Fig. 12.1 (bottom, left), the temperature can be readily correlated to the emission intensity ratio of the $^5D_4 \rightarrow {}^7F_5$ (Tb^{3+}, 545 nm) to $^5D_0 \rightarrow {}^7F_2$ (Eu^{3+}, 613 nm) transition (I_{Tb}/I_{Eu}), which does not require any additional calibration of luminescence intensity. The fact that the temperature can be linearly related to I_{Tb}/I_{Eu} indicates that $Eu_{0.0069}Tb_{0.9931}$-DMBDC is an excellent luminescent thermometer at this temperature range (Fig. 12.1; bottom, left, inset). Because Tb^{3+} and Eu^{3+} within $Eu_{0.0069}Tb_{0.9931}$-DMBDC emit different colors of green at 545 nm and red at 613 nm, respectively, direct visualization of the temperature change, instantly and straightforwardly, is possible. As shown in Fig. 12.1 (bottom, right), the temperature-dependent luminescence colors of $Eu_{0.0069}Tb_{0.9931}$-DMBDC are systematically tuned from the green-yellow to red from 10 to 300 K, which can be clearly and directly observed even by the naked eye or a camera. This phenomenon is attributed to the temperature-dependent energy transfer probability from the Tb^{3+} to Eu^{3+} ions controlled by the phonon-assisted Förster transfer mechanism [9].

Zhou et al. developed a MIL-type MOF, In(OH)(bpydc) (bpydc = 2,2′-bipyridine-5,5′-dicarboxylic acid) for fabricating highly sensitive ratiometric luminescent nanothermometers through straightforward PSM strategy, which highlights the ability of a broad range of nanosized MOFs to construct nanothermometers. The temperature-dependent luminescent behavior of Eu^{3+} and Tb^{3+} in the Eu^{3+}/Tb^{3+}@In-MOF was significantly different from those in the single Eu^{3+}@In-MOF and Tb^{3+}@In-MOF (Fig. 12.2A; left). When the temperature increased from 10°C to 60°C, the Tb^{3+} emission exhibited a much greater decrease of 60%, as compared to 33% for Tb^{3+}@In-MOF (Fig. 12.2B; left). Simultaneously, the Eu^{3+} emission in Eu^{3+}/Tb^{3+}@In-MOF was enhanced, which is contrary to that in Eu^{3+}@In-MOF. The ratiometric and thermometric parameters of Eu^{3+}/Tb^{3+}@In-MOF can be defined as the intensity ratio of $^5D_4 \rightarrow {}^7F_5$ (Tb^{3+}, 545 nm) and $^5D_0 \rightarrow {}^7F_2$ (Eu^{3+}, 613 nm) transitions (I_{Tb}/I_{Eu}). Fig. 12.2C (left) plots the dependence of I_{Tb}/I_{Eu} on temperature, which reveals a good linear relationship between it and temperature within the range of 10 to 60°C with a correlation coefficient (R^2) of 0.9961. The precision of this thermal probe is ±0.48°C, a value limited by the error (0.024) of I_{Tb}/I_{Eu} determined from the data in Fig. 12.2C (left). The temperature-dependent emission spectra of Eu^{3+}/Tb^{3+}@In-MOF excited at 488 nm of the $^7F_6 \rightarrow {}^5D_4$ transition of Tb^{3+} displayed a gradually enhanced Eu^{3+} emission, confirming that the Tb^{3+} to Eu^{3+} energy transfer occurred and was enhanced with the increase in temperature

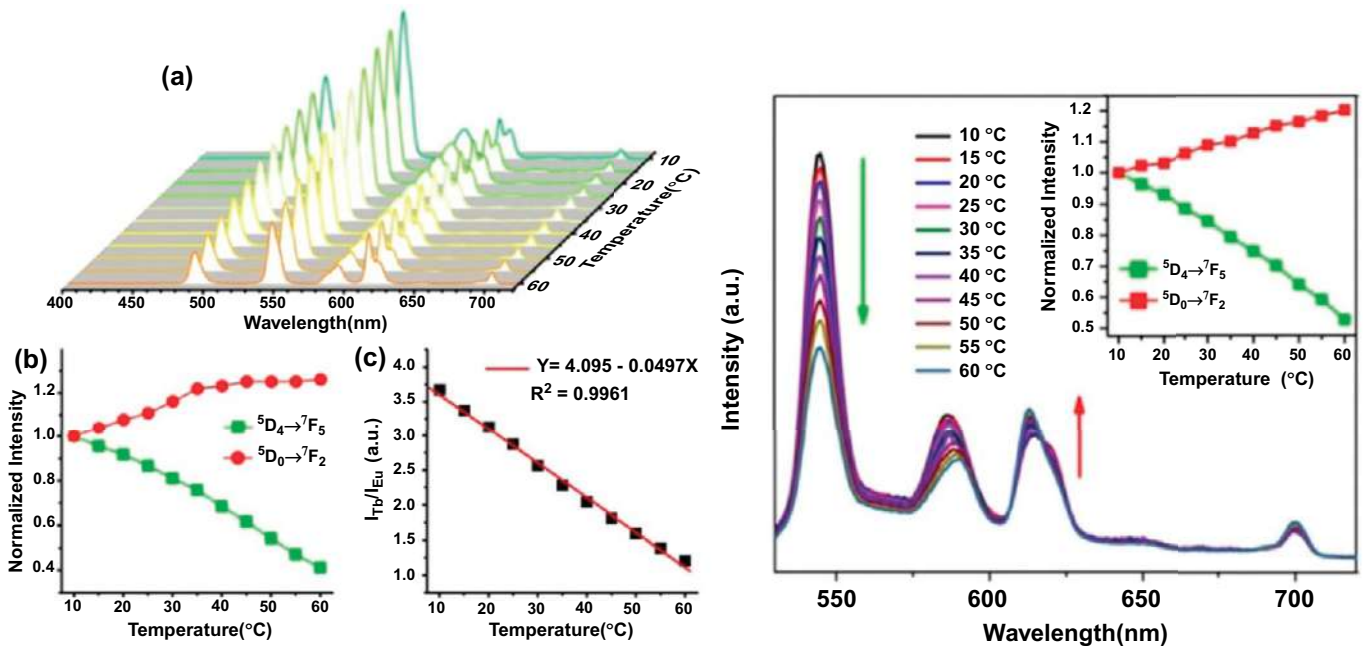

FIG. 12.2 *(Left)* Eu^{3+}/Tb^{3+}@In-MOF nanocrystals show sensitive spectral changes in response to temperature: (A) emission spectra ($\lambda_{ex} = 312$ nm) recorded in the temperature range of 10∼60°C; (B) temperature-dependent intensity of $^5D_4 \rightarrow {}^7F_5$ and $^5D_0 \rightarrow {}^7F_2$ transitions; and (C) the dependence of I_{Tb}/I_{Eu} on temperature. The red line plotted in (C) is the linear fitted curve. *(Right)* Emission spectra ($\lambda_{ex} = 487$ nm) of Eu^{3+}/Tb^{3+}@In-MOF recorded between 10 and 60°C. The inset is the temperature-dependent normalized intensity of Eu^{3+} ($^5D_0 \rightarrow {}^7F_2$) and Tb^{3+} ($^5D_4 \rightarrow {}^7F_5$). *(Reproduced with permission from Y. Zhou, B. Yan, F. Lei, Postsynthetic lanthanide functionalization of nanosized metal–organic frameworks for highly sensitive ratiometric luminescent thermometry. Chem. Commun. 50 (2014) 15235–15238. Copyright 2014 Royal Chemical Society.)*

(Fig. 12.2; right). The thermal activation of nonradiative relaxation included the energy transfer from Tb^{3+} to Eu^{3+} and energy back transfer (B_{EnT}) from the emitting level of Tb^{3+} to the excited triplet state of the H_2bpydc ligand. Another indication provided by Fig. 12.2 (right) is that Eu^{3+}/Tb^{3+}@In-MOF can also be developed as ratiometric optical thermometers when the excitation wavelength is fixed at 487 nm. Nevertheless, the 487-nm excitation is much less cytotoxic than 320 nm, and thus it is preferred in biotechnology [13].

Zhao et al. synthesized a series of RE-MOFs: $\{[RE(L)_2(COO)(H_2O)_2 \cdot H_2O\}_n$ (RE = Eu, Gd, Tb, Dy, Tm, Yb, Y) and codoped RE-MOFs: $Eu_xTb_{1-x}L$ ($x = 0.1$–0.9) with 1,3-bis(4-carboxyphenyl)imidazolium (H_2L). The temperature-dependent luminescent properties of $Eu_{0.2}Tb_{0.8}L$ allows for the design of a thermometer with an excellent linear response to temperature over a wide range from 40 to 300 K. The temperature-dependent emission spectra of codoped MOF $Eu_{0.2}Tb_{0.8}L$ from 40 to 300 K are shown in Fig. 12.3A. The integrated intensities of $^5D_4 \rightarrow {}^7F_5$ (Tb^{3+}, 543 nm) and $^5D_0 \rightarrow {}^7F_2$ (Eu^{3+}, 616 nm) are portrayed in Fig. 12.3B. The codoped MOF $Eu_{0.2}Tb_{0.8}L$ exhibited

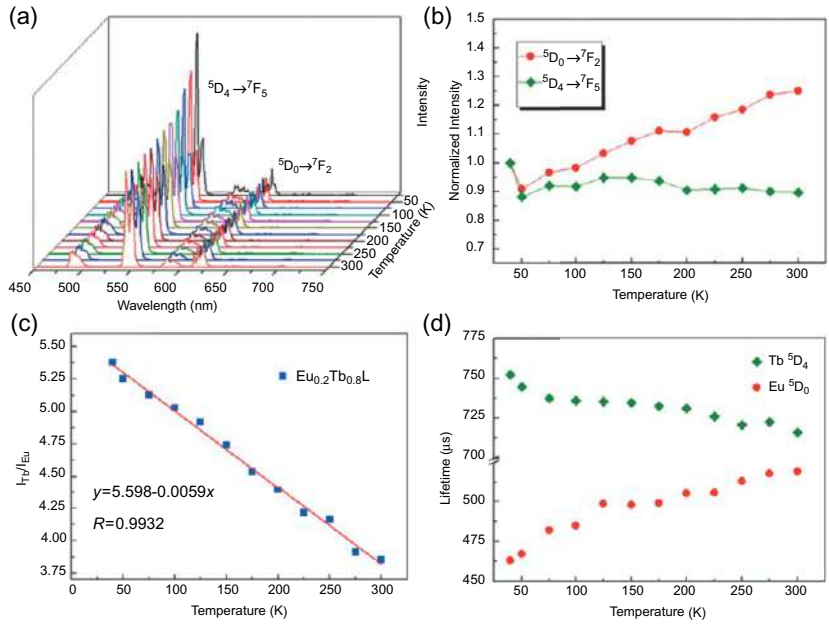

FIG. 12.3 (A) Emission spectra of $Eu_{0.2}Tb_{0.8}L$ recorded between 40 and 300 K (excited at 322 nm); (B) temperature-dependent intensity of the $^5D_4 \rightarrow {}^7F_5$ and $^5D_0 \rightarrow {}^7F_2$ transition for $Eu_{0.2}Tb_{0.8}L$; (C) temperature-dependent intensity ratio of Tb^{3+} (543 nm) to Eu^{3+} (615 nm); (D) temperature dependence of the $^5D_4$ lifetime for TbL and $^5D_0$ lifetime for EuL. Decay curves are monitored at 543 and 615 nm, respectively, and excited at 322 nm. *(Reproduced with permission from S. Zhao, L. Li, X. Song, M. Zhu, Z. Hao, X. Meng, L. Wu, J. Feng, S. Song, C. Wang, H. Zhang, Lanthanide ion codoped emitters for tailoring emission trajectory and temperature sensing. Adv. Funct. Mater. 25 (2015) 1463–1469. Copyright 2015 Wiley.)*

a significantly different temperature-dependent luminescent behavior with respect to the emissions of Tb^{3+} ions at 543 nm and Eu^{3+} ions at 615 nm. The emission intensity of the Tb^{3+} ions decreased as the temperature increased, while that of the Eu^{3+} ions iU. As depicted in Fig. 12.3C, the good linear relationship between the I_{Tb}/I_{Eu} ratio and temperature from 40 to 300 K can be fitted as a function with a correlation coefficient of 0.9932. The remarkable temperature-dependent emissions may be explained by the probability of temperature-dependent energy transfer from the Tb^{3+} to Eu^{3+} ions. The lifetime of $^5D_0$ in $Eu_{0.2}Tb_{0.8}L$ increases by approximately 13%, (Fig. 12.3D) indicating that energy transfer from the Tb^{3+} to Eu^{3+} ions does occur [16].

Yang et al. reported direct growth of mixed Tb/Eu-BTC MOF films on large quartz substrates (4 × 4 cm). Fig. 12.4A shows the emission spectra of the $Tb_{0.980}/Eu_{0.020}$-BTC film as a function of temperature under 296-nm excitation. By contrast, the emission intensity of Eu^{3+} at 617 nm was appreciably enhanced with increasing temperature from 298 to 359 K. The Tb^{3+} -to-Eu^{3+} energy transfer is controlled by a phonon-assisted Förster transfer mechanism. The emission intensity of Tb^{3+} at 549 nm displays a steady decline as the temperature increases (Fig. 12.4B). The researchers estimated the efficiency of the Tb^{3+} -to-Eu^{3+} energy transfer, and the plot of η against temperature in Fig. 12.4C confirms the enhancing of the energy transfer with increasing temperature from 298 to 373 K. The thermometric parameter Δ (the emission intensity ratio of Tb^{3+} ($^5D_4 \rightarrow {}^7F_5$) and Eu^{3+} ($^5D_0 \rightarrow {}^7F_2$)), is plotted in Fig. 12.4D. The plot of the relative sensitivity against temperature in Fig. 12.4E reveals maximum relative sensitivity of 16.14% K^{-1} at 359 K. Notably, a high relative selectivity (Sr) of 9.01% K^{-1} at 353 K was also attained over the physiological temperature range (293–353 K), which outperforms existing luminescence thermometers in this temperature range. The repeatability of the $Tb_{0.980}/Eu_{0.020}$-BTC film was also assessed by cycling the temperature between 298 and 383 K (Fig. 12.4F); the calculated value was larger than 93.25%, which indicates that the maximum experimental deviation during the thermal cycling experiment was lower than 6.75%. The variation of thermal sensitivity on the different temperature cycles can be partly attributed to the release and reabsorption of free solvent that may disturb the local structure of the luminescent RE^{3+} ions.

Zhao et al. use 6-(4-carboxyphenyl)nicotinic acid (H_2cpna) and [2,2′-bipyridine]-5,5′-dicarboxylic acid (H_2bpydc) with carboxylate and pyridine moieties as linkers to fabricate the REMOFs with Tb^{3+} and Eu^{3+} ions, $Tb_{0.95}Eu_{0.05}$cpna and $Tb_{0.95}Eu_{0.05}$bpydc, whose ratiometric parameters feature an excellent S-shaped response to temperature in the range of 25–300 K, with favorable relative sensitivities and low temperature uncertainties. As illustrated in panels a and b of Fig. 12.5 (top), both of them exhibit significantly different temperature-dependent luminescence behavior with respect to the emission peaks of Tb^{3+} at 544 nm and Eu^{3+} at 612 nm. From the emission spectrum of $Tb_{0.95}Eu_{0.05}$cpna (Fig. 12.5A; top), the peak intensity of Tb^{3+} decreased by 0.45% K^{-1} with an increase in temperature from 25 to 150 K, while the emission of Eu^{3+} was

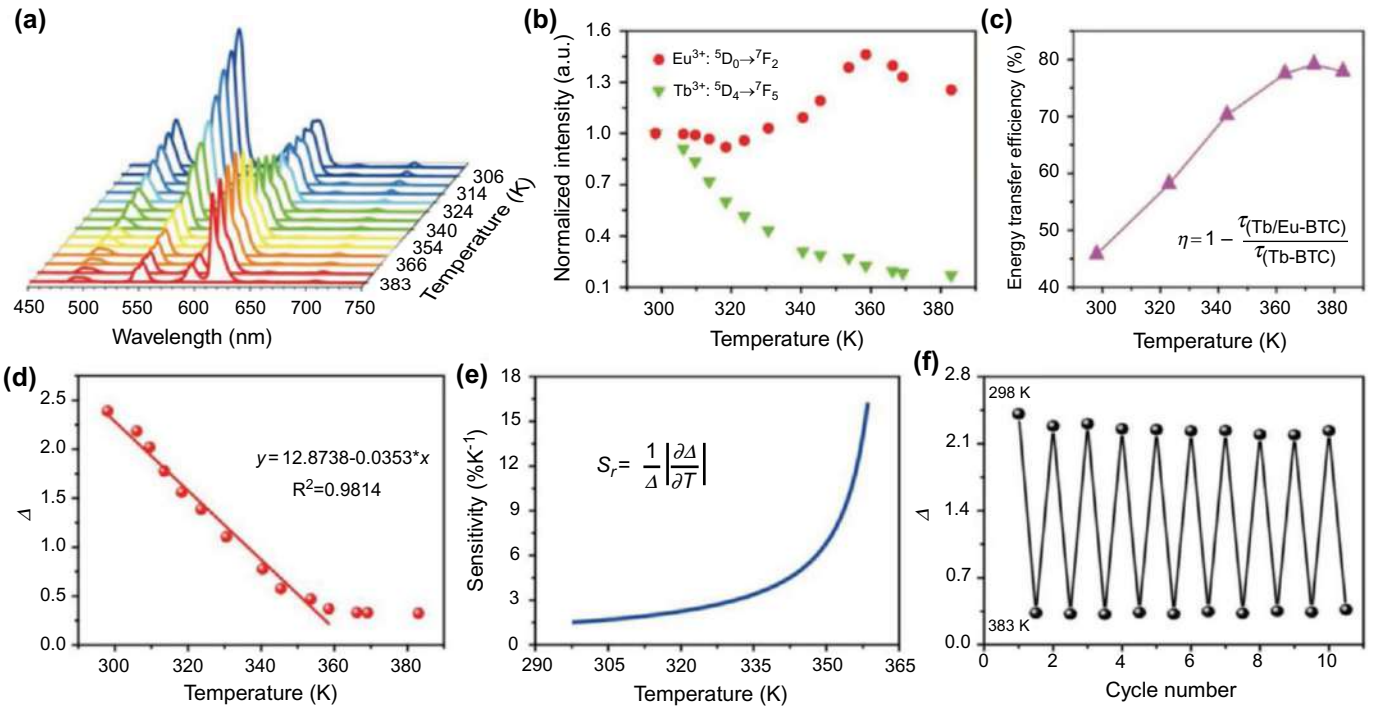

FIG. 12.4 (A) Emission spectra of the $Tb_{0.980}/Eu_{0.020}$-BTC film in temperature range of 298–383 K under excitation of 296 nm. (B) Normalized emission intensity of Tb^{3+} ($^5D_4 \rightarrow {}^7F_5$) and Eu^{3+} ($^5D_0 \rightarrow {}^7F_2$) as a function of temperature. (C) Temperature dependence of Tb^{3+}-to-Eu^{3+} energy transfer. (D) Temperature dependence of emission intensity ratio of Tb^{3+} ($^5D_4 \rightarrow {}^7F_5$) to Eu^{3+} ($^5D_0 \rightarrow {}^7F_2$). (E) Relative thermal sensitivity of the $Tb_{0.980}/Eu_{0.020}$-BTC film in the 298–359 K range. (F) Cyclic stability of the $Tb_{0.980}/Eu_{0.020}$-BTC film. *(Reproduced with permission from X. Yang, H. Zou, X. Sun, T. Sun, C. Guo, Y. Fu, C. L. Wu, X. Qiao, F. Wang, One-step synthesis of mixed lanthanide metal–organic framework films for sensitive temperature mapping. Adv. Opt. Mater. 7 (2019) 1900336. Copyright 2019 Wiley.)*

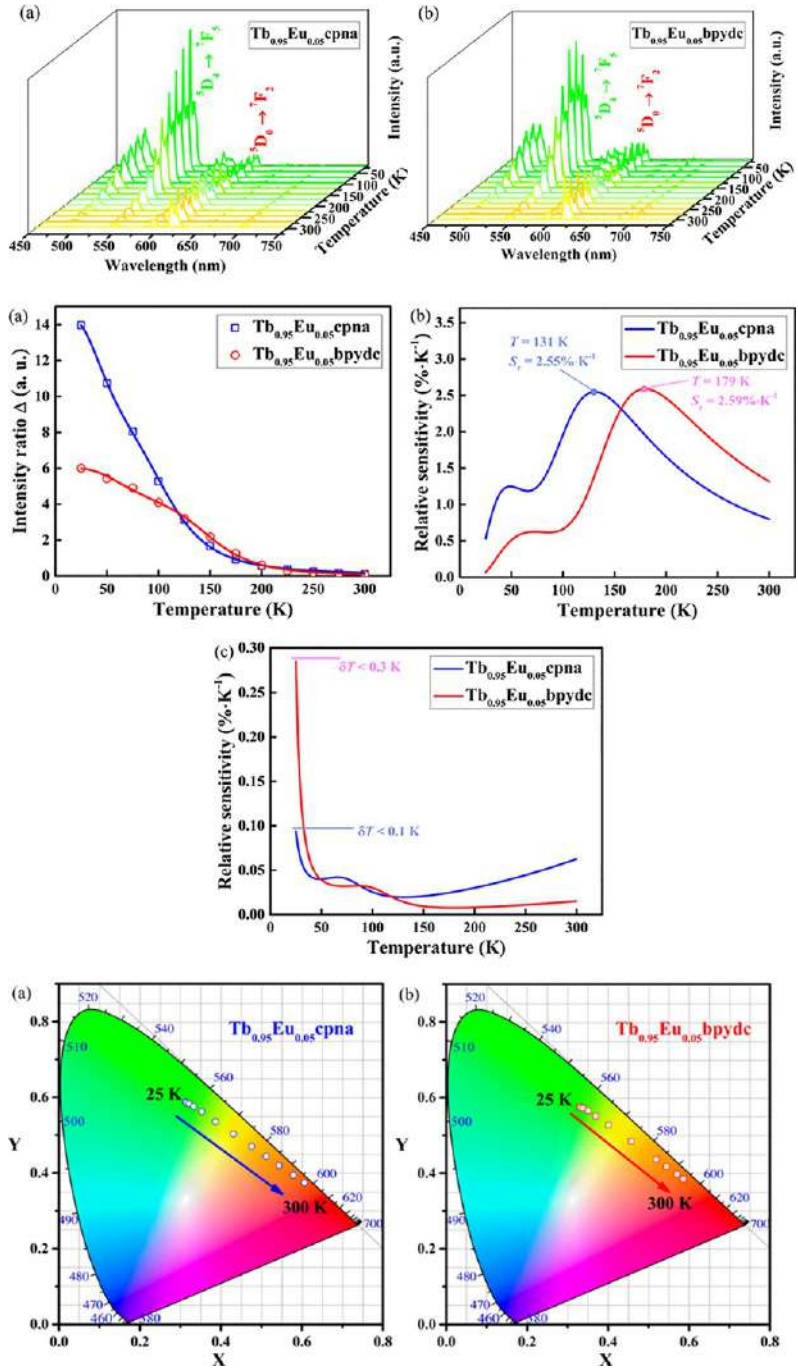

FIG. 12.5 *(Top)* Emission spectra of (A) $Tb_{0.95}Eu_{0.05}$cpna and (B) $Tb_{0.95}Eu_{0.05}$bpydc recorded between 25 and 300 K. *(Middle)* (A) *Blue* and *red* symbols depict the values of the experimental thermometric parameter Δ of $Tb_{0.95}Eu_{0.05}$cpna and $Tb_{0.95}Eu_{0.05}$cpna, respectively, and the solid lines present the best

(Continued)

significantly enhanced. Similar behavior was observed in the isostructural $Tb_{0.95}Eu_{0.05}$bpydc, but it exhibited different extents of change in the corresponding emissions (Fig. 12.5B; top). As shown in Fig. 12.5A (middle), the experimental values of the intensity ratio Δ for $Tb_{0.95}Eu_{0.05}$cpna and $Tb_{0.95}Eu_{0.05}$bpydc are well fitted, with R^2 values for the experimental data points of $Tb_{0.95}Eu_{0.05}$cpna and $Tb_{0.95}Eu_{0.05}$bpydc of 0.9997 and 0.9989, respectively. As shown in Fig. 12.5B (middle), the maximum relative sensitivity of $Tb_{0.95}Eu_{0.05}$cpna was determined to be 2.55% K^{-1} at 131 K, while that of $Tb_{0.95}Eu_{0.05}$bpydc was 2.59% K^{-1} at 179 K. The temperature uncertainty δ_T is another index for assessing the thermometer performance and the minimum temperature uncertainties of $Tb_{0.95}Eu_{0.05}$cpna and $Tb_{0.95}Eu_{0.05}$bpydc were estimated to be 0.02 K (at 131 K) and 0.01 K (at 179 K), respectively (Fig. 12.5C; middle). In addition, they are sensitive luminescent colorimetric probes; the emission color change of these two MOFs with an increase in temperature is depicted on the CIE color diagram in Fig. 12.5 (bottom). The emission colors of both the two probes changed from green (25 K) to red (300*K*) upon heating, which can be easily observed by digital cameras and the naked eye.

Yang et al. synthesized ternary codoped REMOFs, $Eu_xTb_yGd_{1-x-y}L$ (H_4L = 2,6-di(2′,4′−dicarboxyl phenyl) pyridine) and utilized them as ratiometric temperature sensors. The Gd^{3+} ion was introduced to achieve ternary mixed rare earth MOF $Eu_xTb_yGd_{1-x-y}L$ due to its biological interest, silence in f-f emissions, and relatively low price. The ternary mixed rare earth MOFs presented Gd^{3+} -to-Eu^{3+}, Gd^{3+} -to-Tb^{3+}, and Tb^{3+} -to-Eu^{3+} energy transfer, which may provide some new opportunities for designing novel ratiometric luminescent thermometers. Two ternary mixed RE-MOFs, $Eu_xTb_yGd_{1-x-y}L$ ($x = 0.013$, $y = 0.060$; $x = 0.033$, $y = 0.085$) were obtained. As shown in Fig. 12.6, both of them showed similar temperature-dependent luminescent behaviors. The two materials exhibited good linear relationships between the temperature and I_{Tb}/I_{Eu}, which could be fitted with $R^2 = 0.989$ (77–250 K) and $R^2 = 0.990$ (77–280 K), respectively. The $Eu_{0.013}Tb_{0.060}Gd_{0.927}L$ and $Eu_{0.033}Tb_{0.085}Gd_{0.882}L$ had a maximum relative sensitivity of 6.11% K^{-1} at 430 K and 3.62% K^{-1} at 400 K, respectively. This is an unprecedented case of ternary M'RE-MOF ratiometric luminescent thermometers based on energy transfer of different RE^{3+} ions. The Gd^{3+} ions here are considered to play a main

FIG. 12.5—CONT'D, fit of the experimental values. (B) Relative sensitivity of $Tb_{0.95}Eu_{0.05}$cpna and $Tb_{0.95}Eu_{0.05}$bpydc in the range of 25–300 K. (C) Corresponding temperature uncertainty of $Tb_{0.95}Eu_{0.05}$cpna and $Tb_{0.95}Eu_{0.05}$bpydc. *(Bottom)* CIE chromaticity diagram presenting the temperature-dependent color of (A) $Tb_{0.95}Eu_{0.05}$cpna and (B) $Tb_{0.95}Eu_{0.05}$bpydc changing from *green* at 25 K to *red* at 300 K. *(Reproduced with permission from D. Zhao, D. Yue, K. Jiang, L. Zhang, C. Li, G. Qian, Isostructural Tb3+/Eu3+ co-doped metal-organic framework based on pyridine-containing dicarboxylate ligands for ratiometric luminescence temperature sensing. Inorg. Chem. 58 (2019) 2637–2644. Copyright 2019 American Chemical Society.)*

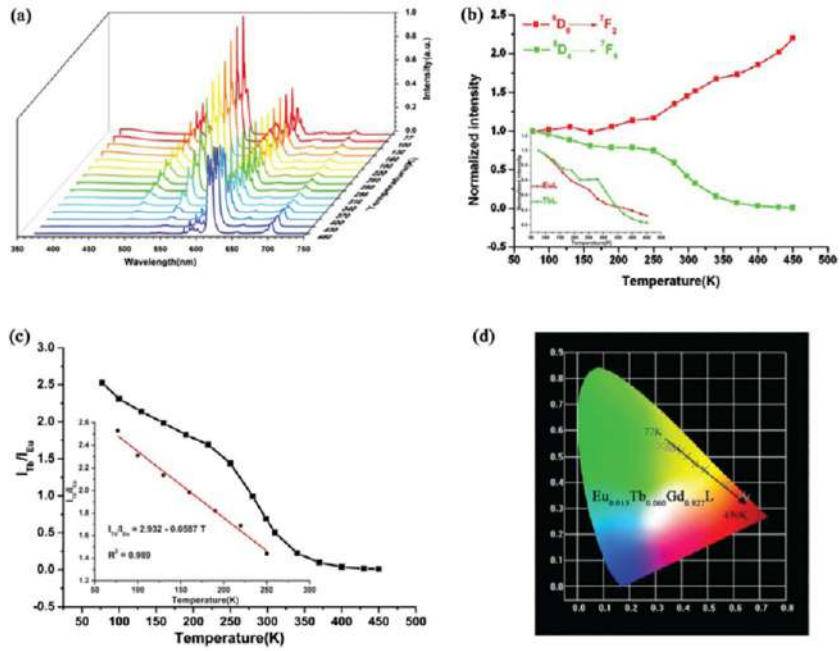

FIG. 12.6 (A) Solid-state emission spectra of $Eu_{0.013}Tb_{0.060}Gd_{0.927}L$ recorded between 77 K and 450 K excited at 335 nm. (B) Temperature-dependent normalized emission intensity of the $^5D_4 \rightarrow {}^7F_5$ and $^5D_0 \rightarrow {}^7F_2$ transitions of $Eu_{0.013}Tb_{0.060}Gd_{0.927}L$. (C) Temperature-dependent intensity ratio of Tb^{3+} (542 nm) to Eu^{3+} (612 nm) for ternary mixed $Eu_{0.013}Tb_{0.060}Gd_{0.927}L$ at different temperatures from 77 K to 450 K. (D) CIE-1931 chromaticity diagram showing the luminescent colors of the ternary mixed $Eu_{0.013}Tb_{0.060}Gd_{0.927}L$. *(Reproduced with permission from Y. Yang, L. Chen, F. Jiang, M. Yu, X. Wan, B. Zhang, M. Hong, A family of doped lanthanide metal–organic frameworks for wide-range temperature sensing and tunable white light emission. J. Mater. Chem. C 5 (2017) 1981–1989. Copyright 2017 Royal Chemical Society.)*

role in acting as a matrix and diluting Eu^{3+} and Tb^{3+}, thereby reducing the quenching effect from concentration [38].

Li et al. fabricated a dual-function ratiometric luminescence sensor based on an $Eu_{0.02}Dy_{0.18}$-MOF of 5-(bis(4-carboxybenzyl)amino)-isophthalic acid (H_4L), in which the two RE^{3+} and ligand (H_4L) formed three luminescence centers and had different sensitivity to temperature. Using the luminescence intensity ratio of Eu^{3+} ($^5D_0 \rightarrow {}^7F_2$, 614 nm) transition to Dy^{3+} ($^4F_{9/2} \rightarrow {}^6H_{13/2}$, 573 nm) transition, the MOF could also sense temperature in the range of 293 to 373 K and 150 to 290 K with high accuracy, excellent linear relationship, reversibility, and recyclability. As shown in Fig. 12.7A (top), the emission intensity of both Eu^{3+} and Dy^{3+} decreased as the temperature increased from 293 to 373 K, and the emission intensity of Dy^{3+} decreased much more slowly than that of Eu^{3+}. The relative intensity Δ ($\Delta = I_{614}/I_{573}$) and temperature have a good linear relationship, which can be fitted with a correction coefficient of

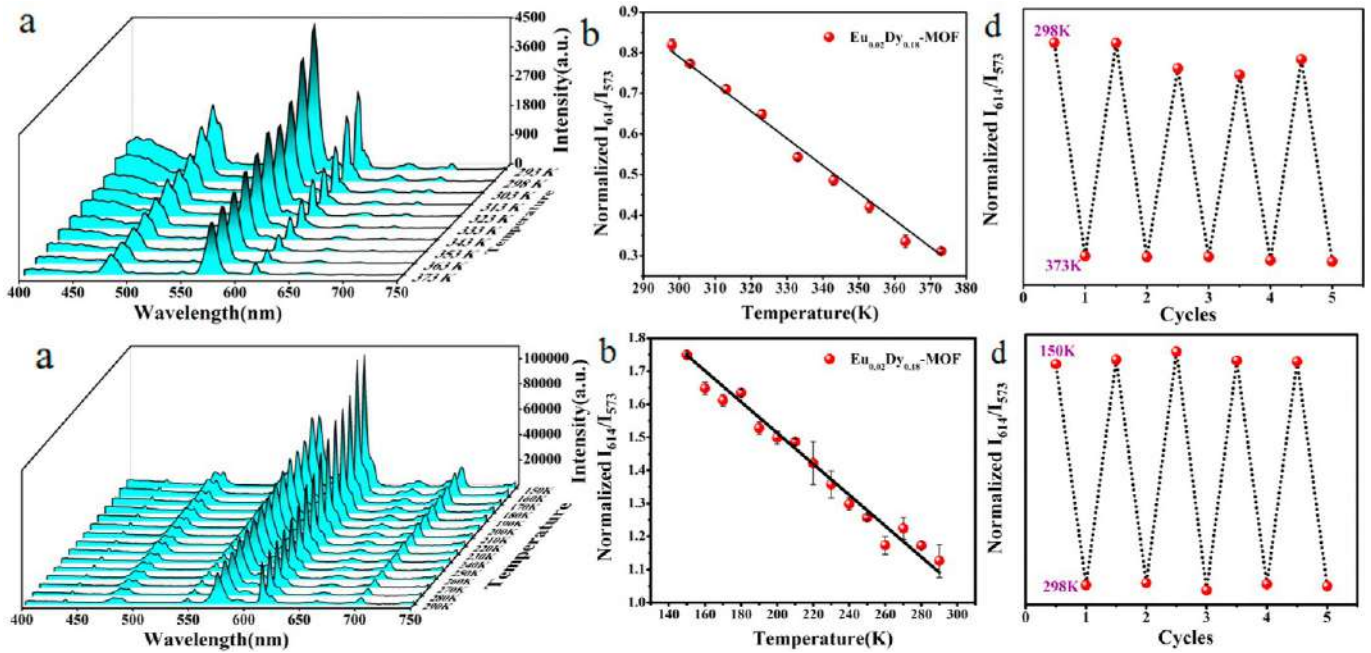

FIG. 12.7 *(Top)* (A) Temperature-dependent emission spectra of $Eu_{0.02}Dy_{0.18}$-MOF from 293 to 373 K. (B) Temperature-dependent intensity ratio of Eu^{3+}(614 nm) to Dy^{3+}(573 nm). (C) Switching cycles of the emission intensities between 298 and 373 K. *(Bottom)* (A) Emission spectra of $Eu_{0.02}Dy_{0.18}$-MOF from 150 to 290 K. (B) Temperature-dependent intensity ratio of Eu^{3+}(614 nm) to Dy^{3+}(573 nm). (C) Switching cycles of the emission intensities between 150 and 298 K. *(Reproduced with permission from H. Li, W. Han, R. Lv, A. Zhai, X. Li, W. Gu, X. Liu, Dual-function mixed-lanthanide metal – organic framework for ratiometric water detection in bioethanol and temperature sensing. Anal. Chem. 91 (2019) 2148–2154. Copyright 2019 American Chemical Society.)*

0.992 (Fig. 12.7B; top). After five cycles, the relative luminescence intensity remained stable (Fig. 12.7D; top). Moreover, with heating and cooling the MOF during 150 and 290 K, the emission intensity of both Eu^{3+} and Dy^{3+} had the same change tendency (Fig. 12.7; bottom) with that at 293 and 373 K. The relationship between the relative intensity Δ ($\Delta = I_{614}/I_{573}$) and temperature could be fitted with a correction coefficient of 0.97 (Fig. 12.7A and B; bottom). Good recyclability was also obtained (Fig. 12.7D; bottom). With raising the temperature from 150 to 290 K and 293 to 373 K, both the emission intensities of Eu^{3+} and Dy^{3+} in the $Eu_{0.02}Dy_{0.18}$-MOF were quenched due to the thermal activation of nonradiative decay pathways. However, the intensity of Eu^{3+} declined faster than that of Dy^{3+} [39].

Zhao et al. developed a near-infrared (NIR) luminescent mixed rare earth MOF, $Nd_{0.866}Yb_{0.134}BTB$ (H_3BTB = 1,3,5-benzenetrisbenzoic acid), as a self-calibrated thermometer in the physiological range. The temperature dependence of its emission spectra was investigated and is presented in Fig. 12.8A and B. At 303 K, the luminescence intensities of Yb^{3+} (980 nm, $^2F_{5/2} \rightarrow {}^2F_{7/2}$) and Nd^{3+} (1060 nm, $^4F_{3/2} \rightarrow {}^4I_{11/2}$) are comparable; they then increase at different rates with temperature, whereas at 333 K, the intensity of Yb^{3+} is more than two times that of Nd^{3+}. A remarkable intensity enhancement for Yb^{3+} of $Nd_{0.866}Yb_{0.134}BTB$ with temperature can be attributed to the efficient energy transfer from Nd^{3+} to Yb^{3+} ions through the thermal driven phonon-assisted energy transfer mechanism. Fig. 12.8C shows a good linear relationship between the intensity ratio Δ and temperature T. The calibrated curve follows a linear-fit function with a correlation coefficient $R^2 = 0.968$, suggesting it is an excellent luminescent thermometer from 303 to 333 K. As shown in Fig. 12.8D, the sensitivity range of $Nd_{0.866}Yb_{0.134}BTB$ is from 2.090% to 4.755% K^{-1} [40].

Zhao et al. presented a type of RE-MOF having NIR absorption and emission features based on efficient Nd^{3+} -to-Yb^{3+} energy transfer at 808-nm photoexcitation. The ratiometric parameter of $Nd_{0.5}Yb_{0.5}TPTC$ (TPTC = 1,1′:4′,1″-terphenyl]-3,3″,5,5″-tetracarboxylic acid) could deliver good exponential-type luminescence response to temperature in the physiological regime (293–328 K). As shown in Fig. 12.9A, $Nd_{0.5}Yb_{0.5}TPTC$ presents the different temperature dependence of the luminescence behavior with respect to the characteristic emissions of Nd^{3+} and Yb^{3+} ions. Fig. 12.9B, which presents the normalized intensity of the $^4F_{3/2} \rightarrow {}^4I_{11/2}$ (1062 nm, Nd^{3+}) and the $^2F_{5/2} \rightarrow {}^2F_{7/2}$ (1026 nm, Yb^{3+}) transition in $Nd_{0.5}Yb_{0.5}TPTC$, displays the temperature dependence. In Fig. 12.9A, one can see that at 293 K, the luminescence intensity of Nd^{3+} at 1062 nm is much stronger than that of Yb^{3+} at 1026 nm. With the rise in temperature, the emission of Nd^{3+} decreased by 1.15% K^{-1} in the range of 293 to 313 K, whereas the peak intensity of Yb^{3+} was significantly increased by a very high rate of 13.14% K^{-1}. At 328 K, the emission intensity of Yb^{3+} was enhanced by 4.6-fold, which is nearly 2.5 times as compared with the emission of Nd^{3+}. As depicted in Fig. 12.9C, the experimental data for $Nd_{0.5}Yb_{0.5}TPTC$ were fitted with a correlation coefficient of

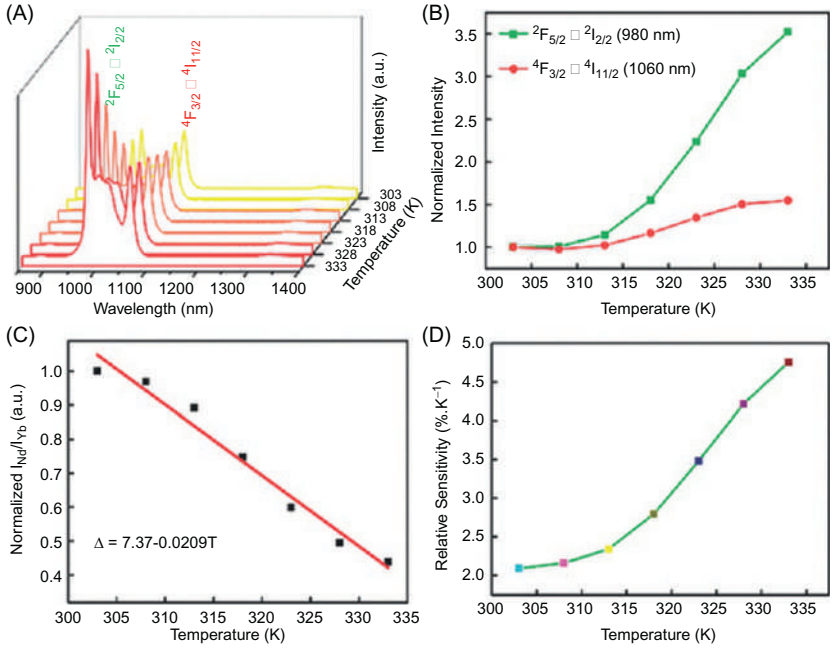

FIG. 12.8 (A) Emission spectra of $Nd_{0.866}Yb_{0.134}BTB$ recorded between 303 and 333 K. Temperature-dependent (B) normalized intensity of the corresponding transitions and (C) intensity ratio of Nd^{3+} (1060 nm) to Yb^{3+} (980 nm) and the fitted curve and (D) relative sensitivity for $Nd_{0.866}Yb_{0.134}BTB$ (excited at 808 nm). *(Reproduced with permission from D. Zhao, J. Zhang, D. Yue, X. Lian, Y. Cui, Y. Yang, G. Qian, A highly sensitive near-infrared luminescent metal–organic framework thermometer in the physiological range. Chem. Commun. 52 (2016) 8259–8262. Copyright 2016 Royal Chemical Society.)*

$R^2 = 0.989$. Such an energy difference was matched with the energy gap between the Nd^{3+} $^4F_{3/2}$ and Yb^{3+} $2F_{5/2}$ levels, which can be considered as the premise of the efficient energy transfer from Nd^{3+} to Yb^{3+} ions [41].

Li et al. presented $(Me_2NH_2)_3[RE_3(FDC)_4(NO_3)_4]\cdot 4H_2O$ (RE-MOF, RE = Eu, Gd; H_2FDC = 9-fluorenone-2,7-dicarboxylic acid), which is a single RE-MOF ratiometric luminescent thermometer based on ion-to-ligand back energy transfer ($\Delta E = 553\ cm^{-1}$). The temperature-dependent emission spectra of Eu-MOF and Gd-MOF in the 12–320 K range are shown in Fig. 12.10. The ligand and Eu^{3+} emission intensities of Eu-MOF (Fig. 12.10C) present a very distinct temperature dependence. Whereas the FDC emission is essentially constant over the low temperature range, decreasing only ≈ 16% up to 150 K and 23% up to 230 K, the Eu^{3+} emission shows a strong temperature quenching, decreasing ≈ 95% up to 150 K and 99% up to 230 K. The intensity decrease of the FDC emission is much more relevant over the high temperature range, reaching 65% for Eu-MOF at 320 K (Fig. 12.10C). For 365-nm excitation (Fig. 12.10A) the I_{FDC} and I_{Eu} are determined integrating the emission spectra,

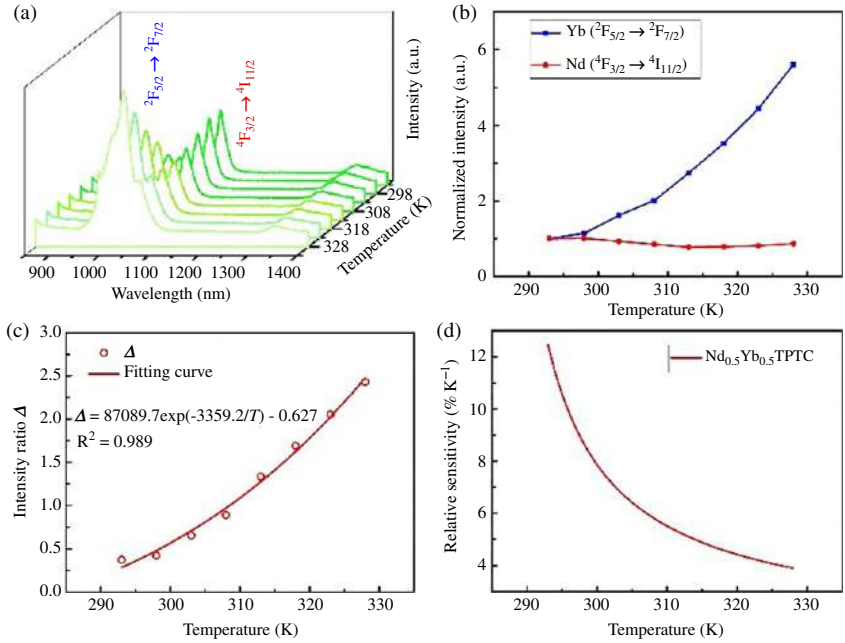

FIG. 12.9 (A) Emission spectra of $Nd_{0.5}Yb_{0.5}TPTC$ recorded in the range of 293 to 328 K (excitation wavelength 808 nm). (B) The normalized intensity of Yb^{3+} ($^2F_{5/2} \rightarrow {}^2F_{7/2}$, 1026 nm) and Nd^{3+} ($^4F_{3/2} \rightarrow {}^4I_{11/2}$, 1062 nm) for $Nd_{0.5}Yb_{0.5}TPTC$. (C) *Red* circular symbols present the values of the experimental parameter ($\Delta = I_{Yb}/I_{Nd}$) of Nd $Nd_{0.5}Yb_{0.5}TPTC$, and the solid *red* line depicts the best fit of the experimental values. (D) Relative sensitivity (Sr) of $Nd_{0.5}Yb_{0.5}TPTC$. *(Reproduced with permission from D. Zhao, X. Han, S. Wang, J. Liu, Y. Lu, C. Li, 808nm-Light-excited near-infrared luminescent lanthanide metal-organic frameworks for highly sensitive physiological temperature sensing. Chem. A Eur. J. 26 (2020) 3145–3151. Copyright 2020 Wiley.)*

respectively, between 450 and 575 nm and 605 and 640 nm. A direct energy transfer occurs from the DSB T_1 state to the $^6P_{7/2}$ level of Gd^{3+}, occupying the higher energy region. From the $^6P_{7/2}$ level, further energy transfer takes place between Gd^{3+} and Eu^{3+}, resulting in a fairly independent Eu^{3+} emission [42].

Xia et al. described the first example of a Dy^{3+}-MOF, Dycpia (H_3cpia = 5-(4-carboxyphenoxy)isophthalic acid), for self-referenced temperature sensing in the range from 298 to 473 K with high sensitivity. Fig. 12.11A (left) shows the normalized spectra in the 435–515-nm wavelength range, and a blue shift in the $^4F_{9/2} \rightarrow {}^6H_{15/2}$ transition can be observed. As shown in Fig. 12.11B (left), the self-calibration thermometric parameter Δ of calcined Dycpia increases exponentially with temperature (where $\Delta = I_1/I_2$, which are the integrated intensities of the $^4I_{15/2} \rightarrow {}^6H_{15/2}$ emission in the 441–462 nm range and the $^4F_{9/2} \rightarrow {}^6H_{15/2}$ emission in the 462–500 nm range, respectively). To judge and compare the performance of different fluorescence thermometers, relative

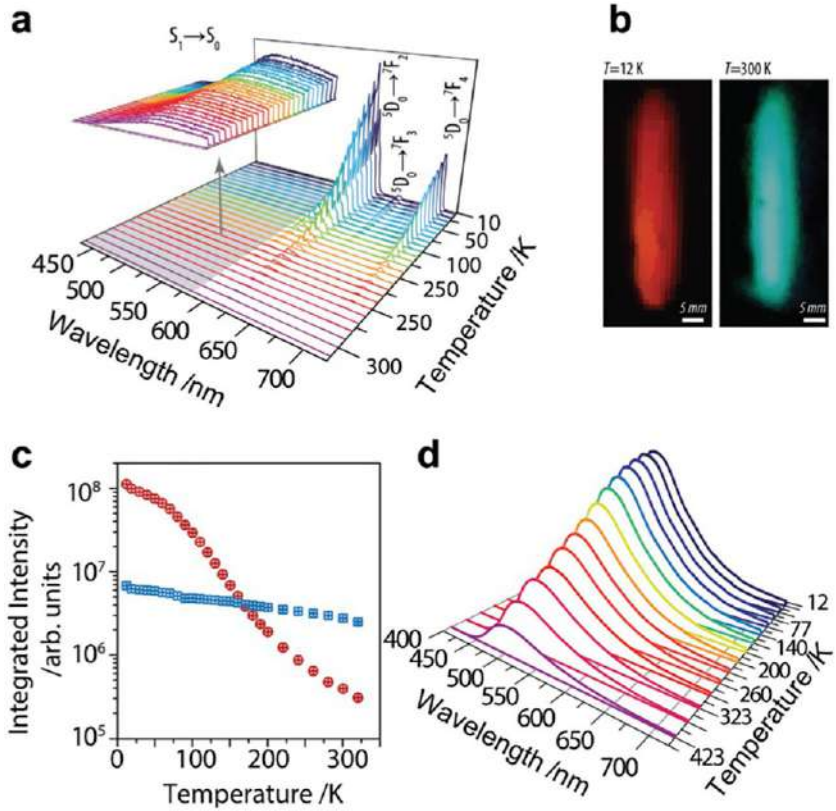

FIG. 12.10 (A) Emission spectra of Eu-MOF recorded between 12 and 423 K (excited at 365 nm). The inset shows a magnification of the FDC ligand emission in the 400∼575 nm region. (B) Digital photographs of Eu-MOF under 365 nm excitation recorded at different temperatures. (C) Integrated areas of the $^5D_0 \rightarrow {}^7F_2$ (Eu^{3+}, *red* circles) and of the FDC ligand emission (*blue* squares). The error bars result from the uncertainty on the integration of the peaks. (D) Emission spectra of Gd-MOF recorded between 12 and 423 K (excited at 365 nm). *(Reproduced with permission from L. Li, Y. Zhu, X. Zhou, C. D. S. Brites, D. Ananias, Z. Lin, F. A. A. Paz, J. Rocha, W. Huang, L. D. Visible-light excited luminescent thermometer based on single lanthanide organic frameworks. Adv. Funct. Mater. 26 (2016) 8677–8684. Copyright 2016 Wiley.)*

sensitivity (Sr) is commonly used and the relative sensitivity Sr of calcined Dycpia steadily increased in the 298–400 K temperature range, and then slowly increased to a stable value at higher temperature (Fig. 12.11A; right). The repeatability of the luminescent thermometer was evaluated by heating-cooling cycles between 298 and 473 K. As shown in Fig. 12.11B (bottom), the calcined Dycpia exhibited a reversible luminescence response under thermal cycling and no noticeable hysteresis was induced by the temperature change [43].

Feng et al. prepared two dual-emitting MOFs with integrated RE^{3+} and luminescent ligand in a UiO-66-type structure, called RE@UiO-66-hybrid

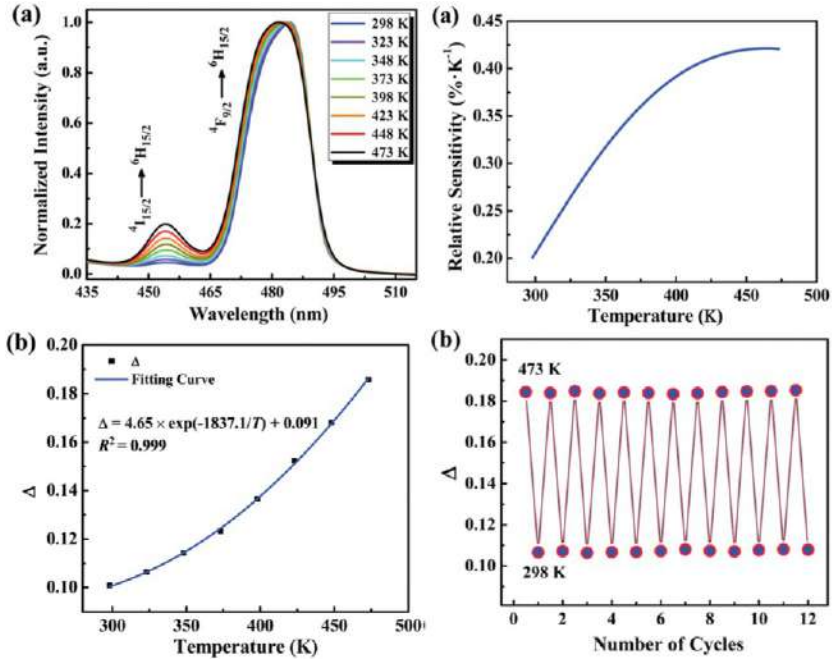

FIG. 12.11 *(Left)* (A) Temperature-dependent normalized spectra of calcined Dycpia excited at 324 nm. (B) Temperature-dependent integrated intensity ratio of the $^4I_{15/2} \rightarrow {}^6H_{15/2}$ to $^4F_{9/2} \rightarrow {}^6H_{15/2}$ transition and the fitting curve for calcined Dycpia. *(Right)* (A) Temperature-dependent relative sensitivity (Sr) of calcined Dycpia. (B) The reversible emission intensity ratio of the $^4I_{15/2} \rightarrow {}^6H_{15/2}$ transition to $^4F_{9/2} \rightarrow {}^6H_{15/2}$ transition between 298 and 473 K. *(Reproduced with permission from T. Xia, Y. Cui, Y. Yang, G. Qian, A luminescent ratiometric thermometer based on thermally coupled levels of a Dy-MOF. J. Mater. Chem. C 5 (2017) 5044–5047. Copyright 2017 Royal Chemical Society.)*

(RE = Eu, Tb), via the combination of postsynthetic modification and postsynthetic exchange methods. Subsequently, the as-synthesized MOFs were deposited onto fluorine tin oxide substrates through electrophoretic deposition by taking advantage of the charges from the unmodified carboxylic groups of the MOFs. The as-prepared Tb@UiO-66-hybrid and Eu@UiO-66-hybrid films were applied to detect temperature changes. As shown in the emission spectra of the Eu@UiO-66-hybrid film shown in Fig. 12.12 (left), the intensity at 430 nm gradually decreased with increasing temperature. In addition, the film exhibited fluorescence with colors ranging from pale pink to red with temperature increasing from 303 to 403 K, which indicates that the temperature change could be observed by the naked eye. Moreover, there is a good function relationship between the intensity ratio (Y) of 616–430 nm and T in the temperature range of 303–403 K, which could be fitted with a correlation coefficient of 0.9954. As shown in Fig. 12.12 (bottom), the intensity at 430 nm decreased

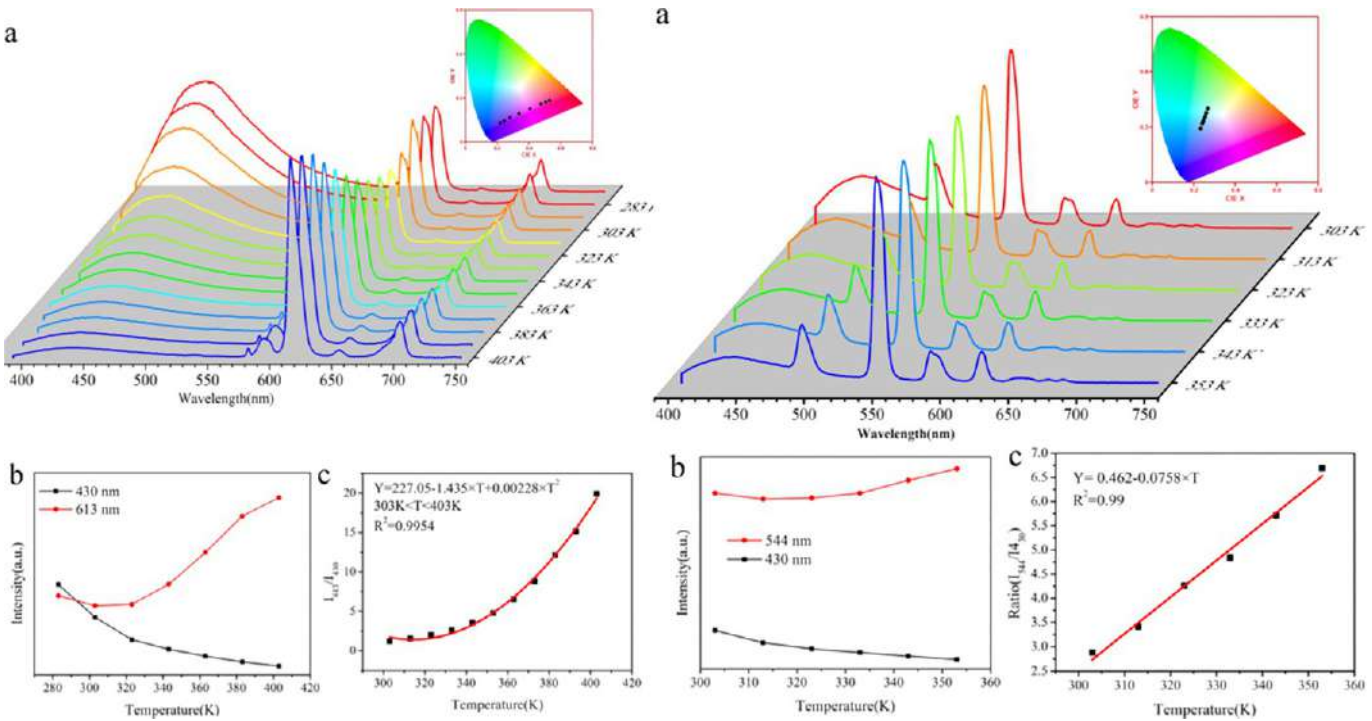

FIG. 12.12 *(Left)* (A) Emission spectra of the Eu@UiO-66-hybrid film recorded in the temperature range of 273–403 K excited at 330 nm (inset: the corresponding CIE picture of Eu@UiO-66-hybrid film); (B) emission intensity at 430 and 613 nm in the temperature range of 303–403 K; and (C) emission intensity ratio of the Eu@UiO-66-hybrid film as a function of temperature with the fitting curve (*red* line, $R^2 = 0.9954$). *(Right)* (A) Emission spectra of the Tb@UiO-66-hybrid film recorded in the temperature range of 303–353 K excited at 330 nm (inset: the corresponding CIE picture of Tb@UiO-66-hybrid film); (B) emission intensity at 430 and 544 nm in the temperature range of 303–353 K; and (C) emission intensity ratio of the Tb@UiO-66-hybrid film as a function of temperature with the fitting curve (*red* line, $R^2 = 0.99$) and the relative sensitivity curve. *(Reproduced with permission from J. Feng, S. Gao, T. Liu, J. Shi, R. Cao, Preparation of dual-emitting ln@UiO-66-hybrid films via electrophoretic deposition for ratiometric temperature sensing. ACS Appl. Mater. Interfaces 10 (2018) 6014–6023. Copyright 2018 American Chemical Society.)*

in quantity with increasing temperature. Similarly, there is a good linear relationship between the ratio (Y) of the intensity at 544–430 nm and temperature in the range of 303–353 K fitted with a correlation coefficient of 0.99. The luminescent lifetimes of the two kinds of hybrid films clearly indicate that energy transfer occurred from the luminescent ligand to the Eu^{3+} or Tb^{3+} ions. The films have a superior temperature-sensing performance as compared to powders [44].

Yan et al. designed and synthesized a smart all-in-one thermometer-heater nanoprobe (THA@Eu-NMOF@Fe/TA), which could achieve precise temperature sensing during PTT under single-beam 808-nm NIR light excitation (TA = trimesic acid, HTHA = (4,4,4-trifluoro-1-(9-hexylcarbazol-3-yl)-1,3-butanedione). HTHA was introduced to sensitize Eu^{3+}, which can absorb 808-nm NIR light excitation to reduce light-induced damage to tissues and increase the depth of light penetrating tissue. Particularly, the long emission lifetime and ultrasensitive transition of the Eu^{3+} endowed the THA@Eu-NMOF probe with the ability to sense temperature. In order to explore the potential efficiency as a molecular thermometer of THA@Eu-NMOF@Fe/TA, the intensity ratio I_{615}/I_{590} was used as the thermometric parameter. The dependence of I_{615}/I_{590} on temperature is plotted in Fig. 12.13A, which reveals a good linear relationship between I_{615}/I_{590} and temperature within the range of 20°C to 60°C (biological range). The linear relationship can be fitted with a correlation coefficient (R^2) of 0.993. As shown in Fig. 12.13B, the maximal sensitivity of the THA@Eu-NMOF@Fe/TA nanoprobe is 0.59% at 60°C. Fig. 12.13C shows the influence of temperature on the lifetime of Eu^{3+} in the nanoprobe THA@Eu-NMOF@Fe/TA, showing that as the temperature increases from 20°C to 60°C, the average lifetime drops rapidly. Fig. 12.13D displays the maximum temperature sensitivity as 0.23% at 60°C (from 20°C to 60°C). Therefore it is more suitable for temperature monitoring in biological systems, which possess the complex biological background interferences [45].

Cui et al. incorporated an organic dye perylene into a porous rare earth MOF ZJU-88 ($[Eu_2(QPTCA)(NO_3)_2(DMF)_4]\cdot(CH_3CH_2OH)_3$) of 1,1′:4′,1″:4″,1‴-quaterphenyl-3,3‴,5,5‴-tetracarboxylic acid (H_4QPTCA) to form the ZJU-88 ⊃ perylene hybrid, and make use of the dual-emitting from organic dyes and Eu^{3+} ions within such a hybrid to realize ratiometric temperature sensing in a physiological temperature range. To assess the potential of ZJU-88 ⊃ perylene as a ratiometric thermometer, the temperature-dependent photoluminescent properties were investigated (Fig. 12.14A). With the increase of temperature from 20°C to 80°C, the luminescence intensity at 473 nm of perylene dye in ZJU-88 ⊃ perylene substantially decreased due to the thermal activation of nonradiative-decay pathways, while the intensity of the $^5D_0 \rightarrow {}^7F_2$ transition of Eu^{3+} at 615 nm increased. The significant luminescence decreases of perylene as well as the enhancement in emission of Eu^{3+} in ZJU-88 ⊃ perylene may be attributed to the energy transfer from perylene molecules to Eu^{3+} ions. Such an energy transfer behavior has been further confirmed by the

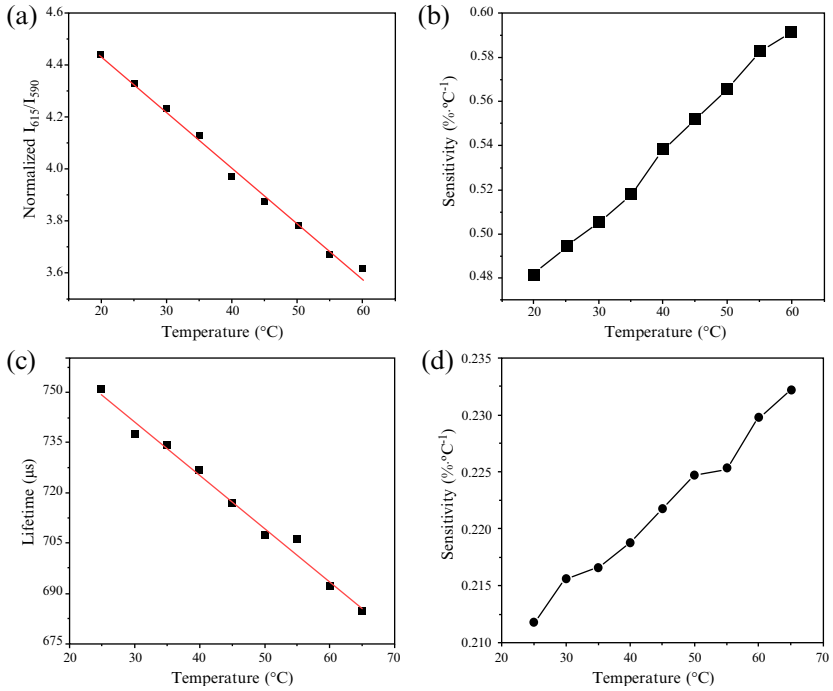

FIG. 12.13 (A) Intensity ratio I_{615}/I_{590} of THA@Eu-NMOF@Fe/TA and the fitted curve. (B) The relative sensitivity (Sr) for THA@Eu-NMOF@Fe/TA. (C) Temperature-dependent lifetime data of THA@Eu-NMOF@Fe/TA and the fitted curve. (D) The relative sensitivity (Sr) of temperature-dependent lifetime for THA@Eu-NMOF@Fe/TA. The experimental details: the sample solution was placed in a fluorescence detector equipped with a temperature-control device (warming procedure: heat for 5 min, keep for 10 min) to collect fluorescence or lifetime signals per 5°C. *(Reproduced with permission from H. Yan, H. Ni, J. Jia, C. Shan, T. Zhang, Y. Gong, X. Li, J. Cao, W. Wu, W. Liu, Y. Tang, Smart all-in-one thermometer-heater nanoprobe based on postsynthetical functionalization of a Eu(III)-metal-organic framework. Anal. Chem. 91 (2019) 5225–5234. Copyright 2019 American Chemical Society.)*

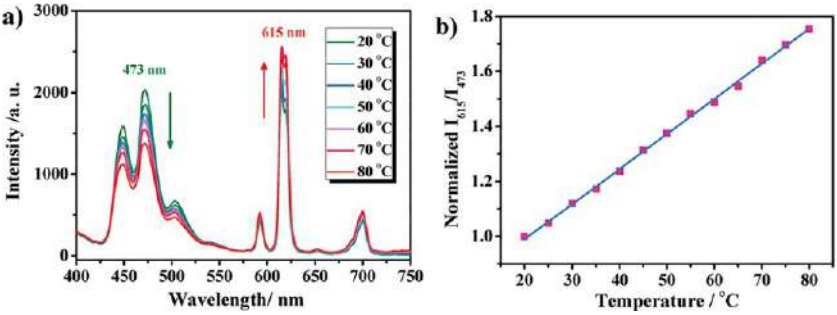

FIG. 12.14 (A) Emission spectra of ZJU-88 ⊃ perylene recorded from 20°C to 80°C, excited at 388 nm. (B) Temperature-dependent intensity ratio of Eu^{3+} (615 nm) to perylene (473 nm) and the fitted curve for ZJU-88 ⊃ perylene. *(Reproduced with permission from Y. Cui, R. Song, J. Yu, M. Liu, Z. Wang, C. Wu, Y. Yang, Z. Wang, B. Chen, G. Qian, Dual-emitting MOF ⊃ dye composite for ratiometric temperature sensing. Adv. Mater. 27 (2015) 1420–1425. Copyright 2015 Wiley.)*

lifetime measurements. Fig. 12.14B plots the ratio of the luminescence intensity at 615 nm (Eu^{3+}) and 473 nm (perylene) versus temperature, normalized to this intensity ratio at 20°C. There is a very good linear relationship between the intensity ratio and temperature, which can be fitted with a correlation coefficient of 0.998 [46].

Liu et al. prepared a dual-emissive $CsPbBr_3$ QD encapsulated Eu-MOF material with expected FIR self-calibrated temperature-sensing activities. Accordingly, the thermo-response luminescence intensity ratio of $CsPbBr^3$ QDs to Eu^{3+} emitters showed an exponential function versus temperature changes, which can effectively serve as a self-calibrating temperature sensor. As shown in Fig. 12.15A, the characteristic green emission of $CsPbBr_3$ QDs centered at around 528 nm decreased gradually as the temperature increased, while the $CsPbBr_3$ QDs do not show any change in emission peak position. In contrast, the emission intensity of Eu^{3+} ions at 618 nm increased as the temperature increased. Such a significant temperature response of Eu^{3+} ions in $CsPbBr_3$@Eu-BTC may be related to the high luminescence efficiency of the encapsulated guest $CsPbBr_3$ QD phase and the host skeleton limiting effect of the Eu-BTC matrix. The opposite temperature-sensing behaviors of $CsPbBr_3$ QDs, and skeleton Eu^{3+} ions will benefit the application of an optical nanothermometer based on the FIR of Eu^{3+} ions (618 nm) to $CsPbBr_3$ (528 nm). Fig. 12.15A (inset) illustrates the chromaticity diagram of $CsPbBr_3$@Eu-BTC at different temperatures. It can be found that with an increase in temperature, the emissive colors evolved from green (0.275, 0.674) to orange (0.536, 0.423). Fig. 12.15B illustrates the relative luminescent intensity ratio of Eu^{3+} ions (618 nm) to $CsPbBr_3$ (528 nm) versus temperature [47].

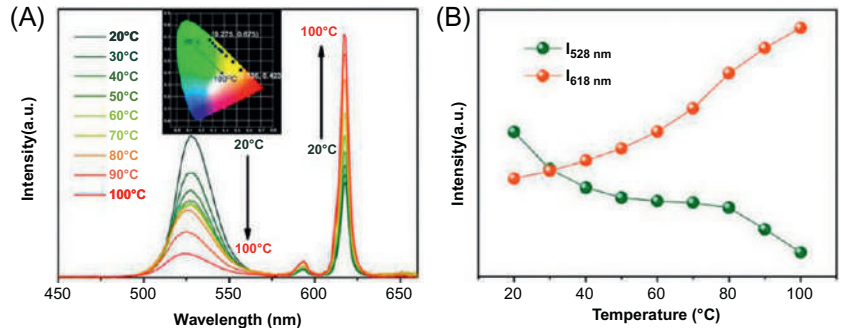

FIG. 12.15 (A) Temperature-dependent luminescent spectra of $CsPbBr_3$@Eu-BTC in the temperature range of 20–100°C excited at 339 nm (inset: the CIE (x, y) coordinate diagram of emission colors at various temperatures). (B) Integrated emission intensities of $CsPbBr_3$ QDs and Eu^{3+}: $^5D_0 \rightarrow {}^7F_2$ versus various temperatures. *(Reproduced with permission from J. Liu, Y. Zhao, X. Li, J. Wu, Y. Han, X. Zhang, Y. Xu, Dual-emissive CsPbBr3@Eu-BTC composite for self-calibrating temperature sensing application. Cryst. Growth Des. 20 (2020) 454–459. Copyright 2015 American Chemical Society.)*

There are some examples of temperature sensing by single luminescence rare earth ion centers. Li et al. synthesized heterometallic 3D Tb^{3+}-K^{+} sulfate and oxalate MOFs via the in-situ generation of sulfate anions, whose tunable luminescence was observed by changing the temperature. This may have potential applications in temperature sensing [48]. Sun et al. designed an Nd-complex from an ESIPT ligand; efficient energy transfer occurred from the triplet keto-state $T_1(K^*)$ of the ligand to the Nd^{3+} centers, resulting in sensitized NIR emission, and it could be substantially modulated by outer interferences related to ESIPT processes. Uniquely, anomalous temperature-enhanced NIR emission was observed in this Nd-complex from 77 to 300 K for the first time, due to the thermally activated triplet states of the unique four energy level attributes in ESIPT ligands. The Nd-complex was further coupled with an optical fiber device to achieve the remote and in-situ detection of temperature over a long range [49]. Kitagawa et al. proposed a design for an effective molecular luminescent thermometer based on long-range electronic coupling in RE-MOFs. The zig-zag orientation of the single polymer chains induced the formation of packed coordination structures containing multiple sites for CH-F intermolecular interactions, resulting in thermal stability above 350°C. The electronic coupling was controlled by changing the concentration of the Gd^{3+} ion in the Eu^{3+} -Gd^{3+} polymer. The emission quantum yield and the maximum relative temperature sensitivity (Sm) of emission lifetimes for the Eu^{3+}-Gd^{3+}-MOF (Eu: Gd = 1:1, $\Phi_{tot} = 52\%$, Sm = 3.73% K^{-1}) were higher than those for the pure Eu^{3+}-MOF ($\Phi_{tot} = 36\%$, Sm =2.70% K^{-1}), respectively. The enhanced temperature-sensing properties are caused by control of long-range electronic coupling based on phosphine oxide with a chrysene framework [50].

12.2 Rare earth metal-organic framework hybrid materials for luminescence responsive chemical sensing of pH value

Another important sensing application is focused on the pH value of aqueous media and further utilization. Solution pH is a pivotal target parameter in a broad range of applications from environmental to industrial to biomedical. A slight pH fluctuation can devastate the lives of plants and animals. The study of pH changes in living cells is important for revealing the mechanism of cell metabolism and different physiological and pathological processes, as well as the intracellular drug delivery process [51–53]. Therefore monitoring the changes and values of pH is highly valuable for exploring and better understanding cellular functions. Also, pH detection is very important and interesting in luminescence sensing research; however, there are few reports of MOF materials as fluorescent pH sensors because most MOFs cannot resist harsh acid and alkali solutions. Among them, MOFs with pH-dependent fluorescent ligands or pH sensitive fluorescent dyes can be used as pH sensors. Some rare earth MOFs have been reported for sensing of pH value, whose luminescence intensity responds to the alternation of pH

value. These facts are strongly correlated to the protonation level of linkers and the ionization constant [54–62].

Han et al. constructed $[Eu_2(_D\text{-cam})(Himdc)_2(H_2O)_2]$ (Eu-MOF) with mixed ligands of D-H_2cam ($_D$-camphoric acid) and 4,5-imidazole dicarboxylic acid (H_3imdc). The imidazole moiety in this Eu-carboxylate system can act as a buffer solution, which is readily protonated/deprotonated without destroying the framework structure. Thus this Eu-MOF is highly stable under a wide pH range and in several boiling solvents and can be used as a pH sensor over a wide pH range from 2 to 11. More significantly, it also shows a highly sensitive and linear pH response in the range of 6.8–8.0 for biological fluids. From Fig. 12.16 (left), the emission intensity of Eu-MOF is correlated with pH values in the whole experimental pH range (2–1), particularly in the range of 5–9. As shown in Fig. 12.16 (right), the luminescent intensity of Eu-MOF increased with increasing pH value and had a linear response to the pH values in the range from 6.8 to 8.0, which is required for working with biological fluids such as blood and culture cell media (Fig. 12.16; right, inset). High sensitivity of up to 1.325% was observed for the Eu-MOF, which makes it potentially useful for designing new miniaturized physiological pH sensor prototypes. In high acidity, the abundance of hydrogen bonds in the Eu-MOF will be destroyed piecemeal, thereby resulting in the decrease of luminescent intensity. However, in alkaline solutions, deprotonation of the imidazole ring in $Himdc^{2-}$ occurs, leading to the more aromatic imidazole ring that favors the energy transfer from ligand to Eu^{3+} ions and hence increases the luminescent intensity [54].

Lu et al. prepared a MOF-253-Eu-TTA hybrid using a PSM, in which Eu^{3+} ions were introduced into MOF-253 first (recorded as MOF-253-Eu), and deprotonated TTA (TTA = 2-thenoyltrifluoroacetone) was used to further

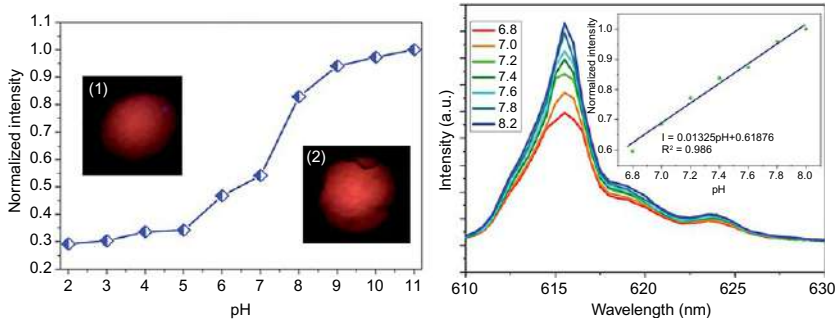

FIG. 12.16 *(Left)* The normalized intensity of the emission spectra of Eu-MOF in different pH (2–11) solutions. *(Right)* The emission spectra of Eu-MOF after immersion in 1 M HEPES aqueous solution with various pH values from 6.8 to 8.0. Inset: linear correlation between the fluorescent response of Eu-MOF and pH. *(Reproduced with permission from Y. Han, C. Tian, Q. Li, S. Du, Highly chemical and thermally stable luminescent EuxTb1-xMOF materials for broad-range pH and temperature sensors. J. Mater. Chem. C 2 (2014) 8065–8070. Copyright 2014 Royal Chemical Society.)*

sensitize the Eu^{3+} ions. The deprotonated TTA could construct a six-membered chelate ring with Eu^{3+} ions. In the PSM, the amount of Eu^{3+} ions was four times that of TTA (according to the feed ratio) for building two different coordination environments of Eu^{3+} ions, one of them only linked by bipyridine, denoted as Eu_1, and the other one having two ligands (bipyridine and TTA), denoted as Eu_2. So, MOF-253-Eu-TTA requires no calibration because only one of the two types of Eu^{3+} is affected by the pH variation in the range from 5 to 7.2. The emission intensity of Eu_1 ($\lambda_{ex} = 330$ nm) remained almost unchanged in different pH solutions (Fig. 12.17A; top). Meanwhile, the emission intensity of Eu_2 ($\lambda_{ex} = 375$ nm) weakened with a decrease of the pH value for the protonation of the a-proton of TTA (Fig. 12.17B; top). The change in the emission intensity corresponds to the results of the excitation spectra, which are obtained by monitoring the emission wavelength at 614 nm (Fig. 12.17C; top). By following the $^5D_0 \rightarrow {}^7F_2$ emission intensity ratio (I_r) of the two Eu^{3+} types (Eu_1/Eu_2), the pH of the solution could be determined. In the pH range of 5.0–7.2, the relationship between the $^5D_0 \rightarrow {}^7F_2$ emission intensity ratio (I_r) and the pH value presented good linearity ($R = 0.9991$) (Fig. 12.17D; top). For the single Eu^{3+} complex with TTA, the free TTA disappeared into the solution after the six-membered chelate ring was broken. However, when the Eu^{3+} complex is assembled into MOFs, some differences will occur. The free TTA would still be present in the pore after the six-membered chelate ring is broken, because MOFs have the adsorption capacity to hold these molecules (TTA). As a consequence, the sensitization from TTA will still exist, but the effect will be lessened. More importantly, the weakened sensitization can maintain the excitation wavelength of Eu_2 at 375 nm and it does not change to 330 nm, even if the six-membered chelate ring is broken (Fig. 12.17; bottom). To further prove the presence of free TTA in the pore, triethylamine was used to recover the luminescence intensity ($\lambda_{ex} = 375$ nm) of MOF-253-Eu-TTA, which was soaked in an aqueous solution of pH 5 (Fig. 12.17; bottom) [55].

Xia et al. presented mixed-RE-MOFs, Eu_xTb_{1-x}Hdpda ($x = 0.097$, 0.205, 0.303, H_4dpda = 4-(3,5-dicar- boxyphenyl)pyridine-2,6-dicarboxylic acid) for self-referencing and colorimetric luminescent pH sensing in a biological pH value range using a single excitation mode. The resultant mixed-rare earth MOFs showed high stability and contained uncoordinated carboxyl groups to interact with H^+ or OH^-. The protonation-deprotonation of uncoordinated carboxyl groups enables these mixed-RE-MOFs' high pH-dependent luminescent emission and significant pH-dependent color change for self-referencing and colorimetric luminescent pH sensors in biotechnology and biomedicine. The emission intensity of Tb^{3+} increased gradually while that of Eu^{3+} almost did not change when increasing the pH from 3.90 to 7.50 (Fig. 12.18; left). Fig. 12.18B (left) plots the ratios of two emission intensities of $^5D_0 \rightarrow {}^7F_2$ (Eu^{3+}, 616 nm) and $^5D_4 \rightarrow {}^7F_5$ (Tb^{3+}, 543 nm) versus pH values, normalized to the intensity ratio at pH 3.90, which decreases exponentially with pH increase. The pH-dependent luminescence colors of $Eu_{0.205}Tb_{0.795}$Hdpda

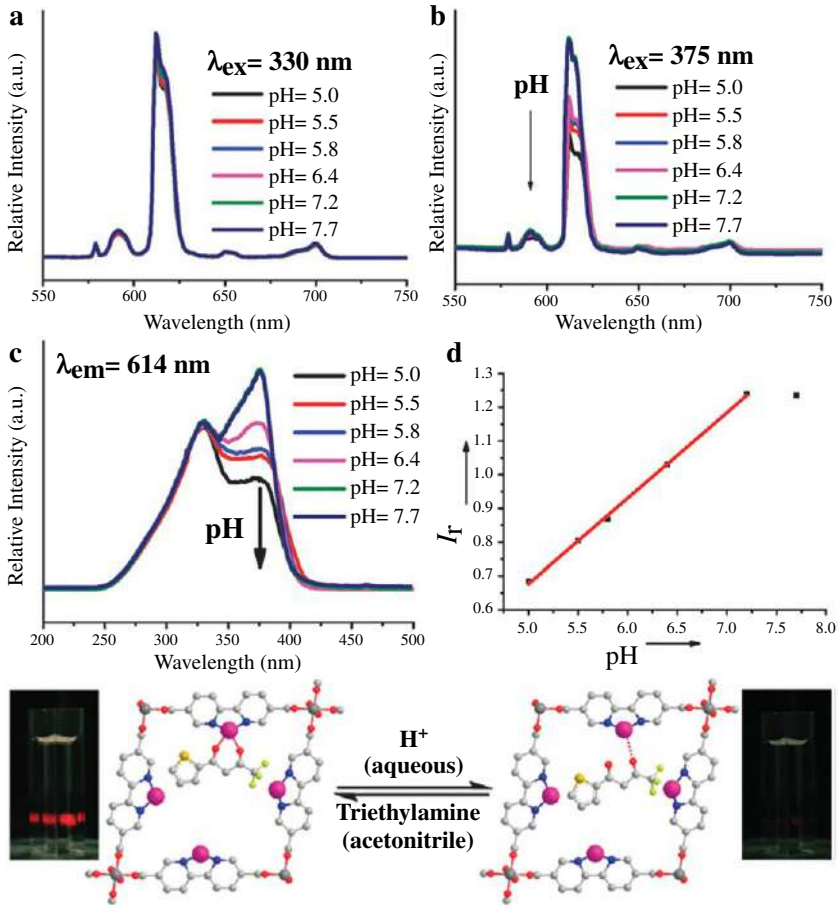

FIG. 12.17 *(Top)* The emission spectra of MOF-253-Eu-TTA in different pH aqueous solutions, $\lambda_{ex} = 330$ nm for (A) and $\lambda_{ex} = 375$ nm for (B); (C) the excitation spectra of MOF-253-Eu-TTA in different pH aqueous solutions ($\lambda_{em} = 614$ nm); (D) the linear variation of the $^5D_0 \rightarrow {}^7F_2$ emission intensity ratio (I_r) of two Eu^{3+} types with different excitation wavelengths, Eu_1 ($\lambda_{ex} = 330$ nm)/Eu_2 (-$\lambda_{ex} = 375$ nm). *(Bottom)* Schematic representation of the pH sensor based on MOF-253; H^+ protons cabd impair the sensitization of TTA to Eu^{3+} by breaking the six-membered chelate ring, and triethylamine can recover the sensitization; the insets show the photographs of MOF-253-Eu-TTA in pH 5 aqueous solution *(right)* and in pH 7.2 aqueous solution *(left)* ($\lambda_{ex} = 375$ nm). *(Reproduced with permission from Y. Lu, B. Yan, A ratiometric fluorescent pH sensor based on nanoscale metal-organic frameworks (MOFs) modified by europium(III) complexes. Chem. Commun. 50 (2014) 13323–13326. Copyright 2014 Royal Chemical Society.)*

change from orange to green when the pH varies from 3.90 to 7.50, which can be directly observed by a camera or the naked eye (insert in Fig. 12.18B; right). The corresponding CIE coordinates change from (0.465, 0.465) at pH 3.90 to (0.295, 0.597) at pH 7.50 (Fig. 12.18A; right), indicating that $Eu_{0.205}Tb_{0.795}$Hdpda can act as a promising colorimetric pH sensor for in-situ

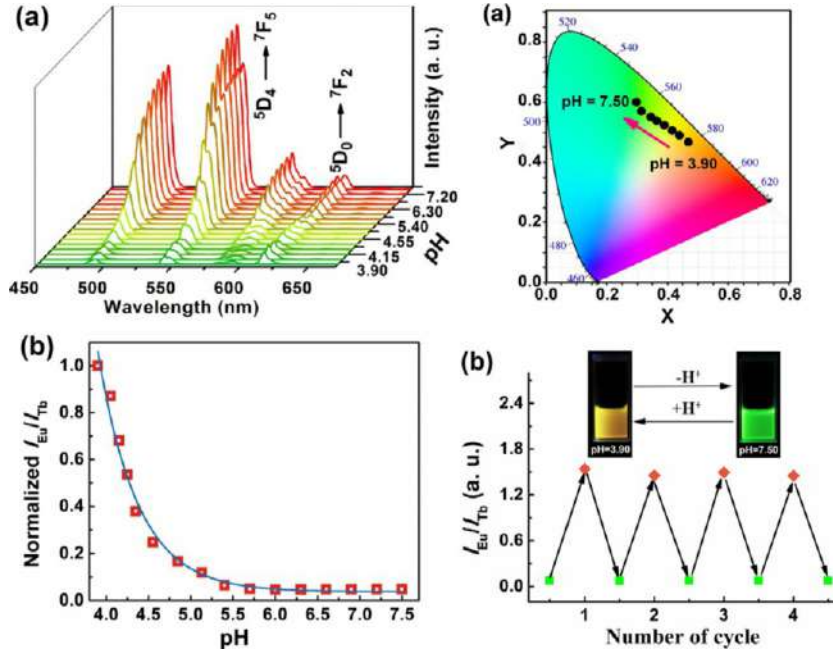

FIG. 12.18 *(Left)* (A) The pH-dependent emission spectra of $Eu_{0.205}Tb_{0.795}$Hdpda in PBS with pH ranging from 3.90 to 7.50. (B) pH-dependent intensity ratios of the $^5D_0 \rightarrow {}^7F_2$ and $^5D_4 \rightarrow {}^7F_5$ transition for $Eu_{0.205}Tb_{0.795}$Hdpda and related fitting curve between I_{Eu}/I_{Tb} and pH. *(Right)* (A) CIE chromaticity diagram of luminescence color of $Eu_{0.205}Tb_{0.795}$Hdpda at different pH values. (B) Reversible luminescence response to pH of four consecutive cycles (Insert: luminescence images of $Eu_{0.205}Tb_{0.795}$Hdpda at pH of 3.90 and 7.50 excited at 365 nm). *(Reproduced with permission from T. Xia, Y. Cui, Y. Yang, G. Qian, Highly stable mixed-lanthanide metal–orgnic frameworks for self-referencing and colorimetric luminescent pH sensing. ChemNanoMat 3 (2017) 51–57. Copyright 2017 Wiley.)*

pH monitoring and imaging. To evaluate the reversibility of $Eu_{0.205}Tb_{0.795}$Hdpda, the pH-dependent luminescence spectra are recorded between pH 3.90 and 7.50 for four consecutive cycles (Fig. 12.18B; right) [56].

Huang et al. designed a MOF-base probe (Tb/GMP/Ag) for pH sensing in undiluted human serum combining Tb^{3+}, water-soluble biomolecules of guanosine monophosphate (GMP), and Ag^+. Tb/GMP/Ag possesses strong luminescence and high quantum yield due to the sensitization by Ag^+ and the fluorescence resonance energy transfer (FRET) from GMP to Tb^{3+}. In alkaline solutions, the luminescence of Tb/Ag/GMP is quenched distinctively because of the strong affinity between OH^- and Ag^+, which results in the extraction of the sensitizer of Ag^+ and the formation of Ag_2O precipitation. Fig. 12.19 (left) depicts the variation in fluorescence of Tb-GMP/Ag in response to different pH in water solutions. The fluorescence intensity of Tb/GMP/Ag reduces linearly with an increase in pH from 7.5 to 13.0. Based on the advantage of

time-resolved fluorescence, the group investigated the achievement of a Tb/GMP/Ag probe for sensing pH in biosamples of human serum (Fig. 12.19; right). In addition, only several hundred microliter samples can be easily detected by the current probe. Therefore, compared with a pH meter, their assay has more practical application value in trace determination [57].

Zhang et al. selected a robust UiO type framework, $Zr_6(\mu_3\text{-}O)_4(OH)_4(bpydc)_{12}$ (known as UiO-67-bpydc, bpydc = 2,2′-bipyridine-5,5′-dicarboxylic acid), which was chosen as a platform to encapsulate Eu^{3+}, and the Eu^{3+} incorporated sample (Eu^{3+}@UiO-67-bpydc) was developed as a pH sensor. Fig. 12.20 (top, left) shows the fluorescence intensity and the emission spectra of Eu^{3+}@UiO-67-bpydc in aqueous solution at various pH values. Significantly, the intensity almost rises along with pH increasing in the whole experimental range, which gives several linear relationships between pH value and fluorescence intensity (Fig. 12.20; top, left). Quantitatively, this phenomenon can be rationalized with an excellent correlation ($R^2 = 0.9989$) to the pH from 1.06–10.99. With a pH value of 1.94 for the solution, Eu^{3+}@UiO-67-bpydc exhibited the same degree of fluorescence quenching after each cycle, and the fluorescence intensity recovered to a similar level when the pH value of the solution was changed to 7.60 (Fig. 12.20; top, right). The protonation and deprotonation of the ligands affects the energy transfer efficiency from the ligands to the Eu^{3+} ions, because the luminescence intensity of Eu^{3+} depends on the efficiency of the ligand-to-Eu energy transfer (Fig. 12.20A; bottom). The protonation of nitrogen atoms in the ligands affects the energy transfer efficiency from the ligands to the Eu^{3+} ions, because the luminescence intensity of Eu^{3+} depends on the efficiency of the ligand-to-Eu^{3+} energy transfer, which results in significant fluorescence quenching of Eu^{3+} ions (Fig. 12.20; top, left). The fluorescence enhancements in the basic solution are assumed to arise from the efficient energy transfer from the ligand to Eu due to deprotonation of the imino group of bipyridine involved in the Eu^{3+}@UiO-67-bpydc framework (Fig. 12.20; bottom). The sensing mechanism of Eu^{3+}@UiO-67-bpydc for pH is based on protonation and deprotonation of the ligands, which changes the excited state energy level of the ligands and affects the ligand-to-Eu^{3+} energy transfer efficiency, leading to different luminescent emissions [59].

Wang et al. designed and prepared RE-MOF nanoplates using yttrium (Y^{3+}) ions as RE^{3+} metal centers and TCCP (4,4,4,4-(Porphine-5,10,15,20-tetrayl)tetrakis(benzoic acid)) as the porphyrin-based planar ligand. Customarily, TCCP exhibits a bright red fluorescence at 645 nm. After the formation of the Y-MOF nanoplates (YTMNs), the fluorescence was quenched via the PET effect. YTMNs exhibited fluorescence recovery under an alkaline medium (pH > 7). These two processes were involved in two different pH ranges. Thus YTMNs was exploited as a fluorescence nanoprobe for pH sensing. Additionally, YTMNs were further cross-linked on paper strips for visual detection. The YTNMs nanoprobe exhibited pH-dependent fluorescence in an alkaline medium, which can be applied for pH sensing. As shown in Fig. 12.21A, no

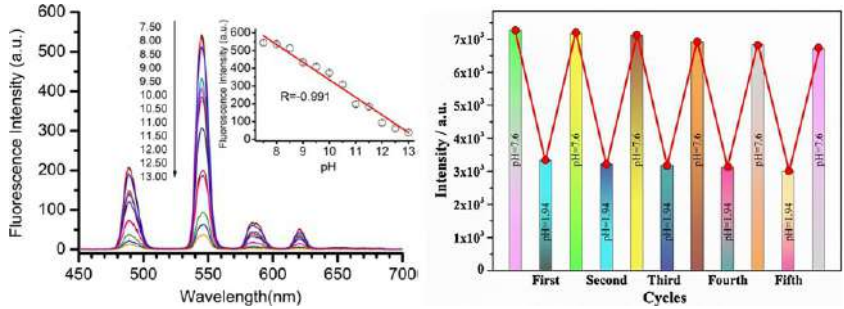

FIG. 12.19 *(Left)* Tb/GMP/Ag probe for sensing pH with range from 7.5 to 13.0 in HEPES buffer solutions. Inset is the linear relationship between the fluorescence intensity of Tb/GMP/Ag CPs at 545 nm and pH. *(Right)* Tb/GMP/Ag probe for sensing pH with range from 7.5 to 13.0 in HEPES buffer solutions. Inset is the linear relationship between the fluorescence intensity of Tb/GMP/Ag CP at 543 nm and pH. *(Reproduced with permission from Y. Huang, B. Liu, Q. Shen, X. Zhu, Y. Hao, Z. Chang, F. Xu, P. Qu, M. Xu, Lanthanide coordination polymer probe for time-gated luminescence sensing of pH in undiluted human serum. Talanta 164 (2017) 427–431. Copyright 2017 Elsevier.)*

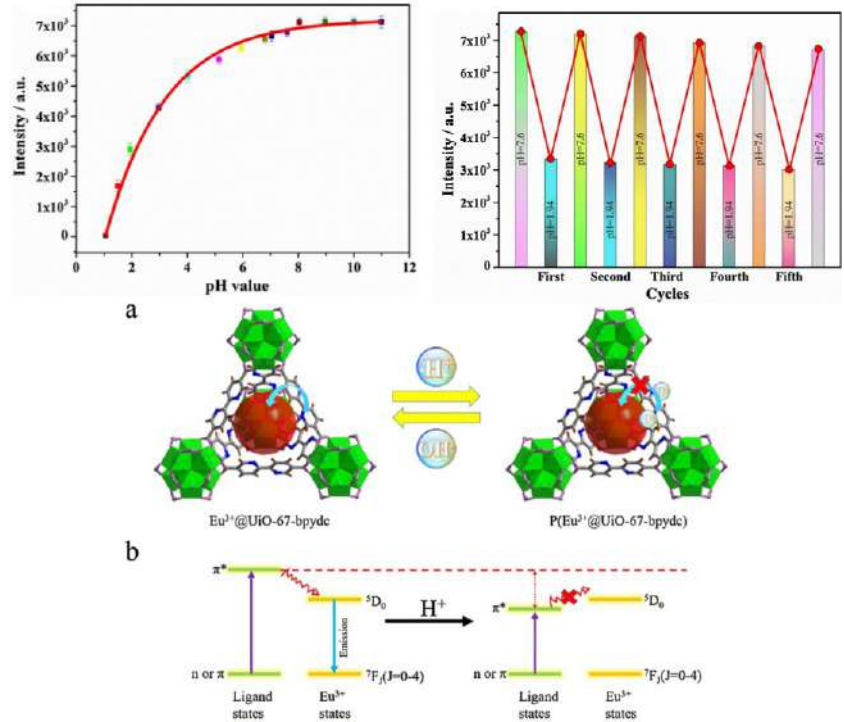

FIG. 12.20 *(Top, Left)* Relationship between the fluorescence intensity of Eu^{3+}@UiO-67-bpydc (at 615 nm) and pH value. *(Top, Right)* The luminescence intensity of Eu^{3+}@UiO-67-bpydc at 615 nm after five recycles ($\lambda_{ex} = 335$ nm). *(Bottom)* (A) Schematic representation of the sensor based on the protonation of the nitrogen atom in the ligands and energy transfer mechanism of fluorescence emission in Eu^{3+}@UiO-67-bpydc. (B) The influence of protons on the ligand-to-Eu energy transfer. *(Reproduced with permission from X. Zhang, K. Jiang, H. He, D. Yue, D. Zhao, Y. Cui, Y. Yang, G. Qian, A stable lanthanide-functionalized nanoscale metal-organic framework as a fluorescent probe for pH. Sens. Actuators B 254 (2018) 1069–1077. Copyright 2018 Elsevier.)*

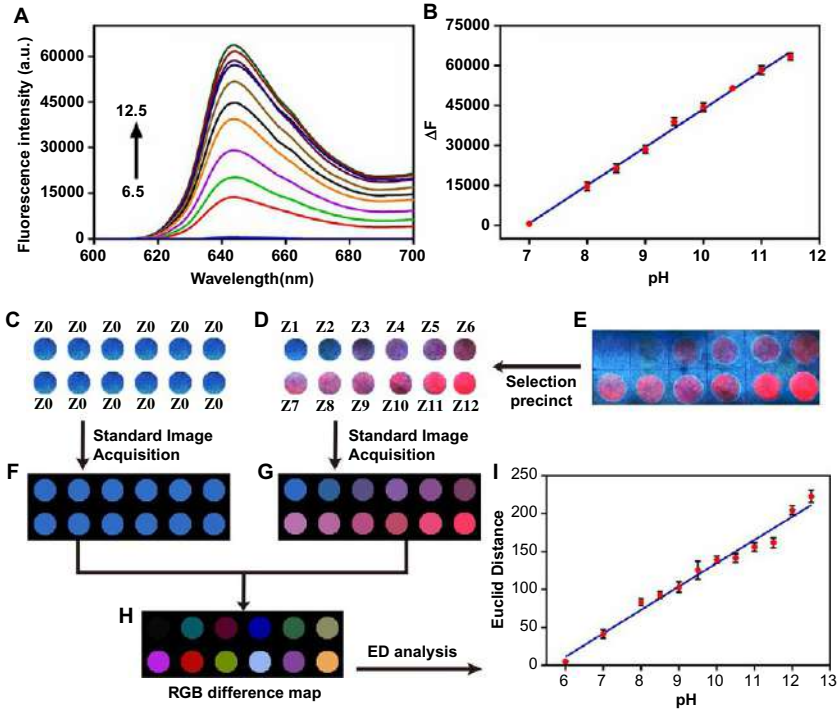

FIG. 12.21 The fluorescence spectrum (A) of YTMNs nanoprobe and corresponding calibration curve (B) with a pH increase from 6 to 12.5. The selection precincts of test zone from YTMNs strip before (C) and after (D) addition of the detection samples. The photograph (E) of YTMNs strip after different pH sensing (6, 7, 8, 8.5, 9, 9.5, 10, 10.5, 11, 11.5, 12, 12.5). The standard images acquisition (F, G) from the selection precincts. The final RGB difference map (H) and corresponding calibration curve (I) from the European Distance of ΔRGB for pH sensing. *(Reproduced with permission from X. Wang, C. Chu, Y. Wu, Y. Deng, J. Zhou, M. Yang, S. Zhang, D. Huo, C. Hou, Synthesis of yttrium (III)-based rare-earth metal-organic framework nanoplates and its applications for sensing of fluoride ions and pH. Sens. Actuators B 321 (2020) 128455. Copyright 2018 Elsevier.)*

fluorescence signal can be observed at the pH of 5. The protonation process destroys the π-electron conjugated state, resulting in the fluorescence quenching of TCCP. In contrast, when the pH is higher than 7, the fluorescence intensity of the YTNMs nanoprobe at 645 nm increases gradually, which results from the imino deprotonation of the TCCP skeleton in YTNMs under an alkaline medium. In the pH range from 7 to 12.5, the response in ΔF exhibits a linear relationship toward the pH value (Fig. 12.21B). The calibration curve obeys with the linear coefficient of 0.994. Customarily, the YTNMs strip had no fluorescence under ultraviolet radiation (Fig. 12.21C). After the addition of different pH samples, the YTNMs strip presented a bright red color (Fig. 12.21D and E). The standard images (Fig. 12.21F and G) and final ΔRGB map (Fig. 12.21H) before and after pH response are automatically achieved using an Intelligent Identification System for Visual Chip. As shown in Fig. 12.21E, the red fluorescent color of the YTNMs strip gradually gets

brighter with the increasing pH values, which is in accordance with the gradually apparent color change of the final RGB difference map (Fig. 12.21H). It realizes the visual monitoring of pH. The calibration curve obeys with R^2 of 0.9708, realizing the digital output for *p*H sensing. To further estimate practicability of YTNMs for pH sensing, river water, tap water and deionized water are applied to prepare the real sample solutions with different pH values. The fluorescence of YTNMs solutions gradually increased with the growing pH values. No obvious fluorescence differences in three real samples were observed at the same pH value. In addition, the fluorescence response also exhibited a linear relation toward the pH change [60].

Liu et al. prepared a broad-range pH sensor with exceptional stability based on the robust framework of UiO-67-bpy, using PSM methods. After the incorporation of Eu^{3+} ions onto UiO-67-bpy, the β-diketonate ligand BTA (BTA = benzoyltrifluoroacetone) was coordinated with the unsaturated Eu^{3+} ions to construct a six-membered chelate ring. Eu^{3+} ions with a new coordination environment displayed a broad-range luminescence response to the aqueous solution pH value (ranging from 1.05 to 9.85). As is illustrated in Fig. 12.22A (left), the emission spectra of UiO-67-bpy-Eu-BTA in aqueous

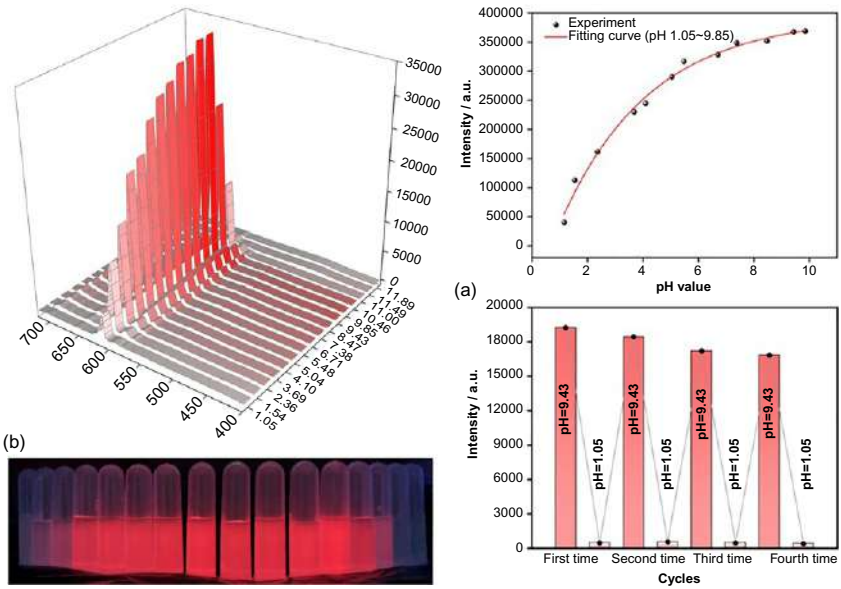

FIG. 12.22 *(Left)* (A) Emission spectra of UiO-67-bpy-Eu-BTA in solutions with pH ranging from 1.05 to 11.89 (λ_{ex} = 363 nm). (B) Photograph of UiO-67-bpy-Eu-BTA in solutions with pH ranging from 1.05 to 11.89 under a 365-nm UV light. *(Right, Top)* Relationship between the fluorescence intensity of UiO-67-bpy-Eu-BTA (at 612 nm) and pH values ranging from 1.05 to 9.85. *(Right, Bottom)* Luminescence intensity of UiO-67-bpy-Eu-BTA at 612 nm after four recycles (λ_{ex} = 363 nm). *(Reproduced with permission from T. Liu, B. Yan, A stable broad-range fluorescent pH sensor based on Eu3 + post-synthetic modification of metal-organic framework. Ind. Eng. Chem. Res. 59 (2020) 1764–1771. Copyright 2020 American Chemical Society.)*

solutions at different pH values indicate that the fluorescence intensity of the solution ($^5D_0 \rightarrow {}^7F_J$, J = 0–4) is positively correlated with pH values ranging from 1.05 to 9.85. Fig. 12.22B (left) shows that the changing trend of fluorescence intensity is visible to the naked eye. Such a quantitative relationship can be fitted well, with R^2 of 0.9899. The fitting curve is shown in Fig. 12.22 (right, top). The quenching effect at pH above 9.85 can be ascribed to partial hydrolysis of zirconium ions, and the structure of the framework is ruined in aqueous solutions with a pH value over 11.49. These results are sufficient to indicate the potential applications of UiO-67-bpy-Eu-BTA in broad-range pH sensing of aqueous solutions. As exhibited in Fig. 12.22 (right, bottom), even after the four sequential cycles, the probe can still emit the characteristic luminescence of Eu^{3+} and the fluorescence intensity is basically recoverable [61].

References

[1] X.D. Wang, O.S. Wolfbeis, R.J. Meier, Luminescent probes and sensors for temperature, Chem. Soc. Rev. 42 (2013) 7834–7869.

[2] Y. Cui, F. Zhu, B. Chen, G. Qian, Metal-organic frameworks for luminescence thermometry, Chem. Commun. 51 (2015) 7420–7431.

[3] D. Jaque, F. Vetrone, Luminescence nanothermometry, Nanoscale 4 (2012) 4301–4326.

[4] C.D.S. Brites, P.P. Lima, N.J.O. Silva, A. Millan, V.S. Amaral, F. Palacio, L.D. Carlos, Lanthanide-based luminescent molecular thermometers, New J. Chem. 35 (2011) 1177–1183.

[5] C.D. Brites, P.P. Lima, N.J. Silva, A. Millan, V.S. Amaral, F. Palacio, L.D. Carlos, Thermometry at the nanoscale, Nanoscale 4 (2012) 4799–4829.

[6] E.J. McLaurin, L.R. Bradshaw, D.R. Gamelin, Chem. Mater. 25 (2011) 1283–1292.

[7] K. Okabe, N. Inada, C. Gota, Y. Harada, T. Funatsu, S. Uchiyama, Intracellular temperature mapping with a fluorescent polymeric thermometer and fluorescence lifetime imaging microscopy, Nat. Commun. 3 (2012) 705.

[8] L.D. Carlos, R.A.S. Ferreira, V. de Zea Bermudez, B. Julian-Lopez, P. Escribano, Progress on lanthanide-based organic-inorganic hybrid phosphors, Chem. Soc. Rev. 40 (2011) 536–549.

[9] Y. Cui, H. Xu, Y. Yue, Z. Guo, J. Yu, Z. Chen, J. Gao, Y. Yang, G. Qian, B. Chen, A luminescent mixed-lanthanide metal–organic framework thermometer, J. Am. Chem. Soc. 134 (2012) 3979–3982.

[10] X. Rao, T. Song, J. Gao, Y. Cui, Y. Yang, C. Wu, B. Chen, G. Qian, A highly sensitive mixed lanthanide metal–organic framework self-clibrated luminescent thermometer, J. Am. Chem. Soc. 135 (2013) 15559–15564.

[11] K. Miyata, Y. Konno, T. Nakanishi, A. Kobayashi, M. Kato, K. Fushimi, Y. Hasegawa, Chameleon luminophore for sensing temperatures: control of metal-to-metal and energy back transfer in lanthanide coordination polymers, Angew. Chem. Int. Ed. 52 (2013) 6413–6416.

[12] Y. Cui, W. Zou, R. Song, J. Yu, W. Zhang, Y. Yang, G. Qian, A ratiometric and colorimetric luminescent thermometer over a wide temperature range based on a lanthanide coordination polymer, Chem. Commun. 50 (2014) 719–721.

[13] Y. Zhou, B. Yan, F. Lei, Postsynthetic lanthanide functionalization of nanosized metal-organic frameworks for highly sensitive ratiometric luminescent thermometry, Chem. Commun. 50 (2014) 15235–15238.

[14] R. Zhao, X. Rao, J. Yu, Y. Cui, Y. Yang, G. Qian, Design and synthesis of an MOF thermometer with high sensitivity in the physiological temperature, Inorg. Chem. 54 (2015) 11193–11199.

[15] X. Liu, S. Akerboom, M. de Jong, I. Mutikainen, S. Tanase, A. Meijerink, E. Bouwman, Mixed-lanthanoid metal–organic framework for ratiometric cryogenic temperature sensing, Inorg. Chem. 54 (2015) 11323–11329.
[16] S. Zhao, L. Li, X. Song, M. Zhu, Z. Hao, X. Meng, L. Wu, J. Feng, S. Song, C. Wang, H. Zhang, Lanthanide ion codoped emitters for tailoring emission trajectory and temperature sensing, Adv. Funct. Mater. 25 (2015) 1463–1469.
[17] X. Shen, B. Yan, Polymer hybrid thin films based on rare earth ion-functionalized MOF: photoluminescence tuning and sensing as a thermometer, Dalton Trans. 44 (2015) 1875–1881.
[18] X. Shen, Y. Lu, B. Yan, Lanthanide complex hybrid system for fluorescent sensing as thermometer, Eur. J. Inorg. Chem. 2015 (2015) 916–919.
[19] G.E. Gomez, A.M. Kaczmarek, R. Van Deun, E.V. Brusau, G.E. Narda, D. Vega, M. Iglesias, E. Gutierrez-Puebla, M.A. Monge, Photoluminescence, unconventional-range temperature sensing, and efficient catalytic activities of lanthanide metal-organic frameworks, Eur. J. Inorg. Chem. 2016 (2016) 1577–1588.
[20] I. N'Dala-Louika, D. Ananias, C. Latouche, R. Dessapt, L.D. Carlos, H. Serier-Brault, Ratiometric mixed Eu-Tb metal-organic framework as a new cryogenic luminescent thermometer, J. Mater. Chem. C 5 (2017) 10933–10937.
[21] T. Xia, F. Zhu, K. Jiang, Y. Cui, Y. Yang, G. Qian, A luminescent ratiometric pH sensor based on a nanoscale and biocompatible Eu/Tb-mixed MOF, Dalton Trans. 46 (2017) 7549–7555.
[22] A.M. Kaczmarek, Y. Liu, C. Wang, B. Laforce, L. Vincze, P. Van Der Voort, R. Van Deun, Grafting of a Eu^{3+}-tfac complex on to a Tb^{3+}-metal organic framework for use as a ratiometric thermometer, Dalton Trans. 46 (2017) 12717–12723.
[23] H. Wang, D. Zhao, Y. Cui, Y. Yang, G. Qian, A Eu/Tb-mixed MOF for luminescent high-temperature sensing, J. Solid State Chem. 246 (2017) 341–345.
[24] D. Zhao, D. Yue, L. Zhang, K. Jiang, G. Qian, Cryogenic luminescent Tb/Eu-MOF thermometer based on a fluorine-modified tetracarboxylate ligand, Inorg. Chem. 57 (2018) 12596–12602.
[25] X. Guo, L. Zhou, L. Cai, Q. Sun, Self-assembled bright luminescent lanthanide-organic polyhedra for ratiometric temperature sensing, Chem. A Eur. J. 24 (2018) 6936–6940.
[26] D. Zhao, H. Wang, G. Qian, Synthesis, structure and temperature sensing of a lanthanide-organic framework constructed from a pyridine-containing tetracarboxylic acid ligand, CrstEngComm 20 (2018) 7395–7400.
[27] Y. Zhu, T. Xia, Q. Zhang, Y. Cui, Y. Yang, G. Qian, A Eu/Tb mixed lanthanide coordination polymer with rare 2D thick layers: synthesis, characterization and ratiometric temperature sensing, J. Solid State Chem. 259 (2018) 98–103.
[28] C. Xia, C. Yu, M. Cao, J. Xia, D. Jiang, G. Zhou, D. Zhang, H. Li, A Eu and Tb co-doped MOF-5 compound for ratiometric high temperature sensing, Ceram. Int. 44 (2018) 21040–21046.
[29] X. Yang, H. Zou, X. Sun, T. Sun, C. Guo, Y. Fu, C.L. Wu, X. Qiao, F. Wang, One-step synthesis of mixed lanthanide metal-organic framework films for sensitive temperature mapping, Adv. Opt. Mater. 7 (2019) 1900336.
[30] X. Zhou, H. Wang, S. Jiang, G. Xiang, X. Tang, X. Luo, L. Li, X. Zhou, Multifunctional luminescent material Eu(III) and Tb(III) complexes with pyridine-3,5-dicarboxylic acid linker: crystal structures, tunable emission, energy transfer, and temperature sensing, Inorg. Chem. 58 (2019) 3780–3788.
[31] D. Zhao, D. Yue, K. Jiang, L. Zhang, C. Li, G. Qian, Isostructural Tb^{3+}/Eu^{3+} co-doped metal–organic framework based on pyridine-containing dicarboxylate ligands for ratiometric luminescence temperature sensing, Inorg. Chem. 58 (2019) 2637–2644.

[32] Y. Pan, H. Su, E. Zhou, H. Yin, K. Shao, Z. Su, A stable mixed lanthanide metal-organic framework for highly sensitive thermometry, Dalton Trans. 48 (2019) 3723–3729.
[33] F. Zhang, J. Li, Z. Zhao, F. Wang, Y. Pu, H. Cheng, Mixed-LnMOFs with tunable color and white light emission together with multi-functional fluorescence detection, J. Solid State Chem. 280 (2019), 120972.
[34] Y. Yang, Y. Wang, Y. Feng, X. Song, C. Cao, G. Zhang, W. Liu, Three isostructural Eu^{3+}/Tb^{3+} co-doped MOFs for wide-range ratiometric temperature sensing, Talanta 208 (2020), 120354.
[35] S. Wang, J. Jiang, Y. Lu, J. Liu, X. Han, D. Zhao, C. Li, Ratiometric fluorescence temperature sensing based on single- and dual-lanthanide metal-organic frameworks, JOL 226 (2020), 117418.
[36] H. Wang, S. Jiang, L. Xiang, Y. Yan, G. Xiang, Y. Li, X. Luo, L. Li, X. Tang, X. Zhou, Synthesis and characterization of Tb^{3+}/Eu^{3+} complexes based on 2,4,6-tris-(4-carboxyphenyl)-1,3,5-triazine ligand for ratiometric luminescence temperature sensing, Spectrochim. Acta A Mol. Biomol. Spectrosc. 244 (2021), 118781.
[37] X. Song, M. Zhang, C. Wang, A.A.A. Shamshooma, H. Meng, W. Xi, Mixed lanthanide coordination polymers for temperature sensing and enhanced NdIII NIR luminescence, JOL 201 (2018) 410–418.
[38] Y. Yang, L. Chen, F. Jiang, M. Yu, X. Wan, B. Zhang, M. Hong, A family of doped lanthanide metal-organic frameworks for wide-range temperature sensing and tunable white light emission, J. Mater. Chem. C 5 (2017) 1981–1989.
[39] H. Li, W. Han, R. Lv, A. Zhai, X. Li, W. Gu, X. Liu, Dual-function mixed-lanthanide metal−-organic framework for ratiometric water detection in bioethanol and temperature sensing, Anal. Chem. 91 (2019) 2148–2154.
[40] D. Zhao, J. Zhang, D. Yue, X. Lian, Y. Cui, Y. Yang, G. Qian, A highly sensitive near-infrared luminescent metal-organic framework thermometer in the physiological range, Chem. Commun. 52 (2016) 8259–8262.
[41] D. Zhao, X. Han, S. Wang, J. Liu, Y. Lu, C. Li, 808nm-Light-excited near-infrared luminescent lanthanide metal-organic frameworks for highly sensitive physiological temperature sensing, Chem. A Eur. J. 26 (2020) 3145–3151.
[42] L. Li, Y. Zhu, X. Zhou, C.D.S. Brites, D. Ananias, Z. Lin, F.A.A. Paz, J. Rocha, W. Huang, L. D., Visible-light excited luminescent thermometer based on single lanthanide organic frameworks, Adv. Funct. Mater. 26 (2016) 8677–8684.
[43] T. Xia, Y. Cui, Y. Yang, G. Qian, A luminescent ratiometric thermometer based on thermally coupled levels of a Dy-MOF, J. Mater. Chem. C 5 (2017) 5044–5047.
[44] J. Feng, S. Gao, T. Liu, J. Shi, R. Cao, Preparation of dual-emitting ln@UiO-66-hybrid films via electrophoretic deposition for ratiometric temperature sensing, ACS Appl. Mater. Interfaces 10 (2018) 6014–6023.
[45] H. Yan, H. Ni, J. Jia, C. Shan, T. Zhang, Y. Gong, X. Li, J. Cao, W. Wu, W. Liu, Y. Tang, Smart all-in-one thermometer-heater nanoprobe based on postsynthetical functionalization of a Eu(III)-metal−organic framework, Anal. Chem. 91 (2019) 5225–5234.
[46] Y. Cui, R. Song, J. Yu, M. Liu, Z. Wang, C. Wu, Y. Yang, Z. Wang, B. Chen, G. Qian, Dual-emitting MOF⊃dye composite for ratiometric temperature sensing, Adv. Mater. 27 (2015) 1420–1425.
[47] J. Liu, Y. Zhao, X. Li, J. Wu, Y. Han, X. Zhang, Y. Xu, Dual-emissive $CsPbBr_3$@Eu-BTC composite for self-calibrating temperature sensing application, Cryst. Growth Des. 20 (2020) 454–459.
[48] Q. Li, Z. Yuan, J. Qian, S. Du, Chemical stability and tunable luminescence of ln(III)-K(I) coordination polymers featuring a tracery-like architecture, RSC Adv. 5 (2015) 49110–49114.

[49] S. Sun, J. Zhang, Z. Wang, Y. Yu, C. Zhu, M. Pan, C. Su, Anomalous thermally-activated NIR emission of ESIPT modulated Nd-complexes for optical fiber sensing devices, Chem. Commun. 54 (2018) 6304–6307.

[50] Y. Kitagawa, M. Kumagai, P.P.F. da Rosa, K. Fushimi, Y. Hasegawa, Long-range LMCT coupling in EuIII coordination polymers for an effective molecular luminescent thermometer, Chem. A Eur. J. 27 (2021) 264–269.

[51] D. Parker, Luminescent lanthanide sensors for pH, pO2 and selected anions, Coord. Chem. Rev. 205 (2000) 109–130.

[52] D. Wencel, T. Abel, C. McDonagh, Optical chemical pH sensors, Anal. Chem. 86 (2014) 15–29.

[53] R.D. Vaughan-Jones, K.W. Spitzer, P. Swietach, Intracellular pH regulation in heart, J. Mol. Cell. Cardiol. 46 (2009) 318–331.

[54] Y. Han, C. Tian, Q. Li, S. Du, Highly chemical and thermally stable luminescent Eu_xTb_{1-x}MOF materials for broad-range pH and temperature sensors, J. Mater. Chem. C 2 (2014) 8065–8070.

[55] Y. Lu, B. Yan, A ratiometric fluorescent pH sensor based on nanoscale metal-organic frameworks (MOFs) modified by europium(III) complexes, Chem. Commun. 50 (2014) 13323–13326.

[56] T. Xia, Y. Cui, Y. Yang, G. Qian, Highly stable mixed-lanthanide metal-organic frameworks for self-referencing and colorimetric luminescent pH sensing, ChemNanoMat 3 (2017) 51–57.

[57] Y. Huang, B. Liu, Q. Shen, X. Zhu, Y. Hao, Z. Chang, F. Xu, P. Qu, M. Xu, Lanthanide coordination polymer probe for time-gated luminescence sensing of pH in undiluted human serum, Talanta 164 (2017) 427–431.

[58] Y. Li, Y. Wang, Q. Liu, The highly connected MOFs constructed from nonanuclear and trinuclear lanthanide-carboxylate clusters: selective gas adsorption and luminescent pH sensing, Inorg. Chem. 56 (2017) 2159–2164.

[59] X. Zhang, K. Jiang, H. He, D. Yue, D. Zhao, Y. Cui, Y. Yang, G. Qian, A stable lanthanide-functionalized nanoscale metal-organic framework as a fluorescent probe for pH, Sens. Actuators B 254 (2018) 1069–1077.

[60] X. Wang, C. Chu, Y. Wu, Y. Deng, J. Zhou, M. Yang, S. Zhang, D. Huo, C. Hou, Synthesis of yttrium(III)-based rare-earth metal-organic framework nanoplates and its applications for sensing of fluoride ions and pH, Sens. Actuators B 321 (2020), 128455.

[61] T. Liu, B. Yan, A stable broad-range fluorescent pH sensor based on Eu^{3+} post-synthetic modification of metal-organic framework, Ind. Eng. Chem. Res. 59 (2020) 1764–1771.

[62] S. Huang, S. Liu, H. Zhang, Z. Han, G. Zhao, X. Dong, S. Zang, Dual-functional proton-conducting and pH-sensing polymer membrane benefiting from a Eu-MOF, ACS Appl. Mater. Interfaces 12 (2020) 28720–28726.

Chapter 13

Molecular logic gate operations of rare earth metal-organic framework hybrid materials for luminescence responsive chemical sensing

13.1 Molecular Boolean logic gates

Rapid growth in the diversity of luminescent chemosensors has laid the groundwork for the emergence of molecule-based logic gates. The modulation of different types of luminescent response processes provides clear "Off-On" or "On-Off" switching characteristics, color changes in absorbance or emission, which typically accompany internal charge transfer or related processes. This increases the chances of signal generation dramatically. The first explicit utilization of a color change in molecular logic design demonstrated that multiple logic behaviors can be extracted from a single system by changing the wavelength of excitation and/or detection. With the recruitment of new photophysical processes, the hunt for chemical equivalents of all 16 Boolean logic operators began. More complicated digital designs will soon follow. Simple molecular Boolean logic gates can be integrated to obtain more complicated combinational molecular gates, allowing a single molecule to process complex operations [1–7].

Zhang et al. constructed a Boolean logical library based on MOFs (MIL-61, Ga-MOF, with linker 1,2,4,5-benzenetetracarboxylic acid (H_4btec)). In this library, MIL-61 and its postsynthesis product (Eu^{3+}@MIL-61) are employed as a signal transducer that exhibits a luminescence change visible to the naked eye under UV lamp. The library embodies some basic logic gates (NOT, NAND, INHIBIT, XNOR), a two-output combinational logic gate, and a cascaded logic gate. Moreover, they also constructed an encoder (to convert data to code), and a parity checker (to distinguish even numbers and odd numbers), which can perform nonarithmetic tasks for further application. The new route for the design of a molecular logic gate library based on RE-MOFs proposed a new possibility for its application. More importantly, this attempt can further

Rare Earth Metal-Organic Framework Hybrid Materials for Luminescence Responsive Chemical Sensors
https://doi.org/10.1016/B978-0-323-91236-5.00009-8

close the gap between RE-MOFs and electrical circuitries and expanded the application of RE-MOFs in the field of molecular logic gates.

13.1.1 Basic molecular Boolean logic gate operation

In terms of this theoretical analysis, a few basic logic gate (NOT, NAND, INHIBIT, XNOR) designs are shown. In this Boolean logical library, the fluorescence of MIL-61 (λ_{375nm}) and Eu^{3+}@MIL-61 (λ_{615nm}) was used as the output with a threshold of 0.5. **(1) The realization of NOT logic gate.** Of all basic logic gates, the NOT logic gate is the simplest to implement using only one input. But it is an important member of the basic logic gate family, and many complex logic calculations must rely on simple logic gates like it. In NOT logic, the output is the opposite of the input. Considering that Fe^{3+} is a fluorescence quencher of many MOFs in the literature, the researchers used Fe^{3+} as the input to construct a NOT gate based on Eu^{3+}@MIL-61 while its fluorescence intensity was used as output. As a result, the fluorescence of Eu^{3+}@MIL-61 is quenched as shown in Fig. 13.1B (left). Inspired by this, they designed a NOT logic gate using λ_{615nm} as the output and Fe^{3+} as input. The presence and absence of Fe^{3+} are denoted as 1 and 0, respectively, with a threshold value of 0.5. When Fe^{3+} is added to the system, the input can be denoted as 1, the fluorescence of Eu^{3+}@MIL-61 is quenched, and the output is 0. The switch effect of Fe^{3+} on the fluorescence intensity is in line with the principle of the NOT gate. The electronic equivalent circuitry and truth table of the NOT gate are also depicted in Fig. 13.1 (left). **(2) The realization of NAND logic gate.** Since the digital NAND logic gate is the inverse of an AND gate, the output signal is 0 only if all inputs are 1. Using this concept, the group constructed a NAND logic gate based on MIL-61. In this NAND logic gate, H^+, Fe^{2+}, and $S_2O_8^{2-}$ are employed as three inputs and the fluorescence of MIL-61 (λ_{375nm}) is the output with a threshold of 1. As can be ascertained from Fig. 13.1C (right), only when all these three ions are added in the MIL-61 system, that is the input is (1/1/1), is the fluorescence quenched, resulting in the output of 0. Upon the addition of $S_2O_8^{2-}$ and H^+ in the solution of MIL-61 containing Fe^{2+}, Fe^{2+} can be oxidized to Fe^{3+}. Fe^{3+} has a quenching effect on the fluorescence, as mentioned previously, so the fluorescence is weak in the presence of these three inputs. It can be seen that only when the three of them coexist does the fluorescence intensity of the MOF change and result in the output 0, so the effect of these three ions is in line with the design principles of NAND logic gates. The truth table is shown in Fig. 13.1D (right). **(3) The realization of INHIBIT logic gate.** Fig. 13.2A (left) shows the design of an INHIBIT gate by using Eu^{3+}@MIL-61 as a signal transducer with output of λ_{615nm}. An INHIBIT gate is a special case of the AND gate, the difference being that in the INHIBIT gate one of the two input lines has an inversion system (NOT gate). Ag^+ and cysteine were designed as the two inputs to construct the INHIBIT gate because of the Ag-thiols interaction. As can be seen from the

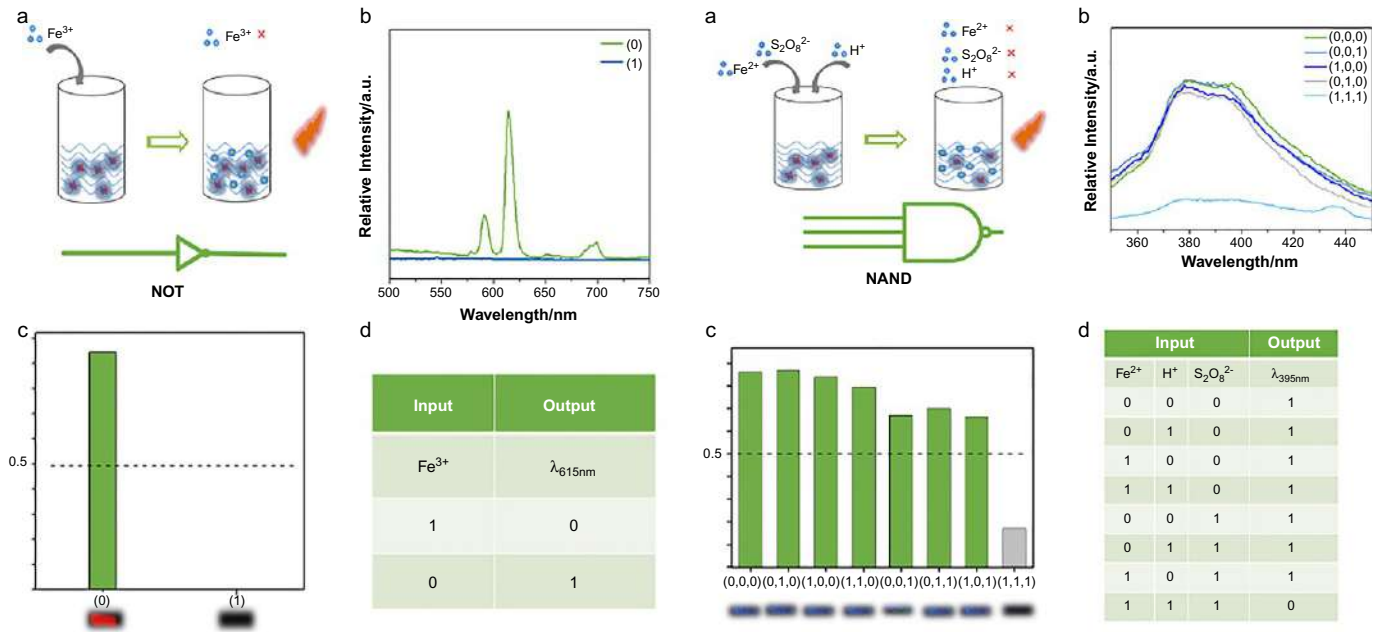

FIG. 13.1 *(Left)* (A) The scheme and electronic equivalent circuitry of NOT logic gate. (B) Luminescent spectra of the NOT gate with the input of Fe^{3+}. (C) Column diagram of the fluorescence intensity: the dashed line shows the threshold. (D) The truth table of the NOT gate. *(Right)* (A) The scheme and electronic equivalent circuitry of NAND logic gate. (B) Luminescent spectra of the NAND gate with the inputs of H^+, Fe^{2+}, and $S_2O_8^{2-}$. (C) Column diagram of the fluorescence intensity: the dashed line shows the threshold. (D) The truth table of the NAND gate. *(Reproduced with permission from Y. Zhang, B. Yan, MIL-61 and Eu3+@MIL-61 as signal transducers to construct an intelligent Boolean logical library based on visualized luminescent metal organic frameworks. ACS Appl. Mater. Interfaces 11 (2019) 20125-20133. Copyright 2019 American Chemical Society.)*

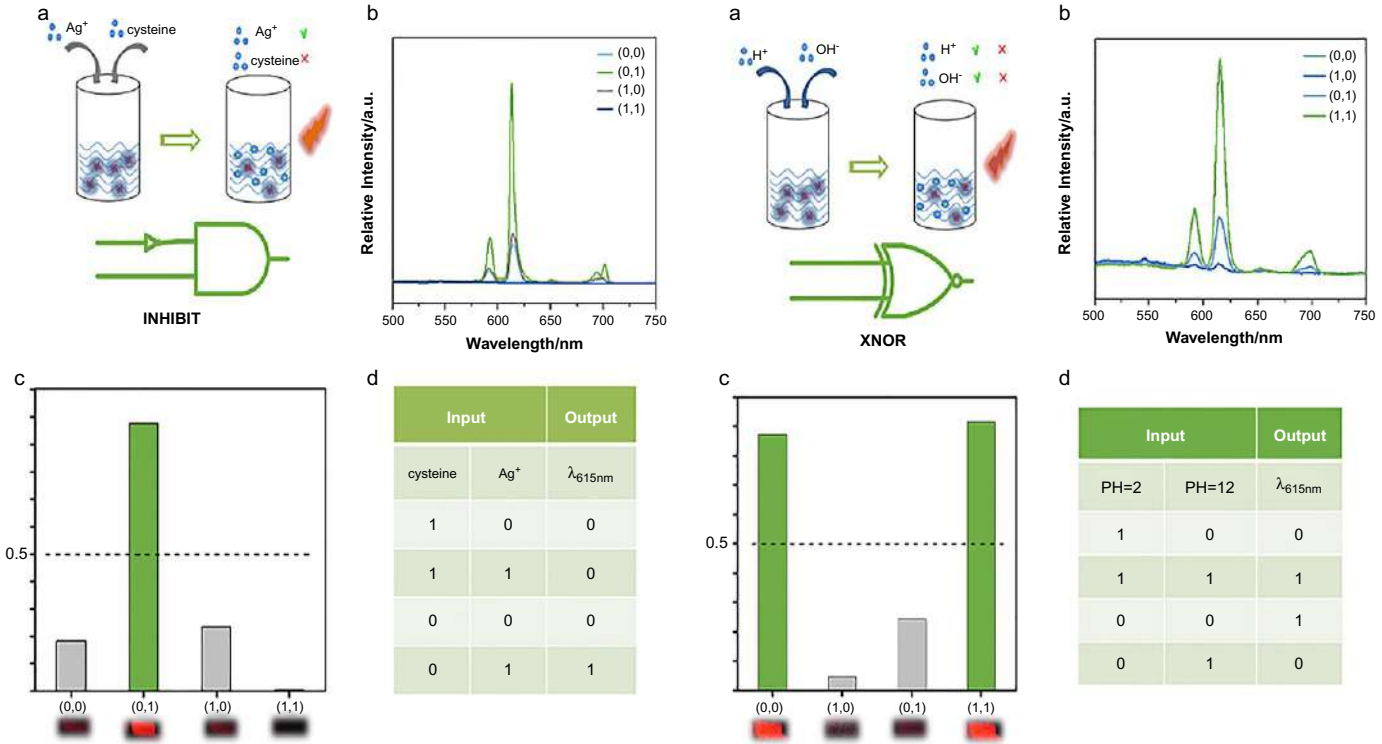

FIG. 13.2 *(Left)* (A) The scheme and electronic equivalent circuitry of INHIBIT logic gate. (B) Luminescent spectra of the INHIBIT gate with the inputs of Ag^+ and cysteine. (C) Column diagram of the fluorescence intensity: the dashed line shows the threshold. (D) The truth table of the INHIBIT gate. *(Right)* (A) The scheme and electronic equivalent circuitry of XNOR logic gate. (B) Luminescent spectra of the XNOR gate with the inputs of pH 2 and pH 12. (C) Column diagram of the fluorescence intensity: the dashed line shows the threshold. (D) The truth table of the XNOR gate. *(Reproduced with permission from Y. Zhang, B. Yan, MIL-61 and Eu3+@MIL-61 as signal transducers to construct an intelligent Boolean logical library based on visualized luminescent metal organic frameworks. ACS Appl. Mater. Interfaces 11 (2019) 20125-20133. Copyright 2019 American Chemical Society.)*

histogram in Fig. 13.2C (left), only the presence of Ag^+ caused the fluorescence to increase greatly. This is because the presence of Ag^+ (0/1) can induce more efficient energy transfer from the ligand to the Eu^{3+} ions, which can result in a great enhancement of fluorescence. As is known, there is an Ag-thiols interaction between Ag^+ and cysteine, so the presence of both Ag^+ and cysteine (1/1) can destroy the induction of Ag^+ and quench the fluorescence. As for the inputs of (0/0) and (1/0), although the fluorescence is not quenched, the intensity of the fluorescence cannot reach the threshold, so the output remains 0. Therefore the interaction between Ag^+ ions and cysteine, which can affect the fluorescence intensity of the MOF, is in accordance with the design principles of INHIBIT logic gates. **(4) The realization of XNOR logic gate.** XNOR can be seen as an exclusive NOR gate. In a XNOR gate, the output is "true" if the inputs are the same and the output is "false" if the inputs are different. This means that the output is 1 only if all of the inputs are either present or absent. Fig. 13.2A (right) depicts the construction of the XNOR logic gate. It can be concluded from the luminescent spectra in Fig. 13.2B (right) that both the lower pH (2) and higher pH (12) can weaken the fluorescence of Eu^{3+}@MIL-61, so an XNOR logic gate can be constructed based on this. When the deionized water (0/0) and equimolar solutions of pH 2 and pH 12 (1/1) are added, the fluorescence of Eu^{3+}@MIL-61 is not affected, because the equal amount of acid and base mix makes the solution neutral. The effect of pH 2 and pH 12 is also in line with the design principles of XNOR logic gates. When Eu^{3+}@MIL-61 is exposed to a strong acid or a strong base with inputs (1/0) or (0/1), they speculated that strong acidity and alkalinity can disrupt the energy transfer between Eu^{3+} and the ligand, so the fluorescence is quenched.

13.1.2 Implementation of a two-output combinational logic gate

Basic logic gates tend to be incapable of accepting a high volume of information and thus are unsuitable for constructing more complex circuits, so the implementation of combinational logic gates is urgently needed. Zhang et al. experimentally realized a combinational logic gate composed of a NOT gate and a NAND gate. In this two-output combinational logic gate, Fe^{3+} and EDTA were used as inputs while the fluorescence of MIL-61 (λ_{375nm}) and Eu^{3+}@MIL-61 (λ_{615nm}) was used as two outputs. From Fig. 13.3B (left), it can be found that Fe^{3+} can quench the fluorescence of both MIL-61 (λ_{375nm}) and Eu^{3+}@MIL-61 (λ_{615nm}) while EDTA can only quench the fluorescence at 615 nm. So if the Fe^{3+} is present (the inputs are 1/1 and 0/1), both the two outputs are (0/0). Another situation occurs if the Fe^{3+} is not present but EDTA is (the input is 1/0): because of the chelation of Eu^{3+} by EDTA, the fluorescence at 615 nm is quenched while at 395 nm it still exists, and so the output is (1/0). When neither Fe^{3+} nor EDTA exists, neither the fluorescence of MIL-61 (λ_{375nm}) nor that of Eu^{3+}@MIL-61 (λ_{615nm}) is affected, so the output is (1/1). The effect of EDTA and Fe^{3+} on the

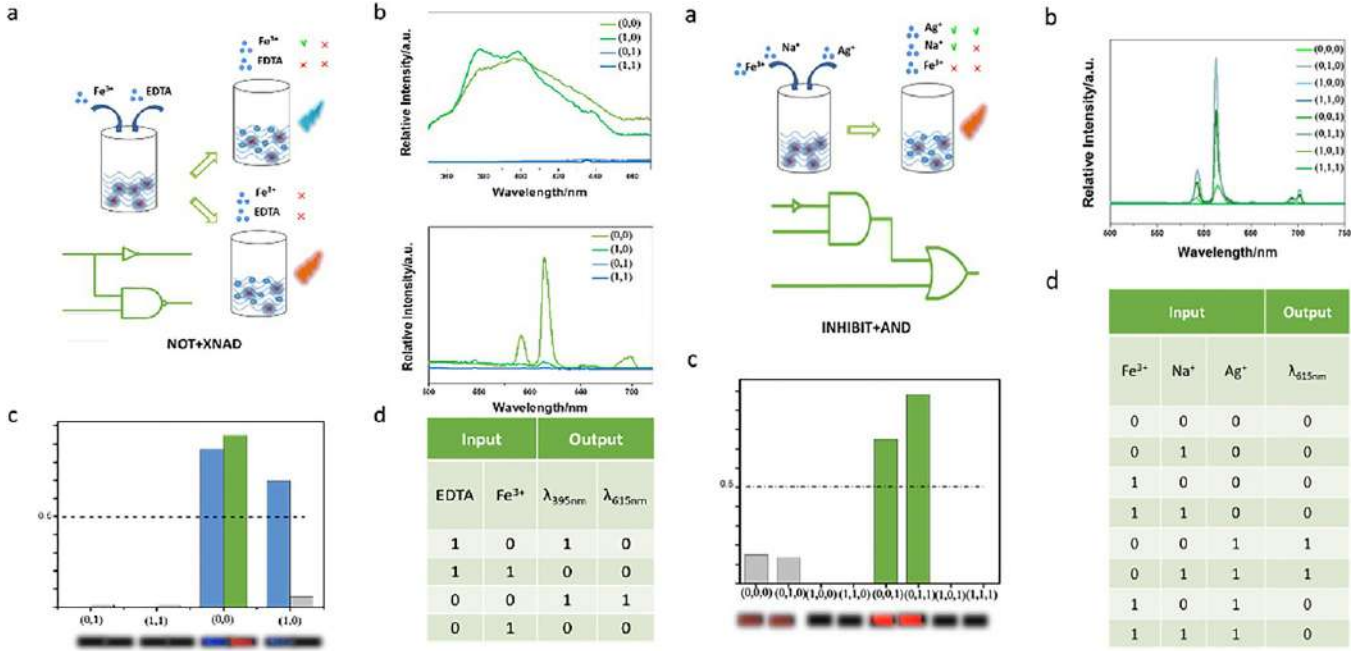

Input		Output	
EDTA	Fe^{3+}	λ_{395nm}	λ_{615nm}
1	0	1	0
1	1	0	0
0	0	1	1
0	1	0	0

Input			Output
Fe^{2+}	Na^{+}	Ag^{+}	λ_{615nm}
0	0	0	0
0	1	0	0
1	0	0	0
1	1	0	0
0	0	1	1
0	1	1	1
1	0	1	0
1	1	1	0

FIG. 13.3 *(Left)* (A) The scheme and electronic equivalent circuitry of the two-output combinational logic gate (NOT+XAND). (B) Luminescent spectra of the combinational logic gate. (C) Column diagram of the fluorescence intensity: the dashed line shows the threshold (the *blue* column represents the fluorescence of 395 nm while the *green* column represents the fluorescence of 615 nm). (D) The truth table of the two-output combinational logic gate. *(Right)* (A) The scheme and electronic equivalent circuitry of the cascaded logic gate (INHIBIT+AND). (B) Luminescent spectra of the cascaded logic gate. (C) Column diagram of the fluorescence intensity: the dashed line shows the threshold. (D) The truth table of the cascaded logic gate. *(Reproduced with permission from Y. Zhang, B. Yan, MIL-61 and Eu3+@MIL-61 as signal transducers to construct an intelligent Boolean logical library based on visualized luminescent metal organic frameworks. ACS Appl. Mater. Interfaces 11 (2019) 20125-20133. Copyright 2019 American Chemical Society.)*

fluorescence intensity of the MOF is in line with the design principles of the combination of NOT and XAND.

13.1.3 Implementation of a cascaded logic gate

The cascaded logic gate is another complex logic gate that is necessary for multilevel integrated circuits. In order to achieve the integrity of this logic gate library, a cascaded logic gate composed of an INHIBIT gate and an AND gate was constructed in this work. In the operation of the combinatorial gate, Ag^+, Fe^{3+}, and Na^+ were chosen as input 1, input 2, and input 3, respectively. The enhancement of fluorescence by Ag^+ and the quenching effect of Fe^{3+} on fluorescence have been mentioned before, and it can be seen from the luminescent spectra in Fig. 13.3B (right) that sodium ions have little effect on the fluorescence at 615 nm. It can clearly be seen through the truth table (Fig. 13.3D; right) that only when the inputs are (0/0/1, 0/1/1), the output is 1, whereas when the inputs are other than that case, the output is 0.

13.1.4 Implementation of logic devices (4-to-2 encoder and parity checker)

One of the most important applications of molecular logic gates is to perform nonarithmetic information processing. From this perspective, a 4-to-2 encoder and a parity checker based on this system were also implemented. An encoder is a device that processes signals or data into signals that can be used for communication, transmission, and storage. Zhang et al. constructed a 4-to-2 encoder based on MIL-61 and Eu^{3+}@MIL-61 that could convert four inputs into two outputs. In this encoder, the four inputs consisted of Fe^{3+}, EDTA, furazolidone, and Na^+ while the outputs were the fluorescence of MIL-61 (λ_{375nm}) or Eu^{3+}@MIL-61 (λ_{615nm}). The effect of Fe^{3+}, EDTA, and Na^+ on the fluorescence at 395 nm and 615 nm has been mentioned previously. In addition, it was found that furazolidone could quench the light at 395 nm and only slightly weaken the light at 615 nm. It can be concluded from the truth table in Fig. 13.4D (left) that this encoder can encode four inputs (1/0/0/0, 0/1/0/0, 0/0/1/0, 0/0/0/1) into four outputs (0/0, 1/0, 0/1, 1/1), respectively.

As for a parity checker, it can be used as a device to detect the presence of erroneous programs in data processing in addition to the simple application of identifying even numbers and odd numbers. In this parity checker, 10 decimal numbers are transformed into corresponding binary numbers, and then K^+, Na^+, Al^{3+}, and Ag^+ are used as four inputs and act as four bits in the meantime. From the truth table in Fig. 13.4D (right), it can be seen that the inputs 0/0/0/1, 0/0/1/1, 0/1/0/1, 0/1/1/1, and 1/0/0/1 are encoded into the output 1 with bright fluorescence, while the inputs 0/0/0/0, 0/0/1/1, 0/1/0/0, 0/1/1/0, and 1/0/0/0 are encoded into the output 0 with weak luminescence. From the photoluminescent spectra in Fig. 13.4B (right), it can be intuitively seen that all the odd numbers

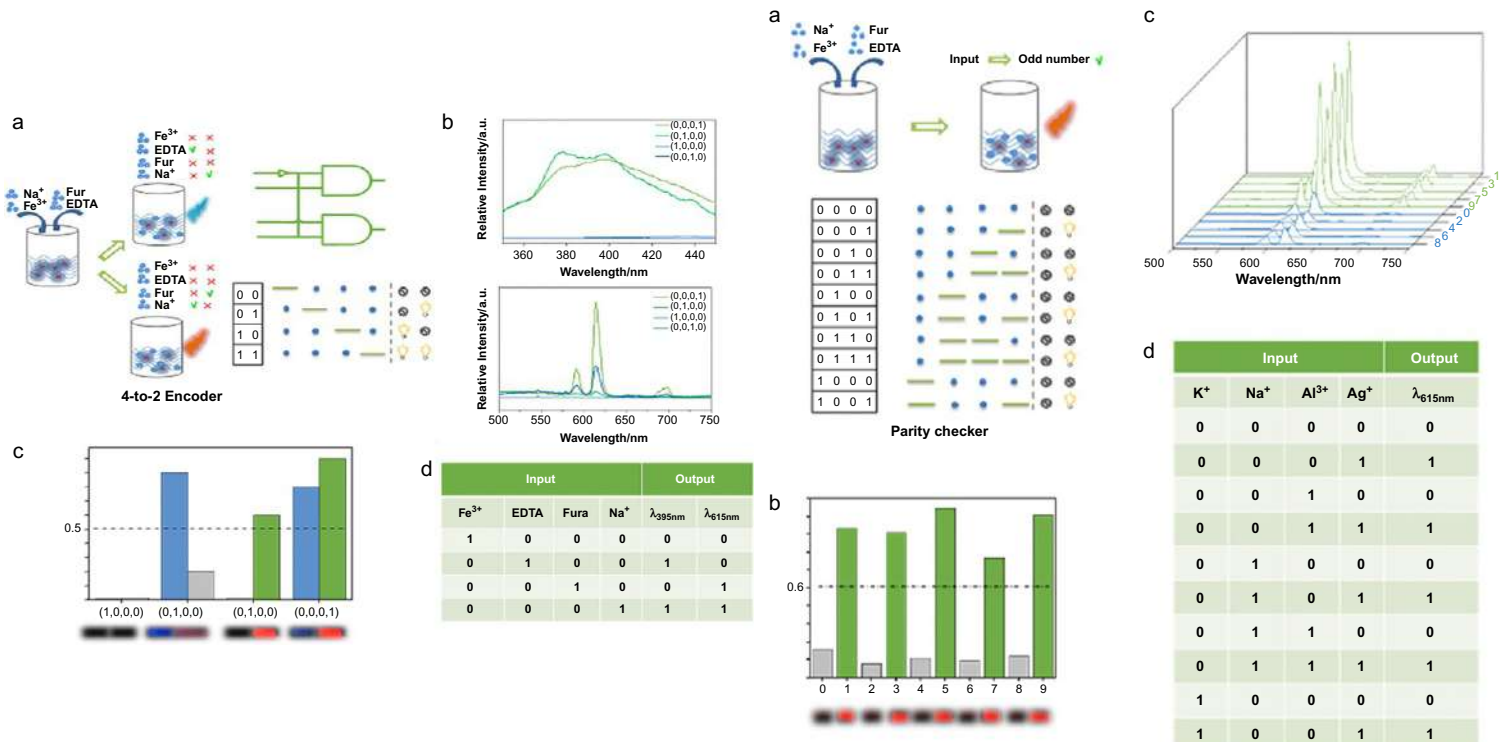

FIG. 13.4 (See figure legend on opposite page)

correspond to strong luminescence intensity, and all even numbers correspond to weak luminescence intensity, so this parity checker is a logical device that can distinguish odd and even numbers conveniently and quickly. What's more, this logical device can be applied to all natural number ranges because the parity of a natural number is determined by its single digit number.

13.2 Luminescence responsive sensing of rare earth metal-organic framework hybrid materials on luminescence for Boolean logic gates

Zhang et al. developed a general strategy for sensing of H_2S utilizing postsynthetic modification of a nano MOF UiO-66-$(COOH)_2$ with Eu^{3+} and Cu^{2+} ions. The constitution of Eu^{3+}@UiO-66-$(COOH)_2$ and Eu^{3+}/Cu^{2+}@UiO-66-$(COOH)_2$ were also verified by studying the spectra in HEPES buffer (pH 7.4) (Fig. 13.5). In the inclusion of Cu^{2+}, the fluorescence intensity of Eu^{3+} in Eu^{3+}/Cu^{2+}@UiO-66-$(COOH)_2$ is remarkably suppressed and the ligand-centered (LC) emission is obviously enhanced (Fig. 13.5A). The emission spectrum of the Eu^{3+}/Cu^{2+}@UiO-66-$(COOH)_2$ suspension allows the observation of two types of luminescence: one is the sharp characteristic emissions of Eu^{3+} and the other is the broad LC emission at 393 nm. The presence of the characteristic emissions of Eu^{3+} in the fluorescence emission spectra validate an energy transfer (ET) from the H_4btec ligands to Eu^{3+}, yet the strong LC emission in the fluorescence emission spectra suggests that the ET efficiency is low (the intensity ratio I_{615}/I_{393} of the $^5D_0 \rightarrow {}^7F_2$ line at 615 nm to that of LC emission at 393 nm is 0.45). In comparison, in the presence of sulfide, the enhanced Eu^{3+} luminescence and the decreased LC emission of Eu^{3+}/Cu^{2+}@UiO-66-$(COOH)_2$ demonstrated the more effective ET ($I_{615}/I_{393} = 4.16$). Moreover, with the two inputs Cu^{2+} (Input 1) and NaHS (Input 2), the emission properties of Eu^{3+}@UiO-66-$(COOH)_2$ are explained as the IMPLICATION type of logic gate. In this system, the presence and absence of the two chemical inputs Cu^{2+} and NaHS can be defined as 1 and 0 states, and the fluorescence intensity ratio of I_{615}/I_{393} as the output for the logic gate. Fig. 13.5A and B shows the luminescence features of the Eu^{3+}@UiO-66-$(COOH)_2$ in the presence of the four possible input combinations (Input 1, Input 2), which are (0, 0), (1, 0), (0, 1),

FIG. 13.4, CONT'D, *(Left)* (A) The scheme and electronic equivalent circuitry of the 4-to-2 encoder. (B) Luminescent spectra of the 4-to-2 encoder. (C) Column diagram of the fluorescence intensity: the dashed line shows the threshold (the *blue* column represents the fluorescence of 395 nm while the *green* column represents the fluorescence of 615 nm). (D) The truth table of the 4-to-2 encoder. *(Right)* (A) The scheme and logic system of the parity checker. (B) Luminescent spectra of the parity checker. (C) Column diagram of the fluorescence intensity: the dashed line shows the threshold. (D) The truth table of the parity checker. *(Reproduced with permission from Y. Zhang, B. Yan, MIL-61 and Eu3+@MIL-61 as signal transducers to construct an intelligent Boolean logical library based on visualized luminescent metal organic frameworks. ACS Appl. Mater. Interfaces 11 (2019) 20125-20133. Copyright 2019 American Chemical Society.)*

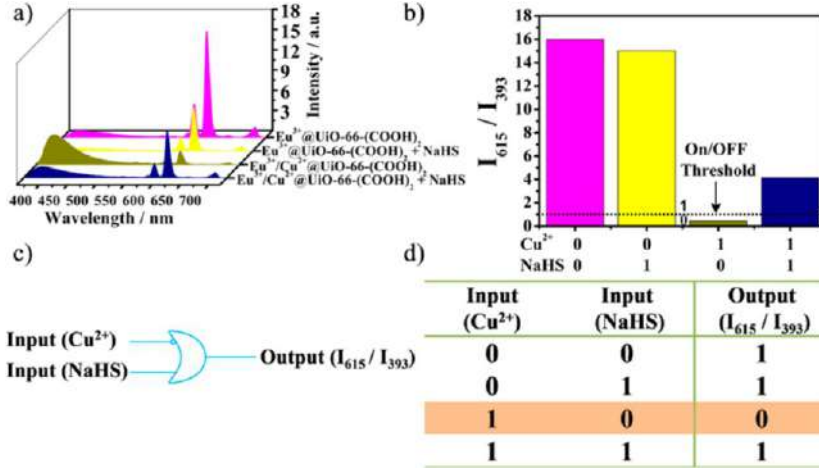

FIG. 13.5 Operations of the IMPLICATION logic gate. (A) Fluorescence spectra of Eu^{3+}@UiO-66-$(COOH)_2$ in the presence of four input modes: (*magenta*) no input; (*yellow*) 5 mM NaHS; (*dark yellow*) 1 mM Cu^{2+}; (*navy*) 5 mM NaHS and 1 mM Cu^{2+}. (B) Fluorescence intensity ratio (I_{615}/I_{393}) in the form of a bar representation, with a threshold of $I_{615}/I_{393}=1$ for output 1 or 0. (C) IMPLICATION logic gate represented using a conventional gate notation; an inactive output signal is obtained when $Cu^{2+}=1$ and NaHS = 0. (D) Truth table for the IMPLICATION logic gate; Cu^{2+} and NaHS are inputs to the system; fluorescence intensity ratio I_{615}/I_{393} is the output signal of Eu^{3+}@UiO-66-$(COOH)_2$. *(Reproduced with permission from X. Zhang, Q. Hu, T. Xia, J. Zhang, Y. Yang, Y. Cui, B. Chen, G. Qian, Turn-on and ratiometric luminescent sensing of hydrogen sulfide based on metal-organic frameworks. ACS Appl. Mater. Interfaces 8 (2016) 32259−32265. Copyright 2016 American Chemical Society.)*

and (1, 1). The fluorescence intensity ratio of I_{615}/I_{393} is greatly reduced only in the presence of Cu^{2+} (1, 0) due to the ET process. However, the fluorescence intensity ratio of I_{615}/I_{393} above the threshold level (1, I_{615}/I_{393}) is observed in the absence (0, 0) and presence of both the inputs (1, 1) and also NaHS alone (0, 1). Therefore monitoring the fluorescence intensity ratio of I_{615}/I_{393} and with the two inputs as Cu^{2+} and NaHS, an IMPLICATION-type logic gate can be constructed. The equivalent combinatorial logic circuit and truth table for the IMPLICATION logic gate are shown in Fig. 13.5C and D [8].

Xu et al. demonstrated and applied Eu(III) functionalized UiO(bpdc) (Eu^{3+}@UMOFs) dual-emission (B_{530} and R_{614}) fluorescence material for recognizing and connecting polluting ions (Hg^{2+}, Ag^{+}, and S^{2-}) in water. The mechanisms for multicomponent recognition can be attributed to the facts that (1) Hg^{2+} can enhance R_{614} by promoting ligand-to-Eu energy transfer; (2) Ag^{+} can quench G_{530} and R_{614} by ligand-to-Eu energy transfer; (3) S^{2-} can trigger B_{485} by producing a new complex. Taking these polluting ions in water as input events, elementary logic operations (NOR, INH, and IMP) and integrative logic operations (OR+INH) are implemented by observing the change in three fluorescence emission bands (B_{485}, G_{530}, and R_{614}). Compared to traditional single-output logic

circuits, the multiple outputs in this system can produce different logic operation by same-ions input, which can increase the information content in the logic library and further improve the ability of information processing. In the logic operations, Eu^{3+}@UMOFs serves as gates, while the polluting ions (Hg^{2+}, Ag^{+}, or S^{2-}) and emission change at 485 nm (B_{485}), 530 nm (G_{530}), and 614 nm (R_{614}) are used as chemical inputs and outputs, respectively. As demonstrated in Fig. 13.6 (top, left), the Eu^{3+}@UMOFs system only exhibits emission at 530 nm (G_{530}) in the absence of Hg^{2+}, Ag^{+}, and S^{2-}. But an obvious fluorescence Turn-Off response occurs for all the other input combinations, correlating well with the proper execution of NOR logic operation. Similarly, an identical NOR logic operation can be implemented by employing emission at 614 nm (R_{614}) as the output, while Ag^{+} and S^{2-} function as double inputs (Fig. 13.6C; top, left). A binary INH logic operation, which is represented by a situation in which the output is 1 only if one particular input is present and the other is absent, can be implemented as well as using emission at 485 nm (B_{485}) as output and Hg^{2+} and S^{2-} (Fig. 13.6B; top, left) as double inputs. These INH logic operations rely on the injection of S^{2-}. Only the addition of S^{2-} (input = 0/1) can trigger the B_{485} Turn-On response (output = 1) due to the destruction of the crystal framework and the formation of new complexes. On the basis of the fact that Ag^{2+} can also interact with S^{2-}, the INH logic operation was implemented by taking Ag^{+} and S^{2-} as double inputs (Fig. 13.6C; top, left). They also constructed an IMP logic operation by defining an R_{614} emission change as output. From the logic gate functions, the Turn-Off of R_{614} (output = 0) is observed only in the presence of one particular input and under other circumstances, output 1 will be observed. Eu^{3+}@UMOFs alone (input = 0/0) have R_{614} emission (output = 1), but the addition of Ag^{+} only (input = 0/1) triggers the fluorescence Turn-Off response (output = 0). However, the R_{614} intensity of Eu^{3+}@UMOFs shows significant fluorescence enhancement by binding to Hg^{2+}, which leads to the output 1 (Fig. 13.6A; top, left). When the Eu^{3+}@UMOFs is injected into the solution of two metal ions (input = 1/1), there is competition between fluorescence quenching by Ag^{+} and enhancing by Hg^{2+}. And the strong fluorescence intensity of R_{614} (output = 1) as shown in Fig. 13.6A (top, left) indicates that the enhancing effect is much stronger than the quenching effect. Similarly, by combining the two input signals Hg^{2+} and S^{2-} in accordance with the truth table (Fig. 13.6B; top, left), only if S^{2-} is present, the R_{614} produces a fluorescence Turn-Off response, resulting in an IMP logic operation. With multiple inputs, the gate can accept and produce a high volume of information. Then it can serve as a basic and versatile building block for constructing more complex circuits. As demonstrated in Fig. 13.6A (top, right), the input state (1/1/1) displays the output: B_{485}, 0; G_{530}, 0; and R_{614}, 1, which is in accordance with the proper execution of the NOR logic gate for G_{530} with a threshold value of 1.62. The gate produces all of the false outputs 0 with different combinations of the inputs reliably. Moreover, the first cascaded gate is constructed by combining an INH gate with an OR gate using R_{614} as output signal (Fig. 13.6B; top, right). The integration of a three-input (Hg^{2+}, Ag^{+}, and S^{2-}) and three-output (B_{485}, G_{530}, and R_{614}) complex logic evolution network

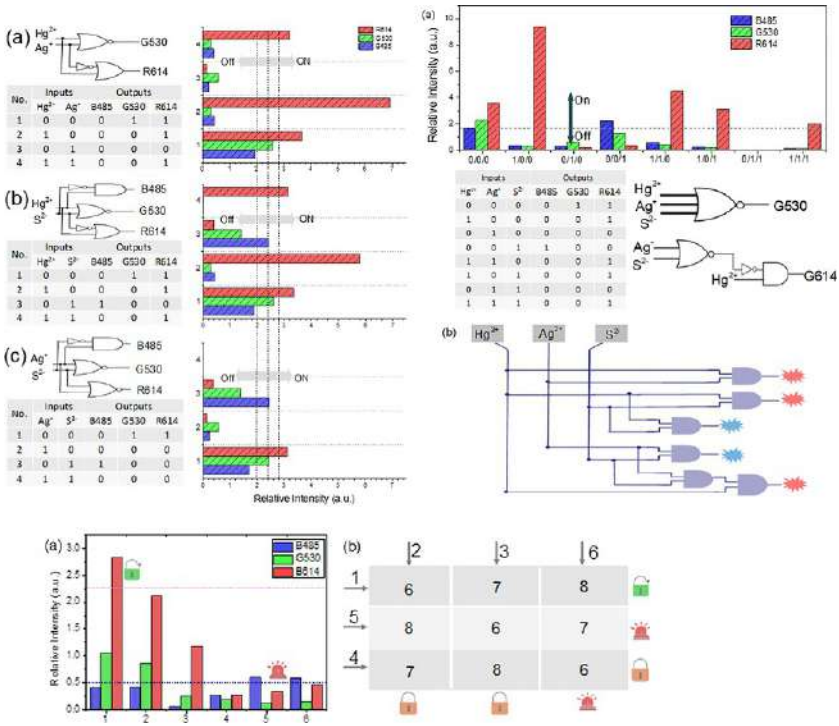

FIG. 13.6 *(Top, Left)* The corresponding electronic equivalent circuitry, truth table, and column diagram of fluorescence intensities of B_{485}, G_{530}, and R_{614}: the *black* dashed lines show the thresholds (B_{485}: 2; G_{530}: 2.2, and R_{614}: 2.8) of the Boolean logic gates containing two input signals: (A) Hg^{2+} and S^{2-}; (B) Hg^{2+} and S^{2-} and (C) Ag^{+} and S^{2-}. The concentration of every ion is 0.01 M. *(Top, Right)* (A) Column diagram of fluorescence intensities of B_{485}, G_{530}, and R_{614}: the *black* dashed lines show the thresholds (R_{614}: 1.8), truth table, and electronic equivalent circuitry of the Boolean logic gates containing three input signals; (B) Symbol of compound logic circuits with three inputs and two output fluorescence (*red* shadow represents the fluorescence signal of R_{614} and *blue* shadow represents the fluorescence signal of B_{485}). *(Bottom)* (A) Column diagram of fluorescence intensities of B_{485}, G_{530}, and R_{614}: the dashed lines show the thresholds (*red*: 2.25 and blue: 0.5) and (B) the keypad-lock security system with different input sequences. 6, 7 and 8 represent Hg^{2+}, Ag^{+}, and S^{2-}, respectively. *(Reproduced with permission from X. Xu, B. Yan, Intelligent molecular searcher from logic computing network based on Eu(III) functionalized UMOFs for environmental monitoring. Adv. Funct. Mater. 27 (2017) 1700247. Copyright 2017 Wiley.)*

is revealed in Fig. 13.6B (top, right), which suggests the powerful molecular recognition function of the Eu^{3+}@UMOFs fluorescence system. As shown in Fig. 13.6A (bottom), the R_{614} is output 1 only when the input sequence is Hg^{2+}-Ag^{+}-S^{2-}. They constructed a keypad-lock security system that can be opened only in the case of knowing the exact password. In addition, multiple outputs of Eu^{3+}@UMOFs can successfully improve the effectiveness of the security system. As illustrated in Fig. 13.6A (bottom), the emission of B_{485} (Th = 0.5) can be

observed only when the input S^{2-} is added first, which can be easily set to alarm emission. Except for closing the lock, the alarm will be triggered after inputting S^{2-} first. Based on this, unauthorized access defined by the input sequence can have limited effectiveness. To visualize the sequence-dependent system directly, Hg^{2+}, Ag^{+}, and S^{2-} ions have been designated as specific numbers 6, 7, and 8, respectively, and constructed as a password for the security system (Fig. 13.6B; bottom). The keypad-lock can be opened when the combination of inputs gives the password "678." On inverting, the other sequence will be negative to open the lock and the alarm can be triggered if one inputs the wrong password "786" or "768." [9]

Zheng et al. constructed a fluorescence system based on an Eu^{3+}@Cu-MOF to recognize and connect multiple components (AA/H_2O_2, H_2S, and Fe^{2+}) for developing dual-emissive (B_{485} and R_{616}) ratiometric fluorescent sensing and integrating Boolean logic operations. In the logic operations, Eu^{3+}@Cu-MOF served as gates, while different analytes (AA/H_2O_2, H_2S, and Fe^{2+}) and fluorescence responses at 485 nm (B_{485}) and 616 nm (R_{616}) were used as chemical inputs and outputs, respectively. The output value was defined as 1 (higher) or 0 (lower) by comparing it with the normalized fluorescence signals, with a set threshold value (B_{485}: 0.6 and R_{616}: 4.0). Subsequently, OR, NOR, AND, XOR, IMP, and INH logic operations were constructed, driven by the two analytes inputs. When H_2O_2/AA and H_2S served as the input, the output of 485 nm was PASS 1 (Fig. 13.7A), which can be seen as a combination of OR and NOR logic gates (Fig. 13.7C). These results are consistent with the proper execution of the combined logic gate. On the other hand, the input states of (1,0) and (1,1) yielded the True output [1] when using the emission at 616 nm (R_{616}) as the output. This can be regarded as the combination of INH and AND logic gates (Fig. 13.2C), consistent with the truth table for the circuit. In particular, in the presence of both inputs (input = 1/1), the output value is different from the output value of H_2S alone (input = 0/1), but similar to the output value of H_2O_2/AA alone (input = 1/0), which showed the same fluorescence intensity (Fig. 13.2B and D). Secondly, a multiple logic circuit was constructed to demonstrate the gate networking necessary for the complex multilevel integrated circuits when H_2O_2/AA and Fe^{2+} served as the input. According to the defined threshold value (B_{485}: 0.6), the True output [1] is observed when the input states are (0/0) and (1,0), while the other input states displayed a False output [0] (Fig. 13.7E), which is consistent with the proper execution of the combination of NOR and INH logic operations (Fig. 13.7G). Meanwhile, the binary XOR logic operation that has the Turn-On output only in the presence of one input could also be implemented by using the fluorescence emission at 616 nm (R_{616}) as the output (Fig. 13.7). Both H_2O_2/AA and Fe^{2+} showed a Turn-On fluorescence effect on the probe Eu^{3+}@Cu-COOH, which did not match well with the output value (0/0) in the truth table (Fig. 13.7E). It is assumed here that Fe^{2+} ions can be oxidized by excess H_2O_2 to generate Fe^{3+}, which may have a quenching effect on the nanocomposite Eu^{3+}@Cu-MOF: $2Fe^{2+}+2H^{+}+2{\bullet}OH$

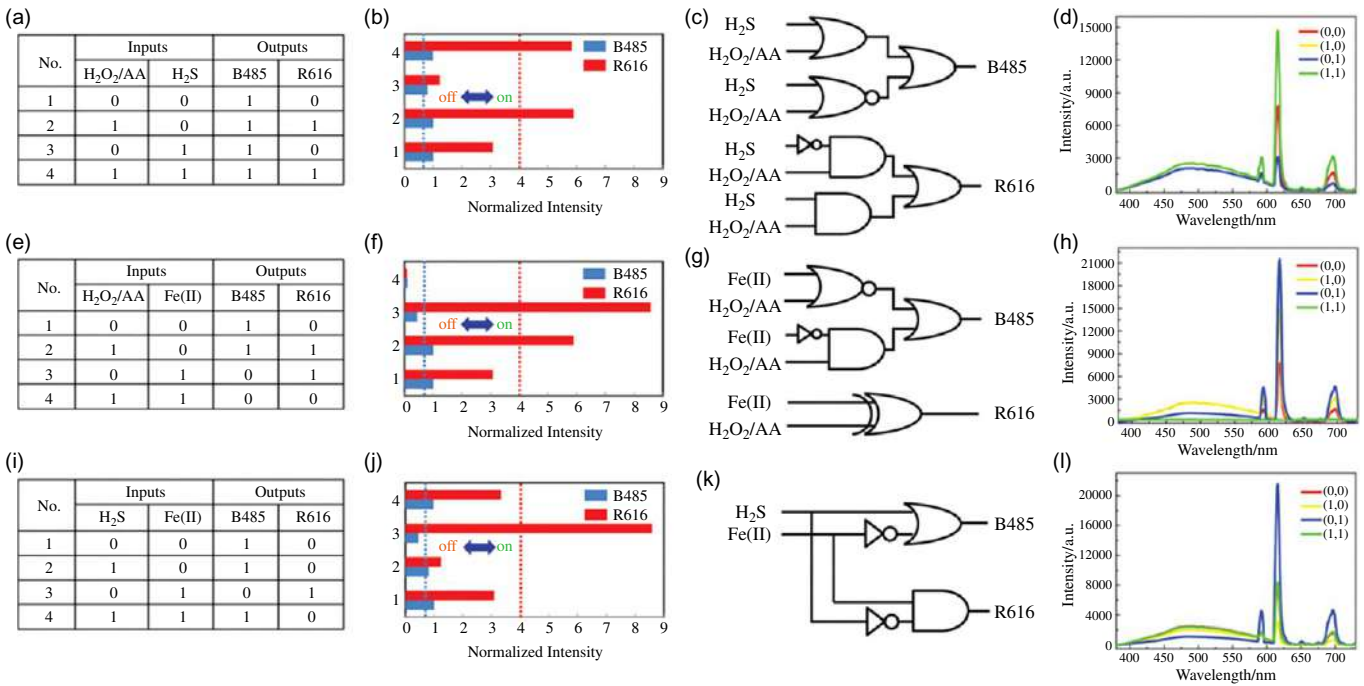

No.	Inputs		Outputs	
	H_2O_2/AA	H_2S	B485	R616
1	0	0	1	0
2	1	0	1	1
3	0	1	1	0
4	1	1	1	1

No.	Inputs		Outputs	
	H_2O_2/AA	Fe(II)	B485	R616
1	0	0	1	0
2	1	0	1	1
3	0	1	0	1
4	1	1	0	0

No.	Inputs		Outputs	
	H_2S	Fe(II)	B485	R616
1	0	0	1	0
2	1	0	1	0
3	0	1	0	1
4	1	1	1	0

FIG. 13.7 Truth table of the Boolean logic gates containing (A) H_2O_2/AA and H_2S, (E) H_2O_2/AA and Fe^{2+} and (I) H_2S and Fe^{2+}. Column diagram of the fluorescence intensities of B_{485} and R_{616} with the thresholds (B_{485}: 0.6 *(blue)*; and R_{616}: 4.0 *(red)*) for (B) H_2O_2/AA and H_2S, (F) H_2O_2/AA and H_2S and (J) H_2S and Fe^{2+}. Electronic equivalent circuitry of the Boolean logic gates containing (C) H_2O_2/AA and H_2S, (G) H_2O_2/AA and Fe^{2+} and (K) H_2S and Fe^{2+}. Fluorescence response spectra with different combinations of (D) H_2O_2/AA and H_2S, (H) H_2O_2/AA and Fe^{2+} and (L) H_2S and Fe^{2+}. *(Reproduced with permission from X. Zheng, R. Fan, K. Xing, A. Wang, X. Du, P. Wang, Dual-emissive nanocomposites based on Eu(III) functionalized Cu(I)-coordination polymer for ratiometric fluorescent sensing and integrating Boolean logic operations. J. Mater. Chem. C 6 (2018) 6229–6239. Copyright 2018 Royal Chemical Society.)*

$\rightarrow 2Fe^{3+}+2H_2O$. Based on the fluorescence properties of Eu^{3+}@Cu-MOF, they constructed another subnetwork by connecting an IMP gate and an INH gate in parallel. An IMP logic operation produces an output of 0 only in the presence of one particular input, which can be implemented by employing the fluorescence emission at 485 nm (B_{485}) as the output, while H_2S and Fe^{2+} functioned as double inputs (Fig. 13.8). As shown in Fig. 13.7I, the turn-off of B_{485} (output = 0) is observed only in the presence of Fe^{2+} and under other circumstances the output 1 will be observed. In other words, Eu^{3+}@Cu-COOH alone (input = 0/0) has B_{485} emission, but the addition of Fe^{2+} (input = 0/1) triggers the fluorescence Turn-Off response (output = 0) (Fig. 13.7L). At the same time, an INH logic operation that has the Turn-On output only in the presence of one particular input can also be implemented by employing the fluorescence emission at 616 nm (R_{616}) as the output. These INH logic operations rely on the injection of Fe^{2+}. Only the addition of Fe^{2+} (input = 0/1) triggers the fluorescence Turn-On response (output = 0). As a result, when the nanocomposite Eu^{3+}@Cu-MOF is introduced to the solution of H_2S and Fe^{2+} ions (input = 1/1), Fe^{2+} can interact with H_2S to diminish the interactions between H_2S and Eu^{3+}@Cu-COOH. After reacting with each other to form FeS for a short time, the remaining Fe^{2+} ions are reactive, but H_2S ions live in silence. The corresponding fluorescence emission spectra for every logic gate are given in Fig. 13.7L. The aforementioned two-input processes show that the nanocomposite Eu^{3+}@Cu-MOF, H_2O_2/AA, H_2S, and Fe^{2+} in solution phase can self-assemble, oxidize, and connect with each other.

Then, they introduce a third analyte as an input to the recognition system, for which the emission spectra can be observed in Fig. 13.8D. With multiple inputs, the gate can accept and produce a high volume of information, and then it can serve as a basic and versatile building block for constructing more complex circuits. As shown in Fig. 13.8A, the input state (1/1/1) displays the output (1/1) with a threshold value (B_{485}: 0.6 and R_{616}: 4.0). Inspired by this interesting fact, a combinatorial gate connecting XOR, INH and OR in series is achieved by using the fluorescence emission at 616 nm (R_{616}) as the output (Fig. 13.8C). In this logic operation, H_2O_2/AA and Fe^{2+} are input to construct the first XOR gate, which is then integrated with the second INH gate into the next OR gate. The second INH gate is constructed by the introduced H_2S and Fe^{2+}. According to the defined threshold value (B_{485}: 0.6; and R_{616}: 4.0), the True output [1] is observed when the input state is (1/0/0, 0/0/1, 1/1/0, 1/1/1), while the other input states (0/0/0, 0/1/0, 1/0/1, 0/1/1) display a False output [0], which is in accordance with the proper execution of the XOR(INH)-OR operation. The integration of three inputs (H_2O_2/AA, H_2S and Fe^{2+}) and two outputs (B_{485} and R_{616}) in the complex logic evolution network are revealed in Fig. 13.8E, suggesting the molecular recognition function of the hybrid system.

Zhang et al. developed and established a fluorescent MOF-based logic platform Eu^{3+}/Ag^{+}@UiO-66-$(COOH)_2$ (EAUC), and realized its potential for a detection of asthma biomarker H_2S in biological samples. The key point of this

(a)

No.	Inputs			Outputs	
	H_2O_2/AA	H_2S	Fe(II)	B485	R616
1	0	0	0	1	0
2	1	0	0	1	1
3	0	1	0	1	0
4	0	0	1	0	1
5	1	1	0	1	1
6	1	0	1	0	0
7	0	1	1	1	0
8	1	1	1	1	1

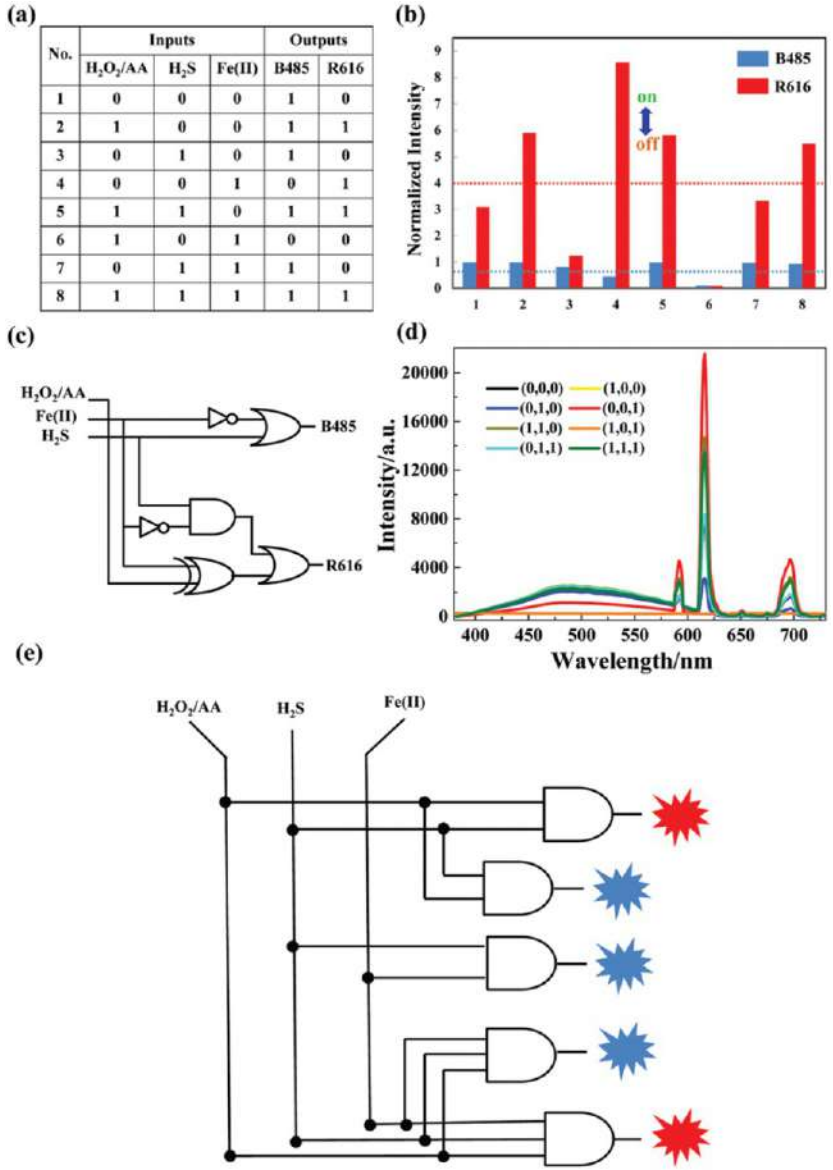

FIG. 13.8 (A) Truth table of the Boolean logic gates containing three input signals. (B) Column diagram of the fluorescence intensities of B_{485} and R_{616} with the thresholds (B_{485}: 0.6 *(blue)*; and R_{616}: 4.0 *(red)*). (C) Electronic equivalent circuitry of the Boolean logic gates containing three input signals. (D) Fluorescence response spectra with different combinations of inputs. (E) Symbols of compound logic circuits with three inputs and two output fluorescence (*red* shadow representing the fluorescence signal of R_{616} and *blue* shadow representing the fluorescence signal of B_{485}). *(Reproduced with permission from X. Zheng, R. Fan, K. Xing, A. Wang, X. Du, P. Wang, Dual-emissive nanocomposites based on Eu(III) functionalized Cu(I)-coordination polymer for ratiometric fluorescent sensing and integrating Boolean logic operations. J. Mater. Chem. C 6 (2018) 6229–6239. Copyright 2018 Royal Chemical Society.)*

platform is to introduce the active metal centers (Ag^+) to the Eu^{3+}@UiO-66-$(COOH)_2$ (EUC) as the Eu^{3+}-luminescence sensitizer and H_2S-responding site. As a result, the INHIBIT logic gate based on EUC can use Ag^+ and H_2S as two inputs and the fluorescence intensity of EUC as the output signal. It is possible to use a MOF-based logic platform for detecting H_2S in biological samples, offering a potential method for a conveniently tentative diagnosis of asthma. In the presence of H_2S, the fluorescence of EAUC can be quenched strongly (Fig. 13.9B and C; top). This is because sulfide has a strong affinity toward Ag^+ ions, which can destroy the sensitization of Ag^+ ions. EUC can serve as an INHIBIT logic gate since the intensity of the emission at 615 nm is responsive to the presence or absence of Ag^+ and H_2S. Thus the logic gate properties of EUC can be established by using two input signals of Ag^+ (Input 1) and H_2S (Input 2), respectively. The presence and absence of two inputs Ag_+ and H_2S can be defined as 1 and 0 states. As shown in Fig. 13.9B and C (top), the fluorescence intensity I_{615} (output) of the EUC is distinctly high (output = 1) only when (Input 1, Input 2) is (1, 0). In contrast, the fluorescence intensity I_{615} holds a low level (output = 0) when (Input 1, Input 2) is (0, 0), (0, 1), or (1, 1), respectively. The pictorial representation and the truth table for the corresponding INHIBIT are given in Fig. 13.9D and E (top). The serum level of H_2S decreases from 75.2 ± 13.0 μM in healthy subjects to 55.8 ± 13.6 μM in patients with stable asthma, 57.8 ± 6.3 μM in patients with mild or acute exacerbation asthma, 40.8 ± 5.1 μM in patients with moderate or acute exacerbation asthma, and 31.3 ± 2.9 μM in patients with severe acute exacerbation of asthma. (Fig. 13.9; bottom). The content of H_2S can be calculated by the fluorescence intensity output of the logic platform to determine whether the patient is suffering from asthma. This luminescent INHIBIT logic platform thus offers a new opportunity for tentative diagnosis of asthma disease associated with H_2S detection in clinical medicine (Fig. 13.9; bottom) [10].

Sun et al. constructed a fluorescent platform based on a novel microscale heterometallic RE-MOF, $Eu_{0.059}Tb_{0.051}Gd_{0.89}$-DPON ($H_3$DPON = 5-(3,4-dicarboxylphenoxy)nicotic acid) for effective combination of molecular/ionic recognition and logic computing. The tri-emission RE-MOF exhibited notable fingerprint correlation between various solvent molecules/cations and the emission intensity ratio of ligands, Tb^{3+}, and Eu^{3+}. It realized multicomponent analysis (Fe^{3+}, VO_4^{3-}, and S^{2-}) in water via construction of a Boolean logic system and had a password lock security system by sequential logic operation. In the Boolean logic operation, $Eu_{0.059}Tb_{0.051}Gd_{0.89}$-DPON served as a gate, while the analyzed substances (Fe^{3+}, VO_4^{3-}, and S^{2-}) and fluorescence emission intensities at 415 nm (B_{415}), 544 nm (G_{544}), and 616 nm (R_{616}) were set as inputs and outputs, respectively. The output was defined by comparing with a threshold value (B_{415}: 0.5, G_{544}: 1 and R_{616}: 1.5), which depends on the fluorescence intensities of different emission centers, higher than the threshold value outputs 1, with lower outputs 0 (Fig. 13.10B). As demonstrated in Fig. 13.10B, E, and H, the fluorescence intensities at 544 nm exceeded the

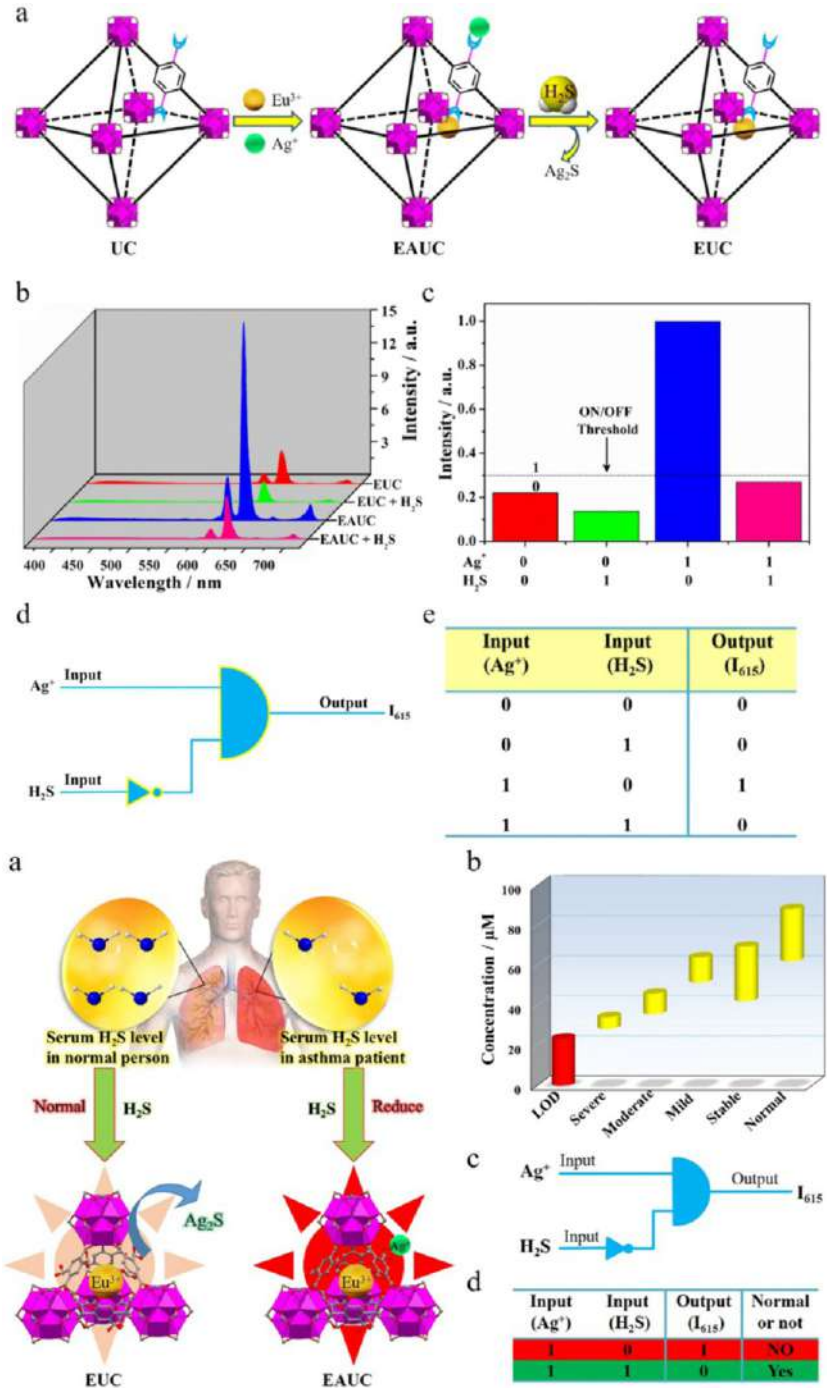

FIG. 13.9 (See figure legend on opposite page)

(a)

No.	Inputs		Outputs		
	Fe^{3+}	VO_4^{3-}	B415	G544	R616
1	0	0	1	1	1
2	1	0	0	0	0
3	0	1	0	0	1
4	1	1	0	0	1

(d)

No.	Inputs		Outputs		
	Fe^{3+}	S^{2-}	B415	G544	R616
1	0	0	1	1	1
2	1	0	0	0	0
3	0	1	1	0	0
4	1	1	0	0	0

(g)

No.	Inputs		Outputs		
	VO_4^{3-}	S^{2-}	B415	G544	R616
1	0	0	1	1	1
2	1	0	0	0	1
3	0	1	1	0	0
4	1	1	1	0	0

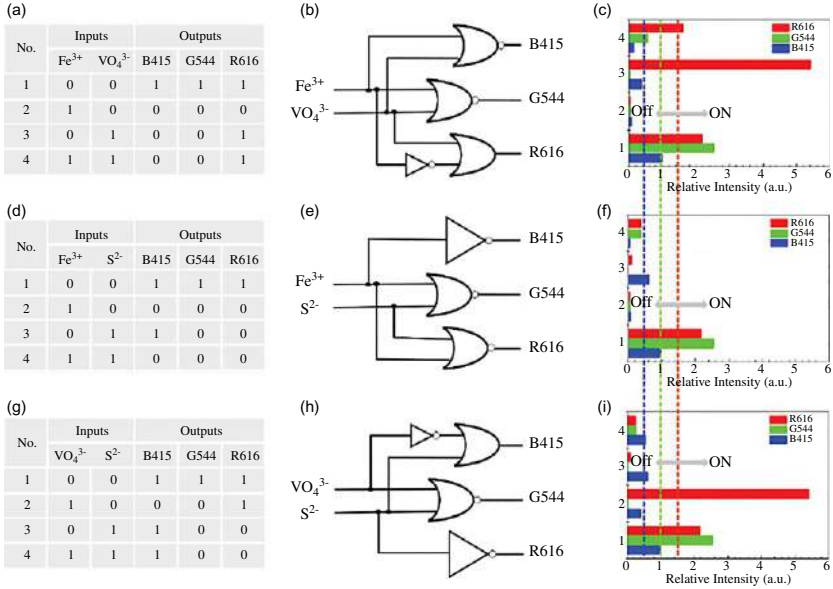

FIG. 13.10 Truth tables of the double input Boolean logic gates (A) $Fe^{3+}+VO_4^{3-}$, (D) $Fe^{3+}+S^{2-}$, and (G) $VO_4^{3-}+S^{2-}$. Electronic equivalent circuitries of the double input Boolean logic gates (B) $Fe^{3+}+VO_4^{3-}$, (E) $Fe^{3+}+S^{2-}$ and (H) $VO_4^{3-}+S^{2-}$. Column diagrams of the fluorescence intensities of B_{415}, G_{544}, and R_{616} in the double input of Boolean logic gates (C) $Fe^{3+}+VO_4^{3-}$, (F) $Fe^{3+}+S^{2-}$ and (I) $VO_4^{3-}+S^{2-}$; the dashed lines represent the thresholds (B_{415}: 0.5, G_{544}: 1 and R_{616}: 1.5). The concentration of each input is 1 mM. *(Reproduced with permission from T. Sun, P. Wang, R. Fan, W. Chen, S. Hao, Y. Yang, Functional microscale single-phase white emission lanthanide MOF for tunable fluorescent sensing and water quality monitoring. J. Mater. Chem. C 7 (2019) 3598–3606. Copyright 2019 Royal Chemical Society.)*

threshold (G_{544}: 1) only in the absence of Fe^{3+}, VO_4^{3-} and S^{2-}; otherwise the output was 0. Similarly, identical NOR logic operation can also be implemented on the B_{415} output of $Fe^{3+}+VO_4^{3-}$ double input logic gate and the R_{616} output of $Fe^{3+}+S^{2-}$ logic gate (Fig. 13.10B and E). The R_{616} output of $Fe^{3+}+VO_4^{3-}$ double input logic gate belongs to the binary IMP logic operation, which produces 0

FIG. 13.9, CONT'D, *(Top)* (A) Synthetic scheme and representative crystalline structure: the tetrahedral cage of UC, EAUC, and EUC. (B) Fluorescence spectra of EUC in the presence of four input modes: *(red)* no input; *(green)* 5 mM H_2S; *(blue)* 1 mM Ag^+; *(pink)* 5 mM H_2S+1 mM Ag^+. (C) Fluorescence intensity changes at 615 nm in the form of a bar representation, with a threshold of $I_{615}=0.3$ (normalized fluorescence intensity) for output 1 or 0. (D) INHIBIT logic gate represented using a conventional gate notation. (E) Truth table for the INHIBIT logic gate; Ag^+ and H_2S are inputs to the system; fluorescence intensity I_{615} is the output signal of EUC. *(Bottom)* (A) The principle of the initial diagnosis of asthma. (B) The relationship between asthma and the concentration of H_2S. (C) INHIBIT logic gate represented using a conventional gate notation; an active output signal is obtained when $Ag^+=1$ and $H_2S=0$. (D) Truth table for the INHIBIT logic gate. *(Reproduced with permission from X. Zhang, L. Fang, K. Jiang, H. He, Y. Yang, Y. Cui, B. Li, G. Qian, Nanoscale fluorescent metal-organic framework composites as a logic platform for potential diagnosis of asthma. Biosens. Bioelectron. 130 (2019) 65–72. Copyright 2019 Elsevier.)*

output only at one particular input (1/0). As shown in Fig. 13.10H, the IMP logic operation can also be implemented on B_{415} output when VO_4^{3-}+S^{2-} acts as a double input. This is because of the framework collapse mechanism of S^{2-}, which makes the VO_4^{3-} live in silence when added together. NOT logic operation also exists in the VO_4^{3-}+S^{2-} logic gate. With the addition of S^{2-}, the characteristic emission of Eu^{3+} disappears and, thus, R_{616} outputs 0. The aforementioned double input logic gate shows that $Eu_{0.059}Tb_{0.051}Gd_{0.89}$-DPON, Fe^{3+}, VO_4^{3-}, and S^{2-} can self-dassemble and interact with each other in aqueous solution.

As seen in Fig. 13.11B, when B_{415} is used as the output signal, the first INH gate is constructed with VO_4^{3-} and S^{2-} double input and its output is integrated with the Fe^{3+} to form the new input for the second NOR gate. The G_{544} input still belongs to the NOR logic operation, since due to the identical quenching effect of three ions, only the 0/0/0 input can produce a 1 input. As for emission at 616 nm (R_{616}), after the NOT logic operation, the Fe^{3+} input is integrated into the next XOR logic operation with S^{2-} input. Moreover, in the presence of all three inputs (1/1/1), Fe^{3+} loses its function through excess connection with VO_4^{3-} and S^{2-}, while the remaining VO_4^{3-} and S^{2-} have their own effects on $Eu_{0.059}Tb_{0.051}Gd_{0.89}$-DPON, resulting in the 1/0/1 output. The integration of a complex logic evolution network with three inputs (Fe^{3+}, VO_4^{3-}, and S^{2-}) and three outputs (B_{415}, G_{544}, and R_{616}) is revealed in Fig. 13.11D. It exhibits the powerful molecular recognition ability of an $Eu_{0.059}Tb_{0.051}Gd_{0.89}$-DPON fluorescence system. As shown in Fig. 13.11E, the emission at 415 nm outputs 1 in A (Fe^{3+}), B (VO_4^{3-}), C (S^{2-}) and B, A, C sequences. Only the A, C, B sequence produces the Turn-On output of R_{616} since the connection of Fe^{3+} and S^{2-} retains the complete framework. The sequence-dependent output characteristics inspired development of the logic operation into a simple password lock (Fig. 13.11F). Blue (B_{415}) and red (R_{616}) emissions are defined as alarm and unlock, respectively, while the 0/0/0 output represents the lock. Obviously, in addition to the correct password (A, C, B), other passwords cannot open the lock, and some wrong passwords (A, B, C and B, A, C) will trigger an alarm, which greatly enhances the security of the password lock [11].

Feng et al. constructed Tb-MOFs with a TMA (trimesic acid) ligand, which can be used as a highly selective luminescent sensor for styrene solution and vapor, showing promise for tracing VOCs. They designed the sensor as a logic gate for further logic application. A logic gate consisting of an INHIBIT gate, AND gate, and OR gate was constructed in this study. There were three inputs, consisting of UV, styrene, and heat, respectively, while the output was the emission intensity of Tb^{3+} at 544 nm (Fig. 13.12A). As shown in Fig. 13.12B, it can be concluded that the prerequisite for the fluorescence of Tb-MOF is the existence of UV. As can be seen from the bar graph in Fig. 13.12C, the relative intensity of I_{544} below and above 0.05 nm can be defined as the threshold value, which relies on the fluorescence intensities of emission centers. As the intensity

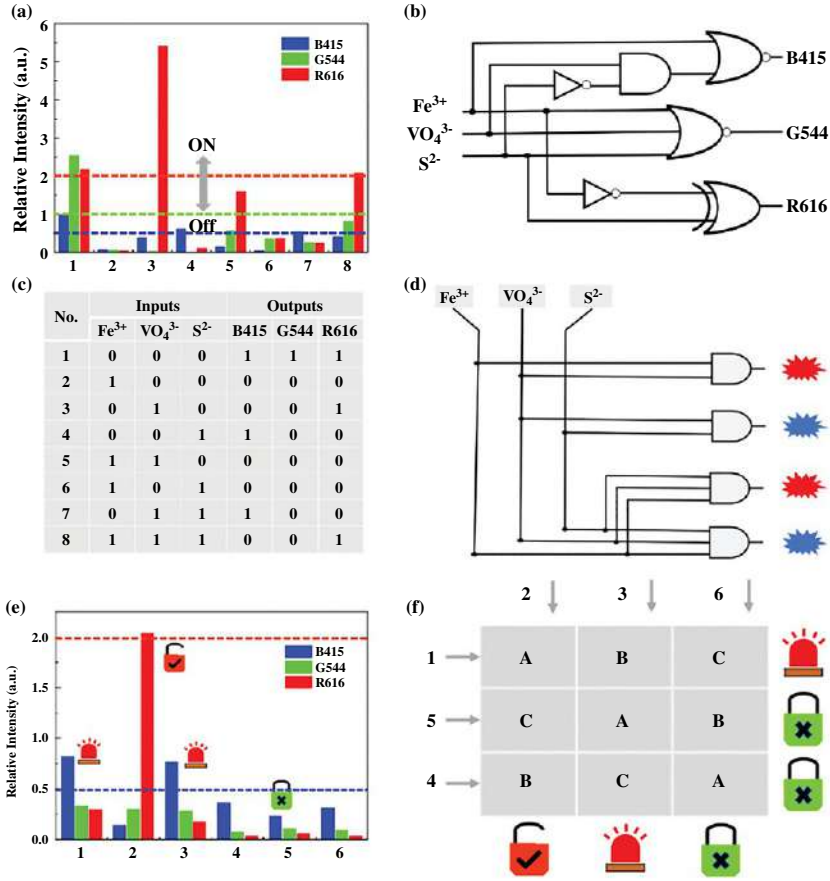

No.	Inputs			Outputs		
	Fe^{3+}	VO_4^{3-}	S^{2-}	B415	G544	R616
1	0	0	0	1	1	1
2	1	0	0	0	0	0
3	0	1	0	0	0	1
4	0	0	1	1	0	0
5	1	1	0	0	0	0
6	1	0	1	0	0	0
7	0	1	1	1	0	0
8	1	1	1	0	0	1

FIG. 13.11 (A) Column diagram of fluorescence intensities of B_{415}, G_{544}, and R_{616}: the dashed lines show the thresholds (B_{415}: 0.5, G_{544}: 1 and R_{616}: 2). (B) Electronic equivalent circuitry of the three input Boolean logic gate. (C) Truth table of the three input Boolean logic gate. (D) Compound logic circuit with three input and two output fluorescence signal (*blue* shadow represents the fluorescence of B_{415} and *red* shadow represents the fluorescence of R_{616}). (E) Column diagram of fluorescence intensities of B_{415}, G_{544}, and R_{616}: the dashed lines show the thresholds (R_{616}: 2 and B_{415}: 0.5). (F) The password lock security system with different input sequences (A, B and C represent Fe^{3+}+VO_4^{3-}, and S^{2-}, respectively). *(Reproduced with permission from T. Sun, P. Wang, R. Fan, W. Chen, S. Hao, Y. Yang, Functional microscale single-phase white emission lanthanide MOF for tunable fluorescent sensing and water quality monitoring. J. Mater. Chem. C 7 (2019) 3598–3606. Copyright 2019 Royal Chemical Society.)*

is higher than the threshold value, the outputs are 1, whereas if it is lower than the threshold value, then the outputs are 0. We can clearly see through the truth table (Fig. 13.12D) that only when the inputs are (1/0/0, 1/0/1, 1/1/1), the output is 1, whereas when the inputs are other than this case, the output is 0. If the output is 0, it implies that the luminescence of Tb-MOF is quenched. The analysis

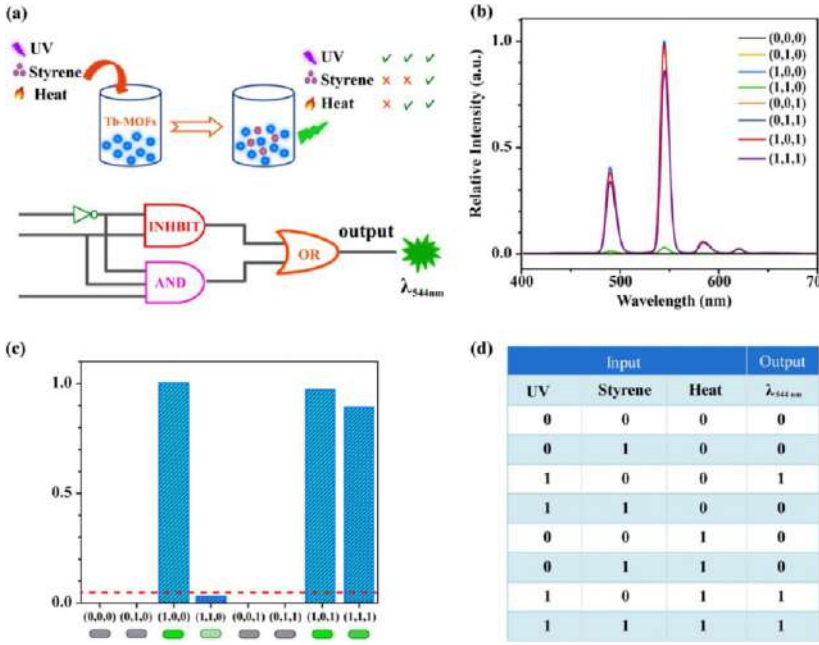

(d)

Input			Output
UV	Styrene	Heat	λ_{544nm}
0	0	0	0
0	1	0	0
1	0	0	1
1	1	0	0
0	0	1	0
0	1	1	0
1	0	1	1
1	1	1	1

FIG. 13.12 (A) Scheme and electronic equivalent circuitry of the logic gate; (B) Emission spectra of the logic gates; (C) Relative emission intensity changes at 544 nm in the form of a bar representation, with a threshold of 0.05; (D) The truth table of the logic gate; UV, styrene and heat are inputs to the system; emission intensity I_{544} is the output signal of Tb-MOF. *(Reproduced with permission from L. Feng, C. Dong, M. Li, L. Li, X. Jiang, R. Gao, R. Wang, L. Zhang, Z. Ning, D. Gao, J. Bi, Terbium-based metal-organic frameworks: highly selective and fast respond sensor for styrene detection and construction of molecular logic gate. J. Hazard. Mater. 388 (2020) 121816. Copyright 2020 Elsevier.)*

of these changes according to the logic operation provides direct detection for styrene and the reusability of Tb-MOF after heating. It is the first report towards the design of a Boolean logic gate system for sensing styrene [12].

Dong et al. prepared a single-phase white light-emitting microscale Eu-MOF, $[Eu_{0.06}Tb_{0.04}Gd_{0.9}(HDPNC)_{1.5}(H_2O)(DMF)]\cdot 2H_2O$ ($H_3DPNC = 5$-(3′,5′-dicarboxylphenyl) nicotinic acid) ($Eu_{0.06}Tb_{0.04}Gd_{0.9}$-DPNC) under 365-nm excitation, by adjusting the molar ratio of Eu^{3+} and different excitation wavelengths, with the CIE coordinates of (0.3328, 0.3296). Additionally, a Boolean logic system was also constructed based on dual-component analysis (MnO_4^- and folic acid (FA)) of $Eu_{0.06}Tb_{0.04}Gd_{0.9}$-DPNC in water. $Eu_{0.06}Tb_{0.04}Gd_{0.9}$-DPNC served as a gate, while the analytes (MnO_4^- and FA) were set as inputs, and relative fluorescence emission intensities at 462 nm (B_{462}), 544 nm (G_{544}), and 613 nm (R_{613}) were set as outputs. The absence and presence of the inputs MnO_4^- and FA were defined as 0 and 1, respectively. A result higher than the threshold value gives the output as 1; otherwise the output is 0, compared to a threshold value (B_{462}: 3.0, G_{544}: 3.3, and

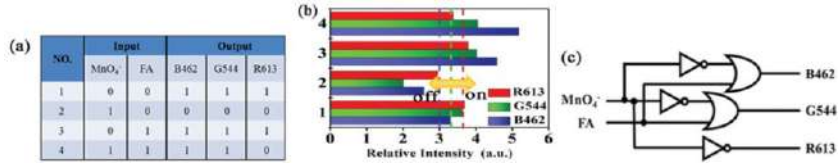

FIG. 13.13 (A) Truth tables of the double input Boolean logic gates. (B) Column diagrams of the fluorescence intensities of B_{462}, G_{544}, and R_{613} in the double inputs of Boolean logic gates; the dashed lines represent the thresholds (B_{462}: 3.0, G_{544}: 3.3 and R_{613}: 3.6). (C) Electronic equivalent circuitries of the double input Boolean logic gates. *(Reproduced with permission from Z. Dong, F. Zhao, L. Zhang, Z. Liu, Y. Wang, A white-light-emitting lanthanide metal-organic framework for luminescence turn-off sensing of MnO4− and turn-on sensing of folic acid and construction of a "turn-on plus" system. New J. Chem. 44 (2020) 10239–10249. Copyright 2020 Royal Chemical Society.)*

R_{613}: 3.6, relative intensity), which depends on the fluorescence intensities of different emission centers. The truth table of the logic gates and the corresponding combinatorial logic circuits are shown in Fig. 13.13A and C. Hence, the binary IMP logic operations can be implemented on both the B_{462} and G_{544} outputs when MnO_4^- and FA act as a double input, which produces 0 output only at one particular input (1/0). When MnO_4^- is added alone, it exhibits a strong quenching effect on the emission at 462 and 544 nm, while upon the addition of FA (input: 1/1), a NOT logic operation exists in the R_{613} output logic gate. With the addition of FA, the characteristic emission of Eu^{3+} disappears; thus R_{613} outputs 0. The corresponding column diagrams of the fluorescence intensities of B_{462}, G_{544}, and R_{613} and electronic equivalent circuitries in the double inputs of Boolean logic gates are shown in Fig. 13.13B and C.

13.3 Luminescence responsive chemical sensing of rare earth metal-organic framework hybrid materials for intelligent molecular searcher applications

It is crucial for environmental protection and monitoring to determine the type and content of polluting ions. Using a Boolean logic operation, as described in the previous section, chemical ions in water can be connected for developing a self-organized logic operation. The logic gates have the peculiarity of manipulating only precise, objective knowledge, i.e., statements that are true (1) and false (0). However, it is not always possible to store accurate information in the chemical process. A certain degree of uncertainty and imprecision appears quite often, especially when there is the nonlinear (sigmoidal) response between the input and output. Therefore it is necessary to adopt soft computing based on a fuzzy logic approach to process the uncertain information. Fuzzy logic has been introduced as a means to deal with inaccuracies and uncertain information through the formulation of fuzzy logic systems (FLSs). A fuzzy variable is a variable that takes on fuzzy sets as values.

Xu et al. took the concentration C of ions and fluorescence F of Eu^{3+}@UMOFs at a given wavelength as the linguistic variable. As illustrated in Fig. 13.14 (left), the C^{+}_{Ag} input variable has been decomposed in three fuzzy sets labeled (1) low, with a $\mu F(x)$ defined by an asymmetrical polynomial curve (whose symbol is zmf, [0.001, 0.1]); (2) medium, with $\mu F(x)$ defined by a triangular shaped curve (whose symbol is trimf, [0.005, 0.5, 1.5]); (3) high, with $\mu F(x)$ defined by an asymmetrical polynomial curve (whose symbol is smf).The next step required to implement Mamdani's FLS entails formulating fuzzy rules: IF-THEN, wherein the IF is called the antecedent and the THEN is called the consequence. The inference engine has been running to map input fuzzy sets into output fuzzy sets in Fig. 13.14 (left), whereas the defuzzifier maps output fuzzy sets produced by the inference engine into crisp numbers. In our case, the crisp number corresponds to the fluorescence intensity of 614 (R_{614}). According to the aforementioned logic operation, we can explain the nonlinear correlation between the concentration of ions and the fluorescence signal by FLS. Then the ion recognition engine can be constructed by a similar FLS function that takes the fluorescence signal as input variable and concentration as output variable. In the three-input logic operation, they obtained an INH gate for R_{614} (Fig. 13.14; right). The self-organizing compiler can perform a Boolean logic function to determine whether Hg^{2+} is present in the solution-based library. If Hg^{2+} is present, the fluorescence of Eu^{3+}@UMOFs at 614 nm is turned on. Fluorescence variable (R_{614}) has been decomposed in three fuzzy sets (Fig. 13.14; right): (1) low (zmf μ_{low} [0.82, 2.13]); (2) medium (trimf μ_{medium} [1.45, 1.85, 2.26]); (3) high (smf μ_{high} [2.13, 3.24]). The inference engine maps $F(R_{614})$ fuzzy sets into C^{2+}_{Hg} fuzzy sets (Fig. 13.14; right). It handles the way in which rules are combined. Finally, the defuzzifier maps C^{2+}_{Hg} fuzzy sets into crisp C^{2+}_{Hg}.

On the basis of Boolean logic and fuzzy logic, Xu et al. realized an intelligent molecular searcher by taking chemical events (Hg^{2+}, Ag^{+}, and S^{2-}) as programmable words and chemical interactions as syntax (Fig. 13.15). Considering the particularity of all the input ions, the approach is helpful in developing an advanced logic program based on Eu^{3+}@UMOFs for application in environmental monitoring. Sensors (MR@Eu-MOF) were created by covalently modifying MR into an -NH_2-rich Eu-MOF, which has a high quantum yield (48%). A double stimuli-responsive fluorescence center was produced via energy transfer from the ligands to Eu^{3+} and MR. Portable sensory hydrogels were obtained by dispersing and solidifying MR@Eu-MOF in water-phase CMC-Na. The hydrogels exhibited a color transition upon "smelling" HI vapor. This transition and shift in the MR-based emission peak are closely related to the HI concentration. Using HI concentration as the input signal and the two fluorescence emissions as output signals, an advanced analytical device based on a one-to-two logic gate was constructed. The four output combinations, NOT (0, 1), YES (1, 0), PASS 1 (1, 1), and PASS 0 (0, 0), allow the direct analysis of HI levels, which can be used for real-time food freshness evaluations. The novel strategy suggested here may be a new application for a molecular logic system in a sensing field.

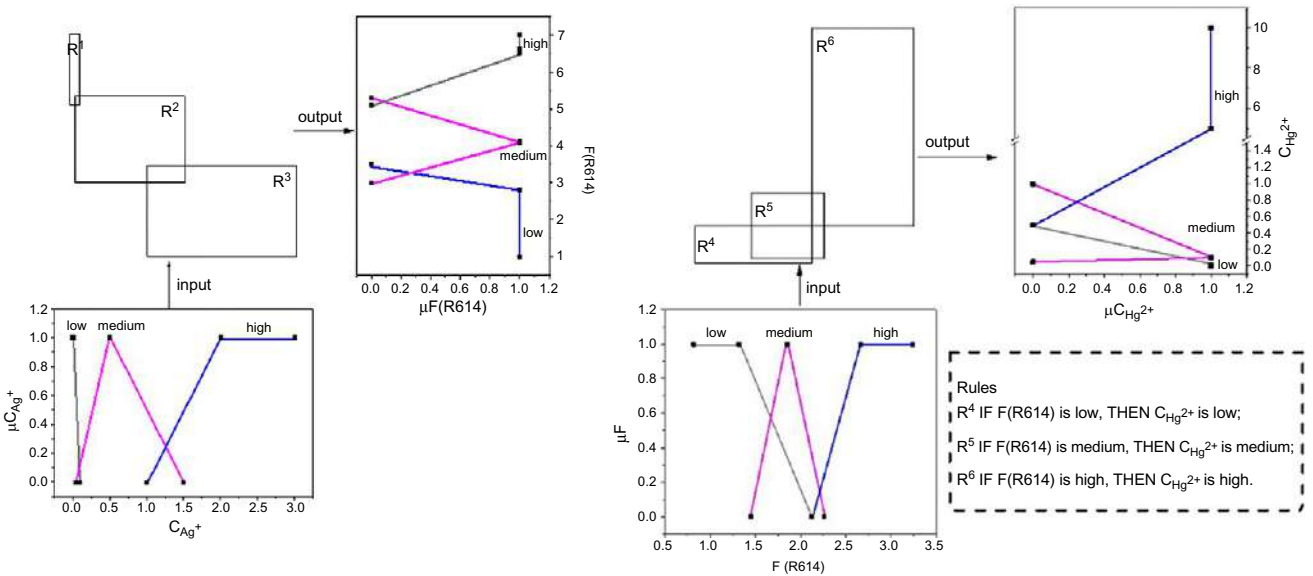

FIG. 13.14 *(Left)* Scheme of fuzzy relation based on fuzzy inference rules mapping input C^{+}_{Ag} to output F (R_{614}). Fuzzy variable of F(R_{614}) is decomposed in three fuzzy sets: (1) low (zmf μ_{low} [1, 3.5]); (2) medium (trimf μ_{medium} [3, 4.1, 5.3]); (3) high (smf μ_{high} [5.1, 7]). *(Right)* (A) Scheme of fuzzy relation based on fuzzy inference rules mapping input C^{2+}_{Hg} to output F(R_{614}). Fuzzy variable of C^{2+}_{Hg} is decomposed in three fuzzy sets: (1) low (zmf μlow [0.1, 0.5]); (2) medium (trimf μmedium [0.05, 0.1, 1]); (3) high (smf μhigh [0.5, 10]). The dashed box gives inference rules. *(Reproduced with permission from X. Xu, B. Yan, Intelligent molecular searcher from logic computing network based on Eu(III) functionalized UMOFs for environmental monitoring. Adv. Funct. Mater. 27 (2017) 1700247. Copyright 2017 Wiley.)*

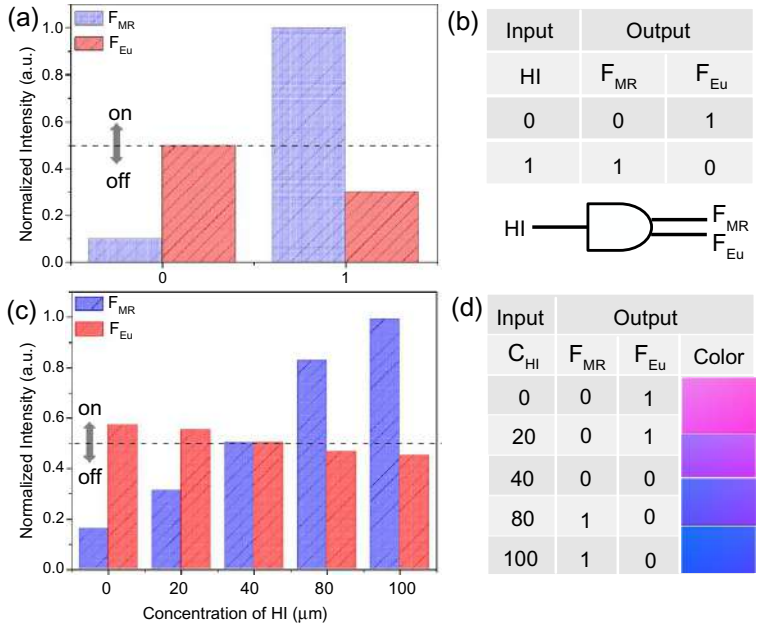

FIG. 13.15 (A) Column diagram of the normalized fluorescence intensity of F_{MR} and F_{Eu} towards HI (250 μM); (B) truth table of the one-to-two decoder logic gate; (C) column diagram of the normalized fluorescence intensity of F_{MR} and F_{Eu} towards different concentrations of HI ranging from 0 to 100 μM; (D) truth table of the logic analytical device for HI monitoring. *(Reproduced with permission from X. Xu, X. Lian, J. Hao, C. Zhang, B. Yan, Double stimuli-responsive fluorescent center for food spoilage monitoring based on dye covalent modified EuMOFs: from sensory hydrogel to logic device. Adv. Mater. 29 (2017) 1702298. Copyright 2017 Wiley.)*

Qin et al. developed highly luminescent, bimetallic MOFs as luminescent sensors for NMF, with a focus on Eu^{3+} and Tb^{3+} complexes as visible emitters with red and green emission. Furthermore, this sensing system was also integrated with AND logic gates using NMF and 300 nm as inputs for intelligent NMF sensing. The simple chemical species NMF was chosen to be the input signal. The fluorescence of I_{544} and I_{614} was the output signal, which is visible and easily detected. According to the defined threshold value of 0.5, the normalized intensity values at 544 nm and 614 nm were defined as the OFF (0) and ON (1) states. The truth table for the logic operation is shown in Fig. 13.16D. As revealed by Fig. 13.16B, each percentage of NMF from 0 to 1 exhibits a corresponding color, which could enable real-time analysis of NMF levels based on the decode procedure. According to the direct color visualization with the naked eye, the percentage of NMF can be readily estimated by comparison with the concentration-dependent CIE chromaticity diagram, thus providing a useful tool for determining NMF distribution. Motivated by the results, an "AND" logic gate was created using similar design strategies (Fig. 13.16E and F).

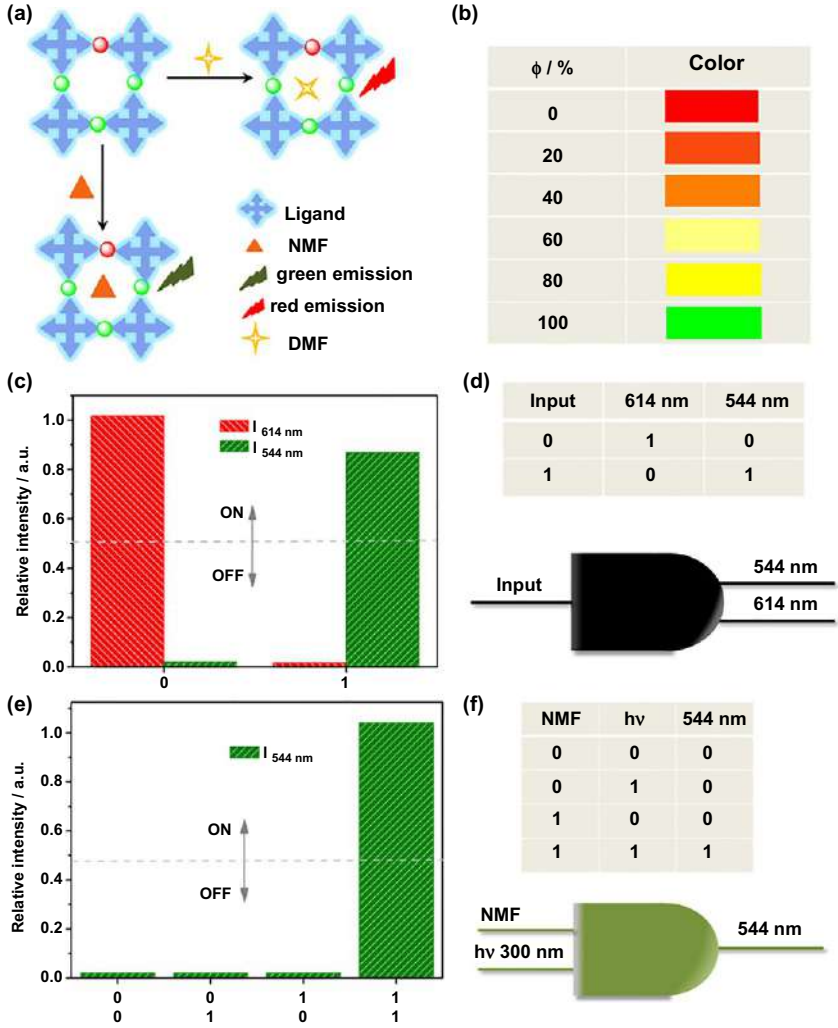

FIG. 13.16 (A) Diagram of the operational design of the sensor. (B) Corresponding color for every NMF volume ratio from 0 to 1. (C) Column diagram of the normalized fluorescence intensities of I_{614} and I_{544} toward NMF. (D) Truth table of the 1-to-2 logic gate. (E) The design of the AND gate, column diagram of the fluorescence intensities in different states; (F) Truth table of the AND gate. *(Reproduced with permission from S. Qin, X. Qu, B. Yan, A self-calibrating bimetallic lanthanide metal-organic luminescent sensor integrated with logic gate operation for detecting N-methylformamide. Inorg. Chem. Front. 5 (2018) 2971-2977. Copyright 2018 Royal Chemical Society.)*

The system performs the "AND" logic function, and the output signal (the green light at 544 nm) is generated (true value 1) only if the system is subjected to both inputs simultaneously. In the absence of any inputs (0, 0) or in the presence of either input (1, 0; 0, 1), no green light at 544 nm would be observed and the output reading would be 0.21. The visible nature of the response signal allows observation of "OFF" and "ON" of the system by the naked eye. This Boolean logic gate can provide an effective systematic pathway and a powerful programming language for monitoring NMF [13].

Zhang et al. proposed an L-MOF-enzyme composite (GO_x-Eu^{3+}@UMOF) that could drive a reaction cascade to generate H_2O_2 and for further detecting of Glu. This will open a new opportunity for the design of an intelligent POC diagnostics molecular logic detector based on the L-MOF-enzyme composite. Based on the superexcellent properties of GOx-Eu^{3+}@UMOF mentioned earlier, a portable, point-of-care (POC) diagnostics logic detector that can realize the self-diagnosis of glucose in urine was designed, shown in Fig. 13.17. Therefore the concentrations of Glu and λ_{ex} were used as the two inputs of the POC diagnostics logic detector and the fluorescent intensity of Eu^{3+} (λ_{614nm}) as the output, and the first combinational logic gate named Gate 1 was designed. It can be seen that only if both $C_{Glu} > 0.1$ μM and λ_{ex} are presented, the output1 is 1, resulting in the Gate 1 open. Considering that they have fixed the excitation into the logic detector, it will not be described in the future. So the function of the first gate is to examine if the concentration of Glu is greater than 0.1 μM but less than 10 μM. If not, the signal can't go through Gate 1, so there is no warning light, and the screen of the logic detector displays "UL (ultra low)" and three green lights. On the other hand, when the first red warning light is on, the screen of the logic detector displays "L (low)" and a bright red light, which is visible with the naked eye. To examine if the concentration of Glu exceeds 10 μM and is less than 10 mM, Gate 2 was designed. In the truth table of Gate 2, it can be seen that if $C_{Glu} > 10$ μM and the Output 1 is 1, then the Output 2 is 1, producing two red warning lights on, a "M (medium)" on the screen, and a dark red light that is visible to the naked eye. If the concentration of Glu exceeds 10 μM, the tandem logic gates come to Gate 3 to examine if the concentration is greater than 10 mM. When the concentration of Glu is greater than 10 mM as well as the Output 2 is 1, the three red warning lights are all on. Meanwhile, the screen of the logic detector displays a dark light that is visible with the naked eye and an "H (high)" on it. The sensing process of this logic detector is simply and intuitively presented in Fig. 13.17C [14].

Zhang et al. constructed a luminescent MOF (Eu^{3+}@Bio-MOF-1) to detect FA in water and food. Experiments showed that the two luminescent centers of Eu^{3+}@Bio-MOF-1 have completely different responses to FA that can offer a reference for each other, so it can be designed as a precise self-calibrating luminescent detector for FA. Based on this, a portable self-calibrating luminescent logic detector capable of gradient detection of FA was designed. The three different outputs of this logic detector were L (low), H (high), VH (very high),

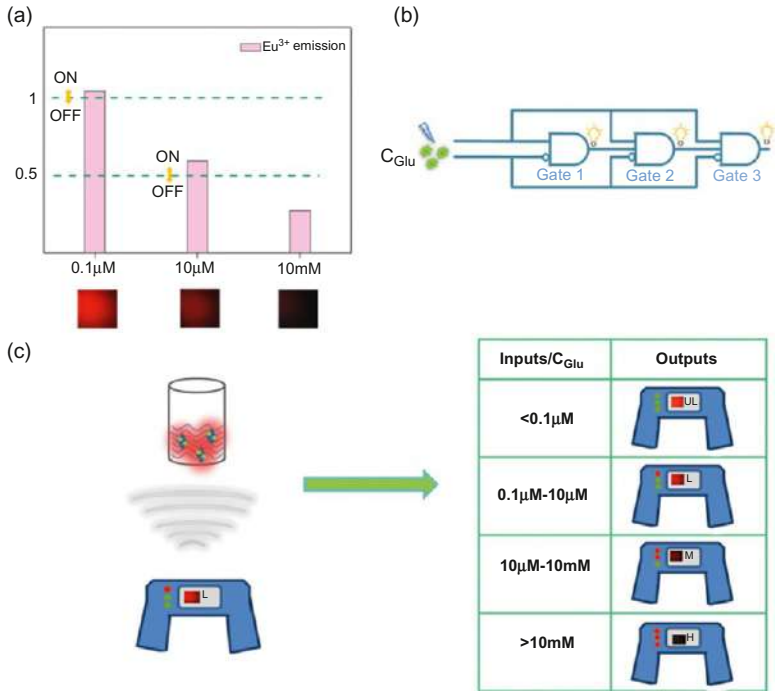

FIG. 13.17 (A) Column diagram of the fluorescence intensity: the dashed line shows the threshold (the inset is the corresponding photographs from Edinburgh FLS920 spectrophotometer with the excitation of 337 nm); (B) The electronic equivalent circuitry of the combinational logic gate system in the logic detector; (C) Simple scheme for the sensing process of the logic detector. *(Reproduced with permission from Y. Zhang, B. Yan, A point-of-care diagnostics logic detector based on glucose oxidase immobilized lanthanide functionalized metal-organic frameworks. Nanoscale 11 (2019) 22946-22953. Copyright 2019 Royal Chemical Society.)*

corresponding to three different inputs (<6 ppm, 6∼10 ppm, >10 ppm). More importantly, the color differences can be easily distinguished by the naked eye under UV light, which makes a significant contribution toward outputting the concentration of FA more intuitively in daily life. As shown in Fig. 13.18B, using the concentrations of FA and λ_{ex} as the double inputs and the intensities of I_L/I_{Eu} as the output, the first logic gate, named Gate 1, was designed. In the truth table of Gate 1 in Fig. 13.18E, only if both FA and λ_{ex} are present, the output1 is 1. It can be clearly concluded that the main function of the first Gate 1 is to detect the presence of FA. If there is no FA, the tandem logic gates are broken. If FA exists, the output1 is 1; as a result the logic detector outputs "L (low)" and a red light visible to the naked eye. Next, the output of Gate 1, the concentrations of FA and λ_{ex}, are used as the three inputs of Gate 2 to detect whether the concentration of FA exceeds 6 ppm. In the histogram for I_L/I_{Eu} in Fig. 13.18A, the threshold of Gate 2 is labeled as 1. In that way the output2

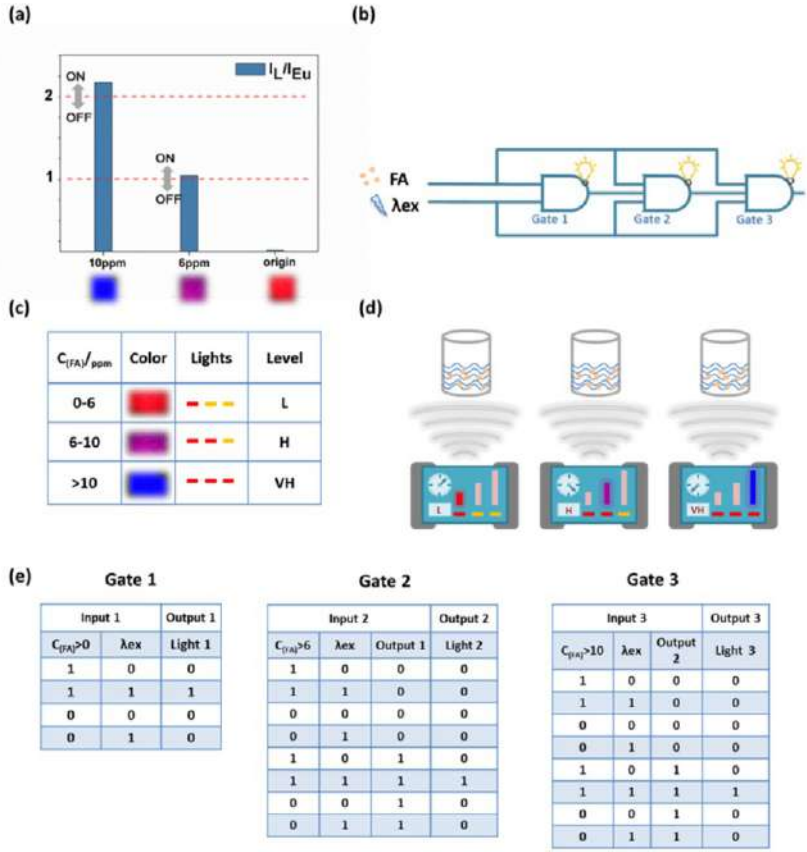

$C_{(FA)}$/ppm	Color	Lights	Level
0-6			L
6-10			H
>10			VH

Input 1		Output 1
$C_{(FA)}$>0	λex	Light 1
1	0	0
1	1	1
0	0	0
0	1	0

Input 2			Output 2
$C_{(FA)}$>6	λex	Output 1	Light 2
1	0	0	0
1	1	0	0
0	0	0	0
0	1	0	0
1	0	1	0
1	1	1	1
0	0	1	0
0	1	1	0

Input 3			Output 3
$C_{(FA)}$>10	λex	Output 2	Light 3
1	0	0	0
1	1	0	0
0	0	0	0
0	1	0	0
1	0	1	0
1	1	1	1
0	0	1	0
0	1	1	0

FIG. 13.18 (A) Column diagram of the fluorescence intensity: the dashed line shows the threshold; (B) The electronic equivalent circuitry of the combinational logic gate system in the logic detector; (C) Corresponding color, lights, and FA level for different concentrations of FA on the screen of the logic detector; (D) Simple scheme for the sensing process of the logic detector. (E) The truth table of Gate 1, Gate 2, and Gate 3. *(Reproduced with permission from Y. Zhang, B. Yan, A portable self-calibrating logic detector for gradient detecting formaldehyde based on luminescent metal organic frameworks hybrids. J. Mater. Chem. C 7 (2019) 5652-5657. Copyright 2019 Royal Chemical Society.)*

is definitely 1, which can be observed in the truth table of Gate 2 in Fig. 13.18E. Consequently a purple light and "H (high)" can be seen presented by the logic detector. If the concentration of FA is over 10 ppm, it goes to Gate 3. With the Gate 2 outputs of 1, the output of Gate 3 is 1 in the presence of the excitation. Hence the logic detector outputs "VH (very high)" and a blue light, which is visible to the naked eye, reminding us that the concentration of FA is at a relatively high value. The process of gradient sensing of FA described here is also vividly and intuitively represented in Fig. 13.18C and D [15].

Lian et al. described a new strategy for the fabrication of an enantio-selective membrane (Eu@Zn-MOF@ZnO) for logic circuit devices. This membrane exhibits a preferential sensing performance to *R*-penicillamine (*R*-Pen) over *S*-penicillamine (*S*-Pen), with a ratiometric luminescence response. They also showed that the enantio-selective response membrane can be used as a logic-gate strategy to be applied in an enantiomer monitor, circulating control electrocircuit and ROM arrays. At first, a logic gate circuit (GC-1) as a half-adder (Fig. 13.19A; top, left), was designed based on the emission change of the Eu@Zn-MOF@ZnO membrane. In consideration of the inputs, the presence and absence of *R*-Pen are defined as 1 and 0, respectively. Ultraviolet excitation is a necessary condition for producing fluorescence, which can be regarded as constant input 1 in logic statements. In the absence of *R*-Pen, Em_{blue} and Em_{red} keep their original states, generating the output (0, 1). After exposure into *R*-Pen, Em_{blue} intensity increased and Em_{red} intensity decreased, generating the output (1, 0). The truth table for the half-adder decoder logic gate is given in Fig. 13.19B (top, left). A more sophisticated detecting strategy was proposed subsequently: the content (e.e.%) of *R*-Pen replaced the input value 0 or 1, and the fluorescence intensity at 0% enantiomeric excess (e.e.) was chosen as the threshold (Fig. 13.19C; top, left). The analysis of these changes according to the logic operation provided direct detection for *R*-Pen levels in the enantiomer mixture, whereafter a reverse gate circuit with input "Em_{blue}" and "Em_{red}" and output "e.e.%" was also designed and actualized. As shown in Fig. 13.19A (top, right), a gate circuit (GC-2) composed of a three-state gate and NAND gate can output three signals: 0, 1, and Z (high impedance). By selecting the same threshold as GC-1, GC-2 could output signal 1 in the presence of Em_{blue} only. In the presence of Em_{red} input only, the GC-2 will output the signal 0, which indicates the negative value of e.e.%. The signal Z is a special output of the three-state gate, which means that the circuit is in the open circuit state at this time. The signal Z is output only when the input signal is (1,1), indicating that the detected mixture is a raceme (e.e.%=0%). The truth table for this logic gate is given in Fig. 13.19B (top, right). Interestingly, the input and output of GC-1 and GC-2 have exactly one-to-one correspondence, and they can make up a reversible cycle circuit. The cycle circuit GC-3 is exhibited in Fig. 13.19A (bottom); the red and blue dotted boxes are GC-1 and GC-2, respectively, and they form a closed loop together. As a steerable electronic component, the LED is supervised by the output value of the circuit. After the first cycle, the output of GC-3 will be changed to 0 causing the LED to turn off. Consequently, 0 and 1 will be output by the GC-3 alternated and uninterrupted (Fig. 13.19B; bottom), and the intelligent control of LED that uninterrupted scintillation between "ON" and "OFF" is achieved. Furthermore, the transformative circuit of GC-3 is applied in ROM arrays. ROM is a common information memory in a computer using binary encoding to achieve huge information storage. As the chart shows (Fig. 13.19C; bottom), the output of GC-1 is used as a ROM decode, and a set of algorithms for decoding and writing information is designed. For

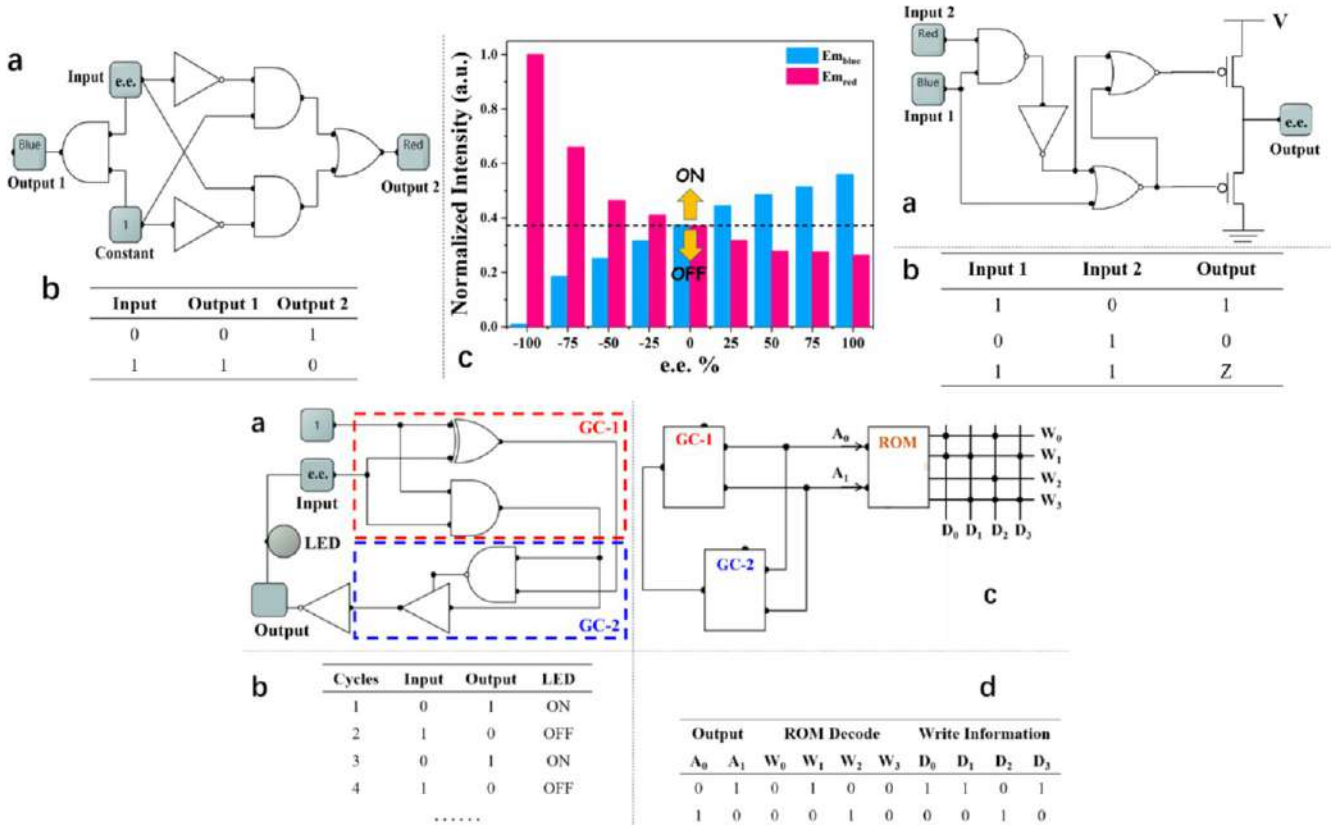

FIG. 13.19 *(Top, Left)* (A) Circuitry for the half-adder GC-1 logic gate; (B) Truth table corresponding to the GC-1 circuit; (C) Column diagram of the normalized fluorescence intensity of I_{blue} and I_{red} toward different enantiomeric excess (e.e.%) of *R*-Pen ranging from −100% to 100%. *(Top, Right)* (A) Circuitry for the GC-2 logic gate; (B) Truth table corresponding to the GC-2 circuit. *(Bottom)* (A) Circuitry for the half-adder GC-3 cycling system; (B) Circuitry for the GC-3 cycling logic gate; (C) Circuitry for the ROM arrays; (D) The decoding and writing information of ROM arrays based on the output A_0 and A_1. *(Reproduced with permission from X. Lian, B. Yan, A luminescent hybrid membrane-based logic device: from enantio-selective discrimination to read-only memory for information processing. ACS Appl. Mater. Interfaces 10 (2018) 29779-29785. Copyright 2018 American Chemical Society.)*

example, when the signal (0, 1) is input into the ROM matrix, the "AND" logic gate code is calculated as (W_0, W_1, W_2, W_3 = 0, 1, 0, 0), and a string (D_0, D_1, D_2, D_3 = 1, 1, 0, 1) is written and stored in the ROM (Fig. 13.19D; bottom). By controlling the e.e.% of *R*-Pen of the solution, and further controlling the intensity of the blue and red emission, the function of information storage is realized. By designing logic circuits and algorithms, the MOFs membrane can integrate ROM and store binary information [16].

Min et al. prepared a fluorescent and electron-deficient hybrid, N-methylated [Eu(pddb)phen$(ox)_{0.5}]_n$ (Eu-MOF-Me) via PSM, which was developed as a visualized fluorescent probe. In this system, Eu-MOF-Me served as the gate; by taking F^-, I^- and S^{2-} as the inputs and fluorescence emission bands (UV_{380}, B_{437}, and R_{612}) as the outputs, some primary logic gates (NOR, IMP, YES, NOT) and the combination of them were realized. For further application, a molecular computing keypad-lock security system was obtained. The aforementioned Boolean logic gates are basically employing a combination of different anions as the inputs, and the outputs haven't been correlated with the adding order of the anions utilized. For the purpose of taking full advantage of the Eu-MOF-Me system in molecular logic gates, its potential in sequential logic was explored, in which the outputs were linked to the sequence of the input signals. Therefore Eu-MOF-Me was able to construct a sequential logic with memory function. Inspired by this important feature, a molecular keypad-lock system based upon Eu-MOF-Me was fabricated. In this system, as shown in Fig. 13.20A, UV_{380} and R_{612} are defined as the outputs with a threshold value of 0.2, 1.2, respectively. To simplify and visualize the description of these sequence-dependent phenomena, as Fig. 13.20C suggests, the input anions

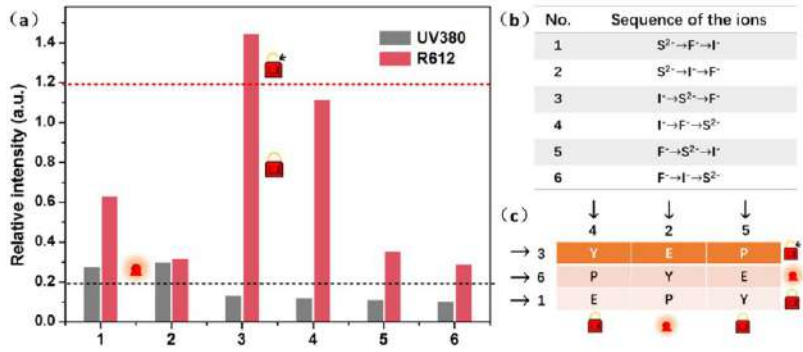

FIG. 13.20 (A) Column diagram of fluorescence intensities at 380 and 614 nm: the dashed lines show the thresholds (*black* one for UV_{380}: 0.2 and *red* one for R_{612}: 1.2); (B) the table showing the adding sequence of anions (C) the keypad-lock security system with different input sequences. Y, E, and P represent I^-, F^-, and S^{2-}, respectively. *(Reproduced with permission from J. Min, X. Qu, B. Yan, Post-modified Eu (III) metal-organic framework as an intelligent molecular logic gate for visual monitoring important anions. Microchim. Acta 187 (2020) 434. Copyright 2020 Springer.)*

I^-, S^{2-}, and F^- were designated as specific letters "Y", "E", "P" separately. This keypad-lock can be opened only when the correct word "YEP" is generated, which means the adding order of these three anions must be $I^- \rightarrow S^{2-} \rightarrow F^-$. All other sequences are invalid and an alarm will be touched off if S^{2-} is selected as the first input anion. Additionally, the keypad-lock system is reusable, since fluorescence responses occur without destroying the structure of the Eu-MOF-Me [17].

Wang et al. selected Ga-MOF ($Ga(OH)(btec)\cdot 0.5H_2O$), a complex 3D hybrid framework whose two noncoordinated carboxyl groups make it possible to introduce RE^{3+} ions by PSM. With addition of CIP, a distinct luminescence enhancement can be observed from the compound. A logic gate strategy was also introduced to the probe to rapidly and conveniently monitor CIP. They defined the normalized logarithm of the fluorescence intensity of them as the threshold value to judge OFF (0) or ON (1) states, as shown in Fig. 13.21A. Fig. 13.21B presents the electronic equivalent circuitry of the Boolean logic gates, Gate 1 and Gate 2. For Gate 1, they chose the concentration of CIP

(a)

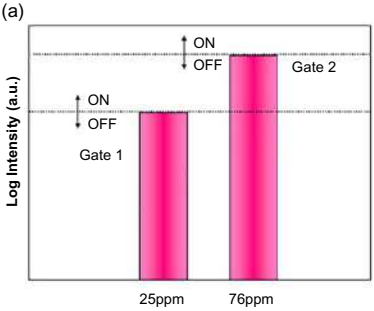

(b)

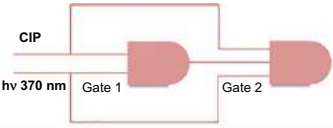

(c)

$C_{(CIP)}$/ppm	Level(exceed)	Color
25	NORMAL	
76	HIGH	

(d)

Input 1		Output 1
$C_{(CIP)}$>25 ppm	hv	614 nm
0	0	0
0	1	0
1	0	0
1	1	1

(e)

Input 2			Output 2
$C_{(CIP)}$>76 ppm	hv	Output 1	614 nm
0	0	0	0
1	0	0	0
0	1	0	0
0	0	1	0
1	1	0	0
0	1	1	0
1	0	1	0
1	1	1	1

FIG. 13.21 (A) Column diagram of the normalized fluorescence intensities and the setting of the threshold; (B) Specific circuitry of the logic gate operation; (C) Corresponding fluorescence, level for the concentrations of CIP; (D) Truth table of the 2-to-1 logic gate Gate 1; (E) Truth table of the 3-to-1 logic gate Gate 2. *(Reproduced with permission from B. Wang, B. Yan, A turn-on fluorescent probe Eu3 + functionalized Ga-MOF integrated with logic gate operation for detecting ppm-level Ciprofloxacin (CIP) in urine. Talanta 208 (2020) 120438. Copyright 2020 Elsevier.)*

and 370-nm excitation wavelength as the double input. The logarithm of the fluorescence intensity of Eu^{3+} at 614 nm was taken as the single output. Different inputs lead to disparate results. The truth table of the 2-to-1 logic gate Gate 1 suggests that only if the system is subjected to both inputs simultaneously is the output signal generated (true value 1). For Gate 2, they used a similar design strategy to create the 3-to-1 logic gate. It is worth mentioning that the output of Gate 1 was the newly added input of Gate 2. If all of the three inputs are satisfied, the tandem logic gate system continues to operate and produce the output signal (true value 1). The corresponding possibilities of Gate 2 are displayed in Fig. 13.21E. While the input of Gate 1 is (0, 1), which means the input of $C_{(cip)}$ is below 25 ppm at the excitation wavelength of 370 nm, the result of the detection of CIP is "LOW". When the input of Gate 2 is (0, 1, 1), the result of the detection of CIP is "NORMAL", meaning the concentration of the CIP in urine is between 25 ppm to 76 ppm. If the input of Gate 2 is (1, 1, 1), the result of the detection of CIP is "HIGH", meaning the concentration of the CIP in urine exceeds 76 ppm. Also, the level of the CIP concentration in urine can be readily estimated by comparison with the concentration-dependent picture, according to the change of the fluorescence (Fig. 13.21C) [18].

References

[1] A.P. de Silva, Molecular Logic-Based Computation, RSC, 2012.

[2] D.C. Magri, Logical sensing with fluorescent molecular logic gates based on photoinduced electron transfer, Coord. Chem. Rev. 426 (2021), 213598.

[3] S. Erbas-Cakmak, S. Kolemen, A.C. Sedgwick, T. Gunnlaugsson, T.D. James, J. Yoon, E.U. Akkaya, Molecular logic gates: the past, present and future, Chem. Soc. Rev. 47 (2018) 2228–2248.

[4] A.P. de Silva, S. Uchiyama, T.P. Vance, B. Wannalerse, A supramolecular chemistry basis for molecular logic and computation, Coord. Chem. Rev. 251 (2007) 1623–1632.

[5] A.P. De Silva, H.Q.N. Gunaratne, C.P. Mccoy, A molecular photoionic and gate based on fluorescent signaling, Nature 364 (1993) 42–44.

[6] J. Andreasson, U. Pischel, Molecules with a sense of logic: a progress report, Chem. Soc. Rev. 44 (2015) 1053–1069.

[7] F.M. Raymo, Digital processing and communication with molecular switches, Adv. Mater. 14 (2002) 401–414.

[8] X. Zhang, Q. Hu, T. Xia, J. Zhang, Y. Yang, Y. Cui, B. Chen, G. Qian, Turn-on and ratiometric luminescent sensing of hydrogen sulfide based on metal-organic frameworks, ACS Appl. Mater. Interfaces 8 (2016) 32259–32265.

[9] X. Xu, B. Yan, Intelligent molecular searcher from logic computing network based on Eu(III) functionalized UMOFs for environmental monitoring, Adv. Funct. Mater. 27 (2017) 1700247.

[10] X. Zhang, L. Fang, K. Jiang, H. He, Y. Yang, Y. Cui, B. Li, G. Qian, Nanoscale fluorescent metal-organic framework composites as a logic platform for potential diagnosis of asthma, Biosens. Bioelectron. 130 (2019) 65–72.

[11] T. Sun, P. Wang, R. Fan, W. Chen, S. Hao, Y. Yang, Functional microscale single-phase white emission lanthanide MOF for tunable fluorescent sensing and water quality monitoring, J. Mater. Chem. C 7 (2019) 3598–3606.

[12] L. Feng, C. Dong, M. Li, L. Li, X. Jiang, R. Gao, R. Wang, L. Zhang, Z. Ning, D. Gao, J. Bi, Terbium-based metal-organic frameworks: highly selective and fast respond sensor for styrene detection and construction of molecular logic gate, J. Hazard. Mater. 388 (2020), 121816.
[13] S. Qin, X. Qu, B. Yan, A self-calibrating bimetallic lanthanide metal-organic luminescent sensor integrated with logic gate operation for detecting N-methylformamide, Inorg. Chem. Front. 5 (2018) 2971–2977.
[14] Y. Zhang, B. Yan, A point-of-care diagnostics logic detector based on glucose oxidase immobilized lanthanide functionalized metal-organic frameworks, Nanoscale 11 (2019) 22946–22953.
[15] Y. Zhang, B. Yan, A portable self-calibrating logic detector for gradient detecting formaldehyde based on luminescent metal organic frameworks hybrids, J. Mater. Chem. C 7 (2019) 5652–5657.
[16] X. Lian, B. Yan, A luminescent hybrid membrane-based logic device: from enantio-selective discrimination to read-only memory for information processing, ACS Appl. Mater. Interfaces 10 (2018) 29779–29785.
[17] J. Min, X. Qu, B. Yan, Post-modified Eu (III) metal-organic framework as an intelligent molecular logic gate for visual monitoring important anions, Microchim. Acta 187 (2020) 434.
[18] B. Wang, B. Yan, A turn-on fluorescent probe Eu^{3+} functionalized Ga-MOF integrated with logic gate operation for detecting ppm-level Ciprofloxacin (CIP) in urine, Talanta 208 (2020), 120438.

Chapter 14

Rare earth metal-organic framework hybrid materials for luminescence responsive chemical sensing imaging

Fluorescence imaging techniques have become powerful tools for noninvasive visualization of biological processes inside living systems in real time with high spatial resolution [1–20]. Compared with methods such as nuclear magnetic resonance (NMR) and microelectrodes, fluorimetry provides a better understanding of cellular internalization pathways and pathogenic processes because of its noninvasive, real-time imaging as well as high spatiotemporal resolution [7]. Fluorescence microscopy is a rapidly developing optical imaging technique ideal for analyzing biological samples at high resolution such that individual cells can be imaged. Diffraction limited microscopy has an image resolution of ca. 200∼250 nm, but further developments in hardware and software have facilitated superresolved fluorescence microscopy at ca. 20∼100-nm image resolution, rendering subcellular components in remarkable detail. For luminescent molecules, the absorption and emission wavelengths, observed lifetime, and quantum yield are key physical parameters that describe the luminescence. Typically, the emitted photon possesses a lower energy than the absorbed photon and this difference in wavelengths is defined as Stokes shift. Consideration of these parameters is critical to the application of luminescent molecules in biological imaging. However, there are significant photophysical and biological advantages to the use of *f*-metal ion coordination compounds in such applications. In particular, the exciting opportunities are afforded by luminescent RE^{3+}-based systems (large Stokes shifts; long luminescent lifetimes) [5].

Confocal fluorescence microscopy (CFM) is a powerful optical technique that makes use of luminescence to generate the image. It is possible to obtain confocal fluorescence microscopes with a range of different light excitation sources, which, together with suitable optics, can deliver a monochromated wavelength to the sample. The use of near-infrared (NIR) light allows better light penetration and improved imaging depth. Multiphoton excitation sources are now also available, potentially allowing low-energy (e.g., NIR) irradiation of samples. The magnitudes of two- and three-photon cross sections thus

Rare Earth Metal-Organic Framework Hybrid Materials for Luminescence Responsive Chemical Sensors
https://doi.org/10.1016/B978-0-323-91236-5.00012-8

determine the required light intensity for excitation and may constrain bioapplicability of a given probe; typical TPA values for organic chromophores are 10 ~ 100 GM, but higher TPA cross sections facilitate lower irradiating light intensities. Significant progress has been made in recent years with the utility of RE^{3+} complexes and optimized cross sections [5–9]. Fluorescence lifetime imaging microscopy (FLIM) is a more advanced form of the technique and creates the image based on the emission lifetime rather than the intensity of the signal. A pulsed light source is required and FLIM commonly employs time-correlated single-photon counting (TCSPC); modern microscopes can have picosecond resolution. The principal advantage of FLIM is that it can deliver quantitative information, since the lifetime of the probe is independent of its concentration, providing measurement of dynamic events and an ability to monitor cellular compartments with good spatial resolution. The equivalent approach that makes explicit use of phosphorescent probes, such as relevant metal complexes, is termed PLIM. In a subtle variation, gated microscopy allows the luminescence signal to be collected after a prescribed time delay, which is particularly useful for removing short-lived fluorescence (to 20 ns) from endogenous (biological) fluorophores [5].

Medical imaging refers to technologies that create visual representations of the inside of a human body to provide precise positional and morphologic information for clinical diagnosis. It allows identification of abnormalities according to a database of normal anatomy and physiology. Traditional diagnostic imaging technologies capture images and report qualities such as water content and density of specific areas. Molecular imaging has emerged as a modern imaging technology, which focuses on tracking biomarkers, collecting information on their surroundings, and giving fundamental molecular pathways and functions in cells, tissues, organs, and organisms. While traditional diagnostic imaging directly visualizes pathological tissues, molecular imaging allows early diagnosis at the molecular and cellular level before tissue damage occurs or typical symptoms of a disease are observed. The major modalities of molecular imaging for clinical diagnosis include positron emission tomography, single photon emission computed tomography (SPECT), magnetic resonance imaging (MRI), and medical optical imaging, each of which has its own strengths and weaknesses in regard to spatial resolution, temporal resolution, sensitivity, and cost. For example, positron emission tomography using radioactive isotopes as tracers has very high sensitivity, but expensive cyclotrons are needed to produce radionuclides. SPECT is significantly less expensive than positron emission tomography, but the spatial resolution is reduced because of less radiation event localization information analyzed. Luminescence imaging has attracted fast-growing interest owing to its high sensitivity and specificity. The rapid development of luminescence imaging microscopes and availability of a variety of emissive probes and labels has facilitated visualization of physiological and pathophysiological processes at cellular, subcellular, and molecular levels. Luminescence bioimaging offers a unique approach for visualizing

morphological details of tissues with subcellular resolution and has become a powerful tool for manipulation as a chemosensor [15].

Foucault-Collet et al. have created unique NIR-emitting nanoscale MOFs (NMOFs) incorporating a high density of Yb^{3+} cations and sensitizers derived from phenylene. They have established that these NMOFs can be incorporated into living cells for NIR imaging. Despite its relatively low quantum yield, nano-Yb-PVDC-3 emits a sufficient number of photons per unit volume to serve as an NIR-emitting reporter for imaging living HeLa and NIH 3T3 cells. NIR microscopy allows for highly efficient discrimination between the NMOF emission signal and the cellular autofluorescence arising from biological material. To confirm that the detected signal observed with confocal microscopy is arising from PVDC emission, they conducted spectral fluorescence microscopy analysis on cells after 24 h of incubation with nano-Yb-PVDC-3. At each individual point of the image (step size = 3 μm), an emission spectrum was recorded. Intensity value averaging between 400 and 600 nm was then used to create an intensity map of the cell (Fig. 14.1; left). This spectral fluorescence microscopy experiment permits the discrimination of nano-Yb-PVDC-3 emission from cellular autofluorescence. Spectra obtained from treated cells result from the overlay of autofluorescence emission and PVDC emission signals (λ_{em} = 455 nm). The ability to use nano-Yb-PVDC-3 as an NIR Yb^{3+}-based imaging agent was tested in an NIR microscopy experimental setup. HeLa and NIH 3T3 cells were incubated with 30 μg mL^{-1} nano-Yb-PVDC-3 for 24 h. In the NIR microscopy mode, the specific Yb^{3+} emission signal was collected with good sensitivity as the result of a high signal-to-noise ratio. In parallel, switching to visible detection mode, the specific fluorescence arising from the PVDC was observed in addition to the cellular autofluorescence, and the resulting images were used as a comparison. The images presented in Fig. 14.1 (right) report on NIR microscopy experiments obtained with a rare earth compound in living cells using a conventional excitation source [21].

Suresh et al. synthesized luminescent NMOFs of $\{[Gd(OPE)(NO_3)(H_2O)_2]\cdot H_2O\}$ (NCP-1, OPE = oligo-(*p*-phenyleneethynylene)dicarboxylate) by coordination-driven self-assembly of OPE and Gd^{3+} in polar solvent under refluxing conditions. NCP-1 forms a stable colloid in DMF, and no precipitation is observed for several months, suggesting the significant solution processability of NCP-1 colloids. Similarly to OPEA, ethanol dispersion of NCP-1 shows a strong linker-based blue emission (λ_{em} = 445 nm) on 330-nm excitation and intense cyan emission (λ_{em} = 463 nm, λ_{ex} = 390 nm) in solid state (Fig. 14.2; left). They further studied the internalization of these nanostructures into mammalian cells for bioimaging applications. Before doing optical imaging studies, NCP-1 was tested for its hydrolytic stability under physiological conditions. Incubation of nanorods of NCP-1 in PBS buffer for 12 h showed no considerable changes in emission properties (λ_{em} = 453 nm, λ_{ex} = 390 nm, only L in PBS emitted at 473 on 390-nm excitation) suggesting the stability of NMOFs in physiological conditions (Fig. 14.2B; left). Due to its self-fluorescence, they

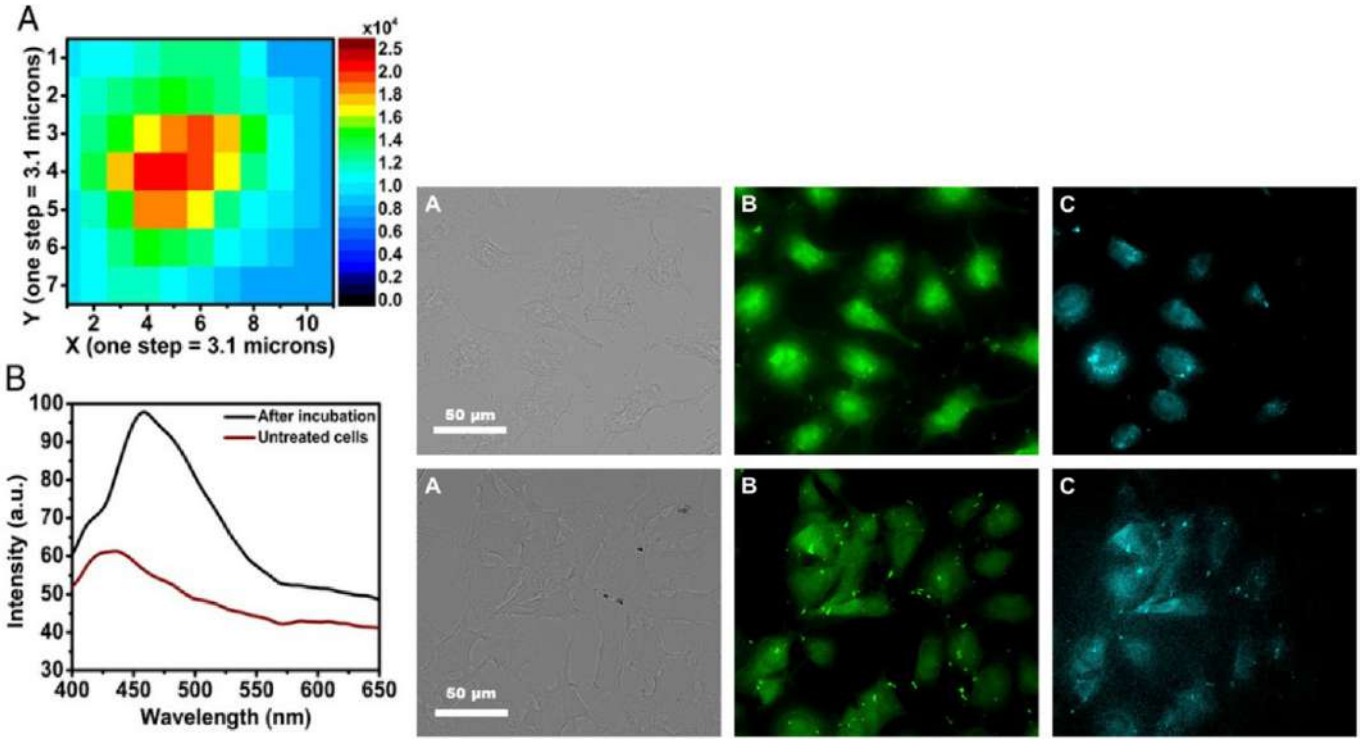

FIG. 14.1 *(Left)* Spectral microscopy of nano-Yb-PVDC-3 in the visible region. (A) Fluorescence intensity map of NIH 3T3 cells after incubation with 30 μg mL^{-1} nano-Yb-PVDC-3 ($\lambda_{ex}=340$ nm, $\lambda_{em}=390\sim650$ nm). (B) Spectra correspond to the mean of intensity of each map. *(Right)* Visible and NIR microscopy images of nano-Yb-PVDC-3 in HeLa cells (Upper) and NIH 3T3 cells *(Lower)* ($\lambda_{ex}=340$ nm). Brightfield (A), H_2-PVDC emission ($\lambda_{ex}=377/50$ nm, $\lambda_{em}=445/50$ nm) (B), and Yb^{3+} emission ($\lambda_{ex}=377/50$ nm, $\lambda_{em}=$long pass 770 nm) (C) images are shown. *(Reproduced with permission from A. Foucault-Collet, K. A. Gogick, K. A. White, S. Villette, A. Pallier, G. Collet, C. Kieda, T. Li, S. J. Geib, N. L. Rosi, S. Petoud, Lanthanide near infrared imaging in living cells with Yb3 + nano metal organic frameworks. PNAS 110 (2013) 17199–17204. Copyright 2011 National Academy of Sciences of the United State of America.)*

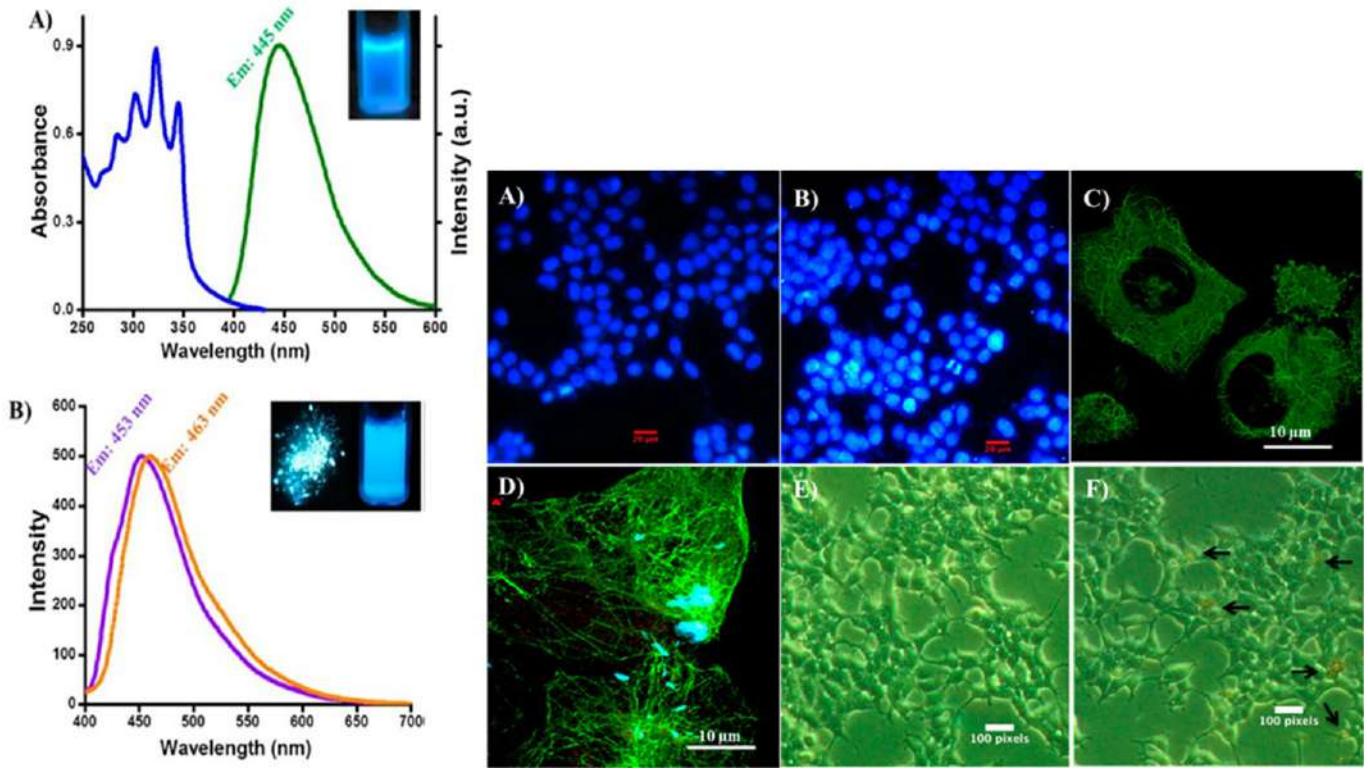

FIG. 14.2 Fluorescence microscope images of HEK 293T cells (A) before and (B) after treating with nanoparticles of NCP-1 showing its nontoxicity. The blue color represents nucleus (DAPI staining), and the cyan color represents NCP-1. (C), (D) confocal microscope images of H1299 cells before and after treating with nanoparticles of NCP-1, respectively. The green color represents the cell cytoskeleton (tubulin staining), and the cyan color represents NCP-1. Inverted microscopic images of H1299 cells (E) before and (F) after treatment with NCP-1. Arrows indicates the nanoparticles. *(Reproduced with permission from V. M. Suresh, S. Chatterjee, R. Modak, V. Tiwari, A. B. Patel, T. K. Kundu, T. K. Maji, Oligo(p-phenyleneethynylene)-derived porous luminescent nanoscale coordination polymer of GdIII: bimodal imaging and nitroaromatic sensing. J. Phys. Chem. C 118 (2014) 12241 – 12249. Copyright 2014 American Chemical Society.)*

studied the distribution of NCP-1 in the previously mentioned cell lines and observed appreciable distribution of NCP-1 throughout 293T cells evidenced through onfocal imaging (Fig. 14.2A and B; right). Immunofluorescence using antitubulin antibody also suggests the internalization of NCP-1 within the cytoplasm of H1299 cells, further strengthening its potential to cross cell membranes (Fig. 14.2C and D; right). It is thought that the nanorods enter the cell line longitudinally due to their nanoscale dimension of width (50∼100 nm). Interestingly, no floating or dead cells were observed even after 24 h of treatment, signifying the nontoxic effect of NCP-1 upon cellular internalization (Fig. 14.2E and F; right). These results suggest that the highly stable, less toxic nanostructures of NCP-1 can be internalized into cells for bioimaging applications under physiological conditions [22].

Wang et al. designed an adenosine-5′-triphosphate (ATP) -aptamer/MOF-RE nanosheet complex, to monitor ATP activity in living cells, where ATP aptamers labeled with FAM and TAMRA are used to assemble multiple dye-aptamer/MOF-RE nanosheets. Dye-labeled ATP aptamers on MOF-La nanosheets are used for intracellular two-color fluorescent imaging of ATP. In the presence of the target ATP, the specific binding of Dye-P2 with ATP induced the formation of a rigid structure. Similar to dsDNA, the affinity of this rigid ATP aptamer conformation for the surface of MOF-La nanosheets was very weak. This ATP sensing was based on the Turn-On of the fluorescence of TAMRA and the Turn-Off of the fluorescence of FAM, upon addition of target ATP. Therefore the dye-P2+MOF-La biosensor can be used for intracellular adenosine probing in MCF-7 human breast cancer cells using confocal microscopy. After MCF-7 cells were incubated with dye-P2+MOF-La, the intracellular adenosine molecules interacted with the dye-P2 (Fig. 14.3A; top). By irradiation with 488-nm light, a distinguishable fluorescence change was observed corresponding to FAM at 500∼550 nm (green) and TAMRA at 550∼650 nm (red). These findings indicate that the dye-P2 targeted adenosines to form a duplex configuration, resulting in the detachment of the dye molecules from the surface of the MOF-La nanosheets and subsequent fluorescence recovery. Adenosine activity in single cells was also monitored by the dye-P2+MOF-La biosensor. As shown in Fig. 14.3B (top), after incubating for 4 h, the fluorescence color in different cells changed from green to red; this difference in color emission was also monitored in single cells (Fig. 14.3C–E; top). Adenosine activity was clearly observed in different cells and different regions of a single cell. By calculating the ratio of F′TAMRA/F′FAM, the adenosine concentration in living cells was semideterminated (data indicated in Fig. 14.3; top). The concentration of adenosines in living cells, incubated with the dye-P2+MOF-La biosensor for 2 or 4 h, could be monitored from 0.5 to 15 nM. When the incubation time was more than 6 h, the ratios of F′TAMRA/F′FAM were beyond the linear range of the method using the prepared dye-P2+MOF-La biosensor. For detecting high concentrations of adenosines (415 nM), more FAM-P2 and TAMRA-P2 should be incubated with the MOF-La nanosheets during the preparation of the dye-P2+MOF-La complex.

Considering that cellular ATP is predominantly produced in the mitochondria during aerobic respiration, the distribution of adenosines and mitochondria in living cells are monitored together. As shown in Fig. 14.3A–C (bottom), after the dye-P2+MOF-La and FMD were contained in MCF-7 cells, some of the adenosines were monitored around mitochondria. As adenosines generally exist in the mitochondria and cytosol, the distribution of adenosines does not overlap well

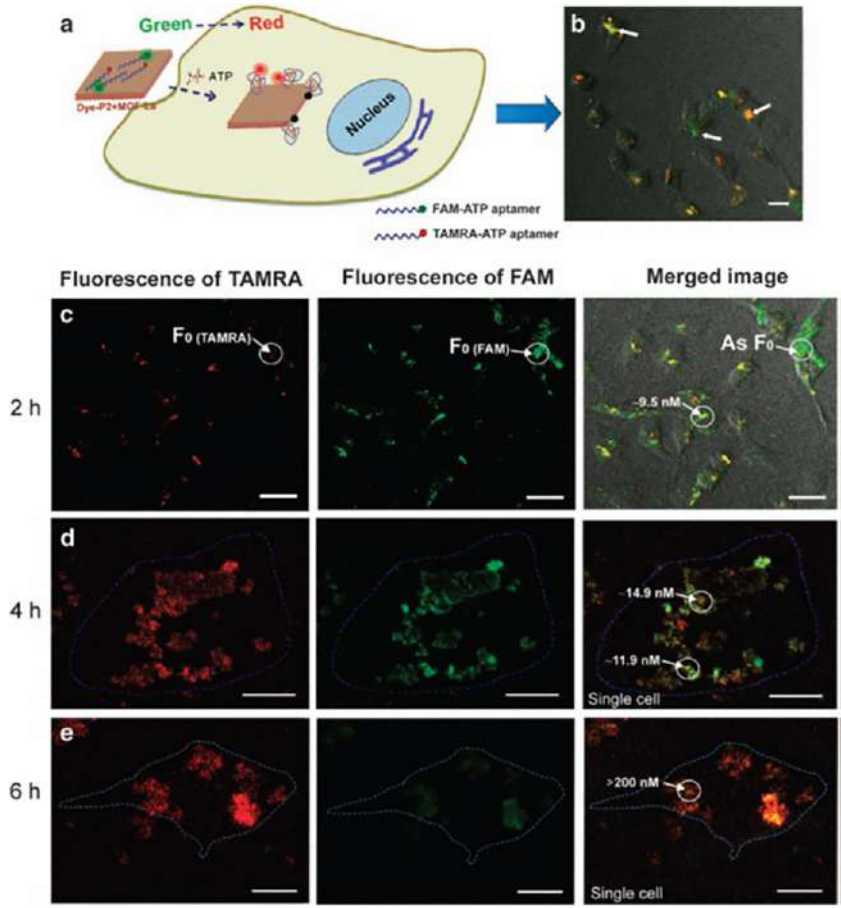

FIG. 14.3 *(Top)* Intracellular fluorescent imaging of adenosines. (A) Schematic illustration of intracellular adenosine probing in living cells using dye-P2+MOF-La. (B) Monitoring of adenosine in living cells. *(Bottom)* (C–E) Confocal images of intracellular visualization for adenosines with an incubation time of 2 to 6 h and quantification of adenosines by two-color fluorescence. Scale bars: B, 25 μm; C, 30 μm; D, E, 10 μm. Fig. 7 Confocal fluorescence images of MCF-7 cells incubated with dye-P2+MOF-La and FMD. (A–C) Single cells incubated with dye-P2 +MOF-La and FMD for 4 h. Scale bars: 10 μm. *(Reproduced with permission from H. Wang, J. Li, J. Li, K. Wang, Y. Ding, X. Xia, Lanthanide-based metal-organic framework nanosheets with unique fluorescence quenching properties for two-color intracellular adenosine imaging in living cells. NPG Asia Mater. 9 (2017) e354. Copyright 2017 Springer Nature.)*

(Continued)

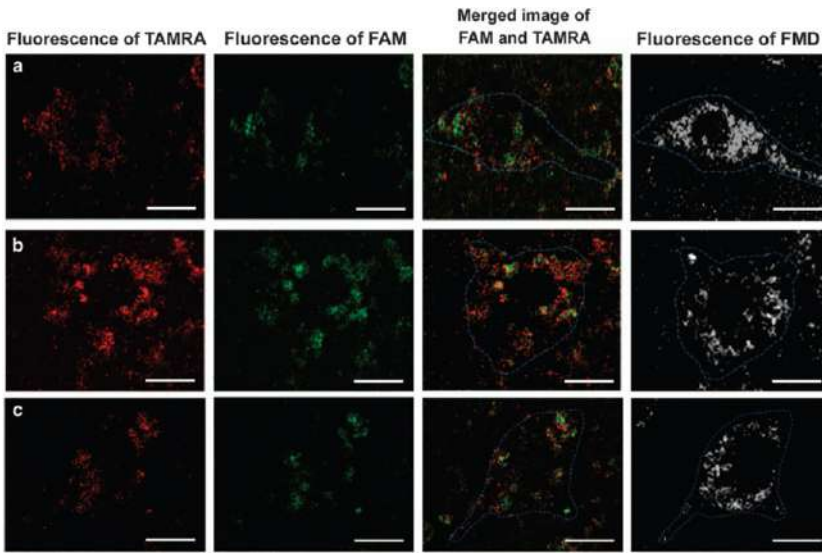

FIG. 14.3—CONT'D

with that of mitochondria (white color in Fig. 14.3 (bottom), $\lambda_{ex} = 644$ nm). In the control experiment, FAM-P3 (a FAM-labeled random DNA P3) and TAMRA-P3 (a TAMRA-labeled random DNA P3) are mixed with the MOF-La nanosheets to prepare a dye-P3+MOF-La complex, which is similar to the dye-P2+MOF-La complex. The dye-P2+MOF-La complex can be used as a selective sensing probe for detecting biomolecules in living cells [23].

Fan et al. designed and synthesized a porous and luminescent Tb-MOF (H_3TATB = 4,4′,4″-striazine- 2,4,6- triyl-tribenzoic acid), which shows enhanced luminescence originating from Tb^{3+} in the presence of Zn^{2+}. This Turn-On pattern was utilized for sensing Zn^{2+}. It has fairly acceptable biocompatibility, which has been fully verified by cytotoxicity testing. The optical microscopy imaging was used to monitor the living state of cells and luminescence of Tb-MOF both in the bright field and luminescent field excited with 365-nm UV light. As shown in Fig. 14.4, the PC12 cells attached closely to the substrate and showed abundant growth of axons and dendrites in the absence of both Tb-MOF and Zn^{2+} (Fig. 14.4A). There was a slight influence on both morphology and amount of PC12 cells on the addition of Zn^{2+} with a concentration of 10^{-3} M (Fig. 14.4B). Afterwards, on the basis of the MTT results, 50 μg mL^{-1} was chosen as the concentration for the imaging experiment. In the case of 50 μg mL^{-1} Tb-MOF, the PC12 cells showed a desirable appearance of neurites emitting compared with the control cells. What's more, Tb-MOF exhibited visible green light under 365-nm UV light excited at the cell atmosphere (Fig. 14.4C). Many MOF clusters

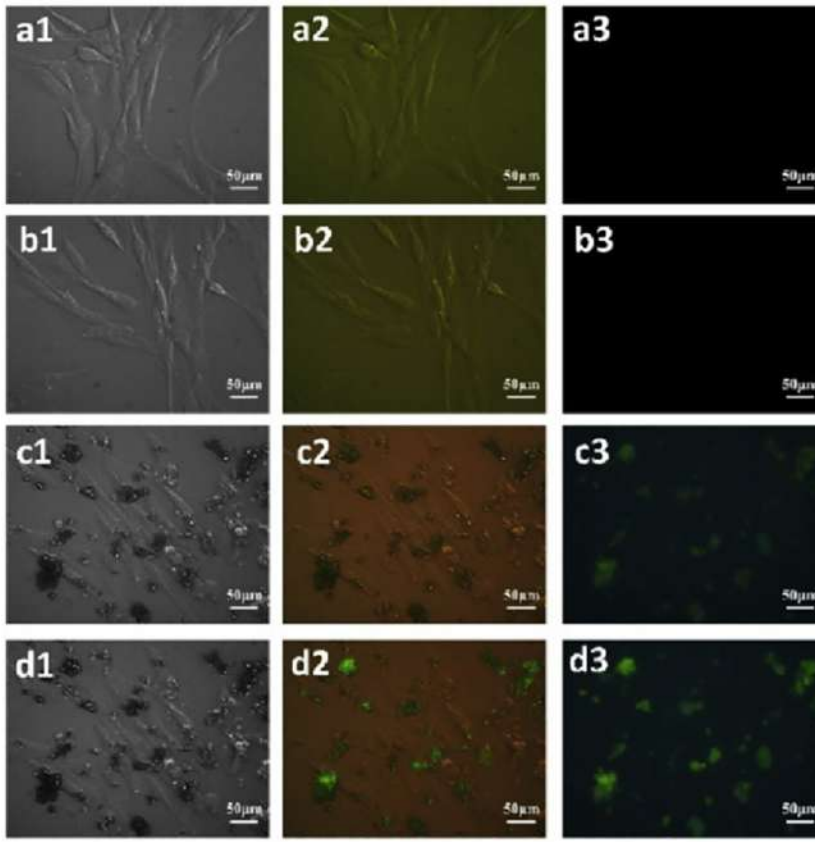

FIG. 14.4 Optical microscopy images of PC12 cells (A) without treatment, (B) incubated with 10^{-3} M Zn^{2+}, (C) incubated with 50 mg mL^{-1} Tb-MOF, and (D) subsequent addition of 10^{-3} M Zn^{2+}. Optical bright field microscopy image for a1, b1, c1, and d1, optical luminescent field microscopy image illuminated with 365-nm light for a3, b3, c3, and d3, overlapped for a2, b2, c2, and d2. *(Reproduced with permission from T. Fan, T. Xia, Q. Zhang, Y. Cui, Y. Yang, G. Qian, A porous and luminescent metal-organic framework containing triazine group for sensing and imaging of Zn2+. Microp. Mesop. Mater. 266 (2018) 1–6. Copyright 2018 Elsevier.)*

were observed as green dots and accumulated around the cells. The colocalized luminescence signals indicated that there were no appreciable changes in the state, morphology, and long stretching microtubular of PC12 cells after the introduction of Tb-MOF, demonstrating the good biocompatibility of Tb-MOF even at a relatively high concentration. Subsequent addition of Zn^{2+} gave rise to a brightness enhancement without affecting the living state of the PC12 cells (Fig. 14.4D). The Turn-On effect in the cell environments agreed well with the phenomenon that was discovered in the luminescence study. The results indicated that Tb-MOF is biocompatible among neuron survival and neurite outgrowth owing to the enriched

neurites. Meanwhile, Tb-MOF exhibits coincident luminescence properties with the spectra study [24].

Zhang et al. fabricated a fluorescent pH sensor based on postsynthetically modified nanoscale UiO-67-bpydc with Eu^{3+} incorporated (Eu^{3+}@UiO-67-bpydc), which was developed as a pH sensor. The MTT analysis showed that Eu^{3+}@UiO-67-bpydc possesses favorable biocompatibility. Furthermore, optical microscopy graphs were used to validate the nontoxic natures of Eu^{3+}@UiO-67-bpydc and cell imaging. PC12 cells were chosen for their enriched neuritis and adherence to the culture plate, which can reflect the state of the cells and can be easily observed under microscopy. PC12 cells were cultured with different concentrations (0, 10, 30, and 50 g mL^{-1}) of Eu^{3+}@UiO-67-bpydc for 24 h and their morphology was analyzed by optical microscopy. In some cells, MOFs were enriched in the growth cone of neurites. Regardless of incubation with Eu^{3+}@UiO-67-bpydc, the appreciable neuritis extension of PC12 cells convincingly indicated good biocompatibility and negligible cytotoxicity Eu^{3+}@UiO-67-bpydc. As shown in Fig. 14.5, PC12 cells loaded with 10 mg mL^{-1} of Eu^{3+}@UiO-67-bpydc showed extremely weak red emission with an excitation of 330 nm. However, a significant increase of fluorescence intensity was observed in the cells coincubated with 30 mg mL^{-1} of Eu^{3+}@UiO-67-bpydc. This suggests probe Eu^{3+}@UiO-67-bpydc is suitable for application in fluorescent pH sensing in living cells [25].

Rosário et al. reported the ability of common flamentous fungi to accumulate RE-MOFs over their cell walls, thereby forming new classes of luminescent biohybrid cells. When microorganisms are cultivated in solutions

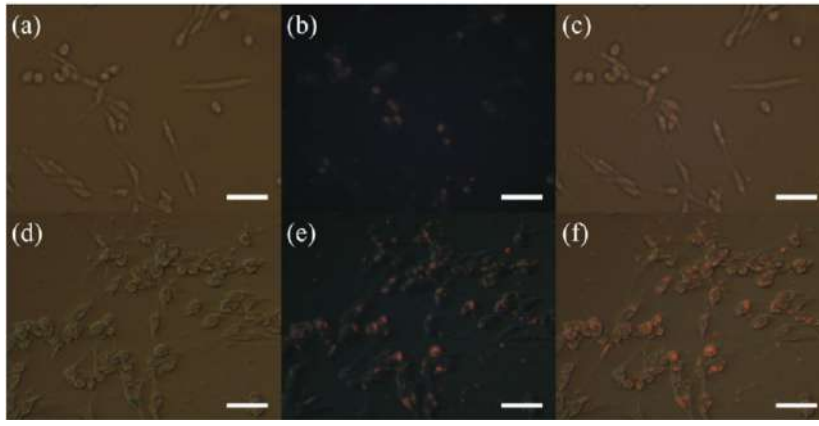

FIG. 14.5 (A) Fluorescent images of PC12 cells incubated with 10 mg mL^{-1} (A, B, and C) and 30 mg mL^{-1} (D, E, and F) Eu^{3+}@UiO-67-bpydc for 24 h. (A, D) Bright-field images; (B, E) Fluorescent images; (C, F) Merge of bright-field images and fluorescent images. The wavelength for excitation is 330 nm. Scale bar = 50 μm. *(Reproduced with permission from X. Zhang, K. Jiang, H. He, D. Yue, D. Zhao, Y. Cui, Yu Yang, G. Qian, A stable lanthanide-functionalized nanoscale metal-organic framework as a fluorescent probe for pH. Sens. Actuators B Chem. 254 (2018) 1069–1077. Copyright 2018 Elsevier.)*

containing a carbon source and discrete particulate RE-MOFs, they deposit these nonbiological objects over mycelia during the physiological process, forming a robust layer on the cellular wall of the fungi. RE-MOFs possess excellent properties that can be useful for in-vivo fungal images, as they do not require any surface modification to be biologically compatible and possess intense photoemission that permits easy discrimination between the target and the background emissions. Biohybrid fungi/RE-MOFs were examined under a conventional fluorescent microscope to display their luminescent properties. In Fig. 14.6A and B, the luminescence is definitely observable, due to the thick layer of green emitter attached to the fungal surface. Although both RE-MOFs presented similar emission intensities for dried biohybrids, a low intensity of the red light can be observed when

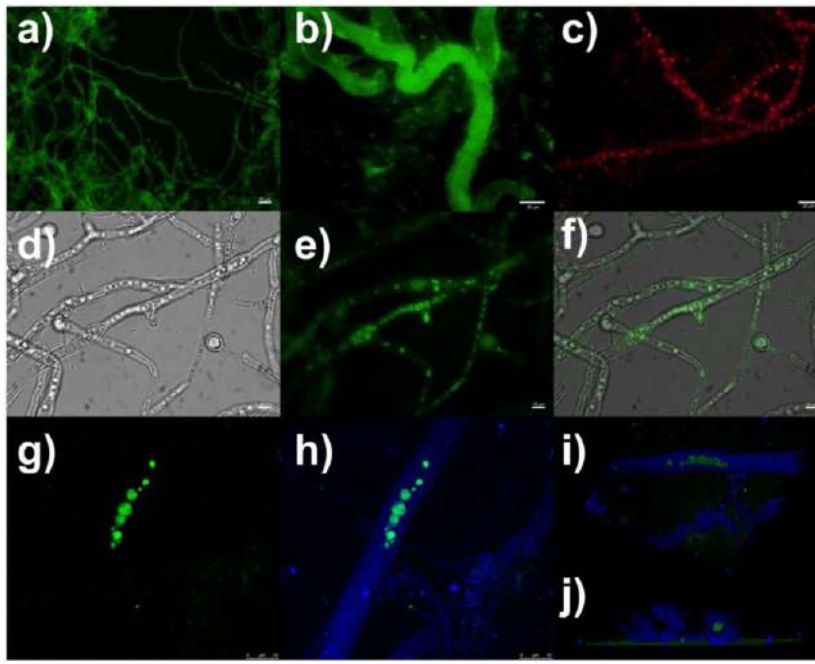

FIG. 14.6 Fungal species labeled with RE-MOFs. Fluorescence images of (A,B) *P. macrosporus*/Tb-MOF, and (C) *Trichoderma* sp./Eu-MOF. Vacuolar system of the *Trichoderma* sp./Tb-MOF biohybrids in (D) bright field, (E) fluorescence, and (F) composite images. The false colors are red and green for Eu-MOF and Tb-MOF, respectively. Confocal scanning laser images of *A. niger*/Tb-MOF: (G) fluorescently labeled organelles and (H) processed image emphasizing the colocalization of the organelles in the hyphal compartment. 3D cell reconstruction of CLSM images in a (I) longitudinal view and an (J) axial view, highlighting the inner localization of the luminescent organelles in the hyphae. *(Reproduced with permission from J. Rosário, L. L. da Luz, R. Geris, J. G. S. Ramalho, A. F. da Silva, S. A. Júnior, M. Malta, Photoluminescent organisms: how to make fungi glow through biointegration with lanthanide metal-organic frameworks. Sci. Rep. 9 (2019) 7302. Copyright 2019 Springer Nature.)*

analyzing living fungi/Eu-MOF investigated under the microscope, which results from the efficient nonradiative deactivation of luminescence through coupling between the hydroxyl group of water (O-H strength) and the *f* electronic levels of the Eu^{3+} ions. Therefore, despite the presence of chromophore species deposited on the fungal surface, the photoluminescence signal is quite low for living fungus/Eu-MOFs in aqueous environments. The group was intrigued by some results of fluorescent microscopy of the fungi/Eu-MOF, where it was possible to observe bright red spheres located along the hyphae (see Fig. 14.6C). RE-MOFs can concentrate at organellar lumen in the inner fungal cells, evidencing luminescence even for Eu-MOF. By selecting arbitrary regions at the periphery of the fungal biohybrid mycelia, the uptake of Tb-MOF improved the visualization of spherical and tubular organelles within cells (Fig. 14.6D and F). In order to confirm that the fluorescent signal arises from internalized RE-MOFs stored in the fungal organelles, additional experiments were performed using confocal scanning laser microscopy (CSLM, Fig. 14.6G–J). Since UV light is known to be prejudicial to the microorganisms, an excitation source was substituted in the experiments by using a low-energy microscope with a wavelength at 405 nm to study these biosystems. Specifically, Fig. 14.6G emphasizes the fluorescent vacuoles of the *A. niger*/Tb-MOF, while Fig. 14.6H shows a representative processed image also considered to be the fungal autofluorescence. Thereby, based on analysis of 3D cell reconstruction (Fig. 14.6H–J), it is confirmed that the fluorescence emission of RE-MOFs originates from organelles within the hyphal compartment [26].

Wang et al. developed new multifunctional water-soluble $NaREF_4$@ MOF-RE nanocomposites with dual-mode luminescence, which is based on Stokes luminescent mesoporous RE-MOFs (MOFs-Y:Eu^{3+}) and anti-Stokes luminescent $NaYF_4$:Tm^{3+}/Yb^{3+} nanoparticles. YF_4:Tm^{3+}/Yb^{3+}@MOF-Y:Eu^{3+} nanocomposites' low concentration in a shorter incubation time results in high-intensity brightness on labeled cells. Therefore, as a fluorescent probe, anti-Stokes luminescent nanomaterials are suitable as a new and potential monitoring tool for early-stage tumor diagnosis. They incubated the supernatant of YF_4:Tm^{3+}/Yb^{3+}@MOF-Y:Eu^{3+} nanocomposites and an aqueous solution with HeLa cells for 4 h for cell imaging. The use of a fluorescence microscope with a 980-nm source to obtain a fluorescent labeling image is shown in Fig. 14.7. It can be observed that the light-emitting cell turnover labeling on the cell and the YF_4:Tm^{3+}/Yb^{3+}@MOF-Y:Eu^{3+} nanocomposite under a bright field coincide. This result indicates that HeLa is efficiently labeled by YF_4:Tm^{3+}/Yb^{3+}@MOF-Y:Eu^{3+} nanocomposites and it is found mainly in the cytoplasm and nanoparticles perinuclear region, as shown in Fig. 14.7B, D, F, and H. Compared to $NaGdF_4$:Tm^{3+}/Yb^{3+}@MOF-Gd:Eu^{3+} nanocomposites (Fig. 14.7I–L), YF_4:Tm^{3+}/Yb^{3+}@MOF-Y:Eu^{3+} nanocomposites have higher brightness and can label cancer cells more completely. This indicates that cellular uptake of YF_4:Tm^{3+}/Yb^{3+}@MOF-Y:Eu^{3+} nanocomposites may be performed by energy-dependent endocytosis [27].

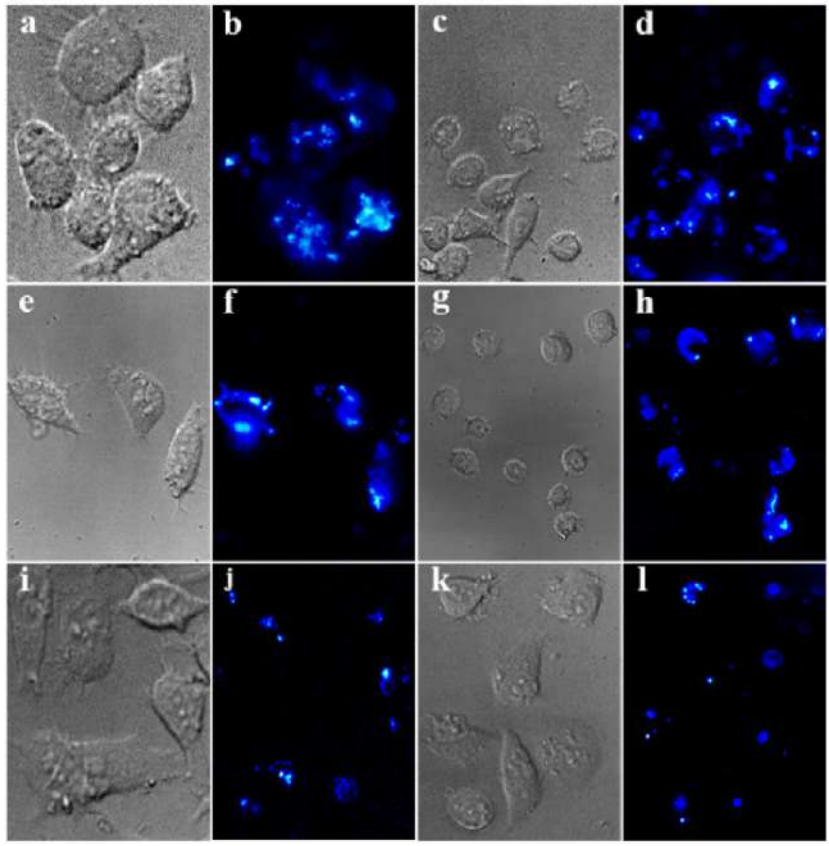

FIG. 14.7 HeLa cells are incubated with (A–D) $NaYF_4$:Tm^{3+}/Yb^{3+}@MOF-Y:Eu^{3+} supernatant, (E–H) $NaYF_4$:Tm^{3+}/Yb^{3+} @MOF-Y:Eu^{3+} solution, and (I–L) $NaGdF_4$:Tm^{3+}/Yb^{3+}@MOF-Gd:Eu^{3+} solution; the fluorescence microscopy images are irradiated with a laser at 980 nm. *(Reproduced with permission from D. Wang, C. Zhao, G. Gao, L. Xu, G. Wang, P. Zhu, Multifunctional NaLnF4@MOF-Ln nanocomposites with dual-mode luminescence for drug delivery and cell imaging. Nanomaterials 9 (2019) 1274. Copyright 2019 MDPI.)*

Sun et al. reported on two MOFs, MOF-1114(Yb) and MOF-1140(Yb), consisting of 2-aminoterephthalate (NH_2-BDC) organic linkers and Yb^{3+}-based inorganic secondary building units (SBUs) with nanoscale porosity that were postsynthetically modified by coupling methyl propiolate (MP) with the linker-bound amine to obtain a high density of short π-systems (2∼4 conjugated π-bonds) confined in MOF pores. They demonstrated that the resulting modified MOFs exhibited longer wavelength absorption and photosensitization (up to 800 nm) of Yb^{3+} NIR emission ($\lambda_{max}=980$ nm). With respect to optical bioimaging applications, they demonstrated that the modified MOFs maintained their structure and emissive properties in aqueous biological conditions

of living cells. Corresponding NIR emission and excitation spectra obtained from these particles showed that they maintained their optical properties with the observation of the characteristic Yb^{3+} NIR emission signal located at 980 nm (Fig. 14.8A, B). These well-dispersed and miniaturized MOFs were incubated with living RAW 264.7 macrophage cells for 18 h. The collected NIR epifluorescence images ($\lambda_{ex}=482$ nm) show the Yb^{3+} emission signal (Fig. 14.8C – E). These results are highly promising, as they reveal that these miniaturized MOFs can sustain the biological conditions of cell culture through the incubation process in the presence of living cells by continuing to generate bright emissions. Such a signal would have been lost had the MOFs dissociated. In addition, Fig. 14.8C – E shows that some of the miniaturized MOFs have been concentrated on or around the macrophages. Notably, MOF fragments observed in Fig. 14.8E are not uniformly bright, which can be explained by the fact that not all organic linkers have been modified by MP during this

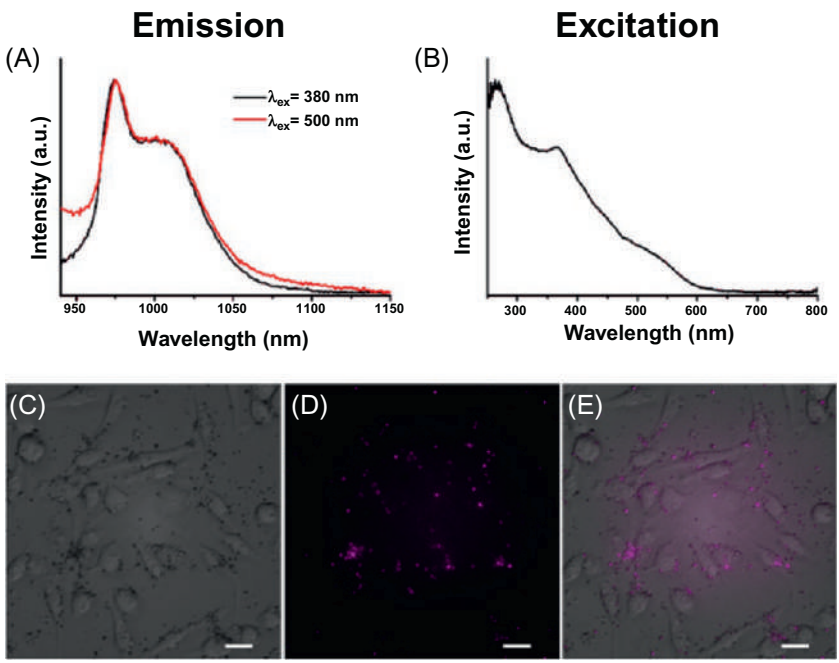

FIG. 14.8 (A) Yb^{3+} emission spectra of miniaturized MOF-1114(Yb) in H_2O with 0.5% Tween-20 under $\lambda_{ex}=380$-nm and $\lambda_{ex}=500$-nm excitation; (B) Yb^{3+} excitation spectra of miniaturized MOF at $\lambda_{em}=980$ nm in H_2O with 0.5% Tween-20; (C – E) Microscopy images of RAW 264.7 cells incubated with miniaturized MOF in water with Tween-20 0.5%. Objective 40×, scale bars = 20 μm: (C) Bright-field imaging; (D) NIR epifluorescence imaging; (E) Merged bright-field and NIR epifluorescence imaging. *(Reproduced with permission from C. Sun, H. Lin, X. Gong, Z. Yang, Y. Mo, X. Chen, J. Gao, DOTA-branched organic frameworks as giant and potent metal chelators. J. Am. Chem. Soc. 142 (2020) 198 – 206. Copyright 2020 American Chemical Society.)*

PSM reaction and the distribution of unmodified linkers throughout an intact crystal is unknown [28].

Muldoon et al. built a series of DOTA-branched MOFs with multiple chelating holes by organizing DOTA layer by layer with DOTA (1,4,7,10-tetraazacyclododecane-1,4,7,10-tetraacetic acid) as both a functioning unit and a constructing junction. Their corresponding polynuclear complex containing Tb^{3+} showed superior imaging properties, excellent feasibility for peripheral modification, and unusual kinetic stability. To further demonstrate the versatility of DBOF, Tb-MOF was prepared for the fluorescence imaging application, whose characterization results are shown in Fig. 14.9A and B. The emission fluorescence spectra of Tb-MOF feature typical Tb^{3+}-based peaks, which originate from electron transitions between the $^5D_4$ state and the ^7F_J ($J=3-6$) ground states (Fig. 14.9C). Tb^{3+} complexes are widely explored as fluorescence probes for cell imaging. However, most of the reported probes are small Tb-MOFs that are quickly excreted from cells. Tb-G2 – G4 was found to localize in lysosomes. Among them, Tb-G2 had the highest colocalization degree (Fig. 14.9D). Upon continuous irradiation, the fluorescence of Lysotracker Green faded away within 20 min, while the fluorescence of Tb-G2 was sustained even after 50 min (Fig. 14.9E), which indicates that Tb-G2 could stay in living cells for a relatively long time. Tb-DBOF Tb-MOF complexes are promising potential fluorescence probes for long-time live cell imaging and lysosome Tb-MOF tracking [29].

Neufeld et al. described the X-ray luminescent properties of two rare earth-NMOFs and their potential as novel platforms for optical molecular imaging techniques such as X-ray excited radioluminescence (RL) imaging. Upon X-ray irradiation, the NMOFs displayed sharp tunable emission peaks that spanned the visible to NIR spectral region (400 ~ 700 nm) based on the identity of the metal (Eu, Tb, or Eu/Tb). Following PEGylation, preliminary toxicity of the NMOFs was assessed toward murine fibroblast (3T3 NIH) and human liver carcinoma (HepG2) cells at both 24 and 72 h, under varying concentrations, with a maximum concentration of 500 μg mL^{-1}. Both particles displayed dose-dependent and time-dependent toxicity with murine epithelial cells displaying increased toxicity compared to human liver cells (Fig. 14.10A and B; top). As seen in Fig. 14.10B (top), Eu-NOMF-PEG and Tb-NOMF-PEG demonstrated minimal cytotoxicity toward HepG2 cells at concentrations ranging from 1.9 to 125 μg mL^{-1}, with cell viability only dropping below 80% at 500 μg mL^{-1}. Murine fibroblasts displayed similar results, except for the significant drop in cell viability at 500 μg mL^{-1} (Fig. 14.10A; top). Furthermore, biological compatibility was qualitatively assessed by live/dead fluorescence to visually evaluate the viability and morphology of HepG2 and 3T3 cells following 24 h exposure to the RE-NMOFs at concentrations of 250 μg mL^{-1} and 125 μg mL^{-1} (Fig. 14.10C; top). As expected, comparison to the untreated controls revealed no significant changes to cell proliferation (blue), cell apoptosis (green), or cell morphology in either cell line when treated with

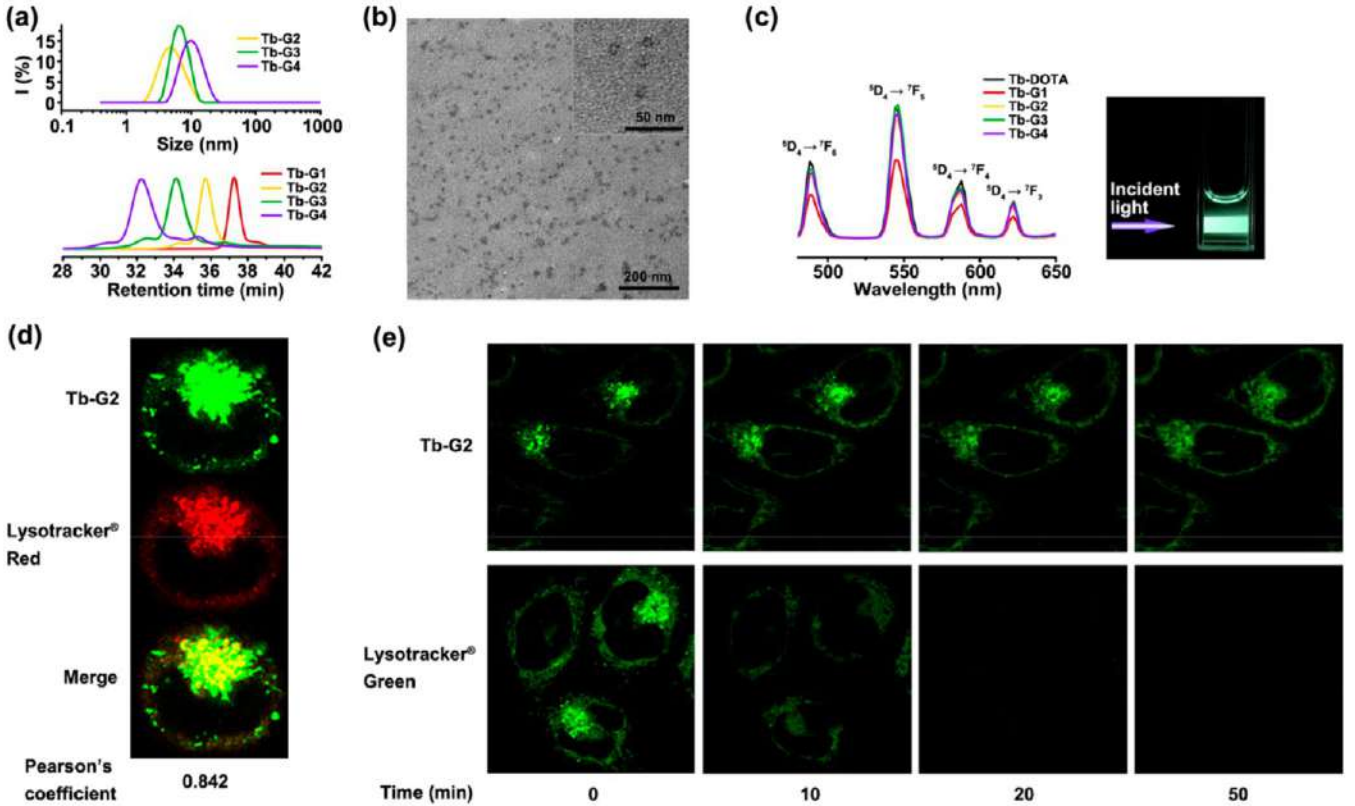

FIG. 14.9 Tb-DBOF complexes for cell imaging. (A) DLS intensity distributions *(top)* and GFC *(bottom)* profiles of Tb-DBOF. (B) Typical TEM images of Tb-G4. (C) Emission spectra of Tb-DBOF and Tb-DOTA *(left)* and an optical photograph of the solution containing Tb-G2 with exciting light *(right)*. (D) Confocal microscopy images of HeLa cells after incubation with Tb-G2 *(top)* and Lysotracker Red *(middle)*; the merged picture *(bottom)* reveals a significant degree of colocalization for both probes. (E) Comparison of photostabilities of Tb-G2 and Lysotracker Green in live HeLa cells. *(Reproduced with permission from P. F. Muldoon, G. Collet, S. V. Eliseeva, T. Luo, S. Petoud, N. L. Rosi, Ship-in-a-bottle preparation of long wavelength molecular antennae in lanthanide metal – organic frameworks for biological imaging. J. Am. Chem. Soc. 142 (2020) 8776 – 8781. Copyright 2020 American Chemical Society.)*

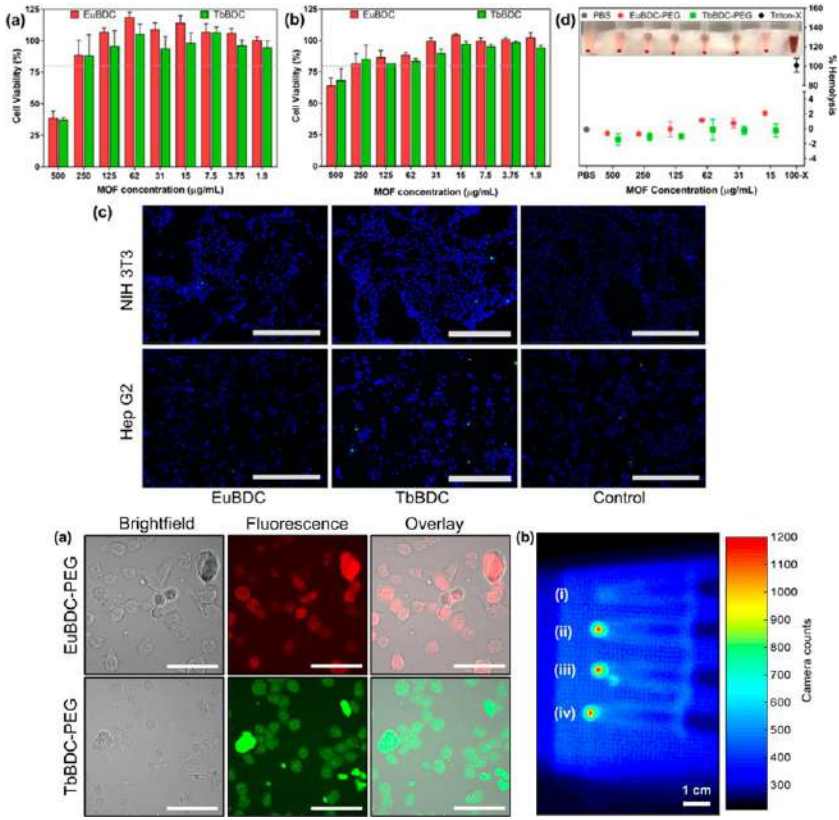

FIG. 14.10 *(Top)* Cell viability of (A) NIH 3T3 and (B) HepG2 cells incubated at various concentrations of Eu-NOMF-PEG and Tb-NOMF-PEG for 24 h. Dotted lines correspond to 80% cell viability. (C) Live/dead fluorescence viability images (*blue*, alive; *green*, dead) for NIH 3T3 and HepG2 cells incubated with 250 μg mL^{-1} of Eu-NOMF-PEG and Tb-NOMF-PEG for 24 h. All scale bars correspond to 400 μm. (D) Ex vivo hemolysis activity of Eu-NOMF-PEG and Tb-NOMF-PEG at various concentrations. All blood data are compared to the positive (PBS) and negative (Triton-X) control. *(Bottom)* Luminescence cell imaging of RE-NMOF. (A) Confocal images of the CT26 cells incubated with Eu-NOMF-PEG and Tb-NOMF-PEG for 3 h. Green and red fluorescence represents the emission from Tb^{3+} and Eu^{3+} of the PEGylated NMOFs, respectively. Scale bars correspond to 50 μm. (B) In vitro RLI of CT26 cell pellets under X-ray excitation of (i) blank cells and cells incubated with (ii) Eu-NOMF-PEG, (iii) Tb-NOMF-PEG, and (iv) Eu_xTb_x-NOMF-PEG for 24 h. *(Reproduced with permission from M. J. Neufeld, H. Winter, M. R. Landry, A. M. Goforth, S. Khan, G. Pratx, C. Sun, Lanthanide metal-organic frameworks for multispectral radioluminescent imaging. ACS Appl. Mater. Interfaces 12 (2020) 26943 – 26954. Copyright 2020 American Chemical Society.)*

Eu-NOMF-PEG or Tb-NOMF-PEG, thus corresponding well with the cell viability experiments. Qualitative fluorescence imaging demonstrated efficient cell uptake for 24 h incubation, indicating the successful uptake of the PEGylated RE-NMOFs. Following an initial 3 h incubation period at an 18 μg mL^{-1} concentration, NMOF uptake was visualized with green and red fluorescence

emissions from Tb^{3+} and Eu^{3+}, respectively (Fig. 14.10A; bottom). Taken together, these data support the utility of these NMOFs as imaging platforms by demonstrating that emission from these luminescent NMOFs is preserved and obtainable following incubation at relatively low NMOF concentration. Further assessment of the efficacy of RE-NMOFs as radioluminescent cell-labeling probes was carried out using an in-vitro X-ray excited RL experiment on CT26 cancer cell pellets, to ensure the retention of X-ray centered luminescent properties. As seen in Fig. 14.10B (bottom), following X-ray irradiation, cell pellets containing Eu-NOMF-PEG, TbBDCPEG, Eu_xTb_x-NOMF-PEG, or EuxTbx-NOMF-PEG displayed relatively high X-ray scintillation light output corresponding to the cells incubated with the PEGylated RE-NMOFs. These discoveries imply that these NMOF materials are promising candidates for X-ray imaging platforms that merit continued investigation in vivo [30].

References

[1] J. Han, K. Burgess, Fluorescent indicators for iiellular pH, Chem. Rev. 110 (2010) 2709–2728.
[2] X. Chen, T. Pradhan, F. Wang, J.S. Kim, J. Yoon, Fluorescent chemosensors based on spiroring-opening of xanthenes and related derivatives, Chem. Rev. 112 (2012) 1910–1956.
[3] Y. Yang, Q. Zhao, W. Feng, F. Li, Luminescent chemodosimeters for bioimaging, Chem. Rev. 113 (2013) 192–270.
[4] Z. Guo, S. Park, J. Yoon, I. Shin, Recent progress in the development of near-infrared fluorescent probes for bioimaging applications, Chem. Soc. Rev. 43 (2014) 1–29.
[5] A.J. Amoroso, S.J.A. Pope, Using lanthanide ions in molecular bioimaging, Chem. Soc. Rev. 44 (2015) 4723–4742.
[6] P.T.C. So, C.Y. Dong, B.R. Masters, K.M. Berland, A useful introduction to TPA fluorescence microscopy, Annu. Rev. Biomed. Eng. 2 (2000) 399–429.
[7] A. D'Aleo, A. Picot, P.L. Baldeck, C. Andraud, O. Maury, Design of dipicolinic acid ligands for the two-photon sensitized luminescence of europium complexes with optimized cross-sections, Inorg. Chem. 47 (2008) 10269–10279.
[8] A. D'Aleo, G. Pompidor, B. Elena, J. Vicat, P.L. Baldeck, L. Toupet, R. Kahn, C. Andraud, O. Maury, Two-photon microscopy and spectroscopy of lanthanide bioprobes, ChemPhysChem 8 (2007) 2125–2132.
[9] A. Bourdolle, M. Allali, J.-C. Mulatier, B. Le Guennic, J.M. Zwier, P.L. Baldeck, J.C.G. Bunzli, C. Andraud, L. Lamarque, O. Maury, Modulating the photophysical properties of azamacrocyclic europium complexes with charge-transfer antenna chromophors, Inorg. Chem. 50 (2011) 4987–4999.
[10] T.D. Ashton, K.A. Jolliffe, F.M. Pfeffer, Luminescent probes for the bioimaging of small anionic species in vitro and in vivo, Chem. Soc. Rev. 44 (2015) 4547–4595.
[11] J. Hou, W. Ren, K. Li, J. Seo, A. Sharma, X. Yu, J.S. Kim, Fluorescent bioimaging of pH: from design to applications, Chem. Soc. Rev. 46 (2017) 2076–2090.
[12] Q. Zhang, X. Tian, H. Zhou, J. Wu, Y. Tian, Lighting the way to see inside two-photon absorption materials: structure–property relationship and biological imaging, Materials 10 (2017) 223.
[13] X. Huang, J. Song, B.C. Yung, X. Huang, Y. Xiong, X. Chen, Ratiometric optical nanoprobes enable accurate molecular detection and imaging, Chem. Soc. Rev. 47 (2018) 2873–2920.

[14] Y. Yang, P. Su, Y. Tang, Stimuli-responsive lanthanide-based smart luminescent materials for optical encoding and bio-applications, ChemNanoMat 4 (2018) 1097–1120.
[15] K.Y. Zhang, Q. Yu, H. Wei, S. Liu, Q. Zhao, W. Huang, Long-lived emissive probes for time-resolved photoluminescence bioimaging and biosensing, Chem. Rev. 118 (2018) 1770–1839.
[16] Y. Ning, M. Zhu, J. Zhang, Near-infrared (NIR) lanthanide molecular probes for bioimaging and biosensing, Coord. Chem. Rev. 399 (2019), 213028.
[17] J.H.S.K. Monteiro, Recent advances in luminescence imaging of biological systems using lanthanide(III) luminescent complexes, Molecules 25 (2020) 2089.
[18] T. Gorai, W. Schmitt, T. Gunnlaugsson, Highlights of the development and application of luminescent lanthanide based coordination polymers, MOFs and functional nanomaterials, Dalton Trans. 50 (2021) 770–784.
[19] J.D. Rocca, D. Liu, W. Lin, Nanoscale metal-organic frameworks for biomedical imaging and drug delivery, Acc. Chem. Res. 44 (2011) 957–968.
[20] Y. Lu, B. Yan, J. Liu, Nanoscale metal–organic frameworks as highly sensitive luminescent sensors for Fe^{2+} in aqueous solution and living cells, Chem. Commun. 50 (2014) 9969–9972.
[21] A. Foucault-Collet, K.A. Gogick, K.A. White, S. Villette, A. Pallier, G. Collet, C. Kieda, T. Li, S.J. Geib, N.L. Rosi, S. Petoud, Lanthanide near infrared imaging in living cells with Yb^{3+} nano metal organic frameworks, PNAS 110 (2013) 17199–17204.
[22] V.M. Suresh, S. Chatterjee, R. Modak, V. Tiwari, A.B. Patel, T.K. Kundu, T.K. Maji, Oligo(p-phenyleneethynylene)-derived porous luminescent nanoscale coordination polymer of GdIII: bimodal imaging and nitroaromatic sensing, J. Phys. Chem. C 118 (2014) 12241–12249.
[23] H. Wang, J. Li, J. Li, K. Wang, Y. Ding, X. Xia, Lanthanide-based metal-organic framework nanosheets with unique fluorescence quenching properties for two-color intracellular adenosine imaging in living cells, NPG Asia Mater. 9 (2017), e354.
[24] T. Fan, T. Xia, Q. Zhang, Y. Cui, Y. Yang, G. Qian, A porous and luminescent metal-organic framework containing triazine group for sensing and imaging of Zn^{2+}, Microporous Mesoporous Mater. 266 (2018) 1–6.
[25] X. Zhang, K. Jiang, H. He, D. Yue, D. Zhao, Y. Cui, Y. Yang, G. Qian, A stable lanthanide-functionalized nanoscale metal-organic framework as a fluorescent probe for pH, Sensors Actuators B Chem. 254 (2018) 1069–1077.
[26] J. Rosário, L.L. da Luz, R. Geris, J.G.S. Ramalho, A.F. da Silva, S.A. Júnior, M. Malta, Photoluminescent organisms: how to make fungi glow through biointegration with lanthanide metal-organic frameworks, Sci. Rep. 9 (2019) 7302.
[27] D. Wang, C. Zhao, G. Gao, L. Xu, G. Wang, P. Zhu, Multifunctional $NaLnF_4$@MOF-Ln nanocomposites with dual-mode luminescence for drug delivery and cell imaging, Nanomaterials 9 (2019) 1274.
[28] C. Sun, H. Lin, X. Gong, Z. Yang, Y. Mo, X. Chen, J. Gao, DOTA-branched organic frameworks as giant and potent metal chelators, J. Am. Chem. Soc. 142 (2020) 198–206.
[29] P.F. Muldoon, G. Collet, S.V. Eliseeva, T. Luo, S. Petoud, N.L. Rosi, Ship-in-a-bottle preparation of long wavelength molecular antennae in lanthanide metal – organic frameworks for biological imaging, J. Am. Chem. Soc. 142 (2020) 8776–8781.
[30] M.J. Neufeld, H. Winter, M.R. Landry, A.M. Goforth, S. Khan, G. Pratx, C. Sun, Lanthanide metal-organic frameworks for multispectral radioluminescent imaging, ACS Appl. Mater. Interfaces 12 (2020) 26943–26954.

Part VI

Summary and prospect for rare earth metal-organic frameworks hybrid materials as luminescence response chemical sensors

Chapter 15

Summary and prospects

15.1 Postsynthetic modification to construct rare earth metal-organic framework hybrid materials

Although there are many new and exciting structures discovered for rare earth MOFs materials with rare earth ions as metal centers, postsynthetic modification (PSM) will always be an indispensable tool to tune rare earth MOFs properties and pave the way for practical uses, especially for constructing versatile rare earth MOFs hybrid materials. In addition, through the PSM path, other MOFs without rare earth ions as centers can also have RE^{3+} ions introduced to embody their luminescent features. So PSM provides a universal strategy to assemble all kinds of rare earth functionalized MOFs hybrid materials, which may cover different structural properties, for instance the metal species in pore systems, framework composition, or crystal morphology. PSM is an important approach for functionalizing MOFs with a wide range of groups that can enhance the chemical and physical properties of the framework. Through covalent and coordinate covalent PSM, various combinations of metal ions and organic components can be added to create frameworks of great complexity. PSM is a highly versatile method and allows for control over the number and type of functional groups introduced into a single framework, which is difficult to achieve through a direct synthetic route. Moreover, PSM has proven to be more than just a functionalization strategy, but also a tool to manipulate the physical properties of the MOFs, providing a clear indication of the opportunities presented from using PSM to functionalize these hybrid materials and improve upon their usefulness in both fundamental and applied studies. PAM approaches to the modification and functionalization of MOFs have become a vibrant area of chemical research and dozens of different chemical reactions have been reported on MOFs, including both organic transformations and inorganic reactions (ligand or metal addition/exchange). The resulting hybrid materials have been shown to engender MOFs with new properties relevant to practical applications. Finally, PSM will lead to MOFs of unprecedented complexity and function that are certain to be important in realizing the full potential of MOFs in a variety of technological applications. PSM has rapidly grown from an area of exploratory chemistry to a mainstream tool within the MOFs community [1–14].

Rare Earth Metal-Organic Framework Hybrid Materials for Luminescence Responsive Chemical Sensors
https://doi.org/10.1016/B978-0-323-91236-5.00015-3

Nevertheless, challenges remain for the field, particularly in the development of PSM methods that allow for precise spatial control over new functionality within the MOFs. Compared to direct molecular synthesis, PSM methods are approaching the wide range of chemical functionality accessible in the realm of small molecules. PSM is first evidenced as a guest exchange process, with encapsulated solvents, counterions, and the like being transported in and out of the open space within these frameworks. Currently, it can have the ability to chemically modify the framework itself, at either the organic struts or the metal ion nodes, becoming a prominent topic in MOFs chemistry. The role of PSM in MOFs, particularly those involving chemical modification of the organic linkers, has recently grown substantially, with the demonstrated ability to incorporate more than one functional modification onto a single MOFs, via a tandem modification approach. Ultimately, covalent PSM of MOFs will provide access to an otherwise inaccessible class of MOFs materials, anticipated to have a prominent and lasting impact on the future of these important compounds. The emergence of PSM brings new inspiration to the limited MOFs in-situ synthesis, and the combination of PSM and MOFs is a great idea. MOFs via PSM not only can obtain a large number of new structures, but also produce some satisfactory property changes of MOFs themselves, such as enhancing the hydrothermal stability, chemical stability, and luminescence stability of MOFs. In addition, PSM will show luminescence changes when contacting with targets so that the purpose of detection can be achieved. Compared with organic luminescent dyes, MOFs can avoid the luminescence quenching caused by aggregation to the greatest extent and can show good photochemical stability. In addition, MOF sensors exhibit high selectivity and sensitivity toward various targets such as inorganic ions, which is more conducive to luminescence sensing applications. The modification of MOFs has undergone a transition process from prefunctionalization to PSM, and from single PSM to tandem PSM. The modification methods have become diversified, and the properties of the synthesized materials have become more efficient, and are more suitable for sensing applications [1–14].

For rare earth MOFs hybrid materials, in addition to the pure rare earth MOFs through molecular design and assembly, rare earth functionalized MOF hybrid materials are constructed using the PSM strategy, which mainly involves the following four aspects.

(1) **Linker covalent PSM and its subsequent coordination PSM.** All kinds of organic ligands behave as linkers in the MOF frameworks, which is the core determining the structure, activity, and luminescent properties of the final MOFs. The abundant composition, functional group of these linkers provide the MOFs the versatile PSM possibility. Considering that the main path for introduction of RE^{3+} into MOFs host is coordination interaction, the coordinated groups for these linkers are important and necessary. Except for some MOFs with free uncoordinated sites of linkers such as multicarboxylate or bipydine derivatives, most of the linkers need to be

further covalently modified to produce the coordinated groups for coordination PSM. The functionalization of linkers has an influence on both reactivity and photophysical properties. In principle, almost all the linkers can be functionalized with covalent modifications, which provide great potential for PSM of MOFs. If the linker possesses the active groups, it is easy to realize the covalent modification and generally keep the whole MOFs system stable. Actually, covalent PSM of MOFs is relatively structurally stable, but the further coordination PSM of RE^{3+} often destroys the MOFs frameworks, for the common covalent modified groups cannot withstand the attack of RE^{3+} as a hard base. Therefore it is still a challenge to solve the problem of how to construct the stable MOFs hybrid materials by the dative modification of covalent-coordination PSM.

(2) **Exchange or substitution reaction for PSM of MOFs units.** For rare earth MOFs hybrid materials, the exchange or substitution reaction is a common PSM path for MOF units of both metal ions and linkers. These exchange or substitution reactions for PSM of MOFs can easily maintain the stability of the whole MOFs framework structure. Rare earth ion exchange often appears in the PSM of anionic MOFs with a simple cation (dimethyl amine cation) to balance the charge of the whole system. Generally, rare earth ion exchange of rare earth MOFs themselves or other trivalent metal cation MOFs are called substitution reactions. So the rare earth ion exchange or substitution reaction for PSM of MOFs is limited to special ones, such as anionic or trivalent metal cation MOFs, including RE-MOFs. Here the linker exchange or substitution reaction for PSM of MOFs should be emphasized, for it is suitable for all the MOFs. Naturally, the linker exchange or substitution reaction requires the similarity of functional groups or coordination performance. The exchanged or substituted linkers may have a special active group for further coordination PSM of RE^{3+}. It is obvious that the exchange of metal ions or ligands in MOFs will be a promising strategy for the desired MOFs that are not accessible by a direct one-pot self-assembly approach, enriching the family of isoreticular MOFs.

(3) **Multiple PSM assembly.** As mentioned earlier, the dative reaction of covalent PSM and coordination PSM belongs to the multiple PSM assembly method for rare earth functionalized MOFs hybrid materials. There are many additional examples. For a rare earth MOF with special free uncoordinated groups, both substitution and coordination PSM can be employed for constructing hybrid materials. For anionic rare earth MOFs, both ionic substitution and ionic exchange can be engaged in the MOFs hybrid materials. On the other hand, the encapsulation or host-guest assembly of special guest molecules can be combined with MOFs together with these PSM methods already discussed, to realize multicomponent composition of hybrid materials. At the basis of this PSM of MOFs, the MOFs can be further composed of other units such as polymer, silica, and so on, resulting in a complicated hybrid material system.

(4) **Thin-film devices and other submicro-/nanoconstruction-based MOFs composites or hybrids.** Thin films of MOFs deposited on suitable substrates clearly carry a lot of potential with regard to a realization of highly complex, multifunctional interfaces with ultimately switchable properties. The ability to load the MOFs after their synthesis with functional molecules or accomplish their PSM functionalization further extends the number of options offered by these molecular frameworks. Certainly, rare earth MOFs hybrid thin films offer the promise of further practical device applications. The hybrid thin films deposited on a conducting substrate are well suited for the application of standard surface science methods. The presence of a homogeneous, flat substrate with defined optical properties opens up a number of optical applications, which is very important for further devices based on rare earth MOFs hybrid thin films. Employing the substrate as an electrode opens up a path for electrical and electrochemical applications, which can be combined and integrated with luminescent responsive sensors. Using some unique fabricating methods such as layer-by-layer processing, the flexibility of MOFs is expected to be extended even further, to produce superlattices consisting of different types of MOFs layers stacked in an arbitrary sequence.

15.2 Luminescence responsive mode and chemical sensing mechanism for rare earth metal-organic framework hybrid materials

For rational fabrication of rare earth MOFs hybrid materials and their application as practical sensors, four major factors are structure, signal, response, and mechanism, whose communication can be useful for identification of relationships between structural features of rare earth MOFs hybrid materials and requirements for other applications. These sensing parameters should be discussed deeply, because there are many common misunderstandings about some topics, including luminescence resonance energy transfer and competitive absorption mechanisms, response and sensitivity and the relationship between the Stern-Volmer constant, response and recovery time, and the dynamic or static nature of the mechanism. With regard to luminescence response chemical sensing research, the general contents involve the following aspects: (i) evaluation of structural stability in aquatic media using characterization techniques; (ii) evaluation of photostability and origination of signal transduction based on charge transfer or energy transfer processes; (iii) examination of selective and sensitive response toward specific analytes using photophysical methods along with determination and definition of response and response time, sensitivity, Stern-Volmer parameters, detection limit, and recovery time; (iv) investigation of selective response toward target analytes in the presence of other interferents; (v) examination of structural stability of the framework in

the presence of target analytes and whether the detection mechanism is based on structural collapse or not; (vi) investigation of the overlap mechanism through combination of the absorption band of target analytes and the excitation and emission band of probes; (vii) investigation of the cation-exchange mechanism using elemental analyses before and after exposing to target analytes; (viii) checking the possible interactive functional groups with target analytes; (ix) assessment of the static or dynamic process in the detection mechanism using luminescence lifetime decay spectroscopy; and (x) theological calculation and analysis of the luminescent response sensing mechanism.

Luminescence is the key feature of rare earth MOFs hybrid materials that facilitates the tuning of chromaticity and efficiency as well as making possible applications for lighting, displaying, and sensing. These materials not only provide a hybrid character of inorganic and organic components that can be beneficially used both for the luminescence that is MOFs' natural feature, but also to provide special advantages for the introduction of rare earth ions to exhibit the abundant luminescence performance complementary to the MOFs host. Accordingly, the latter is driven by processes on the ligand side and on the metal ion side (especially on the rare earth ion side), their electronic interaction or energy transfer is another source of improved luminescence compared to the properties of the single components and even non-rare earth MOFs systems. It is essential that the interaction of the MOFs framework with these analytes can be accompanied by changes in the luminescence of both rare earth ions or linkers, whose changes can be either characterized as "Turn-Off" or "Turn-On" (including the Turn-(On)-Off-On) depending on quenching or on sensitization of a luminescence process of the MOFs. In addition, reversible sensing and irreversible detection must be distinguished, both of which can achieve a luminescence change of potential use for applications, depending on whether the MOFs hybrid is supposed to be used repeatedly. Even the intrinsic cost of otherwise costly rare earth ions thereby proves a lesser hindrance compared to other materials, as most sensors will require only a small amount of material. Probes or chemosensors that exhibit luminescence changes in response to different analytes are more convenient than other types of sensors, as the optical signals can be recognized easily either by fluorimeters or by the naked eye. It has been well established that rare earth MOFs hybrid materials make excellent sensors due to their inherent advantages, such as crystallinity, permanent porosity, structural and functional diversity, and tunable luminescence, as well as multiple luminescence [15–24].

Various MOFs-based sensors with different luminescence responses for sensing and detecting mechanisms have been achieved through rational design. For rare earth MOF hybrid material sensors, they keep the MOF's luminescence response character and protrude the rare earth ions' luminescence response feature. In the majority of these hybrids, especially pure rare earth MOFs materials, rare earth ions belong to the main luminescence center and the MOFs or their linkers behave as the energy sensitizer to RE^{3+} through the "antenna effect." In

this condition, the luminescence responses of rare earth ions involve Turn-(On)-Off and Turn-(On)-On or even Turn-(On)-Off-On modes. Here "Turn-On" means the sensitized luminescence of RE^{3+} by the energy transfer from linkers of the MOFs host. For Turn-(On)-Off mode, the "Turn-(On)" process is effective and then the further luminescence quenching occurs (Turn-Off). For Turn-(On)-On mode, the "Turn-(On)" process is not effective enough and so the analytes may lead to luminescence enhancement (Turn-On). The latter "Turn-(On)-On" mode often can be realized by the "Turn-(On)-Off-On" process using a special quencher to decrease the luminescence of the RE^{3+} ion. If such a quencher is also an analyte, it can perform a universal probe for practical applications. For rare earth ion functionalized MOFs hybrid materials, the actual content of luminescent rare earth ions is relatively limited, which presents the possibility of exhibiting the luminescence of both rare earth ions and linkers of MOFs. The dual emissive center is useful for ratiometric or self-calibration sensing, whose different emissive centers may be expected to have abundant luminescence responses. This luminescence responsive performance seems to be complicated but has great potential in practical detection of analytes. Certainly, other guest species can be encapsulated or functionalized to rare earth MOFs hybrid materials, which can also integrate multiple luminescence responses. In a minority of rare earth MOFs hybrids with weak luminescence or nonemissivity for inert rare earth ions, they are identical to the non-rare earth MOFs materials and here the MOFs luminescence response behavior mainly originates from linkers of their own [15–24].

Turn-Off responsive modes are commonly developed when detecting electron acceptors, where luminescence is quenched through sensor-guest electron transfer accompanied with energy transfer. To increase the sensitivity and selectivity, the Turn-On detection mode has also been implemented into MOFs hybrid sensors, which generally leads to luminescent enhancement or wavelength shifts. Moreover, functional sites have been successfully utilized to detect target compounds. In addition, the embedding of multiluminescent motifs onto the frameworks can produce more than one signal transition, which not only can expand the sensing scale but also can impart self-calibration to MOFs sensors. The majority of rare earth MOFs hybrid sensors operate by the Turn-Off mechanism of luminescent quenching, and many fewer reports are based on the Turn-On mechanism, including the luminescent enhancement or shift of the emission (color change). The Turn-On detection is more sensitive at lower detection limits, because the naked eye can quickly recognize the strong emission and color change in the visible range from a previously dark background or originally low-emitting or nonemitting rare earth MOFs hybrids. In addition, this mechanism also exhibits better selectivity because the shift of the emission peak is frequently specific towards target guest molecules based on guest-host chemistry. More sensors can be fabricated for the Turn-On mechanism by designing a host material with stronger interactions towards a particular analyte. It needs to be stressed that the "Turn-(On)-Off-On" is an effective

strategy for "Turn-On" mode despite the fact that it only happens in some special hybrid systems. Electron and energy transfer between the analyte molecule and related MOFs frameworks is the major contribution for luminescent and electronic responses. Theoretical calculations can effectively predict host-guest interactions and improve the design of the structure of rare earth MOFs hybrid materials. The deep analysis of the sensing mechanism is the most fundamental thing to achieve controllable syntheses of rare earth MOF hybrid sensors with high selectivity for target analytes. Some relationships between structure and luminescent behavior have been revealed through theoretical methods. Based on theoretical results, the direction of charge/energy transfer between MOFs and analyte can be confirmed, so it will be feasible to realize controlled luminescent changes through adjusting the electronic structure with specific functional groups and further achieve MOFs sensor materials through rational design and control of the energy transfer between linkers and RE^{3+}. This is a very important yet challenging issue because of the difficulty in forming target products, because these are affected by various factors. In addition, some issues during practical applications still need to be improved, including the stabilities of recycling, the cost of materials, and portability.

When analytes meet a rare earth MOFs hybrid materials probe, the MOFs host's porous periodic structures consisting of regular arrays of chromophores display additional advantages such as pores and channels of uniform sizes and shapes, ease of synthesis and functionalization, and the ability to introduce luminescence properties in a variety of ways, including the use of luminescent organic linkers, luminescent rare earth ions, and photoactive guest species. The production of a sensing signal must necessarily be triggered by a rare earth MOFs hybrid/analyte association process, which brings the targeted species within the interaction distance with the chromophores of the material. Consequently, the observed spectral changes that are not initiated by rare earth MOFs hybrid/analyte interaction, such as radiative energy transfer, also known as the inner filter effect (IFE), cannot be deemed as true sensing. In addition, care must be taken to ensure that other trivial phenomena like material decomposition do not contribute to the observed spectral changes. In addition, it is desirable that future efforts be directed towards the challenging synthesis of rare earth mesoporous MOFs hybrids to be suitable for the rapid detection of gas phase analytes. One more important future direction is to control the synthesis of the development of composite nanoscale rare earth MOFs hybrid materials externally functionalized in order to form stable colloidal suspensions in sample media, to allow the entry of targeted guests within their pores, which is also adapted to be applied in life science fields. For the rare earth ion luminescence responsive sensing mechanism, its direct interaction with analytes can be attributed to the following aspects: (i) direct coordination interaction between RE^{3+} and analytes with coordination sites; (ii) direct substitution of RE^{3+} by some metal ion analytes. More extensive is the indirect effect on rare earth ion luminescence, which relays on the intramolecular energy transfer from MOFs hosts

(their linkers) to RE^{3+}. Here the analyte sensing is employed by the luminescence response of MOFs or their linkers and it is similar to the small molecule sensing mechanism. It mainly includes three extensive aspects: (a) the fluorescent resonant energy transfer (FRET) or photo-induced electron transfer (PET)), depending on the energy levels between analytes and linkers; (b) the spectral overlap between the MOFs (linkers) emission spectra and the analytes absorption one; (c) the other special interaction leading to the change of MOFs (linkers) from analytes, involving the hydrogen bonding interaction between molecule analytes and MOFs (linkers), ion substitution interaction between some ion analytes (especially metal cations), and the framework ion of MOFs. These interactions strongly affect the MOFs (linkers) and further change their energy transfer to RE^{3+}. For multiple luminescence responsive centers in rare earth hybrid materials, the possible three general luminescence characters correspond to RE^{3+}, MOFs (linkers), and guest species, respectively. The analytes may have different responses to different luminescent centers, but the following sensing mechanisms are still not beyond the previously mentioned range.

15.3 Luminescence responsive chemical sensing of analytes for rare earth metal-organic framework hybrid materials

Luminescent probes with simple and clear signal changes are more convenient than some other sensors. The generated optical signals can be obtained readily using a fluorimeter, and the color changes can be detected with the naked eye in the range of visible light. Rare earth MOFs hybrid materials as potential luminescent sensors have some unique advantages, including crystallinity, porosity, and structural and functional diversity. So far, numerous rare earth MOFs hybrid materials have been reported as luminescent probes to detect heavy ions (live or harmful metal ions, and both simple and complicated oxysalt anions), molecules (general small inorganic and organic molecules; organic solvents and vapor, environmental pollutants, biological molecules, drugs or antibiotics, nitro explosives, pesticides, and biomarkers or biometabolites) as well as temperature and pH value. Although these luminescent hybrid MOFs-based materials have shown a lot of promise, more work is still needed to improve the sensing performance in terms of sensitivity, selectivity, stability, and reusability for all kinds of analytes. (i) The function of rare earth MOFs hybrid materials in each sensing platform should be better understood to fully utilize the advantages of MOFs and to assist with sensor design and performance optimization. In particular, the exact role of the special crystalline and porous structure of MOFs should be evaluated and demonstrated fully. (ii) It is worthwhile to further broaden the MOFs host category with new useful properties for the rare earth MOFs hybrid materials, such as optical/electrical, thermochromic, sensing catalysis, and sensing absorption properties. This will provide more opportunities in sensor design and integration, even creating some multifunctional platforms. (iii) The new PSM or surface functionalization methods are needed to

better tune the MOF host structure of rare earth MOFs hybrid materials and enhance its sensing activity and stability. The stability of MOFs-based hybrid sensing materials needs to be improved, especially for sensors that work under aqueous and/or acid environments. (iv) Most of the sensor demonstrations are conducted using laboratory-prepared samples. Therefore the sensor performance in a complex environmental media, such as real water and special working position, needs to be evaluated and the sensor selectivity and reliability should be improved, as they are the two major critical requirements for practical use of the sensors. (v) Most reported rare earth MOFs hybrid-based sensors are sensitive to a family of guests, whereas selective detection of a specific species is difficult, especially when the analytes have similar chemical structures. More effort in developing general strategies to design such hybrid sensors with Turn-On mechanisms is still needed. The structure-luminescence relationships as well as host-guest interactions have yet to be explored computationally in great detail [9,25–34].

Rare earth MOFs hybrid materials have been extensively utilized in the luminescence responsive sensing of ion analytes, but the reports focus on a few types of ions, such as Fe(III) cation or Cr(VI) oxysalt anion. (1) The rare earth MOFs hybrid materials for luminescence responsive sensing of cations (metal ions) are more extensive than for anions. Metal ion analytes have abundant interactions with MOFs, including the coordination reaction to linkers of MOFs and substitution or exchange with the framework metal ions of MOFs hosts or functionalized RE^{3+} within MOFs hybrids. While anion analytes can only produce a limited interaction with MOFs, which often appears the cationic MOFs to exchange simple balance anions in the porous frameworks of MOFs. (2) For common biologically essential metal ions such as Fe^{3+}/Fe^{2+}, Cu^{2+}, and Zn^{2+}, the reports are mainly focused on Fe^{3+} ions using rare earth MOFs hybrid materials as luminescence responsive probes, as they are a universal cation quencher for luminescence of rare earth MOFs hybrid materials. Additional efforts must be made for the exploration of these hybrid probes for chemical sensing of the other three ions, especially Fe^{2+} and Zn^{2+}. Currently, the reports on Zn^{2+} are very few and those on Fe^{2+} are also rare. (3) For metal ions other than these four essential cations, including the common harmful heavy metal ions (Hg^{2+}, Cd^{2+}, Pb^{2+}), the reports are not extensive for rare earth MOFs hybrid materials as luminescence responsive sensing probes. Thus research in this field needs to be done to develop some new probe systems. Particularly, luminescent responsive sensing of the uranyl ion UO_2^{2+} should be strengthened, to develop an effective probe from these hybrids, for it is a typical harmful species in the environmental field. (4) For simple anions such as halogen ion or pseudohalogen ions, the reports mainly focus on the F^- ion using rare earth MOFs hybrid materials as luminescence responsive probes, while other anions are rarely reported. It is worth pointing out that the luminescent responsive sensing of CN^- should be strengthened to develop an effective probe with these hybrids, for it is another typical harmful species in the environmental field. (5) For complicated oxysalt

anions, the reports mainly focus on the Cr(IV) anion (CrO_4^{2-} and $Cr_2O_7^{2-}$) using rare earth MOFs hybrid materials as luminescence responsive probes, while reports on other anions are relatively few.

Rare earth MOFs hybrid materials have been extensively utilized in luminescence responsive sensing of molecular analytes, much more than in ion species. (1) The number of inorganic molecules is not many, involving O_2, H_2O, H_2O_2, H_2S, HCl, NH_3, NO_x, SO_2, etc. Nowadays, the luminescence responsive sensing of these inorganic molecules has been reported using rare earth MOFs hybrid materials as probes. Comparatively, the number of relevant reports on O_2, H_2O, H_2O_2, H_2S, and NH_3 is greater than for other analytes. Therefore the attempt should be made to discover some rare earth MOF hybrid probe systems for sensing important polluting inorganic gas molecules, such as NO_x, SO_2, CO_2, and CO, whose detection can be combined with other processing of removal and conversion. (2) Organic molecule solvents and their vapors are common in chemical research and industry. In fact, most of these molecules are pollutants, being harmful to the environment and to human health. Currently, the luminescence responsive sensing of these organic compounds concentrates on acetone or benzene series. The highly selective sensing of structural derivatives, whose trace amounts in aqueous solutions are important in daily life, is still very difficult. In addition, much interest centers on organic amines and aldehydes, which are common pollutant gases in particular places. (3) Nitroaromatic explosives (NAEs) are harmful compounds whose luminescence responsive chemical sensing is very extensive. The pure rare earth MOFs have been largely tried for detection of the NAEs, but rare earth functionalized MOFs hybrid materials are rarely used. On the other hand, pesticides and chemical warfare reagents are both common hazardous materials, which attracts the interest of researchers to promote their luminescence responsive sensing using rare earth MOFs hybrids. (4) There are many research works on the luminescence responsive chemical sensing of biomolecules using rare earth MOF hybrid materials as probes, among which amino acid is relatively more common than other biomolecules, such as nucleic acid, etc. It is expected that the luminescence responsive chemical sensing of special biomolecules of nucleotides or special proteins and enzymes will be realized. (5) Drugs and antibiotics enter the environment and become pollutants, which involves luminescent responsive detection. In addition, the pharmacological mechanisms of drugs and antibiotics are very important for practical medical treatment and health, and luminescence responsive sensing is a useful approach to understand this information. (6) Biomarkers or biometabolites are very useful tools to discover the metabolic pathways in organisms, including the human body. The luminescent response chemical sensing of rare earth MOFs hybrid material probes provides a powerful method to detect biomarkers or biometabolites, for they respond easily to special simplified compounds such as biomarkers or biometabolites. The specificity (high selectivity) of sensing of biomarkers is necessary to achieve the ideal luminescence responsive probes of rare earth MOFs hybrid materials.

15.4 Luminescence responsive chemical sensing application for rare earth metal-organic framework hybrid materials

Among the bottlenecks, the ability to process MOFs into workable devices is a prominent challenge involved in taking the features to the level of practical implementation. While the parameters governing sensitivity and selectivity are being explored at the experimental stages, it remains an area that needs significant advancement to achieve the level of performance of real applications. This includes comprehensive evaluation of the response under real-time conditions (temperature, pressure, and mechanical stress) at varying concentrations of both the analytes and the interfering species. In addition to addressing the practicality-focused bottlenecks that have so far limited the widespread adoption of rare earth MOFs hybrid sensor materials, new avenues of research have begun to open up as the field matures. In vivo sensing and the development of rare earth MOFs hybrid-based biomedical devices have recently begun to accelerate. Industrial applications calling for combined absorbance and detection of a specific species, especially when the mechanism of that detection is a colorimetric shift visible to the naked eye, have pushed research in that direction. Combining rare earth MOF hybrid materials with other advanced materials, such as quantum dots, allows researchers to leverage the best qualities of both and create new high-performance devices. As researchers' ability to rationally design these sensors for targeted applications continues to improve, these new avenues of research are expected to yield exciting results. Although excellent sensing performance has been achieved for some rare earth MOFs hybrid materials, many challenges for commercial applications remain to be overcome. (1) The employment of other signal transduction methods has provided access to nonluminescent MOFs, which otherwise display no observable sensing signal. Interferometry, colloidal crystals, and microcantilever devices can be applied to any MOFs material without concern for the properties or structure of specific MOFs materials, which holds great promise for the development of miniaturized, portable sensors. (2) A prominent challenge is to fabricate rare earth MOF hybrid-based sensing materials into workable devices. The development of hybrid membranes and thin films has come closer to practical applications, especially for quantitative sensing of gas-phase analytes. The recent proliferation of MOFs thin-film growth techniques has been essential in enabling the fabrication of these devices. (3) The stability of rare earth MOFs hybrids in different environments (humidity, temperature, acidic or basic conditions, pressure, etc.) is always a key issue to consider for real-time applications. Continued efforts are necessary to design robust MOFs sensors capable of retaining high performance over multiple cycles. (4) Although the sensing performance of rare earth MOFs hybrids has been constantly improved under laboratory conditions, further development is required to make them suitable for real-world commercial applications; enabling their integration in microelectronic, microfluidic, and lab-on-a-chip systems will be a crucial step.

(5) The high cost of large-scale production of rare earth MOFs hybrids has substantially hampered their widespread practical applications. In spite of their excellent performance in laboratory conditions, extensive research and development are still needed in order to see this technology being commercialized. (6) Wearable devices for personalized and preventive medicine and the development of these devices is driving a renaissance in sensor technology. Usually, wearable sensors are capable of real-time, on-body monitoring, which can yield significant, additional insights into the overall health state and performance of individuals. Wearable devices focus on the measurement of physical characteristics, but sensors have been developed for the capture and biochemical analysis of body fluids, offering a high clinical value. Rare earth MOFs hybrid materials can be prepared for use in wearable healthcare devices for luminescence responsive chemical sensing [9,25–34].

The thin-film fabrication of rare earth MOFs hybrid materials for practical luminescence responsive chemical sensors is a fundamental approach for all kinds of new devices and real applications. (1) When new techniques are implemented to grow MOFs material structures on substrates, this technique will not only be able to access different length scales of MOF structures, but also will create good interfaces between MOFs and support surfaces. In certain cases, clever design tricks may be used to install sophisticated recognition elements into MOFs. In principle, each analyte interacts with the series differently to produce a unique fingerprint. In practice, the effectiveness of the approach is somewhat limited, because the "unique fingerprint" changes with analyte concentration. Additionally, the array or nose addresses only the problem of identification, and not the problem of signals from interferents. Widespread implementation of high throughput screening of MOFs for highly specific analyte adsorption, therefore, will likely become practical only when significantly greater computational power becomes routinely available and/or when reliable approximate methods for handling more complex molecule/MOF interactions have been devised and validated. Subsequently, it may be possible to identify MOFs capable of discriminating between relatively similar molecules. (2) Rare earth MOFs hybrid materials have the potential to move beyond the pore exclusion approach to develop new sensing devices. Recent advancements in the photophysics of these hybrid materials foreshadow that light harvesting and energy transfer are facets that can be implemented towards the rational construction of a novel platform with unrevealed sensing benefits. The natural photosystem can be utilized as a model to integrate the mentioned photophysical processes inside a single rare earth MOFs hybrid-based material, creating a "three-in-one" sensing platform. Since light harvesting is the first step in the development of novel rare earth MOFs hybrid-based sensors of this kind, it is essential for these scaffolds to possess wide absorption profiles achieved through efficient coupling of multiple chromophores. In addition to tunability and high surface area, the main advantage to developing energy transfer-based

sensors using MOFs hybrid is framework crystallinity, which allows for the precise determination of the distances and angles between self-assembled organic linkers. (3) MOFs hybrids can be viewed as the next generation of "smart materials," whose sensing ability is controlled as a function of the external stimuli, including excitation wavelength, heat, pressure, or pH. Due to porosity and structural modularity, MOFs can also be employed as tunable nanoreactors, with the potential to act as a "sensor flask." Integration of all the discussed aspects inside one material, along with integration into a sensing device, is still an inexhaustible challenge [9,15–34].

The multiple luminescence responses of rare earth MOFs hybrid materials, when used as sensing probes, provide some advantages, such as abundant color change for visualization and complicated responsive detection. These materials are thus expected to be suitable for applications in logic gate operation and device stimulation. The origins and rapid growth of this field can in part be attributed to pioneering research on chemosensors and logic gates. The progress of molecular logic gates is already impressive, but the coming era of molecular logic devices, whether they are based on rare earth MOFs hybrid materials or not, will have a transformative impact on modern science. It is expected to see a rise of information processing molecular devices with "disruptive" potential, such as autonomous therapeutic applications. (1) The wide sensing applications of rare earth MOFs hybrid materials have caused them to become an important member in the club of "smart materials." Making up of DNA-based circuits effectively, rare earth MOF hybrids have well-defined structures in which a large number of chromophoric sensitizers and rare earth cations can be incorporated, whose host framework-guest interactions (such as coordination bonds, π-π interactions and hydrogen bonding) give rise to their high sensing sensitivity. Assembly of rare earth MOFs hybrids is achieved by the facile PSM method, which is a more cost-effective and less complicated operational process than DNA modification. So, rare earth MOFs hybrid materials can be considered and proven to be a special molecular system that has promising candidates for the construction of logical devices. (2) Boolean logical library containing basic logic gates (NOT, NAND, INHIBIT, XNOR) and combinational gates have been easily constructed, even can be realized with the same MOFs host through the different functionalization of RE^{3+} and other functional species. This verifies that the rare earth MOFs hybrid materials are candidates for creating logic gate operations. Through the different units, the different luminescence centers, the different luminescence responses, and the different analytes and their concentrations, all kinds of molecular logic gate operation and stimulators can be designed, resulting in the boolean logical library. (3) For further application of luminescence responsive chemical sensing based on rare earth MOFs hybrid materials, some complicated logic devices have been designed and constructed, including a computing keypad-lock security system using sequential logic operation, fuzzy logic computing, molecular searcher, circuit

controller, and information memorizer. This provides more opportunities for the development of artificial intelligence in environmental monitoring. (4) On the basis of the Boolean logical operation, it can be expected to further establish some platform using luminescence responsive rare earth MOFs hybrid material sensors, such as intelligent logic detector point-of-care diagnostics, food spoilage logic detector, artificial neural networks, and visual molecular robots. A future effort should be made to develop these stimulated logic gate operation as the real workable device or platform to engage in practical fields of commerce and industry.

Rare earth nano-metal-organic framework (NMOF) hybrid materials have stable pores in their assembly, which is a potential concern in optical imaging for biomedical applications, involving bioimaging and cellular imaging. They have become a powerful imaging modality due to the capability of noninvasively distinguishing between healthy tissues and tumors or other contaminated tissues centered on the differential dye accumulations. (1) Considering the biomedical applications, rare earth nano-metal-organic framework hybrid materials should be synthesized with nanoscale of MOFs host particles. Nowadays, a particle size of MOFs hybrids can be achieved of $50 \sim 100$ nm through the adjusting of the synthesis reaction condition parameters of the MOFs host. (2) Rare earth MOFs hybrid materials contain heavy metal elements, which usually show certain toxicity to cells. Thus it is necessary to decrease the rare earth ion content in the hybrid material probes. Certainly, rare earth ion functionalized MOFs with special kinds of central metal ions (e.g., Zn^{2+}) are an effective method due to the low content of RE^{3+}. (3) The focus of probe design will be put on the maximization of the luminescence lifetime response to the analyte, to benefit from the time-resolved photoluminescence measurement and imaging. Multiple luminescence responsive probes with different luminescence lifetimes can be used simultaneously, which can be distinguished via time-resolved photoluminescence techniques, even if they emit with similar intensity at the same wavelength. (4) There are limited examples of long-lived emissive probes used for in-vivo time-resolved photoluminescence imaging due to a lack of long-lived near-infrared (NIR) emissive probes and imaging techniques. Thus development of NIR emissive probes based on some rare earth (Yb^{3+}, Nd^{3+}, and Er^{3+}) MOFs hybrid materials with long lifetime and time-resolved photoluminescence techniques suitable for live animal models will broaden the scope of time-resolved photoluminescence applications in vivo. (5) Combination of time-resolved detection with modern imaging techniques, such as stimulated emission depletion microscopy, terahertz imaging, and fluorescence anisotropy imaging, will open up new directions in the development of imaging techniques. The future development of new rare earth MOFs hybrid systems for biomedical imaging, together with the advancement of new imaging techniques, will undoubtedly see rare earth ions continue to play a pivotal role in the design of next-generation imaging and therapeutic agents [35–38].

References

[1] K.K. Tanabe, S.M. Cohen, Postsynthetic modification of metal-organic frameworks—a progress report, Chem. Soc. Rev. 40 (2011) 498–519.

[2] S.M. Cohen, Postsynthetic methods for the functionalization of metal-organic frameworks, Chem. Rev. 112 (2012) 970–1000.

[3] V. Valtchev, G. Majano, S. Mintova, J. Perez-Ramırez, Tailored crystalline microporous materials by post-synthesis modification, Chem. Soc. Rev. 42 (2013) 263–290.

[4] J.D. Evans, C.J. Sumby, C.J. Doonan, Post-synthetic metalation of metal-organic frameworks, Chem. Soc. Rev. 43 (2014) 5933–5951.

[5] P. Deria, J.E. Mondloch, O. Karagiaridi, W. Bury, J.T. Hupp, O.K. Farha, Beyond post-synthesis modification: evolution of metal-organic frameworks via building block replacement, Chem. Soc. Rev. 43 (2014) 5896–5912.

[6] S.M. Cohen, The postsynthetic renaissance in porous solids, J. Am. Chem. Soc. 139 (2017) 2855–2863.

[7] T. Islamoglu, S. Goswami, Z. Li, A.J. Howarth, O.K. Farha, J.T. Hupp, Postsynthetic tuning of metal – organic frameworks for targeted applications, Acc. Chem. Res. 50 (2017) 805–813.

[8] Z. Yin, S. Wan, J. Yang, M. Kurmoo, M. Zeng, Recent advances in post-synthetic modification of metal-organic frameworks: new types and tandem reactions, Coord. Chem. Rev. 378 (2019) 500–512.

[9] Q. Yu, Z. Li, Q. Cao, S. Qu, Q. Jia, Advances in luminescent metal-organic framework sensors based on post-synthetic modification, Trends Anal. Chem. 129 (2020), 115939.

[10] C.K. Brozek, M. Dinca, Cation exchange at the secondary building units of metal-organic frameworks, Chem. Soc. Rev. 43 (2014) 5456–5467.

[11] Y. Han, J. Li, Y. Xie, G. Guo, Substitution reactions in metal-organic frameworks and metal-organic polyhedral, Chem. Soc. Rev. 43 (2014) 5952–5981.

[12] S.A.A. Razavi, A. Morsali, Linker functionalized metal-organic frameworks, Coord. Chem. Rev. 399 (2019), 213023.

[13] P. Li, X. Wang, Y. Zhao, Click chemistry as a versatile reaction for construction and modification of metal-organic frameworks, Coord. Chem. Rev. 380 (2019) 484–518.

[14] M. Xu, Q. Chen, L. Xie, J. Li, Exchange reactions in metal-organic frameworks: new advances, Coord. Chem. Rev. 421 (2020), 213421.

[15] Y. Zhang, S. Yuan, G. Day, X. Wang, X. Yang, H. Zhou, Luminescent sensors based on metal-organic frameworks, Coord. Chem. Rev. 354 (2018) 28–45.

[16] T. Rasheed, F. Nabeel, Luminescent metal-organic frameworks as potential sensory materials for various environmental toxic agents, Coord. Chem. Rev. 401 (2019), 213065.

[17] B. Yan, Luminescence response mode and chemical sensing mechanism for lanthanide functionalized metal-organic frameworks hybrids, Inorg. Chem. Front. 8 (2021) 201–233.

[18] Y. Cui, B. Chen, G. Qian, Lanthanide metal-organic frameworks for luminescent sensing and light-emitting applications, Coord. Chem. Rev. 273–274 (2014) 76–86.

[19] L.E. Kreno, K. Leong, O.K. Farha, M. Allendorf, R.P. Van Duyne, J.T. Hupp, Metal-organic framework materials as chemical sensors, Chem. Rev. 112 (2012) 1105–1125.

[20] F. Yi, D. Chen, M. Wu, L. Han, H. Jiang, Chemical sensors based on metal-organic frameworks, ChemPlusChem 81 (2016) 67–690.

[21] I. Stassen, N. Burtch, A. Talin, P. Falcaro, D.M. Allendorfc, R. Ameloot, An updated roadmap for the integration of metal-organic frameworks with electronic devices and chemical sensors, Chem. Soc. Rev. 46 (2017) 3185–3241.

[22] W.P. Lustig, S. Mukherjee, N.D. Rudd, A.V. Desai, J. Li, S.K. Ghosh, Metal-organic frameworks: functional luminescent and photonic materials for sensing applications, Chem. Soc. Rev. 46 (2017) 3242–3285.
[23] E.A. Dolgopolova, A.M. Rice, C.R. Martin, N.B. Shustova, Photochemistry and photophysics of MOFs: steps towards MOF-based sensing enhancements, Chem. Soc. Rev. 47 (2018) 4710–4728.
[24] S.A. Diamantis, A. Margariti, A.D. Pournara, G.S. Papaefstathiou, M.J. Manos, T. Lazarides, Luminescent metal-organic frameworks as chemical sensors: common pitfalls and proposed best practices, Inorg. Chem. Front. 5 (2018) 1493–1511.
[25] R. Lin, S. Liu, J. Ye, X. Li, J. Zhang, Photoluminescent metal-organic frameworks for gas sensing, Adv. Sci. 3 (2016) 1500434.
[26] Y. Li, A. Xiao, B. Zou, H. Zhang, K. Yan, Y. Lin, Advances of metal-organic frameworks for gas sensing, Polyhedron 154 (2018) 83–97.
[27] H. Li, S. Zhao, S. Zang, J. Li, Functional metal-organic frameworks as effective sensors of gases and volatile compounds, Chem. Soc. Rev. 49 (2020) 6364–6401.
[28] K. Müller-Buschbaum, F. Beuerle, C. Feldmann, MOF based luminescence tuning and chemical/physical sensing, Microporous Mesoporous Mater. 216 (2015) 171–199.
[29] B. Chen, S. Xiang, G. Qian, Metal-organic frameworks with functional pores for recognition of small molecules, Acc. Chem. Res. 43 (2010) 1115–1124.
[30] Z. Hu, B.J. Deibert, J. Li, Luminescent metal-organic frameworks for chemical sensing and explosive detection, Chem. Soc. Rev. 43 (2014) 5815–5840.
[31] X. Fang, B. Zong, S. Mao, Metal-organic framework-based sensors for environmental contaminant sensing, Nano-Micro Lett. 10 (2018) 64.
[32] H. Wang, W.P. Lustig, J. Li, Sensing and capture of toxic and hazardous gases and vapors by metal-organic frameworks, Chem. Soc. Rev. 47 (2018) 4729–4756.
[33] J. Tang, X. Ma, J. Yang, D. Feng, X. Wang, Recent advances in metal-organic frameworks for pesticide detection and adsorption, Dalton Trans. 49 (2020) 14361–14372.
[34] L. Chen, D. Liu, J. Peng, Q. Du, H. He, Ratiometric fluorescence sensing of metal-organic frameworks: tactics and perspectives, Coord. Chem. Rev. 404 (2020), 213113.
[35] K.Y. Zhang, Q. Yu, H. Wei, S. Liu, Q. Zhao, W. Huang, Long-lived emissive probes for time-resolved photoluminescence bioimaging and biosensing, Chem. Rev. 118 (2018) 1770–1839.
[36] Y. Ning, M. Zhu, J. Zhang, Near-infrared (NIR) lanthanide molecular probes for bioimaging and biosensing, Coord. Chem. Rev. 399 (2019), 213028.
[37] Z. Guo, S. Park, J. Yoon, I. Shin, Recent progress in the development of near-infrared fluorescent probes for bioimaging applications, Chem. Soc. Rev. 43 (2014) 1–29.
[38] A.J. Amoroso, S.J.A. Pope, Using lanthanide ions in molecular bioimaging, Chem. Soc. Rev. 44 (2015) 4723–4742.

Index

Note: Page numbers followed by *f* indicate figures.

S

T

V

W

WOODHEAD PUBLISHING SERIES IN ELECTRONIC AND OPTICAL MATERIALS

Rare Earth Metal-Organic Framework Hybrid Materials for Luminescence Responsive Chemical Sensors primarily focuses on rare earth metal-organic framework (MOF) hybrid materials, especially on rare earth functionalized MOFs hybrid materials for sensing applications. First sections cover an introduction to the field and key concepts like luminescence, rare earth ion luminescence and luminescence response for chemical sensing. Second sections emphasize the luminescence response mode and sensing mechanisms of these important materials, including single mode and dual mode sensing, as well as chemical sensing mechanisms. Third sections outline different kinds of sensing analytes by rare earth MOFs hybrids and develops into emerging applications. Final section gives the summary and prospect. This book is suitable for materials scientists and engineers, chemists, and chemical engineers. In addition, the material is appropriate for those working in academia and R&D in industry.

Key Features

- Authored by one of the world's leading experts on rare earth metal-organic framework (MOF) hybrid materials
- Introduces advanced concepts in luminescence response and sensing mechanisms of rare earth metal-organic framework hybrid materials
- Outlines the progress of luminescence responsive chemical sensors (based on rare earth metal organic frameworks hybrid materials) on all kinds of typical analytes
- Discusses the use of luminescence responsive chemical sensors (based on rare earth metal organic frameworks hybrid materials) for logic gate or imaging applications

About the Author

Dr. Bing Yan received his BSc and MSc in Applied Chemistry from Harbin Institute of Technology in 1992 and 1995, respectively. He studied at Changchun Institute of Applied Chemistry, where he got his Ph.D. in Inorganic Chemistry in 1998. In 1998-2001, he went to City University of Hong Kong to be a Research Assistant and then became PostD fellow in Peking University and University of Sherbrooke. At the end of 2001, he joined Tongji University as a Professor at the School of Chemical Science and Engineering, Tongji University in Shanghai, China. Dr. Yan is a member of the technical committees on Rare Earth Luminescence and Rare Earth Molecular Materials and Supramolecular Devices for the Chinese Society of Rare Earth. His research specialties include rare earth chemistry, hybrid materials, micro-nano materials, photophysical devices, and chemical sensors. He has published more than 600 research papers in international peer reviewed journals indexed by the Web of Science. His publications have been cited more than 10000 times. He has been elected as the Most Cited Researchers in China (Material Science, 2014-2019) and (Chemistry, 2020) by Elsevier. He has written one English monograph, one English Chapter and one Chinese Chapter. His group has made systematic research achievements in photo functional rare earth materials, especially in photo functional rare earth hybrid materials, becoming the leading research group in this field.

ELSEVIER
WP
WOODHEAD PUBLISHING
An imprint of Elsevier
elsevier.com/books-and-journals

ISBN 978-0-323-91236-5
9 780323 912365